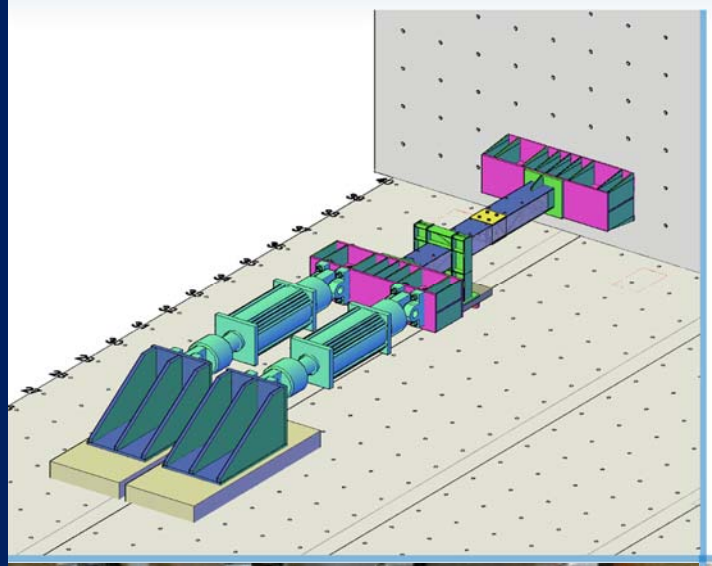
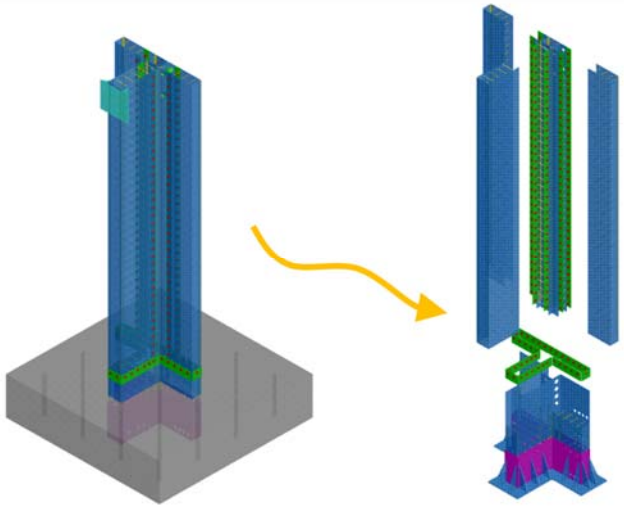
Bolted Splice Details for Composite Plate Shear Walls—Concrete Filled

(CPF Research Grant # 02-21)









Jia-Hau Liu
Michel Bruneau

University at Buffalo
The State University of New York

University at Buffalo
Department of Civil, Structural and Environmental Engineering

Bolted Splice Details for Composite Plate Shear Walls—Concrete Filled

Research Report

Submitted to

Charles Pankow Foundation

(CPF Research Grant # 02-21)

by
Jia-Hau Liu
Graduate Research Assistant
Michel Bruneau
SUNY Distinguished Professor

University at Buffalo
Department of Civil, Structural and Environmental Engineering
Buffalo, NY

August 2024





Acknowledgments

This research was conducted with support from the Charles Pankow Foundation (CPF), the American Institute of Steel Construction (AISC), the MKA Foundation, and Atlas Tube/Zekelman through CPF research grant #02-21 “Bolted Splice Details for Composite Plate Shear Walls – Concrete Filled” awarded to Michel Bruneau from the University at Buffalo.

The researchers are also grateful to members of Project Advisory Group:

- Glen Bell, Consulting Engineer, Director, CROSS-US;
- Devin Huber, Director of Research, AISC;
- Ron Klemencic, Chairman & CEO, Magnusson Klemencic Associates (MKA);
- Christopher Raebel, Vice President, American Institute of Steel Construction (AISC);
- Larry Kruth, Former Vice President, American Institute of Steel Construction (AISC);
- Jim Malley, Senior Principal, Degenkolb Engineers, and;
- Rafael Sabelli, Principal and Director of Seismic Design, Walter P. Moore & Associates

for their technical guidance.

The researchers also thank all at AISC, Magnusson Klemencic Associates (Russell Larson, Joshua Mouras, Jeremy Hasselbauer), Cives Steel Co. (Gregory Orff), and Banker Steel (Ron Meng), for their outstanding support, donation of steel, and fabrication of specimens in the experimental projects cross-references as part of this study, as well as current (Stuart Harrison) and former (Mark Perniconi and Anne Ellis) Executive Directors of the Charles Pankow Foundation, for this valuable support.

Abstract

Composite Plate Shear Walls—Concrete Filled (C-PSW/CF) consist of two steel faceplates with concrete infill sandwiched between them. This structural system has garnered national attention for implementation in non-seismic regions, where bolted connections are preferred over welded ones. This research investigates bolted splice details for C-PSW/CF to facilitate their use in such regions. Objectives include assessing the applicability of existing AISC strength equations, comparing splice details, evaluating stiffness equations, understanding ultimate behavior, and validating numerical models.

The first part of the research involved testing and analyzing C-PSW/CF components through an experimental program with six tension and six shear tests on various splice designs, including blind bolts, Shuriken details, and through rods with pipe-sleeves. All splice details met the design strength per AISC equations. Proposed simplified spring models successfully replicated the hysteresis curves and modeled the behavior of tension specimens, including friction sliding, bearing, net and gross section yielding, and concrete behaviors. Finite element models accurately captured the behavior of tension and shear specimens under monotonic and cyclic loading, showing significant reduction in friction forces as bolt hole elongation increased, indicating the impact of bolt hole deformation on friction development. This work provides valuable insights into the expected behavior of bolted C-PSW/CF components under various design limit states.

The second part involved testing and analyzing a large-scale T-shaped C-PSW/CF specimen with bolted splices. The horizontal splice was designed to develop approximately 60% of the faceplate yield strength in tension, while vertical splices used steel component and composite section approaches for slip-critical design. A proposed simplified method calculated the target flexural strength of the horizontal splice to develop bearing strength of $2.4dtF_u$ and $3.0dtF_u$. The tested wall achieved the target flexural strength and

maintained at least 80% of peak strength until 2.4% positive drift and -4.3% negative drift, with no slip observed in vertical splices. Finite element models of the wall specimen were developed to investigate its inelastic behavior. Monotonic pushover analyses assessed the ultimate behavior, while cyclic loading analyses compared inelastic behavior with test results. This research demonstrated the satisfactory inelastic behavior of a bolted C-PSW/CF under axial and cyclic lateral loads that can be obtained when designed such that the bolts in horizontal splices are governed by bearing strength and the bolts in vertical splices are governed by slip-critical resistance.

1 TABLE OF CONTENTS

ACKNOWLEDGMENTS I

ABSTRACT II

1 TABLE OF CONTENTS IV

2 LIST OF FIGURES XI

3 LIST OF TABLES XLVI

SECTION 1 INTRODUCTION 1

SECTION 2 LITERATURE REVIEW 5

2.1 GENERAL 5

2.2 DEVELOPMENT OF STEEL PLATE COMPOSITE WALLS 5

2.3 RECENT APPLICATIONS AND REQUIREMENTS FOR BOLTED SPLICE DETAILS 18

2.4 TARGET LIMIT STATES OF BOLTED SPLICE CONNECTIONS 24

2.4.1 Previous Research on Bearing-Type Bolted Connections 26

2.5 KNOWLEDGE GAP 49

SECTION 3 DESIGN OF COMPONENT SPECIMENS 50

3.1 GENERAL 50

3.2 DESIGN OF TENSION COMPONENT TESTS 52

3.2.1 List of Specimens 52

3.2.2 Design Limit States 55

3.2.3 Primarily Finite Element Analyses 59

3.2.4 Summary of Tension Test Specimens 61

3.2.5 Test Set-up 62
3.2.6 Material Properties of Tension Specimens 70
3.2.7 Instrumentations for Tension Tests 72
3.2.8 Loading Protocol 77
3.3 DESIGN OF SHEAR COMPONENT TESTS 78
3.3.1 List of Specimens 78
3.3.2 Design Limit States 79
3.3.3 Preliminary Finite Element Analyses 81
3.3.4 Summary of Shear Test Specimens 82
3.3.5 Test Set-up 83
3.3.6 Material Properties of Shear Specimens 89
3.3.7 Instrumentations for Shear Tests 91
3.3.8 Loading Protocol 94
SECTION 4 COMPONENT LEVEL TEST 95
4.1 GENERAL 95
4.2 TEST OBSERVATIONS AND RESULTS OF TENSION SPECIMENS 95
4.2.1 Specimen T1 95
4.2.2 Specimen T2 111
4.2.3 Specimen T3 128
4.2.4 Specimen T4 143
4.2.5 Specimen T5 159
4.2.6 Specimen T6 173
4.3 TEST OBSERVATIONS AND RESULTS OF SHEAR SPECIMENS 189
4.3.1 Specimen S1 189

4.3.2 Specimen S2 198
4.3.3 Specimen S3 209
4.3.4 Specimen S4 223
4.3.5 Specimen S5 232
4.3.6 Specimen S6 245
SECTION 5 NUMERICAL ANALYSES OF COMPONENT LEVEL TESTS 255
5.1 GENERAL 255
5.2 SIMPLIFIED SPRING ANALYSIS 255
5.2.1 Introduction 255
5.2.2 Bearing Spring 256
5.2.3 Elongation of Bolt Holes due to Bearing Stresses 258
5.2.4 Friction and Bearing Spring 261
5.2.5 Spring Models and Properties 264
5.2.6 Loading Protocol 274
5.2.7 Analysis Results of Specimens T1 and T2 (Displacement History from Test) 275
5.2.8 Analysis Results of Specimen T3 (Displacement History from Test) 284
5.2.9 Analysis Results of Specimens T5 and T6 (Displacement History from Test) 290
5.2.10 Analysis Results of Specimens T1 and T2 (Symmetric Displacement History) 298
5.2.11 Analysis Results of Specimen T3 (Symmetric Displacement History) 300
5.2.12 Analysis Results of Specimens T5 and T6 (Symmetric Displacement History) 301
5.2.13 Summary of Spring Analysis 303
5.3 FINITE ELEMENT MODELS FOR TENSION SPECIMENS 305
5.3.1 Finite Element Models 305
5.3.2 Elements 308

5.3.3 Material Constitutive Models 309
5.3.4 Contact and Constraint Properties 310
5.3.5 Pretension of Bolts and Through Rods 312
5.3.6 Boundary Conditions and Loading Areas 314
5.3.7 Results of Finite Element Analysis 317
5.4 FINITE ELEMENT MODELS OF SHEAR SPECIMENS 377
5.4.1 Shear Model Properties 377
5.4.2 Inclination of Actuator 384
5.4.3 Results of Finite Element Analysis 389
5.4.4 Results of Finite Element Analysis (Considering Inclination from the Actuator) 416
5.5 WALL CASE SCENARIO FOR SHEAR SPLICES 423
5.5.1 Shear Models and Properties 423
5.5.2 Design Limit States 426
5.5.3 Results of Finite Element Analysis of Models W1 to W4 428

SECTION 6 IMPACT OF BOLT PRETENSION ON BEARING STRENGTH OF BOLTED CONNECTIONS 448

6.1 GENERAL 448
6.2 FINITE ELEMENT MODELS OF STEEL BOLTED CONNECTIONS 448
6.3 FRICTION FORCES IN STEEL BOLTED CONNECTIONS 452
6.3.1 Single-Bolt Connection (Model 1) 452
6.3.2 Double-Bolt Connection (Model 2 to Model 4) 463
6.4 FRICTION FORCES IN C-PSW/CF BOLTED CONNECTIONS 477
6.4.1 C-PSW/CF Bolted Connections in Tension 477
6.4.2 C-PSW/CF Bolted Connections in Compression 483

SECTION 7 DESIGN OF WALL SPECIMENS 491

7.1 GENERAL 491

7.2 DESIGN OF HORIZONTAL SPLICES 496

7.2.1 Tributary Area Approach 496

7.2.2 Flexural Strength of Faceplates 500

7.2.3 Flexural Strength of Horizontal Splices 504

7.2.4 Summary of Moment Capacity for Test Specimen 509

7.3 DESIGN OF VERTICAL SPLICES 511

7.3.1 Shear Strength by Steel Component Approach 511

7.3.2 Shear Strength by Composite Section Approach 514

7.4 TEST SETUP 517

7.5 MATERIAL PROPERTIES 520

7.6 INSTRUMENTATIONS 522

7.7 LOADING PROTOCOL 528

7.8 PROPOSED REPAIR SCHEME FOR RESILIENCE OF BOLTED CPSW/CF 531

SECTION 8 WALL SPECIMEN TEST 533

8.1 GENERAL 533

8.2 TEST OBSERVATIONS AND RESULTS OF WALL SPECIMENS 533

8.3 POST-TEST OBSERVATIONS 569

8.4 TEST DATA ANALYSIS 577

8.4.1 Shear Force of the Wall 577

8.4.2 Flexural Strength of the Wall 579

8.4.3 Records from Strain Gauges and Vertical and Horizontal String Potentiometers 582

8.5 SUMMARY OF WALL SPECIMEN TEST 620

SECTION 9 NUMERICAL ANALYSES OF WALL SPECIMEN TESTS 622

9.1 GENERAL 622

9.2 FINITE ELEMENT MODELS 623

9.2.1 Finite Element Model of the Wall Specimen 623

9.2.2 Wall Properties 624

9.3 RESULTS OF FINITE ELEMENT ANALYSIS 629

9.3.1 Monotonic Pushover Analyses 629

9.3.2 Cyclic Loading Analysis 655

9.3.3 Comparison between Test Data and Finite Element Analysis 678

9.3.4 Double-Shear Connection for Horizontal Splices 702

9.4 SUMMARY OF FINITE ELEMENT ANALYSIS 712

SECTION 10 SUMMARY AND CONCLUSIONS 715

10.1 SUMMARY AND DETAILED FINDINGS 715

10.2 OVERARCHING CONCLUSIONS 728

10.3 FUTURE RESEARCH 730

SECTION 11 REFERENCES 731

APPENDIX A. POWERPOINT SLIDES PRESENTED AT FIRST PROJECT ADVISORY GROUP (OCTOBER 7, 2021) 735

APPENDIX B. POWERPOINT SLIDES PRESENTED AT SECOND PROJECT ADVISORY GROUP (DECEMBER 9, 2021) 748

APPENDIX C. POWERPOINT SLIDES PRESENTED AT THIRD PROJECT ADVISORY GROUP (DECEMBER 14, 2022) 759

APPENDIX D. POWERPOINT SLIDES PRESENTED AT FOURTH PROJECT ADVISORY GROUP (APRIL 26, 2023) 771

APPENDIX E. POWERPOINT SLIDES PRESENTED AT FIFTH PROJECT ADVISORY GROUP (FEBRUARY 13, 2024) 777

APPENDIX F. DRAWINGS OF SPECIMENS (COMPONENT LEVEL TEST) 785

APPENDIX G. ANALYSIS OF SPECIMENS (COMPONENT LEVEL TEST) 803

APPENDIX H. INSTRUMENTATION (COMPONENT LEVEL TEST) 829

APPENDIX I. DRAWINGS OF THE SPECIMEN (WALL SPECIMEN TEST) 840

APPENDIX J. ANALYSIS OF SPECIMENS (WALL SPECIMEN TEST) 849

APPENDIX K. INSTRUMENTATION (WALL SPECIMEN TEST) 860

APPENDIX L. BILL OF MATERIAL (COMPONENT LEVEL TEST) 864

2 LIST OF FIGURES

FIGURE 2-1. (A) STEEL-PLATE (SC) COMPOSITE WALL, (B) MEMBRANE FORCES, (C) PLANE VIEW AND DEFORMATIONS (VARMA ET AL., 2011 AND 2014)....6

FIGURE 2-2. FREE BODY DIAGRAM AND FORCE EQUILIBRIUM FOR STEEL-PLATE COMPOSITE (SC) SECTION (VARMA ET AL., 2011 AND 2014)....7

FIGURE 2-3. CFSSP SPECIMENS: (A) CFSSP-NB1; (B) CFSSP-NB2; (C) CFSSP-B1; (D) CFSSP-B2 (ALZENI AND BRUNEAU, 2017)....10

FIGURE 2-4. TEST SETUP FOR CFSSP SPECIMENS (ALZENI AND BRUNEAU, 2017)....11

FIGURE 2-5. TEST RESULTS OF CFSSP SPECIMENS: (A) CFSSP-NB1; (B) CFSSP-NB2; (C) CFSSP-B1; (D) CFSSP-B2 (ALZENI AND BRUNEAU, 2017)....11

FIGURE 2-6. DETAILS OF PLANAR C-PSW/CF SPECIMENS (SHAFAEI ET AL., 2021)....14

FIGURE 2-7. TEST RESULTS OF PLANAR C-PSW/CF SPECIMENS (SHAFAEI ET AL., 2021)....15

FIGURE 2-8. DETAILS OF C-SHAPED C-PSW/CF SPECIMENS (KENARANGI ET AL., 2021)....15

FIGURE 2-9. TEST RESULTS OF C-SHAPED C-PSW/CF SPECIMENS (KENARANGI ET AL., 2021)....15

FIGURE 2-10. DETAILS OF T-SHAPED C-PSW/CF SPECIMENS: (A) 3D TEST SPECIMEN (B) T-SHAPE SPECIMEN CROSS-SECTION DIMENSIONS (KIZILARSLAN AND BRUNEAU, 2023)....17

FIGURE 2-11. TEST RESULTS OF T-SHAPED C-PSW/CF SPECIMENS: (A) SPECIMEN T1; (B) SPECIMEN T2; (C) SPECIMEN T3; (D) SPECIMEN T4 (KIZILARSLAN AND BRUNEAU, 2023)....17

FIGURE 2-12. 3D RENDERING VIEW OF RAINIER SQUARE (AISC DESIGN GUIDE 38, VARMA ET AL., 2023)....19

FIGURE 2-13. PHOTOGRAPHS OF COUPLED C-PSW/CF SYSTEM UNDER CONSTRUCTION IN RAINIER SQUARE (AISC DESIGN GUIDE 38, VARMA ET AL., 2023)....20

FIGURE 2-14. 3D RENDERING VIEW OF 200 PARK AVENUE (AISC DESIGN GUIDE 38, VARMA ET AL., 2023)....20

FIGURE 2-15. CLOSE-UP VIEW OF COUPLED C-PSW/CF SYSTEM UNDER CONSTRUCTION IN 200 PARK AVENUE (AISC DESIGN GUIDE 38, VARMA ET AL., 2023)....21

FIGURE 2-16. ELEVATION SHOWING VERTICAL AND HORIZONTAL SPLICES IN BOSTON PROJECT (PERSONAL COMMUNICATION, MKA, JUNE 2021.) 23
FIGURE 2-17. FREE-BODY DIAGRAM OF A WALL SEGMENT WITH VERTICAL AND HORIZONTAL SPLICES 23
FIGURE 2-18. BEARING CRITICAL TEST SPECIMENS (FRANK AND YURA, 1981) 28
FIGURE 2-19. TEST RESULTS OF THE UN-TORQUED SPECIMENS (FRANK AND YURA, 1981) 28
FIGURE 2-20. TEST RESULTS OF THE TORQUED AND UN-TORQUED SPECIMENS (FRANK AND YURA, 1981) 29
FIGURE 2-21. BENDING OF SPLICE PLATES (FRANK AND YURA, 1981) 30
FIGURE 2-22. INFLUENCE OF TYPE OF SPECIMEN ON THE BEARING (KULAK ET AL., 1987) 31
FIGURE 2-23. TEST SETUP OF BOLTED CONNECTION SPECIMENS (LEWIS AND ZWERNEMAN, 1996) 34
FIGURE 2-24. COMPARISON OF 5/8 IN. SINGLE-BOLT TEST DATA TO VARIOUS DESIGN EQUATIONS (LEWIS AND ZWERNEMAN, 1996) 34
FIGURE 2-25. TEST SETUP OF BOLTED CONNECTION SPECIMENS (KIM AND YURA, 1996) 35
FIGURE 2-26. LOAD-DISPLACEMENT CURVE OF BEARING TEST SPECIMEN BO200 (KIM AND YURA, 1996) 35
FIGURE 2-27. COMPARISON BETWEEN TEST AND PREDICTION AT 0.25-IN. DEFORMATION (KIM AND YURA, 1996) 36
FIGURE 2-28. COMPARISON BETWEEN TEST AND PREDICTION AT ULTIMATE DEFORMATION (KIM AND YURA, 1996) 36
FIGURE 2-29. TEST SETUP OF BOLTED TENSION TESTS (BROWN ET AL., 2007) 38
FIGURE 2-30. TEST RESULTS FOR SINGLE-BOLTS CONNECTIONS (MOŽE, 2018) 41
FIGURE 2-31. TEST RESULTS FOR TWO-BOLTS CONNECTIONS (MOŽE, 2018) 42
FIGURE 2-32. FRICTION FORCE IN RELATION TO THE (A) FRICTION COEFFICIENT AND (B) TO THE END DISTANCE (MOŽE, 2018) 43
FIGURE 2-33. BOLT TENSION IN RELATION TO THE FRICTION FORCE (MOŽE, 2018) 44
FIGURE 2-34. TEST PROGRAMS FOR SINGLE-BOLTED CONNECTIONS (KIM AND LEE, 2020) 47
FIGURE 2-35. RESULTS OF BEARING-FAILURE IN SINGLE-BOLTED CONNECTIONS: (A) SPECIMEN C400-09-24 (B) SPECIMEN C400-15-24 (KIM AND LEE, 2020) 47

FIGURE 2-36. RESULTS OF TEAR-OUT FAILURE IN SINGLE-BOLTED CONNECTIONS (A) SPECIMEN T400-06-24-50 (B) SPECIMEN T400-15-24-50 (KIM AND LEE, 2020)....48
FIGURE 2-37. COMPARISON OF AISC 360 AND PROPOSED DESIGN APPROACH FOR SINGLE-BOLTED CONNECTIONS (KIM AND LEE, 2020)....48
FIGURE 3-1. BLIND BOLTS (CONCEPTUALLY SHOW HERE BY MKA) 53
FIGURE 3-2. THROUGH BOLTS (CONCEPTUALLY SHOW HERE BY MKA)....53
FIGURE 3-3. I-SHAPED ANCHORS 53
FIGURE 3-4. DESIGNED WALL SEGMENT....56
FIGURE 3-5. FINITE ELEMENT ANALYSIS OF CASE 1A....59
FIGURE 3-6. FINITE ELEMENT ANALYSIS OF CASE 4A....60
FIGURE 3-7. 3D VIEW OF TENSION TEST SETUP 63
FIGURE 3-8. TENSION TEST SETUP FOR SPECIMEN T1 64
FIGURE 3-9. TENSION TEST SETUP FOR SPECIMENS T2 AND T3....65
FIGURE 3-10. TENSION TEST SETUP FOR SPECIMEN T4 66
FIGURE 3-11. TENSION TEST SETUP FOR SPECIMEN T5 67
FIGURE 3-12. TENSION TEST SETUP FOR SPECIMEN T6 68
FIGURE 3-13. TENSION TEST SPECIMENS (DURING CASTING CONCRETE)....69
FIGURE 3-14. MATERIAL TEST OF TENSION SPECIMEN....71
FIGURE 3-15. AXIAL DEFORMATION MEASUREMENT OF TENSION SPECIMEN....74
FIGURE 3-16. STRING POTS FOR TENSION SPECIMENS....74
FIGURE 3-17. LINEAR POTS OF SPECIMEN T1 (ELEVATION) 74
FIGURE 3-18. LINEAR POTS OF SPECIMEN T1 (3D VIEW) 75
FIGURE 3-19. PHOTOS OF LINEAR POTS FOR SPECIMEN T1....75
FIGURE 3-20. STRAIN GAUGES OF SPECIMEN T1 (ELEVATION) 76
FIGURE 3-21. STRAIN GAUGES OF SPECIMEN T1 (3D VIEW) 76

FIGURE 3-22. FINITE ELEMENT ANALYSIS OF COMPOSITE SHEAR STRENGTH 81
FIGURE 3-23. FINITE ELEMENT ANALYSIS OF NON-COMPOSITE SHEAR STRENGTH 82
FIGURE 3-24. PANTOGRAPH (3D VIEW WITHOUT SPECIMEN IN PLACE) 84
FIGURE 3-25. 3D VIEW OF SHEAR TEST SETUP 85
FIGURE 3-26. REUSABLE PARTS FOR SHEAR SPECIMENS 85
FIGURE 3-27. SHEAR SPECIMENS S1 AND S2 86
FIGURE 3-28. SHEAR SPECIMENS S3 AND S4 (ELEVATION) 87
FIGURE 3-29. SHEAR SPECIMENS S5 AND S6 87
FIGURE 3-30. SHEAR TEST SPECIMENS (BEFORE CASTING CONCRETE) 88
FIGURE 3-31. MATERIAL TEST OF SHEAR SPECIMEN 90
FIGURE 3-32. STRAIN GAUGES ON SPECIMENS S1 TO S4 92
FIGURE 3-33. STRAIN GAUGES ON SPECIMENS S5 AND S6 92
FIGURE 3-34. STRING POTS OF ALL SHEAR SPECIMENS 93
FIGURE 3-35. LINEAR POTS OF ALL SHEAR SPECIMENS 93
FIGURE 4-1. GLOBAL VIEW OF SPECIMEN T1 95
FIGURE 4-2. TIMBER SUPPORT FOR SPECIMEN T1 96
FIGURE 4-3. ACTUATOR DISPLACEMENT AND LOAD HISTORY FOR SPECIMEN T1 97
FIGURE 4-4. DEMONSTRATION OF NORTH VIEW 98
FIGURE 4-5. NORTH VIEW OF SPECIMEN T1 (STEPS 1 TO 4) 99
FIGURE 4-6. NORTH VIEW OF SPECIMEN T1 (STEPS 5 TO 8) 100
FIGURE 4-7. INSTALLING DYWIDAG RODS ON BUTTRESSES 102
FIGURE 4-8. ACTUATOR DISPLACEMENT AND LOAD HISTORY 104
FIGURE 4-9. BENDING IN COMPRESSION OF SPECIMEN T1 (STEP 7) 106
FIGURE 4-10. TIMER SUPPORT BEING CRUSHED IN STEP 7 106
FIGURE 4-11. SPECIMEN T1 (STEP 9, PEAK ACTUATOR DISPLACEMENT=0.86") 107

FIGURE 4-12. RELATIVE MOVEMENT BETWEEN FACEPLATES AND SPLICE PLATES (STEP 9) 107
FIGURE 4-13. FACEPLATES AFTER REMOVING SPLICE PLATES 108
FIGURE 4-14. BLIND BOLTS INSIDE THE CONNECTION 108
FIGURE 4-15. TEST RESULTS OF SPECIMEN T1 109
FIGURE 4-16. TEST RESULTS OF SPECIMEN T1 WITH DESIGN LIMIT STATE 110
FIGURE 4-17. BEARING BEHAVIOR IN STEP 8 110
FIGURE 4-18. ACTUATOR DISPLACEMENT AND LOAD HISTORY FOR SPECIMEN T2 112
FIGURE 4-19. NORTH VIEW OF SPECIMEN T2 (STEPS 1 TO 4) 113
FIGURE 4-20. NORTH VIEW OF SPECIMEN T2 (STEPS 5 TO 8) 114
FIGURE 4-21. NORTH VIEW OF SPECIMEN T2 (STEPS 9 TO 12) 115
FIGURE 4-22. SOUTH VIEW OF SPECIMEN T2 116
FIGURE 4-23. STEEL SUPPORTS UNDER THE SPREADER BEAM 116
FIGURE 4-24. SPECIMEN T2 (STEP 5, PEAK ACTUATOR DISPLACEMENT=0.77") 118
FIGURE 4-25. SIDE VIEWS OF SPECIMEN T2 (STEP 6, PEAK ACTUATOR DISPLACEMENT=0.90") 119
FIGURE 4-26. TOP VIEW OF SPECIMEN T2 SHOWING 0.5" GAP DUE TO SLIDING BETWEEN SPLICE PLATE AND FACEPLATE (STEP 6, PEAK ACTUATOR DISPLACEMENT=0.90") 119
FIGURE 4-27. SIDE VIEWS OF SPECIMEN T2 (STEP 7, PEAK ACTUATOR DISPLACEMENT=1.10") 120
FIGURE 4-28. SIDE VIEWS OF SPECIMEN T2 (STEP 8, PEAK ACTUATOR DISPLACEMENT=1.30") 121
FIGURE 4-29. SIDE VIEWS OF SPECIMEN T2 (STEP 9, PEAK ACTUATOR DISPLACEMENT=1.60") 121
FIGURE 4-30. TOP VIEW OF SPECIMEN T2 (STEP 9, PEAK ACTUATOR DISPLACEMENT=1.60") 122
FIGURE 4-31. SIDE VIEWS OF SPECIMEN T2 (STEP 10, PEAK ACTUATOR DISPLACEMENT=2.50") 122
FIGURE 4-32. SIDE VIEWS OF SPECIMEN T2 (STEP 11, PEAK ACTUATOR DISPLACEMENT=3.20") 123
FIGURE 4-33. BEARING DEFORMATION INSIDE THE SPLICE PLATE (STEP 11, PEAK ACTUATOR DISPLACEMENT=3.20") 123
FIGURE 4-34. SIDE VIEWS OF SPECIMEN T2 (STEP 12, PEAK ACTUATOR DISPLACEMENT=5.0") 124
FIGURE 4-35. TEST RESULTS OF SPECIMEN T2 125

FIGURE 4-36. CLOSE-UP VIEW SHOWING FIRST OBSERVATION OF SLIDING IN SPECIMEN T2 125
FIGURE 4-37. TEST RESULTS OF SPECIMEN T2 WITH DESIGN LIMIT STATES 126
FIGURE 4-38. COMPARISON BETWEEN SPECIMENS T1 AND T2 (SP) 126
FIGURE 4-39. COMPARISON BETWEEN SPECIMENS T1 AND T2 (LP) 127
FIGURE 4-40. ACTUATOR DISPLACEMENT AND LOAD HISTORY FOR SPECIMEN T3 129
FIGURE 4-41. NORTH VIEW OF SPECIMEN T3 (STEPS 1 TO 5) 130
FIGURE 4-42. NORTH VIEW OF SPECIMEN T3 (STEPS 6 TO 10) 131
FIGURE 4-43. NORTH VIEW OF SPECIMEN T3 (STEPS 11 TO 12) 132
FIGURE 4-44. SPECIMEN T3 (STEP 1, PEAK ACTUATOR DISPLACEMENT=0.09") 132
FIGURE 4-45. FIRST SLIDING OF SPECIMEN T3 133
FIGURE 4-46. SPECIMEN T3 (STEP 4, PEAK ACTUATOR DISPLACEMENT=0.74") 133
FIGURE 4-47. SPECIMEN T3 (STEP 5, PEAK ACTUATOR DISPLACEMENT=0.96") 134
FIGURE 4-48. FOOTING SLIPPAGE AT STEP 6 135
FIGURE 4-49. SPECIMEN T3 (STEP 6, AFTER THE SLIPPAGE OF THE FOOTING) 135
FIGURE 4-50. INSTALLATION OF DYWIDAG RODS ON CONCRETE FOOTINGS 135
FIGURE 4-51. SPECIMEN T3 (STEP 8, PEAK ACTUATOR DISPLACEMENT=1.16") 136
FIGURE 4-52. SPECIMEN T3 (STEP 9, PEAK ACTUATOR DISPLACEMENT=1.40") 136
FIGURE 4-53. SPECIMEN T3 (STEP 10, PEAK ACTUATOR DISPLACEMENT=1.75") 137
FIGURE 4-54. TOP VIEW OF SPECIMEN T3 (STEP 10, PEAK ACTUATOR DISPLACEMENT=1.75") 137
FIGURE 4-55. SPECIMEN T3 (STEP 11, PEAK ACTUATOR DISPLACEMENT=2.20") 138
FIGURE 4-56. NET SECTION FRACTURE AT TOP FACEPLATES (PEAK ACTUATOR DISPLACEMENT=2.50") 139
FIGURE 4-57. SPECIMEN T3 (STEP 12, PEAK ACTUATOR DISPLACEMENT=3.00") 139
FIGURE 4-58. NET SECTION FRACTURE ON TOP AND BOTTOM FACEPLATES 140
FIGURE 4-59. TEST RESULTS OF SPECIMEN T3 141
FIGURE 4-60. TEST RESULTS OF SPECIMEN T3 WITH DESIGN LIMIT STATES 141

FIGURE 4-61. COMPARISON BETWEEN SPECIMENS T2 AND T3 (SP) 142
FIGURE 4-62. COMPARISON BETWEEN SPECIMENS T2 AND T3 (LP) 142
FIGURE 4-63. ACTUATOR DISPLACEMENT AND LOAD HISTORY FOR SPECIMEN T4 144
FIGURE 4-64. NORTH VIEW OF SPECIMEN T4 (STEPS 1 TO 4) 145
FIGURE 4-65. NORTH VIEW OF SPECIMEN T4 (STEPS 5 TO 8) 146
FIGURE 4-66. NORTH VIEW OF SPECIMEN T4 (STEPS 9 TO 11) 147
FIGURE 4-67. STRAIN GAUGES FOR SPECIMEN T4 (ELEVATION) 148
FIGURE 4-68. STRAIN GAUGES FOR SPECIMEN T4 (3D VIEW) 149
FIGURE 4-69. SPECIMEN T4 (STEP 1, PEAK ACTUATOR DISPLACEMENT=0.075") 150
FIGURE 4-70. SPECIMEN T4 (STEP 2, PEAK ACTUATOR DISPLACEMENT=0.185") 151
FIGURE 4-71. SPECIMEN T4 (STEP 3, PEAK ACTUATOR DISPLACEMENT=0.3") 151
FIGURE 4-72. SPECIMEN T4 (STEP 4, PEAK ACTUATOR DISPLACEMENT=0.46") 152
FIGURE 4-73. SPECIMEN T4 (STEP 5, PEAK ACTUATOR DISPLACEMENT=0.6") 152
FIGURE 4-74. SPECIMEN T4 (STEP 6, PEAK ACTUATOR DISPLACEMENT=0.74") 153
FIGURE 4-75. SPECIMEN T4 (STEP 7, PEAK ACTUATOR DISPLACEMENT=0.82") 153
FIGURE 4-76. SPECIMEN T4 (STEP 8, PEAK ACTUATOR DISPLACEMENT=0.99") 154
FIGURE 4-77. SPECIMEN T4 (STEP 9, PEAK ACTUATOR DISPLACEMENT=1.25") 154
FIGURE 4-78. SPECIMEN T4 (STEP 10, PEAK ACTUATOR DISPLACEMENT=1.5") 155
FIGURE 4-79. TOP VIEW OF SPECIMEN T4 (STEP 10) 155
FIGURE 4-80. SPECIMEN T4 (STEP 11, PEAK ACTUATOR DISPLACEMENT=2.8") 155
FIGURE 4-81. TEST RESULTS OF SPECIMEN T4 156
FIGURE 4-82. TEST RESULTS OF SPECIMEN T4 WITH DESIGN LIMIT STATES 157
FIGURE 4-83. TOP VIEW OF SPECIMEN T4 SHOWING ROD HOLES MOVEMENT 157
FIGURE 4-84. SPECIMEN T4 (CLOSE VIEW SHOWING THE BENDING OF RODS) 157
FIGURE 4-85. BRITTLE FAILURE SURFACES OF THE RODS 158

FIGURE 4-86. ACTUATOR DISPLACEMENT AND LOAD HISTORY FOR SPECIMEN T5 160
FIGURE 4-87. NORTH VIEW OF SPECIMEN T5 (STEPS 1 TO 4) 161
FIGURE 4-88. NORTH VIEW OF SPECIMEN T5 (STEPS 5 TO 8) 162
FIGURE 4-89. NORTH VIEW OF SPECIMEN T5 (STEPS 9 TO 10) 163
FIGURE 4-90. SPECIMEN T5 (STEP 1, PEAK ACTUATOR DISPLACEMENT=0.155") 163
FIGURE 4-91. SPECIMEN T5 (STEP 2, PEAK ACTUATOR DISPLACEMENT=0.455") 164
FIGURE 4-92. SPECIMEN T5 (STEP 3, PEAK ACTUATOR DISPLACEMENT=0.66") 164
FIGURE 4-93. SPECIMEN T5 (STEP 4, PEAK ACTUATOR DISPLACEMENT=1.00") 165
FIGURE 4-94. SPECIMEN T5 (STEP 4, PEAK ACTUATOR DISPLACEMENT=-0.55") 166
FIGURE 4-95. SPECIMEN T5 (AFTER 5 CYCLES OF STEP 4) 166
FIGURE 4-96. SPECIMEN T5 (STEP 5, PEAK ACTUATOR DISPLACEMENT=1.5") 167
FIGURE 4-97. SPECIMEN T5 (STEP 6, PEAK ACTUATOR DISPLACEMENT=2.0") 167
FIGURE 4-98. SPECIMEN T5 (STEP 7, PEAK ACTUATOR DISPLACEMENT=2.50") 167
FIGURE 4-99. SPECIMEN T5 (STEP 7, PEAK ACTUATOR DISPLACEMENT=-0.1") 168
FIGURE 4-100. SPECIMEN T5 (STEP 8, PEAK ACTUATOR DISPLACEMENT=3.0") 168
FIGURE 4-101. SPECIMEN T5 (STEP 8, PEAK ACTUATOR DISPLACEMENT=-0.1") 169
FIGURE 4-102. SPECIMEN T5 (STEP 9, PEAK ACTUATOR DISPLACEMENT=3.25") 169
FIGURE 4-103. GROSS SECTION FRACTURE IN STEPS 9 AND 10 OF SPECIMEN T5 170
FIGURE 4-104. TEST RESULTS OF SPECIMEN T5 171
FIGURE 4-105. TEST RESULTS OF SPECIMEN T5 WITH DESIGN LIMIT STATES 171
FIGURE 4-106. LINEAR POTS SHIFTED DUE TO THE BUCKLING OF THE SPLICE PLATES 172
FIGURE 4-107. SHURIKEN CONNECTORS AFTER TEST 172
FIGURE 4-108. ACTUATOR DISPLACEMENT AND LOAD HISTORY FOR SPECIMEN T6 174
FIGURE 4-109. NORTH VIEW OF SPECIMEN T6 (STEPS 1 TO 4) 175
FIGURE 4-110. NORTH VIEW OF SPECIMEN T6 (STEPS 5 TO 8) 176

FIGURE 4-111. NORTH VIEW OF SPECIMEN T6 (STEPS 9 TO 10) 177
FIGURE 4-112. SPECIMEN T6 (STEP 2, PEAK ACTUATOR DISPLACEMENT=0.325") 177
FIGURE 4-113. FIRST SLIDING OF SPECIMEN T6 (STEP 3) 178
FIGURE 4-114. SPECIMEN T6 (STEP 3, PEAK ACTUATOR DISPLACEMENT=0.74") 178
FIGURE 4-115. SPECIMEN T6 (STEP 4, PEAK ACTUATOR DISPLACEMENT=1.00") 179
FIGURE 4-116. SPECIMEN T6 (STEP 5, PEAK ACTUATOR DISPLACEMENT=1.50") 180
FIGURE 4-117. SPECIMEN T6 (STEP 5, CLOSE VIEW OF LOCAL BUCKLING) 180
FIGURE 4-118. SPECIMEN T6 (STEP 6, PEAK ACTUATOR DISPLACEMENT=2.00") 181
FIGURE 4-119. SPECIMEN T6 (STEP 6, CLOSE VIEW OF LOCAL BUCKLING) 181
FIGURE 4-120. SPECIMEN T6 (STEP 7, PEAK ACTUATOR DISPLACEMENT=2.50") 181
FIGURE 4-121. SPECIMEN T6 (STEP 7, CLOSE VIEW OF LOCAL BUCKLING) 182
FIGURE 4-122. SPECIMEN T6 (STEP 8, PEAK ACTUATOR DISPLACEMENT=3.00") 182
FIGURE 4-123. SPECIMEN T6 (STEP 8, ACTUATOR DISPLACEMENT=0.80") 183
FIGURE 4-124. SPECIMEN T6 (STEP 9, PEAK ACTUATOR DISPLACEMENT=3.30") 184
FIGURE 4-125. SPECIMEN T6 (STEP 9, FRACTURE ON WEST BOTTOM FACEPLATE) 184
FIGURE 4-126. SPECIMEN T6 (STEP 10, PEAK ACTUATOR DISPLACEMENT=4.00") 185
FIGURE 4-127. SPECIMEN T6 (FRACTURED RODS AFTER TEST) 185
FIGURE 4-128. SPECIMEN T6 (TOP FACEPLATES IN SPLICE REGION AFTER TEST) 185
FIGURE 4-129. SPECIMEN T6 (BOTTOM FACEPLATES IN SPLICE REGION AFTER TEST) 186
FIGURE 4-130. TEST RESULTS OF SPECIMEN T6 187
FIGURE 4-131. TEST RESULTS OF SPECIMEN T6 WITH DESIGN LIMIT STATES 187
FIGURE 4-132. COMPARISON BETWEEN SPECIMENS T5 AND T6 188
FIGURE 4-133. ACTUATOR DISPLACEMENT AND LOAD HISTORY FOR SPECIMEN S1 190
FIGURE 4-134. DEMONSTRATION OF NORTH VIEW 190
FIGURE 4-135. SPECIMEN S1 (STEP 1, PEAK ACTUATOR DISPLACEMENT=0.47") 191

FIGURE 4-136. FIRST SLIDING OF SPECIMEN S1 (STEP 1) 191
FIGURE 4-137. SPECIMEN S1 (STEP 2, PEAK ACTUATOR DISPLACEMENT=0.96") 192
FIGURE 4-138. SPECIMEN S1 (STEP 3, PEAK ACTUATOR DISPLACEMENT=1.26") 192
FIGURE 4-139. SPECIMEN S1 (STEP 4, PEAK ACTUATOR DISPLACEMENT=1.68") 193
FIGURE 4-140. SPECIMEN S1 (STEP 4, PEAK ACTUATOR DISPLACEMENT=-1.95") 193
FIGURE 4-141. SPECIMEN S1 (STEP 5, PEAK ACTUATOR DISPLACEMENT=2.20") 194
FIGURE 4-142. SPECIMEN S1 (STEP 5, PEAK ACTUATOR DISPLACEMENT=-2.50") 194
FIGURE 4-143. SPECIMEN S1 (STEP 6, PEAK ACTUATOR DISPLACEMENT=2.90") 195
FIGURE 4-144. SPECIMEN S1 (STEP 6, PEAK ACTUATOR DISPLACEMENT=-3.20") 195
FIGURE 4-145. SPECIMEN S1 (STEP 7, PEAK ACTUATOR DISPLACEMENT=-5.00") 196
FIGURE 4-146. SPECIMEN S1 (AFTER TEST) 196
FIGURE 4-147. TEST RESULTS OF SPECIMEN S1 WITH DESIGN LIMIT STATES 197
FIGURE 4-148. ACTUATOR DISPLACEMENT AND LOAD HISTORY FOR SPECIMEN S2 199
FIGURE 4-149. SPECIMEN S2 (STEP 2, PEAK ACTUATOR DISPLACEMENT=0.27") 199
FIGURE 4-150. SPECIMEN S2 (STEP 3, PEAK ACTUATOR DISPLACEMENT=0.45") 200
FIGURE 4-151. SPECIMEN S2 (STEP 4, PEAK ACTUATOR DISPLACEMENT=0.75") 200
FIGURE 4-152. SPECIMEN S2 (STEP 5, PEAK ACTUATOR DISPLACEMENT=1.05") 201
FIGURE 4-153. SPECIMEN S2 (STEP 6, PEAK ACTUATOR DISPLACEMENT=1.50") 201
FIGURE 4-154. SPECIMEN S2 (STEP 6, PEAK ACTUATOR DISPLACEMENT=-1.70") 202
FIGURE 4-155. SPECIMEN S2 (STEP 7, PEAK ACTUATOR DISPLACEMENT=2.00") 202
FIGURE 4-156. SPECIMEN S2 (STEP 7, PEAK ACTUATOR DISPLACEMENT=-2.30") 203
FIGURE 4-157. SPECIMEN S2 (STEP 7, PEAK ACTUATOR DISPLACEMENT=-2.30") 203
FIGURE 4-158. SPECIMEN S2 (STEP 8, PEAK ACTUATOR DISPLACEMENT=2.50") 204
FIGURE 4-159. SPECIMEN S2 (STEP 8, PEAK ACTUATOR DISPLACEMENT=-2.80") 204
FIGURE 4-160. SPECIMEN S2 (STEP 8, PEAK ACTUATOR DISPLACEMENT=-2.80") 205

FIGURE 4-161. SPECIMEN S2 (STEP 9, PEAK ACTUATOR DISPLACEMENT=3.00") 205
FIGURE 4-162. SPECIMEN S2 (STEP 9, PEAK ACTUATOR DISPLACEMENT=-3.30") 206
FIGURE 4-163. SPECIMEN S2 (STEP 9, PEAK ACTUATOR DISPLACEMENT=-3.30") 206
FIGURE 4-164. SPECIMEN S2 (AFTER TEST) 207
FIGURE 4-165. TEST RESULTS OF SPECIMEN S2 WITH DESIGN LIMIT STATES 208
FIGURE 4-166. TEST RESULTS OF SPECIMENS S1 AND S2 208
FIGURE 4-167. ACTUATOR DISPLACEMENT AND LOAD HISTORY FOR SPECIMEN S3 210
FIGURE 4-168. SPECIMEN S3 (STEP 1, PEAK ACTUATOR DISPLACEMENT=0.11") 210
FIGURE 4-169. SPECIMEN S3 (STEP 2, PEAK ACTUATOR DISPLACEMENT=0.21") 211
FIGURE 4-170. SPECIMEN S3 (STEP 3, PEAK ACTUATOR DISPLACEMENT=0.30") 211
FIGURE 4-171. SPECIMEN S3 (STEP 4, PEAK ACTUATOR DISPLACEMENT=0.42") 212
FIGURE 4-172. SPECIMEN S3 (STEP 4, PEAK ACTUATOR DISPLACEMENT=-0.53") 212
FIGURE 4-173. FIRST SLIDING OF SPECIMEN S3 (STEP 4) (-144 K) 213
FIGURE 4-174. SPECIMEN S3 (STEP 5, PEAK ACTUATOR DISPLACEMENT=0.66") 213
FIGURE 4-175. SPECIMEN S3 (STEP 6, PEAK ACTUATOR DISPLACEMENT=0.90") 214
FIGURE 4-176. SPECIMEN S3 (STEP 7, PEAK ACTUATOR DISPLACEMENT=1.14") 214
FIGURE 4-177. SPECIMEN S3 (STEP 8, PEAK ACTUATOR DISPLACEMENT=1.48") 214
FIGURE 4-178. SPECIMEN S3 (STEP 8, PEAK ACTUATOR DISPLACEMENT=1.48") 215
FIGURE 4-179. SPECIMEN S3 (STEP 8, PEAK ACTUATOR DISPLACEMENT=-1.59") 215
FIGURE 4-180. SPECIMEN S3 (STEP 9, PEAK ACTUATOR DISPLACEMENT=1.92") 216
FIGURE 4-181. SPECIMEN S3 (STEP 9, PEAK ACTUATOR DISPLACEMENT=-2.03") 216
FIGURE 4-182. SPECIMEN S3 (STEP 9, PEAK ACTUATOR DISPLACEMENT=-2.03") 216
FIGURE 4-183. SPECIMEN S3 (STEP 10, PEAK ACTUATOR DISPLACEMENT=2.46") 217
FIGURE 4-184. SPECIMEN S3 (STEP 10, PEAK ACTUATOR DISPLACEMENT=2.46") 217
FIGURE 4-185. SPECIMEN S3 (STEP 10, PEAK ACTUATOR DISPLACEMENT=-2.57") 217

FIGURE 4-186. SPECIMEN S3 (STEP 11, PEAK ACTUATOR DISPLACEMENT=3.1") 218
FIGURE 4-187. SPECIMEN S3 (STEP 11, PEAK ACTUATOR DISPLACEMENT=3.1") 218
FIGURE 4-188. FRACTURE OF NORTH BOTTOM FACEPLATE (STEP 11)....219
FIGURE 4-189. SPECIMEN S3 (STEP 12, PEAK ACTUATOR DISPLACEMENT=4.0") 220
FIGURE 4-190. FRACTURE OF BOTTOM FACEPLATES (STEP 12)....220
FIGURE 4-191. SPECIMEN S3 (AFTER TEST") 221
FIGURE 4-192. TEST RESULTS OF SPECIMEN S3 WITH DESIGN LIMIT STATES....222
FIGURE 4-193. ACTUATOR DISPLACEMENT AND LOAD HISTORY FOR SPECIMEN S4 224
FIGURE 4-194. SPECIMEN S4 (STEP 4, PEAK ACTUATOR DISPLACEMENT=0.46") 224
FIGURE 4-195. SPECIMEN S4 (STEP 5, PEAK ACTUATOR DISPLACEMENT=0.69") 225
FIGURE 4-196. SPECIMEN S4 (STEP 6, PEAK ACTUATOR DISPLACEMENT=0.92") 225
FIGURE 4-197. SPECIMEN S4 (STEP 7, PEAK ACTUATOR DISPLACEMENT=1.15") 226
FIGURE 4-198. SPECIMEN S4 (STEP 8, PEAK ACTUATOR DISPLACEMENT=1.48") 226
FIGURE 4-199. SPECIMEN S4 (STEP 9, PEAK ACTUATOR DISPLACEMENT=1.91") 227
FIGURE 4-200. SPECIMEN S4 (STEP 9, PEAK ACTUATOR DISPLACEMENT=1.91") 227
FIGURE 4-201. SPECIMEN S4 (STEP 9, PEAK ACTUATOR DISPLACEMENT=-2.02") 227
FIGURE 4-202. SPECIMEN S4 (STEP 10, PEAK ACTUATOR DISPLACEMENT=2.44") 228
FIGURE 4-203. SPECIMEN S4 (STEP 10, PEAK ACTUATOR DISPLACEMENT=2.44") 228
FIGURE 4-204. SPECIMEN S4 (STEP 10, PEAK ACTUATOR DISPLACEMENT=-2.58") 229
FIGURE 4-205. SPECIMEN S4 (STEP 10, 3RD CYCLE)....229
FIGURE 4-206. SPECIMEN S4 (AFTER TEST) 229
FIGURE 4-207. TEST RESULTS OF SPECIMEN S4 WITH DESIGN LIMIT STATES....230
FIGURE 4-208. TEST RESULTS OF SPECIMENS S3 AND S4....231
FIGURE 4-209. ACTUATOR DISPLACEMENT AND LOAD HISTORY FOR SPECIMEN S5 233
FIGURE 4-210. SPECIMEN S5 (STEP 1, PEAK ACTUATOR DISPLACEMENT=0.53") 234

FIGURE 4-211. FIRST SLIDING OF SPECIMEN S5 (STEP 1) (47.7K) 234
FIGURE 4-212. GLOBAL BEHAVIOR OF SPECIMEN S5 (STEP 2) 235
FIGURE 4-213. SPECIMEN S5 (STEP 2, 9TH CYCLE) 235
FIGURE 4-214. SPECIMEN S5 (STEP 3, PEAK ACTUATOR DISPLACEMENT=1.70") 236
FIGURE 4-215. SPECIMEN S5 (STEP 3, PEAK ACTUATOR DISPLACEMENT=1.70") 236
FIGURE 4-216. SPECIMEN S5 (STEP 4, PEAK ACTUATOR DISPLACEMENT=2.14") 236
FIGURE 4-217. SPECIMEN S5 (STEP 4, PEAK ACTUATOR DISPLACEMENT=2.14") 237
FIGURE 4-218. SPECIMEN S5 (STEP 4, PEAK ACTUATOR DISPLACEMENT=-1.53") 237
FIGURE 4-219. SPECIMEN S5 (STEP 5, PEAK ACTUATOR DISPLACEMENT=2.58") 238
FIGURE 4-220. SPECIMEN S5 (STEP 5, PEAK ACTUATOR DISPLACEMENT=2.58") 238
FIGURE 4-221. SPECIMEN S5 (STEP 5, PEAK ACTUATOR DISPLACEMENT=-2.18") 239
FIGURE 4-222. SPECIMEN S5 (STEP 6, PEAK ACTUATOR DISPLACEMENT=3.02") 239
FIGURE 4-223. SPECIMEN S5 (STEP 6, PEAK ACTUATOR DISPLACEMENT=3.02") 240
FIGURE 4-224. SPECIMEN S5 (STEP 6, PEAK ACTUATOR DISPLACEMENT=-2.83") 240
FIGURE 4-225. SPECIMEN S5 (STEP 7, PEAK ACTUATOR DISPLACEMENT=3.46") 241
FIGURE 4-226. SPECIMEN S5 (STEP 7, PEAK ACTUATOR DISPLACEMENT=3.46") 241
FIGURE 4-227. SPECIMEN S5 (STEP 7, PEAK ACTUATOR DISPLACEMENT=-3.48") 242
FIGURE 4-228. SPECIMEN S5 (STEP 7, 3RD CYCLE) 242
FIGURE 4-229. SPECIMEN S5 (AFTER TEST) 243
FIGURE 4-230. TEST RESULTS OF SPECIMEN S5 WITH DESIGN LIMIT STATES 244
FIGURE 4-231. ACTUATOR DISPLACEMENT AND LOAD HISTORY FOR SPECIMEN S6 246
FIGURE 4-232. SPECIMEN S6 (STEP 3 PEAK ACTUATOR DISPLACEMENT=0.5") 246
FIGURE 4-233. SPECIMEN S6 (STEP 4 PEAK ACTUATOR DISPLACEMENT=0.75") 247
FIGURE 4-234. SPECIMEN S6 (STEP 5 PEAK ACTUATOR DISPLACEMENT=0.94") 247
FIGURE 4-235. SPECIMEN S6 (STEP 6 PEAK ACTUATOR DISPLACEMENT=1.13") 248

FIGURE 4-236. SPECIMEN S6 (STEP 7 PEAK ACTUATOR DISPLACEMENT=1.32") 248
FIGURE 4-237. SPECIMEN S6 (STEP 8 PEAK ACTUATOR DISPLACEMENT=1.61") 249
FIGURE 4-238. SPECIMEN S6 (STEP 8 PEAK ACTUATOR DISPLACEMENT=1.61") 249
FIGURE 4-239. SPECIMEN S6 (STEP 8 PEAK ACTUATOR DISPLACEMENT=-1.84") 249
FIGURE 4-240. SPECIMEN S6 (STEP 9 PEAK ACTUATOR DISPLACEMENT=2.00") 250
FIGURE 4-241. SPECIMEN S6 (STEP 9 PEAK ACTUATOR DISPLACEMENT=2.00") 250
FIGURE 4-242. SPECIMEN S6 (STEP 9 PEAK ACTUATOR DISPLACEMENT=-2.25") 250
FIGURE 4-243. SPECIMEN S6 (STEP 10 PEAK ACTUATOR DISPLACEMENT=2.49") 251
FIGURE 4-244. SPECIMEN S6 (STEP 10 PEAK ACTUATOR DISPLACEMENT=2.49") 251
FIGURE 4-245. FRACTURE ON BOTTOM FACEPLATE OF SPECIMEN S6 (STEP 10) 252
FIGURE 4-246. SPECIMEN S6 (AFTER TEST) 252
FIGURE 4-247. TEST RESULTS OF SPECIMEN S6 WITH DESIGN LIMIT STATES 254
FIGURE 4-248. TEST RESULTS OF SPECIMENS S5 AND S6 254
FIGURE 5-1. BEARING SPRING MODEL WITH HOOK/GAP 257
FIGURE 5-2. GAP AND HOOK ELEMENTS IN SAP2000 258
FIGURE 5-3. THE CHANGE OF HOOK AND GAP VALUES IN TENSION 258
FIGURE 5-4. BOLT HOLE DEFORMATION UNDER CYCLIC LOADING 259
FIGURE 5-5. BEARING SPRING ANALYSIS UNDER CYCLIC LOADING 260
FIGURE 5-6. FRICTION AND BEARING SPRING MODEL 262
FIGURE 5-7. FRICTION AND BEARING SPRING MODEL 262
FIGURE 5-8. FRICTION AND BEARING SPRING ANALYSIS UNDER CYCLIC LOADING 263
FIGURE 5-9. EXAMPLE OF CPSW/CF CONNECTIONS 265
FIGURE 5-10. SIMPLIFIED SPRING MODELS 265
FIGURE 5-11. COMPARISON BETWEEN LOWER-BOUND AND UPPER-BOUND MODEL 265
FIGURE 5-12. LOWER-BOUND SPRING MODEL (SAP2000) 270

FIGURE 5-13. UPPER-BOUND SPRING MODEL (SAP2000)....270
FIGURE 5-14. SPRING PROPERTIES FOR SIMPLIFIED SPRING MODELS....270
FIGURE 5-15. COMPRESSIVE FORCE DEVELOPMENT OF CONCRETE (SECTION CUT IN THE MIDDLE)....271
FIGURE 5-16. COMPRESSIVE STRESSES OF CONCRETE IN FINITE ELEMENT MODELS (TOP VIEW)....271
FIGURE 5-17. AXIAL COMPRESSION FORCE IN VARIOUS ELEMENTS ALONG THE LENGTH OF THE SPLICE REGION FOR SPECIMEN T3, FROM FINITE ELEMENT ANALYSIS....272
FIGURE 5-18. DISPLACEMENT HISTORY FROM SPECIMEN T2....274
FIGURE 5-19. SYMMETRIC DISPLACEMENT HISTORY FOR SPECIMEN T2....275
FIGURE 5-20. COMPARISON OF SP AND ACTUATOR DISPLACEMENT HISTORIES FOR SPECIMEN T2....276
FIGURE 5-21. MOVING AVERAGE OF SP AND ACTUATOR DISPLACEMENT HISTORIES FOR SPECIMEN T2....277
FIGURE 5-22. MODIFIED SP HISTORIES FOR SPECIMEN T2....277
FIGURE 5-23. DIFFERENT SPRING MODELS WITH TEST RESULTS....278
FIGURE 5-24. ANALYSIS RESULTS OF LOWER-BOUND SPRING MODEL (SPECIMENS T1 AND T2)....279
FIGURE 5-25. COMPARISON BETWEEN TEST RESULT AND LOWER-BOUND SPRING ANALYSIS (SPECIMENS T2)....281
FIGURE 5-26. ELASTIC STIFFNESS OF SIMPLIFIED SPRING MODEL T2....281
FIGURE 5-27. ANALYSIS RESULTS OF UPPER-BOUND SPRING MODEL (SPECIMEN T2)....283
FIGURE 5-28. COMPARISON OF LOWER AND UPPER-BOUND (SPECIMENS T2)....283
FIGURE 5-29. COMPARISON BETWEEN TEST RESULT AND UPPER-BOUND SPRING ANALYSIS (SPECIMENS T2)....284
FIGURE 5-30. ANALYSIS RESULTS OF LOWER-BOUND SPRING MODEL (SPECIMEN T3)....285
FIGURE 5-31. NET SECTION SPRING RESPONSE AT EACH CYCLE (T3_LOWER-BOUND)....286
FIGURE 5-32. COMPARISON BETWEEN TEST RESULT AND SIMPLIFIED SPRING ANALYSIS (SPECIMENS T3)....287
FIGURE 5-33. ELASTIC STIFFNESS OF SIMPLIFIED SPRING MODEL T3....288
FIGURE 5-34. ANALYSIS RESULTS OF UPPER-BOUND SPRING MODEL (SPECIMEN T3)....289
FIGURE 5-35. COMPARISON OF LOWER AND UPPER-BOUND (SPECIMEN T3)....289
FIGURE 5-36. COMPARISON BETWEEN TEST RESULT AND UPPER-BOUND SPRING ANALYSIS (SPECIMENS T3)....290

FIGURE 5-37. ANALYSIS RESULTS OF LOWER-BOUND SPRING MODEL (SPECIMENS T5 AND T6).....292
FIGURE 5-38. NET SECTION SPRING RESPONSE AT EACH CYCLE (SPECIMENS T5 AND T6_LOWER-BOUND) 293
FIGURE 5-39. COMPARISON BETWEEN TEST RESULT AND SIMPLIFIED SPRING ANALYSIS (SPECIMENS T6) 294
FIGURE 5-40. ELASTIC STIFFNESS OF SIMPLIFIED SPRING MODEL.....295
FIGURE 5-41. ELASTIC STIFFNESS COMPARISONS BETWEEN SPRING MODEL AND TEST RESULTS.....295
FIGURE 5-42. ANALYSIS RESULTS OF UPPER-BOUND SPRING MODEL (SPECIMENS T5 AND T6).....296
FIGURE 5-43. COMPARISON OF LOWER AND UPPER-BOUND (SPECIMENS T5 AND T6).....297
FIGURE 5-44. COMPARISON BETWEEN TEST RESULT AND UPPER-BOUND SPRING ANALYSIS (SPECIMENS T6).....297
FIGURE 5-45. ANALYSIS RESULTS OF LOWER-BOUND SPRING MODEL (SPECIMENS T1 AND T2).....299
FIGURE 5-46. ANALYSIS RESULTS OF LOWER-BOUND SPRING MODEL (SPECIMEN T3) 300
FIGURE 5-47. ANALYSIS RESULTS OF UPPER-BOUND SPRING MODEL (SPECIMENS T5 AND T6).....302
FIGURE 5-48. FINITE ELEMENT MODEL OF SPECIMEN T1.....305
FIGURE 5-49. FINITE ELEMENT MODEL OF SPECIMEN T2.....306
FIGURE 5-50. FINITE ELEMENT MODEL OF SPECIMEN T3.....306
FIGURE 5-51. FINITE ELEMENT MODEL OF SPECIMEN T4.....307
FIGURE 5-52. FINITE ELEMENT MODEL OF SPECIMEN T5.....307
FIGURE 5-53. FINITE ELEMENT MODEL OF SPECIMEN T6.....308
FIGURE 5-54. TYPICAL CONTACT INTERFACES IN THE FINITE ELEMENT MODEL 311
FIGURE 5-55. TENSION FORCE FROM FINITE ELEMENT ANALYSIS OF T2 SPECIMEN WITH DIFFERENT BOLT PRETENSION VALUES.....313
FIGURE 5-56. SLIP RESISTANCE FROM TENSION TESTS (R_{TEST}).....313
FIGURE 5-57. BOUNDARY CONDITION FOR FINITE ELEMENT MODELS.....315
FIGURE 5-58 LOADING AREA FOR FINITE ELEMENT MODELS 315
FIGURE 5-59. FINITE ELEMENT RESULTS OF TWO DIFFERENT LOADING AREAS 316
FIGURE 5-60 STRESS DISTRIBUTION OF CONCRETE OF TWO DIFFERENT LOADING AREAS.....316

FIGURE 5-61. FINITE ELEMENT RESULTS OF LOAD-DEFORMATION CURVE OF SPECIMEN T1.....319

FIGURE 5-62. LENGTH OF FINITE ELEMENT MODEL AND LP MEASUREMENT 319

FIGURE 5-63. VON MISES STRESSES OF ALL STEEL AT 2.0-IN. DEFORMATION IN TENSION (SPECIMEN T1) 321

FIGURE 5-64. VON MISES STRESSES AT BOLT SECTION AT 2.0-IN. DEFORMATION IN TENSION (SPECIMEN T1) 321

FIGURE 5-65. COMPARISON OF FINITE ELEMENT MODEL AND TEST OF SPECIMEN T1 322

FIGURE 5-66. ELONGATION OF BOLT HOLES AT 2.0-IN. DEFORMATION IN TENSION (SPECIMEN T1) 323

FIGURE 5-67. BEARING CURVE VS GLOBAL RESPONSE (SPECIMEN T1) 324

FIGURE 5-68. FINITE ELEMENT RESULTS FOR BOUNDARY CONDITIONS OF SPECIMEN AND OF WALL MODELS (SPECIMEN T1) 325

FIGURE 5-69. NORMAL-STRESSES FOR B.C. OF SPECIMEN MODEL (SPECIMEN T1, DISP.=1" IN TENSION) 326

FIGURE 5-70. NORMAL-STRESSES FOR B.C. OF WALL MODEL (SPECIMEN T1, DISP.=1" IN TENSION).....326

FIGURE 5-71. CYCLIC LOADING PROTOCOL OF FINITE ELEMENT MODEL (SPECIMEN T1) 328

FIGURE 5-72. FINITE ELEMENT RESULTS OF HYSTERESIS LOOP OF SPECIMEN T1.....328

FIGURE 5-73. CYCLIC INTERACTION BETWEEN CONCRETE AND STEEL (SPECIMEN T1) 329

FIGURE 5-74. AXIAL STRENGTHS OF CONCRETE AND STEEL (SPECIMEN T1).....330

FIGURE 5-75. INTERACTION BETWEEN CONCRETE AND BLIND BOLTS (SPECIMEN T1).....330

FIGURE 5-76. DETAILS OF POINTS 2 AND 3 (SPECIMEN T1) 331

FIGURE 5-77. FINITE ELEMENT RESULTS OF LOAD-DEFORMATION CURVE OF SPECIMEN T2.....333

FIGURE 5-78. VON MISES STRESSES OF STEEL PARTS (SPECIMEN T2, AT 2.0-IN. DEFORMATION IN TENSION).....334

FIGURE 5-79. VON MISES STRESSES AT ROD SECTION (SPECIMEN T2 AT 2.0-IN. DEFORMATION IN TENSION).....334

FIGURE 5-80. DEFORMATION OF RODS (SPECIMEN T2) 335

FIGURE 5-81. COMPARISON OF FINITE ELEMENT MODEL AND TEST OF SPECIMEN T2 (LP=2.0 IN. IN TENSION).....335

FIGURE 5-82. ELONGATION OF BOLT HOLES (SPECIMEN T2, AT 2.0-IN. DEFORMATION IN TENSION) 336

FIGURE 5-83. BEARING DEFORMATION VS GLOBAL RESPONSE (SPECIMEN T2).....337

FIGURE 5-84. FINITE ELEMENT RESULTS OF BOUNDARY CONDITIONS OF SPECIMEN AND OF WALL (SPECIMEN T2).338

FIGURE 5-85. NORMAL STRESSES FOR SPECIMEN MODEL (SPECIMEN T2, AT 2.0-IN. DEFORMATION IN TENSION) 338
FIGURE 5-86. NORMAL STRESSES FOR WALL MODEL (SPECIMEN T2, AT 2.0-IN. DEFORMATION IN TENSION) 339
FIGURE 5-87. CYCLIC LOADING PROTOCOL OF FINITE ELEMENT MODEL (SPECIMEN T2) 340
FIGURE 5-88. FINITE ELEMENT RESULTS OF HYSTERESIS LOOP OF SPECIMEN T2.....340
FIGURE 5-89. CYCLIC INTERACTION BETWEEN CONCRETE AND STEEL (SPECIMEN T2) 341
FIGURE 5-90. AXIAL STRENGTHS OF CONCRETE AND STEEL (SPECIMEN T2) 342
FIGURE 5-91. FINITE ELEMENT RESULTS OF LOAD-DEFORMATION CURVE OF SPECIMEN T3.....344
FIGURE 5-92. VON MISES STRESSES OF STEEL PARTS (SPECIMEN T3, AT 2.0-IN. DEFORMATION IN TENSION).....345
FIGURE 5-93. VON MISES STRESSES AT ROD SECTION (SPECIMEN T3, AT 2.0-IN. DEFORMATION IN TENSION).....345
FIGURE 5-94. DEFORMATION OF RODS (SPECIMEN T3) 346
FIGURE 5-95. ELONGATION OF BOLT HOLES (SPECIMEN T3, AT 2.0-IN. DEFORMATION IN TENSION) 347
FIGURE 5-96. BEARING DEFORMATION VS GLOBAL RESPONSE (SPECIMEN T3).....347
FIGURE 5-97. FINITE ELEMENT RESULTS OF BOUNDARY CONDITIONS OF SPECIMEN AND OF WALL (SPECIMEN T3).348
FIGURE 5-98. NORMAL STRESSES OF SPECIMEN MODEL (SPECIMEN T3, AT 2.0-IN. DEFORMATION IN TENSION) 348
FIGURE 5-99. NORMAL STRESSES OF WALL MODEL (SPECIMEN T3, AT 2.0-IN. DEFORMATION IN TENSION).....349
FIGURE 5-100. CYCLIC LOADING PROTOCOL OF FINITE ELEMENT MODEL (SPECIMEN T3).....350
FIGURE 5-101. FINITE ELEMENT RESULTS OF HYSTERESIS LOOP OF SPECIMEN T3.....350
FIGURE 5-102. CYCLIC INTERACTION BETWEEN CONCRETE AND STEEL (SPECIMEN T3) 351
FIGURE 5-103. AXIAL STRENGTHS OF CONCRETE AND STEEL (SPECIMEN T3) 352
FIGURE 5-104. SIDE VIEW OF NORMAL STRESSES OF SPECIMEN T3.....353
FIGURE 5-105. FINITE ELEMENT RESULTS OF LOAD-DEFORMATION CURVE OF SPECIMEN T4.....354
FIGURE 5-106. VON MISES STRESSES OF SPECIMEN T4 (DEFORMATION=0.55" IN TENSION) 355
FIGURE 5-107. VON MISES STRESSES OF SPECIMEN T4 (REVEAL FACEPLATES, DEFORMATION=0.55" IN TENSION) .355
FIGURE 5-108. DEFORMATION OF RODS (SPECIMEN T4) 356
FIGURE 5-109. DEVELOPMENT OF COMPRESSION STRUT OF SPECIMEN T4 (FINITE ELEMENT MODEL VS TEST) 358

FIGURE 5-110. MIDDLE SECTION CUT (SPECIMEN T4, AT 0.6-IN. DEFORMATION IN TENSION).....359
FIGURE 5-111. AXIAL-FORCE COMPONENTS OF SPECIMEN 4 AT SECTION CUTS 1 AND 2.....359
FIGURE 5-112. AXIAL STRENGTHS OF CONCRETE AND STEEL (SPECIMEN T4, SECTION CUT 1).....360
FIGURE 5-113. AXIAL STRENGTHS OF CONCRETE AND STEEL (SPECIMEN T4, SECTION CUT 2).....360
FIGURE 5-114. CYCLIC LOADING PROTOCOL OF FINITE ELEMENT MODEL (SPECIMEN T4).....361
FIGURE 5-115. FINITE ELEMENT RESULTS OF HYSTERESIS LOOP OF SPECIMEN T4.....362
FIGURE 5-116. DEVELOPMENT OF COMPRESSION STRUTS FROM CYCLIC LOAD ANALYSIS (SPECIMEN T4).....363
FIGURE 5-117. FINITE ELEMENT RESULTS OF MONOTONIC CURVE OF SPECIMEN T5.....365
FIGURE 5-118. VON MISES STRESSES OF SPECIMEN T5 (DEFORMATION=2.0" IN TENSION).....365
FIGURE 5-119. VON MISES STRESSES OF SPECIMEN T4 (REVEAL FACEPLATES, DEFORMATION=2.0" IN TENSION) ...366
FIGURE 5-120. VON MISES STRESSES AT BOLT SECTION (SPECIMEN T5, DEFORMATION=2.0" IN TENSION).....366
FIGURE 5-121. ELONGATION OF FACEPLATES (SPECIMEN T5, DEFORMATION=2" IN TENSION).....367
FIGURE 5-122. ELONGATION OF DIFFERENT SEGMENTS (SPECIMEN T5).....368
FIGURE 5-123. NORMAL STRESSES FOR SPECIMEN MODEL (SPECIMEN T5).....369
FIGURE 5-124. FINITE ELEMENT RESULTS OF BOUNDARY CONDITIONS OF SPECIMEN AND OF WALL (SPECIMEN T5) 369
FIGURE 5-125. NORMAL STRESSES FOR WALL MODEL (SPECIMEN T5).....370
FIGURE 5-126. FINITE ELEMENT RESULTS OF LOAD-DEFORMATION CURVE OF SPECIMEN T6.....371
FIGURE 5-127. VON MISES STRESSES OF SPECIMEN T6 (DEFORMATION=2.0" IN TENSION)).....371
FIGURE 5-128. VON MISES STRESSES OF SPECIMEN T6 (REVEAL FACEPLATES, DEFORMATION=2.0" IN TENSION) ...372
FIGURE 5-129. VON MISES STRESSES AT ROD SECTION (SPECIMEN T6, DEFORMATION=2" IN TENSION) 372
FIGURE 5-130. ELONGATION OF FACEPLATES (SPECIMEN T6, DEFORMATION=2" IN TENSION).....374
FIGURE 5-131. ELONGATION OF DIFFERENT SEGMENTS (SPECIMEN T6).....374
FIGURE 5-132. CYCLIC LOADING PROTOCOL OF FINITE ELEMENT MODEL (SPECIMEN T6).....375
FIGURE 5-133. FINITE ELEMENT RESULTS OF HYSTERESIS LOOP OF SPECIMEN T6.....376

FIGURE 5-134. TEST ASSEMBLY AND FINITE ELEMENT MODEL 378
FIGURE 5-135. FINITE ELEMENT MODEL OF SPECIMEN S1 379
FIGURE 5-136. FINITE ELEMENT MODEL OF SPECIMEN S2 379
FIGURE 5-137. FINITE ELEMENT MODEL OF SPECIMEN S3 380
FIGURE 5-138. FINITE ELEMENT MODEL OF SPECIMEN S4 380
FIGURE 5-139. FINITE ELEMENT MODEL OF SPECIMEN S5 381
FIGURE 5-140. FINITE ELEMENT MODEL OF SPECIMEN S6 381
FIGURE 5-141. TOP CONSTRAINT (UZ) FOR SHEAR SPECIMENS 382
FIGURE 5-142. SLIP RESISTANCE FROM SHEAR TESTS (R_{TEST}) 383
FIGURE 5-143. BOUNDARY CONDITION FOR FINITE ELEMENT MODELS OF SHEAR SPECIMENS 383
FIGURE 5-144. TEST SETUP OF SHEAR SPECIMEN S1/S2 385
FIGURE 5-145. RED LASER MEASURING INCLINATION OF ACTUATOR 385
FIGURE 5-146. ANGLE OF INCLINATION OF SHEAR SPECIMENS 386
FIGURE 5-147. FINITE ELEMENT MODELS WITH AND WITHOUT CONSIDERING AXIAL LOAD 387
FIGURE 5-148. SHEAR STRENGTH OF MODELS 1 AND 2 387
FIGURE 5-149. SHEAR STRENGTH OF STEEL AND CONCRETE OF MODELS 1 AND 2 388
FIGURE 5-150. FINITE ELEMENT RESULTS OF LOAD-DEFORMATION CURVE OF SPECIMEN S1 390
FIGURE 5-151. VON MISES STRESS OF S1 FINITE ELEMENT MODEL (LATERAL DISP. = 2.0 IN.) 391
FIGURE 5-152. FINITE ELEMENT RESULTS OF LOAD-DEFORMATION CURVE OF SPECIMEN S2 393
FIGURE 5-153. VON MISES STRESS OF S2 FINITE ELEMENT MODEL 393
FIGURE 5-154. SHEAR STRENGTHS OF CONCRETE AND STEEL (SPECIMEN S2) 395
FIGURE 5-155. SECTION CUT IN THE MIDDLE OF SHEAR SPECIMENS 395
FIGURE 5-156. COMPARISON OF SHEAR STRENGTHS OF S1 AND S2 FINITE ELEMENT MODELS 396
FIGURE 5-157. COMPARISON OF SHEAR STRENGTHS OF S2 CONCRETE AND "S2-S1" 396
FIGURE 5-158. CYCLIC LOADING PROTOCOL OF FINITE ELEMENT MODEL (SPECIMEN S2) 397

FIGURE 5-159. FINITE ELEMENT RESULTS OF HYSTERESIS LOOP OF SPECIMEN S2 397
FIGURE 5-160. VON MISES STRESSES OF FACEPLATES DURING CYCLING LOADING (SPECIMEN S2) 398
FIGURE 5-161. FINITE ELEMENT RESULTS OF LOAD-DEFORMATION CURVE OF SPECIMEN S3 400
FIGURE 5-162. VON MISES STRESS OF S3 FINITE ELEMENT MODEL 400
FIGURE 5-163. FINITE ELEMENT RESULTS OF LOAD-DEFORMATION CURVE OF SPECIMEN S4 402
FIGURE 5-164. VON MISES STRESS OF S4 FINITE ELEMENT MODEL 402
FIGURE 5-165. SHEAR STRENGTHS OF CONCRETE AND STEEL (SPECIMEN S4) 403
FIGURE 5-166. COMPARISON OF SHEAR STRENGTHS OF S3 AND S4 FINITE ELEMENT MODELS 404
FIGURE 5-167. COMPARISON OF SHEAR STRENGTHS OF S4 CONCRETE AND "S4-S3" 404
FIGURE 5-168. CYCLIC LOADING PROTOCOL OF FINITE ELEMENT MODEL (SPECIMEN S4) 405
FIGURE 5-169. FINITE ELEMENT RESULTS OF HYSTERESIS LOOP OF SPECIMEN S4 405
FIGURE 5-170. VON MISES STRESSES OF FACEPLATES DURING CYCLING LOADING (SPECIMEN S4) 406
FIGURE 5-171. FINITE ELEMENT RESULTS OF LOAD-DEFORMATION CURVE OF SPECIMEN S5 408
FIGURE 5-172. VON MISES STRESS OF S5 FINITE ELEMENT MODEL 408
FIGURE 5-173. FINITE ELEMENT RESULTS OF BACKBONE CURVE OF SPECIMEN S6 410
FIGURE 5-174. VON MISES STRESS OF S6 FINITE ELEMENT MODEL 410
FIGURE 5-175. SHEAR STRENGTHS OF CONCRETE AND STEEL (SPECIMEN S6) 412
FIGURE 5-176. COMPARISON OF SHEAR STRENGTHS OF S5 AND S6 FINITE ELEMENT MODELS 412
FIGURE 5-177. COMPARISON OF SHEAR STRENGTHS OF S6 CONCRETE AND "S6-S5" 413
FIGURE 5-178. CYCLIC LOADING PROTOCOL OF FINITE ELEMENT MODEL (SPECIMEN S6) 414
FIGURE 5-179. FINITE ELEMENT RESULTS OF HYSTERESIS LOOP OF SPECIMEN S6 414
FIGURE 5-180. VON MISES STRESSES OF FACEPLATES DURING CYCLING LOADING (SPECIMEN S4) 415
FIGURE 5-181. APPLIED AXIAL FORCE FZ IN SHEAR SPECIMENS 417
FIGURE 5-182. FINITE ELEMENT RESULTS OF LOAD-DEFORMATION CURVE OF SPECIMEN S1 WITH AND WITHOUT CONSIDERING FZ 419

FIGURE 5-183. FINITE ELEMENT RESULTS OF LOAD-DEFORMATION CURVE OF SPECIMEN S2 WITH AND WITHOUT CONSIDERING FZ 419
FIGURE 5-184. FINITE ELEMENT RESULTS OF LOAD-DEFORMATION CURVE OF SPECIMEN S3 WITH AND WITHOUT CONSIDERING FZ 420
FIGURE 5-185. FINITE ELEMENT RESULTS OF LOAD-DEFORMATION CURVE OF SPECIMEN S4 WITH AND WITHOUT CONSIDERING FZ 420
FIGURE 5-186. FINITE ELEMENT RESULTS OF LOAD-DEFORMATION CURVE OF SPECIMEN S5 WITH AND WITHOUT CONSIDERING FZ 421
FIGURE 5-187. FINITE ELEMENT RESULTS OF LOAD-DEFORMATION CURVE OF SPECIMEN S6 WITH AND WITHOUT CONSIDERING FZ 421
FIGURE 5-188. FINITE ELEMENT MODEL OF SPECIMEN W1....424
FIGURE 5-189. FINITE ELEMENT MODEL OF SPECIMEN W2....424
FIGURE 5-190. FINITE ELEMENT MODEL OF SPECIMEN W3....425
FIGURE 5-191. FINITE ELEMENT MODEL OF SPECIMEN W4....425
FIGURE 5-192. FINITE ELEMENT RESULTS OF LOAD-DEFORMATION CURVE OF MODEL W1 430
FIGURE 5-193. FINITE ELEMENT RESULTS OF LOAD-DEFORMATION CURVE OF MODEL W2 431
FIGURE 5-194. FINITE ELEMENT RESULTS OF LOAD-DEFORMATION CURVE OF MODEL W3 431
FIGURE 5-195. FINITE ELEMENT RESULTS OF LOAD-DEFORMATION CURVE OF MODEL W4 432
FIGURE 5-196. UNIT LENGTH SHEAR STRENGTH VERSUS SHEAR DEFORMATION (MODELS W1 TO W4) 432
FIGURE 5-197. VON MISES STRESS OF MODEL W1 (LATERAL DISP. = 2.0 IN.) 434
FIGURE 5-198. VON MISES STRESS OF MODEL W2 (LATERAL DISP. = 2.0 IN.) 435
FIGURE 5-199. VON MISES STRESS OF MODEL W3 (LATERAL DISP. = 2.0 IN.) 436
FIGURE 5-200. VON MISES STRESS OF MODEL W4 (LATERAL DISP. = 2.0 IN.) 437
FIGURE 5-201. COMPRESSION STRUT OF MODEL W1 (LATERAL DISP. = 0.2 IN.) 439
FIGURE 5-202. COMPRESSION STRUT OF MODEL W2 (LATERAL DISP. = 0.2 IN.) 440

FIGURE 5-203. COMPRESSION STRUT OF MODEL W3 (LATERAL DISP. = 0.2 IN.) 441
FIGURE 5-204. COMPRESSION STRUT OF MODEL W4 (LATERAL DISP. = 0.2 IN.) 442
FIGURE 5-205. COMPRESSION STRUT OF MODEL W4 (LATERAL DISP. = 2.0 IN.) 443
FIGURE 5-206. FINITE ELEMENT MODEL OF SPECIMENS W4 AND W4_CORE.....445
FIGURE 5-207. FINITE ELEMENT RESULTS OF LOAD-DEFORMATION CURVE OF MODEL W4_CORE 446
FIGURE 6-1. FINITE ELEMENT MODEL OF: (A) SINGLE, AND; (B) DOUBLE-BOLT CONNECTIONS 450
FIGURE 6-2. TYPICAL CONTACT INTERFACES IN THE FINITE ELEMENT MODEL 451
FIGURE 6-3. LOAD-DEFORMATION CURVE OF MODEL 1 (WITH PRETENSION) 453
FIGURE 6-4. LOAD-DEFORMATION CURVE OF MODEL 1 (WITHOUT PRETENSION).....454
FIGURE 6-5. VON MISES STRESSES OF MODEL 1 AT DIFFERENT DEFORMATIONS (BOLT SHANK NOT SHOWN).....456
FIGURE 6-6. DEFORMATION AROUND BOLTS OF MODEL 1 (DEFORMATION = 2 IN.) 456
FIGURE 6-7. FREE-BODY DIAGRAM OF SPRING SYSTEM OF BOLTED CONNECTIONS (PRELOAD STAGE) 457
FIGURE 6-8. FREE-BODY DIAGRAM OF SPRING SYSTEM OF BOLTED CONNECTIONS (PRELOAD AND DEFORMED STAGES).....457
FIGURE 6-9. DEFORMATION OF CONNECTION MODEL 1 (BOLTS NOT SHOWN).....458
FIGURE 6-10. THICKNESS CHANGE AROUND BOLT HOLES (MODEL 1).....458
FIGURE 6-11. THICKNESS CHANGE AROUND BOLT HOLES (MODEL 1).....459
FIGURE 6-12. BENDING AND YIELDING OF BOLTS (MODEL 1).....459
FIGURE 6-13. ELEVATION VIEWS OF CONTACT INTERFACES SHOWING CLAMPING STRESS VECTORS (MODEL 1).....460
FIGURE 6-14. NORMAL AND FRICTION STRESSES ON THE SURFACE OF THE SPLICE PLATE (MODEL 1) 461
FIGURE 6-15. NORMAL AND FRICTION STRESSES ON THE SURFACE OF THE FACEPLATE (MODEL 1).....461
FIGURE 6-16. CLAMPING FORCE AND BOLT HOLE ELONGATION CURVE (MODEL 1) 462
FIGURE 6-17. TOTAL AXIAL FORCE AND FRICTION FORCE OF MODEL 2 465
FIGURE 6-18. TOTAL AXIAL FORCE AND FRICTION FORCE OF MODEL 3 465
FIGURE 6-19. TOTAL AXIAL FORCE AND FRICTION FORCE OF MODEL 4 466

FIGURE 6-20. VON MISES STRESSES OF MODEL 2 AT DIFFERENT DEFORMATIONS (BOLT SHANK NOT DISPLACED) .467

FIGURE 6-21. VON MISES STRESSES OF MODEL 3 AT DIFFERENT DEFORMATIONS (BOLT SHANK NOT DISPLACED) .468

FIGURE 6-22. VON MISES STRESSES OF MODEL 4 AT DIFFERENT DEFORMATIONS (BOLT SHANK NOT DISPLACED) .468

FIGURE 6-23. DEFORMATION OF DOUBLE-BOLTS CONNECTIONS (DEFORMATION = 2.0 IN.).....470

FIGURE 6-24. DEFORMATION OF CONNECTION MODEL 3 (BOLTS SHANK NOT SHOWN).....470

FIGURE 6-25. ELEVATION VIEWS OF CONTACT INTERFACES SHOWING CLAMPING STRESS VECTORS (MODEL 2).....471

FIGURE 6-26. ELEVATION VIEWS OF CONTACT INTERFACES SHOWING CLAMPING STRESS VECTORS (MODEL 3).....471

FIGURE 6-27. ELEVATION VIEWS OF CONTACT INTERFACES SHOWING CLAMPING STRESS VECTORS (MODEL 4).....472

FIGURE 6-28. CLAMPING FORCE AND BOLT HOLE ELONGATION CURVE (MODEL 2) 472

FIGURE 6-29. CLAMPING FORCE AND BOLT HOLE ELONGATION CURVE (MODEL 3) 473

FIGURE 6-30. CLAMPING FORCE AND BOLT HOLE ELONGATION CURVE (MODEL 4) 473

FIGURE 6-31. NORMAL AND FRICTION STRESSES ON THE SURFACE OF THE SPLICE PLATE (MODEL 2) 474

FIGURE 6-32. NORMAL AND FRICTION STRESSES ON THE SURFACE OF THE FACEPLATE (MODEL 2).....474

FIGURE 6-33. NORMAL AND FRICTION STRESSES ON THE SURFACE OF THE SPLICE PLATE (MODEL 3) 475

FIGURE 6-34. NORMAL AND FRICTION STRESSES ON THE SURFACE OF THE FACEPLATE (MODEL 3).....475

FIGURE 6-35. NORMAL AND FRICTION STRESSES ON THE SURFACE OF THE SPLICE PLATE (MODEL 4) 476

FIGURE 6-36. NORMAL AND FRICTION STRESSES ON THE SURFACE OF THE FACEPLATE (MODEL 4).....476

FIGURE 6-37. FORCE-DEFORMATION CURVE OF SPECIMEN T1 WITH DIFFERENT PRETENSIONS 479

FIGURE 6-38. FORCE-DEFORMATION CURVE OF SPECIMEN T2 WITH DIFFERENT PRETENSIONS 479

FIGURE 6-39. FORCE-DEFORMATION CURVE OF SPECIMEN T3 WITH DIFFERENT PRETENSIONS 480

FIGURE 6-40. CLAMPING STRESS VECTORS IN SPECIMEN T2 481

FIGURE 6-41. CLAMPING FORCE-HOLE DEFORMATION CURVE OF MODELS T1 TO T3.....482

FIGURE 6-42. FORCE-DEFORMATION CURVE OF MODEL T1 IN COMPRESSION.....484

FIGURE 6-43. INITIATION OF CONCRETE CRACKS OF MODEL T1 IN COMPRESSION 485

FIGURE 6-44. BOLT HOLE ELONGATION AT -0.20 IN. DEFORMATION.....485

FIGURE 6-45. GLOBAL FREE-BODY DIAGRAM OF MODEL T1 488
FIGURE 6-46. LOCAL FREE-BODY DIAGRAM OF MODEL T1 488
FIGURE 6-47. AXIAL FORCES ON FACEPLATES AND SPLICE PLATES AND BEARING FORCES IN MODEL T1 489
FIGURE 6-48. FRICTION FORCES IN MODEL T1 489
FIGURE 6-49. FORCE EQUILIBRIUM OF MODEL T1 490
FIGURE 7-1. 3D VIEW OF WALL TEST SETUP 493
FIGURE 7-2. ELEVATIONS OF T-SHAPED WALL 494
FIGURE 7-3. TYPICAL CROSS SECTION OF T-SHAPED WALL 495
FIGURE 7-4. TRIBUTARY AREA APPROACH 498
FIGURE 7-5. CROSS SECTION OF T-SHAPED WALL WITH HORIZONTAL SPLICE 499
FIGURE 7-6. 3D ASSEMBLY OF THE WALL SPECIMEN 499
FIGURE 7-7. STRESS PROFILE OF T-SHAPED C-PSW/CF (WEB IN COMPRESSION, ELASTIC) 501
FIGURE 7-8. STRESS PROFILE OF T-SHAPED C-PSW/CF (WEB IN COMPRESSION, YIELDING STAGE) 501
FIGURE 7-9. STRESS PROFILE OF T-SHAPED C-PSW/CF (FLANGE IN COMPRESSION, ELASTIC) 502
FIGURE 7-10. P-M INTERACTION CURVE FOR THE T-SHAPED SECTION FOR A MAXIMUM TENSION STRESS LIMITED TO $0.6F_Y$ 502
FIGURE 7-11. NEUTRAL AXIS LOCATION OF THE T-SHAPED SECTION FOR A MAXIMUM TENSION STRESS LIMITED TO $0.6F_Y$ 503
FIGURE 7-12 FORCE DISTRIBUTION OF BOLTS IN HORIZONTAL SPLICES (WEB IN COMPRESSION) (A) ELASTIC DISTRIBUTION (B) ELASTIC DISTRIBUTION WITH COMPRESSION LIMIT 506
FIGURE 7-13. FORCE DISTRIBUTION OF BOLTS IN HORIZONTAL SPLICES (FLANGE IN COMPRESSION) 506
FIGURE 7-14. P-M INTERACTION CURVE FOR THE HORIZONTAL SPLICES (BEARING STRENGTH = $2.4dtF_U$) 507
FIGURE 7-15. NEUTRAL AXIS LOCATION OF THE T-SHAPED SECTION (BEARING STRENGTH = $2.4dtF_U$) 507
FIGURE 7-16. P-M INTERACTION CURVE FOR THE T-SHAPED SECTION (BEARING STRENGTH = $3.0dtF_U$) 508
FIGURE 7-17. NEUTRAL AXIS LOCATION OF THE HORIZONTAL SPLICES (BEARING STRENGTH = $3.0dtF_U$) 508

FIGURE 7-18. CROSS SECTION OF VERTICAL SPLICES 512
FIGURE 7-19. ELEVATIONS OF T-SHAPED C-PSW/CF 513
FIGURE 7-20. SHEAR FLOW ON THE T-SHAPED SECTION 513
FIGURE 7-21. DESIGNED BOLT SPACING FOR VERTICAL SPLICES 514
FIGURE 7-22. ELEVATIONS OF T-SHAPED C-PSW/CF ABOVE HORIZONTAL SPLICES 516
FIGURE 7-23. SECTION FORCES OF T-SHAPED C-PSW/CF (WEB IN COMPRESSION) 516
FIGURE 7-24. ELEVATION OF THE VERTICAL ACTUATORS 518
FIGURE 7-25. CONSTRUCTION SEQUENCE OF THE TEST SPECIMEN 518
FIGURE 7-26. FINISHED TEST SETUP FOR THE WALL TEST 519
FIGURE 7-27. MATERIAL TEST OF WALL SPECIMEN 520
FIGURE 7-28. STRAIN GAUGES ON WALL SPECIMEN 523
FIGURE 7-29. INSTALLED STRAIN GAUGES FROM SOUTHWEST VIEW 524
FIGURE 7-30. LINEAR POTENTIOMETERS ON WALL SPECIMEN 524
FIGURE 7-31. LINEAR POTENTIOMETERS FROM SOUTHWEST VIEW 525
FIGURE 7-32. VERTICAL STRING POTENTIOMETERS ON WALL SPECIMEN 525
FIGURE 7-33. DEFORMED VSP ON WEST AND EAST SIDES OF THE WALL 526
FIGURE 7-34. HORIZONTAL STRING POTENTIOMETERS ON WALL SPECIMEN (PLAN VIEW) 526
FIGURE 7-35. HORIZONTAL STRING POTENTIOMETERS ON WALL SPECIMEN (ELEVATION VIEW) 527
FIGURE 7-36. FORCE-DISPLACEMENT BEHAVIOR PREDICTED FROM PRELIMINARY FINITE ELEMENT ANALYSIS RESULT 529
FIGURE 7-37. PROPOSED REPAIR SCHEME BY WELDING AT THE TOP OF THE HORIZONTAL SPLICE 532
FIGURE 8-1. AXIAL STRAINS AT VERTICAL LOADING STAGE IN (A) ELEVATION AND (B) 3D 536
FIGURE 8-2. VERTICAL LOADING HISTORY 537
FIGURE 8-3. REINFORCING BOTTOM OF VERTICAL ACTUATORS WITH WIDE FLANGE BEAMS 537
FIGURE 8-4. ACTUATOR DISPLACEMENT AND LOAD HISTORY 539

FIGURE 8-5. FREE-BODY DIAGRAM FOR CALCULATING THE SHEAR FORCE OF THE WALL 540
FIGURE 8-6. LP DEFORMATION AT POSITIVE AND NEGATIVE PEAKS IN STEP 2 IN (A) ELEVATION AND (B) 3D 541
FIGURE 8-7. STEP 3, PEAK ACTUATOR DISPLACEMENT=0.94" 543
FIGURE 8-8. STEP 3, PEAK ACTUATOR DISPLACEMENT=-0.5" 543
FIGURE 8-9. DEFORMATION OF LP IN STEP 3 IN (A) ELEVATION AND (B) 3D 544
FIGURE 8-10. STEP 4, PEAK ACTUATOR DISPLACEMENT=1.38" 544
FIGURE 8-11. STEP 4, PEAK ACTUATOR DISPLACEMENT=-0.9" 545
FIGURE 8-12. NO GAP INITIATION ON WEB IN STEP 4, PEAK ACTUATOR DISPLACEMENT=-0.9" 545
FIGURE 8-13. HYSTERESIS CURVE IN STEPS 1 TO 4 546
FIGURE 8-14. STEP 5, PEAK ACTUATOR DISPLACEMENT=1.85" 548
FIGURE 8-15. STEP 5, PEAK ACTUATOR DISPLACEMENT=-1.3" 548
FIGURE 8-16. YIELDING LINES NEAR BOLTS ON THE NORTH SIDE OF THE WALL IN STEP 5, PEAK ACTUATOR DISPLACEMENT=1.85" 548
FIGURE 8-17. GAP VISIBLE ON THE WEB IN STEP 5, PEAK ACTUATOR DISPLACEMENT=-1.3" 549
FIGURE 8-18. STEP 6, PEAK ACTUATOR DISPLACEMENT=2.35" 549
FIGURE 8-19. STEP 6, PEAK ACTUATOR DISPLACEMENT=-1.7" 550
FIGURE 8-20. YIELDING LINES ON THE NORTH SIDE OF THE WALL IN STEP 6, PEAK ACTUATOR DISPLACEMENT=2.35" 550
FIGURE 8-21. GAP ON THE WEB IN STEP 6, PEAK ACTUATOR DISPLACEMENT=-1.7" 551
FIGURE 8-22. STEP 7, PEAK ACTUATOR DISPLACEMENT=2.85" 552
FIGURE 8-23. STEP 7, PEAK ACTUATOR DISPLACEMENT=-2.1" 553
FIGURE 8-24. STEP 8, PEAK ACTUATOR DISPLACEMENT=3.50" 553
FIGURE 8-25. STEP 8, PEAK ACTUATOR DISPLACEMENT=-2.6" 553
FIGURE 8-26. BUCKLING ON HORIZONTAL SPLICE ON WEB IN STEP 8, PEAK ACTUATOR DISPLACEMENT=3.5" 554
FIGURE 8-27. CLOSE VIEW OF BUCKLING ON HORIZONTAL SPLICE ON WEB IN STEP 8, PEAK ACTUATOR DISPLACEMENT=3.5" 554
FIGURE 8-28. STEP 9, PEAK ACTUATOR DISPLACEMENT=4.25" 555
FIGURE 8-29. STEP 9, PEAK ACTUATOR DISPLACEMENT=-3.2" 555

FIGURE 8-30. CLOSE VIEW OF BUCKLING ON HORIZONTAL SPLICE ON WEB IN STEP 9, PEAK ACTUATOR DISPLACEMENT=4.25” 556
FIGURE 8-31. CLOSE VIEW OF FRACTURES OF TIE-RODS DURING STEP 9 556
FIGURE 8-32. CONCRETE SPALLING OBSERVED AFTER STEP 9 557
FIGURE 8-33. HYSTERESIS CURVE IN STEPS 7 TO 9 557
FIGURE 8-34. STEP 10, PEAK ACTUATOR DISPLACEMENT=-3.9” 558
FIGURE 8-35. STEP 11, PEAK ACTUATOR DISPLACEMENT=-4.6” 559
FIGURE 8-36. BEARING DEFORMATION ON SPLICE PLATE WEB AT STEP 11, PEAK ACTUATOR DISPLACEMENT=-4.6” 559
FIGURE 8-37. STEP 12, PEAK ACTUATOR DISPLACEMENT=-5.6” 560
FIGURE 8-38. STEP 13, PEAK ACTUATOR DISPLACEMENT=-7.0” 560
FIGURE 8-39. STEP 14, PEAK ACTUATOR DISPLACEMENT=-8.0” 560
FIGURE 8-40. STEP 15, PEAK ACTUATOR DISPLACEMENT=-9.5” 561
FIGURE 8-41. FRACTURES DUE TO BEARING FAILURE OBSERVED AT STEP 14, PEAK ACTUATOR DISPLACEMENT=-8.0” 561
FIGURE 8-42. HYSTERESIS CURVE IN STEPS 10 TO 15 562
FIGURE 8-43. SOUTHWEST VIEW OF THE SPECIMEN (STEPS 7 TO 10) 563
FIGURE 8-44. SOUTHWEST VIEW OF THE SPECIMEN (STEPS 11 TO 15) 564
FIGURE 8-45. SOUTHEAST VIEW OF THE SPECIMEN (STEPS 7 TO 10) 565
FIGURE 8-46. SOUTHEAST VIEW OF THE SPECIMEN (STEPS 11 TO 14) 566
FIGURE 8-47. NORTHWEST VIEW OF THE SPECIMEN (STEPS 7 TO 10) 567
FIGURE 8-48. NORTHWEST VIEW OF THE SPECIMEN (STEPS 11 TO 15) 568
FIGURE 8-49. PHOTOS REVEALING FACEPLATES AFTER TEST 570
FIGURE 8-50. PHOTO REVEALING FACEPLATES ON WESTERN WEB AFTER TEST 571
FIGURE 8-51. CROSS SECTION VIEW OF LOWER PART OF WALL AFTER TEST 572
FIGURE 8-52. CROSS SECTION VIEW OF UPPER PAT OF WALL AFTER TEST 572
FIGURE 8-53. CLEAN-CUT ON THE BOTTOM INSIDE HORIZONTAL SPLICE PLATES 573
FIGURE 8-54. REQUESTED WELDING ON BOTTOM OF INSIDE AND OUTSIDE SPLICE PLATES 573

FIGURE 8-55. WELDING ON BOTTOM OF HORIZONTAL SPLICE IN SHOP DRAWING 574
FIGURE 8-56. PHOTOS SHOWING ALL OUTSIDE HORIZONTAL SPLICE PLATES AFTER TEST 574
FIGURE 8-57. MEASURED ROTATION AT HORIZONTAL SPLICE AFTER TEST 576
FIGURE 8-58. HYSTERESIS CURVES OF (A) HACTF VS TOP LATERAL DISPLACEMENT (B) SHEAR FORCE VS TOP LATERAL DISPLACEMENT 577
FIGURE 8-59. HYSTERESIS CURVES OF SHEAR FORCE VS TOP LATERAL DRIFT 578
FIGURE 8-60. INCLINATION ANGLE OF VERTICAL ACTUATORS AT ZERO DISPLACEMENT AND FREE BODY DIAGRAM OF THE WALL SPECIMEN AT ZERO DISPLACEMENT (KIZILARSLAN AND BRUNEAU, 2023) 580
FIGURE 8-61. ADJUSTED FREE BODY DIAGRAM OF THE WALL SPECIMEN AT ZERO DISPLACEMENT 580
FIGURE 8-62. CALCULATED EXPERIMENTAL M_{SP} VS TOP LATERAL DRIFT CURVE 581
FIGURE 8-63. AXIAL STRAINS AT POSITIVE PEAK IN STEP 2 IN (A) ELEVATION AND (B) 3D 585
FIGURE 8-64. AXIAL STRAINS AT NEGATIVE PEAK IN STEP 2 IN (A) ELEVATION AND (B) 3D 586
FIGURE 8-65. AXIAL STRAINS AT POSITIVE PEAK IN STEP 4 IN (A) ELEVATION AND (B) 3D 587
FIGURE 8-66. AXIAL STRAINS AT NEGATIVE PEAK IN STEP 4 IN (A) ELEVATION AND (B) 3D 588
FIGURE 8-67. AXIAL STRAINS AT POSITIVE PEAK IN STEP 5 IN (A) ELEVATION AND (B) 3D 589
FIGURE 8-68. AXIAL STRAINS AT NEGATIVE PEAK IN STEP 5 IN (A) ELEVATION AND (B) 3D 590
FIGURE 8-69. AXIAL STRAINS AT POSITIVE PEAK IN STEP 6 IN (A) ELEVATION AND (B) 3D 591
FIGURE 8-70. AXIAL STRAINS AT NEGATIVE PEAK IN STEP 6 IN (A) ELEVATION AND (B) 3D 592
FIGURE 8-71. AXIAL STRAINS AT POSITIVE PEAK IN STEP 7 IN (A) ELEVATION AND (B) 3D 593
FIGURE 8-72. AXIAL STRAINS AT NEGATIVE PEAK IN STEP 7 IN (A) ELEVATION AND (B) 3D 594
FIGURE 8-73. AXIAL STRAINS AT POSITIVE PEAK IN STEP 8 IN (A) ELEVATION AND (B) 3D 595
FIGURE 8-74. AXIAL STRAINS AT NEGATIVE PEAK IN STEP 8 IN (A) ELEVATION AND (B) 3D 596
FIGURE 8-75. AXIAL STRAINS AT POSITIVE PEAK IN STEP 9 IN (A) ELEVATION AND (B) 3D 597
FIGURE 8-76. AXIAL STRAINS AT NEGATIVE PEAK IN STEP 9 IN (A) ELEVATION AND (B) 3D 598
FIGURE 8-77. AXIAL STRAINS AT NEGATIVE PEAK IN STEP 10 IN (A) ELEVATION AND (B) 3D 599
FIGURE 8-78. AXIAL STRAINS AT NEGATIVE PEAK IN STEP 11 IN (A) ELEVATION AND (B) 3D 600

FIGURE 8-79. AXIAL STRAINS AT NEGATIVE PEAK IN STEP 12 IN (A) ELEVATION AND (B) 3D 601
FIGURE 8-80. AXIAL STRAINS AT NEGATIVE PEAK IN STEP 13 IN (A) ELEVATION AND (B) 3D 602
FIGURE 8-81. AXIAL STRAINS AT NEGATIVE PEAK IN STEP 14 IN (A) ELEVATION AND (B) 3D 603
FIGURE 8-82. AXIAL STRAINS AT NEGATIVE PEAK IN STEP 15 IN (A) ELEVATION AND (B) 3D 604
FIGURE 8-83. LATERAL DISPLACEMENT AND DRIFT AT POSITIVE PEAKS IN EACH STEP 605
FIGURE 8-84. LATERAL DISPLACEMENT AND DRIFT AT NEGATIVE PEAKS IN EACH STEP 605
FIGURE 8-85. NORMALIZED LATERAL DISPLACEMENT AT POSITIVE PEAKS IN EACH STEP 606
FIGURE 8-86. NORMALIZED LATERAL DISPLACEMENT AT NEGATIVE PEAKS IN EACH STEP 606
FIGURE 8-87. FREE-BODY DIAGRAM OF WALL FOR FIRST AND SECOND-ORDER ANALYSES 607
FIGURE 8-88. LATERAL DISPLACEMENT AT POSITIVE PEAKS IN EACH STEP (FIRST-ORDER ANALYSIS) 608
FIGURE 8-89. LATERAL DISPLACEMENT AT POSITIVE PEAKS IN EACH STEP (SECOND-ORDER ANALYSIS) 609
FIGURE 8-90. LATERAL DISPLACEMENT AT NEGATIVE PEAKS IN EACH STEP (FIRST-ORDER ANALYSIS) 610
FIGURE 8-91. LATERAL DISPLACEMENT AT NEGATIVE PEAKS IN EACH STEP (SECOND-ORDER ANALYSIS) 611
FIGURE 8-92. DEFORMATION OF VSP AT POSITIVE PEAK IN STEP 4 IN (A) ELEVATION AND (B) 3D 612
FIGURE 8-93. DEFORMATION OF VSP AT NEGATIVE PEAK IN STEP 4 IN (A) ELEVATION AND (B) 3D 612
FIGURE 8-94. DEFORMATION OF VSP AT POSITIVE PEAK IN STEP 5 IN (A) ELEVATION AND (B) 3D 613
FIGURE 8-95. DEFORMATION OF VSP AT NEGATIVE PEAK IN STEP 5 IN (A) ELEVATION AND (B) 3D 613
FIGURE 8-96. DEFORMATION OF VSP AT POSITIVE PEAK IN STEP 6 IN (A) ELEVATION AND (B) 3D 614
FIGURE 8-97. DEFORMATION OF VSP AT NEGATIVE PEAK IN STEP 6 IN (A) ELEVATION AND (B) 3D 614
FIGURE 8-98. DEFORMATION OF VSP AT POSITIVE PEAK IN STEP 8 IN (A) ELEVATION AND (B) 3D 615
FIGURE 8-99. DEFORMATION OF VSP AT NEGATIVE PEAK IN STEP8 IN (A) ELEVATION AND (B) 3D 615
FIGURE 8-100. DEFORMATION OF VSP AT POSITIVE PEAK IN STEP 9 IN (A) ELEVATION AND (B) 3D 616
FIGURE 8-101. DEFORMATION OF VSP AT NEGATIVE PEAK IN STEP 9 IN (A) ELEVATION AND (B) 3D 616
FIGURE 8-102. DEFORMATION OF VSP AT NEGATIVE PEAK IN STEP 10 IN (A) ELEVATION AND (B) 3D 617
FIGURE 8-103. DEFORMATION OF VSP AT NEGATIVE PEAK IN STEP 11 IN (A) ELEVATION AND (B) 3D 617

FIGURE 8-104. DEFORMATION OF VSP AT NEGATIVE PEAK IN STEP 12 IN (A) ELEVATION AND (B) 3D 618
FIGURE 8-105. DEFORMATION OF VSP AT NEGATIVE PEAK IN STEP 13 IN (A) ELEVATION AND (B) 3D 618
FIGURE 8-106. DEFORMATION OF VSP AT NEGATIVE PEAK IN STEP 14 IN (A) ELEVATION AND (B) 3D 619
FIGURE 8-107. DEFORMATION OF VSP AT NEGATIVE PEAK IN STEP 15 IN (A) ELEVATION AND (B) 3D 619
FIGURE 9-1. FINITE ELEMENT MODEL OF WALL SPECIMEN AND FOUNDATION.....623
FIGURE 9-2. MESHT SIZE DETAILS OF THE WALL SPECIMEN.....626
FIGURE 9-3. MESH SIZE DETAILS OF THE CONCRETE FOUNDATION 626
FIGURE 9-4. FINITE ELEMENT ELASTIC STIFFNESS OF WALL SPECIMEN FOR VARIOUS ELASTIC MODULUS OF CONCRETE COMPARED TO FIRST CYCLE FROM WALL SPECIMEN TEST 627
FIGURE 9-5. MAXIMUM VON MISES STRESS ON STEEL IN FOUNDATION FROM POSITIVE AND NEGATIVE FINITE ELEMENT ANALYSES 628
FIGURE 9-6. BOUNDARY CONDITION OF THE WALL MODEL 628
FIGURE 9-7. IMPACT OF PRETENSION OF BOLTS FROM PUSHOVER ANALYSIS 630
FIGURE 9-8. SHEAR FORCE AND TOP LATERAL DRIFT CURVE FROM TEST AND FINITE ELEMENT ANALYSIS.....632
FIGURE 9-9. MOMENT AND TOP LATERAL DRIFT CURVE FROM TEST AND FINITE ELEMENT ANALYSIS 632
FIGURE 9-10. VON MISES STRESSES OF THE WALL MODEL IN POSITIVE PUSHOVER ANALYSIS (SOUTHWEST VIEW).633
FIGURE 9-11. VON MISES STRESSES OF THE WALL MODEL IN POSITIVE PUSHOVER ANALYSIS (SOUTHEAST VIEW) .634
FIGURE 9-12. BUCKLING OF HORIZONTAL SPLICE AT 1.5% DRIFT 635
FIGURE 9-13. BUCKLING OF FACEPLATE AND HORIZONTAL SPLICE AT 3.0% DRIFT 635
FIGURE 9-14. CONTACT BETWEEN UPPER AND LOWER PARTS OF FACEPLATES AT DRIFT OF 2.3%.....636
FIGURE 9-15. VON MISES STRESSES OF THE WALL MODEL IN NEGATIVE PUSHOVER ANALYSIS (SOUTHWEST VIEW) 637
FIGURE 9-16. VON MISES STRESSES OF THE WALL MODEL IN NEGATIVE PUSHOVER ANALYSIS (SOUTHEAST VIEW) 638
FIGURE 9-17. YIELDING NEAR BOLT HOLES ON SPLICE WEB AT -3% DRIFT 639

FIGURE 9-18. DEVELOPMENT OF CRACKS OF CONCRETE IN POSITIVE PUSHOVER ANALYSIS (SOUTH VIEW).....641
FIGURE 9-19. FRICTION AND BEARING FORCES AT EACH ROW OF BOLT (DRIFT = 0.1%) 644
FIGURE 9-20. FRICTION AND BEARING FORCES AT EACH ROW OF BOLT (DRIFT = 0.3%) 644
FIGURE 9-21. FRICTION AND BEARING FORCES AT EACH ROW OF BOLT (DRIFT = 0.5%) 645
FIGURE 9-22. FRICTION AND BEARING FORCES AT EACH ROW OF BOLT (DRIFT = 1.0%) 645
FIGURE 9-23. FRICTION AND BEARING FORCES AT EACH ROW OF BOLT (DRIFT =2.0%).....646
FIGURE 9-24. FRICTION AND BEARING FORCES AT EACH ROW OF BOLT (DRIFT = 3.0%) 646
FIGURE 9-25. DEVELOPMENT OF BOLT HOLE DEFORMATION ON COMPRESSION AND TENSION EDGES 647
FIGURE 9-26. FRICTION AND BEARING FORCES AT EACH ROW OF BOLT (DRIFT = -0.1%).....648
FIGURE 9-27. FRICTION AND BEARING FORCES AT EACH ROW OF BOLT (DRIFT = -0.3%).....648
FIGURE 9-28. FRICTION AND BEARING FORCES AT EACH ROW OF BOLT (DRIFT = -0.5%).....649
FIGURE 9-29. FRICTION AND BEARING FORCES AT EACH ROW OF BOLT (DRIFT = -1.0%).....649
FIGURE 9-30. FRICTION AND BEARING FORCES AT EACH ROW OF BOLT (DRIFT = -2.0%).....650
FIGURE 9-31. FRICTION AND BEARING FORCES AT EACH ROW OF BOLT (DRIFT = -3.0%).....650
FIGURE 9-32. SUMMATION OF FRICTION AND BEARING FORCES AT EACH ROW OF BOLT (DRIFT = 1.17%).....652
FIGURE 9-33. SUMMATION OF FRICTION AND BEARING FORCES AT EACH ROW OF BOLT (DRIFT =1.54%).....652
FIGURE 9-34. SUMMATION OF FRICTION AND BEARING FORCES AT EACH ROW OF BOLT (DRIFT = -0.77%) 653
FIGURE 9-35. SUMMATION OF FRICTION AND BEARING FORCES AT EACH ROW OF BOLT (DRIFT =-1.0%).....653
FIGURE 9-36. IMPACT OF PRETENSION OF BOLTS FROM CYCLIC LOADING ANALYSIS.....656
FIGURE 9-37. IMPACT OF PRETENSION OF BOLTS FROM CYCLIC LOADING ANALYSIS (-0.3% TO 0.8% DRIFT).....656
FIGURE 9-38. IMPACT OF PRETENSION OF BOLTS FROM CYCLIC LOADING ANALYSIS (STEPS 1 TO 8).....657
FIGURE 9-39. CYCLIC LOADING PROTOCOL OF FINITE ELEMENT MODEL 660
FIGURE 9-40. SHEAR FORCE AND TOP LATERAL DRIFT CURVE FROM TEST AND FINITE ELEMENT ANALYSIS.....660
FIGURE 9-41. MOMENT AND TOP LATERAL DRIFT CURVE FROM TEST AND FINITE ELEMENT ANALYSIS 661
FIGURE 9-42. VON MISES STRESSES OF THE WALL MODEL IN CYCLIC LOADING ANALYSIS (SOUTHWEST VIEW) 662

FIGURE 9-43. VON MISES STRESSES OF THE WALL MODEL IN CYCLIC LOADING ANALYSIS (SOUTHEAST VIEW) 663
FIGURE 9-44. BUCKLING OF WEB HORIZONTAL SPLICE AT 1.41% DRIFT.....664
FIGURE 9-45.YIELDING NEAR BOLTS AT POSITIVE AND NEGATIVE PEAKS.....664
FIGURE 9-46. SHEAR STRENGTHS OF CONCRETE AND STEEL, DEPICTING (A) ABOVE, (B) AT, (C) BELOW HORIZONTAL SPLICE LEVEL 665
FIGURE 9-47. FLEXURAL STRENGTHS OF CONCRETE AND STEEL AT HORIZONTAL SPLICE LEVEL 665
FIGURE 9-48. PERCENTAGE OF CONCRETE SHEAR FORCE IN CYCLIC LOADING HISTORY (ABOVE HORIZONTAL SPLICE LEVEL).....666
FIGURE 9-49. PERCENTAGE OF CONCRETE SHEAR FORCE IN CYCLIC LOADING HISTORY (HORIZONTAL SPLICE LEVEL) 666
FIGURE 9-50. PERCENTAGE OF CONCRETE MOMENT IN CYCLIC LOADING HISTORY (HORIZONTAL SPLICE LEVEL) ..667
FIGURE 9-51. DEVELOPMENT OF CRACKS OF CONCRETE IN CYCLIC LOADING ANALYSIS (SOUTH VIEW) 668
FIGURE 9-52. FRICTION AND BEARING FORCES AT EACH ROW OF BOLT (STEP 2 POSITIVE, DRIFT =0.32%) 670
FIGURE 9-53. FRICTION AND BEARING FORCES AT EACH ROW OF BOLT (STEP 2 NEGATIVE, DRIFT =-0.18%).....670
FIGURE 9-54. FRICTION AND BEARING FORCES AT EACH ROW OF BOLT (STEP 3 POSITIVE, DRIFT =0.57%) 671
FIGURE 9-55. FRICTION AND BEARING FORCES AT EACH ROW OF BOLT (STEP 3 NEGATIVE, DRIFT =-0.30%).....671
FIGURE 9-56. FRICTION AND BEARING FORCES AT EACH ROW OF BOLT (STEP 4 POSITIVE, DRIFT =0.84%) 672
FIGURE 9-57. FRICTION AND BEARING FORCES AT EACH ROW OF BOLT (STEP 4 NEGATIVE, DRIFT =-0.55%).....672
FIGURE 9-58. FRICTION AND BEARING FORCES AT EACH ROW OF BOLT (STEP 5 POSITIVE, DRIFT =1.12%) 673
FIGURE 9-59. FRICTION AND BEARING FORCES AT EACH ROW OF BOLT (STEP 5 NEGATIVE, DRIFT =-0.79%).....673
FIGURE 9-60. FRICTION AND BEARING FORCES AT EACH ROW OF BOLT (STEP 6 POSITIVE, DRIFT =1.42%) 674
FIGURE 9-61. FRICTION AND BEARING FORCES AT EACH ROW OF BOLT (STEP 6 NEGATIVE, DRIFT =-1.03%).....674
FIGURE 9-62. FRICTION AND BEARING FORCES AT EACH ROW OF BOLT (STEP 7 POSITIVE, DRIFT =1.73%) 675
FIGURE 9-63. FRICTION AND BEARING FORCES AT EACH ROW OF BOLT (STEP 7 NEGATIVE, DRIFT =-1.27%).....675
FIGURE 9-64. SUMMATION OF FRICTION AND BEARING FORCES AT EACH ROW OF BOLT (DRIFT =1.00%).....676

FIGURE 9-65. SUMMATION OF FRICTION AND BEARING FORCES AT EACH ROW OF BOLT (DRIFT = -0.70%) 676
FIGURE 9-66. AXIAL STRAINS AT POSITIVE PEAK IN STEP 2 IN (A) ELEVATION AND (B) 3D 680
FIGURE 9-67. AXIAL STRAINS AT NEGATIVE PEAK IN STEP 2 IN (A) ELEVATION AND (B) 3D 681
FIGURE 9-68. AXIAL STRAINS AT POSITIVE PEAK IN STEP 4 IN (A) ELEVATION AND (B) 3D 682
FIGURE 9-69. AXIAL STRAINS AT NEGATIVE PEAK IN STEP 4 IN (A) ELEVATION AND (B) 3D 683
FIGURE 9-70. AXIAL STRAINS AT POSITIVE PEAK IN STEP 5 IN (A) ELEVATION AND (B) 3D 684
FIGURE 9-71. AXIAL STRAINS AT NEGATIVE PEAK IN STEP 5 IN (A) ELEVATION AND (B) 3D 685
FIGURE 9-72. AXIAL STRAINS AT POSITIVE PEAK IN STEP 6 IN (A) ELEVATION AND (B) 3D 686
FIGURE 9-73. AXIAL STRAINS AT NEGATIVE PEAK IN STEP 6 IN (A) ELEVATION AND (B) 3D 687
FIGURE 9-74. AXIAL STRAINS AT POSITIVE PEAK IN STEP 7 IN (A) ELEVATION AND (B) 3D 688
FIGURE 9-75. AXIAL STRAINS AT NEGATIVE PEAK IN STEP 7 IN (A) ELEVATION AND (B) 3D 689
FIGURE 9-76. PRINCIPAL STRESS VECTORS S11 WITH LOCATION OF STRAIN GAUGES (STEP 4, DRIFT =-0.55%) 690
FIGURE 9-77. PRINCIPAL STRESS VECTORS S33 IN POSITIVE DIRECTION AT (A) STEP 4 (B) STEP 5 (C) STEP 6 (D) STEP 7 691
FIGURE 9-78. PRINCIPAL STRESS VECTORS S11 IN NEGATIVE DIRECTION AT (A) STEP 4 (B) STEP 5 (C) STEP 6 (D) STEP 7 692
FIGURE 9-79. RECORD OF LINEAR POTENTIOMETER AT POSITIVE PEAK IN STEP 1 IN (A) ELEVATION AND (B) 3D 693
FIGURE 9-80. RECORD OF LINEAR POTENTIOMETER AT NEGATIVE PEAK IN STEP 1 IN (A) ELEVATION AND (B) 3D 694
FIGURE 9-81. RECORD OF LINEAR POTENTIOMETER AT POSITIVE PEAK IN STEP 2 IN (A) ELEVATION AND (B) 3D 695
FIGURE 9-82. RECORD OF LINEAR POTENTIOMETER AT NEGATIVE PEAK IN STEP 2 IN (A) ELEVATION AND (B) 3D 696
FIGURE 9-83. RECORD OF LINEAR POTENTIOMETER AT POSITIVE PEAK IN STEP 3 IN (A) ELEVATION AND (B) 3D 697
FIGURE 9-84. RECORD OF LINEAR POTENTIOMETER AT NEGATIVE PEAK IN STEP 3 IN (A) ELEVATION AND (B) 3D 698
FIGURE 9-85. RECORD OF LINEAR POTENTIOMETER AT POSITIVE PEAK IN STEP 4 IN (A) ELEVATION AND (B) 3D 699
FIGURE 9-86. RECORD OF LINEAR POTENTIOMETER AT NEGATIVE PEAK IN STEP 4 IN (A) ELEVATION AND (B) 3D 700
FIGURE 9-87. LP DEFORMATION AFFECTED BY BENDING AND ROTATION OF STEEL PLATES 701

FIGURE 9-88. MERGE OF NODES FOR DOUBLE-SHEAR CONNECTION 702
FIGURE 9-89. SHEAR FORCE AND TOP LATERAL DRIFT CURVE FROM SINGLE-SHEAR AND DOUBLE-SHEAR FINITE ELEMENT ANALYSIS 704
FIGURE 9-90. MOMENT AND TOP LATERAL DRIFT CURVE FROM SINGLE-SHEAR AND DOUBLE-SHEAR FINITE ELEMENT ANALYSIS 704
FIGURE 9-91. VON MISES STRESSES OF THE DOUBLE-SHEAR WALL MODEL IN POSITIVE PUSHOVER ANALYSIS (SOUTHWEST VIEW) 706
FIGURE 9-92. VON MISES STRESSES OF THE DOUBLE-SHEAR WALL MODEL IN POSITIVE PUSHOVER ANALYSIS (SOUTHEAST VIEW) 707
FIGURE 9-93. BUCKLING OF HORIZONTAL SPLICE AT 1.65% DRIFT (DOUBLE-SHEAR) 708
FIGURE 9-94. BUCKLING OF FACEPLATE AND HORIZONTAL SPLICE AT 3.0% DRIFT (DOUBLE-SHEAR) 708
FIGURE 9-95. VON MISES STRESSES OF THE DOUBLE-SHEAR WALL MODEL IN NEGATIVE PUSHOVER ANALYSIS (SOUTHWEST VIEW) 709
FIGURE 9-96. VON MISES STRESSES OF THE DOUBLE-SHEAR WALL MODEL IN NEGATIVE PUSHOVER ANALYSIS (SOUTHEAST VIEW) 710
FIGURE 9-97. YIELDING NEAR BOLT HOLES ON FACEPLATE WEB AT -3% DRIFT 711

3 LIST OF TABLES

TABLE 2-1. EXPERIMENTAL RESULTS AND ANALYTICAL COMPARISONS FOR SC PANEL SPECIMENS SUBJECTED TO AXIAL COMPRESSION AND IN-PLANE SHEAR. (VARMA ET AL., 2011 AND 2014) 7

TABLE 2-2. EXPERIMENTAL RESULTS AND ANALYTICAL COMPARISONS FOR SC PANEL SPECIMENS SUBJECTED TO AXIAL COMPRESSION AND IN-PLANE SHEAR. (VARMA ET AL., 2011 AND 2014) 9

TABLE 2-3. SUMMARY OF BEARING TEST (FRANK AND YURA, 1981) 29

TABLE 2-4. SUMMARY OF BEARING TEST (KIM AND YURA, 1996) 37

TABLE 2-5. SUMMARY OF BEARING TEST (MOŽE, 2018) 43

TABLE 3-1. TENSION TEST SPECIMENS 54

TABLE 3-2 DESIGN LIMIT STATES FOR TENSION TEST 1A/2A/2B/1C/2C 58

TABLE 3-3 DESIGN LIMIT STATES FOR TENSION TEST 4A 58

TABLE 3-4 DESIGN LIMIT STATES FOR TENSION TEST 1A/2A/2B/1C/2C (ACTUAL MATERIAL STRENGTH) 58

TABLE 3-5 DESIGN LIMIT STATES FOR TENSION TEST 4A (ACTUAL MATERIAL STRENGTH) 58

TABLE 3-6. LIST OF TENSION TESTS 61

TABLE 3-7. COUPON TEST RESULTS 71

TABLE 3-8. ORIGINAL LOADING PROTOCOL FOR TENSION TEST 77

TABLE 3-9. SHEAR TEST SPECIMENS 79

TABLE 3-10. DESIGN LIMIT STATES FOR SHEAR TEST 80

TABLE 3-11. DESIGN LIMIT STATES FOR SHEAR TEST (ACTUAL MATERIAL STRENGTH) 81

TABLE 3-12. LIST OF SHEAR TESTS 82

TABLE 3-13. COUPON TEST RESULTS 90

TABLE 3-14. LOADING PROTOCOL FOR SHEAR TEST 94

TABLE 4-1. MODIFIED LOADING PROTOCOL FOR T1 97

TABLE 4-2. MODIFIED LOADING PROTOCOL FOR T2 111

TABLE 4-3. MODIFIED LOADING PROTOCOL FOR T3 128

TABLE 4-4. DEVELOPMENT OF GROSS SECTION AND NET SECTION STRAINS FOR T3 128

TABLE 4-5. MODIFIED LOADING PROTOCOL FOR T4 143
TABLE 4-6. DEVELOPMENT OF GROSS SECTION AND NET SECTION STRAINS FOR T4 149
TABLE 4-7. DEVELOPMENT OF STRAIN I-SHAPED ANCHOR AND ON THE SPLICE PLATES 150
TABLE 4-8. MODIFIED LOADING PROTOCOL FOR T5 159
TABLE 4-9. DEVELOPMENT OF GROSS SECTION AND NET SECTION STRAINS FOR T5 159
TABLE 4-10. MODIFIED LOADING PROTOCOL FOR T6 173
TABLE 4-11. DEVELOPMENT OF GROSS SECTION AND NET SECTION STRAINS FOR T6 173
TABLE 4-12. MODIFIED LOADING PROTOCOL FOR S1 189
TABLE 4-13. MODIFIED LOADING PROTOCOL FOR S2 198
TABLE 4-14. MODIFIED LOADING PROTOCOL FOR S3 209
TABLE 4-15. MODIFIED LOADING PROTOCOL FOR S4 223
TABLE 4-16. MODIFIED LOADING PROTOCOL FOR S5 232
TABLE 4-17. MODIFIED LOADING PROTOCOL FOR S6 245
TABLE 5-1. SPRING NAME AND LENGTH 265
TABLE 5-2. SUMMARY OF SPRING PROPERTIES 273
TABLE 5-3. SPRING NAME AND LENGTH 278
TABLE 5-4. MATERIAL PROPERTIES FOR STEEL 310
TABLE 5-5. MATERIAL PROPERTIES FOR CONCRETE 310
TABLE 5-6. PRESTRESS VALUE USED IN FINITE ELEMENT MODELS 314
TABLE 5-7. MATERIAL PROPERTIES FOR STEEL PARTS 382
TABLE 5-8. MATERIAL PROPERTIES FOR CONCRETE PARTS 382
TABLE 5-9. PRESTRESS VALUE USED IN FINITE ELEMENT MODELS 382
TABLE 5-10. AXIAL LOAD OF SPECIMENS CONSIDERING DIFFERENT ECCENTRICITIES FROM CENTER OF SPECIMEN 386
TABLE 5-11. SUMMARIES OF EFFECT OF AXIAL LOAD 388

TABLE 5-12. ACTUATOR FORCES OF SHEAR SPECIMENS WHEN CONSIDERING INCLINATION 417

TABLE 5-13. COMPARISON OF PEAK SHEAR FORCES OF SHEAR SPECIMENS WITH AND WITHOUT CONSIDERING INCLINATION.....422

TABLE 5-14. DESIGN LIMIT STATES FOR MODELS W1 TO W4.....427

TABLE 5-15. THE RATIOS OF ECCENTRIC BEARING STRENGTH TO NON-ECCENTRIC BEARING STRENGTH IN MODELS W1 TO W4.....427

TABLE 5-16. MAXIMUM TOTAL SHEAR STRENGTH (V_T) IN MODELS W1 TO W4.....433

TABLE 5-17. MAXIMUM STEEL SHEAR STRENGTH V.S. BEARING STRENGTH IN MODELS W1 TO W4 434

TABLE 5-18. CONCRETE SHEAR STRENGTH V.S. ACI SHEAR STRENGTH EQUATION IN MODELS W1 TO W4 439

TABLE 5-19. SHEAR STRENGTH COMPARISON BETWEEN MODELS W4 AND W4_CORE 446

TABLE 5-20. SHEAR STRENGTH PER UNIT LENGTH COMPARISON BETWEEN MODELS W4 AND W4_CORE.....446

TABLE 6-1. GEOMETRIES OF FINITE ELEMENT MODELS.....451

TABLE 6-2. MATERIAL PROPERTIES FOR STEEL PARTS 451

TABLE 6-3. DESIGN LIMIT STATES OF FINITE ELEMENT MODELS (STRENGTH FOR TWO BOLTS IN CASES 2, 3, AND 4) 451

TABLE 6-4. CALCULATED SLIP RESISTANCE FOR MODELS 2, 3, AND 4.....466

TABLE 6-5. INITIAL AND RESIDUAL FRICTION FORCES IN MODELS 2, 3, AND 4.....466

TABLE 6-6. GEOMETRIES OF SPECIMENS T1, T2, AND T3.....478

TABLE 6-7. NOMINAL STRENGTH OF CONCRETE FOR FE MODELS T1, T2, AND T3.....480

TABLE 7-1. PERCENTAGE OF GROSS SECTION YIELDING STRENGTH DEVELOPED BY BOLTED SPLICES 498

TABLE 7-2. SUMMARY OF MOMENT CAPACITY FOR TEST SPECIMEN (DESIGN STAGE).....510

TABLE 7-3. SUMMARY OF MOMENT CAPACITY FOR TEST SPECIMEN (ACTUAL MATERIAL STRENGTH).....510

TABLE 7-4. COUPON TEST RESULTS.....521

TABLE 7-5. ORIGINAL LOADING PROTOCOL FOR WALL TEST 530

TABLE 8-1. MODIFIED LOADING PROTOCOL 538

TABLE 8-2. DEFORMED HOLE DIMENSIONS ON OUTSIDE SPLICE PLATES (UNIT: IN.).....575

TABLE 8-3. DEFORMED HOLE DIMENSIONS ON FACEPLATES (UNIT: IN.) 575

TABLE 9-1. MATERIAL PROPERTIES FOR STEEL PARTS 627

TABLE 9-2. MATERIAL PROPERTIES FOR CONCRETE PARTS 627

TABLE 9-3. FLEXURAL STRENGTH OF BOLTS FROM SIMPLIFIED METHOD AND FINITE ELEMENT ANALYSIS.....654

TABLE 9-4. FLEXURAL STRENGTH OF BOLTS FROM SIMPLIFIED METHOD AND FINITE ELEMENT ANALYSIS.....677

TABLE 9-5. SHEAR AND FLEXURAL STRENGTH COMPARISONS BETWEEN SINGLE-SHEAR AND DOUBLE-SHEAR MODELS.....705

SECTION 1
INTRODUCTION

A Composite Plate Shear Wall/Concrete Filled (C-PSW/CF) consists of two steel faceplates with concrete infill sandwiched in-between. The steel faceplates are connected to each other using tie bars that are embedded in the concrete infill and, in some instances, steel headed stud anchors. The steel faceplates serve as the primary reinforcement for the concrete infill and they also serve as stay-in-place formwork during construction. The concrete infill prevents the inwards local buckling of the steel faceplates thus improving their stability. Recent research co-funded by the CPF and the American Institute of Steel Construction (AISC) has validated the use of this structural system in seismic regions, and has led to implementation in ASCE-7 and AISC 360 and 341.

Most particularly, construction of the 58 story Rainier Square Project in Seattle has showcased the massive reduction in construction time made possible by use of this structural system. This has attracted national attention and a considerable interest for implementation in non-seismic regions. Contractors in many of these regions typically prefer bolted assembly on-site; although many such bolted details for horizontal splices and vertical joints can be developed, none have been experimentally verified. The fact that there exists no experimentally-verified bolted splice details for these walls creates a critical hurdle in large parts of the country where established construction practice relies on field bolting. It is therefore critical to create and experimentally validate the knowledge and details needed to design and build this innovative type of core walls across the nation in those regions where field bolting is the practice.

It is the objective of this research to develop and experimentally validate such bolted splice details for C-PSW/CF, to enable nationwide application of this structural system. Focus here is for application in non-seismic regions, such as New York City and Boston, where bolted splices are preferred over welded ones, and other places where wind demands exceed elastic seismic demands and govern splice design. However, in the process, cyclic response up to the limits permitted by the ASCE Pre standard for Performance-Based Wind Design are to be considered. In parallel, some limited consideration is given to investigate if bolted splices could be used (without being onerous or impractical) in some regions where seismic design governs, with the understanding that splices in that case would have to resist the full yield strength of the connected plates. This could be useful in regions of moderate seismicity, such as Nevada, Idaho, Utah, South Carolina, and many more.

The specific questions to be answered by this research are: (1) whether existing strength equations for steel-only connections are applicable to C-PSW/CF for the desirable and recommended failure mode of bearing failure, particularly with respect to the contribution of friction to the development of that strength; (2) whether different types of bolted splice details can provide equally satisfactory performance; (3) whether the existing stiffness equations can be used for C-PSW/CF with bolted splice plates; (4) what is the ultimate behavior of C-PSW/CF with bolted splices of the type considered here, to better understand what is likely to occur in instances of demands exceeding design levels, and (5) what is the ability of simplified as well as more complex finite element models to capture and explain the behavior of bolted C-PSW/CF.

Chapter 2 of this dissertation reviews the historical development of various composite shear walls across multiple applications, highlights recent advancements, and underscores the necessity of examining bolted

splices in composite plate shear walls. A particular focus of this chapter is to provide a literature review of work on the development of bearing strength equations for bolted connection, as it is the dominant limit state for this study.

The initial phase of the research, presented in Chapters 3 and 4, involved the design and testing of component composite specimens having bolted splices representative of C-PSW/CF connections. The first series, termed Tension Component Tests, included six splice connection specimens subjected to cyclic axial loads. This was followed by a second series, called Shear Component Tests, which comprised six shear splice specimens designed to evaluate connection behavior under cyclic shear and flexural forces. These tension and shear components tests aimed to capture some of the fundamental behaviors of different types of horizontal and vertical splice connections details to be used in wall applications.

Chapter 5 presents findings from analyses conducted to replicate the behaviors observed during the component test. Proposed simplified spring models and finite element analyses were used for this purpose. The simplified spring models were first used to compare with the results from Tension Component Tests. These models were developed to provide a simple and fast approach to replicate the complex behaviors of bolted C-PSW/CF connections. Then, finite element models were developed to replicate the behavior of the tension and shear component specimens and provide more insights on aspects of behavior that could not be experimentally measured. For both tension and shear specimens, the results from finite element models subjected to both monotonic and cyclic loading were compared with the test results.

In Chapter 6, the impact of bolt pretension on the bearing strength of bolted connections was explored. Initially, finite element models of steel-only bolted connections were developed. These models included a single-bolt configuration as well as three double-bolt connection models with different diameters of bolts. The analyses also included a bolted C-PSW/CF connection in tension and in compression similar to the one investigated in Chapter 5. These analyses aimed to develop a better understanding of the relationship between bearing and friction forces in various conditions, and of the related load transfer mechanisms.

Chapters 7 and 8 focuses on the design and test of a C-PSW/CF specimen having vertical and horizontal bolted splices. Chapter 7 describes the design approach for the horizontal and vertical splices, and corresponding test details. Chapter 8 presents the test observations and results for the wall specimen, as well as analysis of the test data.

Finally, Chapter 9 presents the numerical results obtained from the finite element models of the wall specimen featuring bolted splices, to investigate the inelastic behavior of the tested wall specimen and provide more insights on behavior. Monotonic pushover analyses were used to assess the ultimate behavior of the wall specimen, while cyclic loading analyses were conducted to compare inelastic behavior with test results. The overall objectives of this section are to replicate the hysteretic behavior of the tested specimens and to generate additional information from the finite element models that could not be investigated or measured from the test specimen.

SECTION 2
LITERATURE REVIEW

2.1 General

This section offers an overview of previous research conducted on Composite Plate Shear Wall/Concrete Filled (C-PSW/CF) systems. It also examines recent applications of these walls and highlights the critical necessity to develop detailed bolted splice connections. To delve deeper into the specifics of bolted connection behavior, previous research regarding bearing tests of bolted connections have been reviewed to investigate the design of bolted connection details for the C-PSW/CF system.

2.2 Development of Steel Plate Composite Walls

A C-PSW/CF is a lateral force-resistant system comprised of two steel plates separated by concrete infill. Tie bars are used to connect the steel plates together, and the same tie bars and (optionally) steel-headed stud anchors are used to connect these steel plates to the concrete. These walls offer potential advantages over typical reinforced concrete walls due to their relatively high shear strength, high stiffness, deformation capacity, and speed of construction in the field.

The development of composite plate shear walls has been ongoing since the late 1970s. Throughout their evolution over the past decades, these walls have been referred to by various names, such as steel-plate composite (SC) walls, steel/concrete/steel sandwich construction, double skin composite walls, or Bi-Steel™. More recently, the names "Composite Plate Shear Wall/Concrete Filled (C-PSW/CF)" and "SpeedCore" have been adopted for these walls in North America, specifically following the AISC-341 seismic requirements, as a subset of the broader group.

Significant research efforts have been carried out in recent years to explore and understand the behavior, analysis, and design of the C-PSW/CF system. Here, focus is on the in-plane shear and flexural behavior of composite plate shear walls.

An early research effort investigated the in-plane shear behavior of steel-plate composite (SC) walls designed for safety-related nuclear facilities, as shown in Figure 2-1. Varma et al. (2011 and 2014) introduced a mechanics-based model (MBM) for predicting the behavior of SC wall panels under the influence of in-plane membrane forces. Figure 2-2 shows the membrane forces (S_x, S_y, and S_{xy}) and the stress and strain matrices associated with the MBM. In the MBM concept, concrete properties after cracking were assumed to be orthotropic, and the yielding of steel faceplates was determined using the von Mises stress criterion. Table 2-1 presents a comparison between experimental results and calculated values using the MBM. The yield stress ratio between experimental data and calculated values ranged from 1.00 to 1.14.

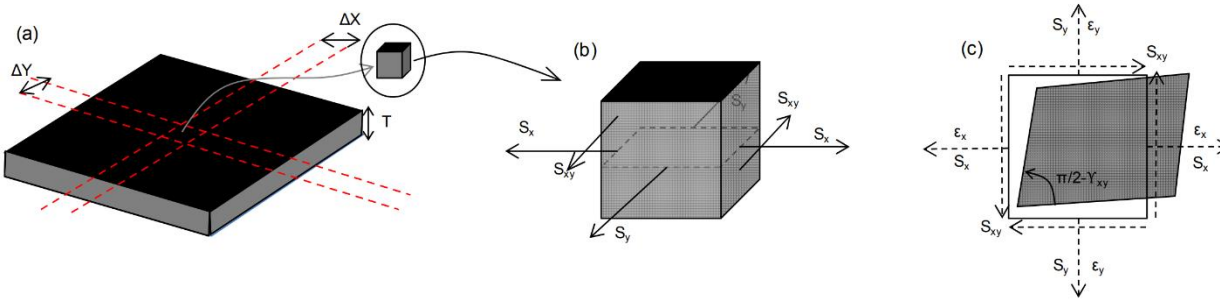


Figure 2-1. (a) Steel-plate (SC) composite wall, (b) Membrane forces, (c) Plane View and Deformations (Varma et al., 2011 and 2014)

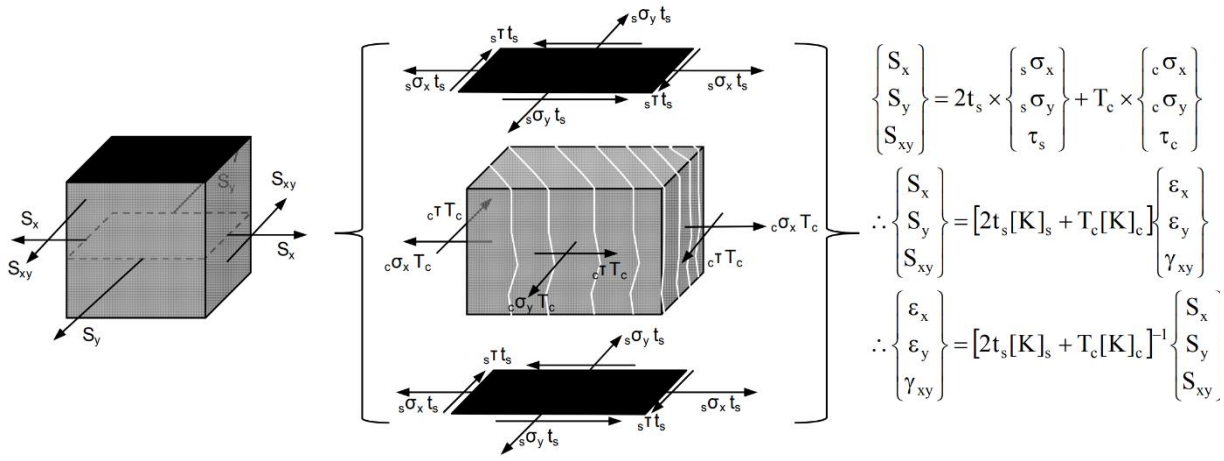


Figure 2-2. Free Body Diagram and Force Equilibrium for Steel-Plate Composite (SC) Section (Varma et al., 2011 and 2014)

Table 2-1. Experimental Results and Analytical Comparisons for SC Panel Specimens Subjected to Axial Compression and In-Plane Shear. (Varma et al., 2011 and 2014)

Specimen	Steel Plate properties		Concrete strength	Stud properties		Experimental Axial Cracking Yielding			Experimental to Analytical Result Comparisons	
	t_p (in.)	F_y (ksi)	f'_c (ksi)	d (in.)	Stud s/t_p	S_x^{exp} (kips)	S_{cr}^{exp} (kips)	$S_{xy}^{Y\text{-}exp}$ (kips)	$\frac{S_{cr}^{exp}}{S_{cr}^{calc}}$	$\frac{S_{xy}^{Y-exp}}{S_{xy}^{Y-calc}}$
S2-00-NN	0.09	49.3	6.1	0.16	30	0	65.8	493.9	1.01	1.14
S2-15-NN	0.09	49.3	6.1	0.16	30	-79	97.2	518.6	1.05	1.11
S2-30-NN	0.09	49.3	6.1	0.16	30	-158	121.7	568.0	1.08	1.15
S3-00-NN	0.13	50.9	6.1	0.20	31	0	69.8	689.2	1.04	1.14
S3-15-NN	0.13	50.9	6.1	0.20	31	-79	86.2	700.4	0.91	1.11
S3-30-NN	0.13	50.9	6.1	0.20	31	-158	86.4	691.4	0.76	1.05
S4-00-NN	0.18	50.2	6.2	0.35	30	0	78.3	793.6	1.10	1.00

Based on the MBM concept, Seo et al. proposed an in-plane shear strength (V_n^{MBM}) formula (Equations 2-1 to 2-3) in 2015 as follows:

$$V_n^{MBM} = \frac{K_s + K_{sc}}{\sqrt{3K_s^2 + K_{sc}^2}} A_s f_y \quad \text{Equation 2-1}$$

$$K_{sc} = \frac{1}{\frac{4}{0.7E_c A_c} + \frac{2(1-\nu_s)}{E_s A_s}} \quad \text{Equation 2-2}$$

$$K_s = G_s A_s \quad \text{Equation 2-3}$$

In these equations, $K_s =$ plane stress properties of steel faceplates; $K_{sc} =$ orthotropic properties for the 45˚ cracked concrete; $G_s =$ shear modulus of steel; and A_s and $A_c =$ cross-sectional area of steel faceplates and of concrete infill. This in-plane shear strength corresponds to the limit state of von Mises yielding of the steel faceplates and includes the contribution of the concrete infill in the principal compression direction.

Table 2-2 presents a comparative database of the MBM-based in-plane shear strength (V_n^{MBM}) in contrast to the shear strengths of Reinforced Concrete (RC) Walls using the ACI 349M-06 code (V_n^{ACI}) and safety-related facilities utilizing the AISC N690s1 standards (V_n^{AISC}). The dataset consists of 26 specimens analyzed using the mentioned approaches. The table reveals that the ACI 349M-06 code equation overestimates the in-plane shear strength for eight of the 26 SC wall specimens. In contrast, the MBM and AISC N690s1 code equations predict the in-plane shear strength conservatively because they focus on the limit state of faceplate yielding, which was achieved during the test.

Table 2-2. Experimental Results and Analytical Comparisons for SC Panel Specimens Subjected to Axial Compression and In-Plane Shear. (Varma et al., 2011 and 2014)

Comparison of complete database with design equations.

		Specimen name	$\frac{V^{,exp}}{A_g f'_c}$	$\frac{V^{,exp}}{V_n^{ACI}}$	$\frac{V^{,exp}}{V_n^{MBM}}$	$\frac{V^{,exp}}{V_n^{AISC}}$
SC wall specimens with flange walls	Funakoshi et al. [7]	BS70T05	0.49	1.07	1.26	1.24
		BS50T10	0.33	1.31	1.54	1.56
		BS70T10	0.34	1.22	1.42	1.44
		BS85T10	0.31	1.15	1.34	1.36
		BS70T14	0.31	1.46	1.74	1.81
	Takeuchi et al. [8]	H07T10	0.29	1.22	1.51	1.50
		H10T05	0.39	0.91	1.12	1.04
		H10T10	0.20	0.93	1.14	1.16
		H10T10N	0.25	1.13	1.39	1.41
		H10T10V	0.39	1.77	2.18	2.21
		H10T15	0.27	1.57	2.04	2.12
		H15T10	0.21	1.02	1.21	1.22
	Fujita et al. [9]	No. 1	0.24	0.89	1.05	1.05
		No. 2	0.38	1.04	1.23	1.19
		No. 3	0.42	1.14	1.34	1.30
		No. 4	0.35	1.12	1.31	1.28
	Varma et al. [10]	WH1	0.29	0.90	1.02	1.04
SC wall panel specimens	Ozaki et al. [5]	S200NN	0.22	0.97	1.16	1.17
		S215NN	0.23	1.02	1.21	1.23
		S230NN	0.25	1.12	1.32	1.35
		S300NN	0.31	1.00	1.17	1.14
		S315NN	0.31	1.02	1.19	1.16
		S330NN	0.32	1.00	1.17	1.15
		S400NN	0.34	0.86	1.02	0.99
	Lee et al. [6]	S30/400F3.2 N00-2	0.10	0.61	0.72	0.70
		S30/400F3.2 N08	0.10	0.61	0.72	0.70
Mean of 24 tests (not including Lee et al.)				1.12	1.34	1.34
Coefficient of variation (not including Lee et al.)				0.20	0.22	0.24

Furthermore, this MBM-based in-plane shear strength formula was adopted in AISC 360-22, and the equation for K_{sc} was updated with an algebraically equivalent equation as shown in Equation 2-4:

$$K_{sc} = \frac{0.7(E_c A_c)(E_s A_{sw})}{4E_s A_{sw} + E_c A_c} \qquad \text{Equation 2-4}$$

Recent research was also conducted to study the in-plane inelastic flexural behavior of C-PSW/CF toward the goal of implementation into AISC-341 and AISC-360. Alzeni and Bruneau (2014, 2017) conducted tests on four large-scale Concrete-filled sandwich steel panel (CFSSP) wall specimens to investigate the in-plane flexural behavior of walls with and without boundary elements. Figure 2-3 and Figure 2-4 show the details of the tested specimens and the test setup. The test results for the four specimens are presented in Figure 2-5. The four tested specimens demonstrated the ability to maintain their strength up to drift levels exceeding 3%. These specimens were reported to exhibit displacement ductility ratios (Δ_u/Δ_y) ranging from 3.67 to 5.5.

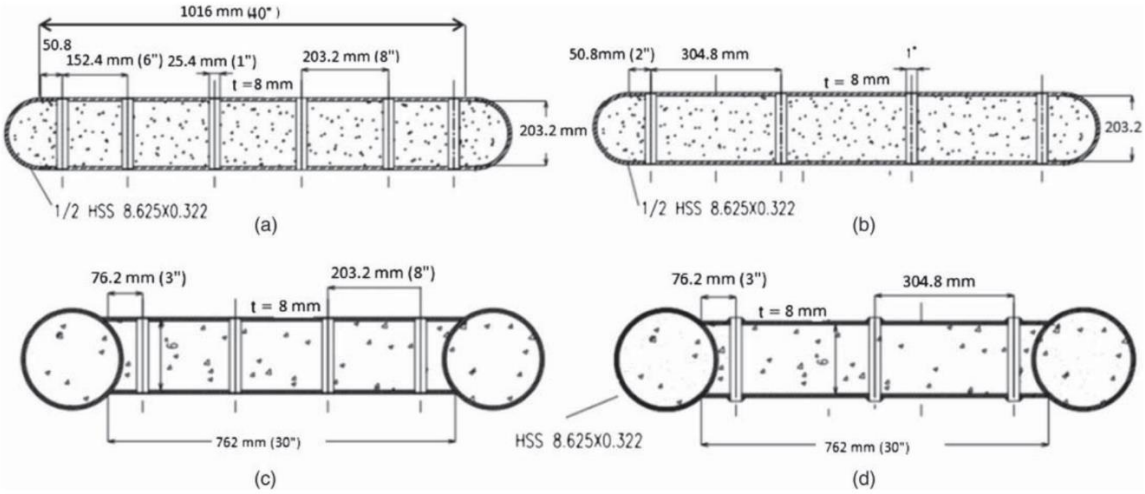
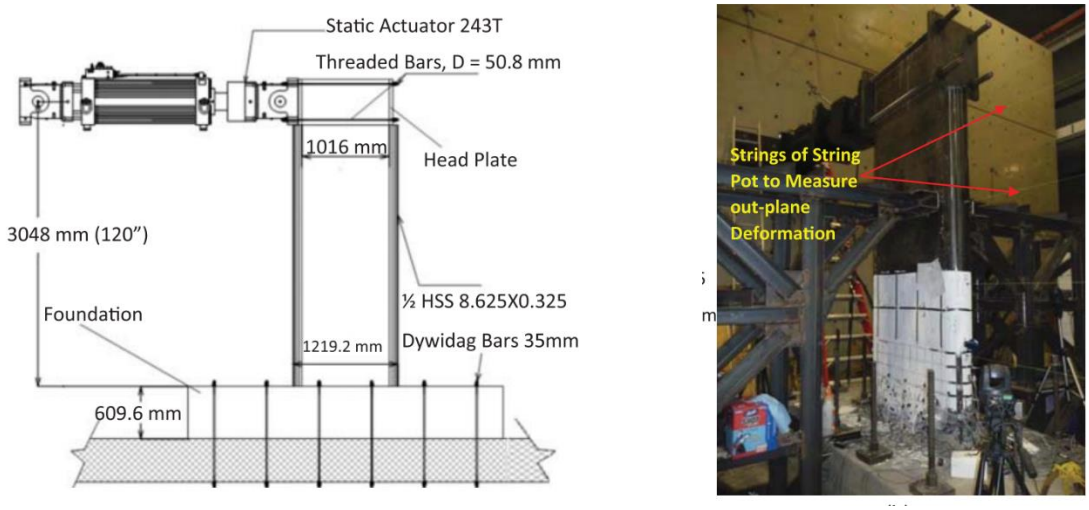


Figure 2-3. CFSSP Specimens: (a) CFSSP-NB1; (b) CFSSP-NB2; (c) CFSSP-B1; (d) CFSSP-B2 (Alzeni and Bruneau, 2017)



(a) Elevation of Test Setup (b) Photo of Test Setup

Figure 2-4. Test Setup for CFSSP Specimens (Alzeni and Bruneau, 2017)

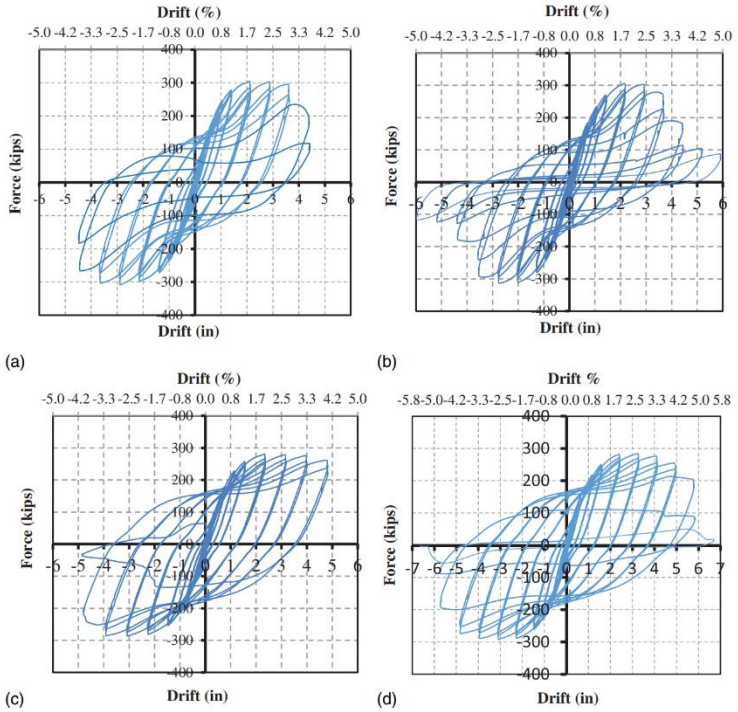


Figure 2-5. Test Results of CFSSP Specimens: (a) CFSSP-NB1; (b) CFSSP-NB2; (c) CFSSP-B1; (d) CFSSP-B2 (Alzeni and Bruneau, 2017)

Shafaei et al. (2021) conducted experiments involving five planar C-PSW/CF specimens that were subjected to both axial compression and cyclic lateral loading. Figure 2-6 shows detailed information about these C-PSW/CF specimens. In the set of five specimens tested, the tie spacing ratio (S_{tie}/t_{sc}) varied ranging from 0.5 to 1.0. Additionally, the applied axial load was varied across the specimens, with values ranging from 10% to 30% of the compressive strength of the concrete area ($A_g f'_c$).

Figure 2-7 shows the test results obtained for the five planar C-PSW/CF specimens. The peak flexural strength for these specimens was recorded during a loading cycle corresponding to 3 times the yielding displacement of the wall, referred to as Δ_y. The load capacity dropped to less than 80% of its maximum during the loading cycles at $4\Delta_y$. The displacement ductility ratio across all specimens ranged from 4.1 to 5.6.

Kenarangi et al. (2021) conducted tests on two large-scale C-shaped C-PSW/CF (Composite Plate Shear Wall/Concrete Filled) specimens subjected to axial load and lateral cyclic loading. Figure 2-8 shows the cross-section detail and the test setup of the C-shaped specimen. The dimensions of the C-shaped specimen were: wall height (H) at 166 in., flange length (h) at 97.5 in., web length (b) at 30 in., steel plate thickness (t) at 0.1875 in., flange thickness (d) at 6 in., web thickness (c) at 8.375 in., tie spacing at 6 in., and tie diameter at 0.5 in. The two C-shaped specimens, C1 and C2, differed in terms of their concrete strength (f'_c) and applied axial loads. Specimen C1 had a concrete strength of 4.5 ksi and an axial load of 19% of $A_g f'_c$, while specimen C2 had a concrete strength of 5.1 ksi and an axial load of 15% of $A_g f'_c$.

Figure 2-9 shows the test results of the C-shaped specimens. Both specimens reached their peak strength at the same lateral displacement, corresponding to $2\Delta_y$' (where Δ_y' represents the equivalent yield displacement obtained from a bi-linear backbone curve of the hysteretic behavior). Local buckling was

observed during the loading cycle at $1.5\Delta_y$', while fracture initiation occurred during the loading cycle at $3\Delta_y$'. The displacement ductility ratio for both specimens exceeded 4 when the flexural strength dropped to 80% of its peak value. Additionally, both specimens reached or exceeded their calculated plastic moment capacities in the positive and negative directions, respectively.

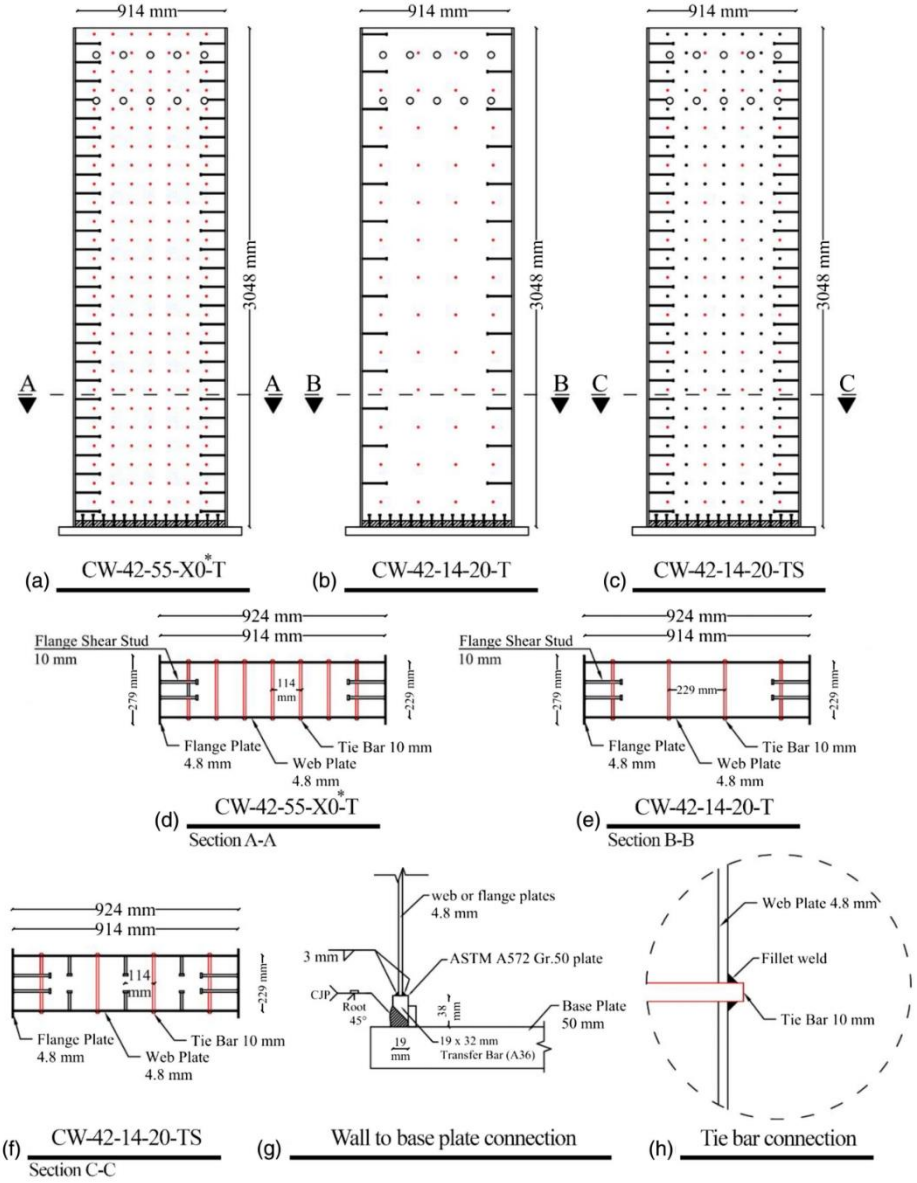


Figure 2-6. Details of planar C-PSW/CF Specimens (Shafaei et al., 2021)

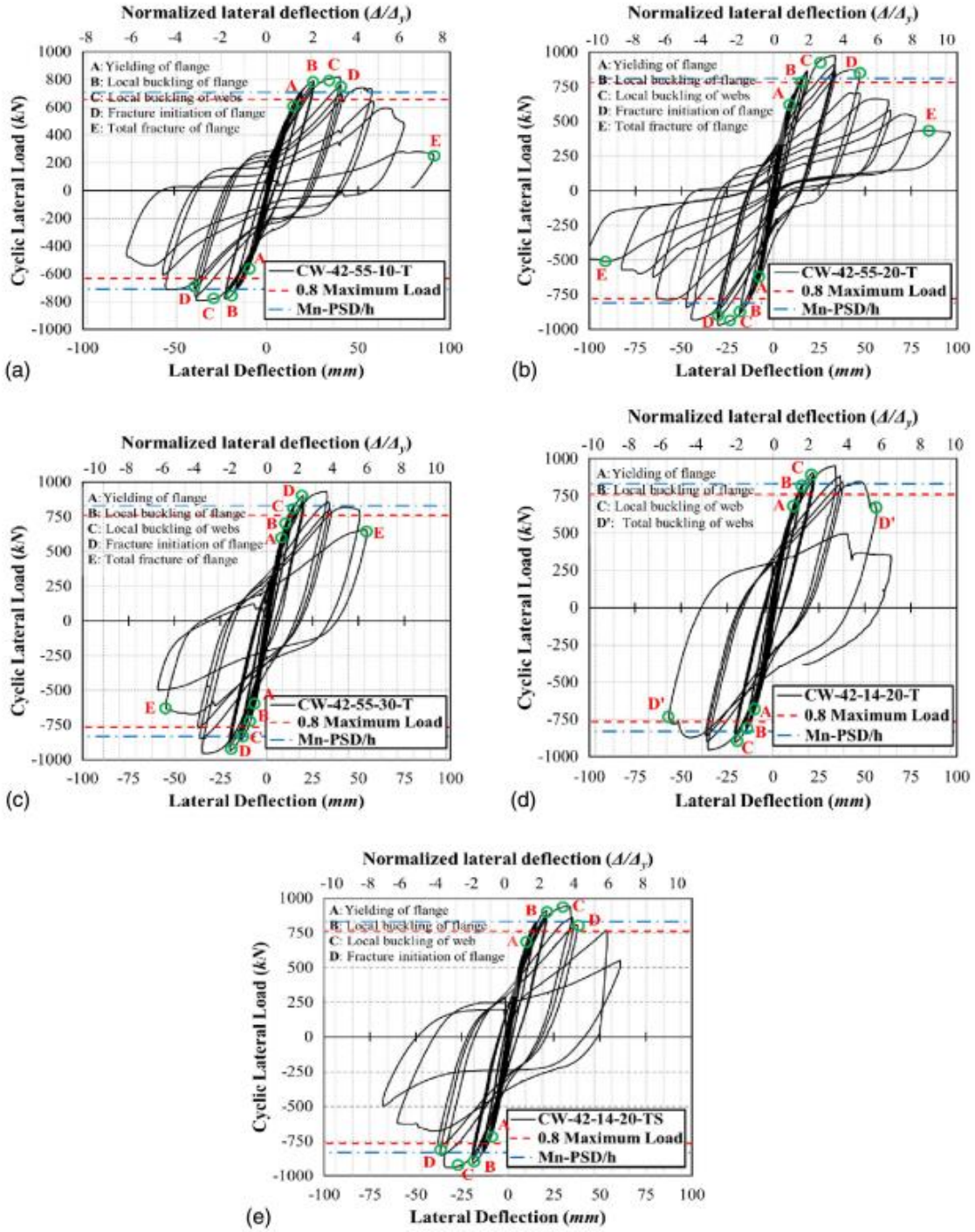
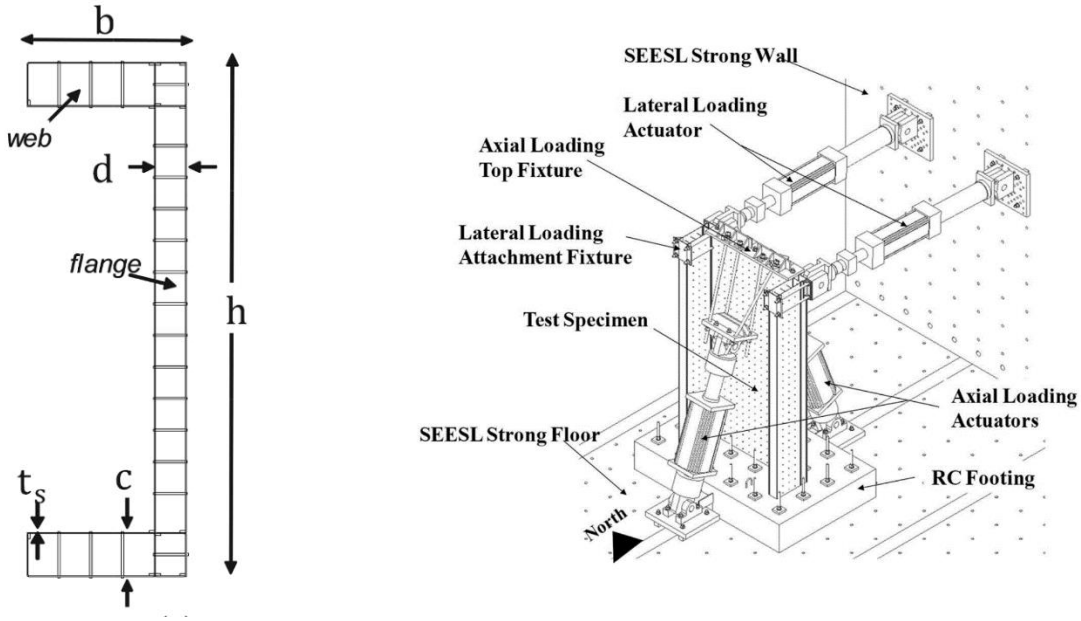
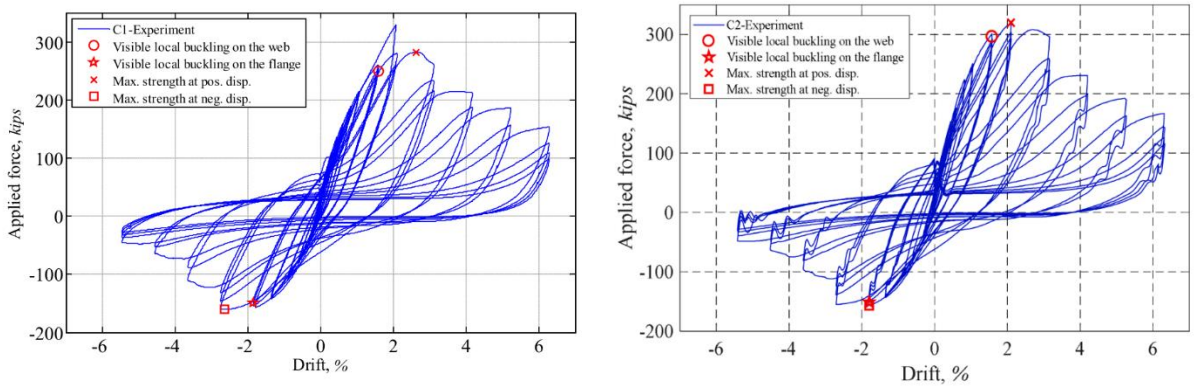


Figure 2-7. Test Results of planar C-PSW/CF Specimens (Shafaei et al., 2021)



(a) Cross-Section Details (b) Test Setup 3D

Figure 2-8. Details of C-Shaped C-PSW/CF Specimens (Kenarangi et al., 2021)



(a) Specimen C1 (b) Specimen C2

Figure 2-9. Test Results of C-Shaped C-PSW/CF Specimens (Kenarangi et al., 2021)

Kizilarslan and Bruneau (2023) conducted experiments on four T-shaped C-PSW/CF (Composite Plate Shear Wall/Concrete Filled) specimens subjected to axial load and cyclic lateral load. The T-shaped specimens were designed with dimensions corresponding to half of the C-shaped walls previously tested by Kenarangi et al. (2021). This reduction in concrete area allowed for the application of axial loads up to 30% of $A_g f'_c$. All four specimens shared the same dimensions except for tie spacing and tie diameter: Among the four specimens, the tie diameter was changed from 0.5 in. to 0.25 in. and the tie spacing was varied from 6 in. to 4.5 in.

Figure 2-11 shows the test results of the four T-shaped specimens. Note that specimen T1 was subjected to 2120 cycles up to a local peak strain of $1.5\varepsilon_y$ as a wind loading protocol, while seismic loading protocols were applied to specimens T2, T3, and T4. The peak strength was achieved at drifts of 1.81%/-1.66% for specimen T2 and at drifts of 1.35%/-2.49% for specimens T3 and T4. At a displacement amplitude of $1.5\Delta y'$, local buckling initiation was observed at the bottom of all specimens. However, the capacity of the walls did not start to drop until the steel plates started to fracture. The displacement ductility ratios, calculated at the point when flexural strength dropped to 80% of the peak value developed, were 2.13/-3.23, 3.07/-2.77, and 2.29/-2.60 for Specimens T2, T3, and T4, respectively.

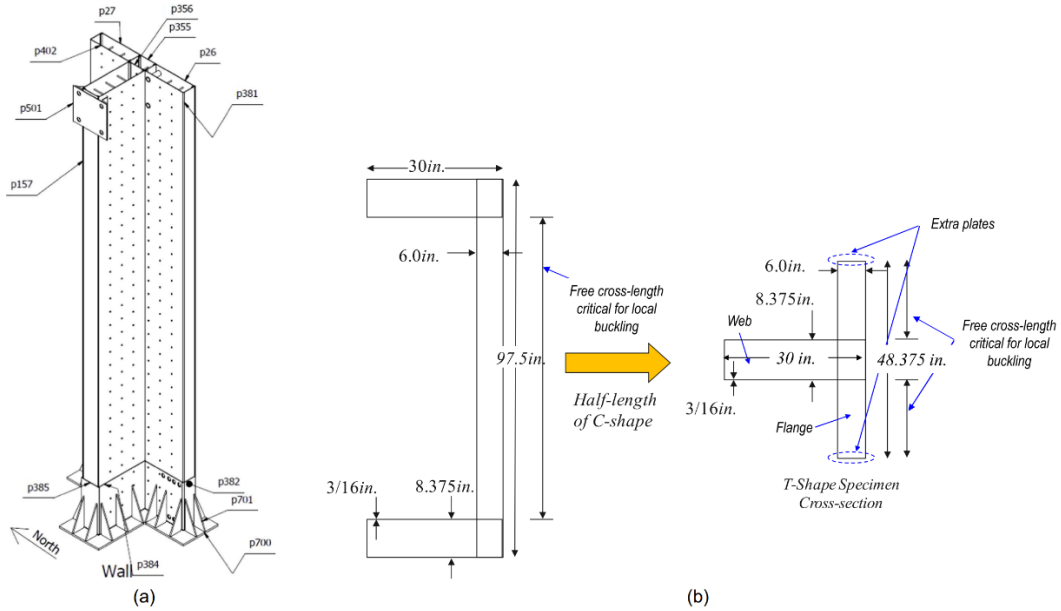


Figure 2-10. Details of T-shaped C-PSW/CF Specimens: (a) 3D Test Specimen (b) T-shape specimen cross-section dimensions (Kizilarslan and Bruneau, 2023)

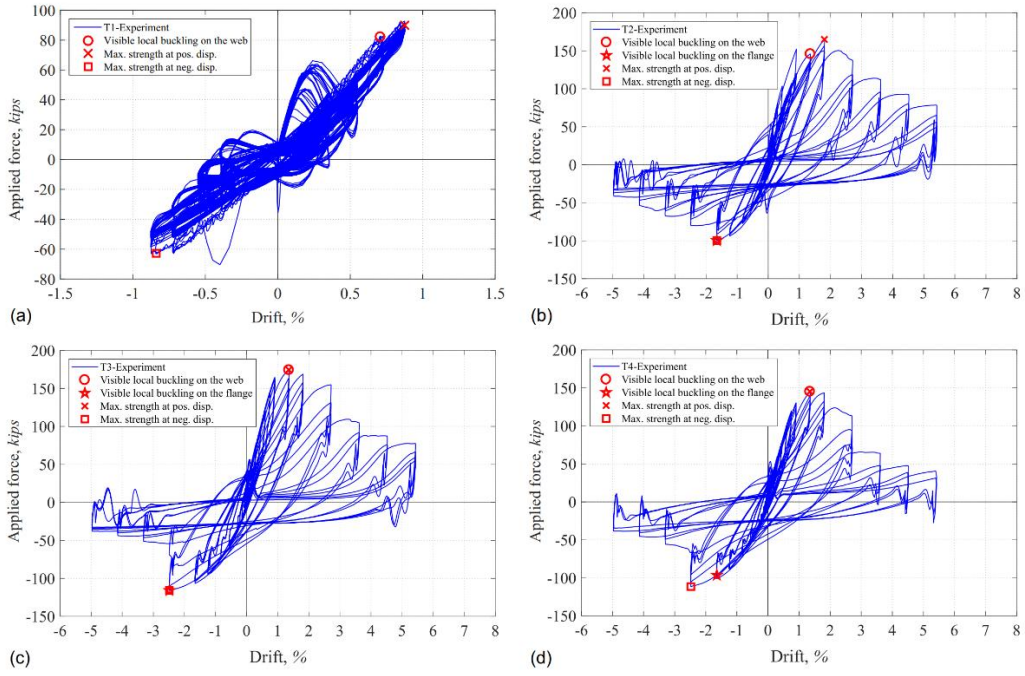


Figure 2-11. Test Results of T-shaped C-PSW/CF Specimens: (a) Specimen T1; (b) Specimen T2; (c) Specimen T3; (d) Specimen T4 (Kizilarslan and Bruneau, 2023)

From 2016 to the present, the AISC (American Institute of Steel Construction) has published updated versions of its AISC-360 and AISC-341 specifications. The above research results on C-PSW/CFs have been incorporated into these standards. C-PSW/CF design requirements were first introduced in AISC 341-16, focusing on planar walls with half-circular or circular boundaries (Alzeni and Bruneau, 2014), and planar walls without boundary elements (Kurt et. al., 2016). In the AISC 341-22 edition, design for C-shaped, I-shaped, and planar walls were also included, however, the planar walls without boundary elements were not permitted anymore based on the research from Agrawal et al. (2020). Design requirements for planar walls with closure or flange plates were also updated in AISC 341-22 based on test data from Shafaei et al. (2021).

2.3 Recent Applications and Requirements for Bolted Splice Details

The 58-story Rainier Square tower (Figure 2-12), situated in downtown Seattle, was the pioneering structure in a severe seismic region to use C-PSW/CF (Composite Plate Shear Wall/Concrete Filled) as its force-resisting system. Since walls were used for the elevator core, with multiple openings, the building actually used a coupled composite plate shear walls/concrete-filled (CC-PSW/CF) system (Figure 2-13). As detailed in the AISC Design Guide 38 (Varma et al. 2023) and elsewhere (e.g., Russell Fortmeyer, 2021), the composite wall had various thicknesses over its height, ranging from 45 in. at its base to approximately 21 in. at its upper levels. The tie bars, with a diameter of 1 in., were positioned at 12-in. intervals in both horizontal and vertical orientations. The typical thickness of the steel plates used was 0.5 in., with some thicker plates used locally near openings. Trade literature referring to this and other recent projects typically used the term SpeedCore instead of C-PSW/CF and CC-PSW/CF.

The construction of the Rainier Square tower leveraged the advantages of the SpeedCore system. The original construction schedule for the reinforced concrete (RC) shear walls alternative was estimated to be 21 months after the arrival of steel on-site. However, switching to the SpeedCore system significantly reduced the construction schedule to just 12 months, representing a 43% reduction in schedule for this first implementation of the SpeedCore system in a high-rise building.

Following the Rainier Square project, the second building is a severe seismic region to use the SpeedCore system was the 200 Park Avenue building (Figure 2-14). This is a 19-story, 1.3-million-square-foot commercial office building situated in San Jose, California. The primary lateral force resisting system used in this structure was a CC-PSW/CF system, as shown in Figure 2-15.



Figure 2-12. 3D rendering view of Rainier Square (AISC Design Guide 38, Varma et al., 2023)

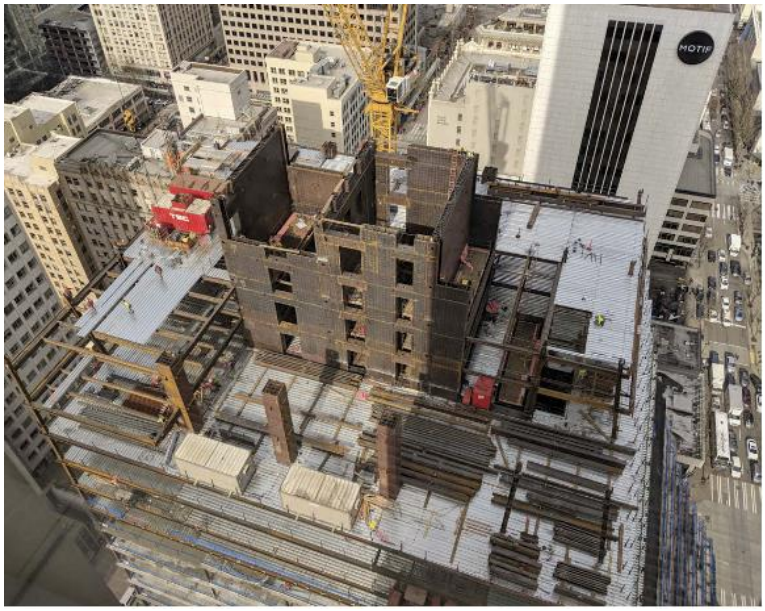


Figure 2-13. Photographs of coupled C-PSW/CF system under construction in Rainier Square (AISC Design Guide 38, Varma et al., 2023)



Figure 2-14. 3D rendering view of 200 Park Avenue (AISC Design Guide 38, Varma et al., 2023)

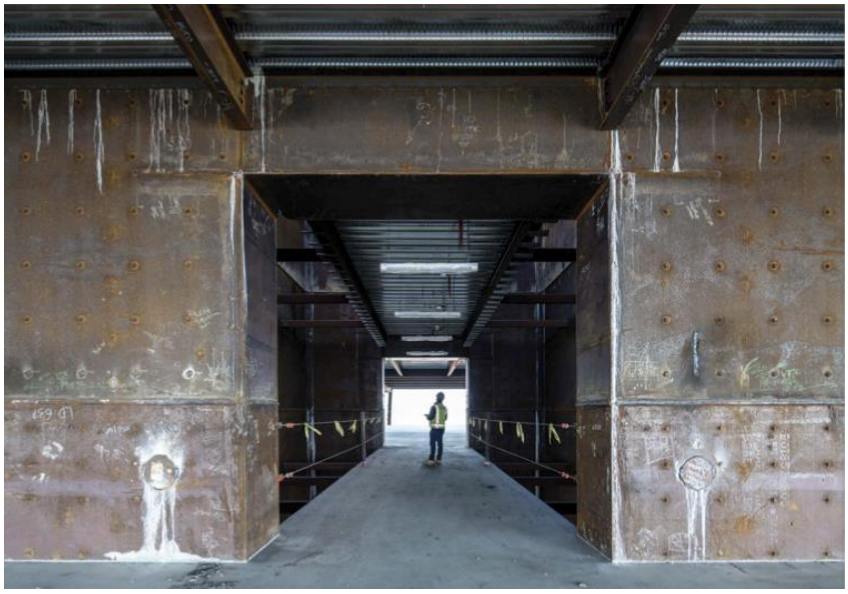


Figure 2-15. Close-up view of coupled C-PSW/CF system under construction in 200 Park Avenue (AISC Design Guide 38, Varma et al., 2023)

More relevant to the research presented in the next chapters, focusing on Speedcore with bolted splices for buildings located in low-seismic areas or those designed based on wind load considerations, a recent project in Boston has proposed to use bolted connection for all splice regions (ENR 2023). Note that in many parts of the United States, it is common practice to use bolted splices instead of welding, marking a significant departure in detailing from the Rainier Square and 200 Park Avenue projects. Due to the absence of prior research on the bolted connections of the SpeedCore system, it is desirable to experimentally validate the behavior of bolted splice connections in C-SPW/CF.

Figure 2-16 shows a typical elevation of the C-PSW/CF wall system implemented in the Boston project. The figure schematically identifies the locations of vertical and horizontal splices. When a specific wall panel is subjected to lateral forces, as shown in Figure 2-17, it results in story shear forces and bending moments at the base of the wall panel. In the splice system, the vertical splices are required to transfer vertical shear forces (or shear flows) between individual panels. Meanwhile, the horizontal splices are designed to resist both the story shear force and bending moment generated by the lateral forces. In the context of tall buildings, wall design is predominantly influenced by flexural behavior. Consequently, the in-depth investigation into the localized behavior of such bolted splices presented in the next chapters is timely.

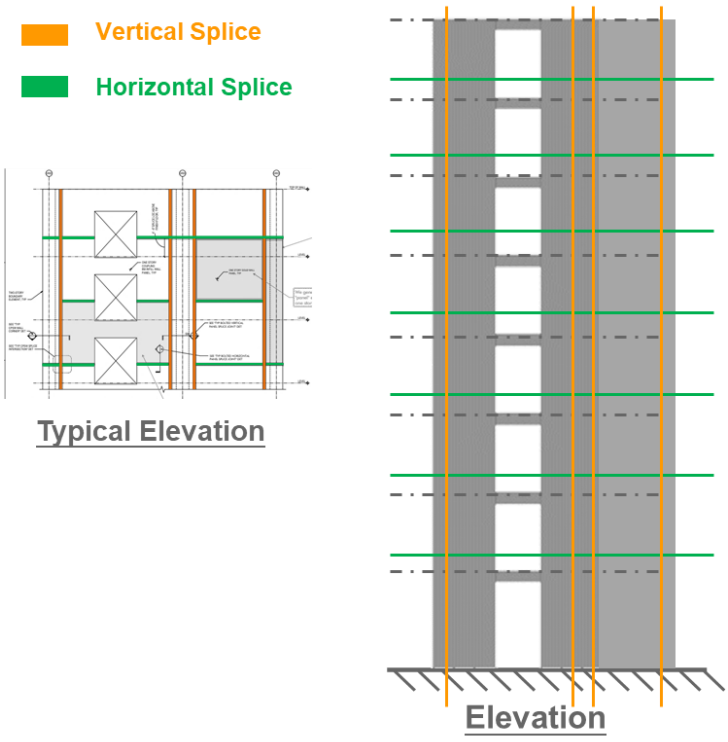


Figure 2-16. Elevation showing Vertical and Horizontal Splices in Boston Project (personal communication, MKA, June 2021.)

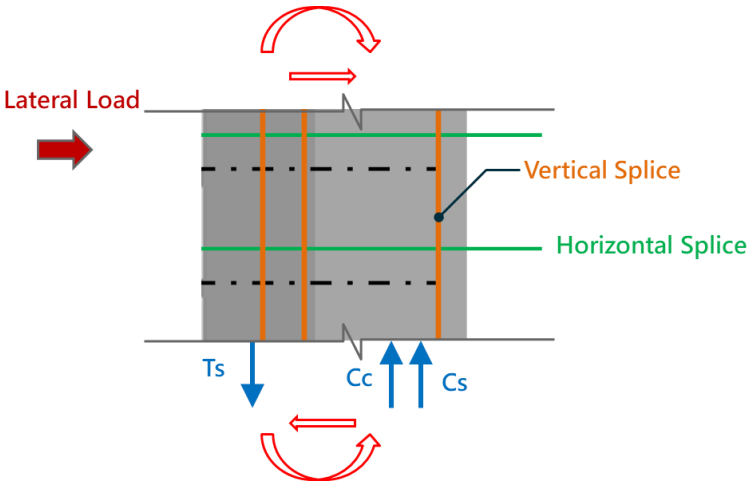


Figure 2-17. Free-Body Diagram of a Wall Segment with Vertical and Horizontal Splices

2.4 Target Limit States of Bolted Splice Connections

When designing a bolted splice connection for buildings, several types of design limit states are considered. These limit states include slip-critical resistance, bearing strength, tear-out strength, net section and gross section yielding strengths, net section rupture, block shear, and bolt shear strength. The dominant limit states for this study will be the bearing strength, as demonstrated later. A brief literature review on this topic is therefore warranted at this point.

In previous studies, bearing and tear-out strength were often examined together due to the challenge of separating them. The bearing and tear-out strength of bolted connections specified in AISC 360 Specification are defined by the following equations, qualified as to whether deformation at the bolt hole at service load is a design consideration (Equations 2-5 and 2-7) or not (Equations 2-6 and 2-8):

Bearing Strength

$$R_n = 2.4dtF_u \quad \text{Equation 2-5}$$

$$R_n = 3.0dtF_u \quad \text{Equation 2-6}$$

Tear-out Strength

$$R_n = 1.2L_ctF_u \quad \text{Equation 2-7}$$

$$R_n = 1.5L_ctF_u \quad \text{Equation 2-8}$$

where d is the bolt diameter, t is the thickness of the plate, L_c is the clear distance (in the direction of force) between the edge of the hole and the edge of the adjacent hole or edge of the material, and F_u is the tensile strength of the plate.

As reported in the commentary of the Specification, Frank and Yura (1981) demonstrated that hole elongation greater than 0.25 in. will generally begin to develop as the bearing force is increased beyond $2.4dtF_u$, especially if it is combined with high tensile stress on the net section, even though rupture does not occur. An upper bound of $3.0dtF_u$ is specified, which anticipates hole ovalization, defined as a deformation greater than 0.25 in. at maximum strength. However, it remains unclear how this specific value was derived, under what conditions bearing stresses reach this limit, and the progression of bearing stresses during loading. To gain a more comprehensive understanding of this bearing behavior in bolted connection, the subsequent section provides a review of prior relevant research.

2.4.1 Previous Research on Bearing-Type Bolted Connections

Frank and Yura (1981) conducted an experimental study on bolted shear connections. Figure 2-18 shows the typical test specimens using a symmetric butt splice designed to fail in its splice plates. The splice plates consisted of nominal 0.25-in. A36 steel plates, and 1 in. diameter A490 bolts were used to resist double shear stresses. The specimens with standard holes had widths ranging from 2 to 8 in., and edge distance *L* varying from 3 to 9 in (*L/d* = 3 to 9), while the bolt spacing remained constant at 3 in.

The plate bearing stress σ_b in the report calculated using the following equation:

$$\sigma_b = \frac{P}{ndt} \qquad \text{Equation 2-9}$$

where P is the applied axial load of the connection, n is the number of bolts, d is the diameter of bolts, and t is the thickness of the steel plate.

Figure 2-19 shows a typical comparison between bearing failure and net section failure types of the un-torqued (snug-tightened) specimens. In the figure, Load Stage 1 (LS1) corresponds to the elastic limit of the specimen, Load Stage 2 (LS2) represents the yielding of the net section of the specimen, and Load Stage 3 (LS3) indicates slight necking and extensive yielding for net section failure-type connections. In the bearing-controlled connections, the bearing stress reached approximately $2.0F_u$ at a deformation close to 0.2 in (elastic limit). At a 0.25-in. deformation (measured from the center of an end bolt to the edge of the steel plate.), the bearing stress was equal to $2.238F_u$, and failure occurred at a bearing stress of $2.67F_u$ at a deformation close to 1.0 in. In comparison, for net section failure type connections, both bearing deformation and net section elongation contributed to some extent to the deformation value at LS2. At net section failure stage (LS3), the splice plates reached their net section tensile strength before the bearing stress reached the previous stress limit of $2.67F_u$.

To compare the effect of bolt clamping forces, Figure 2-20 shows the test results for specimens with torqued and un-torqued bolts for the bearing and net section failure type connections. The findings indicate that fully torqued bolts exhibit a 10 percent higher capacity compared to snugged bolts when failure is defined as the point when deformation is equal to 0.25 in. However, no increase in capacity is observed when failure is defined in terms of ultimate load for the bearing-controlled connections.

Table 2-3 summarizes all bearing test results conducted by Frank and Yura (1981). In the table, it can be observed that for the bearing-controlled connections (Labeled "2" in column 3 in the table) with round holes, the bearing strength ranged from $2.25F_u$ to $2.35F_u$ at 0.25 in. deformation, but the ultimate bearing strength developed ranged from $2.57F_u$ to $2.85F_u$. Frank and Yura mentioned that since bearing-type connections did not gain much capacity after 0.25 in. deformation, this deformation value was then chosen as a limit state for bolt hole deformation. They also indicated that the value of bearing stress at failure is significantly influenced by the amount of lateral confinement applied to the stressed material. In cases where surfaces are fully restrained, such as the inside splice plates of symmetrical butt splices tested by Struik and Wittermans (1968) with fully torqued bolts, the connections achieved ultimate load at bearing stresses ranging from $3.0F_u$ to $3.5\ F_u$ (no corresponding deformation data was reported). However, on unrestrained surfaces, such as the outside splice plates of symmetrical butt splices, ultimate load was reached at bearing stresses of $2.0F_u$ to $2.8F_u$. Also, as shown in Figure 2-21, bending of the splice plates due to bolt deformation was observed in the free end of the plate (i.e., beyond the last bolt) during the test.

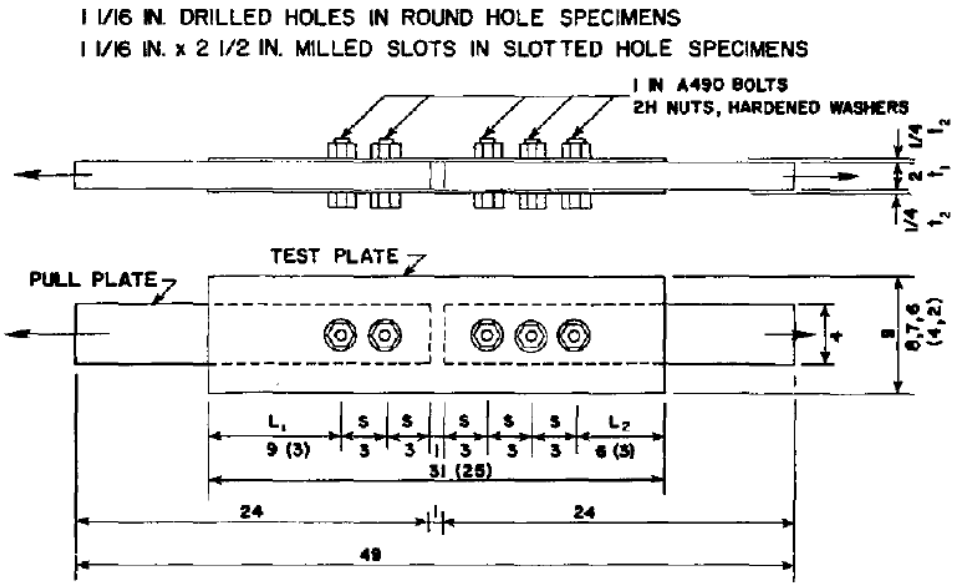


Figure 2-18. Bearing Critical Test Specimens (Frank and Yura, 1981)

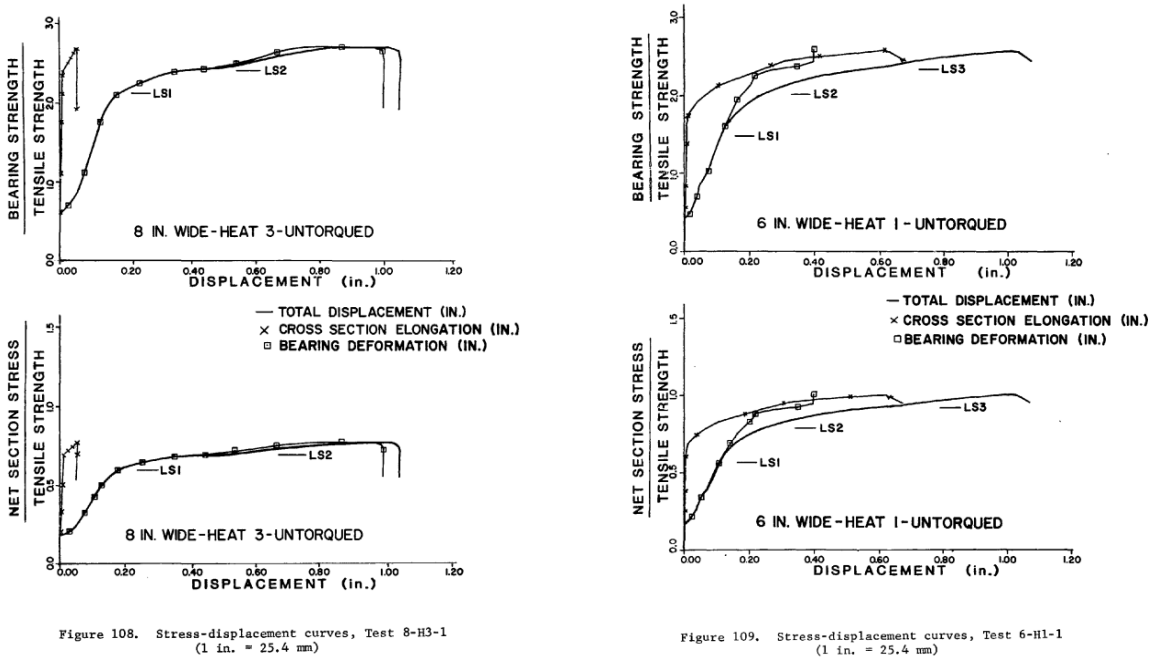
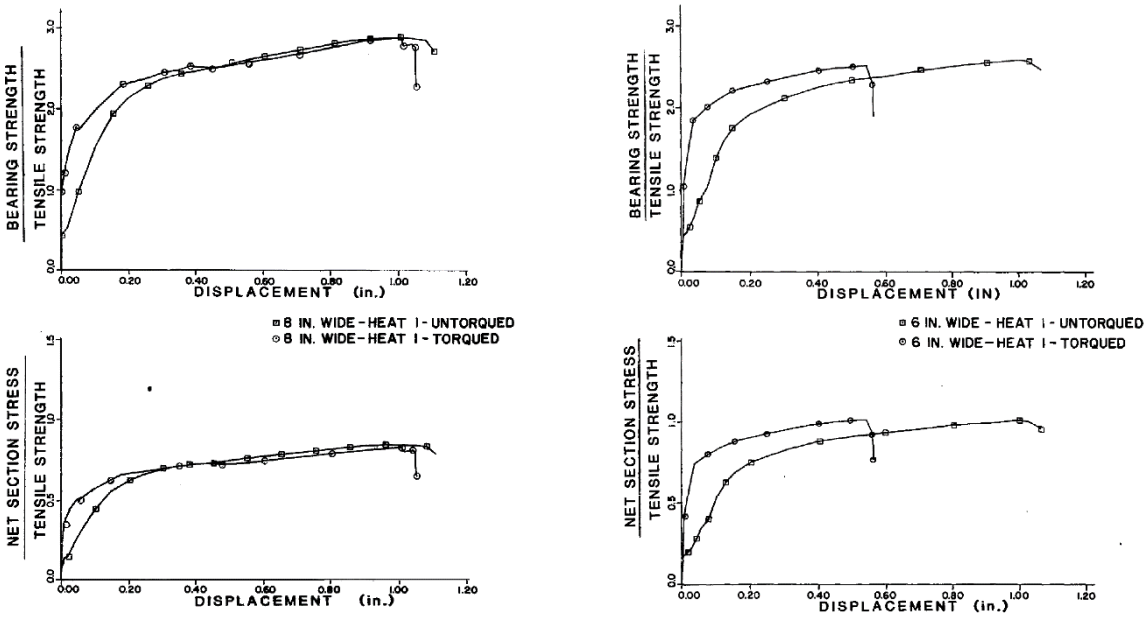


Figure 108. Stress-displacement curves, Test 8-H3-1 (1 in. = 25.4 mm)

Figure 109. Stress-displacement curves, Test 6-H1-1 (1 in. = 25.4 mm)

(a) Bearing Failure Type (b) Net Section Failure Type

Figure 2-19. Test Results of the Un-torqued Specimens (Frank and Yura, 1981)



(a) Bearing Failure Type (b) Net Section Failure Type

Figure 2-20. Test Results of the Torqued and Un-torqued Specimens (Frank and Yura, 1981)

Table 2-3. Summary of bearing test (Frank and Yura, 1981)

Test No. (1)	Bearing Ratio (Eq. 5) (2)	Type of Failure* (3)	$P_{0.25}$ (kips) (4)	P_u (kips) (5)	$\left(\frac{\text{Net Ten. Stress}}{F_u}\right)_{.25}$ (6)	$\left(\frac{\text{Net Ten. Stress}}{F_u}\right)_u$ (7)	$\left(\frac{\text{Bearing Stress}}{F_u}\right)_{.25}$ (8)	$\left(\frac{\text{Bearing Stress}}{F_u}\right)_u$ (9)
8-H1-2	3.46	2	133.77	168.65	0.658	0.829	2.255	2.842
6-H1-1	2.53	1	119.2	151.8	0.780	0.993	2.008	2.558
6-H1-2(3)	1.65	0	132.9	145.0	0.905	0.988	1.493	1.629
6-H1-2	2.48	1	113.1	145.0	0.771	0.988	1.906	2.444
4-H1-1	1.48	0	85.2	88.4	0.965	1.001	1.436	1.489
4-H1-1(3)	0.99	0	90.15	92.7	1.021	1.049	1.013	1.041
2-H1-1	0.471	0	29.2	30.4	1.055	1.095	0.493	0.512
8-H1-1C	3.49	2	139.4	169.3	0.671	0.815	2.349	2.853
6-H1-1C	2.48	1	136.0	148.2	0.919	1.001	2.293	2.497
4-H1-2C	1.490	0	91.7	92.2	1.025	1.030	1.546	1.554
2-H1-2C	0.475	0	--**	42.7	--**	1.686	--**	0.720
8-H3-1	3.51	2	150.6	179.9	0.634	0.757	2.238	2.672
8-H3-2	3.51	3	129.7	178.3	0.547	0.752	1.923	2.649
7-H3-1	3.01	2	151.5	173.1	0.737	0.842	2.252	2.572
6-H3-1	2.51	1	131.7	172.4	0.767	1.003	1.958	2.562
6-H3-2	2.50	3	123.0	146.1	0.718	0.854	1.827	2.171

*Code for Types of Failure (1 kip = 4.45 kN)
0 Net Section
1 Mixed Mode
2 Bearing Failure
3 End Tearout
**Did not slip until net section failure.

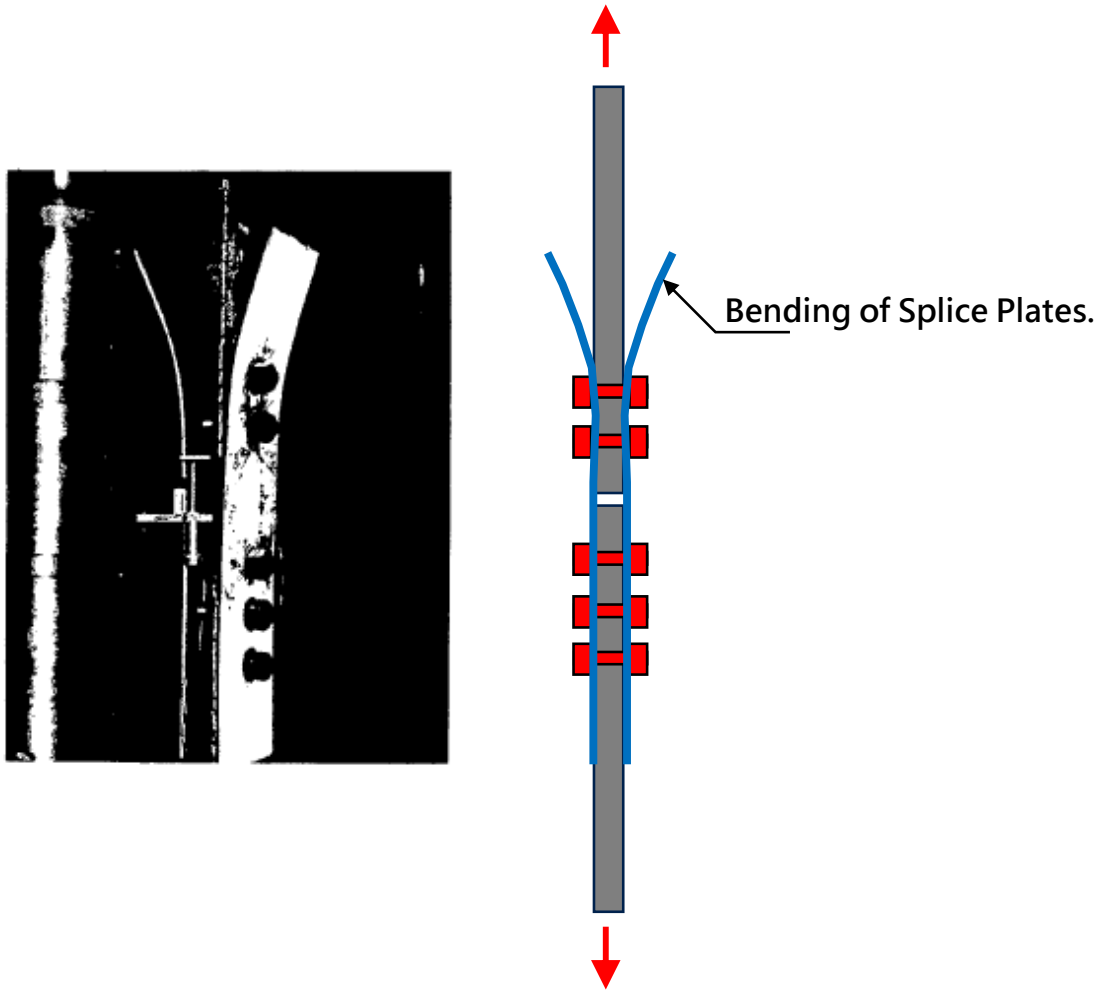


Figure 2-21. Bending of Splice Plates (Frank and Yura, 1981)

In the 2nd edition of the book "Design Criteria for Bolted and Riveted Joints", Kulak et al. compared previous bearing test results conducted by Jones (1958), Munse (1959), Back and Jong (1968), and Frank and Yura (1981). This collected test data is shown in Figure 2-22, together with the proposed Equation 2-10 for bearing strength as a function of the end distance ratio (*L/d*). In this equation, *L* is the edge distance from the bolt center to the plate edge, d is the diameter of the bolts, σ_b denotes the bearing stress (as defined in Equation 2-9), and σ_u^p d represents the tensile strength of the plates.

$$\frac{L}{d} \geq 0.5 + 0.715\frac{\sigma_b}{\sigma_u^p} \qquad \text{Equation 2-10}$$

The test results show that the application of a clamping force increased the ultimate bearing strength, suggesting partial load transmission through friction. For single bolt connections, the ultimate bearing stress sometimes reached values beyond $3.5F_u$ when a large end distance was present. However, Kulak et al. recommended that in order to limit deformations of the hole, the bearing ratio σ_b/σ_u^p should not exceed 3.0 at the factored load level. Note that all specimens in Figure 2-22, except those marked with a dash, experienced critical failure in the middle plate surrounded by the splice plates. Conversely, when specimens experienced bending on thin splice plates, as shown in Figure 2-21, reduced bearing strength were observed before failure.

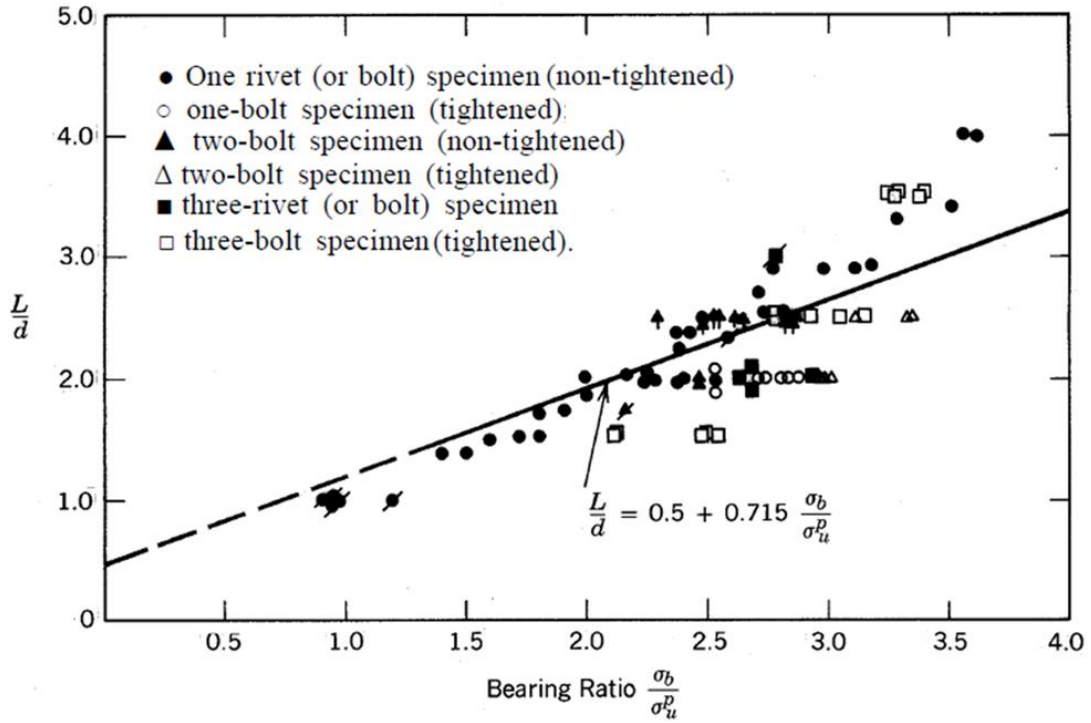


Figure 2-22. Influence of type of specimen on the bearing (Kulak et al., 1987)

Lewis and Zwerneman (1996) followed that work with a series of bearing tests on bolted connections. Figure 2-23 shows the test setup for the single and double-bolt connection specimens. The specimens were made from ASTM A36 steel bars of various thickness (1/4 in., 1/2 in., and 3/4 in. thick) with bolts of ASTM A325 or A490 of various diameter (5/8 in., 3/4 in., and 1 in. diameter). Clear end distances varied between 0.125 in. and 2.75 in, and bolt spacings varied between 1.05 in. and 2.85 in. Lap splices were used, and both single-bolt and two-bolt connections were tested. Note that the specimen design included a gap between the test specimen and the fixture (splice plates) to allow some out-of-plane movement of the plates, thus preventing friction in the connection.

Figure 2-24 shows the test results for a 5/8-in. single-bolt connection comparing with various design equations. It can be observed that when the clear end distance (L_c) exceeds twice the bolt diameter ($2d$), the bearing strength developed at 0.25-in. deformation surpassed $2.4dtF_u$. Lewis and Zwerneman concluded that a maximum bearing stress of $2.4dtF_u$ is suitable for use in design equations, even though this value overpredicts the capacity of a 1-in. diameter single-bolt connection when 0.25-in. deformation is used as the failure criterion. Lewis and Zwerneman also noted that the test plates were "unconfined" during load application because the bolts were not pretensioned.

Kim and Yura (1996) conducted a series of bolted connection tests, specifically focusing on bearing behavior, as illustrated in Figure 2-25. The plates used in the test program had a nominal thickness of 3/16 in., and all specimens were fastened with 3/4-in. diameter A490 bolts with 13/16-in. diameter standard holes. For one-bolt splices, bolt holes were made with clear end distances of *0.5d*, *1.0d*, *1.5d*, and *2.0d*, where *d* is the diameter of the bolt. The two-bolt splices had clear end distances varying from *2.0d* to *3.0d*, and bolt spacing varying from *1.0d* to *3.0d*. Note that a 3/16-in. gap was intentionally included between the splice plates and the test plate to prevent the development of surface friction.

One of the test results from this series is shown in Figure 2-26 to. In this figure, the bearing strength at 0.25-in. deformation reached 27.5 kips, equivalent to $2.48dtF_u$, while the ultimate bearing strength was 29.9 kips, equivalent to $2.70dtF_u$.

In the report, the bearing and tear-out strength were combined and expressed as follows. This combined approach was referred to as the clear distance approach as defined below:

For single-bolt Connections:

$$R_n = 1.2L_c tF_u \leq 2.4dtF_u \qquad \text{Equation 2-11}$$

For two or more bolts in the line of force:

$$R_n = 1.5L_c tF_u \leq 3.0dtF_u \qquad \text{Equation 2-12}$$

As shown in Figure 2-27, the report indicates that the force obtained from all of the test results at a 0.25-in. deformation exceeded the force calculated by Equation 2-11. However, at ultimate displacements (Figure 2-28), only 64% of the tested specimens developed a strength larger than the value calculated by Equation 2-12. Table 2-4 summarizes the geometry, material properties, test strengths, and predicted strengths of the specimens. The table provides strengths at both 1/4-in. deformation and ultimate deformation ($P_{1/4}$ and P_u, respectively), along with predicted strengths according to AISC-LRFD (1993), labeled as $P_{1/4,LRFD}$ and $P_{u,LRFD}$, and those predicted by the clear distance approach, defined as $P_{1/4,clear}$ and $P_{u,clear}$.

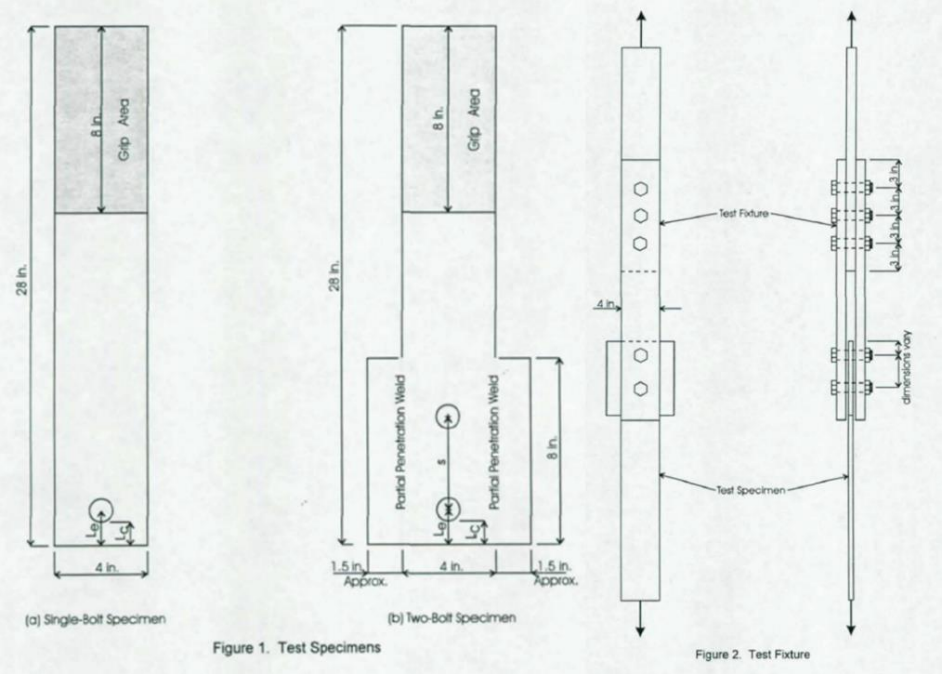


Figure 2-23. Test Setup of Bolted Connection Specimens (Lewis and Zwerneman, 1996)

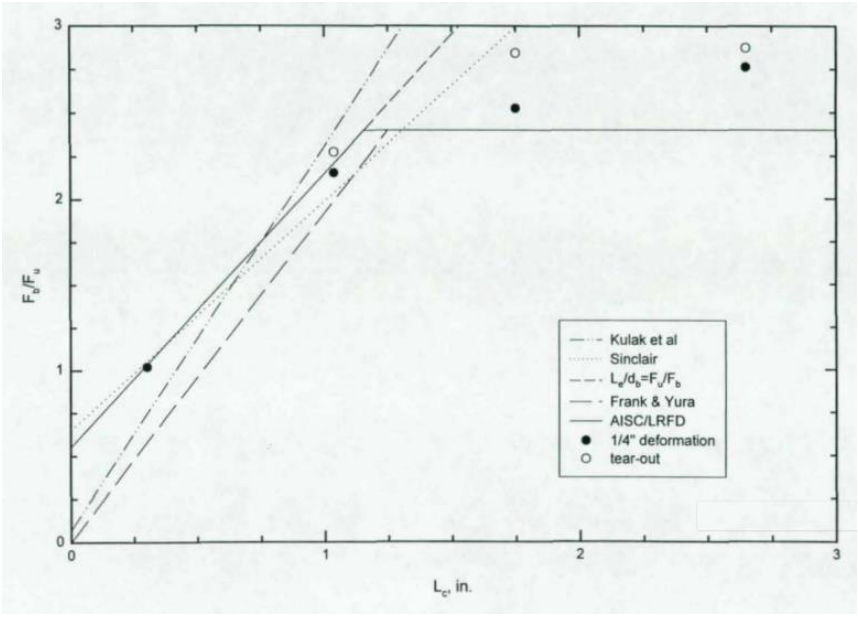


Figure 2-24. Comparison of 5/8 in. Single-Bolt Test Data to Various Design Equations (Lewis and Zwerneman, 1996)

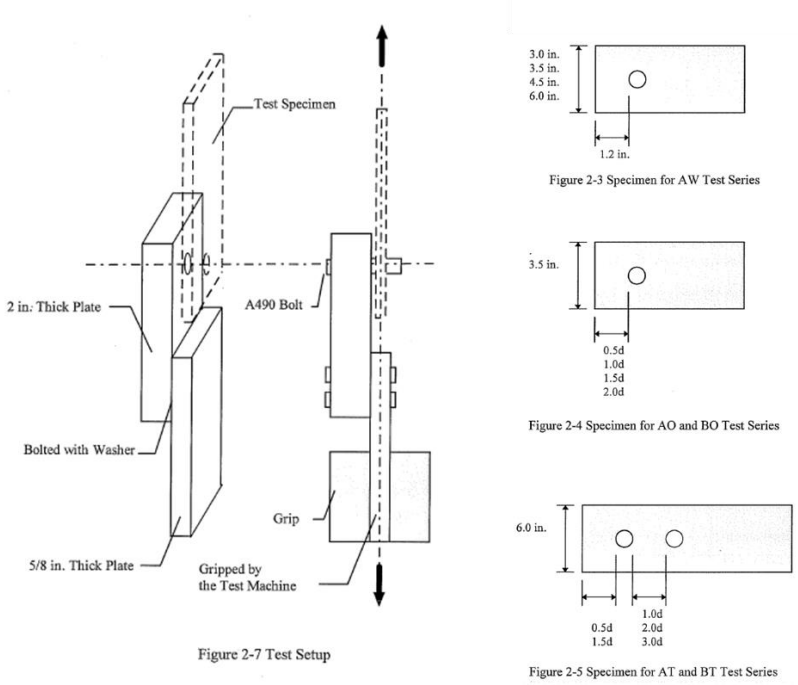


Figure 2-7 Test Setup

Figure 2-3 Specimen for AW Test Series

Figure 2-4 Specimen for AO and BO Test Series

Figure 2-5 Specimen for AT and BT Test Series

Figure 2-25. Test Setup of Bolted Connection Specimens (Kim and Yura, 1996)

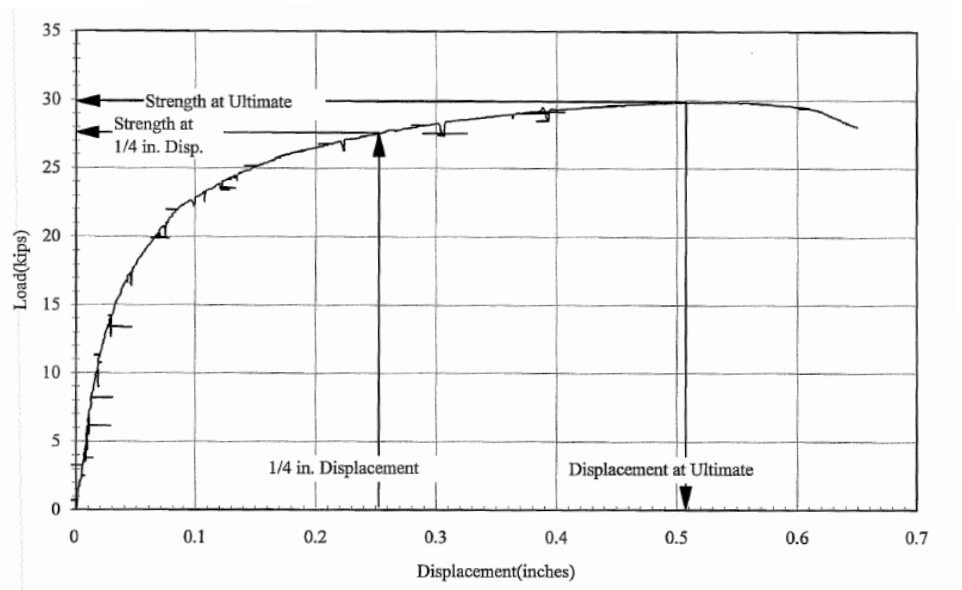


Figure 3-1 Plot of Modified Displacement and Load Data(BO200)

Figure 2-26. Load-Displacement Curve of Bearing Test Specimen BO200 (Kim and Yura, 1996)

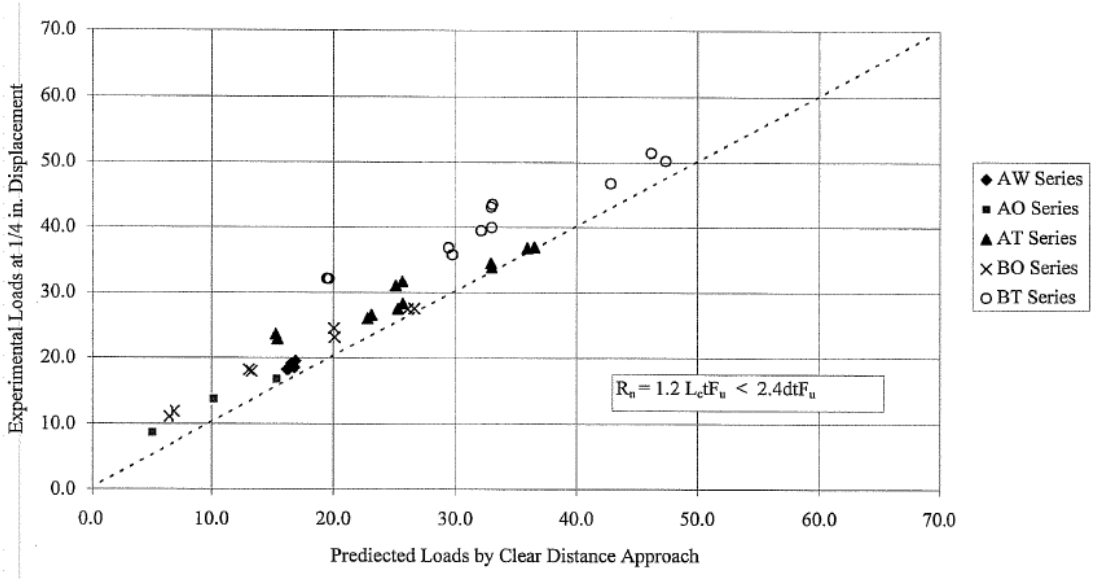


Figure 2-27. Comparison between test and prediction at 0.25-in. deformation (Kim and Yura, 1996)

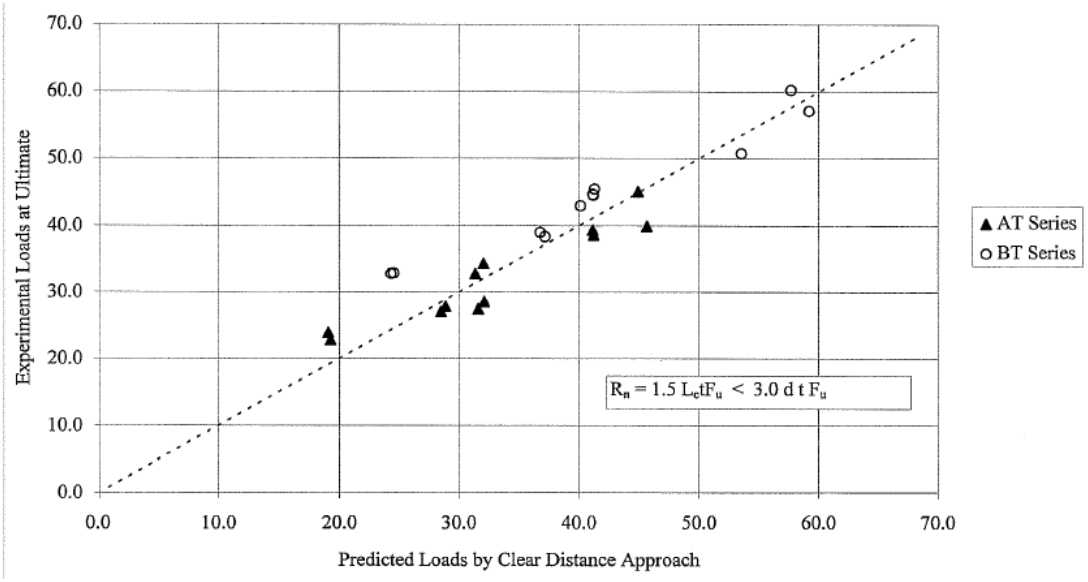


Figure 2-28. Comparison between test and prediction at ultimate deformation (Kim and Yura, 1996)

Table 2-4. Summary of bearing test (Kim and Yura, 1996)

Specimen	C1	C2	w	t	F_y	F_u	$P_{1/4}$	P_u	$Delta_u$	$P_{1/4, LRFD}$	$P_{u, LRFD}$	$P_{1/4, Clear}$	$P_{u, Clear}$
AW300	1.20	-	3.00	0.182	38.7	62.3	18.2	20.0	0.42	18.2	-	16.3	-
AW350	1.23	-	3.53	0.183	38.7	62.3	18.5	19.5	0.37	18.6	-	16.8	-
AW35R	1.23	-	3.53	0.182	38.7	62.3	18.6	19.9	0.40	18.6	-	16.7	-
AW45S	1.24	-	4.54	0.183	38.7	62.3	19.5	20.3	0.42	18.7	-	16.9	-
AW45U	1.18	-	4.54	0.183	38.7	62.3	18.2	20.0	0.47	18.1	-	16.2	-
AW600	1.22	-	5.95	0.182	38.7	62.3	19.1	20.2	0.34	18.4	-	16.6	-
AO050	0.36	-	3.54	0.183	38.7	62.3	8.5	8.5	0.19	8.7	-	4.9	-
AO050R	0.36	-	3.53	0.183	38.7	62.3	8.6	8.6	0.21	8.8	-	4.9	-
AO100	0.74	-	3.54	0.184	38.7	62.3	13.7	13.8	0.27	13.1	-	10.2	-
AO150	1.12	-	3.53	0.183	38.7	62.3	16.7	18.2	0.52	17.4	-	15.4	-
AT0510	0.37	0.76	5.99	0.183	38.7	62.3	22.8	22.8	0.23	22.5	-	15.4	19.3
AT0510R	0.37	0.76	5.96	0.182	38.7	62.3	23.6	23.9	0.30	22.3	-	15.3	19.1
AT0520	0.36	1.32	5.96	0.182	38.7	62.3	26.0	27.1	0.33	28.6	-	22.8	28.5
AT0520R	0.38	1.31	5.99	0.183	38.7	62.3	26.5	27.9	0.34	28.9	-	23.1	28.9
AT0530	0.36	2.20	5.97	0.182	38.7	62.3	27.5	27.5	0.21	29.1	-	25.3	31.6
AT0530R	0.38	2.18	5.96	0.183	38.7	62.3	28.3	28.6	0.27	29.5	-	25.7	32.1
AT1510	1.09	0.74	5.96	0.183	38.7	62.3	31.0	32.8	0.40	30.5	-	25.1	31.4
AT1510R	1.11	0.76	5.98	0.183	38.7	62.3	31.6	34.3	0.47	31.0	-	25.7	32.1
AT1520	1.09	1.33	5.99	0.182	38.7	62.3	33.9	38.6	0.57	37.1	-	33.0	41.2
AT1520R	1.13	1.30	5.96	0.181	38.7	62.3	34.5	39.4	0.58	37.0	-	32.9	41.2
AT1530	1.17	2.20	5.98	0.183	38.7	62.3	37.0	39.9	0.37	41.1	43.6	36.5	45.7
AT1530R	1.13	2.20	5.98	0.183	38.7	62.3	36.9	45.1	0.69	41.1	43.1	35.9	44.9
BO050	0.36	-	3.55	0.187	70.1	79.1	11.1	11.1	0.25	11.3	-	6.4	-
BO050R	0.39	-	3.55	0.187	70.1	79.1	11.9	11.9	0.23	11.7	-	6.9	-
BO100	0.74	-	3.61	0.189	70.1	79.1	17.9	18.1	0.33	17.2	-	13.3	-
BO100R	0.73	-	3.61	0.188	70.1	79.1	18.1	18.4	0.30	16.9	-	13.1	-
BO150	1.13	-	3.61	0.188	70.1	79.1	23.1	24.3	0.48	22.8	-	20.1	-
BO150R	1.13	-	3.56	0.187	70.1	79.1	24.5	25.2	0.37	22.7	-	20.1	-
BO200	1.51	-	3.61	0.187	70.1	79.1	27.5	29.9	0.51	26.6	-	26.6	-
BO200R	1.47	-	3.54	0.187	70.1	79.1	27.4	29.9	0.62	26.6	-	26.1	-
BT0510	0.35	0.75	6.04	0.187	70.1	79.1	32.1	32.8	0.35	28.7	-	19.5	24.4
BT0510R	0.36	0.74	6.09	0.188	70.1	79.1	32.1	32.9	0.37	28.9	-	19.7	24.6
BT0520	0.36	1.31	6.09	0.188	70.1	79.1	35.8	38.4	0.48	37.4	-	29.8	37.2
BT0520R	0.35	1.31	6.03	0.187	70.1	79.1	36.9	39.0	0.41	37.0	-	29.4	36.8
BT0530	0.31	2.19	6.05	0.187	70.1	79.1	39.5	43.0	0.43	37.2	-	32.1	40.2
BT0530R	0.36	2.18	6.10	0.187	70.1	79.1	40.0	44.6	0.45	37.9	-	33.0	41.2
BT1510	1.10	0.75	6.10	0.188	70.1	79.1	43.1	44.6	0.38	40.0	-	32.9	41.2
BT1510R	1.11	0.75	6.03	0.187	70.1	79.1	43.5	45.4	0.43	40.0	-	33.0	41.3
BT1520	1.09	1.31	6.03	0.188	70.1	79.1	46.8	50.7	0.52	48.2	-	42.8	53.5
BT1530	1.17	2.20	6.10	0.187	70.1	79.1	50.2	57.1	0.53	53.3	56.6	47.4	59.2
BT1530R	1.10	2.18	6.05	0.187	70.1	79.1	51.4	60.2	0.77	53.3	55.6	46.2	57.7

Brown et al. (2007) conducted a series of bolted connection tension tests to verify the influence of different hole making processes (punched or drilled) for single-bolt and two-bolts connections. Figure 2-29 shows the test setup for these specimens, which consisted of 6-inch wide A36 or A572 Gr. 50 plates with 7/8-inch nominal bolt diameters. The study also compared the performance of snug-tight bolts with that of pretensioned bolts. Note that the clear end distance L_c was less than $2d$ for all the specimens, thus the failure mode was tear-out and the upper limit for bearing strength ($2.4dtF_u$ or $3.0dtF_u$) did not control any of the design strength obtained. Brown et al. highlighted that the use of pretensioned bolts significantly increased the experimental strength of all specimens in those cases. Also, the difference in strength between punched hole and drilled hole specimens decreased due to the influence of the pretensioned bolts. When comparing the two bearing strength equations presented in AISC 360-05 ($R_n = 1.2L_ctF_u \leq 2.4dtF_u$ versus $R_n = 1.5L_ctF_u \leq 3.0dtF_u$), it was found that using the equation $1.5L_ctF_u$, when bolt hole deformation is not a design consideration, is not conservative based on the test results. However, this case is only for when tear-out governs, and the primary focus here is on bolted connections governed by bearing behavior.

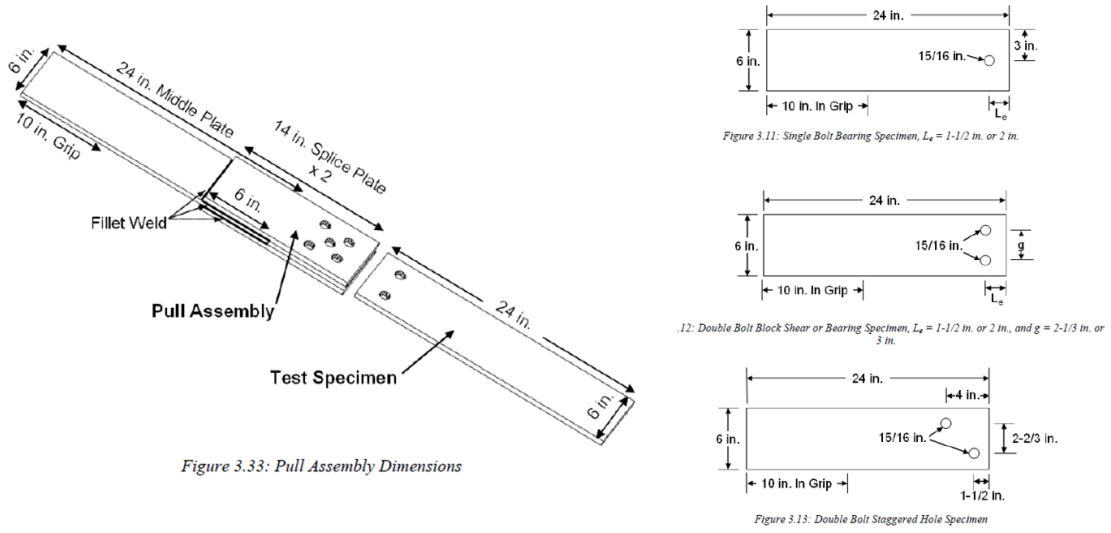


Figure 2-29. Test Setup of Bolted Tension Tests (Brown et al., 2007)

Može (2018) conducted a series of bearing tests on bolted connections with large end distances and bolt spacings. The specimens used were 10-mm thick steel plates with an average yield strength of f_y = 342 MPa and an average tensile strength of f_u = 447 MPa. The bolts had a diameter (d) of 27 mm with a 30-mm diameter (d_0) bolt hole. All bolts were snug-tightened to minimize the influence of friction. The edge distance to bolt hole diameter ratio (e_1/d_0) ranged from 3.0 to 5.0 for single-bolt connections and from 1.5 to 5.0 for two-bolt connections. Additionally, the bolt spacing to bolt hole diameter ratio (p_1/d_0) ranged from 2.2 to 4.0.

A nondimensional resistance, $\bar{F}$, was introduced in the report, as in the following equation:

$$\bar{F} = \frac{\sigma_b}{F_u} = \frac{F}{dtF_u} \qquad \text{Equation 2-13}$$

where σ_b is the bearing stress of a bolt ($\sigma_b = F/dt$), F is the applied axial load of the connection, d is the diameter of bolts, and t is the thickness of the steel plate.

The test results for one-bolt and two-bolts connections are shown in Figure 2-30 and Figure 2-31, along with a summary of the results in Table 2-5. In these figures, displacement u represents the hole elongation, and results are presented in terms of the nondimensional resistance $\bar{F}$ and displacements (u/d). For single-bolt connections, $\bar{F}$ ranged from 3.55 to 5.45, and u/d varied from 1.06 to 1.23. For two-bolt connections, $\bar{F}$ ranged from 4.03 to 8.30, and u/d varied from 0.71 to 1.26. Note that in Table 2-5, the two-bolt connections with edge distances less than *3.0d* are highlighted in boxes. This represents cases where the edge tear-out strength is smaller than the bearing strength of the edge bolt. The $\bar{F}$ in the report is defined based on the applied axial load divided by the bearing area of one bolt; therefore, the values reported in the Table are high for two-bolt connections, and generally exceed twice the strength of the equivalent single-bolt connection when the connection is designed governed by bearing.

In the report, several finite element models for single-bolt connections were analyzed using ABAQUS to investigate the development of friction force during axial tensile loading. Figure 2-32 shows the relationship between normalized friction force (friction force F_f divided by dtF_u) and normalized deformation (deformation u divided by bolt diameter d) curve. In Figure 2-32 (a), two different friction coefficients (k=0.15 and k=0.25) were considered to investigate the effect of friction on connection strength. Additionally, the analysis included a preloaded connection with k=0.15 for comparison. This figure demonstrates that friction forces are generated between contact interfaces during axial loading, even without bolt pretension, and that these forces increase when the friction coefficient is greater. Figure 2-32(b) explores the impact on connection strength of various edge distances (e_1), ranging from $1.5d_0$ to $5d_0$ (d_0 being the bolt hole dimension, equivalent to 30mm for M27 bolts). It shows that an increase in edge distance significantly boosts the development of friction force. In addition, the friction forces in the preloaded model show no significant difference compared to those without preload once large deformations are developed. In both figures, results with elastic bolts are plotted with thin lines, indicating that in the absence of inelastic deformation of bolts, friction can develop further, reaching higher value. Figure 2-33 provides the evidence from analysis results showing that the tension force in the bolt and the friction force stop increasing once the bolt has yielded.

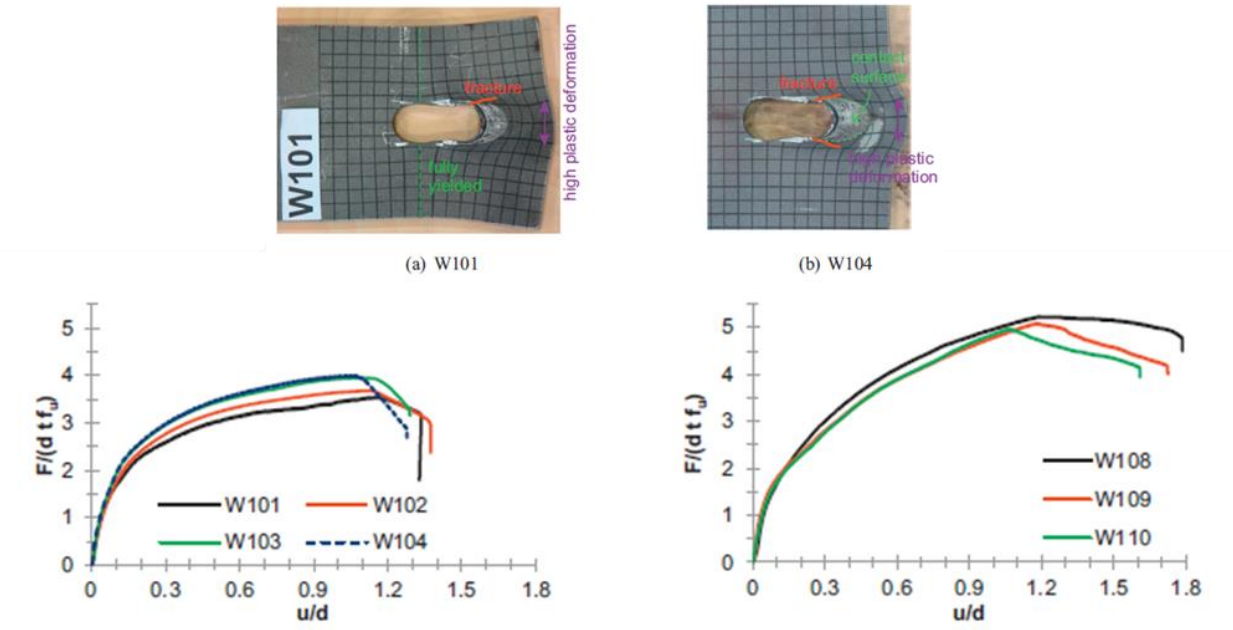


Figure 2-30. Test Results for Single-Bolts Connections (Može, 2018)

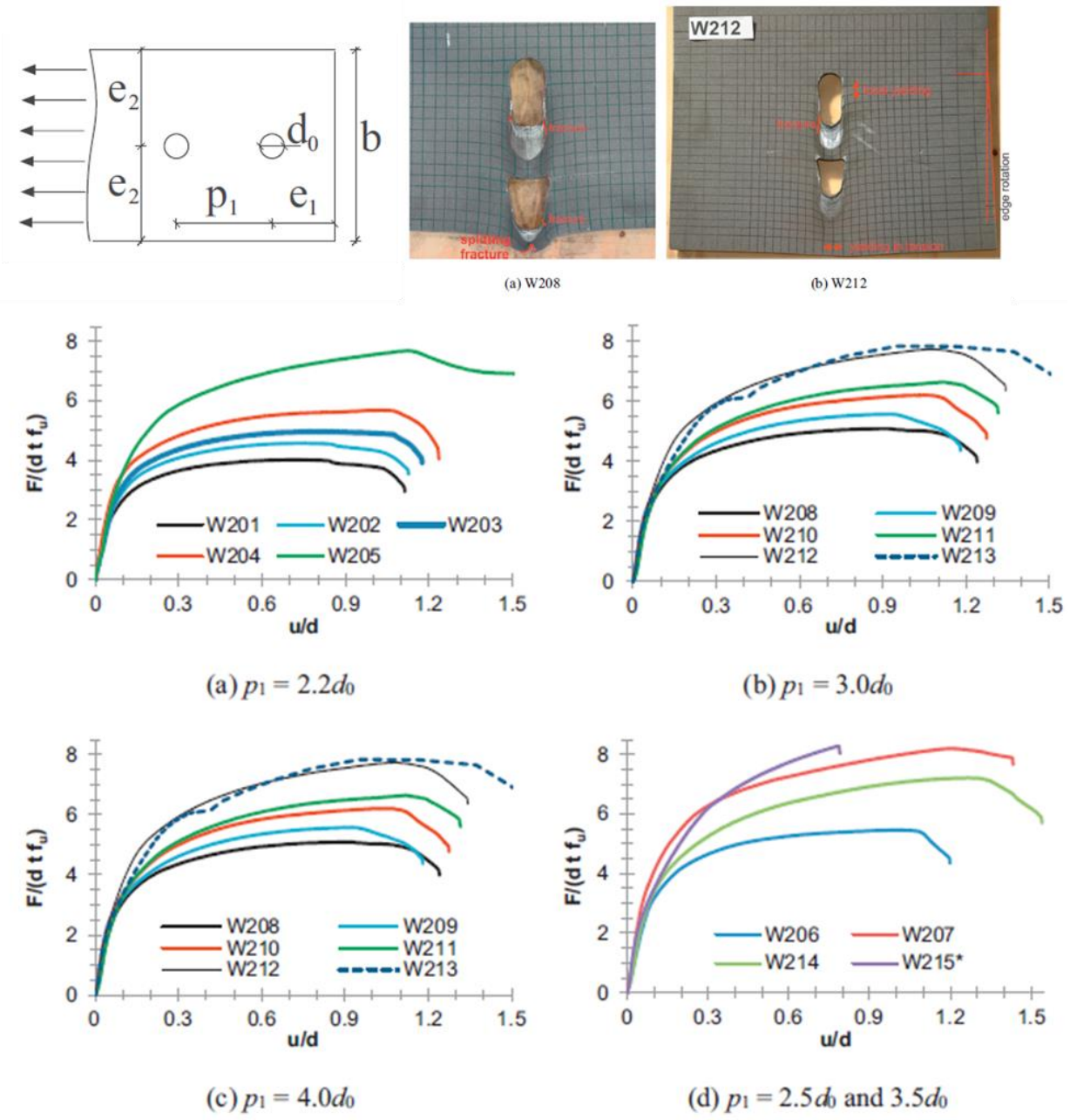


Figure 2-31. Test Results for Two-Bolts Connections (Može, 2018)

Table 2-5. Summary of bearing test (Može, 2018)

Table 1
Geometry of the test specimens.

Spec.	Actual relative distances			Actual absolute distances [mm]				Fracture location	F_{max} [kN]	$\overline{F}_{max}$	u/d
	e_1/d_0	e_2/d_0	p_1/d_0	b	e_2	e_1	p_1				
W101	3.03	2.43		145.8	72.9	90.8	/	1	427	3.55	1.16
W102	3.00	3.07		180.7	92.0	90.0	/	1	443	3.68	1.10
W103	2.99	4.03		241.0	120.8	89.8	/	1	476	3.96	1.08
W104	3.01	5.01		300.0	150.2	90.3	/	1	482	4.00	1.06
W105	3.49	5.01		300.5	150.2	104.7	/	1	536	4.45	1.23
W106	3.83	7.52		450.5	225.5	114.8	/	1	591	4.91	1.08
W107	4.44	7.51		450.5	225.2	133.2	/	1	657	5.45	1.12
W108	5.04	3.36		200.9	100.7	151.1	/	1	630	5.23	1.19
W109	5.00	5.03		300.5	150.8	149.9	/	1	613	5.09	1.18
W110	4.94	7.47		448.0	224.0	148.2	/	1	599	4.97	1.06
W201	1.53	5.03	2.21	301.0	150.8	45.8	66.4	2	485	4.03	0.71
W202	2.02	5.02	2.21	300.5	150.5	60.6	66.2	2	552	4.58	0.74
W203	2.36	4.99	2.21	299.0	149.7	70.7	66.3	2	599	4.97	0.79
W204	3.02	5.03	2.20	300.5	150.8	90.6	66.1	3	686	5.69	1.01
W205	5.01	5.03	2.22	301.0	150.8	150.4	66.5	3	926	7.69	1.12
W206	2.52	5.01	2.51	299.5	150.3	75.6	75.4	2	658	5.47	1.00
W207	5.02	5.02	2.51	300.0	150.5	150.6	75.2	3	988	8.21	1.20
W208	1.53	6.68	3.01	400.0	200.4	45.9	90.4	2 (1, 3)	614	5.10	0.90
W209	2.05	6.69	3.01	401.0	200.7	61.4	90.3	2, 3	672	5.58	0.93
W210	2.53	6.68	3.01	401.0	200.5	75.8	90.2	2, 3	748	6.21	1.06
W211	3.01	6.69	3.01	401.0	200.6	90.3	90.3	3	800	6.65	1.12
W212	4.01	6.68	2.99	401.0	200.5	120.2	89.8	3	933	7.75	1.08
W213	5.01	6.68	3.01	401.0	200.5	150.4	90.4	3	944	7.84	0.95
W214	3.02	6.70	3.52	400.0	200.9	90.6	105.7	2, 3	869	7.22	1.26
W215[a]	5.02	6.71	3.50	402.0	201.2	150.6	105.1	[a]	997[a]	8.28[a]	0.78[a]
W216	2.02	6.67	4.00	400.0	200.2	60.6	119.9	2, 3	758	6.30	0.97
W217	3.04	6.70	4.01	401.5	201.0	91.1	120.2	3	920	7.64	1.08
W218[a]	4.03	6.69	4.02	401.0	200.7	120.8	120.5	[a]	998[a]	8.29[a]	0.91[a]
W219[a]	5.05	6.70	4.01	401.5	200.9	151.4	120.4	[a]	1000[a]	8.30[a]	0.61[a]

Single Bolt

Two Bolts

F_{max} maximum resistance.
$\overline{F}_{max}$ non-dimensional maximum resistance.
u bolt hole elongation (bolt hole deformation due to bearing).
d bolt diameter.
$d_0 = 30$ mm for all connections (bolts M27).
1 shear fracture at end bolt.
2 splitting fracture.
3 shear fracture at inner bolt.
[a] The capacity of the testing machine was reached – failure was not observed.

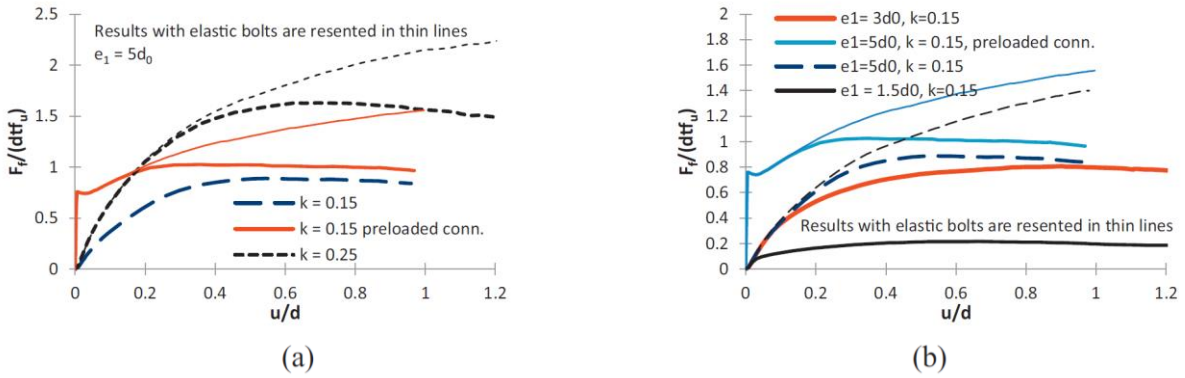
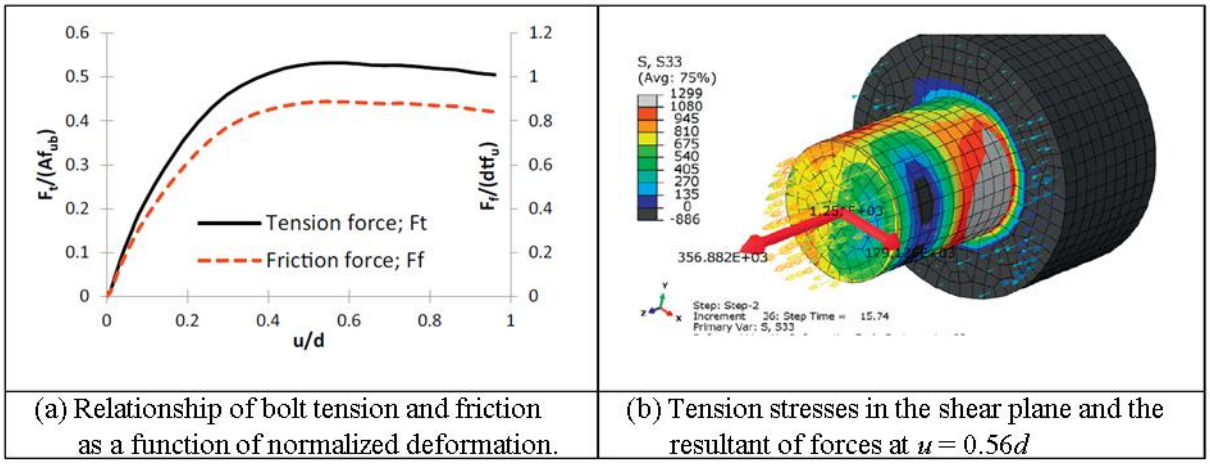


Figure 2-32. Friction Force in Relation to the (a) Friction Coefficient and (b) to the end distance (Može, 2018)



(a) Relationship of bolt tension and friction as a function of normalized deformation.

(b) Tension stresses in the shear plane and the resultant of forces at $u = 0.56d$

Figure 2-33. Bolt Tension in Relation to the Friction Force
(Može, 2018)

Kim and Lee (2020) conducted extensive tests on single-bolt bearing connections. The testing program encompassed both bearing-controlled (referred to as "closed boundary condition") and tear-out-controlled (referred to as "open boundary condition") single-bolt connections, as shown in Figure 2-34. Similar tests had been done before by Crawford and Kulak (1968, 1971), however, at that time, their focus was limited to a single combination consisting of 3/4-in. diameter A325 bolt and A36 steel plate, with test results primarily governed by the shear rupture of the bolt. Kim and Lee's objective was to explore similar single-bolted connections, but subjected to bearing, tear-out, and bolt shear rupture failure modes across a range of material strengths using SS400, SM490, SM570, and HSA800 steel plates (F_u= 400 MPa to 800 MPa), plate thicknesses (t= 6 mm to 25 mm), and bolt diameters (d=20 mm to 30 mm). Figure 2-35 and Figure 2-36 show typical test results for connections governed by bearing and tear-out failure, and Figure 2-37 summarizes the test results, incorporating previous test data from Jones 1958, Munse 1959, de Back and de Jong 1968, Hirano 1970, Rex and Easterling 2003, Wang et al. 2017, together with the newer tests results by Kim and Lee (Labeled as "T400" and "T490" in the figure). Note that the T400 and T490 in the figure refer to the specimens with tear-out failure using SS400 and SM490 steel. Based on the test results, new

design formulas for bearing and tear-out strength ($R_{b,closed}$ and $R_{b,open}$, respectively) were proposed as follows (if not constrained by limitations on hole elongation values):

$$R_{b,closed} = 3.0F_u dt \quad \text{Equation 2-14}$$

$$R_{b,open} = \left(0.9\frac{L_c}{d} + 0.3\right)F_u dt = aF_u dt \leq 3.0F_u dt \quad \text{Equation 2-15}$$

As shown in Figure 2-37, a comparison was made between the proposed design formula and the AISC 360 equations for connections governed by bearing and tear-out failure. The results indicated that the current AISC 360 Specification is not conservative when compared to the combined test data, particularly evident when contrasting the tear-out and bearing strength of $1.5L_ctF_u$ and $3.0dtF_u$.

The objective of the Kim and Lee study was to develop a generalized load-deformation relationship that can be used when designing group-bolted connections based on the instantaneous center of rotation method (ICRM). Therefore, for this purpose, they proposed the following updated load-deformation curves that matched the test results:

$$R = R_{ult}(1 - e^{-\mu\Delta}) \quad \text{Equation 2-16}$$

$$R_{ult} = \min\left(aF_u dt, n_s \times 0.6F_{ub}A_b\right) \quad \text{Equation 2-17}$$

$$K_{closed} \cong \frac{\frac{0.04F_y t^2}{d}}{1 + \frac{F_y t^2}{n_s F_y' t'^2}}, \qquad K_{open} \cong \frac{0.0133F_y t L_c (t/d)^2}{1 + \frac{F_y t^2}{n_s F_y' t'^2}} \quad \text{Equation 2-18}$$

$$\mu = (K_{closed}\ or\ K_{open})/R_{ult} \quad \text{Equation 2-19}$$

$$\Delta_{ult} = 4(a + 0.5)\left(\frac{aF_u dt}{n_s \times 0.6F_{ub}A_b}\right)^{-0.4(a+0.5)} \quad \text{Equation 2-20}$$

where R_{ult} is the ultimate load attainable by bolts, which is governed by minimum of the bearing strength as defined in Equation 2-15, and the shear strength of bolts, $n_s \times 0.6F_{ub}A_b$. K_{closed} and K_{open} are the initial stiffness of the connection governed by bearing and tear-out failure modes, and Δ_{ult} is the ultimate deformation of single bolted joint.

As shown in Figure 2-35, the load-deformation curve derived by Crawford and Kulak in the past does not exhibit a close match with some of the experimental results when compared to the proposed load-deformation curve. Notably, it tends to underestimate the ductility and strength of the connection, particularly as the plate thickness increases. In contrast, Kim and Lee proposed a bearing load-deformation relationship for single-bolted connections to cover a broader range of limit states, as well as various material strengths, plate thicknesses, bolt diameters, and edge distances.

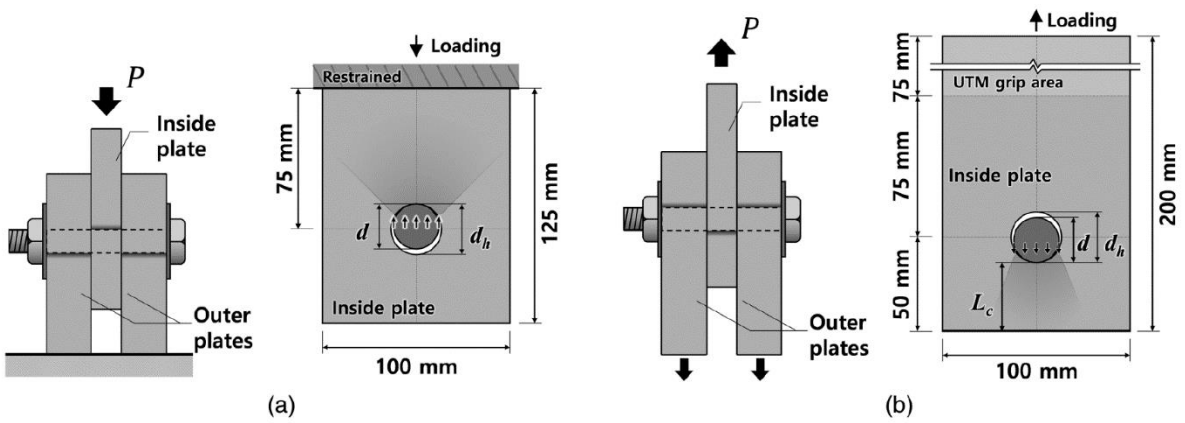


Figure 2-34. Test Programs for Single-Bolted Connections (Kim and Lee, 2020)

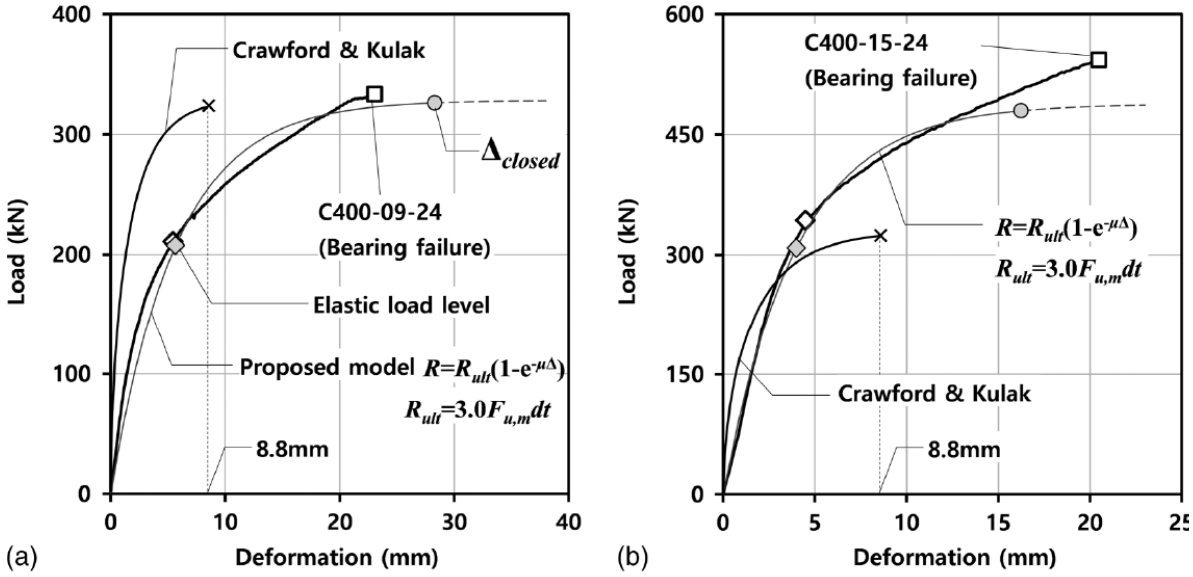


Figure 2-35. Results of Bearing-Failure in Single-Bolted Connections:
(a) Specimen C400-09-24 (b) Specimen C400-15-24
(Kim and Lee, 2020)

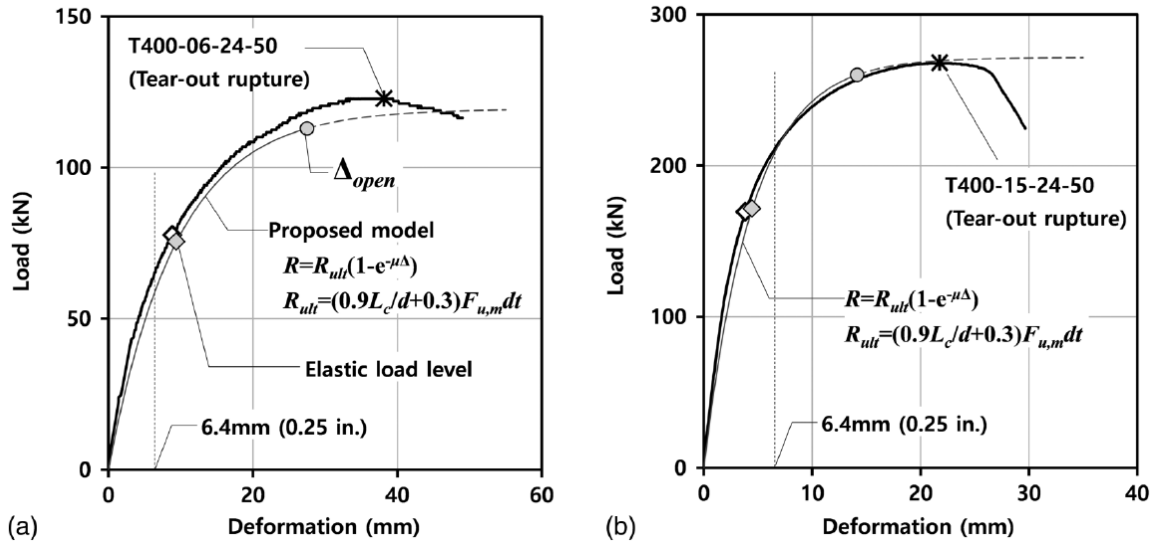


Figure 2-36. Results of Tear-Out Failure in Single-Bolted Connections
(a) Specimen T400-06-24-50 (b) Specimen T400-15-24-50
(Kim and Lee, 2020)

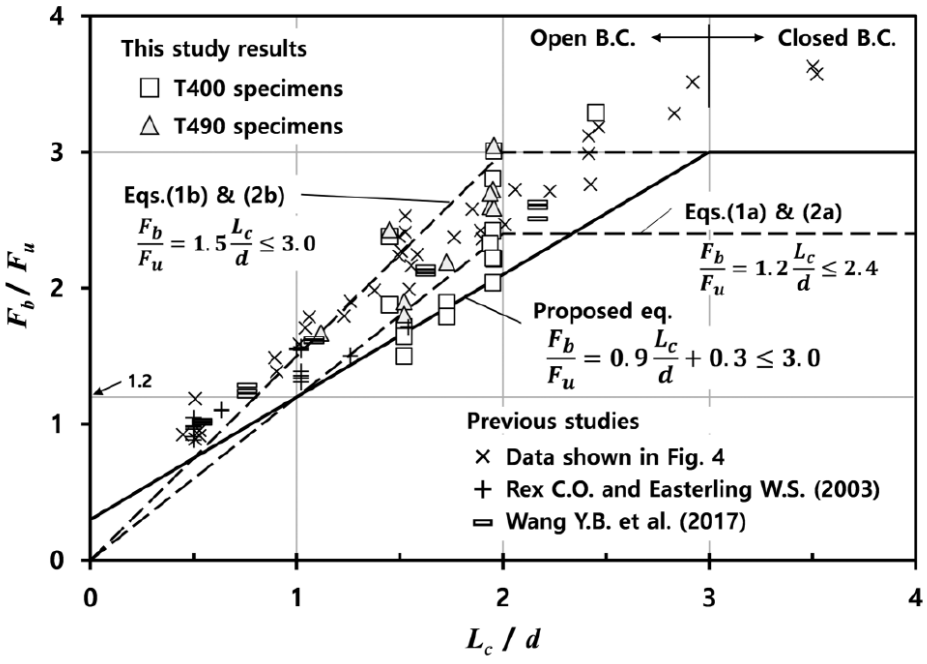


Figure 2-37. Comparison of AISC 360 and Proposed Design Approach for Single-Bolted Connections
(Kim and Lee, 2020)

2.5 Knowledge gap

The previous sections have reviewed some relevant research on the in-plane behavior of C-PSW/CF. Also, in the perspective of C-PSW/CF having bolted splices of the type described in subsequent chapters, a review of previous bolt bearing tests has been conducted.

While the reviewed information is instructive, it remains that no research has been conducted to investigate the behavior of C-PSW/CFs having bolted splices. Also, while many researchers have mentioned the fact that slip-resistance strength is not additive to bearing strength, the physical mechanisms that explain this observation have not been definitively identified – something important to resolve to be able to develop design equations for the splices of C-PSW/CF. Therefore, recognizing the above knowledge gap, and the desire by structural engineers to build C-PSW/CF in regions where field bolting is the practice (rather than field welding), it is essential to investigate the behavior of bolted splices in C-PSW/CFs.

SECTION 3
DESIGN OF COMPONENT SPECIMENS

3.1 General

A set of different bolted details were developed and evaluated, both at the prototype and specimen scale. The objective was to keep connections simple enough to be designed using simple hand-calculation methods, but preliminary finite element simulations were performed to predict the expected ultimate performance of the specimens beyond their target service levels.

A preliminary set of possible configurations was developed and presented to the Project Advisory Group in a first meeting (via WebEx) on October 7, 2021, during which some steel fabricators and erectors were invited to participate. The PowerPoint slides presented at that meeting are included in Appendix A. Taking into account the comments of steel fabricators and structural engineers collected during this meeting, and the additional feedback received subsequently from the project sponsors, a revised set of connection configuration was developed and presented to the Project Advisory Group on December 9, 2021 (via Zoom). PowerPoint slides presented at that meeting are included in Appendix B. This proposed testing program followed the philosophy presented in Sections 3.2 and 3.3 below.

The Phase I Test (Component Level Test) of the Bolted Connection of C-PSW/CF was separated into two test series. The first test series consisted of six splice connection specimens that were subjected to cyclic axial loads. The second test series consisted of six shear splices to verify the connection behavior under cyclic shear and flexural forces. After the proposed concept was approved, the specimen design progressed to 90% completion. However, slight modifications occurred to take into account insights from refined

analyses and due to geometric laboratory constraints that impacted design of the final test set-up and experimental plan. As a result, Sections 3.2 and 3.3 of this report present the final design details for the specimens that were tested in tension and shear, respectively. In both cases, testing was accomplished at the component level using a test set-up that made it possible to swap and test multiple splice details relatively expeditiously. Appendix L provides the bill of material that was used to estimate the fabrication effort. Appendix F provides the final set of drawings for these specimens and their test set-up. The twelve specimens were fabricated by Banker Steel, and received at the University at Buffalo on 8/26/2022. The axial splice tests were performed from 9/1/2022 to 1/31/2023, and the shear splice tests were conducted from 2/1/2023 to 5/5/2023.

A testing protocol was proposed for these specimens, with the understanding that some adjustment would be performed as each test unfolds, based on experimental observations. The specific number of cycles initially foresee as part of this conceptual testing protocol, presented in Sections 3.2 and 3.3, allowed: (i) to verify that the connection detail can resist set specific design loads, and; (ii) to investigate the extent to which a stable cyclic behavior can be developed beyond those specified design loads. Different specimens were designed to exhibit different hierarchy of limit states, such as to compare and contrast different ultimate behaviors. Note that while performance under demands from wind load is the primary focus here, a few of the details considered will allow engineers to consider whether it may be possible to implement some of the proposed details in moderate seismic regions.

The following sections present the proposed set of splice specimens that were tested at the component level.

3.2 Design of Tension Component Tests

3.2.1 List of Specimens

In the tension tests, a number of connections details were investigated, considering different fastener types, configurations, and governing limit states. Three types of tension splice configurations were considered, namely: Type 1 - Blind Bolts (3-1); Type 2 - Through Bolts (3-2), and; Type 4 - I-Shaped Anchors (Figure 3-3) (a Type 3 originally considered was dropped along the way). Figures 3-1 and 3-2 show details as conceptually developed by Magnusson Klemencic Associates (MKA). These were eventually modified to the final details presented later. In particular, double splice plates were used to minimize the number of bolts. Types 1 and 2 are designed as conventional steel connections, neglecting the presence of concrete. Type 4 is a concept intended to take advantage of the presence of concrete, relying on a load path that develops compressive diagonal struts contributing to the design strength of the splice.

In addition, the designation Case A, B, and C is used to represent different governing limit states, namely: bearing, slip-critical, and yield strength control, respectively. In all cases, a specific hierarchy of limit states was imposed to favor ductile failure modes over brittle ones. Out of all possibilities (combining Types and Cases), the six tension test specimens shown in Table 3-1 were selected.



(a) Nut-welding type (b) Shuriken products

Figure 3-1. Blind Bolts (conceptually show here by MKA)

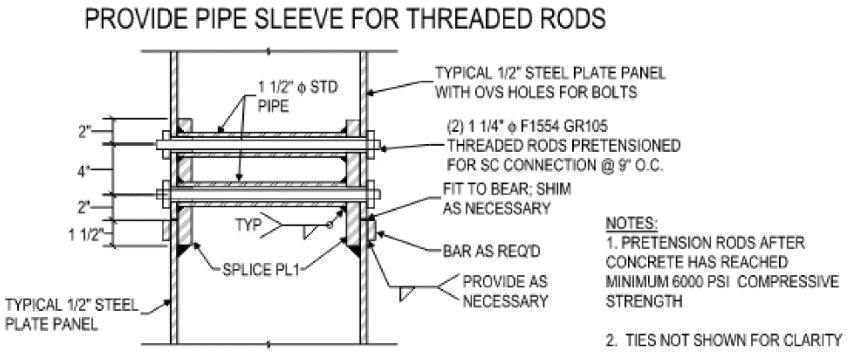


Figure 3-2. Through Bolts (conceptually show here by MKA)

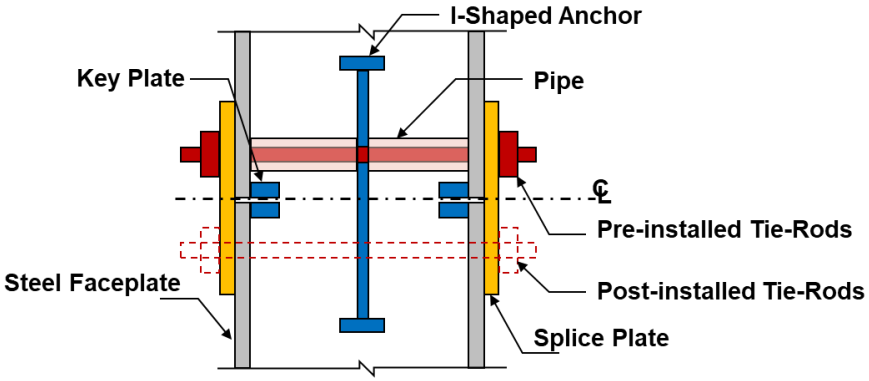


Figure 3-3. I-Shaped Anchors

Table 3-1. Tension Test Specimens

Limit States / Fasteners	Case A (Bearing)	Case B (Slip-Critical)	Case C (Yielding)
Type 1 (Blind Bolts)	Case 1A	-	Case 1C
Type 2 (Through Bolts)	Case 2A	Case 2B	Case 2C
Type 4 (I-Shaped Anchors)	Case 4A	-	-

3.2.2 Design Limit States

Table 3-2 and Table 3-3 show the design strength for each connection under different limit states assuming a yield strength, R_yF_y, of 55ksi. In that table, "target load" refers to the assumed tension force that the splice would have to be designed to resist over that segment of wall of a given width, where this width is selected to be the same for all tension component test specimens. Note that in these tables, for each proposed connection, the term "sequence" is used to rank (from weakest to strongest) the strengths obtained considering various limit states for each wall segment.

Figure 3-4 shows a corresponding wall segment subjected to story shear force and overturning moment resulting from the lateral load. As an example, a double shear connection is shown to represent a segment of the wall horizontal splice, subjected to a tension load from the overturning moment. The maximum width considered for the tension component tests was selected to be able to reach the failure strength of the specimens using two 420 kips actuators (for a maximum applied load equal to 840 kips (details of the test set-up are presented later). As a result, a 14 in. component width was chosen to satisfy this design limitation.

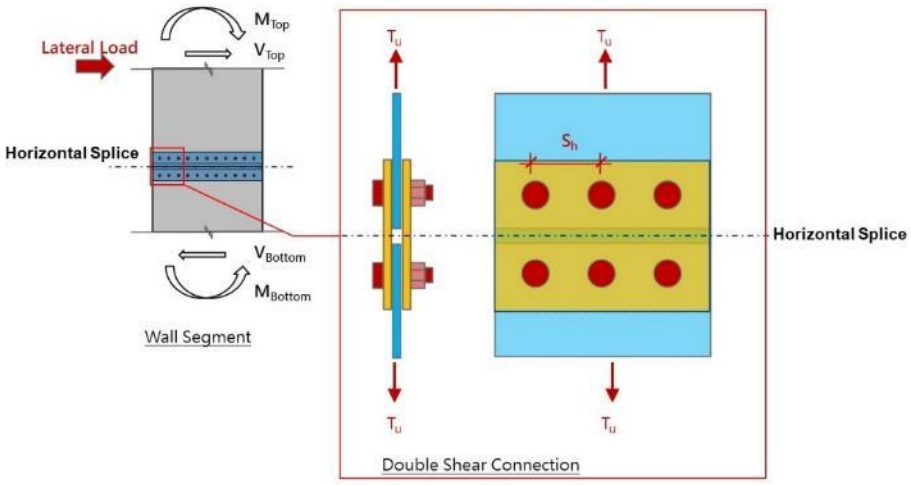


Figure 3-4. Designed Wall Segment

In developing the chosen details, the limit states of "bolt shear strength", "net section rupture", "tear-out", and "filet weld strength" were deemed to be non-ductile, and the limit states of "sliding" (corresponding to slip-critical strength of bolted connections), "bearing", "net section yielding" and "gross section yielding" were deemed to be ductile. Except for the last case, all these ductilities would be only localized in the splice itself, with limited benefit if interested in attaining large inelastic story drifts, but possibly of some benefits to meet Performance-Based Wind Design objectives. The column labelled "Sequence" in Table 3-2 and Table 3-3 orders the various limit states from weakest to strongest.

In Cases A, the bolted connections were not designed to be slip resistant, and the design was governed by the bearing capacity of the bolted connection – anticipated to provide some ductile behavior when occurring together with some energy dissipation provided during sliding of the connections.

In Cases B, the bolted connections were designed to be slip resistant connections, and the design was governed by that limit state. The hierarchy of limit states was also selected such that net section yielding would be the second limit state to develop (once sliding stops at the ends of the bolt holes). As the net section gains strength due to strain hardening, the bearing capacity of the bolted connection would then be reached. Together, the combination of these three ductile modes would be expected to maximize the amount of ductility and energy dissipation that would be developed in the splice.

In Cases C, the objective was to develop (allowing bolt slippage) the full yield capacity of the wall plates, after some extent of strain hardening after yielding of net section – anticipating that the net section could

exhibit an extended elastic range after this strain hardening, which would be possible if the steel plates do not yield in compression during a wind cyclic loading scenario.

After specimens were received, steel coupon tests and concrete cylinder tests were performed and values for the design limit states were updated accordingly and are shown in Table 3-4 and Table 3-5. Note that initial stages of cyclic loading during the experiment were done on the basis of the actual strength from three steel coupon tests (F_y=62 ksi), but results obtained (Table 3-4 and Table 3-5) were compared on the basis of actual material values from nine steel coupon tests (F_y=63 ksi).

All detailed calculation of analysis of specimens are provided in Appendix G.

Table 3-2 Design Limit States for Tension Test 1A/2A/2B/1C/2C

	Case 1A/2A		Case 2B		Case 1C/2C	
Target Loading Tu (kips)	257.40		393.14		577.50	
Limit States	Strength (kips)	Sequence	Strength (kips)	Sequence	Strength (kips)	Sequence
1. Slip-Critical Resistance	173.57/167.74	1	393.14	1	284.76/283.06	1
2. Net Section Yiled (AeRyFy)	484.69	5	407.34	2	505.31	2
3. Gross Area Yield (AgRyFy)	577.50	7	577.50	6	577.50	3
4. Bearing Capacity	257.40	2	482.63	4	579.15	4
5. Tear-out Capacity	313.71	3	639.48	7	876.77	7
6. Net Section Rupture (AeRuFu)	630.09	8	529.55	5	656.91	5
7. Bolt Shear Strength	530.61	6	1243.63	8	895.41	8
8. Block Shear Strength	409.92	4	479.53	3	713.21	6

Table 3-3 Design Limit States for Tension Test 4A

	Case 4A	
Target Loading Tu (kips)	259.78	
Limit States	Strength (kips)	Sequence
1. Corner Bending Resistance	259.78	1
2. Concrete Failure	336.00	4
3. t2 Yielding Force (RyFy)	288.75	2
4. t3 Shear Strength	315.00	3
5. t1 Yielding Force (RyFy)	577.50	6
6. Bolt Tension Strength	530.14	5

Table 3-4 Design Limit States for Tension Test 1A/2A/2B/1C/2C (Actual Material Strength)

	Case 1A/2A		Case 2B		Case 1C/2C	
Target Loading Tu (kips)	298.80		393.13		661.50	
Limit States	Strength (kips)	Sequence	Strength (kips)	Sequence	Strength (kips)	Sequence
1. Slip-Critical Resistance	167.74	1	393.13	1	283.06	1
2. Net Section Yiled (AeRyFy)	555.19	6	466.59	2	578.81	2
3. Gross Area Yield (AgRyFy)	661.50	7	661.50	6	661.50	3
4. Bearing Capacity	298.80	2	560.25	4	672.30	4
5. Tear-out Capacity	364.16	3	742.33	7	1017.79	8
6. Net Section Rupture (AeRuFu)	731.44	8	614.72	5	762.56	5
7. Bolt Shear Strength	530.61	5	1243.63	8	895.41	7
8. Block Shear Strength	473.57	4	553.61	3	827.93	6

Table 3-5 Design Limit States for Tension Test 4A (Actual Material Strength)

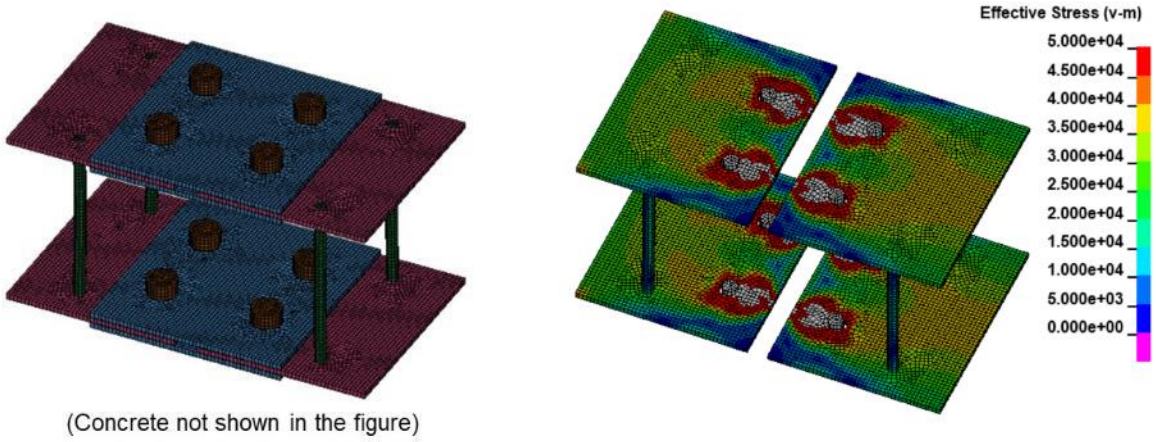
	Case 4A	
Target Loading Tu (kips)	327.33	
Limit States	Strength (kips)	Sequence
1. Corner Bending Resistance	327.33	1
2. Concrete Failure	369.60	3
3. t2 Yielding Force (RyFy)	330.75	2
4. t3 Shear Strength	396.90	4
5. t1 Yielding Force (RyFy)	661.50	6
6. Bolt Tension Strength	530.19	5

3.2.3 Primarily Finite Element Analyses

A large number of analyses were conducted to investigate whether the desired hierarchy of limit states could be expected to develop as intended, and to assess the ultimate strength of the proposed details. For brevity, most of these analyses are not presented here (some are summarized in Appendix B). These included simple strength-based approaches (using conventional design equations), SAP2000 analyses using elastic or inelastic hysteretic materials, and finite element analyses.

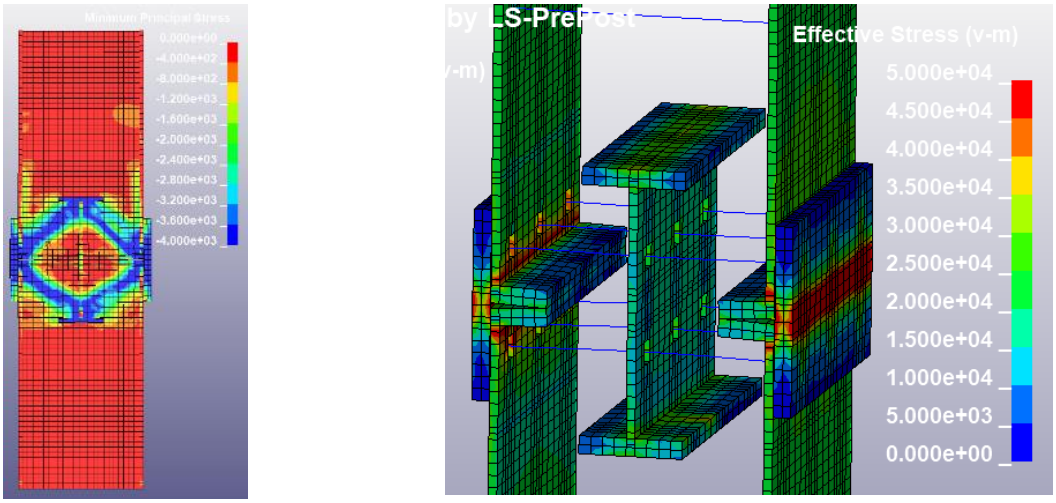
Finite element models were used to predict the structural behavior and ultimate strength developed by the splice connections. For example, Figure 3-5 shows one finite element analysis results for Case 1A. In this model, an elasto-perfectly-plastic steel model with *50 ksi* yield strength was used together with concrete having a *6 ksi* compressive strength. Concrete tensile strength was ignored in the analysis. Likewise, for illustration purposes, Figure 3-6 shows results for the Case 4A model, which uses an I-shape "anchor" to

successfully develop compressive struts and keep the steel plates from failing due to their out-of-plane bending at the “corners”, for two different concrete tensile strength scenarios.

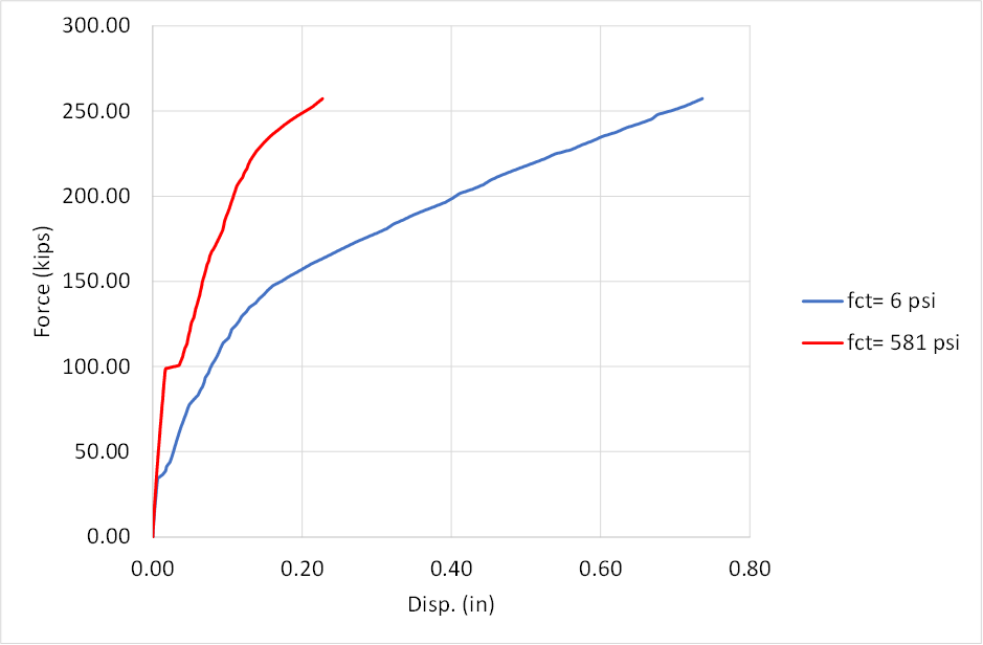


(a) Tensile Stress Contour (b) von Mises Stresses around bolt holes

Figure 3-5. Finite Element Analysis of Case 1A



(a) Compressive Strut (b) von Mises stress of steel plates



(c) Load-Displacement Curve

Figure 3-6. Finite Element Analysis of Case 4A

3.2.4 Summary of Tension Test Specimens

There is a total of six tension tests in the component test series. From here on, instead of using the previously nomenclature that referred to specific types of behavior (i.e., Case 1A, Case 2A, etc.), the text will refer to Specimens T1 to T6 in the sequence they were tested. Cross-correlation to the cases that describe their expected behavior is provided in Table 3-6.

Table 3-6. List of Tension Tests

Specimens	Name
T1	Case 1A
T2	Case 2A
T3	Case 2B
T4	Case 4A
T5	Case 1C
T6	Case 2C

3.2.5 Test Set-up

Figure 3-7 shows a 3D view of the test setup and a specimen assembled at SEESL at the University at Buffalo. The set-up consists of two 420 kips actuators connected to a spreader beam. Each specimen is connected to that spreader beam as well as to a similar spreader beam at its other end that distributes the load to multiple anchors attached to the laboratory's strong wall. The specimens were designed to allow casting the concrete in the tension specimens in the lab, and the composite specimens to be swapped and sequentially tested. A small frame was included to keep the specimen aligned (by necessity due to the fact that the servo-controlled actuators have pins at both of their ends). Figures 3-8 to 3-12 provide plan views and elevations views of the test setup for all six tension test specimens. Larger drawings are provided in Appendix F.

Steel specimens were delivered to the laboratory fully assembled, with all connections with blind bolts (including the one with Shuriken) torqued to their pretension value. Connections with pipe sleeves had to be torqued after concrete was poured; Specimen T3 was torqued with a hydraulic torque wrench to 2000 ft-lb, while Specimens T2, T4, and T6 were torqued using a bolt-gun to approximately 400 ft-lb (a value estimated after the tests, based on results obtained). Concrete was cast on site, with all specimens disposed sideways, as shown in Figure 3-13.

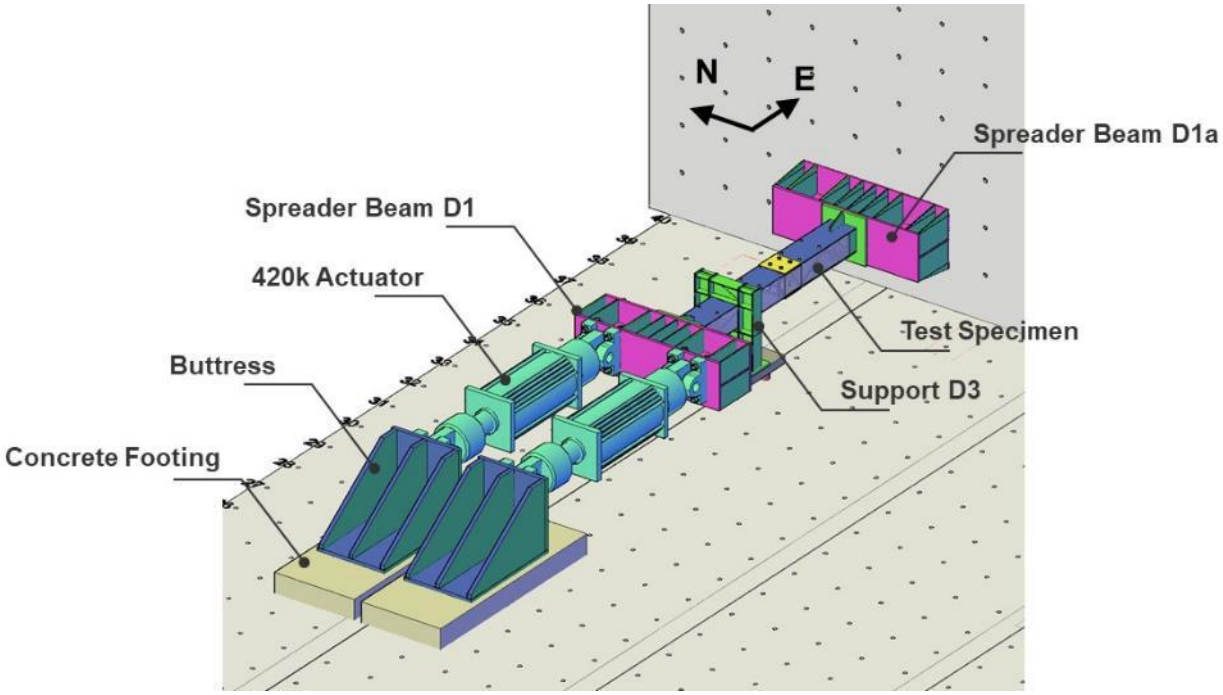
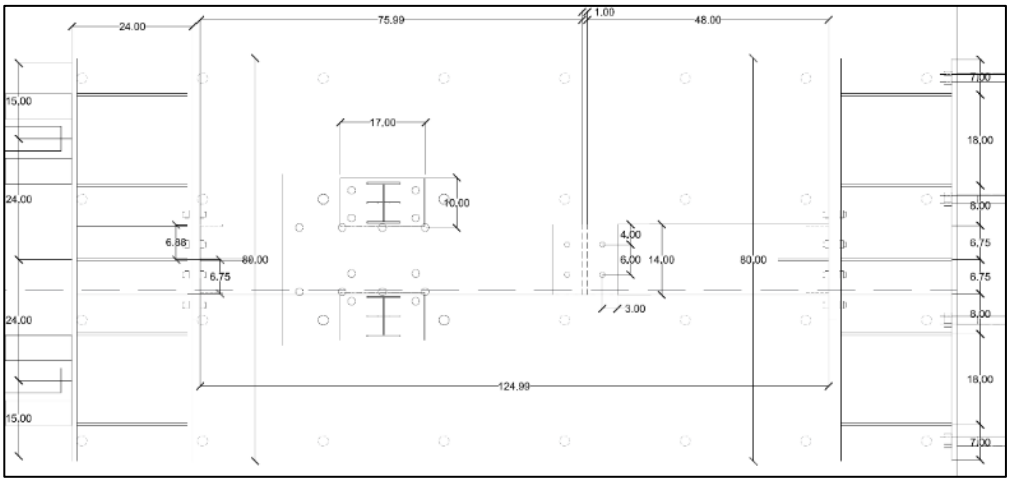
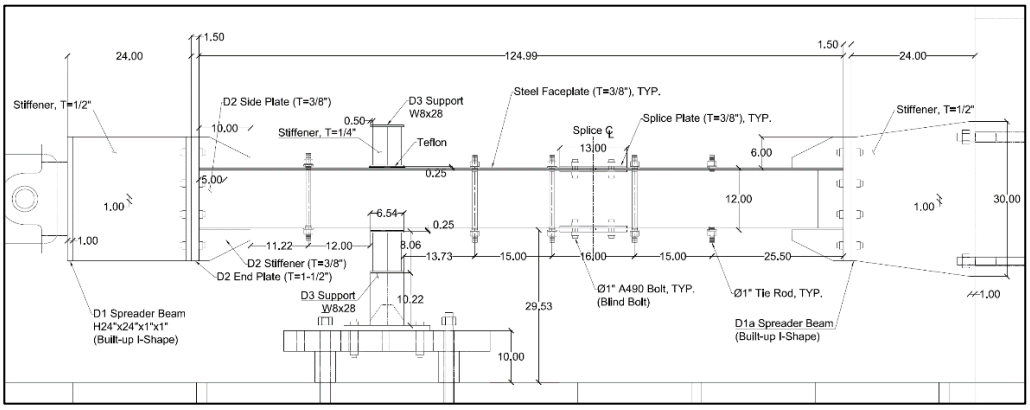


Figure 3-7. 3D View of Tension Test Setup

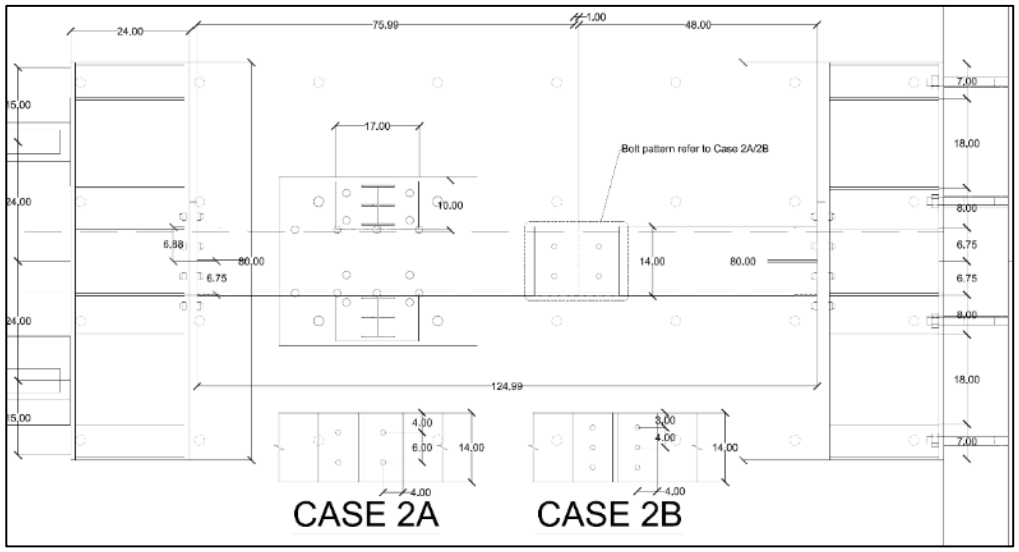


(a) Plan

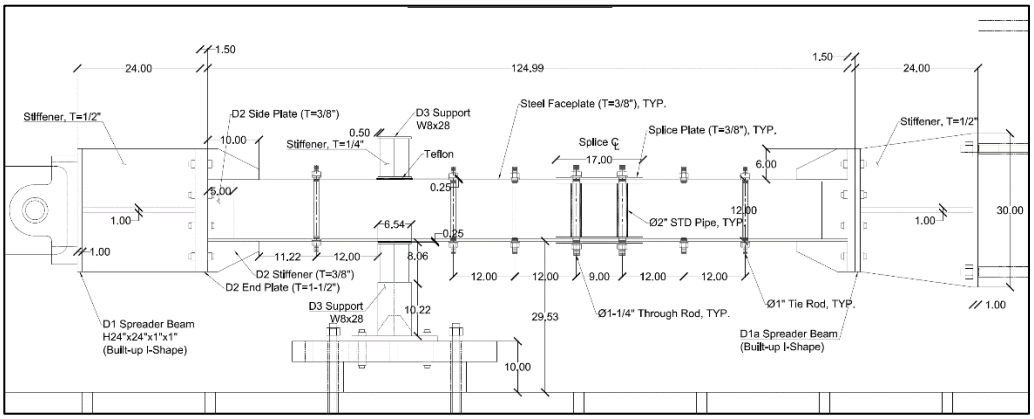


(b) Elevation

Figure 3-8. Tension Test Setup for Specimen T1

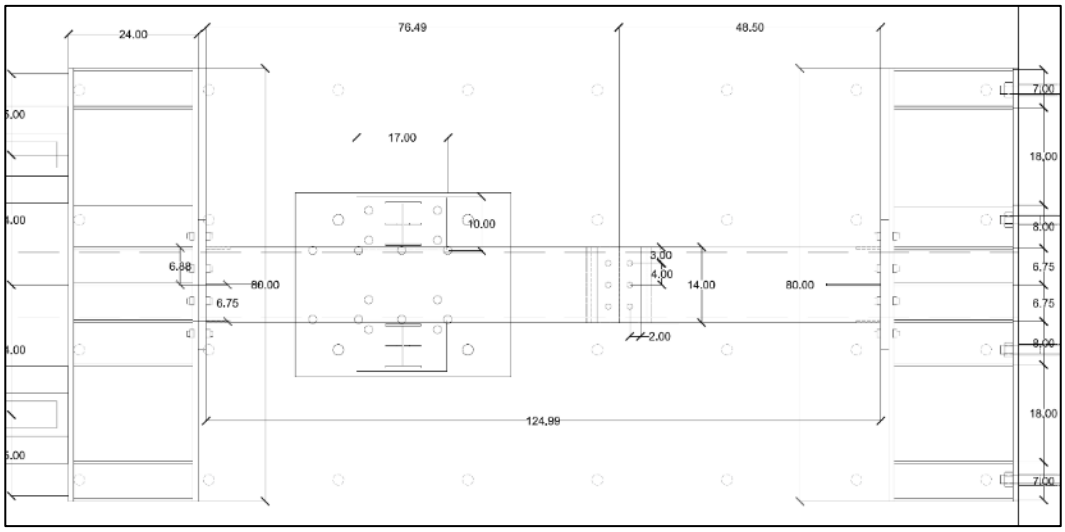


(a) Plan

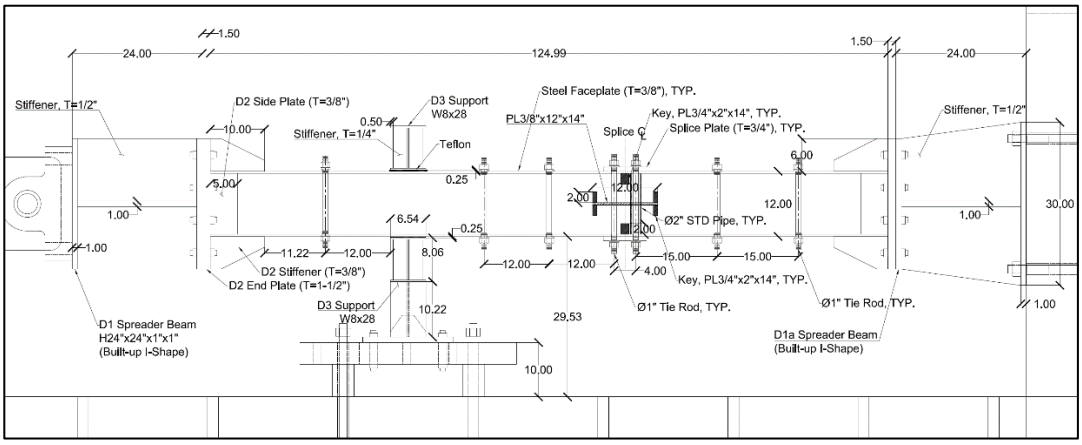


(b) Elevation

Figure 3-9. Tension Test Setup for Specimens T2 and T3

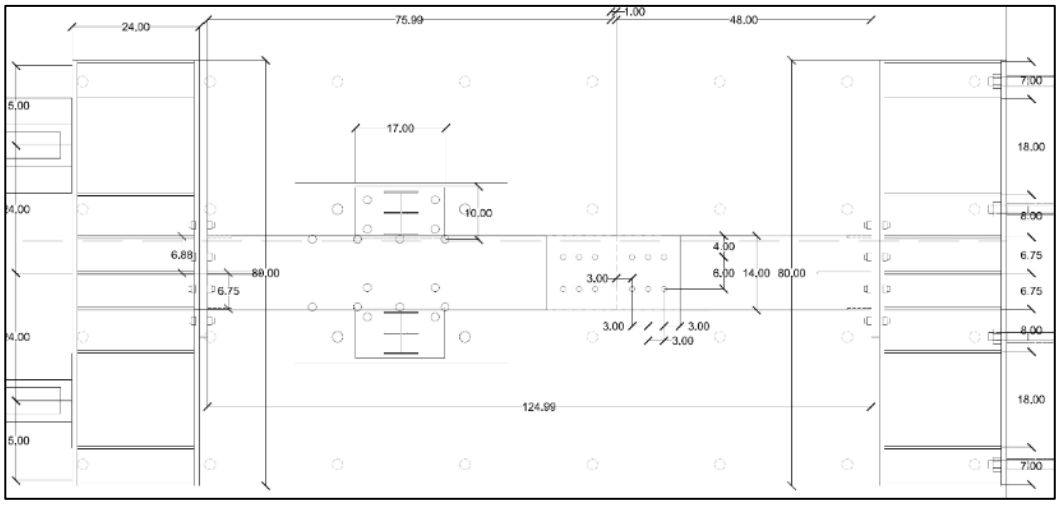


(a) Plan

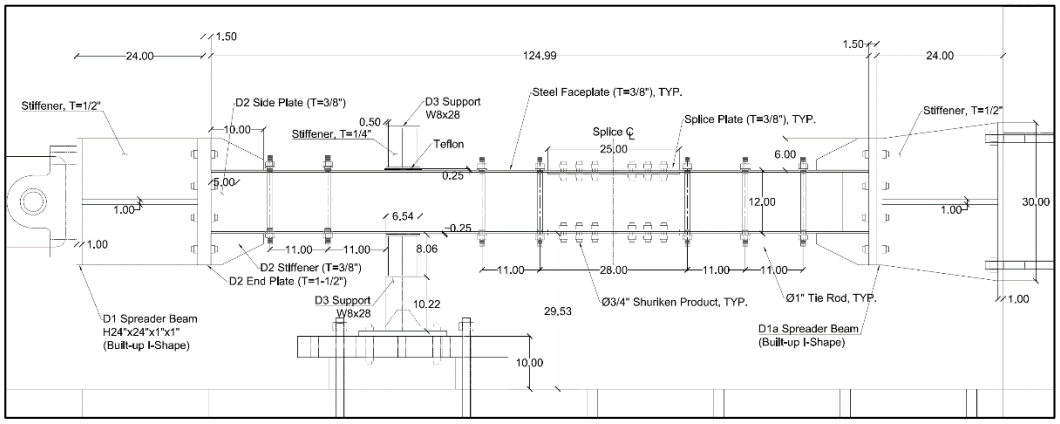


(b) Elevation

Figure 3-10. Tension Test Setup for Specimen T4

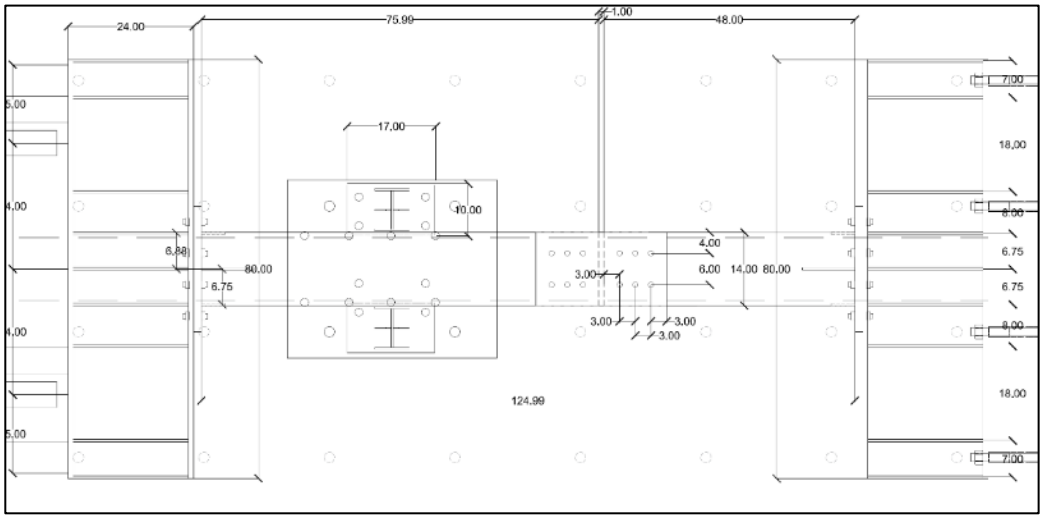


(a) Plan

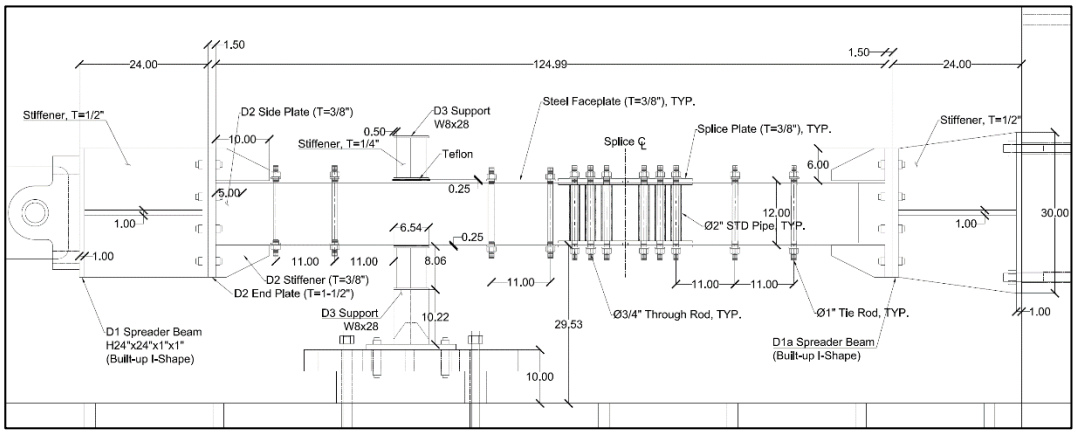


(b) Elevation

Figure 3-11. Tension Test Setup for Specimen T5



(a) Plan



(b) Elevation

Figure 3-12. Tension Test Setup for Specimen T6

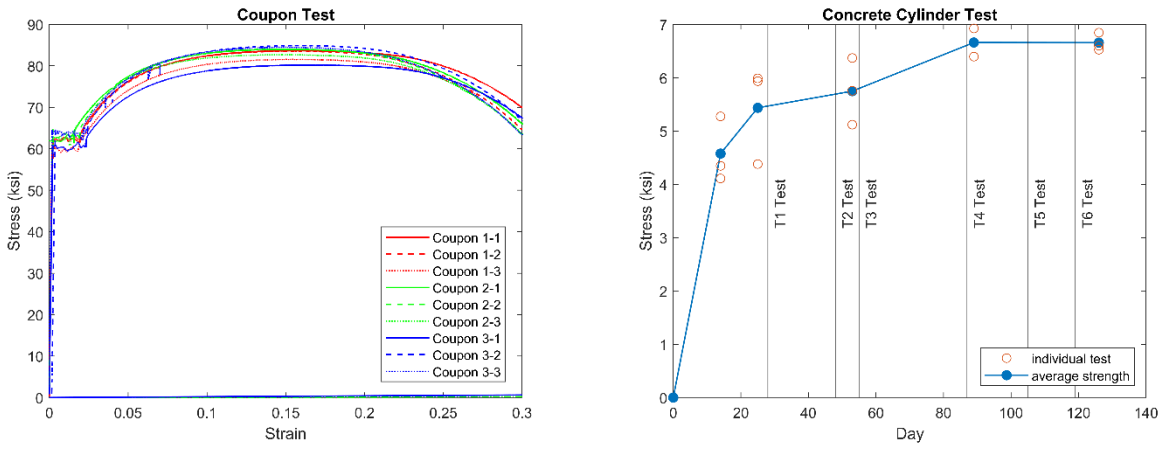


Figure 3-13. Tension Test Specimens (During Casting Concrete)

3.2.6 Material Properties of Tension Specimens

A572 Gr. 50 steel was used in the construction of all specimens. According to the plate information provided by the fabricator, all of the 3/8" thick steel plates used for tension specimens (including the faceplates and splice plates) came from two different plate sheets, labelled FS382320 and FS382321. The first three coupon specimens (Coupon Group 1) were received a month after the specimens arrived, and the fabricator indicated that these coupons were cut from sheet FS382320. To cross-verify the material properties, three coupon specimens (Coupon Group 2) were cut from the faceplate of specimen T4, and another three coupon specimens (Coupon Group 3) were cut from the splice plate of specimen T6. These coupon specimens were used to represent the materials of plate sheets FS382320 and FS382321, respectively. All coupon specimens were tested under uniaxial tension. Results are presented in Figure 3-14 (a) and in Table 3-7. A "Yield plateau" was observed in the stress-strain behavior of the tested coupons. The average yield strength, F_y, for the steel plate is 63.0 ksi, and the average ultimate strength, F_u, for each coupon test is 83.0 ksi.

For concrete, fifteen 6in. x12in. cylinders were taken on the day of concrete pouring from the concrete batch used for the foundation and the infill of the tension specimens. The number of cylinders was taken to keep track of concrete strength over time. Figure 3-14 (b) shows the development of concrete strength over time, and the number of days of curing on the date of each tension tests (T1 Test to T6 Test) is marked in the figure.



(a) Steel Coupon Test

(b) Concrete Cylinder Test

Figure 3-14. Material Test of Tension Specimen

Table 3-7. Coupon Test Results

Coupon Specimen	F_y (ksi)	F_u (ksi)
1-1	62.81	83.66
1-2	62.65	83.55
1-3	62.23	81.35
2-1	62.73	83.99
2-2	64.70	84.05
2-3	62.83	82.69
3-1	61.64	80.20
3-2	64.55	84.91
3-3	64.38	84.51
Average	**63.17**	**83.21**

3.2.7 Instrumentations for Tension Tests

Linear pots, string pots, and strain gauges were used to measure the deformation of each tension specimen during cyclic axial loadings. The measurements focused on documenting the axial deformation of the specimens and some local effects of the connection and test setup. As shown in Figure 3-15, the axial deformation of the specimens was measured over three ranges.

The first range is the global response (labeled "GR"), which is the displacement read from the actuators. GR includes the sum of the deformation from the specimen, gap openings at various points between parts of the test setups and specimens, and the sliding displacements of the foundations.

The second range is the overall deformation of the specimen measured using string pots, which was labeled "SP". SP measures the axial deformation of the specimen from the left end to the right end of the specimen (Figure 3-16), which include all deformations taking place over the bolted splice connection and the gross section elongations of the C-PSW/CF members. Note that because of the way the instruments were connected, SP also measured gap openings between end plates and spreader beams, but this amounted on average to 0.44% of the total SP value measured, with a 0.77% standard deviation (in only one case, this contributed to more than 1% of the total value). A pair of string pots, positioned above and below the specimen and labeled SP1 and SP2, were used for this purpose, and the value of SP is calculated as the average of SP1 and SP2.

The third range focuses on the connection behavior in the splice region and the deformation there, which is labeled as "LP". These deformations were measured using linear pots located at L9 to L12 in Figures 3-17 and 3-18. LP measures the movement of the outside splice plate with respect to faceplates. In other words, the value of LP includes the sum of the sliding distances between splice plates and faceplates, the gross

section deformation outside the connection from the end of splice plates to the points where the linear pots are connected to the faceplate plate. As such, it includes all deformations that happen inside the splice region, such as bearing deformations and both net and gross section deformations of the faceplates and splice plates. To calculate the value of LP, the sum of L9, L10, L11, and L12 is divided by two. Figures 3-17 and 3-18 shows the locations of all the linear pots installed for Specimen T1. Additionally, 3-19 shows photographs of some of the linear pots used during the test.

As shown in Figures 3-17 and 3-19, additional linear pots (L1 to L8) were installed at the edge of the faceplates in the connection area to obtain localized information on net section elongation in the spliced region, with strains to be obtained by dividing the linear pot deformations by the length over which that measurement was taken.

In addition, strain gauges were installed to measure the strain of the net section and gross section area. Figures 3-20 and 3-21 show the locations of strain gauges installed in Specimen T1, where S1 to S8 measured edge plate deformations, which represent the net section strain at those points, and S9 to S12 captured gross section strains at mid-width of the top and bottom faceplates. Drawings showing the generic locations/labeling of all instrumentation is provided in Appendix H (i.e., without dimensions showing gage lengths for the linear pots).

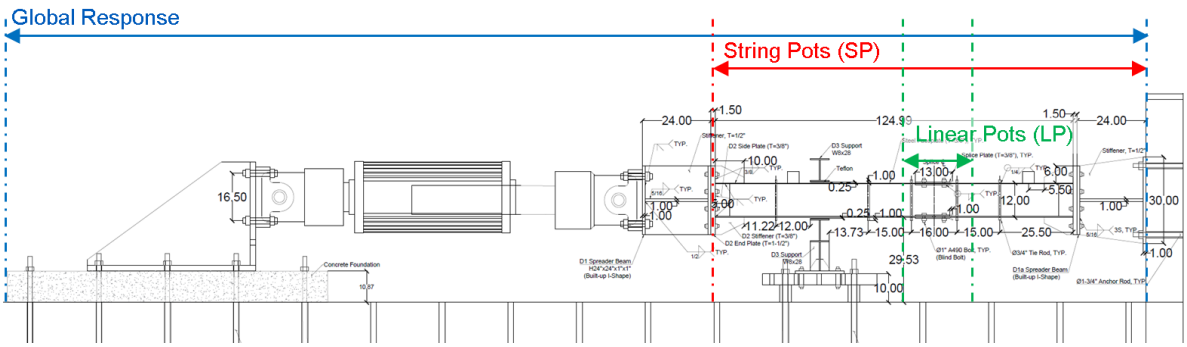


Figure 3-15. Axial Deformation Measurement of Tension Specimen

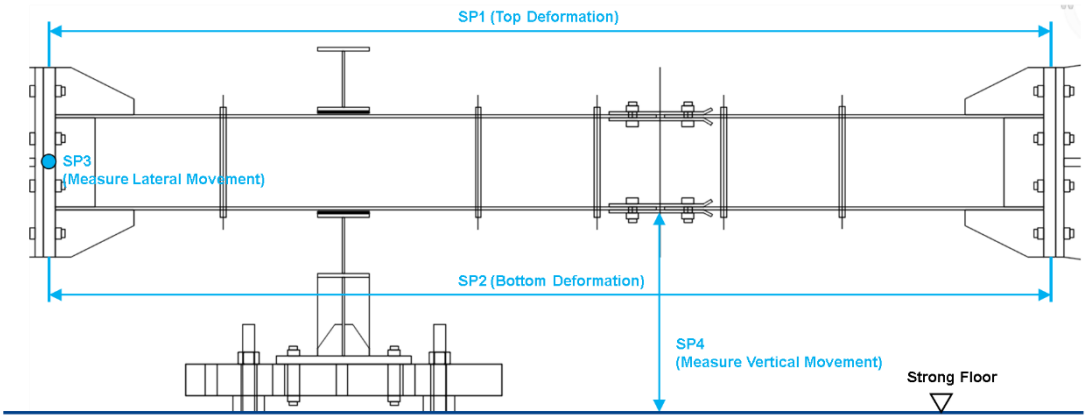


Figure 3-16. String Pots for Tension Specimens

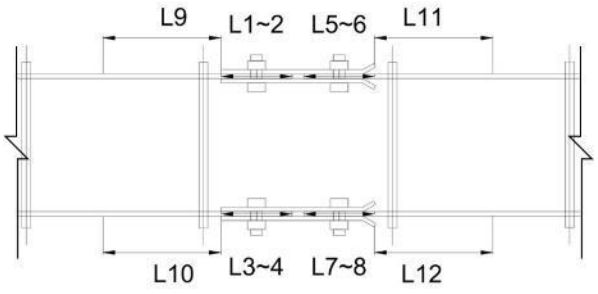


Figure 3-17. Linear Pots of Specimen T1 (Elevation)

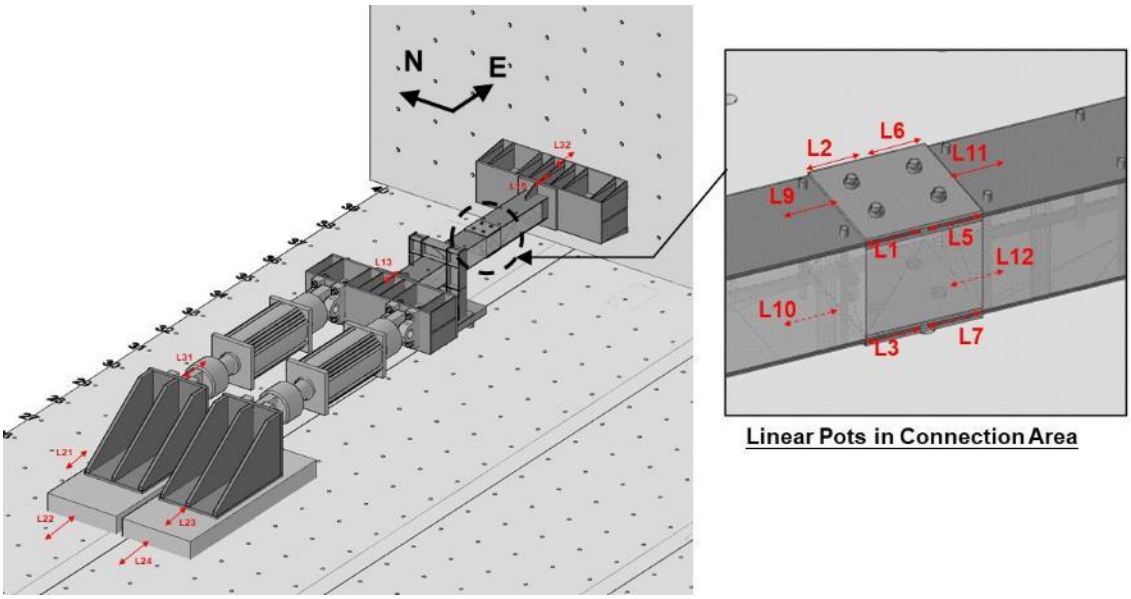


Figure 3-18. Linear Pots of Specimen T1 (3D View)



(a) South View (b) Top View

Figure 3-19. Photos of Linear Pots for Specimen T1

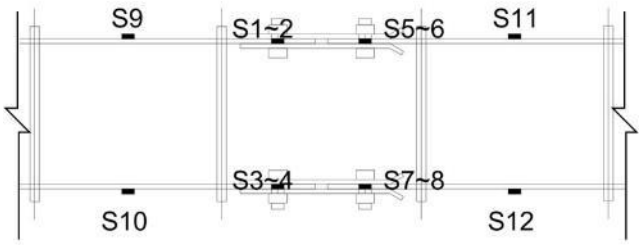


Figure 3-20. Strain Gauges of Specimen T1 (Elevation)

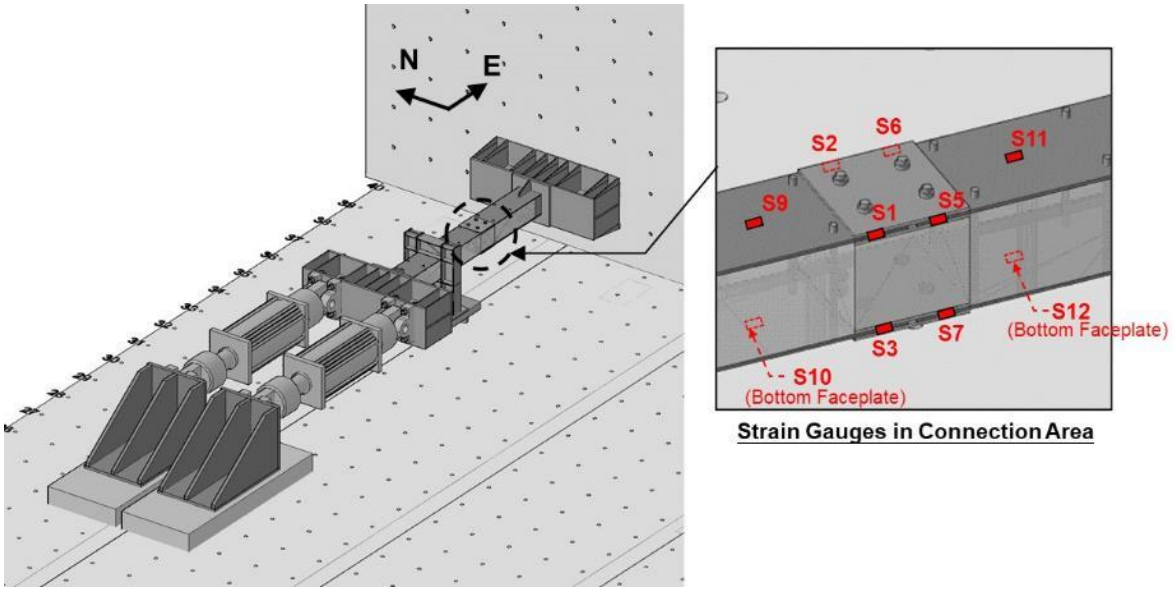


Figure 3-21. Strain Gauges of Specimen T1 (3D View)

3.2.8 Loading Protocol

Table 3-8 shows the originally planned loading protocols for each tension test. Since Specimens 1 to 4 are designed to be governed by wind load, loading cycles in Table 3-8(a) are proposed to test the component behaviors under typical and performance-based wind load. The approach consists of first applying cyclic loading up to the design strength, to verify the ability of the splice to resist the design loads. Then, beyond that, further cycles would be applied in incremental steps of strains beyond yield up to failure, to determine the ultimate failure and confirm development of the intended hierarchy of limit states. For Specimens 5 to 6, loading cycles in Table 3-8 (b) are proposed, but fewer cycles are applied as the intent here is to yield the steel plate of the walls, thus imposing a loading protocol closer to what is conventionally used in earthquake engineering. In essence, although not reflected in Table 3-8, the expectation is that the ability of the splice to provide ductile behavior (Specimens 1 to 4) is significantly less than what can be provided by yielding of the base material (Specimens 5 to 6).

Note that the loading protocols described above were slightly modified for each specimen based on observations while running the test. The updated loading protocols are discussed in the later sections.

Table 3-8. Original Loading Protocol for Tension Test

*Pw = design wind load for Tension/Shear

Phase	TYP. Wind	P.B. Wind
1	10 cycles @ 0.5Pw	10 cycles @ 0.5εy
2	10 cycles @ 0.75Pw	10 cycles @ 0.75εy
3	10 cycles @ 1.0Pw	10 cycles @ 1.0εy
4	-	10 cycles @ 1.5εy
5	-	10 cycles @ 2.0εy
6	-	10 cycles @ 3.0εy
7	-	10 cycles @ 4.0εy
8	-	10 cycles @ 5.0εy

Keep increasing until failure

(a) For Specimens T1 to T4

Phase	TYP. Wind	P.B. Wind/Seismic
1	10 cycles @ 0.5Pw	10 cycles @ 0.5εy
2	10 cycles @ 0.75Pw	10 cycles @ 0.75εy
3	10 cycles @ 1.0Pw	10 cycles @ 1.0εy
4	-	10 cycles @ 1.5εy
5	-	2 cycles @ 2.0εy
6	-	2 cycles @ 3.0εy
7	-	2 cycles @ 4.0εy
8	-	2 cycles @ 5.0εy

Keep increasing until failure

(b) For Specimens T5 to T6

3.3 Design of Shear Component Tests

3.3.1 List of Specimens

In the shear tests, connections details vary to account for different fastener types used and desired governing limit states. Similarly to what was presented for the tension specimens, Table 3-9 shows a summary of shear test specimens selected for the test program. There are two types of splice configurations considered in this case, namely, Type 1 - Blind Bolts and Type 2 - Through Bolts, conceptually identical to what was presented earlier. The designation Case A, B, and C is again used to represent different governing limit states, namely: bearing, slip-critical, and yield strength control.

In shear, it is unescapable that the presence of concrete will allow development of a diagonal compression strut acting simultaneously to the strength provided by the steel splice. To be able to separate the contribution of steel and concrete, special details were developed to allow (for each Case) the testing of a specimen without in the splice region and one for which full composite action can develop. A lowercase character “c” was added to the name of specimens in Table 6 for which the full composite action would develop – e.g., “Case 5Ac”.

Table 3-9. Shear Test Specimens

Limit States / Fasteners	Case A (Bearing)	Case B (Slip-Critical)	Case C (Yielding)
Type 1 (Blind Bolts)	-	Case 5B/5Bc	-
Type 2 (Through Bolts)	Case 6A/6Ac	-	Case 6C/6Cc

3.3.2 Design Limit States

Following the same approach described in Section 3.2.2, Table 3-10 shows the design strength for each splice connection for its different limit states, assuming a yield strength, R_yF_y, of 55ksi. In that table, "target load" refers to the assumed shear force that the splice would have to be designed to resist over that segment of wall of a given width. Note that in these tables, for each proposed connection, the term "sequence" is used to rank (from weakest to strongest) the strengths obtained considering various limit states for each wall segment. Similarly compared to tension specimens, all design limit states were calculated using AISC equations. Note that, although connection eccentricity would typically not be an issue in the long splices of walls, since the eccentricity of shear connection is unavoidable for the specimens considered here, bearing strength subjected to combined shear force and torsion in the system were also calculated (using the elastic method from the AISC Steel Manual, but replacing bolt strength by bearing strength) and are included in the table for comparison purposes. However, note that when establishing the hierarchy of limit states during design of the specimen, these eccentricities were neglected. For Cases 6A and 5B, the presence of eccentricity reduces strength without affecting the hierarchy of limit states. For Cases 6C/6Cc, the eccentric

bearing strength would not be engaged before slip resistance of the connection is exceeded. Also note that the composite shear strength computed using AISC equations for fully welded C-SPW/CF walls is also listed in that table (it was used as a theoretical upper limit checked against the 420 kips maximum capacity of the pantograph test set-up).

After specimens were received, steel coupon tests and concrete cylinder tests were performed and values for the design limit states were updated accordingly and are shown in Table 3-11. Note that initial stages of cyclic loading during the experiment were done on the basis of the design strength values (because no extra material had been received to allow getting the actual steel strength before testing, and steel coupons had to be taken from splice plates after the test), but results obtained were compared on the basis of actual material values.

Detailed calculations for analysis of the specimens are provided in Appendix G.

Table 3-10. Design Limit States for Shear Test

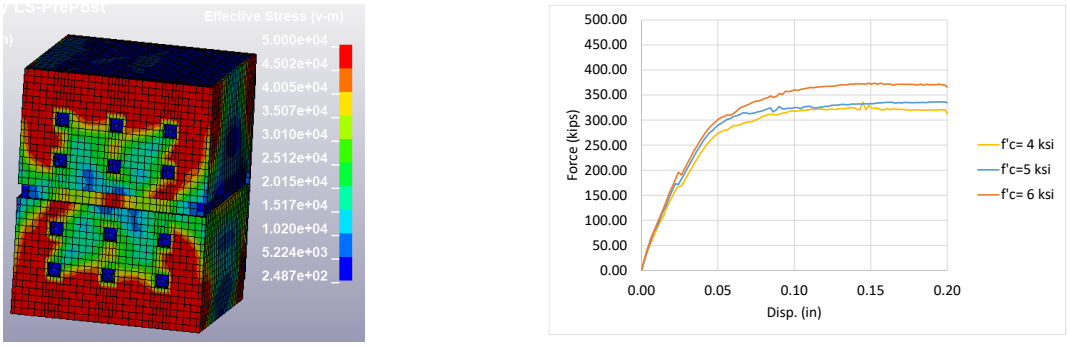
	S1/S2		S3/S4		S5/S6	
Target Loading Tu (kips)	171.60		141.53		231.00	
Limit States	Strength (kips)	Sequence	Strength (kips)	Sequence	Strength (kips)	Sequence
A. Slip-Critical Resistance (kips)	167.74	3	141.53	2	188.70	3
B. Net Section Yiled (0.6AeRyFy) (kips)	193.88	5	187.69	4	202.13	4
C. Gross Area Yield (0.6AgRyFy) (kips)	231.00	6	231.00	6	231.00	5
D. Bearing Capacity (kips)	171.60	4	193.05	5	257.40	6
E. Tear-out Capacity (kips)	356.61	10	378.06	10	745.39	11
F. End Tear-out & Bearing (kips)	233.27	7	238.63	7	434.36	9
G. Net Section Rupture (0.6AeRuFu) (kips)	252.04	8	243.99	8	262.76	7
H. Bolt Shear Strength (kips)	530.61	11	445.32	11	593.76	10
I. Eccentric Bearing Capacity 2.4dtFu (kips)	131.83	1	140.84	1	143.58	1
J. Eccentric Bearing Capacity 3.0dtFu (kips)	164.78	2	176.05	3	179.47	2
K. Composite Shear Strength (kips)	318.01	9	318.01	9	318.01	8

Table 3-11. Design Limit States for Shear Test (Actual Material Strength)

	S1/S2		S3/S4		S5/S6	
Target Loading Tu (kips)	175.06		142.38		268.21	
Limit States	Strength (kips)	Sequence	Strength (kips)	Sequence	Strength (kips)	Sequence
A. Slip-Critical Resistance (kips)	167.74	1	142.38	1	189.84	3
B. Net Section Yiled (0.6AeRyFy) (kips)	225.11	5	217.92	5	234.69	4
C. Gross Area Yield (0.6AgRyFy) (kips)	268.21	8	268.21	8	268.21	7
D. Bearing Capacity (kips)	175.06	4	196.94	4	262.58	5
E. Tear-out Capacity (kips)	363.79	9	385.67	9	760.40	11
F. End Tear-out & Bearing (kips)	237.97	6	243.44	6	443.11	9
G. Net Section Rupture (0.6AeRuFu) (kips)	257.11	7	248.91	7	268.05	6
H. Bolt Shear Strength (kips)	530.61	11	445.32	11	593.76	10
I. Eccentric Bearing Capacity 2.4dtFu (kips)	134.48	2	143.67	2	146.47	1
J. Eccentric Bearing Capacity 3.0dtFu (kips)	168.10	3	179.59	3	183.08	2
K. Composite Shear Strength (kips)	406.17	10	406.17	10	406.17	8

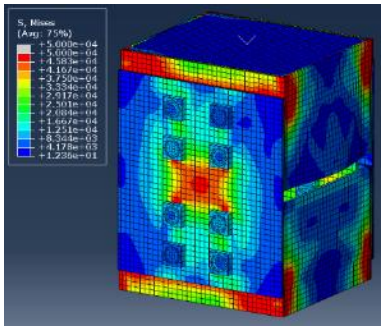
3.3.3 Preliminary Finite Element Analyses

Finite element models were used to predict the structural behavior and the ultimate strength of the shear splice specimens, considering various design options and modeling assumptions. For brevity, these analysis results are not presented here, except for Figures 3-22 and 3-23, to illustrate the comparison between finite element analysis results for composite and non-composite shear strength for one of the specimens.

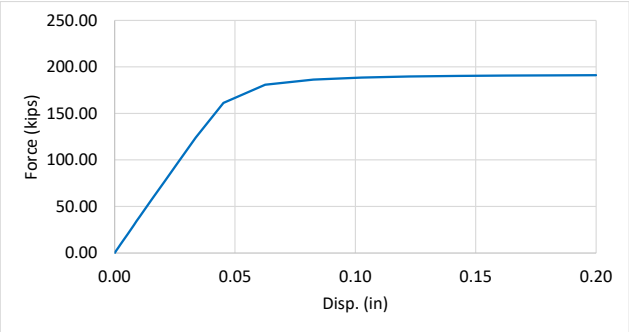


(a) von Mises stress (b) Load-Displacement Curve for different f'c

Figure 3-22. Finite Element Analysis of Composite Shear Strength



(a) von Mises stress



(b) Load-Displacement Curve

Figure 3-23. Finite Element Analysis of Non-Composite Shear Strength

3.3.4 Summary of Shear Test Specimens

There is a total of six tension tests in the component test series. From here on, instead of using the previously nomenclature that referred to specific types of behavior (i.e., Case 6A, Case 6Ac, etc.), the text will refer to Specimens S1 to S6 in the sequence they were tested. Cross-correlation to the cases that describe their expected behavior is provided in Table 3-12.

Table 3-12. List of Shear Tests

Specimens	Name
S1	Case 6A
S2	Case 6Ac
S3	Case 5B
S4	Case 5Bc
S5	Case 6C
S6	Case 6Cc

3.3.5 Test Set-up

Figure 3-24 shows that the Pantograph that was used in all shear tests. The purpose of a pantograph is to apply a condition of pure shear at mid-height of the specimen (which would be the splice location in this case). This Pantograph already exists at the University at Buffalo and has been used successfully in prior research, including for tests of concrete-filled steel tubes (the largest of those developing a strength of 410 kips). The maximum load that can be applied using this set-up is 420 kips. Figure 3-25 shows a 3D view of the test setup and a specimen assembled at SEESL at the University at Buffalo.

Note that a concept was developed to allow re-use of the steel framing the specimen outside of the splice region. As shown in Figure 3-26, it consisted of bolted rectangular "collars" framing around the specimens, to keep their "free length" short and therefore develop an ultimate behavior dominated by shear instead of flexure. This concept also allowed concrete to be cast into all of the specimens at the same time and in the lab, and made it possible to swap and sequentially test each composite specimen. Figures 3-27 to 3-29 show the shear test setups for all six specimens.

Specimens were shipped to the lab fully assembled. All except S2 and S4 were disassembled prior to pouring concrete. This was done for S1, S3, and S5 because it was needed to be able to pour concrete only outside of their splice region. This was done for S6 because the outside splice plate needed to be cut to make it shorter vertically to provide a larger ability to rotation during the test without touching the top and bottom plates delimiting the free region (if needed). Also, S2 and S6 were designed with the internal pipe sleeves and therefore were required to be torqued after concrete was poured. All were re-assembled using a torque-gun. Turn-of-the nut method was used for S3, applying a rotation of 1/3 of a turn after snug tight. Even though the bolts for S4 were pre-tensioned by the fabricator, a torque was applied to the bolts while

in the lab, which resulted in 1/8 of a turn of the nut for 6 out of the 12 of the bolts, and no additional rotation for the remaining six. All others were re-assembled using a torque gun applying a torque of approximately 400 ft-lb (a value estimated based on results obtained during the tests).

Figure 3-30 shows test preparation for concrete cast into the shear specimens, either over their full height (Specimens S2, S4, and S6) or in their top and bottom parts outside the splice region (Specimens S1, S3, and S5).

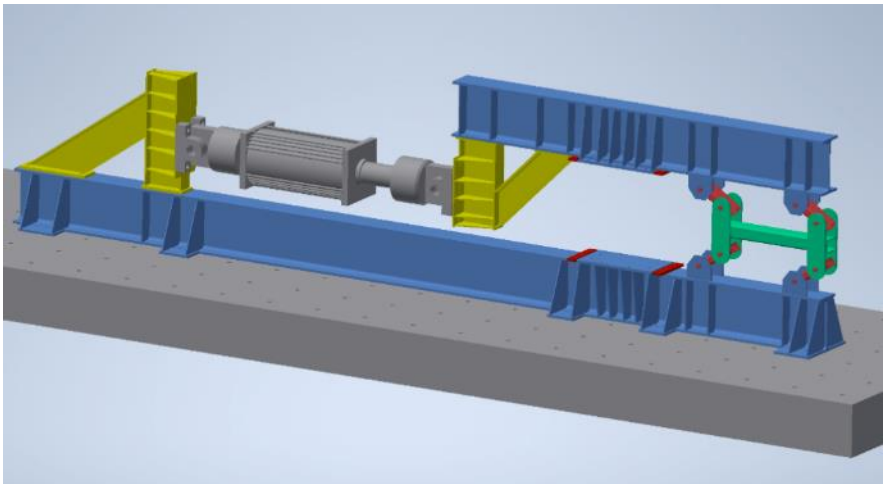


Figure 3-24. Pantograph (3D View without specimen in place)

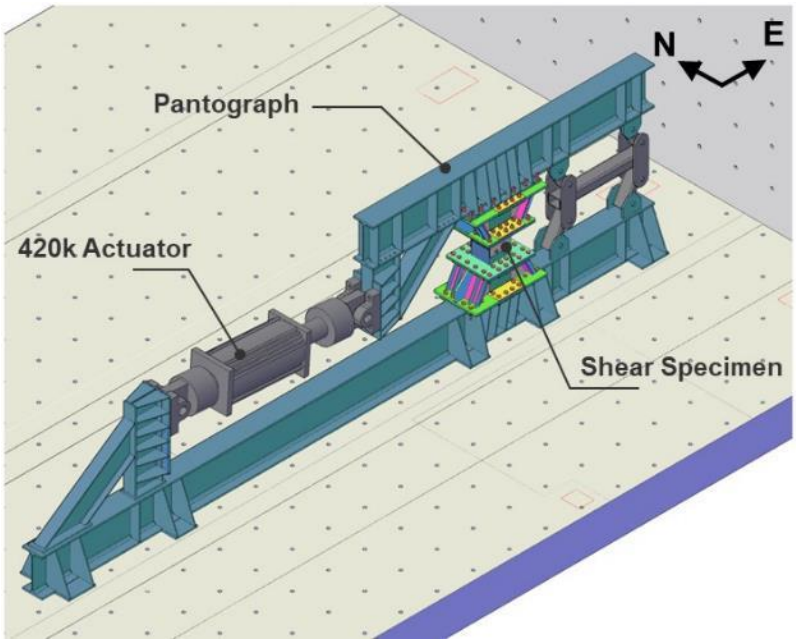


Figure 3-25. 3D View of Shear Test Setup

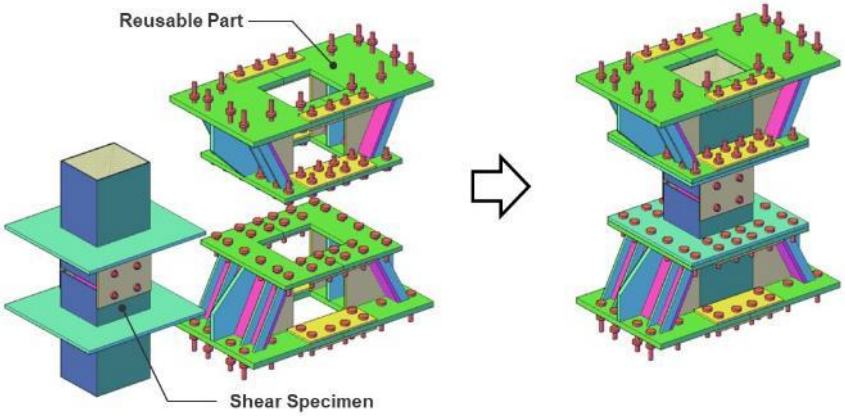
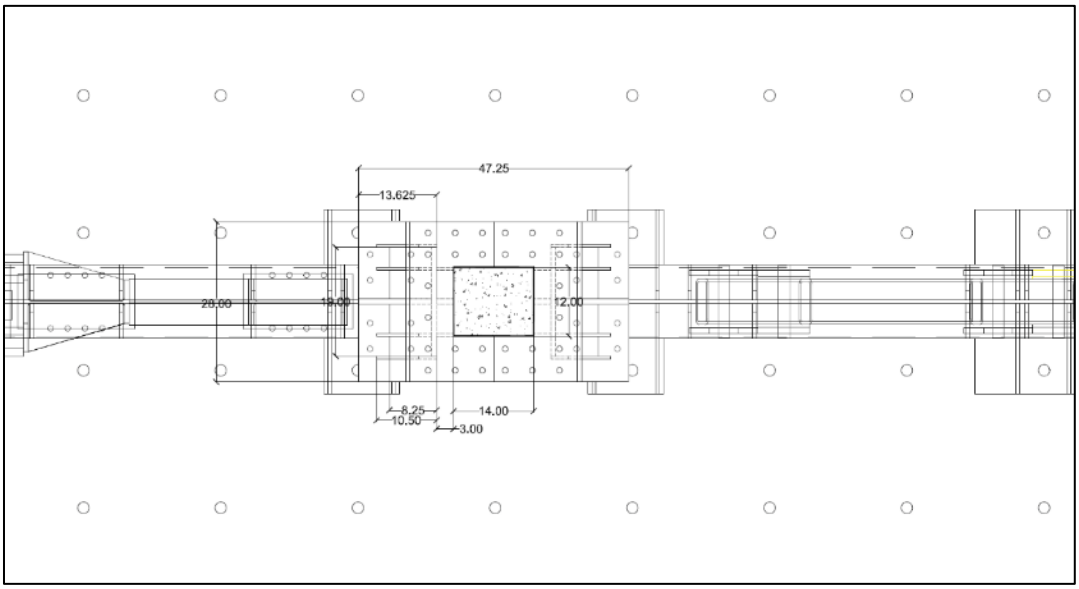
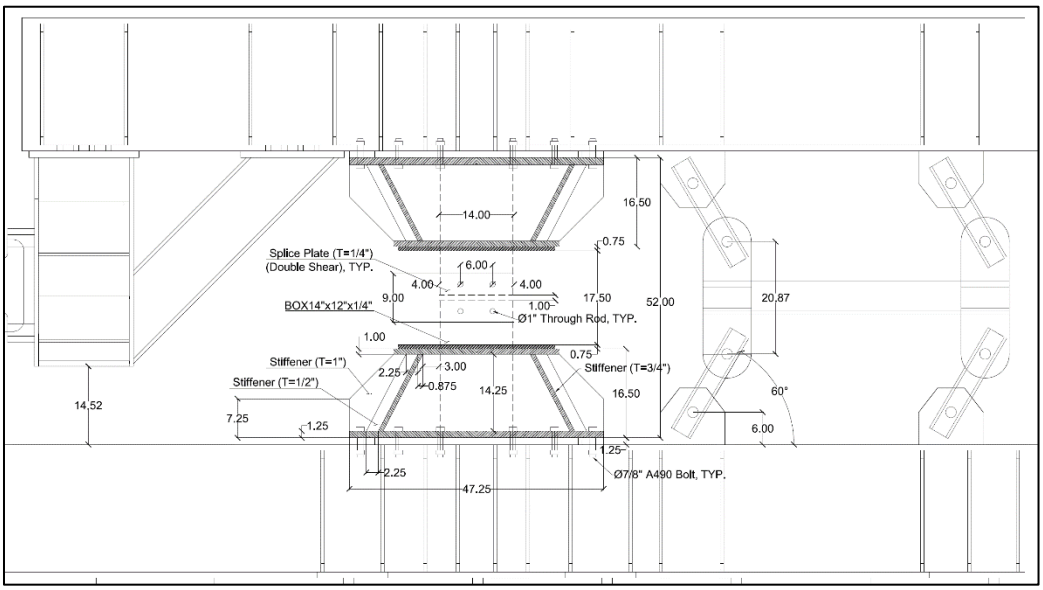


Figure 3-26. Reusable Parts for Shear Specimens



(a) Plan (for all shear tests)



(b) Elevation

Figure 3-27. Shear Specimens S1 and S2

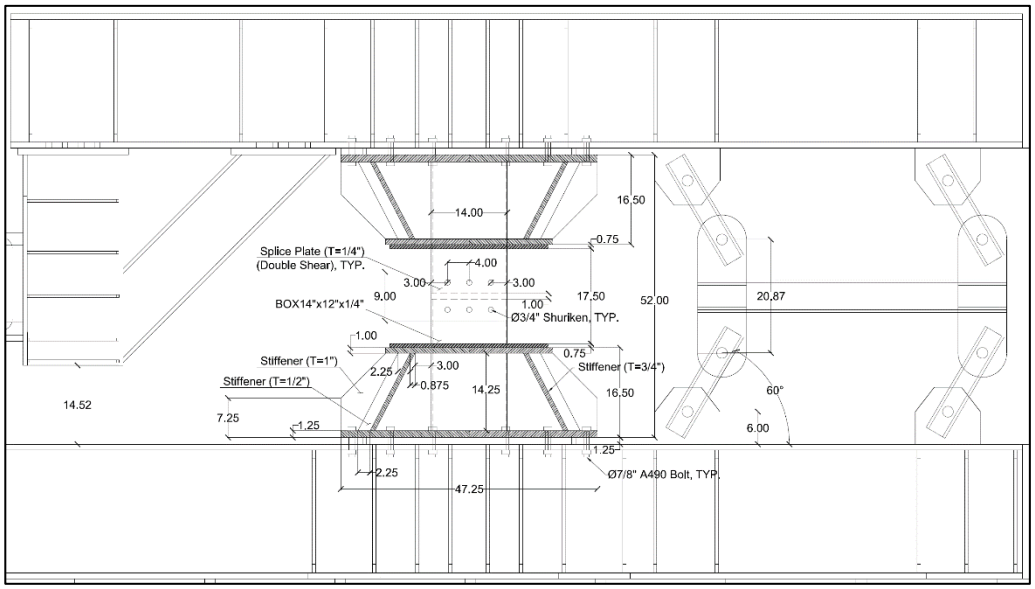


Figure 3-28. Shear Specimens S3 and S4 (Elevation)

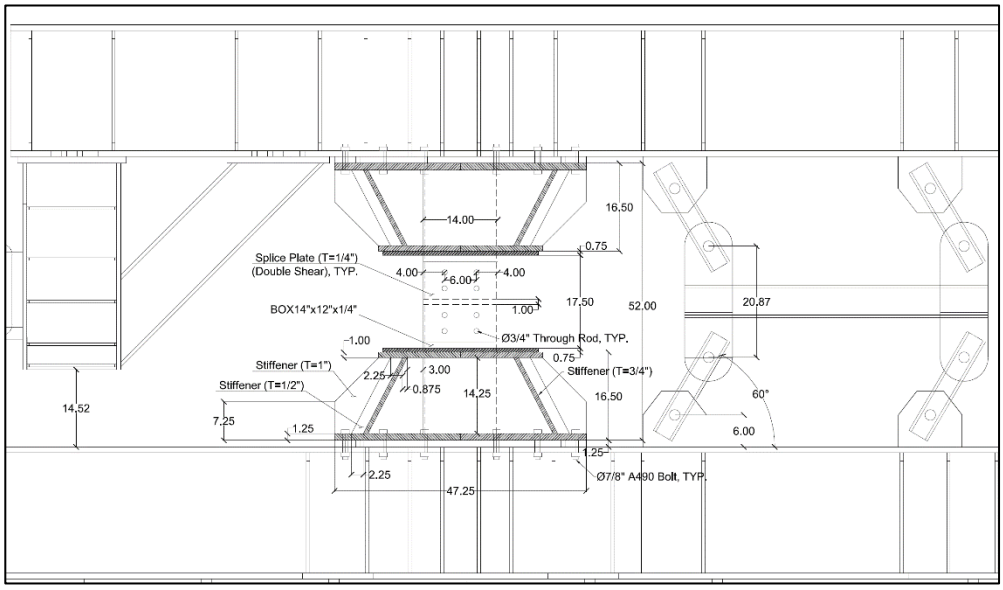


Figure 3-29. Shear Specimens S5 and S6

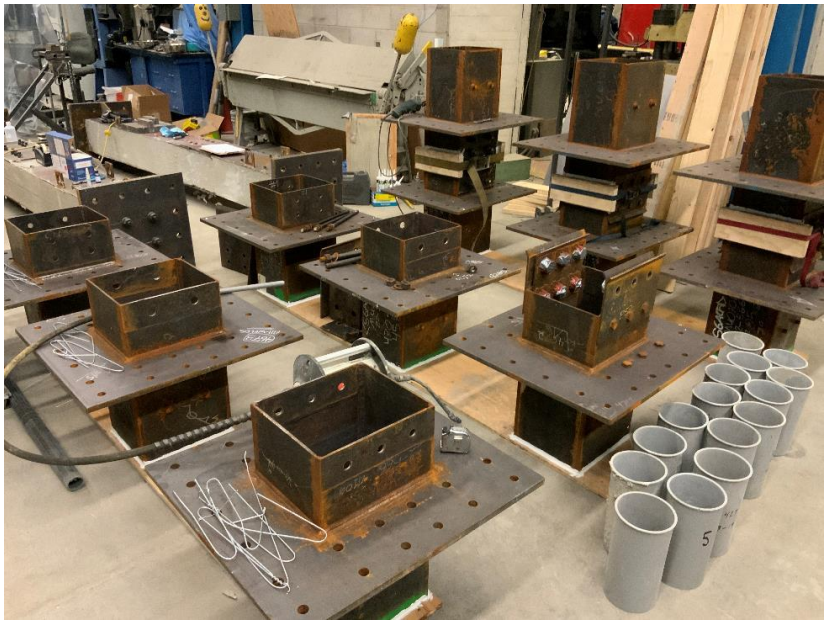
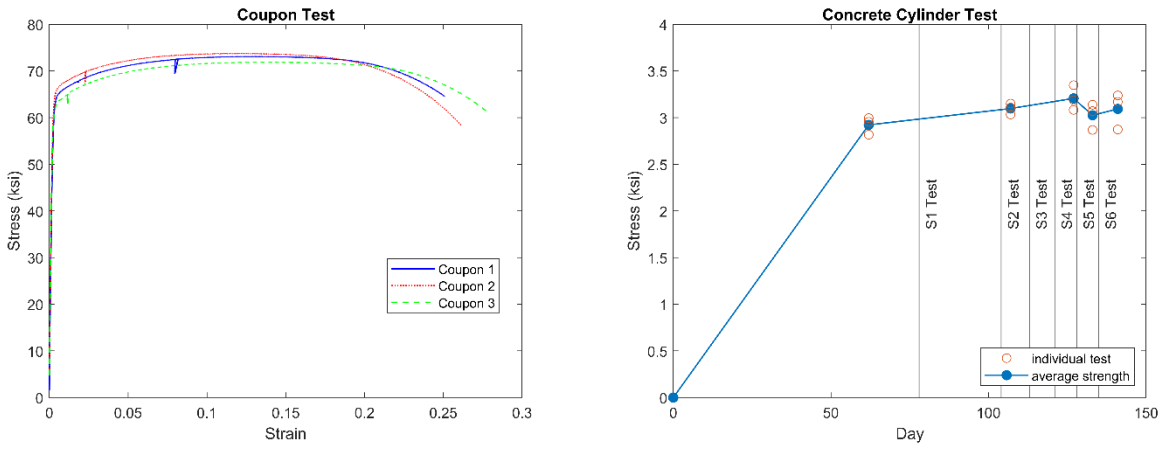


Figure 3-30. Shear Test Specimens (Before Casting Concrete)

3.3.6 Material Properties of Shear Specimens

A572 Gr. 50 steel was used in the construction of all specimens. All of the ¼ in. thick steel plates used for the shear specimens were cut from the same sheet. Three coupon specimens were cut from the splice plate of specimen S1, and the coupon specimens were tested under uniaxial tension. Results are presented in Figure 3-31 (a) and Table 3-13. However, no "yield plateau" was observed in the stress-strain behavior of the test coupons. Using the 0.2% offset method, the average yield strength, F_y, of the plates was determined to be 63.86 ksi. The average ultimate strength, Fu, for each coupon test is 72.94 ksi.

For concrete, fifteen 6in. x12in. cylinders were taken on the day of pouring from the concrete batch used for the infill of the shear specimens. The number of cylinders was taken to keep track of concrete strength over time. Figure 3-31 (b) shows the development of concrete strength over time, and the number of days of curing on the date of each shear tests (S1 Test to S6 Test) is marked in the figure. Note that concrete was purposely ordered to have an f'_c of less than 4ksi, to ensure that the shear specimens could develop their maximum strength with an adequate margin against reaching the maximum load that could be applied by the pantograph.



(a) Steel Coupon Test (b) Concrete Cylinder Test

Figure 3-31. Material Test of Shear Specimen

Table 3-13. Coupon Test Results

Coupon Specimen	F_y (ksi)	F_u (ksi)
1	63.86	73.12
2	65.20	73.79
3	62.53	71.91
Average	**63.86**	**72.94**

3.3.7 Instrumentations for Shear Tests

Strain gauges, string pots, and linear pots were used to measure the deformation of each shear specimen during cyclic axial loadings. The measurements focused on documenting the shear deformation of the specimens and tracking some local effects of the connection and test setup. According to Figures 3-32 and 3-33, a total of 14 strain gauges were affixed to the shear specimens. For specimens S1 to S4, strain gauges S1 to S12 were placed on both the top and bottom surfaces of the faceplates to measure shear strains on gross section areas. This was done using three gages at each location, at angles of -45, 0 and 45 degrees from the vertical, creating a strain gage rosette that also allowed to read each strain individually. Strain gauges S13 and S14 were installed to monitor the normal strain at the corners of cap plates. In the case of specimens S5 and S6, due to limited space, strain gauges S1 to S6 were instead placed on the external splice plates, to indirectly be able to infer strains on the hidden faceplates by measuring shear strains on the outer splice plates.

String pots were used to measure the shear deformation and the vertical deformation of the specimens. As shown in Figure 3-34, six string pots were installed around the specimen. String pots SP1 and SP2 were used to obtain the shear deformation (SP2-SP1) over the free length of the connection by measuring the displacement at the top and bottom of this free length of the specimen. String pots SP3 to SP6 were used to measure the vertical movements between the plates at the end of the specimen's free length, as well as between the top and bottom of the reusable parts.

Finally, four linear potentiometers (Figure 3-35) were installed at four different levels on the specimen and reusable parts. Their purpose was to measure the relative movements between the pantograph and the reusable part, as well as between the reusable part and the connection part.

Drawings showing the generic locations/labeling of all instrumentation is provided in Appendix H (i.e., without dimensions showing gage lengths for the linear pots).

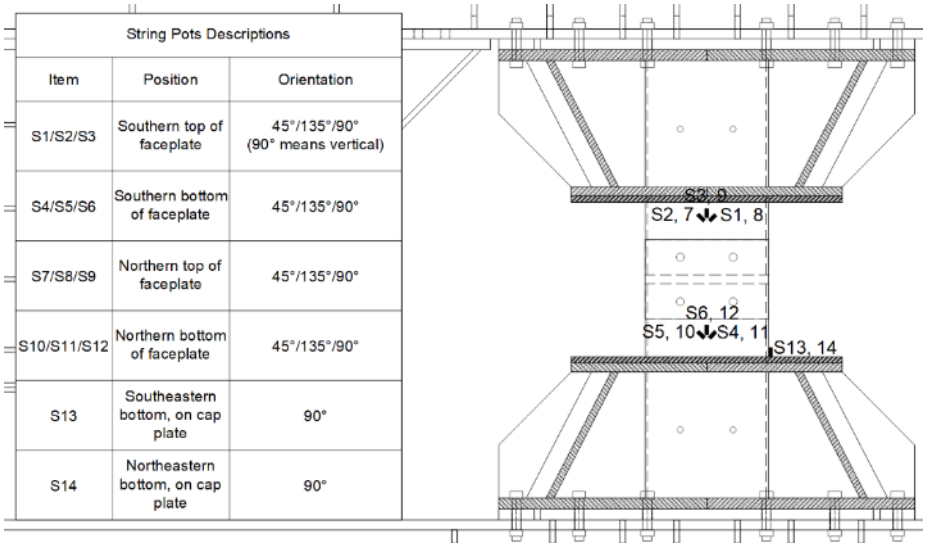


Figure 3-32. Strain Gauges on Specimens S1 to S4

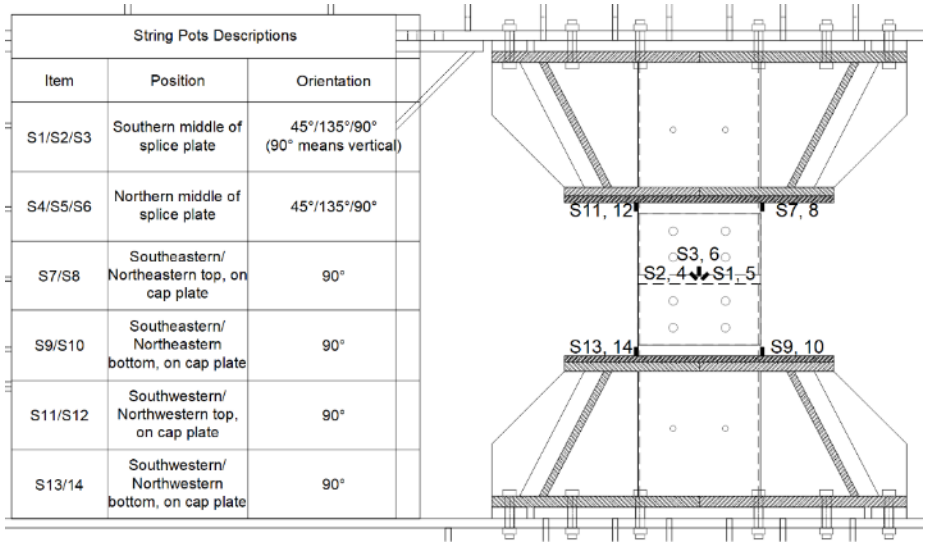


Figure 3-33. Strain Gauges on Specimens S5 and S6

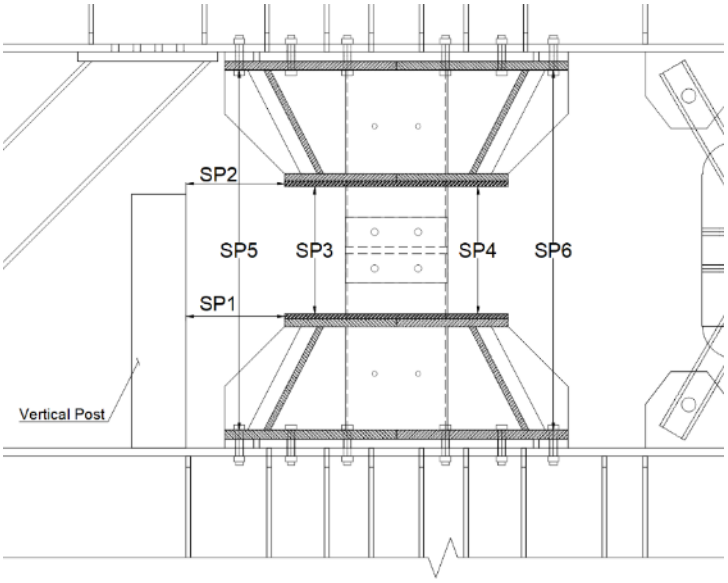


Figure 3-34. String Pots of All Shear Specimens

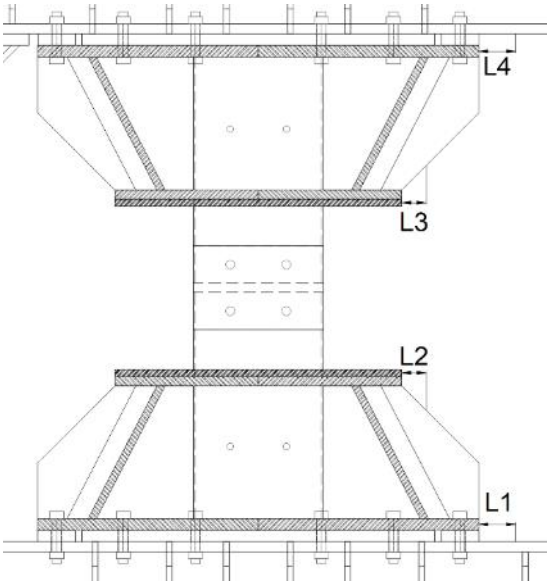


Figure 3-35. Linear Pots of All Shear Specimens

3.3.8 Loading Protocol

Table 3-14 shows the loading protocols for each shear test. The approach taken here is similar to the one presented in Section 2.2.5, with the difference that shear distortion angle is used here instead of axial strains.

Note that the loading protocols described above were slightly modified for each specimen based on observations while running the test. The updated loading protocols are discussed in the later sections.

Table 3-14. Loading Protocol for Shear Test

Phase	TYP. Wind	P.B. Wind
1	10 cycles @ 0.5Pw	10 cycles @ 0.5γy
2	10 cycles @ 0.75Pw	10 cycles @ 0.75γy
3	10 cycles @ 1.0Pw	10 cycles @ 1.0γy
4	-	10 cycles @ 1.5γy
5	-	10 cycles @ 2.0γy
6	-	10 cycles @ 3.0γy
7	-	10 cycles @ 4.0γy
8	-	10 cycles @ 5.0γy

Keep increasing until failure

(a) For Specimens S1 to S4

Phase	TYP. Wind	P.B. Wind/Seismic
1	10 cycles @ 0.5Pw	10 cycles @ 0.5γy
2	10 cycles @ 0.75Pw	10 cycles @ 0.75γy
3	10 cycles @ 1.0Pw	10 cycles @ 1.0γy
4	-	10 cycles @ 1.5γy
5	-	2 cycles @ 2.0γy
6	-	2 cycles @ 3.0γy
7	-	2 cycles @ 4.0γy
8	-	2 cycles @ 5.0γy

Keep increasing until failure

(b) For Specimens S5 to S6

SECTION 4
COMPONENT LEVEL TEST

4.1 General

This chapter presents the results and findings of the component level test. The tests were comprised of two series: six tension tests (T1 to T6) and six shear tests (S1 to S6), both designed to investigate the splice behavior in C-PSW/CF members, as mentioned earlier. The observations and results for the tension tests and shear tests are presented in Sections 4.2 and 4.3, respectively.

4.2 Test Observations and Results of Tension Specimens

4.2.1 Specimen T1

Testing of Specimen T1 started on 10/21/2022. A global view of the specimen is shown in 4-1. To prevent the downward movements from the actuators, timber supports were placed underneath the spreader beam before starting the test (Figures 4-1 and 4-2).



Figure 4-1. Global View of Specimen T1

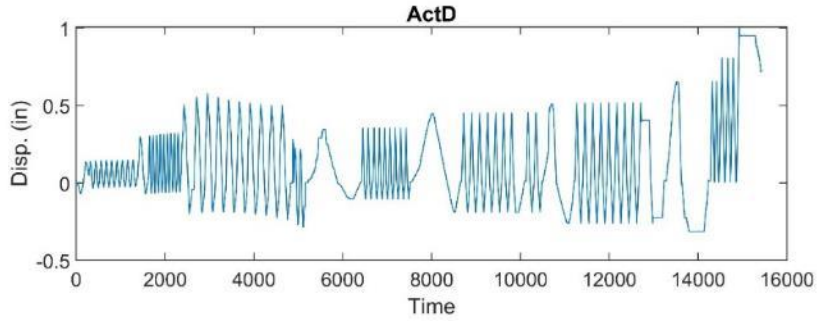


Figure 4-2. Timber Support for Specimen T1

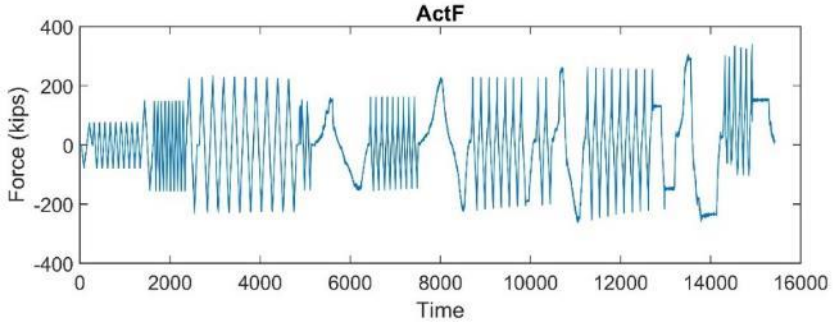
Testing unfolded following the loading protocol shown in Table 4-1 (slightly modified from the reference protocol shown in Table 3-8). Figure 4-3 shows the corresponding actuator displacement and load history during the test. The test began with the loads being applied in force control, with one actuator slaved to apply the same load as the other actuator, but (as can be inferred from Figure 4-3) changed to displacement-control starting from the fourth amplitude of applied cycles (corresponding to 50% of the design strength), with one actuator slaved to apply the same displacement as the other. Figure 4-4 provides a definition for the term "north view" (and, implicitly, all other cardinal directions) used throughout this report to monitor the condition of the specimens, the progression of cracks, and movements of parts of the connection throughout the entire test program for tension component. Figures 4-5 and 4-6 present a collection of photos of the splice region from the north view of Specimen T1 to illustrate the behavior at different displacement amplitudes, in support of the descriptions below.

Table 4-1. Modified Loading Protocol for T1

Step	Disp. (in) +	Disp. (in) -	Force (kips) +	Force (kips) -	Cycles	Note 1	Note 2
0	0.00	0.00	0	0	-		
1	0.14	0.03	75	75	10	0.25Pw	
2	0.30	0.07	150	150	10	0.5Pw	
3	0.50	0.20	225	225	10	0.75Pw	Base Slip
4	0.35	0.11	150	150	10	0.5Pw	
5	0.45	0.20	225	225	10	0.75Pw	
6	0.51	0.28	260	260	10	0.86Pw	
7	0.65	0.36	300	260	3	1.0Pw	
8	0.80	0.00	330	100	3		
9	1.00	0.00	339	-	-		Base Slip



(a) Average Displacement History



(b) Resulting Load History

Figure 4-3. Actuator Displacement and Load History for Specimen T1

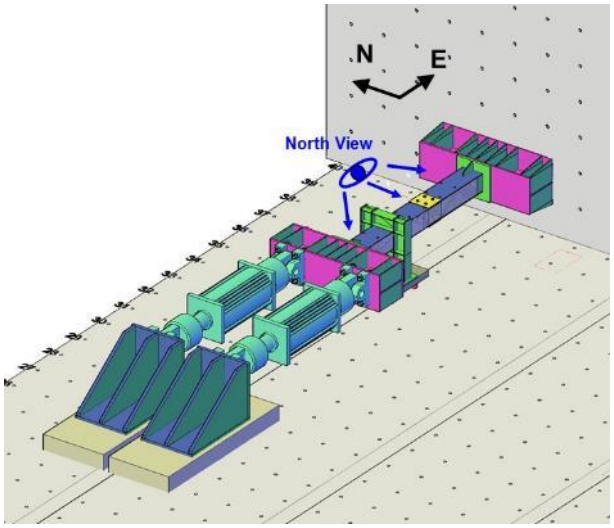


Figure 4-4. Demonstration of North View

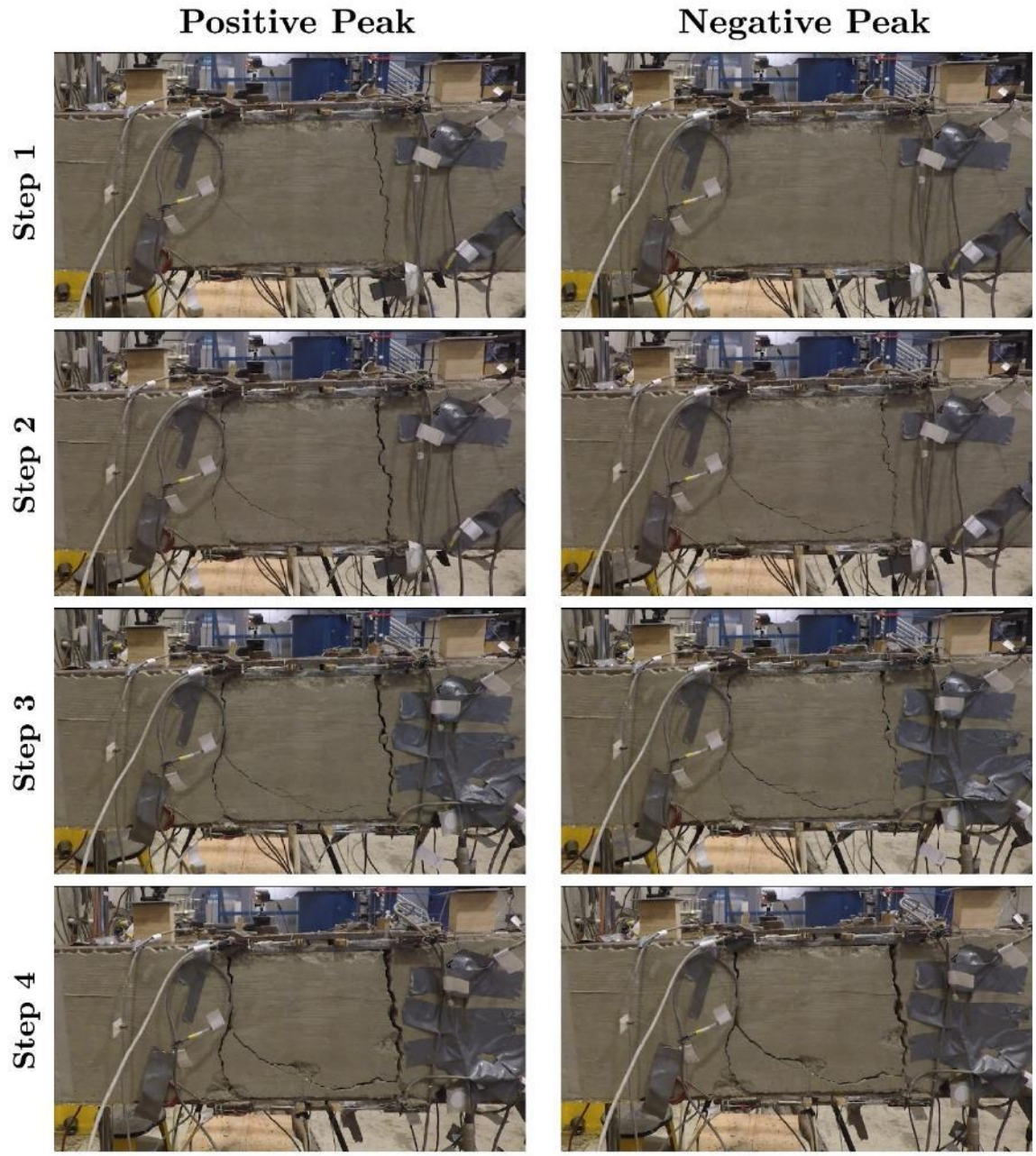


Figure 4-5. North View of Specimen T1 (Steps 1 to 4)

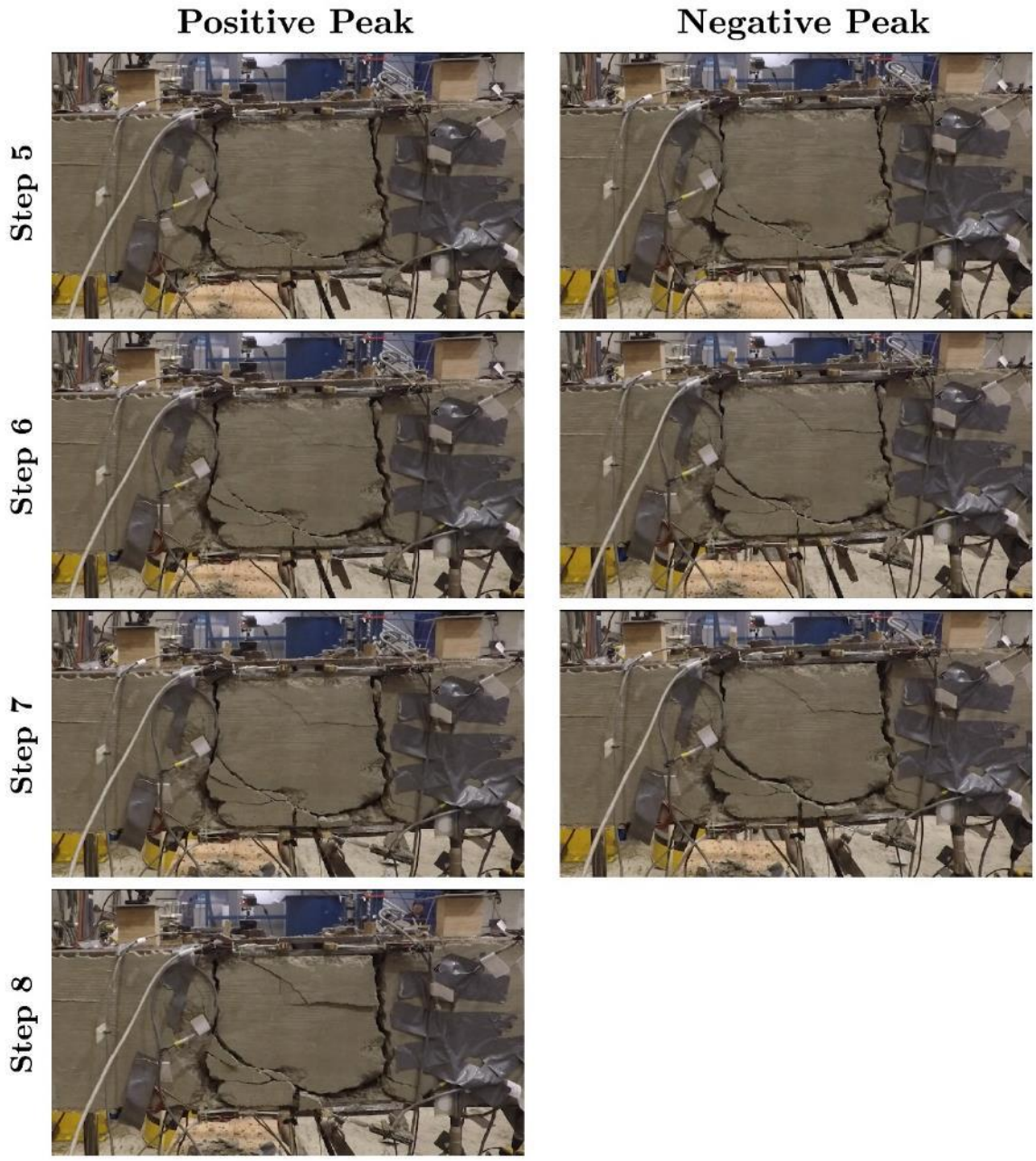


Figure 4-6. North View of Specimen T1 (Steps 5 to 8)

The first step of the test consisted of running 10 cycles at 25% of the design strength ($0.25P_w$). The corresponding axial force was 75 kips, and the resulting average actuator displacements in tension and compression were 0.15 in. and -0.07 in., respectively. Note that both actuators underwent different displacements. For example, in Step 1, the southern actuator had a tension displacement of 0.15 in. and a compression displacement of -0.10 in., while the northern actuator exhibited a tension displacement of 0.16 in. and a compression displacement of -0.04 in. The gross section strains measured on the wall plate ranged from -141 to 272 με (corresponding to -6% to 13% of the yield strain ε_y=2172με), and the net section strains measured from the edge of faceplates by strain gauges S1 to S8 ranged from -118 to 302 με (i.e., approximately -5% to 14% of ε_y). Two vertical cracks were observed, at end of the splice plates, and one diagonal crack running west to east also initiated. At that point, the value recorded by LP was 0.09 in. which is much greater than the product of the maximum measured net section strain by the splice length of 13 in. (i.e., splice length (13 in.) × 302με=0.00040 in.). This indicates that the plates in the bolted splice connection had already slipped during Step 1, despite the slip-critical strength being calculated to be about 174 kips, which is significantly higher than the force applied in this step.

During Step 2, applying 10 cycles at 0.5 P_w, the applied load reached 150 kips and the resulting average actuator displacements in tension and compression reached 0.32 in. and -0.07 in., respectively. The southern actuator had a tension displacement of 0.36 in. and a compression displacement of -0.06 in., while the northern actuator exhibited a tension displacement of 0.30 in. and a compression displacement of -0.12 in. The gross section strain on the wall plate ranged from -267 to 555 με (-12% to 26% ε_y), and the net section strain varied from -217 to 706 με (-10% to 33% ε_y). The two vertical cracks became more severe, and the diagonal crack propagated west to east near the bottom of the specimen during the 10-cycles of loading.

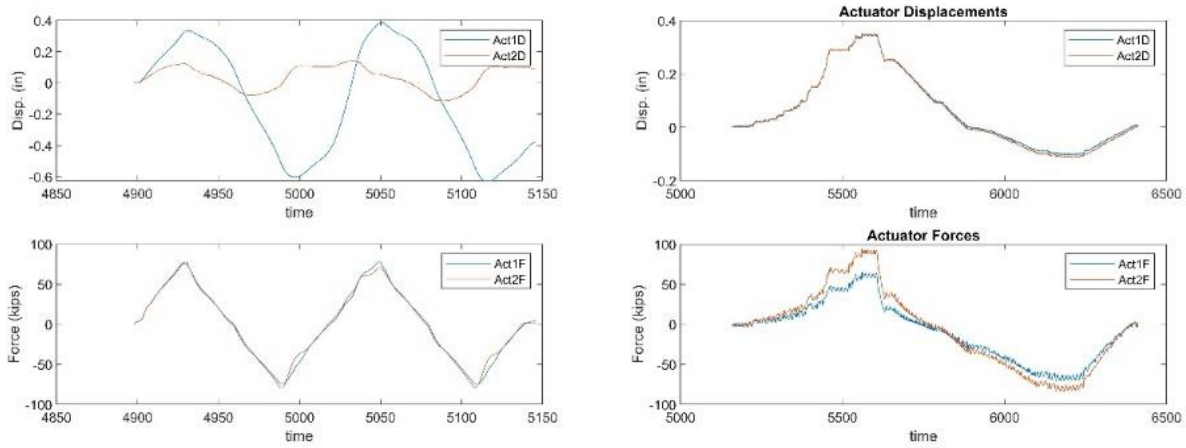
The apply load was increased to 225 kips during the Step 3 cycles, and the resulting average actuator displacements in tension and compression were 0.58 in. and -0.24 in., respectively. The southern actuator had a tension displacement of 0.70 in. and a compression displacement of -0.07 in., while the northern actuator exhibited a tension displacement of 0.52 in. and a compression displacement of -0.49 in. The gross section strains on the wall plate ranged from -468 to 833 με (-22% to 38% ε_y), and the net section strains ranged from -878 to 906 με (-40% to 42% ε_y). During Step 3, the crack pattern remained similar, and all previously observed cracks were found to be slightly more severe compared to the previous step. However, significant sliding of the reaction buttresses was observed during the Step 3 cycles, and the test was paused to increase the clamping force of the buttress to the lab strong floor, such as to increase its friction resistance. This was done by replacing some of the threaded rods with Dywidag rods on the buttresses (Figure 4-7).



Figure 4-7. Installing Dywidag Rods on Buttresses

Testing resumed by restarting the loading cycle, with the intention of repeating the forces in Step 2 for Step 4 (i.e., repeating cycles at 0.5 P_w). However, at the beginning of Step 4, it was observed that the two actuators underwent different displacements when the specimen was in tension, and as a result, the spreader beam moved horizontally 3 in. sideways, which caused the specimen to bend sideways. As a result of the

specimen bending sideways, the test was paused again. The actuator was unloaded to zero force before resuming the test. At this point, the recorded gross section strains on the wall plates ranged from -188 to 462 με (-9% to 21% ε_y), and the net section strains ranged from -1274~934 με (-59% to 43% ε_y). Since all strain gauges indicated elastic behavior, the specimen was loaded for two more cycles of Step 4. However, it was observed that the two actuators still exhibited different displacements. One actuator had displaced from -0.63 in. to 0.38 in. during the cycle, and the other went from -0.11 in. to 0.14 in, while applied loading went from -75 to 75 kips. To prevent further bending of the specimen, it was decided to continue testing using displacement control, applying displacements as needed to reach the target loads applied by the actuators to the specimen, until the end of the test (with one actuator slaved to apply the same displacement as the other actuator, as mentioned earlier). After applying one cycle of Step 4 in displacement control, the load, combined from two actuators, reached 150 kips and the resulting average actuator displacements in tension and compression reached 0.35 in. and -0.11 in. Figure 4-8 provides a comparison between cycles 2 to 3 and cycle 4 in Step 4, showing the differences between force control and displacement control. Then the test continued to apply the remaining 9 cycles of Step 4. Through these cycles, the recorded gross section strains on the wall plate ranged from -391 to 572 με (-18% to 26% ε_y), and the net section strains ranged from -1360~934 με (-63% to 43% ε_y).



(a) 2nd and 3rd Cycles in Step 4 (Force Control)

(b) 4th Cycle in Step 4 (Displacement Control)

Figure 4-8. Actuator Displacement and Load History

Similarly, the intent of Step 5 was to repeat cycles at the same applied force as in Step 3. The load reached 225 kips and the resulting average actuator displacements in tension and compression reached 0.45 in. and -0.2 in. The obtained gross section strains on the wall plate ranged from -478 to 850 με (-22% to 39% ε_y), and net section strains ranged from -1324~792 με (-61% to 36% ε_y). Note that all peak strain readings did not change significantly during the 10 cycles in this step. This suggests that the specimen exhibited a stable state under repeated cycles.

Per the original target loading protocol, the next step of testing should have been to apply to reach 100% of the load corresponding to the target limit state, which in this case the bearing strength defined by AISC as $2.4dtF_u$. However, based on previous research by Frank and Yura (1981), localized yielding due to bearing around bolts is expected to occur when the force applied reaches approximately 83% of the AISC bearing strength expressed as $2.4dtF_u$, which is therefore equivalent to 2.0dtFu. Frank and Yura (as well as other

researchers) also emphasized that the $2.4dtF_u$, strength is typically reached after bolts holes have elongated by ¼" under the bearing pressures. As a result, the target force in Step 6 was set to approximately capture this yield point. Therefore, during Step 6 (which overshot a bit the target value, up to an applied load of 0.86 P_w), the applied force reached 260 kips, and resulting average actuator displacements in tension and compression were 0.52 in. and -0.26 in., respectively. After these cycles, the gross section strains on the wall plates ranged from -767 to 967 με (-35% to 45% ε_y), and the net section strains ranged from -1521 to 823 με (-70% to 38% ε_y).

A force of 1.0 P_w was then applied in Step 7. The corresponding axial load applied was 300 kips, and the corresponding average actuator displacements in tension and compression were 0.66 in. and -0.32 in., respectively. The obtained gross section strains on the wall plates ranged from -1042 to 1174 με (-48% to 54% ε_y), and net section strain ranged from -2179~778 με (-100% to 36% ε_y). No failure was observed when the connection reached the target loading of 1.0 P_w. However, the presence of cracks in the concrete resulted in a significant gap in the splice region, causing the specimen to bend downwards despite the presence of timber supports underneath the spreader beam. This can be observed in Figures 4-9 and 4-10. Thus, to prevent further bending and concrete cracking of the specimen under compression, the maximum actuator displacement in compression was limited to zero for all subsequent cycles.

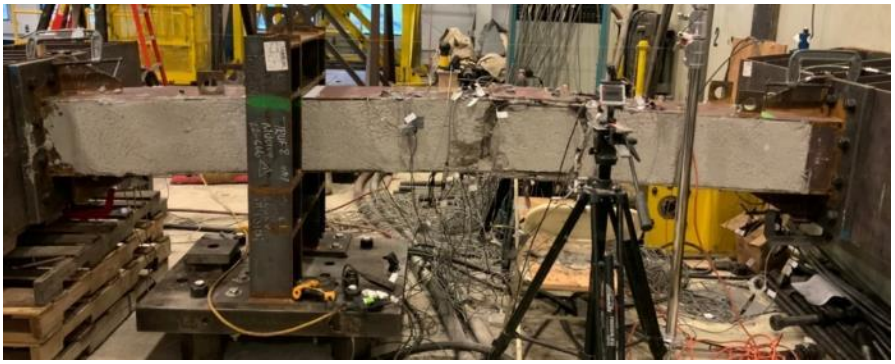


Figure 4-9. Bending in Compression of Specimen T1 (Step 7)



Figure 4-10. Timer Support being crushed in Step 7

In Step 8, the average actuator displacements reached a displacement of 0.8 in. in tension and a tensile force of 330 kips, but no significant differences between Steps 7 and 8 were observed. After Step 8, the obtained gross section strains on the wall plates ranged from -740 to 1287 με (-34% to 59% ε_y), and net section strains ranged from -3526~382 με (-162% to 18% ε_y).

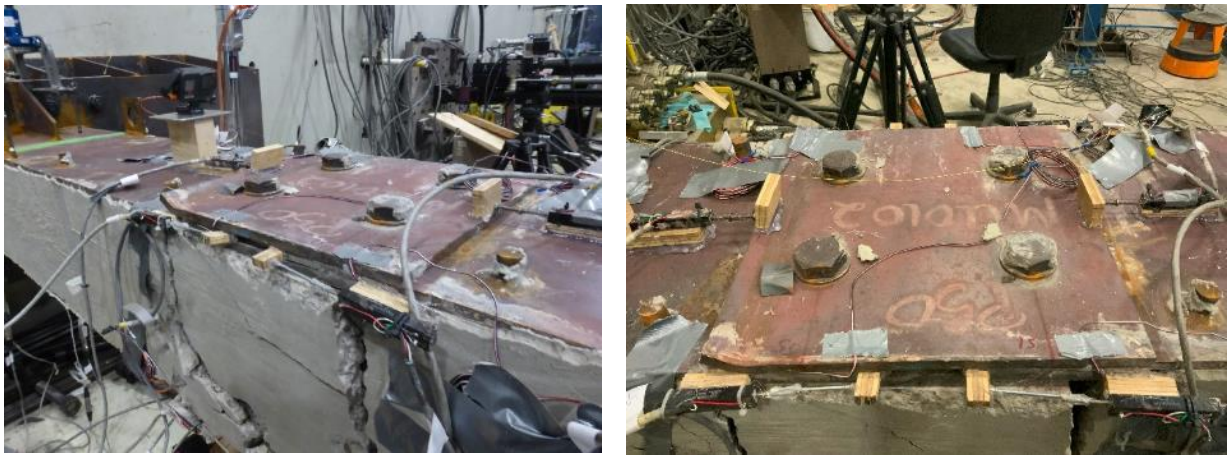
In Step 9, the specimen was pulled to a displacement of 1.00 in. when a loud “bang” was heard, and the load applied dropped from a peak of 338 kips to a value of 92 kips. At that point, it was assumed that

bearing failure had occurred in the steel plate hidden by the splice plate, which prompted termination of the test. Figure 4-11 illustrates the condition of the specimen at this stage, with more cracks observed in the concrete, and Figure 4-12 shows the relative movement between faceplates and splice plates. The obtained gross section strains on wall plates ranged from -685 to 1329 με (-32% to 61% ε_y), and net section strains ranged from -3854~123 με (-177% to 6% ε_y).



(a) South View (b) North View

Figure 4-11. Specimen T1 (Step 9, Peak Actuator Displacement=0.86")



(a) View 1 (b) View 2

Figure 4-12. Relative Movement between Faceplates and Splice Plates (Step 9)

After the test, the specimen was removed from the test set-up, the splice plates were removed, and it was found that complete bearing failure had not occurred after all, even though elongation of the bolt holes was on the order of 0.5 in. (Figure 4-13). No failure was observed on the welds of the blind bolts (Figure 4-14). Further investigation of the test data revealed that sliding of almost 0.6 in. had occurred on the north footing under the steel buttress. This lead to the decision to not stop the testing any of the remaining tension specimens until clear evidence of failure was observed, pulling the specimens to extreme deformations in tension if necessary for that purpose.



(a) Top Faceplates



(b) Bottom Faceplates

Figure 4-13. Faceplates after removing Splice Plates



Figure 4-14. Blind Bolts inside the Connection

Figure 4-15 presents the results obtained using GR, SP, and LP. The comparison between the hysteresis curves of SP and LP, along with design limit states, is shown in Figure 4-16. In the figure, there is no obvious plateau observed in the hysteresis loop to determine a specific slip-critical force in this case. Additionally, the bearing strengths corresponding to $2.0dtF_u$ and $2.4dtF_u$ are marked in Figure 37 to illustrate the yielding of bearing and the theoretical bearing capacity of the specimen. Results indicate that the target bearing strength limit state was reached and exceeded, but it is important to note that upon repeated cycles, the strength reached in previous cycles is not reached anew until previous peak displacement is not reached again, as the bolts must slide within their elongated holes before bearing on steel again. This phenomenon which occurred in all cycles after bearing strength was developed can be observed in Figure 4-17, which demonstrates this typical bearing behavior for the three cycles in Step 8.

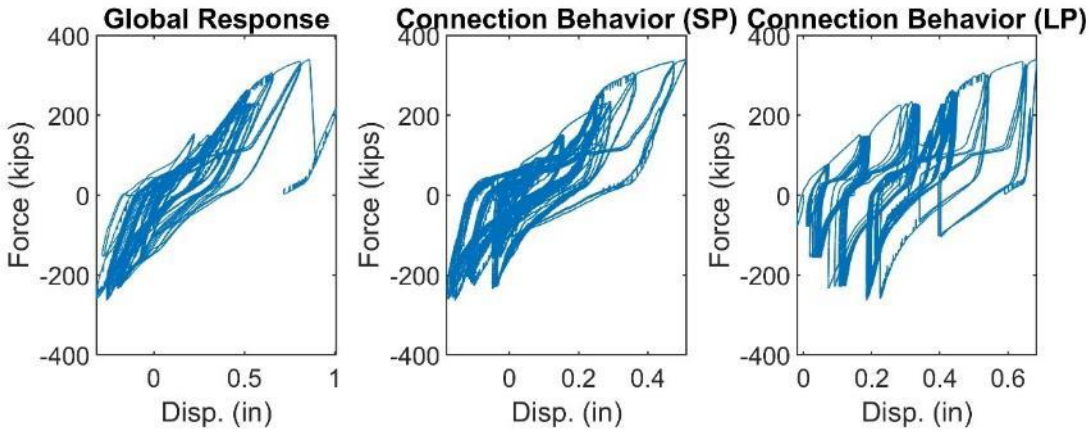


Figure 4-15. Test Results of Specimen T1

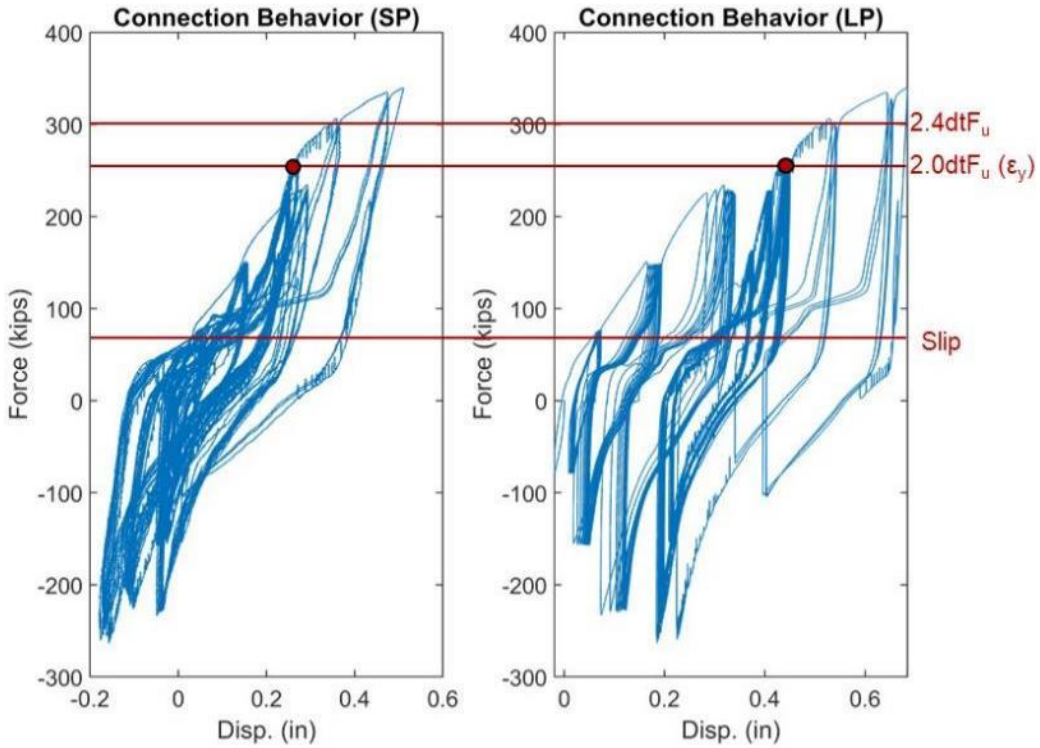


Figure 4-16. Test Results of Specimen T1 with Design Limit State

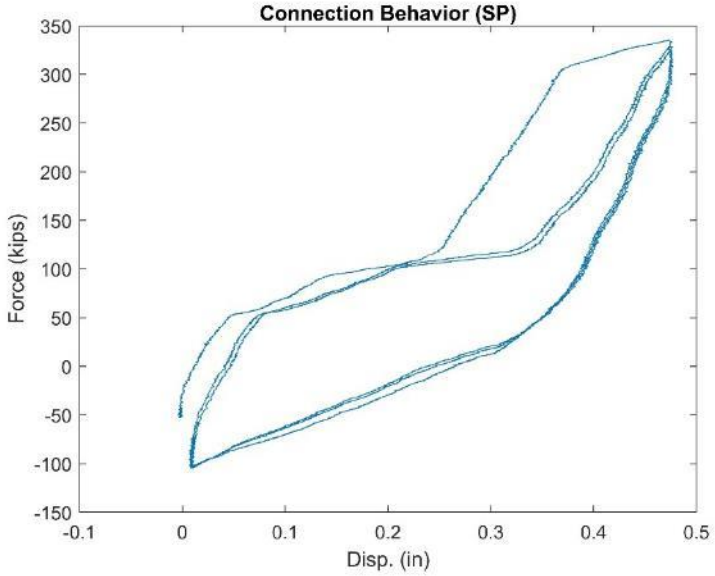


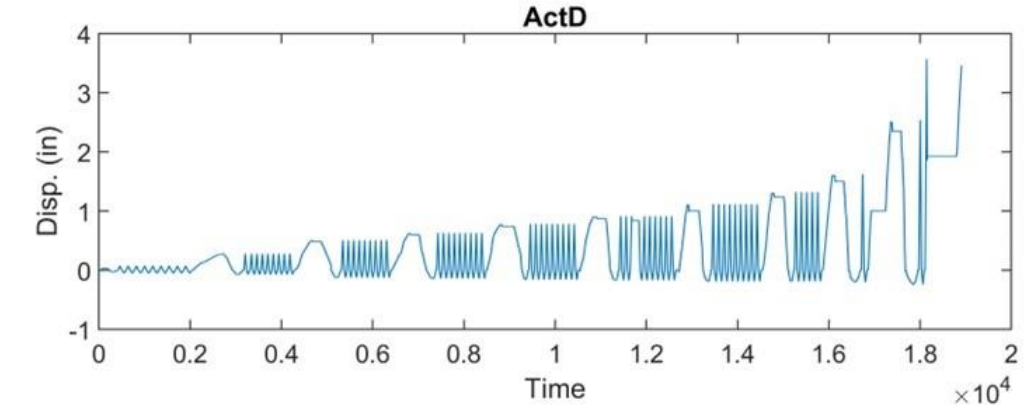
Figure 4-17. Bearing Behavior in Step 8

4.2.2 Specimen T2

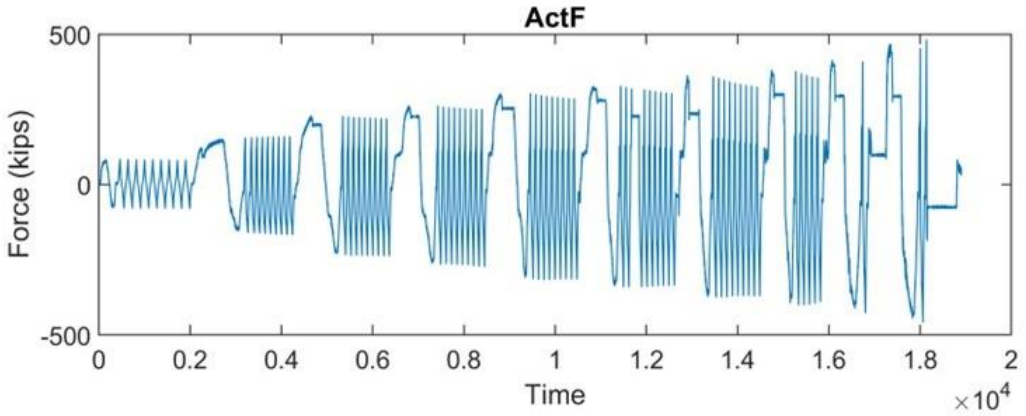
Testing of Specimen T2 started on 11/10/2022, and unfolded following the loading protocol shown in Table 4-2. Figure 4-18 shows the corresponding actuator displacement and load history during the test. Figures 4-19 to 4-21 present a collection of photos of the splice region from the north view of Specimen T2 to illustrate the behavior at different displacement amplitudes, in support of the descriptions below.

Table 4-2. Modified Loading Protocol for T2

Step	Disp. (in) +	Disp. (in) -	Force (kips) +	Force (kips) -	Cycles	Note 1	Note 2
0	0.00	0.00	0	0	-		
1	0.07	0.05	75	75	10	0.25Pw	
2	0.28	0.07	150	150	10	0.5Pw	Conn Slip
3	0.50	0.12	225	225	10	0.75Pw	
4	0.62	0.14	260	260	10	0.86Pw	
5	0.77	0.16	300	300	10	1.0Pw	
6	0.90	0.17	327	327	10	-	
7	1.10	0.19	360	360	10	-	
8	1.30	0.18	390	390	6	-	
9	1.60	0.20	400	400	2	-	
10	2.50	0.23	450	450	2	-	
11	3.20	-	480	-	-	Failure	
12	5.00	-	30	-	-	Final	



(a) Average Displacement History



(b) Resulting Load History

Figure 4-18. Actuator Displacement and Load History for Specimen T2

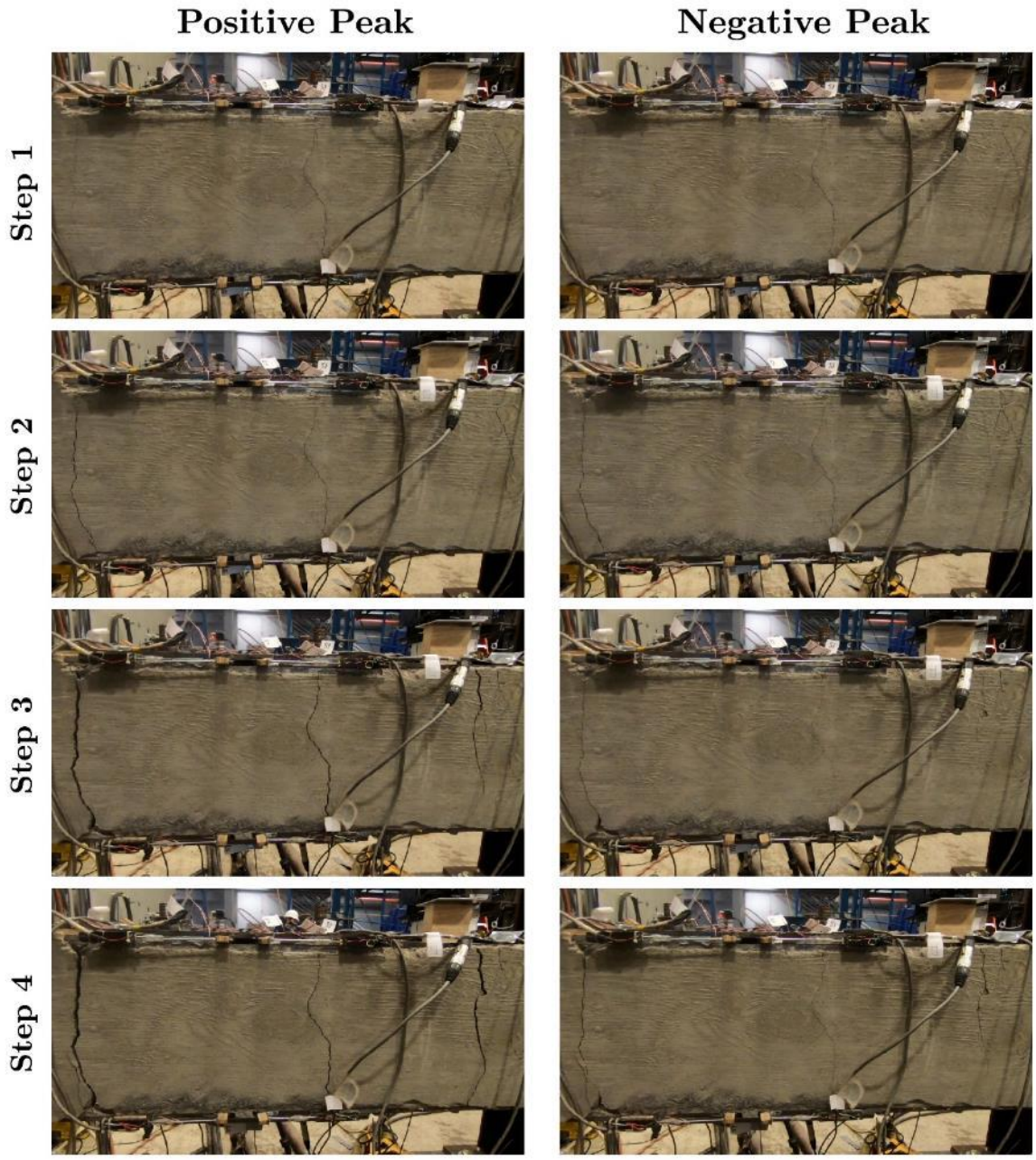


Figure 4-19. North View of Specimen T2 (Steps 1 to 4)

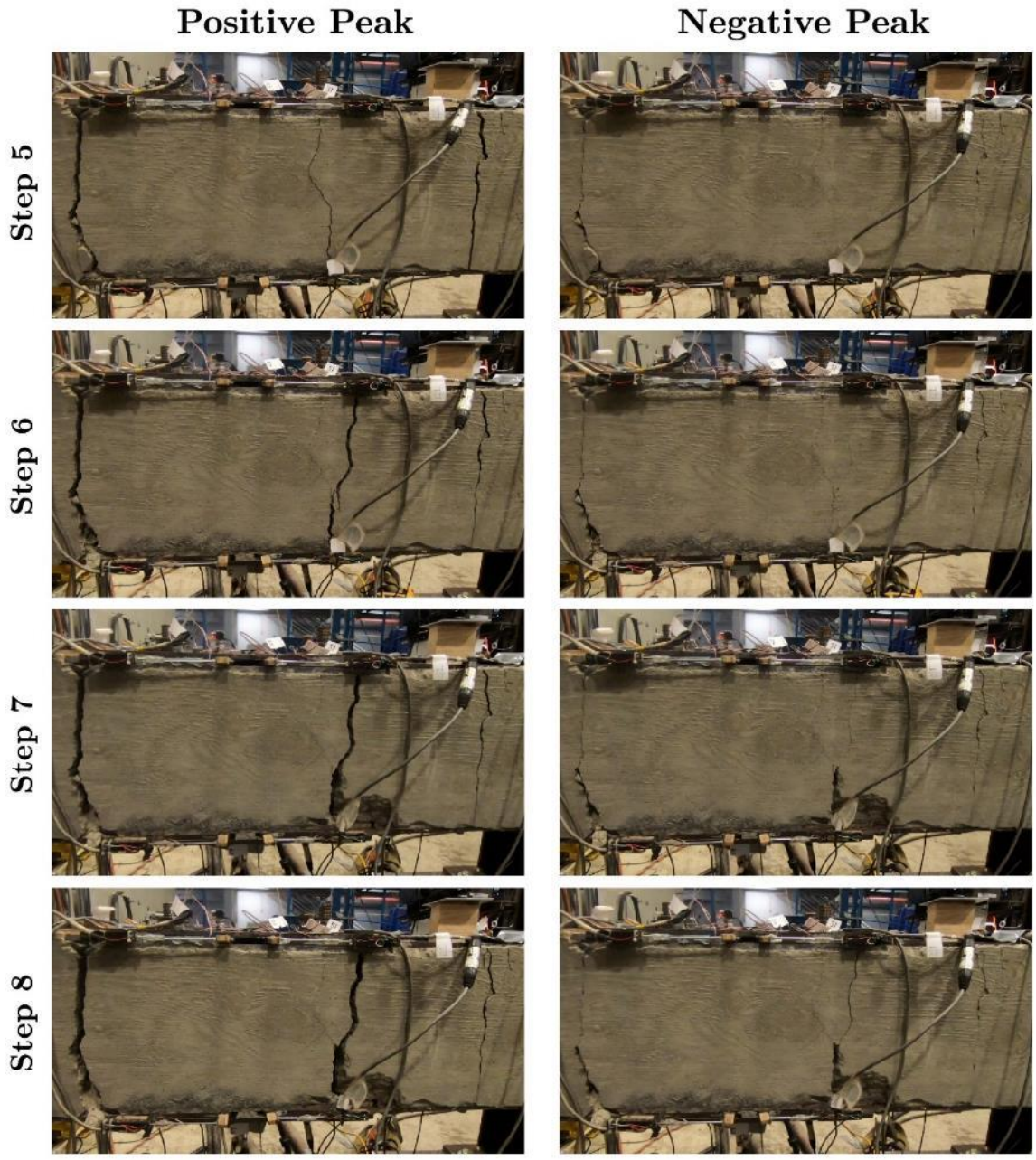


Figure 4-20. North View of Specimen T2 (Steps 5 to 8)

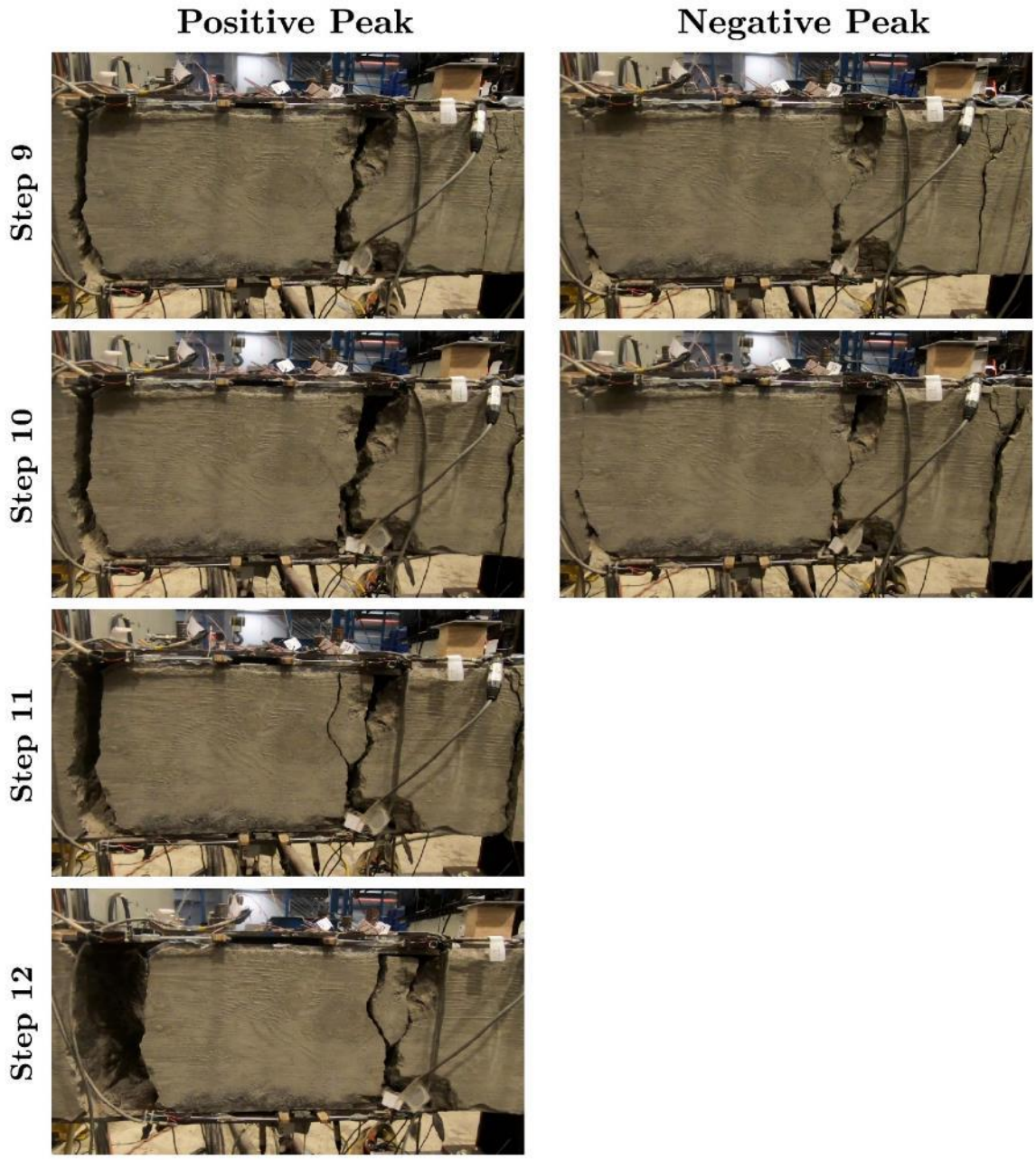


Figure 4-21. North View of Specimen T2 (Steps 9 to 12)

Before testing Specimen T2, two steel supports were placed under the spreader beam (Figure 4-22), between the actuators and the specimen, to replace the timber supports used in Specimen T1. Teflon plates were installed on top of these supports (Figure 4-23), allowing the spreader beam to slide on them with minimal friction and preventing it from moving downwards.



Figure 4-22. South View of Specimen T2



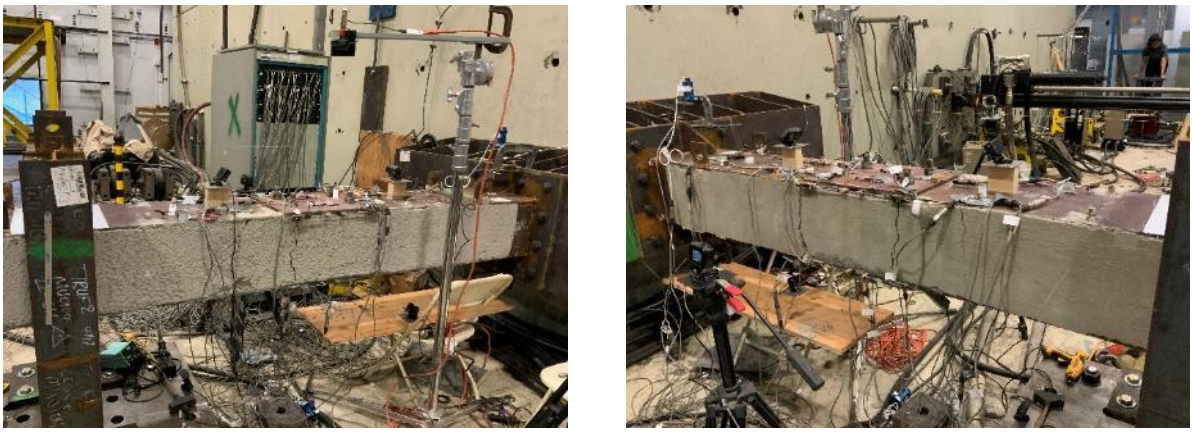
Figure 4-23. Steel Supports under the Spreader Beam

The test started with the loads being applied in displacement control, with one actuator slaved to apply the same displacement as the other actuator. The first loading cycles (Step 1) was 10 cycles at 25% of the design strength ($0.25P_w$). The corresponding axial force was 75 kips, and the resulting actuator displacements in tension and compression were 0.07 in. and -0.05 in., respectively. At this step, the gross section strain ranged from -194 to 218 με (corresponding to -9% to 10% of the yield strain ε_y=2172με), and the net section strain ranged from. -189 to 94 με (i.e., approximately -9% to 4% of εy). Several vertical cracks were observed at the two ends of the splice plates and at the locations of tie-rods. The test proceeded to Step 2, undergoing 10 cycles at $0.5P_w$. The applied load reached 150 kips, resulting in actuator displacements of 0.28 in. in tension and -0.07 in. in compression, respectively. The gross section strain ranged from -419 to 554 με (-19% to 26% ε_y), and the net section strain ranged from -395 to 105 με (-18% to 5% ε_y). Note that while it is counter-intuitive for the net section strains to be less than the gross section strains, this is because bearing deformations in the longitudinal direction laterally displaced the segment of net section between the bolt and the faceplate free edge, inducing compression on the edge of the faceplate due to that bending effect (this will be illustrated using finite element analysis results later on). During these 10 cycles, a loud "bang" was heard. As there was no evidence of set-up problems, it was assumed that the noise occurred as a result of sliding between the splice plates and faceplates, which was deemed logical given that similar noises occurred throughout the entire remaining cyclic loading program at similar values of applied loading. The crack pattern appeared similar to that of the previous step.

The load increased to 225 kips during the Step 3 cycles, and actuator displacements in tension and compression were 0.50 in. and -0.12 in., respectively. The gross section strain ranged from -462 to 819 με (-21% to 38% ε_y), and the net section strain ranged from -347 to 219 με (-16 to 10% ε_y). Notably, the crack widths appeared more severe, specifically at the edge of the splice plate on the east side. During the Step 4

cycles, the load increased to 260 kips, with actuator displacements of 0.62 in. in tension and -0.14 in. in compression. The gross section strain ranged from -524 to 920 με (-24% to 42% ε_y), and the net section strain ranged from -322 to 377 με (-15 to 17% ε_y). The crack pattern observed in Step 4 remained consistent to what was observed in the previous step, but slightly more severe.

In the subsequent Step 5, the load further increased to 300 kips, with actuator displacements of 0.77 in. in tension and -0.16 in. in compression. The gross section strain ranged from -558 to 1076 με (-26% to 50% ε_y), and the net section strain ranged from -204 to 668 με (-9 to 31% ε_y). Despite reaching the target loading of 1.0 P_w, no failure was observed. Figure 4-24 provides south and north views for the specimen in Step 5. The crack pattern remained similar to that of the previous steps.

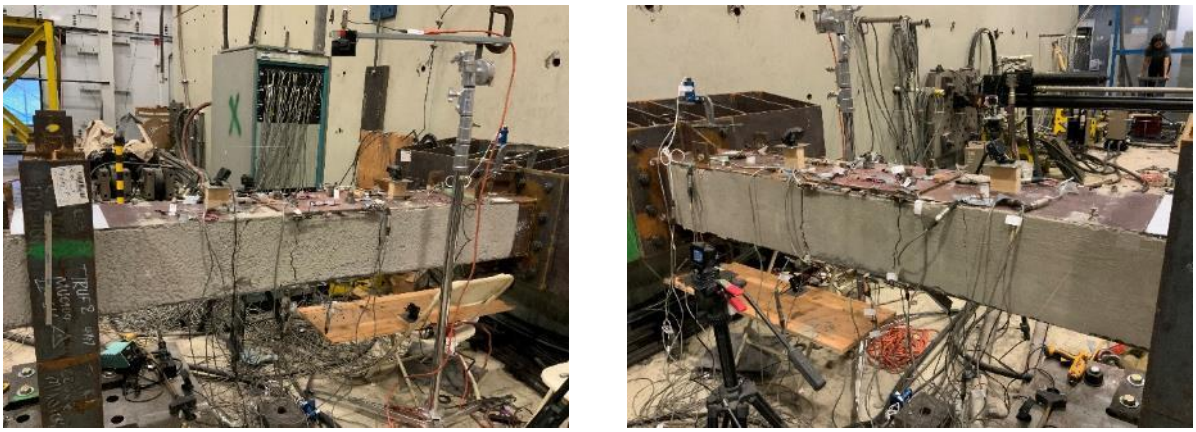


(a) South View (b) North View

Figure 4-24. Specimen T2 (Step 5, Peak Actuator Displacement=0.77”)

During Step 6, the load increased to 327 kips, and actuator displacements in tension and compression were 0.90 in. and -0.17 in., respectively. The gross section strain ranged from -602 to 1181 με (-28% to 54% ε_y), and the net section strain ranged from -110 to 861 με (-5 to 40% ε_y). Figure 4-25 shows the side views of the specimen and the crack condition of the concrete. Figure 4-26 provides a top view of the specimen.

From the top view, an approximately 0.5-in. relative movement between splice plates and faceplates was observed.



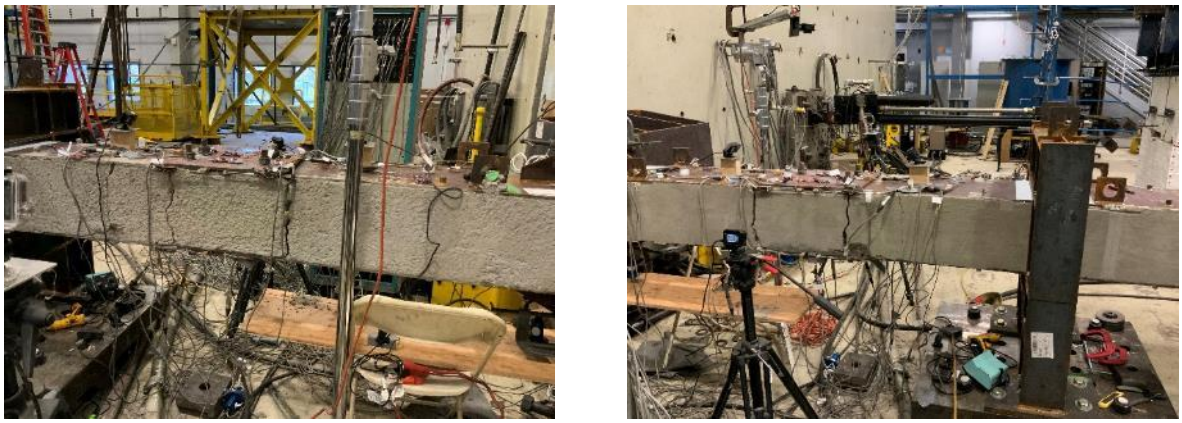
(a) South View (b) North View

Figure 4-25. Side Views of Specimen T2 (Step 6, Peak Actuator Displacement=0.90”)



Figure 4-26. Top View of Specimen T2 showing 0.5” gap due to sliding between splice plate and faceplate (Step 6, Peak Actuator Displacement=0.90”)

In Step 7, the load increased to 360 kips, and actuator displacements in tension and compression were 1.10 in. and -0.19 in., respectively. The gross section strain ranged from -690 to 1304 με (-32% to 60% ε_y), and the net section strain ranged from 57 to 1054 με (3 to 49% ε_y). A side view from the north (Figure 4-27) shows that a piece of concrete fell at the bottom corner of the connection.



(a) South View (b) North View

Figure 4-27. Side Views of Specimen T2 (Step 7, Peak Actuator Displacement=1.10")

During Step 8, the load increased to 390 kips, and actuator displacements of 1.30 in. in tension and -0.18 in. in compression were recorded. The gross section strain ranged from -729 to 1400 με (-34% to 64% ε_y), and the net section strain ranged from 211 to 1127 με (10 to 52% ε_y). In the subsequent Step 9 cycles, the load increased to 400 kips, with actuator displacements of 1.60 in. in tension and -0.20 in. in compression. The gross section strain ranged from -779 to 1529 με (-36% to 70% ε_y), and the net section strain ranged from 228 to 1274 με (10 to 59% ε_y). Side views of the specimen in Steps 8 and 9 are illustrated in Figures 4-28 and 4-29. The crack patterns in both steps are similar.

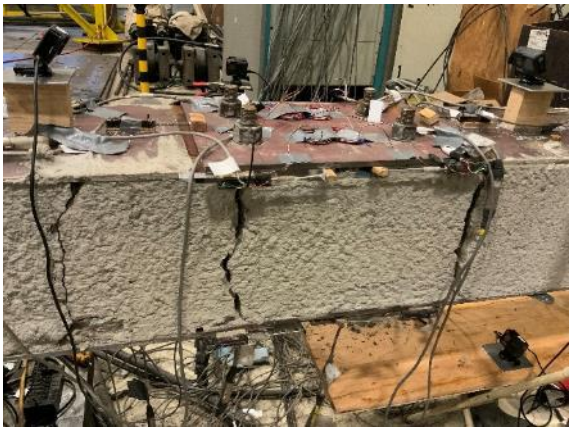


(a) South View

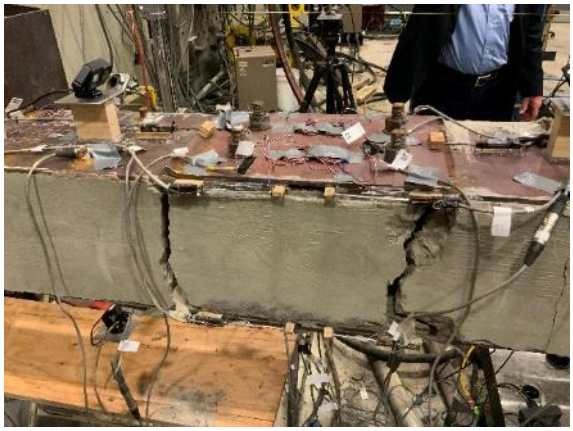


(b) North View

Figure 4-28. Side Views of Specimen T2 (Step 8, Peak Actuator Displacement=1.30”)



(a) South View



(b) North View

Figure 4-29. Side Views of Specimen T2 (Step 9, Peak Actuator Displacement=1.60”)

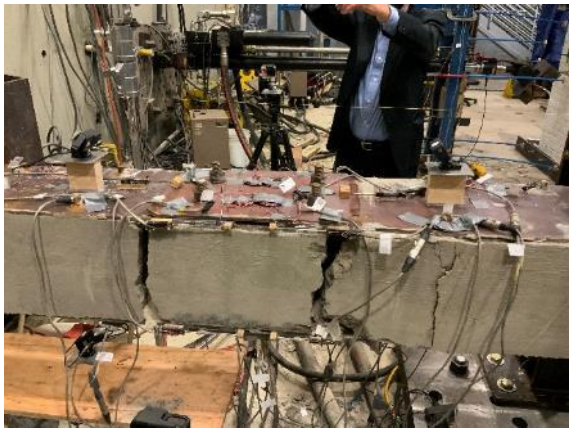


Figure 4-30. Top View of Specimen T2 (Step 9, Peak Actuator Displacement=1.60")

Step 10 witnessed a further increase in load to 450 kips, with actuator displacements of 2.50 in. in tension and -0.23 in. in compression. The gross section strain ranged from -738 to 1825 με (-34% to 84% ε_y), and the net section strain ranged from -2249 to 1479 με (-104 to 68% ε_y). Figure 4-31 demonstrates the condition when the specimen was pulled to a 2.50 in. deformation.



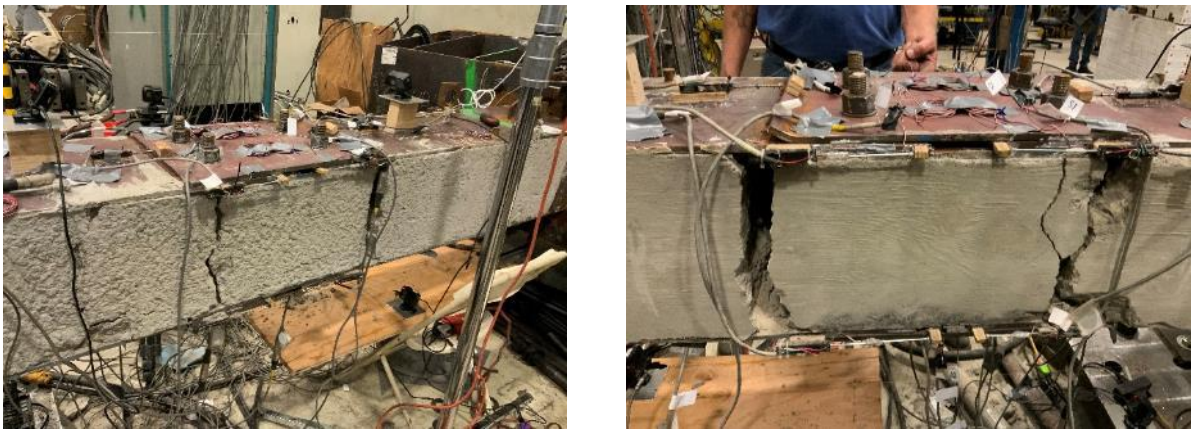
(a) South View



(b) North View

Figure 4-31. Side Views of Specimen T2 (Step 10, Peak Actuator Displacement=2.50")

In Step 11, the specimen was pulled to 3.2 in. in tension, and the load was increased to 480 kips, which was the peak force reached during this test. The gross section strain ranged from -502 to 1870 με (-23% to 86% ε_y), and the net section strain ranged from -4593 to 1858 με (-211 to 86% ε_y). Figure 4-32 illustrates the side views when the specimen reached the peak force, and Figure 4-33 shows the bearing deformation inside the top splice plate.



(a) South View (b) North View

Figure 4-32. Side Views of Specimen T2 (Step 11, Peak Actuator Displacement=3.20")

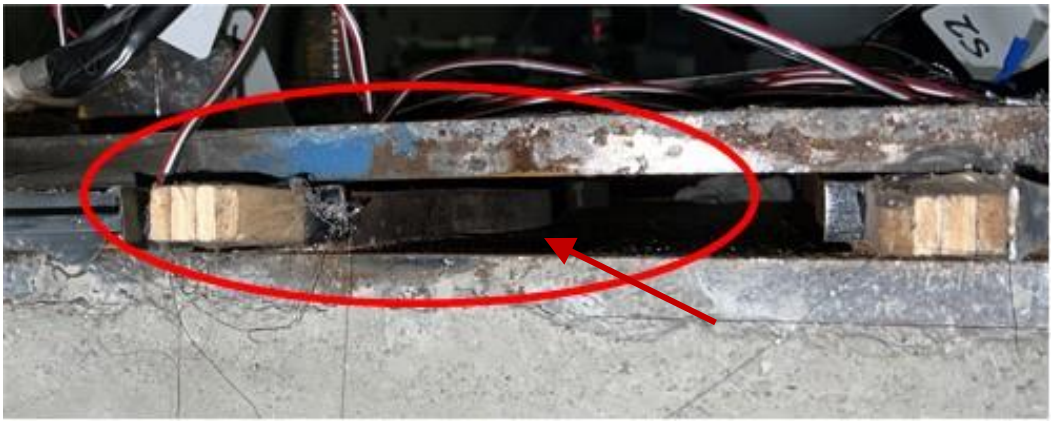
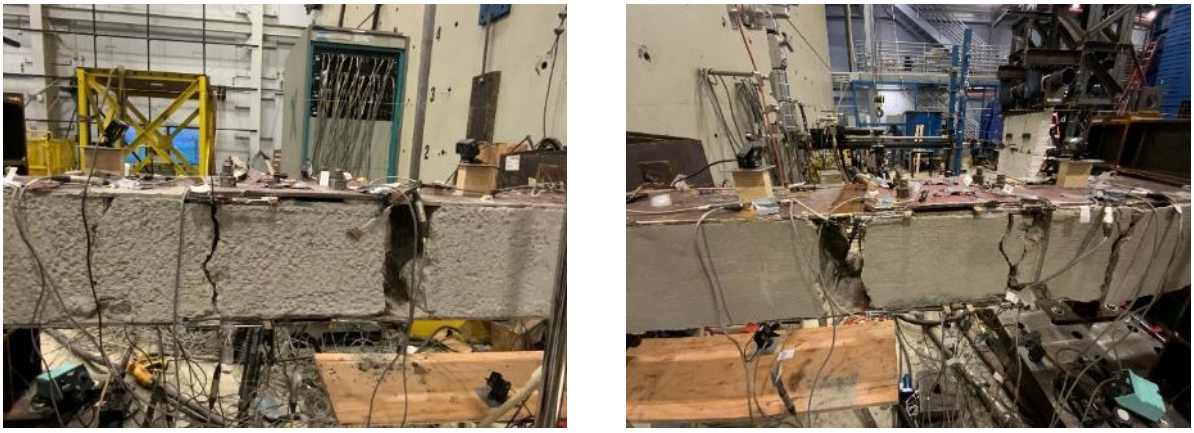


Figure 4-33. Bearing Deformation inside the Splice Plate (Step 11, Peak Actuator Displacement=3.20")

Finally, during Step 12, the specimen was pulled to 5.0 in. in tension, as its tension strength progressively dropped to a residual strength of 30 kips. Figure 4-34 shows the specimen at the end of this final step.



(a) South View (b) North View

Figure 4-34. Side Views of Specimen T2 (Step 12, Peak Actuator Displacement=5.0")

Figure 4-35 presents the results obtained using GR, SP, and LP. Figure 4-36 provides a close-up view of the half-cycle during which the first instance of sliding of the connection was recorded, at a force of 122.0 kips, which was lower than the calculated slip-critical value of 167.74 kips. Figure 4-37 compares the hysteresis curves of SP and LP and shows the design limit states. Bearing strengths corresponding to $2.0dtF_u$, $2.4dtF_u$, and $3.0dtF_u$ are marked to represent the progressive development of higher bearing stresses in tension. The strength continued to increase after the specimen developed $3.0dtF_u$ until the peak force of 480 kips, which corresponded to $3.84dtF_u$. Figures 4-38 and 4-39 compares specimens T1 and T2 and demonstrates that the slip-critical resistance of T1 was smaller than T2. Therefore, the initial sliding strength of T1 was much smaller than T2. However, as shown in 4-38, after bearing strength developed, when both T1 and T2 specimens reached 0.5 in. deformation, the strength of T1 and T2 started to become nearly identical.

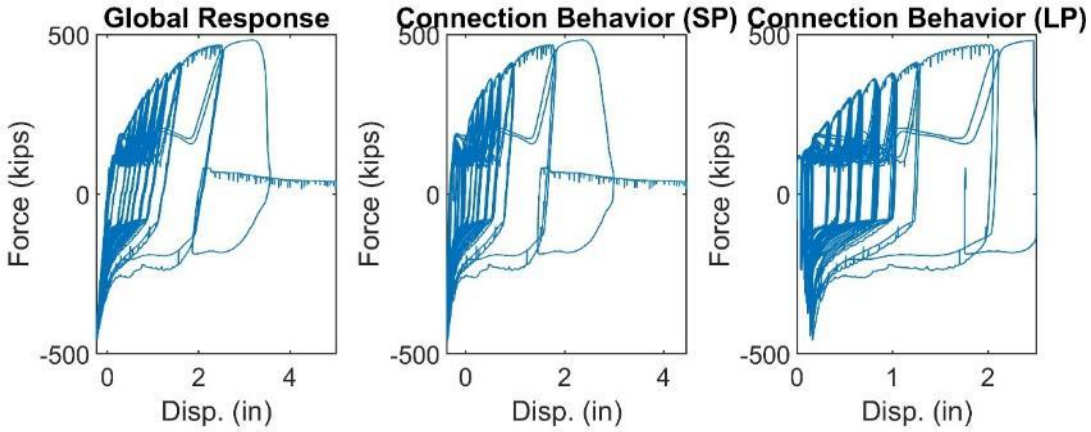


Figure 4-35. Test Results of Specimen T2

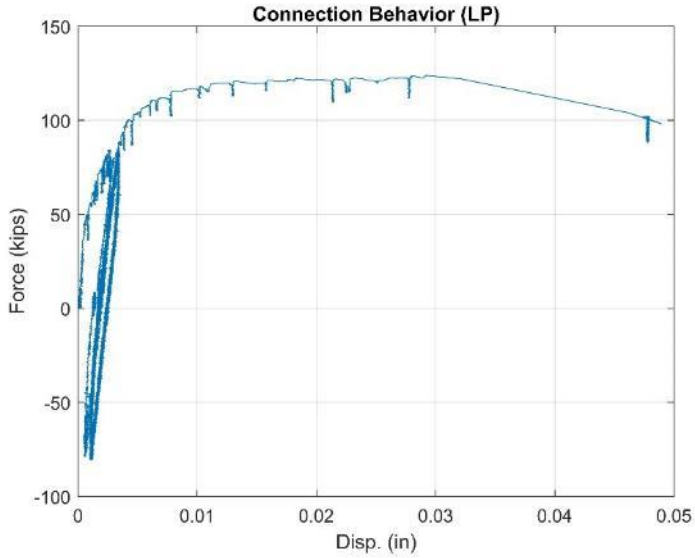


Figure 4-36. Close-up View Showing First Observation of Sliding in Specimen T2

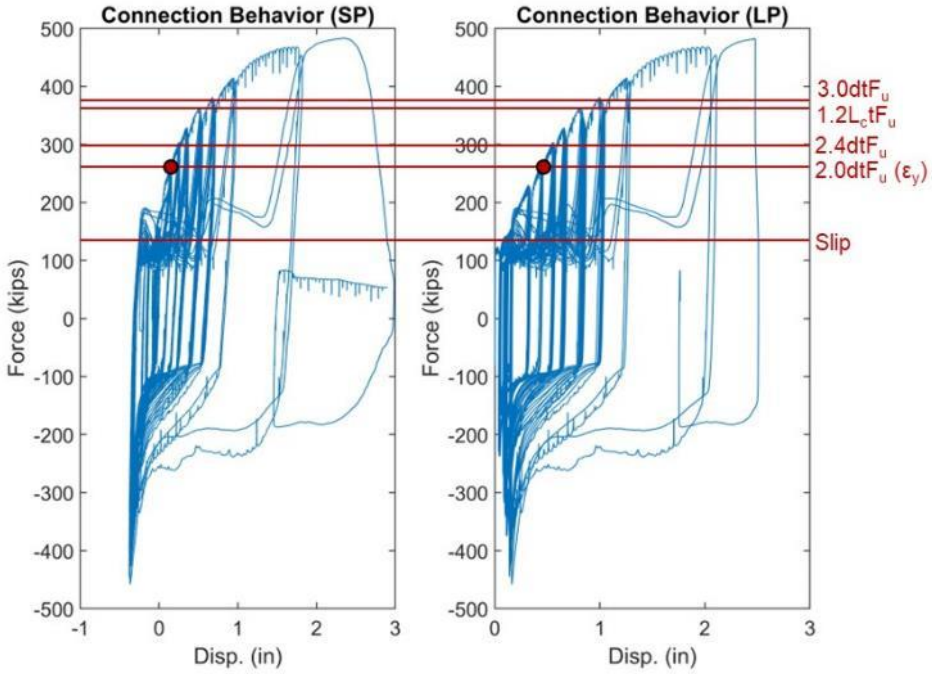


Figure 4-37. Test Results of Specimen T2 with Design Limit States

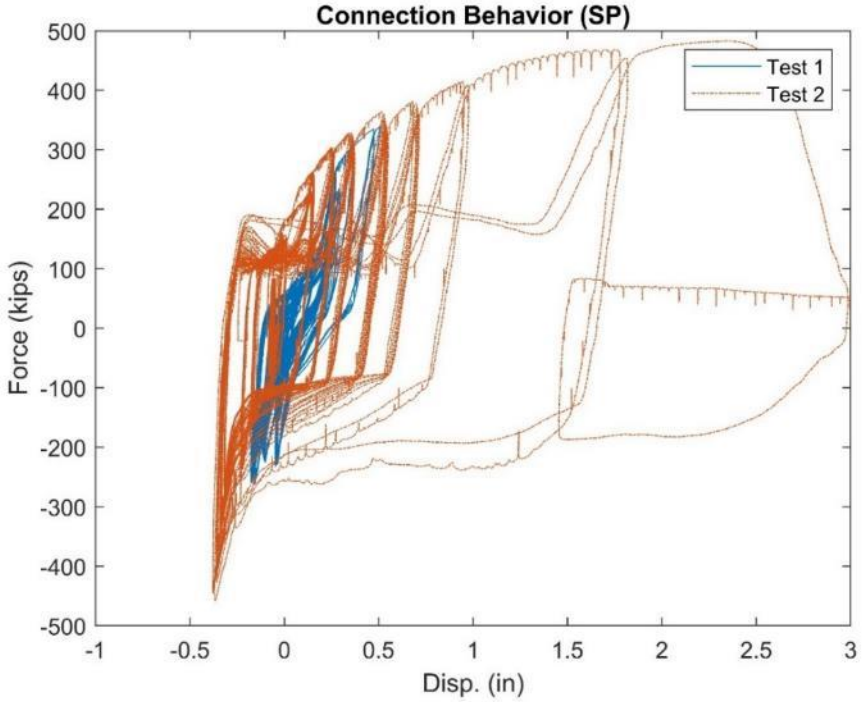


Figure 4-38. Comparison between Specimens T1 and T2 (SP)

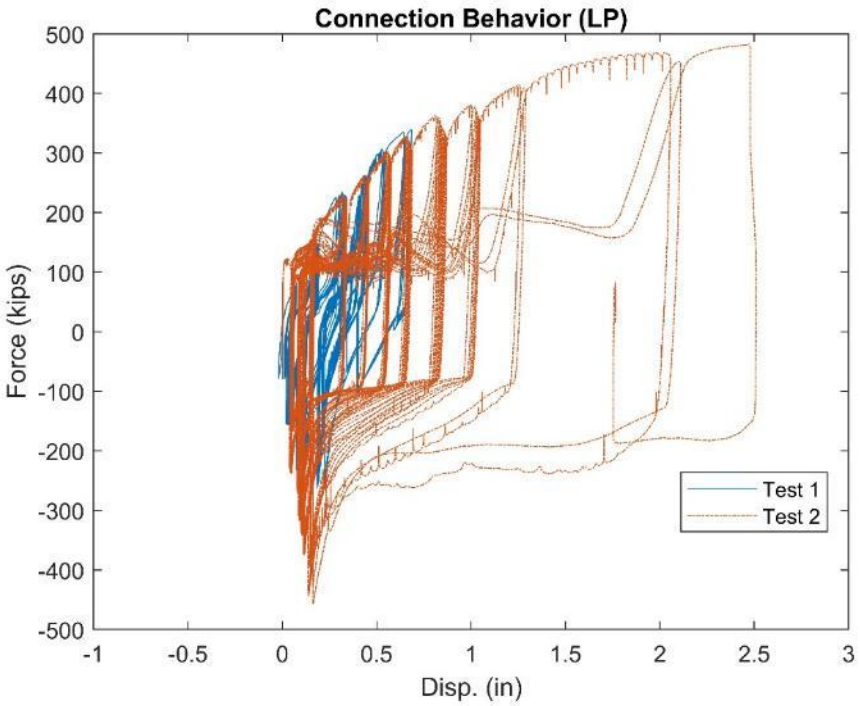


Figure 4-39. Comparison between Specimens T1 and T2 (LP)

4.2.3 Specimen T3

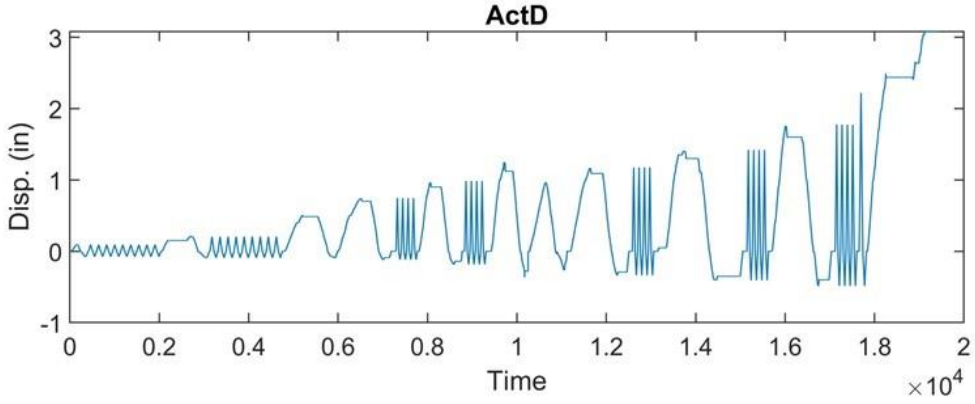
The testing of Specimen T3 started on 11/17/2022, following the loading procedure outlined in Table 4-3. The average actuator displacement and resulting load history for the experiment can be observed in Figure 4-40. Table 4-4 provides an overview of the development of the maximum gross section and net section strains developed during each step of the test. To further support the descriptions, a series of photographs illustrating the splice region from the north perspective of Specimen T3 at different displacement amplitudes are presented in Figures 4-41 to 4-43.

Table 4-3. Modified Loading Protocol for T3

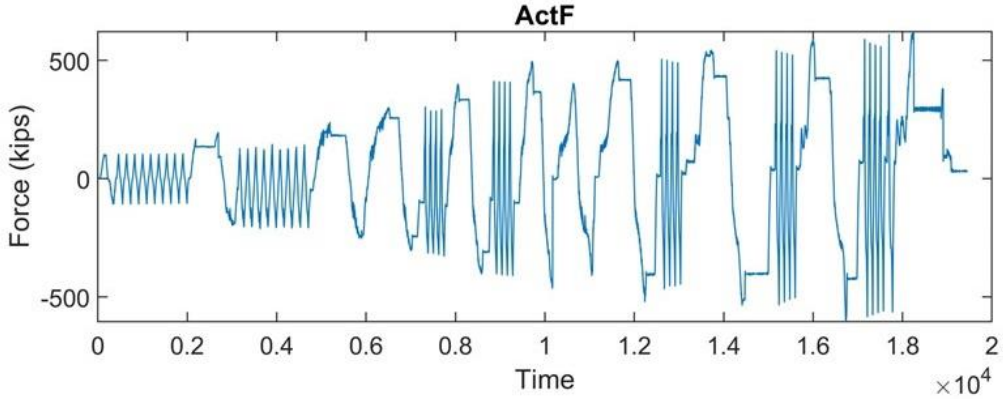
Step	Disp. (in) +	Disp. (in) -	Force (kips) +	Force (kips) -	Cycles	Note 1	Note 2
0	0.00	0.00	0	0	-		
1	0.09	0.08	100	100	10	0.25Pw	
2	0.20	0.09	200	200	10	0.5Pw	(Slip)
3	0.50	0.09	240	255	1	0.6Pw	
4	0.74	0.12	300	300	5	0.75Pw	
5	0.96	0.18	400	400	5	1.0Pw	
6	1.24	Slip	500	500	1	AeFy	(Δy)
7	0.96	0.26	400	400	1		
8	1.16	0.33	500	500	5	AeFy	
9	1.40	0.40	540	530	5		
10	1.75	0.48	600	530	5		
11	2.20	0.48	600	530	1		
12	3.00	-	619	-	-	Failure	

Table 4-4. Development of Gross Section and Net Section Strains for T3

Step	Min. ε_{Gross} (με)	Max. ε_{Gross} (με)	Min. ε_{Net} (με)	Max. ε_{Net} (με)	Min. ε_{Gross} (%ε_y)	Max. ε_{Gross} (%ε_y)	Min. ε_{Net} (%ε_y)	Max. ε_{Net} (%ε_y)
0	0	0	0	0	0	0	0	0
1	-181	274	-134	118	-8%	13%	-6%	5%
2	-783	671	-461	226	-36%	31%	-21%	10%
3	-853	825	-448	322	-39%	38%	-21%	15%
4	-1055	1159	-405	631	-49%	53%	-19%	29%
5	-1242	1532	-326	2489	-57%	71%	-15%	115%
6	-1257	1782	-120	2741	-58%	82%	-6%	126%
7	-1242	1532	-326	2489	-57%	71%	-15%	115%
8	-1314	1771	148	3302	-61%	82%	7%	152%
9	-1477	1894	303	3493	-68%	87%	14%	161%
10	-1528	2303	599	22175	-70%	106%	28%	1021%
11	-1528	2303	599	22175	-70%	106%	28%	1021%



(a) Average Displacement History



(b) Resulting Load History

Figure 4-40. Actuator Displacement and Load History for Specimen T3

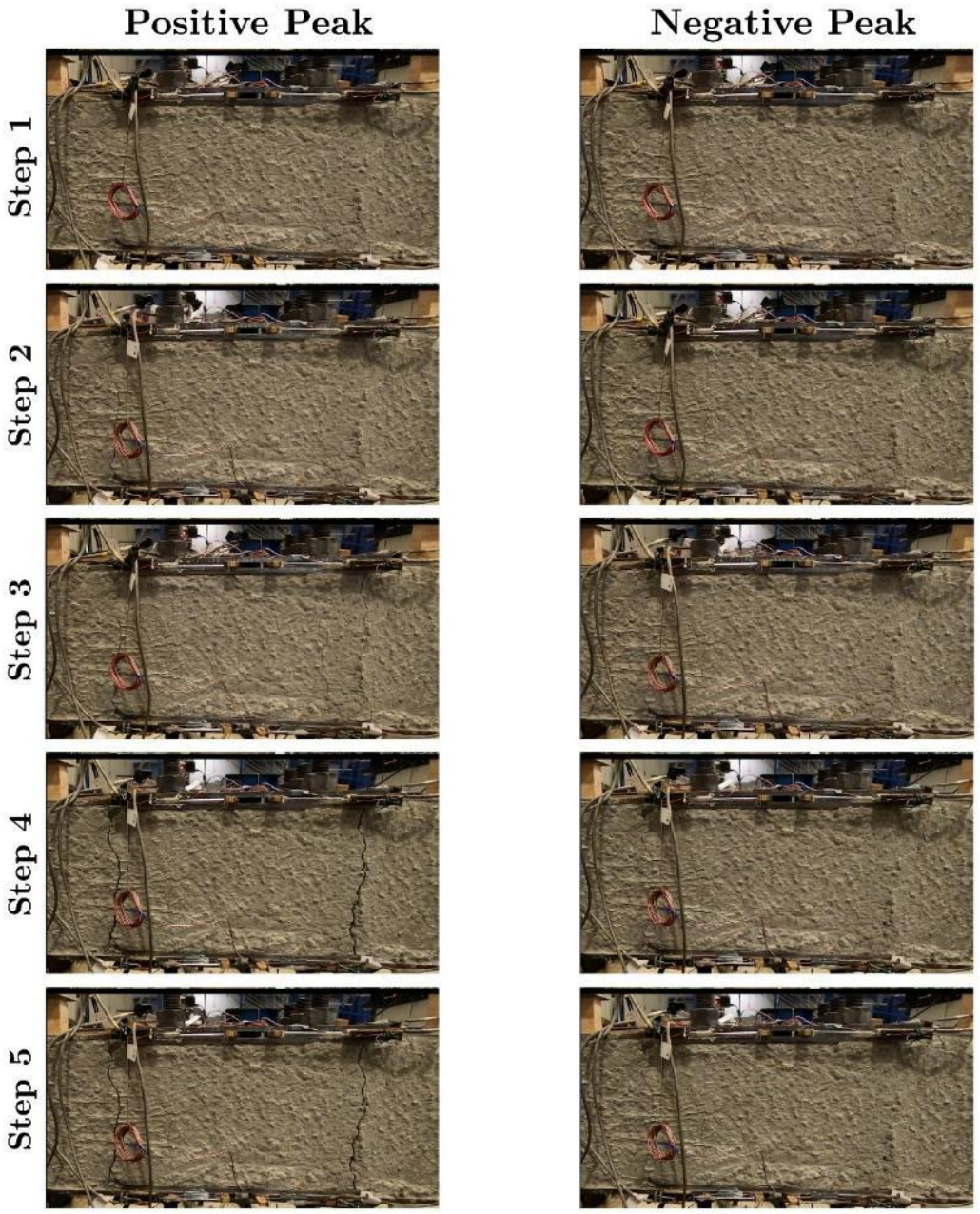


Figure 4-41. North View of Specimen T3 (Steps 1 to 5)

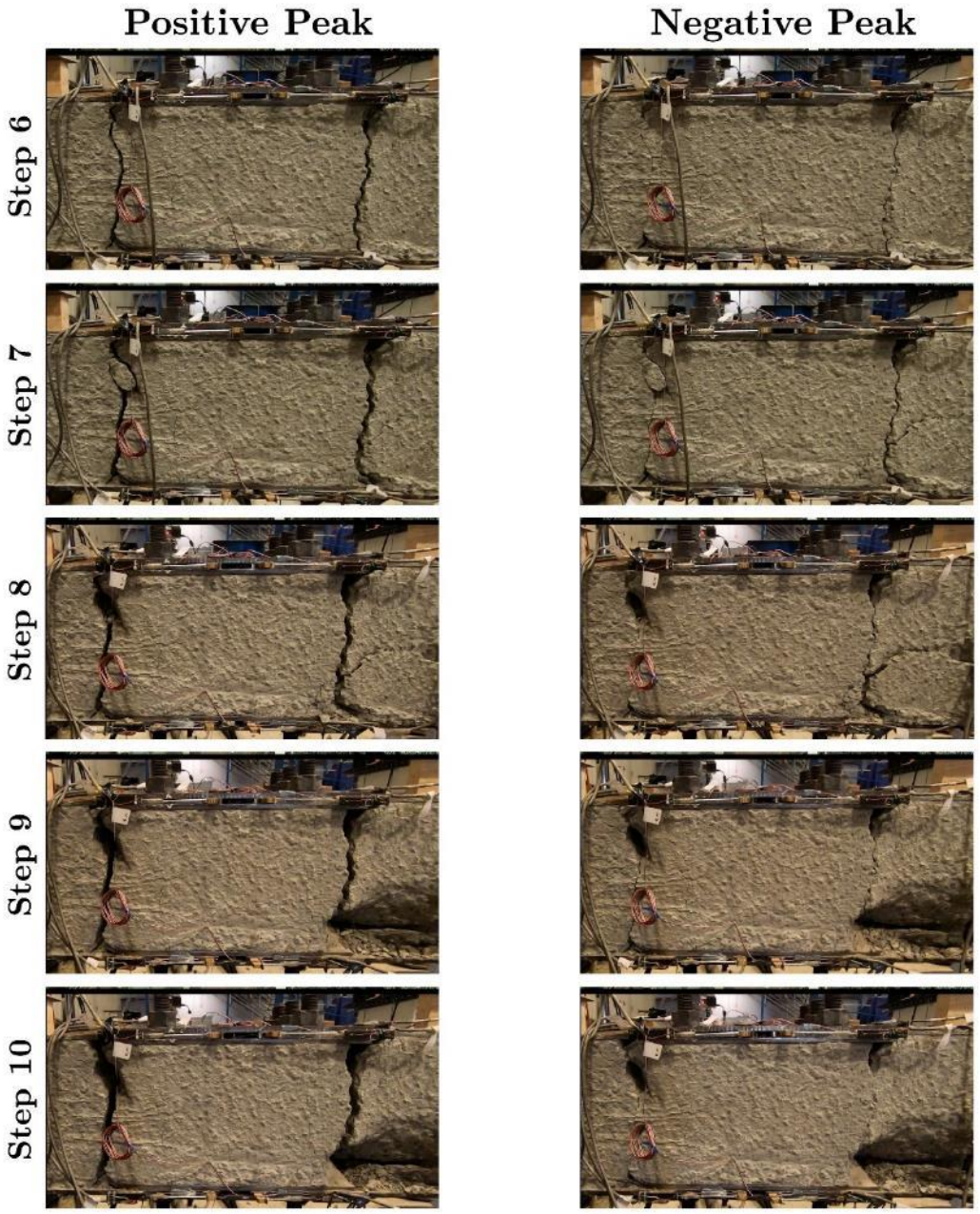


Figure 4-42. North View of Specimen T3 (Steps 6 to 10)

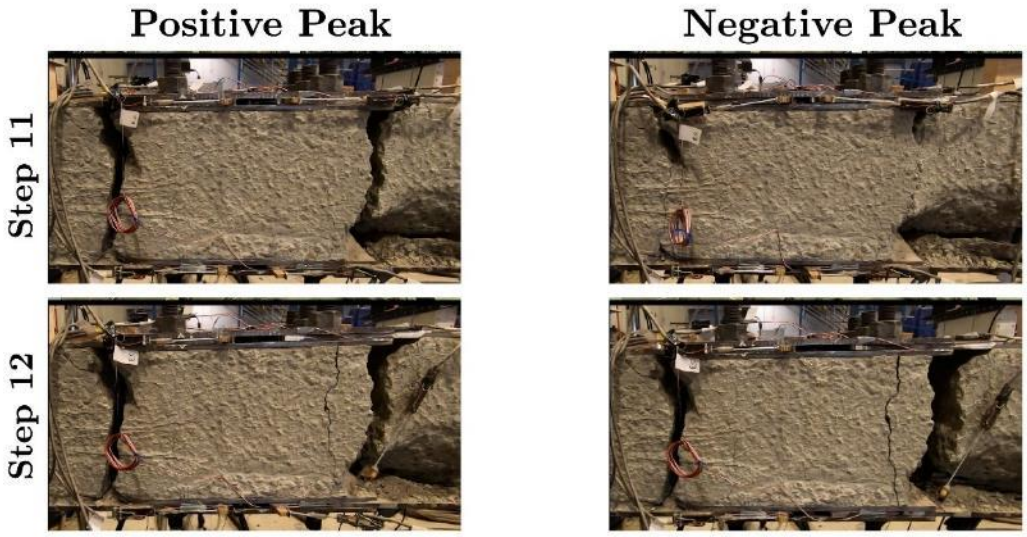
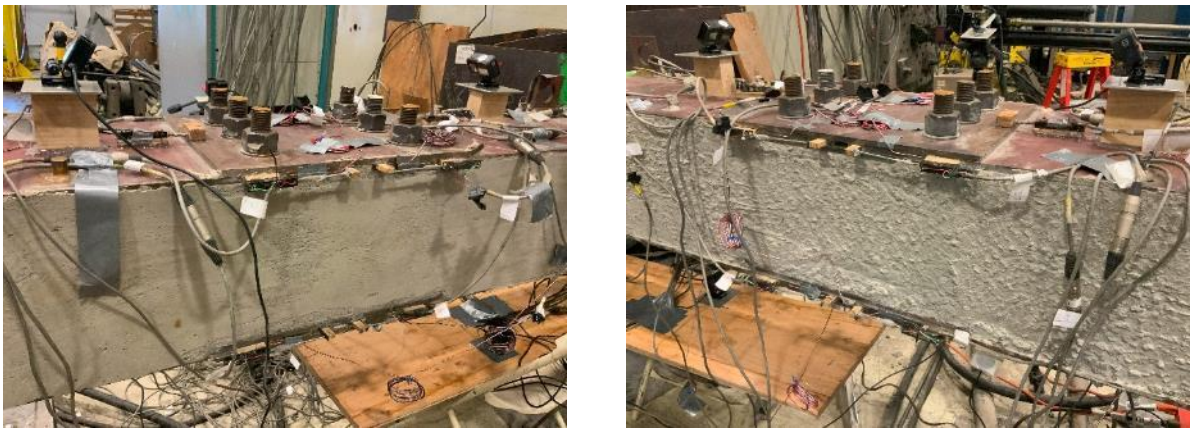


Figure 4-43. North View of Specimen T3 (Steps 11 to 12)

The test started with the loads being applied in displacement control, with one actuator slaved to apply the same displacement as the other actuator. After completing 10 loading cycles in Step 1, the actuator reached 25% of design load P_w. Figure 4-44 shows there was no visible crack observed at this point.



(a) South View (b) North View

Figure 4-44. Specimen T3 (Step 1, Peak Actuator Displacement=0.09")

Subsequently, the test proceeded to Step 2 ($0.5P_w$). However, during the first cycle in Step 2, a loud "bang" was heard due to the connection sliding. Figure 4-45 provides the force and LP deformation curve, which demonstrate a slip-critical value of 170.0 kips. Similar to Step 1, there was no visible crack on the concrete surfaces at this point.

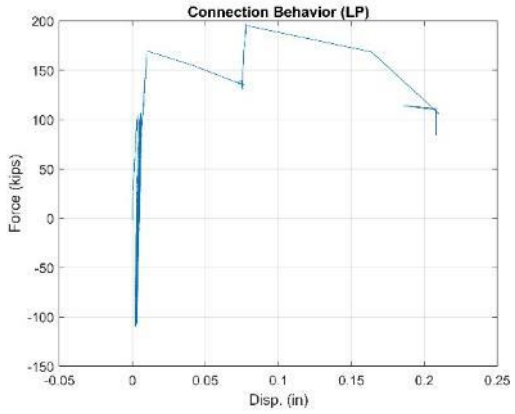
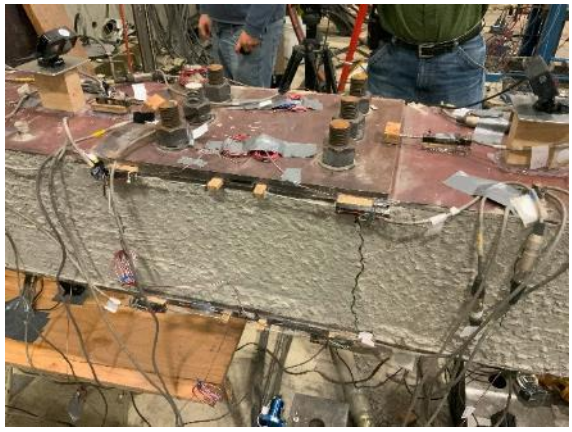


Figure 4-45. First Sliding of Specimen T3

The test progressed further with Steps 3 and 4 (0.6 and $0.75P_w$). As the load increased, more visible cracks became apparent in Step 4. As depicted in Figure 4-46, three vertical cracks were identified, namely occurring at both ends of the splice plates and at the tie bar position.



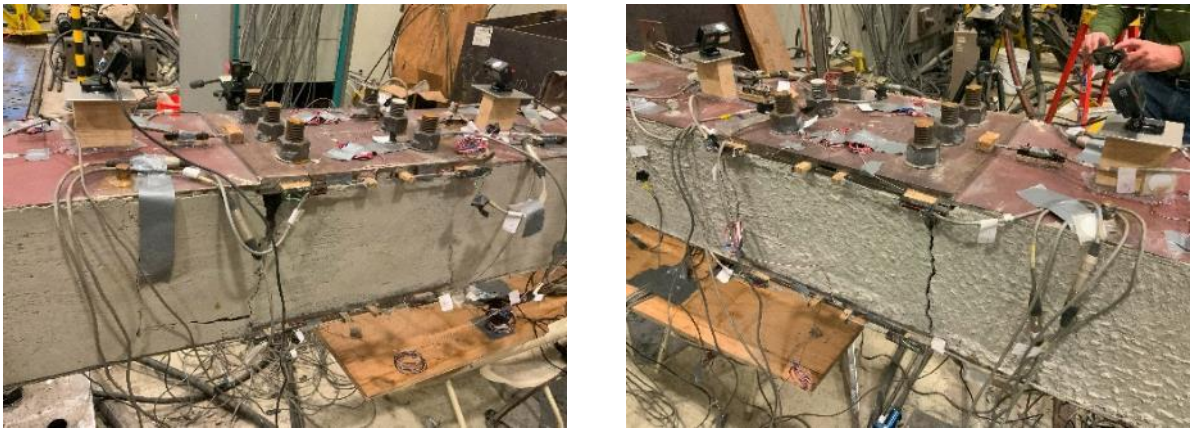
(a) South View



(b) North View

Figure 4-46. Specimen T3 (Step 4, Peak Actuator Displacement=0.74")

In Step 5 of the testing process, the applied force reached 100% P_w. Figure 4-47 depicts the condition after 5-cycles of loading in Step 5. At this stage, it was observed that the crack width had increased, indicating the progression of damage. Additionally, a new horizontal crack appeared near the bottom of the concrete surface on the south side of the specimen, outside the splice region.



(a) South View (b) North View

Figure 4-47. Specimen T3 (Step 5, Peak Actuator Displacement=0.96”)

During the first cycle in Step 6, the footing under the reaction buttress slid when the applied force reached -461 kips in compression. Figure 4-48 shows the global response (GR) at this stage, and the applied force that dropped suddenly because of this footing slippage. In response to this issue, the test was paused to address and rectify the issue associated with the footing's slippage. Figure 4-49 recorded the condition of the test specimen after the slippage of the footing. To increase the clamping force of the footings to the lab strong floor, eight of the threaded rods on the concrete footings were replaced with Dywidag rods (Figure 4-50).

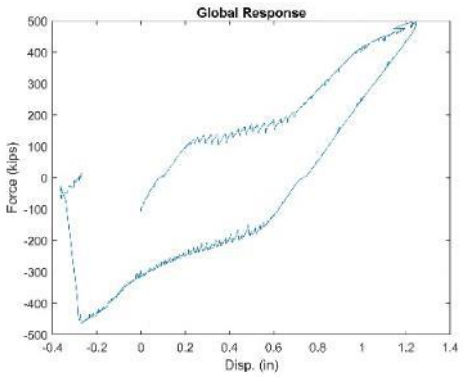
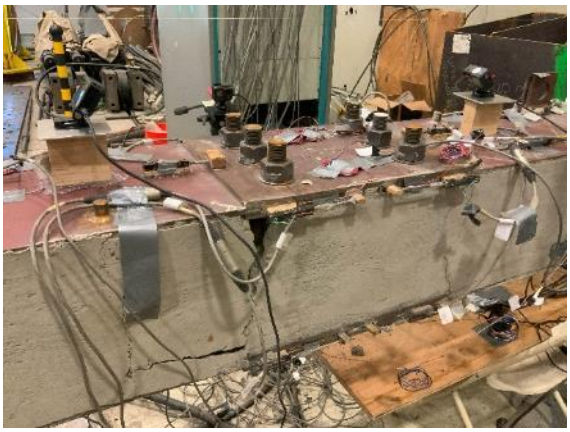
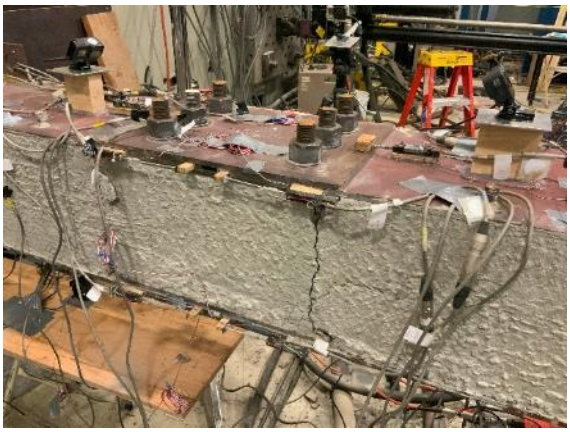


Figure 4-48. Footing Slippage at Step 6



(a) South View



(b) North View

Figure 4-49. Specimen T3 (Step 6, After the Slippage of the Footing)

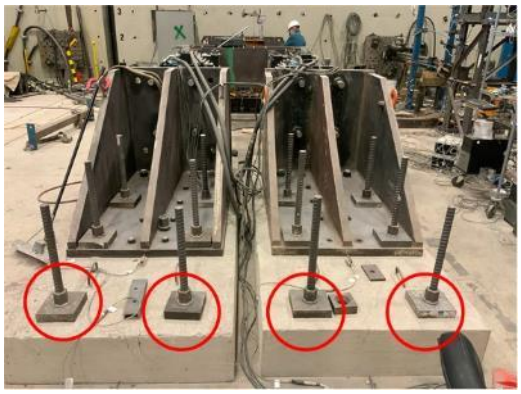


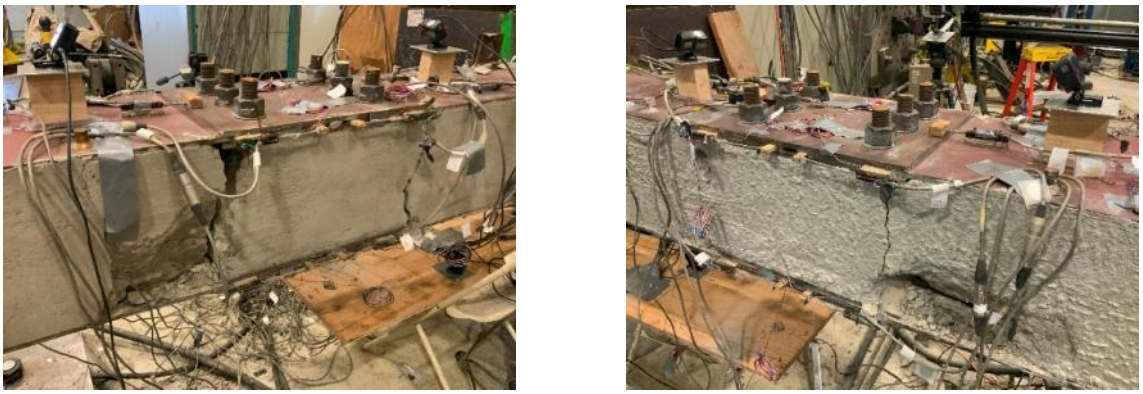
Figure 4-50. Installation of Dywidag Rods on Concrete Footings

After the installation of these Dywidag rods on the concrete footings, testing resumed on 11/22/2022. The test resumed from Step 7, which involved repeating one cycle of loading at 100% of P_w. Subsequently, the test progressed to Step 8, where the applied load was increased to 500 kips, which corresponded to the load level when the footing previously experienced sliding. Figure 4-51 shows the condition after finishing one cycle of loading in Step 8. At this stage, it can be observed that a bottom piece of concrete on each of the south and north sides had detached. The test then proceeded to Step 9, where the applied load reached 530 kips. During this step, a comparable crack pattern was observed as in the previous step, but more severe (Figure 4-52).



(a) South View (b) North View

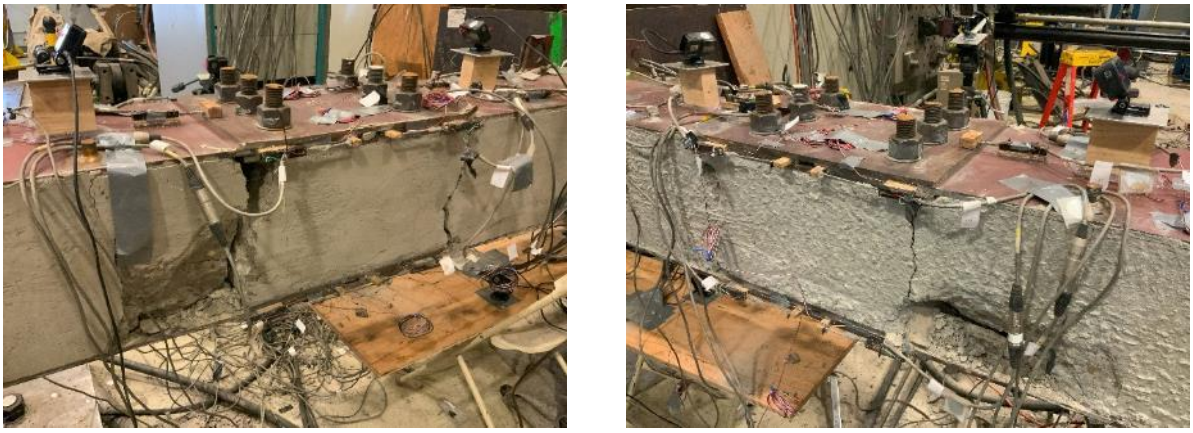
Figure 4-51. Specimen T3 (Step 8, Peak Actuator Displacement=1.16”)



(a) South View (b) North View

Figure 4-52. Specimen T3 (Step 9, Peak Actuator Displacement=1.40”)

In Step 10 of the testing process, the applied force reached 600 kips while the actuator displacement was 1.75 inches. Figure 4-53 provides a summary of the crack condition on both the south and north sides at that stage. Figure 4-54 shows that by that time, an approximate 1-inch relative movement had developed between the top faceplate and splice plate.



(a) South View (b) North View

Figure 4-53. Specimen T3 (Step 10, Peak Actuator Displacement=1.75”)



Figure 4-54. Top View of Specimen T3 (Step 10, Peak Actuator Displacement=1.75”)

The test progressed to Step 11, where the average actuator displacement was increased to 2.2 inches. Figure 4-55 presents the crack condition observed at this stage, indicating that the cracks are similar to those observed in the previous step but again more severe.



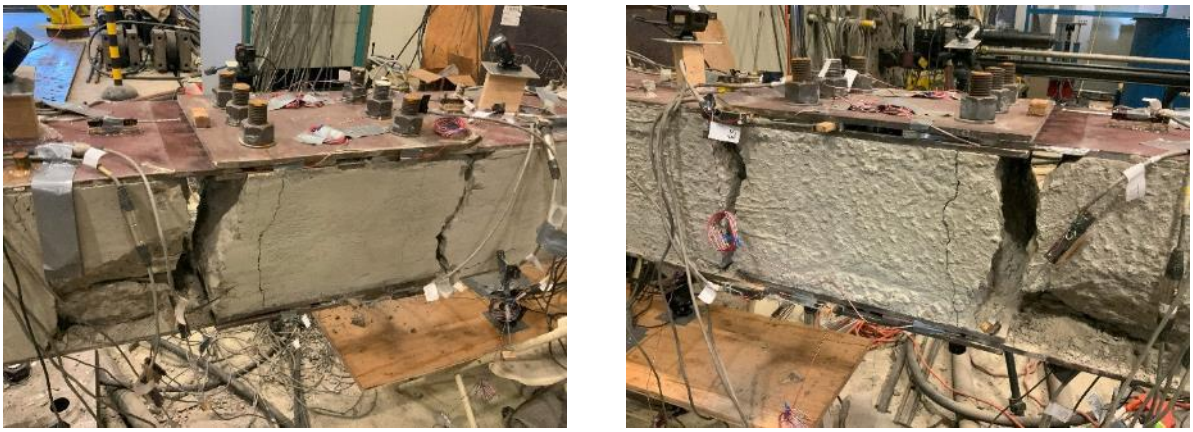
(a) South View (b) North View

Figure 4-55. Specimen T3 (Step 11, Peak Actuator Displacement=2.20”)

The test proceeded to Step 12 with the intention of applying an average actuator displacement of 3.0 inches. However, during the pulling phase, when the average actuator displacement reached 2.50 inches, a loud "bang" sound was heard, and a peak load of 622 kips was recorded before it abruptly dropped. This event was accompanied by the occurrence of a net section fracture on the top faceplate, as depicted in Figure 4-56. Following the fracture, further displacement was applied until reaching the target of 3.0 inches to verify that the entire width of both faceplates (top and bottom) had fractured. Figure 4-57 illustrates the crack condition observed at this final stage of the test.



Figure 4-56. Net Section Fracture at Top Faceplates (Peak Actuator Displacement=2.50”)



(a) South View (b) North View

Figure 4-57. Specimen T3 (Step 12, Peak Actuator Displacement=3.00”)

After the completion of the test, the splice plates were removed from the specimen. Figure 4-58 shows the path of the net section fracture observed on the western side (top and bottom) of the faceplates.



(a) Top Faceplates (b) Bottom Faceplates

Figure 4-58. Net Section Fracture on Top and Bottom Faceplates

Figure 4-59 presents the results obtained using GR, SP, and LP. Figure 4-60 compares the hysteresis curves of SP and LP and shows calculated strength for various design limit states. Strengths corresponding to net section yielding, bearing strength corresponding to 2.4dtFu, block shear, and net section fracture are labeled to represent the progressive development of higher bearing stresses in tension. Remarkably, it was observed that the peak force recorded during the test, which reached 622 kips, was close to the value associated with net section fracture. This indicates that the test results matched the predicted the failure mode of the specimen. Figures 4-61 and 4-62 compare the hysteresis loop of specimens T2 and T3 to highlight the differences in behavior between a connection governed by bearing failure and a connection governed by net section fracture. By defining the yield LP deformation (Δ_{LPy}) for specimens T2 and T3 as the forces corresponding to $2.0dtF_u$ and A_eF_y, respectively, and the ultimate LP deformation (Δ_{LPu}) as the point at which the strength reached its peak value, the ductility of the connection can be defined by calculating the ratio of Δ_{LPu} to Δ_{LPy}. As shown in 4-62, the ductility of the connection in T2 was calculated to be 5.5 (2.48/0.45=5.5), while the ductility in T3 was determined to be 2.25 (2.25/1.00=2.25). Consequently, it can be observed that the connection governed by bearing failure demonstrates a more ductile behavior.

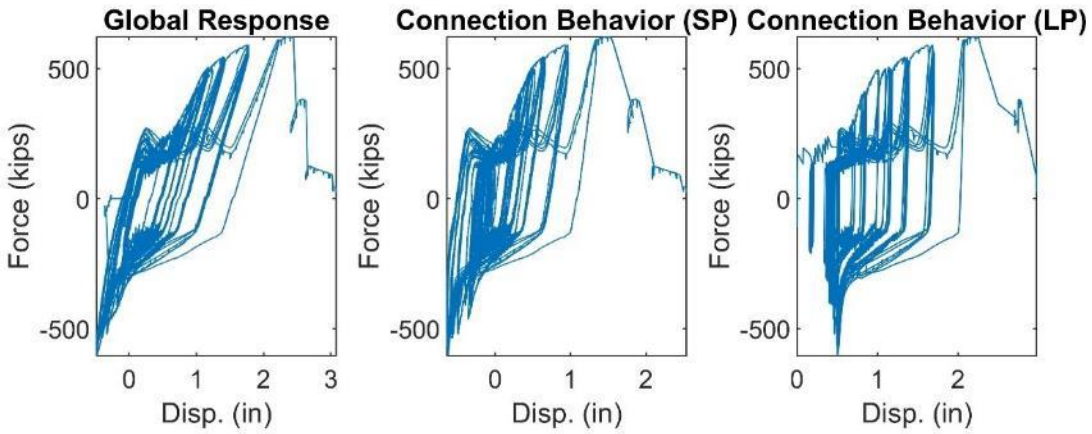


Figure 4-59. Test Results of Specimen T3

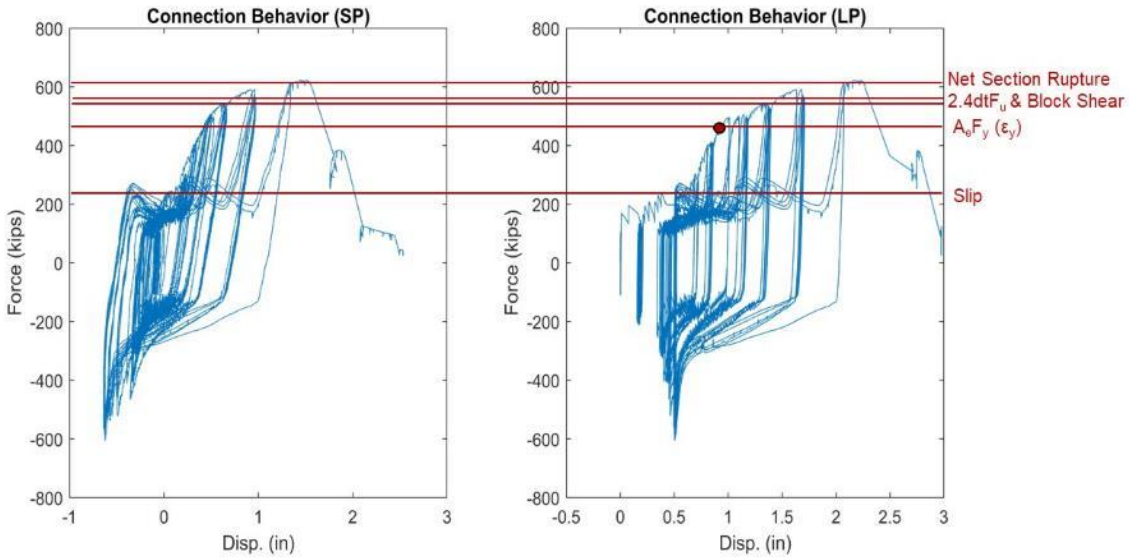


Figure 4-60. Test Results of Specimen T3 with Design Limit States

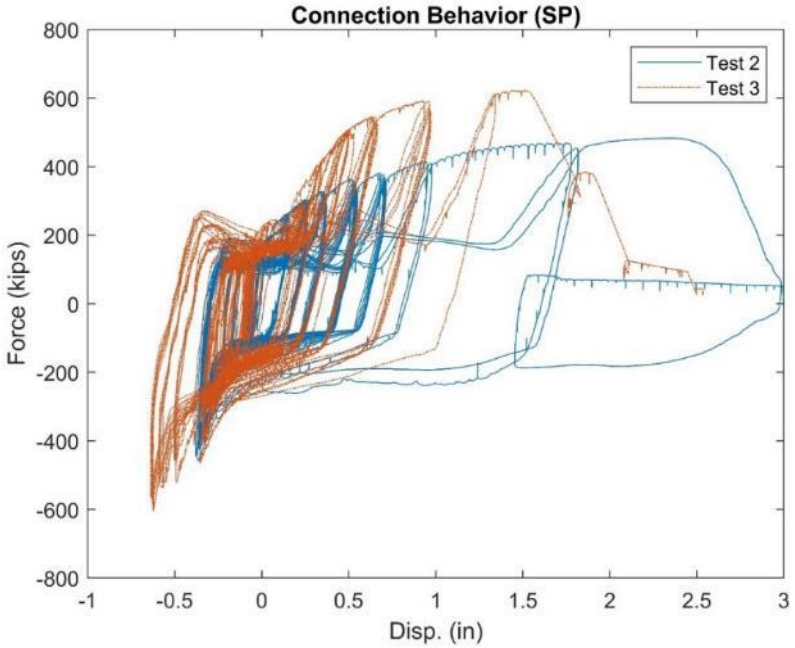


Figure 4-61. Comparison between Specimens T2 and T3 (SP)

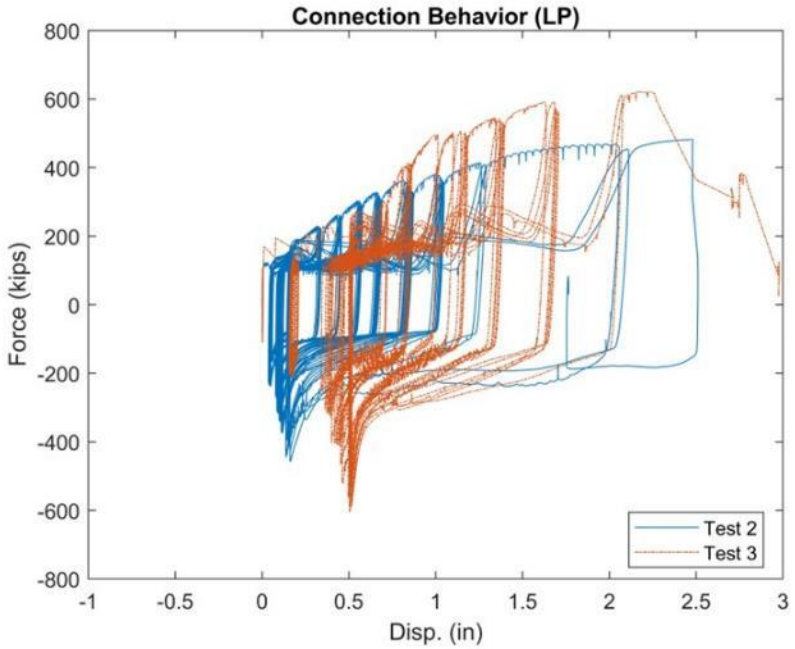


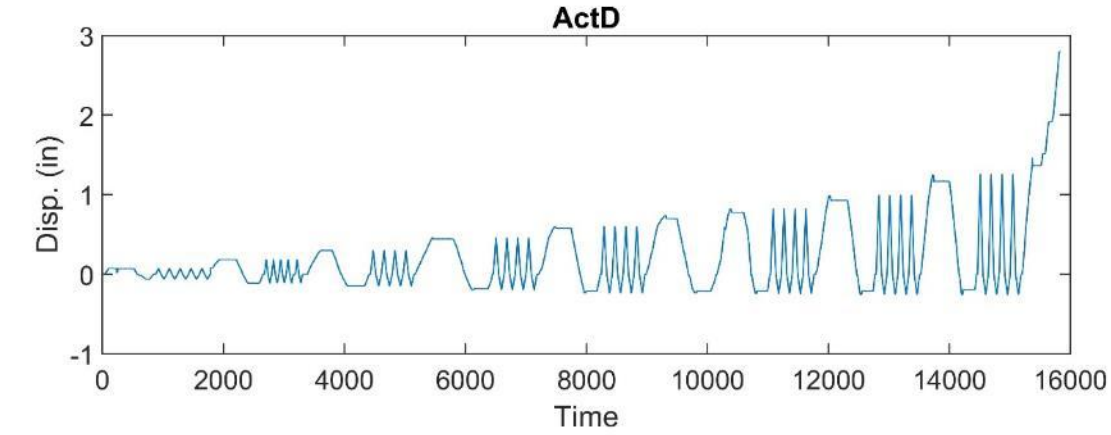
Figure 4-62. Comparison between Specimens T2 and T3 (LP)

4.2.4 Specimen T4

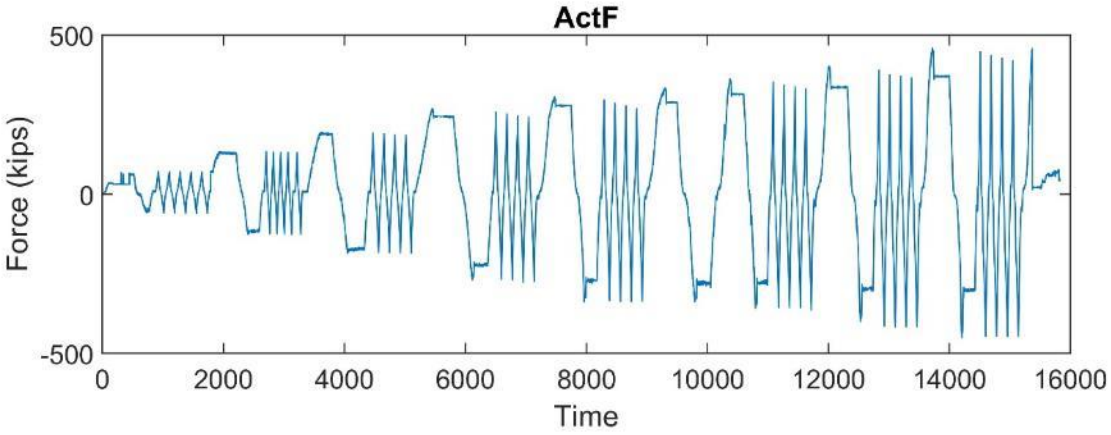
The testing of Specimen T4 started on 12/19/2022, following the loading procedure outlined in Table 4-5. The average actuator displacement and resulting load history for the experiment can be observed in Figure 4-63. To provide additional support for the descriptions, a series of photographs illustrating the splice region (taken from the north perspective of Specimen T4) at different displacement amplitudes are presented in Figures 4-64 to 4-66.

Table 4-5. Modified Loading Protocol for T4

Phase	Disp. (in) +	Disp. (in) -	Force (kips) +	Force (kips) -	Cycles	Note 1	Note 2
0	0.00	0	0	0	-		
1	0.08	0.063	65	65	6	0.25Pw	
2	0.19	0.11	130	130	6	0.5Pw	
3	0.30	0.145	195	195	5	0.75Pw	
4	0.46	0.195	260	260	5	1.0Pw	
5	0.60	0.23	300	300	5		
6	0.74	0.23	330	330	2	t2 Yielding	
7	0.82	0.24	350	350	5	Concrete Fail	
8	0.99	0.25	400	400	5		
9	1.25	0.25	450	450	5		
10	1.50	-	460	-	-	Failure	
11	2.80	-	-	-	-	Final	



(a) Average Displacement History



(b) Resulting Load History

Figure 4-63. Actuator Displacement and Load History for Specimen T4

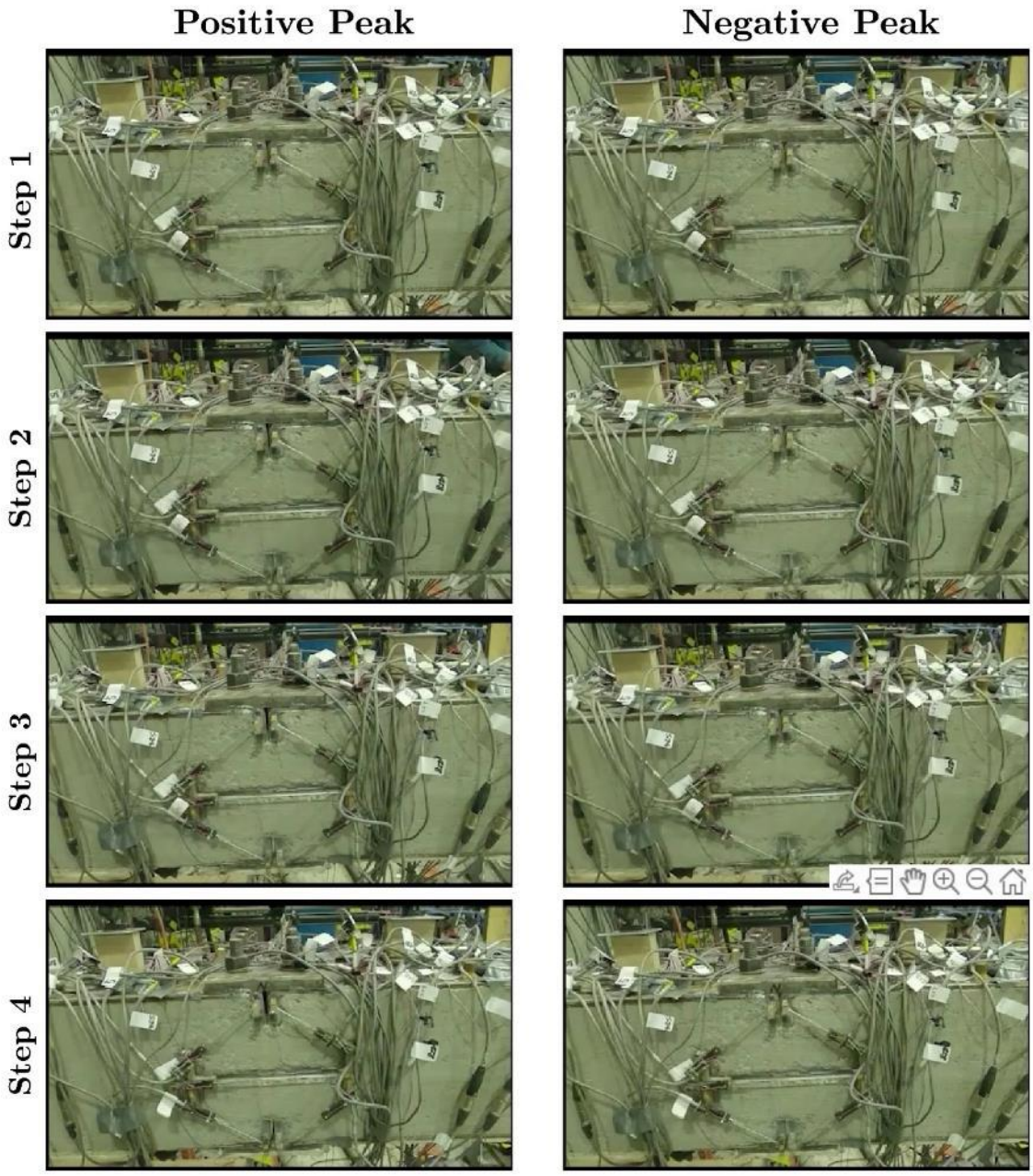


Figure 4-64. North View of Specimen T4 (Steps 1 to 4)

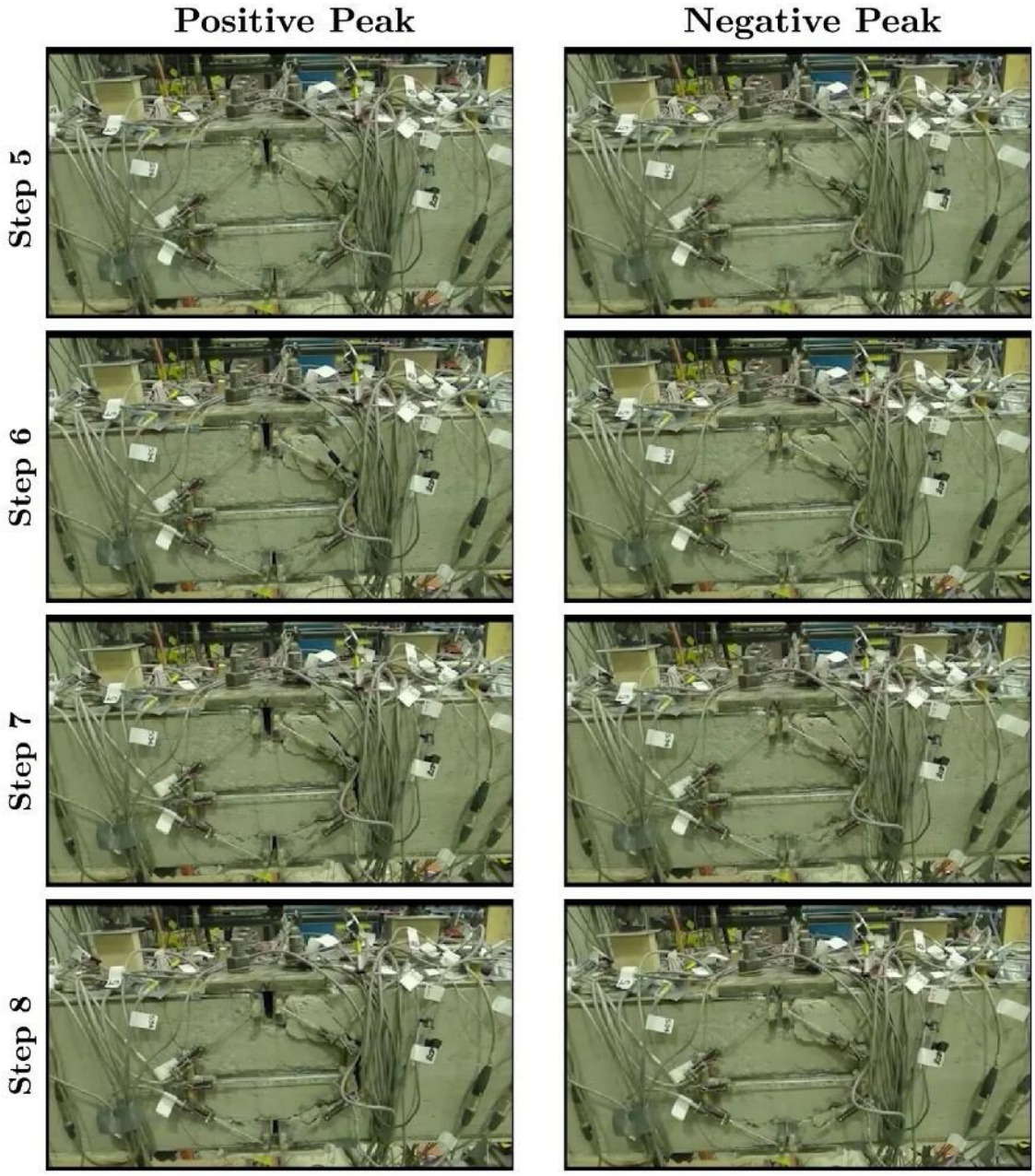


Figure 4-65. North View of Specimen T4 (Steps 5 to 8)

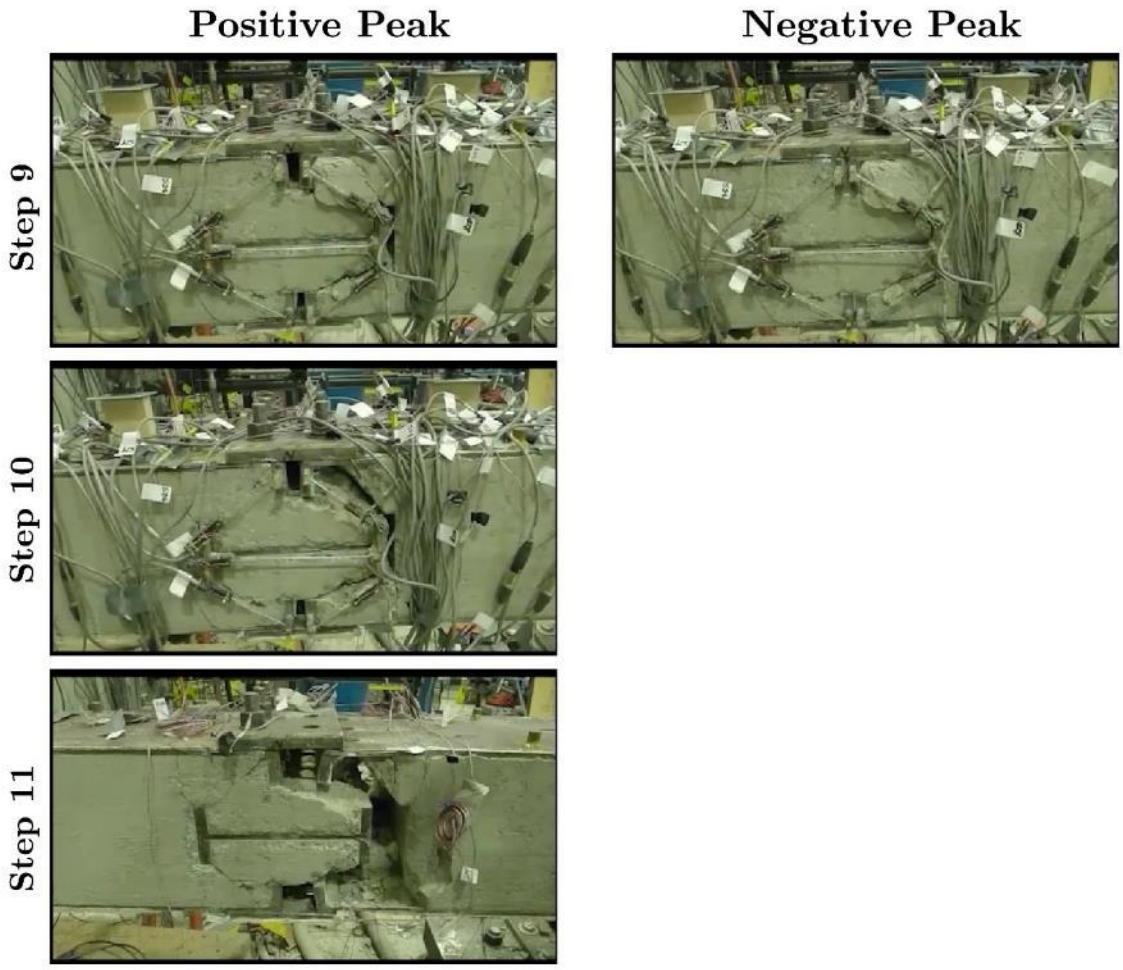


Figure 4-66. North View of Specimen T4 (Steps 9 to 11)

As shown in Figure 3-3, an I-shaped anchor and four key plates were installed in the connection. In an attempt to capture both the general behavior in the splice region and the flexural strain behavior of the I-shaped anchor in Specimen T4, a number of strain gauges were installed. Figures 4-67 and 4-68 provide detailed drawings for the position of strain gauges on Specimen T4. As shown in the figure, the strain gauges labeled S1 to S16 were installed prior to the casting of concrete. They were placed to measure the flexural strains occurring on the flange of the I-shaped anchor ($\varepsilon_{I\text{-}Flange}$) and at the corners of the key plates (ε_{Key}). For capturing the bending strains (ε_{Splice}) in the middle of the splice plates, strain gauges S17 and S18 were positioned on the middle section of the splice plates. To measure the net section strains at specific locations, strain gauges S19 to S26 were affixed to the edge of the faceplates. Gross section strains on the faceplates were measured using strain gauges S27 to S30. Finally, strain gauges S31 and S32 were installed on the web of the I-shaped anchor ($\varepsilon_{I\text{-}Web}$) to monitor the elongation of the anchor.

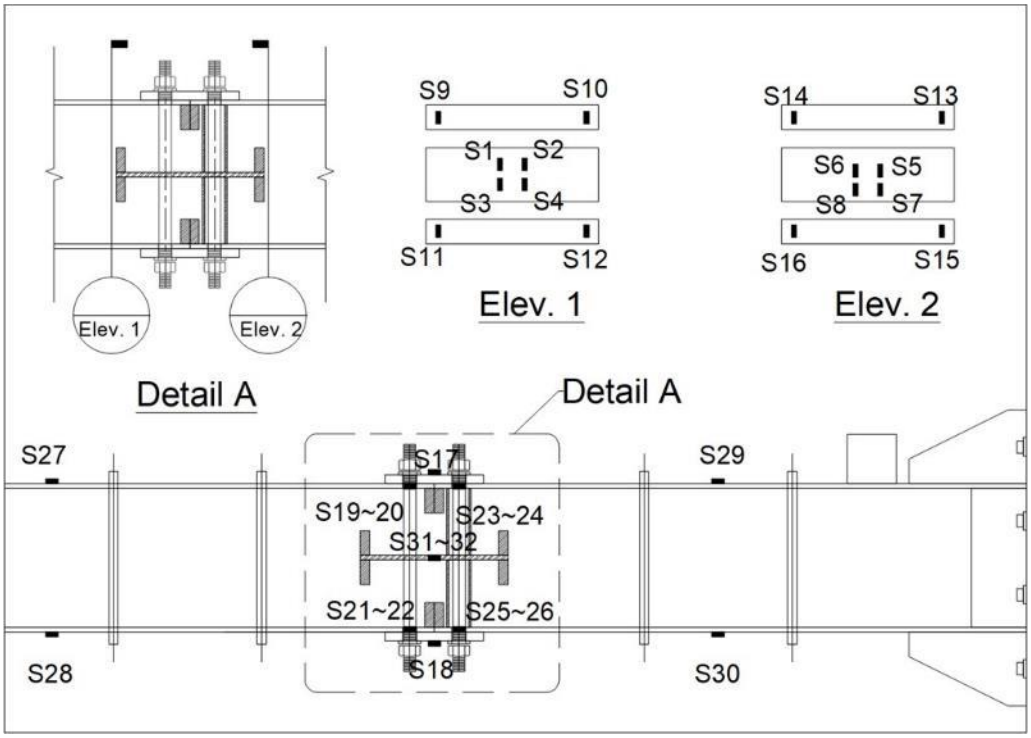


Figure 4-67. Strain Gauges for Specimen T4 (Elevation)

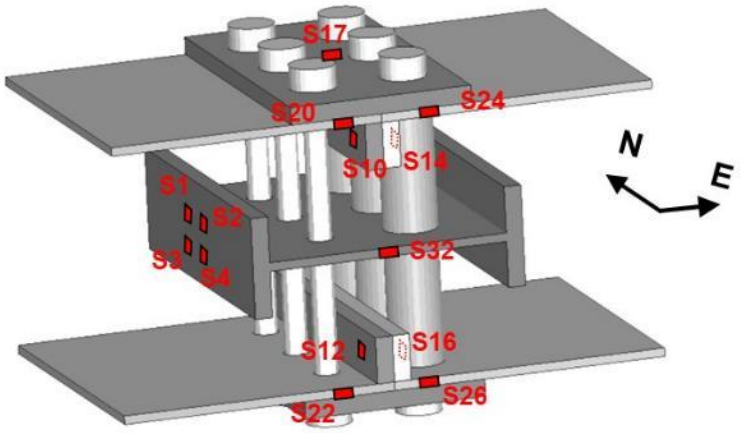


Figure 4-68. Strain Gauges for Specimen T4 (3D View)

Throughout the duration of the test, Table 4-6 provides an overview of the development of gross section and net section strains. Table 4-7 summarizes the strains on the I-shaped anchor and on the splice plates. Note that strain gauges located inside the concrete, namely $\varepsilon_{I\text{-}Flange}$ and ε_{Key}, failed early, during or immediately after Step 4, due to damage caused by concrete cracking.

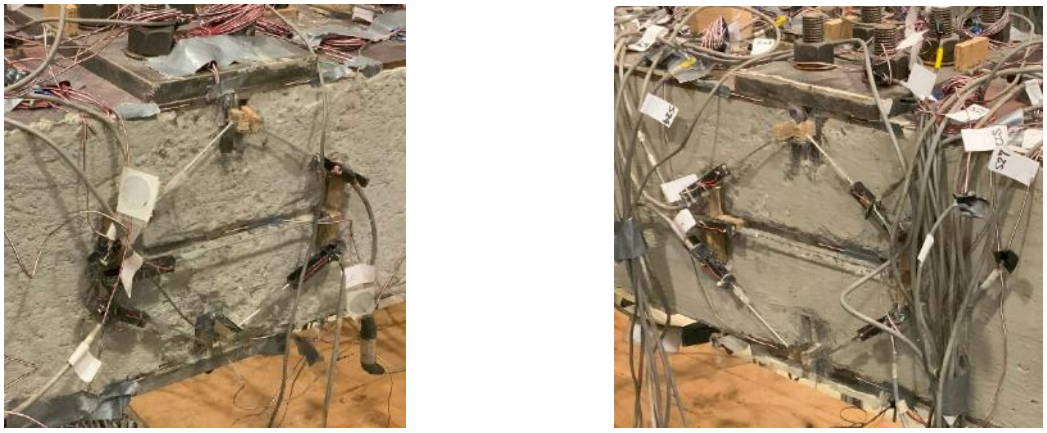
Table 4-6. Development of Gross Section and Net Section Strains for T4

Step	Min. ε_{Gross} (με)	Max. ε_{Gross} (με)	Min. ε_{Net} (με)	Max. ε_{Net} (με)	Min. ε_{Gross} (%εy)	Max. ε_{Gross} (%ε_y)	Min. ε_{Net} (%εy)	Max. ε_{Net} (%εy
0	0	0	0	0	0	0	0	0
1	-276	414	-159	260	-13%	19%	-7%	12%
2	-457	858	-272	567	-21%	39%	-13%	26%
3	-754	992	-516	701	-35%	46%	-24%	32%
4	-1230	1383	-714	1074	-57%	64%	-33%	49%
5	-945	1595	-764	1371	-43%	73%	-35%	63%
6	-599	1797	-907	1549	-28%	83%	-42%	71%
7	-707	2028	-1032	1730	-33%	93%	-48%	80%
8	-783	3210	-1211	1927	-36%	148%	-56%	89%
9	-894	5166	-1770	2124	-41%	238%	-82%	98%
10	-333	7872	-1582	2189	-15%	362%	-73%	101%

Table 4-7. Development of Strain I-shaped anchor and on the splice plates

Step	Min. $\varepsilon_{I\text{-}Flange}$ (με)	Max. $\varepsilon_{I\text{-}Flange}$ (με)	Min. ε_{Key} (με)	Max. ε_{Key} (με)	Min. ε_{Splice} (με)	Max. ε_{Splice} (με)	Min. $\varepsilon_{I\text{-}Web}$ (με)	Max. $\varepsilon_{I\text{-}Web}$ (με
0	0	0	0	0	0	0	0	0
1	-150	141	-367	174	-80	114	-200	161
2	-650	231	-428	353	-130	499	-237	582
3	-488	248	-436	439	-141	1009	-136	1141
4	-645	1967	-	-	-200	1902	261	1923
5	-	-	-	-	-327	2482	577	1959
6	-	-	-	-	-388	2173	734	1890
7	-	-	-	-	-531	2238	673	1879
8	-	-	-	-	-426	2041	719	1655
9	-	-	-	-	-254	1856	876	1578
10	-	-	-	-	47	849	1111	1439

The test started with the loads being applied in displacement control, with one actuator slaved to apply the same displacement as the other actuator. Figure 4-69 shows the condition of the connection after completing 6 loading cycles in Step 1 (0.25 P_w). On the north surface, several tiny cracks were observed near the flange of the I-shaped anchor and the top key plate.

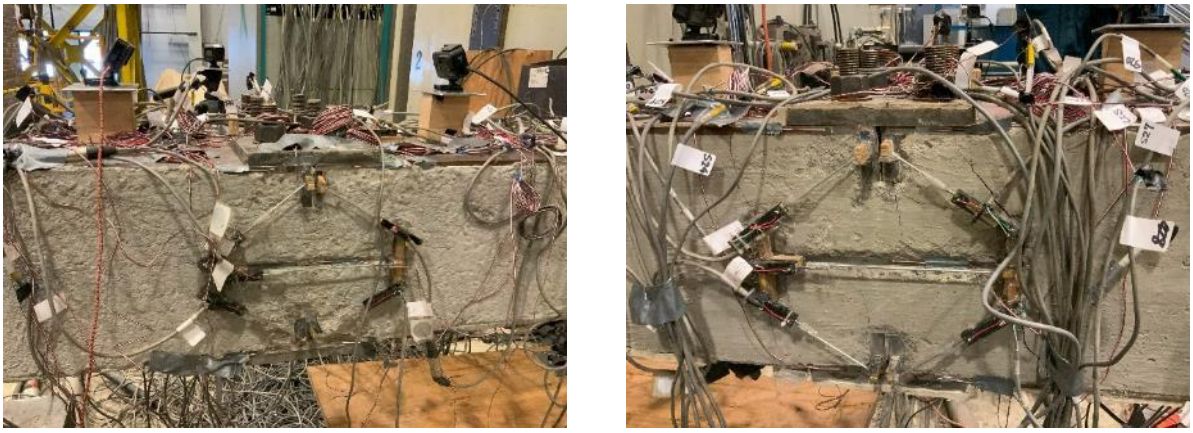


(a) South View (b) North View

Figure 4-69. Specimen T4 (Step 1, Peak Actuator Displacement=0.075")

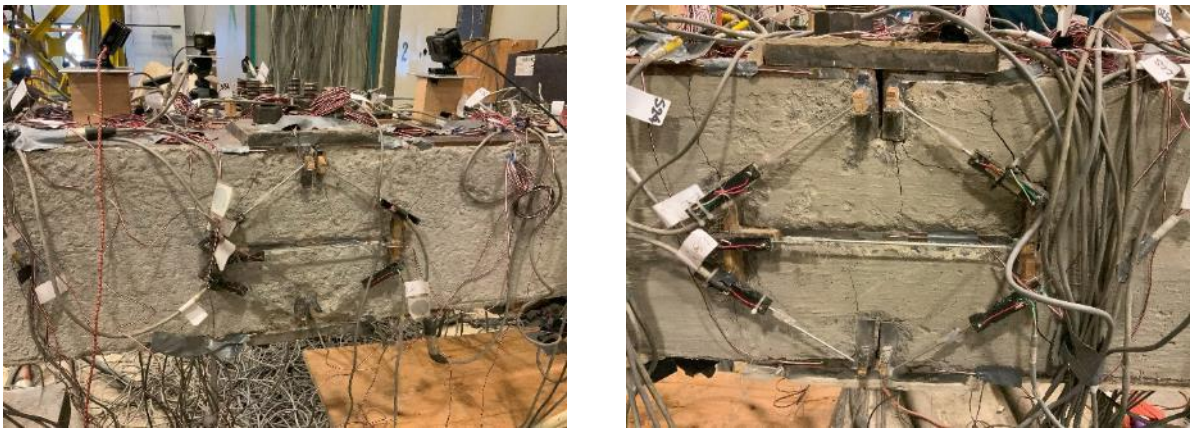
The test proceeded with 6 cycles in Step 2 (0.5 P_w) and 5 cycles in Step 3 (0.75 P_w). Figures 4-70 and 4-71 show south and north views of the connection for Steps 2 and 3, respectively. It can be observed that more cracks appeared around the I-shaped anchor and key plates, and the cracks were more severe on the

northwestern top of the connection. As cracks became more severe, the gap between key plates became larger, particularly on the northern top of the connection.



(a) South View (b) North View

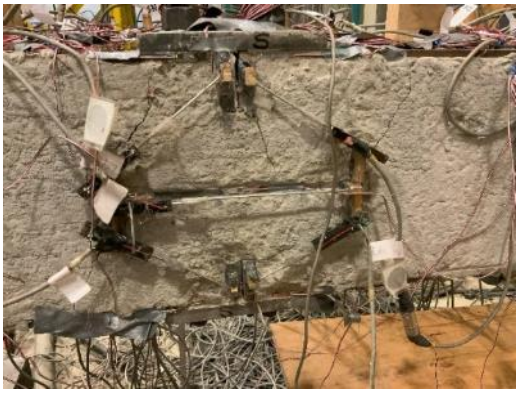
Figure 4-70. Specimen T4 (Step 2, Peak Actuator Displacement=0.185")



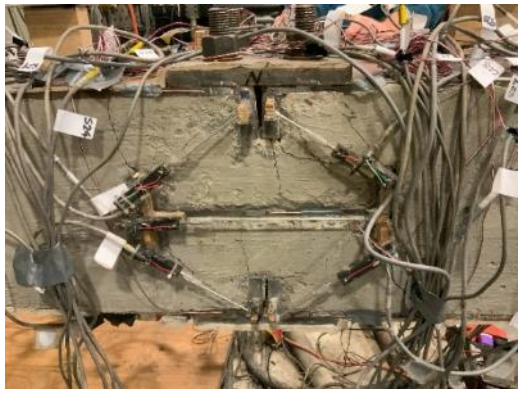
(a) South View (b) North View

Figure 4-71. Specimen T4 (Step 3, Peak Actuator Displacement=0.3")

During the test, the load was further increased to 260 kips (1.0 P_w) in Step 4, and 5 cycles of loading were completed. Figure 4-72 provides a visual representation of the crack pattern observed on the connection at this stage. As depicted in the figure, the crack pattern in Step 4 was similar to the previous step but more severe.



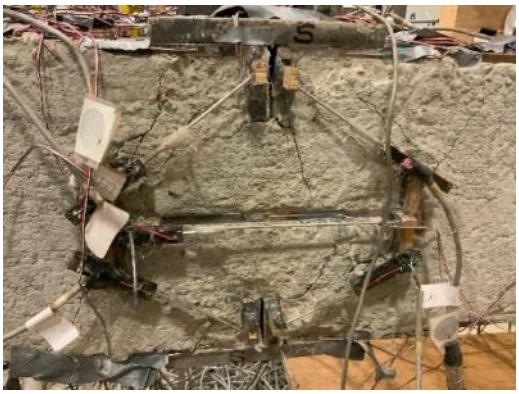
(a) South View



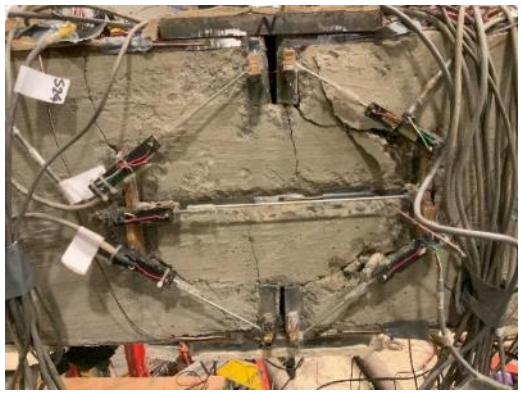
(b) North View

Figure 4-72. Specimen T4 (Step 4, Peak Actuator Displacement=0.46”)

During Steps 5 to 7, the applied actuator force was increased from 300 to 350 kips, respectively. Figures 4-73 to 4-75 provide an illustration of the cracking condition observed at these stages. After the loading cycles, four diagonal cracks are visible, particularly on the northwestern side of the connection. Note that while a 45-degree compression strut was assumed to develop between the flange of the embedded I-shape and the key plates, the large cracks shown on the northwest side of the specimen developed at a shallower angle and intersected this assumed compression strut location. Additionally, it can be observed that a piece of concrete on the northwestern top was ready to fall off, and that the separation between northern top key plates increased to approximately 0.5 inches.



(a) South View

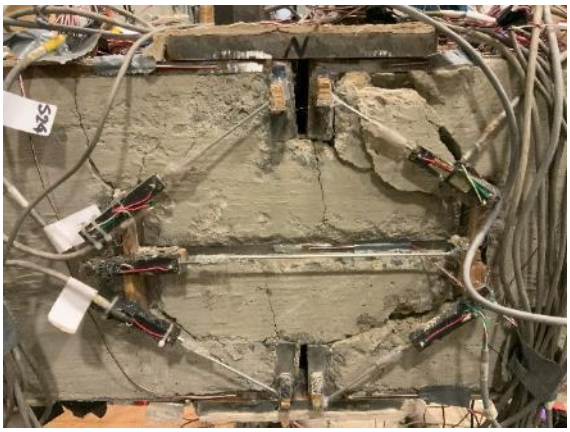


(b) North View

Figure 4-73. Specimen T4 (Step 5, Peak Actuator Displacement=0.6”)



(a) South View

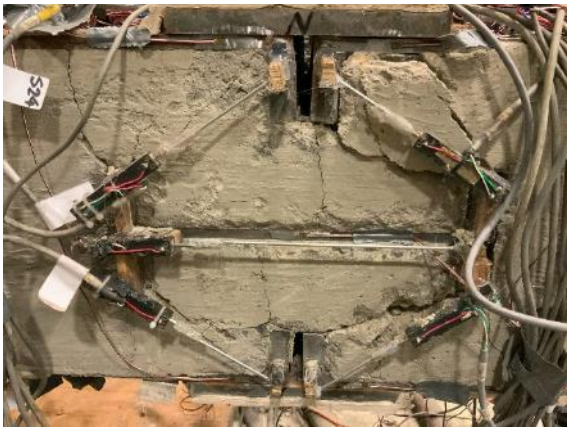


(b) North View

Figure 4-74. Specimen T4 (Step 6, Peak Actuator Displacement=0.74”)



(a) South View



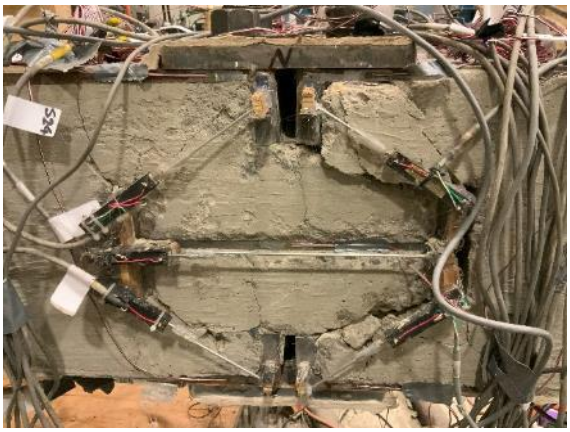
(b) North View

Figure 4-75. Specimen T4 (Step 7, Peak Actuator Displacement=0.82”)

Figures 4-76 and 4-77 depict the crack propagation observed during Steps 8 and 9. As the applied forces increased, the cracks extended further, and the gap distance between the key plates increased to approximately 0.75 inches. This separation indicated that the cracks had propagated almost throughout the width of the concrete, reducing the effectiveness of the compression strut forces.



(a) South View

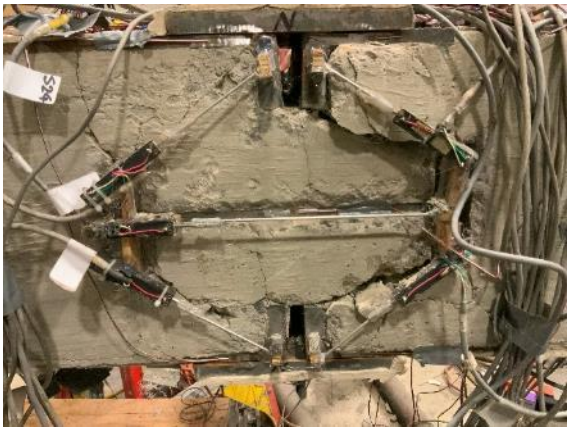


(b) North View

Figure 4-76. Specimen T4 (Step 8, Peak Actuator Displacement=0.99”)



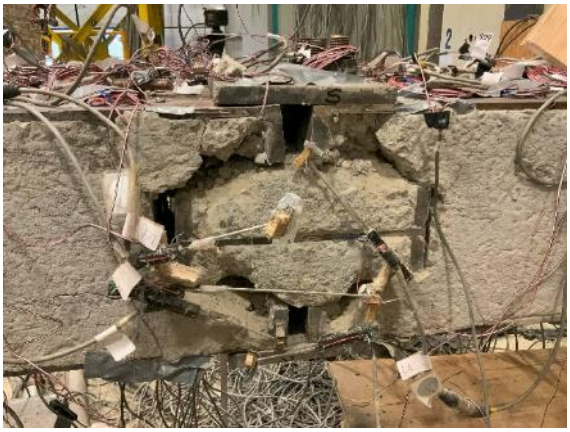
(a) South View



(b) North View

Figure 4-77. Specimen T4 (Step 9, Peak Actuator Displacement=1.25”)

In Step 9 of the test, the target actuator displacement was set to 1.5 in. However, a loud “bang” was heard when the actuator displacement reached 1.37 in. Figures 4-78 and 4-79 show the side and top views of the connection after this event. It can be observed that three rods on the western side of the connection broke, resulting in a substantial gap between the eastern and western parts of the wall. After Step 9, the actuator displacement was further increase to 2.8 in, as shown in Figure 4-80, to confirm that the western and eastern parts of the wall were by then completely separated.



(a) South View



(b) North View

Figure 4-78. Specimen T4 (Step 10, Peak Actuator Displacement=1.5”)



Figure 4-79. Top View of Specimen T4 (Step 10)



(a) South View



(b) North View

Figure 4-80. Specimen T4 (Step 11, Peak Actuator Displacement=2.8”)

Figure 4-81 presents the results obtained using GR, SP, and LP. Figure 4-82 compares the hysteresis curves of SP and LP and shows calculated strength for various design limit states. The design limit states corresponding to the flexural yielding at the corner of key plates (labeled "Corner Bending" in the figure), the yielding at the web of the I-shaped anchor ("t2 Yielding & Concrete Failure"), and the shear yielding at the corner of key plates ("t3 Shear Yielding") are marked in the figure. It is worth noting that according to Table 3-5, the rod fracture strength under pure tensile force is specified as 530.2 kips. However, in the test, the rods fractured earlier than expected, at a peak force of 459 kips, as they were observed to be under the combined effect of tensile and large bending stresses locally, as observed by the deflected shape of the threaded rod exposed when removing some of the concrete (Figures 4-83 and 4-84). Evidence of this bending effect can be observed from the radiating marks that developed on the brittle failure surfaces of the rods (Figure 4-85).

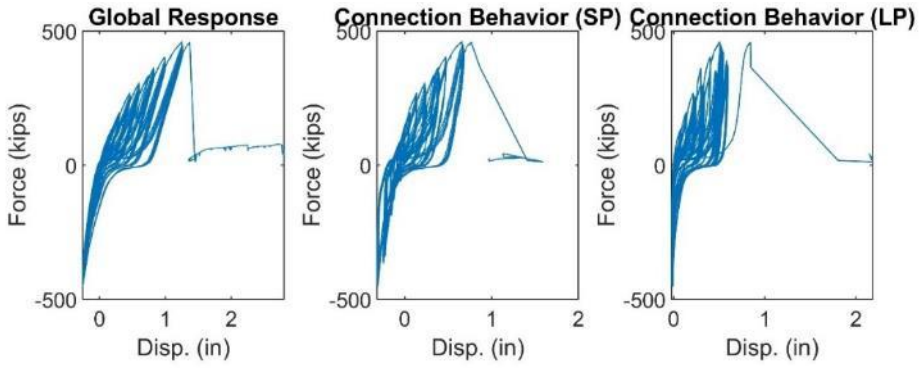


Figure 4-81. Test Results of Specimen T4

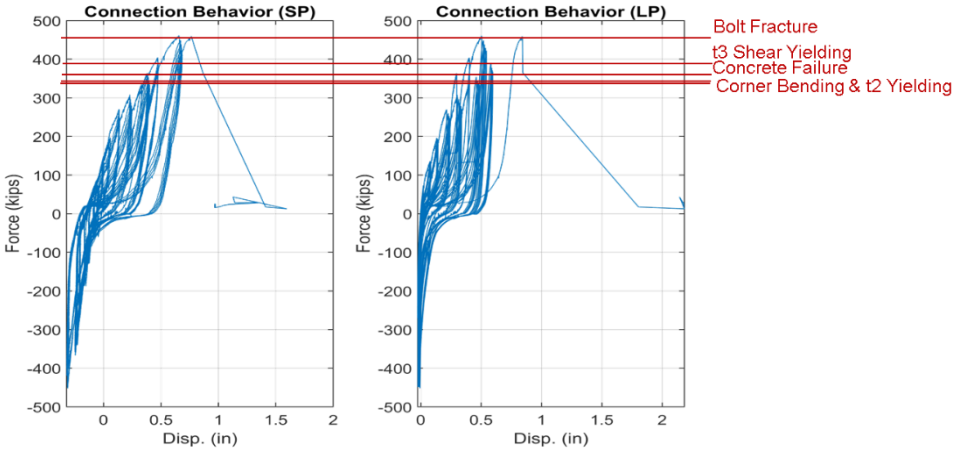
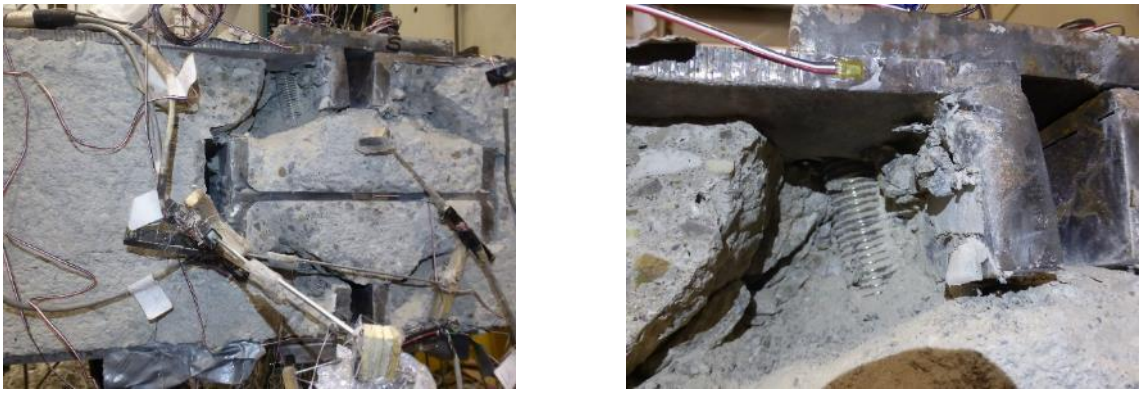


Figure 4-82. Test Results of Specimen T4 with Design Limit States



Figure 4-83. Top View of Specimen T4 showing Rod Holes Movement



(a) South View (b) North View

Figure 4-84. Specimen T4 (Close View showing the Bending of Rods)



Figure 4-85. Brittle Failure Surfaces of the Rods

4.2.5 Specimen T5

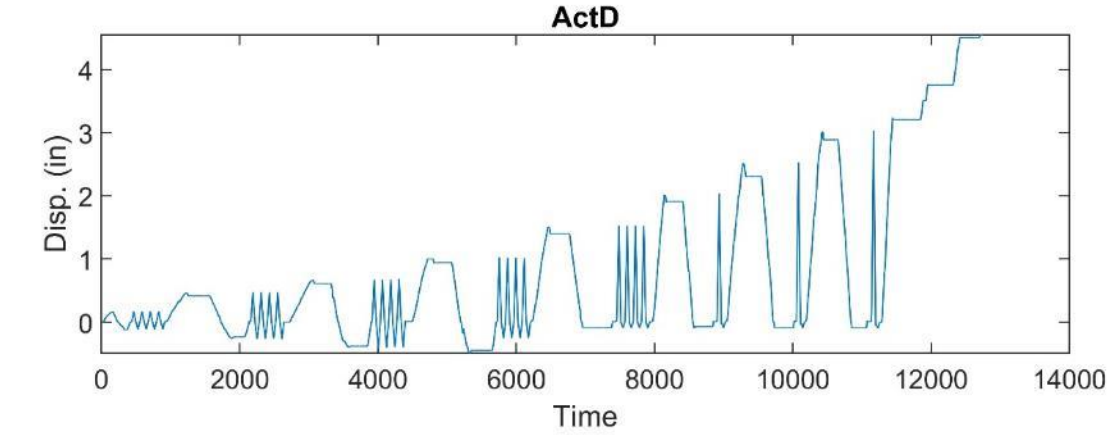
The testing of Specimen T5 started on 1/6/2022, following the loading procedure outlined in Table 4-8. The average actuator displacement and resulting load history for the experiment can be observed in Figure 4-86. To further support the descriptions, a series of photographs illustrating the splice region from the north perspective of Specimen T5 at different displacement amplitudes are presented in Figures 4-87 to 4-89. Table 4-9 provides an overview of the development of the maximum gross section and net section strains developed during each step of the test. Note that during or after Step 5, all strains exhibit significantly large values due to the buckling of the connection in Step 4.

Table 4-8. Modified Loading Protocol for T5

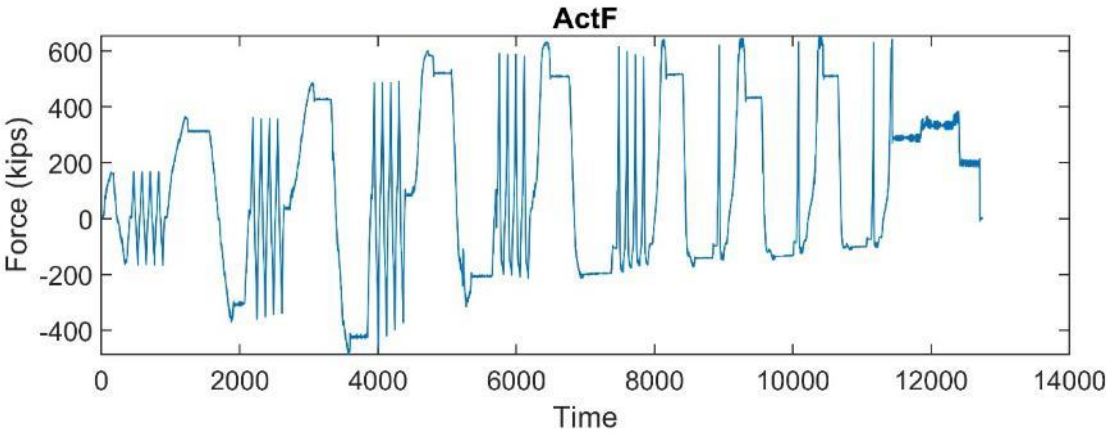
Step	Disp. (in) +	Disp. (in) -	Force (kips) +	Force (kips) -	Cycles	Note 1	Note 2
0	0	0	0	0	-		
1	0.155	0.12	163	163	5	0.25Pw	
2	0.455	0.265	325	325	5	0.5Pw	Conn. Slip
3	0.66	0.4	488	488	5	0.75Pw	
4	1.00	0.55	600	317	5	0.92Pw	AeFy
5	1.5	0.1	630	210	5	1.0Pw	AgFy
6	2	0.1	640	175	2		
7	2.5	0.1	646	150	2		
8	3	0.1	653	110	2		
9	3.25	-	650	-	-		Failure
10	4.5	-	-	-	-		Final

Table 4-9. Development of Gross Section and Net Section Strains for T5

Step	Min. ε_{Gross} (με)	Max. ε_{Gross} (με)	Min. ε_{Net} (με)	Max. ε_{Net} (με)	Min. ε_{Gross} (%εy)	Max. ε_{Gross} (%ε_y)	Min. ε_{Net} (%εy)	Max. ε_{Net} (%εy
0	0	0	0	0	0	0	0	0
1	-490	537	-572	412	-23%	25%	-26%	19%
2	-944	1185	-953	1009	-43%	55%	-44%	46%
3	-1634	1742	-1041	1231	-75%	80%	-48%	57%
4	-1343	2367	-906	3558	-62%	109%	-42%	164%
5	-1459	6544	-21680	21813	-67%	301%	-998%	1004%
6	-1084	21576	-21811	21813	-50%	993%	-1004%	1004%
7	5376	21576	-21811	21813	248%	993%	-1004%	1004%
8	15346	21576	175	22027	707%	993%	8%	1014%
9	15976	21800	203	22027	736%	1004%	9%	1014%



(a) Average Displacement History



(b) Resulting Load History

Figure 4-86. Actuator Displacement and Load History for Specimen T5

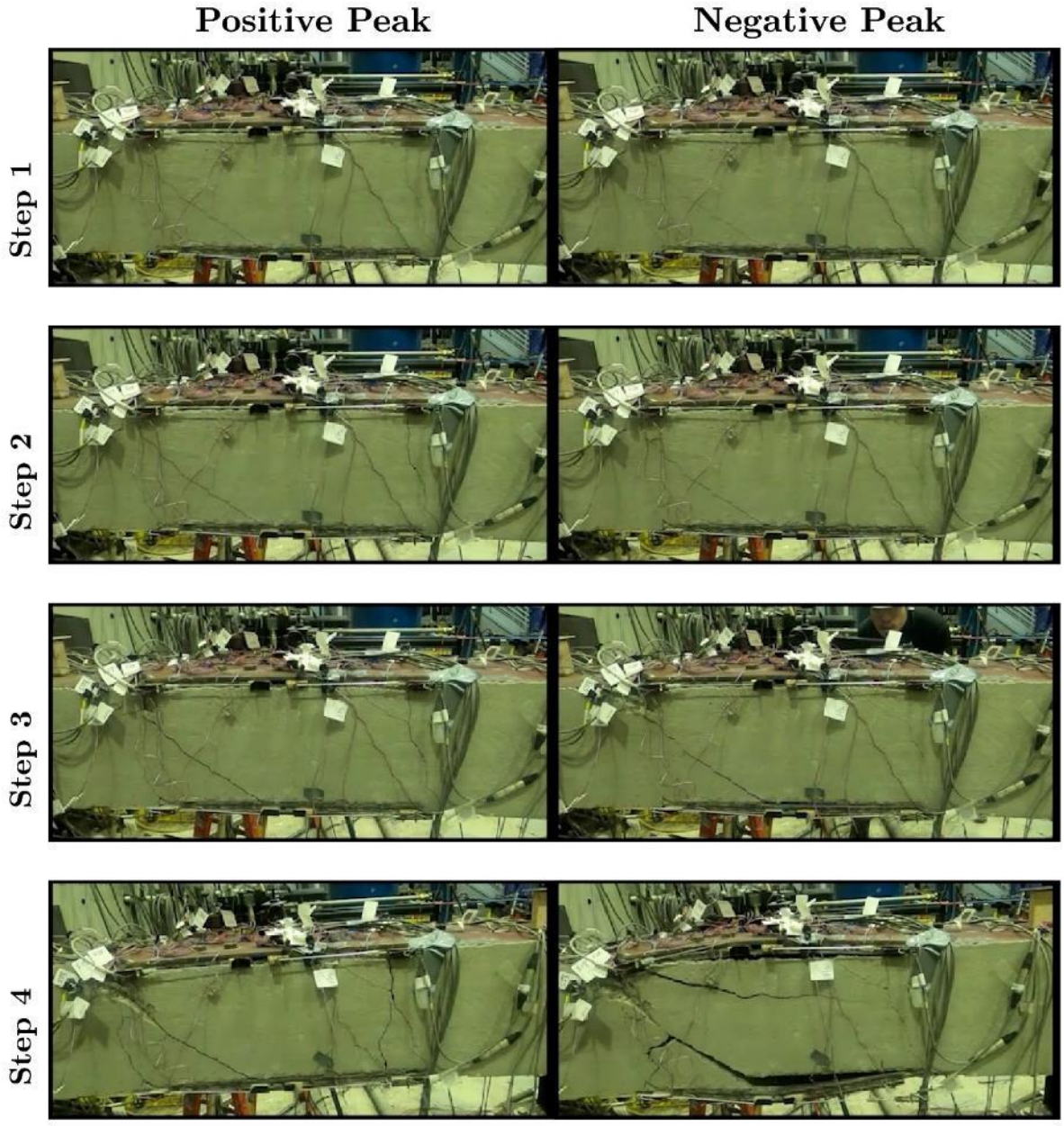


Figure 4-87. North View of Specimen T5 (Steps 1 to 4)

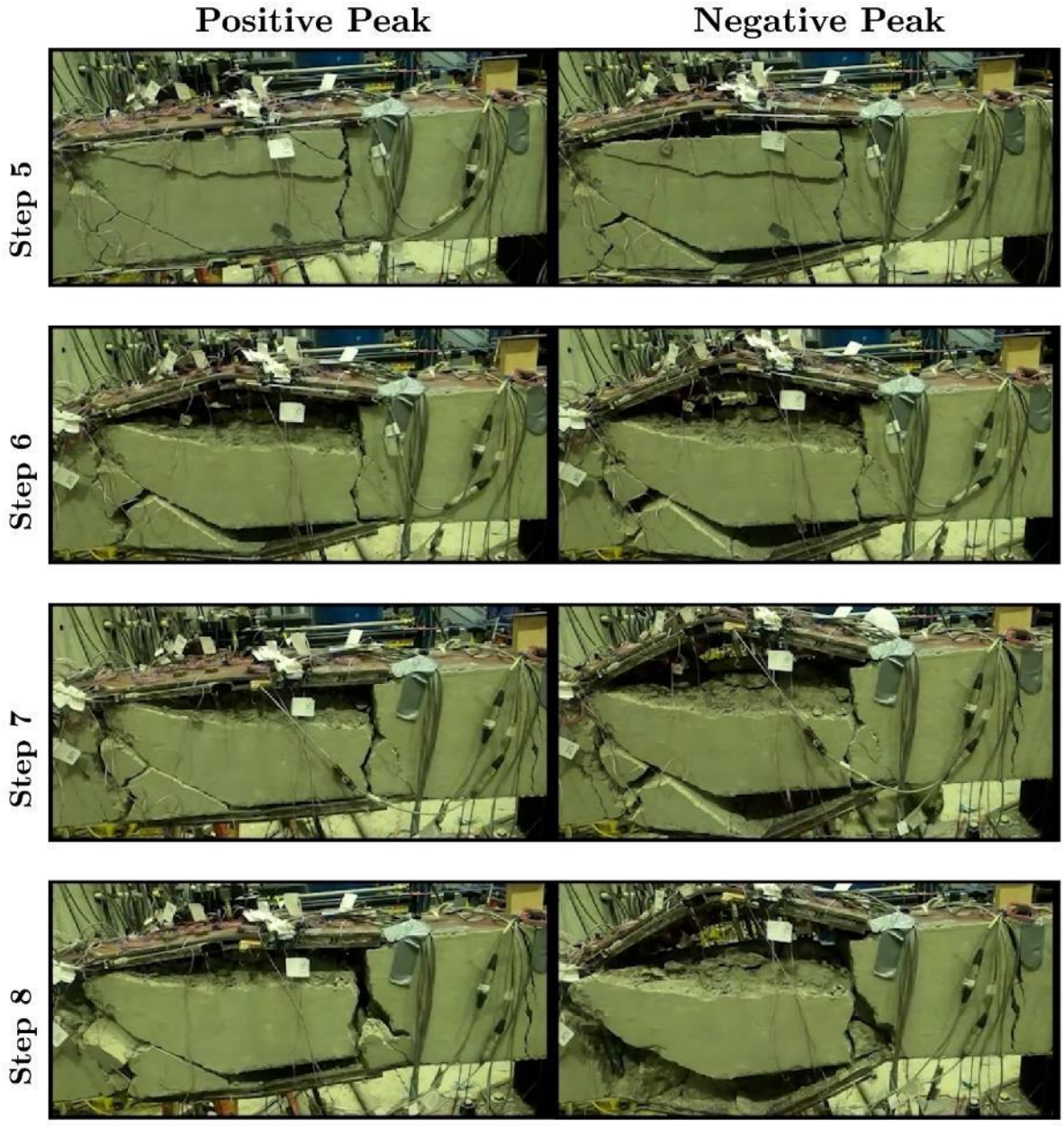


Figure 4-88. North View of Specimen T5 (Steps 5 to 8)

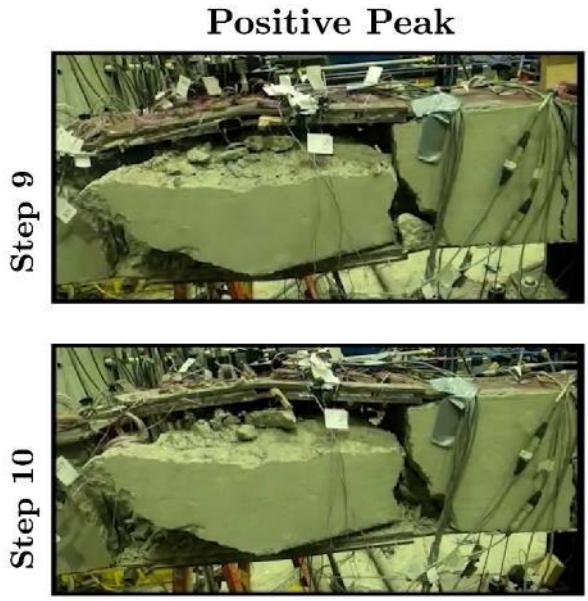


Figure 4-89. North View of Specimen T5 (Steps 9 to 10)

The test started with loads applied in displacement control. After completing 5 loading cycles in Step 1 (0.25 P_w), Figure 4-90 displays the condition of the connection. On the north surface of the connection, there was a vertical crack near the west end, and a diagonal crack propagated from the top eastern area to the middle bottom.



(a) South View (b) North View

Figure 4-90. Specimen T5 (Step 1, Peak Actuator Displacement=0.155")

The test continued with 5 cycles of Step 2 (0.5 Pw) and Step 3 (0.75 Pw). Figure 4-91 shows the south view of the connection for Step 2, while Figure 4-92 displays the north view for Step 3. It can be observed that in Step 2, the previously mentioned diagonal crack also initiated on the south surface. In Step 3, a vertical crack appeared at the position of the tie bar.



(c) South View

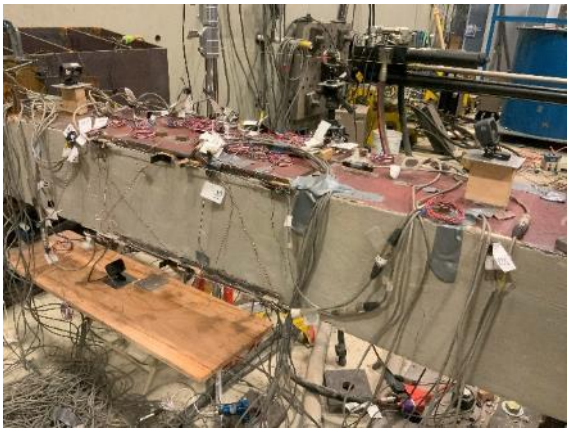


(d) North View

Figure 4-91. Specimen T5 (Step 2, Peak Actuator Displacement=0.455”)



(c) South View



(d) North View

Figure 4-92. Specimen T5 (Step 3, Peak Actuator Displacement=0.66”)

During Step 4, the applied tensile load was increased to 600 kips (0.92 P_w), and Figure 4-93 shows the crack pattern observed on the connection at this stage. More cracks were observed on both south and north surfaces. When the actuator moved in the negative direction (compression), the connection was observed to buckle at the top and bottom, as depicted in Figure 4-94. After buckling was noticed, the average actuator displacement in compression was limited to -0.2 in. to complete the remaining 4 cycles. Figure 4-95 shows the crack pattern of the connection, and it can be observed that top and bottom pieces of concrete fell off on the north side, and a top piece of concrete on the south surface was dislodged and ready to come out. To prevent further stability issue, the actuator displacement in compression was further limited again, this time to -0.1 in. for the subsequent loading cycles.



(c) South View



(d) North View

Figure 4-93. Specimen T5 (Step 4, Peak Actuator Displacement=1.00”)



(a) South View

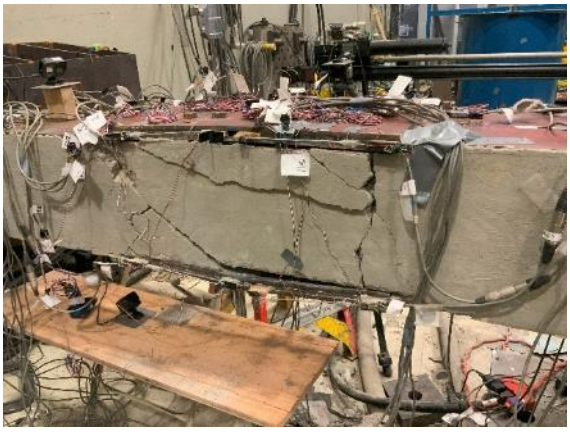


(b) North View

Figure 4-94. Specimen T5 (Step 4, Peak Actuator Displacement=-0.55”)



(a) South View



(b) North View

Figure 4-95. Specimen T5 (After 5 cycles of Step 4)

During Steps 5 to 7, the applied average actuator displacement was increased from 1.5 in. to 2.5 in. Figures 4-96 to 4-98 show the progressive damage to concrete during these steps. Throughout the loading cycles, it can be observed that an increasing number of concrete pieces fell off, and as a result, some of the previously embedded tie-rods and bolts became exposed. Although the applied displacement in compression was limited to -0.1 in., there was still large plate deformations due to buckling as shown in Figure 4-99.



(c) South View



(d) North View

Figure 4-96. Specimen T5 (Step 5, Peak Actuator Displacement=1.5”)



(c) South View



(d) North View

Figure 4-97. Specimen T5 (Step 6, Peak Actuator Displacement=2.0”)



(c) South View

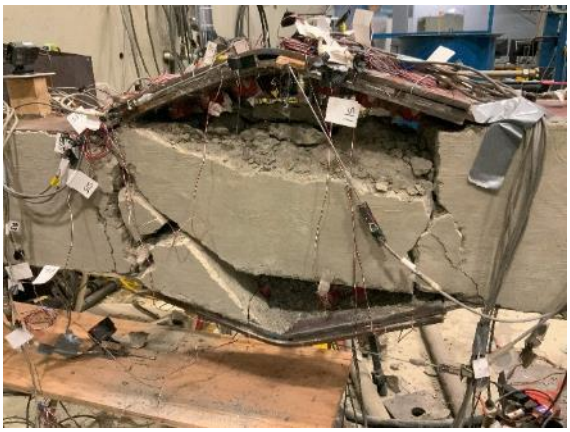


(d) North View

Figure 4-98. Specimen T5 (Step 7, Peak Actuator Displacement=2.50”)



(a) South View



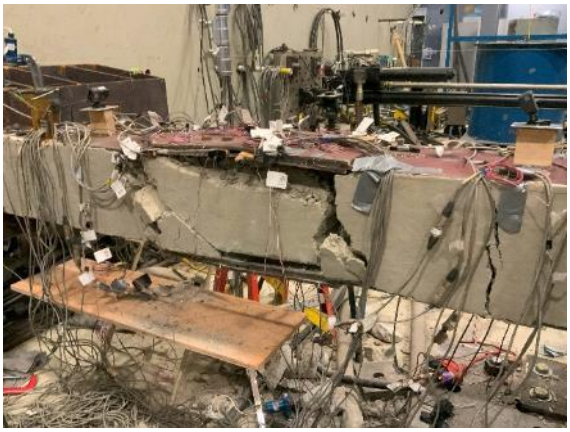
(b) North View

Figure 4-99. Specimen T5 (Step 7, Peak Actuator Displacement=-0.1”)

Figures 4-100 and 4-101 depict the specimen condition in Step 8 when the connection was in tension and compression. The gaps in concrete were more severe when the connection was in tension, and when in compression, the entire concrete in the connection seemed about to fall out due to buckling.



(c) South View



(d) North View

Figure 4-100. Specimen T5 (Step 8, Peak Actuator Displacement=3.0”)



(c) South View



(d) North View

Figure 4-101. Specimen T5 (Step 8, Peak Actuator Displacement=-0.1")

During Step 9 of the test, the target actuator displacement was pulled to 3.5 in. However, a loud "bang" was heard when the actuator displacement reached 3.25 in. Figure 4-102 show the side and top views of the connection after this event, and Figure 4-103 (a) provides a top view showing the gross section fracture that occurred on the eastern top of the faceplate at one of the location where the faceplate was developing a plastic hinge during buckling. After Step 9, the actuator displacement further increased to 4.5 in. to completely separate the western and eastern parts of the wall in Step 10 (Final Step). As shown in Figure 4-103 (b), this was achieved, with complete fracture of the top and bottom faceplates.



(c) South View



(d) North View

Figure 4-102. Specimen T5 (Step 9, Peak Actuator Displacement=3.25")



(a) Step 9



(b) Step 10 (Final Step)

Figure 4-103. Gross Section Fracture in Steps 9 and 10 of Specimen T5

Figure 4-104 presents the results obtained using GR, SP, and LP. Figure 4-105 compares the hysteresis curves of SP and LP and shows calculated strength for various design limit states. In the figure, there is no obvious plateau observed in the hysteresis loop to determine a specific slip-critical force in this case. Strengths corresponding to net section yielding and gross section yielding are labeled in the figure to demonstrate the tensile strength development. During the test, it was noted that the peak force reached 654 kips, which was close to the calculated gross section yield strength of 661.5 kips. This observation suggests that the connection experienced gross section yielding in tension, consistently with the predicted behavior during the specimen's design phase. Note that the LP deformation in Figure 4-105 shifted by approximately 1 to 2 in. due to movement of the linear pots during buckling of the connection (Figure 4-106). The curves have not been corrected to subtract this effect, as this can be done visually.

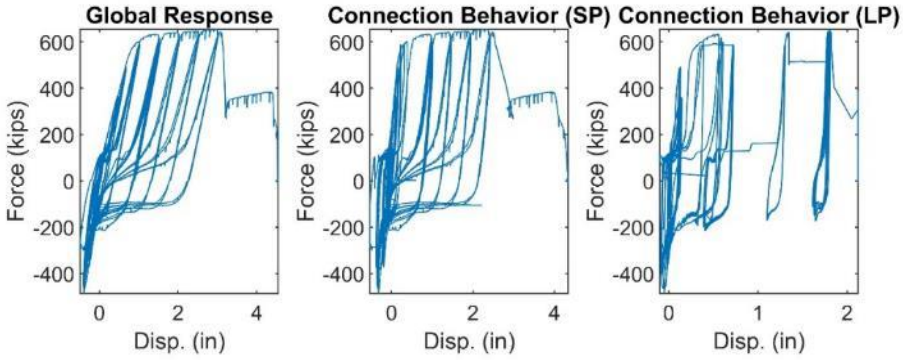


Figure 4-104. Test Results of Specimen T5

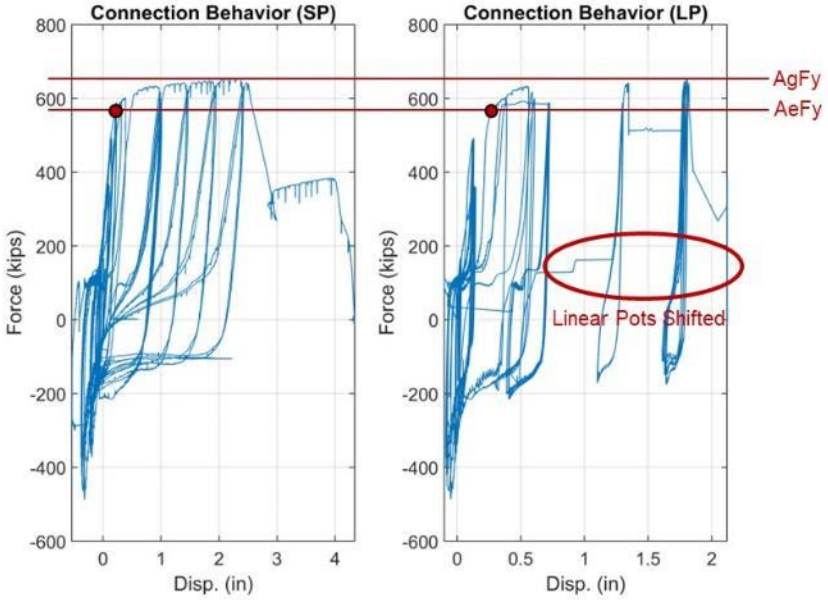


Figure 4-105. Test Results of Specimen T5 with Design Limit States

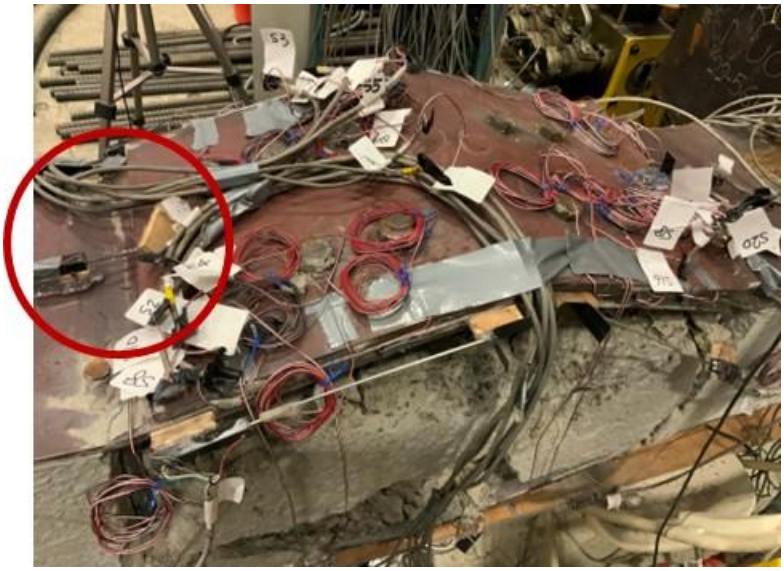


Figure 4-106. Linear Pots Shifted due to the Buckling of the Splice Plates

After completion of the test, it was found that all of the Shuriken connectors on the back side of the plates were in good condition (i.e., none of the Shuriken corner tack welds had failed), as shown in Figure 4-107.



Figure 4-107. Shuriken Connectors after Test

4.2.6 Specimen T6

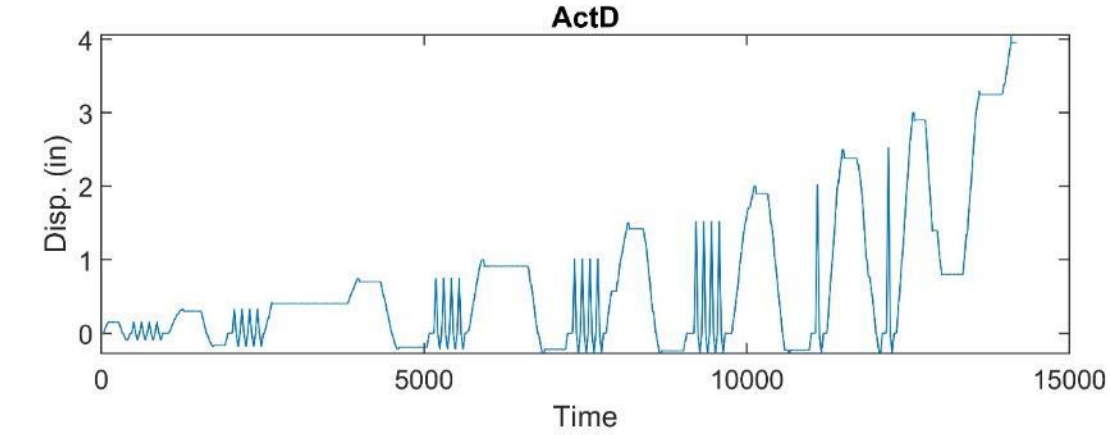
The testing of Specimen T6 started on 1/20/2022, following the loading procedure outlined in Table 4-8. The average actuator displacement and resulting load history for the experiment can be observed in Figure 4-108. To further support the descriptions, a series of photographs illustrating the splice region from the north perspective of Specimen T6 at different displacement amplitudes are presented in Figures 4-109 to 4-111. Table 4-11 provides an overview of the development of the maximum gross section and net section strains developed during each step of the test. Note that during or after Step 6, most strain gages recorded significantly large values due to the buckling on the faceplates in Step 5.

Table 4-10. Modified Loading Protocol for T6

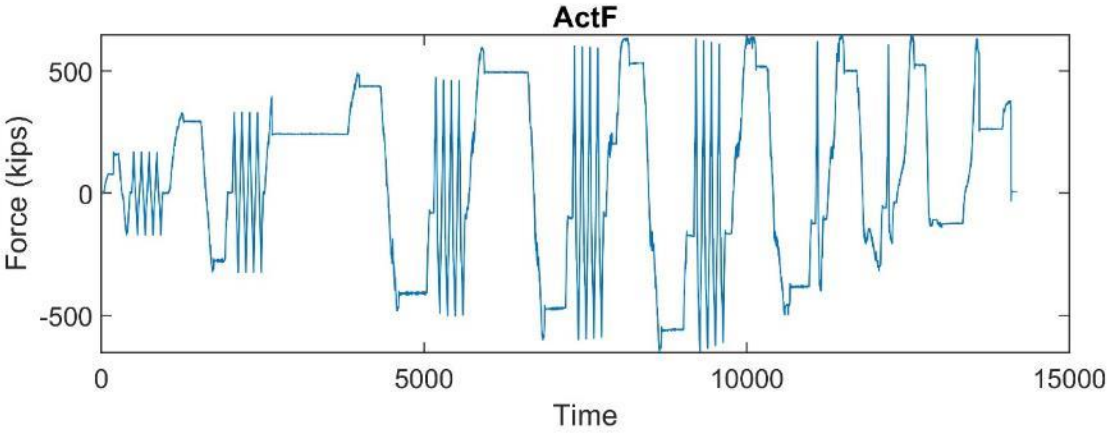
Step	Disp. (in) +	Disp. (in) -	Force (kips) +	Force (kips) -	Cycles	Note 1	Note 2
0	0.00	0	0	0	-		
1	0.15	0.095	163	163	5	0.25Pw	
2	0.33	0.18	325	325	5	0.5Pw	
3	0.74	0.215	488	488	5	0.75Pw	Conn. Slip
4	1.00	0.27	600	600	5	0.92Pw	AeFy
5	1.50	0.27	635	650	5	1.0Pw	AgFy
6	2.00	0.27	640	500	2		
7	2.50	0.27	645	319	2		
8	3.00	-	650	140	1		
9	3.30	-	635	-	-		Failure
10	4.00	-	-	-	-		Final

Table 4-11. Development of Gross Section and Net Section Strains for T6

Step	Min. ε_{Gross} (με)	Max. ε_{Gross} (με)	Min. ε_{Net} (με)	Max. ε_{Net} (με)	Min. ε_{Gross} (%εy)	Max. ε_{Gross} (%ε_y)	Min. ε_{Net} (%εy)	Max. ε_{Net} (%εy)
0	0	0	0	0	0	0	0	0
1	-322	483	-263	440	-15%	22%	-12%	20%
2	-542	1072	-467	822	-25%	49%	-22%	38%
3	-1025	1807	-920	1117	-47%	83%	-42%	51%
4	-1027	2387	-857	2210	-47%	110%	-39%	102%
5	-1473	2468	-273	4773	-68%	114%	-13%	220%
6	-1340	21780	115	21749	-62%	1003%	5%	1001%
7	-594	21974	294	21749	-27%	1012%	14%	1001%
8	-21974	21974	368	22084	-1012%	1012%	17%	1017%
9	-21974	21974	368	22084	-1012%	1012%	17%	1017%



(a) Average Displacement History



(b) Resulting Load History

Figure 4-108. Actuator Displacement and Load History for Specimen T6

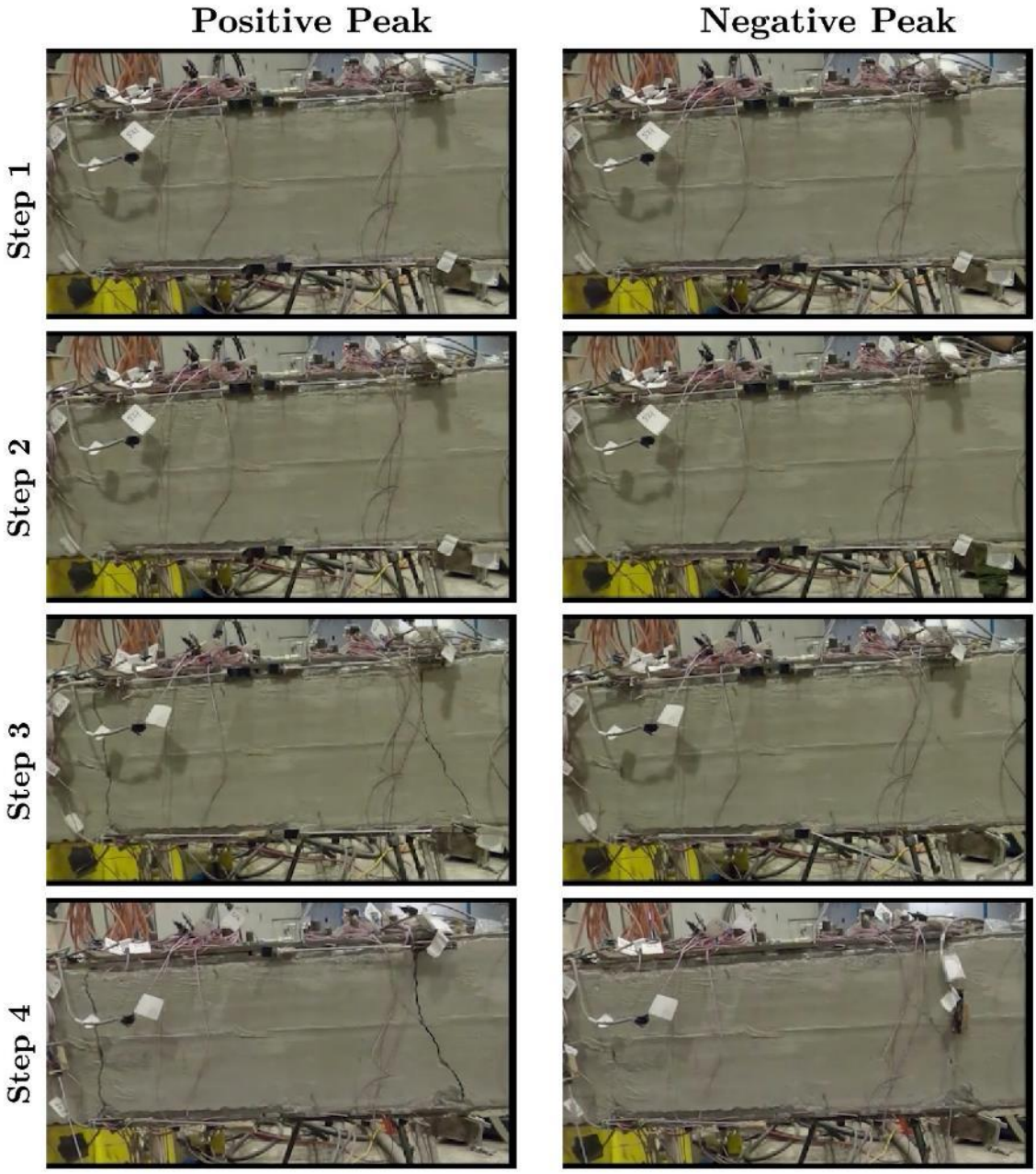


Figure 4-109. North View of Specimen T6 (Steps 1 to 4)

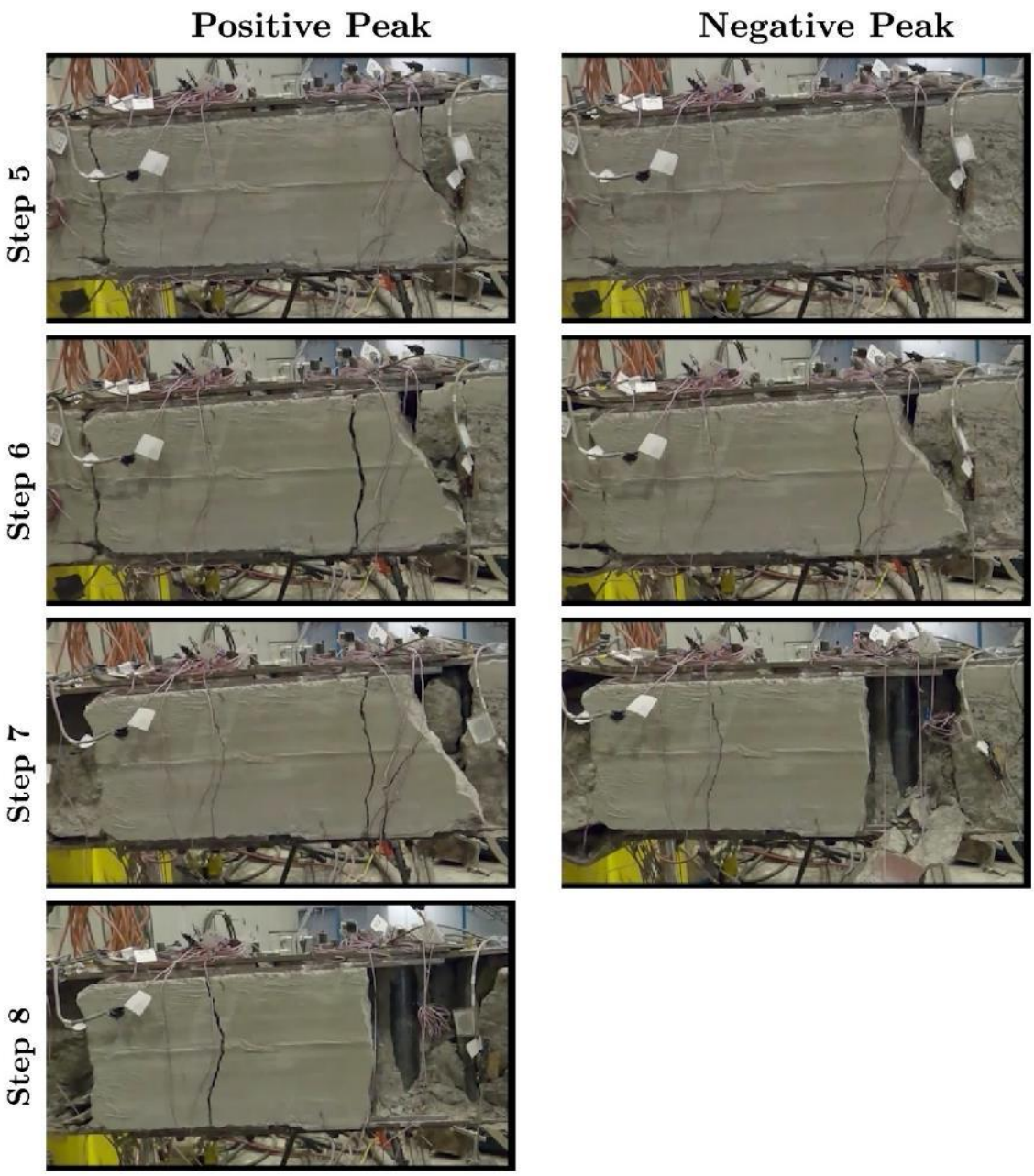


Figure 4-110. North View of Specimen T6 (Steps 5 to 8)



Figure 4-111. North View of Specimen T6 (Steps 9 to 10)

The test started with loads applied in displacement control. Figure 4-112 shows the south and north view after completing 5 loading cycles in Step 1 (0.25 P_w) and Step 2(0.5 P_w). The figure displays the condition of the connection in Step 2. Several tiny vertical cracks appeared on the south and north concrete surfaces at this point.



(a) South View (b) North View

Figure 4-112. Specimen T6 (Step 2, Peak Actuator Displacement=0.325")

The test then proceeded to Step 3 ($0.75P_w$). When the load reached 400 kips in tension, a loud "bang" was heard due to beginning of sliding between the plates in the connection. Figure 4-113 provides the force-deformation curve, on which can be seen the point when this first sliding occurred. In Figure 4-114, vertical cracks at both ends of the splice plate can be clearly observed.

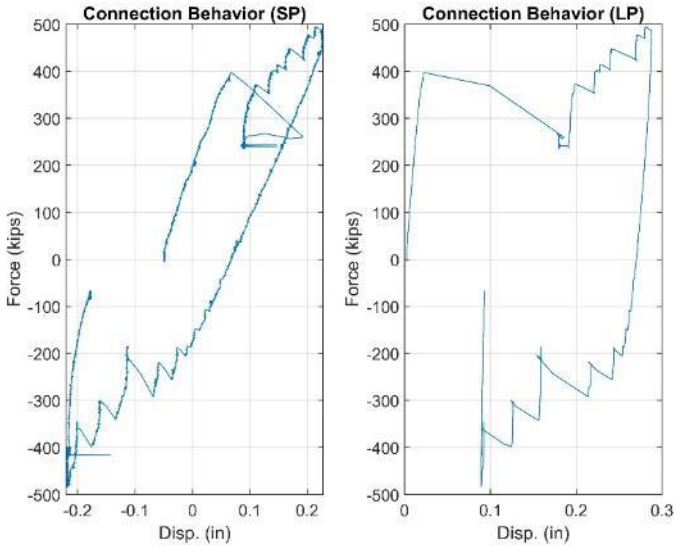
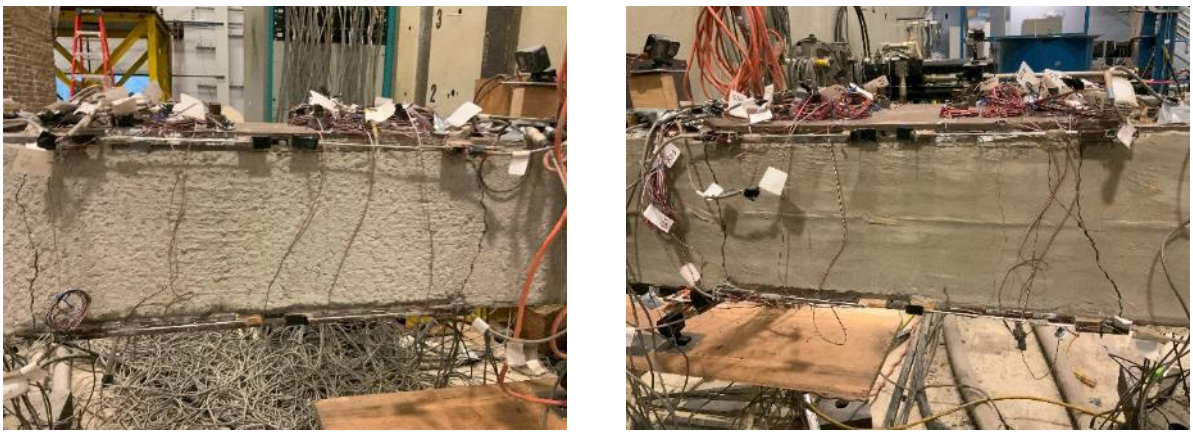


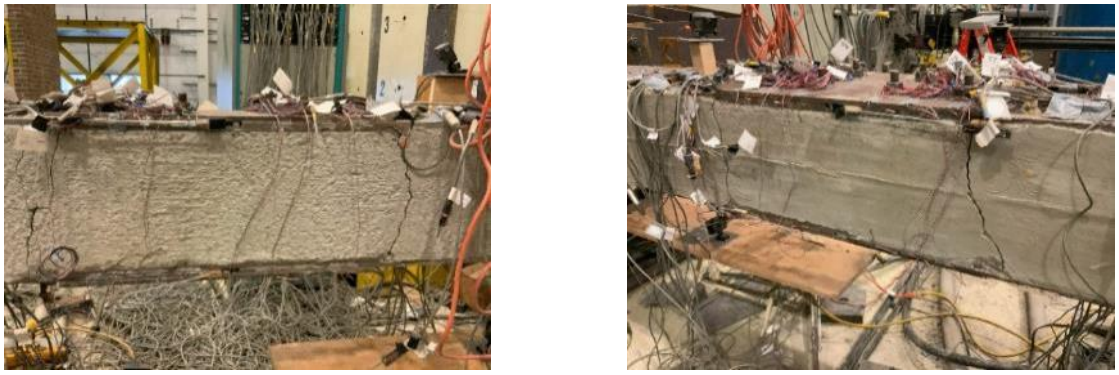
Figure 4-113. First Sliding of Specimen T6 (Step 3)



(a) South View (b) North View

Figure 4-114. Specimen T6 (Step 3, Peak Actuator Displacement=0.74")

In Steps 4 and 5, the applied tensile load was increased to 600 kips and 635 kips, respectively, resulting in the crack pattern observed on the connection shown in Figures 115 and 116. Additional cracks were observed on both the south and north surfaces, and a section of concrete on the northwest side detached from the surface. Note that when the actuator moved in the negative direction in Step 5, a slight buckling of the top faceplate was observed on the faceplate outside of the splice region, as illustrated in Figure 4-117. Note that at that location, the spacing of the ties was 34.5 in. rather than the 11 in. used elsewhere, because it was planned that the restraining frame could serve that role in preventing plate buckling, which did not happen because the small gap between the top of the specimen and the restraining beam above it had not been filled with shims. Note that after this buckling was observed, at the peak of the next cycle in tension (with the buckle flattened out), steel shims were introduced there to roughly recreate the originally intended restraint and limit the occurrence of further bucking there, but as out-of-plane deformations of the faceplate had already been induced, local buckling occurred in front of the frame in subsequent cycles.



(a) South View (b) North View

Figure 4-115. Specimen T6 (Step 4, Peak Actuator Displacement=1.00”)



(a) South View



(b) North View

Figure 4-116. Specimen T6 (Step 5, Peak Actuator Displacement=1.50”)



(a) Northwest View 1



(b) Northwest View 2

Figure 4-117. Specimen T6 (Step 5, Close View of Local Buckling)

Figure 4-118 illustrates the progress of damage on both the south and north views observed during Step 6. Additionally, Figure 4-119 shows local buckling of the top and bottom faceplates when the actuators were moved in the negative direction. During Step 7, an increased number of concrete pieces fell off, and the tie-rods and pipe sleeves in the connection region became exposed, as shown in Figure 4-120. Figure 4-121 illustrates the more severe local buckling observed during Step 7.



(a) South View



(b) North View

Figure 4-118. Specimen T6 (Step 6, Peak Actuator Displacement=2.00”)



(a) South View



(b) North View

Figure 4-119. Specimen T6 (Step 6, Close View of Local Buckling)



(a) South View



(b) North View

Figure 4-120. Specimen T6 (Step 7, Peak Actuator Displacement=2.50”)



(a) Southwest View



(b) Southeast View

Figure 4-121. Specimen T6 (Step 7, Close View of Local Buckling)

In Step 8, several large chunks of concrete were observed to be almost dislodging from the specimen (Figure 4-122). Additionally, when the actuator displacement was reversed from 3.0 in. to 0.8 in., the entire connection portion moved downward (Figure 4-123) due to the formation of plastic hinges in the steel plates at both ends of the connection. To prevent further bending failure, undesirable in the tension test, it was decided to apply tension-only loading for further loading amplitudes.



(a) South View



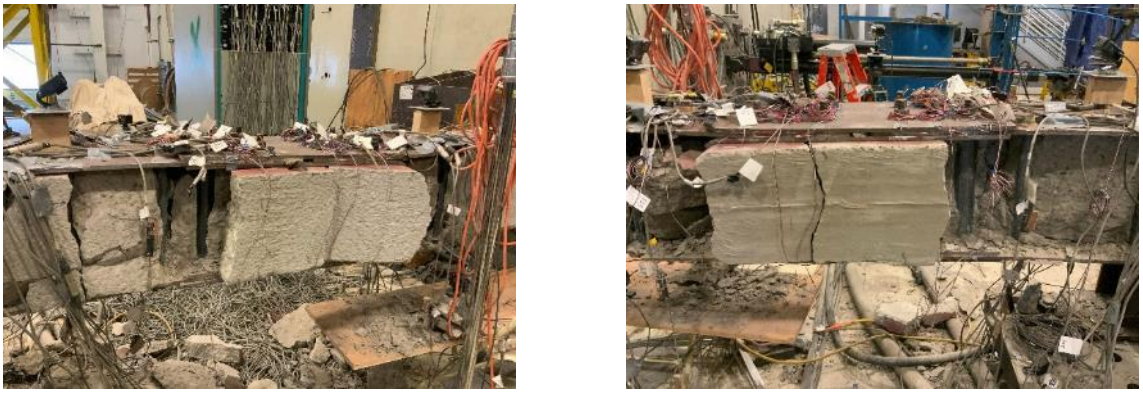
(b) North View

Figure 4-122. Specimen T6 (Step 8, Peak Actuator Displacement=3.00”)



Figure 4-123. Specimen T6 (Step 8, Actuator Displacement=0.80”)

During Step 9, a loud “bang” was heard when the applied actuator displacement was increased to 3.30 in. Figure 4-124 illustrates the condition of the connection at this stage, while Figure 4-125 displays the gross section fracture on the west bottom of the faceplate outside the splice region. After Step 9, the connection was further pulled to a 4.0 in. displacement in Step 10 (Final Step). This time, an abrupt and loud noise was heard, and it was discovered that the six rods on the east side of the connection had fractured. Figures 4-126 and 4-127 provide several views of the damage to the rods.



(a) South View (b) North View

Figure 4-124. Specimen T6 (Step 9, Peak Actuator Displacement=3.30”)



Figure 4-125. Specimen T6 (Step 9, Fracture on West Bottom Faceplate)



(a) South View



(b) South Top View

Figure 4-126. Specimen T6 (Step 10, Peak Actuator Displacement=4.00”)



Figure 4-127. Specimen T6 (Fractured Rods after Test)

After the test, the splice plates were removed to show the condition of the faceplates inside the connection region after the test. As can be seen in Figures 4-128 and 4-129, only a small amount of bearing deformation can be observed.



(a) South View



(b) South Top View

Figure 4-128. Specimen T6 (Top Faceplates in Splice Region after Test)



Figure 4-129. Specimen T6 (Bottom Faceplates in Splice Region after Test)

Figure 4-130 presents the results obtained using GR, SP, and LP. Figure 4-131 compares the hysteresis curves of SP and LP and illustrates the calculated strength for various design limit states. The figure also labels strengths corresponding to net section yielding and gross section yielding to demonstrate that yielding of the faceplates occurred during the test. During the test, the peak force before failure reached 650 kips, which was close to the calculated gross section yield strength of 661.5 kips. This further confirms that the connection underwent gross section yielding in tension, consistent with the expected behavior that governed that specimen's design. Note that the LP deformation in Figure 4-131 shifted by approximately 1 in. due to the movement of the linear pots during buckling of the faceplates. No adjustments have been made to the curves to compensate for this effect, as it can be visually accounted for. Figure 4-132 provides a comparison between specimens T5 and T6. The result shows that both connections have similar behavior. Both connections developed gross section yielding and failed in the gross section outside the connection. This failure occurred because of a combination of tension and bending, primarily due to buckling effects.

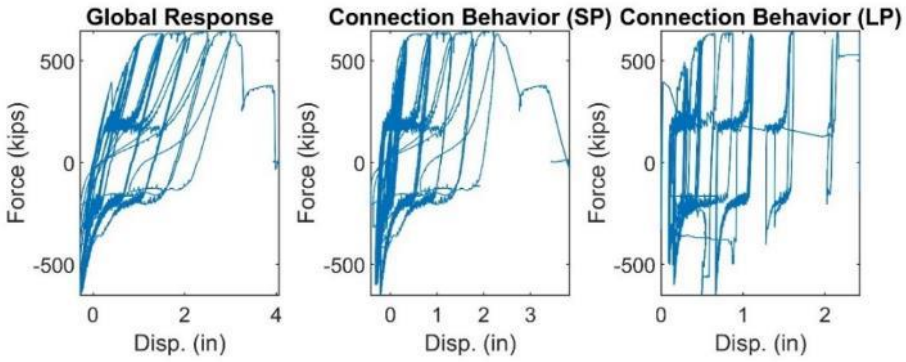


Figure 4-130. Test Results of Specimen T6

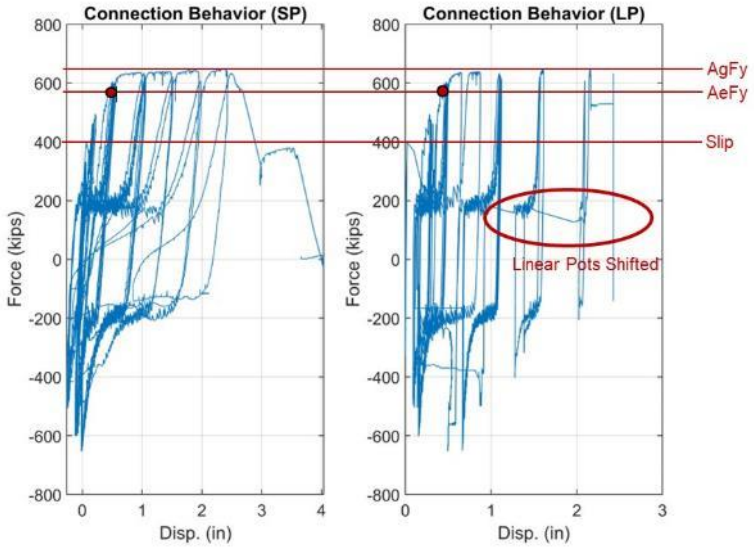


Figure 4-131. Test Results of Specimen T6 with Design Limit States

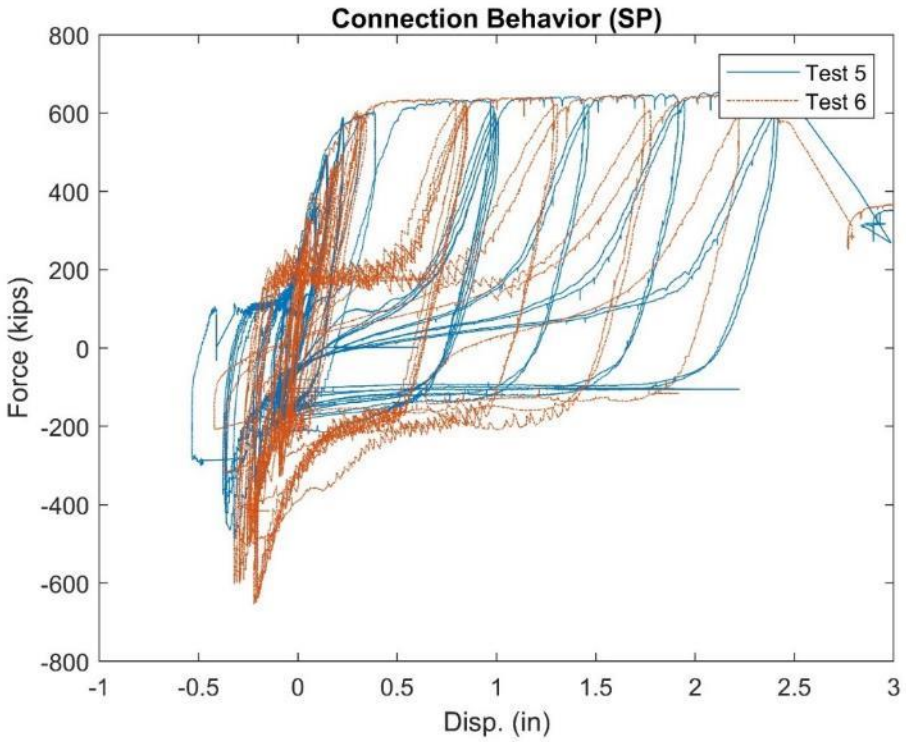


Figure 4-132. Comparison between Specimens T5 and T6

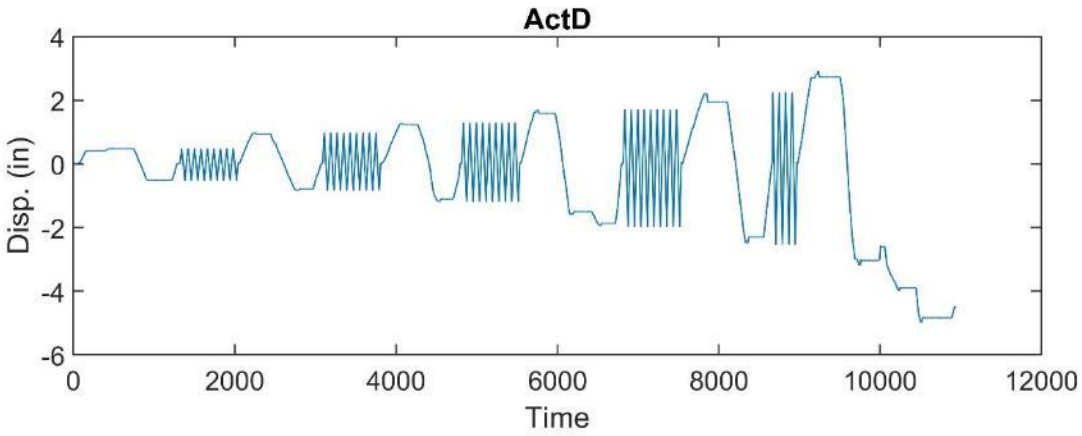
4.3 Test Observations and Results of Shear Specimens

4.3.1 Specimen S1

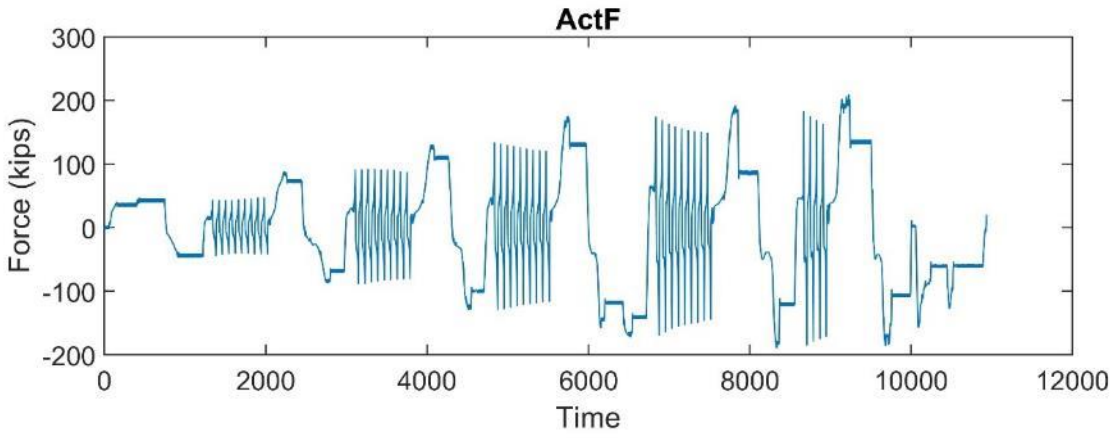
The testing of Specimen S1 started on 3/9/2023, following the loading procedure outlined in Table 4-12. The average actuator displacement and resulting load history for the experiment can be observed in Figure 4-133. Cycles up to $1.0P_w$ were applied to develop similar forces in both loading directions. Thereafter, loading was accomplished by increasing actuator displacement by an amount either equal to the increase observed in the previous step, or by approximately proportionally larger values in the positive and negative directions (also trying to balance the magnitude of positive and negative displacement increments whenever possible). Note that this approach was take for all shear specimens, and this clarification will therefore not be mentioned again, unless deviations from this scenario occurred in specific cases.

Table 4-12. Modified Loading Protocol for S1

Step	Disp. (in) +	Disp. (in) -	Force (kips) +	Force (kips) -	Cycles	Note 1	Note 2
0	0.00	0.00	0	0	-		
1	0.47	0.53	43	43	10	0.25Pw	
2	0.96	0.84	86	86	10	0.5Pw	
3	1.26	1.19	129	129	10	0.75Pw	
4	1.68	1.95	172	172	10	1.0Pw	
5	2.20	2.50	185	190	5		
6	2.90	3.20	209.7	184	-	Failure	
7	-	5.00	-	-	-	Final	



(a) Average Displacement History



(b) Resulting Load History

Figure 4-133. Actuator Displacement and Load History for Specimen S1

Figure 4-134 provides a definition for the term "north view" (and, implicitly, all other cardinal directions) used throughout this report to monitor the condition of the shear specimens, the progression of damage, and movements of parts of the connection throughout the entire test program for shear components.

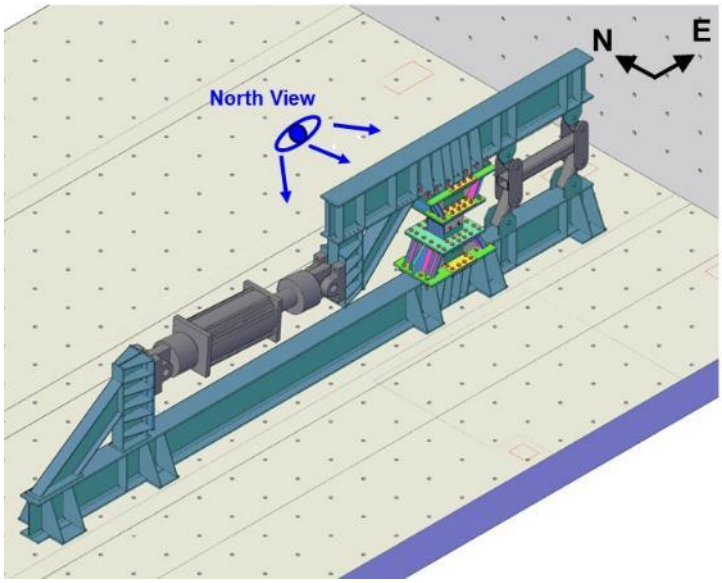
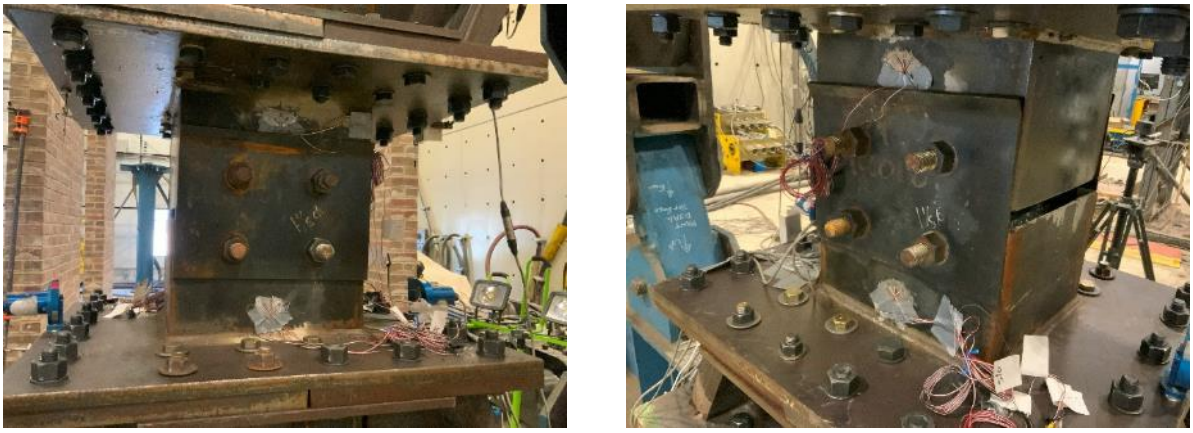


Figure 4-134. Demonstration of North View

Figure 4-135 illustrates the condition of the connection at the peak actuator displacement of Step 1 (0.25 P_w). During Step 1, the first occurrence of sliding between the splice plates and faceplates was observed, accompanied by a loud "bang" when the actuator moved towards the positive peak displacement, as depicted in Figure 4-136. The slippage caused slight rotation of the splice plate.



(a) South View (b) Northwest View

Figure 4-135. Specimen S1 (Step 1, Peak Actuator Displacement=0.47")

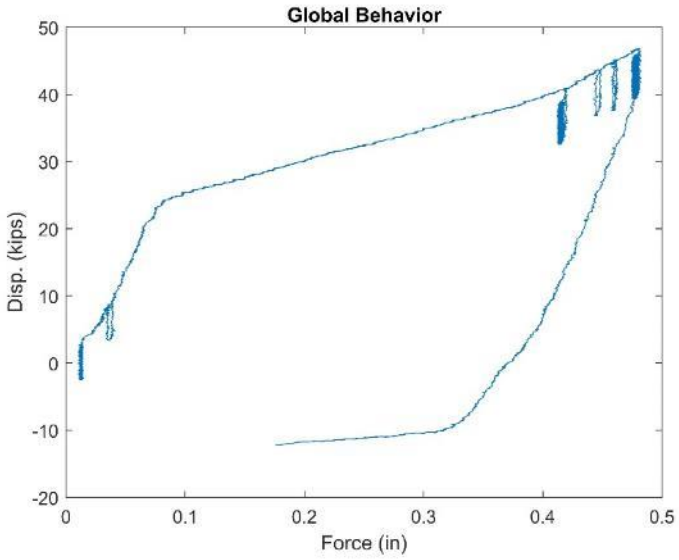


Figure 4-136. First Sliding of Specimen S1 (Step 1)

The test continued with applied actuator loads ranging from 86 to 172 kips in Steps 2 to 4 (0.5 to 1.0 Pw). Figures 4-137 to 4-140 display photos taken during these steps. Note that in Step 4, additional displacement was needed to achieve the target load in the negative direction compared to the positive direction. More severe rotation of the splice plates can be observed in subsequent steps.



(a) South View



(b) North View

Figure 4-137. Specimen S1 (Step 2, Peak Actuator Displacement=0.96”)



(a) South View



(b) North View

Figure 4-138. Specimen S1 (Step 3, Peak Actuator Displacement=1.26”)



(a) South View



(b) North View

Figure 4-139. Specimen S1 (Step 4, Peak Actuator Displacement=1.68")



(a) South View



(b) North View

Figure 4-140. Specimen S1 (Step 4, Peak Actuator Displacement=-1.95")

After the specimen reached the target load (1.0 P_w), the test continued to Step 5. The applied forces in the positive and negative direction reached 185 and -195 kips, respectively. Figures 4-141 and 4-142 show the rotation of splice plates in this step, and noticeable vertical displacement of the rods from their initial position can be observed as highlighted in 4-142 (b).



(a) South View

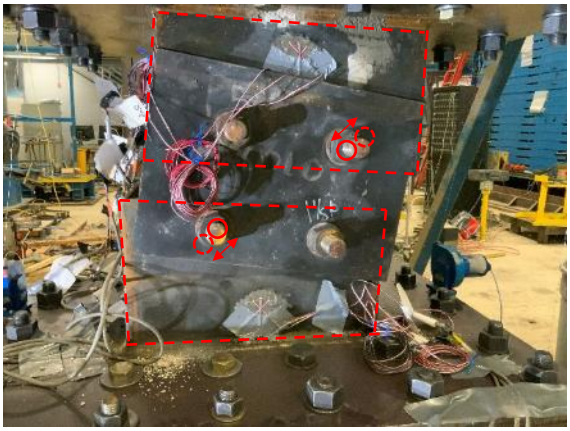


(b) North View

Figure 4-141. Specimen S1 (Step 5, Peak Actuator Displacement=2.20”)



(a) South View



(b) North View

Figure 4-142. Specimen S1 (Step 5, Peak Actuator Displacement=-2.50”)

Then the test proceeded with Step 6, where the applied forces reached 209.7 and -184 kips in the positive and negative direction, respectively. When the actuator was at the negative peak, a load "bang" was heard, and the force dropped abruptly due to the failure of the connection. Figures 4-143 and 4-144 depict the condition at this point. Following this step, the specimen was further pulled up to a -5.0 in. displacement in Step 7, leading to clear tear-out damage. Figure 4-145 provides the condition of tear-out damage at this final step. Figure 4-146 shows photos taken from the north and south views after the splice plates were removed.



(a) South View

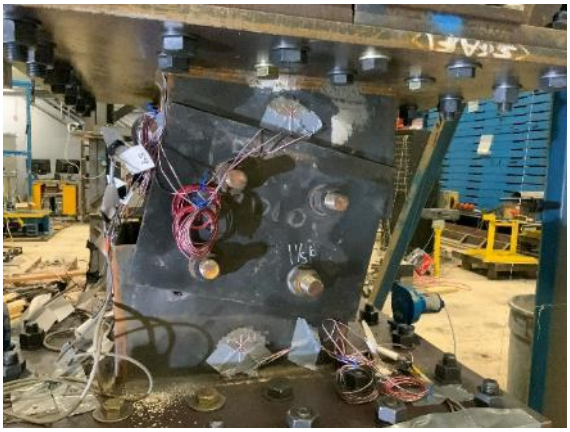


(b) North View

Figure 4-143. Specimen S1 (Step 6, Peak Actuator Displacement=2.90")



(a) South View



(b) North View

Figure 4-144. Specimen S1 (Step 6, Peak Actuator Displacement=-3.20")



(a) South View



(b) North View

Figure 4-145. Specimen S1 (Step 7, Peak Actuator Displacement=-5.00”)



(a) South View



(b) North View

Figure 4-146. Specimen S1 (After Test)

Figure 4-147 compares the hysteresis curves of global response and link behavior, along with design limit states. The link behavior refers to the shear force versus shear deformation of the specimen over its free length. The figure includes markings for the bearing strengths at $2.4dtF_u$ and $3.0dtF_u$, considering combined shear force and torsion. Additionally, the bearing strength at $2.4dtF_u$ specifically considering only shear force is also marked. These markings allow for a comparison between the theoretical design values and the actual test results. Results indicate that the target bearing strength limit state was reached and exceeded, and the specimen finally failed by bearing considering eccentricity.

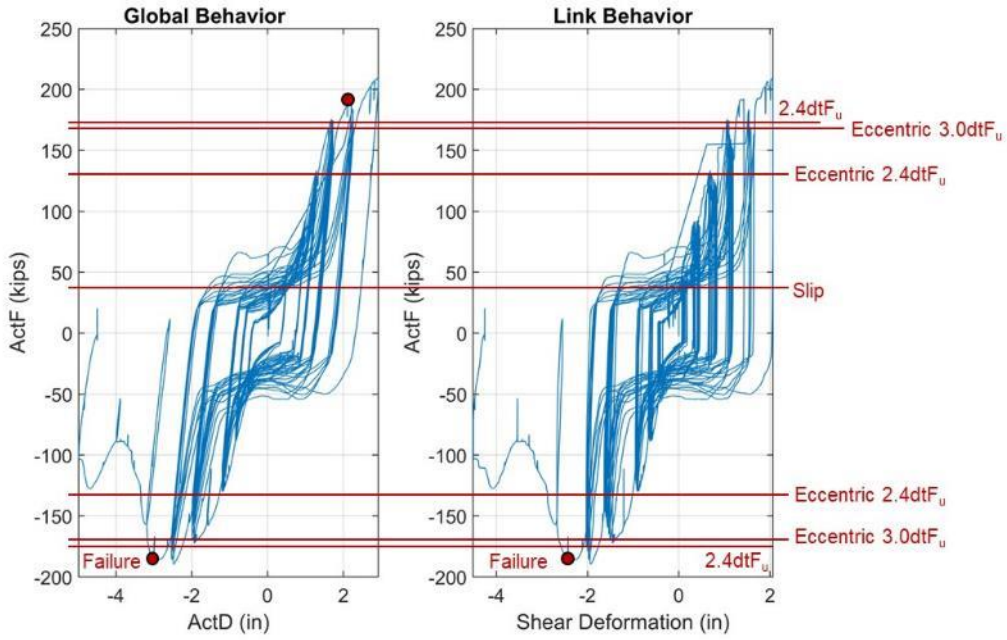


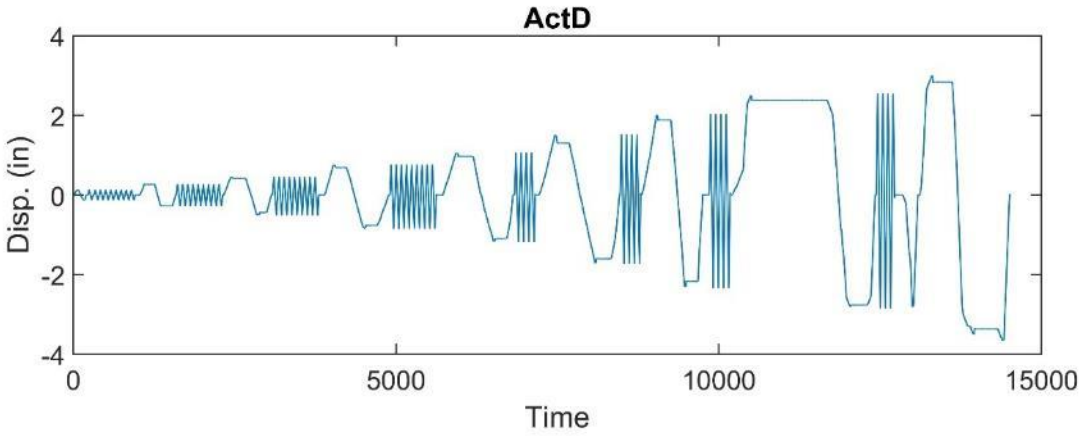
Figure 4-147. Test Results of Specimen S1 with Design Limit States

4.3.2 Specimen S2

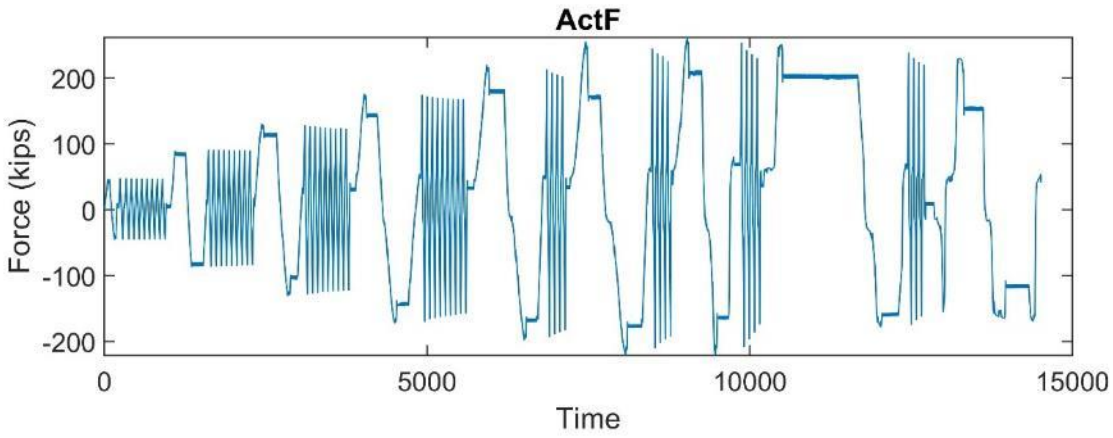
The testing of Specimen S2 started on 4/4/2023, following the loading procedure outlined in Table 4-13. The average actuator displacement and resulting load history for the experiment can be observed in Figure 4-148.

Table 4-13. Modified Loading Protocol for S2

Step	Disp. (in) +	Disp. (in) -	Force (kips) +	Force (kips) -	Cycles	Note 1	Note 2
0	0.00	0.00	0	0	-		
1	0.12	0.13	43	43	10	0.25Pw	
2	0.27	0.28	86	86	10	0.5Pw	
3	0.45	0.50	129	129	10	0.75Pw	
4	0.75	0.83	172	172	10	1.0Pw	
5	1.05	1.16	219	199	5		
6	1.50	1.70	255	222	5		
7	2.00	2.30	251	220	5		
8	2.50	2.80	251	175	4		
9	3.00	3.30	216	160	1	Failure	



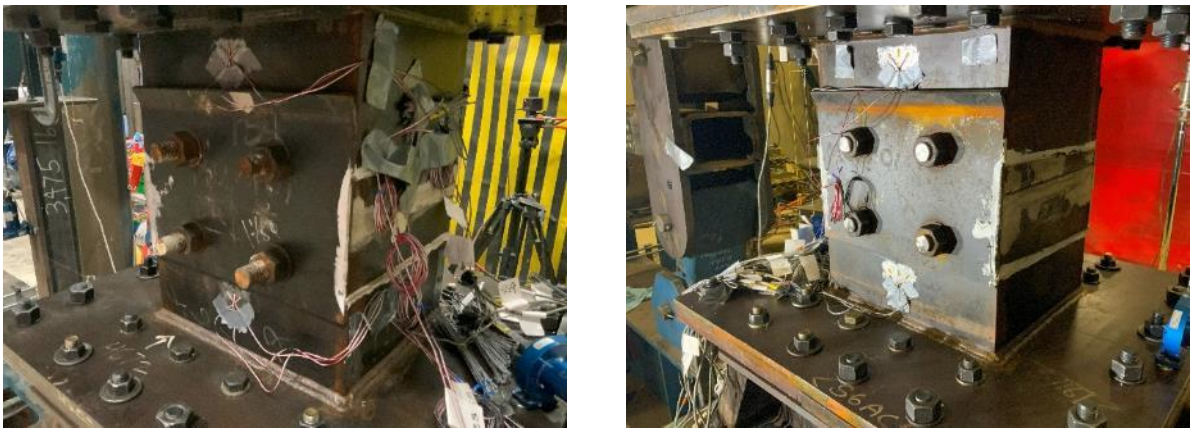
(a) Average Displacement History



(b) Resulting Load History

Figure 4-148. Actuator Displacement and Load History for Specimen S2

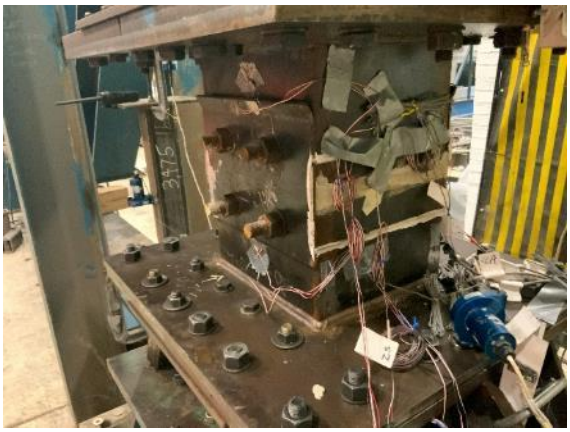
After completing 10 loading cycles in Steps 1 and 2, the actuator reached 0.25 and 0.50 P_w. Figure 4-149 provides a southeast and northwest views in Step 2, and there was no visible damage of concrete surface observed in this step.



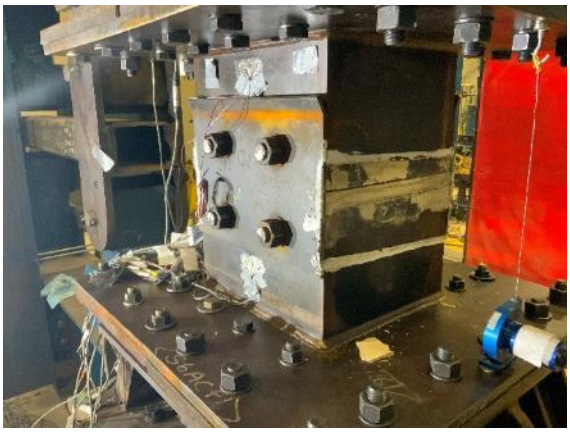
(a) Southeast View (b) Northwest View

Figure 4-149. Specimen S2 (Step 2, Peak Actuator Displacement=0.27")

During Steps 3 to 4 of the experiment, the applied force increased to 0.75Pw and 1.00Pw, respectively. Similarly, there was no visible concrete damage observed during this stage as shown in Figures 4-150 and 4-151.



(a) Southeast View

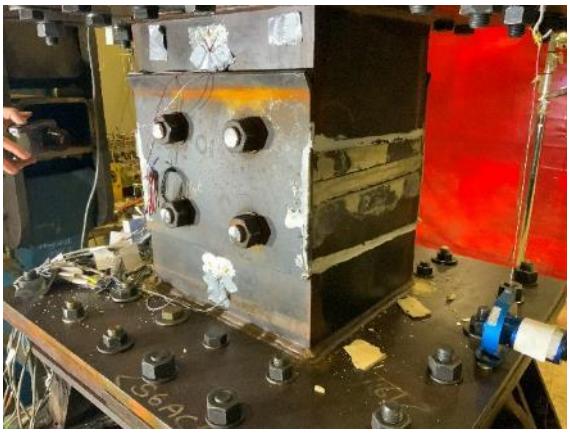


(b) Northwest View

Figure 4-150. Specimen S2 (Step 3, Peak Actuator Displacement=0.45")



(a) Southeast View



(b) Northwest View

Figure 4-151. Specimen S2 (Step 4, Peak Actuator Displacement=0.75")

Figures 4-152 to 4-154 provide a southeast and northwest view of the specimen during Steps 5 to 6. In Step 6, the applied force reached 255 and -222 kips in the positive and negative direction, respectively. Notably, during these steps, several pieces of concrete between the cap plates detached and fell off.



(a) Southeast View



(b) Northwest View

Figure 4-152. Specimen S2 (Step 5, Peak Actuator Displacement=1.05”)



(a) Southeast View



(b) Northwest View

Figure 4-153. Specimen S2 (Step 6, Peak Actuator Displacement=1.50”)



(a) Southeast View



(b) Northwest View

Figure 4-154. Specimen S2 (Step 6, Peak Actuator Displacement=-1.70”)

In Step 7, the applied forces reached 251 and -220 kips in the positive and negative direction, respectively. The applied forces were slightly lower than in the previous step, meaning that the shear strength had plateaued. Figures 4-155 to 4-157 shows the rotation of splice plates and the concrete damage in this step. The connection damage became more severe, and the rotation of splice plate became quite noticeable at this point.



(a) Southeast View



(b) Northwest View

Figure 4-155. Specimen S2 (Step 7, Peak Actuator Displacement=2.00”)



(a) Southeast View



(b) Northwest View

Figure 4-156. Specimen S2 (Step 7, Peak Actuator Displacement=-2.30”)



(a) South View



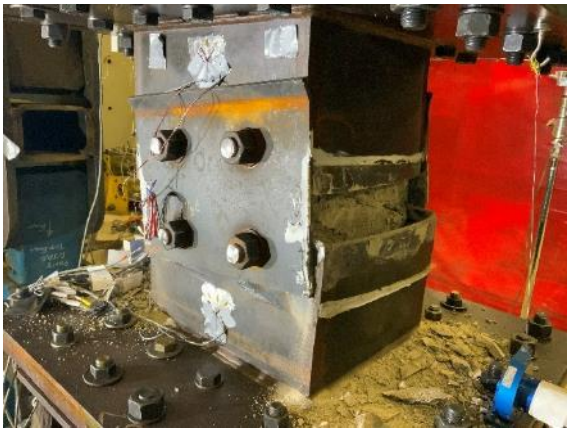
(b) North View

Figure 4-157. Specimen S2 (Step 7, Peak Actuator Displacement=-2.30”)

In Step 8, the applied force reached 251 and -175 kips in the positive and negative direction, respectively. Note that the shear strength in the negative direction experienced a decrease of approximately 45 kips compared to the previous step, which shear strength was sustained in the positive direction. Figures 4-158 to 4-160 show the movements occurring between the top and bottom walls. Notably, in this step, the cap plates exhibited a noticeable outward bending.



(a) Southeast View



(b) Northwest View

Figure 4-158. Specimen S2 (Step 8, Peak Actuator Displacement=2.50”)



(a) Southeast View

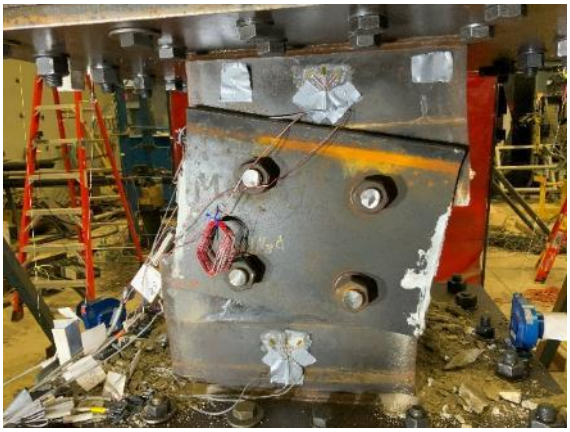


(b) Northwest View

Figure 4-159. Specimen S2 (Step 8, Peak Actuator Displacement=-2.80”)



(a) South View



(b) North View

Figure 4-160. Specimen S2 (Step 8, Peak Actuator Displacement=-2.80”)

In Step 9, the applied force reached 216 and -160 kips in the positive and negative direction, respectively, corresponding to drops of 39 and 62 kips in the positive and negative direction compared to the peak strength. Figures 4-161 to 4-163 illustrate the condition of the connection at this step. Furthermore, the figures from the south and north views reveal that the rods had torn out of the faceplates. At this point, it was decided to terminate the test and return the actuator back to zero displacement. After the test, the splice plates were removed and Figure 4-164 shows the failure mechanism from the south and north views.



(a) Southeast View



(b) Northwest View

Figure 4-161. Specimen S2 (Step 9, Peak Actuator Displacement=3.00”)



(a) Southeast View



(b) Northwest View

Figure 4-162. Specimen S2 (Step 9, Peak Actuator Displacement=-3.30”)



(a) South View



(b) North View

Figure 4-163. Specimen S2 (Step 9, Peak Actuator Displacement=-3.30”)



(a) South View (b) North View

Figure 4-164. Specimen S2 (After Test)

Figure 4-165 compares the hysteresis curves of global response and link behavior, along with design limit states. The figure also labels strengths corresponding to bearing strength considering pure shear force, combined shear and eccentric forces, and net section shear yielding strength. Results indicate that the target bearing strength limit state was reached and exceeded, and that the connection developed its shear yielding strength in the positive direction. Figure 4-166 provides a comparison between Specimens S1 and S2 to illustrate the difference between non-composite and composite wall connection. The composite section was initially stiffer and reached peak force with significantly less sliding. The peak force increased 45.3 and 32 kips in Specimen S2 compared to Specimen S1. The peak strength of S2 was also sustained over a range of deformations, whereas that of S1 progressively increased with larger deformations up to failure, However, at large deformations, the strength of S2 progressively degraded to approach that of S1 before failure.

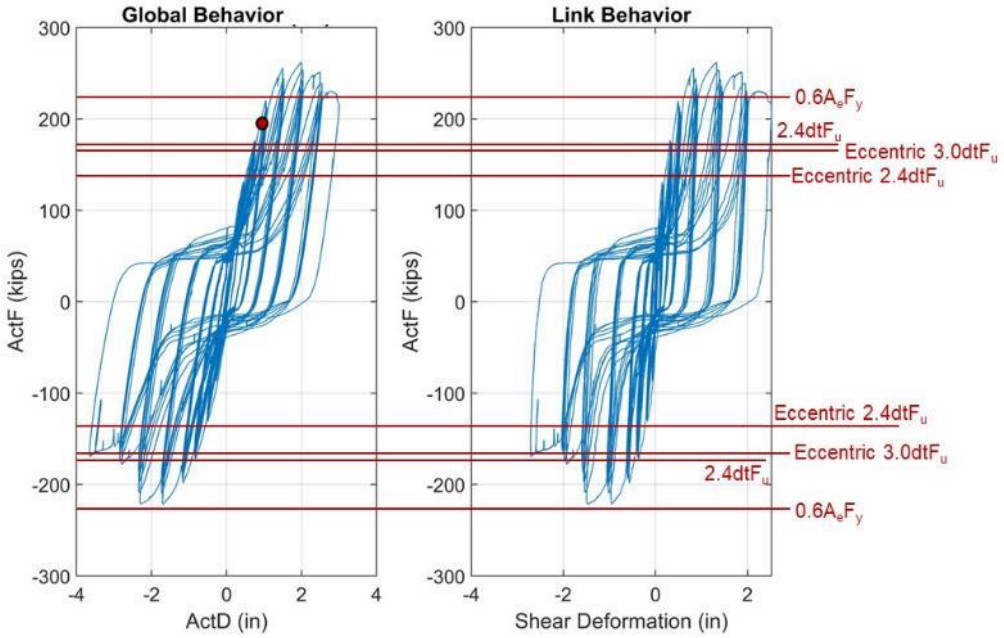


Figure 4-165. Test Results of Specimen S2 with Design Limit States

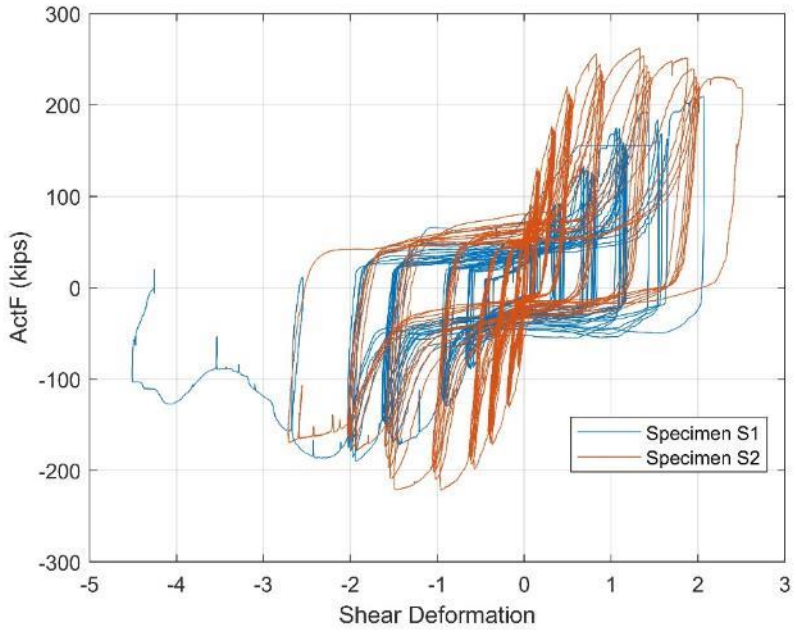


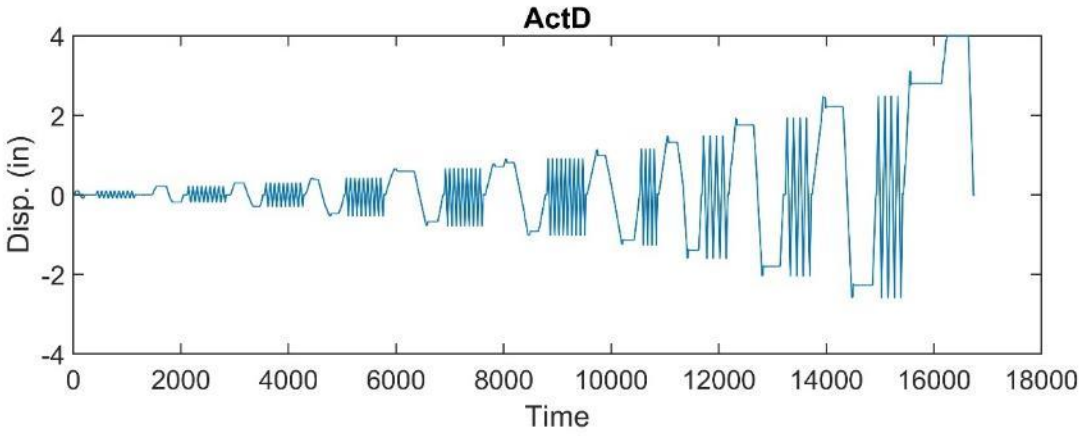
Figure 4-166. Test Results of Specimens S1 and S2

4.3.3 Specimen S3

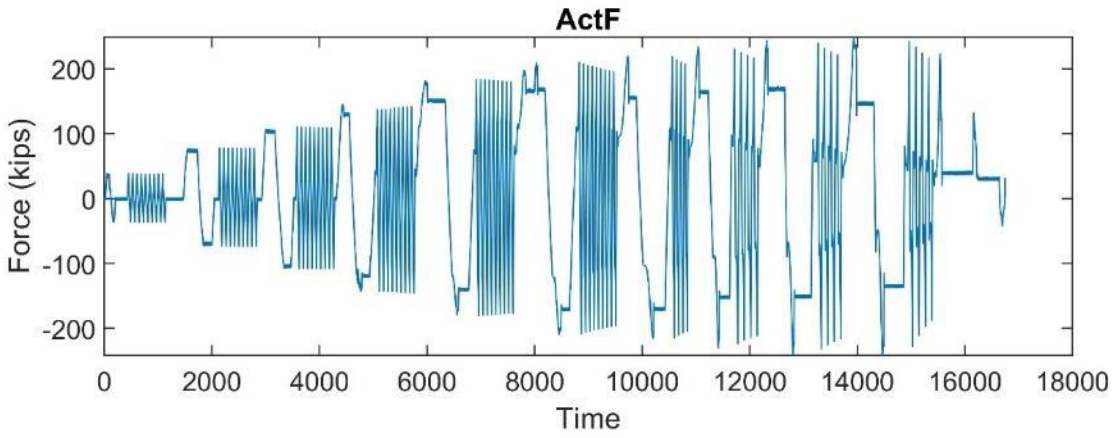
The testing of Specimen S3 started on 4/13/2023, following the loading procedure outlined in Table 4-14. The average actuator displacement and resulting load history for the experiment can be observed in Figure 4-167.

Table 4-14. Modified Loading Protocol for S3

Step	Disp. (in) +	Disp. (in) -	Force (kips) +	Force (kips) -	Cycles	Note 1	Note 2
0	0.00	0.00	0	0	-		
1	0.11	0.08	36	36	10	0.25Pw	
2	0.21	0.19	72	72	10	0.5Pw	
3	0.30	0.29	107	107	10	0.75Pw	
4	0.42	0.53	143	143	10	1.0Pw	Slip-Critical
5	0.66	0.77	182	180	10		
6	0.90	1.01	211	210	10	2.4dtFu	
7	1.14	1.25	220	216	5		
8	1.48	1.59	234	231	5	0.6AgFy	
9	1.92	2.03	244	240	5	0.6AeFu	
10	2.46	2.57	249	242	5		
11	2.70	-	224	-	-	Failure	
12	4.00	-	-	-	-	Final	



(a) Average Displacement History



(b) Resulting Load History

Figure 4-167. Actuator Displacement and Load History for Specimen S3

The test started with 10 loading cycles in each of Steps 1 to 3, and the applied forces increased from 0.25 to 0.75 P_w. Figures 4-168 to 4-170 provide southeast and northwest views in these steps. No sliding between plates was observed during these steps.



(a) Southeast View

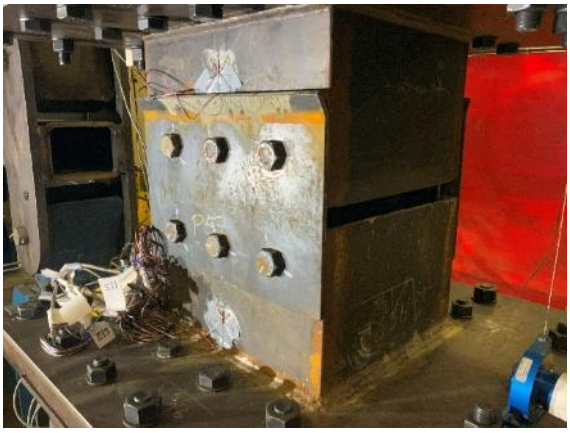


(b) Northwest View

Figure 4-168. Specimen S3 (Step 1, Peak Actuator Displacement=0.11")



(a) Southeast View



(b) Northwest View

Figure 4-169. Specimen S3 (Step 2, Peak Actuator Displacement=0.21”)



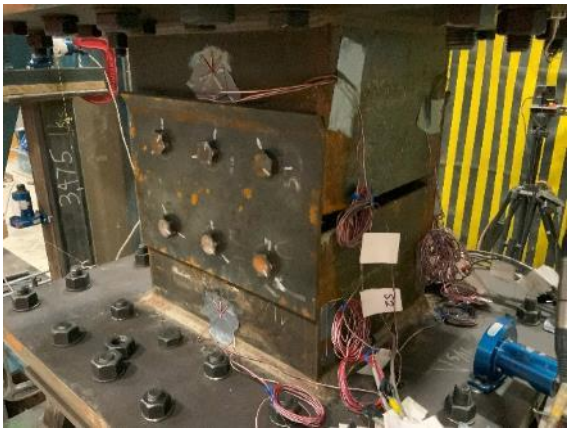
(a) Southeast View



(b) Northwest View

Figure 4-170. Specimen S3 (Step 3, Peak Actuator Displacement=0.30”)

During Step 4, the applied forces increased to 1.00 P_w. Figures 4-171 and 4-172 show the condition of the specimen at peak deformations in the positive and negative directions. When the actuator moved toward negative direction, a loud “band” was heard due to the sliding between splice plates and faceplates. The load-displacement curve in Figure 4-173 shows when this slippage occurred. The peak force before sliding was -144 kips, which was close to the hand-calculated slip-critical resistance of -141.53 kips.



(a) Southeast View



(b) Northwest View

Figure 4-171. Specimen S3 (Step 4, Peak Actuator Displacement=0.42”)



(a) Southeast View



(b) Northwest View

Figure 4-172. Specimen S3 (Step 4, Peak Actuator Displacement=-0.53”)

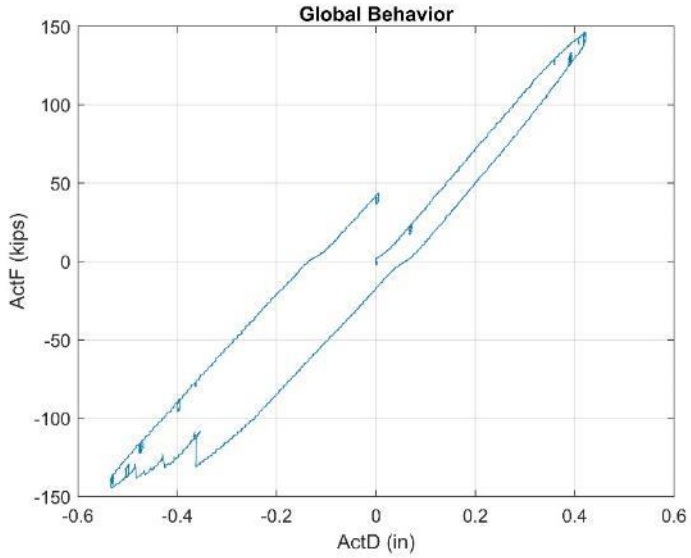


Figure 4-173. First Sliding of Specimen S3 (Step 4) (-144 k)

The test progressed through Steps 5 to 8, with the applied forces increasing from 182 to 234 kips. Figures 4-174 to 4-179 show the condition of the specimen during these steps. Rotation of splice plates became noticeable and progressively more severe through these successive steps.



(a) Southeast View



(b) Northwest View

Figure 4-174. Specimen S3 (Step 5, Peak Actuator Displacement=0.66”)



(a) Southeast View



(b) Northwest View

Figure 4-175. Specimen S3 (Step 6, Peak Actuator Displacement=0.90”)



(a) Southeast View



(b) Northwest View

Figure 4-176. Specimen S3 (Step 7, Peak Actuator Displacement=1.14”)



(a) South View



(b) North View

Figure 4-177. Specimen S3 (Step 8, Peak Actuator Displacement=1.48”)



(c) Southeast View



(d) Northwest View

Figure 4-178. Specimen S3 (Step 8, Peak Actuator Displacement=1.48”)



(a) Southeast View



(b) Northwest View

Figure 4-179. Specimen S3 (Step 8, Peak Actuator Displacement=-1.59”)

Figures 4-180 to 4-185 show the specimen during Steps 9 and 10. Following Step 10, the applied forces reached the peak values of 249 and -242 kips in the positive and negative directions, respectively. Again, the figures show the increasing amplitude of plate rotations through the steps, with noticeable movement in the corner bolts indicating the development of bearing deformations in the faceplates.



(a) Southeast View



(b) Northwest View

Figure 4-180. Specimen S3 (Step 9, Peak Actuator Displacement=1.92”)



(a) Southeast View



(b) Northwest View

Figure 4-181. Specimen S3 (Step 9, Peak Actuator Displacement=-2.03”)



(a) South View



(b) North View

Figure 4-182. Specimen S3 (Step 9, Peak Actuator Displacement=-2.03”)



(a) South View



(b) North View

Figure 4-183. Specimen S3 (Step 10, Peak Actuator Displacement=2.46”)



(a) Southeast View



(b) Northwest View

Figure 4-184. Specimen S3 (Step 10, Peak Actuator Displacement=2.46”)



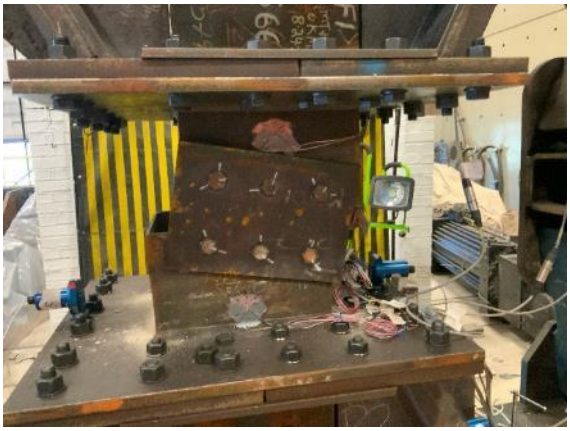
(c) Southeast View



(d) North View

Figure 4-185. Specimen S3 (Step 10, Peak Actuator Displacement=-2.57”)

During Step 11, the applied displacement reached 3.1 in. in the positive direction. Note that the force experienced a sudden drop when the load reached 224 kips and the displacement reached 2.7 in. Figures 4-186 and 4-187 provide views of the connection from south and north. Notably, in Figure 4-188, a fracture on the north bottom faceplate can be observed (looking between the splice plates, which makes it hard to see).



(a) South View



(b) North View

Figure 4-186. Specimen S3 (Step 11, Peak Actuator Displacement=3.1")



(a) Southeast View



(b) Northwest View

Figure 4-187. Specimen S3 (Step 11, Peak Actuator Displacement=3.1")



Figure 4-188. Fracture of North Bottom Faceplate (Step 11)

In Step 12 (Final Step), the applied displacement was increased to 4.0 in. During this step, excessive bolt movements became even more severe, as depicted in Figure 4-189. Figure 4-190 shows the fracture of bottom faceplates between splice plates as highlighted in the figure. After the test, the splice plates were removed, and the damage shown in Figure 4-191provides information on the failure mechanism of the specimen. The top faceplates exhibit severe bearing deformations, while the bottom plates show a combined failure mechanism involving bearing failure and net section fracture.



(a) South View



(b) North View

Figure 4-189. Specimen S3 (Step 12, Peak Actuator Displacement=4.0”)



Figure 4-190. Fracture of Bottom Faceplates (Step 12)



(a) Top Part



(b) Bottom Part

Figure 4-191. Specimen S3 (After Test")

Figure 4-192 compares the hysteresis curves of global response and link behavior, along with design limit states. The figure labels strengths corresponding to bearing strength considering only shear force, bearing strength considering combined shear and eccentric forces, as well as the net section shear yielding and net section rupture strength. Results indicate that the target limit state (net section shear yielding) was reached and exceeded, and that the connection developed its net section rupture strength in shear in the positive direction.

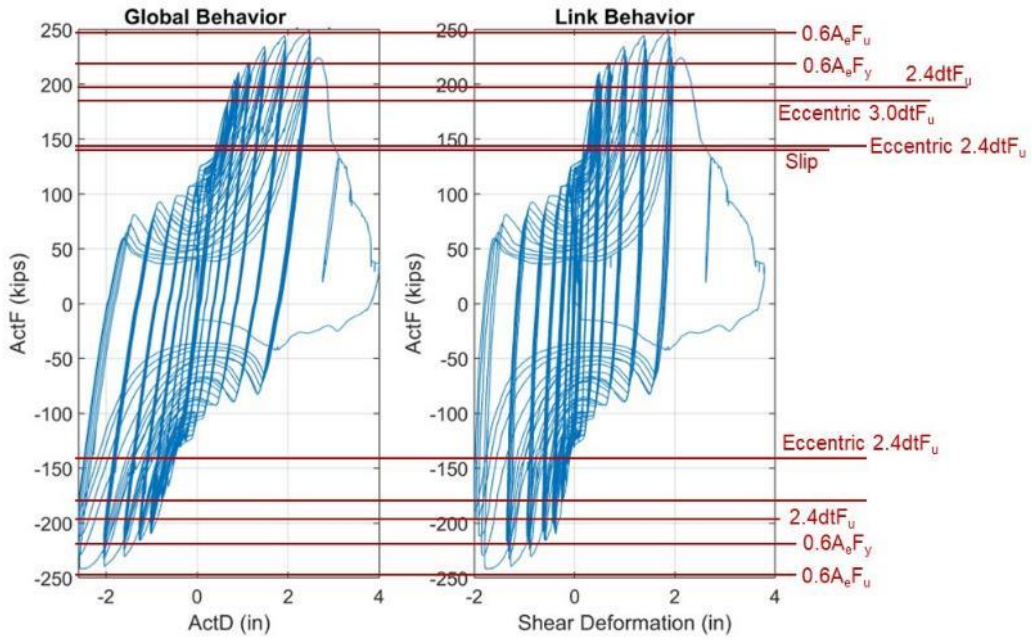


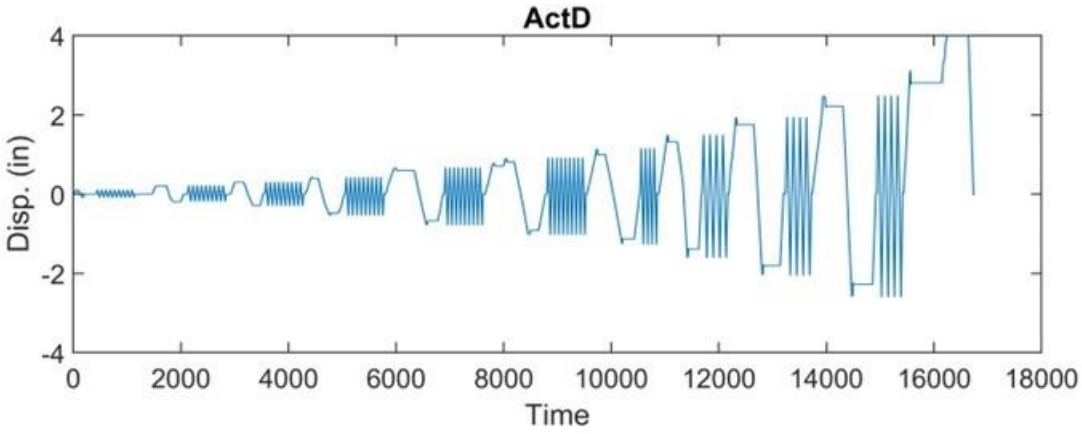
Figure 4-192. Test Results of Specimen S3 with Design Limit States

4.3.4 Specimen S4

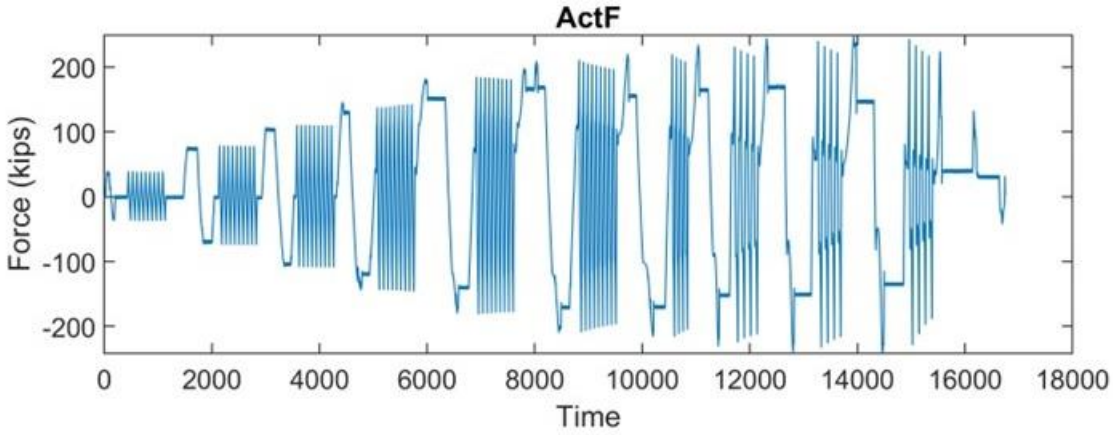
The testing of Specimen S4 started on 4/21/2023, following the loading procedure outlined in Table 4-14. The average actuator displacement and resulting load history for the experiment can be observed in Figure 4-167.

Table 4-15. Modified Loading Protocol for S4

Step	Disp. (in) +	Disp. (in) -	Force (kips) +	Force (kips) -	Cycles	Note 1	Note 2
0	0.00	0.00	0	0	-		
1	0.10	0.09	36	36	10	0.25Pw	
2	0.20	0.18	72	72	10	0.5Pw	
3	0.30	0.30	107	107	10	0.75Pw	
4	0.46	0.42	143	143	10	1.0Pw	Slip-Critical
5	0.69	0.68	188	188	10	AeFy	
6	0.92	0.94	247	236	10	0.6AeFu	
7	1.15	1.20	282	271	5		
8	1.48	1.56	313	300	5		
9	1.91	2.02	305	292	5		
10	2.44	2.58	276	246	4	Failure	



(a) Average Displacement History



(b) Resulting Load History

Figure 4-193. Actuator Displacement and Load History for Specimen S4

The test started with 10 loading cycles in each of Steps 1 to 4, and the applied forces increased from 0.25 to 1.00 P_w. Figure 4-194 shows the southeast and northwest views in Step 4. No sliding or damage of concrete were observed during these steps. The connection remained in a similar condition throughout Steps 5 and 6, as shown in Figures 4-195 and 4-196.



(a) Southeast View

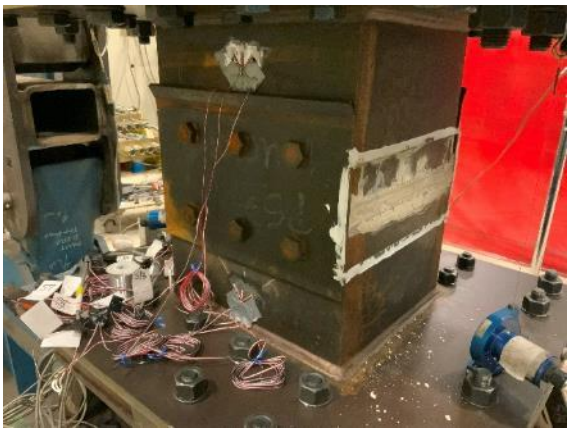


(b) Northwest View

Figure 4-194. Specimen S4 (Step 4, Peak Actuator Displacement=0.46")



(a) Southeast View



(b) Northwest View

Figure 4-195. Specimen S4 (Step 5, Peak Actuator Displacement=0.69”)



(a) Southeast View



(b) Northwest View

Figure 4-196. Specimen S4 (Step 6, Peak Actuator Displacement=0.92”)

The test continued with 5 cycles in each of Steps 7 and 8, and during Step 8, the applied load reached its peak values of 313 kips in the positive direction and -300 kips in the negative direction. Figures 4-197 and 4-198 provide the condition of the specimen during these steps. Notably, some of the concrete began to fall off during these loading cycles.



(a) Southeast View

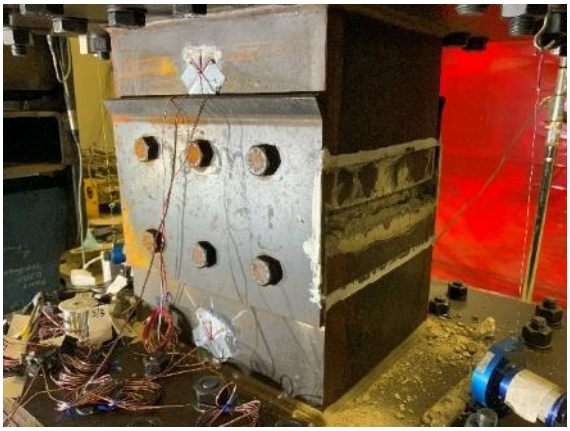


(b) Northwest View

Figure 4-197. Specimen S4 (Step 7, Peak Actuator Displacement=1.15”)



(a) Southeast View



(b) Northwest View

Figure 4-198. Specimen S4 (Step 8, Peak Actuator Displacement=1.48”)

In Step 9, the applied load reached 305 kips in the positive direction and -292 kips in the negative direction. Note that the maximum applied loads reached during these cycles decreased compared to the previous step. Figures 4-199 to 4-201 show the plate movements observed in this step. A slight rotation of the splice plate can be observed, and the concrete damage on the became progressively more severe.



(a) South View



(b) North View

Figure 4-199. Specimen S4 (Step 9, Peak Actuator Displacement=1.91”)



(a) Southeast View



(b) Northwest View

Figure 4-200. Specimen S4 (Step 9, Peak Actuator Displacement=1.91”)



(a) Southeast View



(b) Northwest View

Figure 4-201. Specimen S4 (Step 9, Peak Actuator Displacement=-2.02”)

At the first cycle of Step 10, the applied load reached 276 kips in the positive direction and -246 kips in the negative direction, respectively, corresponding to drops of 37 and 54 kips in the positive and negative direction, respectively, compared to the peak strength. Figures 4-202 to 4-204 illustrate the condition of the connection at this step. The strength dropped to 38 kips in the positive direction during the third cycle of Step 10. Figure 4-205 shows the excessive movement of the plates that occurred in this step. Fractures on bottom faceplates can even be observed in the figure. After the test, the splice plates were removed. As shown in Figure 4-206, the failure mechanism that ultimately developed was similar to the one for specimen S3.



(c) South View



(d) North View

Figure 4-202. Specimen S4 (Step 10, Peak Actuator Displacement=2.44")



(c) Southeast View



(d) Northwest View

Figure 4-203. Specimen S4 (Step 10, Peak Actuator Displacement=2.44")



(c) Southeast View



(d) Northwest View

Figure 4-204. Specimen S4 (Step 10, Peak Actuator Displacement=-2.58")



(a) South View



(b) North View

Figure 4-205. Specimen S4 (Step 10, 3rd Cycle)



(a) Top Faceplates



(b) Bottom Faceplates

Figure 4-206. Specimen S4 (After Test)

Figure 4-207 compares the hysteresis curves of global response and link behavior, along with design limit states. The figure also labels strengths corresponding to bearing strength considering only shear force, bearing strength considering combined shear and eccentric forces, as well as the net section shear yielding and fracture strength, and the gross section shear yielding strength. Results indicate that the target limit state (net section yielding) was reached and exceeded, and that the connection also even developed its gross section yielding shear strength. Figure 4-208 provides a comparison between Specimens S3 and S4 to illustrate the difference between non-composite and composite wall connection. Again, the composite section was initially stiffer, and it reached peak strength with significantly less sliding. The positive and negative peak strengths increased by 64 and 58 kips, respectively, in Specimen S4 compared to Specimen S3. The peak strength of S4 was also maintained over a range of deformations, whereas that of S3 progressively increased with larger deformations up to failure. However, after 1.5-in. deformation, the strength of S4 progressively degraded to approach that of S3 before failure.

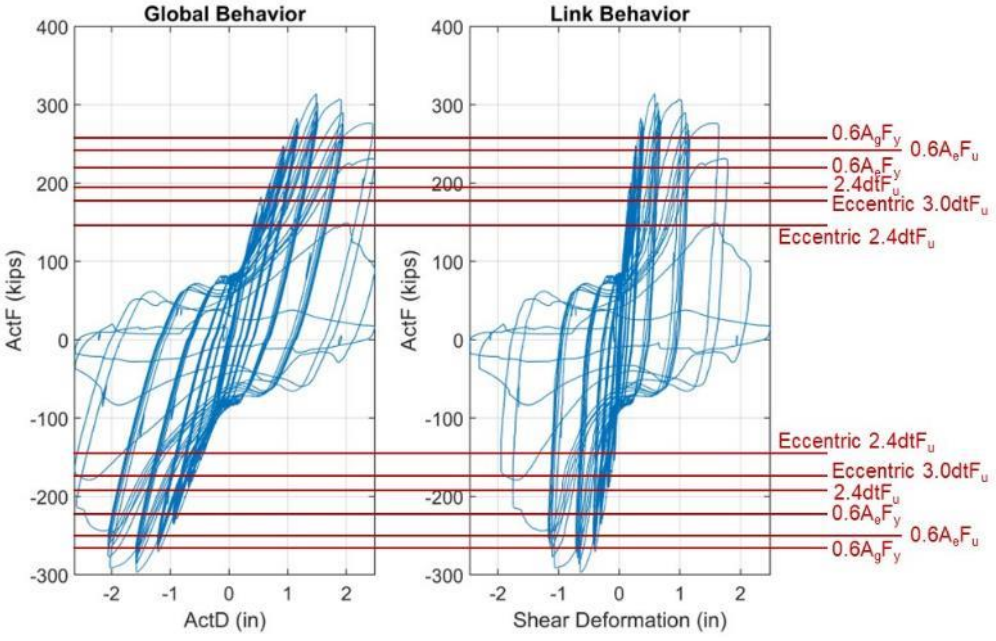


Figure 4-207. Test Results of Specimen S4 with Design Limit States

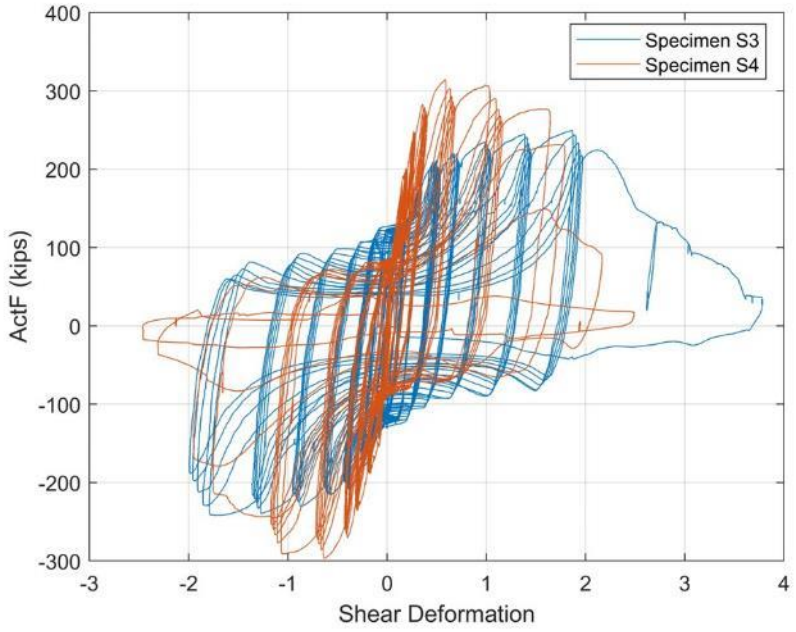


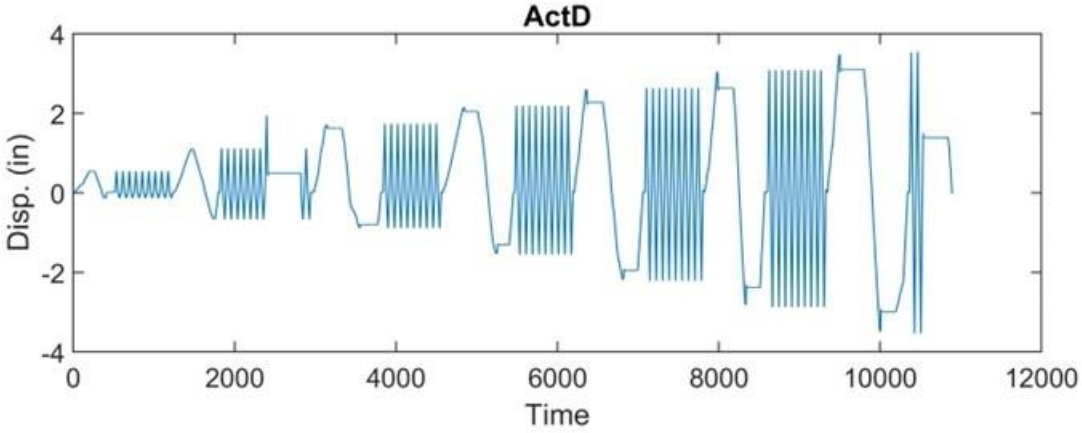
Figure 4-208. Test Results of Specimens S3 and S4

4.3.5 Specimen S5

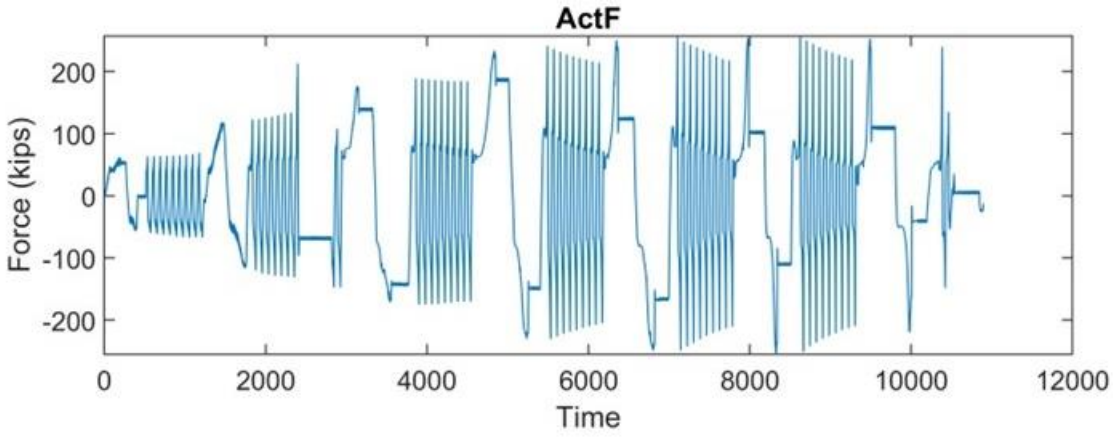
The testing of Specimen S5 started on 4/28/2023, following the loading procedure outlined in Table 4-16. The average actuator displacement and resulting load history for the experiment can be observed in Figure 4-209.

Table 4-16. Modified Loading Protocol for S5

Step	Disp. (in) +	Disp. (in) -	Force (kips) +	Force (kips) -	Cycles	Note 1	Note 2
0	0.00	0.00	0	0	-		
1	0.53	0.14	58	58	10	0.25Pw	
2	1.09	0.67	116	116	10	0.5Pw	
3	1.70	0.88	173	173	10	0.75Pw	
4	2.14	1.53	231	231	10	1.0Pw	0.6AgFy
5	2.58	2.18	248	252	10	2.4dtFu	
6	3.02	2.83	252	258	10		
7	3.46	3.48	252	222	2	Failure	



(a) Average Displacement History



(b) Resulting Load History

Figure 4-209. Actuator Displacement and Load History for Specimen S5

The test started with 10 loading cycles of Step 1, with applied forces of 0.25 P_w. Figure 4-210 shows the southeast and northwest views in Step 1. It was observed that sliding between splice plates and faceplates occurred when the force reached 47.7 kips, as shown in Figure 4-211. Subsequently, the test continued with 10 loading cycles in Step 2 for the applied force equal to 0.5 P_w. In this step, the actuator displacement was intended to be 1.09 in. and -0.67 in. in the positive and negative direction, respectively. However, an inadvertent error occurred in setting the actuator control commands, resulting in a displacement of 1.9 in. on the 9th cycle of this step instead of the intended 1.09 in. This error brought the peak force to 213 kips, as shown in Figure 4-212. The test was paused immediately to check the specimen, shown in Figure 4-213, and no damage observed in this step.



(a) Southeast View



(b) Northwest View

Figure 4-210. Specimen S5 (Step 1, Peak Actuator Displacement=0.53”)

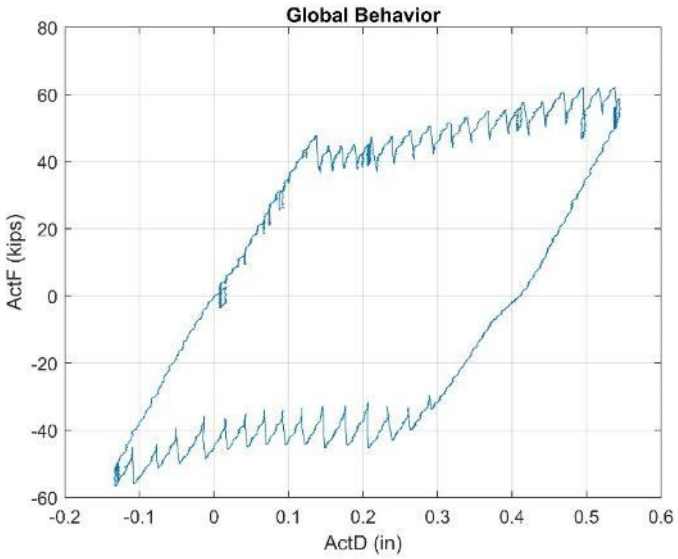


Figure 4-211. First Sliding of Specimen S5 (Step 1) (47.7k)

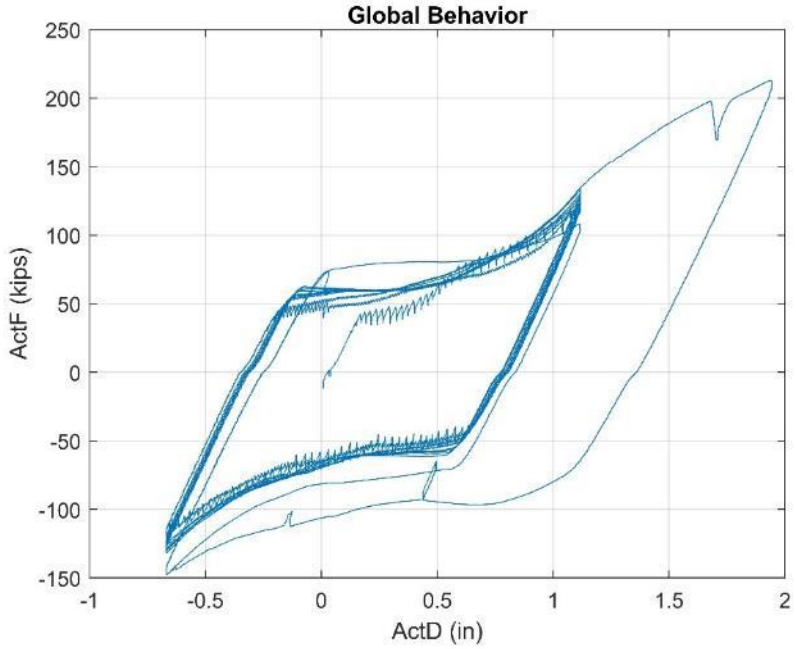


Figure 4-212. Global Behavior of Specimen S5 (Step 2)



(a) Southeast View (c) Northwest View

Figure 4-213. Specimen S5 (Step 2, 9th Cycle)

During Steps 3 and 4, the applied forces increased from 0.75 to 1.0 P_w. Figures 4-214 to 4-217 show the condition of the specimen in these steps. Rotation of splice plates can be observed, and became progressively more severe through successive steps.



(a) South View



(b) North View

Figure 4-214. Specimen S5 (Step 3, Peak Actuator Displacement=1.70”)



(c) Southeast View



(d) Northwest View

Figure 4-215. Specimen S5 (Step 3, Peak Actuator Displacement=1.70”)



(a) South View

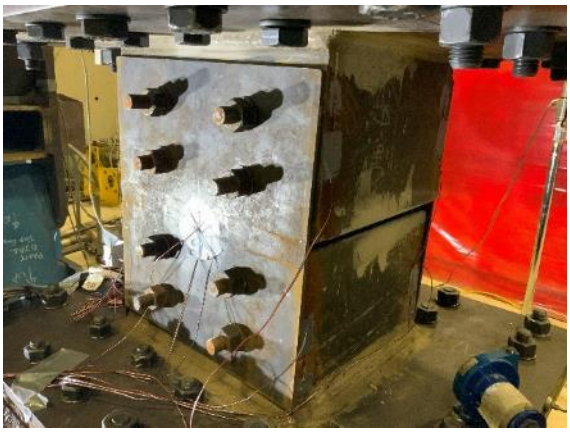


(b) North View

Figure 4-216. Specimen S5 (Step 4, Peak Actuator Displacement=2.14”)



(a) Southeast View

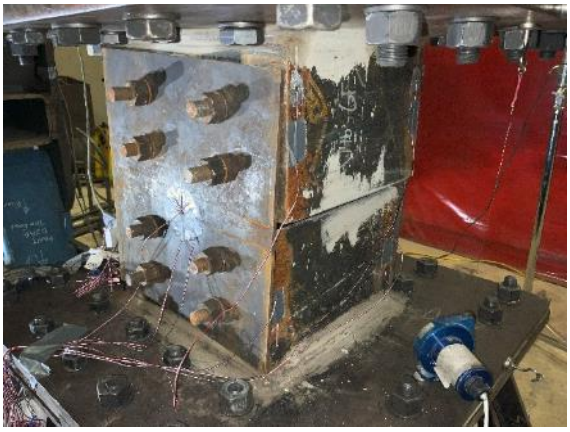


(b) Northwest View

Figure 4-217. Specimen S5 (Step 4, Peak Actuator Displacement=2.14”)



(a) Southeast View

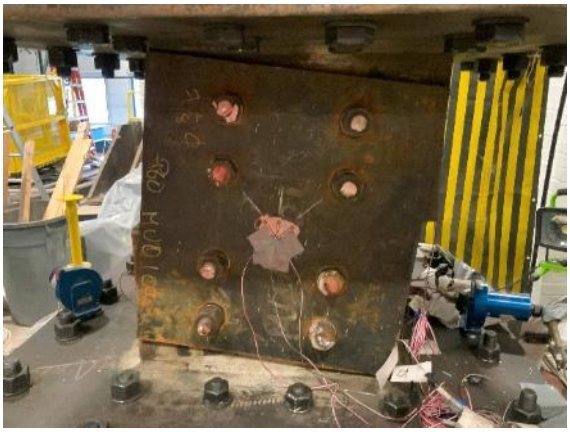


(b) Northwest View

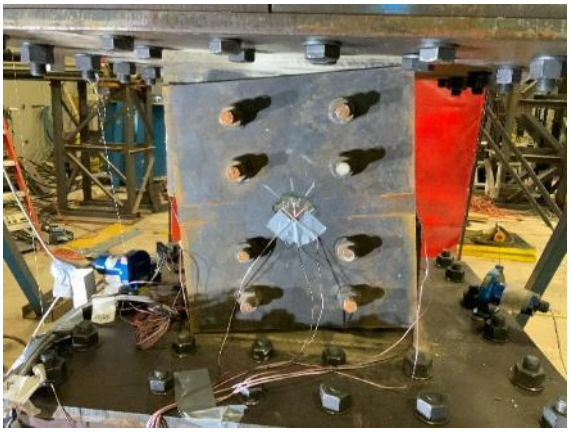
Figure 4-218. Specimen S5 (Step 4, Peak Actuator Displacement=-1.53”)

Figures 4-219 to 4-224 show the specimen during Steps 5 and 6. In Step 6, the applied load reached its peak values of 252 kips in the positive direction and -258 kips in the negative direction. Again, the rotation of splice plates became even more severe during these steps.

\



(a) South View



(b) North View

Figure 4-219. Specimen S5 (Step 5, Peak Actuator Displacement=2.58”)



(a) Southeast View



(b) Northwest View

Figure 4-220. Specimen S5 (Step 5, Peak Actuator Displacement=2.58”)



(a) Southeast View



(b) Northwest View

Figure 4-221. Specimen S5 (Step 5, Peak Actuator Displacement=-2.18”)



(a) South View



(b) North View

Figure 4-222. Specimen S5 (Step 6, Peak Actuator Displacement=3.02”)



(a) Southeast View



(b) Northwest View

Figure 4-223. Specimen S5 (Step 6, Peak Actuator Displacement=3.02”)



(a) Southeast View



(b) Northwest View

Figure 4-224. Specimen S5 (Step 6, Peak Actuator Displacement=-2.83”)

In Step 7 (Final Step), the applied loads reached 252 and -222 kips in the positive and negative direction, respectively. Note that the applied force dropped about 36 kips in the negative direction compared to its peak. Figures 4-225 to 4-227 show the plate movements in the first cycle of this step. On the 3rd cycle of Step 7, the bottom faceplate fractured and moved sideways as shown in Figure 4-228. This resulted in significant bearing deformation and tearing out of the edge of the faceplate at this point. Therefore, the test was terminated. Figure 4-229 shows the failure mechanism of the specimen after the test. The top faceplates exhibit severe bearing deformations and some fractures, while the bottom plates show a combined failure mechanism involving bearing failure and net section fracture.



(a) South View



(b) North View

Figure 4-225. Specimen S5 (Step 7, Peak Actuator Displacement=3.46")



(a) Southeast View



(b) Northwest View

Figure 4-226. Specimen S5 (Step 7, Peak Actuator Displacement=3.46")



(a) Southeast View

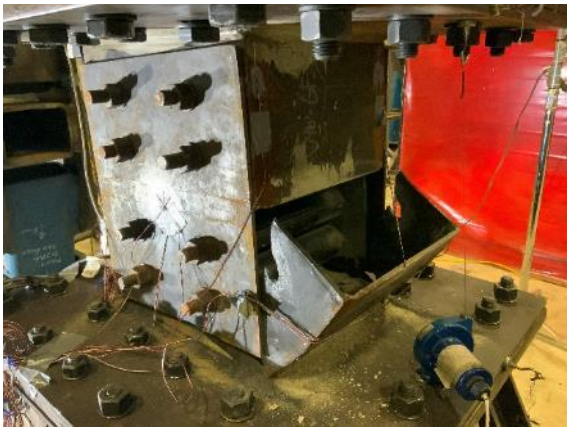


(b) Northwest View

Figure 4-227. Specimen S5 (Step 7, Peak Actuator Displacement=-3.48”)



(a) Southeast View



(b) Northwest View

Figure 4-228. Specimen S5 (Step 7, 3rd Cycle)



(a) South View (b) North View

Figure 4-229. Specimen S5 (After Test)

Figure 4-230 compares the hysteresis curves of global response and link behavior, along with design limit states. The figure labels strengths corresponding to bearing strength considering only shear force, bearing strength considering combined shear and eccentric forces, as well as the net section and gross section shear yielding. Results indicate that the peak strength (258 kips) in the test, was 3.7% lower than the target limit state of gross section shear yielding, which was 268 kips, which could be attributed to the effect of eccentric loading (i.e., shear and torsion) on the connection.

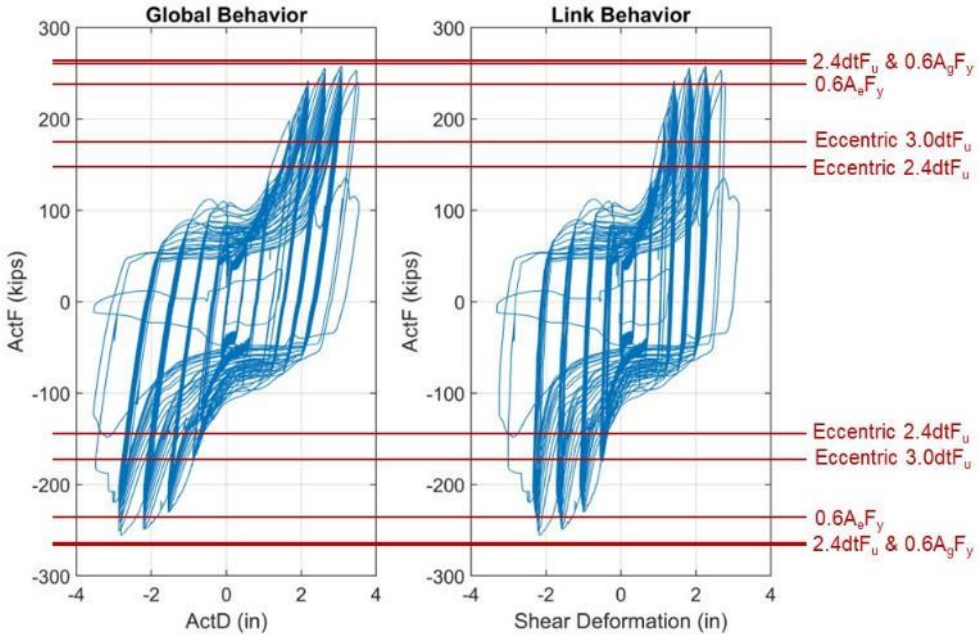


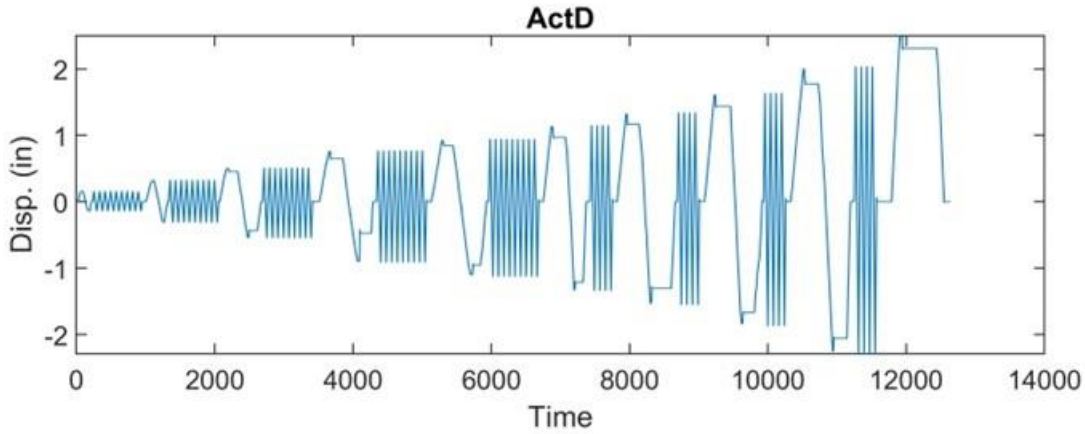
Figure 4-230. Test Results of Specimen S5 with Design Limit States

4.3.6 Specimen S6

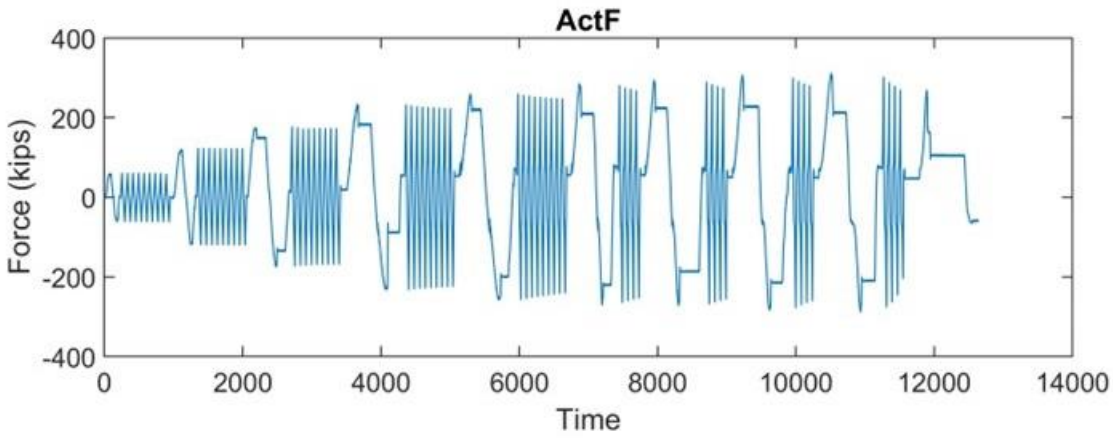
The testing of Specimen S6 started on 5/5/2023, following the loading procedure outlined in Table 4-17. The average actuator displacement and resulting load history for the experiment can be observed in Figure 4-231.

Table 4-17. Modified Loading Protocol for S6

Step	Disp. (in) +	Disp. (in) -	Force (kips) +	Force (kips) -	Cycles	Note 1	Note 2
0	0.000	0.000	0	0	-		
1	0.155	0.140	58	58	10	0.25Pw	
2	0.320	0.310	116	116	10	0.5Pw	
3	0.500	0.540	173	173	10	0.75Pw	
4	0.750	0.900	231	231	10	1.0Pw	0.6AgFy
5	0.940	1.110	258	258	10	2.4dtFu	
6	1.130	1.320	286	272	5		
7	1.320	1.530	295	274	5		
8	1.610	1.840	308	285	5		
9	2.000	2.250	312	289	5		
10	2.490	-	260	-	-	Failure	



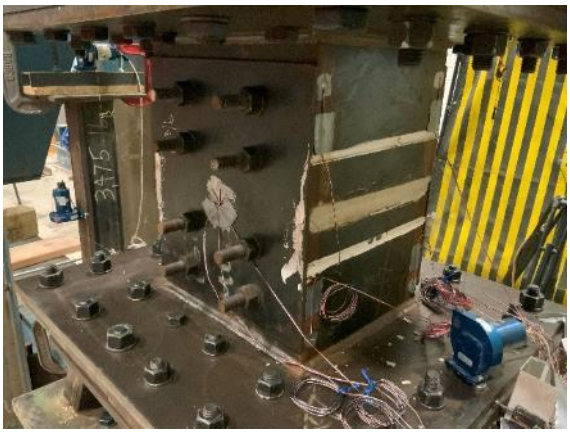
(a) Average Displacement History



(b) Resulting Load History

Figure 4-231. Actuator Displacement and Load History for Specimen S6

The test started with 10 loading cycles in each of Steps 1 to 4, and the applied forces increased from 0.25 to 1.00 P_w. Figures 4-232 and 4-233 show the condition of the specimen in Steps 3 and 4. No sliding or damage of concrete were observed during these steps.



(a) Southeast View



(b) Northwest View

Figure 4-232. Specimen S6 (Step 3 Peak Actuator Displacement=0.5")



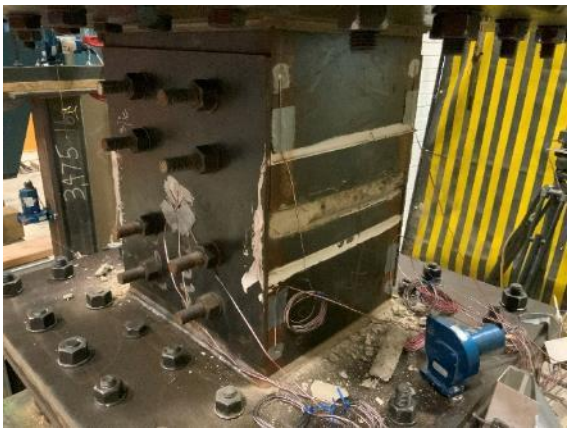
(a) Southeast View



(b) Northwest View

Figure 4-233. Specimen S6 (Step 4 Peak Actuator Displacement=0.75”)

The test proceeded with Steps 5 to 7, and in Step 7, and the applied force reached 295 and -274 kips in the positive and negative direction, respectively. Figures 4-234 to 4-236 show the southeast and northwest views in these steps. No significant rotation of splice plates was observed, but some of the concrete on the side began to fall off.



(a) Southeast View



(b) Northwest View

Figure 4-234. Specimen S6 (Step 5 Peak Actuator Displacement=0.94”)



(a) Southeast View



(b) Northwest View

Figure 4-235. Specimen S6 (Step 6 Peak Actuator Displacement=1.13”)



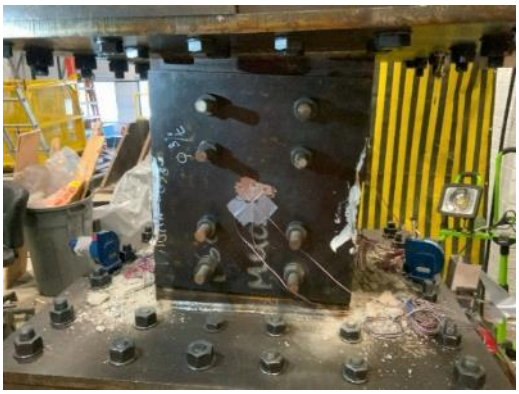
(a) Southeast View



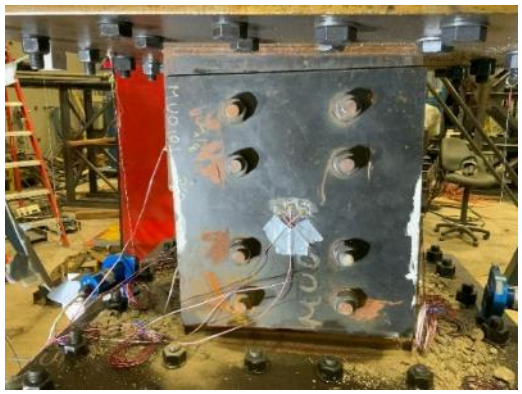
(b) Northwest View

Figure 4-236. Specimen S6 (Step 7 Peak Actuator Displacement=1.32”)

Figures 4-237 to 4-242 show the specimen during Steps 8 and 9. In Step 9, the applied load reached its peak values of 312 and -289 kips in the positive direction and in the negative direction, respectively. The rotation of splice plates and the damage of concrete became more severe during these steps. During the five loading cycles in Step 9, the peak strength reached in each cycle force decreased from 312 to 268 kips in the positive direction and from -289 to -191 kips in the negative direction. This indicates that the connection began to exhibit signs of failure at certain positions.



(a) South View

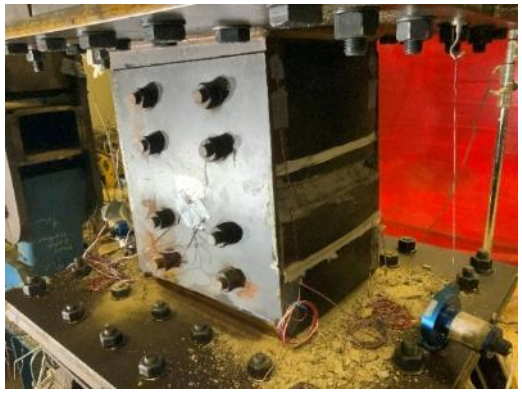


(b) North View

Figure 4-237. Specimen S6 (Step 8 Peak Actuator Displacement=1.61”)



(c) Southeast View

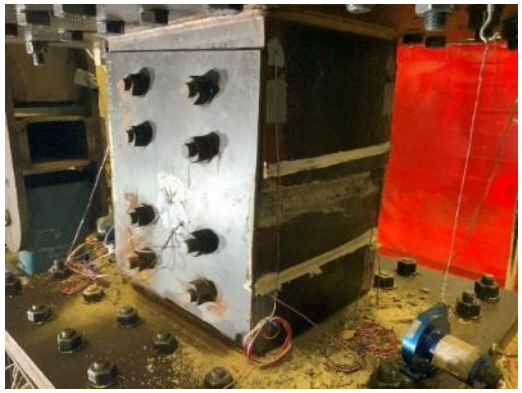


(d) Northwest View

Figure 4-238. Specimen S6 (Step 8 Peak Actuator Displacement=1.61”)



(a) Southeast View

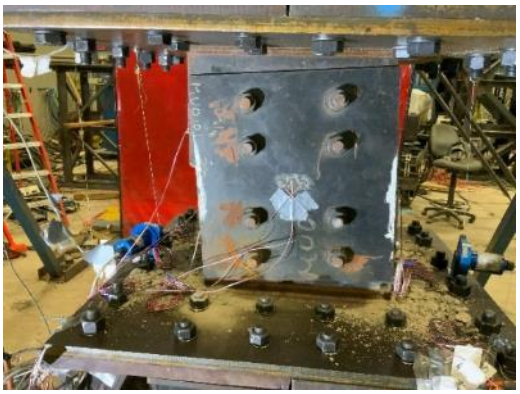


(b) Northwest View

Figure 4-239. Specimen S6 (Step 8 Peak Actuator Displacement=-1.84”)

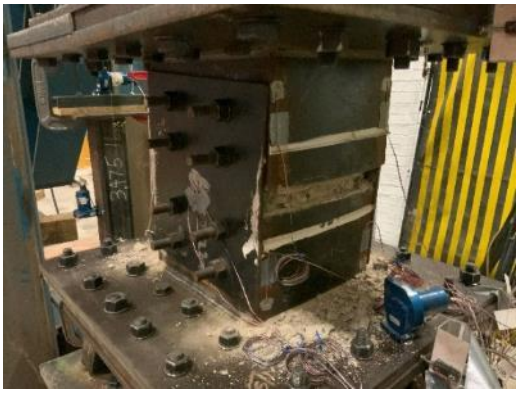


(e) South View

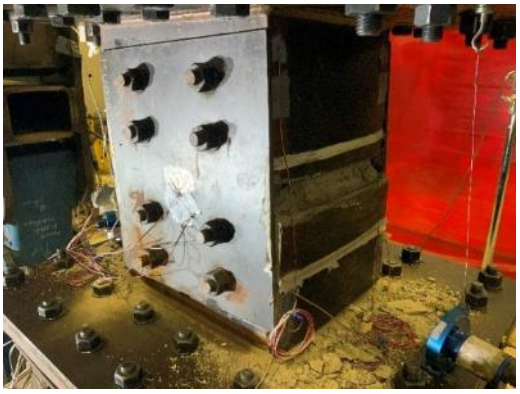


(f) North View

Figure 4-240. Specimen S6 (Step 9 Peak Actuator Displacement=2.00”)



(g) Southeast View



(h) Northwest View

Figure 4-241. Specimen S6 (Step 9 Peak Actuator Displacement=2.00”)



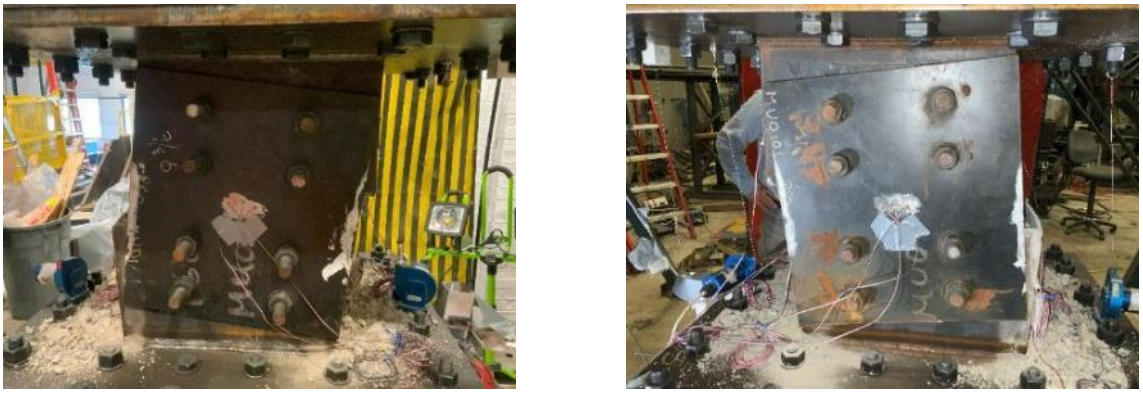
(c) Southeast View



(d) Northwest View

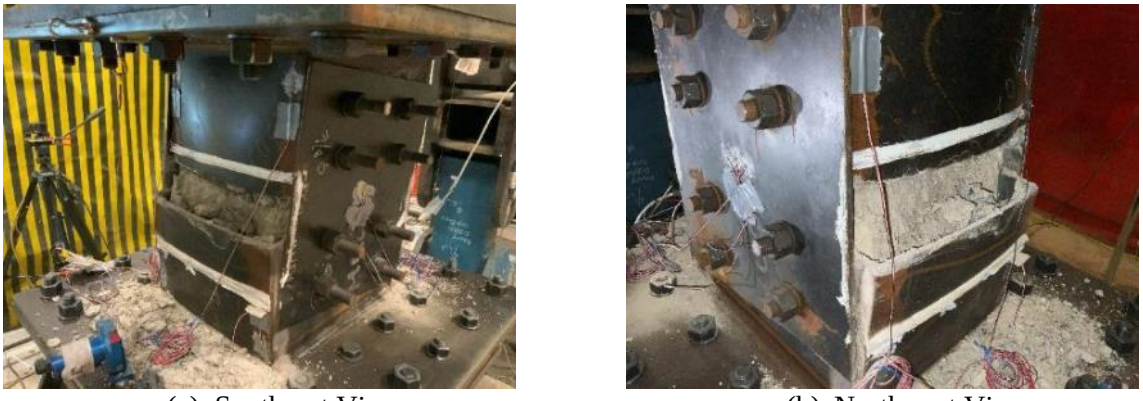
Figure 4-242. Specimen S6 (Step 9 Peak Actuator Displacement=-2.25”)

In Step 10 (Final Step), the applied loads reached 269 kips then dropped abruptly in the positive direction. Figures 4-243 and 4-244 show the plate movements and damage of concrete at this point. Figure 4-245 highlights the area where a fracture was observed on the bottom faceplate. Testing stopped there, without pushing the specimen to similar failure in the negative direction, to allow removing the splice plates and observe the damage of the faceplate in this state of immediate failure (i.e., without inducing additional large deformations as in prior shear specimens). Figure 4-246 show this failure mechanism of the specimen after the test, with the splice plates removed. The top faceplates exhibit severe bearing deformations, while the bottom plates show a combined failure mechanism involving bearing failure and net section fracture.



(a) South View (b) North View

Figure 4-243. Specimen S6 (Step 10 Peak Actuator Displacement=2.49”)



(a) Southeast View (b) Northwest View

Figure 4-244. Specimen S6 (Step 10 Peak Actuator Displacement=2.49”)



Figure 4-245. Fracture on Bottom Faceplate of Specimen S6 (Step 10)



(a) South View (b) North View

Figure 4-246. Specimen S6 (After Test)

Figure 4-247 compares the hysteresis curves of global response and link behavior, along with design limit states. The figure labels strengths corresponding to bearing strength considering only shear force, bearing strength considering combined shear and eccentric forces, as well as the net section and gross section shear

yielding. Results indicate that the target limit state (gross section yielding) was reached and exceeded. Figure 4-248 provides a comparison between Specimens S5 and S6 to illustrate the difference between non-composite and composite wall connection. Again, the composite section displayed greater initial stiffness and achieved its peak strength with significantly less sliding. The positive and negative peak strengths increased by 60 and 31 kips, respectively, in Specimen S6 compared to Specimen S5. Specimens S5 and S6 both experienced a rapid drop in strength in the positive direction after reaching their peak strength, but Specimen S5 sustained peak loads over a longer deformation range in this loading direction. Because testing of S6 was stopped there after failure in the positive direction, without similarly pushing it in the negative direction (for reasons mentioned earlier), a comparison of maximum deformation at sustained peak strength is not possible in that direction.

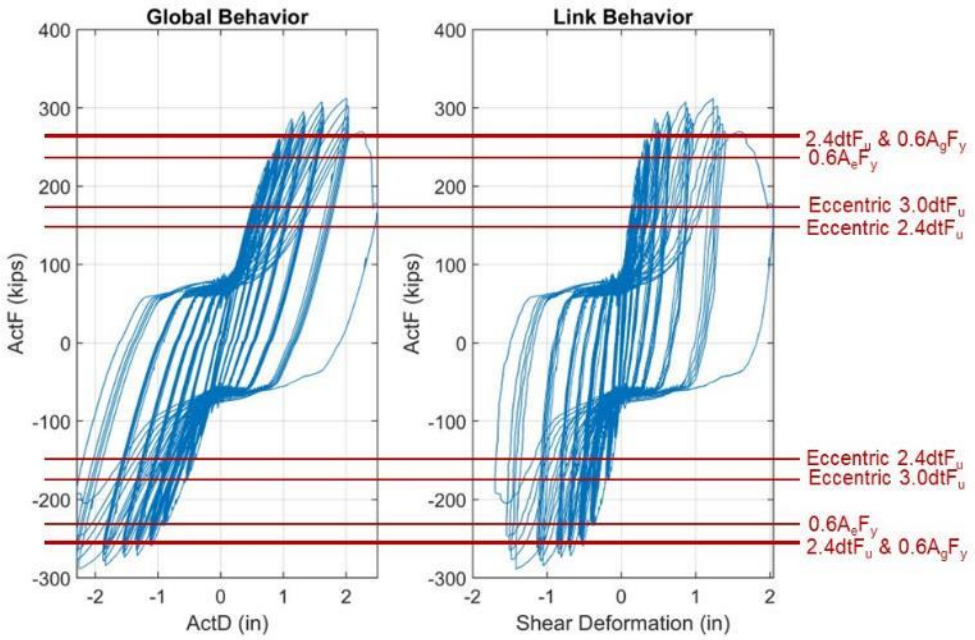


Figure 4-247. Test Results of Specimen S6 with Design Limit States

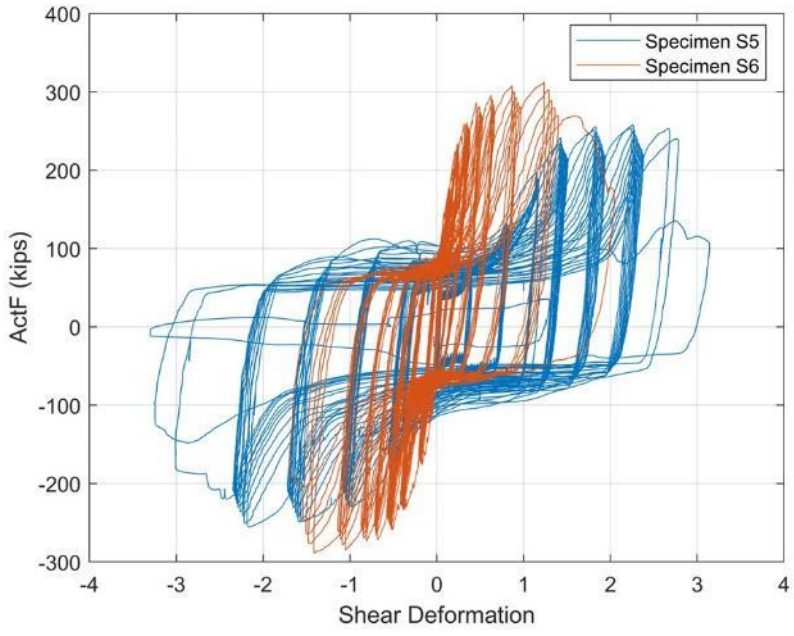


Figure 4-248. Test Results of Specimens S5 and S6

SECTION 5
NUMERICAL ANALYSES OF COMPONENT LEVEL TESTS

5.1 General

This chapter presents the results and findings from numerical analyses of the component level tests presented in Chapter 4. The analyses were comprised of two series: six tension tests (T1 to T6) and six shear tests (S1 to S6). For tension specimens, simplified spring models and finite element models were adopted to analyze the specimens and compare them with test results. For shear specimens, finite element models were used for comparison with the test results. The numerical analyses for the tension tests are presented in Sections 5.2 and 5.3, while the analyses for shear tests are presented in Section 5.4.

5.2 Simplified Spring Analysis

5.2.1 Introduction

Composite Plate Shear Walls—Concrete Filled (C-PSW/CF) designed in accordance with AISC 341-22 rely on welded splices as they are intended for use in seismic regions. They have a demonstrated capacity to develop high strength and ductility in flexure, and implicitly in the parts of the walls cross-sections undergoing tension and compression regions under this bending action.

For non-seismic applications with bolted splices, the behavior of the walls will be more or less ductile depending on the governing limit state, with many of these controlling limit states occurring in the splice regions. These design limit states of steel bolted connection include slip-critical resistance, bearing and tear-out strength, net section rupture, block shear fracture, gross section yielding, and bolt shear strength. As mentioned in the previous interim report, in all the bolted tension test specimens considered (Case 1A, 1B, 2B, 1C, and 2C), the splices were designed such that tear-out, block shear fracture, and bolt shear strength were not the controlling limit states (because these are considered to be relatively less ductile limit

states). As a result, all the connections considered here can be analyzed, in a preliminary way, using simplified spring analysis models, in which various springs can be used to model behaviors due to friction, bearing deformations, gross and net section yielding of plates, and concrete compression. The details of these analyses are presented in Section 5.2.7 to 5.2.12, first considering the modeling of various limit states, and then of the specific connections considered.

5.2.2 Bearing Spring

The development of bearing strength depends on the contact behavior between bolt shanks and plates. Since the bearing strength will develop only when the bolt hits the edge of the hole, a hook or gap element was included to model the clearance between bolts and plates. Figure 5-1 shows the bearing spring model containing hook and gap elements. Note that the bearing spring here is separated into a tension-only bearing spring (BT) and a compression-only bearing spring (BC) to reflect the fact that the connection can be subjected to tension and compression load.

Figure 5-2 shows the gap and hook elements in SAP2000. For the gap element, when the compressive displacement is larger than the gap opening, the opening will close, and a spring with stiffness *k* will be compressed. Likewise, for the hook element, when the tensile displacement is larger than the hook opening, the hook will start to elongate a spring of stiffness *k*. Note that the stiffness *k* on the gap and hook elements will affect the effective stiffness of the whole bearing model since they are connected in series with the bearing spring. As a result, a large value of stiffness was assigned to the gap and hook springs to minimize their influence on total deformations.

Figure 5-3 shows the typical bearing behavior of a CPSW/CF connection (as expressed by this model) when subjected to tension, in three stages labelled Stages 1 to 3 in the figure. Stage 1 is the initial condition,

assuming that all bolts are initially centered in holes having a 1/8” greater diameter than the bolt diameter. Note that, in tension, the hook value must be zero for the member to start developing its bearing strength, whereas in compression, the gap value must be zero to start doing the same. In Stage 2, for illustration purpose, bolts remain centered in the cover plate holes, but the faceplate has moved 1/16”, putting it in contact with the bolt shank. In Stage 3, a similar 1/16” of sliding has occurred to also put the cover plates in contact with the bolt shank, for a total sliding of 1/8” before bearing strength starts to develop. Since sliding occurs in opposite directions on both sides of the connection centerline, this adds up to ¼” of slippage before bearing behavior is engaged. In tension, this ¼” represent the total slippage that must develop in the connection before the bolt shanks contact both the faceplates and splice plates represents the initial hook values. In other words, to represent the above behavior, if all bolts are initially positioned at the center of the bolt holes, the initial hook value must be set to be 1/8 in. x 2 = 1/4 in (i.e., to model both sides of the splice connection). However, note that in actual implementations, the bolts may not be precisely centered, and as a result, the hook and gap values of each bolt may need to be adjusted to correctly fit actual clearances (which are unknown) if the objective is to more perfectly replicate behavior of actual conditions.

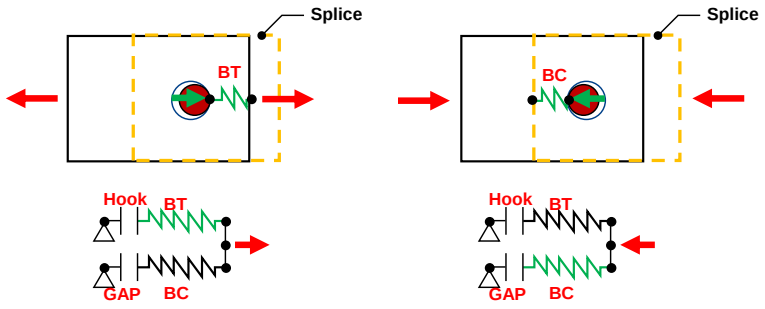


Figure 5-1. Bearing Spring Model with Hook/Gap

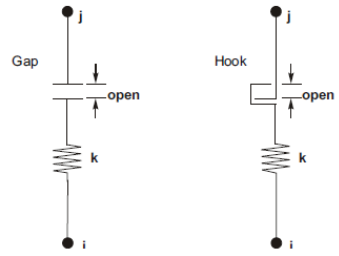


Figure 5-2. Gap and Hook Elements in SAP2000

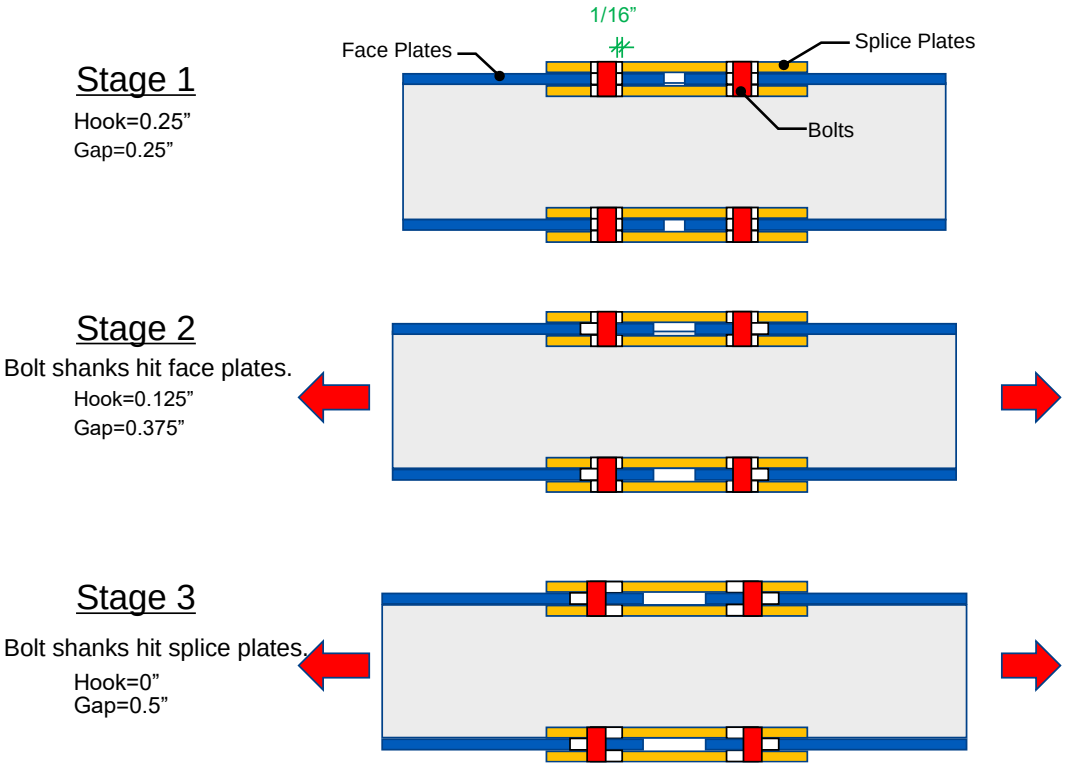


Figure 5-3. The Change of Hook and Gap Values in Tension

5.2.3 Elongation of Bolt Holes due to Bearing Stresses

When a force is resisted by bearing, the bearing spring starts to deform; therefore, the geometry of the bolt hole changes. Figure 5-4 shows a typical bolt hole deformation under cyclic loadings. In the Figure, H and d_b represent the original hole dimension and bolt diameter, and Δ_B corresponds to the bolt hole deformation

due to bearing stresses. For example, when the connection was in tension (Steps 1 to 2), the bolt slipped to the right in contact with the plate, then the bolt hole dimension increased due to the bearing load. Similarly, when the connection was in compression (Steps 3 to 4), the bolt shank moved to the left and forced the left edge to deform. This cyclic load-displacement behavior, considering the non-recoverable hole elongations, is adequately modeled using bearing springs with hook/gap elements.

Figure 5-5 shows a typical cyclic analysis result for this bearing spring model. As shown in Cycle 1, the bearing spring first exhibited slippage (due to the gap between bolts and plates) until the gap closed, and then (upon further loading) the bearing strength was developed with a corresponding inelastic deformation. After the first cycle, due to hole elongation, the gap between the bolts and plates became larger, and likewise in each subsequent cycle of progressively larger displacement amplitude (see Cycles 2 to 5) as a result of the bearing spring elastoplastic behaviors. It can be noted that the residual deformation of the bearing spring represents the elongation of the bolt hole dimension (or gap and hook opening length).

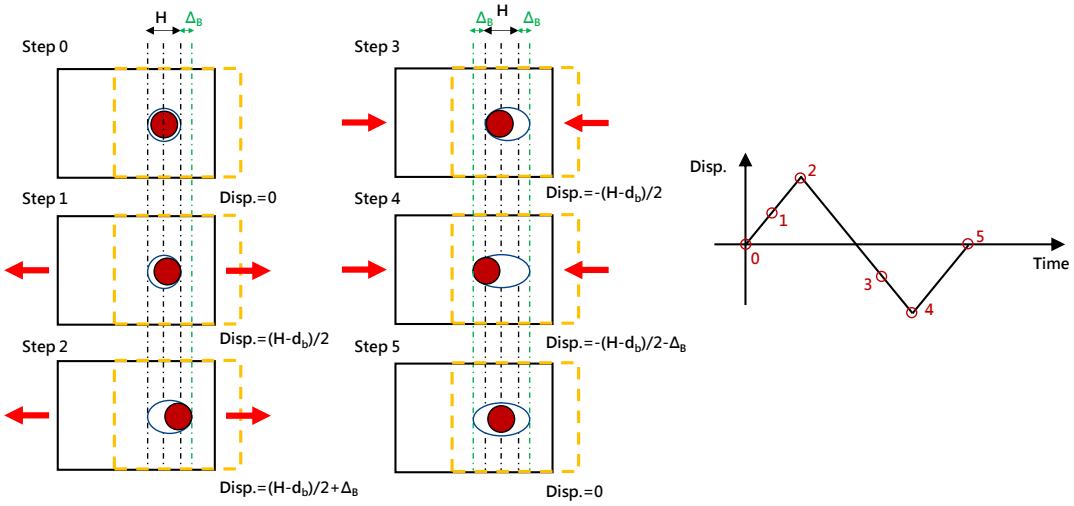


Figure 5-4. Bolt Hole Deformation under Cyclic Loading

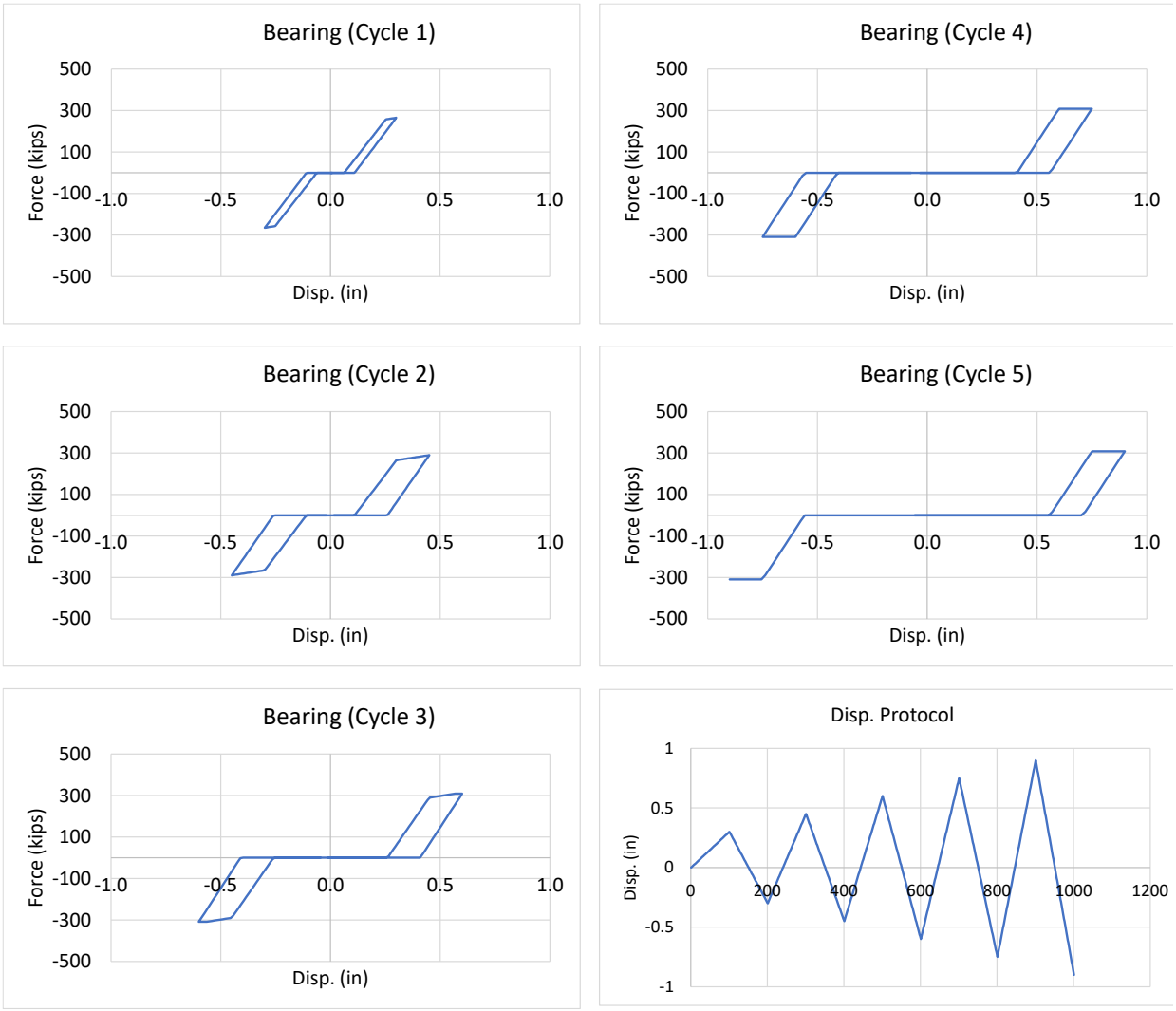


Figure 5-5. Bearing Spring Analysis under Cyclic Loading

5.2.4 Friction and Bearing Spring

Information presented in Section 5.2.3 was for bearing strength with non-pretensioned bolts (i.e., with sliding occurring at the point of zero applied load). In bearing connections with pretensioned bolts, slippage will occur when the load applied reaches the slip-critical resistance of the connection. After slippage, the bolt will contact the plate, and the bearing strength will develop. However, as observed in some experiential tests (Frank and Yura, 1981), the pretension sometimes barely increases the ultimate strength of a bolted connection. That is, the bearing strength (usually estimated to be 2.4 to 3.0 times the bearing stress (AISC 360)) that governs the maximum strength of a bolted connection can be the same with or without pretension. As a result, when the friction force reaches the slip-critical value, the connection will slip to the edge of the hole, after which the strength of the connection will continue to increase until it reaches the ultimate bearing strength. Note that the connection in this example is assumed to be designed such that other failure modes (such as tear-out, net section fracture, block shear rupture, etc.) are precluded.

Figure 5-6 shows the friction and bearing spring model used to model this behavior. Note that the friction and bearing springs here were assumed to resist external forces simultaneously, therefore they were connected in parallel. Since the ultimate strength is the summation of friction and bearing spring forces in the SAP2000 model, the bearing spring strength is modified here to deduct from the slip-critical value (to be consistent with the above observation that ultimate strength is not increased due to the presence of friction). Figure 5-7 shows the definition of “additional bearing strength”, which is equal to the calculated bearing strength minus the slip-critical value.

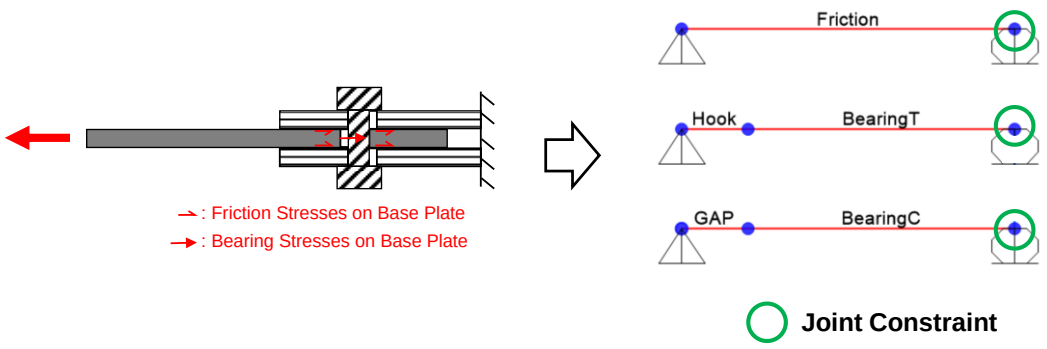


Figure 5-6. Friction and Bearing Spring Model

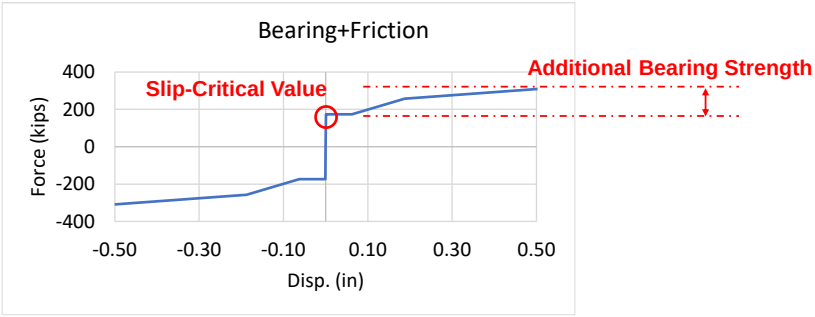


Figure 5-7. Friction and Bearing Spring Model

Figure 5-8 shows typical results from this friction and bearing spring analysis under cyclic loading. Compared to the bearing spring case studied previously, here the connection initially reached the slip-critical resistance, then slippage happened. After that, the bearing strength was developed, and the connection developed plastic deformations. As described before, the slip distance became larger and larger under each load cycle of progressively increasing displacement, and the residual deformation corresponds to the increase in bolt hole dimension or gap.

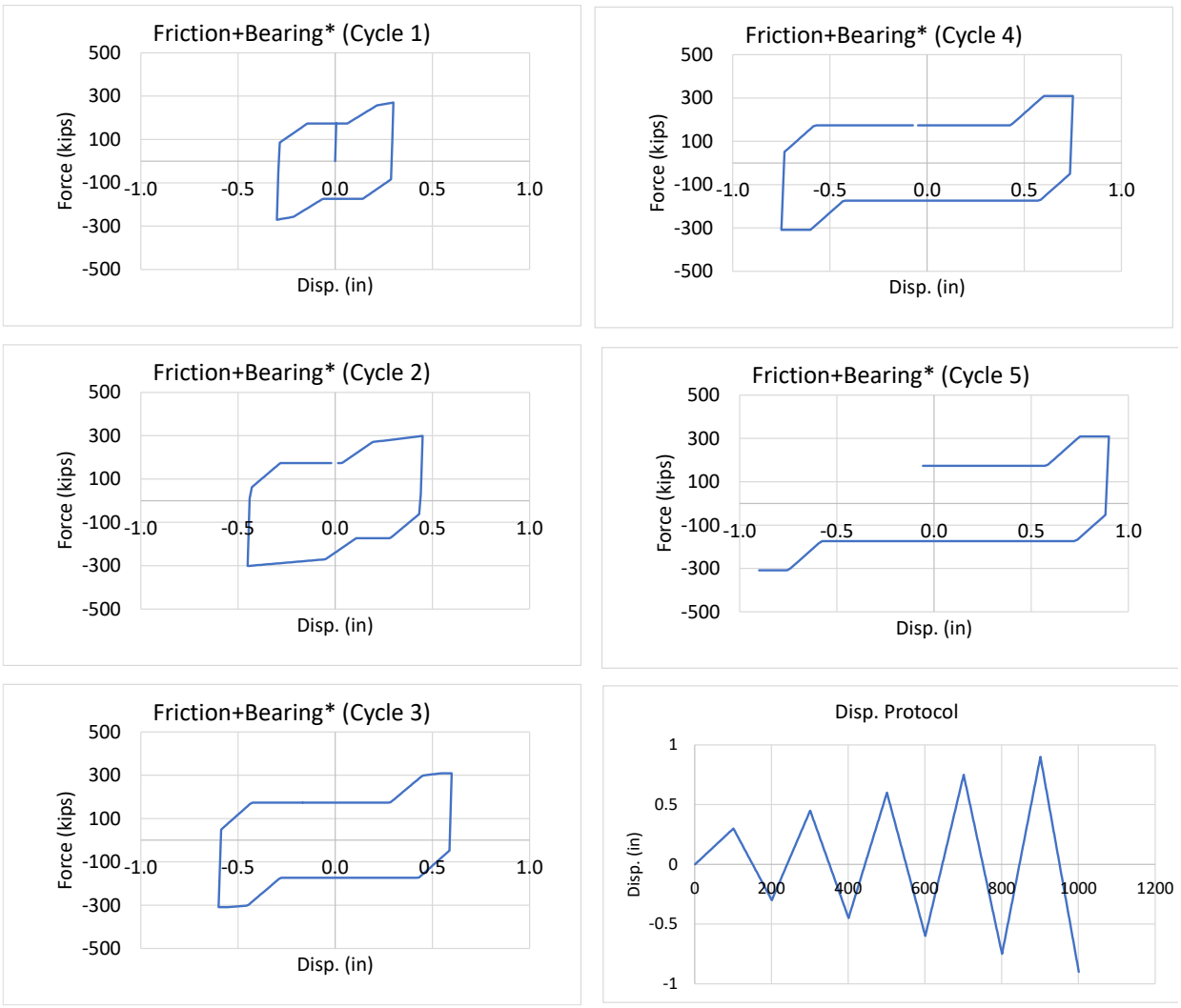


Figure 5-8. Friction and Bearing Spring Analysis under Cyclic Loading

5.2.5 Spring Models and Properties

5.2.5.1 Spring Models (Lower-Bound and Upper-Bound)

The behavior of a CPSW/CF bolted splice connection can be complicated to model using simple springs, because it is an "amalgam" of different springs connected in series or parallel and intended to represent various components of the total behavior. Some assumptions regarding this behavior are required, which give rise to different models that could possibly predict different chains of events and different ultimate behavior. Figure 5-9 show a typical CPSW/CF splice specimen for the tension tests, where L_1 and L_2 represent the length outside the splice region, while L_3 is the length inside the splice region. To simplify the entire specimens into simplified spring models, Table 5-1provides a comprehensive list of the spring names and corresponding lengths employed. Figure 5-10 show such models that are expected to provide Lower-Bound and Upper-Bound estimates of actual strength and behavior (the true behavior probably lies somewhere in between these limits). The reason for the difference between the two models is due to the uncertain manner by which friction forces developing locally near the bolt heads can affect the overall splice behavior, as schematically illustrated in Figure 5-11. In the Lower-Bound model, net section stresses are assumed to develop after bearing of the bolt occurs; in the Upper-Bound model, net section stresses and friction develop simultaneously. In reality, the friction spring and net section spring interact a little bit in both manners, implying that they are connected "partially in series" and "partially in parallel." At best, the Lower-Bound and Upper-Bound models can be useful to predict the minimum and maximum strengths and ductilities of the splices, for these limit states, which can be useful for various purposes.

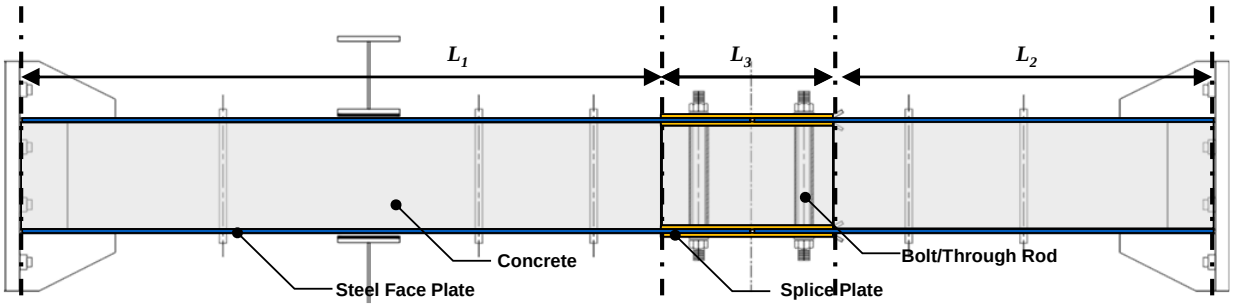
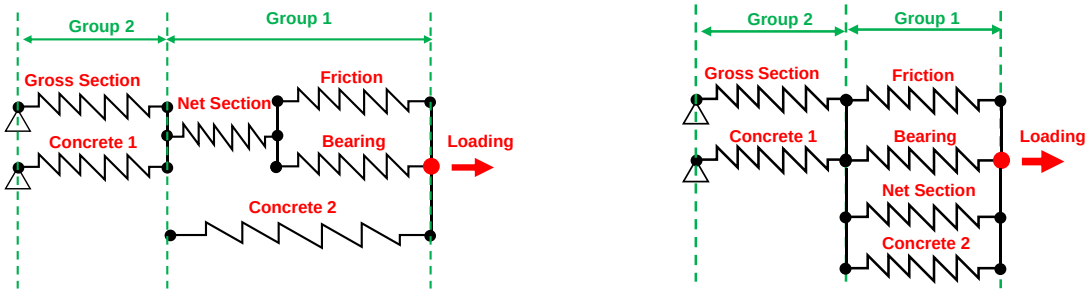


Figure 5-9. Example of CPSW/CF connections

Table 5-1. Spring Name and Length

Spring Name	Length
Net Section	$2\times N_{rows}\times D_{Holes}$
Gross Section	$L_1 + L_2$
Concrete 1	$L_1 + L_2$
Concrete 2	L_3



(a) Lower-Bound Spring Model (b) Upper-Bound Spring Model

Figure 5-10. Simplified Spring Models

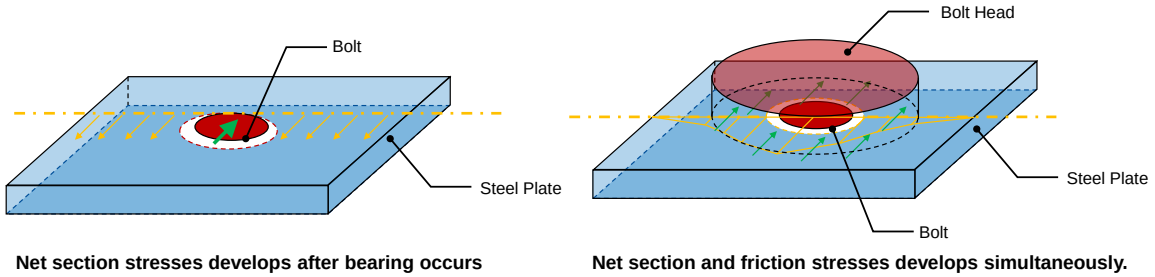


Figure 5-11. Comparison between Lower-Bound and Upper-Bound Model

5.2.5.2 Spring Properties

Figures 5-12 and 5-13 show the simplified spring models developed and analyzed using the SAP2000 program for both Lower-Bound and Upper-Bound conditions of the bolted splices considered. More specifically, the spring models are created by assembling two groups of springs. Group 1 consists of springs inside the splice region, which model steel friction (Spring No. 3), bearing (Spring No. 1 and 2), net section (Spring No. 4), and concrete stiffness and strengths (Spring No. 7 or 8). Group 2 represents the springs outside the splice region, which model steel gross section and concrete stiffness and strengths (Spring No. 5 and 6). To be more correct, a steel gross section spring could also have been included inside the splice region, but this would only slightly affect the total stiffness results in analyses conducted here. As mentioned previously, in Group 1 for the Lower-Bound spring model, the net section spring is connected in series with the friction and bearing springs. On the other hand, in the Upper-Bound spring model, the net section spring is connected in parallel with the friction and bearing springs.

Figure 5-14 shows the spring models used in the simplified spring analysis, and Table 5-2 summarizes all the spring properties used. Bi-linear spring properties were used for the steel friction and gross section springs. Similarly, bi-linear spring properties were assigned to the concrete springs under compression. For the steel net section and concrete springs under tension, trilinear properties were employed. For the bearing springs, a quadrilinear spring model was adopted to represent the progressive increase in bearing strength from 2.0 to 3.0dtF_u, where *2.0dtFu* is assumed to correspond to the start of elongation of bolt holes under bearing.

Symbols P_1, P_2, P_3, P_4, Δ_1, Δ_2, Δ_3, and Δ_4 represent forces and displacements on the curves for all spring properties, per Figure 5-14. Note that all spring properties are symmetric in tension and compression, except for the concrete springs. In addition, for all curves, the last segment assumes that the strength remains

constant up to infinite deformations, as expressed by a flat plateau (in other words, strength degradation and failure are not modeled here).

For the friction springs, the slip-critical resistance was determined through experimental observations to obtain the P_1 and P_2 values, and the Δ_1 value was arbitrarily defined to be 0.001 in. to include a large initial stiffness to simulate the connection behavior before slip.

For the gross section and net section springs, by using results from coupon tests for the steel material properties, the yield strength of faceplates (A_gF_y) was calculated and assigned as the P_1 and P_2 values to the gross section springs (i.e., neglecting strain hardening of the gross section, deemed unlikely to develop in this connection). Similarly, the net section yield strength (A_eF_y) was calculated as the P_1 value, and the net section tensile strength (A_eF_u) was calculated and assigned as the P_2 and P_3 values in the net section springs. In addition, their Δ_1 values was calculated by multiplying the yield strain (ε_y), taken here as 0.002, by the spring length. Furthermore, for the Net Section spring, the Δ_2 value for the Net Section spring was taken as equal to an ultimate strain (ε_u), taken as 0.15, times the springs length.

For the bearing springs, the bearing strengths corresponding to $2.0dtF_u$ and $2.4dtF_u$ were adopted to define the P_1 and P_2 values, respectively, while the strength corresponding to $3.0dtF_u$ was used to define the P_3 and P_4 values. Referring to the research by Frank et. al. (1981), a hole elongation approximately equal to 0.25 in. typically has developed when the bearing strength reaches $2.4dtF_u$. However, here the deformations of bearing springs were defined based on the test result obtained from Specimen T2. Therefore, a displacement of 0.19 in. was chosen as the Δ_1 value. This displacement represents the point where the bearing strength corresponding to $2.0dtF_u$ is developed. In addition, the Δ_2 value for the Bearing springs

was determined to be twice the value of Δ_1, and the Δ_3 value was taken as equal to four times the value of Δ_1.

The labels CONC1 and CONC2 were used to represent the concrete springs inside and outside the splice region, and the compressive strength ($A_c f'_c$) was used to determine the P_1 and P_2 values under compression.

For the CONC 2 spring, note that inside the splice region, the net area of concrete reduced at the location of the bolts or rods in their pipe sleeves. Figure 5-15 shows a comparison of the compressive strength transferred by the concrete alone by cutting a section in the middle of the connection, as obtained from finite element analyses for Specimens T1, T2, and T3, which are connections having two blind bolts, two through rods, and three through rods, respectively. Figure 5-16 shows corresponding compressive stress contours. It can be observed that as the number of bolts/rods participating in the connection increased, there was a greater reduction in the compression transferred within the splice region, due to a reduction in the effective concrete cross-sectional area at that location.

To better understand the above phenomenon and its implication in the spring model, Figure 5-17 shows the axial compression force obtained from finite element analysis in various elements along the length of the splice region for Specimen T3. In this figure, the axial forces are plotted for various cross-sections taken along the X-coordinate, and the force resisted by a number of components within the splice region are plotted individually to assess their contributions. It is observed that the axial force resisted by the concrete through the splice reduces from the value resisted outside the splice. This is because some of the force resisted by concrete is transferred through the splice plates and through the pipe sleeves. Note that the total compressive force within the splice region remains constant – only that it is resisted by different components. Since the splice plates, and pipe sleeves were not included in the spring analysis for simplicity, they can be

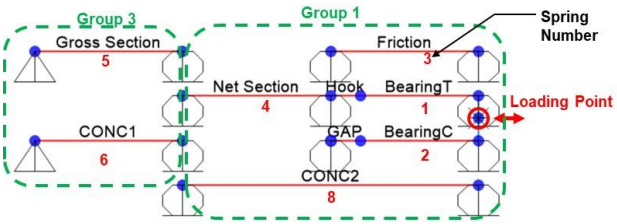
considered as part of the concrete spring in the splice region. Therefore, in the spring analysis, it was assumed that there is no loss of strength in the CONC2 spring, as it is assumed to account for the force transfer mechanism described above.

For the concrete springs in tension, a value of $0.1A_c f'_c$ was assigned for the P_1 values. The P_2 and P_3 values in tension were set to zero to represent the tensile behavior of concrete.

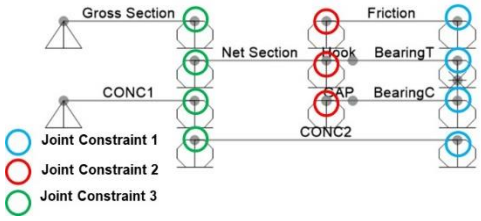
For concrete spring (CONC1 and CONC2) under compression, the Δ_1 values were assumed to be 0.003 times the length of the springs. These values represent the displacements when the concrete springs reach their compressive strengths. When concrete springs are in tension, the Δ_1 values were calculated to be P_1 divided by axial stiffness (EA/L) of the concrete springs. The Δ_2 values, representing the displacements when the tensile strengths drop to zero, were assumed to be 0.002 times the length of springs.

The Δ_2 values in the bilinear springs, the Δ_3 values in the trilinear springs, and the Δ_4 value in the quadrilinear spring were assigned to be equal to the maximum displacement considered in the spring analyses conducted. Note that, for simplicity, this is equivalent to defining all the spring properties as ultimately elongating to infinity after reaching their maximum strength (i.e., without failure mechanisms at specific deformations).

Analysis results are discussed in Sections 5.2.7 to 5.2.12, after a description of the loading protocols used in Section 5.2.6.

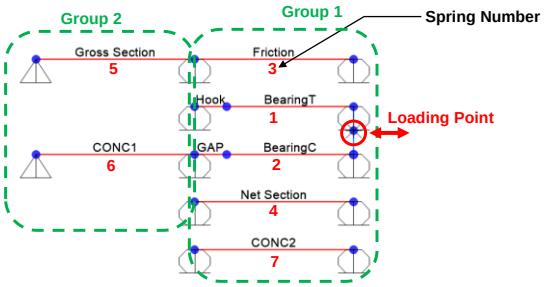


(a) SAP2000 Model (Lower-Bound)

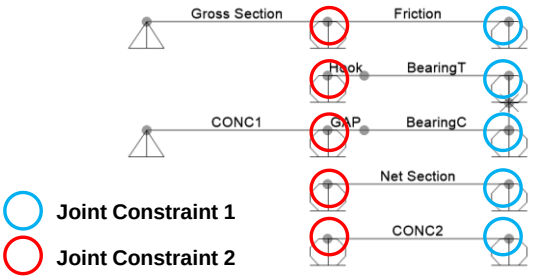


(b) Joint Constraints

Figure 5-12. Lower-Bound Spring Model (SAP2000)



(a) SAP2000 Model (Upper-Bound)



(b) Joint Constraints

Figure 5-13. Upper-Bound Spring Model (SAP2000)

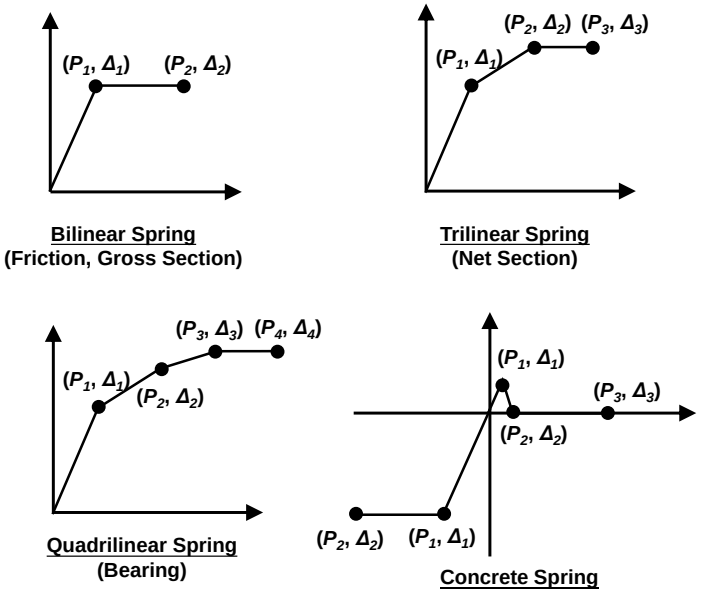


Figure 5-14. Spring Properties for Simplified Spring Models

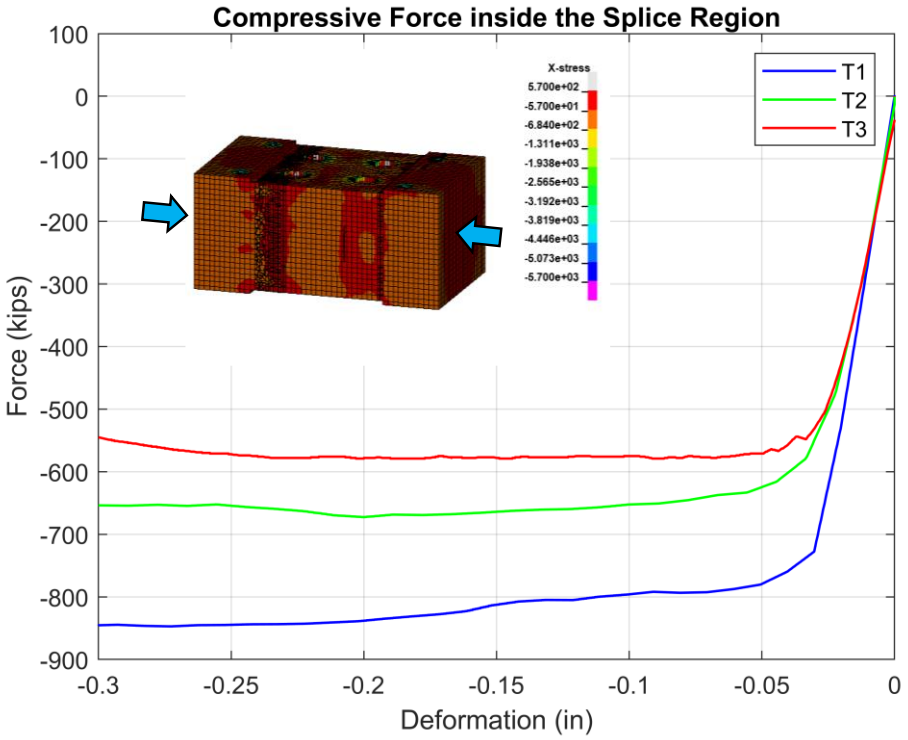


Figure 5-15. Compressive Force Development of Concrete (Section Cut in the middle)

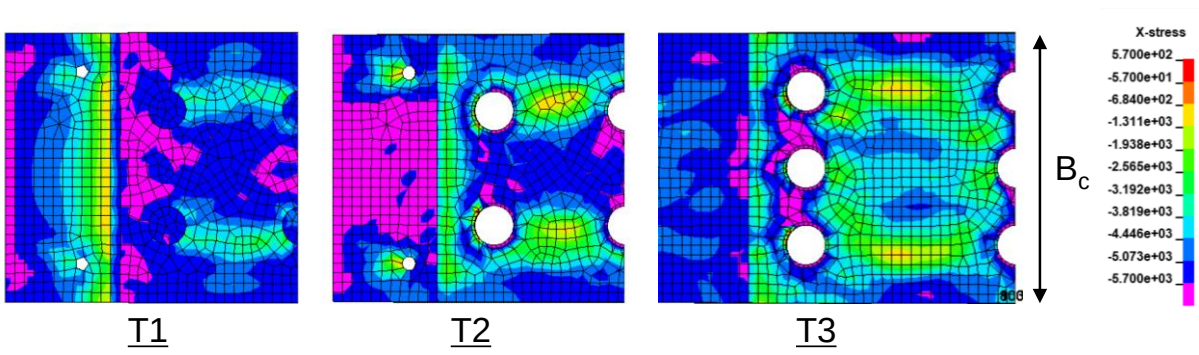


Figure 5-16. Compressive Stresses of Concrete in Finite Element Models (Top View)

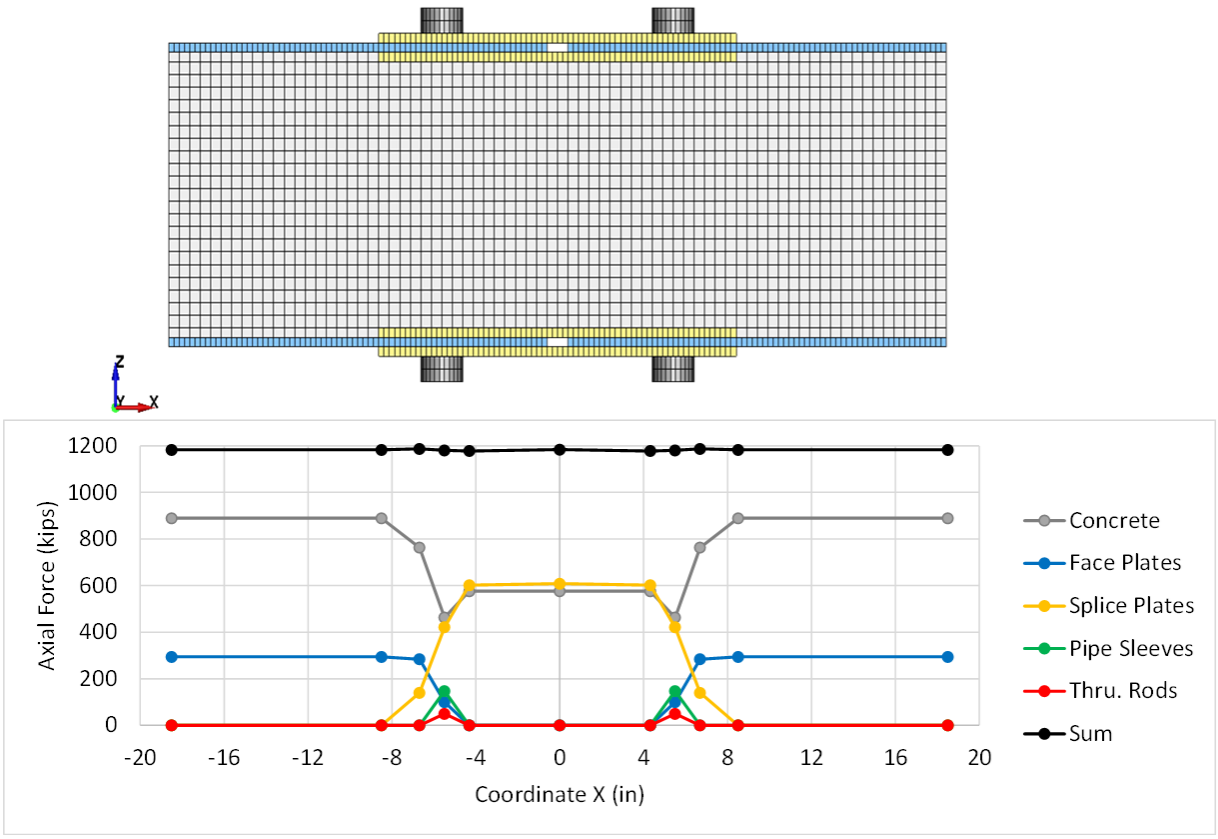


Figure 5-17. Axial Compression Force in Various Elements Along the Length of the Splice Region for Specimen T3, from Finite Element Analysis

Table 5-2. Summary of Spring Properties

(a) Specimen T2

ITEM	Spring Name	Hardening Model	Spring Length (in)	P1 (kips)	P2 (kips)	P3 (kips)	P4 (kips)	Δ1 (in)	Δ2 (in)	Δ3 (in)	Δ4 (in)
A	Friction	Isotropic	13.856	122.0	122.0	-		0.001	3.500	-	-
B	Bearing	Isotropic	-	249.0	298.8	373.5	373.5	0.190	0.380	0.76	3.50
C	Net Section	Kinematic	2.250	555.2	731.4	731.4	-	0.005	0.338	3.50	-
D	Gross Section	Isotropic	107.000	661.5	661.5	-	-	0.214	3.500	-	-
E	Concrete1_Compression	Concrete	107.000	897.8	897.8	-	-	0.321	3.500	-	-
F	Concrete1_Tension	Concrete	107.000	89.8	0.0	0.0	-	0.014	0.214	3.50	-
G	Concrete2_Compression	Concrete	18.000	655.2	655.2	-	-	0.054	3.500	-	-
H	Concrete2_Tension	Concrete	18.000	65.5	0.0	0.0	-	0.002	0.036	3.50	-

(b) Specimen T3

ITEM	Spring Name	Hardening Model	Spring Length (in)	P1 (kips)	P2 (kips)	P3 (kips)	P4 (kips)	Δ1 (in)	Δ2 (in)	Δ3 (in)	Δ4 (in)
A	Friction	Isotropic	10.4	170.0	170.0	-	-	0.001	3.500	-	-
B	Bearing	Isotropic	-	466.9	560.3	700.3	700.3	0.190	0.380	0.76	3.50
C	Net Section	Kinematic	2.8	466.6	614.7	614.7	-	0.006	0.413	3.50	-
D	Gross Section	Isotropic	107.0	661.5	661.5	-	-	0.214	3.500	-	-
E	Concrete1_Compression	Concrete	107.0	897.8	897.8	-	-	0.321	3.500	-	-
F	Concrete1_Tension	Concrete	107.0	89.8	0.0	0.0	-	0.014	0.214	3.50	-
G	Concrete2_Compression	Concrete	18.0	579.0	579.0	-	-	0.054	3.500	-	-
H	Concrete2_Tension	Concrete	18.0	57.9	0.0	0.0	-	0.002	0.036	3.50	-

(c) Specimen T6

ITEM	Spring Name	Hardening Model	Spring Length (in)	P1 (kips)	P2 (kips)	P3 (kips)	P4 (kips)	Δ1 (in)	Δ2 (in)	Δ3 (in)	Δ4 (in)
A	Friction	Isotropic	25.9	200.0	200.0	-	-	0.001	4.040	-	-
B	Bearing	Isotropic	-	560.3	672.3	840.4	840.4	0.190	0.380	0.76	4.04
C	Net Section	Kinematic	5.3	578.8	762.6	762.6	-	0.011	0.788	4.04	-
D	Gross Section	Isotropic	100.0	661.5	661.5	-	-	0.200	4.040	-	-
E	Concrete1_Compression	Concrete	100.0	945.0	945.0	-	-	0.300	4.040	-	-
F	Concrete1_Tension	Concrete	100.0	94.5	0.0	0.0	-	0.014	0.200	4.04	-
G	Concrete2_Compression	Concrete	25.0	655.2	655.2	-	-	0.075	4.040	-	-
H	Concrete2_Tension	Concrete	25.0	65.5	0.0	0.0	-	0.003	0.050	4.04	-

5.2.6 Loading Protocol

5.2.6.1 Displacement History from Tests

To compare with the test results, displacement histories from the tension tests were used to conduct the simplified spring analysis. More specifically, the recorded SP histories from the tension tests were used because they include the deformation of the entire specimen, including both inside and outside the splice region, which is consistent with the spring model presented above.

Figure 5-18 shows the displacement history used in Specimen T2. Note that the given displacement in the negative direction (compression) is much smaller than in the positive one (tension).

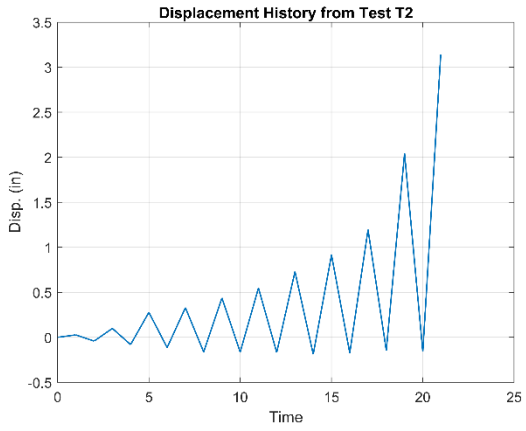


Figure 5-18. Displacement History from Specimen T2

5.2.6.2 Symmetric Displacement History

For comparison, to investigate what would be the behavior if there was no limitation on the compressive and tensile loads that could be applied to the bolted splice during the test, a symmetric displacement history is also considered. In this displacement history, the given displacement in the negative direction (compression) is always equal to the positive one (tension). Figure 5-19 shows a symmetric displacement

history that mirrors in the negative direction the displacements reached in the positive direction for Specimen T2.

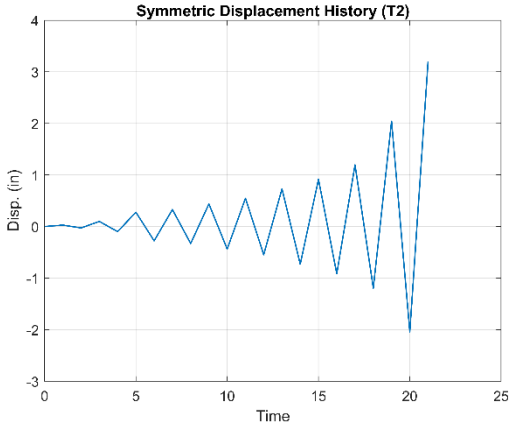


Figure 5-19. Symmetric Displacement History for Specimen T2

5.2.7 Analysis Results of Specimens T1 and T2 (Displacement History from Test)

5.2.7.1 Lower-Bound Analysis

The design limit state of Specimens T1 and T2 was the bearing strength of the connection. Given that specimens T1 and T2 are identical except for the type of bolts used in the splice region (i.e., blind bolts vs threaded rods with pipe sleeves), the spring model remains the same for both specimens. Additionally, since specimen T2 was tested until failure (contrary to T1), the test results of specimen T2 were used to compare with the results obtained from the simplified spring analysis result.

To compare the simplified spring model with the test results, the SP history (Figure 5-20) from the test was used in the spring analysis. However, it was discovered that there was a drift in the recorded SP history, with some negative deformation values being smaller than the actuator displacement, which is not

physically possible. To address and correct this drift issue, a moving average technique was implemented to shift the SP history.

Figure 5-21 provides the curves L1 and L2, which represent the moving averages for the SP and actuator displacement histories, respectively. To obtain the modified SP history, the difference between curves L2 and L1 (labelled L2 - L1) was calculated, resulting in a new curve with corrected Δ values. By varying the correction of the Δ values by various percentages, ranging from 0.5 to 1.0 times the magnitude of (L2-L1), four modified SP histories were obtained, plotted in Figure 5-22.

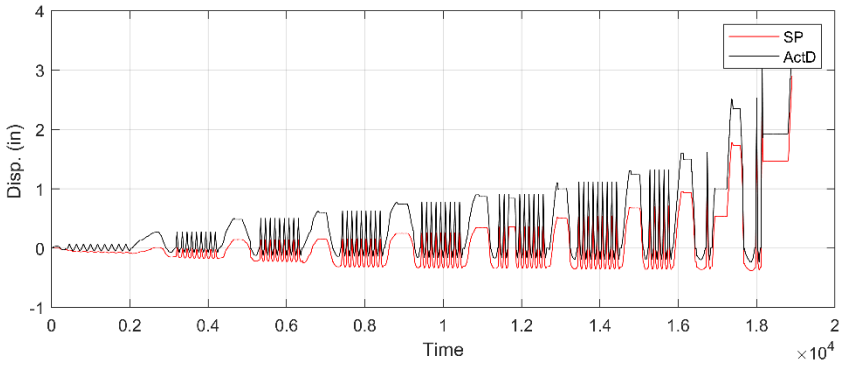


Figure 5-20. Comparison of SP and Actuator Displacement Histories for Specimen T2

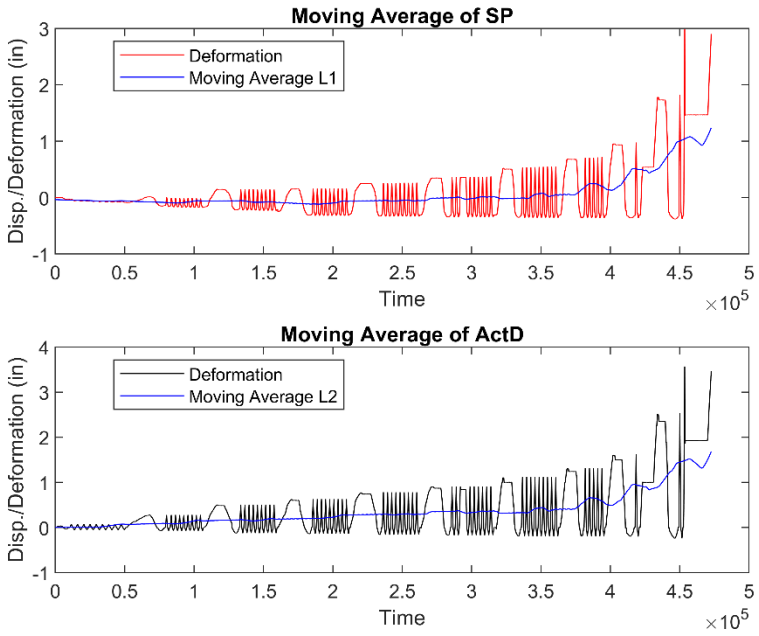


Figure 5-21. Moving Average of SP and Actuator Displacement Histories for Specimen T2

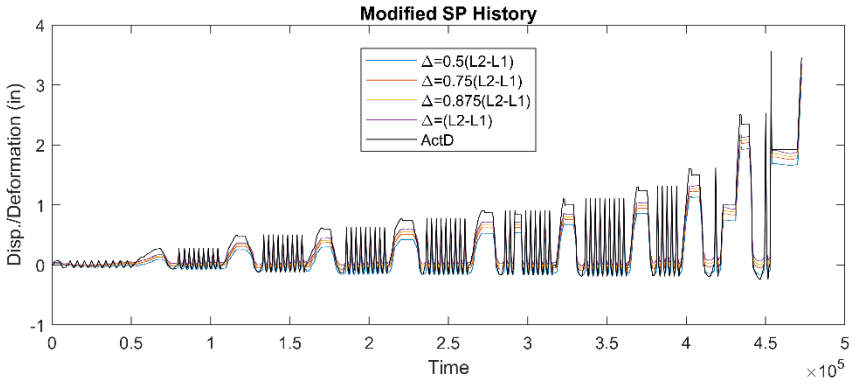


Figure 5-22. Modified SP Histories for Specimen T2

A total of sixteen spring models were analyzed and compared by varying the Δ values, hook values, and gap values. Table 5-3 presents the parameters used in the last three specific spring models considered (which gave better results), while Figure 5-23 shows the comparison between the force-displacement curves

obtained for the spring model and the corresponding test results. For the detailed spring analysis results presented in this section, the "T2_L16" model was used.

Table 5-3. Spring Name and Length

Model	Hook	Gap	Δ Values
T2_L14	0.125”	0.375”	Δ=(L2-L1)x0.875
T2_L15	0	0.5”	Δ=(L2-L1)x0.5
T2_L16	0.08"	0.42"	Δ=(L2-L1)x0.75

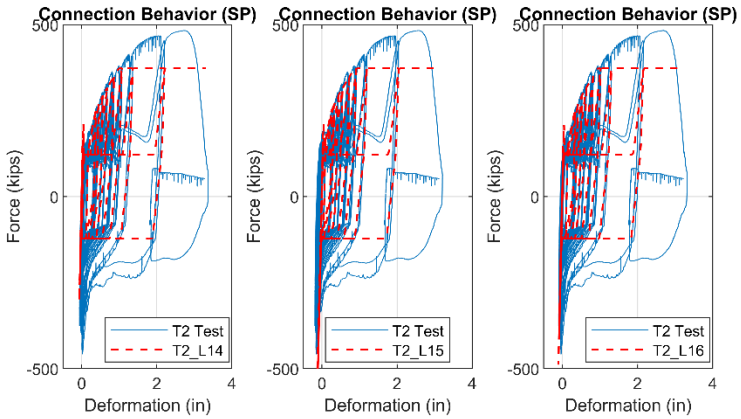


Figure 5-23. Different Spring Models with Test Results

Figure 5-24 shows the resulting cyclic behavior of the Lower-Bound spring model in Specimens T2. Figure 5-24 (i) shows the applied displacement history. The global response of spring analysis is shown in Figure 5-24 (h), and the maximum tensile force is 373.5 kips, which is the ultimate bearing strength given in Table 5-2.

The results for the friction and bearing springs are shown in Figure 5-24 (a) and (b), and they are the primary energy-dissipating components of the total spring model in this case. Note that due to the high stiffness of the concrete spring, the bearing strength was far from developed in compression. Figure 5-24 (c) and (d) are the net and gross section deformation of the steel plates, respectively, and they both remain elastic under cyclic loading in this case. All concrete spring results are shown in Figure 5-24 (e) and (f). As shown in the

figures, all concrete springs performed in a predominantly compression behavior, and their compressive strengths were not reached due to the limited amplitude of the given displacement protocol.

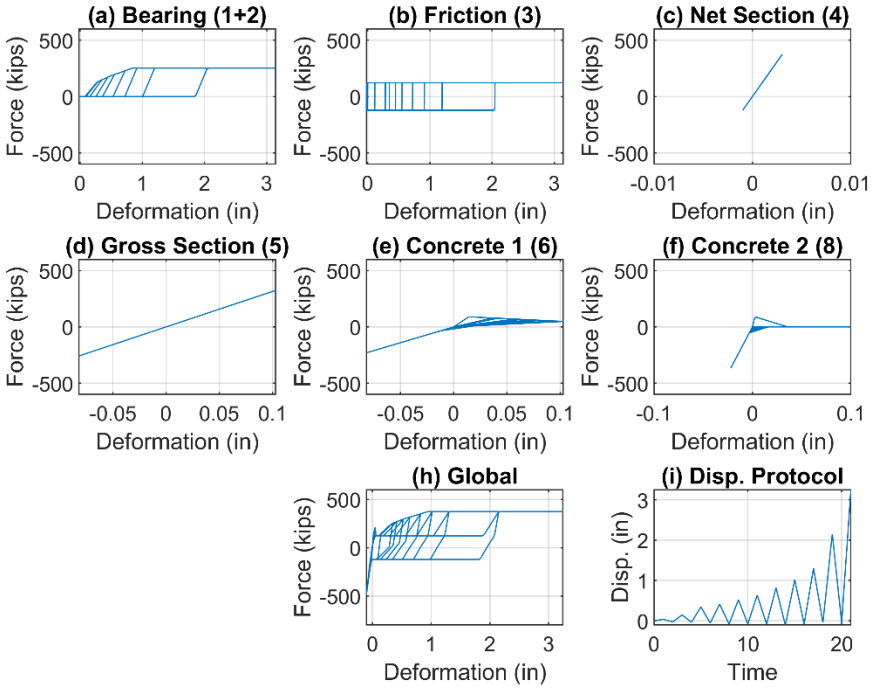


Figure 5-24. Analysis Results of Lower-Bound Spring Model (Specimens T1 and T2)

Figure 5-25 shows the comparison between the test and the analysis. The ultimate tensile strength obtained in the test is higher than the one predicted by the simplified spring analysis, as Specimen T2 develop a bearing strength equivalent to $3.84dtF_u$, whereas the bearing strength considered in the spring model was limited to 3.00dtFu. However, the spring model captures well the overall inelastic behavior of the specimen upon load-reversal, with a “plateau” when sliding occurs, until bolts reach the edge of holes elongated in previous cycles and develop anew their bearing strength. While it may be tempting in this case to attribute the value of "$3.84dtF_u$" obtained in the test to represent the combined friction and bearing strength of the connection, it might not be the case. Note that previous research conducted by Frank and Yura (1981)

suggested that variations in torquing of bolts did not significantly increase the capacity of the connection (although at low bearing deformations, below the ultimate bearing strength, some difference in the force resisted occurs as a function of clamping forces values, as confirmed by Gomes et. al. (2019). To study the effect of pretension on the combined friction and bearing strength, different pretension values will be applied in the Finite Element Analyses presented in a later section.

Figure 5-26 shows experimental and analytical elastic stiffness for spring model T2 before sliding of the connection. In this figure, values of elastic stiffness were shown on the spring elements that contributed to the total stiffness calculation, namely those in two spring groups connected in series. The resulting elastic stiffness of the spring model is determined to be 8586 k/in, which matches well the average stiffness observed from the test result.

It is also interesting to compare this value with the axial stiffness of the entire specimen if considering it as a continuous member (i.e., without the bolted splice). The elastic axial stiffness of the entire composite section before cracking can be calculated as $(E_sA_s+E_cA_c)/L$. Based on the geometries of the test specimens and the concrete cylinder tests, the following parameters can be determined: E_s= 29000 ksi, A_s= 10.5 in², E_c= 4303 ksi, A_c= 157.5 in², L= 125 in. Substituting these values into the formula, the axial stiffness is calculated to be 7858 k/in. This stiffness is 8.5% lower than obtained from the above spring model of the connection and from the one obtained from the test. This difference can be attributed to the high stiffness contributed by the friction spring within the splice region, which is the primary source of stiffness in the spring model compared to the stiffness of the entire specimen considered as a continuous member.

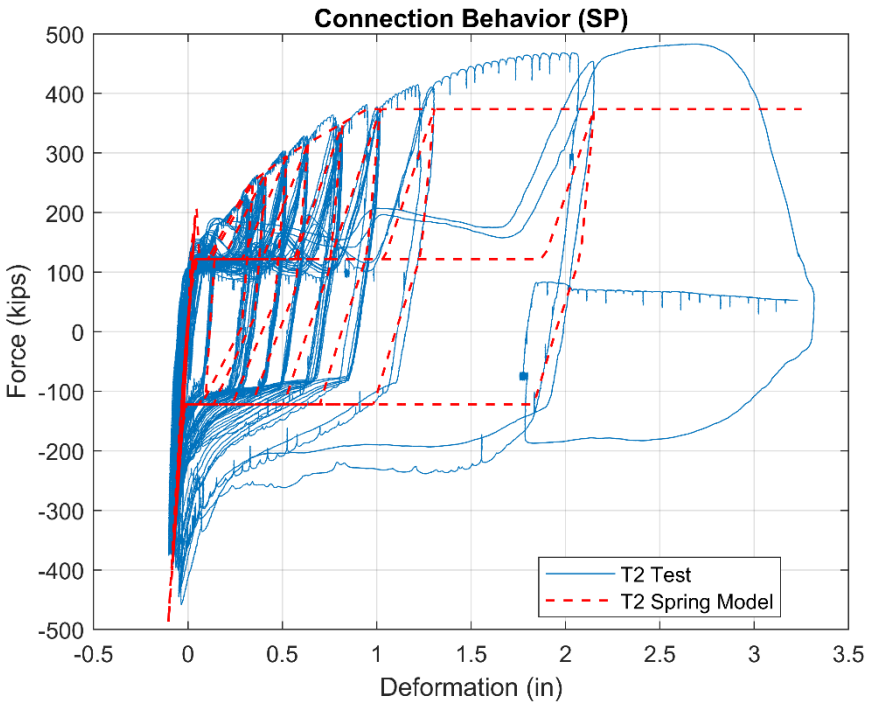


Figure 5-25. Comparison between Test Result and Lower-Bound Spring Analysis (Specimens T2)

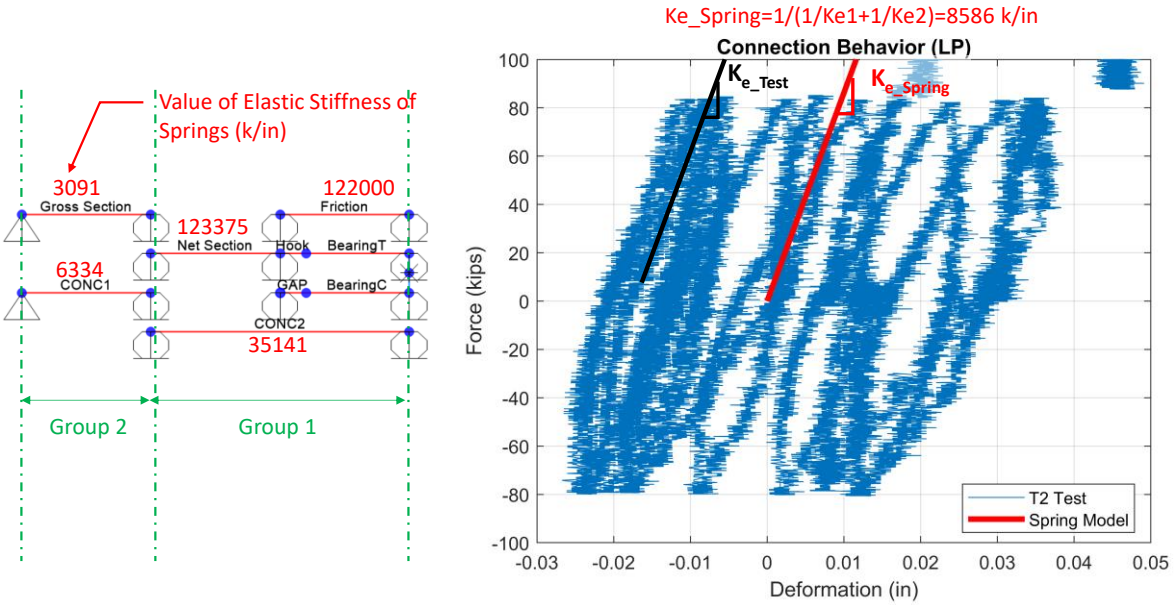


Figure 5-26. Elastic Stiffness of Simplified Spring Model T2

5.2.7.2 Upper-Bound Analysis

Figure 5-30 shows the cyclic analysis results of the Upper-Bound spring model in Specimens T1 and T2. As shown in Figure 5-30 (h), the maximum tensile force is 661.5 kips, which is the yield strength of the gross section spring given in Table 5-2.

Results for the friction, bearing, and net section springs are shown in Figure 5-24 (a), (b), and (c). In this case, the bearing spring did not deform under cyclic loadings due to the high stiffness provided by the net section spring. It can be observed that the summation of the slip-critical strength of friction and net section springs (see P_1 values in Table 5-2) is about 677.2 kips, which is slightly larger than the gross section yielding (661.5 kips). Therefore, the gross section spring (Figure 5-30 (d)) yielded first in tension under the cyclic analysis and developed a full hysteretic behavior. All concrete spring results are shown in Figure 5-30 (e) and (f), and their compressive strengths were again not reached due to the limited amplitude of the displacement protocol. A comparison of the Lower and Upper-Bound models is provided in Figures 5-28 and 5-29 show the comparison between the Upper-Bound model and the test result. From the observation, it can be concluded that the analysis results from the Lower-Bound model exhibit a better match with the test results. This implies that the net section stresses are more likely to develop after bearing of the bolt occurs.

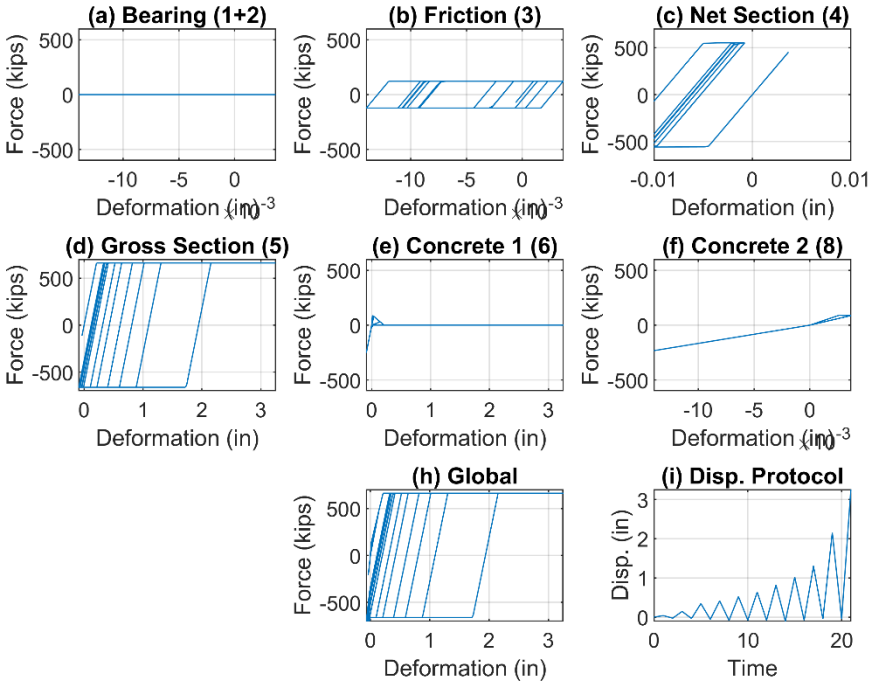


Figure 5-27. Analysis Results of Upper-Bound Spring Model (Specimen T2)

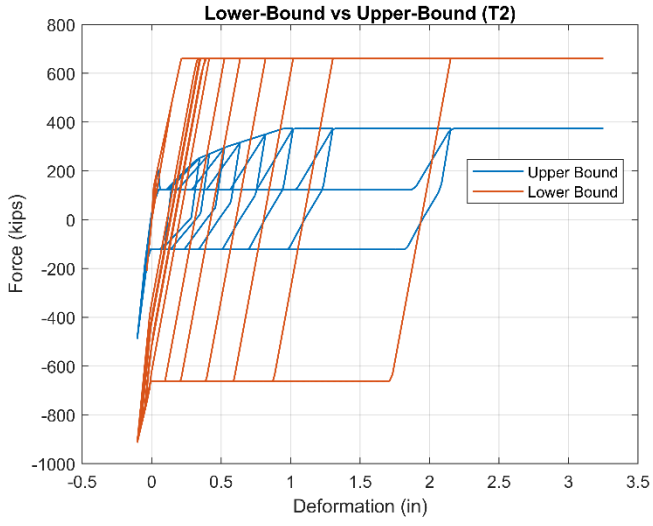


Figure 5-28. Comparison of Lower and Upper-Bound (Specimens T2)

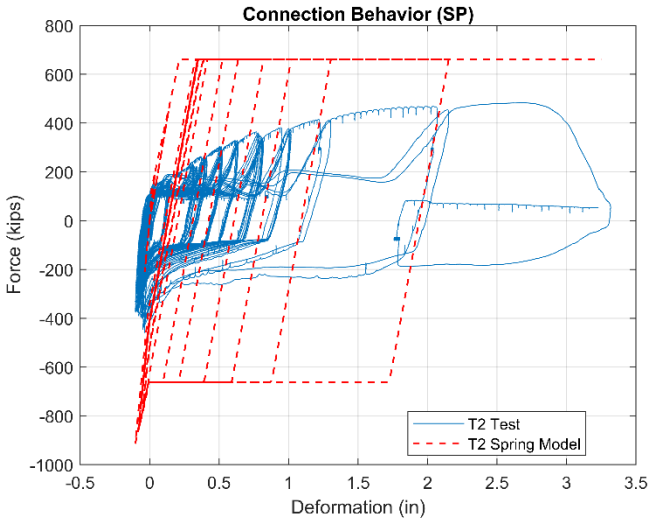


Figure 5-29. Comparison between Test Result and Upper-Bound Spring Analysis (Specimens T2)

5.2.8 Analysis Results of Specimen T3 (Displacement History from Test)

5.2.8.1 Lower-Bound Analysis

For Specimen T3, the design limit state was the slip-critical resistance of the connection. After the connection slips, the connection was designed to undergo significant deformation and failure in the net section area. Following the previous approach, the shifting value Δ for the modified SP history was set to be "L2-L1", and the hook and gap values were set to be 0.5 in. and 0, respectively, in the T3 spring model.

Figure 5-30 shows the resulting cyclic behavior of the Lower-Bound spring model in Case 2B, and Figure 5-30 (i) and 18 (h) show the displacement protocol and the global response. In the Figure, the maximum tensile force is 614.7 kips, which is the strength of the net section rupture given in Table 5-2.

The results for the friction and bearing springs are shown in Figure 5-30 (a) and (b), and the response of the net section spring is shown in Figure 5-30 (c). Note that the net section yielding strength (466.59 kips) is larger than the slip-critical strength (170 kips) in this case. Therefore, the connection slipped first, then

the bearing and net section springs deformed subsequently. In this analysis, the plastic response was mainly contributed by friction, bearing, and net section springs, and all other springs remained elastic.

It is essential to keep track of the ductility developed in the net section spring since net section rupture is a brittle failure mode that should be avoided. Figure 5-31 shows the detailed net section spring analysis under each cycle. However, it is observed that during loading Cycle 11 and the final step of the analysis, the net section strain ranging from 0.25 to 0.75, which exceeds the maximum strain capacity of the steel and indicates that the net section has undergone fracture. As such, results for the spring model presented in this analysis concur with the occurrence of net section fracture during the test of Specimen T3.

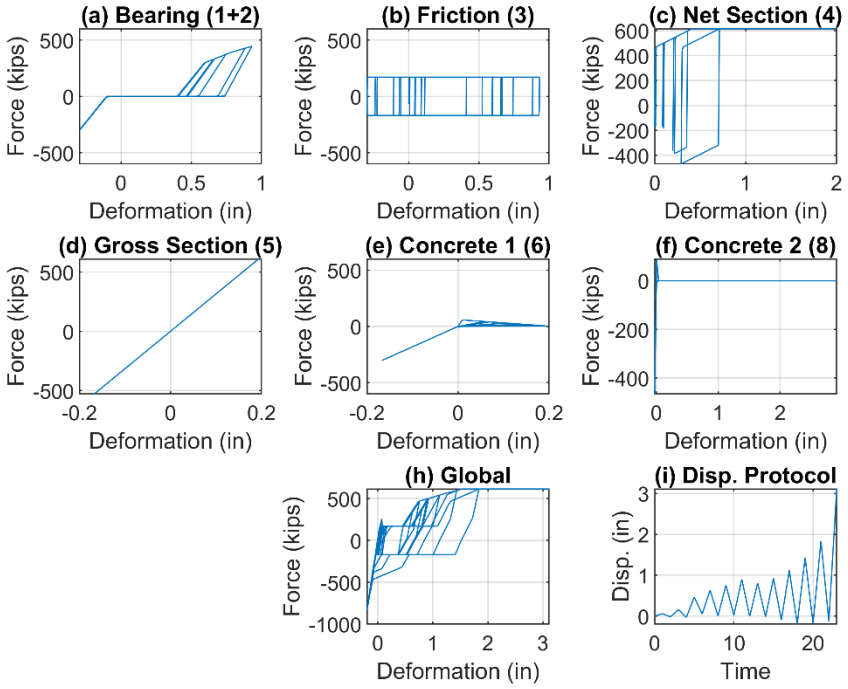


Figure 5-30. Analysis Results of Lower-Bound Spring Model (Specimen T3)

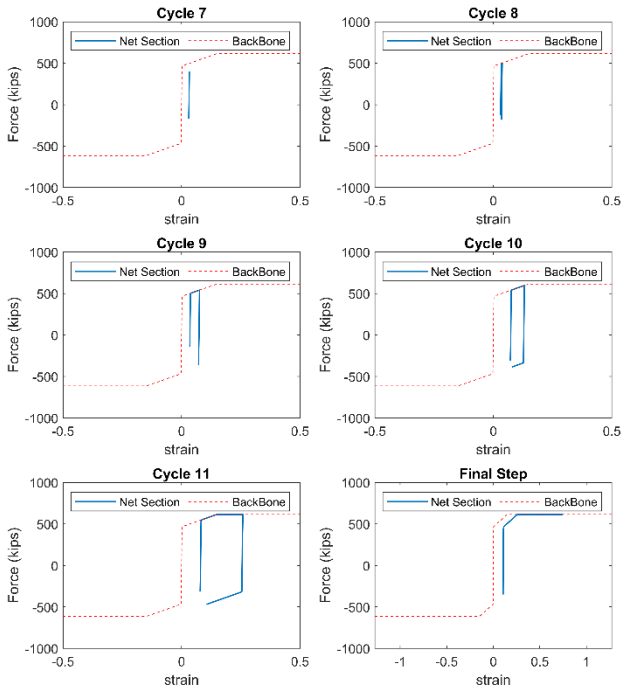


Figure 5-31. Net Section Spring Response at Each Cycle (T3_Lower-Bound)

Figure 5-32 shows the comparison between the experimental and analysis results. The spring model captures well the overall inelastic behavior of the specimen. The hysteretic curves incorporate a "plateau" that models the sliding behavior observed during the test. Furthermore, the spring model simulates the combined development of bearing and net section strengths, resulting in a hysteresis response that closely matches the experimental results. Notably, the peak force 622 kips reached during the test closely aligns with the peak force obtained from the simplified spring model.

Figure 5-33 shows the elastic stiffness values of the individual springs that contribute to total stiffness before sliding of the connection. Similarly to the calculation for Specimen T2, the elastic stiffness of the spring model is 8547 k/in. The figure also presents the elastic stiffness observed during the first 10 cycles of the test. Note that the experimentally obtained stiffness was not constant during these cycles. Three

stiffness values (K_{e1} to K_{e3}) are shown in the figure, ranging from 53641 to 5370 k/in. It is speculated that the high initial stiffness observed (K_{e1}) at the start of the test could be attributed to the fact that the specimen was initially resting on the reaction frame designed to prevent upward movement of the specimen, which could have provided additional frictional stiffness to initiate movement of the specimen (although this cannot be proven). However, and more importantly, without considering this transient stiffness at the beginning of the test, the elastic stiffness of the test ranged from 5370 to 11870 k/in, which brackets the value from the spring model.

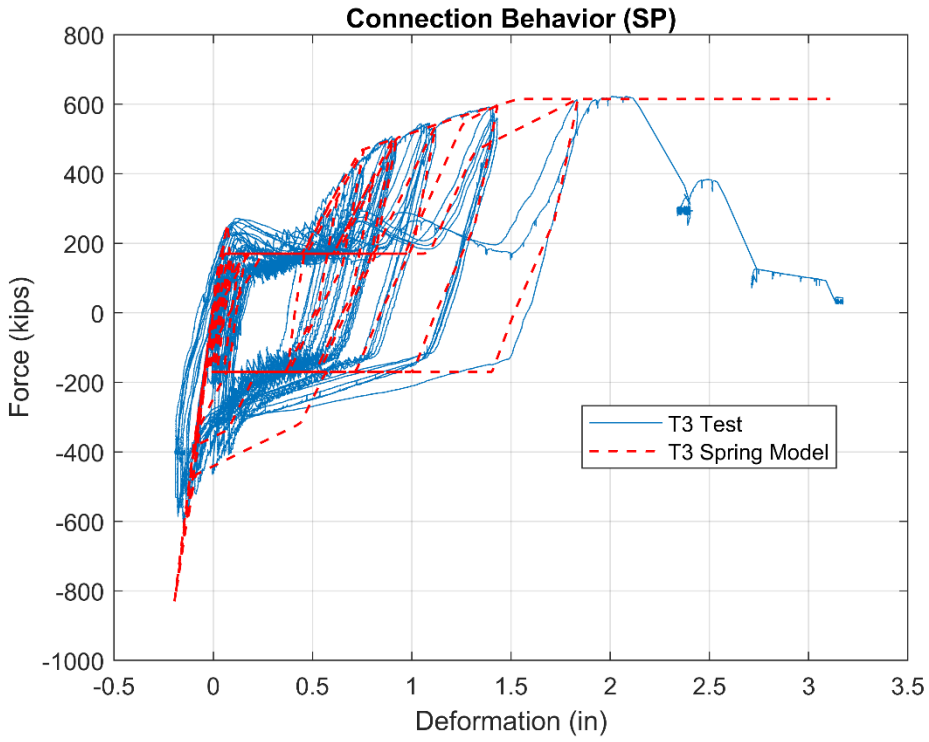


Figure 5-32. Comparison between Test Result and Simplified Spring Analysis (Specimens T3)

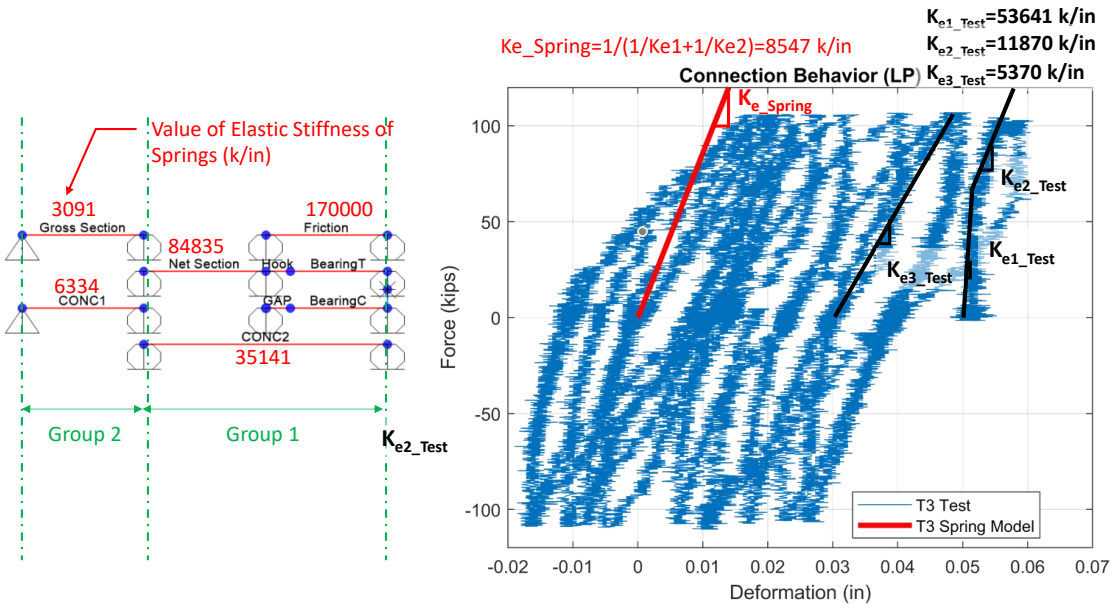


Figure 5-33. Elastic Stiffness of Simplified Spring Model T3

5.2.8.2 Upper-Bound Analysis

Figure 5-34 shows the cyclic analysis results of the Upper-Bound spring model in Specimen T3. Figure 5-34 (i) and (h) show the displacement protocol and the global response. The maximum tensile force is about 661.5 kips, which is the gross section yield strength given in Table 5-2.

Results for the friction, bearing, and net section springs are shown in Figure 5-34 (a), (b), and (c). Similarly, there was no significant contribution by the bearing spring because of the high stiffness of the net section spring. Here, as was the case for the Upper-Bound analysis in Specimens T1 and T2, the gross section spring (Figure 5-34 (d)) was the primarily energy-dissipating component. The comparison of the Lower and Upper-Bound models is provided in Figure 5-35, and Figure 5-36 shows the comparison between the Upper-Bound model and the test result. Similar as mentioned before, the Lower-Bound model provides more accurate analysis compared to the test result.

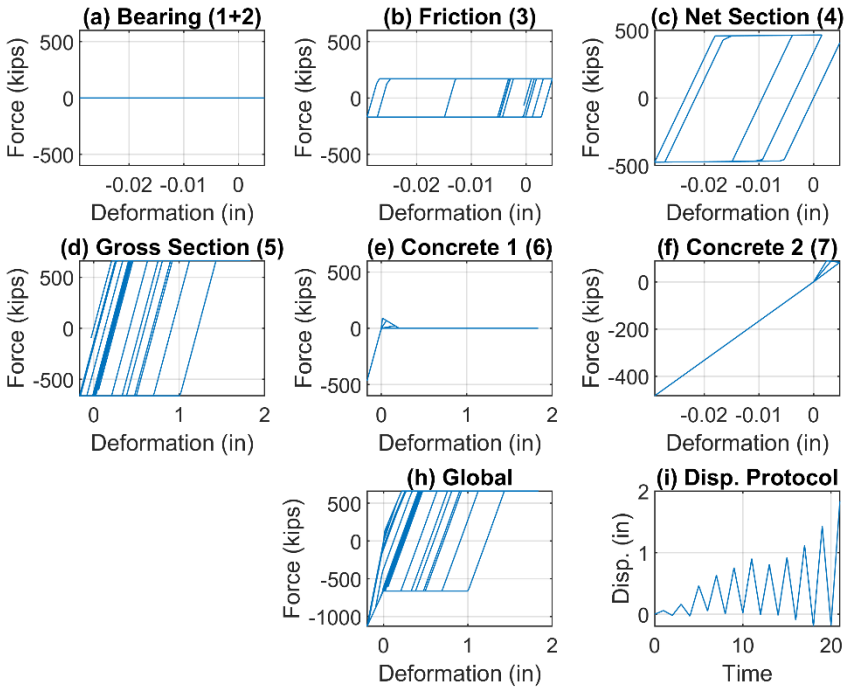


Figure 5-34. Analysis Results of Upper-Bound Spring Model (Specimen T3)

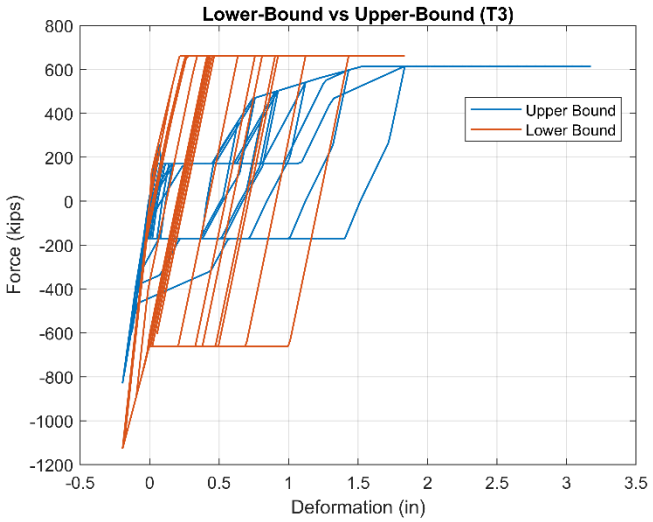


Figure 5-35. Comparison of Lower and Upper-Bound (Specimen T3)

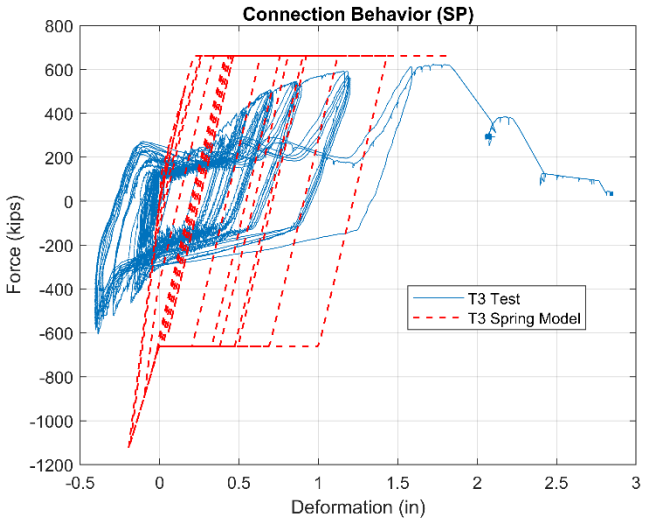


Figure 5-36. Comparison between Test Result and Upper-Bound Spring Analysis (Specimens T3)

5.2.9 Analysis Results of Specimens T5 and T6 (Displacement History from Test)

5.2.9.1 Lower-Bound Analysis

The design limit state for Specimens T5 and T6 was the yield strength of the gross section. The connection here was designed to resist seismic loads; therefore, it is important to investigate the detailed behavior when the connection reaches the full yielding of the faceplates. The hook and gap values are 0.25 in. in the model, and the original SP history, without any modification, was used in this spring analysis.

Figure 5-37 shows the cyclic behavior of the Lower-Bound spring model in Specimens T5 and T6. The maximum tensile force is 661.59 kips, which is close to the gross section yielding strength given in Table 5-2.

The results of the friction and bearing springs are shown in Figure 5-37 (a) and (b). Figure 5-37 (c) and (d) show the net and gross section springs results. After the connection underwent sliding, the inelastic response primarily occurred in the gross section spring. After the sliding of the connection, both bearing and net section kept increasing until the gross section reached the yielding strength, 661.5 kips. Note that the net section experienced strain-hardening, but it remained elastic upon unloading while gross section yielding occurred in tension and compression. This net section spring essentially behaved over an extended elastic range.

The gross section spring developed a full hysteresis loop, representing the cyclic deformation and energy dissipation within the connection. Note that the gross section spring was an elasto-perfectly plastic model, i.e., not given the ability to strain harden.

Similarly, Figure 5-38 shows details of the net section spring under each cycle. In the spring model, the maximum net section strain was found to be 0.127. This value can be compared to the maximum net section strain obtained from the Lower-Bound spring model in test T3, which exceeds 0.5. This allows for a comparison of net section strain between the failure mechanisms of the connection, specifically whether it is primarily governed by net section fracture (T3) or gross section yielding (T5 and T6).

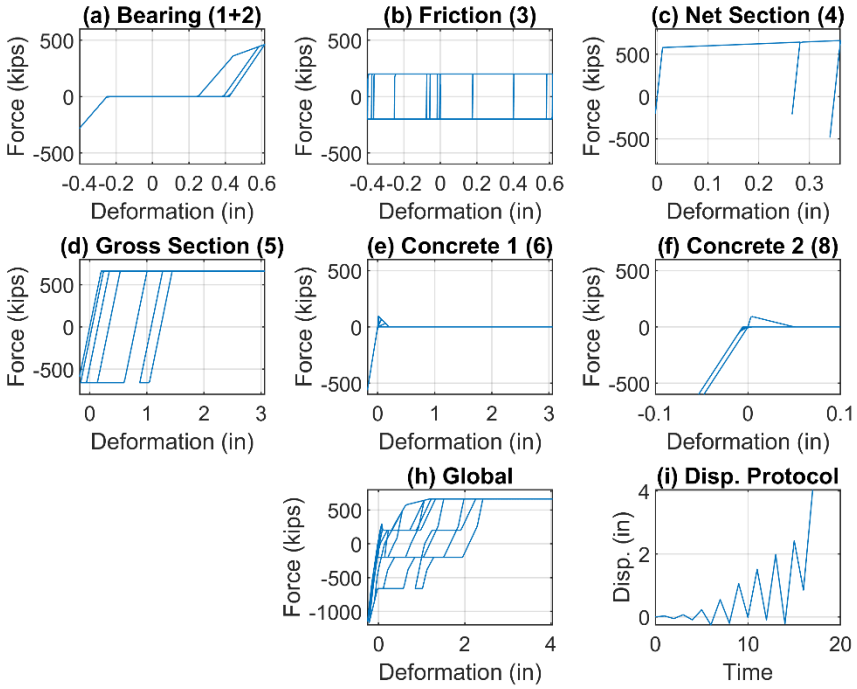


Figure 5-37. Analysis Results of Lower-Bound Spring Model (Specimens T5 and T6)

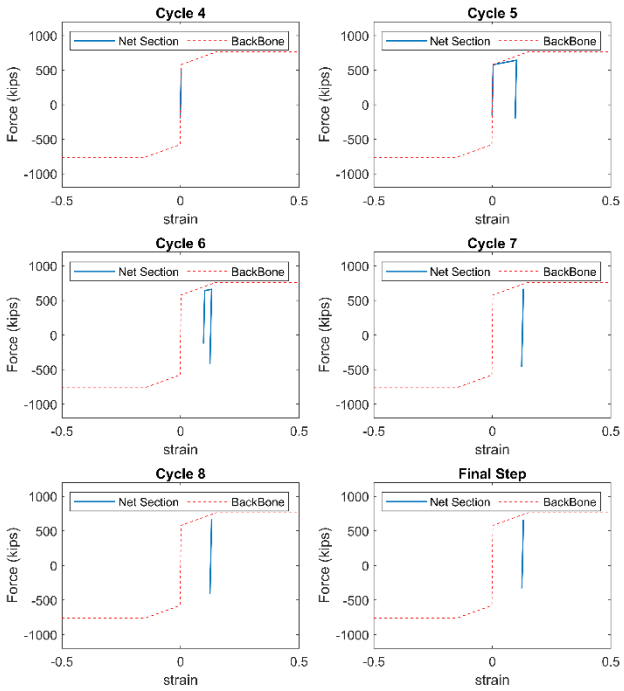


Figure 5-38. Net Section Spring Response at Each Cycle (Specimens T5 and T6_Lower-Bound)

Figure 5-39 shows the comparison between the test and the analysis. The peak force recorded during the test, reaching 650 kips, is close to the peak force of 661.5 kips obtained from the simplified spring model.

Figure 5-40 shows the elastic stiffness values of the individual springs before sliding of the connection, and used to calculate the total elastic stiffness of the spring model of 8966 k/in. Similar to the findings for Specimen T3, the elastic stiffness during the initial 5 cycles of the test is not constant from the test results of Specimens T5 and T6 (Figure 5-41. The stiffness values (K_{e1} to K_{e3}) of Specimen T5 are shown in the figure, ranging from 29555 to 4089k/in, while the stiffness values (K_{e1} to K_{e2}) of Specimen T6 are 34028 and 4187 k/in. Note the value of K_{e1} is dismissed here for the same reasons provided earlier for Specimen T3. It can be observed that the elastic stiffness can vary between Specimens T5 and T6, which were supposed to be identical since they were only different in the type of bolts used. The spring model appears to align better with the elastic stiffness of Specimen T5.

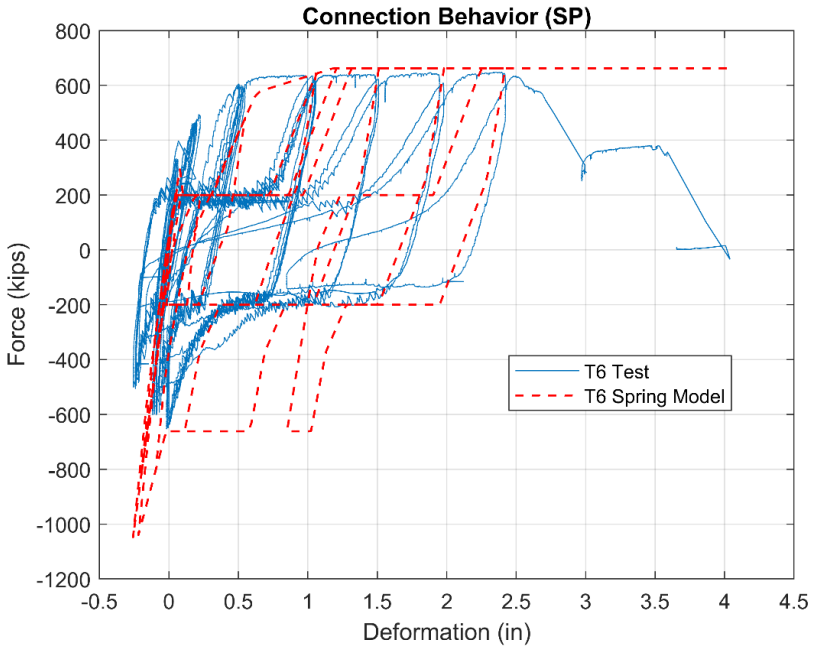


Figure 5-39. Comparison between Test Result and Simplified Spring Analysis (Specimens T6)

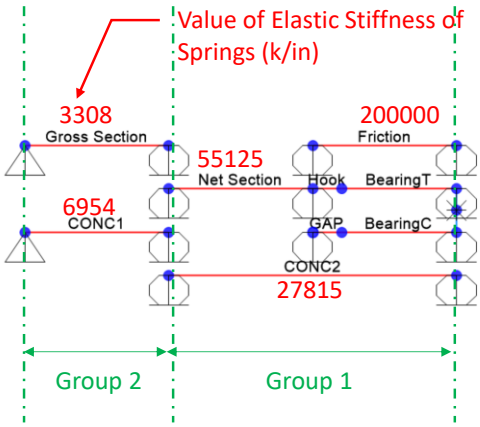
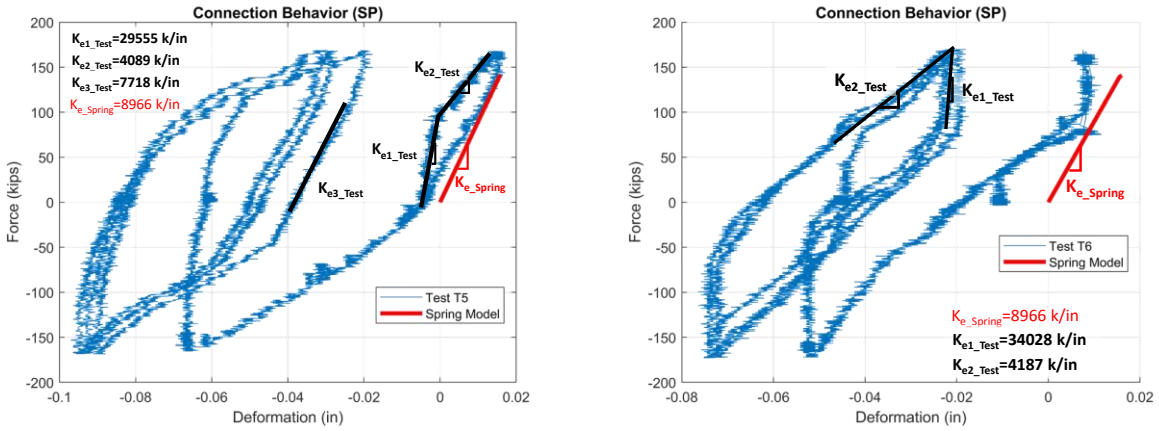


Figure 5-40. Elastic Stiffness of Simplified Spring Model



(a) Spring Model v.s. Specimen T5 (b) Spring Model v.s. Specimen T6

Figure 5-41. Elastic Stiffness Comparisons between Spring Model and Test Results

5.2.9.2 Upper-Bound Analysis

Figure 5-42 shows the cyclic analysis results of the Upper-Bound spring model in Case 1C/2C. Figure 5-42 (i) and A25 (h) show the displacement protocol and the global response. The maximum tensile force is about 671 kips, and the gross yield strength is given in Table 5-2.

The analysis result was similar to the Upper-Bound Analyses in Specimens T1, T2 and T3 (Figure 5-27 and Figure 5-34) since the gross section spring was the primary energy dissipating component. A comparison of the Lower and Upper-Bound models is provided in Figure 5-43, and Figure 5-44 shows the comparison between the Upper-Bound model and the test result. There is no significant difference between Lower and Upper-Bound analysis results in this case. However, again, the Lower-Bound model provides more accurate analysis compared to the test result.

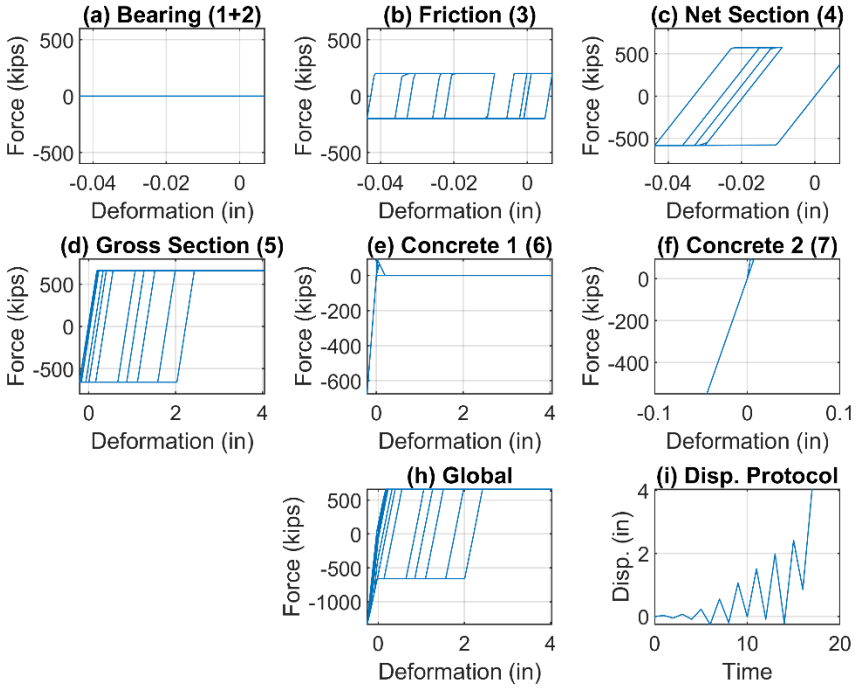


Figure 5-42. Analysis Results of Upper-Bound Spring Model (Specimens T5 and T6)

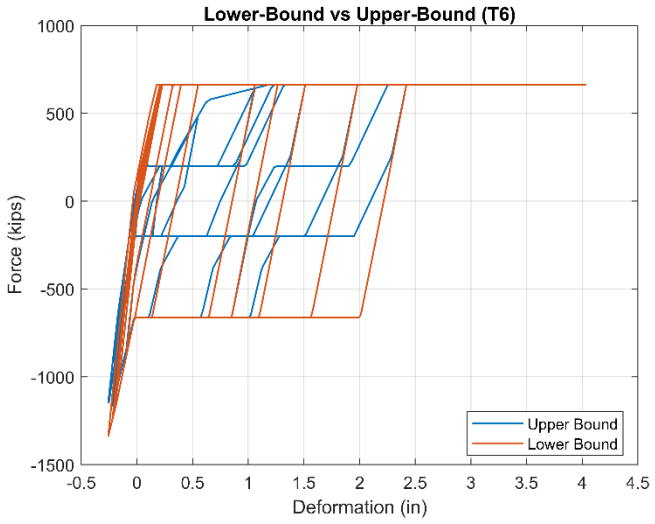


Figure 5-43. Comparison of Lower and Upper-Bound (Specimens T5 and T6)

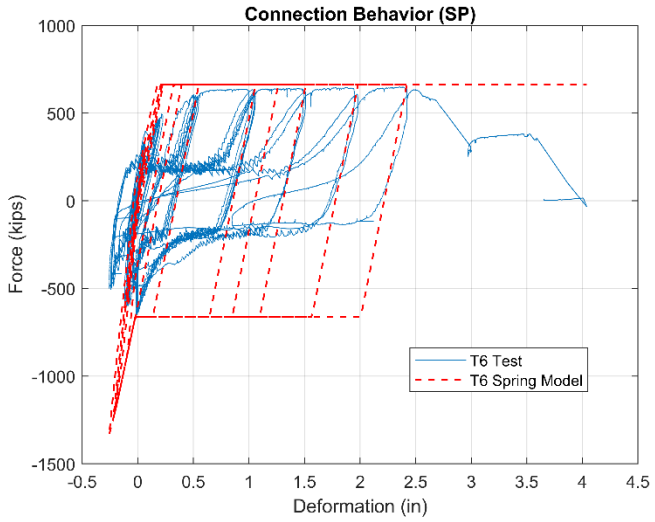


Figure 5-44. Comparison between Test Result and Upper-Bound Spring Analysis (Specimens T6)

5.2.10 Analysis Results of Specimens T1 and T2 (Symmetric Displacement History)

Analysis was conducted for the case mentioned in Section 5.2.6.2, whereby symmetric displacement histories are applied in tension and compression, to analyze the spring models under this worst case condition. Note that only the Lower-Bound analysis was performed for these spring models when subjected to symmetric displacement histories. These analyses provide a complementary evaluation of the possible connection's behavior during cyclic strain events.

5.2.10.1 Lower-Bound Analysis

Figure 5-45 shows the cyclic behavior of the Lower-Bound spring model in Specimens T1 and T2 using the displacement-controlled protocol. Different from the displacement history from the test, the compressive displacements in this case are the same as in their corresponding tension cycles. Therefore, large compressive strength was expected as shown in Figure 5-45 (h), and the maximum tensile and compressive forces are about 373.5 and -1271.3 kips.

The friction and bearing springs (Figure 5-45 (a) and (b)) were the primary energy-dissipating components in tension as the same in previous case in Section 5.2.7.1. However, in this scenario, the Concrete 2 spring developed a significant inelastic response in compression, leading to a large plastic response in the overall behavior of the connection in compression.

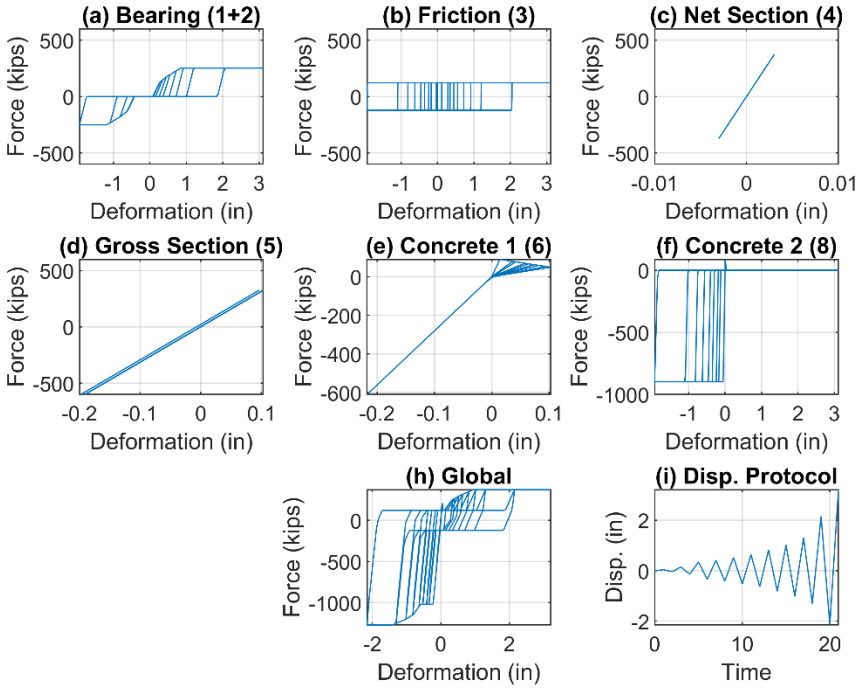


Figure 5-45. Analysis Results of Lower-Bound Spring Model (Specimens T1 and T2)

5.2.11 Analysis Results of Specimen T3 (Symmetric Displacement History)

5.2.11.1 Lower-Bound Analysis

Figure 5-46 shows the cyclic behavior of the Lower-Bound spring model in Specimen T3 using the displacement-controlled protocol. As shown in Figure 5-46 (h), the maximum tensile and compressive forces are about 614.7 and -1513 kips.

Figure 5-46 (a), (b), and (c) represent the response of the friction, bearing, and net section springs after analysis. The friction, bearing, and net section springs developed significant plastic deformations in both tension and compression. Similar to the analysis in Section 5.2.8.1, the net section spring developed a significant inelastic response. In addition, without the compression limit, the gross section and concrete 1 springs yielded in compression. (Figure 5-46 (d) and (f))

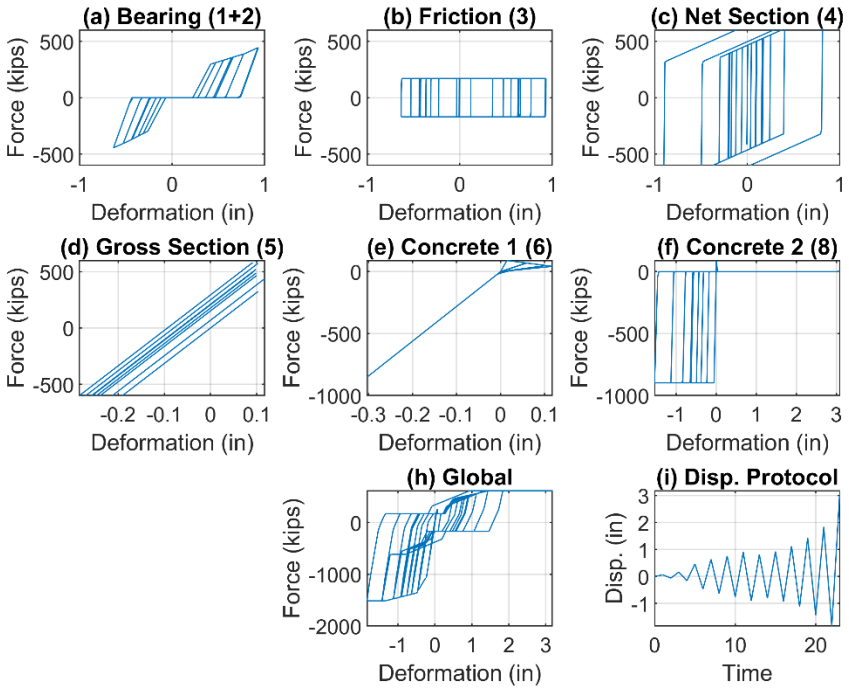


Figure 5-46. Analysis Results of Lower-Bound Spring Model (Specimen T3)

5.2.12 Analysis Results of Specimens T5 and T6 (Symmetric Displacement History)

5.2.12.1 Lower-Bound Analysis

Figure 5-47 shows the cyclic behavior of the Lower-Bound spring model in Specimens T5 and T6 using the displacement-controlled protocol. As shown in Figure 5-47 (h), the maximum tensile and compressive forces are about 661.59 and -1607 kips.

Figure 5-47 (a), (b), and (c) represent the response of the friction, bearing, and net section springs after analysis. Figure 5-47 (d), (e), (g) show the cyclic behavior of the gross section and concrete springs. The gross section spring contributed the primary energy dissipation in this simplified spring analysis. The bearing, friction, and net section springs also developed certain inelastic deformations. In this case, the net section spring was not limited to response along an extended elastic range after it strain hardened, which is a significant difference in behavior compared with the results for the previous displacement history protocol.

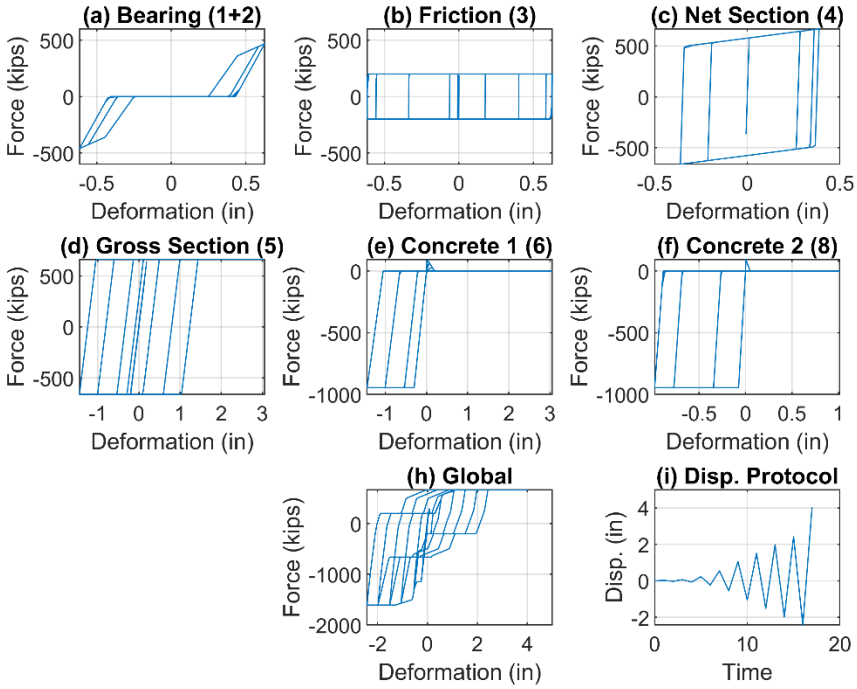


Figure 5-47. Analysis Results of Upper-Bound Spring Model (Specimens T5 and T6)

5.2.13 Summary of Spring Analysis

In this section, a series of simplified spring models were used to analyze the cyclic inelastic behavior of bolted C-PSW/CF connections.

A detailed bearing spring combined with gap/hook elements was proposed to model the development of bearing stresses with bolt hole deformations. In accordance to results from previous research, the ultimate combined friction and bearing strength was assumed to not increase with the pretension of bolts.

To better understand the load transfer sequence between the friction and net section stresses, a Lower-Bound and an Upper-Bound spring model were established to predict the possible maximum and minimum responses. Detailed models were developed by using different springs properties as mentioned in Section 5.2.5.2. All the spring properties used in the simplified spring analysis are summarized in Table 5-2. It was found that the Lower-Bound model matched better with the test results. This implies that the net section stresses are more likely to develop after bearing of the bolt occurs.

Two types of displacement histories were employed in the spring analyses: displacement histories from the tests and symmetric displacement histories. By using the displacement histories obtained from tests, the analysis results were compared with the test data. Friction strength used in the models were set to be the values observed experimentally. Other properties were set based on steel coupon and concrete cylinder values. The connection used for Specimens T1/T2, T3, and T5/T6, were analyzed, and the spring models proved capable of accurately capturing the overall inelastic response observed in the tests. By comparing the analysis results with symmetric displacement histories, the simplified spring models can be used to predict the behavior of the connections under cyclic behavior of that type. This displacement history also

served to show that the compressive strength of CPSW/CF connections is typically several times larger than the strength in tension, as explained in Sections 5.2.10 to 5.2.12.

All the analyses in this section were performed to show how they could be used to predict the axial behavior of the various bolted C-PSW/CF connections considered in this project. The proposed spring models presented here are relatively simple and could be used by engineers to investigate similar connections subjected to cyclic axial loading.

5.3 Finite Element Models for Tension Specimens

This section provides details of the Finite Element Models built to replicate the connection behavior observed in the tested tension specimens. These finite element models of the tested specimens were built in LS-DYNA (Hallquist 2006).

5.3.1 Finite Element Models

Figures 5-48 to 5-53 show the finite element models (and the various parts of the assembled models) for tension specimens T1 to T6. The reference coordinate system (X, Y, and Z directions) is also shown in the figures. These models consist of faceplates, splice plates, bolts or through rods with pipe-sleeves, infill concrete, and tie bars. For simplicity and efficiency, only the region near the connection was modeled.

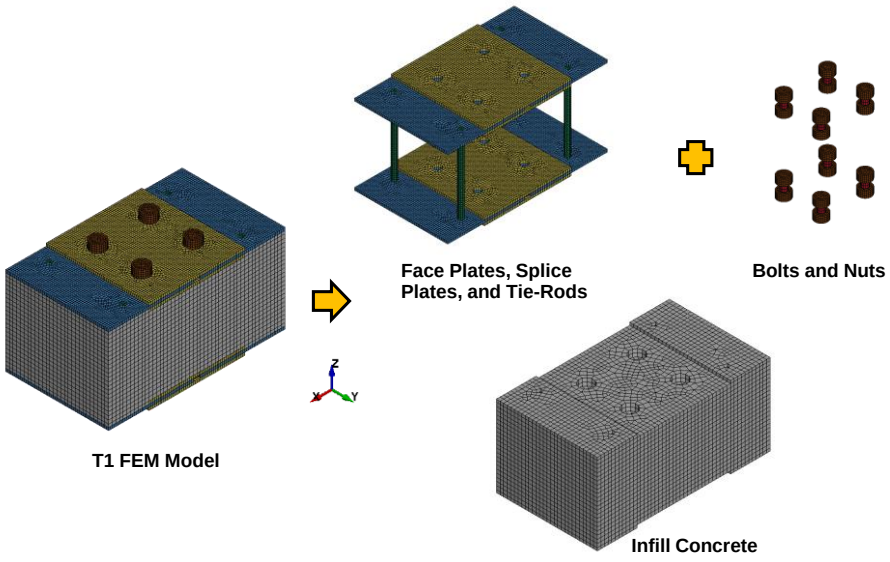


Figure 5-48. Finite Element Model of Specimen T1

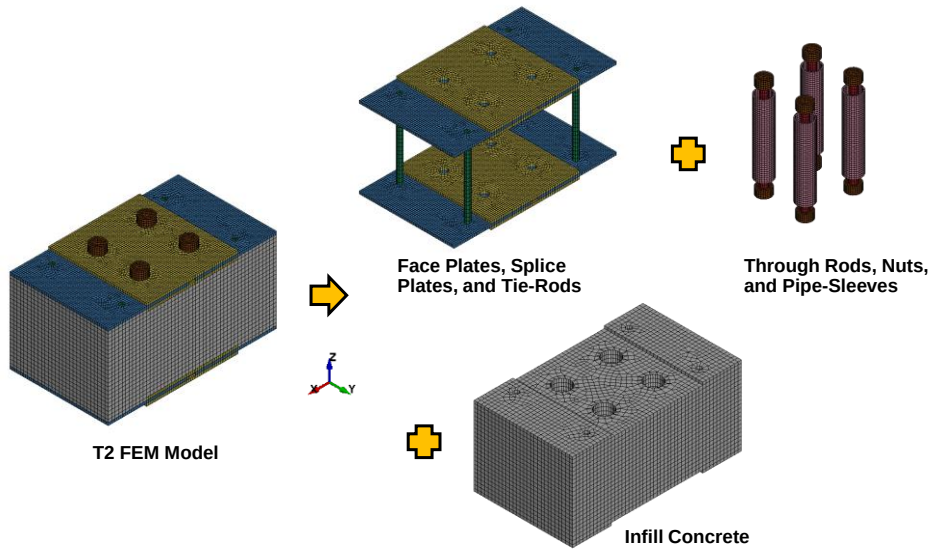


Figure 5-49. Finite Element Model of Specimen T2

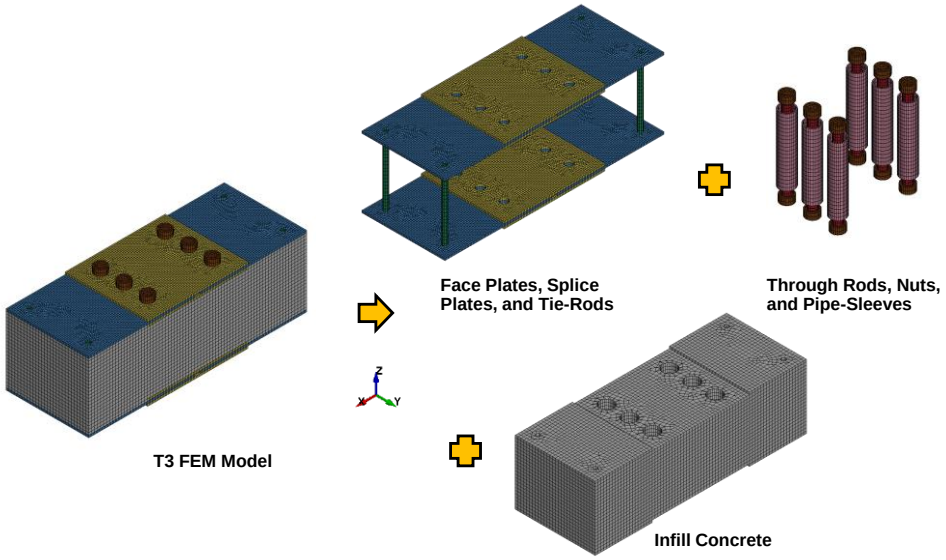


Figure 5-50. Finite Element Model of Specimen T3

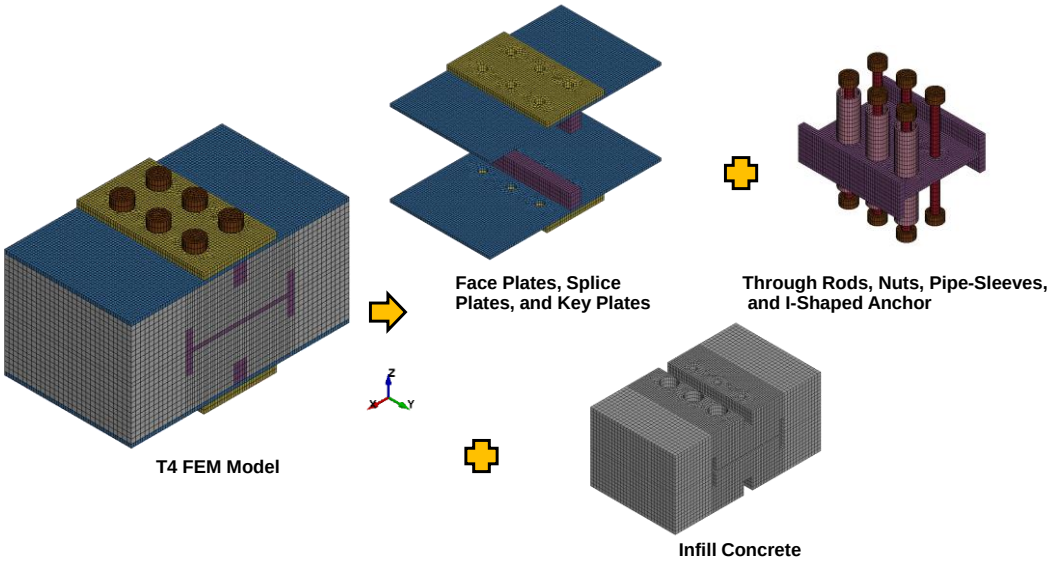


Figure 5-51. Finite Element Model of Specimen T4

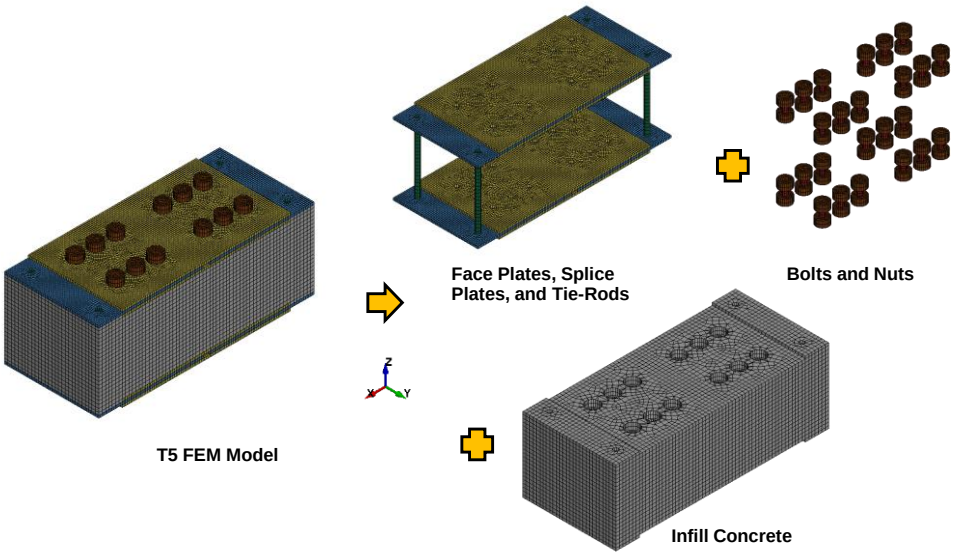


Figure 5-52. Finite Element Model of Specimen T5

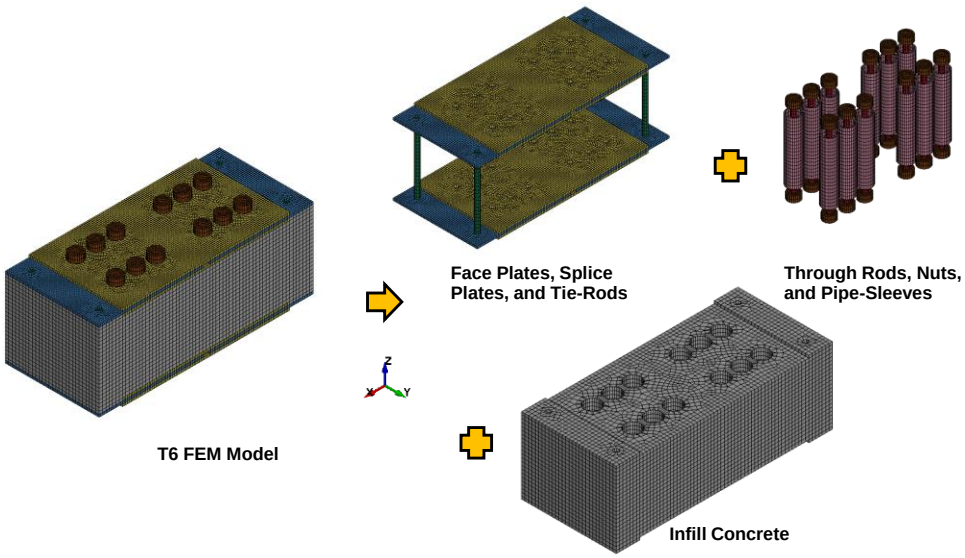


Figure 5-53. Finite Element Model of Specimen T6

5.3.2 Elements

All steel parts in the model were meshed using fully integrated solid elements (ELFORM = -1 in LS-DYNA). A total of eight integration points were employed through the thickness of the elements. The mesh size on the surface of the steel plates was set to 0.5 in. × 0.5 in. (width × length), while the element heights varied from 0.25 in. to 0.5 in.

Fully integrated solid elements (ELFORM = 1 in LS-DYNA) were used to model the infill concrete. The typical size of the solid elements for the concrete was 0.5 in. × 0.5 in. × 0.5 in, except in areas where the concrete elements are in contact with the bolts, pipe-sleeves, or I-shaped anchor, where a finer element size of approximately 0.5 in. × 0.5 in. × 0.25 in. was adopted.

5.3.3 Material Constitutive Models

All steel (plates, bolts, etc.) was modeled using the *plastic_kinematic* (MAT_003) bilinear material model with kinematic hardening. The properties of the steel material used in the finite element analyses are presented in Table 5-4. The parameters included the Elastic Modulus (E_s), Poisson's ratio, yield strength (F_y), Tangent Modulus (E_t), and Hardening parameter (β). Note that a value of zero for the hardening parameter β represents zero isotropic hardening.

The Winfrith concrete material model (MAT_085 in LS-DYNA) was used for all concrete elements. The material model parameters include the elastic modulus (E_c), Poisson's ratio, concrete strength (f'_c), tensile strength of concrete (f_t), fracture energy (FE), and aggregate size (ASIZE). The same Poisson's ratio of 0.2 and aggregate size of 0.5 were used in all specimen models.

The elastic modulus of concrete was calculated using the equation in Section 19.2.2 of ACI 318-19 (Equation 1.1 below). The tensile strength (f_t) of concrete was taken as 10% of the compressive strength of concrete (0.1* f'_c). The fracture energy (FE) was determined using Equation 1.2, where G_f represents the area under the stress-crack opening relationship as the crack width at which crack normal tensile stress goes to zero (a constant value of 0.514 was used for all specimens).

$$E_c = 57{,}000\sqrt{f'_c} \ \ (in\ psi) \qquad \text{Equation 5-1}$$

$$w_c = \frac{2G_f}{f_t} \qquad \text{Equation 5-2}$$

The input values for infill concrete in the Winfrith models for all specimens are summarized in Table 5-5.

Table 5-4. Material Properties for Steel

Part	E_s (ksi)	Possion's Ratio	F_y (ksi)	E_t (ksi)	β
Face Plates	29000	0.3	63	145.7	0.0
Splice Plates	29000	0.3	63	145.7	0.0
Key Plates	29000	0.3	63	145.7	0.0
I-Shaped Anchor	29000	0.3	63	145.7	0.0
Bolts/Rods	29000	0.3	120	221.2	0.0
Others	29000	0.3	55	108.8	0.0

Table 5-5. Material Properties for Concrete

Specimen	E_c (ksi)	Possion's Ratio	f'_c (psi)	f_t (psi)	FE	ASIZE
T1	4227	0.2	5500	550	0.00187	0.500
T2	4303	0.2	5700	570	0.00180	0.500
T3	4303	0.2	5700	570	0.00180	0.500
T4	4631	0.2	6600	660	0.00156	0.500
T5	4631	0.2	6600	660	0.00156	0.500
T6	4631	0.2	6600	660	0.00156	0.500

5.3.4 Contact and Constraint Properties

For the surfaces between bolt shanks and nuts and between pipe-sleeves and inner splice plates, the tie constraints *tie_surface_to_surface* was adopted to simulate that they are perfectly connected. The nodes between tie bar and faceplates were merged to represent the welded connection between the two parts.

Figure 5-54 shows the other contact interfaces in the finite element models. These interfaces include the contact surfaces between steel plates, between bolts and steel plates, and between steel and concrete. All these contact interfaces in the analysis were defined using the *automatic_surface_to_surface_mortar* contact model. This contact model uses a segment-to-segment penalty-based approach. It considers overlapping and penetrating segments on both sides of the contact interface and applies a consistent nodal force assembly, taking into account the individual shape functions of the segments. It does so using a penalty-based slave-node master-surface interaction, where a compression spring with a specific stiffness

is inserted between the slave-node and master-surface to generate the contact force. This contact model is particularly suitable for contacts involving higher order elements and may provide more accurate results.

In the models, a static interface friction coefficient of 0.3 was assigned, and the contact stiffness was adjusted from the default value. Based on the findings of Polat and Bruneau (2018), it was observed that when using the default contact stiffness in the contact model (SFS, SFM=1 in LS-DYNA), slippage of the concrete core under large deformations occurred. To address this issue, the contact stiffness of their wall models was increased in the contact model definition, effectively eliminating the slippage of the concrete core. Furthermore, based on the study conducted by Emre and Bruneau (2020), it was found that the issue of slippage in the concrete core could be completely eliminated by setting the contact stiffness to a value of 10. Therefore, to prevent the occurrence of slippage in the simulations, a contact stiffness of 10 (i.e., SFS=SFM=10) was used in this analysis.

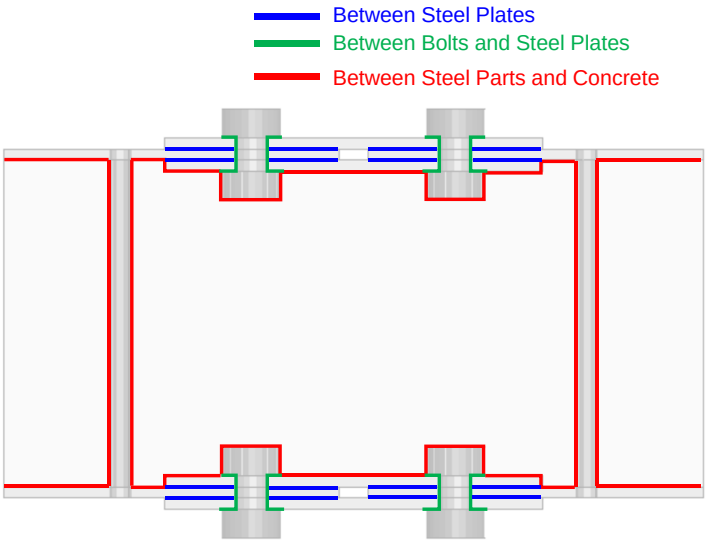


Figure 5-54. Typical Contact Interfaces in the Finite Element Model

5.3.5 Pretension of Bolts and Through Rods

To simulate the pretension of bolts/through rods, the cross sections at the center of the bolt/through rods were defined using the *Database_Cross_Section_Plane* keywords in LS-DYNA. Subsequently, the pretension stresses were applied to these sections using the *Initial_Stress_Section* keyword. This allowed for the incorporation of the desired pretension forces in the analysis.

As previously mentioned, investigating the effect of pretension's value on the combined friction and bearing strength is of interest. Figure 5-55 displays the finite element analysis results of the T2 model subjected to monotonic tension. The analysis considers various applied pretension values, ranging from 0 to 105 ksi. The results indicate that the pretension of bolts increases the strength of the connection up to a deformation of 0.75 in. However, beyond 0.75 in. deformation, the strength remains consistent. This suggests that the slip resistance and bearing strength in the connection are not additive under large deformation.

Table 5-6 presents a summary of the pretension values used in the finite element models. The table includes the diameter (d_b) and area (A_b) of bolts or through rods, the initial stress (*Prestress*) and pretension force (T_b) of bolts or through rods, and the coefficient of friction (μ). The theoretical slip resistance (R_{theory}) can be calculated using the formula $T_b \times \#\ of\ bolts \times \mu \times 2$ (for double shear), as indicated in the table. Additionally, the table also includes the observed slip resistances from the tests (R_{test}), as shown in Figure 5-56. Note that the slip resistance from tests is provided in the table only when there is a noticeable sliding plateau, and the average sliding force from the test is recorded.

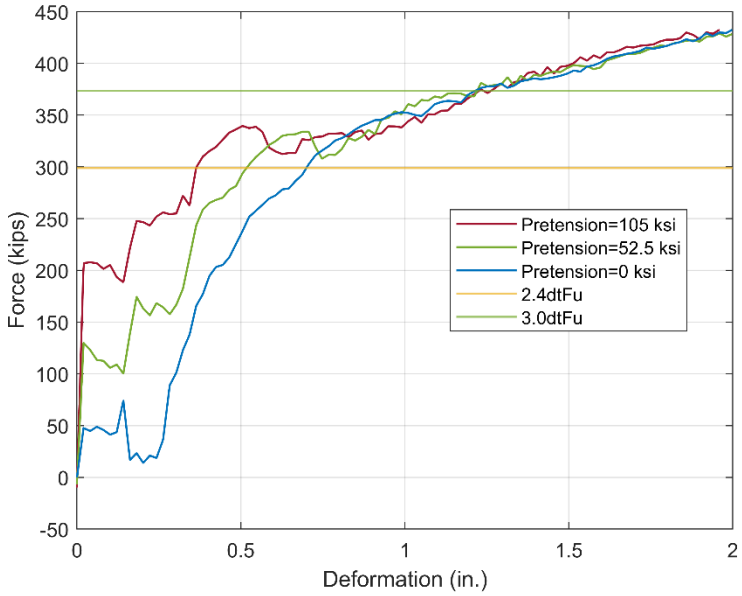


Figure 5-55. Tension Force from Finite Element Analysis of T2 Specimen with Different Bolt Pretension Values

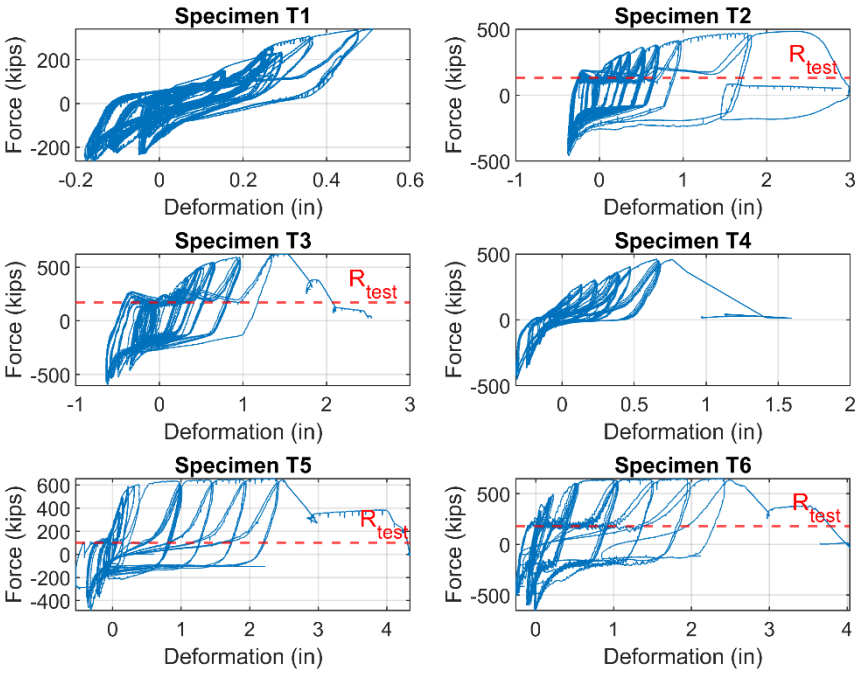


Figure 5-56. Slip Resistance from Tension Tests (R_{test})

Table 5-6. Prestress Value used in Finite Element Models

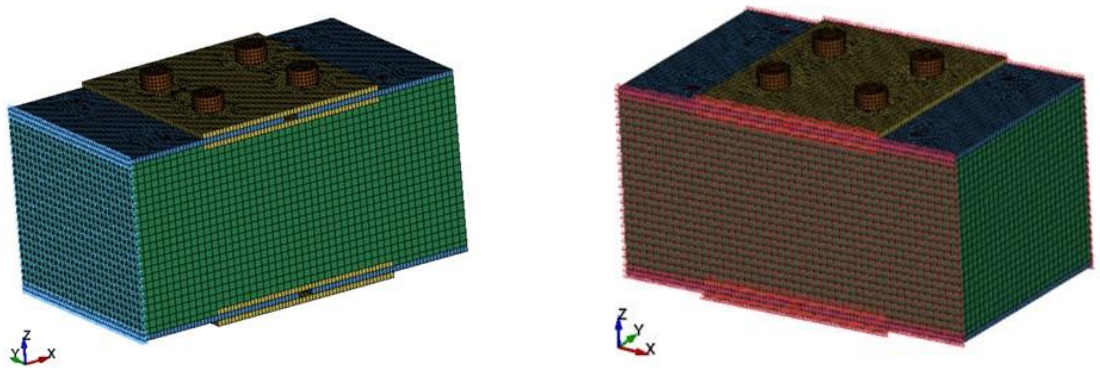
Specimen	d_b	A_b (in_2)	Prestress (ksi)	T_b (kips)	# of Bolts	μ	R_{theory} (kips)	R_{test} (kips)
T1	1	0.785	52.5	41.23	4	0.30	98.96	-
T2	1	0.785	52.5	41.23	4	0.30	98.96	130
T3	1.25	1.227	52.5	64.43	6	0.30	231.94	170
T4	1	0.785	52.5	41.23	6	0.30	148.44	-
T5	0.75	0.442	52.5	23.19	12	0.30	167.00	100
T6	0.75	0.442	52.5	23.19	12	0.30	167.00	178

5.3.6 Boundary Conditions and Loading Areas

Figure 5-57 shows the typical boundary conditions implemented in the finite element models. In the case of tension specimens, the left end of the C-PSW/CF section was restrained in all directions (fixed-end), as shown in Figure 5-57 (a). To simulate the lateral confinement in real wall scenarios, for some analyses, an additional side restraint (Figure 5-57 (b)) was applied to the specimen models. This lateral restraint was used to compare the behavior between test specimens (where lateral expansion of the material along the wall axis occurred) and the actual wall connections (where lateral expansion of the material along the wall axis would not occur, as restrained by other similar segments of wall in tension). Detailed analysis results are presented in Sections 5.3.7.1 to 5.3.7.6.

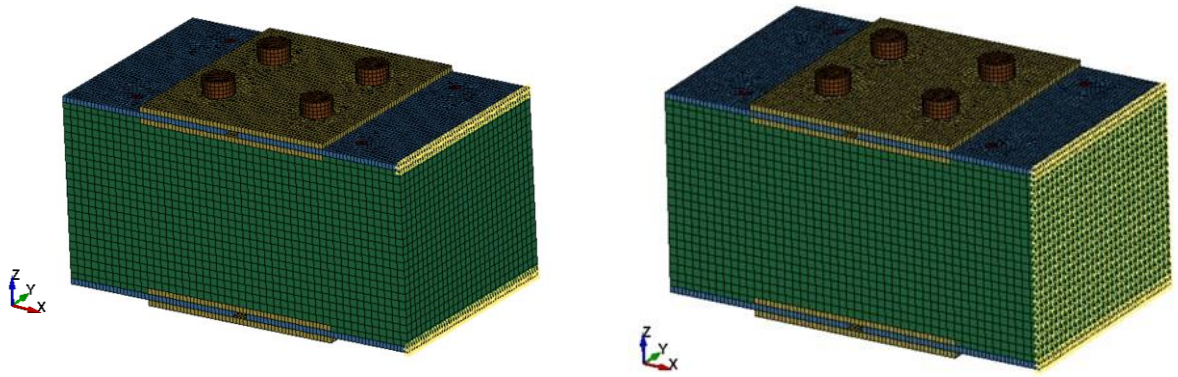
Figure 5-58 compares the effect of two distinct ways to apply tension to the specimens in the finite element models. These two scenarios were used to compare the effect of having the load applied solely to the steel faceplates with the case where the load is applied to the entire section. When the connection is subjected to compression, it is appropriate to apply the load to the entire cross-section. However, when the connection is in tension, the applied load could be (at the extreme) applied only on the faceplates. Figures 5-59 and 5-60 show the comparison between the results obtained from these two analyses. Note that while the stresses in the concrete were distributed more uniformly when the load was applied to the entire section, there was no significant difference in the overall force-deformation response of the connection. This suggests that

whether tension is applied solely to the faceplates or to the entire section, does not significantly influence the overall behavior of the connection. Therefore, for simplicity, in all subsequent finite element models for cyclic load analysis, the axial load was applied to the entire section.



(a) Fixed End at Left End (b) Joint Restraint on Y-Direction (UY=0)

Figure 5-57. Boundary Condition for Finite Element Models



(a) Loading on Faceplate Only (b) Loading on Whole Section

Figure 5-58 Loading Area for Finite Element Models

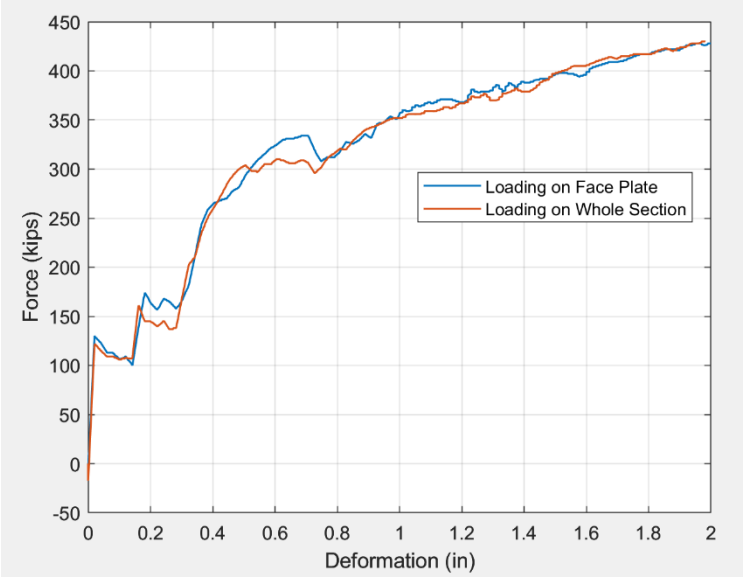
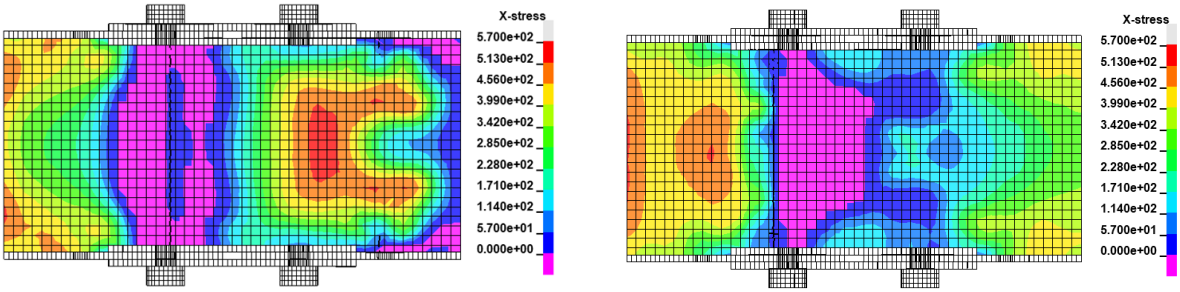


Figure 5-59. Finite Element Results of Two Different Loading Areas



(a) Loading on Faceplate Only (b) Loading on Whole Section

Figure 5-60 Stress Distribution of Concrete of Two Different Loading Areas

5.3.7 Results of Finite Element Analysis

This section provided analysis results from finite element model as mentioned in Section 5.3.1.

5.3.7.1 Specimen T1

Figure 5-61 shows the comparison of the axial load-deformation curves between the finite element model and the test results. Monotonic tension and compression finite element analyses were first performed to investigate the ultimate behavior of the connection under these loading conditions. Figure 5-62 shows that the lengths of finite element model and LP measurement by linear pots installed in the test are both taken as 24 in. here (there is actually a small difference between the two lengths because the 24 in. distance is from the end of the LP attachment points and the distance between mid-points of the LP attachment is actually 19.4 in., with negligible differences (<1%) in the results because the ends of the faceplates away from the splice plates remains elastic). As the length of the finite element models is approximately the same as the length measured by the linear pots, therefore the deformation recorded by the linear pots (LP deformation) was used to plot the test result and compared with the finite element analysis.

The finite element result indicates that the compressive strength of the connection is approximately 2.5 times larger (-1072 kips at -0.4 in. deformation) than its tensile strength (420 kips at 2.0 in. deformation). Furthermore, the tensile strength predicted by the finite element model aligns well with the strength observed in the test result up to a deformation of 0.7 in. Note that Specimen T1 experienced undesired bending throughout the entire test, which explains its lower axial stiffness compared to the finite element result.

Since the tested specimens did not have lateral confinement during testing, some of the concrete fell off from the sides during the cyclic loading tests. Also, once the cracked parts of the concrete infill separated

due to tension, when subsequently subjected to compression, part of the concrete that fell as debris into the cracks also participated and produced contact forces. In contrast, in the finite element analyses, the concrete surfaces that separated upon cracking remained "intact" (i.e., without debris). Also, in the finite element models, the concrete did not fall out from the open edges (even without lateral restraints).These discrepancies explain why the compressive strengths obtained from finite element analyses differed and were typically much higher than those observed in the tests. Therefore, the finite element analysis results in this section mainly focus on comparing tensile behaviors to the test results.

Figure 5-63 shows the von Mises stresses of all steel elements, and Figure 5-64 shows the distribution of von Mises stresses obtained from a cross-section taken along the bolt line when the connection reached a deformation of 2.0 inches under monotonic tensile load. These figures indicate that the steel predominantly remained within the elastic range ($\sigma < 63{,}000\ psi$), with the exception of regions near the bolt holes. Figure 5-65 shows a comparison between the finite element results and the test at an LP deformation of 0.69 in. in tension. The figure shows the normal stress in the X direction from the finite element model (excluding the splice plates and bolts). Additionally, the figure shows the visible cracks generated using the Winfrith concrete model. Both the finite element model and the test specimen exhibit vertical cracks in the concrete near the ends of the splice plates.

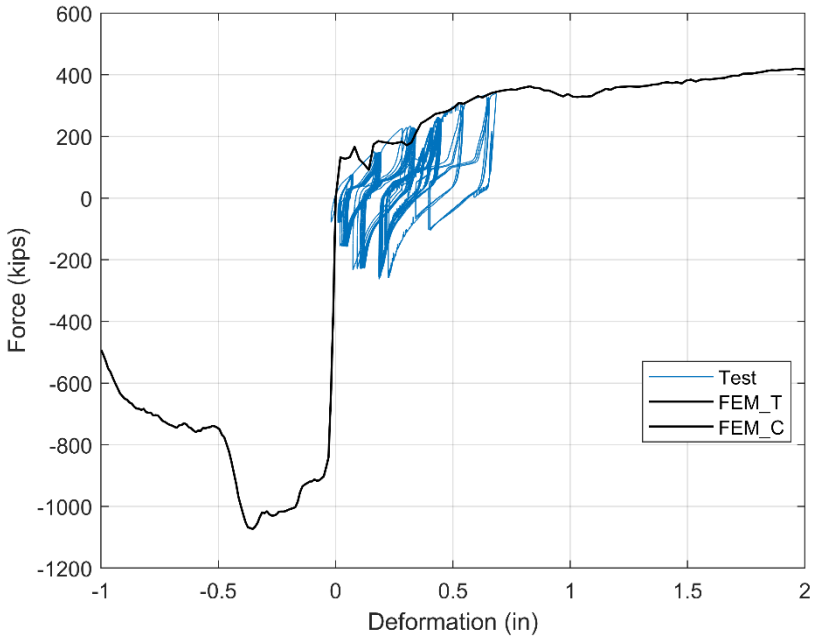


Figure 5-61. Finite Element Results of Load-Deformation Curve of Specimen T1

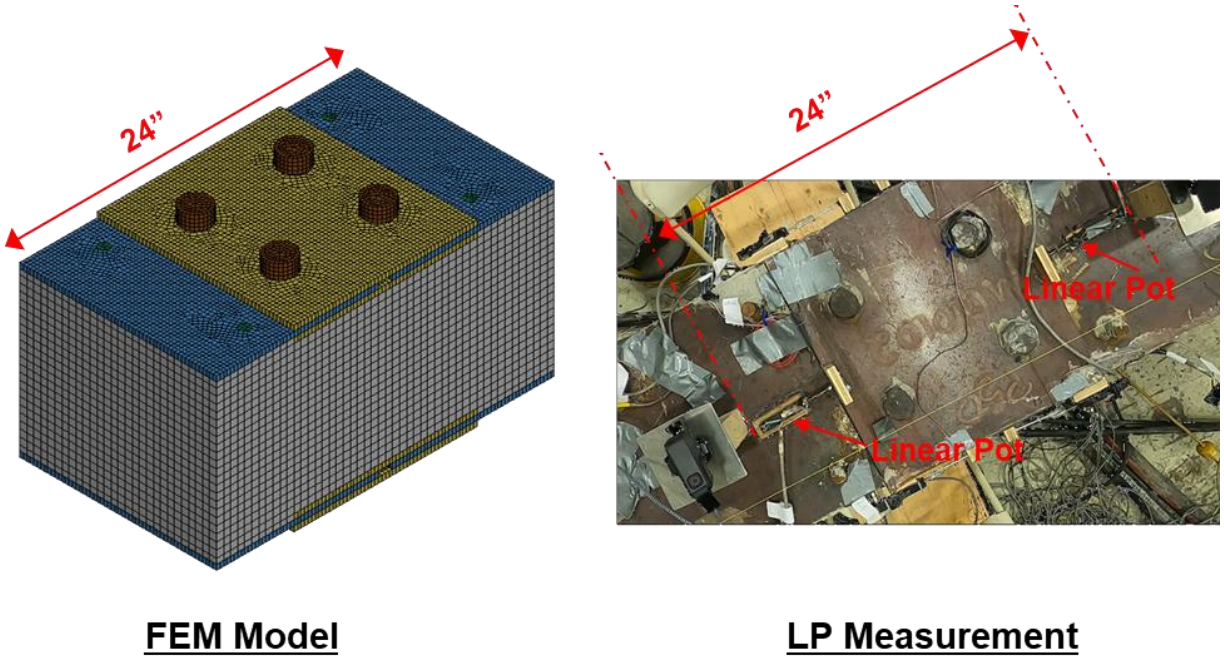
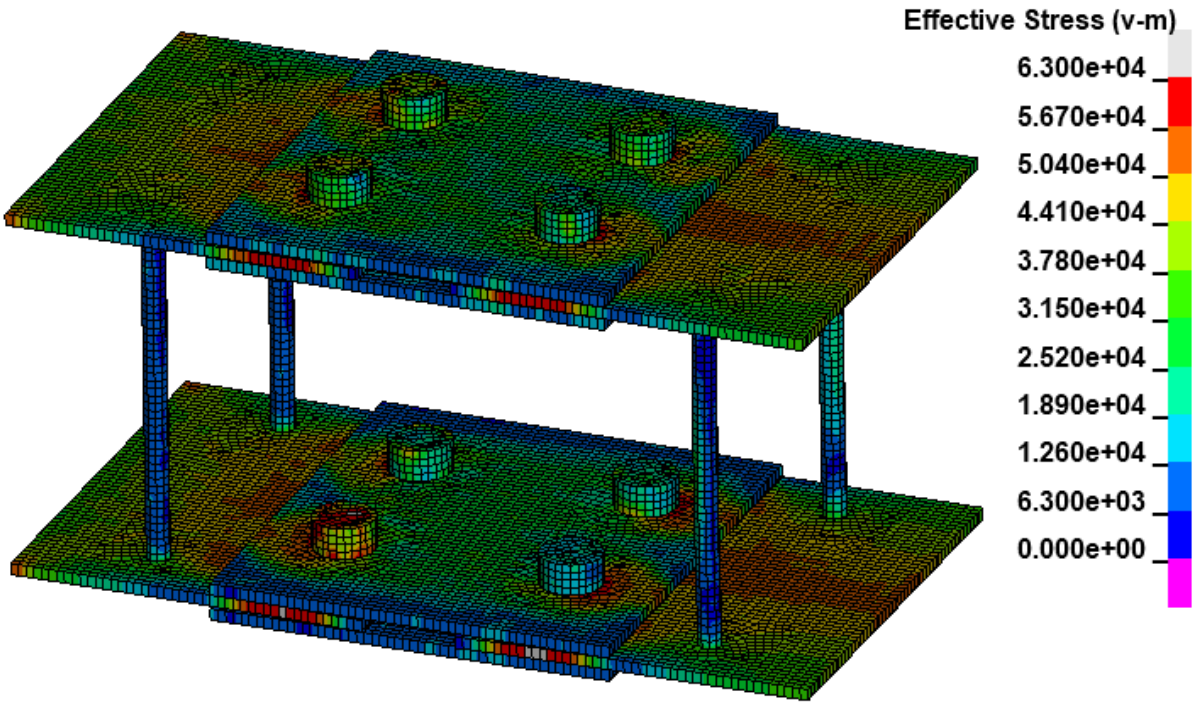
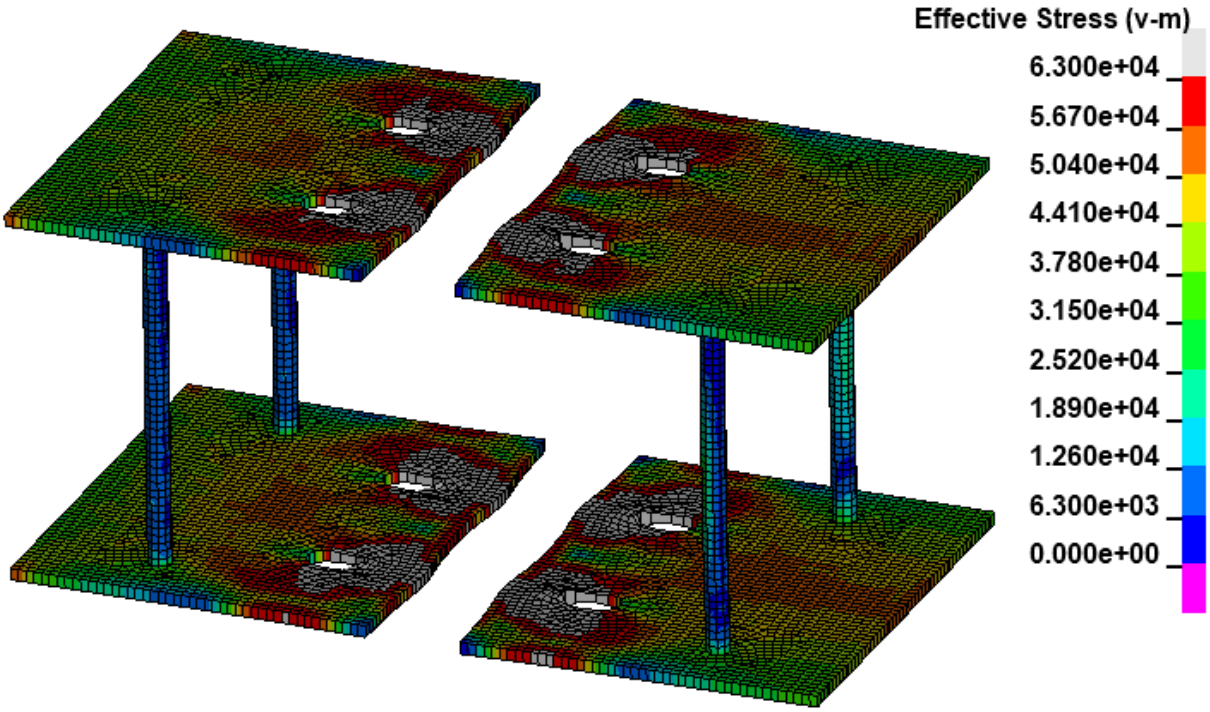


Figure 5-62. Length of Finite Element Model and LP Measurement



(a) All Steel



(b) Reveal Faceplates

Figure 5-63. von Mises Stresses of All Steel at 2.0-in. Deformation in Tension (Specimen T1)

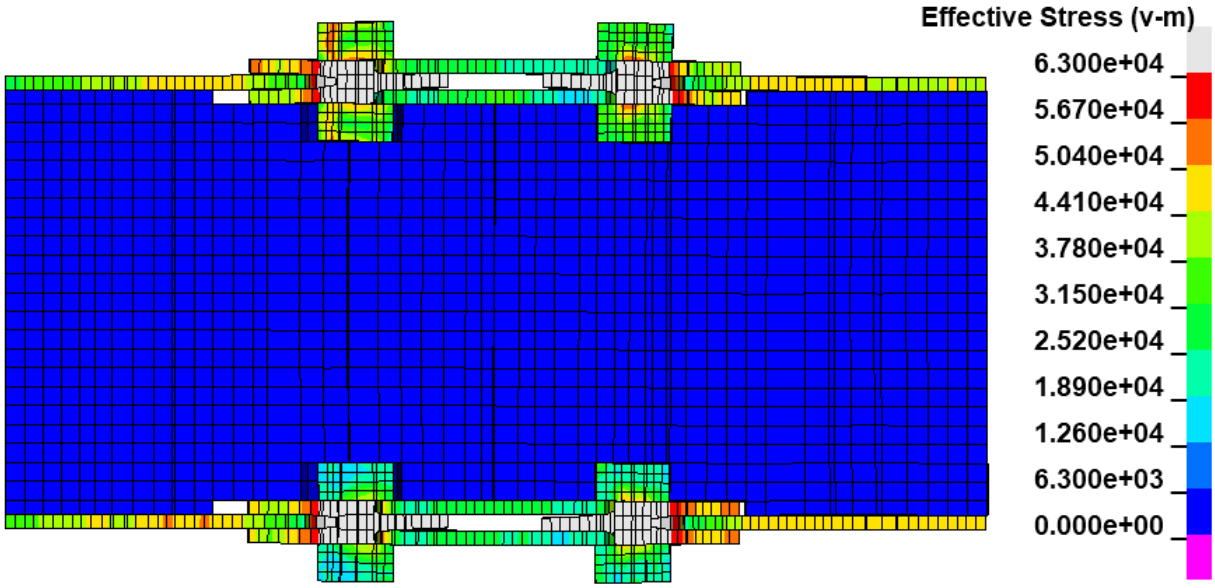
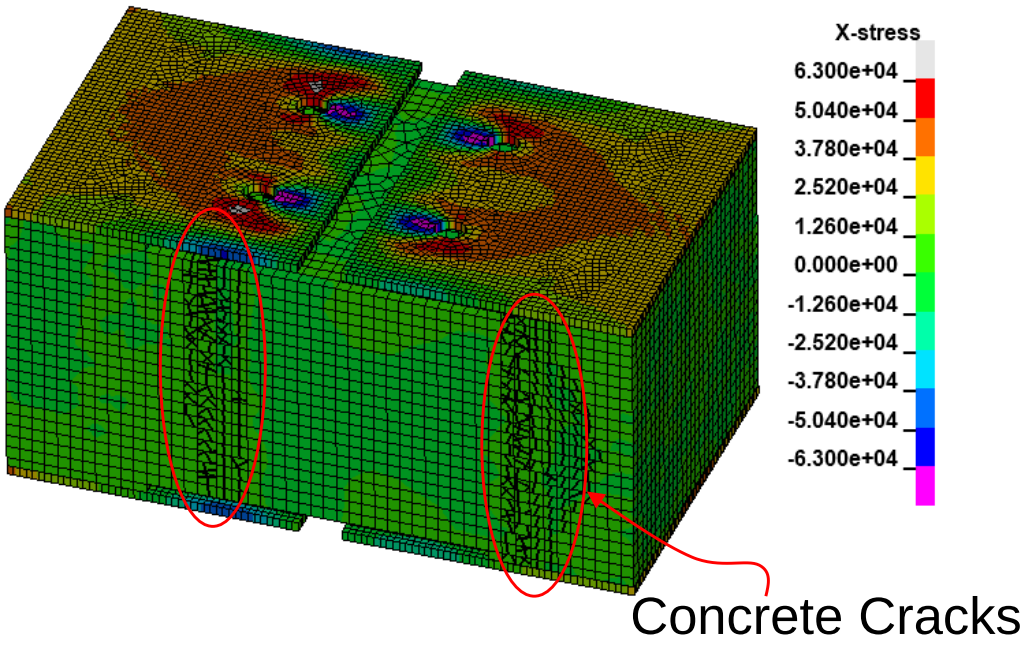


Figure 5-64. von Mises Stresses at Bolt Section at 2.0-in. Deformation in Tension (Specimen T1)



(a) Finite Element Model (at 0.69-in. Deformation in Tension)



(b) Test of Speciment T1 (LP=0.69 in.)

Figure 5-65. Comparison of Finite Element model and Test of Specimen T1

Figure 5-66 shows the elongation of bolt holes in the finite element result of Specimen T1 subjected to monotonic tensile load. To further study the bearing behavior, the hole elongations from both sides, $\Delta_{hole,\ L}$ and $\Delta_{hole,\ R}$, are summed to create a force versus bolt hole deformation (Δ_{hole}) curve, as shown in Figure 5-67. This curve represents the bearing curve in the connection and is compared with the global response.

In Figure 5-67, the applied deformation of the connection is 2.0 in., while the bolt hole deformation developed a 1.40-in. deformation. It can be observed that the bearing strength reached $2.4dtF_u$ and $3.0dtF_u$ when the deformation reached 0.21 in. and 0.9 in. Furthermore, also plotted as a dotted line in that figure is the top part of the bearing curve shifted by 0.25 in., which represents the sliding distance, and it is seen to closely align with the global response curve. This indicates that the bearing strength begins to develop after approximately 0.25-in. in slippage deformation.

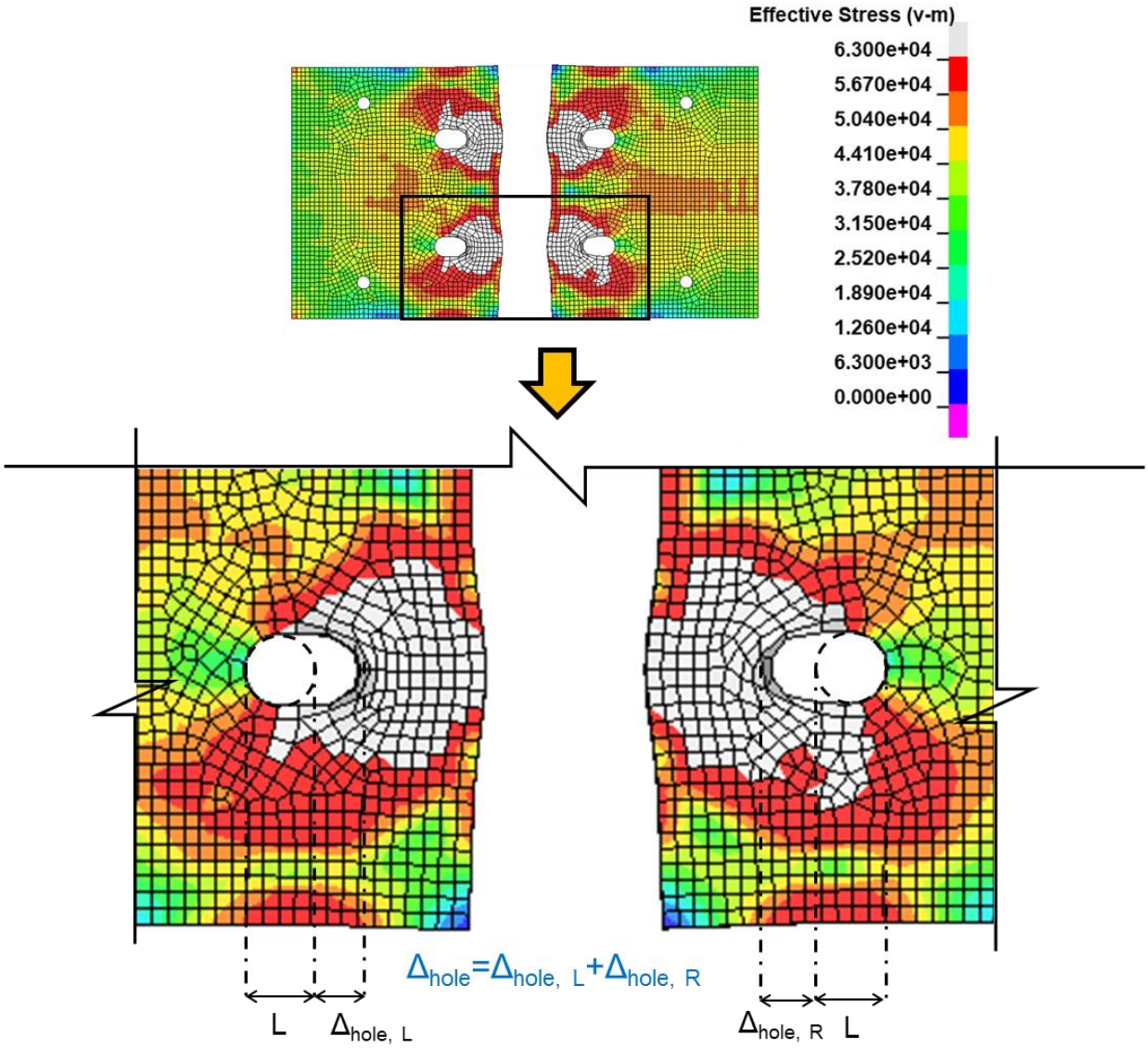


Figure 5-66. Elongation of Bolt Holes at 2.0-in. Deformation in Tension (Specimen T1)

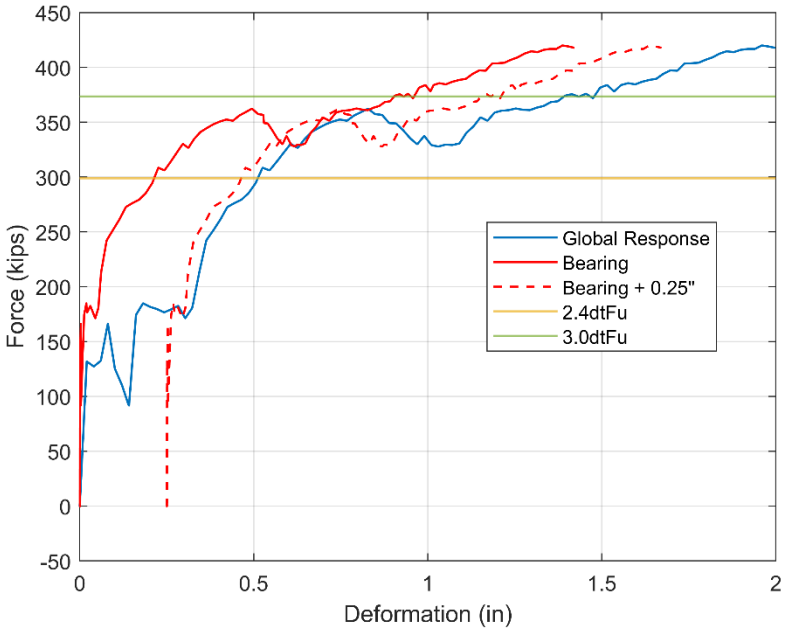


Figure 5-67. Bearing Curve vs Global Response (Specimen T1)

As discussed in Section 5.3.6, an additional side restraint (UY=0) was incorporated into the boundary condition to simulate the lateral confinement to model the effect of continuity in actual walls. To compare the effects of this restraint, the monotonic tensile load was applied to both boundary conditions, namely that of Specimen T1 and that with the additional side restraint (referred to as "the wall scenario"). Figure 5-68 shows the comparison between these two models. Results are generally in good agreement, and no significant difference is observed between different boundary conditions. This confirms that the behavior of the specimen is representative of that of wall segments in tension.

Furthermore, Figures 5-69 and 5-70 provide further comparison by presenting the distribution of net section normal stresses for these two models. It can be observed that for the boundary condition of the specimen, the edge shows a negative stress (compression), which occur because, as the bolt bears on the plate, it

pushes the steel outward at the longitudinal free-edge, creating bending stresses near that free edge when the connection is subjected to tension.

On the contrary, for the boundary condition of the wall, the entire net section displays a positive stress distribution, because the side-restraints prevent the development of that bending behavior (i.e., the expected wall behavior). Note that in the actual wall condition, the stresses at the middle and the edge should be approximately the same due to symmetry. However, due to the presence of tie bars nearer to the edge of the faceplates in the specimen (i.e., they are not laid-out in a symmetric pattern with respect to the bolts here, as should be the case if this was a perfect slice of a wall), the corresponding finite element result do not exhibit perfect symmetry.

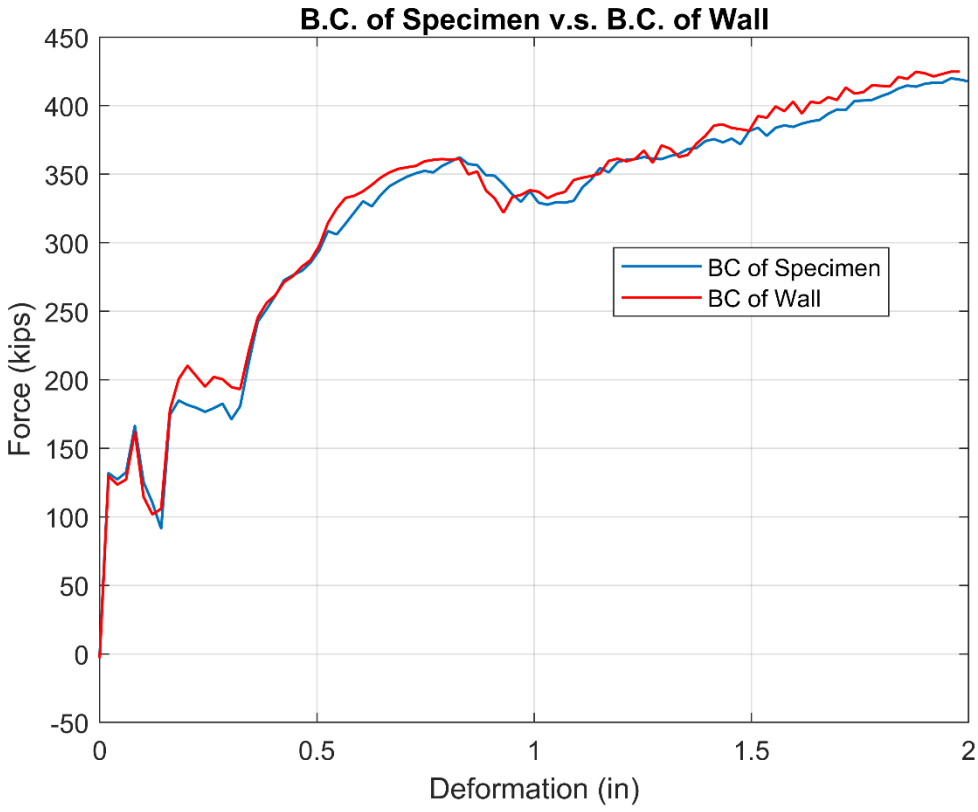


Figure 5-68. Finite Element Results for Boundary Conditions of Specimen and of Wall Models (Specimen T1)

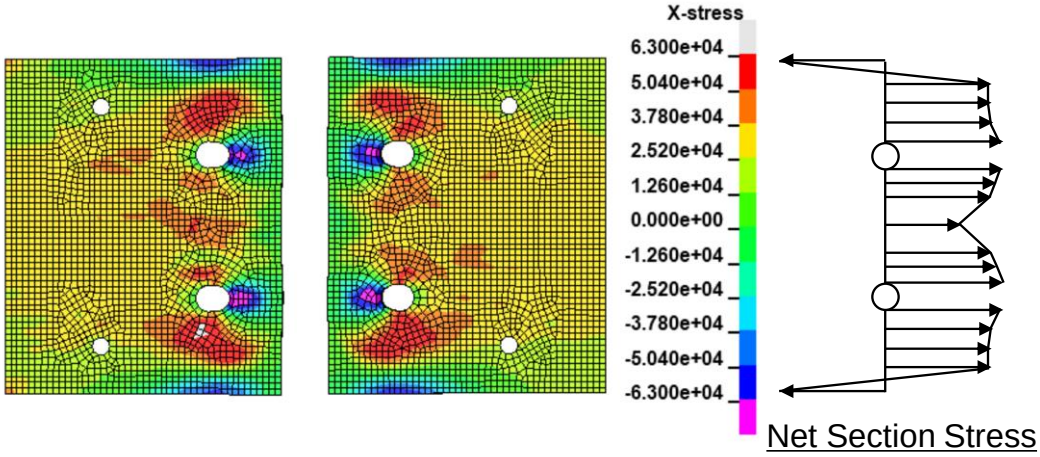


Figure 5-69. Normal-Stresses for B.C. of Specimen Model (Specimen T1, Disp.=1" in Tension)

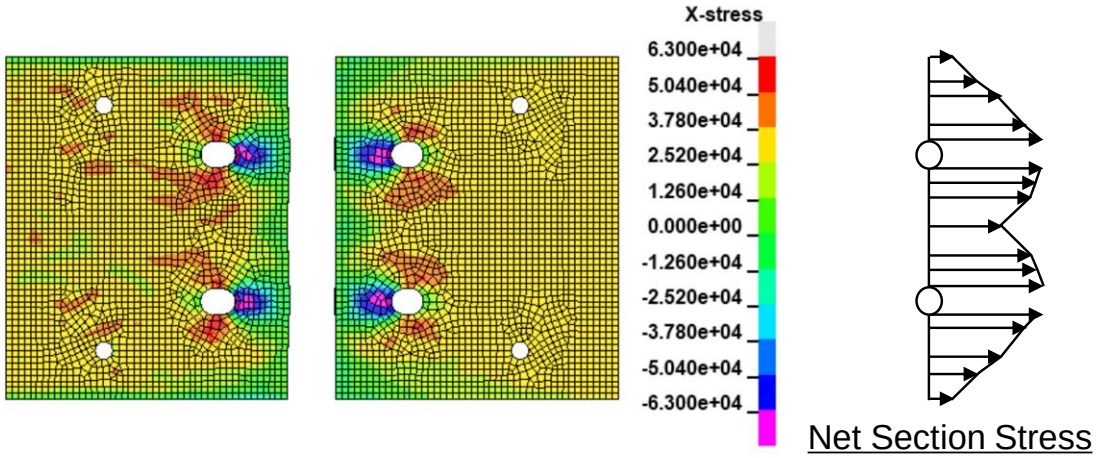


Figure 5-70. Normal-Stresses for B.C. of Wall Model (Specimen T1, Disp.=1" in Tension)

Figure 5-71 shows the load protocol obtained from the recorded LP history for the cyclic load finite element analysis, while Figure 5-72 shows the corresponding finite element result. Again, the test result shows a lower stiffness initially due to the bending observed during the test. However, the finite element model captures well the overall response upon the subsequent loading and unloading curves. The analysis result closely matches the peak tension force, particularly under large deformation.

Figure 5-73 provides an overview of the interaction between concrete and steel during the cyclic load analysis. The figure highlights stress contours obtained at five points (which are arbitrarily selected different points), with Points 1 and 3 representing the connection in compression, and the remaining Points representing the connection in tension. Figure 5-74, on the other hand, shows the respective contributions concrete and steel in resisting forces throughout the cyclic loading. The same five points are also marked in the figure for reference. The figures indicate that the concrete reached its maximum compressive strength during Point 1. As anticipated, the contribution of tensile strength provided by the concrete was negligible.

Figure 5-75 shows a closer detail of the local behavior of blind bolts interacting with the concrete in Points 3 and 5. Free-body diagrams are presented by cutting a section near the middle of the connection. In these diagrams, T_{FP} represents the tensile force on the faceplates, C_{FP} represents the compressive force on the faceplates, M_{mid} represents the bending moment at the middle of the splice plates, and C_C represents the contact force between the concrete and nuts. In tension (Point 2), there is no direct interaction between the right bolt nuts and the concrete, as the gap between the concrete and nuts increases. In compression (Point 3), a bending moment (M_{mid}) is observed in the middle of the splice plates due to the contact forces from the concrete (C_C), with corresponding movement of the cover plates away from the concrete (note that this behavior was not observed during the test due to the large undesirable global bending of the specimen that occurred due to imperfections in the specimen). Note that the axial forces within the connection are in compression, even as the applied displacement remains positive. Figure 5-76 shows the relationship between the faceplates, splice plates, and bolts at Points 2 and 3 during the cyclic analysis. The figure shows that as the load is reversed from Point 2 to Point 3, the splice plates maintain contact with the bolts, resisting deformations and preventing the splice plates from returning to their initial position (i.e., with bolts centered in the holes), leading to some residual elongation in the splice plates. This residual elongation results in compressive forces in the faceplates, despite the applied displacement being positive.

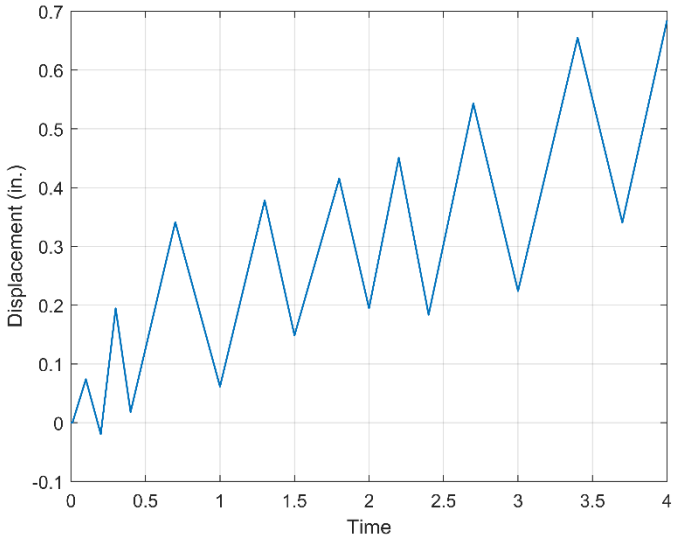


Figure 5-71. Cyclic Loading Protocol of Finite Element Model (Specimen T1)

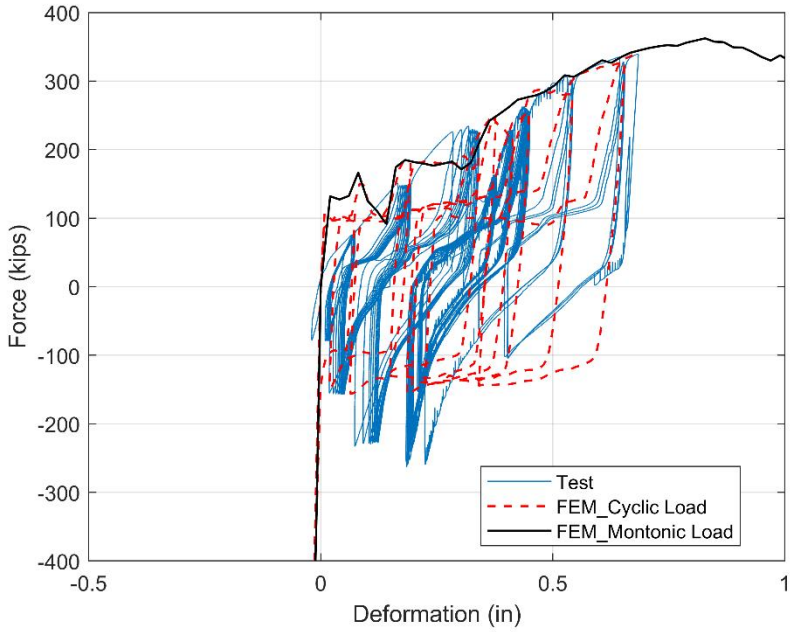


Figure 5-72. Finite Element Results of Hysteresis Loop of Specimen T1

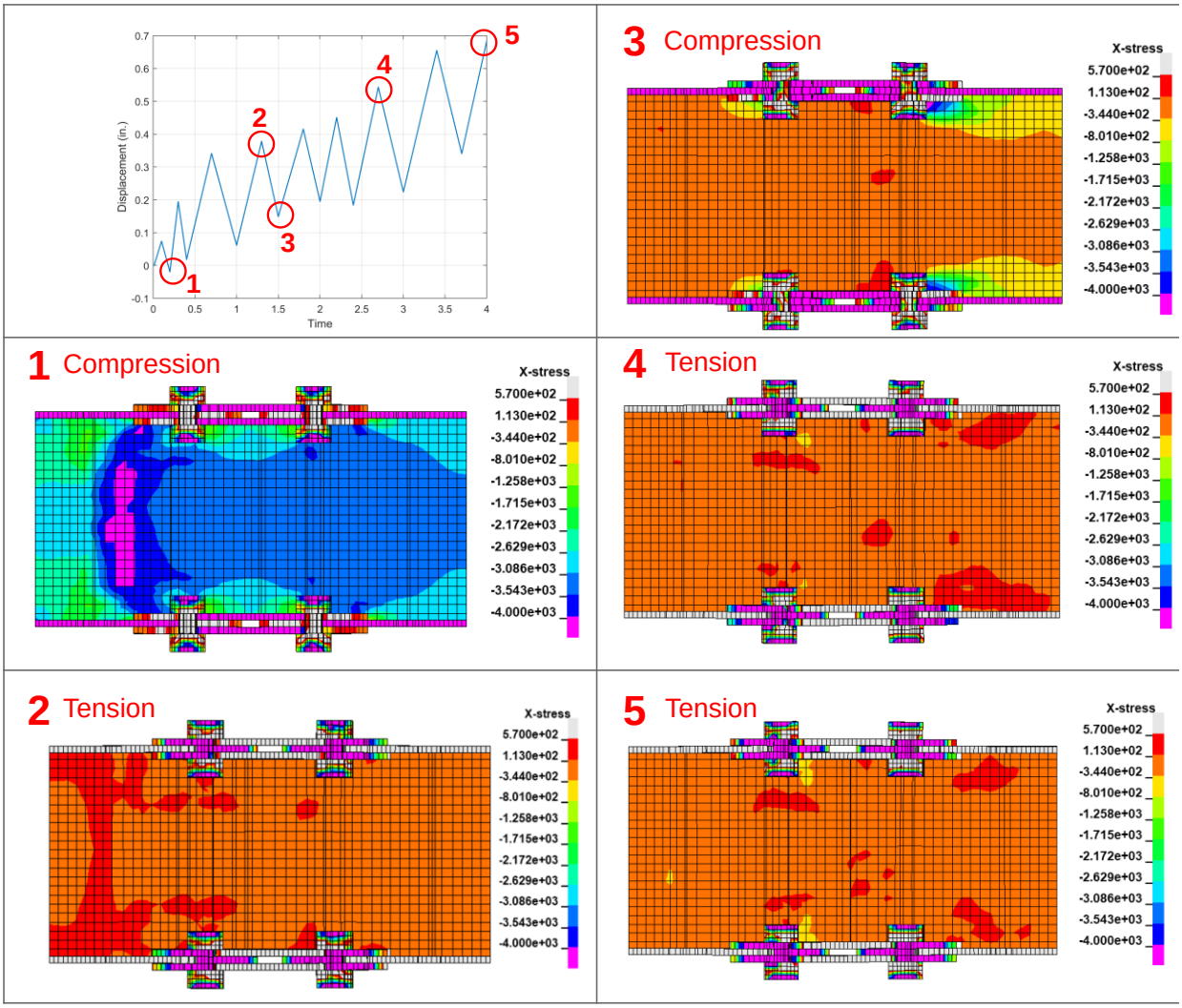


Figure 5-73. Cyclic Interaction between Concrete and Steel (Specimen T1)

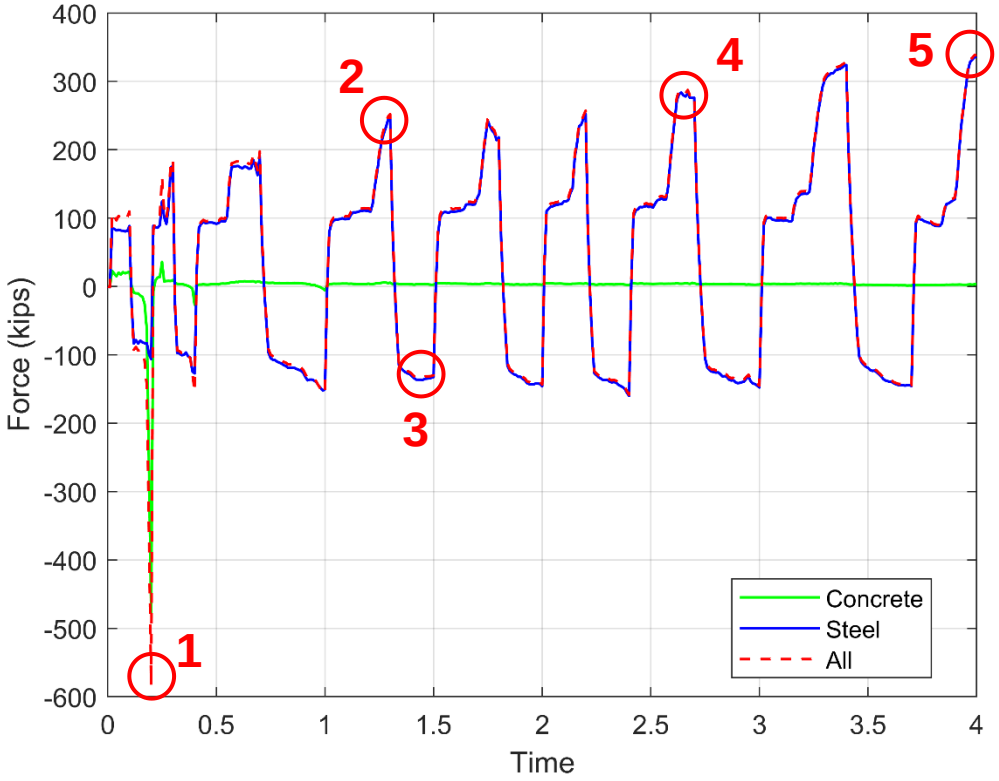
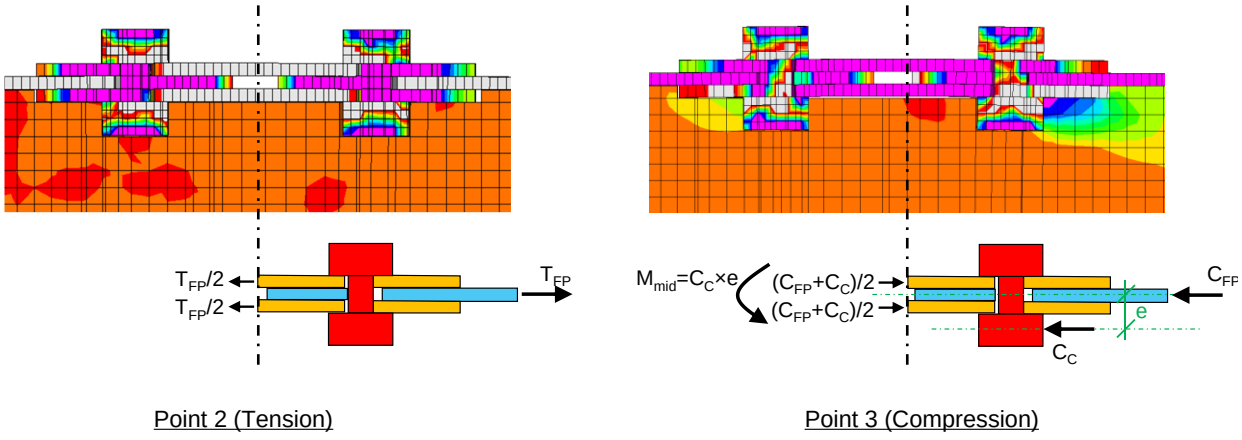


Figure 5-74. Axial Strengths of Concrete and Steel (Specimen T1)



Point 2 (Tension) Point 3 (Compression)

Figure 5-75. Interaction between Concrete and Blind Bolts (Specimen T1)

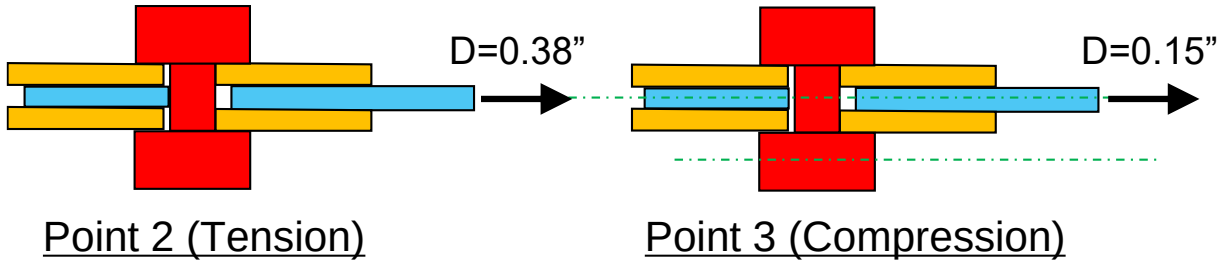


Figure 5-76. Details of Points 2 and 3 (Specimen T1)

5.3.7.2 Specimen T2

Figure 5-77 shows the comparison of the axial load-deformations curve between the finite element model and the test results. The finite element result exhibits a tensile strength of 428 kips and a compressive strength of -1039 kips. The corresponding deformation are 2.0 in. in tension and -0.4 in. in compression. The finite element model accurately predicts the tensile strength in line with the test results up to a deformation of 0.70 in., with a slight 8% underestimation observed when the deformation reaches 2.0 in.

Figure 5-78 shows the distribution of von Mises stresses in all the steel elements, while Figure 5-79 shows the von Mises stresses obtained from a cross-section taken along the center line of the through rod when the connection reached 2.0in. deformation in tension. Furthermore, Figure 5-80 shows the deformation of a rod extracted from the right-hand side of the previous figure, together with a magnified deformation plot. The figure shows that the rod experienced slight bending during the loading process.

These figures indicate that the steel mostly remained within the elastic range ($\sigma < 63{,}000$ psi), except for regions near the rod holes. Again, Figure 5-81 shows a comparison between the finite element model and the test at an LP deformation of 2.0 in. in tension. The figure shows the normal stress in the X direction from the finite element model (excluding the splice plates and bolts). Both finite element model and test show vertical cracks in the concrete near the ends of the splice plates.

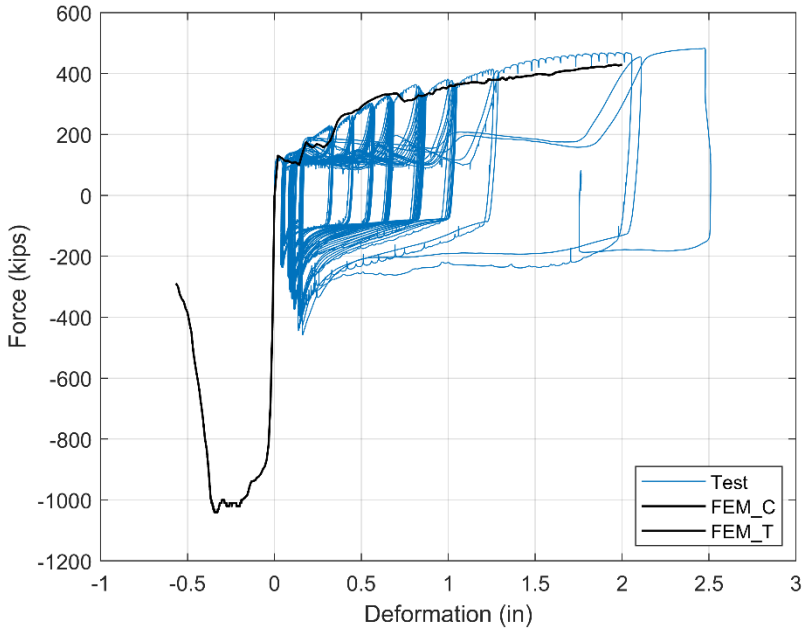
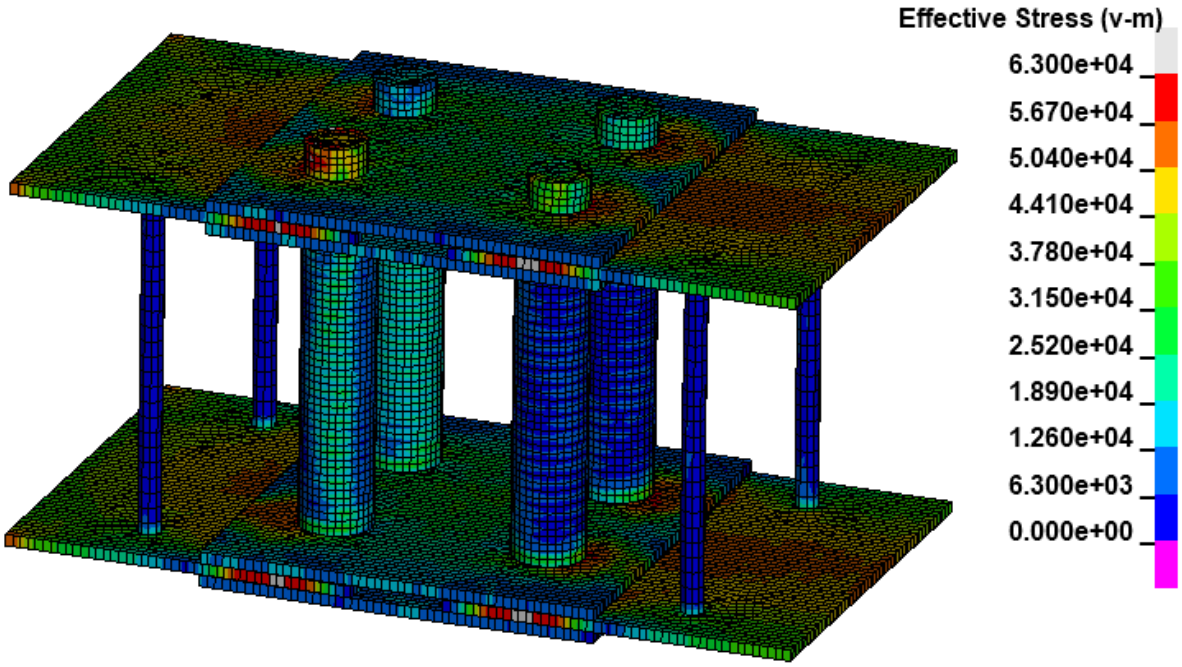
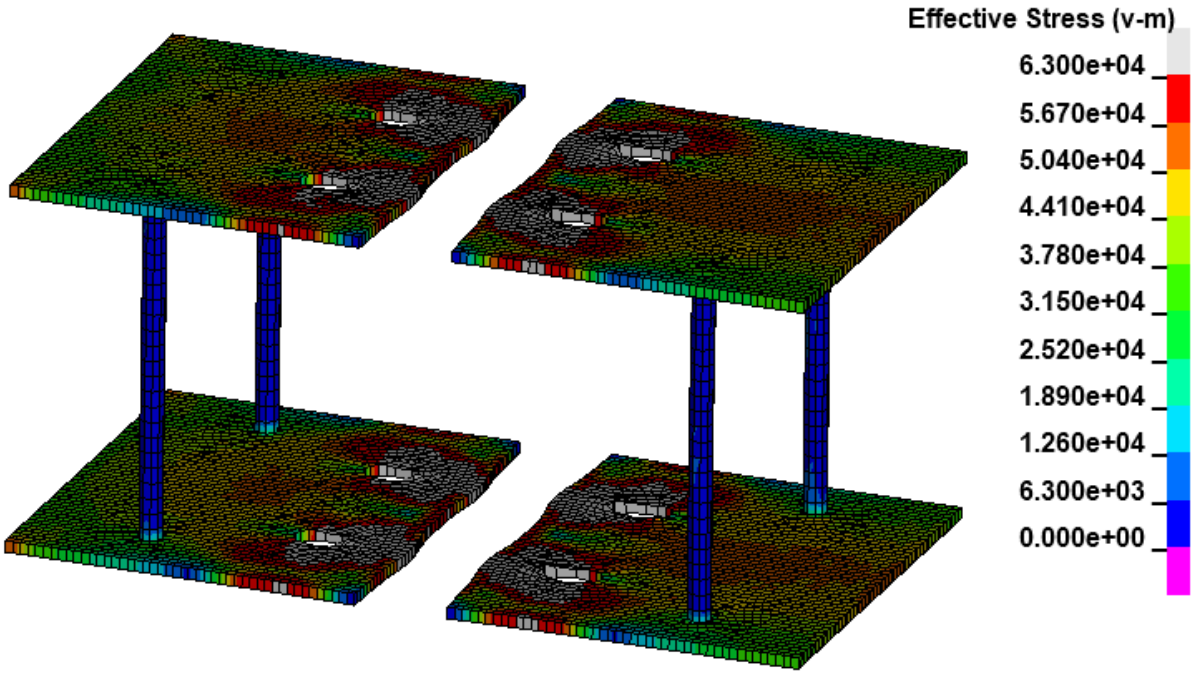


Figure 5-77. Finite Element Results of Load-Deformation Curve of Specimen T2



(a) All Steel



(b) Reveal Faceplates

Figure 5-78. von Mises Stresses of Steel Parts (Specimen T2, at 2.0-in. Deformation in Tension)

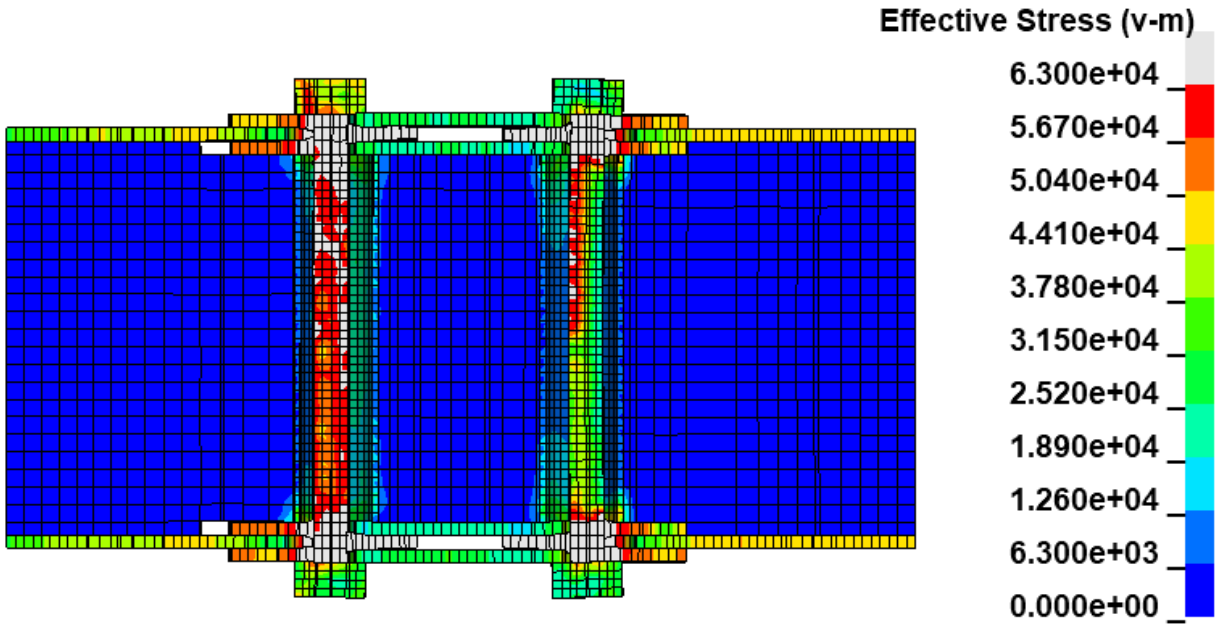


Figure 5-79. von Mises Stresses at Rod Section (Specimen T2 at 2.0-in. Deformation in Tension)

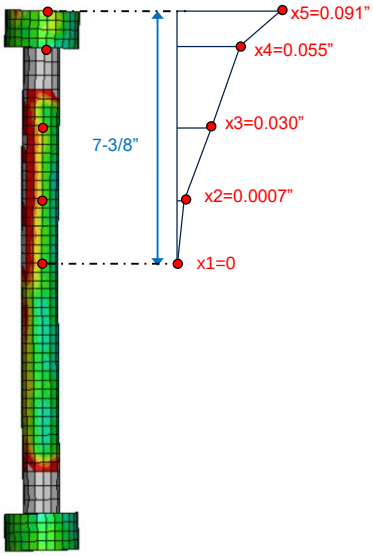


Figure 5-80. Deformation of Rods (Specimen T2)

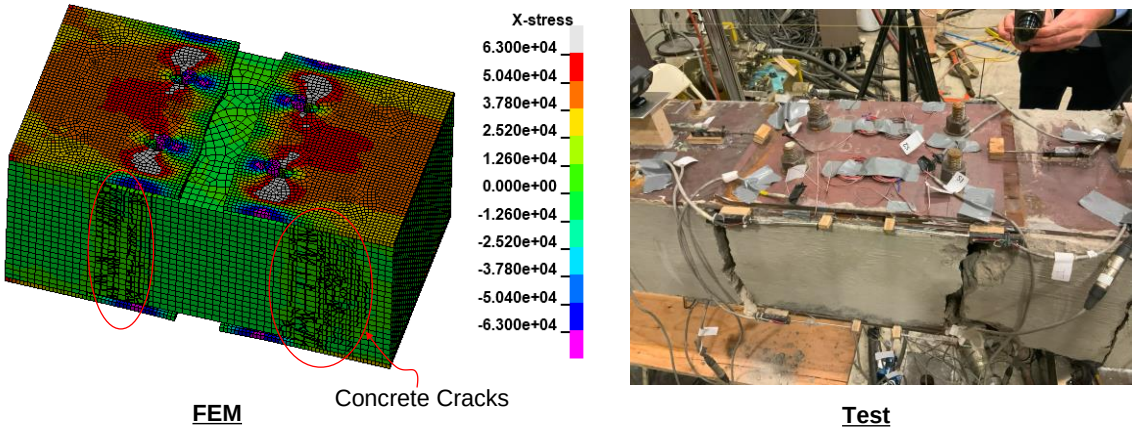


Figure 5-81. Comparison of Finite Element Model and Test of Specimen T2 (LP=2.0 in. in Tension)

Figure 5-82 shows the elongation of the rod holes in the finite element result of Specimen T2 under monotonic tensile load. The bearing curve, obtained by summing the rod hole deformations, is shown in Figure 5-83.

The bearing strength reaches $2.4dtF_u$ and $3.0dtF_u$ at deformations of 0.21 in. and 0.8 in., respectively. Additionally, when the bearing curve is shifted by 0.30 in. (shown as dotted line in the figure), it closely matches the global response, indicating that the development of bearing strength occurs after approximately 0.30 in. of deformation.

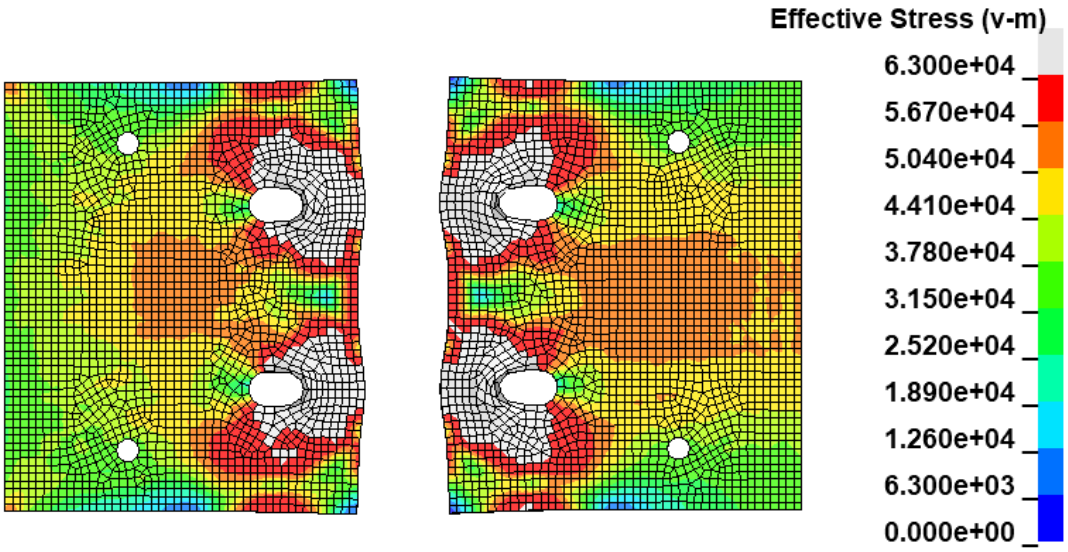


Figure 5-82. Elongation of Bolt Holes (Specimen T2, at 2.0-in. Deformation in Tension)

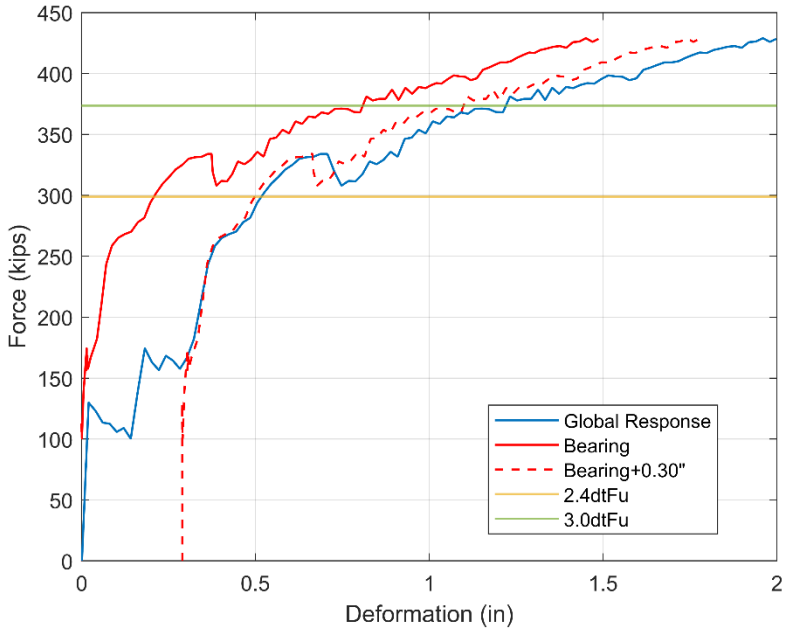


Figure 5-83. Bearing Deformation vs Global Response (Specimen T2)

Similarly, a comparison of results for boundary conditions corresponding to Specimen T2 and the wall scenario was conducted. Figure 5-84 shows the comparison between these two models, with and without the additional side restraints. The overall response showed no significant difference between the two models. Furthermore, Figures 5-85 and 5-86 provide a further comparison by presenting the distribution of net section normal stress for these two models. Again, in the absence of side restraints (boundary condition of the specimen), the edge of the faceplates shows a negative stress (compression) due to the bending stresses near the free edge.

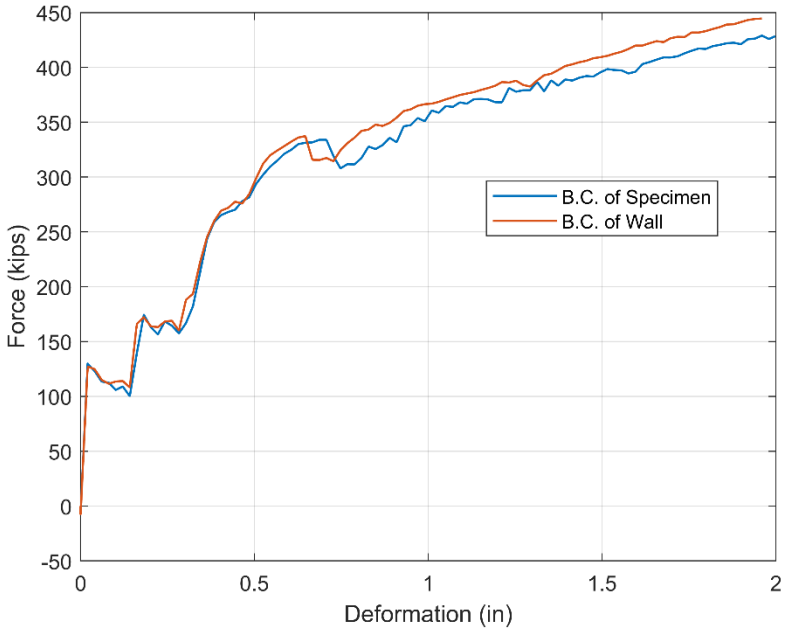


Figure 5-84. Finite Element Results of Boundary Conditions of Specimen and of Wall (Specimen T2)

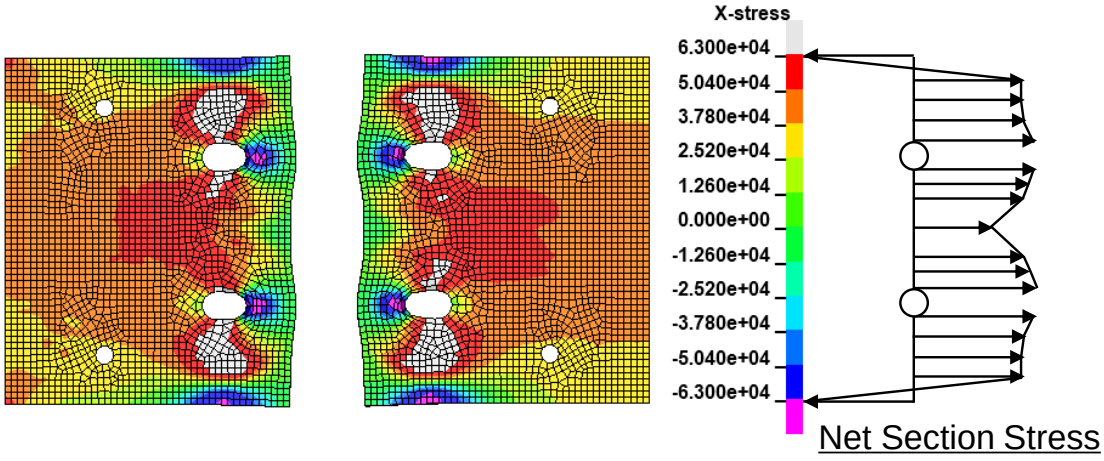


Figure 5-85. Normal Stresses for Specimen Model (Specimen T2, at 2.0-in. Deformation in Tension)

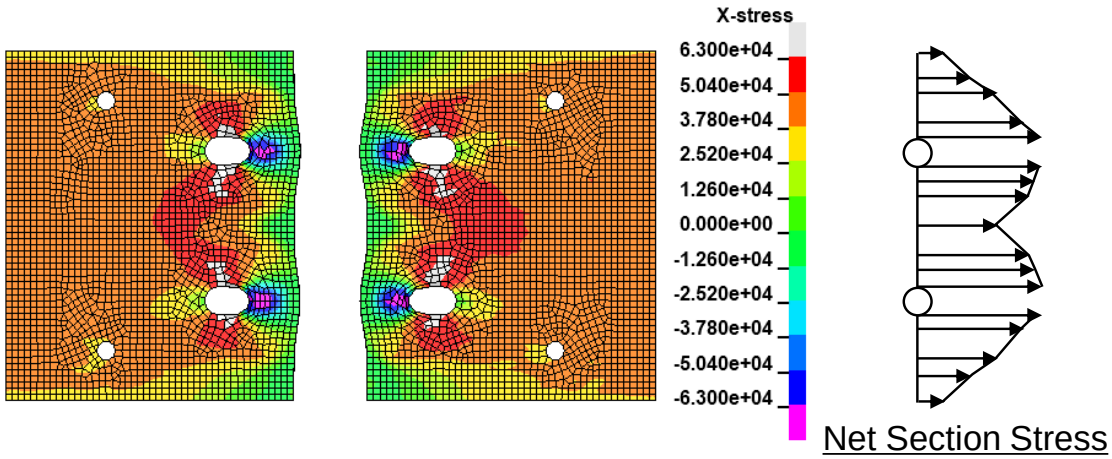


Figure 5-86. Normal Stresses for Wall Model (Specimen T2, at 2.0-in. Deformation in Tension)

Figure 5-87 shows the load protocol obtained from the recorded LP history for the cyclic load finite element analysis, while Figure 5-88 shows the corresponding finite element result. The finite element model demonstrates a good overall hysteresis response that closely resembles the loading and unloading curves of the test. The analysis result closely matches the peak force up to a deformation of 0.8 in. However, beyond this point, the strength of the finite element result begins to deviate from the test result. Specifically, at a deformation of 1.8 in., the strength of the finite element result is approximately 13% lower than to the corresponding value observed in the test.

Figure 5-89 provides a comprehensive view of the interaction between concrete and steel during the cyclic load analysis. This figure focuses on the normal stresses of concrete to investigate the stress concentration during cyclic loading. In addition, Figure 5-90 shows the axial strengths of concrete and steel throughout the cyclic loading process. Five distinct arbitrarily chosen points (selected in Figure 1-85) have been highlighted in the figure to represent various loading conditions experienced during cyclic loading. The figures indicate that the concrete reached its maximum compressive strength during Point 2. Beyond that point 2, the concrete still contributed approximately 25% to 40% of the compressive strength at compressive

peaks. Note that Specimen T2 was pushed further in compression than Specimen T1, which is why higher compression forces (per the mechanism described earlier) are observed. Similar to Specimen T1, the tensile strength of concrete is negligible.

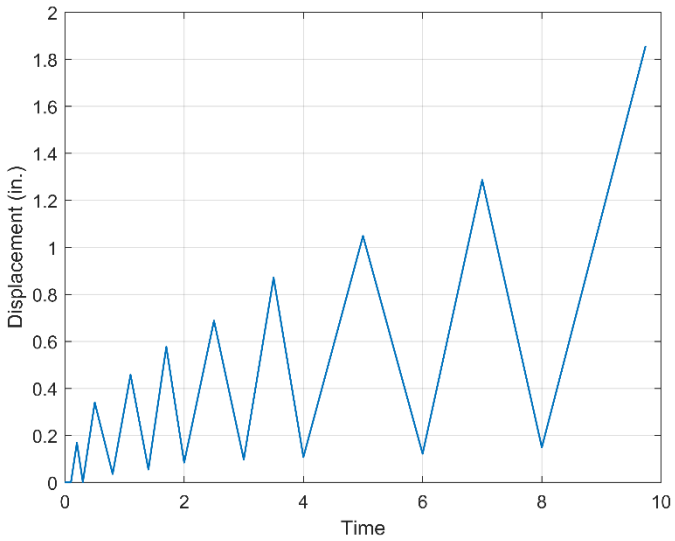


Figure 5-87. Cyclic Loading Protocol of Finite Element Model (Specimen T2)

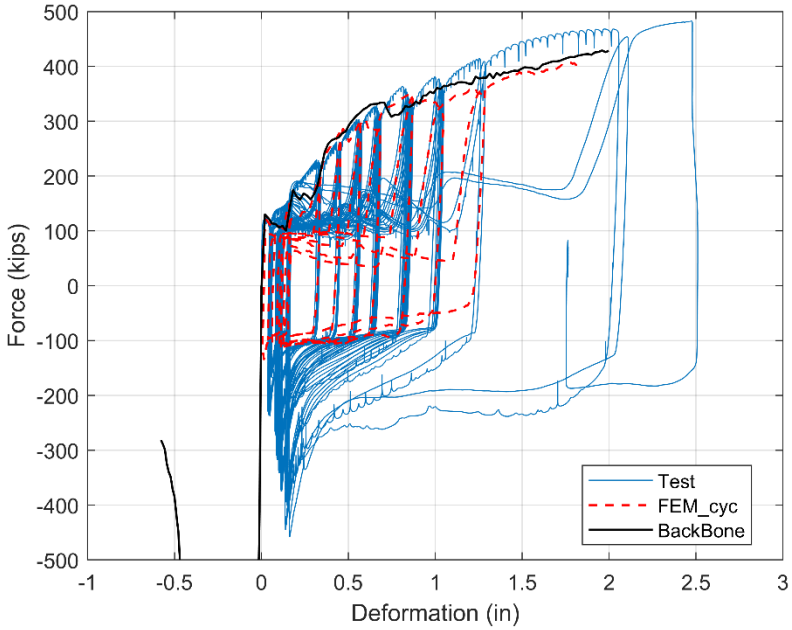


Figure 5-88. Finite Element Results of Hysteresis Loop of Specimen T2

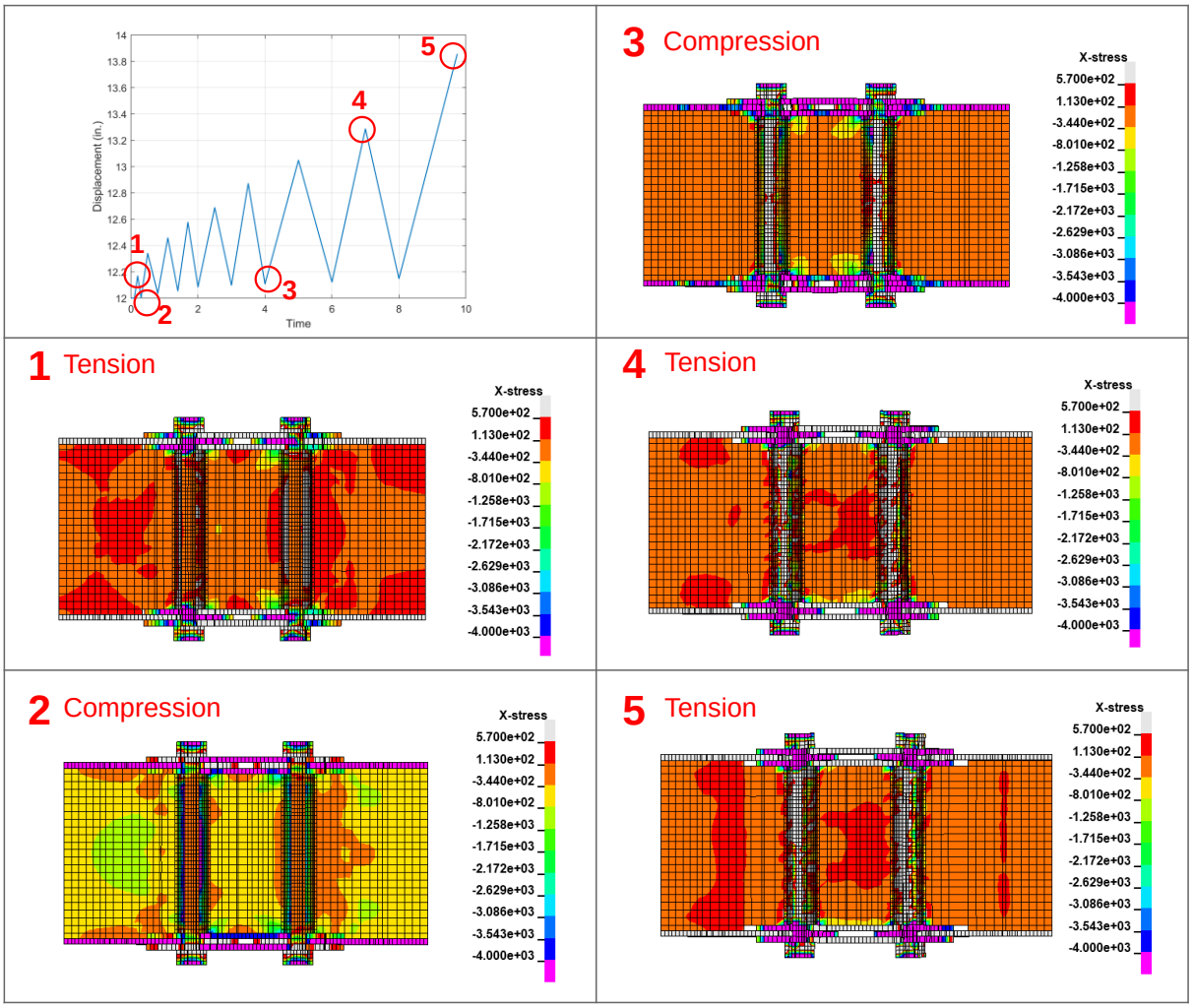


Figure 5-89. Cyclic Interaction between Concrete and Steel (Specimen T2)

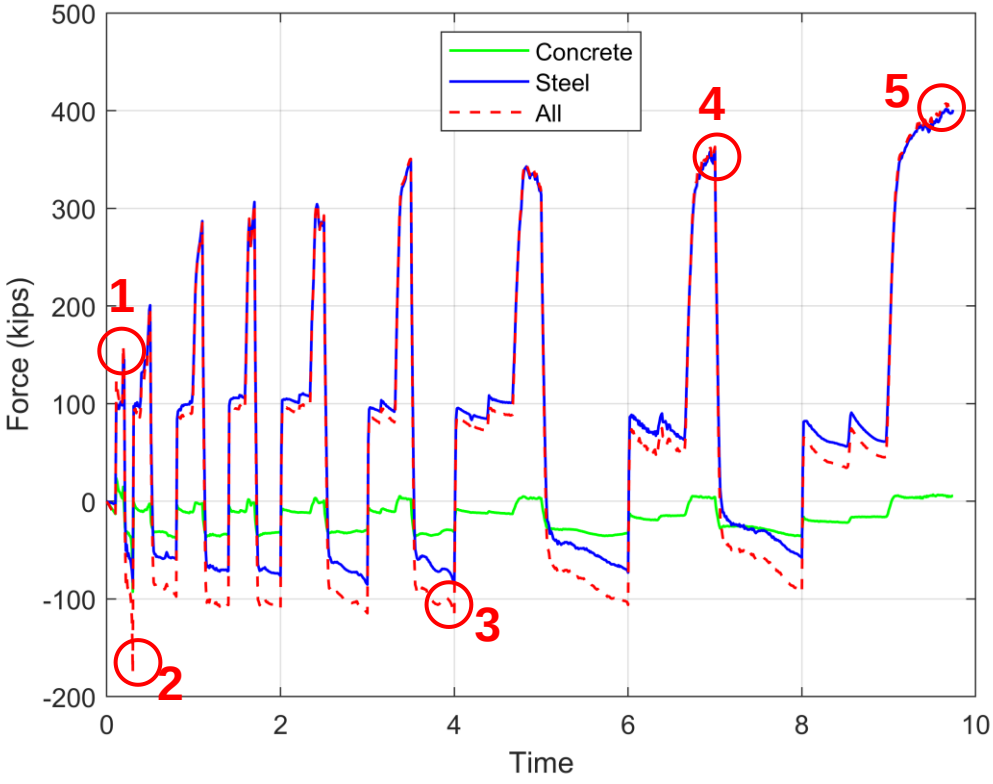


Figure 5-90. Axial Strengths of Concrete and Steel (Specimen T2)

5.3.7.3 Specimen T3

Figure 5-91 shows the axial load-deformation curve from monotonic loading of finite element model, compared to the test results. The tensile and compressive strengths of the finite element results are 577 kips and -1310 kips, and the corresponding deformation are 2.0 in. and -0.4 in. The maximum tensile load obtained from the finite element result is 7.0% lower than the value (620 kips) from the test result at a deformation of 2.0 in. in tension. The figure shows an amount of sliding observed in the finite element result that is less than in the test. In the finite element model, all the through rods were initially positioned at the center of the rod holes (corresponding to hook and gap values of 0.25 in. in the spring analysis). However, in the test, the observed amount of sliding is close to 0.5 in. In the spring model of Specimen T3, the hook and gap values were adjusted to 0.5 in. and 0, respectively, to better match the test result. Such an adjustment was not done for the finite element model.

Figure 5-92 shows the distribution of von Mises stresses all steel elements, while Figure 5-93 shows the von Mises stresses obtained from a cross-section taken along the center line of the through rods when the connection reached a deformation of 2.0 in. under monotonic tensile load. The steel mostly remained within the elastic range, except near the rod holes.

From Figure 5-93, it is noticeable that the edges of the splice plates curve when the connection is subjected to tension, primarily due to the bending of the rods. Furthermore, Figure 5-94 shows the deformation of a rod extracted from the right-hand side of the previous figure, together with a magnified deformation plot. The finite element results indicate that under a specimen deformation of 2.0 in. in tension, the rod experienced a relative bending deformation of 0.123 in. from its middle to its top.

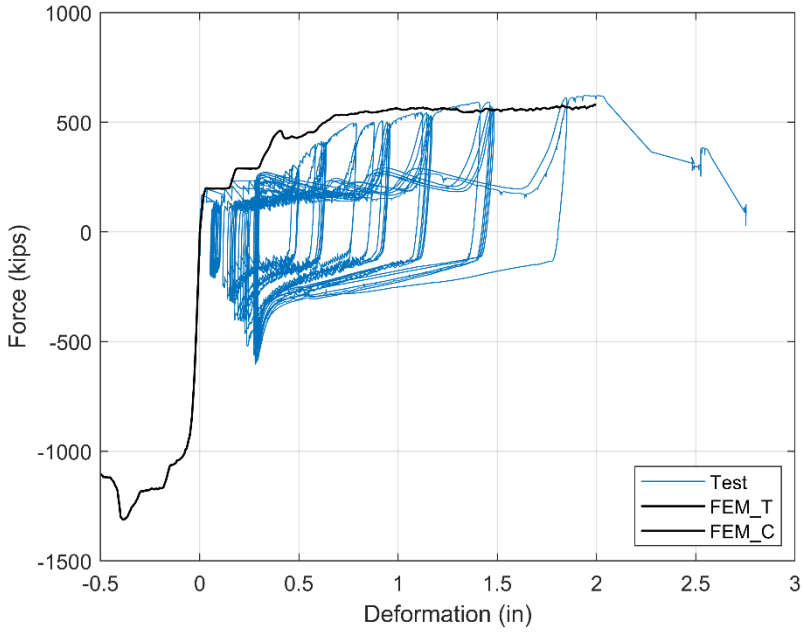
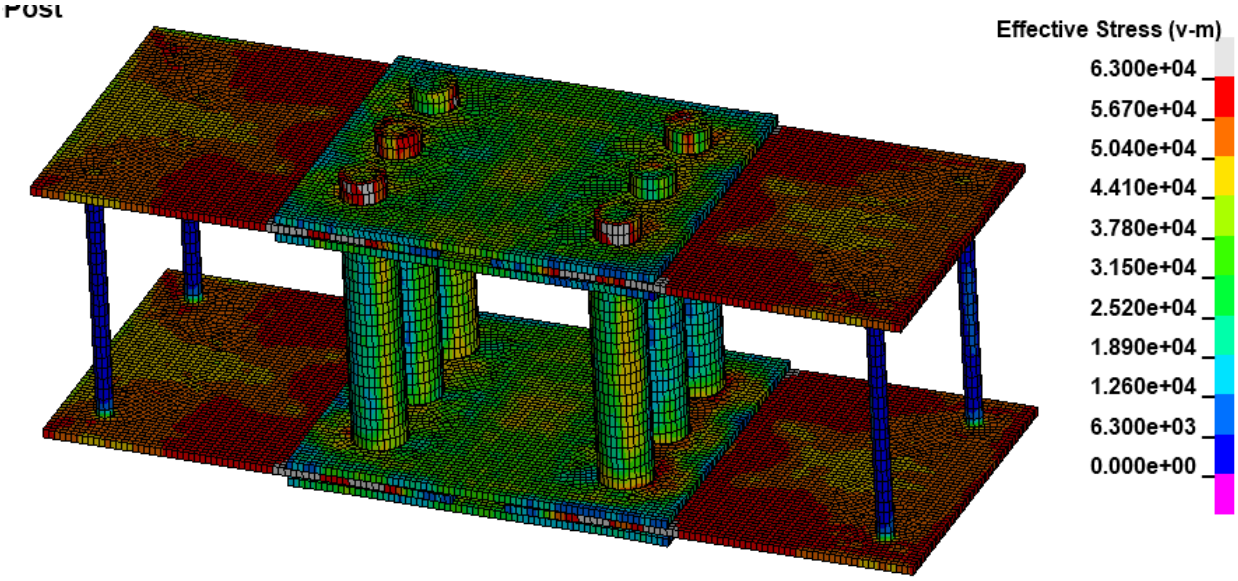
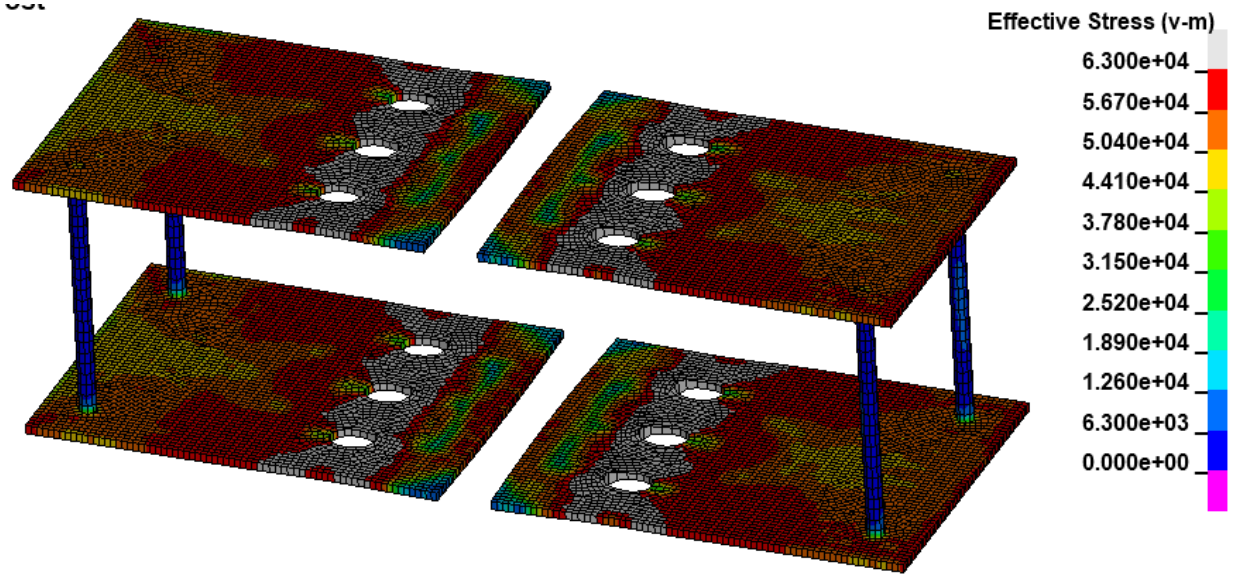


Figure 5-91. Finite Element Results of Load-Deformation Curve of Specimen T3



(a) All Steel



(b) Reveal Faceplates

Figure 5-92. von Mises Stresses of Steel Parts (Specimen T3, at 2.0-in. Deformation in Tension)

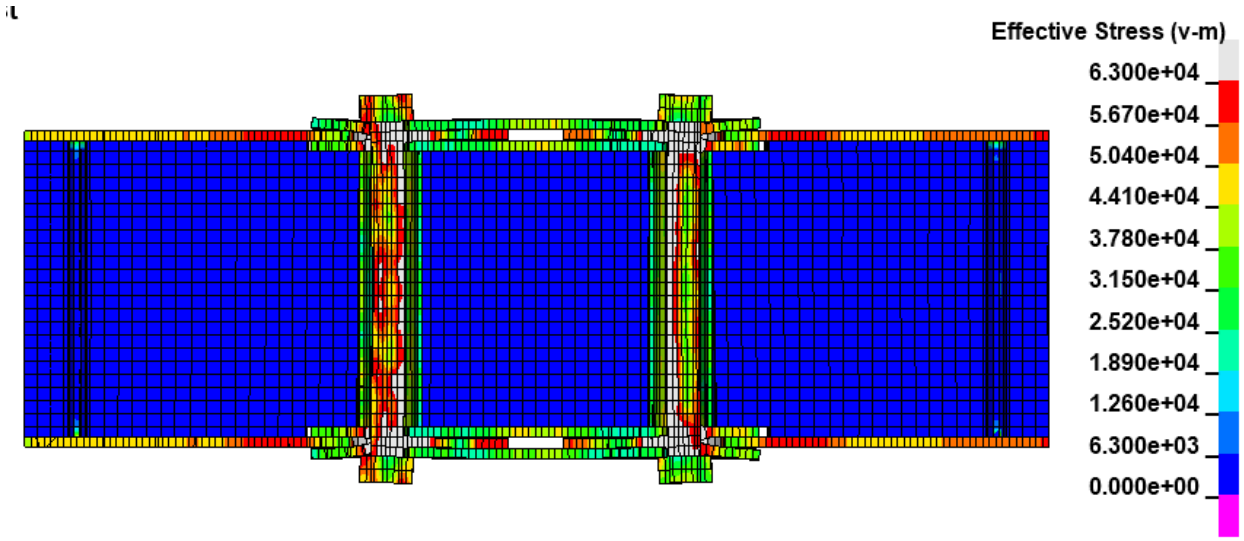


Figure 5-93. von Mises Stresses at Rod Section (Specimen T3, at 2.0-in. Deformation in Tension)

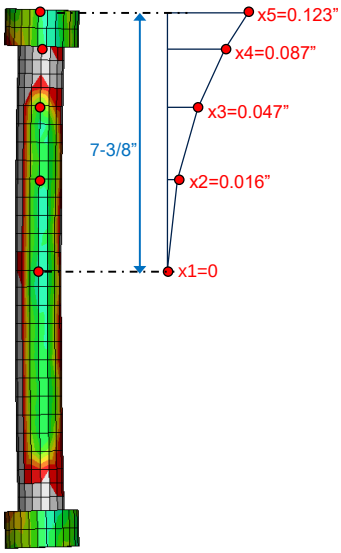


Figure 5-94. Deformation of Rods (Specimen T3)

Figure 5-95 shows the elongation of the rod holes in the finite element result of Specimen T3 under monotonic tensile load at a deformation of 2.0 in. Figure 5-96 compares the bearing curve with the global response, where the bearing curve is obtained by calculating hole elongation (note that the three holes elongation values are within 1.5% of each other). As Specimen T3 was designed to be governed by net section rupture, the connection experienced net section yielding after sliding. Following net section yielding, the axial stiffness of the connection significantly decreases, as depicted in the figure. The bearing curve intersects with $2.4dtF_u$ at a deformation of 0.6 inches. Note that this 0.6-in. deformation is primarily attributed to net section elongation around the rod holes.

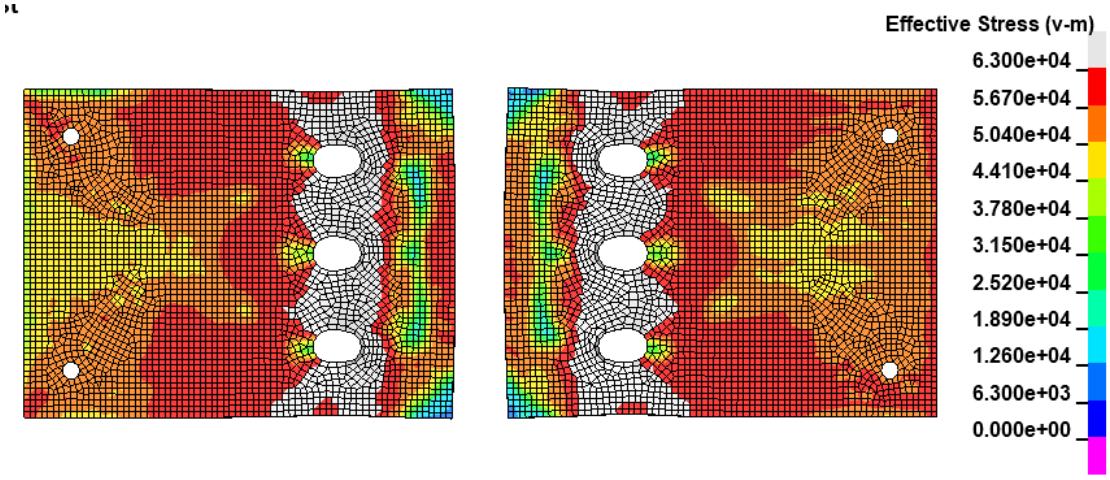


Figure 5-95. Elongation of Bolt Holes (Specimen T3, at 2.0-in. Deformation in Tension)

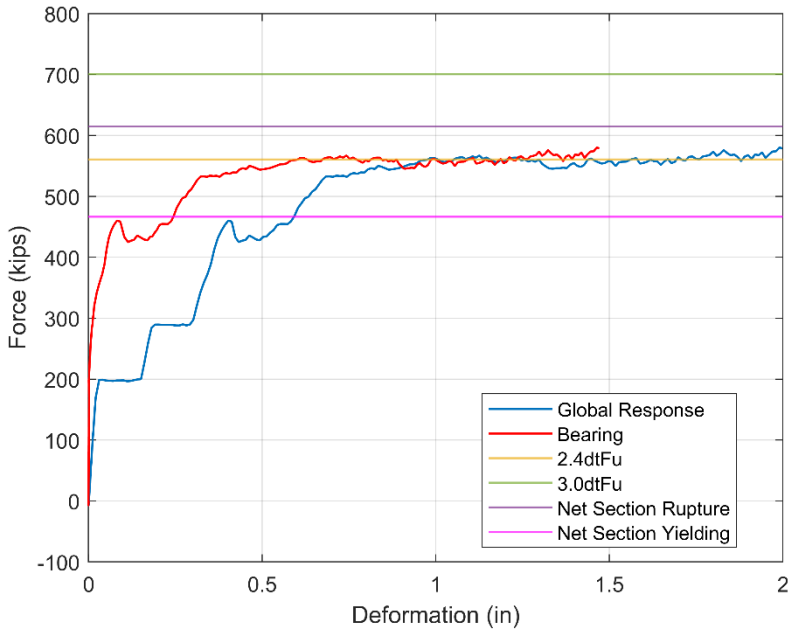


Figure 5-96. Bearing Deformation vs Global Response (Specimen T3)

Similarly, a comparison was made between Specimen T3 and the wall scenario in terms of boundary conditions. Figure 5-97 shows the comparison between these two models, with and without side restraints. The overall response showed no significant difference between the two models. Additionally, Figure 5-98 and Figure 5-99 provide a detailed comparison by presenting the distribution of net section normal stress

in these two models. In contrast to Specimens T1 and T2, the edge stress in Specimen T3 remains in tension in both the specimen and wall boundary conditions. As previously mentioned, Specimen T3 underwent net section yielding prior to reaching the bearing strength corresponding to $2.4dtF_u$. Therefore, the negative stresses resulting from bending along the free edge are not present in this case. All net section normal stresses remain in tension.

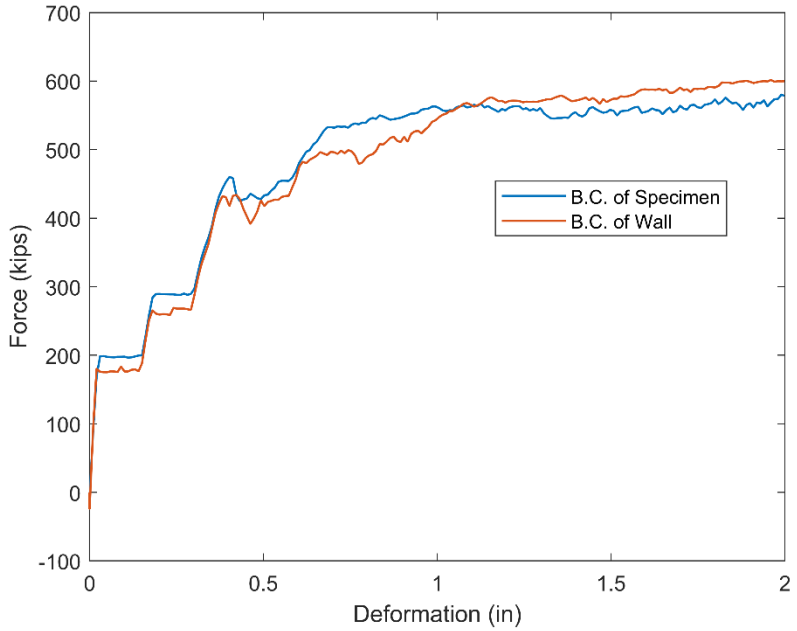


Figure 5-97. Finite Element Results of Boundary Conditions of Specimen and of Wall (Specimen T3)

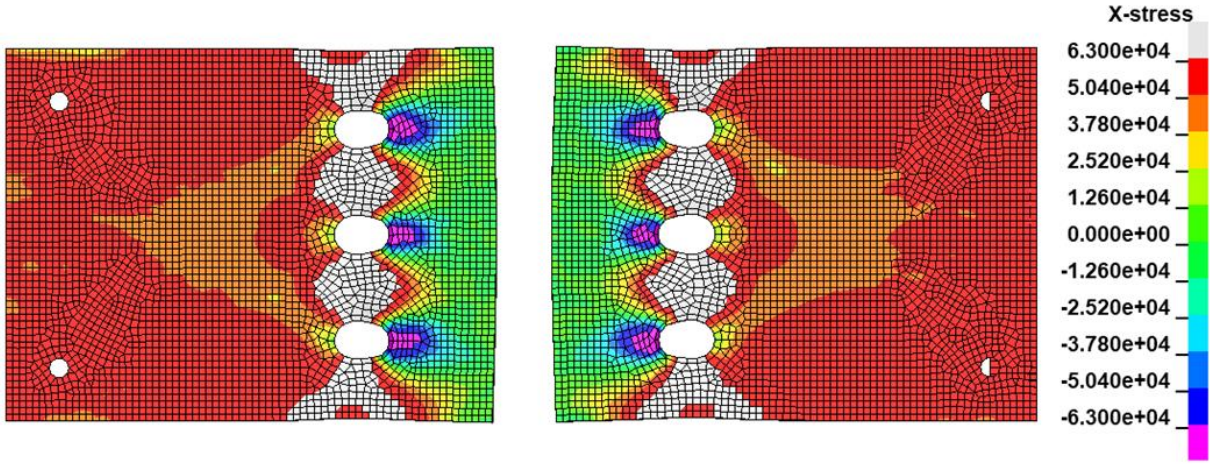


Figure 5-98. Normal Stresses of Specimen Model (Specimen T3, at 2.0-in. Deformation in Tension)

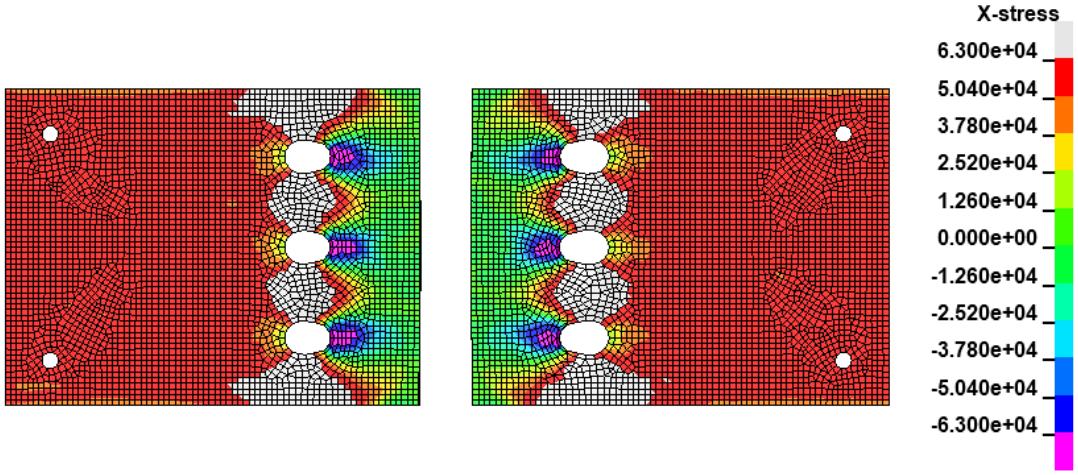


Figure 5-99. Normal Stresses of Wall Model (Specimen T3, at 2.0-in. Deformation in Tension)

Figure 5-100 shows the load protocol obtained from the recorded LP history for the cyclic load finite element analysis, while Figure 5-101 shows the corresponding finite element result. Although the finite element model shows a higher strength initially compared to the test, the analysis result captures well the overall hysteresis response upon the subsequent loading and unloading curves. The finite element analysis recorded a peak force of 571 kips at a 2.0-in. deformation, which is 8.2% lower than the corresponding value observed in the test.

Figure 5-102 provides an overview of the interaction between concrete and steel during the cyclic load analysis, while Figure 5-103 shows the proportion of the axial force resisted by concrete and steel by cutting a cross-section at the middle of the connection. The figures highlight five arbitrary selected points that represent different loading conditions during cyclic loading. It is observed that the concrete in the middle of the connection consistently remains in compression throughout the cyclic loading process, contributing approximately 30% to 50% of the compressive strength at compressive peaks. Figure 5-104 shows points 3 and 4 from the cyclic loading analysis, providing a side view of the specimen. Vertical cracks initially

appeared through the full depth of the concrete at both ends of the splice plates. Subsequently, the concrete in the middle of the specimen remained in compression throughout the cyclic analysis, per the behavior described earlier.

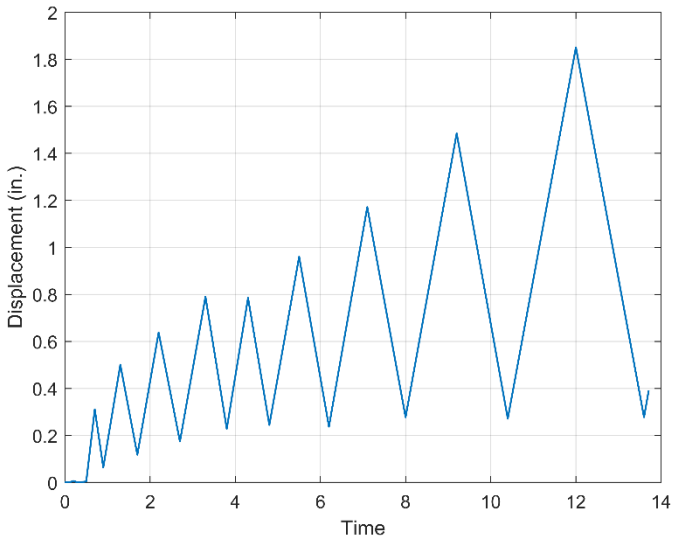


Figure 5-100. Cyclic Loading Protocol of Finite Element Model (Specimen T3)

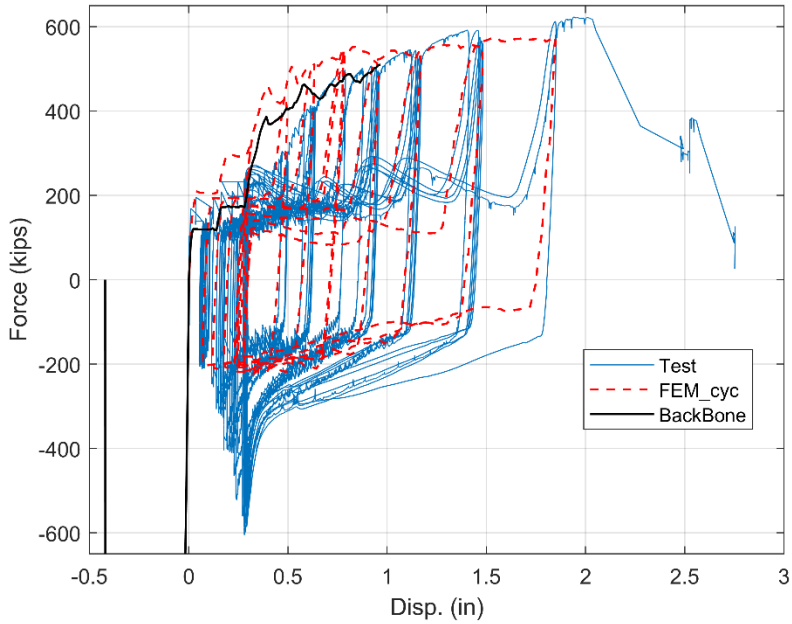


Figure 5-101. Finite Element Results of Hysteresis Loop of Specimen T3

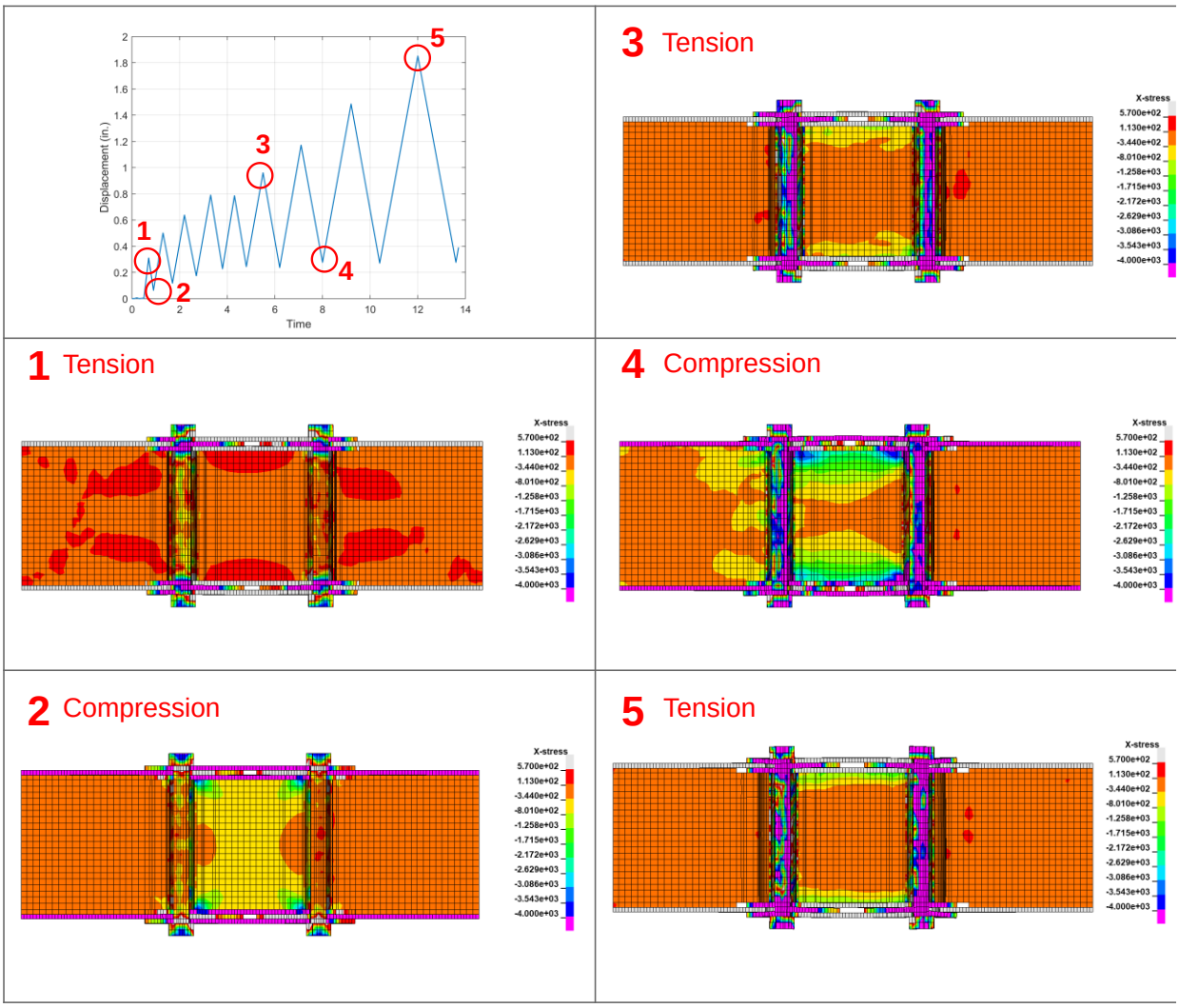


Figure 5-102. Cyclic Interaction between Concrete and Steel (Specimen T3)

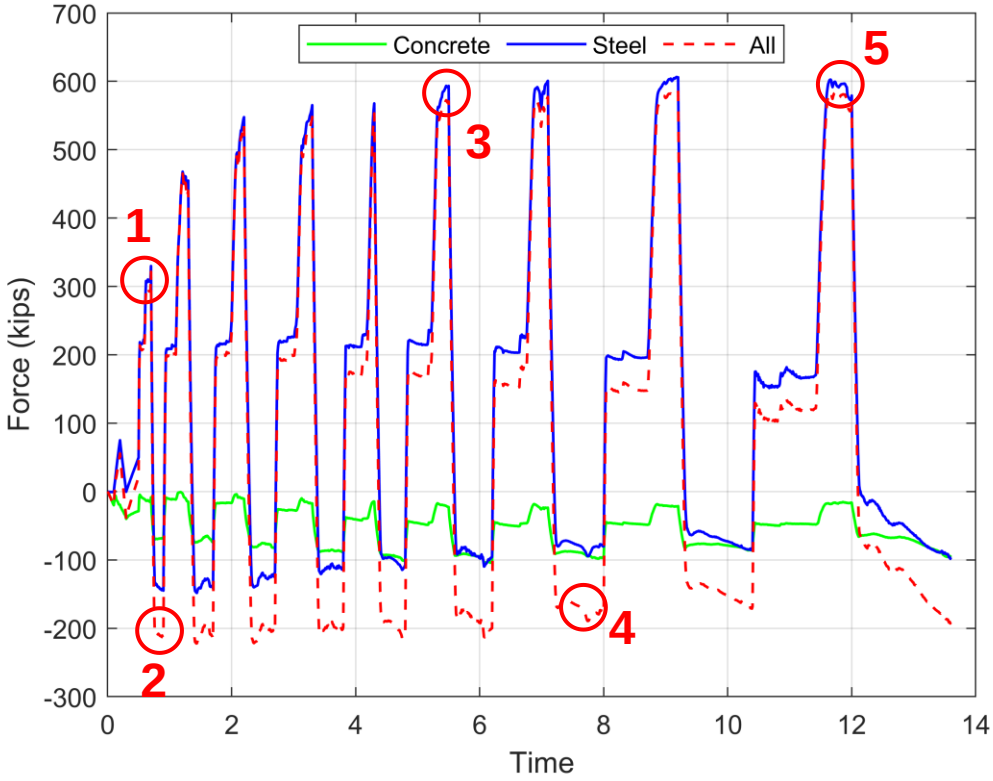


Figure 5-103. Axial Strengths of Concrete and Steel (Specimen T3)

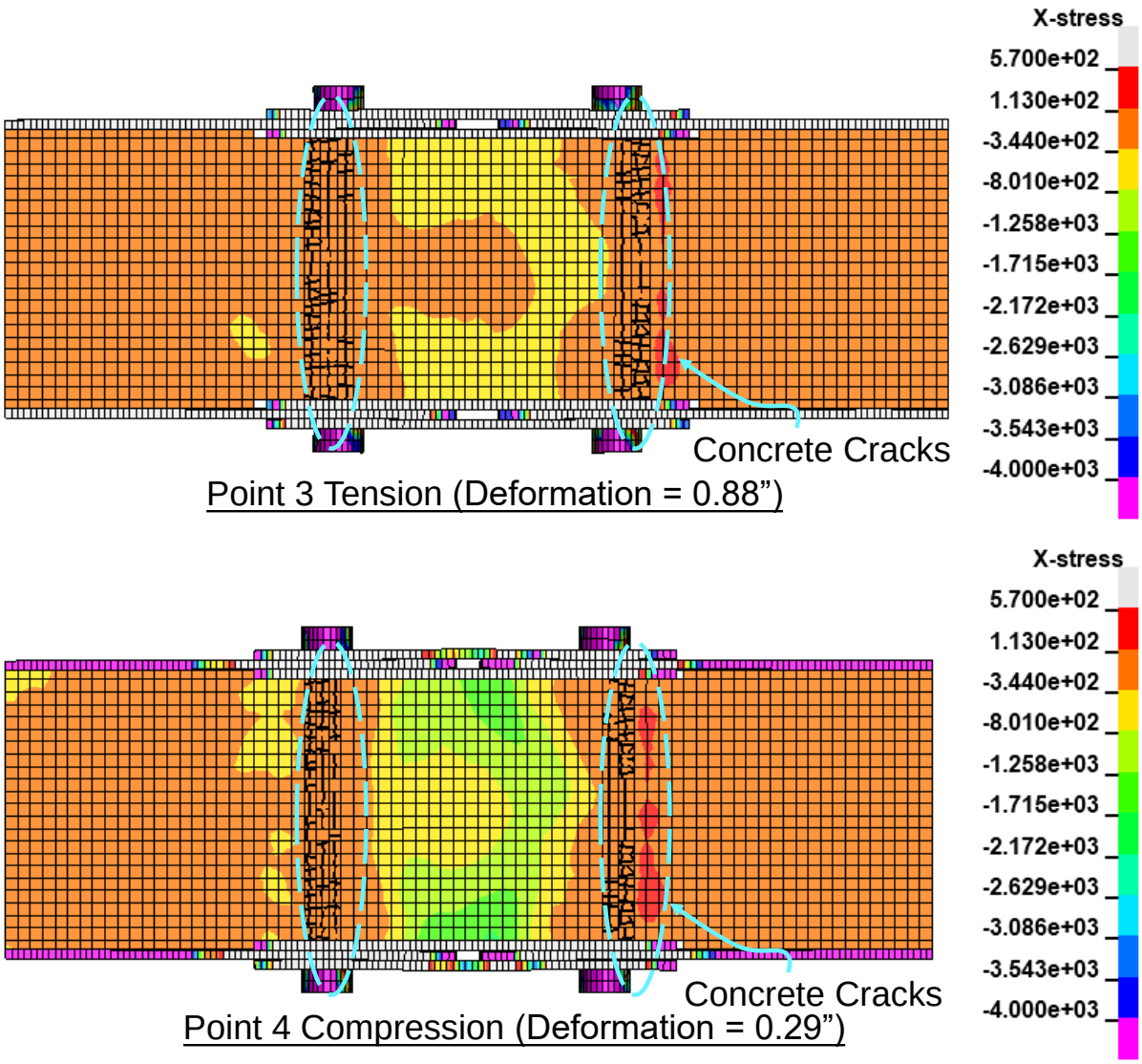


Figure 5-104. Side View of Normal Stresses of Specimen T3

5.3.7.4 Specimen T4

Figure 5-105 compares the axial load-deformation curve between the finite element model and the test results. The tensile strength from finite element analysis reaches 551 kips at 0.5-in. deformation. The finite element results exhibit higher stiffness and strength in comparison to the test results. The maximum load obtained from the finite element result is approximately 20.0% higher than the corresponding value of 460 kips observed in the test. The figure also shows the expected strength corresponding to corner bending and concrete failure, which are 259.78 kips and 396.60 kips, respectively. The figure indicates that the axial strength in the finite element result reaches the limit state of corner bending at a deformation of 0.09 in., and the limit state of concrete failure at a deformation of 0.25 in. On the other hand, the axial strength in the test result reaches the limit state of corner bending at a deformation of 0.2 in., and the limit state of concrete failure at a deformation of 0.39 in.

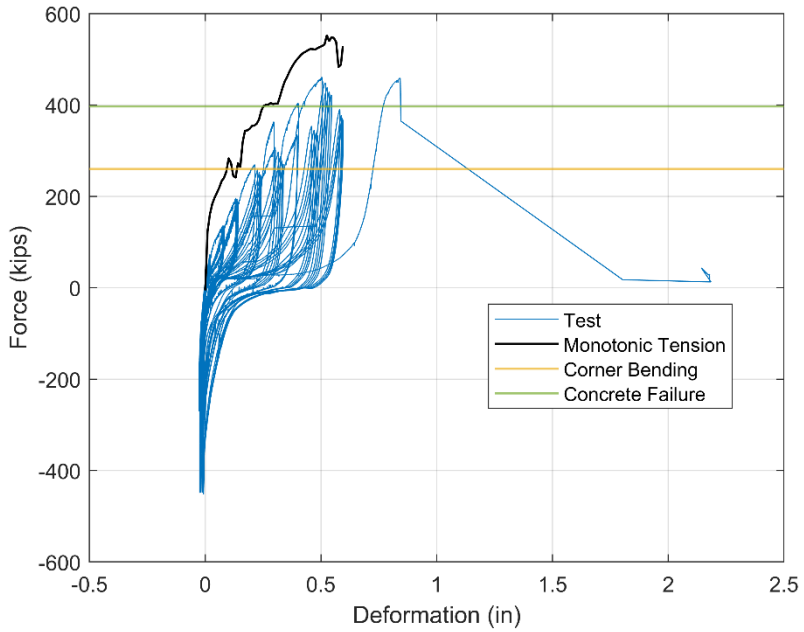


Figure 5-105. Finite Element Results of Load-Deformation Curve of Specimen T4

Figure 5-106 shows the distribution of von Mises stresses in all the steel elements, while Figure 5-107 shows the stresses around rod holes by visually removing the splice plates and pipe-sleeves. Under a deformation of 0.55 in. in tension, the area near the rod holes on faceplates experienced yielding, and the rods were bent due to the tensile force pulling on the splice. The deformation of a typical rod is shown in Figure 5-108, revealing that it behaved in double-curvature bending.

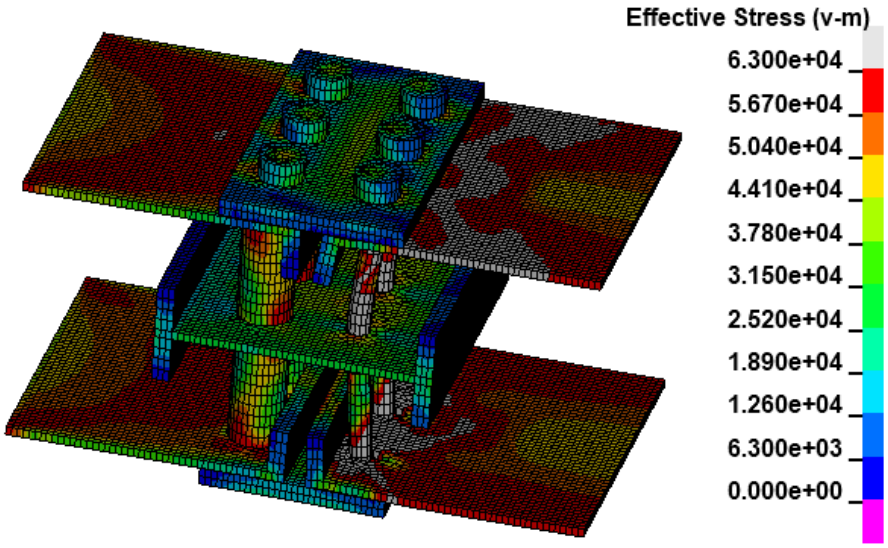


Figure 5-106. von Mises Stresses of Specimen T4 (Deformation=0.55” in Tension)

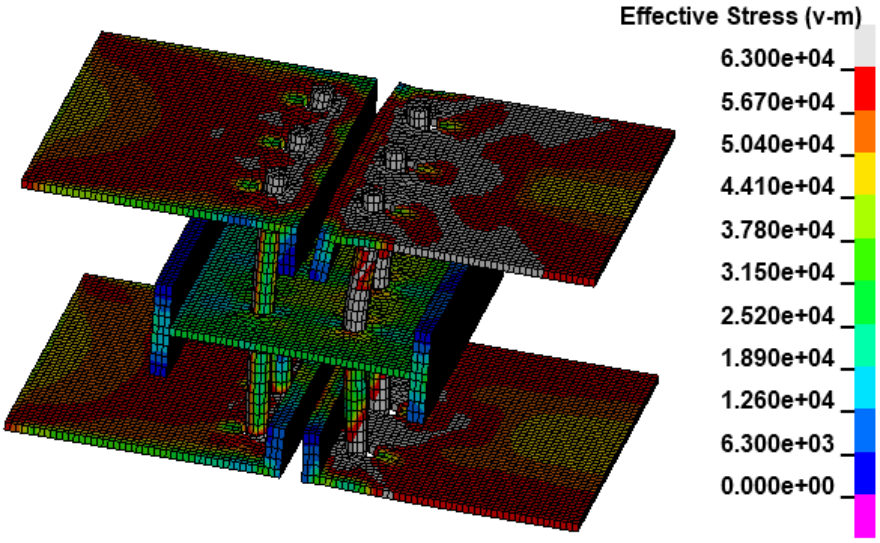


Figure 5-107. von Mises Stresses of Specimen T4 (Reveal Faceplates, Deformation=0.55” in Tension)

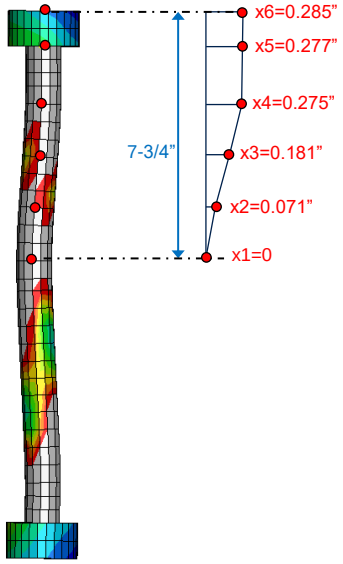


Figure 5-108. Deformation of Rods (Specimen T4)

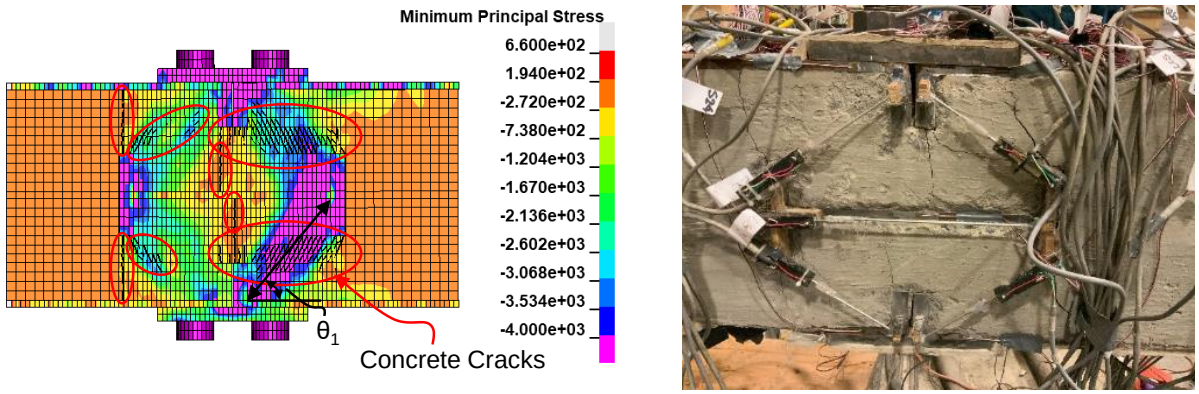
Figure 5-109 shows the development of compression struts on the north face (side view) of the specimen, comparing it with the corresponding test result at various LP deformation stages. At an axial deformation of 0.14 in., the angle of the compression struts shown in the figure (θ_1) is approximately 50˚, which is close to the theoretical value of 45˚ assumed for design. Also shown in this figure are the concrete cracks generated from the Winfrith concrete model. As the deformation increases, more concrete cracks are observed in the connection.

Additionally, while Figure 5-106 looked at stresses at the edge of the specimen (i.e., North face), Figure 5-110 presents results at a section taken at the middle of one of the rods, revealing the presence of a compression strut there with an angle within the section(θ_2) of 68˚. A noticeable difference in the angles (θ_1 and θ_2) of the compression strut is observed between the side view and section cut at the middle of rods.

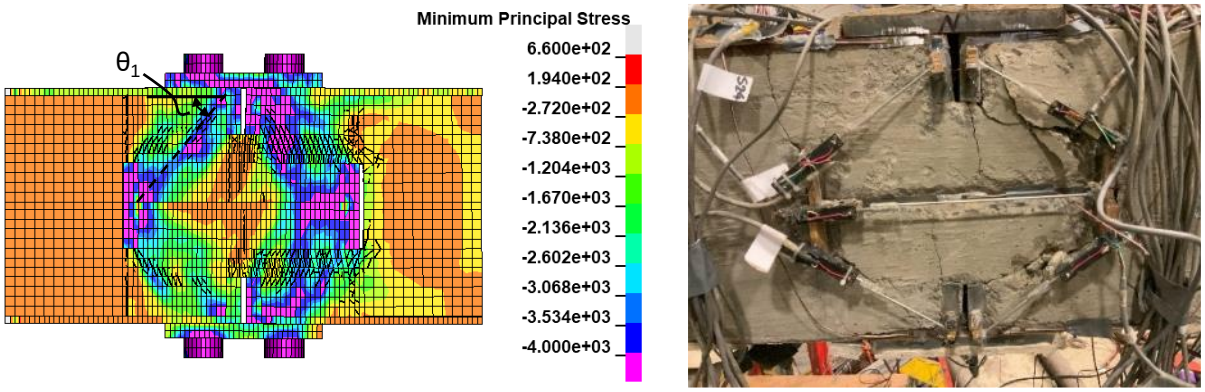
Figure 5-111 shows two section cuts of Specimen T4, illustrating the axial force components at the respective locations. Section Cut 1 corresponds to the middle of the compression struts, while Section Cut 2 corresponds to the middle of the connection. Additionally, the following notation is used:

- T_u: represents the total axial force applied to the connection.
- C_1: represents the sum of the horizontal component of the two compression struts forces.
- T_2: represents the sum of the axial forces in the top and bottom faceplates.
- T_3: represents the sum of the axial forces in the top and bottom splice plates.
- T_4: represents the axial force in the web of the I-Shaped Anchor.
- C_5: represents the sum of the axial forces acting on the top and bottom nuts.

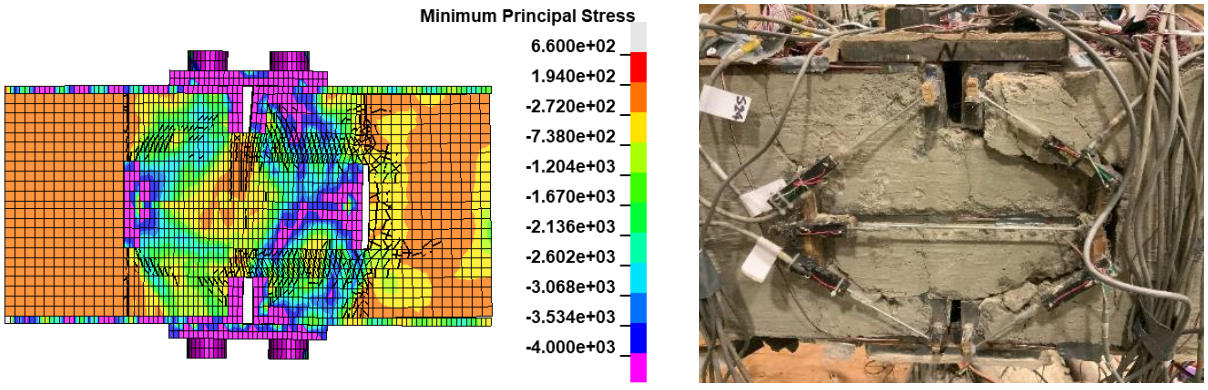
Figures 5-112 and 5-113 show the axial forces contributed by each component at respective Section Cuts. The theoretical expected strength of 396.6 kips corresponding to failure of the compression strut is also indicated in these two figures. In 5-112, it can be observed that the compression strut force reaches a plateau (at a horizontal component of approximately 150 kips) after the connection reaches 0.1-in. deformation, indicating a compression-strut contribution lower than expected. At that section cut, the tension force in the web of the I-shaped anchor is in equilibrium with the horizontal component of the compression strut forces. At that cut, tension from the faceplate has not yet been significantly transferred to the splice plates. 5-113 shows that, at 0.25-in. deformation, when the theoretical expected strength of 396.6 kips is reached, equilibrium at the mid-length of the splice indicates that the splice plates transfer 44% of the total tension force, while the web of the I-shaped anchor transfer 52% of it. Results also indicate that the force transfer mechanism exhibits a decreased effectiveness of the compression strut, with the splice plates progressively taking over a greater portion of the axial forces as the deformation further increases.



(a) LP=0.14 in.



(b) LP=0.3 in.



(c) LP=0.6 in.

Figure 5-109. Development of Compression Strut of Specimen T4 (Finite Element Model vs Test)

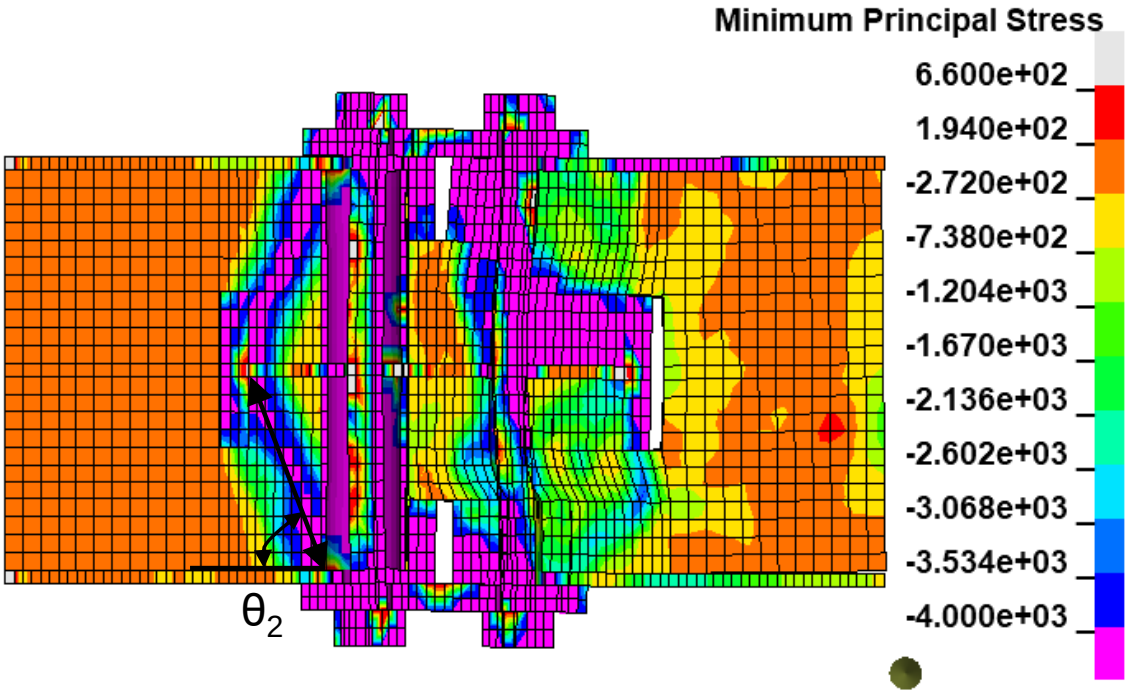


Figure 5-110. Middle Section Cut (Specimen T4, at 0.6-in. deformation in Tension)

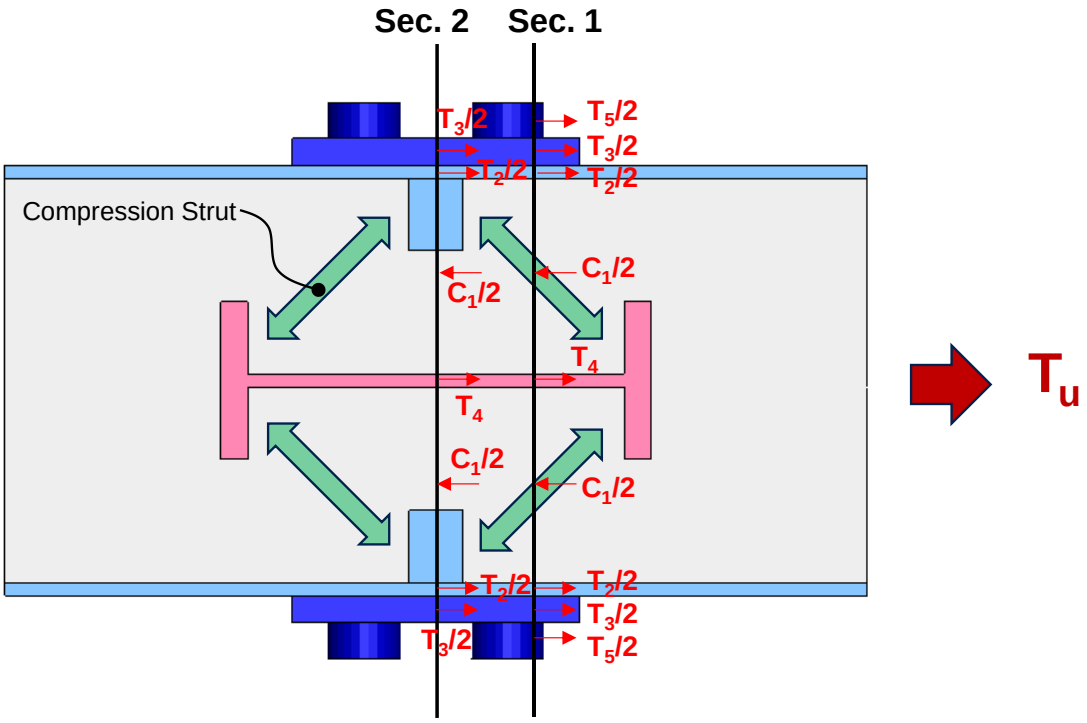


Figure 5-111. Axial-Force Components of Specimen 4 at Section Cuts 1 and 2

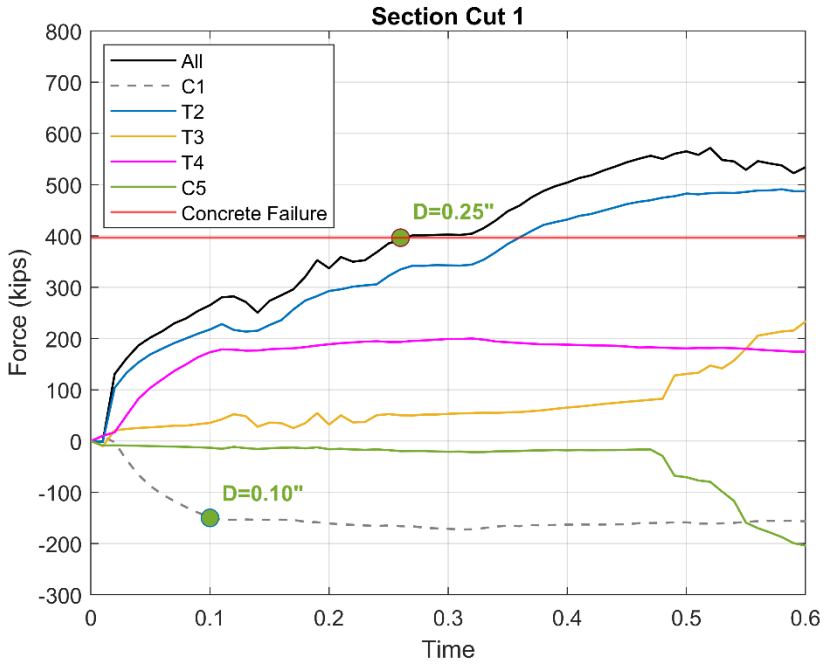


Figure 5-112. Axial Strengths of Concrete and Steel (Specimen T4, Section Cut 1)

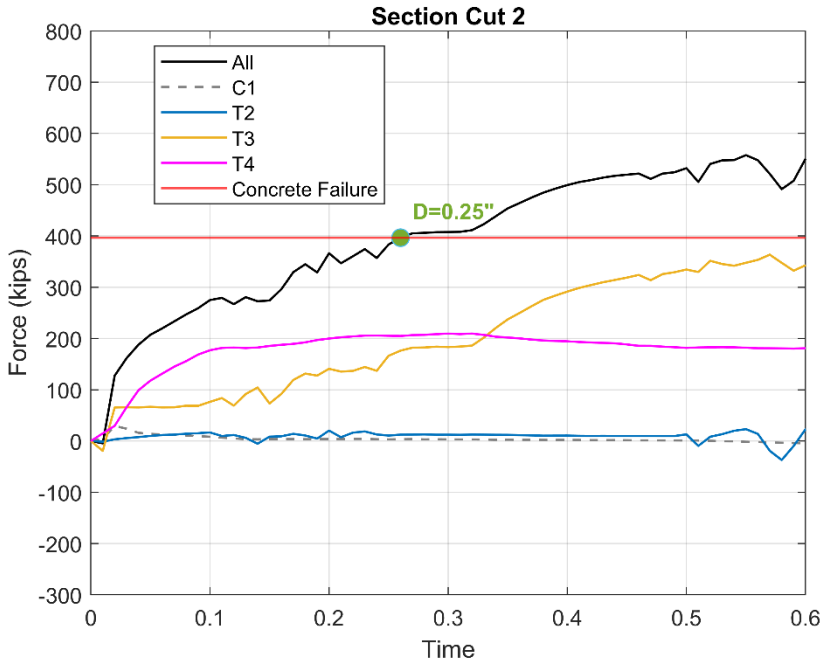


Figure 5-113. Axial Strengths of Concrete and Steel (Specimen T4, Section Cut 2)

Figure 5-114 shows the load protocol derived from the recorded LP history for the cyclic load finite element analysis, while Figure 5-115 shows the corresponding finite element results. The envelope of the cyclic load analysis aligns with the monotonic tension curve, and as observed previously, the finite element results overestimate the strength of the connection by approximately 20%.

In Figure 5-116, the evolution of the compression struts during the cyclic load analysis at five selected tensile peaks (points) is presented from the side view (north face). As was the case for monotonic loading, a compression strut at an angle of approximately 50 is observed on the north face of the connection during the analysis up to Point 2. However, as the deformation exceeds 0.25 in. and the axial strength of the concrete surpasses 390.6 kips (the concrete failure strength), the compression struts become less prominent and the cracks in the concrete increase.

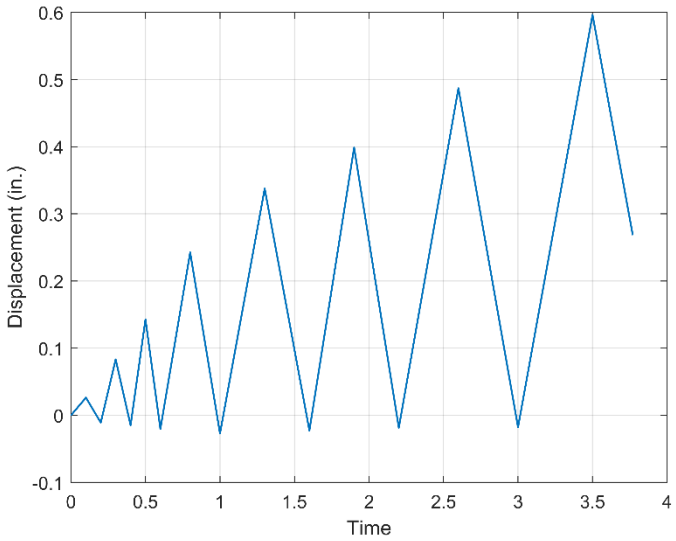


Figure 5-114. Cyclic Loading Protocol of Finite Element Model (Specimen T4)

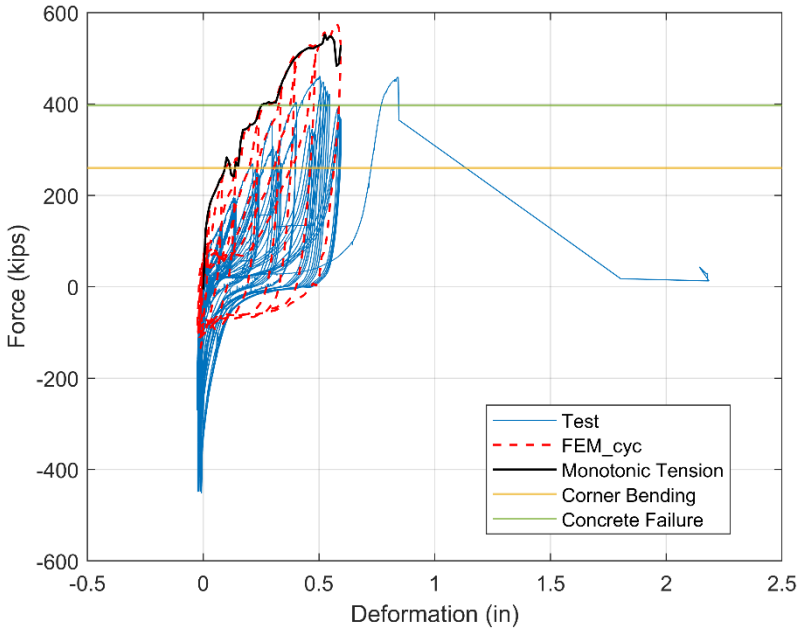


Figure 5-115. Finite Element Results of Hysteresis Loop of Specimen T4

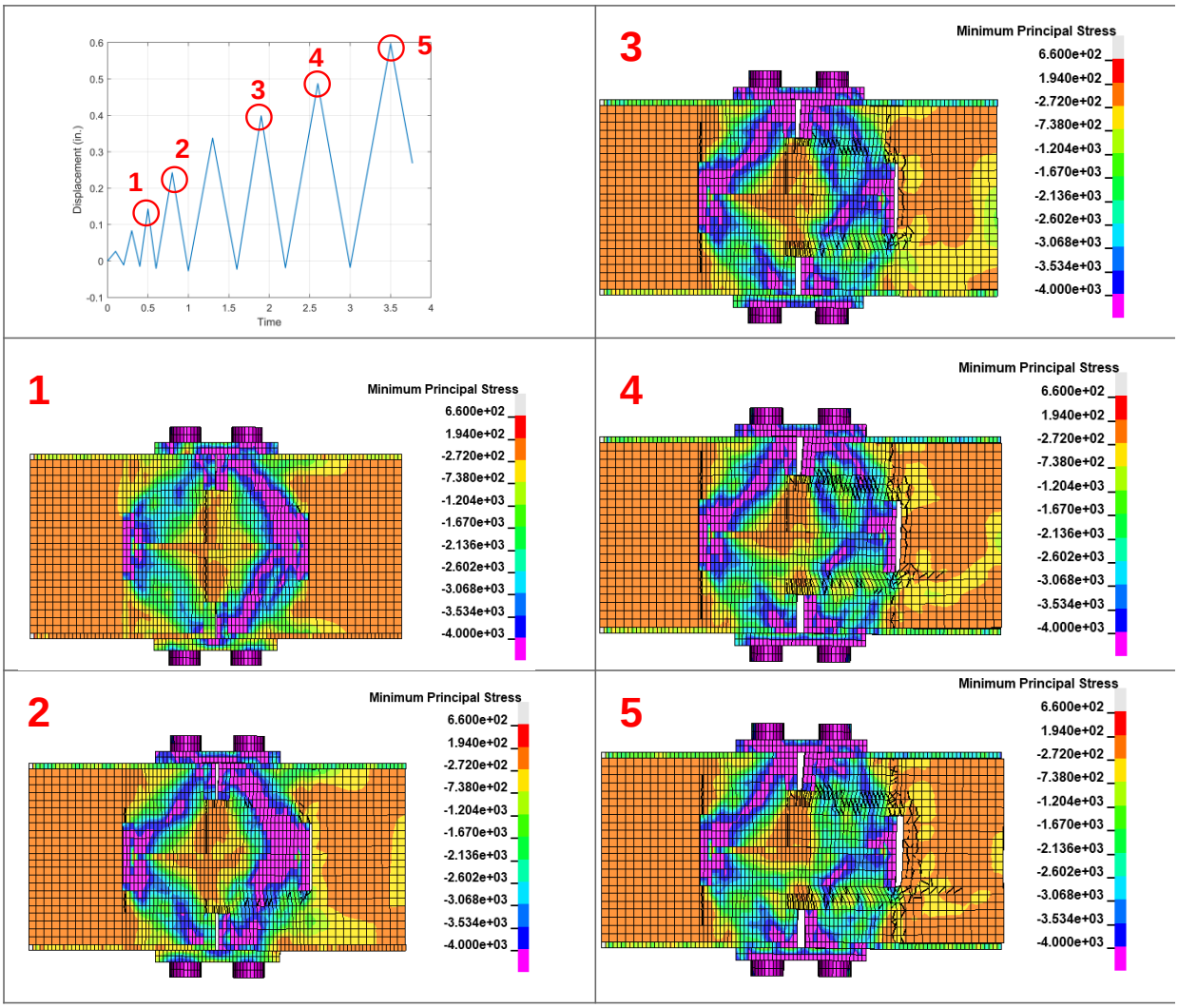


Figure 5-116. Development of Compression Struts from Cyclic Load Analysis (Specimen T4)

5.3.7.5 Specimen T5

Figure 5-117 shows the comparison of the axial load-deformation curve between the finite element model and the test results. The tensile and compressive strengths of the finite element results are 715 kips and -1417 kips, and the corresponding deformation are 2.0 in. and -0.22 in. Note that buckling of splice plates occurred in the test after LP deformation reached 0.71 in. Also, after LP reached 0.71 in., the experimental curve includes some "horizontal plateaus" that are not actual elongations but rather shifts in recorded values because the instruments attachments failed due to the buckling of splice plates and could not be easily reconnected because the plate was curved, losing the reference points in the process. Therefore, in the finite element analysis, monotonic loading displacements beyond 0.71 in. are exploratory and not intended to replicate test results., and comparison of cyclic response is limited to 0.71 in.

Figures 5-118 and 5-119 show the distribution of von Mises stresses of Specimen T5 when the connection reaches 2.0 in. deformation. Figure 5-120 shows the von Mises stresses obtained from a cross-section taken along the center line of the bolts. The result shows that both net section and gross section area of the faceplates experienced yielding in the analysis.

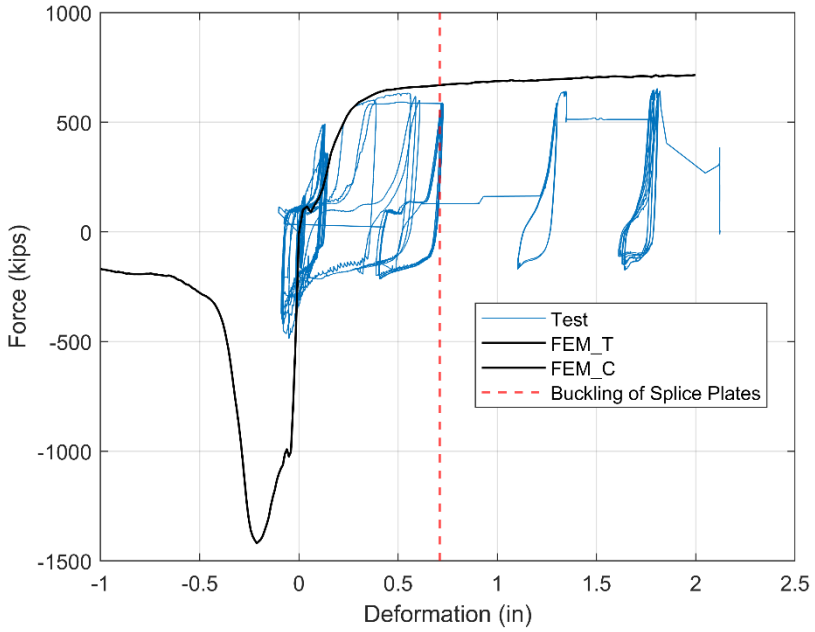


Figure 5-117. Finite Element Results of Monotonic curve of Specimen T5

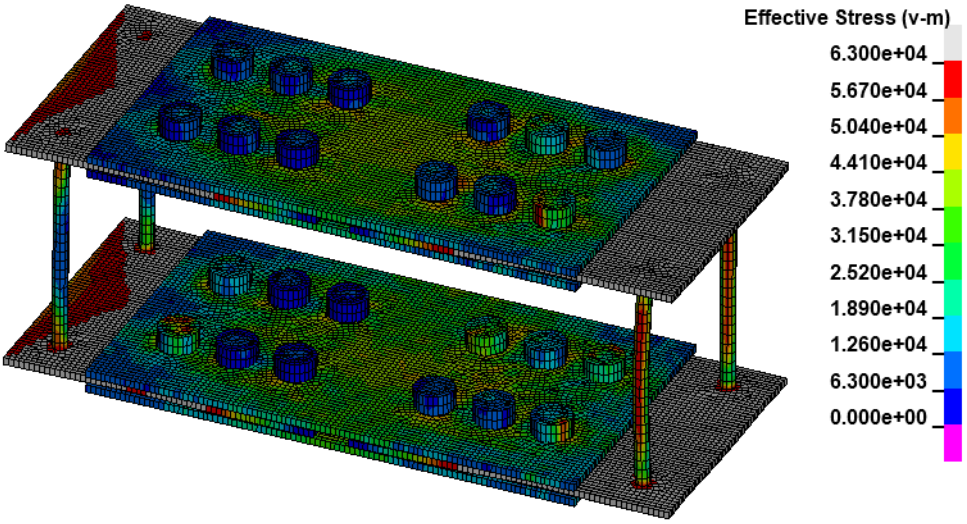


Figure 5-118. von Mises Stresses of Specimen T5 (Deformation=2.0” in Tension)

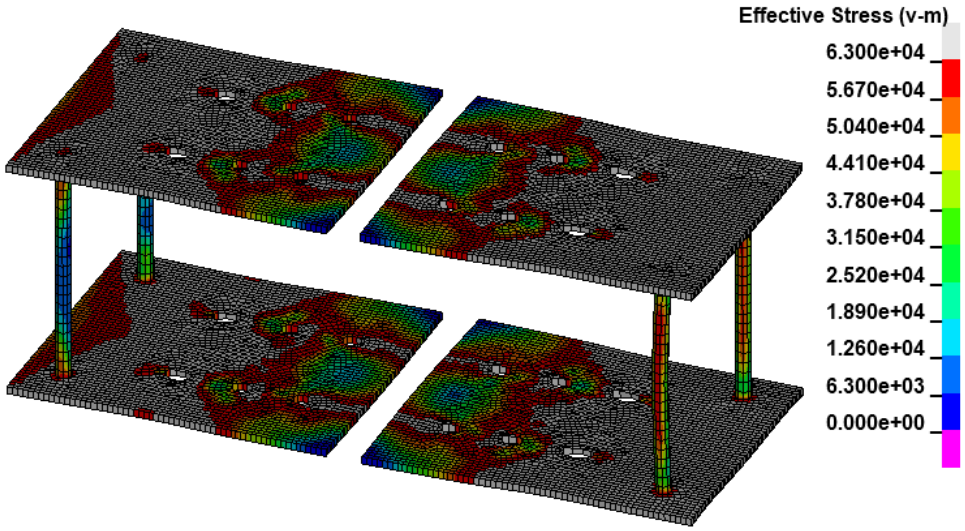


Figure 5-119. von Mises Stresses of Specimen T4 (Reveal Faceplates, Deformation=2.0” in Tension)

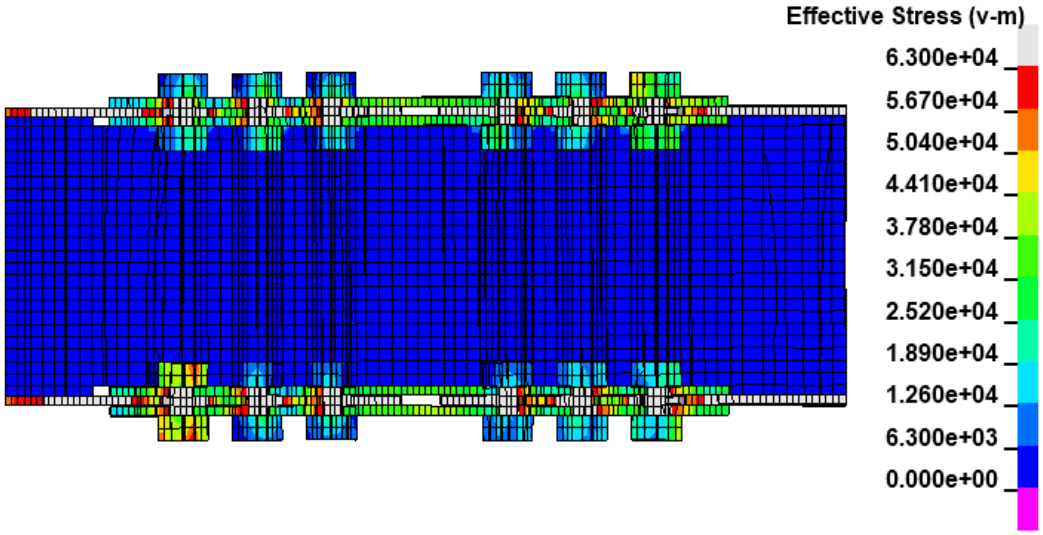


Figure 5-120. von Mises Stresses at Bolt Section (Specimen T5, Deformation=2.0” in Tension)

Figure 5-121 shows the elongation of the faceplates at a deformation of 2.0 in. The elongations are divided into various segments, such as the gross section of the faceplates, net section of the faceplates, end part of the faceplates, and the gap. By combining the deformations from these different segments, the global response of the faceplates can be determined.

Figure 5-122 shows the elongations contributed by different segments of the faceplates, as well as the global response. The figure indicates that the gross sections and net sections of the faceplates experience elongation, while the end part of the faceplates actually undergoes some shortening. This is because, while the plate is displaced in tension, the bolts locally prevent this elongation and compress the end part of the faceplate, as shown in Figure 5-123 for x-direction stresses (rather than effective stresses as in Figure 5-121). During the applied 2.0-in deformation (Global Response), the gross section deformation contributes an elongation of 0.56 in., the net section deformation contributes an elongation of 1.24 in., the end part deformation contributes a shortening of -0.40 in., and the gap between the plates increases by 0.60 in. It is notable that the net section deformation contributes the largest portion of the overall deformation in this subassembly, but one must keep in mind that gross section yielding would actually extend over a much longer distance than only the localized splice plate region that is the focus of analysis here, and would therefore contribute most substantially to the wall deformation over the entire length of gross section yielding.

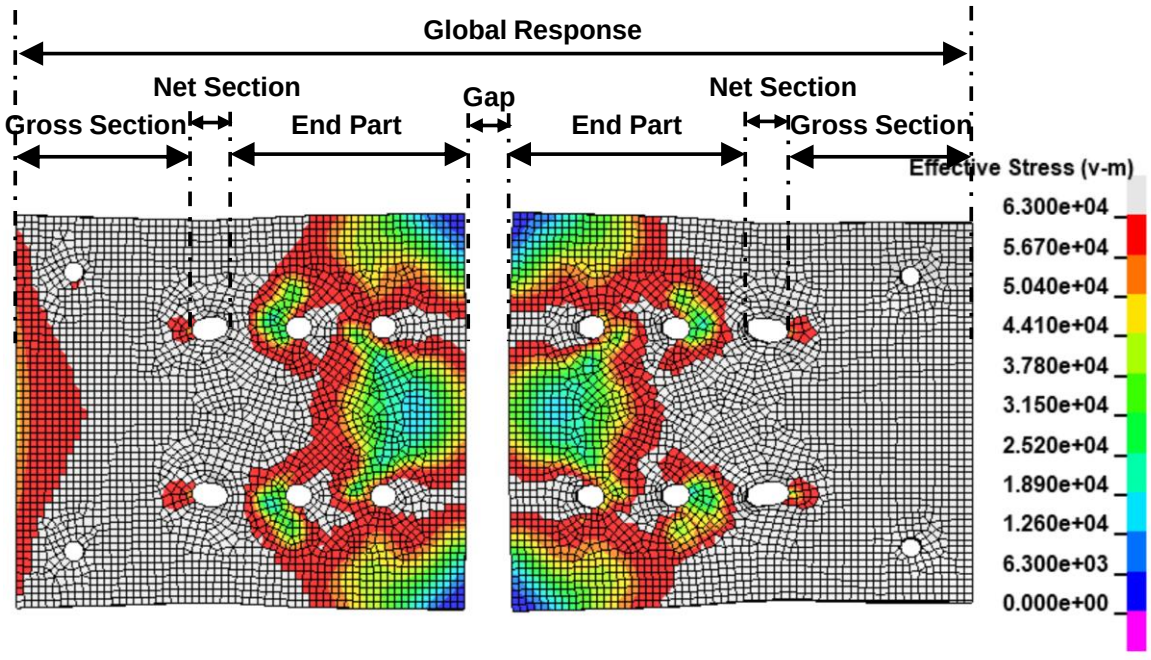


Figure 5-121. Elongation of Faceplates (Specimen T5, Deformation=2” in Tension)

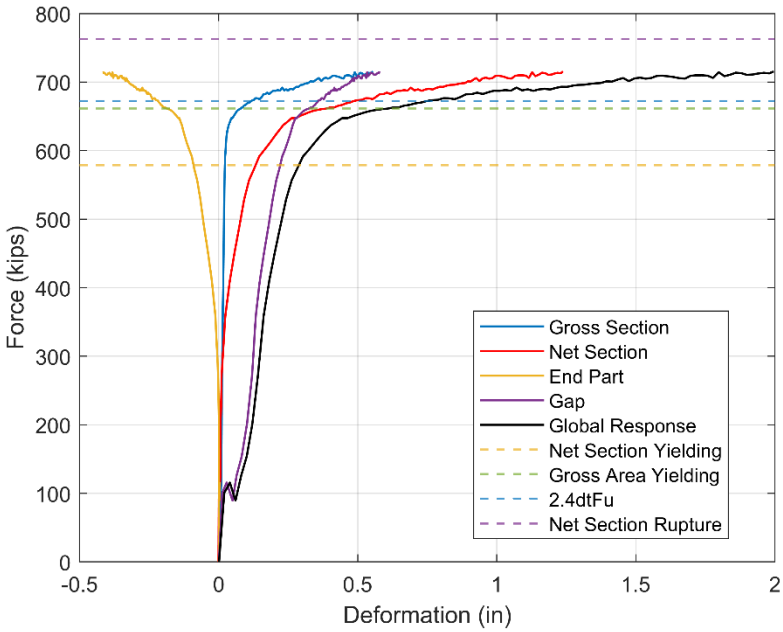


Figure 5-122. Elongation of Different Segments (Specimen T5)

Figure 5-124 shows the comparison between boundary conditions of specimen and wall scenarios, and Figure 5-123 shows the normal stresses on the faceplates in both models. The overall responses showed no significant difference between the two models before the axial strength reaches net section yielding. However, after net section yielding, the axial strength of the wall model exceeds that of the specimen model under the same deformation. This is logical since the presence of transverse restraints is known to increase the yield strength of steel, as can be demonstrated using Mohr Circles (Bruneau et al. 2011).

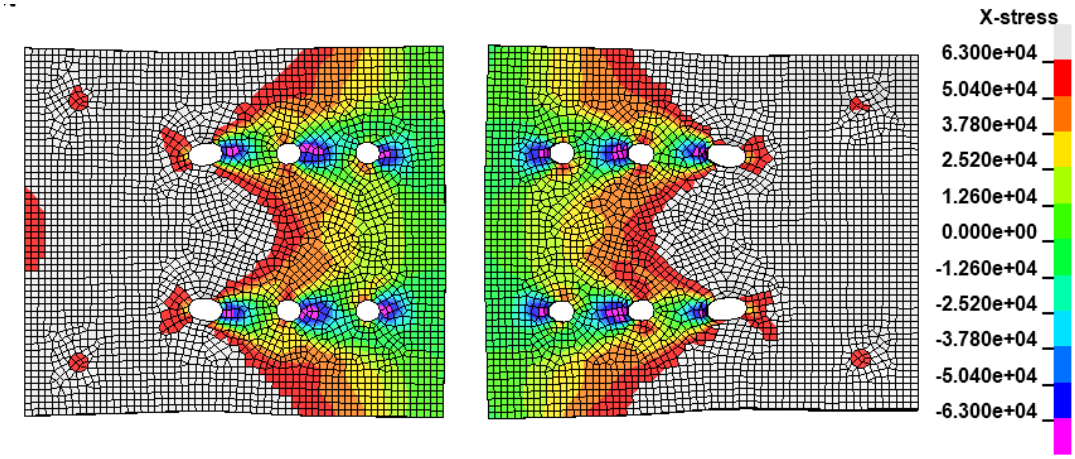


Figure 5-123. Normal Stresses for Specimen Model (Specimen T5)

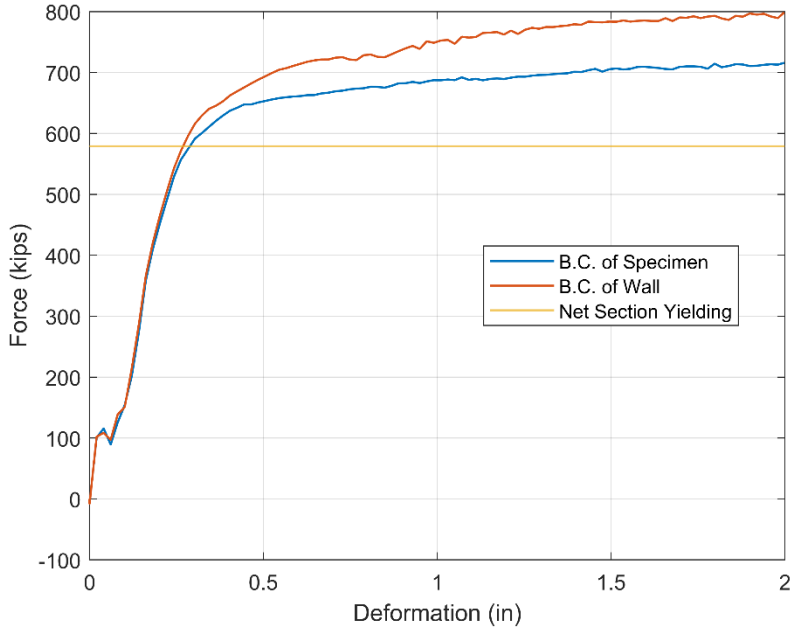


Figure 5-124. Finite Element Results of Boundary Conditions of Specimen and of Wall (Specimen T5)

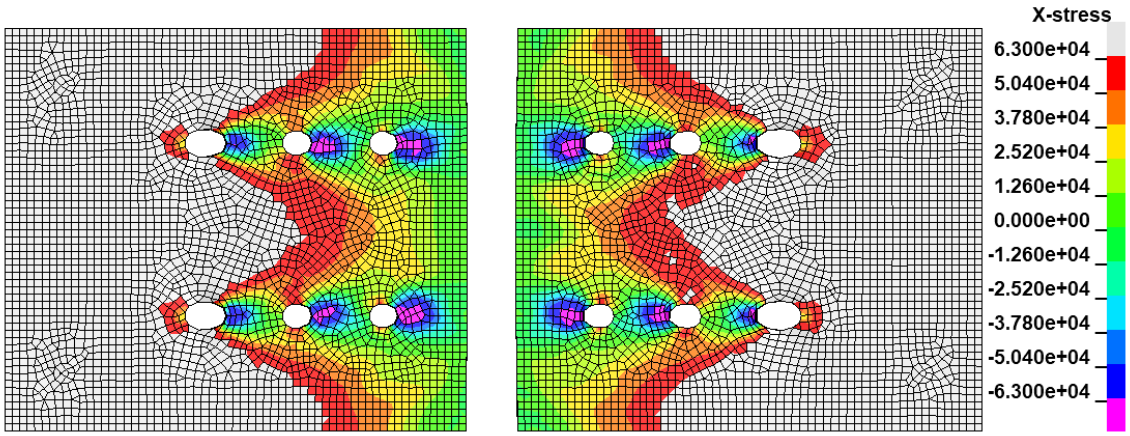


Figure 5-125. Normal Stresses for Wall Model (Specimen T5)

5.3.7.6 Specimen T6

Figure 5-126 shows the comparison of the axial load-deformation curve between the finite element model and the test results. The tensile and compressive strengths of the finite element results are 721 kips and -1628 kips, and the corresponding deformation are 2.0 in. and -0.33 in. Note that during the test, local buckling of the faceplates occurred once the LP deformation reached 0.87 in. Additionally, beyond an LP deformation of 0.87 in., the experimental curve exhibits some "horizontal plateaus" that do not represent actual elongations. These plateaus are caused by the failure of instrument attachments due to the local buckling of the faceplates. Reconnecting the instruments became challenging because the plate was curved, losing the reference points in the process. Therefore, in the finite element analysis, monotonic loading displacements beyond 0.87 in. are considered exploratory and not intended to replicate the test results. The comparison of cyclic response is limited to an LP deformation of 0.87 in.

Figures 5-127 and 5-128 show the distribution of von Mises stresses for Specimen T6 at a deformation of 2.0 in. in tension. Figure 5-129 shows the von Mises stresses obtained from a cross-section taken along the

center line of the rods. Again, both net section and gross section area of faceplates experienced yielding in the analysis.

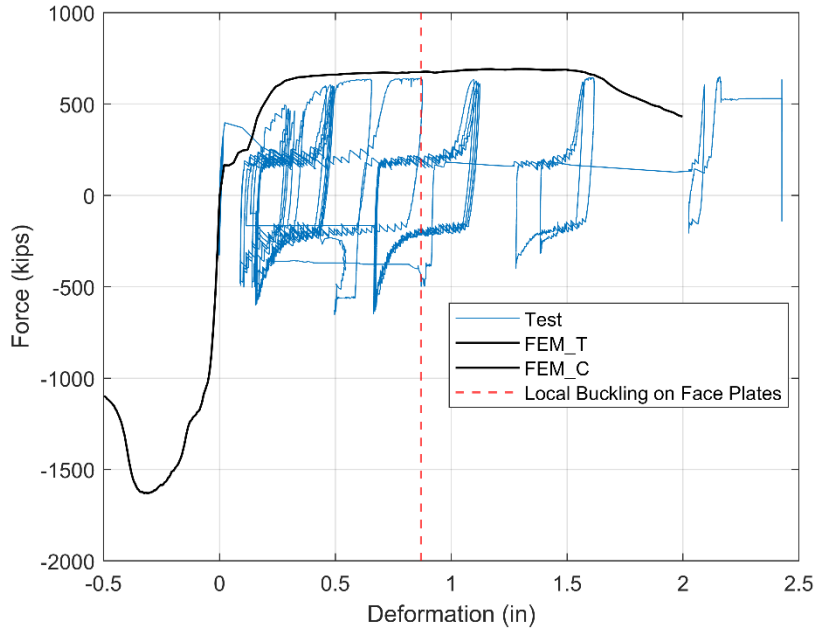


Figure 5-126. Finite Element Results of Load-Deformation Curve of Specimen T6

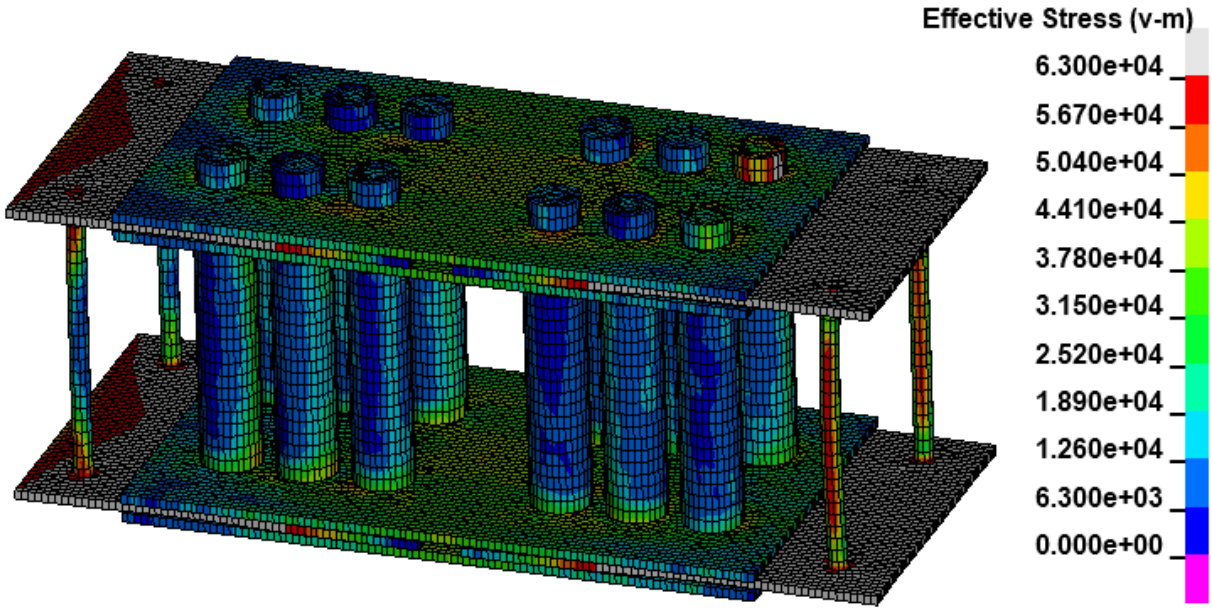


Figure 5-127. von Mises Stresses of Specimen T6 (Deformation=2.0” in Tension))

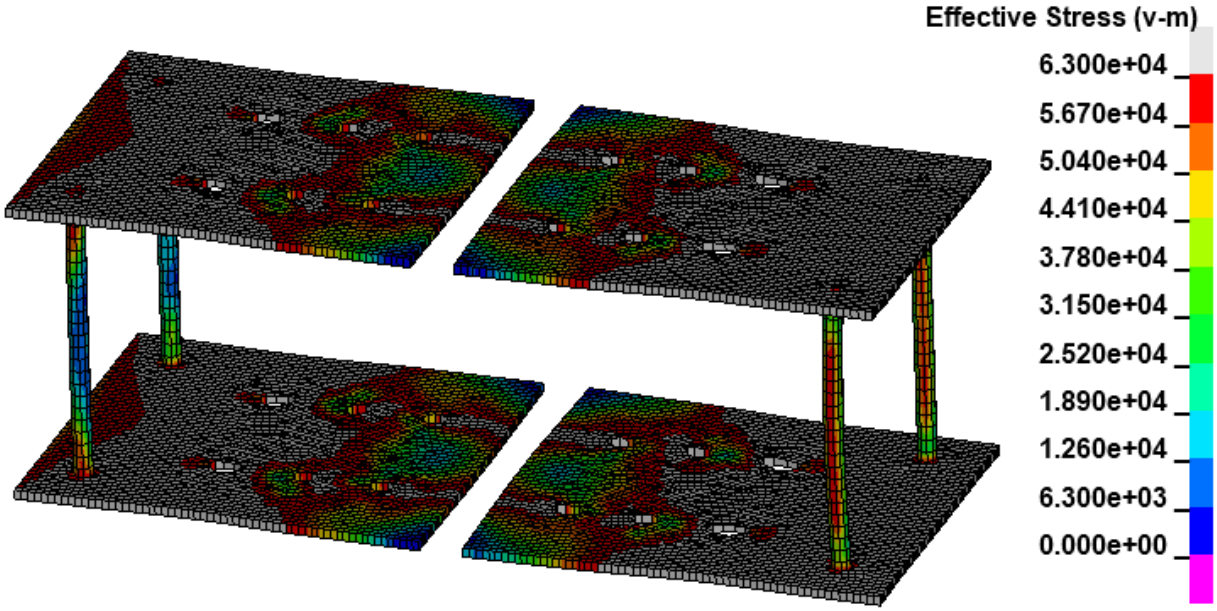


Figure 5-128. von Mises Stresses of Specimen T6 (Reveal Faceplates, Deformation=2.0” in Tension)

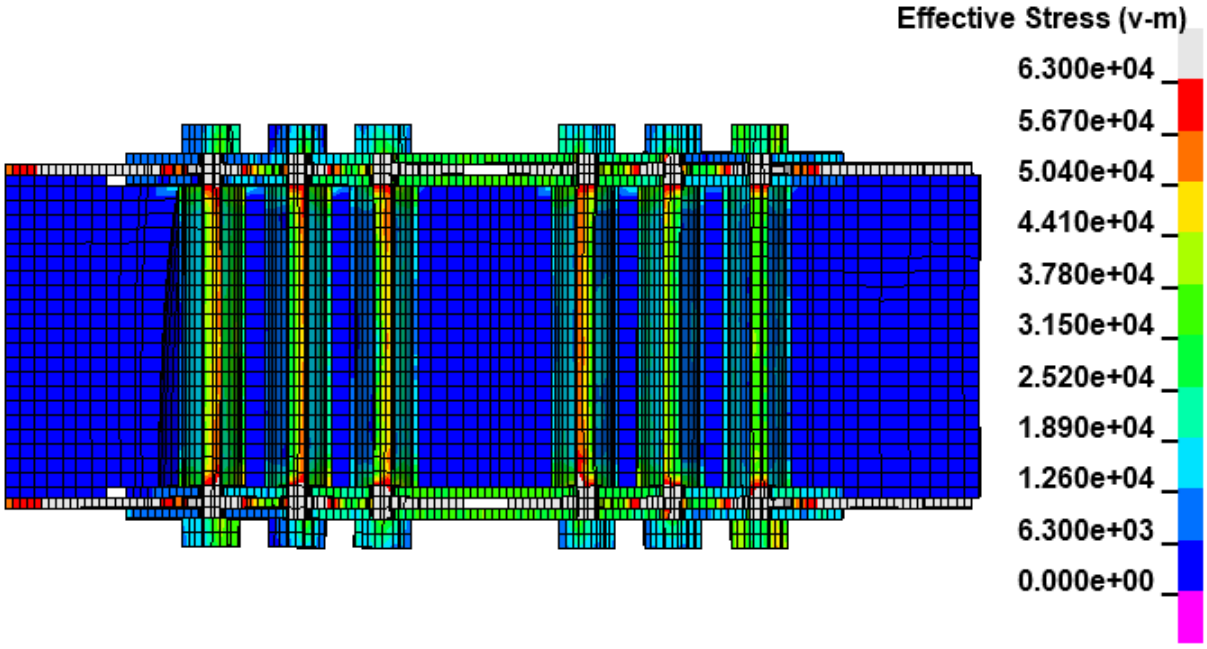


Figure 5-129. von Mises Stresses at Rod Section (Specimen T6, Deformation=2” in Tension)

Similarly, Figure 5-130 shows the elongation of faceplates with different segments at a deformation of 2.0 in. Figure 5-131 shows the elongations contributed by different segments of the faceplates, as well as the global response. The figure indicates that the gross section and net section of the faceplates experience elongation, while the end part of the faceplates undergoes shortening, for the same reasons described earlier for Specimen T5.

During the applied 2.0-in deformation (Global Response), the gross section deformation contributes an elongation of 0.51 in., the net section deformation contributes an elongation of 1.26 in., the end part deformation contributes a shortening of -0.38 in., and the gap between the plates increases by 0.61 in. It is notable that the net section deformation contributes the largest portion of the overall deformation in this subassembly. However, as described in Specimen T5, the gross section yielding would actually extend over a much longer distance than only the localized splice plate region that is the focus of analysis here and would therefore contribute most substantially to the wall deformation over the entire length of gross section yielding.

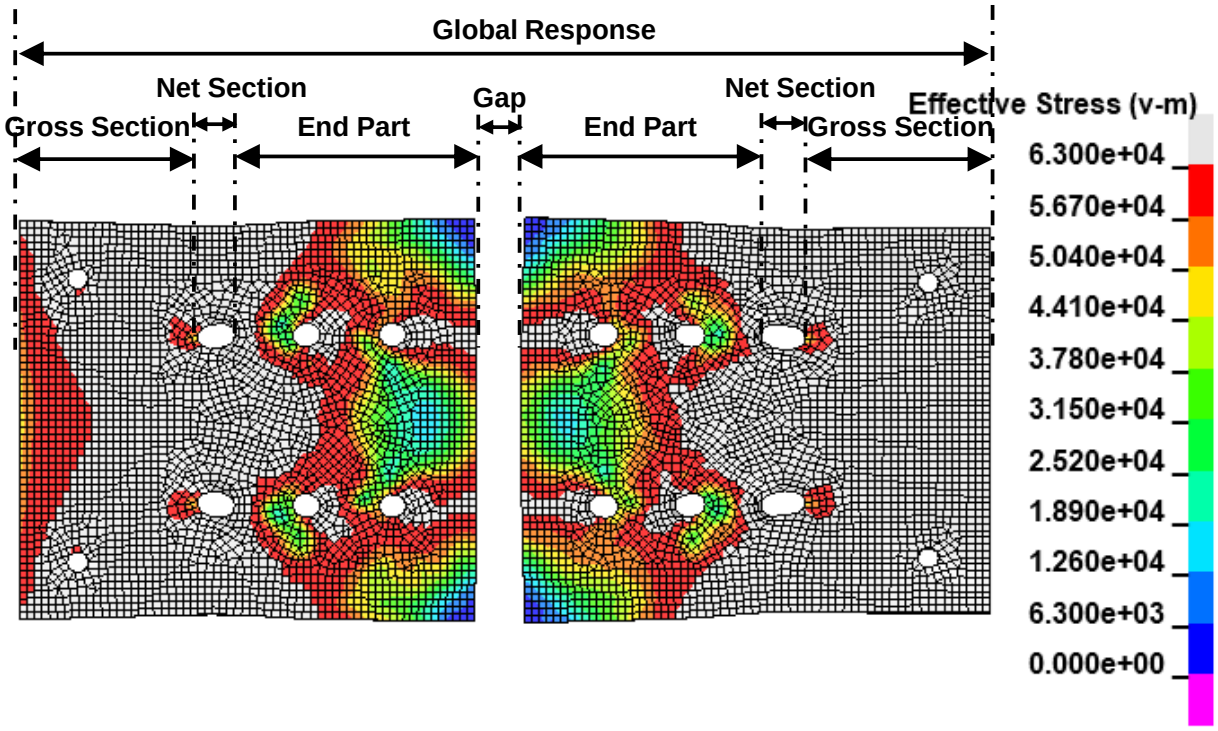


Figure 5-130. Elongation of Faceplates (Specimen T6, Deformation=2" in Tension)

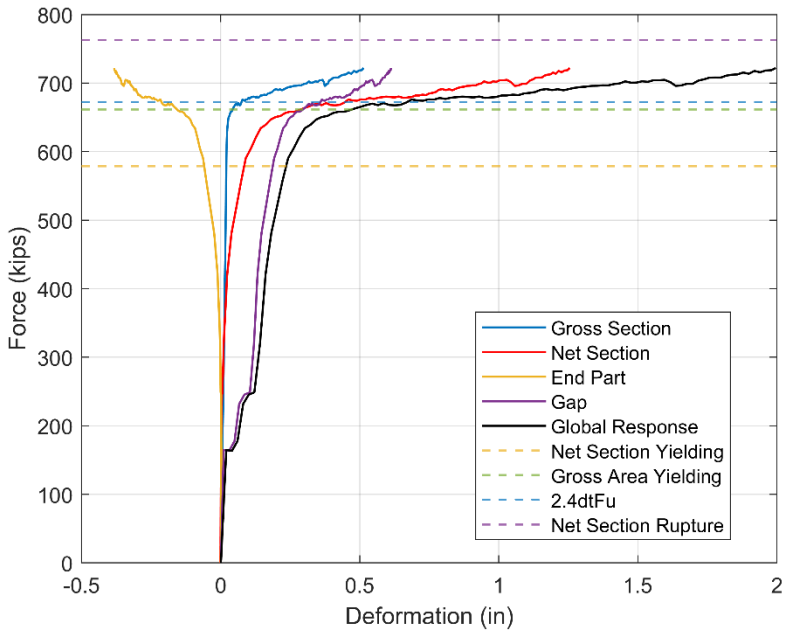


Figure 5-131. Elongation of Different Segments (Specimen T6)

Figure 5-132 shows the load protocol obtained from the recorded LP history for the cyclic load finite element analysis, while Figure 5-133 shows the corresponding finite element result. The analysis result demonstrates a 7% higher peak tensile strength compared to the test results. The hysteresis curve obtained from the finite element analysis captures well the overall response, aligning relatively well with the loading and unloading curves.

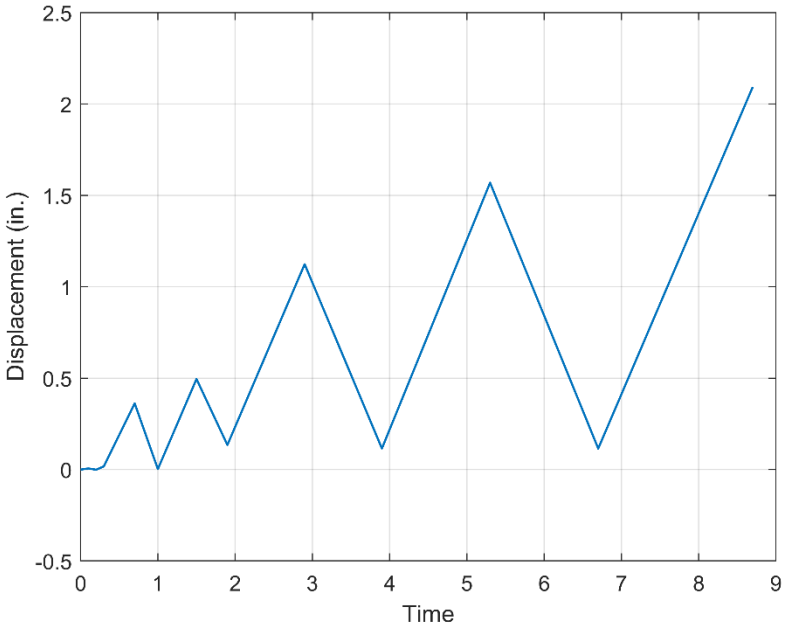


Figure 5-132. Cyclic Loading Protocol of Finite Element Model (Specimen T6)

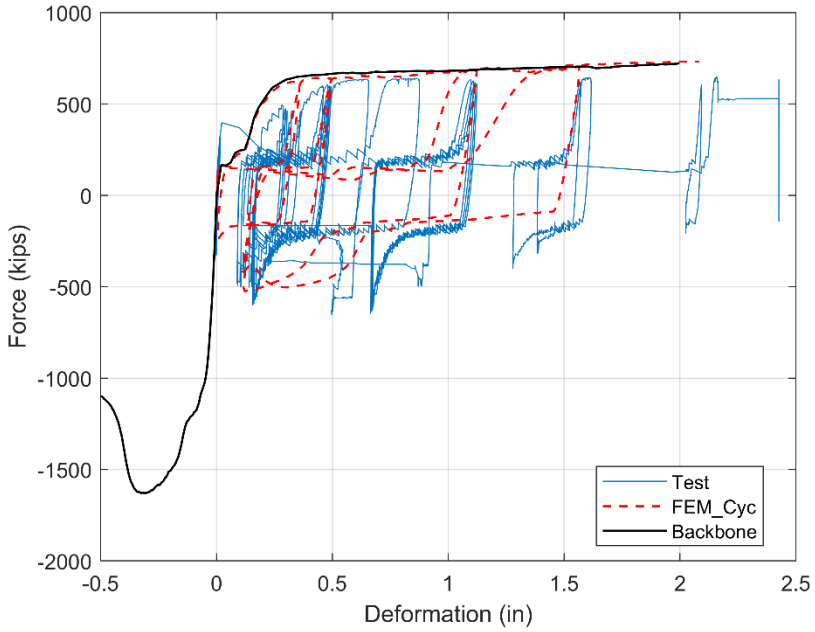


Figure 5-133. Finite Element Results of Hysteresis Loop of Specimen T6

5.4 Finite Element Models of Shear Specimens

This section provides details of the Finite Element Models built to replicate the connection behavior observed in the tested shear specimens. These finite element models of the tested specimens were built in LS-DYNA (Hallquist 2006).

The finite element analyses in this section are conducted to replicate the behavior of the tested shear specimens. Note that the tested specimens were limited to a width of 14 in. due to the capacity of the actuator (420 kips) in the Pantograph used for testing. However, in real wall scenarios, the width is typically much wider, and the connection often includes multiple bolts arranged in a row, which would result in a different behavior than observer here. However, the analyses conducted here allow to develop confidence in the finite element model, which will then be used to investigate the behavior of longer wall splices in shear in subsequent work.

5.4.1 Shear Model Properties

Finite element models of shear specimens were built to replicate the free length region of the shear test assembly as shown in Figure 5-134. Figures 5-135 to 5-140 show the finite element models for shear specimens S1 to S6. The corresponding coordinate system (X, Y, and Z directions) is shown in the figures. These models consist of faceplates, splice plates, bolts or through rods with pipe-sleeves, and infill concrete.

Material properties, element, meshing, contact and constraint properties, etc. for the shear models were the same as for the tension properties, except for the following differences:

- The material properties for the steel and concrete elements unique to these shear specimens, respectively summarized Tables 5-7 and 5-8.

- The different boundary conditions applicable to the shear specimens. In particular, here, to replicate the effect of the wall continuity at the top face of the shear specimens, all the nodes on the top and bottom of the specimens were constrained in the vertical (Z) direction. This constraint ensured that the top surface of the specimens remained horizontal during the analysis, simulating a pure shear behavior for a segment of wall represented by the specimen.
- The unique pretension values applied to the bolts/rods in the finite element models of the shear specimens, as listed in Table 5-9, and as explained in Section 5.3.5. Figure 5-142 shows the observed slip resistances from the tests (R_{test}).

With respect to the second point above, Figure 5-143 shows the boundary conditions implemented in the finite element models of the shear specimens. The bottom face of the models was fully constrained (fixed end) in all directions, while the applied displacement was imposed on the top surface of the models.

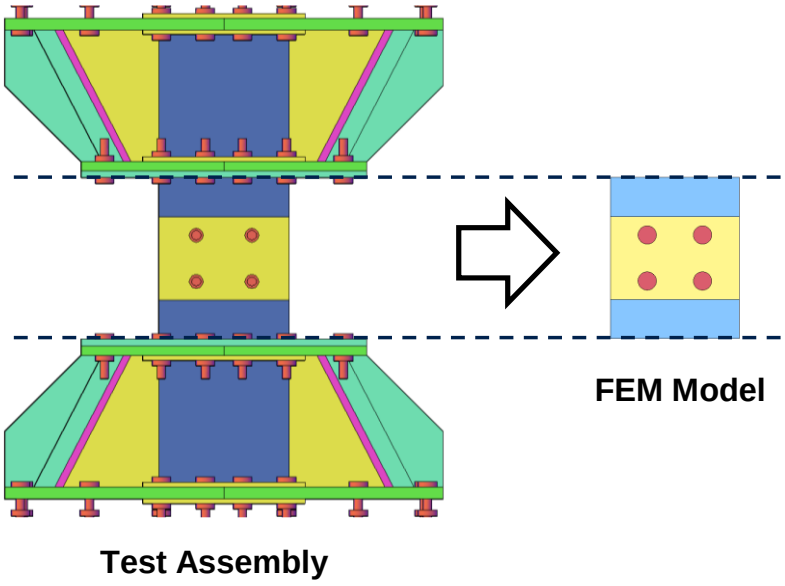


Figure 5-134. Test Assembly and Finite Element Model

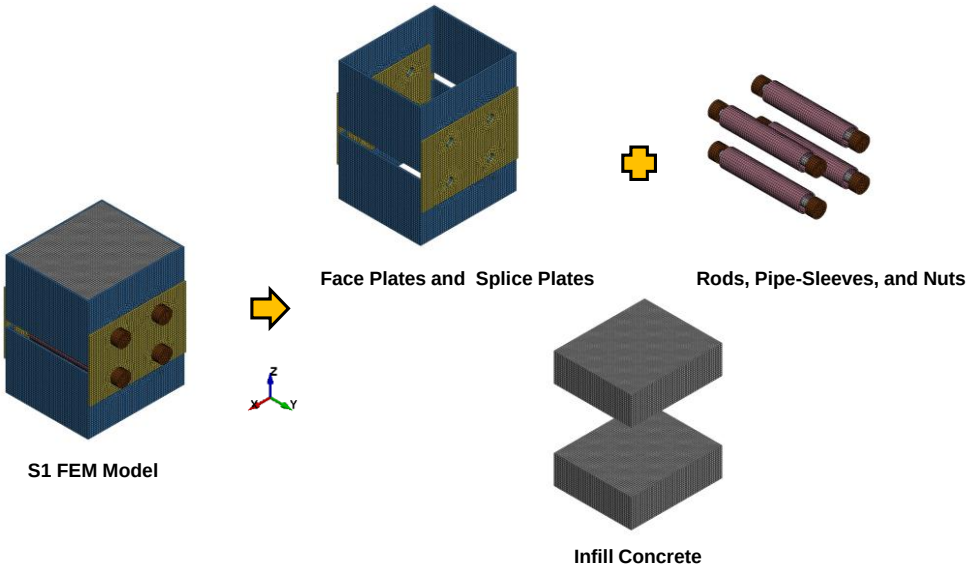


Figure 5-135. Finite Element Model of Specimen S1

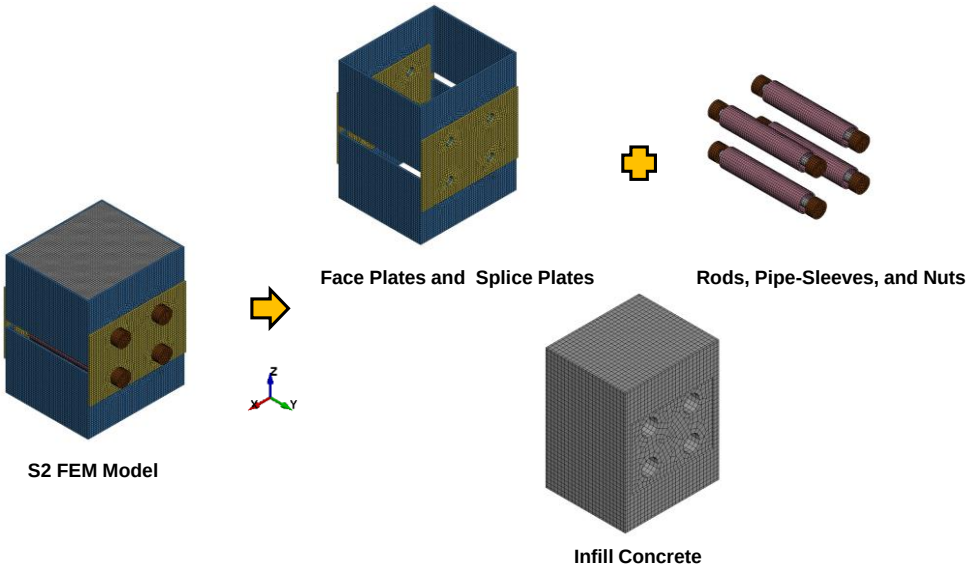


Figure 5-136. Finite Element Model of Specimen S2

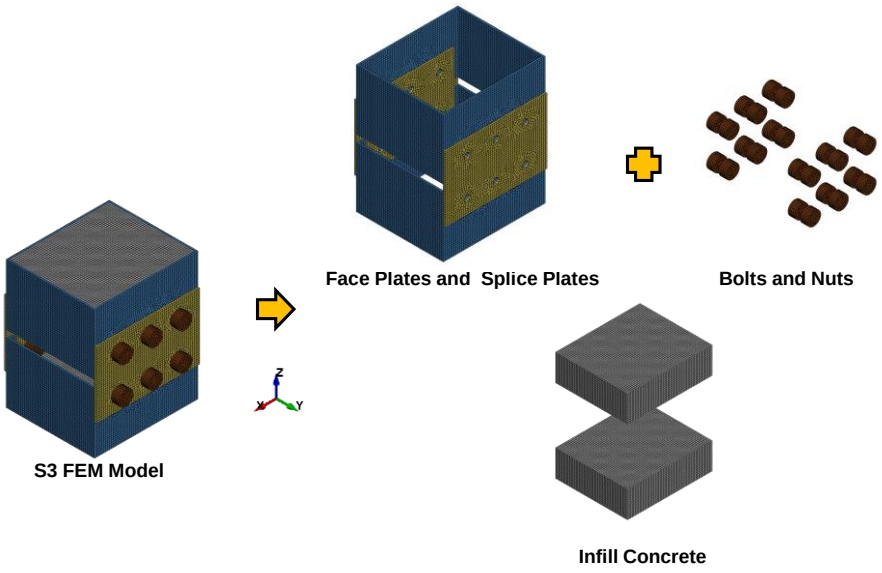


Figure 5-137. Finite Element Model of Specimen S3

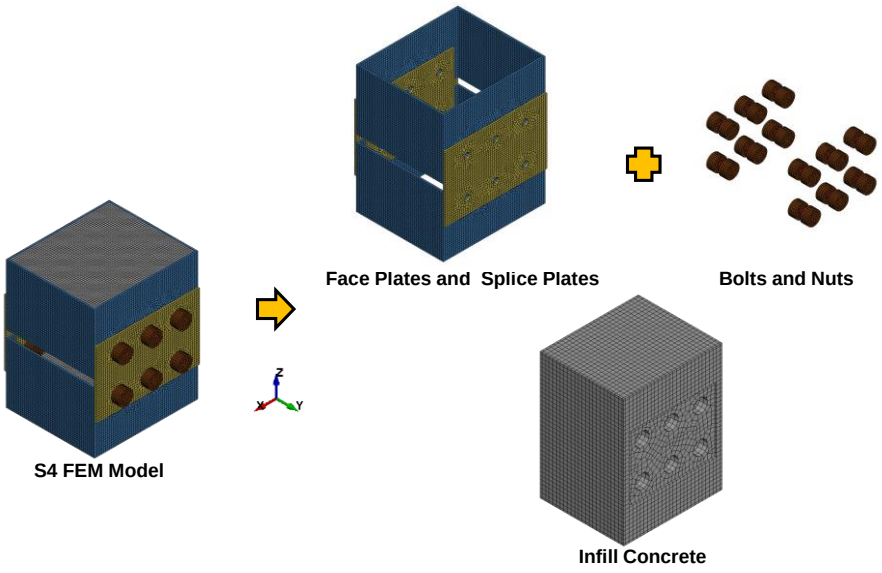


Figure 5-138. Finite Element Model of Specimen S4

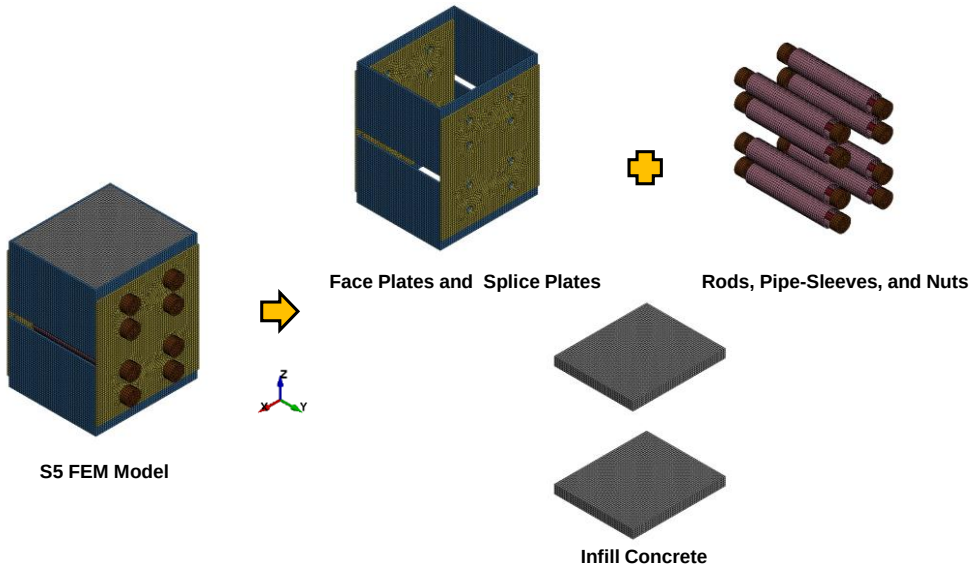


Figure 5-139. Finite Element Model of Specimen S5

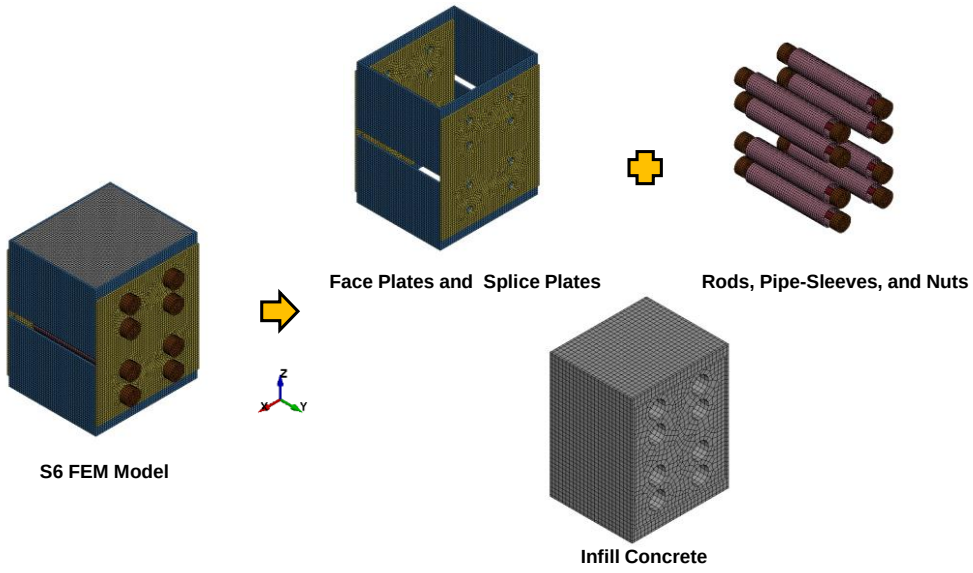


Figure 5-140. Finite Element Model of Specimen S6

Table 5-7. Material Properties for Steel Parts

Part	E_s (ksi)	Possion's Ratio	F_y (ksi)	E_t (ksi)	β
Face Plates	29000	0.3	63	66.0	0.0
Splice Plates	29000	0.3	63	66.0	0.0
Bolts/Rods	29000	0.3	120	221.2	0.0
Others	29000	0.3	55	108.8	0.0

Table 5-8. Material Properties for Concrete Parts

Specimen	E_c (ksi)	Possion's Ratio	f'_c (psi)	f_t (psi)	FE	ASIZE
S1	3122	0.2	3000	300	0.00343	0.500
S2	3122	0.2	3000	300	0.00343	0.500
S3	3122	0.2	3000	300	0.00343	0.500
S4	3122	0.2	3000	300	0.00343	0.500
S5	3122	0.2	3000	300	0.00343	0.500
S6	3122	0.2	3000	300	0.00343	0.500

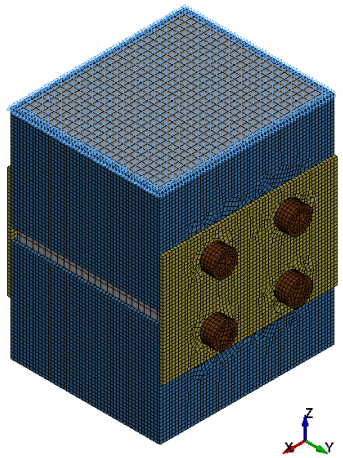


Figure 5-141. Top Constraint (UZ) for Shear Specimens

Table 5-9. Prestress Value used in Finite Element Models

Specimen	d_b	A_b (in_2)	Prestress (ksi)	T_b (kips)	# of Bolts	μ	R_{theory} (kips)	R_{test} (kips)
S1	1	0.785	52.5	41.23	4	0.30	98.96	40
S2	1	0.785	52.5	41.23	4	0.30	98.96	70
S3	0.75	0.442	52.5	23.19	6	0.30	83.50	80
S4	0.75	0.442	52.5	23.19	6	0.30	83.50	80
S5	0.75	0.442	52.5	23.19	8	0.30	111.33	80
S6	0.75	0.442	52.5	23.19	8	0.30	111.33	80

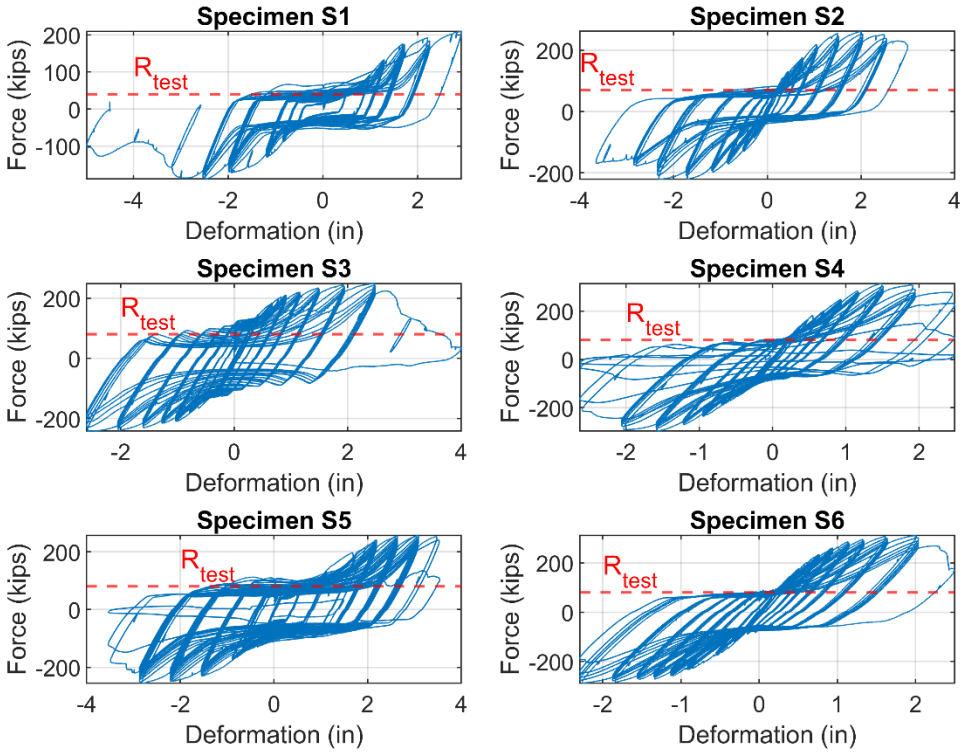
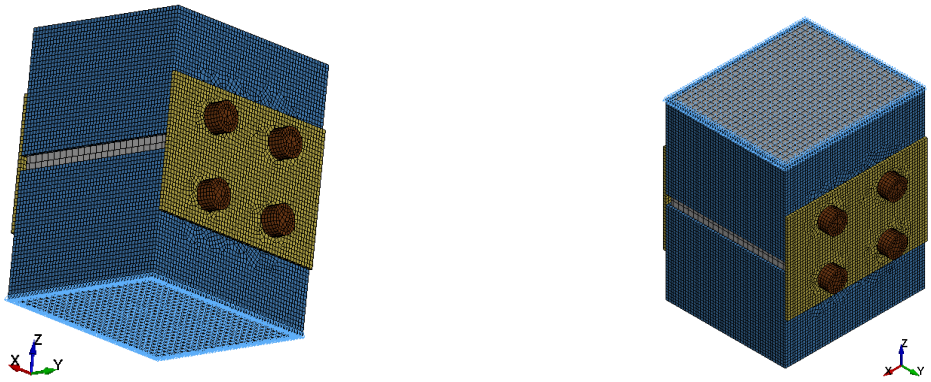


Figure 5-142. Slip Resistance from Shear Tests (R_{test})



(a) Fixed End at Bottom Face (b) Loading Area

Figure 5-143. Boundary Condition for Finite Element Models of Shear Specimens

5.4.2 Inclination of Actuator

One issue that arose with the pantograph during test set-up is the inability to install the actuator perfectly horizontally such as to have the line of action of the applied force perfectly intersect the center of the specimen while applying only a shear force to it. This constraint, unforeseen at the specimen design stage, occurred as a consequence of interference between the actuator connector plates and the fixed stiffener spacing in the two vertical pieces of the pantograph to which the actuator is to be connected. Resolving this issue via modifications to the pantograph would have incurred costs and delays that the project could not bear. It was also judged to be likely unnecessary given the limited consequence of applying the load at a small angle, and analyses were conducted to substantiate that this was indeed the case.

Figure 5-144 shows the test setup for the shear specimens, highlighting the presence of an inclination in the actuator for a typical shear test positioned into the pantograph. To assess the significance of condition, it was crucial to accurately measure the angle of inclination of the actuator. Figure 5-145 shows photos of the actuator and a specimen, using a red laser to measure the inclination angle of the actuator. The red laser measurement indicated that the eccentricity of the actuator resulted in a load applied 1.75 in. away from the center of the specimen at an angle of 3.81˚.

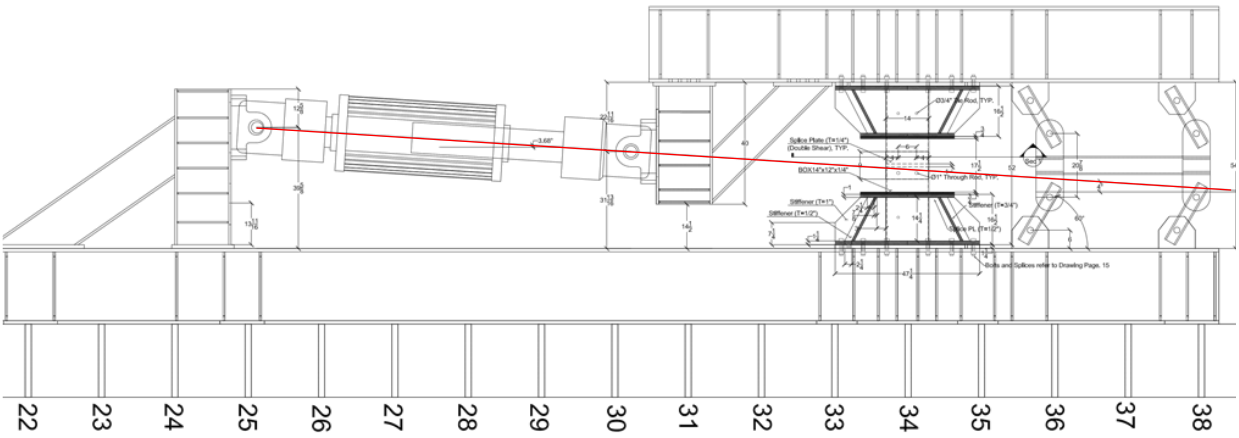
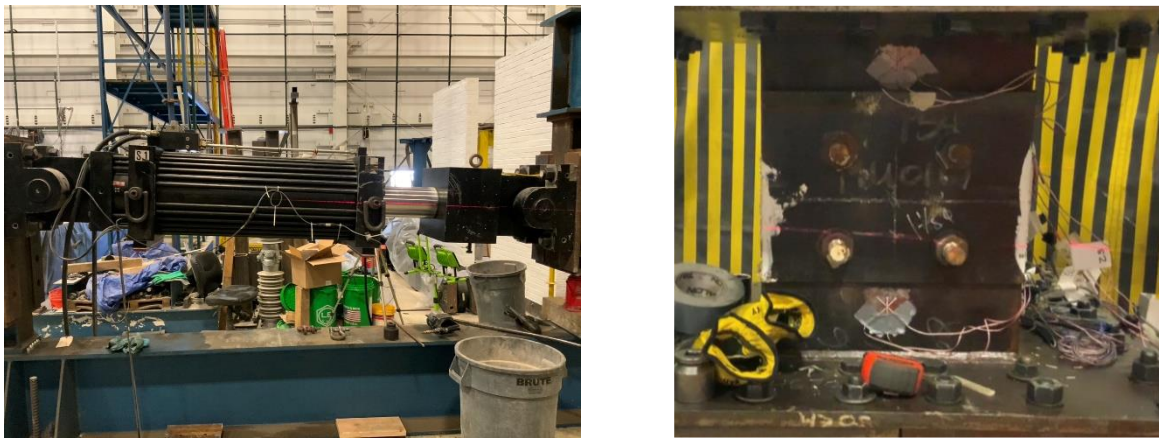


Figure 5-144. Test Setup of Shear Specimen S1/S2



(a) Red Laser on Actuator (b) Red Laser on Specimen

Figure 5-145. Red Laser Measuring Inclination of Actuator

Figure 5-146 shows the geometry of the shear test setup, depicting the relationship between the inclination of the actuator and the eccentricity for the known actuator "far-end" elevation as connected to the pantograph, and arbitrary hypothetical values of eccentric loading considered to assess the impact of this effect. The figure indicates that as the eccentricity from the center of the specimen varies from 0 to 3 in., the angle of the actuator θ changes from 3.34˚ to 4.14˚. Assuming a maximum actuator load (ActF) of 420 kips applied to the specimen (which is a worst-case scenario, given that none of the specimen tested

developed that strength), the calculated corresponding horizontal and vertical components (ActF_X and ActF_Z) are listed in Table 5-10. Results show no impact on the applied shear value, and in the most conservative case considered, with an eccentricity of 3.0 inches, a maximum axial force (ActF_Z) applied to the shear specimen equal to approximately 30 kips, or 7% of the applied shear load.

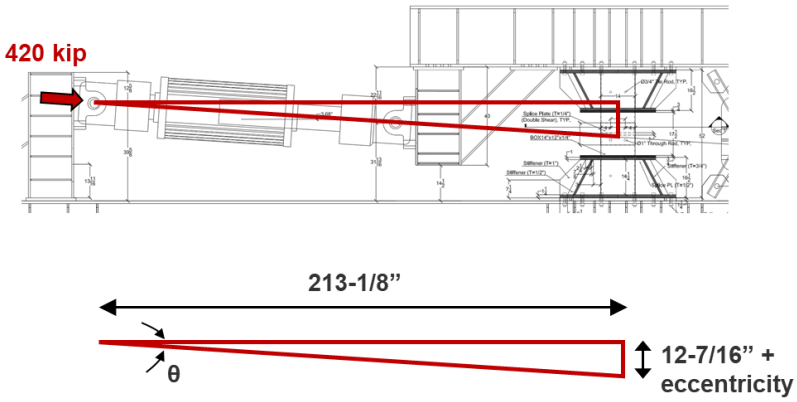


Figure 5-146. Angle of Inclination of Shear Specimens

Table 5-10. Axial Load of Specimens Considering Different Eccentricities from center of specimen

Eccentricity (in)	Angle (degree)	ActF (kips)	ActF_X (kips)	ActF_Z (kips)
0.00	3.34	420.00	419.29	24.47
1.00	3.61	420.00	419.16	26.45
1.75	3.81	420.00	419.72	27.91
3.00	4.14	420.00	418.90	30.32

Figure 5-147 compares results for two monotonically loaded finite element models (Models 2 and 1): one considering the axial load effect (F_z) and the other without it. Since the shear strength of concrete tends to be lower under tensile loads, a tensile axial load of 30 kips was applied in Model 2. Figure 5-148 shows a comparison of the resulting force-displacement relationship for the two models up to a displacement of 1.0 inch. Additionally, Figure 5-149 shows the relative contribution of concrete and steel to resist the applied shear force, as obtained by cutting cross sections in the middle of the specimen. Table 5-11 summarizes the differences in maximum base shear, shear strength of steel in the middle of the connection, and concrete

strength in the middle of the connection between the two models. Based on the results, it can be concluded that considering the effect of this eccentricity (i.e., producing an axial load in tension equal to 7.1% of the applied shear) leads to a reduction of approximately 6.9% in the maximum shear strength of steel and a reduction of approximately 4.0% in the maximum shear strength of concrete in the connection. Therefore, as this eccentricity was determined to have a negligible impact, all subsequent shear finite element analyses conducted to compare with experimental results did not consider the axial load effect.

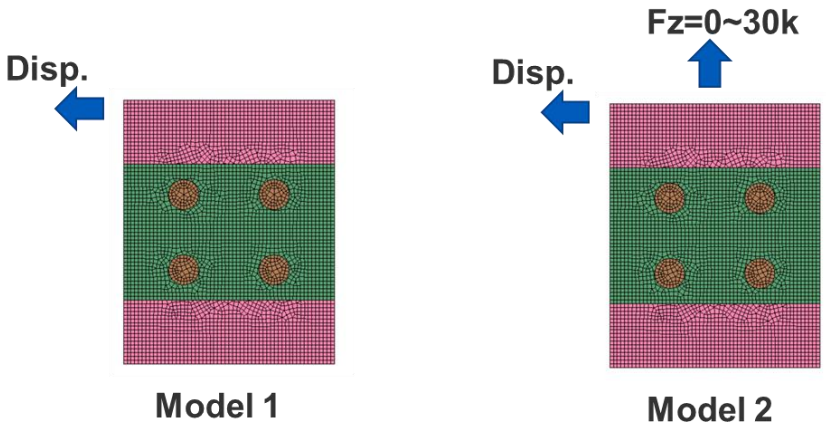


Figure 5-147. Finite Element Models with and without Considering Axial Load

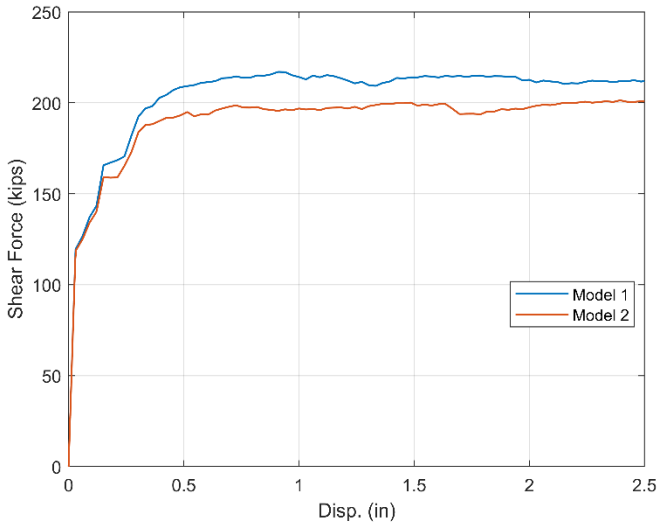


Figure 5-148. Shear Strength of Models 1 and 2

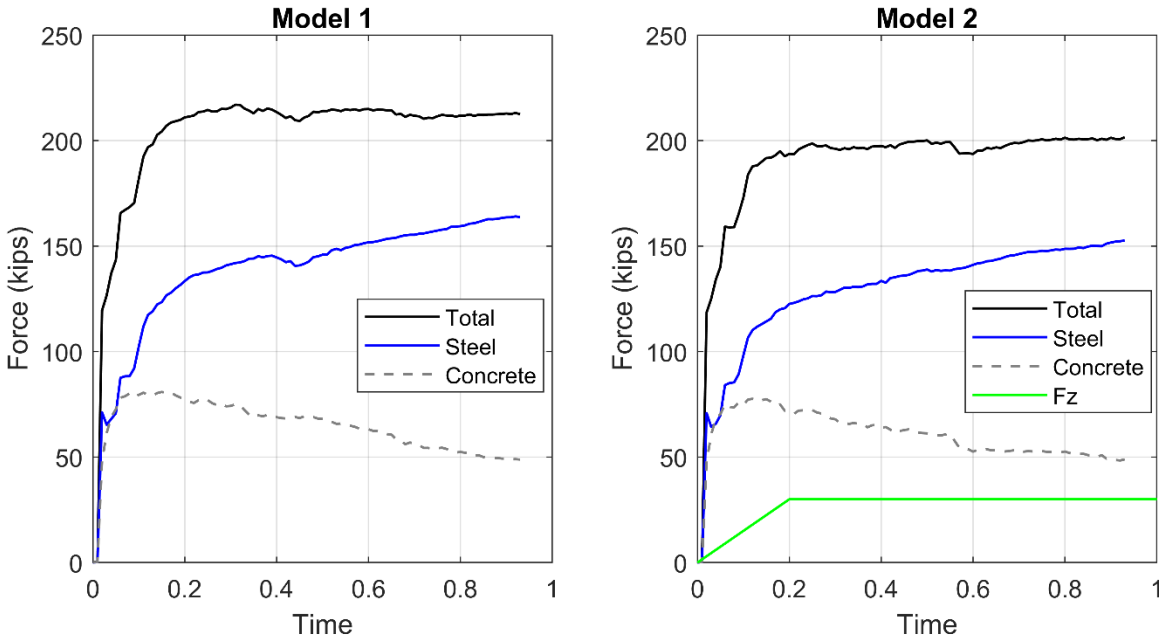


Figure 5-149. Shear Strength of Steel and Concrete of Models 1 and 2

Table 5-11. Summaries of Effect of Axial Load

Model	Max. Base Shear (kips)	Max. Mid. Vs (kips)	Max. Mid. Vc (kips)	Max. Fz (kips)
1	216.91	164.07	80.87	0.00
2	201.58	152.67	77.63	30.00

5.4.3 Results of Finite Element Analysis

This section provided analysis results from finite element model as mentioned in Section 5.4.1. Models were subjected to top lateral displacements to apply shear deformations similar to what was done to the specimens during testing.

5.4.3.1 Specimen S1

A monotonic lateral displacement of 2.0 in. was applied to the top of the finite element model of Specimen S1. Figure 5-150 shows the comparison between the resulting finite element model's monotonic loading curve and the hysteresis curve obtained from the test. The figure includes markings for the bearing strengths at $2.4dtF_u$ and $3.0dtF_u$, considering combined shear force and torsion. Additionally, the bearing strength at $2.4dtF_u$ specifically considering only shear force is also marked. These markings allow for a comparison between the theoretical design values and the finite element results. Both finite element and test results achieved the target bearing strength limit states. The finite element model reached a peak strength of 194.0 kips at 2.0-in. displacement, while the test specimen reached peak strengths of 209.7 kips in the positive direction and -184 kips in the negative direction.

While the monotonic loading curve from the finite element results reached similar maximum strength, it typically overestimated strength at lower deformations compared to what would be a backbone of the experimentally obtained hysteretic curves. The slip resistance observed in the test was 40 kips, which was lower than the slip resistance (70 kips) obtained from the finite element analysis. As explained in Section 5.2.7.1 for tension Specimens T1 and T2, the higher pretension in the finite element model resulted in higher strength at smaller deformations, leading to the overestimation at lower deformations.

Figure 5-151 (a) shows the distribution of von Mises stresses in the steel cover plates and rods, while Figure 5-151(b) shows the von Mises stresses in the faceplates (after removing the splice plates and rods). The figures reveal that when the applied displacement on the top reached 2.0 in, a rotation of approximately 10° occurred in the splice plate. Furthermore, it can be observed that all holes were elongated by the bearing pressure from the rods, but the two holes pushed toward a free edge (due to rotation) deformed more than the others under monotonic loading. Yielding of the steel in the faceplates, as indicated by von Mises stresses exceeding 63,000 psi in the figure, initiated from the rod holes and propagated over a significant area.

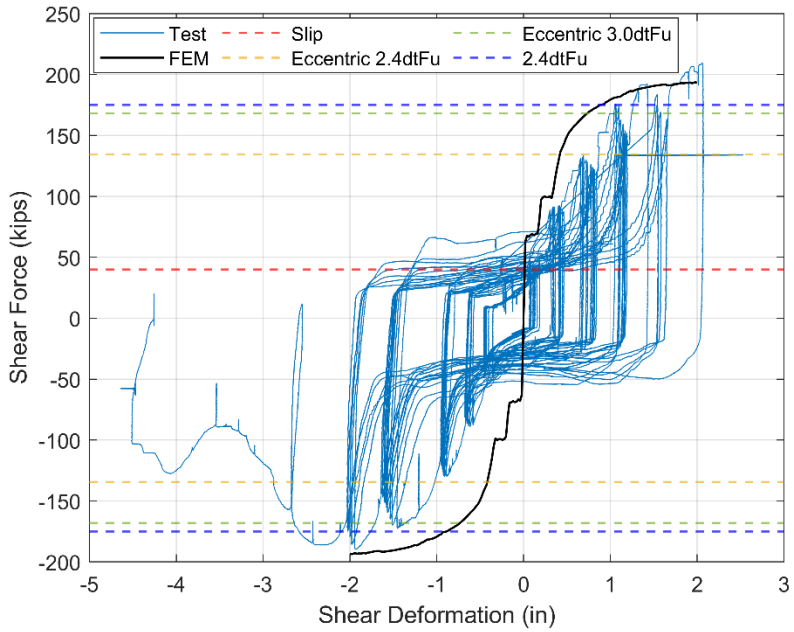
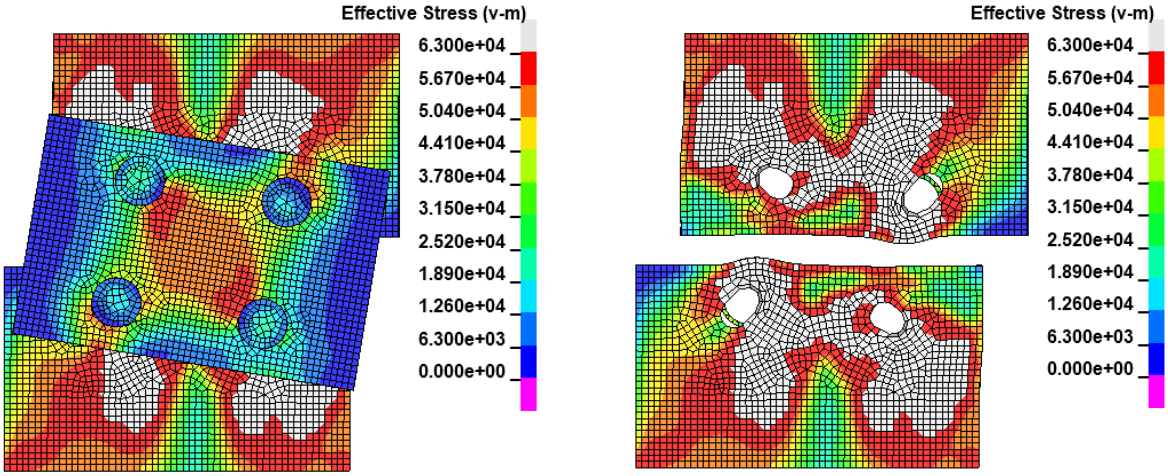


Figure 5-150. Finite Element Results of Load-Deformation Curve of Specimen S1



(a) All Steel (b) Faceplate Only

Figure 5-151. von Mises Stress of S1 Finite Element Model (Lateral Disp. = 2.0 in.)

5.4.3.2 Specimen S2

A monotonic lateral displacement of 2.0 in. was applied to the top of the finite element model of Specimen S2. Figure 5-152 shows the comparison between the resulting finite element model's monotonic loading curve and the hysteresis curve obtained from the test. The figure labels strengths corresponding to bearing strength considering pure shear force, combined shear and eccentric forces, and net section shear yielding strength. Both finite element and test results achieved the target bearing strength limit states and reached the net section shear yielding strength. The finite element model reached a peak strength of 240 kips at 1.0-in. displacement, while the test specimen reached peak strengths of 255 kips in the positive direction and -222 kips in the negative direction. Since Specimen S2 is a composite section with higher slip resistance compared to Specimen S1, the finite element result captures well the overall response observed in the test.

Figure 5-153 (a) shows the distribution of von Mises stresses in the steel cover plates and rods, while Figure 5-153 (b) shows the von Mises stresses in the faceplates (after removing the splice plates and rods). Similarly, a rotation of approximately 10° occurred in the splice plate when the applied displacement on the top reached 2.0 in. Furthermore, in Specimen S2, as it reached the strength corresponding to net section shear yielding, yielding occurred over a larger portion of the plate compared to the finite element result of Specimen S1. However, due to the presence of the eccentric load effect and torsional response, this yielding region was oriented in a direction similar to what was observed for Specimen S1 but with greater severity.

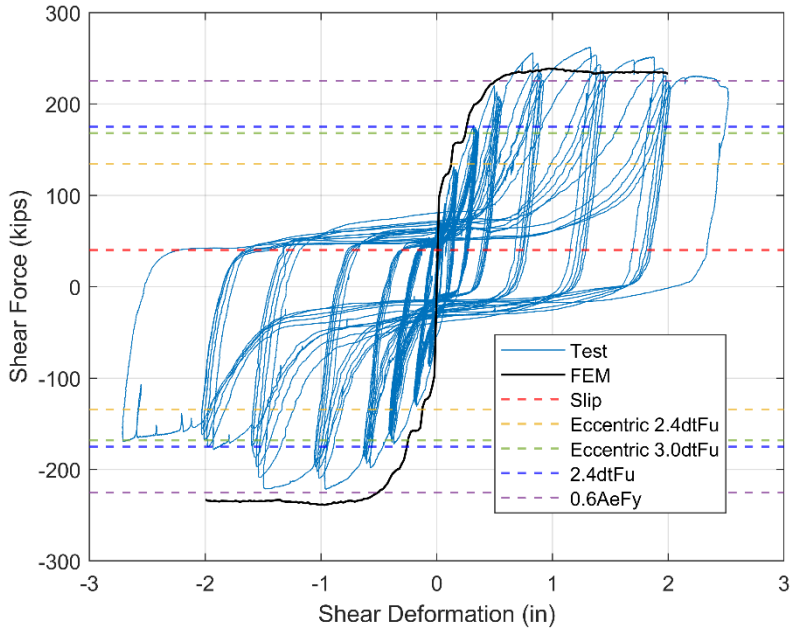
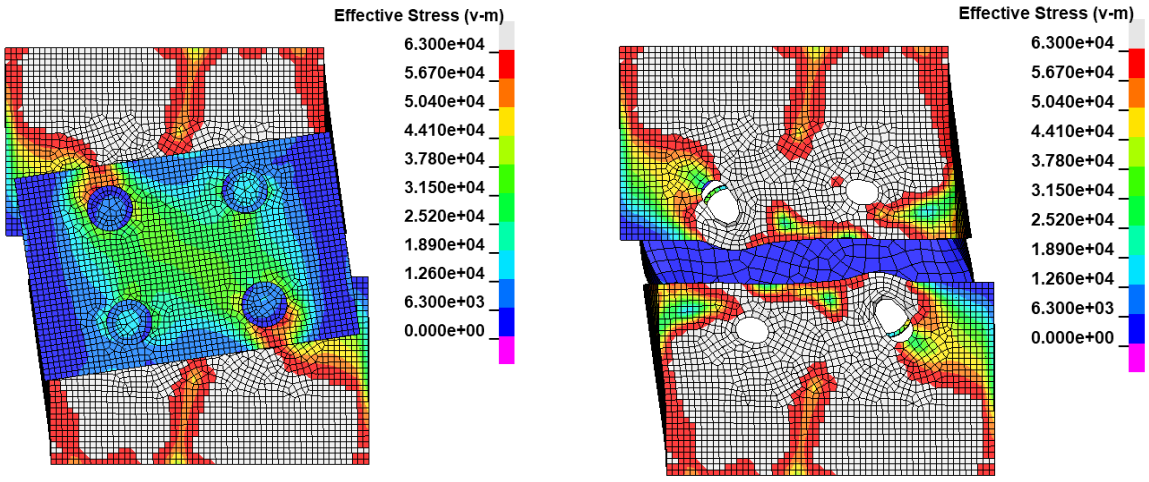


Figure 5-152. Finite Element Results of Load-Deformation Curve of Specimen S2



(a) All Steel (b) Faceplate

Figure 5-153. von Mises Stress of S2 Finite Element model

To understand the contribution of shear strength from steel and concrete, Figure 5-154 shows the shear strength of concrete, steel, and the entire section in the middle of the connection. This is achieved by cutting a cross section in the middle of finite element model as shown in Figure 5-155. It is observed that the

concrete reaches its peak shear strength (70 kips) at a deformation of 0.15 in., with a progressively reducing strength beyond that point, while the steel reaches 84% of its peak shear strength at a deformation of 0.5 in., progressively increasing to its peak strength of 187 kips at a deformation of 1.90 in.

To further assess the contribution of concrete in the composite connection, Figure 5-156 shows a comparison of shear strengths obtained from the S1 and S2 finite element models. The peak shear strengths for S1 and S2 are 194 kips and 240 kips, respectively. By subtracting the shear strength of S1 from S2 over the entire deformation range, the shear strength provided by the concrete component can be somewhat inferred, and is labeled "S2-S1" in the figure. The "S2-S1" shear strength reaches a peak strength of 70 kips at a shear deformation of 0.30 in., and it decreases to 53 kips at a shear deformation of 2.0 in. Finally, the shear strength of concrete obtained from S2 finite element model is compared with the "S2-S1" shear strength as shown in Figure 5-157. Note that models S1 and S2 do not exhibit perfect “synchronization” of their behavior. For example, the two models experienced sliding at different deformation levels. Therefore, using the "S2-S1" method to calculate the contribution of concrete to total strength may lead to some inaccuracies.

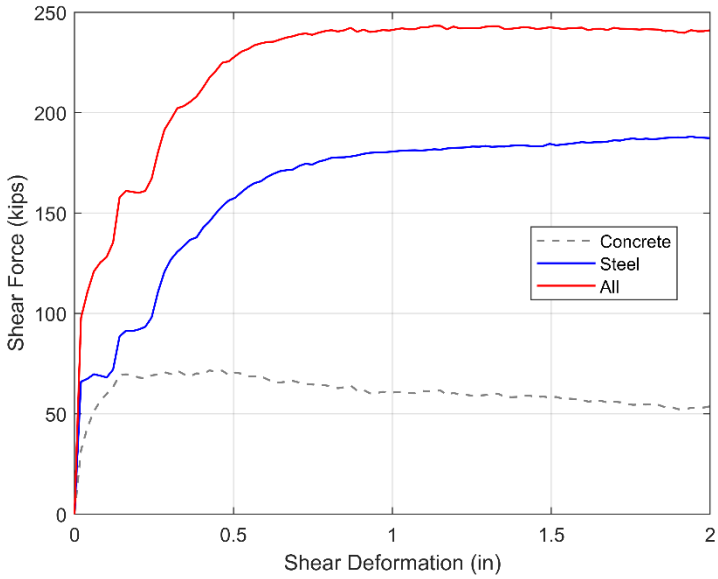


Figure 5-154. Shear Strengths of Concrete and Steel (Specimen S2)

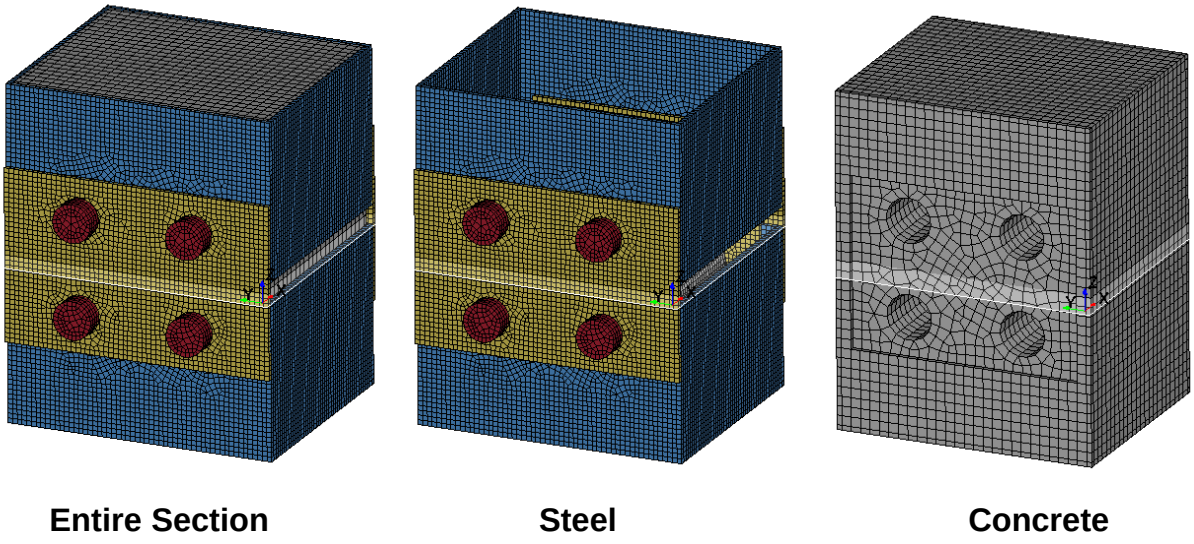


Figure 5-155. Section Cut in the Middle of Shear Specimens

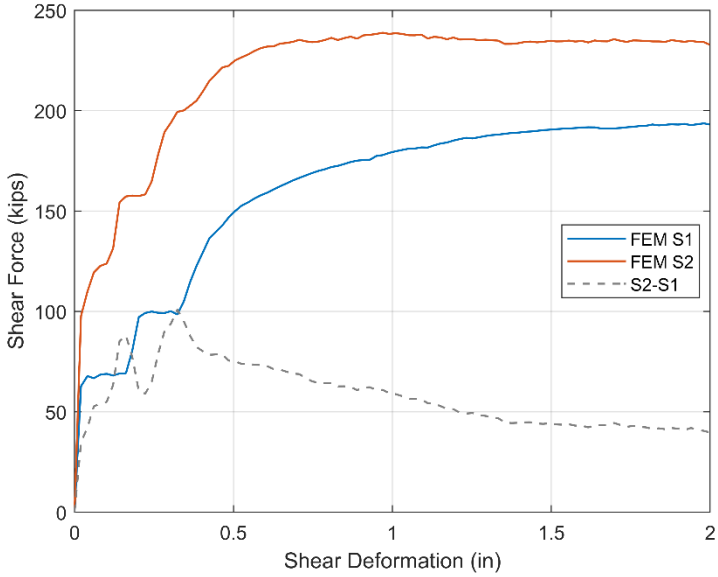


Figure 5-156. Comparison of Shear Strengths of S1 and S2 Finite Element models

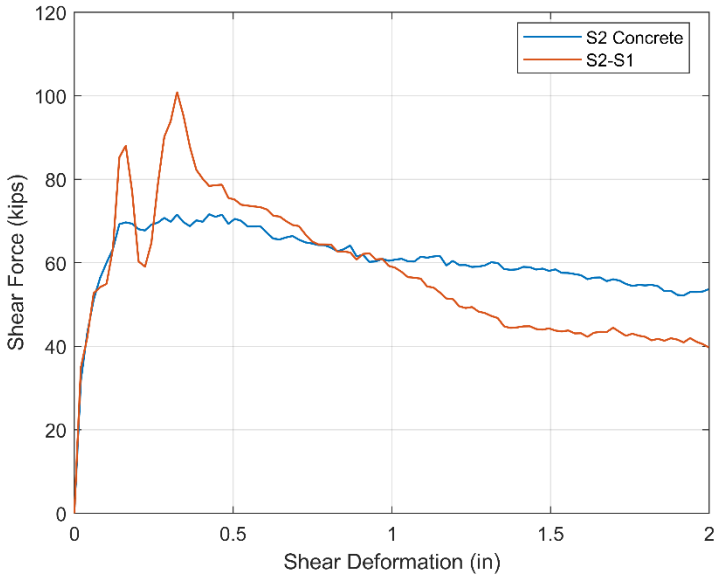


Figure 5-157. Comparison of Shear Strengths of S2 Concrete and "S2-S1"

Figure 5-158 shows the load protocol for the cyclic analysis of Specimen S2, while Figure 5-159 shows the corresponding finite element result. The analysis result closely matches the loading and unloading

branches of the hysteretic curves obtained experimentally (a similarly good match to what was obtained for the monotonic loading curves). Furthermore, Figure 5-160 shows the von Mises stresses of the faceplates during cyclic loading. Five arbitrary points were selected to demonstrate the distribution of stress and deformation of the faceplates. It can be observed that, unlike what was observed for the monotonic loading case, all rod holes show similar elongation levels during the cyclic loading analysis.

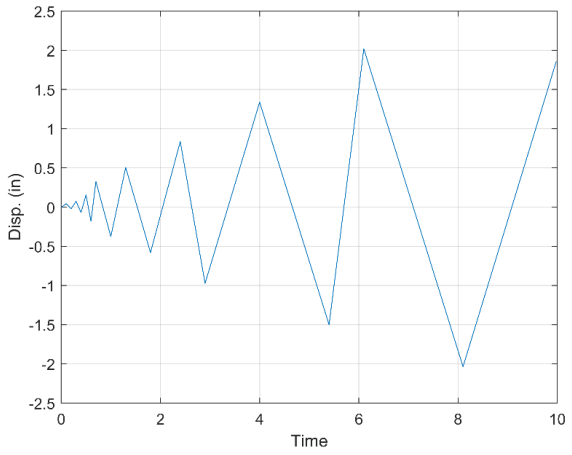


Figure 5-158. Cyclic Loading Protocol of Finite Element Model (Specimen S2)

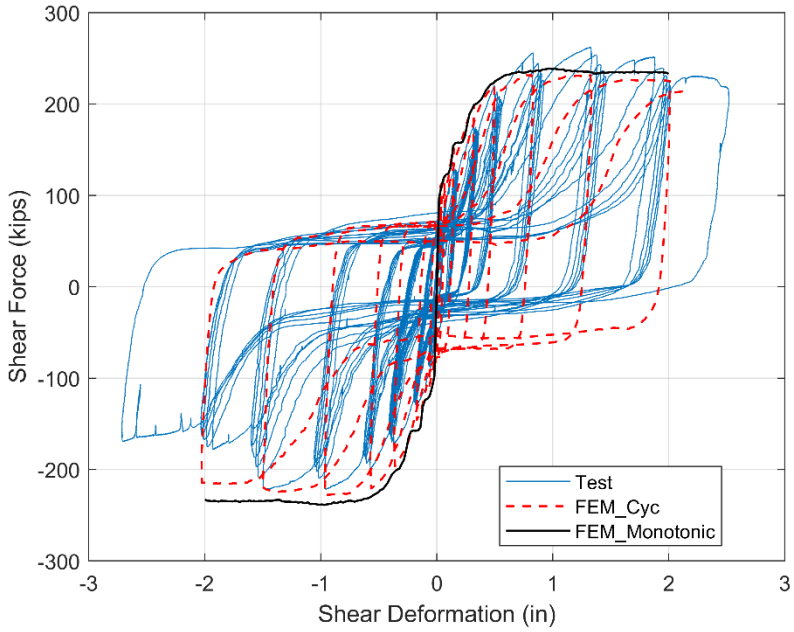


Figure 5-159. Finite Element Results of Hysteresis Loop of Specimen S2

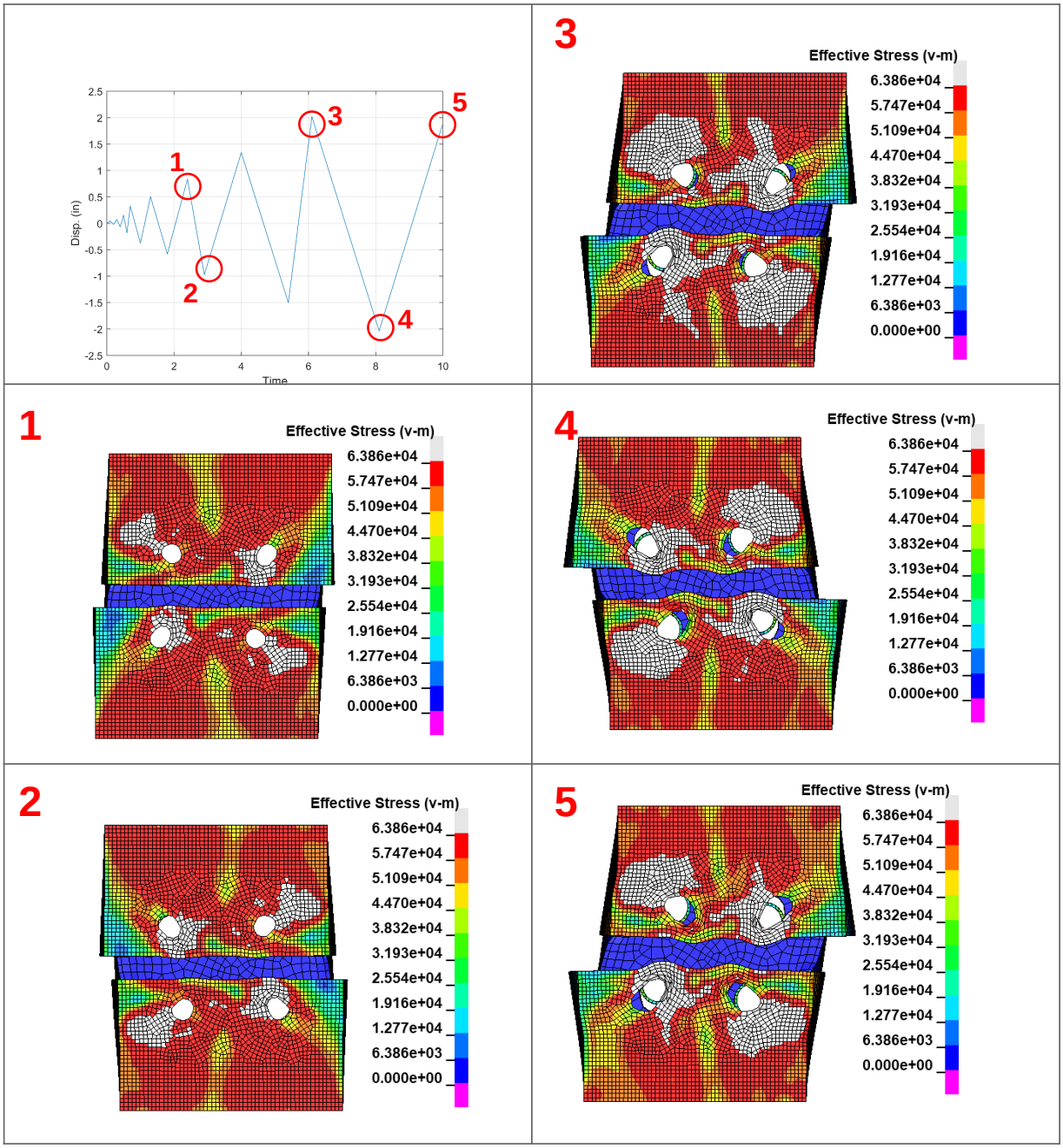


Figure 5-160. von Mises Stresses of Faceplates during Cycling Loading (Specimen S2)

5.4.3.3 Specimen S3

A monotonic lateral displacement of 2.0 in. was applied to the top of the finite element model of Specimen S3. Figure 5-161 shows the comparison between the resulting finite element model's monotonic loading curve and the hysteresis curve obtained from the test. The figure labels strengths corresponding to bearing strength considering pure shear force, combined shear and eccentric forces, and net section shear yielding strength and net section rupture strength. Both finite element and test results reached the target limit state (net section shear yielding), and the test result reached the net section rupture strength in the positive direction. The finite element model reached a peak strength of 231.3 kips at 2.0-in. displacement, while the test specimen reached peak strengths of 249 kips in the positive direction and -242 kips in the negative direction. The finite element results exhibit a slightly lower shear strength compared to the test results. Specifically, the shear strength of the finite element results is approximately 7% lower in the positive peak strength and 5% lower in the negative peak strength compared to the test result.

Figure 5-162 (a) shows the distribution of von Mises stresses in the steel cover plates and bolts, while Figure 5-162 (b) shows the von Mises stresses in the faceplates (after removing the splice plates and bolts). The figures show that the splice plates rotated by 8° when the top of the connection experienced a lateral displacement of 2.0 in. Three bolt holes in the figure exhibit different directions of elongation. It can be observed that the middle holes mainly moved horizontally, indicating a pure shear state, unlike the corner bolts. This observation highlights the influence of torsional forces acting on those bolts. The yielding area (σ_{von} > 63,000 psi) of faceplates shown in the figure started around the bolt holes and propagated over a certain range. As Specimen S3 reached the limit states of bearing strength and net section shear yielding strength, as mentioned earlier, a pair of corner bolt holes experienced severe outward pulling, resulting in serious torsional yielding similar to Specimens S1 and S2.

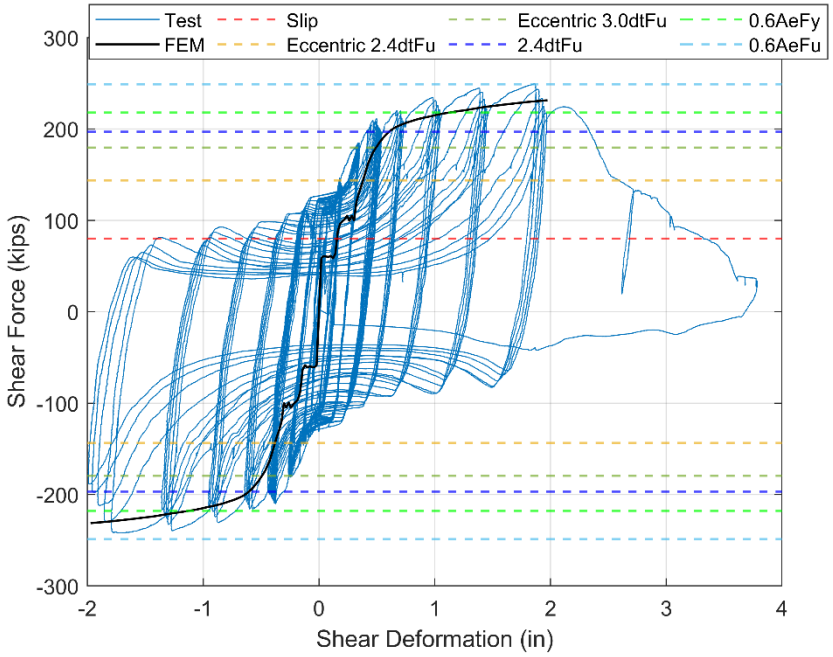
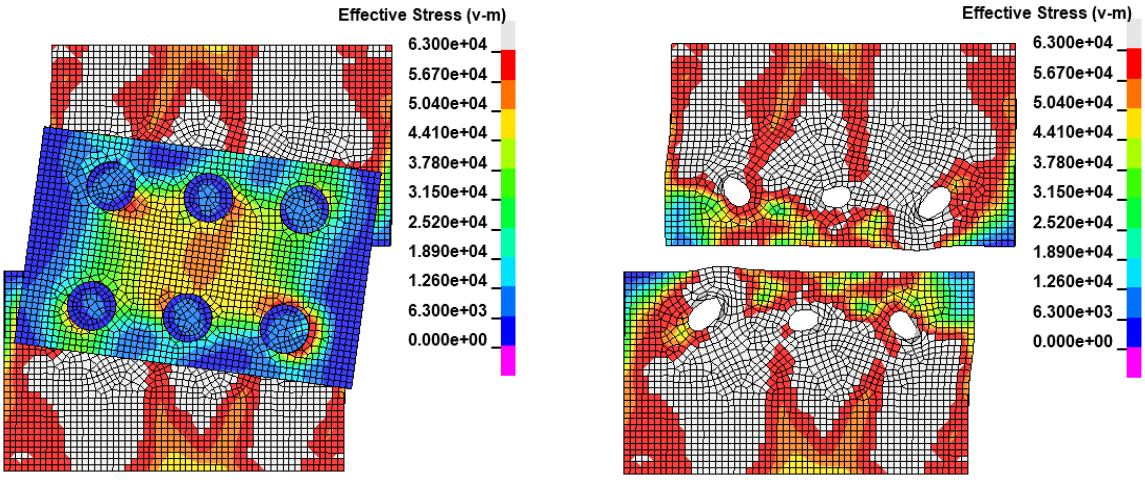


Figure 5-161. Finite Element Results of Load-Deformation Curve of Specimen S3



(a) All Steel (b) Faceplate Only

Figure 5-162. von Mises Stress of S3 Finite Element model

5.4.3.4 Specimen S4

A monotonic lateral displacement of 2.0 in. was applied to the top of the finite element model of Specimen S4. Figure 5-163 shows the comparison between the resulting finite element model's monotonic loading curve and the hysteresis curve obtained from the test. The figure labels strengths corresponding to bearing strength considering combined shear and eccentric forces, as well as the net section shear yielding and fracture strength, and the gross section shear yielding strength. Both the finite element and test results exceeded the target limit state of net section shear yielding and reached the gross section shear yielding strength. The finite element model reached a peak strength of 270 kips at 1.0-in. displacement, while the test specimen reached peak strengths of 313 kips in the positive direction and -300 kips in the negative direction. The peak strength of the finite element results underestimates the test results by approximately 14% and 9% in the positive and negative direction, respectively.

Figure 5-164 (a) shows the distribution of von Mises stresses in the steel cover plates and bolts, while Figure 5-164 (b) shows the von Mises stresses in the faceplates (after removing the splice plates and bolts). The figures show an approximate rotation of 7° in the splice plates when the top of the connection reached a lateral displacement of 2.0 in. In contrast to Specimen S3, Specimen S4 reached the strength of gross section shear yielding. As a result, at a deformation of 2.0 in., a significant portion of the gross section of faceplates exhibited yielding away from the row of bolts (i.e., before transferring forces to the splice plates through via the bolts).

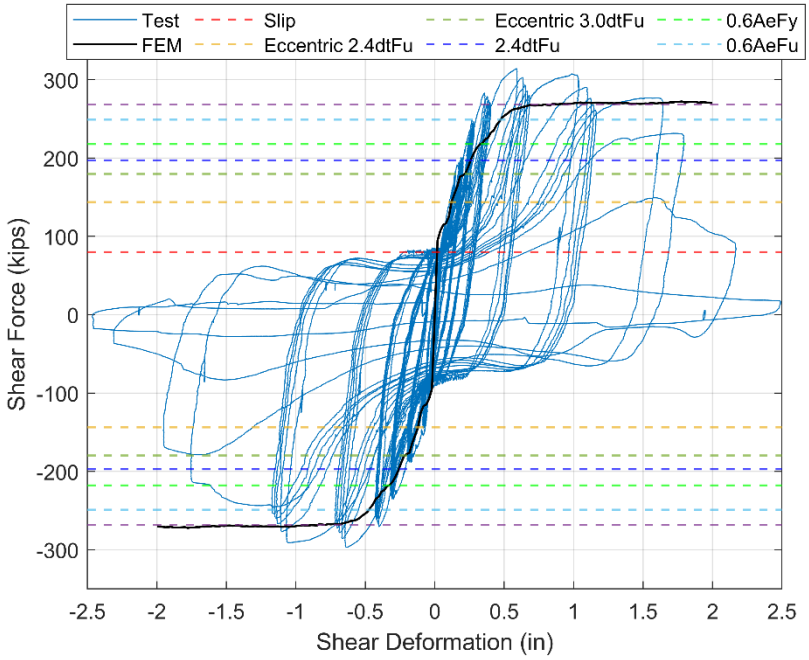
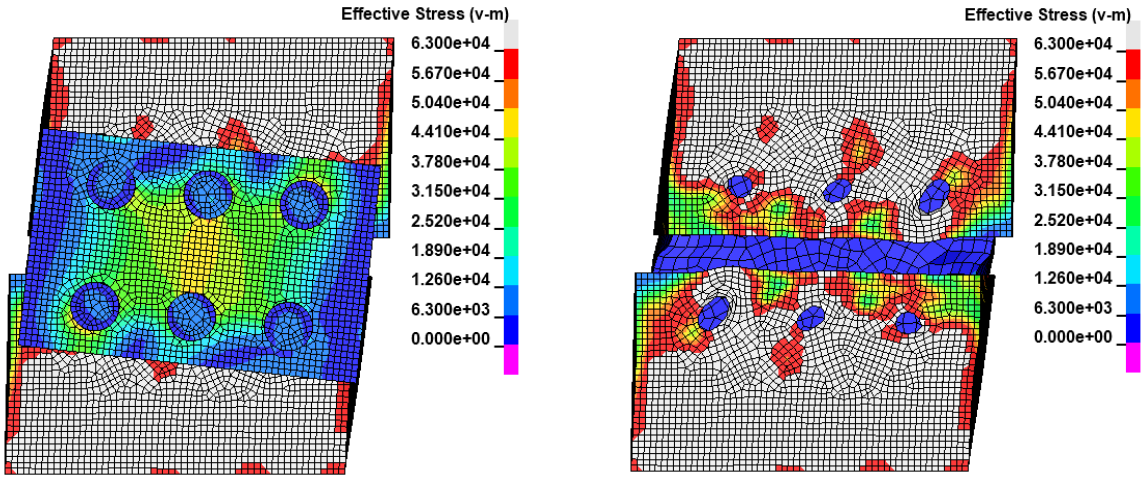


Figure 5-163. Finite Element Results of Load-Deformation Curve of Specimen S4



(a) All Parts (b) Faceplate

Figure 5-164. von Mises Stress of S4 Finite Element model

To understand the contribution of shear strength from steel and concrete, Figure 5-165 shows the shear strength of concrete, steel, and the entire section in the middle of the connection. It is observed that the concrete reaches its peak shear strength (84 kips) at a deformation of 0.33 in., with a progressively reducing

strength beyond that point, while the steel reaches 82% of its peak shear strength at a deformation of 0.5 in., progressively increasing to its peak strength of 220 kips at a deformation of 2.0 in.

To further assess the contribution of concrete in the composite connection, Figure 5-166 shows a comparison of shear strengths obtained from the S3 and S4 finite element models. The peak shear strengths for S3 and S4 are 231.3 kips and 270 kips, respectively. By subtracting the shear strength of S3 from S4 over the entire deformation range, the shear strength provided by the concrete component can be somewhat inferred, and is labeled "S4-S3" in the figure. The "S4-S3" shear strength reaches a peak strength of 113 kips at a shear deformation of 0.30 in., and it decreases to 39 kips at a shear deformation of 2.0 in. Finally, the shear strength of concrete obtained from S4 finite element model is compared with the "S4-S3" shear strength as shown in Figure 5-167. Again, models S3 and S4 do not exhibit perfect “synchronization.” Consequently, when comparing the results obtained from the "S4-S3" analysis, there is a larger fluctuation observed in the deformation range of 0 to 0.5 in., which corresponds to the region where the results were more sensitive to the occurrence of sliding.

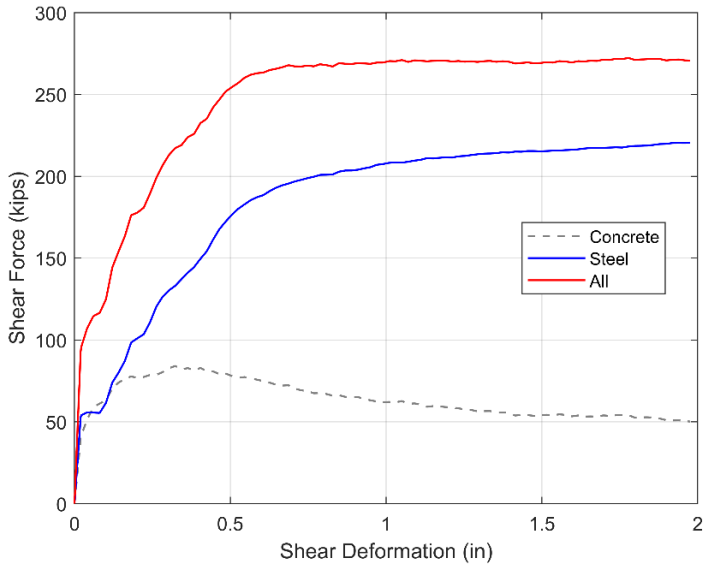


Figure 5-165. Shear Strengths of Concrete and Steel (Specimen S4)

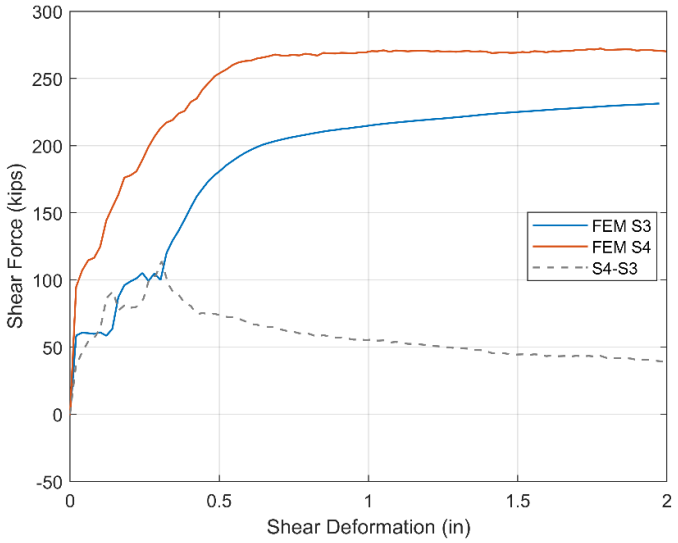


Figure 5-166. Comparison of Shear Strengths of S3 and S4 Finite Element Models

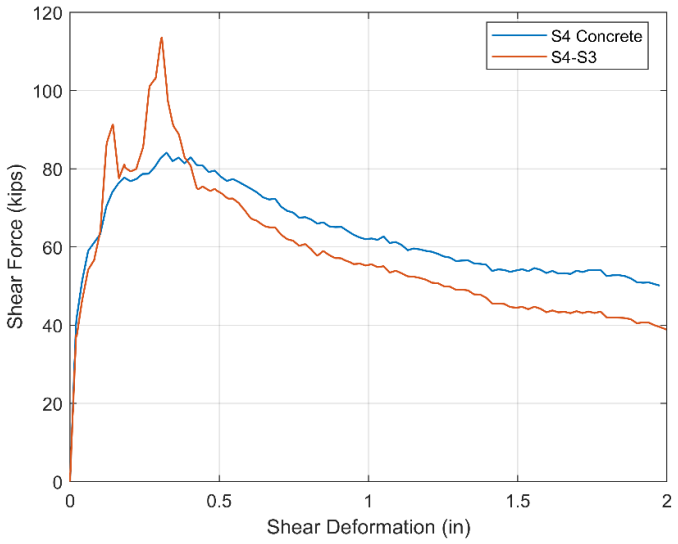


Figure 5-167. Comparison of Shear Strengths of S4 Concrete and "S4-S3"

Figure 5-168 shows the load protocol for the cyclic analysis of Specimen S4, while Figure 5-169 shows the corresponding finite element results. The analysis results closely match the overall response observed in the loading and unloading curves. However, the peak strength of the finite element results underestimates the test results by approximately 9% to 14%, which is consistent with the findings from the monotonic load

analysis. Furthermore, Figure 5-170 shows the von Mises stresses of the faceplates during cyclic loading. Five arbitrary points were selected to demonstrate the distribution of stress and deformation of the faceplates. The bolt holes in the cyclic analysis experienced elongation in both directions due to the cyclic loads. As a result, the four corner holes, which are subjected to torsional effects, exhibited similar amounts of elongation. Additionally, the middle bolt holes showed more predominant elongation in the left and right directions, closer to a pure shear behavior.

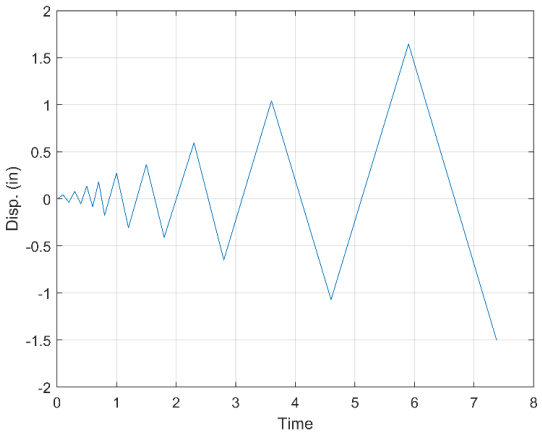


Figure 5-168. Cyclic Loading Protocol of Finite Element Model (Specimen S4)

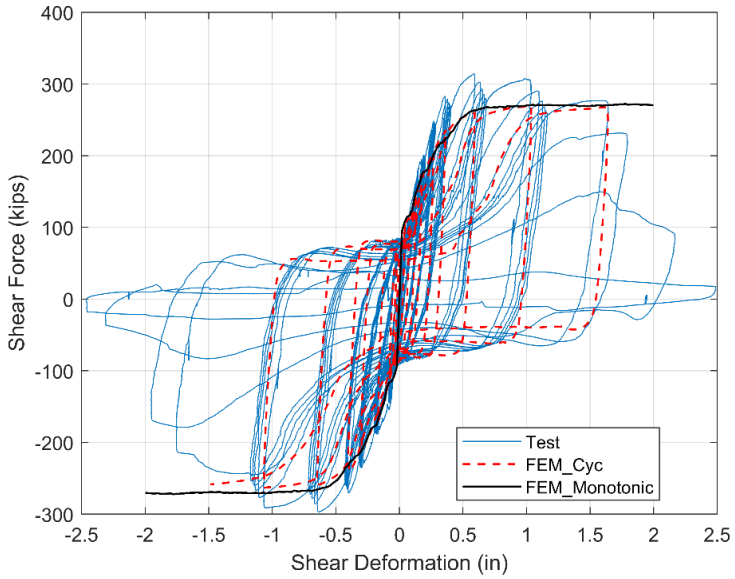


Figure 5-169. Finite Element Results of Hysteresis Loop of Specimen S4

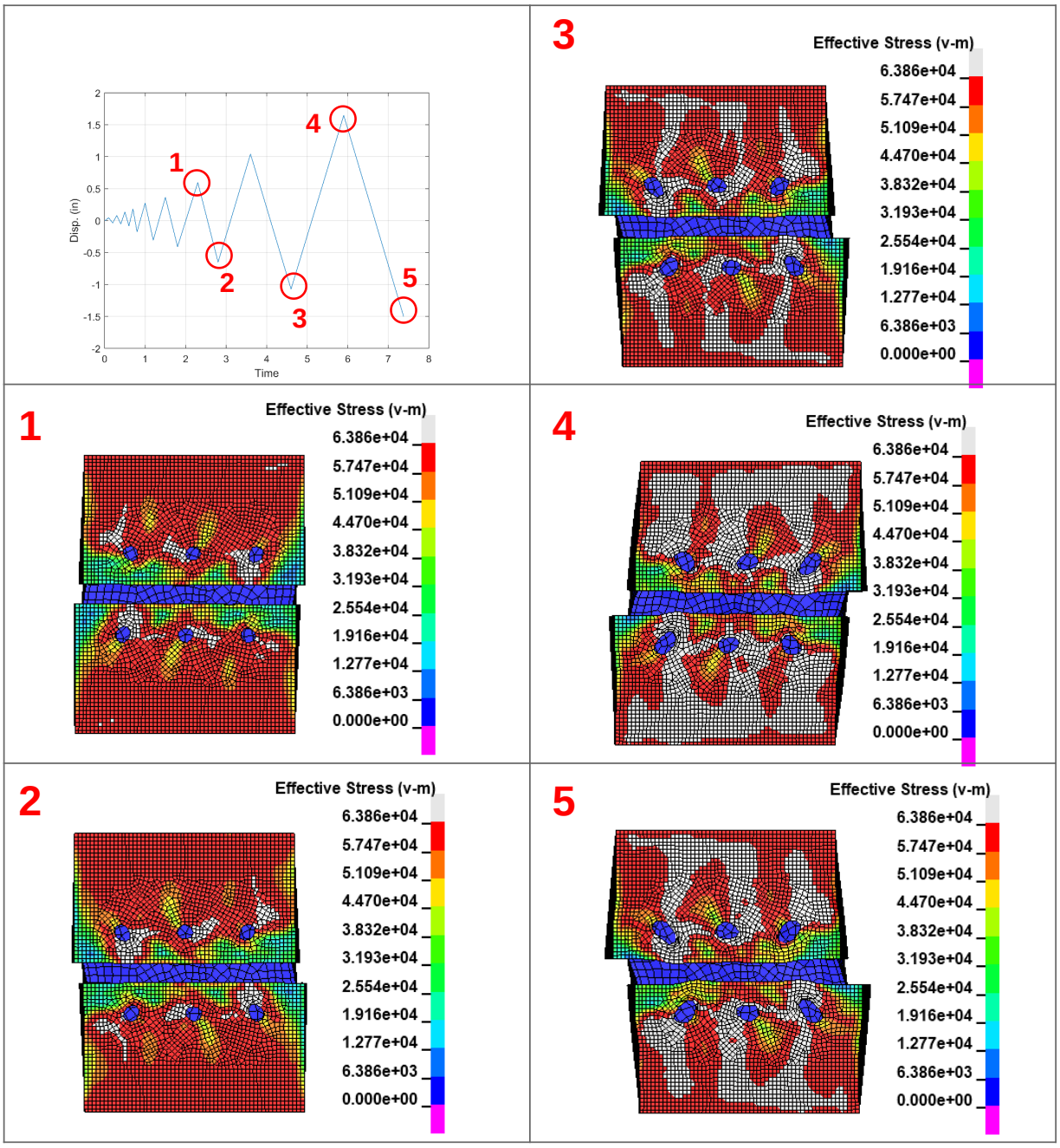


Figure 5-170. von Mises Stresses of Faceplates during Cycling Loading (Specimen S4)

5.4.3.5 Specimen S5

A monotonic lateral displacement of 2.0 in. was applied to the top of the finite element model of Specimen S5. Figure 5-171 shows the comparison between the resulting finite element model's monotonic loading curve and the hysteresis curve obtained from the test. The figure labels strengths corresponding to bearing strength considering pure shear force, bearing strength considering combined shear and eccentric forces, as well as the net section and gross section shear yielding. The finite element analysis reached the limit state of eccentric bearing ($3.0dtF_u$), whereas the test result reached the limit state of net section shear yielding strength. The finite element model reached a peak strength of 224.0 kips at 2.0-in. displacement, while the test specimen reached peak strengths of 252 kips in the positive direction and -258 kips in the negative direction. The peak strength of the finite element results underestimates the test results by approximately 13.2% and 11.2 in the positive and negative direction, respectively.

Figure 5-172 (a) shows the distribution of von Mises stresses in the steel cover plates and rods, while Figure 5-172 (b) shows the von Mises stresses in the faceplates (after removing the splice plates and rods). The figures show that the splice plates rotated by 7° when the top of the connection experienced a lateral displacement of 2.0 in. Furthermore, the four rod holes located on the top and bottom of the faceplates exhibited different deformations due to the eccentric torsion. As the connection reached the strength of eccentric bearing ($3.0dtF_u$), severe yielding occurred around the rod holes because of the rods pushing the holes in different directions. Consequently, the gross section of the faceplates primarily exhibited yielding along the bearing direction of the rod holes.

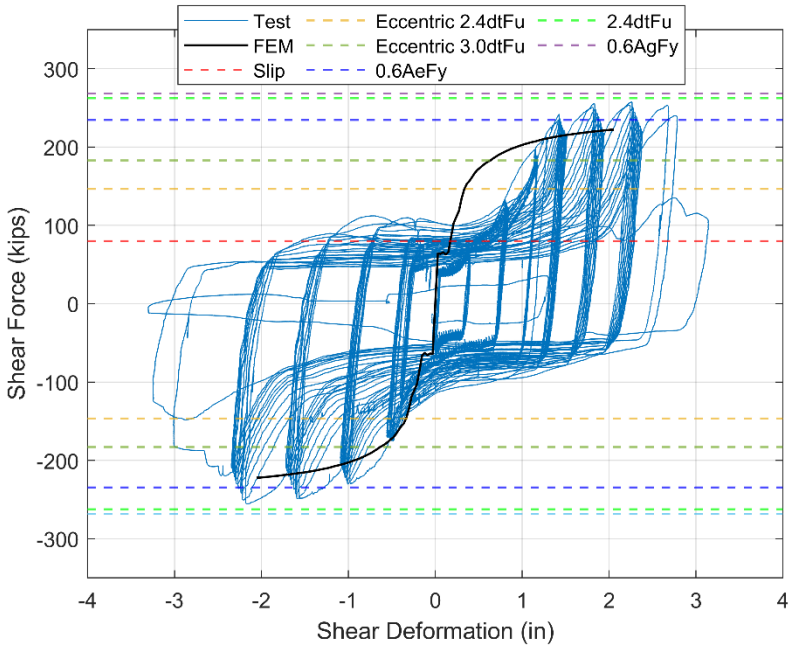
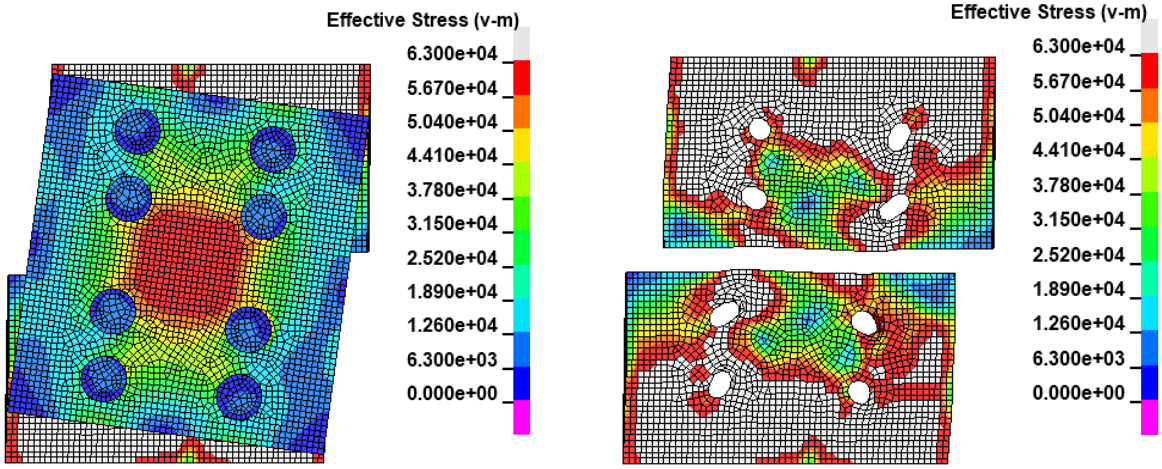


Figure 5-171. Finite Element Results of Load-Deformation Curve of Specimen S5



(a) All Steel (b) Faceplate Only

Figure 5-172. von Mises Stress of S5 Finite Element Model

5.4.3.6 Specimen S6

A monotonic lateral displacement of 2.0 in. was applied to the top of the finite element model of Specimen S6. Figure 5-173 shows the comparison between the resulting finite element model's monotonic loading curve and the hysteresis curve obtained from the test. The figure labels strengths corresponding to bearing strength considering pure shear force, bearing strength considering combined shear and eccentric forces, as well as the net section and gross section shear yielding. Both the finite element and test results reached the limit state of gross section shear yielding. The finite element model reached a peak strength of 278 kips at 1.15-in. displacement, while the test specimen reached peak strengths of 312 kips in the positive direction and -289 kips in the negative direction. The peak strength of finite element results closely matches the test results at an approximately 1.5-in. lateral displacement.

Figure 5-174 (a) shows the distribution of von Mises stresses in the steel cover plates and rods, while Figure 5-174 (b) shows the von Mises stresses in the faceplates (after removing the splice plates and rods). Similarly, a rotation of approximately 7° occurred in the splice plate when the applied displacement on the top reached 2.0 in. As Specimen S6 reached the strength of gross section shear yielding, the gross section of the faceplates exhibited more severe yielding compared to the S5 finite element model.

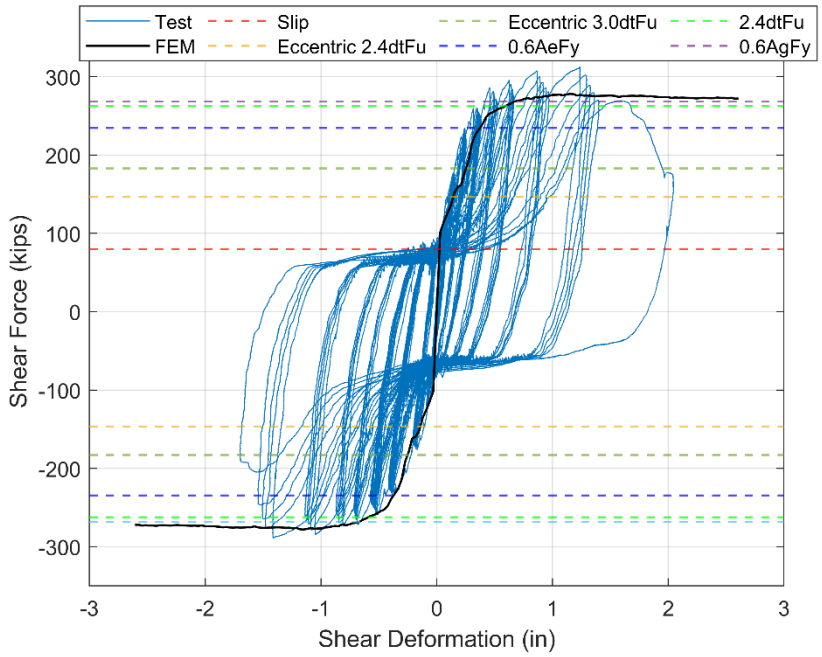
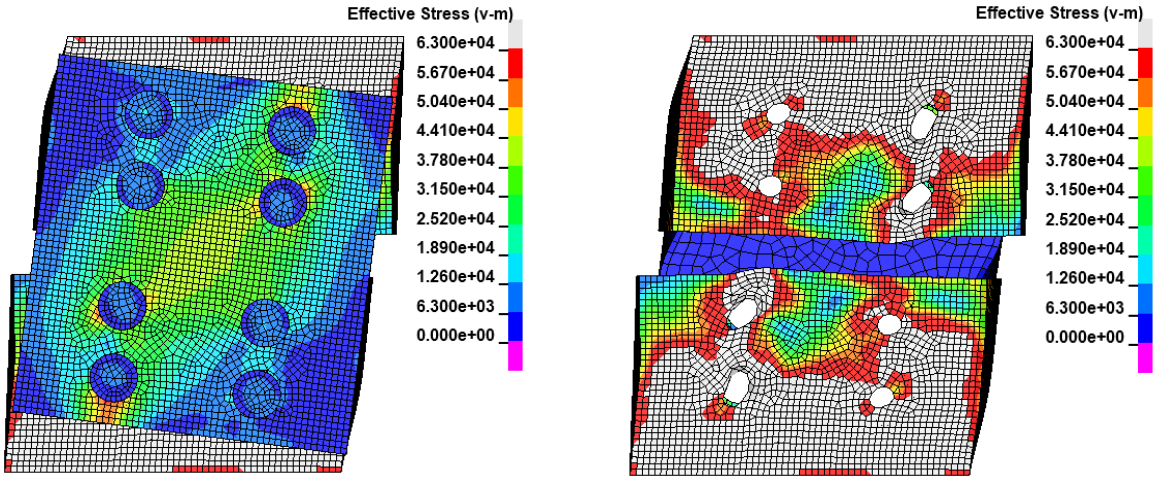


Figure 5-173. Finite Element Results of Backbone curve of Specimen S6



(a) All Steel (b) Faceplate

Figure 5-174. von Mises Stress of S6 Finite Element model

To understand the contribution of shear strength from steel and concrete, Figure 5-175 shows the shear strength of concrete, steel, and the entire section in the middle of the connection. It is observed that the concrete reaches its peak shear strength (72 kips) at a deformation of 0.32 in., with a progressively reducing

strength beyond that point, while the steel reaches 81% of its peak shear strength at a deformation of 0.5 in., progressively increasing to its peak strength of 229 kips at a deformation of 2.0 in.

To further assess the contribution of concrete in the composite connection, Figure 5-176 shows a comparison of shear strengths obtained from the S5 and S6 finite element models. The peak shear strengths for S5 and S6 are 224 kips and 278 kips, respectively. By subtracting the shear strength of S5 from S6 over the entire deformation range, the shear strength provided by the concrete component can be somewhat inferred, and is labeled "S6-S5" in the figure. The "S6-S5" shear strength reaches a peak strength of 111.6 kips at a shear deformation of 0.34 in., and it decreases to 58 kips at a shear deformation of 2.0 in. Finally, the shear strength of concrete obtained from S6 finite element model is compared with the "S6-S5" shear strength as shown in Figure 5-177. Similar to previous observations, models S5 and S6 do not exhibit perfect “synchronization” of the force-deformation curve. The result obtained from the "S6-S5" analysis has a peak shear strength of 111.7 kips at 0.27-in. shear deformation, while the result obtained from model S6’s section cut has a peak shear strength of 72 kips at 0.33-in shear deformation. However, this difference decreases to 5% when their shear deformation reaches 2.0 in.

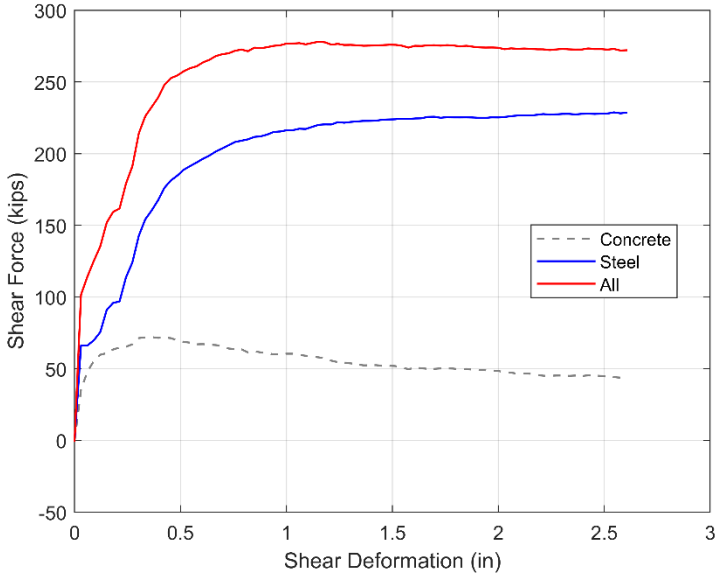


Figure 5-175. Shear Strengths of Concrete and Steel (Specimen S6)

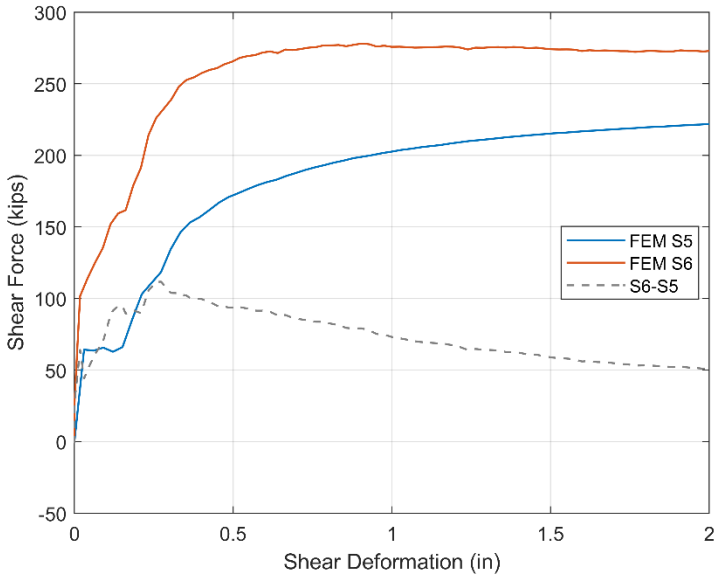


Figure 5-176. Comparison of Shear Strengths of S5 and S6 Finite Element Models

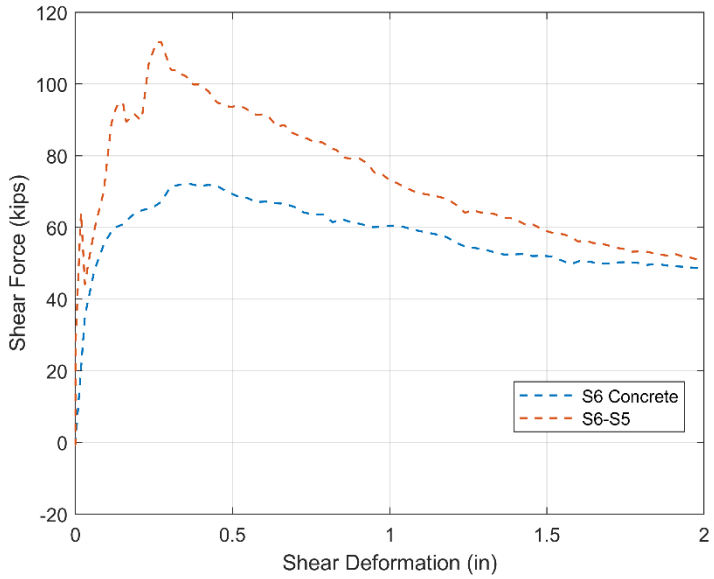


Figure 5-177. Comparison of Shear Strengths of S6 Concrete and "S6-S5"

Figure 5-178 shows the load protocol for the cyclic analysis of Specimen S6, while Figure 5-179 shows the corresponding finite element result. The finite element result shows the hysteresis process of cyclic loading. Similar to the monotonic loading curve, the analysis result closely matches the peak strength of the test result when the shear deformation reaches 1.5 in. Furthermore, Figure 5-180 shows the von Mises stresses of the faceplates during cyclic loading. Five arbitrary points were selected to demonstrate the distribution of stress and deformation of the faceplates. During the cyclic loading analysis, the four rod holes on the top and bottom faceplate elongated in different directions due to the torsional effect. This resulted in yielding paths along the bolt lines and the formation of a block shear failure pattern.

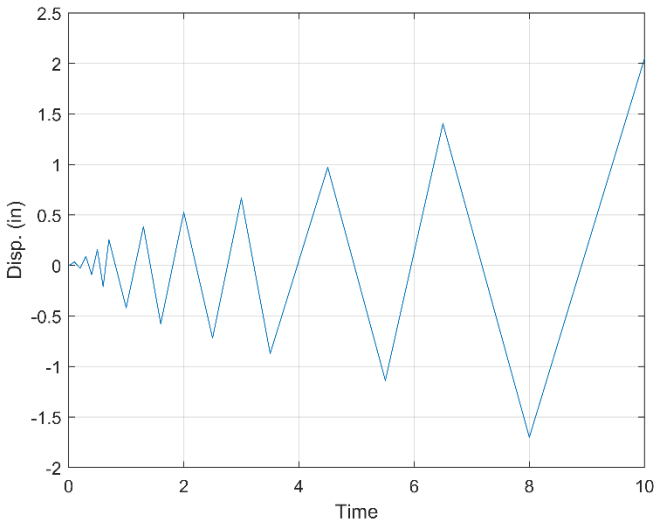


Figure 5-178. Cyclic Loading Protocol of Finite Element Model (Specimen S6)

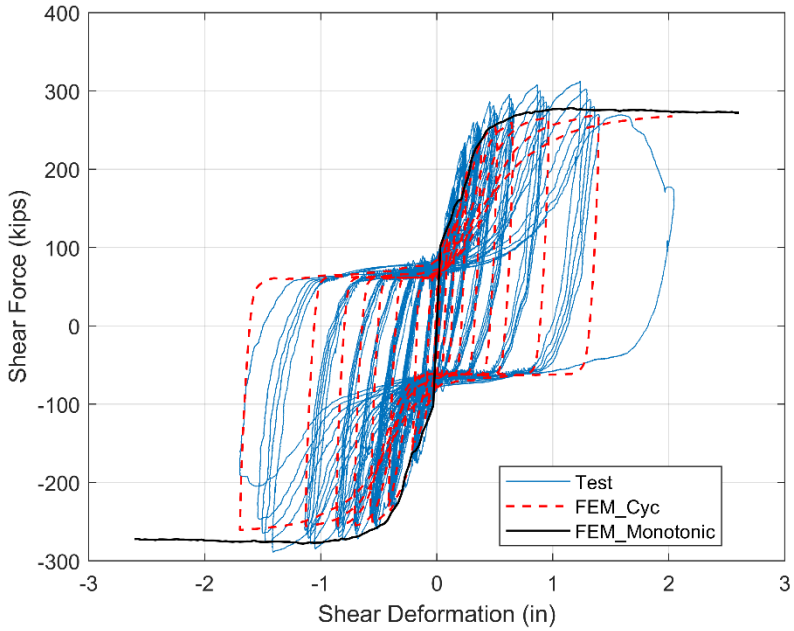


Figure 5-179. Finite Element Results of Hysteresis Loop of Specimen S6

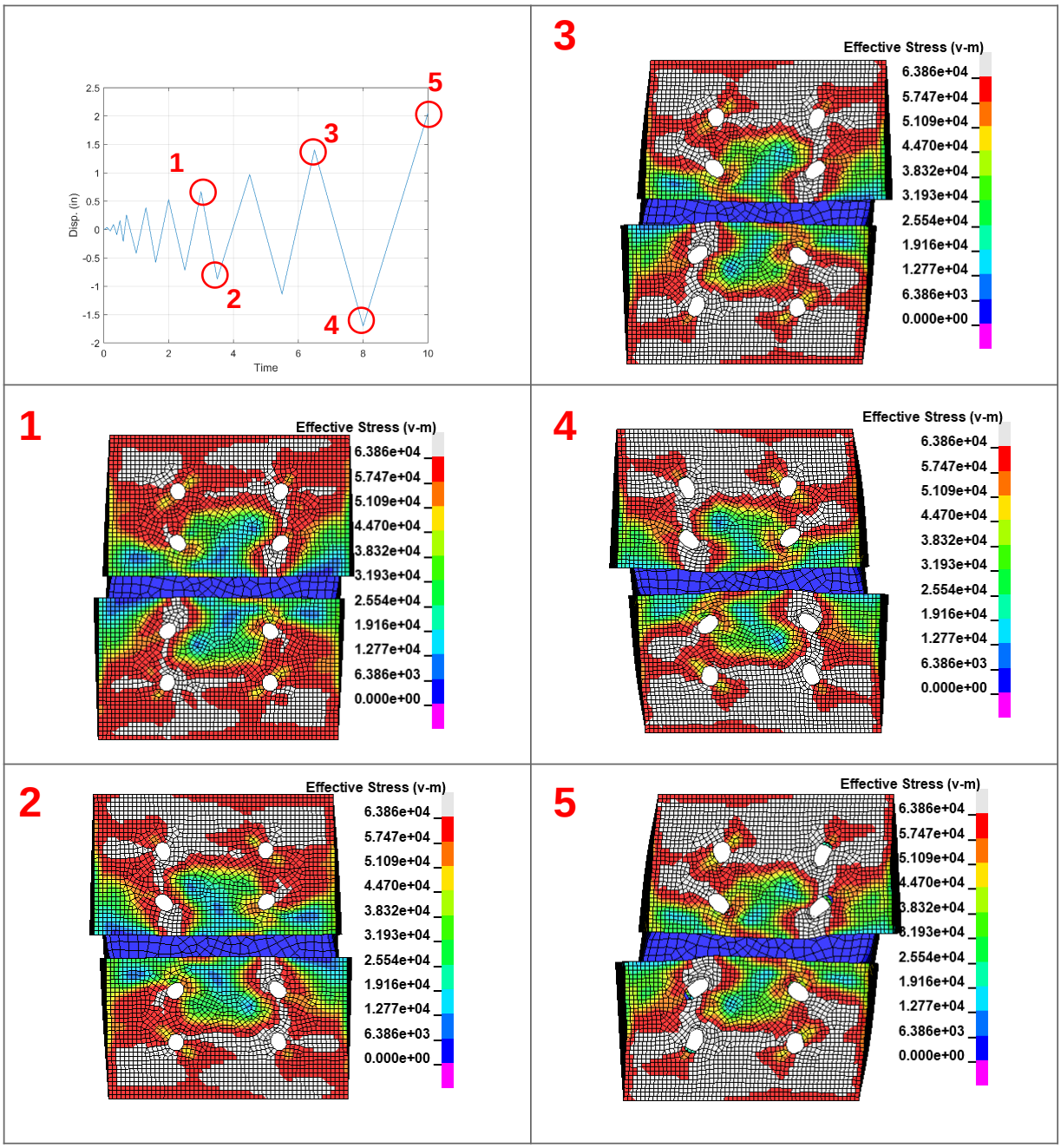


Figure 5-180. von Mises Stresses of Faceplates during Cycling Loading (Specimen S4)

5.4.4 Results of Finite Element Analysis (Considering Inclination from the Actuator)

The previous work provided analysis results for the finite element model described in Section 5.4.1, by subjecting the models to top lateral displacements to induce shear deformations, replicating the conditions applied to the specimens during testing. Here, vertical axial forces are also applied to the specimens in the finite element analyses to simulate the inclination effects generated by the actuator, and quantify to what extent this affects the results.

As discussed in Section 5.4.2, a vertical eccentricity of 1.75 in. and a corresponding actuator angle of 3.81 degrees were measured during the shear component tests. To indirectly account for this effect in the finite element analyses here, a vertical axial load was applied to the specimen, increasing simultaneously with the applied horizontal load. Figure 5-181 illustrates the applied vertical load (Fz) in the finite element models of the shear specimens, along with the shear force (V_{FEM}) obtained from the finite element model. To replicate the monotonic shear force-shear deformation curve, a bilinear curve was used for applying Fz. This bilinear curve indicates that the applied Fz gradually increases until the shear deformation reaches 0.5 in. Beyond this point, Fz reaches a plateau. The magnitude of that plateaued force was calculated by geometry, at the angle mentioned above, for the maximum shear forces obtained from Section 5.4.3. The resulting vertical actuator force, ActF_Z, for the corresponding total actuator force, ActF, are summarized in Table 5-12. Note that Fz is in compression during the positive direction, while it is in tension during the negative direction.

Table 5-12. Actuator Forces of Shear Specimens when Considering Inclination

Specimen	Ecc. (in.)	Angle (degree)	ActF (kips)	ActF_X (kips)	ActF_Z (kips)
S1	1.75	3.81	194.43	194.00	12.91
S2	1.75	3.81	240.53	240.00	15.98
S3	1.75	3.81	231.81	231.30	15.40
S4	1.75	3.81	270.60	270.00	17.97
S5	1.75	3.81	224.50	224.00	14.91
S6	1.75	3.81	278.62	278.00	18.51

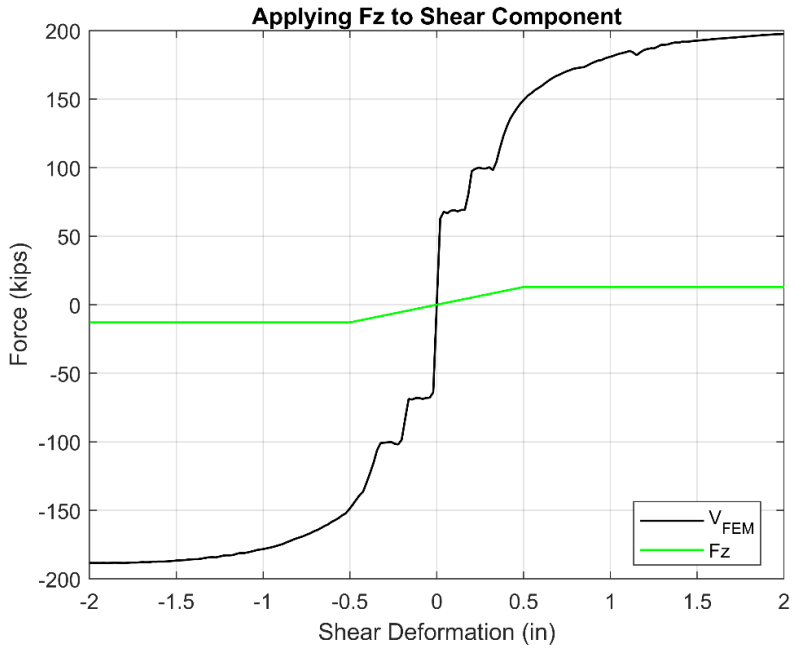


Figure 5-181. Applied Axial Force Fz in Shear Specimens

Figures 182 to 187 show the finite element analysis results for Specimens S1 to S6, considering the inclination of the actuator. In these figures, the analysis results with and without considering inclination are plotted together to illustrate the impact of the applied axial load, Fz, on the shear strength of the specimens. Table 5-13 summarizes the analysis results for both scenarios. In the table, V_{FEM+} and V_{FEM-} denote the positive and negative peak shear forces obtained from the monotonic finite element analysis without

considering the inclination of the actuators, while V_{FEM_Act+} and V_{FEM_Act-} denote those considering the inclination.

For composite specimens (S2, S4, and S6), with the axial load Fz in compression in the positive direction, it was expected that the peak shear force from the analysis would be slightly higher, as the compressive axial load tends to increase the shear strength of concrete. Conversely, when Fz is in tension in the negative direction, it was expected to reduce the peak shear force as the axial force reduces the concrete shear capacity. The finite element analysis results confirm this behavior, indicating an increase in peak shear forces in the positive direction and a decrease in the negative direction for composite specimens. The results also indicate that adding the applied axial loads Fz in the analysis resulted in a change of shear strength that ranged from 0% to 4% for Specimens S1 to S6 (with practically no visible difference for Specimens S3, S4 and S5). This further confirms that the impact of the actuator inclination during the tests can be considered negligible. However, in some cases, considering this factor here has enhanced the match between the finite element results of the test results..

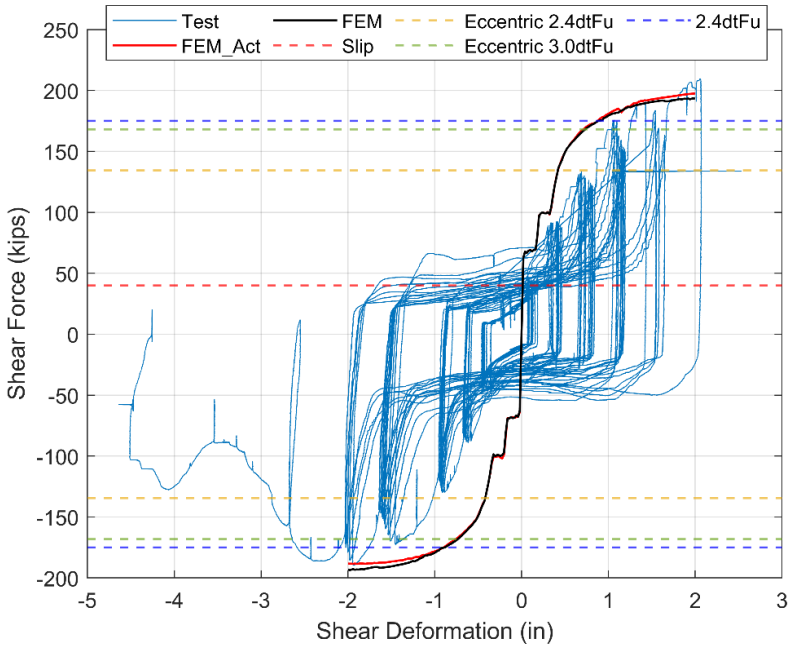


Figure 5-182. Finite Element Results of Load-Deformation Curve of Specimen S1 with and without Considering Fz

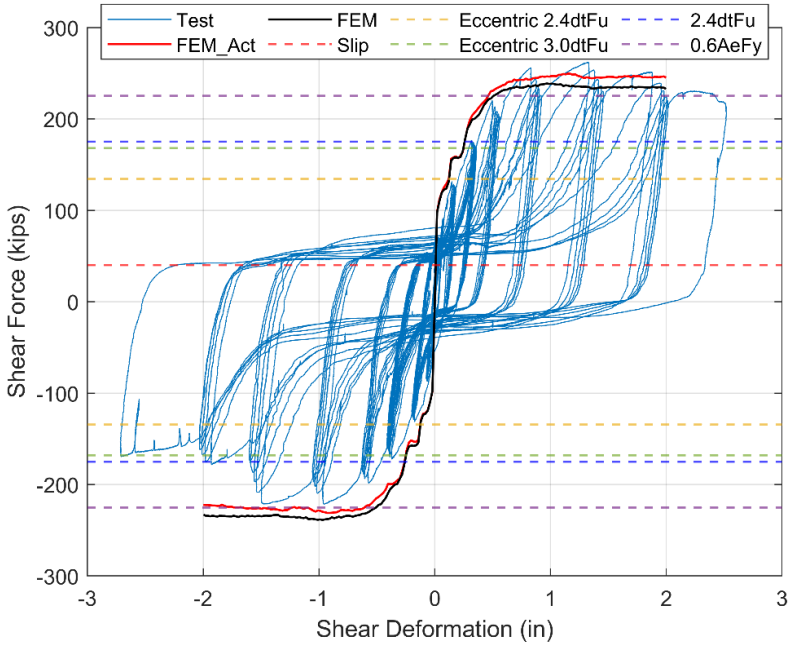


Figure 5-183. Finite Element Results of Load-Deformation Curve of Specimen S2 with and without Considering Fz

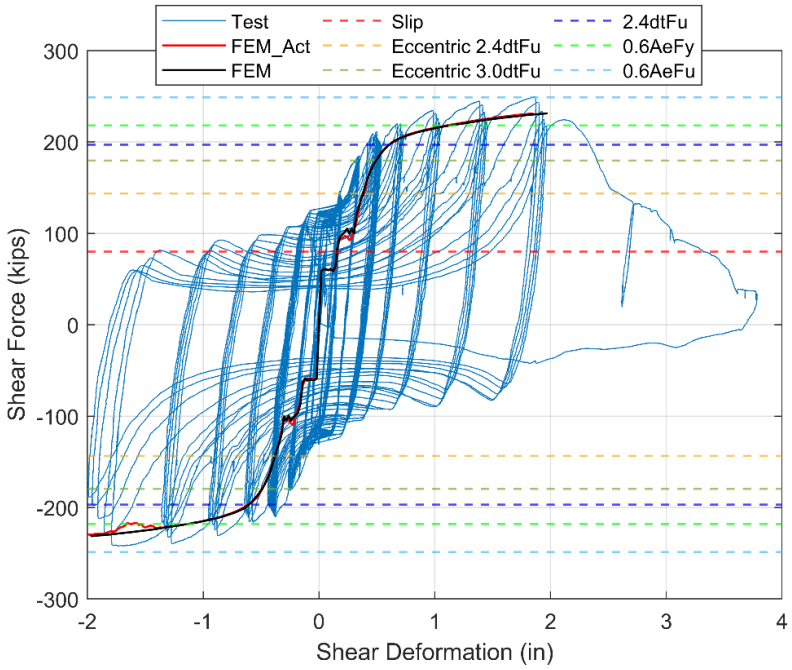


Figure 5-184. Finite Element Results of Load-Deformation Curve of Specimen S3 with and without Considering Fz

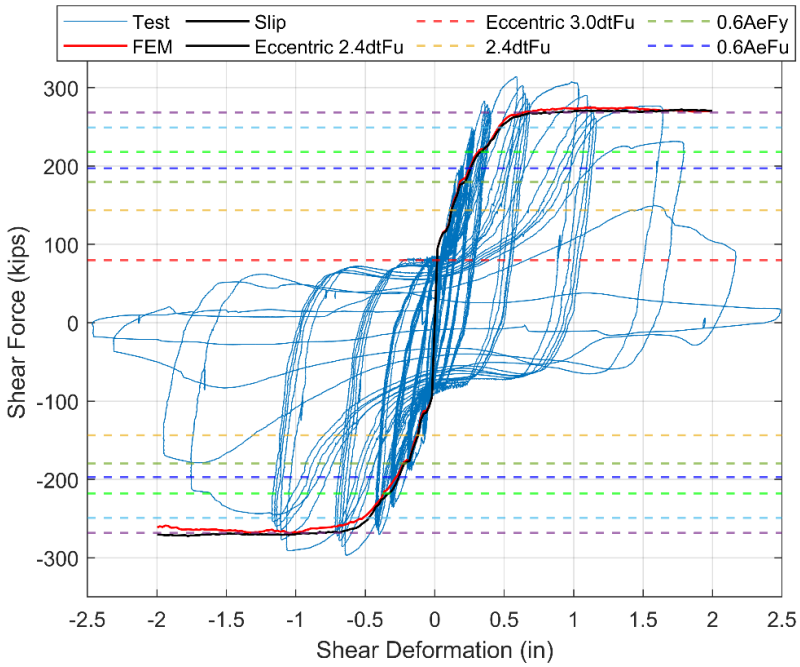


Figure 5-185. Finite Element Results of Load-Deformation Curve of Specimen S4 with and without Considering Fz

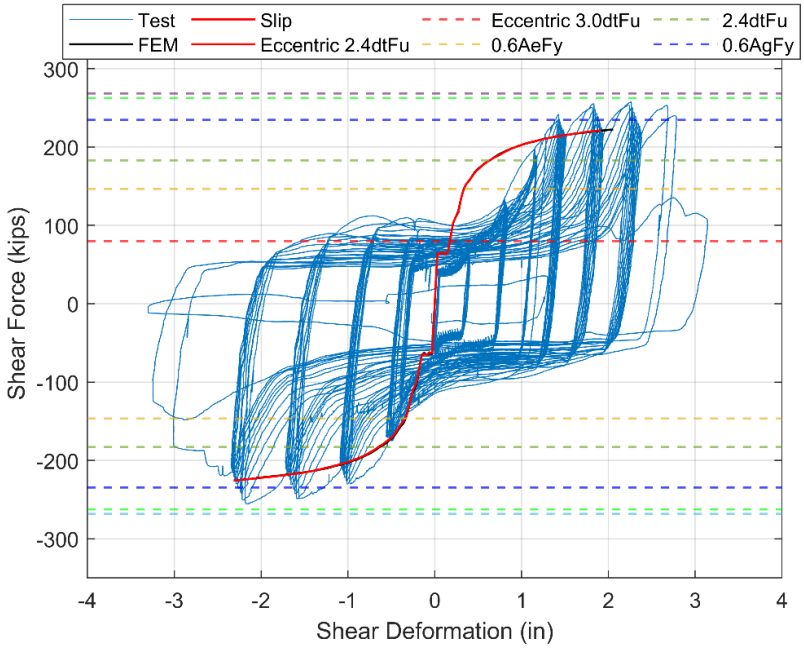


Figure 5-186. Finite Element Results of Load-Deformation Curve of Specimen S5 with and without Considering Fz

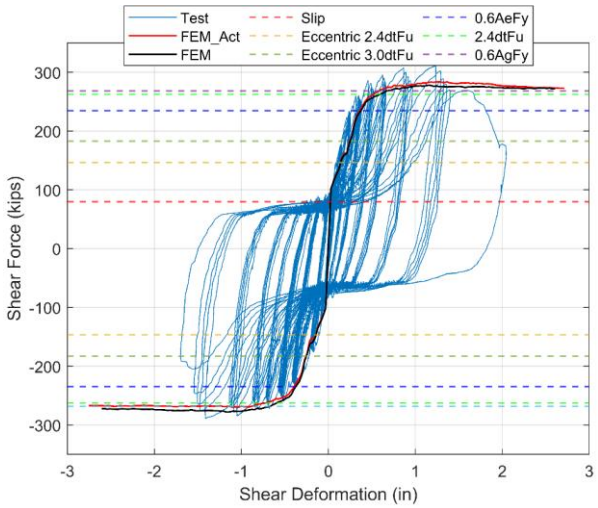


Figure 5-187. Finite Element Results of Load-Deformation Curve of Specimen S6 with and without Considering Fz

Table 5-13. Comparison of Peak Shear Forces of Shear Specimens with and without Considering Inclination

Specimen	V_{FEM+} (kips)	V_{FEM-} (kips)	V_{FEM_Act+}	V_{FEM_Act-}	V_{FEM+}/V_{FEM_Act+}	V_{FEM-}/V_{FEM_Act}
S1	194.0	194.0	197.5	188.5	0.98	1.03
S2	240.0	240.0	249.5	231.1	0.96	1.04
S3	231.3	231.3	230.9	229.9	1.00	1.01
S4	270.0	270.0	274.7	268.7	0.98	1.00
S5	224.0	224.0	221.3	225.4	1.01	0.99
S6	278.0	278.0	283.8	269.4	0.98	1.03

5.5 Wall Case Scenario for Shear Splices

In Section 5.4, the six 14-in. wide tested shear specimens were replicated in the LS-DYNA finite element models. Here, wider walls with bolted splices are examined to investigate the behavior of connections governed by shear while minimizing the influence of localized end-effects. It is expected that in a wider wall segment, the impact of the eccentricity of the bolt groups would be reduced, to become negligible once the wall width increases beyond a certain value. Thus, the objective is to investigate the shear capacity of bolted splices in a more realistic C-PSW/CF scenario.

5.5.1 Shear Models and Properties

Figures 5-188 to 5-191 show four shear models (W1 to W4) constructed in LS-DYNA. These shear models maintain the same wall thickness T (12 in.) and height H (17.5 in.) as those studied in Section 5.4. Four shear models (W1 to W4) with width-to-thickness ratios (B/T) of 1.167, 2.167, 3.167, and 4.167, and width-to-height ratios (B/H) of 0.8, 1.486, 2.171, and 2.857, were analyzed in this study to understand the effects of increasing wall width. One row of bolts was placed at both the top and bottom of the faceplates, with the number of bolts increasing from two in Model W1 to eight in Model W4. All bolt spacings are set to 6 in., with horizontal and vertical edge distances (measured from the bolt center to the edge of the steel plate) of 4 inches and 2 inches, respectively. All shear models in this section share the same properties as the shear specimens S1 to S6 (refer to Section 5.4.1).

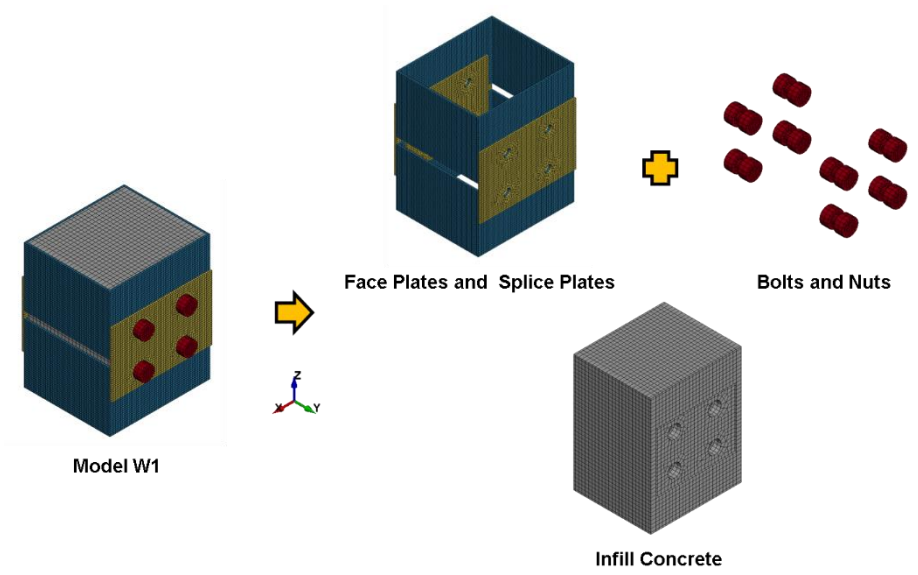


Figure 5-188. Finite Element Model of Specimen W1

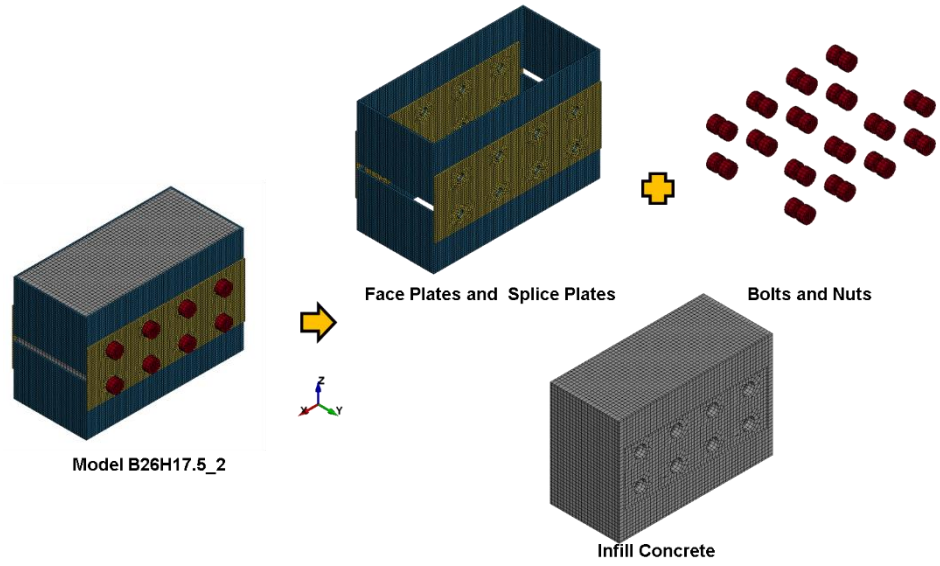


Figure 5-189. Finite Element Model of Specimen W2

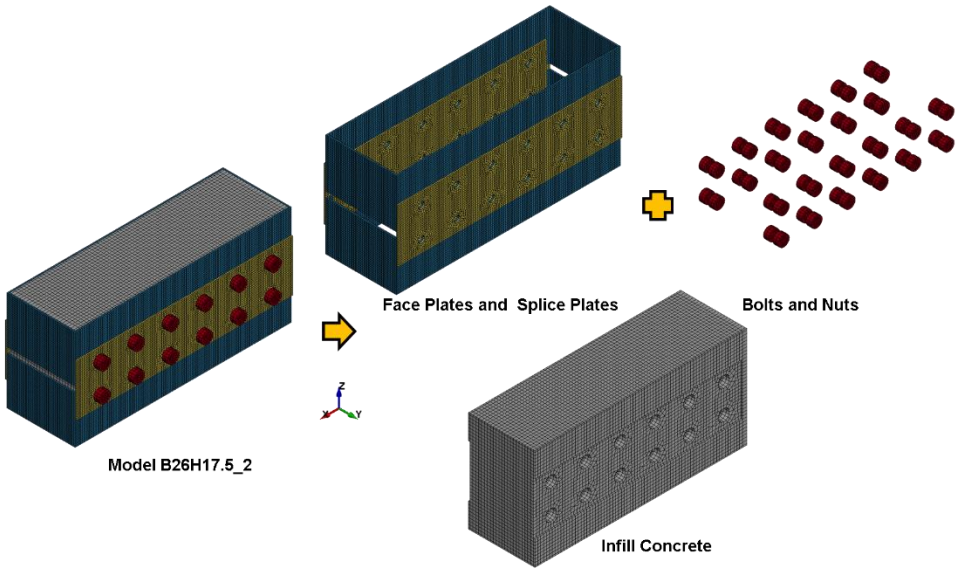


Figure 5-190. Finite Element Model of Specimen W3

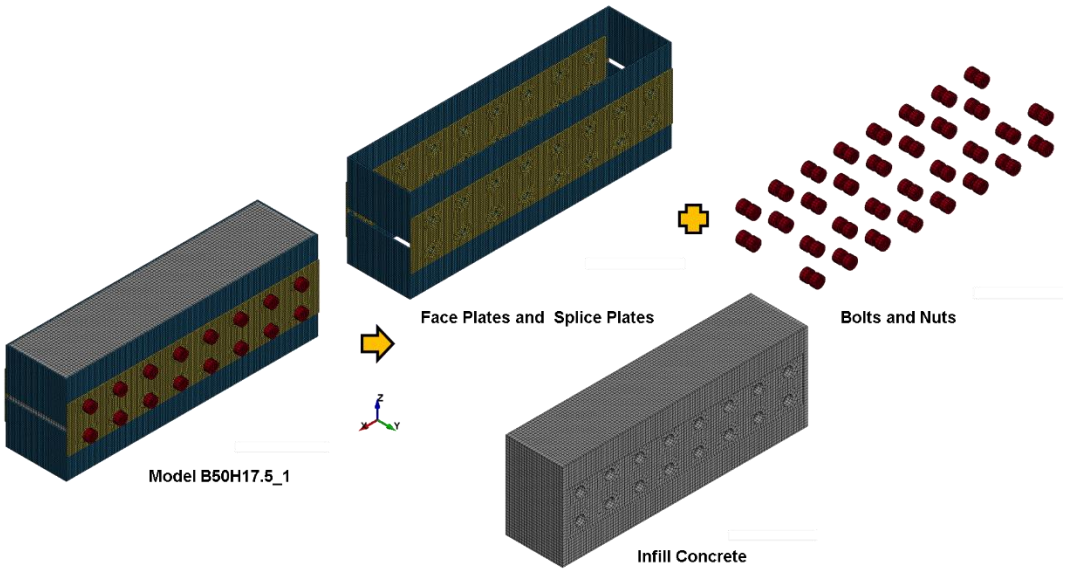


Figure 5-191. Finite Element Model of Specimen W4

5.5.2 Design Limit States

Following the methodology outlined in Section 3.3.2, Table 5-14 presents the design strengths of Models W1 to W4 under various limit states using AISC equations. These calculations assume a yield strength (F_y) of 63.86 ksi and a tensile strength (F_u) of 72.94 ksi. In the table, the term "sequence" ranks the strengths from weakest to strongest for each wall model across different limit states. All limit states were computed using AISC equations as introduced in Section 3.3.2, and all shear models were designed to be governed by bearing strength.

As previously discussed in Section 3.3.2, the bearing strength considering eccentricity is included in the limit states. Table 5-15 compares the "Eccentricity Ratios", representing the ratio of eccentric bearing strength ($Ecc.\ 2.4dtF_u$) to non-eccentric (pure shear) bearing strength ($2.4dtF_u$) for Models W1 to W4. These ratios vary from 0.77 to 0.96, indicating that the impact of eccentricity diminishes as the wall's width increases. Specifically, for Models W3 and W4, the ratios are 0.94 and 0.96, respectively. These values are close to 1.0, which represents the condition in a wall case scenario where the impact of eccentricity is negligible. The following section compares the finite element analysis results from Models W1 to W4, providing deeper insights into the influence of wall width when the "Eccentricity Ratios" changes.

Table 5-14. Design Limit States for Models W1 to W4

	W1		W2		W3		W4	
Limit States	**Strength (kips)**	**Sequence**	**Strength (kips)**	**Sequence**	**Strength (kips)**	**Sequence**	**Strength (kips)**	**Sequence**
A. Slip-Critical Resistance (kips)	98.96	1	197.92	1	296.88	1	395.84	1
B. Net Section Yiled (0.6AeRyFy) (kips)	225.11	5	411.90	5	598.69	5	785.48	5
C. Gross Area Yield (0.6AgRyFy) (kips)	268.21	8	498.11	8	728.00	8	957.90	8
D. Bearing Capacity 2.4dtFu (kips)	175.06	4	350.11	3	525.17	3	700.22	3
E. Tear-out Capacity (kips)	363.79	9	790.49	10	1217.19	10	1643.89	10
F. End Tear-out & Bearing (kips)	237.97	6	413.02	6	588.08	4	763.13	4
G. Net Section Rupture (0.6AeRuFu) (kips)	257.11	7	470.46	7	683.81	7	897.16	7
H. Bolt Shear Strength (kips)	530.61	11	1061.23	11	1591.84	11	2122.46	11
I. Eccentric Bearing Capacity 2.4dtFu (kips)	134.48	2	313.15	2	494.57	2	674.68	2
J. Eccentric Bearing Capacity 3.0dtFu (kips)	168.10	3	391.44	4	618.22	6	843.35	6
K. Composite Shear Strength (kips)	406.17	10	754.31	9	1102.46	9	1450.60	9

Table 5-15. The ratios of eccentric bearing strength to non-eccentric bearing strength in Models W1 to W4

	W1	**W2**	**W3**	**W4**
Width B (in)	14.00	26.00	38.00	50.00
Thickness T (in)	12.00	12.00	12.00	12.00
B/T	1.17	2.17	3.17	4.17
$2.4dtF_u$ (kips)	175.06	350.11	525.17	700.22
Ecc. $2.4dtF_u$ (kips)	134.48	313.15	494.57	674.68
Ecc. $2.4dtF_u$/$2.4dtF_u$	0.77	0.89	0.94	0.96

5.5.3 Results of Finite Element Analysis of Models W1 to W4

This section presents analysis results from the finite element models W1 to W4, as detailed in Section 5.5.1. The models were subjected to top lateral displacements to induce shear deformations, similar to the procedure described in Section 5.4.

A monotonic lateral displacement of 2.0 in. was applied to the top of Models W1 to W4. Figures 5-192 to 5-195 show the load-deformation curves for these models, with markings of the limit states discussed in Section 5.5.2. The figures also display the analysis results for Models W1 to W4, which were subjected to a monotonic lateral displacement of 2.0 in. These figures reveal the behavior of total shear force (V_T), steel shear force (V_s), and concrete shear force (V_c) under increasing shear deformations. The load-deformation curves for each model are as follows:

The figures also display the analysis results for Models W1 to W4, which were subjected to a monotonic lateral displacement of 2.0 in. These figures reveal the behavior of the total shear force (V_T), steel shear force (Vs), and concrete shear force (Vc) under increasing shear deformations.

- **Model W1**: The total shear force (V_T) reaches a peak value of 247.5 kips at a deformation of 1.2 in. The maximum steel shear force (V_s) is 198.7 kips at 1.9 in. of deformation, while the maximum concrete shear force (V_c) is 67.4 kips at 0.26 in. of deformation. The concrete shear strength degrades progressively with increased deformation, with the "V_c *ratio*" (the ratio of V_c to V_T) decreasing from 33% at 0.2 in. to 17% at 2.0 in.
- **Model W2**: The total shear force (V_T) reaches a peak value of 541.0 kips at a deformation of 0.73 in. The maximum steel shear force (V_s) is 438.2 kips at 1.88 in. of deformation, while the maximum concrete shear force (V_c) is 157.0 kips at 0.24 in. of deformation. The concrete shear strength

degrades progressively with increased deformation, with the "V_c *ratio*" (the ratio of V_c to V_T) decreasing from 35% at 0.2 in. to 15% at 2.0 in.

- **Model W3**: The total shear force (V_T) reaches a peak value of 826.6 kips at a deformation of 0.5 in. The maximum steel shear force (V_s) is 667.9 kips at 1.9 in. of deformation, while the maximum concrete shear force (V_c) is 254.7 kips at 0.2 in. of deformation. The concrete shear strength degrades progressively with increased deformation, with the "V_c *ratio*" (the ratio of V_c to V_T) decreasing from 36% at 0.2 in. to 16% at 2.0 in.
- **Model W4**: The total shear force (V_T) reaches a peak value of 1117 kips at a deformation of 0.58 in. The maximum steel shear force (V_s) is 911.7 kips at 1.96 in. of deformation, while the maximum concrete shear force (V_c) is 350.8 kips at 0.22 in. of deformation. The concrete shear strength degrades progressively with increased deformation, with the "V_c *ratio*" (the ratio of V_c to V_T) decreasing from 37% at 0.2 in. to 15% at 2.0 in.

In addition to the shear strength mentioned above, Figure 5-196 shows the shear strength per unit length of walls, including total shear strength, steel shear strength, and concrete shear strength, for Models W1 to W4. As shown in the figure, the shear strengths per unit length increase for the wider walls as the effect of eccentricity diminishes and converge in Models W3 and W4 for cases where the eccentricity ratio is close to 1. This behavior is observed for the total strength and the steel shear strength per unit length, but not as markedly for the concrete shear strength per unit length.

Table 5-16 lists the total shear strengths (V_T) in Models W1 to W4, comparing with the bearing strength of $2.4dtF_u$, gross section yielding strength ($0.6A_gF_y$), and composite shear strength calculated using AISC 360-22 equation I4-2. The maximum total shear strength of Model W1 reached and exceeded the bearing strength of $2.4dtF_u$ and the net section yielding strength ($0.6A_eF_y$). For Models W2 to W4, their maximum

total shear strength reached and exceeded the gross section yielding strength ($0.6A_gF_y$). However, none of the splice total shear strengths achieved the composite shear strength of a solid wall expressed by equation I4-2 in AISC 360. To better understand the contribution of steel and concrete when the composite wall is governed by bearing strength under shear force, the following section further explores how the shear strengths of steel and concrete develop separately in Models W1 to W4.

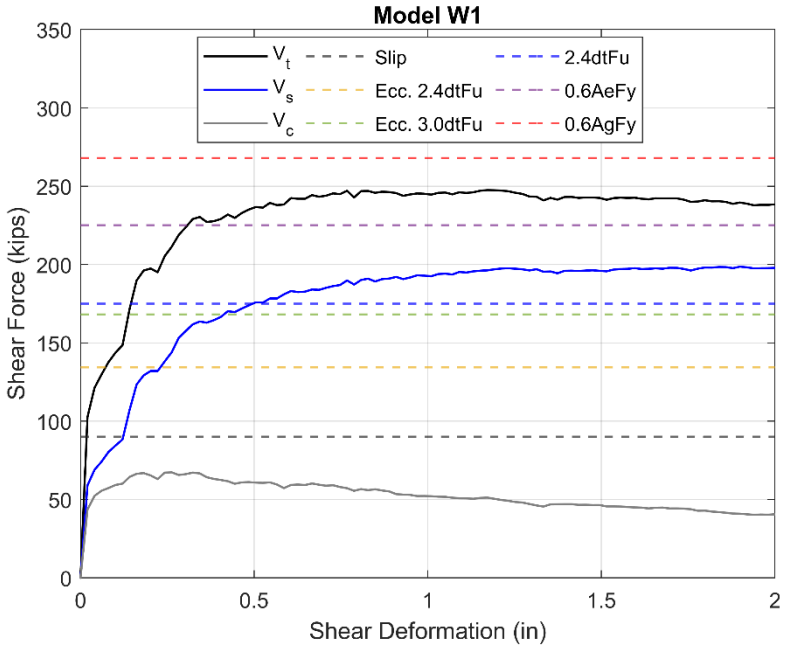


Figure 5-192. Finite Element Results of Load-Deformation Curve of Model W1

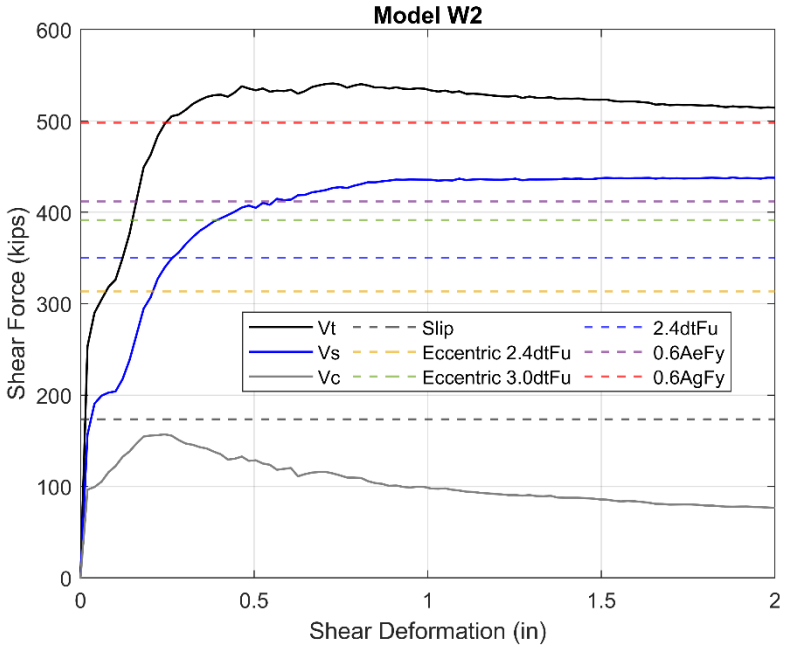


Figure 5-193. Finite Element Results of Load-Deformation Curve of Model W2

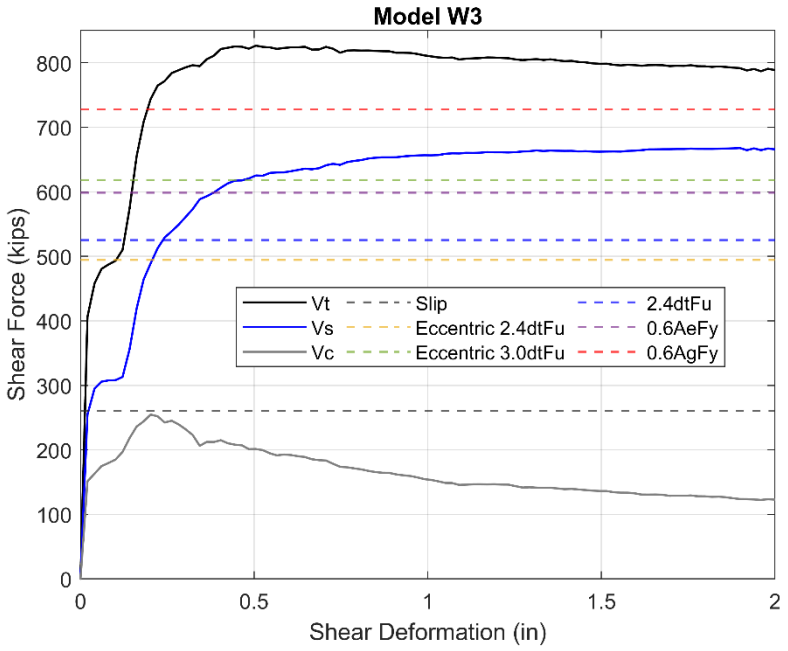


Figure 5-194. Finite Element Results of Load-Deformation Curve of Model W3

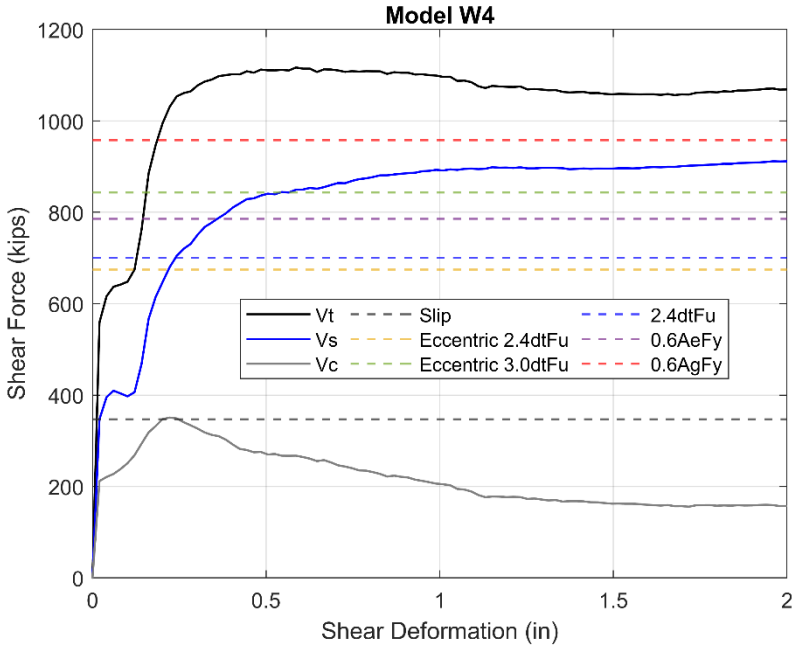


Figure 5-195. Finite Element Results of Load-Deformation Curve of Model W4

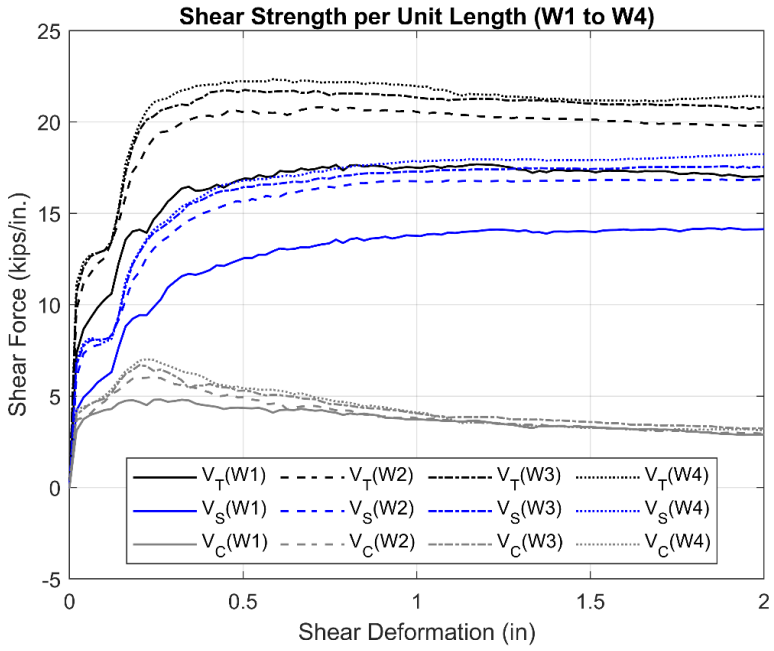


Figure 5-196. Unit Length Shear Strength versus Shear Deformation (Models W1 to W4)

Table 5-16. Maximum Total Shear Strength (V_T) in Models W1 to W4

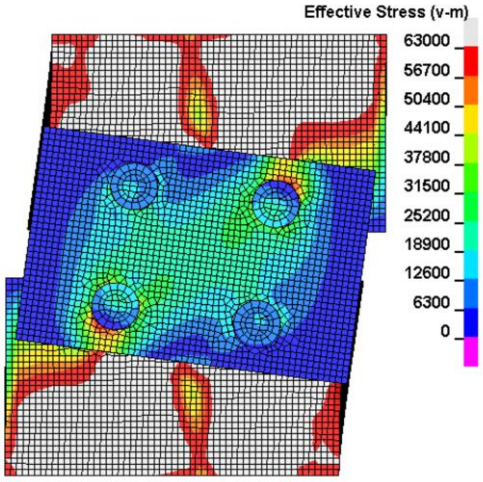
Model	B (in)	B/T	$V_{T,max}$ (kips)	$2.4dtF_u$ (kips)	$0.6A_eF_y$ (kips)	$0.6A_gF_y$ (kips)	$V_{composite}$ (kips)
W1	14	1.17	247.52	175.06	225.11	268.21	406.17
W2	26	2.17	540.98	350.11	411.90	498.11	754.31
W3	38	3.17	826.57	525.17	598.69	728.00	1102.46
W4	50	4.17	1116.79	700.22	785.48	957.90	1450.60

Table 5-17 compares the maximum steel shear strength ($V_{S,max}$) in Models W1 to W4, along with bearing strength of $2.4dtF_u$ and $3.0dtF_u$. All steel shear strengths reached and exceeded the bearing strength considering eccentricity (*Ecc.* $2.4dtF_u$ and *Ecc.* $3.0dtF_u$), as well as the bearing strength of $2.4dtF_u$ neglecting eccentricity. Additionally, the shear strengths in Models W2 to W4 reached and exceeded the bearing strength of $3.0dtF_u$ neglecting eccentricity. As expected, as the wall width increases, the impact of eccentricity diminishes, leading to an increase in steel shear strength.

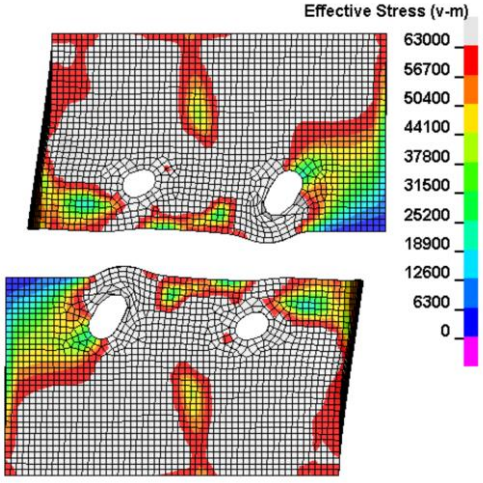
Figures 5-197 (a) to 5-200 (a) show the distribution of von Mises stresses in the steel splice plates and bolts, while Figures 5-197 (b) to 5-200 (b) show the von Mises stresses in the faceplates (after removing the splice plates and bolts). Yielding of the steel in the faceplates, as indicated by von Mises stresses exceeding 63,000 psi in the figures, initiated from the bolt holes and propagated over a significant area. When the applied displacement at the top reached 2.0 in., rotations of approximately 7.7°, 2.32°, 1.32°, and 0.95° were observed in the splice plates of Models W1, W2, W3, and W4, respectively. Additionally, by measuring displacement of the bolts in x and z directions (Δ_x and Δ_z), the angle θ of bolt hole deformation can be calculated as $\theta = tan^{-1}(\Delta_z/\Delta_x)$. Calculated values of θ for the bolt holes of the middle bolts on the bottom row indicated that these holes elongated at angles of 52°, 22°, 15°, and 12° in Models W1, W2, W3, and W4, respectively. These observations indicate that as the wall width increases, both the rotation of splice plates and the angle of bolt hole elongation decrease.

Table 5-17. Maximum Steel Shear Strength V.S. Bearing Strength in Models W1 to W4

Model	B (in)	B/T	$V_{S,max}$ (kips)	$2.4dtF_u$ (kips)	$3.0dtF_u$ (kips)
W1	14	1.17	198.66	175.06	218.82
W2	26	2.17	438.16	350.11	437.64
W3	38	3.17	667.90	525.17	656.46
W4	50	4.17	911.67	700.22	875.28

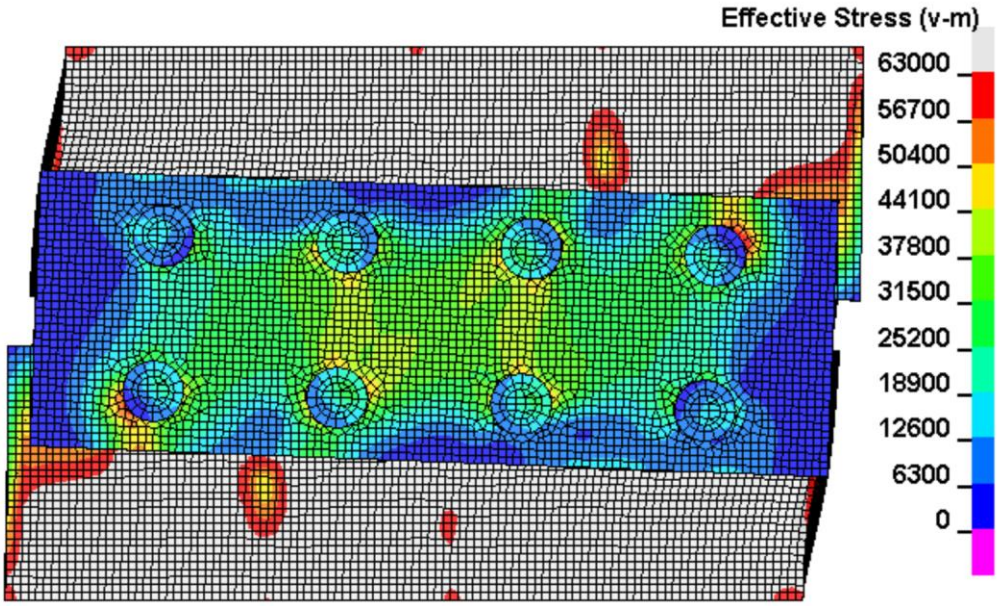


(a) All Steel

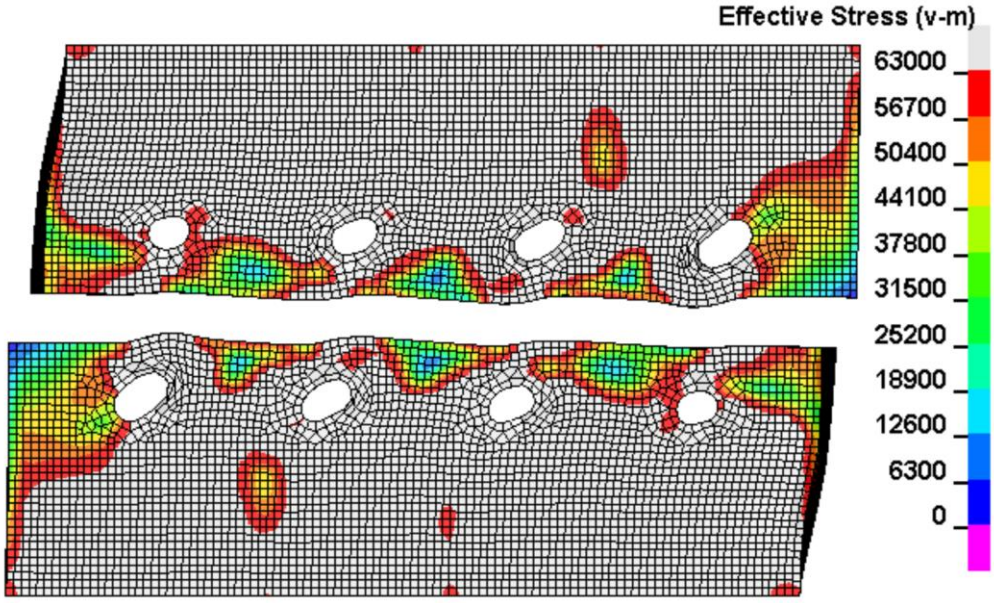


(b) Faceplate Only

Figure 5-197. von Mises Stress of Model W1 (Lateral Disp. = 2.0 in.)

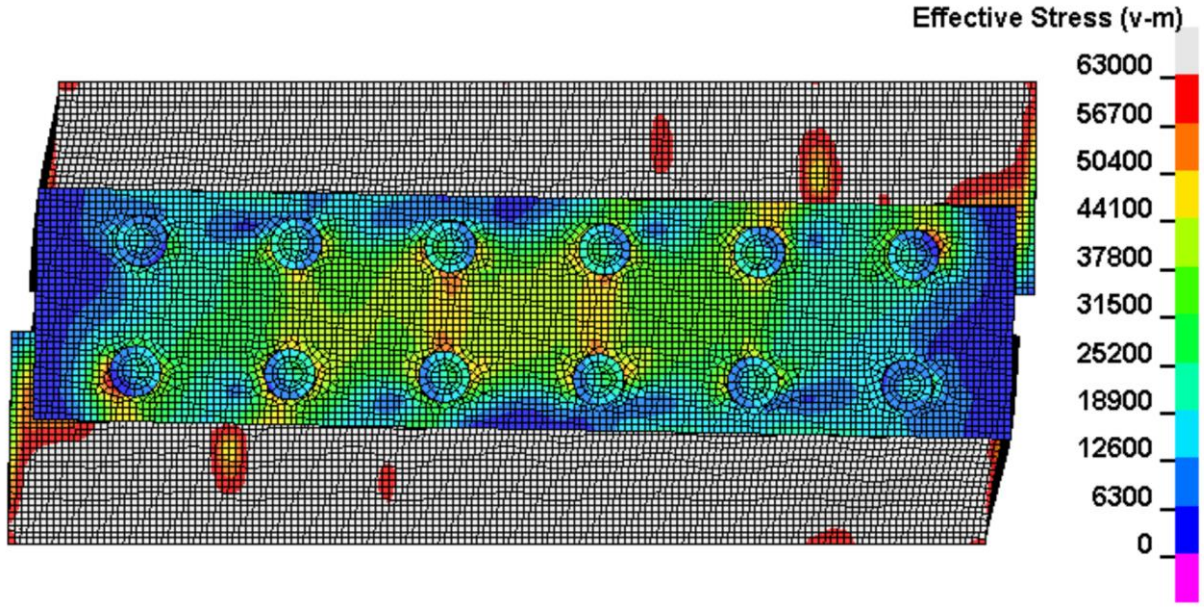


(a) All Steel

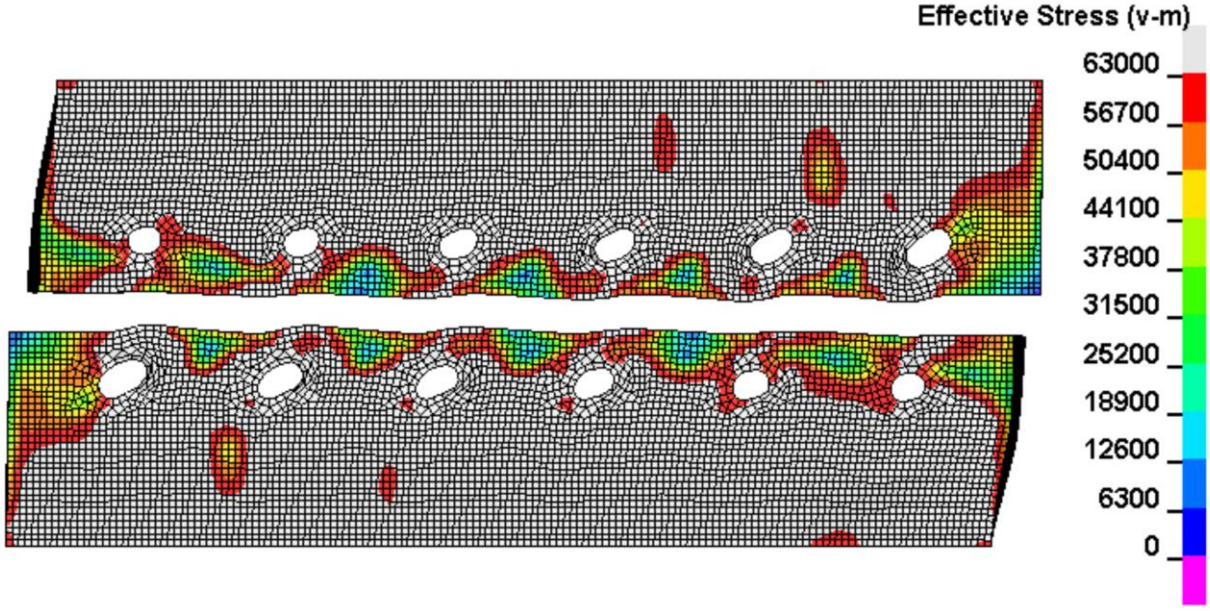


(b) Faceplate Only

Figure 5-198. von Mises Stress of Model W2 (Lateral Disp. = 2.0 in.)

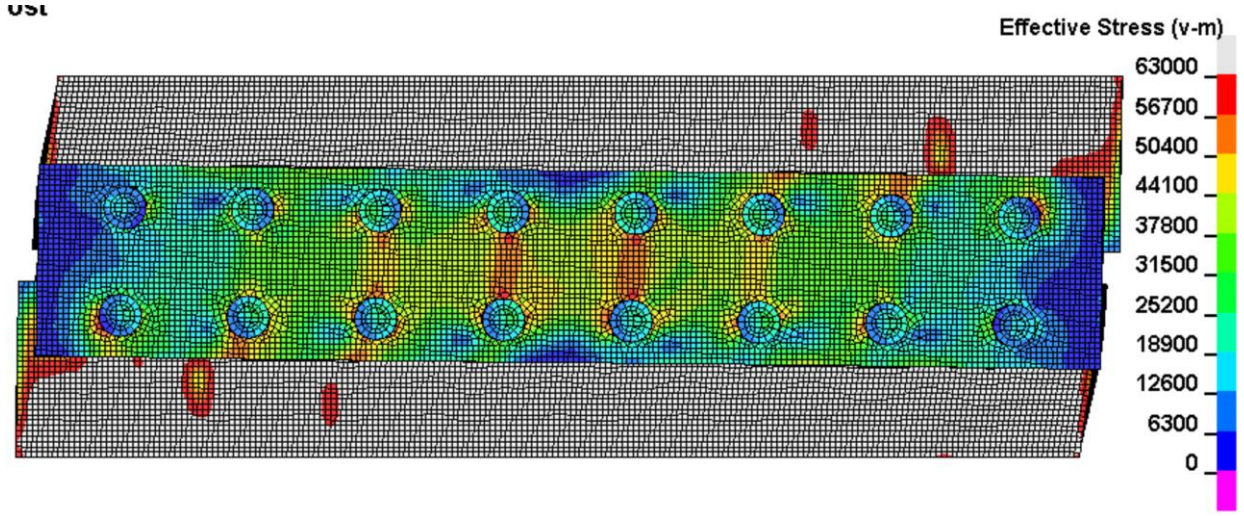


(a) All Steel

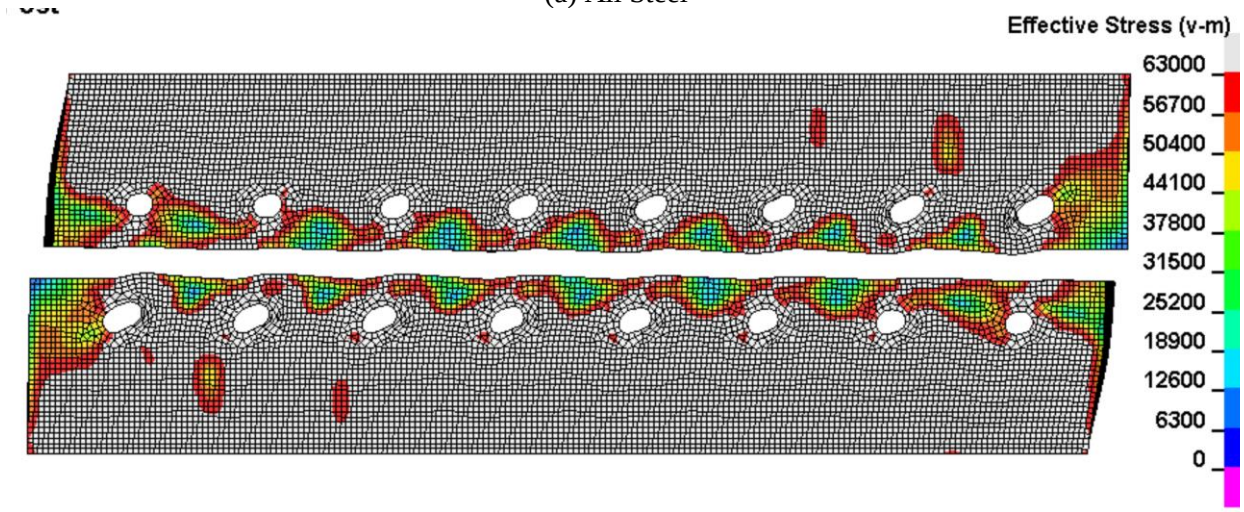


(b) Faceplate Only

Figure 5-199. von Mises Stress of Model W3 (Lateral Disp. = 2.0 in.)



(a) All Steel



(b) Faceplate Only

Figure 5-200. von Mises Stress of Model W4 (Lateral Disp. = 2.0 in.)

The concrete shear strength specified for special structural walls in ACI 318-19 equation 18.10.4.1 was adopted here to compare with the concrete shear strength obtained in the shear models as shown below:

$$V_c = \alpha_c \lambda \sqrt{f_c'} A_{cv} \quad \text{Equation 5-3}$$

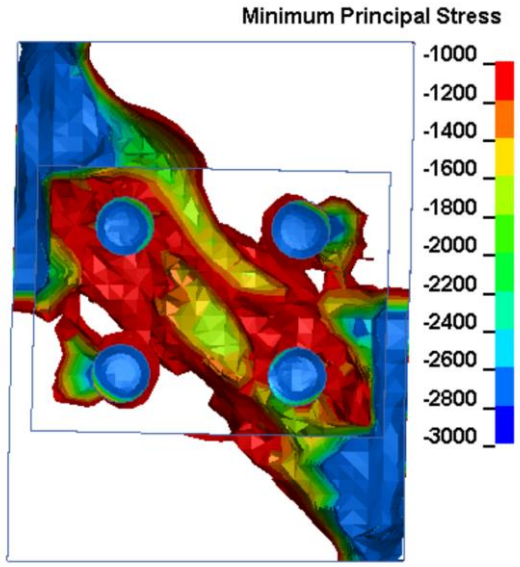
where α_c=3 for H/B ≤1.5 and α_c=2 for H/B ≥2, λ=0.75 for light-weight concrete, and $\lambda = 1$ for normal-weight concrete, and A_{cv} is the gross area of the concrete section bounded by web thickness and length of the section in the direction of shear force.

Table 5-18 summarizes the maximum concrete shear strengths ($V_{C,max}$) and residual concrete shear strengths ($V_{C,residual}$) in Models W1 to W4. The maximum concrete shear strengths occurred at deformations ranging from 0.2 to 0.26 in., while the residual concrete shear strengths were obtained at a deformation of 2.0 in. It was observed that the ratio of concrete shear strength (V_C) to total shear strength (V_T) ranges from 33% to 37% at a deformation of 0.2 in., whereas at a deformation of 2.0 inches, the ratios drop to 15% to 17%. Although the concrete shear strength decreases with increasing shear deformation, it was observed that the residual concrete shear strengths ($V_{C,residual}$) are still higher than the shear strengths obtained using the ACI equation 18.10.4.1.

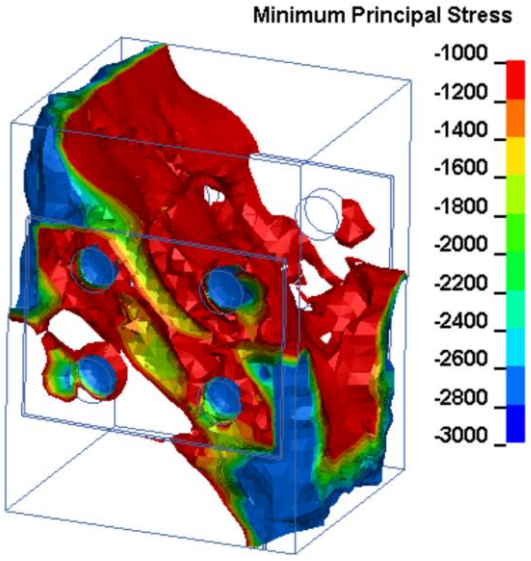
Figures 5-201 to 5-204 show the minimum principal stresses (i.e., maximum compression stresses) in Models W1 to W4 at a deformation of 0.2 in., with stress contours plotted within a range of -1000 to -3000 psi. These figures illustrate the development of the compression strut in concrete as the concrete shear strength approaches its peak. As previously mentioned, the concrete shear strength decreases as shear deformation increases. Figure 5-205 illustrates the minimum principal stresses in Model W4 at a deformation of 2.0 in., providing a comparison with Figure 5-204 to demonstrate the reduction of compression strut forces as shear deformation increases.

Table 5-18. Concrete Shear Strength V.S. ACI Shear Strength Equation in Models W1 to W4

Model	B (in)	B/D	$V_{C,max}$ (kips)	$V_{C,residual}$ (kips)	$V_{C,ACI}$ (kips)
W1	14	1.17	67.39	40.62	27.61
W2	26	2.17	157.03	76.69	51.27
W3	38	3.17	254.69	122.85	74.93
W4	50	4.17	350.77	157.42	98.59

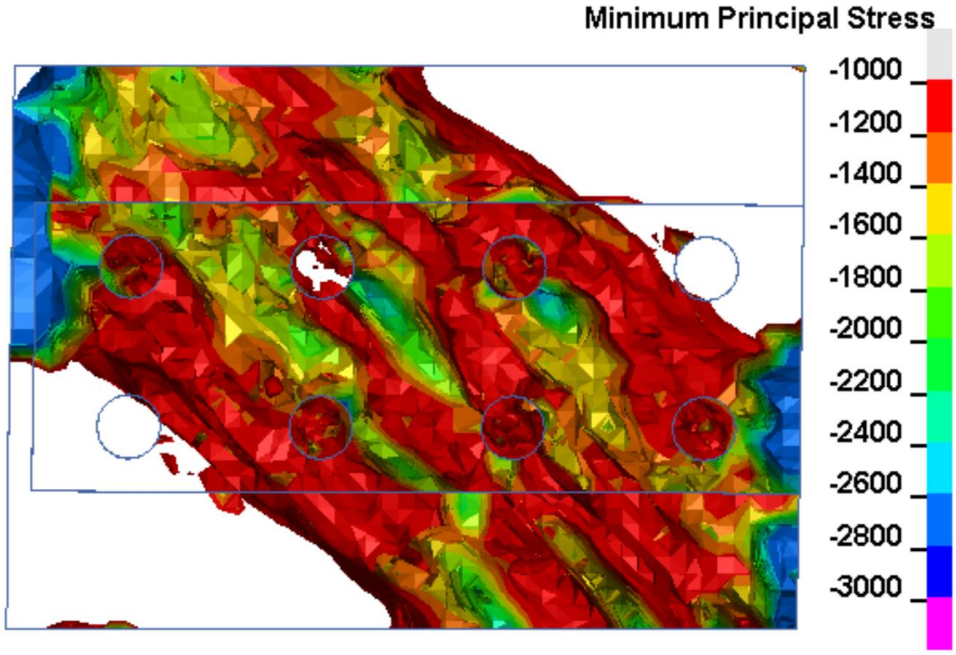


(a) Front View

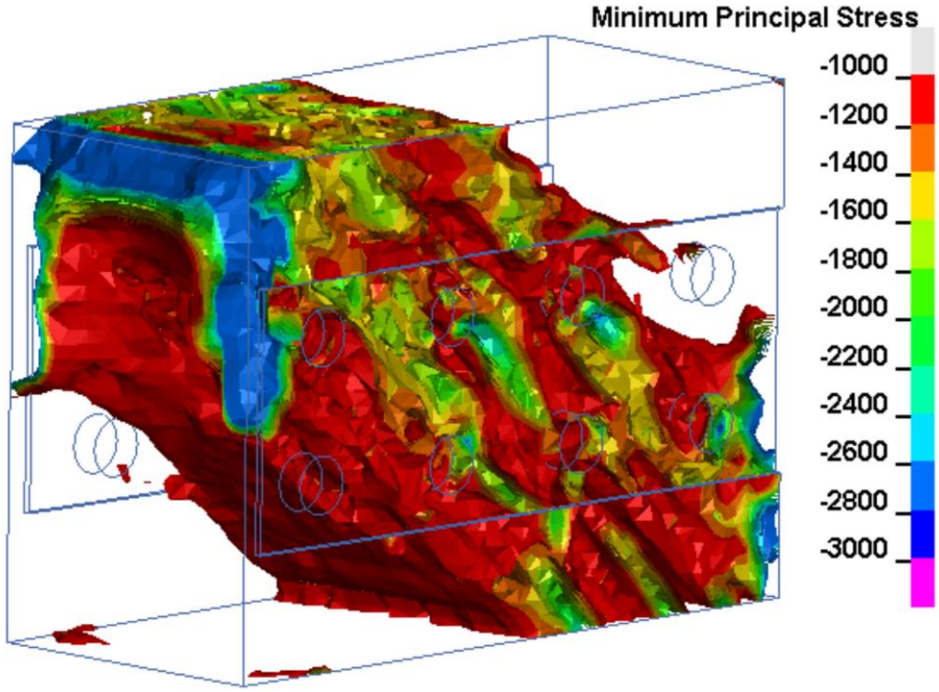


(b) 3D View

Figure 5-201. Compression Strut of Model W1 (Lateral Disp. = 0.2 in.)

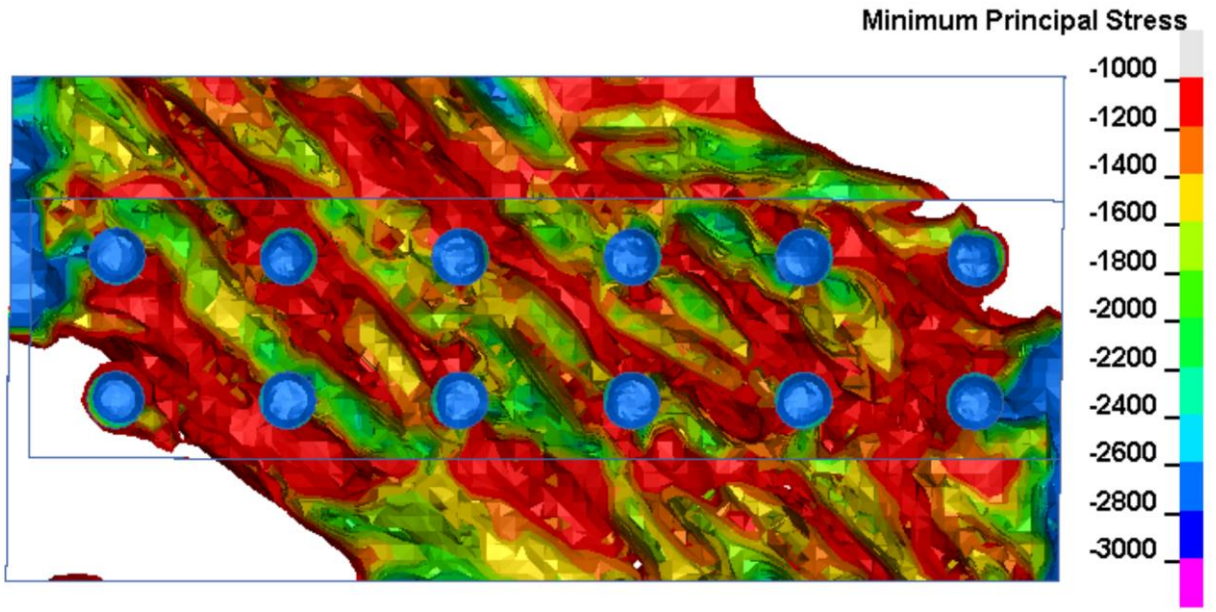


(a) Front View

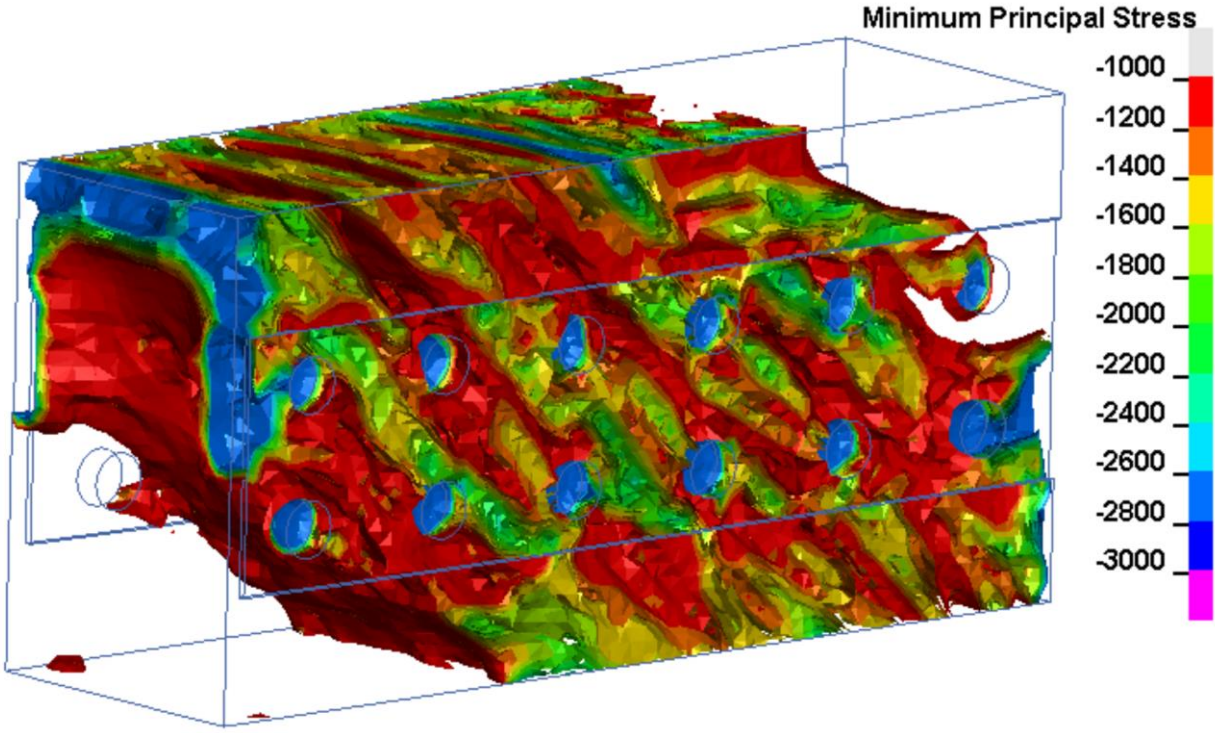


(b) 3D View

Figure 5-202. Compression Strut of Model W2 (Lateral Disp. = 0.2 in.)

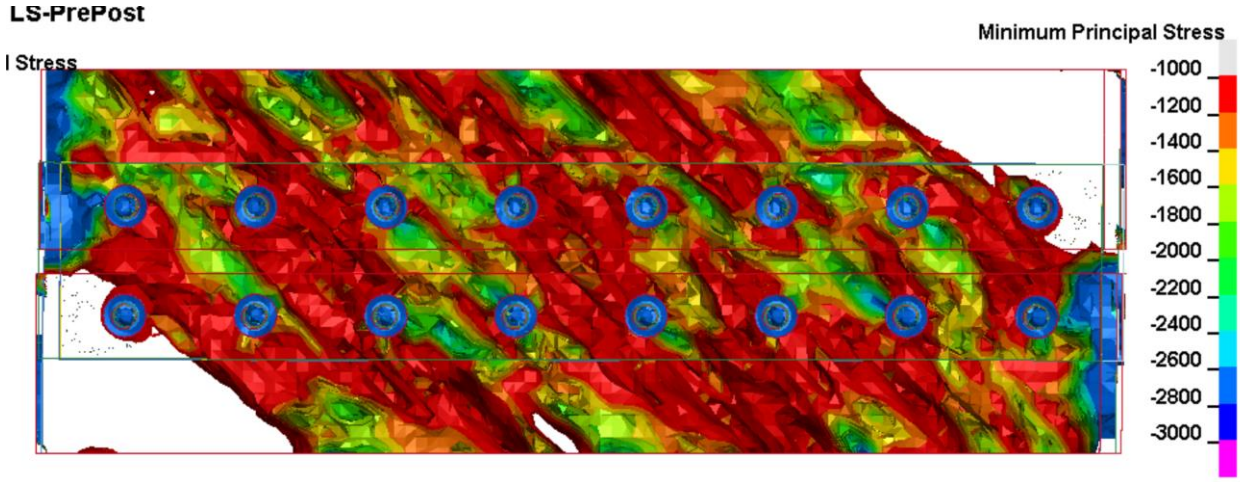


(a) Front View

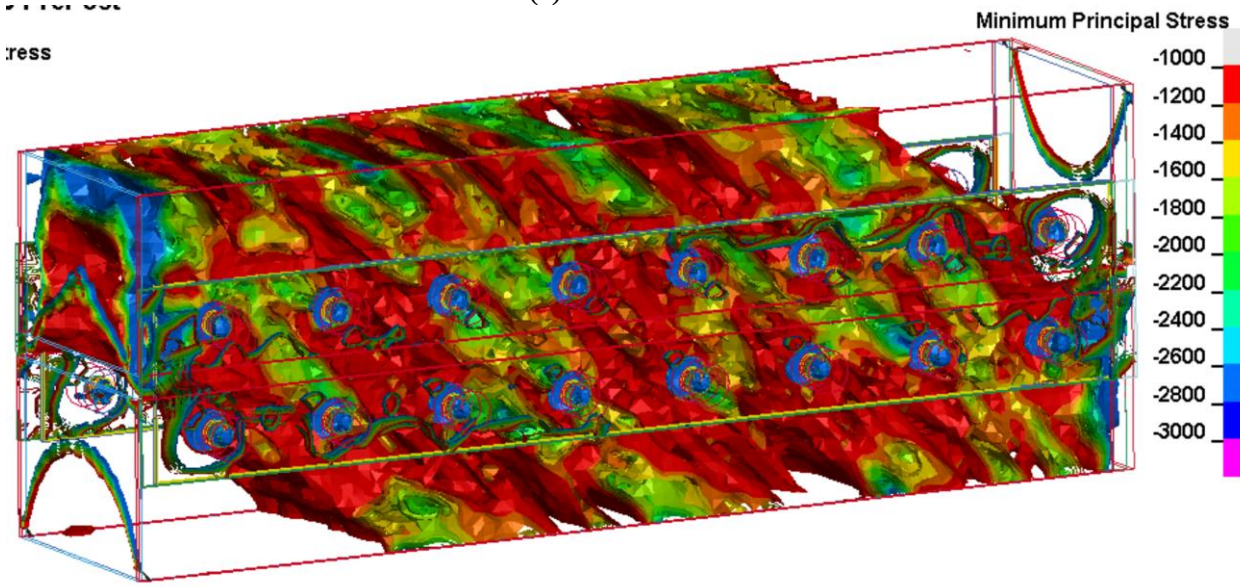


(b) 3D View

Figure 5-203. Compression Strut of Model W3 (Lateral Disp. = 0.2 in.)

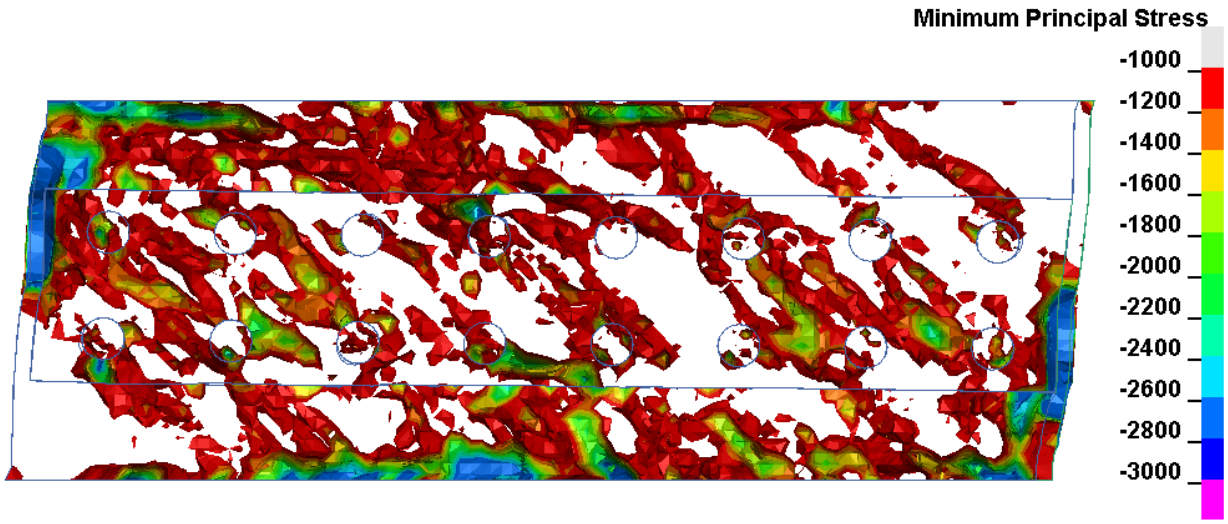


(a) Front View

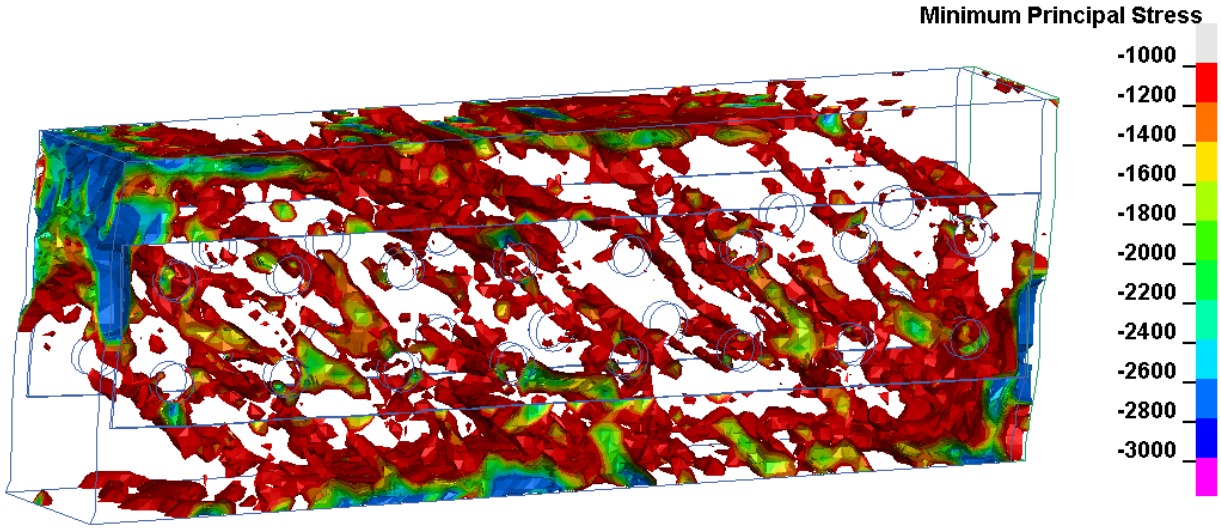


(b) 3D View

Figure 5-204. Compression Strut of Model W4 (Lateral Disp. = 0.2 in.)



(a) Front View



(b) 3D View

Figure 5-205. Compression Strut of Model W4 (Lateral Disp. = 2.0 in.)

The above analyses for Models W1 to W4 encompass the shear strength of the entire model, including faceplates and cap plates at the edges. A further analysis was conducted based on Model W4, focusing solely on the center core of Model W4 to eliminate the edge effects caused by the cap plates. This condition was labeled as "Model W4_Core," representing the wall scenario without the influence of edge cap plates. Figure 5-206 illustrates the comparison between W4 and W4_Core in LS-DYNA, while Figure 5-207 shows the load-deformation curve of W4_Core obtained from finite element analysis. The figure also marks the bearing strength of $2.4dtF_u$ and the ACI concrete shear strength mentioned above. Table 5-19 summarizes the shear strength values of the total, steel, and concrete components in Model W4_Core, along with the corresponding shear strength calculated using the bearing strength of $2.4dtF_u$ and $3.0dtF_u$, and the ACI concrete shear strength equations. In addition, Table 5-20 shows the shear strength per unit length derived from Table 5-19. Note that strength per unit length is slightly higher for Model W4_Core. The results of Model W4_Core indicate that, for a wall case without edge effect, the steel shear strength V_s can achieve the bearing strength of $3.0dtF_u$, and the concrete shear strength is greater than the value calculated by the ACI equation. This indicates that Equation 5-3 above could be conservatively used if one wishes to add the contribution of concrete to the calculated shear strength of bolted splices. Note that while peak concrete strength was roughly three times greater than the value provided by that equation, it remains that the contribution of concrete to total shear strength of the bolted splice remains significantly less than that of the steel. Therefore, efforts to develop an improved equation for the concrete contribution were not pursued here, particularly as it would have required extensive additional studies considering different wall geometries and steel-to-concrete ratios.

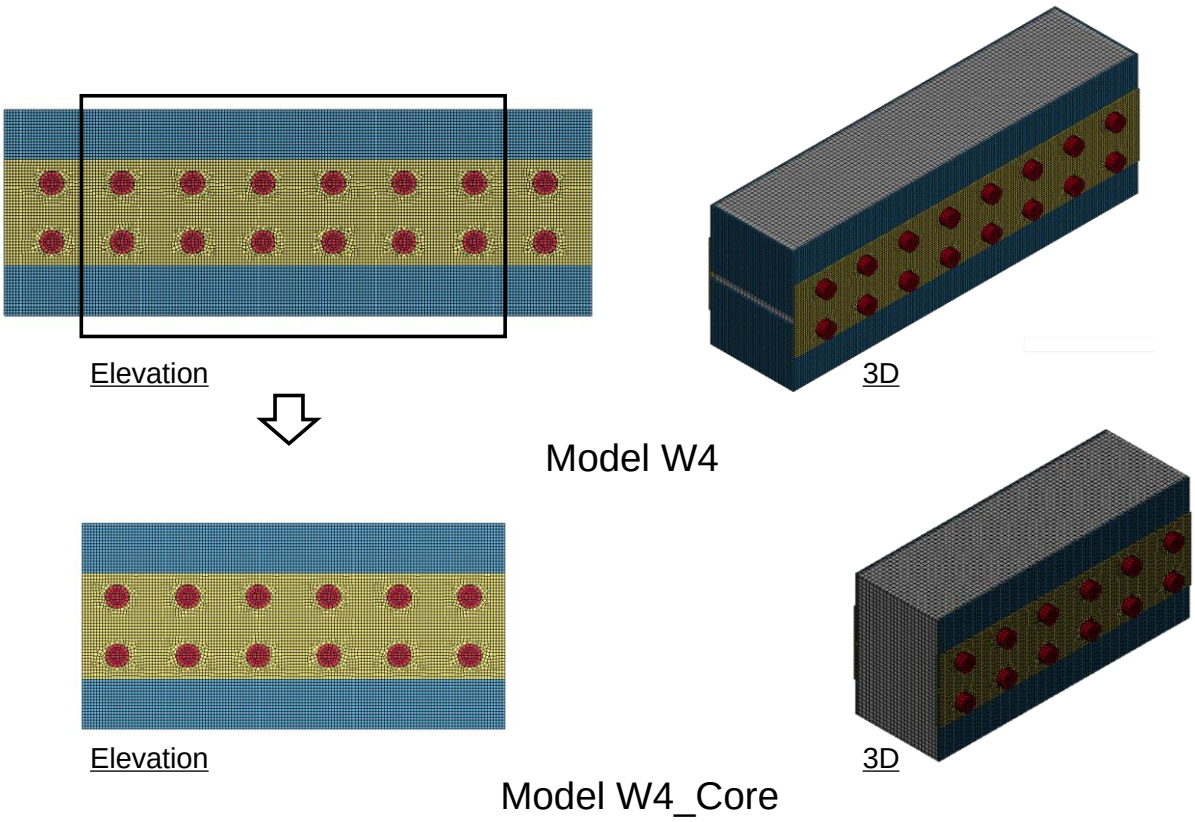


Figure 5-206. Finite Element Model of Specimens W4 and W4_Core

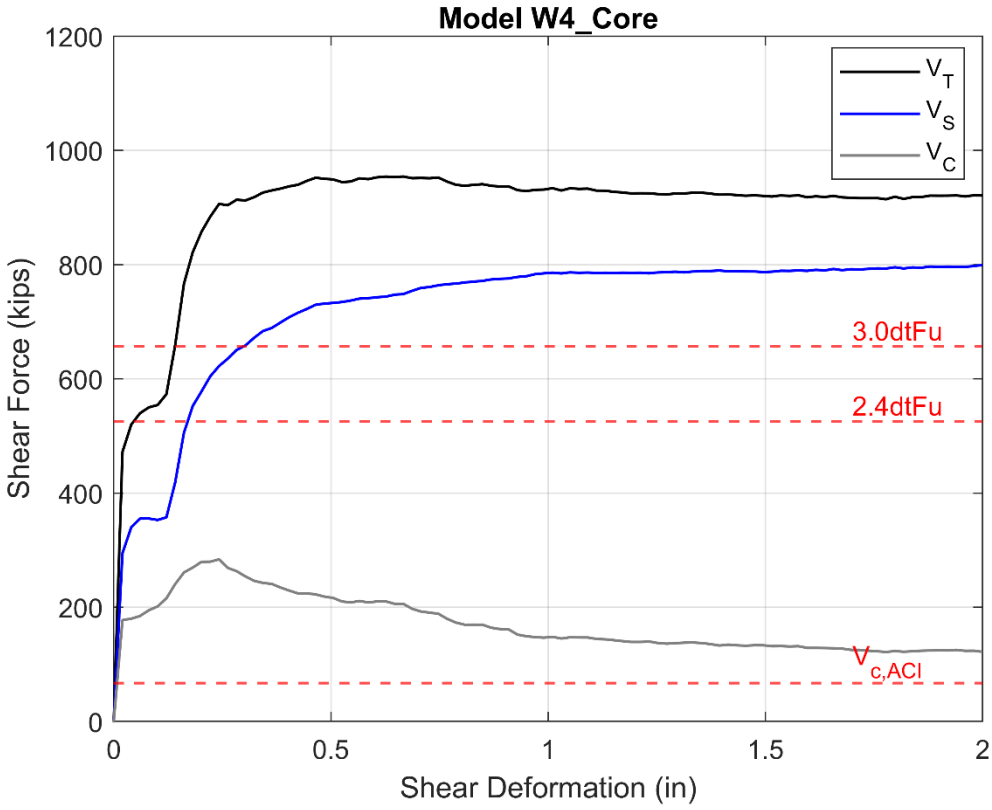


Figure 5-207. Finite Element Results of Load-Deformation Curve of Model W4_Core

Table 5-19. Shear Strength Comparison between Models W4 and W4_Core

Model	$V_{T,max}$ (kips)	$V_{S,max}$ (kips)	$V_{C,max}$ (kips)	$V_{C,residual}$ (kips)	$V_{C,ACI}$ (kips)	$V_{2.4dtFu}$ (kips)	$V_{3.0dtFu}$ (kips)
W4	1116.79	911.67	350.77	157.42	98.59	700.22	875.28
W4_Core	954.08	799.01	283.81	121.96	67.04	525.17	656.46

Table 5-20. Shear Strength per Unit Length Comparison between Models W4 and W4_Core

Model	$V_{T,max}$ (k/in)	$V_{S,max}$ (k/in)	$V_{C,max}$ (k/in)	$V_{C,residual}$ (k/in)	$V_{C,ACI}$ (k/in)	$V_{2.4dtFu}$ (k/in)	$V_{3.0dtFu}$ (k/in)
W4	22.34	18.23	7.02	3.15	1.97	14.00	17.51
W4_Core	28.06	23.50	8.35	3.59	1.97	15.45	19.31

The analysis results of shear models W1 to W4 and W4_Core summarize the shear strength of C-PSW/CF with bolted connection where the design limit state is governed by bearing strength, with varying wall widths to investigate the impact of wall width and eccentricity of bolt group. It can be concluded that for walls with higher eccentricity ratios (Models W2 to W4), where the eccentricity of bolt group is less significant, the contribution of steel, V_s, to the total shear strength can reach and exceed the bearing strength of $3.0dtF_u$ calculated parallel to the splice direction. However, for V_s to reach $3.0dtF_u$, it requires the bolt holes to develop large deformations. Controlling the bearing strength to $2.4dtF_u$ allows for the shear deformation to be kept below 0.2 in. (refer to Figure 5-207), helping to maintain the serviceability of the connection. Therefore, it is recommended to keep the design steel shear strength at $2.4dtF_u$. In addition, the contribution of concrete, V_c, to the total shear strength can reach and exceed the shear strength value given by ACI equation 18.10.4.1 in all shear models introduced previously. Consequently, when bearing strength is the governing limit state for steel, the nominal shear strength V_n of C-PSW/CF with bolted connection can be conservatively obtained combining the shear strength of steel and concrete, as expressed below:

$$V_n = V_s + V_c = 2.4dtF_u + \alpha_c\lambda\sqrt{f_c'}A_{cv} \qquad \text{Equation 5-4}$$

SECTION 6
IMPACT OF BOLT PRETENSION ON BEARING STRENGTH OF BOLTED CONNECTIONS

6.1 General

This chapter presents the results and findings from numerical analyses aimed at investigating the impact of bolt pretension on the bearing strength of bolted connections. The splice components considered as part of these analyses are steel bolted connections with single or double bolts, relying on the limit state of bolt bearing strength to resist tension forces. The objective of these analyses is to capture the physical behavior of such connections under progressively increasing tension loading up to peak bearing strength, with a particular focus on understanding the evolution of the contribution of friction forces present between the splice plates due to bolt pre-tension. The subsequent discussion will highlight key factors that contribute to the reduction of clamping and friction forces in bolted splice connections as the applied loading is increased. Similar comparisons will be made for C-PSW/CF connections with bolted splices, using the finite element models presented in Chapter 5.

6.2 Finite Element Models of Steel Bolted Connections

Analyses were first conducted on all-steel bolted connections. Figure 6-1 shows the geometries and finite element models of bolted splice connections relying on a single bolt or two bolts to transfer an applied tension loading, along with the reference coordinate system used for the analyses (X, Y, and Z directions). These models consist of faceplates, splice plates, and bolts (the term “faceplate” is used here by analogy with the splices in C-PSW/CF that will be addressed later). Table 6-1 outlines the geometries used in the finite element models considered. The table shows that the steel plate thickness “*t*” (including faceplates and splice plates) and width “*W”* remain constant across all models. "W_e" is the net width of the connection,

"n" denotes the number of bolts, "d" and "d_h" are the diameter of the bolt and the bolt hole, respectively, "e" is the edge distance from the bolt center to the plate edge, and "S" is the spacing between bolts. The term "BR" in the table refers to the bearing ratio, which can be expressed as shown in the following equation.

$$BR = \frac{A_e F_u}{ndtF_u} = \frac{W_e t F_u}{ndtF_u} = \frac{W_e}{nd} \qquad \text{Equation 6-1}$$

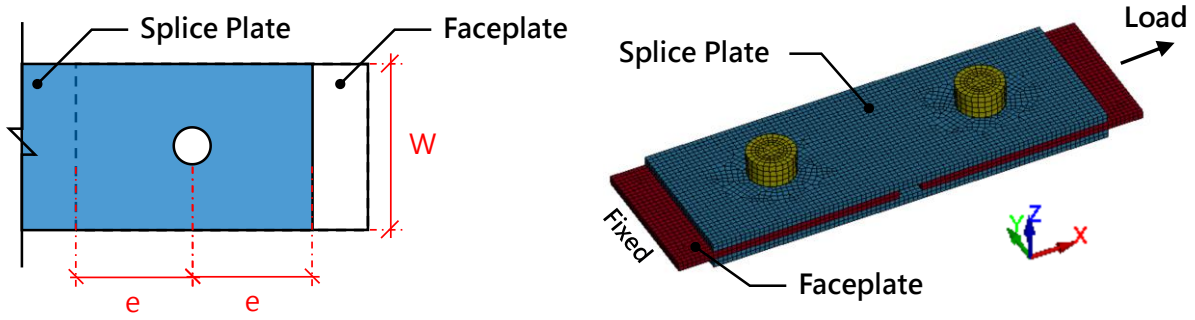
Equivalently, BR can be defined as the net section area, A_e, divided by the total bearing area, ndt. Consequently, for a steel plate to have a net section rupture strength greater than a bearing strength of $3.0dtF_u$, the BR value must be larger than 3.0.

The material properties for the steel elements in these bolted specimens are summarized in Table 6-2. In all the bolted connection models considered here, the edge distance to bolt center, e, and center-to-center bolt spacing, S, (as shown in Figure 6-1) have been chosen to prevent tear-out (as per 2-7) being the controlling limit state. Calculated strength for the limit states of bearing strength ($2.4dtF_u$ and $3.0dtF_u$ as per Equations 2-5 and 2-6), net section rupture strength (A_eF_u), gross section yielding strength (A_gF_y), and bolt shear strength, are summarized in Table 6-3 for the finite element models considered. Single-bolt (Model 1) and double-bolt (Models 2 to 4) connections were considered. Three different bolt diameters were used in double-bolt connections (Models 2 to 4) to assess the influence of bending and shear deformation of bolts on the development of bearing strength. Except for Model 2 where net section failure occurs shortly after the onset of bearing deformations, all bolted connection models are governed by the bearing limit state.

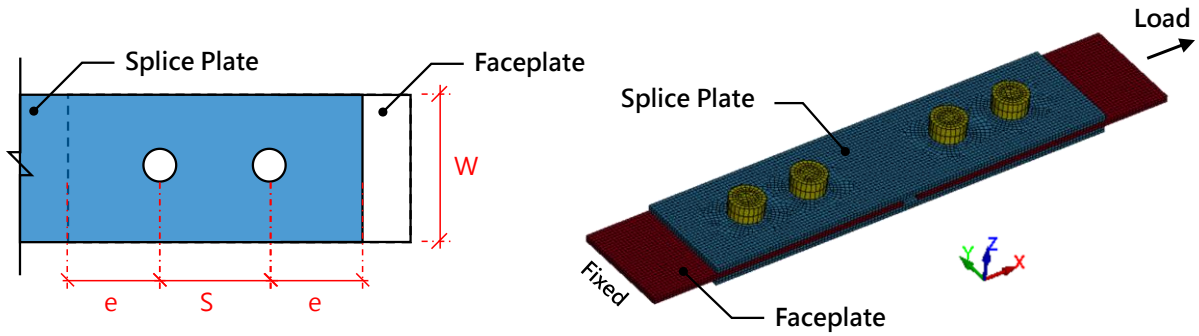
For all finite element models analyzed, fixed boundary conditions were applied at one end, and a progressively increasing axial deformation was imposed at the other end to induce axial loading on the

splices. Additionally, all bolts were preloaded to a stress equal to 105 ksi before any axial loading was applied to the splices.

Figure 6-2 schematically shows the typical contact interfaces in the finite element models. These interfaces include the contact surfaces between steel plates, between bolts and steel plates, and between nuts and splice plates. Consistent with Chapter 5, all these contact interfaces in the analysis were specified using the *automatic_surface_to_surface_mortar* contact model with a static interface friction coefficient set to 0.3.



(a) Geometries and Finite Element Model of Single-Bolt Connection



(b) Geometries and Finite Element Model of Double-Bolt Connection

Figure 6-1. Finite Element Model of: (a) Single, and; (b) Double-Bolt Connections

Table 6-1. Geometries of Finite Element Models

Model	t (in)	W (in)	W_e (in)	Rows	n	d_h (in)	d (in)	e (in)	S (in)	BR
1	0.375	6	4.875	1	1	1.125	1	4.00	-	4.875
2	0.375	6	4.875	2	2	1.125	1	4.00	4.00	2.438
3	0.375	6	5.188	2	2	0.8125	0.75	4.00	4.00	3.458
4	0.375	6	5.313	2	2	0.6875	0.625	4.00	4.00	4.250

Table 6-2. Material Properties for Steel Parts

Part	Es (ksi)	Possion's Ratio	Fy (ksi)	Et (ksi)	β
Face Plates	29000	0.3	55.0	108.8	0.0
Splice Plates	29000	0.3	55.0	108.8	0.0
Bolts	29000	0.3	120.0	221.2	0.0

Table 6-3. Design Limit States of Finite Element Models (strength for two bolts in Cases 2, 3, and 4)

Model	A_eF_u (kips)	A_gF_y (kips)	$2.4dtF_u$ (kips)	$3.0dtF_u$ (kips)	Bolt Shear Strength (kips)	Govering Limit State
1	127.97	123.75	63	78.75	131.95	Bearing
2	127.97	123.75	126	157.50	263.89	Gross Section Yielding
3	136.17	123.75	94.5	118.13	148.44	Bearing
4	139.45	123.75	78.75	98.44	103.08	Bearing

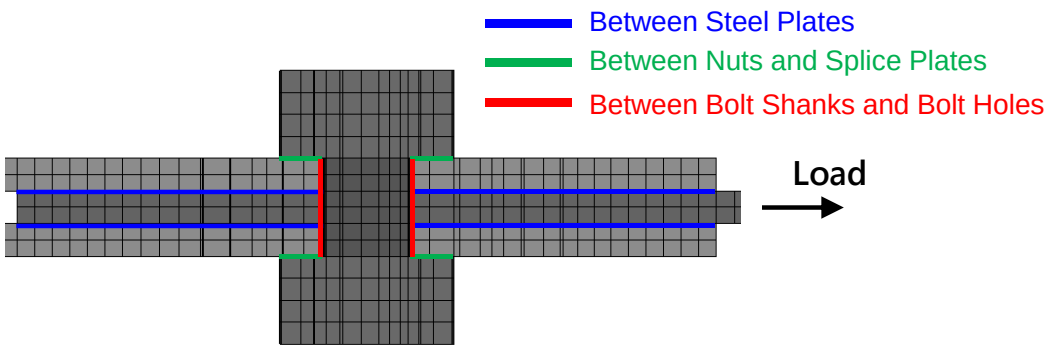


Figure 6-2. Typical Contact Interfaces in the Finite Element Model

6.3 Friction Forces in Steel Bolted Connections

6.3.1 Single-Bolt Connection (Model 1)

Figures 6-3 and 6-4 show the load-deformation curve obtained from the finite element analysis of Model 1 with and without applying bolt pretension. In these figures, deformation is from end-to-end of the specimen. The load-deformation curves compare the total axial force in the connection with the friction and bearing forces obtained from the contact interfaces. To evaluate the impact of the inelasticity of bolts on behavior, separate analyses were conducted, first with the material properties of the bolts modeled as elastic, and then using the inelastic bolt material properties listed in Table 6-2. Both results considering regular (i.e., inelastic) and elastic bolt material are shown in Figures 6-3 and 6-4.

For the bolted connection with bolt pretension (Figures 6-3), the preloaded stress is 105 ksi on 1 in.-diameter bolts, and the pretension force (T_b) is calculated as $(\pi/4) \times 1^2 \times 105 = 82.47$ kips. Therefore, the calculated slip resistance is $\mu T_b \times 2 = 0.3 \times 82.47 \times 2 = 49.48$ kips, and the value is close to the numerically obtained initial friction (51.6 kips) marked in Figures 6-3. After the connection slid, the bearing force started to develop. It can be observed that as the bearing force and deformations increased, the friction force decreased simultaneously. At a deformation of 2.0 in., the maximum axial forces for regular and elastic bolt models reached 104.3 kips and 108.9 kips, while the maximum bearing forces reached 88.72 kips and 80.52 kips, respectively. The residual friction forces for regular and elastic bolt models were 17.5 kips and 30.36 kips at 2.0-in. deformation, representing 34% and 59% of the initial friction force, respectively. By comparing the regular and elastic bolt material, there is an approximately 25% loss (59% - 34%) of friction force due to the partial yielding of bolts.

For the bolted connection without bolt pretension, as shown in Figure 6-4, sliding occurred immediately after applying the axial load. After sliding, the bearing and friction forces developed simultaneously, with

friction induced as a consequence of bearing. Similarly, the load-deformation curve shows the analysis results from both regular and elastic bolt models. The maximum axial forces in the regular and elastic bolt models reached 104.0 kips and 111.7 kips at 2.0-in. deformation, while the corresponding maximum bearing forces were 81.4 kips and 89.2 kips, respectively. The maximum friction forces reached 28.0 kips at 0.73-in. deformation and 37.6 kips at 1.03-in. deformation in the regular and elastic bolt models. The residual friction forces at 2.0-in. deformation were 16.2 kips and 32.2 kips in the regular and elastic bolt models, respectively, which are values nearly identical to the case with pre-tension.

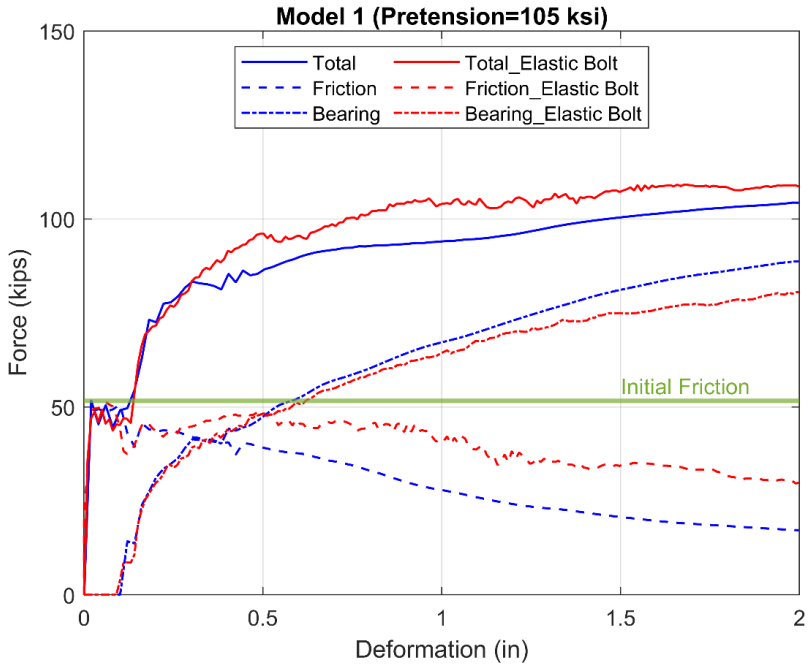


Figure 6-3. Load-Deformation Curve of Model 1 (With Pretension)

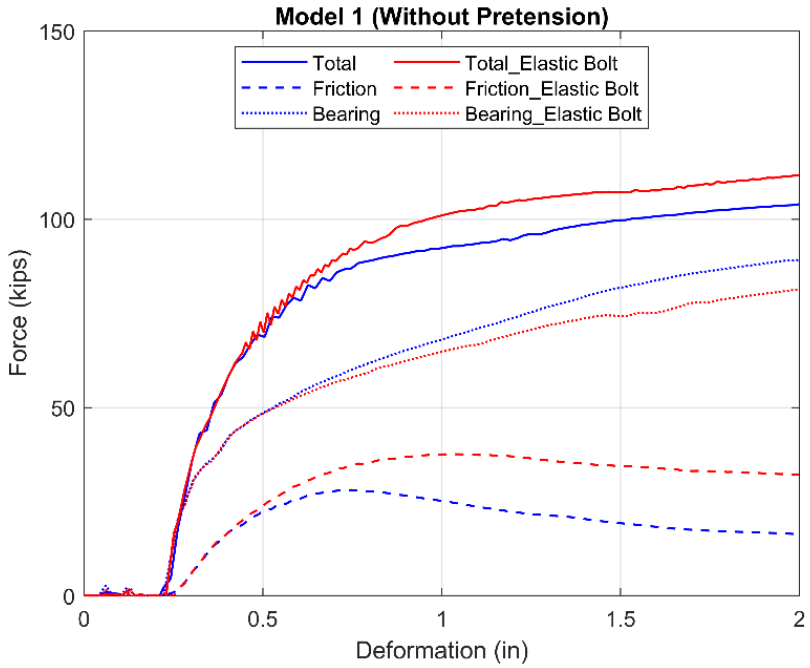


Figure 6-4. Load-Deformation Curve of Model 1 (Without Pretension)

Further analysis of the results was performed to identify the causes for this progressive reduction in friction forces (and for the development of friction in the cases without pretension). Figure 6-5 shows the von Mises stress distribution in the connection at different deformation stages, illustrating the growth of the yielding "field" in the faceplate as hole elongation increases. Figure 6-6 shows typical deformations of this single-bolt connection at 2.0-in. deformation. The observed deformations in both figures around the bolt include hole elongation, thickness changes in the plates, and bending of plates and bolts.

A free-body diagram of the connection system showing contact springs is presented in Figure 6-7. In this diagram, nuts, splice plates, and faceplates are interconnected by contact springs, forming a system of springs in series. Note there is no gap for the contact spring in the bolted connection studied here. Upon applying axial deformations to the connection, relative movements develop between the plates, and the

faceplate undergoes substantial hole elongation, as illustrated in Figure 6-8. As this occurs, the initial contact spring loses contact area and contact stiffness due to hole elongation and thinning of the faceplate in tension due to Poisson's effect (Figure 6-9). Figure 6-10 highlights the thickness change around bolt holes in the spliced plate at three different positions (P1, P2, and P3, respectively located at left, middle, and right end of the bolt hole), and Figure 6-11 shows the thickness change along with the axial deformation of the connection. These show an increase in the spliced plate thickness as it is compressed by the bolts in bearing. This increase in the thickness of the faceplate at the bolt bearing point increases the distance between the bolt head and the nut on that one side of each bolt, resulting in bolt bending and yielding (Figure 6-12).

These factors collectively influence the behavior of the contact springs on both sides of the bolt. A net reduction in contact forces results in decreased clamping and friction forces. These behaviors contribute significantly to the reduction in friction observed across all finite element models.

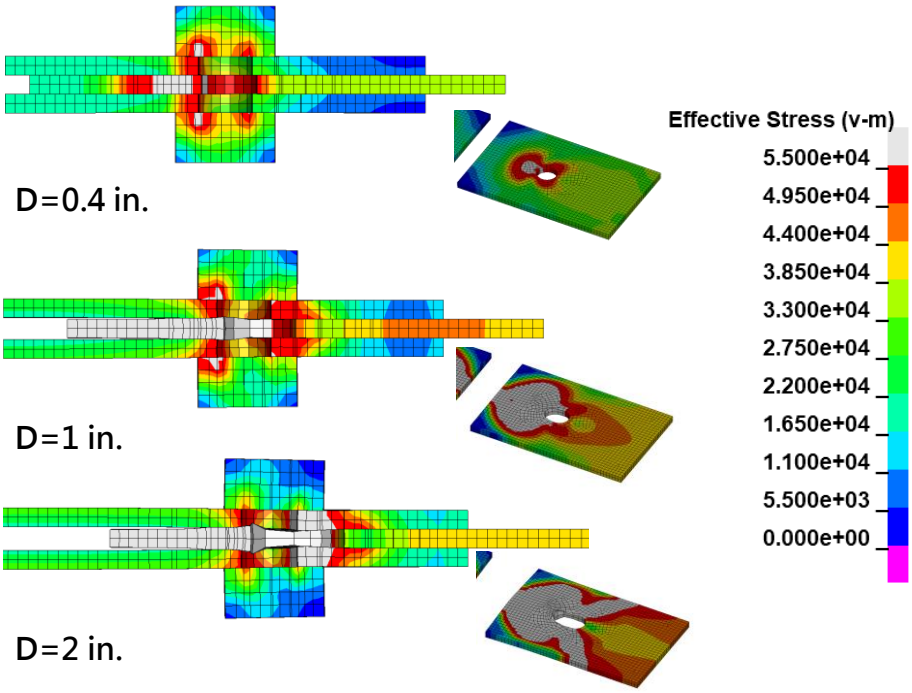


Figure 6-5. Von Mises Stresses of Model 1 at Different Deformations (Bolt Shank not Shown)

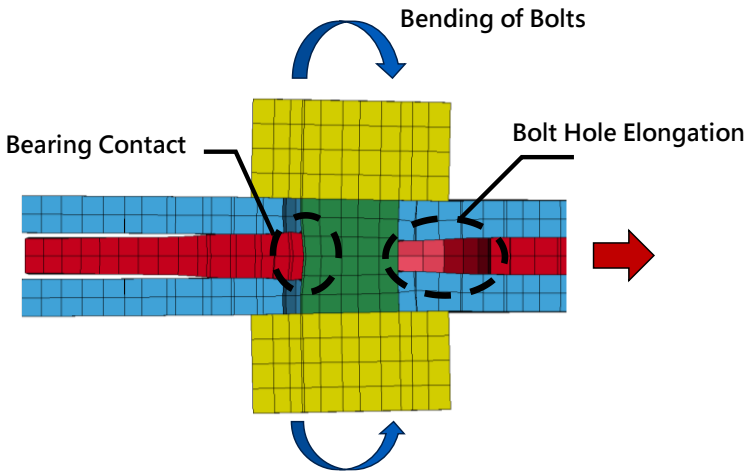


Figure 6-6. Deformation around Bolts of Model 1 (Deformation = 2 in.)

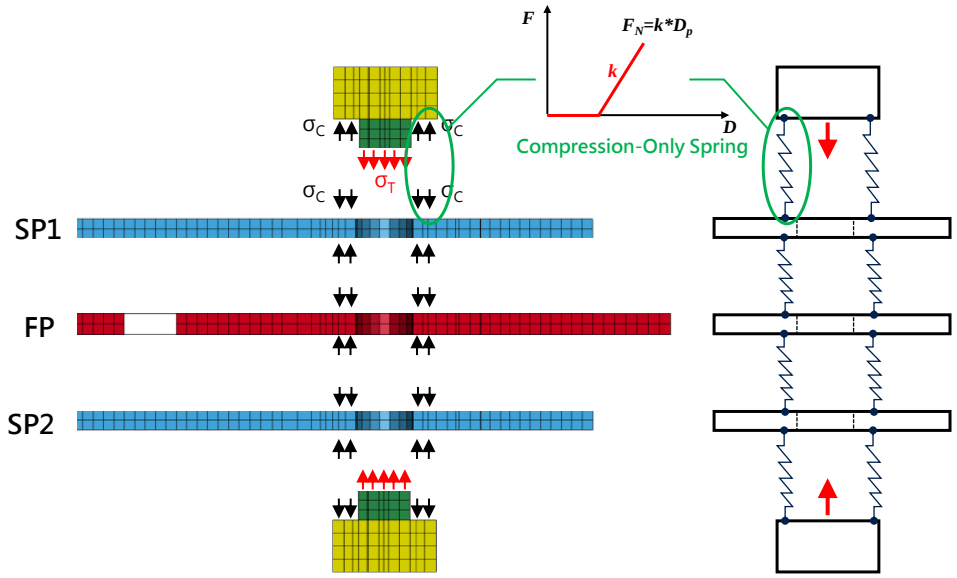


Figure 6-7. Free-Body Diagram of Spring System of Bolted Connections (Preload Stage)

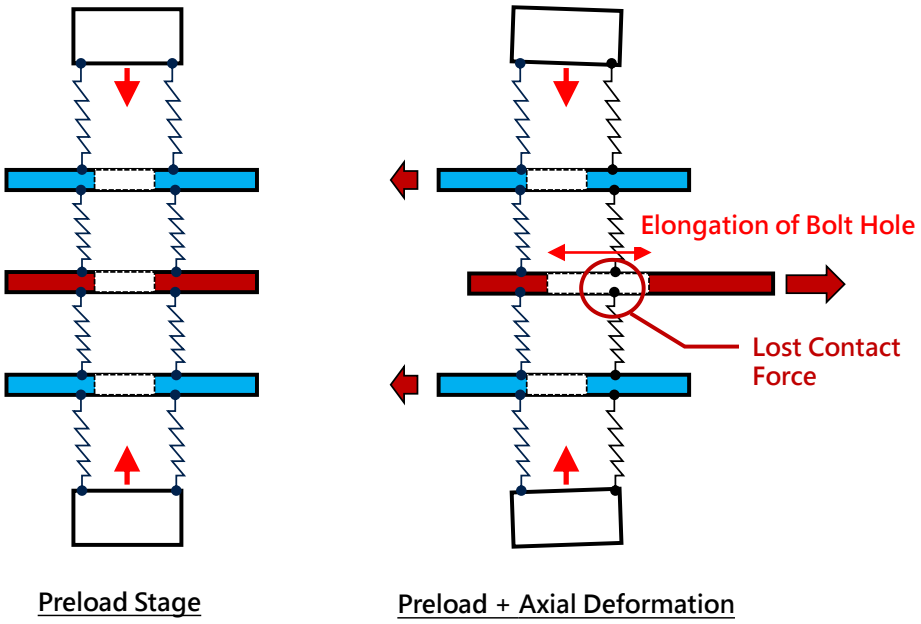


Figure 6-8. Free-Body Diagram of Spring System of Bolted Connections (Preload and Deformed Stages)

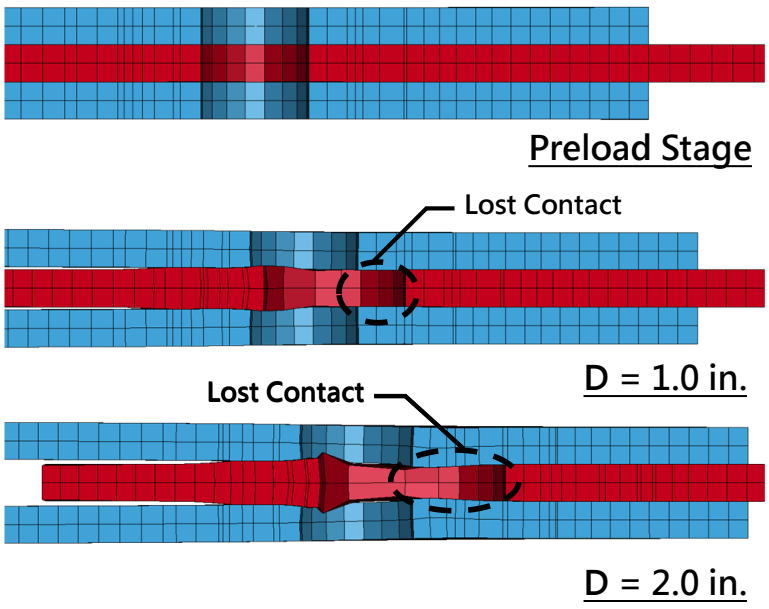


Figure 6-9. Deformation of Connection Model 1 (Bolts not Shown)

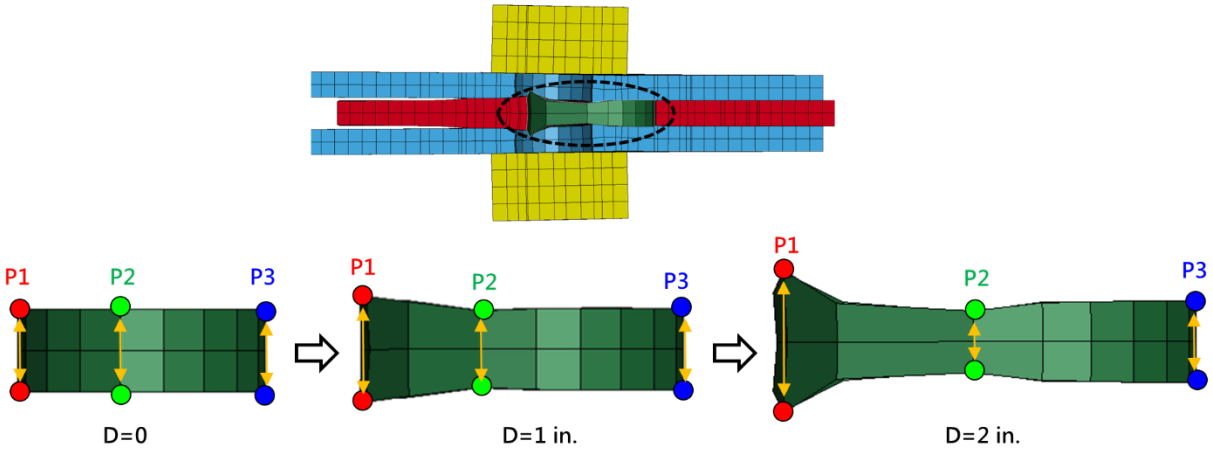


Figure 6-10. Thickness Change around Bolt Holes (Model 1)

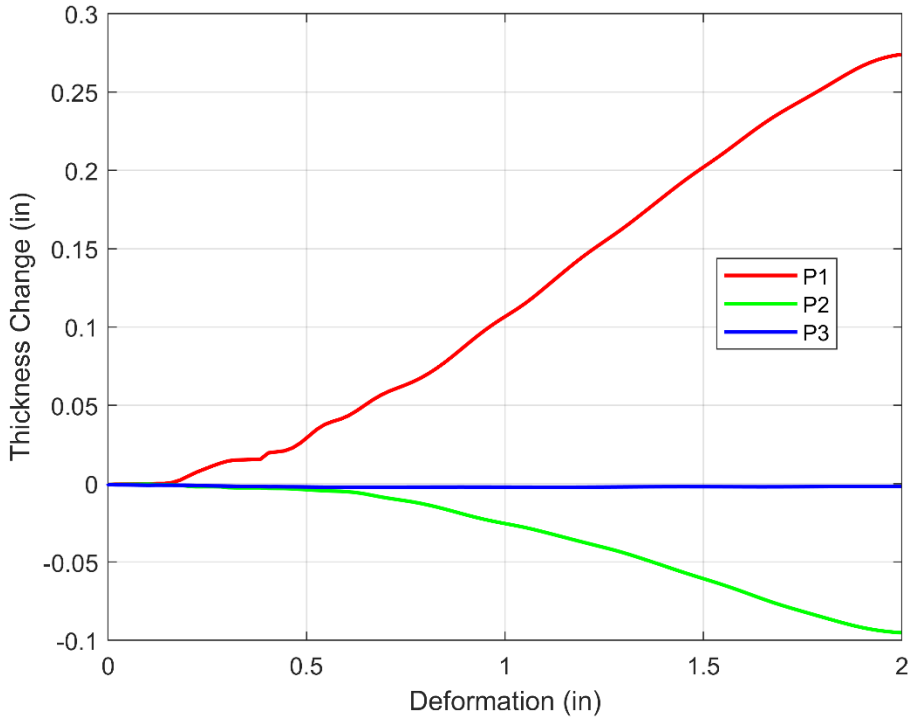


Figure 6-11. Thickness Change around Bolt Holes (Model 1)

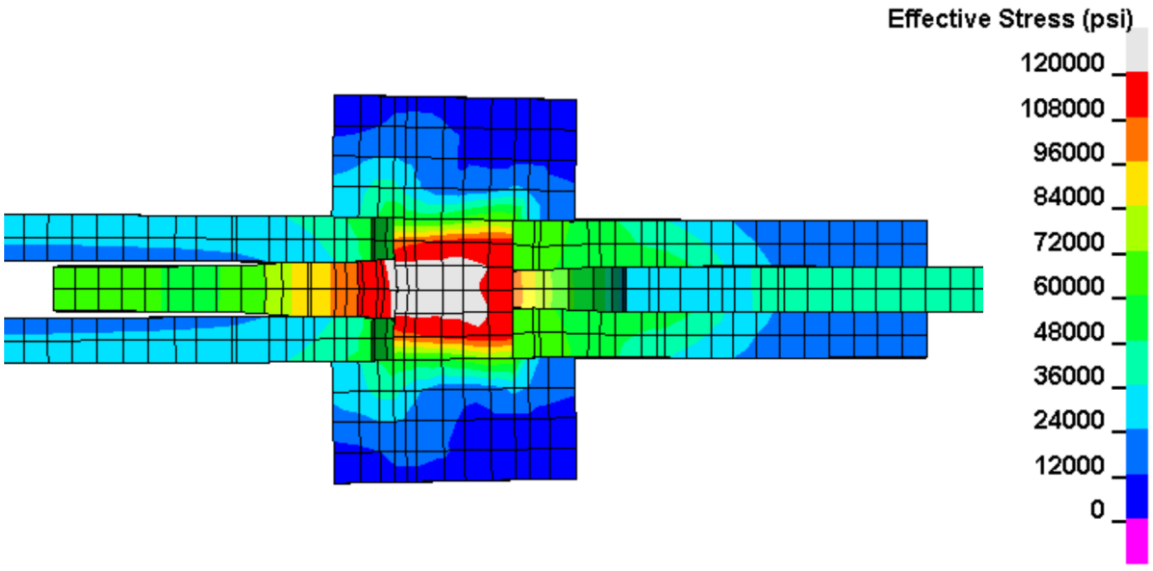


Figure 6-12. Bending and Yielding of Bolts (Model 1)

Figure 6-13 shows the history of clamping stress vectors at different values of connection axial deformation. For the reasons mentioned earlier, the clamping stress vectors on the right (the side where the hole elongates in that figure) lost contact area and stiffness, resulting in a significant reduction in magnitude of the stress vectors with the application of axial deformation. Simultaneously, the thickness of the faceplate around the bolt hole became thinner there, leading to reduced clamping stresses around the bolt hole. Figure 6-14 and Figure 6-15 show the 2D distribution of these clamping and friction stress vectors on a splice plate and the faceplate. Similarly, the clamping stress vectors are shown to significantly reduce as hole elongation increase. Figure 6-16 shows the variation in the clamping force and bolt tensile force as a function of bolt hole elongation. The clamping force decreasing from initial value of 85 kips to 31 kips as the hole elongated to 0.8-in. deformation, and the axial force in the bolt correspondingly reduced by the same amount.

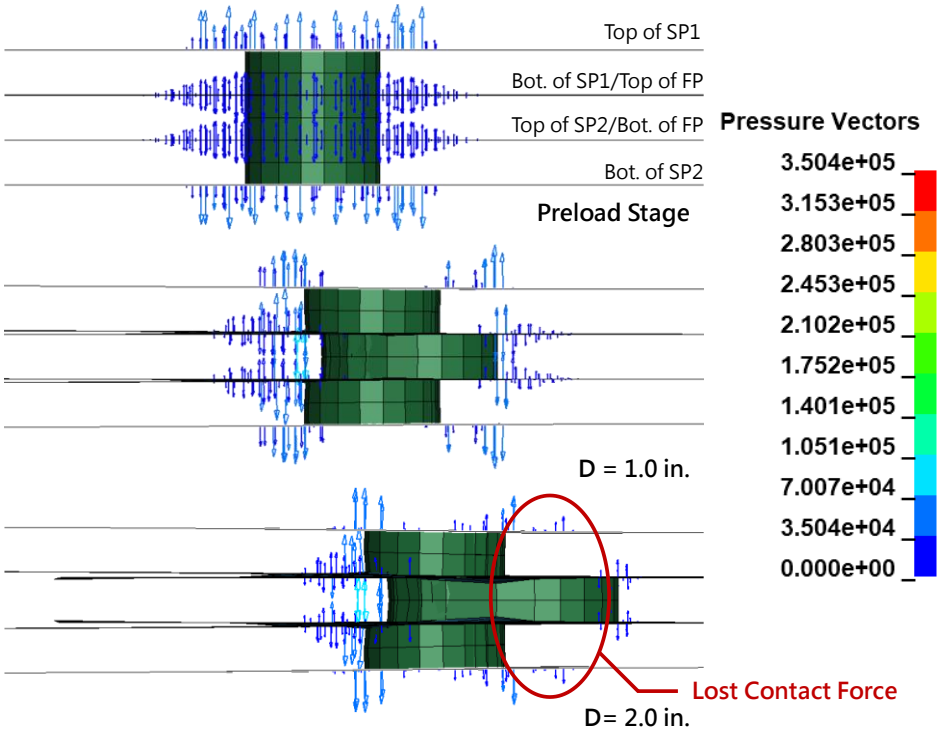


Figure 6-13. Elevation Views of Contact Interfaces showing Clamping Stress Vectors (Model 1)

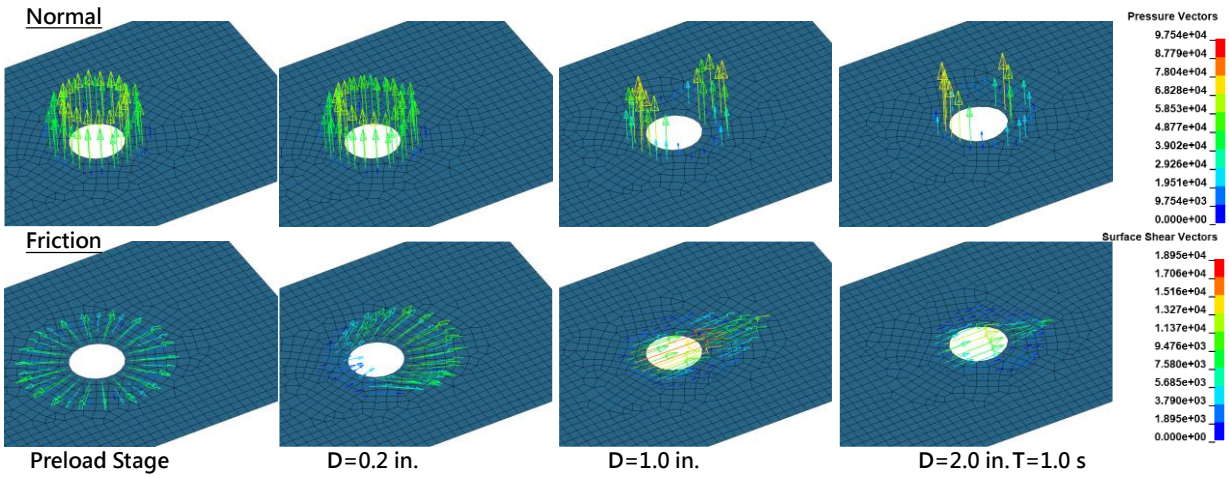


Figure 6-14. Normal and Friction Stresses on the Surface of the Splice Plate (Model 1)

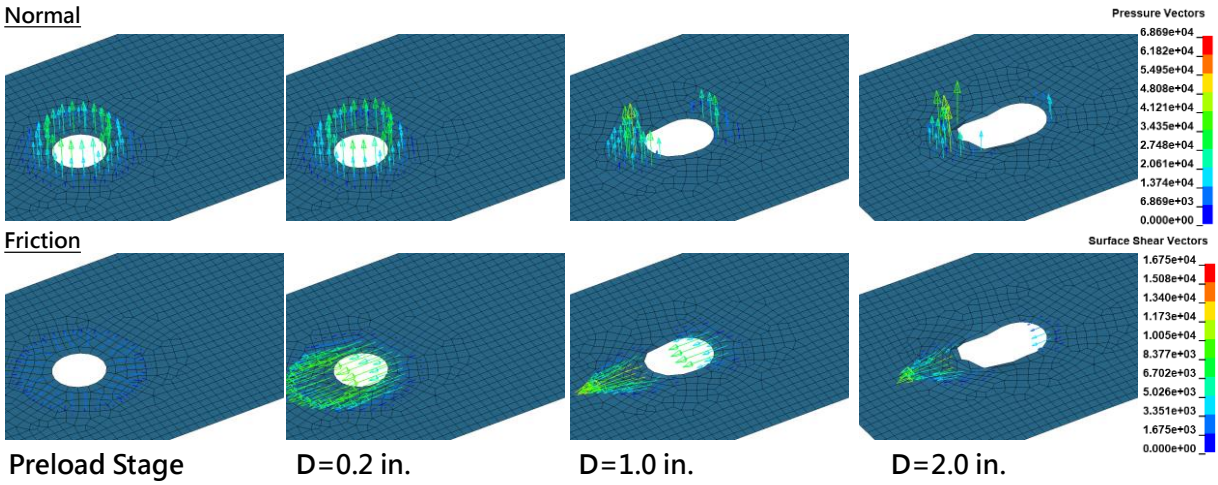


Figure 6-15. Normal and Friction Stresses on the Surface of the Faceplate (Model 1)

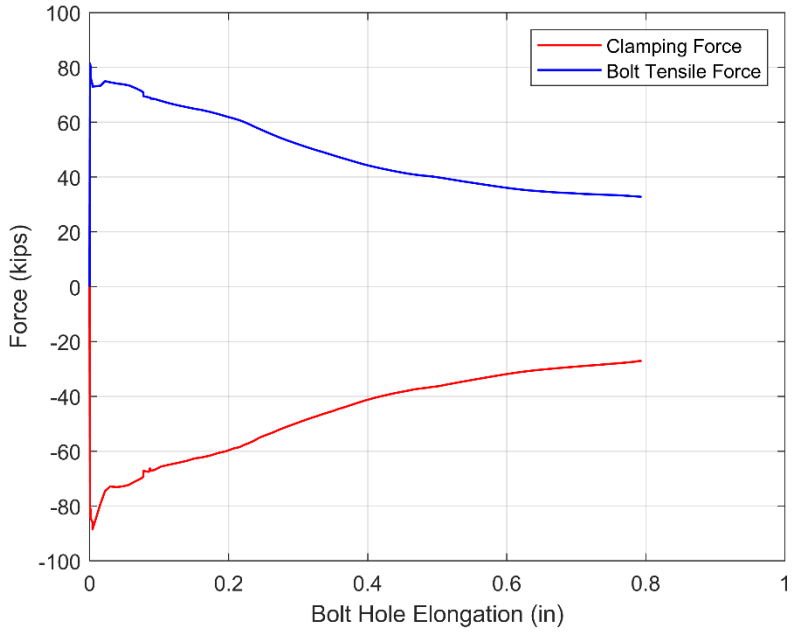


Figure 6-16. Clamping Force and Bolt Hole Elongation Curve (Model 1)

6.3.2 Double-Bolt Connection (Model 2 to Model 4)

As mentioned earlier, Models 2 to 4 are used for investigating the clamping effect considering various bolt diameters (1 in., 0.75 in, and 5/8 in. in Models 2, 3, and 4, respectively), with bearing ratio (*BR*) ranging from 2.44 to 4.25. As previously noted in Figure 6-6, Model 1 exhibited some bolt bending behaviors. Consequently, there is keen interest in exploring this behavior under double-bolt connections in Models 2 to 4. The aim is to assess whether the bending of bolts will be mitigated in these configurations and to understand the influence on the development of friction. Figures 6-17 to 6-19 show the load-deformation curves of the finite element analysis for Models 2 to 4. Table 6-4 provides the calculated slip resistance for the models.

In Model 2 (6-17), the calculated slip resistance and numerically obtained initial friction force are 98.96 kips and 97.70 kips, respectively. After the connection slip, the bearing force started to develop, reaching its maximum value at the end of the analysis (arbitrarily stopped at 2.0-in. deformation). As mentioned in Table 6-3, the governing limit state in Model 2 is gross section yielding. Accordingly, the total axial force reached a plateau near 120 kips after 0.4-in. deformation, closely approaching the gross section yielding strength. The peak total axial force reached 125 kips at a deformation of 2.0 in., exceeding the gross section yielding strength of 123.75 kips and approaching the bearing strength of $2.4dtF_u$, set at 126 kips. At 2.0-in. deformation, the residual friction force is 40 kips, representing a 59% reduction compared to the initial friction force. When comparing Models 1 and 2, both featuring 1-in. bolt diameters and including single-bolt and double-bolt connections, it is observed that the residual friction in Models 1 and 2 is 34% and 41% of their initial friction force, respectively. This suggests that there is a greater reduction in friction in single-bolt connections compared to double-bolt connections under large bolt hole deformation due to bearing.

In Model 3 (Figure 6-18), the calculated slip resistance and numerically obtained initial friction force are 55.67 kips and 52.70 kips, respectively. The bearing force developed after connection slip, and it reached $2.4dtF_u$ at 0.8-in. deformation. Concurrently, the total axial force reached the bearing strength of $2.4dtF_u$ at a deformation of 0.23 in., and it achieved the bearing strength of $3.0dtF_u$ at a deformation of 0.89 in. At 2.0-in. deformation, the peak total axial force reached 126.5 kips at 2.0-in. deformation, which is larger than the gross section yielding strength (123.75 kips). Meanwhile, the residual friction force is 18 kips, representing a 66% reduction compared to the initial friction force.

Finally, for Model 4 (6-19), the calculated slip resistance and initial friction force are 38.66 kips and 37.00 kips, respectively. The bearing force developed after connection slip, and it reached $2.4dtF_u$ and $3.0dtF_u$ at 0.51-in. and 0.81-in. deformations. Meanwhile, the total axial force attained the bearing strength of $2.4dtF_u$ at a deformation of 0.29 in., and it achieved the bearing strength of $3.0dtF_u$ at a deformation of 0.61 in. The peak total axial force attained 126.0 kips at 2.0-in. deformation, surpassing the gross section yielding strength of 123.75 kips. At this point, the residual friction force at this stage is 8 kips, representing a 78% reduction compared to the initial friction force. Table 6-5 compares Models 2 to 4, which have bolt diameters of 1.0 in., 0.75 in., and 0.625 in., respectively. It summarizes the maximum axial forces at a 2.0-inch deformation and details the initial and residual friction forces. Notably, the residual friction forces in Models 2 to 4 are 40 kips, 18 kips, and 8 kips respectively, representing 41%, 34%, and 22% of their respective initial friction forces. The data shows that smaller bolt diameters lead to greater reductions in friction due to increased bending and shear deformations in bolted connections.

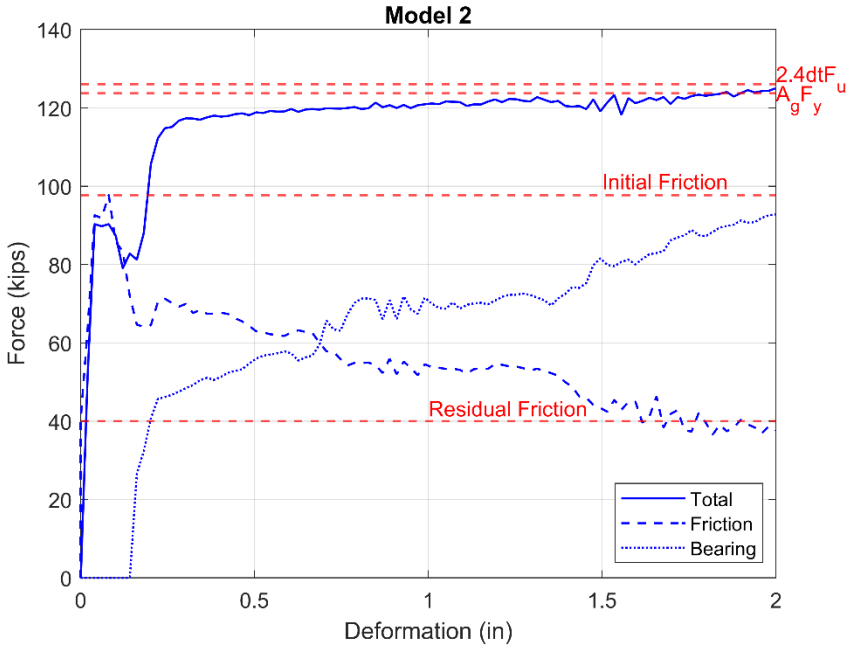


Figure 6-17. Total Axial Force and Friction Force of Model 2

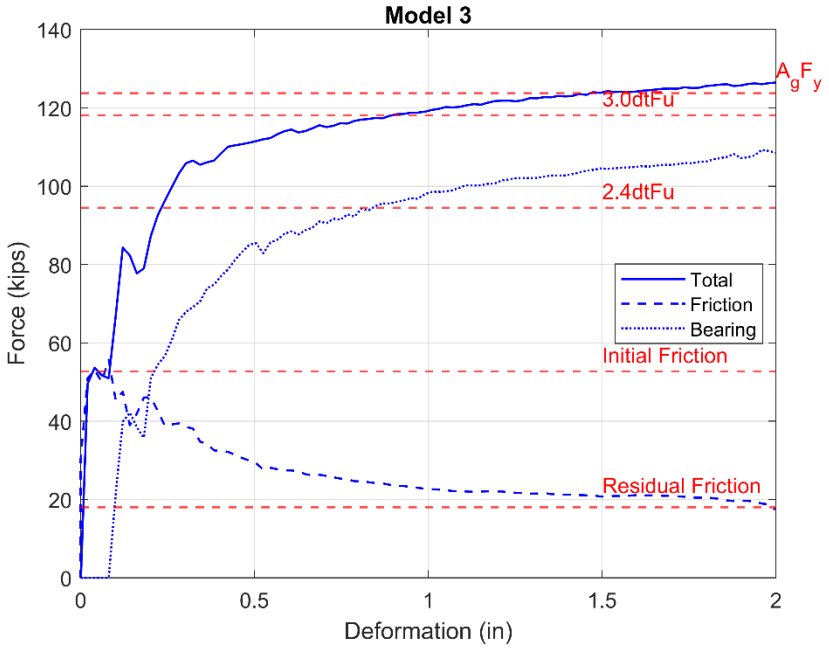


Figure 6-18. Total Axial Force and Friction Force of Model 3

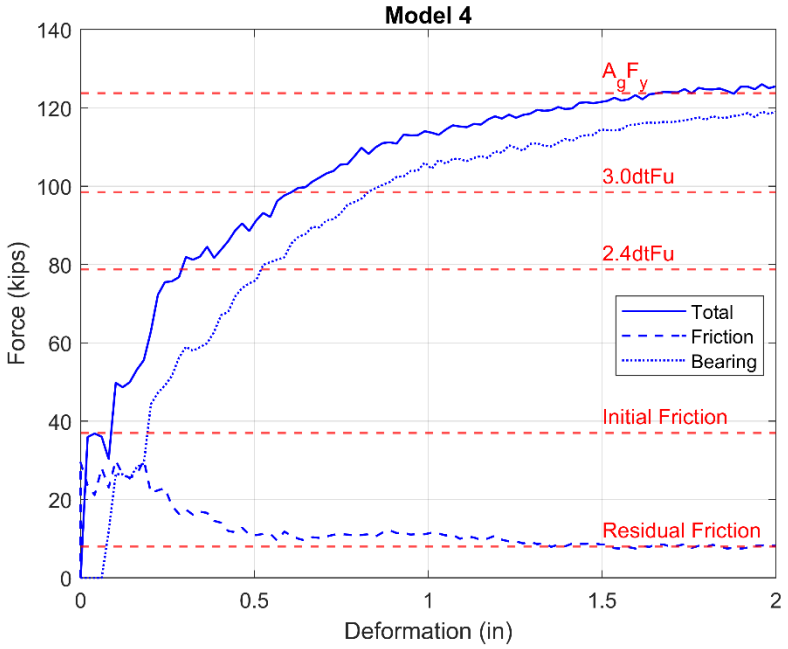


Figure 6-19. Total Axial Force and Friction Force of Model 4

Table 6-4. Calculated Slip Resistance for Models 2, 3, and 4

Model	Pretension T_b (kips)	Slip Resistance (kips)
2	82.47	98.96
3	46.39	55.67
4	32.21	38.66

Table 6-5. Initial and Residual Friction Forces in Models 2, 3, and 4

Model	Max. Axial Force (kips)	Initial Friction Force (kips)	Residual Friction Force (kips)
2	125.0	97.7	40.0
3	126.4	52.7	18.0
4	125.0	37.0	8.0

Figures 6-20 to 6-22 show the von Mises stresses distribution of these models at different deformation stages, highlighting the progressive yielding on the plates. As previously noted, the peak axial forces in Models 2 to 4 reached the gross section yielding strength, leading to observable whole section yielding around the inner bolts. In contrast, Model 1, which features a single-bolt connection and is shown in Figure 6-5, did not achieve the gross section yielding strength. In this model, yielding initiated around the bolt and extended towards the free edge, illustrating a different pattern of bearing stress distribution compared to the double-bolt connections.

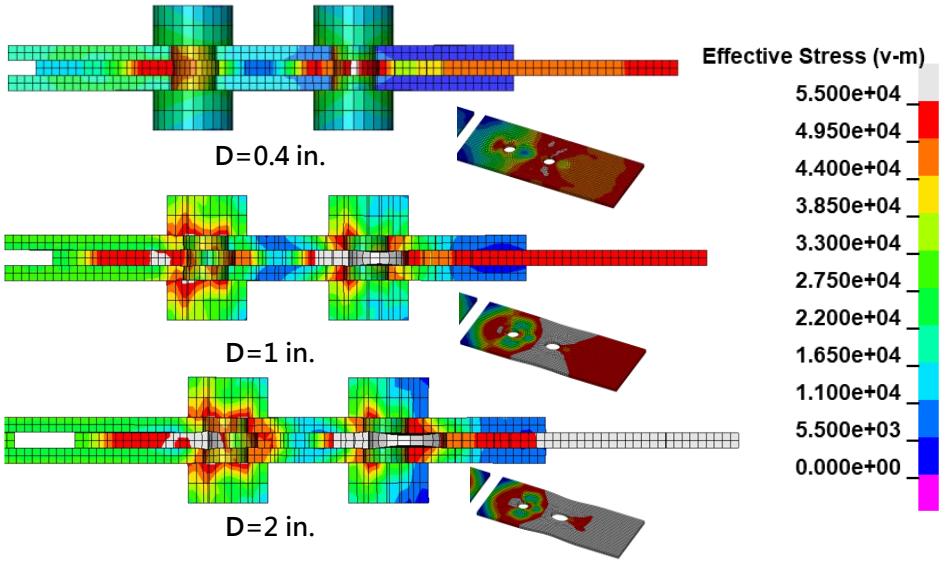


Figure 6-20. Von Mises Stresses of Model 2 at Different Deformations (Bolt Shank Not Displaced)

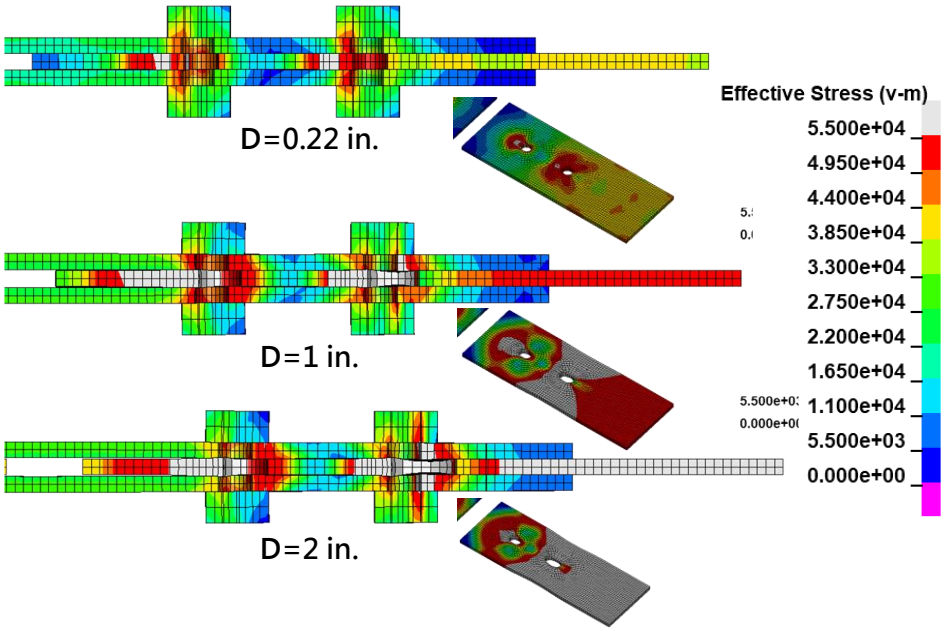


Figure 6-21. Von Mises Stresses of Model 3 at Different Deformations (Bolt Shank Not Displaced)

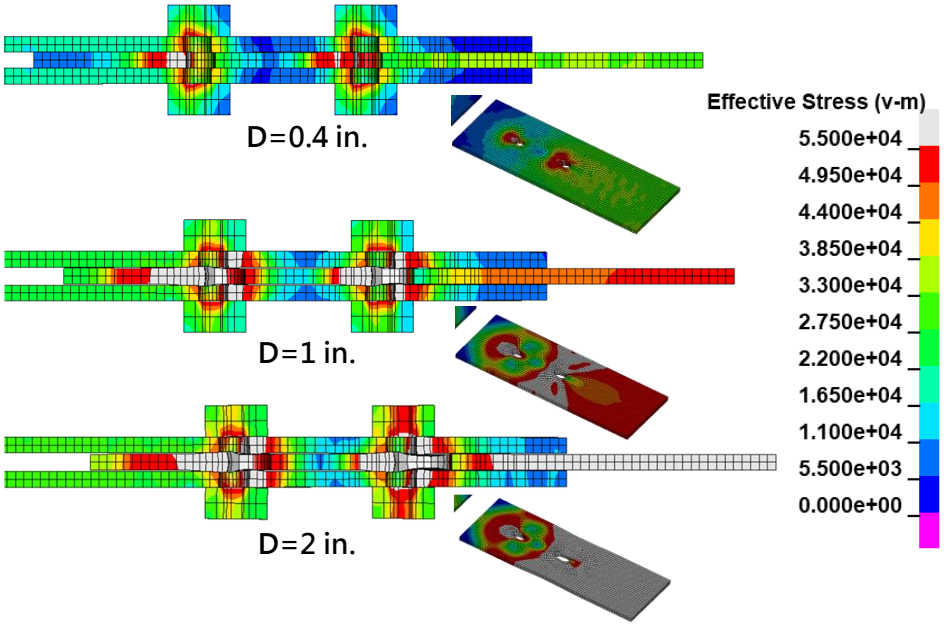


Figure 6-22. Von Mises Stresses of Model 4 at Different Deformations (Bolt Shank Not Displaced)

Figure 6-23 shows the deformation of double-bolts connections (Models 2 to 4) at 2.0-in. deformation. Recall that these models have various bolt diameters, equal to 1 in., 0.75, and 5/8 in. in Model 2, 3, and 4, respectively. It is noticeable that as the bolt diameter decreases, the bolt shanks exhibit more pronounced bending behavior (although, in Model 2, behavior was more dominantly governed by plate yielding rather that bolt bearing). Figure 6-24 shows the deformation of Model 3 (design governed by bearing) without showing the bolt shanks, providing a clearer view to observe the thickness change around bolt holes at locations identified as “Bolt 1” and “Bolt 2” in the figure. It can be observed that the bolt hole elongation is larger at location "Bolt 1" (closer to the edge of splice plates), while the elongation is smaller at location "Bolt 2" (closer to the center of the splice plates).

Recall from Figure 6-8, that as axial deformations are applied to the connection, relative movements occur between the plates, resulting in significant hole elongation in the faceplate. Figures 6-25 to 6-27 show the history of clamping stress vectors over axial deformation in Models 2 to 4. In the case of Model 2, where the design is governed by gross section yielding, the hole elongation of Bolt 2 is significantly less than that of Bolt 1. Therefore, the reduction of clamping stress vectors at Bolt 2 is less significant than at Bolt 1. Conversely, in Models 3 and 4, where the design is governed by bearing with smaller diameters of bolts, the bolts experience more bending, and the bolt holes have larger elongations, resulting in a more significant loss of clamping stress vectors. This phenomenon can also be observed by plotting the clamping force to hole elongation curves as shown in Figures 6-28 to 6-30. Also, the same conclusions were found by observing the clamping and friction stress vectors on the splice plate and faceplate as shown from Figure 6-31 to 6-36.

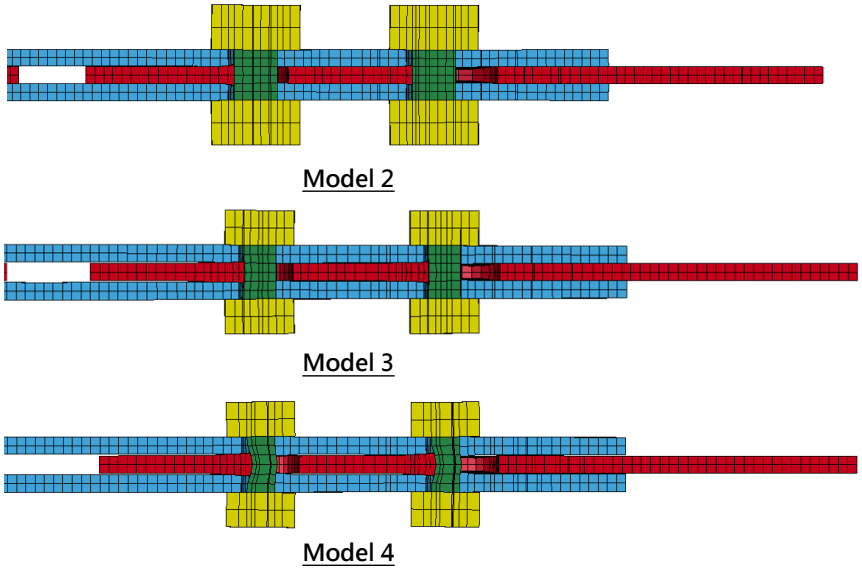


Figure 6-23. Deformation of Double-Bolts Connections (Deformation = 2.0 in.)

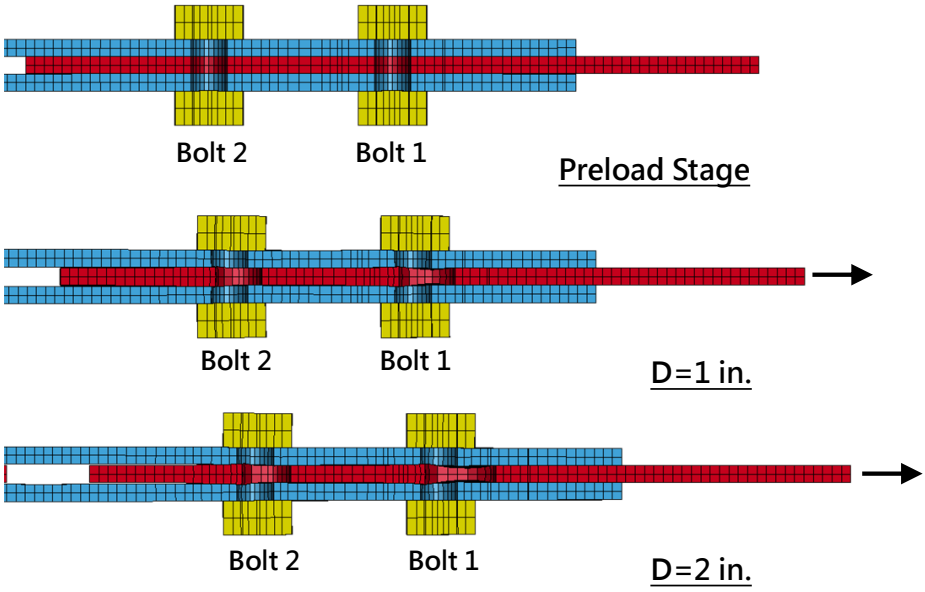


Figure 6-24. Deformation of Connection Model 3 (Bolts Shank not Shown)

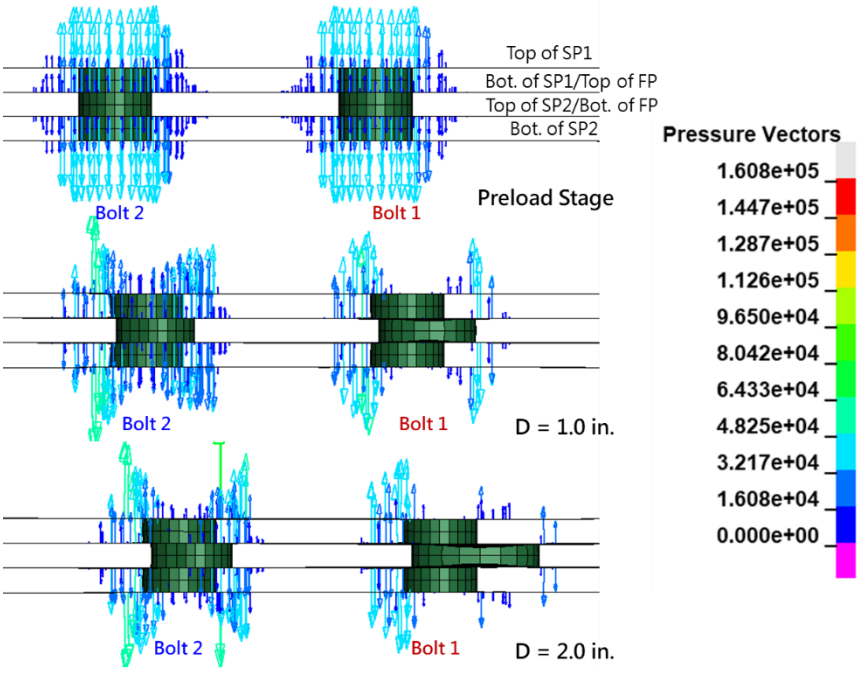


Figure 6-25. Elevation Views of Contact Interfaces showing Clamping Stress Vectors (Model 2)

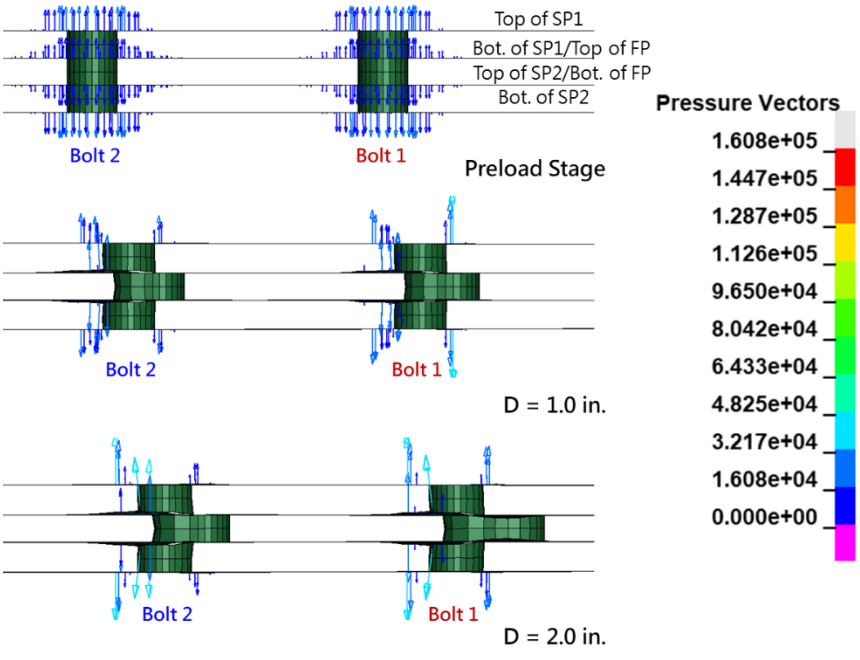


Figure 6-26. Elevation Views of Contact Interfaces showing Clamping Stress Vectors (Model 3)

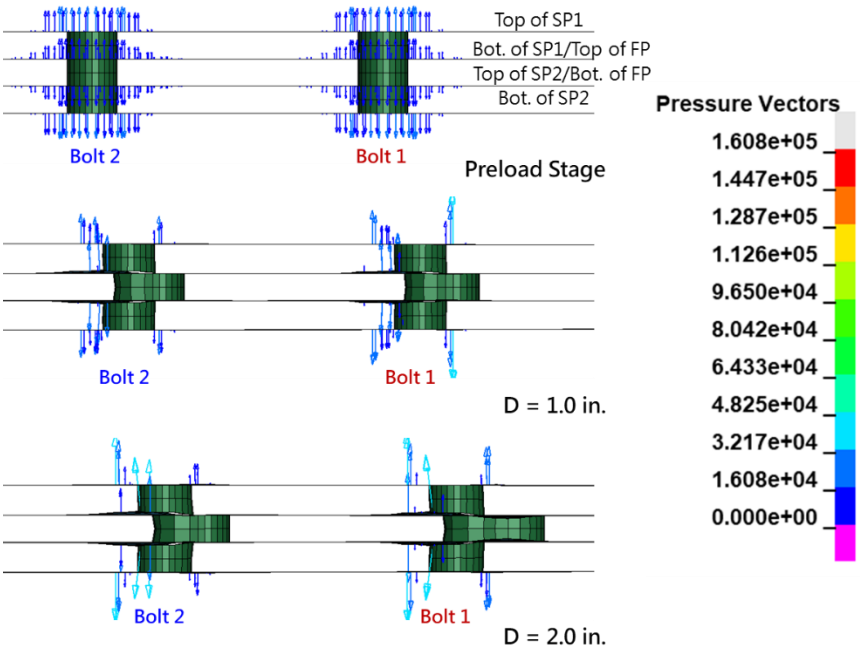


Figure 6-27. Elevation Views of Contact Interfaces showing Clamping Stress Vectors (Model 4)

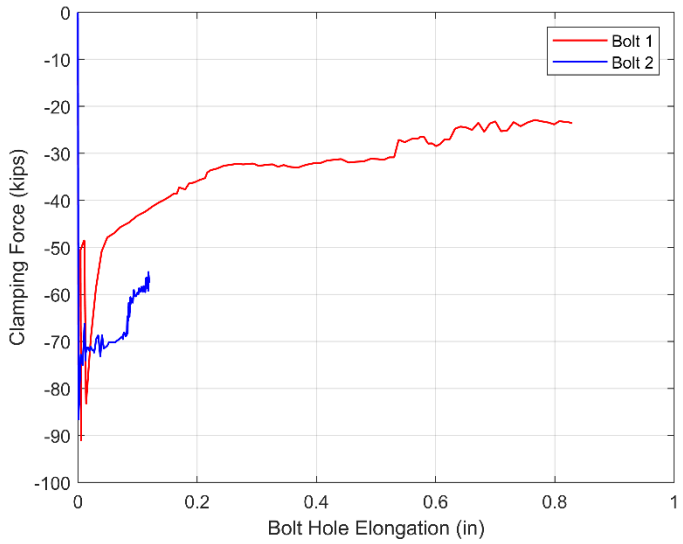


Figure 6-28. Clamping Force and Bolt Hole Elongation Curve (Model 2)

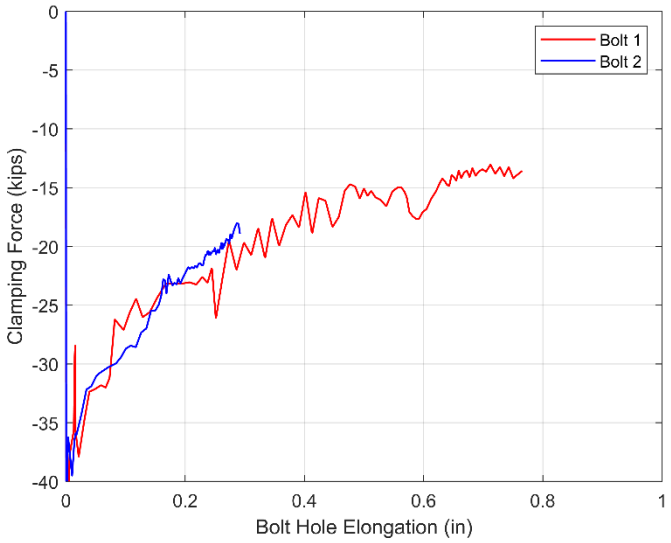


Figure 6-29. Clamping Force and Bolt Hole Elongation Curve (Model 3)

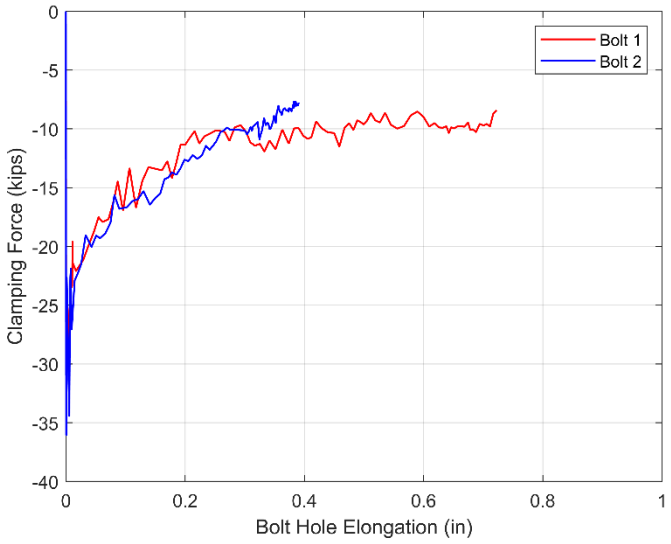


Figure 6-30. Clamping Force and Bolt Hole Elongation Curve (Model 4)

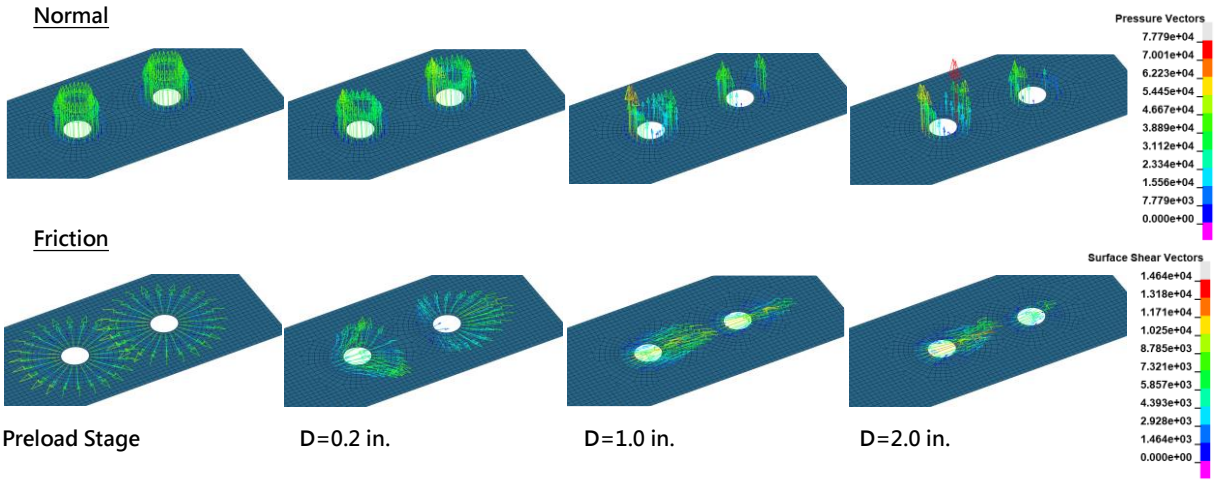


Figure 6-31. Normal and Friction Stresses on the Surface of the Splice Plate (Model 2)

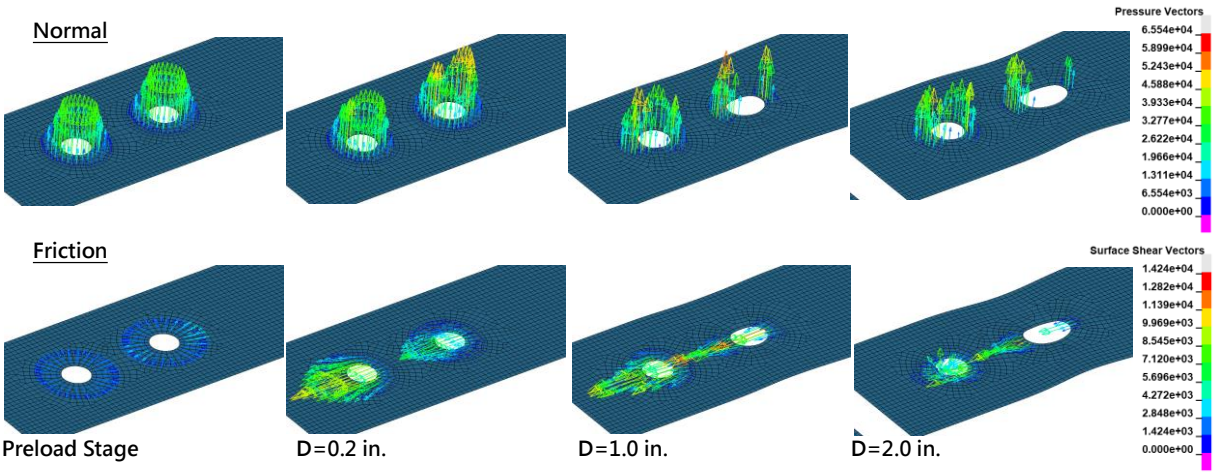


Figure 6-32. Normal and Friction Stresses on the Surface of the Faceplate (Model 2)

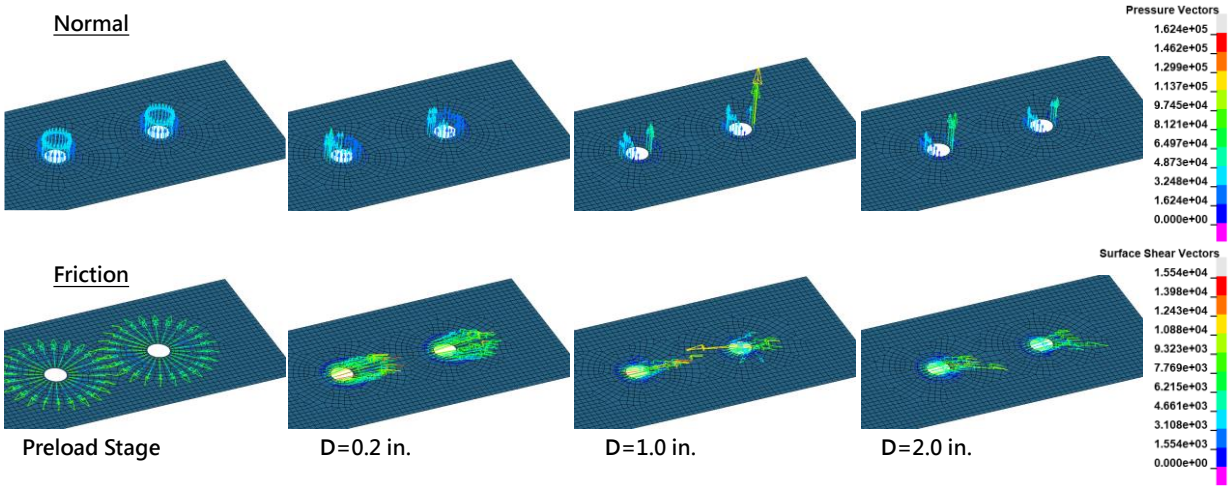


Figure 6-33. Normal and Friction Stresses on the Surface of the Splice Plate (Model 3)

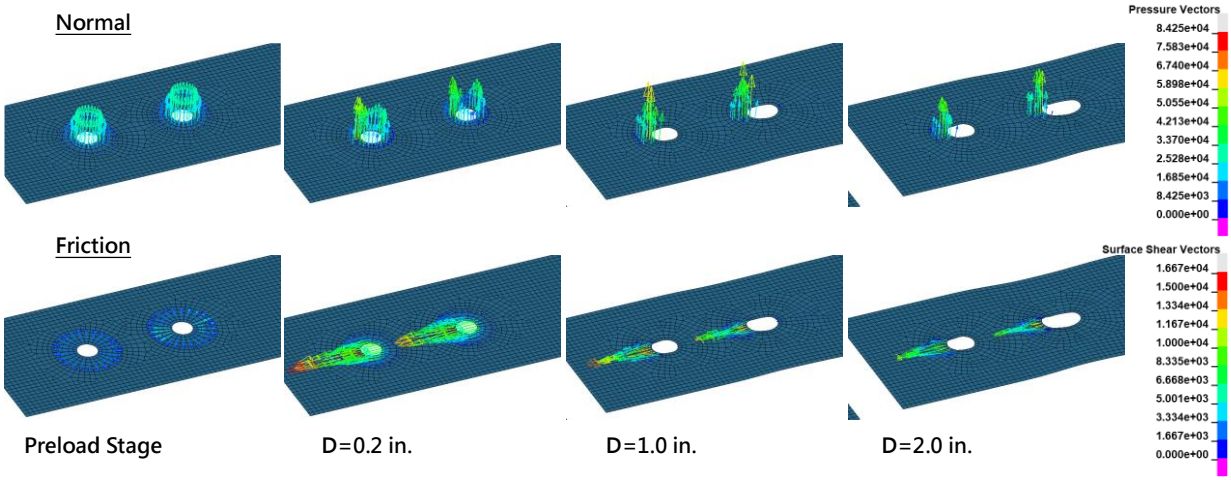


Figure 6-34. Normal and Friction Stresses on the Surface of the Faceplate (Model 3)

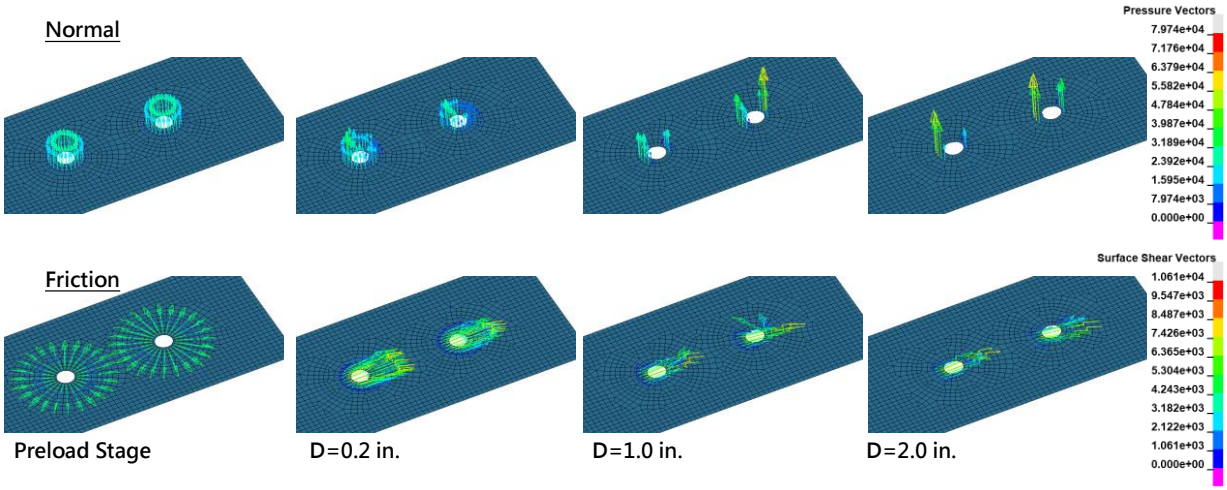


Figure 6-35. Normal and Friction Stresses on the Surface of the Splice Plate (Model 4)

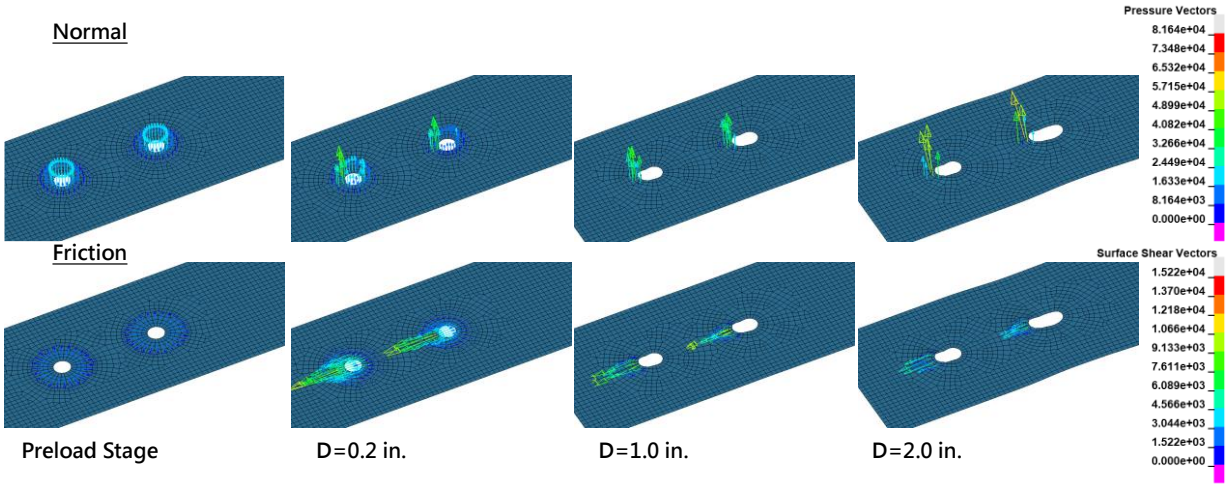


Figure 6-36. Normal and Friction Stresses on the Surface of the Faceplate (Model 4)

6.4 Friction Forces in C-PSW/CF Bolted Connections

6.4.1 C-PSW/CF Bolted Connections in Tension

Finite element analyses of the C-PSW/CF components were performed in Section 5. Specimens T1, T2, and T3 are selected here to study the clamping effect in tension for bolted C-PSW/CF connections. Similar to Table 6-1, Table 6-6 provides information on the geometry of the connections, and on the bearing ratio (*BR*) which ranges from 2.6 to 5.9 for the cases considered. The results from Specimens T1 and T2 are used to investigate friction development in scenarios where the connection is primarily governed by bearing strength. In contrast, Specimen T3 is utilized for comparison in situations where net section yielding occurs before bearing strength $2.4dtF_u$.

Figures 6-37 to 6-39 present analysis results for Specimens T1 to T3, showing the total axial forces and friction forces as a function of axial deformation. These results consider different pretension values in the bolts or through rods of the C-PSW/CF connections, with corresponding test results included in the figures. More specifically, the analyses of Specimens T1 to T3 consider three pretension stress values, namely: 0 ksi (no pretension), 52.5 ksi (50% pretension), and 105 ksi (full pretension). These values correspond to axial forces of 0, 41.23 kips, and 82.47 kips for the 1-in. diameter bolts/rods used in Specimens T1 and T2, and 0, 64.43 kips, and 128.85 kips for the 1.25-in. diameter rods used in Specimen T3. As shown in Table 5-6, the experimentally observed initial friction forces for Specimens T2 and T3 are 130 kips and 170 kips, respectively, corresponding to pretension values of 69 ksi and 39 ksi. A similar value could not be determined for Specimen T1, as explained in Section 5.3.5.

The behaviors of steel bolted connections and C-PSW/CF bolted connections in tension show similarities. In both types, the bearing force begins to develop after connection slip, and the friction force starts decreasing following the development of the bearing force. In Specimens T1 and T2 (bearing-controlled

case the total axial forces reached $2.4dtF_u$ and $3.0dtF_u$ at axial deformations of approximately 1.3 in. and 1.2 in., regardless of the applied pretension values. For Specimen T3 (net section yielding-controlled case), the peak axial load reached net section yielding strength A_eF_y at deformations of 0.2 in., 0.55 in., and 0.82 in., for the cases of bolts pretensioned to values of 105 ksi, 52.5 ksi, and 0 ksi. The axial loads in the models plateaued after reaching net section yielding. Subsequently, regardless of pretension values, the axial load reached the bearing strength of $2.4dtF_u$ at deformation of 1.5 in.

While the curves indicate a significant drop in friction forces as axial deformation increases regardless of the initially assigned pretension value, it can be observed there is no significant difference in the residual friction forces among each model under large axial deformation of connections, i.e., when the connections reach their maximum bearing strength. Figure 6-40 shows the development of clamping stress vectors in Specimen T2, exhibiting a reduction behavior similar to the one described in the case of pure steel bolted connections. Figure 6-41 shows the clamping force versus bolt hole deformation curve for Specimens T1 to T3, each under a pretension value of 52.5 ksi. The initial clamping forces for Specimens T1 to T3 are 38 kips, 38 kips, and 55 kips, while the residual clamping forces are 16 kips, 18 kips, and 30 kips, representing 42%, 47%, and 55% of the initial clamping force. T1 and T2 show similar reductions in clamping force, likely due to having identical bolt numbers and diameters. T3 exhibits a smaller reduction in clamping force, likely due to its lower bearing ratio (*BR*).

Table 6-6. Geometries of Specimens T1, T2, and T3

Specimen	t (in)	W (in)	W_e (in)	Rows	n	d_h (in)	d (in)	e (in)	S (in)	BR
T1	0.375	14	11.750	1	2	1.125	1	4.00	-	5.875
T2	0.375	14	11.750	1	2	1.125	1	4.00	-	5.875
T3	0.375	14	9.875	1	3	1.375	1.25	4.00	-	2.633

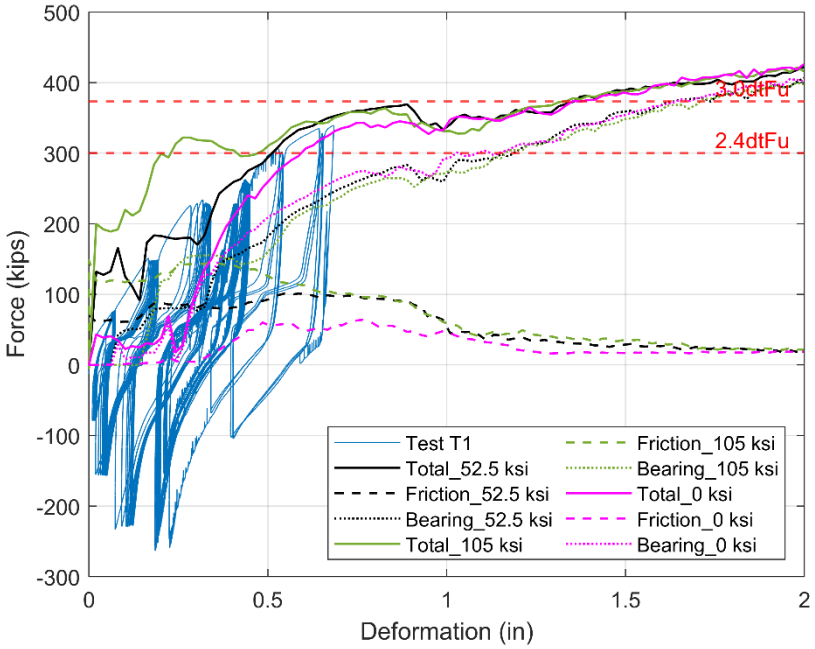


Figure 6-37. Force-Deformation Curve of Specimen T1 with Different Pretensions

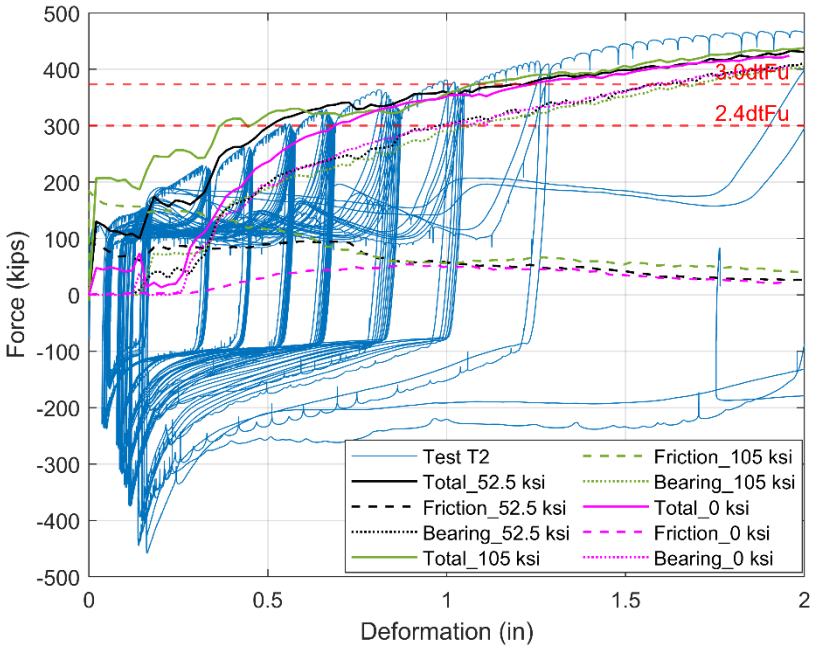


Figure 6-38. Force-Deformation Curve of Specimen T2 with Different Pretensions

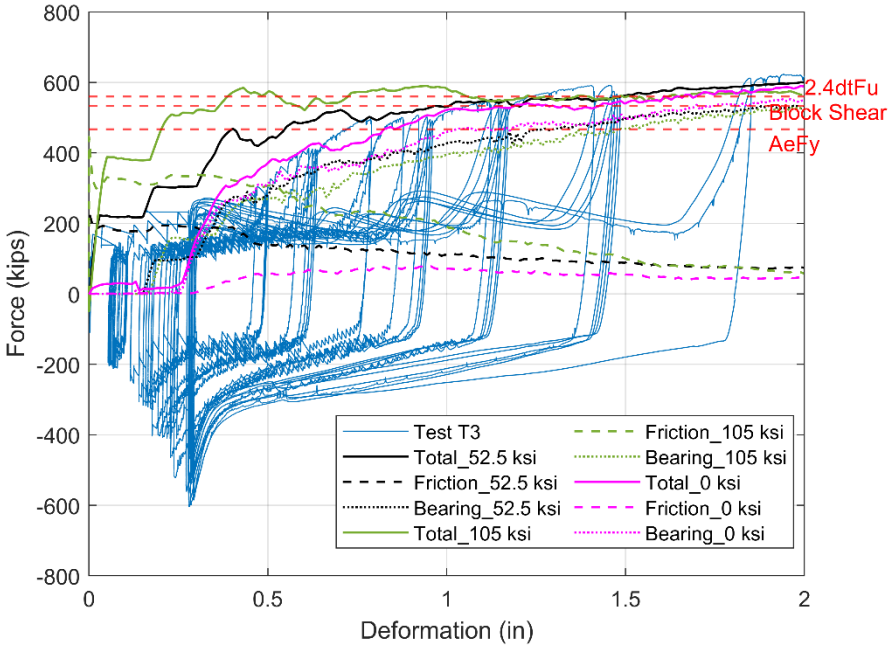


Figure 6-39. Force-Deformation Curve of Specimen T3 with Different Pretensions

Table 6-7. Nominal Strength of Concrete for FE Models T1, T2, and T3

Specimen	f'_c (psi)	f_t (psi)	A_c (in^2)	P_c (kips)	P_t (kips)
T1	5500	550	147	687.23	80.85
T2	5700	570	147	712.22	83.79
T3	5700	570	147	712.22	83.79

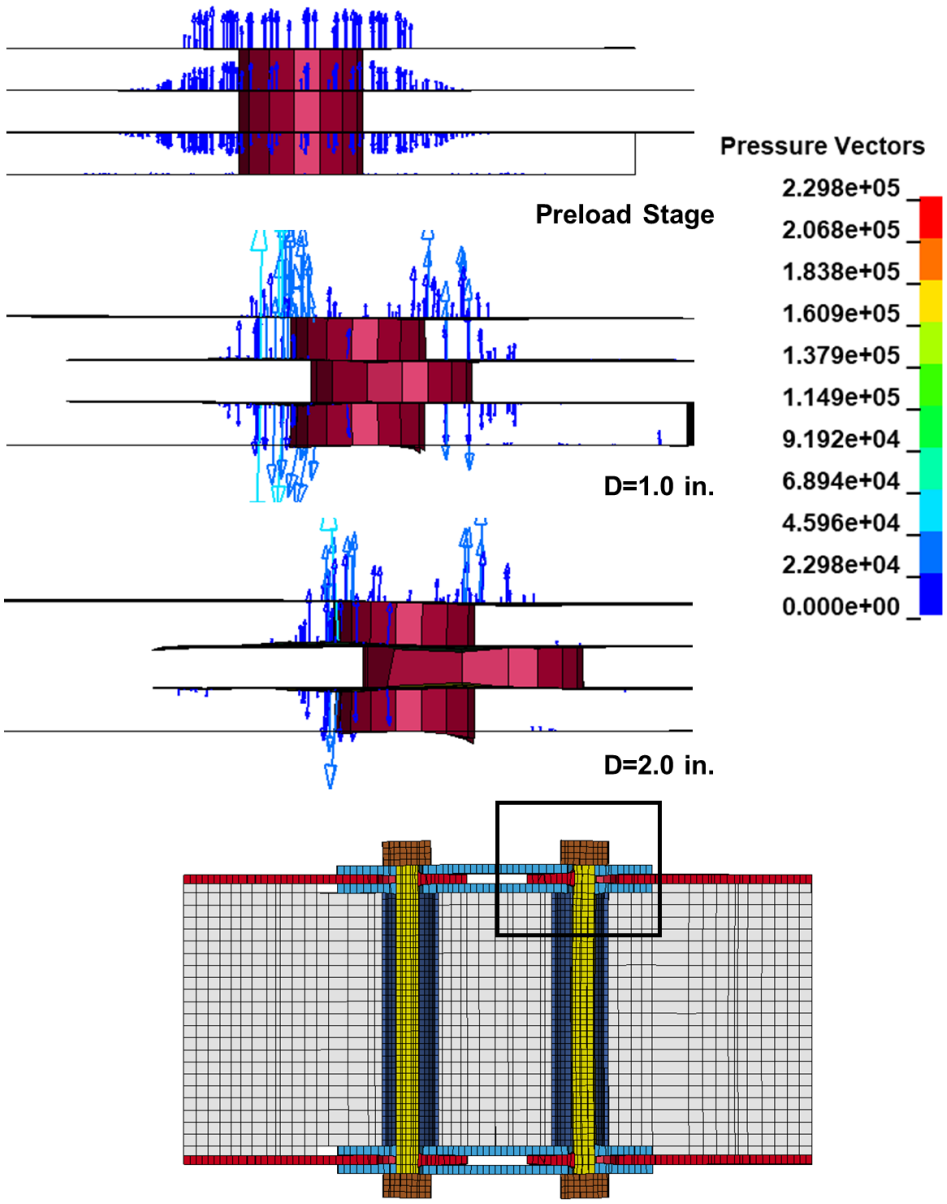


Figure 6-40. Clamping Stress Vectors in Specimen T2

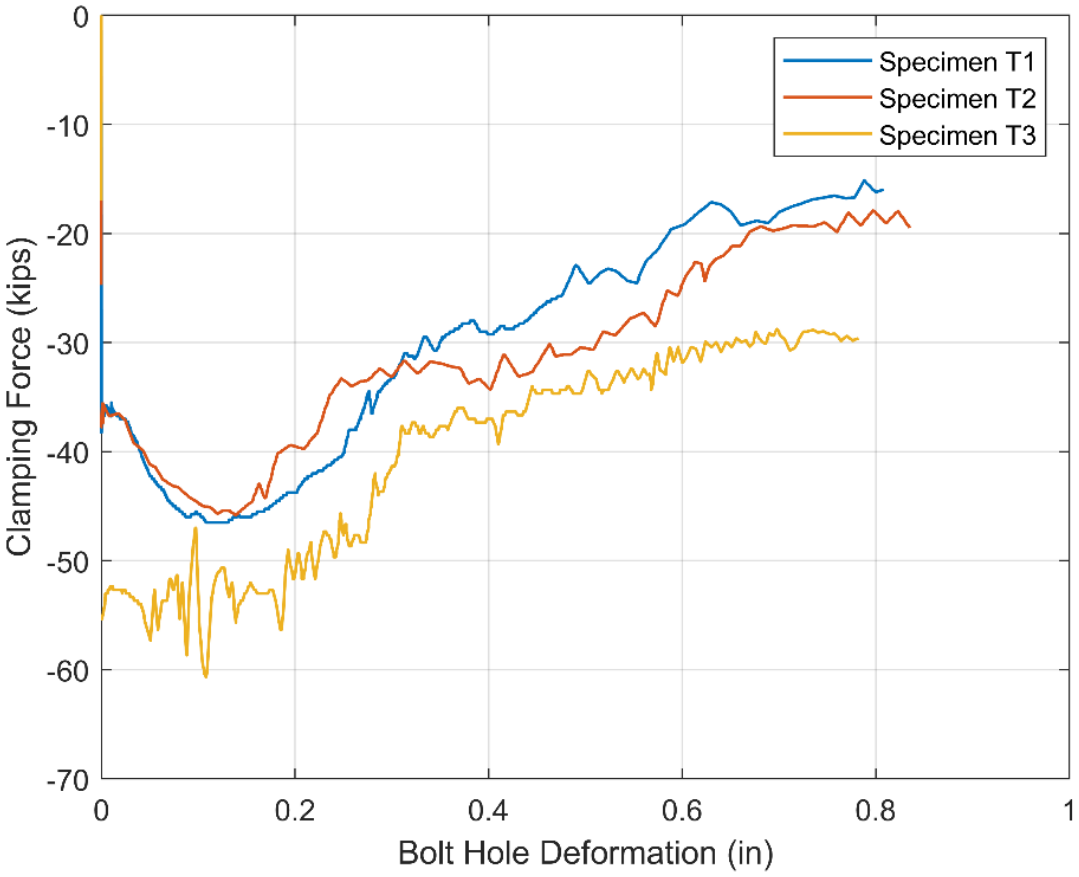


Figure 6-41. Clamping Force-Hole Deformation Curve of Models T1 to T3

6.4.2 C-PSW/CF Bolted Connections in Compression

When a C-PSW/CF bolted connection is in compression, the high strength and stiffness of concrete contribute significantly to the axial load capacity. Specimen T1 was chosen to numerically explore the friction force that develops in the bolted splice region between the steel components as well as between the steel and concrete when the C-PSW connection is in compression. To simulate lateral confinement in real wall scenarios, the same side restraint previously used in Figure 5-57(b) was applied to the model.

Figure 6-42 shows the load-deformation curves obtained from the finite element analysis of Specimen T1 (Model T1) in compression, in terms of the total axial force, axial force in steel, and axial force in concrete. The steel plates started sliding at a deformation of -0.01 in, corresponding to an axial load in steel equal to 100 kips (labeled as P_1 in the figure), and concrete resist ed 261 kips (70% of the total axial load). At this point, the total axial load, P_{T1}, reached -372 kips. For comparison, the theoretical axial load in steel and concrete (P_{S1} and P_{C1}) predicted using relative elastic stiffness are:

$$P_{T1} = -372\ kips$$

$$P_{S1} = P_{T1} \times \frac{E_s A_s}{E_s A_s + E_c A_c} = -85.6\ kips \qquad \text{Equation 6-2}$$

$$P_{C1} = P_{T1} \times \frac{E_s A_s}{E_s A_s + E_c A_c} = -286.4\ kips$$

where the young's modulus of steel and concrete (E_s and E_c) are equal to 29000 ksi and 4227 ksi, and the area of steel and concrete (A_s and A_c) are 7 in^2 and 161 in^2, respectively.

The member axial stiffness did not change significantly after sliding of steel plates started, and the concrete alone resisted the additional axial load. At a deformation of -0.04 in, when the total axial load reached -

993 kips (labeled as P_2 in the figure), some concrete cracks were observed at this point as the infill concrete elements reached its compressive strength (5500 psi), as shown in Figure 6-43, leading to a significant change in axial stiffness. At that point, the concrete resisted -871 kips, which is 88% of the total applied axial load. Peak strength for the connection was 1126 kips, reached at -0.2-in. deformation. For comparison, the nominal axial strength of the connection can be calculated as:

$$P_{T,n} = A_s F_y + 0.85 A_c f_c' = -1193.68\ kips \qquad \text{Equation 6-3}$$

where the compressive strength of concrete f_c' is equal to 5.5 ksi. The peak strength reached by the numerical model is less that this value because the strength of the steel splice is governed by bearing, which developed at stresses less than F_y. For comparison, at peak total strength in the numerical model, the average stress developed in the steel and concrete area was -17.5 ksi and -6.32 ksi, respectively. At that deformation level, bolts are bearing on the bolt holes but have not produced large hole deformations yet, as shown in Figure 6-44.

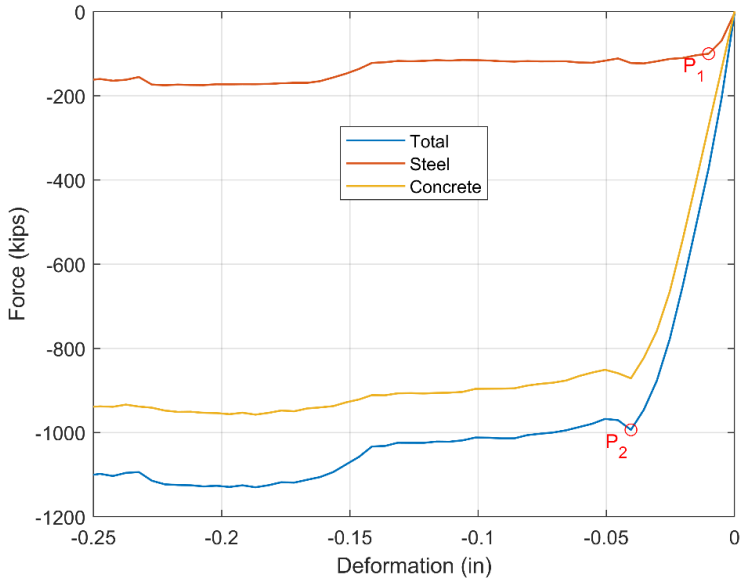


Figure 6-42. Force-Deformation Curve of Model T1 in Compression

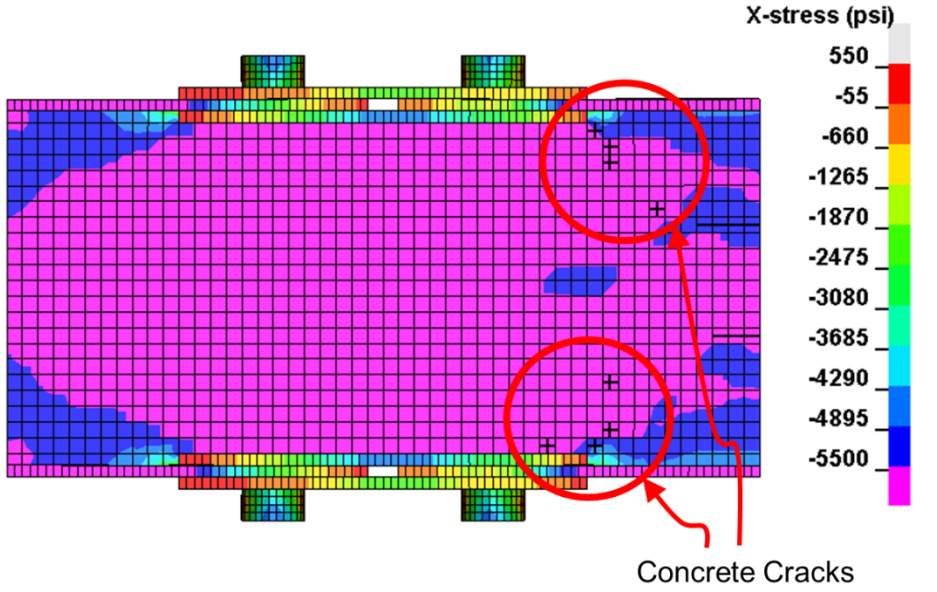


Figure 6-43. Initiation of Concrete Cracks of Model T1 in Compression

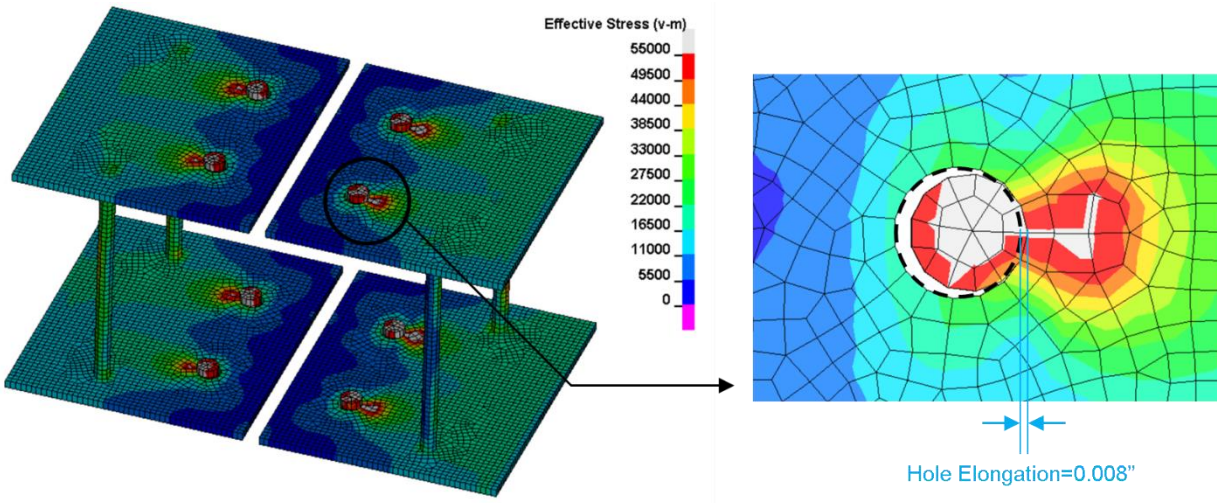


Figure 6-44. Bolt Hole Elongation at -0.20 in. Deformation

To investigate the load-transfer mechanisms that develop in the splice region, Figures 6-45 and 6-46 provide global and local free-body diagrams of the forces between steel plates and between steel and concrete there. All force components shown in the free-body diagrams are plotted in Figures 6-47 and 6-48. The force equilibrium formulas are presented below, and Figure 6-49 shows the results of these formulas, confirming compliance with force equilibrium.

$$sumG1 = P_{FP} - F_{r5} + F_6 - P_{SP1} - P_{SP2}$$
$$sumG2 = P_{FP} + F_{r1} + F_{r4} - F_{r5} - B_1 + B_2 + B_3 - P_{SP1} - P_{SP2}$$
$$sumL1 = F_{r1} + F_{r4} + B_2 - P_{SP1} \qquad \text{Equation 6-4}$$
$$sumL2 = P_{FP} - B_1 - F_{r2} - F_{r3}$$
$$sumL3 = F_{r3} + F_{r4} - F_{r5} + P_{FP} + B_3 - P_{SP2}$$

At the initial stage (before connection slip and at -0.01-in. deformation), the axial forces P_{FP}, P_{SP1} and P_{SP2} were 46.2 kips, 27.6 kips and 22.0 kips, respectively. At this stage, the friction forces F_{r2} and F_{r3}, each contributing 23.1 kips, reached their slip-critical state. Meanwhile, the friction forces F_{r1} and F_{r4} were -0.9 kips, and 4.2 kips, respectively. After the connection slip, the axial forces P_{FP}, P_{SP1}, and the friction forces F_{r2} and F_{r3} remained unchanged as they were in plateau. However, the axial force P_{SP2} and friction force F_{r4} kept increasing and plateaued at 42.7 kips and 20.0 kips at deformation of -0.05 in. At this point, the contact force F_6 acting on nuts reached 17 kips.

It can be observed that the bearing force B_1 initiated at a deformation of -0.12 in. and continued to increase until it plateaued at 45 kips at -0.17-in. deformation. During this period, the axial force P_{FP} increased to 87 kips and the axial force P_{SP1} rose to 42 kips, approaching the magnitude of P_{SP2}. Concurrently, the friction

force F_{r1} changed from -3.3 kips to 20.7 kips, reaching its plateau at deformation of -0.17 in. Furthermore, the contact force F_6 changed from 11.3 kips to -2 kips. At a deformation of -0.23 in., the bearing forces acting on splice plates (B_2 and B_3) began to develop.

In other words, the sequence of events can be described as follows: When the axial load on the faceplate (P_{FP}) increased to the slip-critical resistance of bolts at a deformation of -0.01in., the sliding intended to occur on the friction forces between faceplate and splice plate (F_{r2} and F_{r3}). However, the sliding was prevented because the nuts embedded inside concrete could not move. Between deformation of -0.01in to -0.05in, the friction force between the bolt nut and inside splice plate (F_{r4}), the contact force between the bolt nut and concrete(F_6), and the axial force on the inside splice plate (P_{SP2}) continued to increase to a plateau at a deformation of -0.05in. After the bolt shank started touching bolt holes at a deformation of -0.12in., the axial forces on the faceplate and splice plate (P_{FP} and P_{SP1}), bearing force on the faceplate (B_1) and friction force between the bolt head and the outside splice plate (F_{r1}) started to develop. These forces increased to a plateau until the bearing force on the faceplate (B_1) reached its plateau at a deformation of -0.17in. Finally, at -0.23-in. deformation, the axial forces on the faceplate (P_{FP}), and the axial forces on the splice plates (P_{SP1} and P_{SP2}) increased again as the bearing forces splice plates (B_2 and B_3) started to develop.

During the above compressive deformation, the friction forces did not experience a significant reduction compared to the connection subjected to tension, as the hole elongations are limited due to the presence of the concrete.

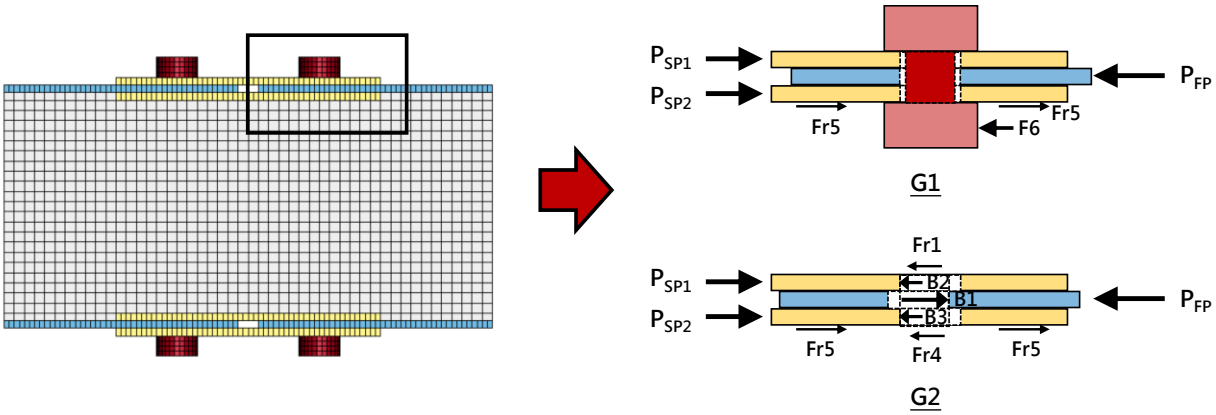


Figure 6-45. Global Free-Body Diagram of Model T1

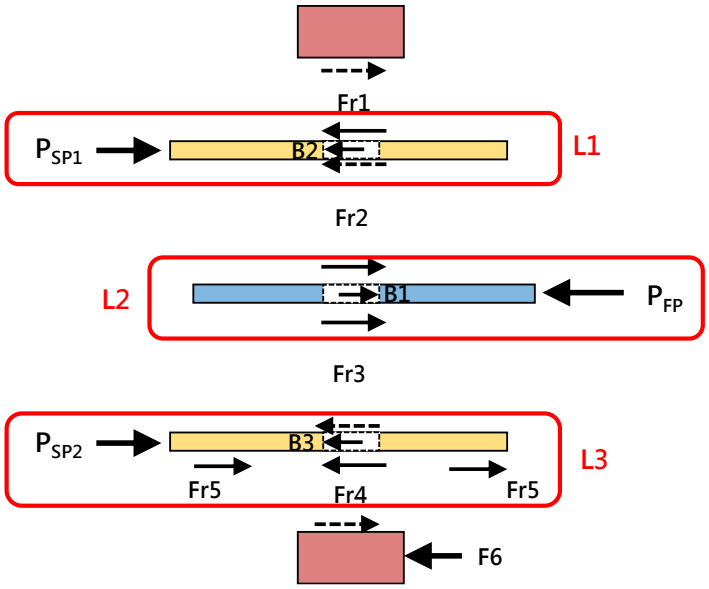


Figure 6-46. Local Free-Body Diagram of Model T1

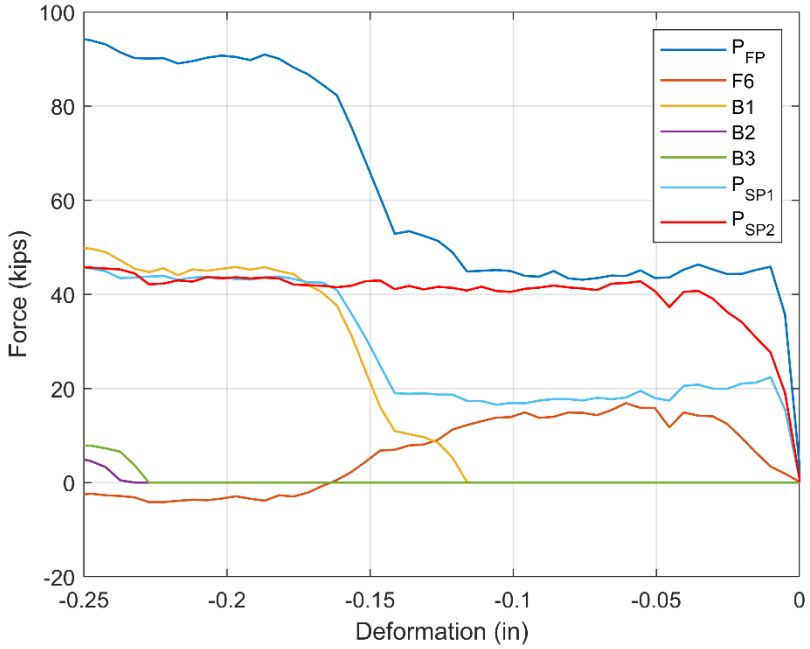


Figure 6-47. Axial Forces on Faceplates and Splice Plates and Bearing Forces in Model T1

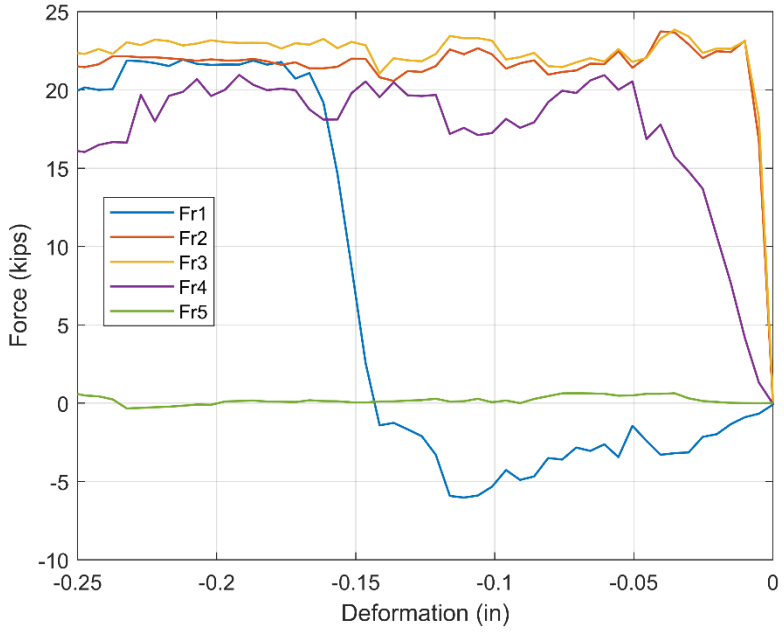


Figure 6-48. Friction Forces in Model T1

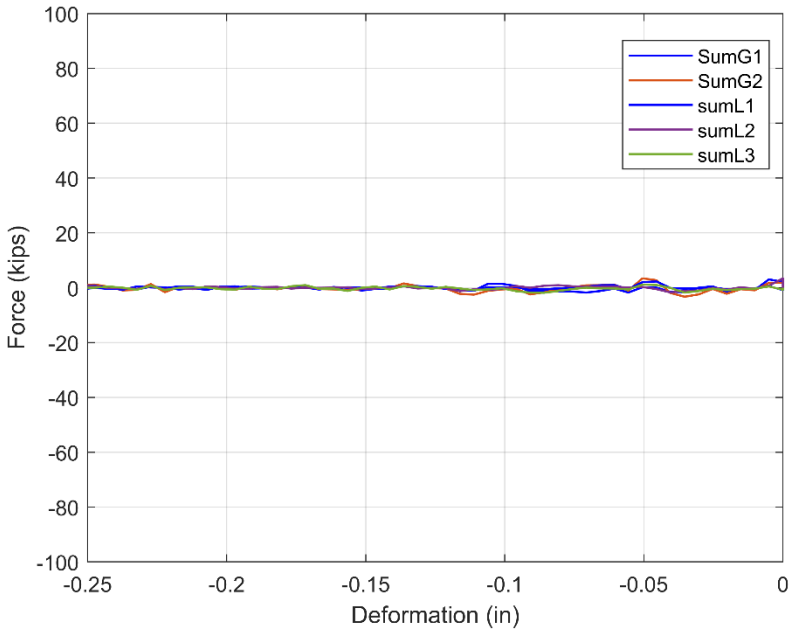


Figure 6-49. Force Equilibrium of Model T1

SECTION 7
DESIGN OF WALL SPECIMENS

7.1 General

A previously T-shaped C-PSW/CF tested by Kizilarslan and Bruneau (2023) was adopted for the Wall Specimen Test. The wall specimen to be tested is a vertical cantilever embedded at its base into a reinforced concrete footing needed to transfer the base moment into the laboratory strong floor. The set-up consists of two 420-kips diagonal (nearly vertical) actuators intended to apply an axial load to the wall, and one 220-kips horizontal actuators connected to the top of the wall and used to apply cyclic lateral loading (Figure 7-1). The dimensions of the T-shaped wall matched that of the previous specimen, with the addition of horizontal and vertical splices. Figure 7-2 shows the west and south elevations of the T-shaped wall, while Figure 7-3 shows the cross-section dimensions of the T-shaped wall. The faceplates have a thickness of 3/16 in. and are connected by 0.25-in. diameter tie bars at 4.5-in. center-to-center spacing. The objective of this large-scale test was to investigate the behavior of bolted C-PSW/CF connections. Simple hand calculations were used to design the bolted splice and set-up the layout of the splice details, and preliminary finite element simulations were used to predict the expected ultimate performance of the specimens beyond their target service levels.

A preliminary set of possible splice locations, bolt layouts for horizontal and vertical splices were developed and shared with the Project Advisory Group during the third and fourth project meetings, conducted via Zoom on December 14, 2022, and April 26, 2023. The PowerPoint slides presented during these meetings are included in Appendices C and D. This proposed testing program followed the philosophy presented in Sections 7.2 to 7.3 below.

Appendix I contains the final drawings of the specimen. Fabrication of the wall specimen was carried out by Cives and delivered to the University at Buffalo on December 22, 2023. The testing took place from February 27 to February 28, 2024.

The T-shaped wall with horizontal and vertical bolted splices was subjected to gravity and cyclic lateral loads, following a loading protocol that was developed and presented to the Project Advisory Group on February 13, 2024. PowerPoint slides presented at that meeting are included in Appendix E. It was understood that the proposed testing protocol for this specimen would be adjusted as each test unfolds, based on experimental observations. The specific number of cycles initially foreseen as part of this conceptual testing protocol, presented in Section 7.7, allowed: (i) to verify that the connection detail can resist set specific design loads, and; (ii) to investigate the extent to which a stable cyclic behavior can be developed beyond those specified design loads.

More detailed information on the specimen design and properties, test set-up, instrumentation and loading protocol for this T-shaped wall with bolted splice specimen is presented below.

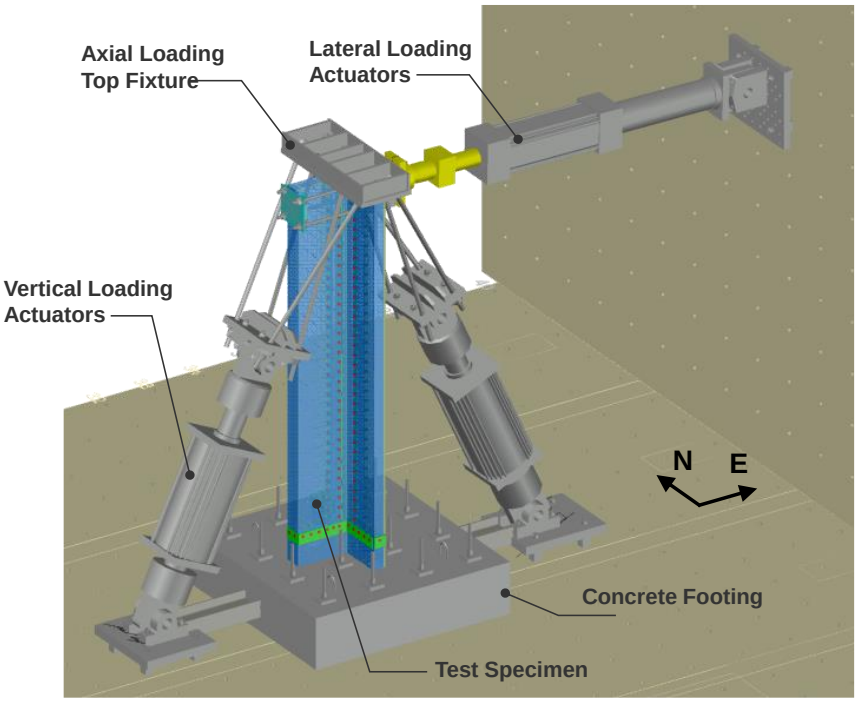


Figure 7-1. 3D View of Wall Test Setup

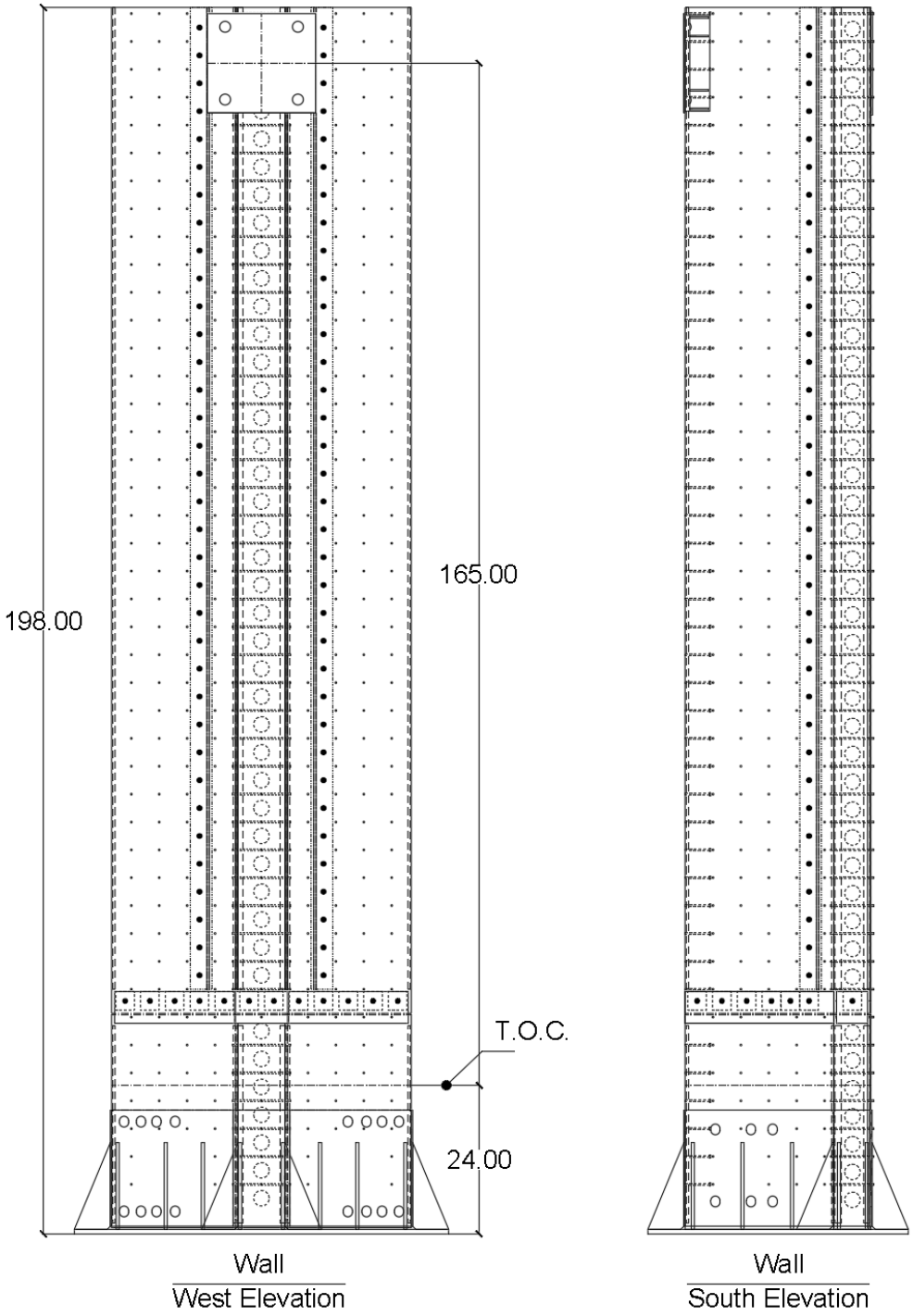


Figure 7-2. Elevations of T-shaped Wall

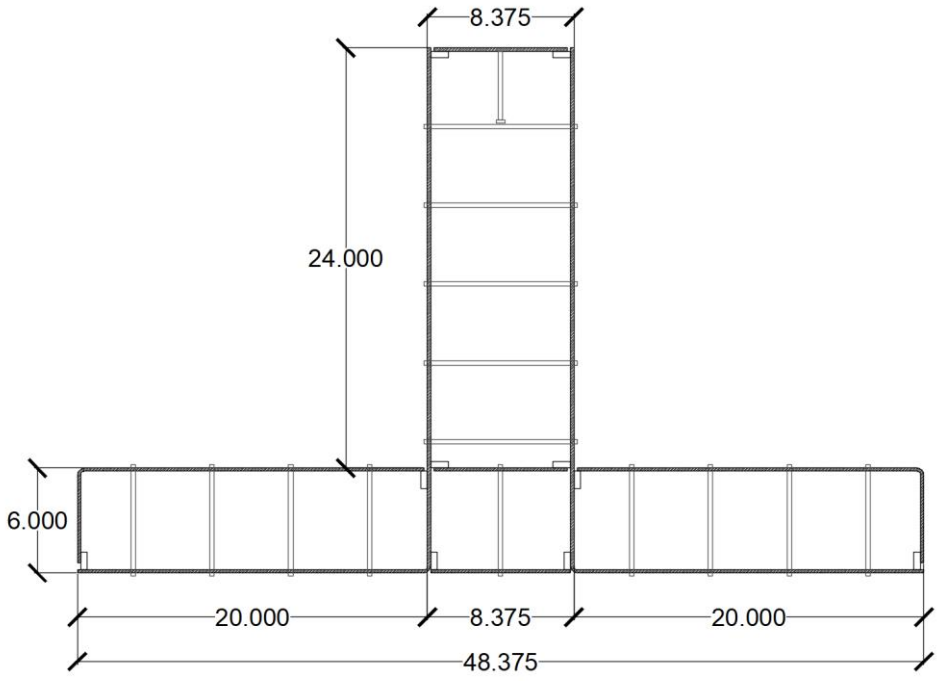


Figure 7-3. Typical Cross Section of T-shaped Wall

7.2 Design of Horizontal Splices

7.2.1 Tributary Area Approach

In this section, a simple hand calculation considering the area of the faceplate tributary to each bolt was used to design the bolt spacing required to achieve a specific target strength value. As shown in Figure 7-4, a tributary area A_g (equal to the bolt spacing S times plate thickness t, *i.e.*, $A_g = S \times t$) is identified, and this area is used to determine the gross section yield strength (A_gF_y) and to compare it with the tension strength (R_n) of the bolted connection. To calculate the tension strength of the bolted connection in this tributary area, AISC formulas are used to account for the various design limit states, including slip-critical resistance (AISC 360-16 J3-4), bearing strength (AISC 360-16 J3-6a), bolt shear strength (AISC 360-16 J3-1), and net section rupture strength (A_eF_u). The percentage of gross section yielding strength (A_gF_y) that can be developed by the connection is defined as the target strength value, expressed by Equation 7-1.

$$R_n = P = \alpha A_g F_y \qquad \text{Equation 7-1}$$

where P is the external force applied to the connection, and α represents the percentage of yield strength that has been developed.

Considering expected yield strength (R_yF_y) and tensile strength (R_uF_u) of faceplates equal to 55 ksi and 71.5 ksi, Table 7-1 shows the percentage of the gross section yielding strength developed by the tensile strength of the connection over its tributary area. In the table, these values are listed by comparing 1-1/4 in. and 3/4 in. diameter bolts for different bolt spacings, as well as various faceplate thicknesses. The objective was to design a specimen that would develop a percentage of the gross section yielding similar to what has been used in a SpeedCore project in Boston with bolted splices, designed by Magnusson Klemencic Associates (MKA). The Boston project used 3/8-in. faceplates with horizontal splices having 1-1/4-in. diameter A490

bolts spaced between 6 and 18 in. The corresponding range of the percentage of gross section yielding values for the Boston project is highlighted in the table. Values are also color coded to indicate which failure mode governs for the corresponding bolted tributary area: bearing strength in blue, net section rupture in green, and bolt shear failure in red. Although the slip-critical resistance was 2% less than the bearing strength ($2.4dtF_u$) in the design, it was disregarded because the desired failure mode for the connection was bearing failure, which requires slip to develop. Note that a double-shear connection was considered in these calculations, consistently with the fact that double splice plates were used in the Boston project.

It is noted in the table that, for the Boston project (with 3/8 in. faceplate thickness), when the design limit state is governed by bearing failure (i.e,, with strength of $2.4\,d\,t\,F_u$), the corresponding strength of the bolted tributary area with 6-in. spacing is equivalent to 65% of its gross section yielding strength. Therefore, a similar value was targeted for the design of the test specimen, where the thickness of faceplates and splice plates are 3/16 in., and the bolt diameter is 3/4 in. As shown in Table 7-1, a 4-in. bolt spacing for the test specimen can develop approximately 60% of the gross section yielding strength. Therefore, based on the information above, a detailed bolt layout for the horizontal splices of the wall specimen was developed using a spacing equal to (or close to) 4 in., as shown in Figure 7-5. Figure 7-6 shows the resulting 3D assembly of the T-shaped wall with vertical and horizontal splices. Inside and outside splice plates were designed for a double shear connection. While implementations may be all-bolts, at the specimen scale, it was elected to use a configuration with welding at the bottom of the splice plates and bolting at their top. Note that to facilitate construction in the field, oversized holes measuring 15/16” would be used in the faceplates, which are the central ply in the horizontal splice and outer ply in the vertical splices, so the specimen was similarly designed, with oversized holes measuring 15/16” for the 3/4” bolts used.

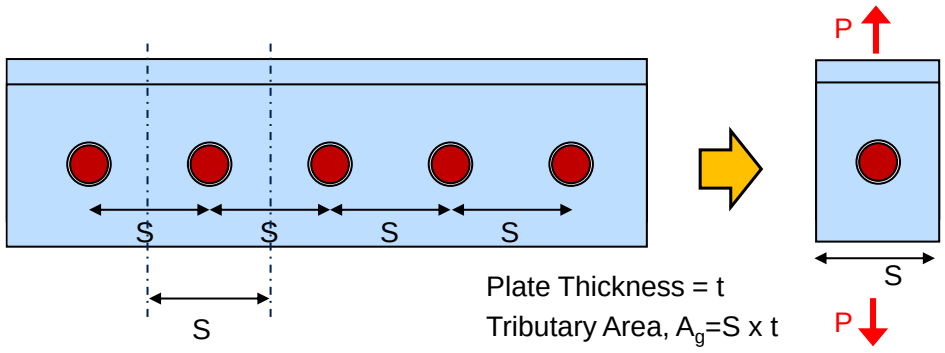


Figure 7-4. Tributary Area Approach

Table 7-1. Percentage of Gross Section Yielding Strength Developed by Bolted Splices

	For 3/4" Bolt								
	Spacing in Inches								
Plate Thickness	2	4	6	8	10	12	14	16	18
3/16	69%	59%	39%	29%	23%	20%	17%	15%	13%
1/4	69%	59%	39%	29%	23%	20%	17%	15%	13%
5/16	69%	59%	39%	29%	23%	20%	17%	15%	13%
3/8	69%	59%	39%	29%	23%	20%	17%	15%	13%
1/2	69%	55%	36%	27%	22%	18%	16%	14%	12%
3/4	69%	36%	24%	18%	15%	12%	10%	9%	8%
1	55%	27%	18%	14%	11%	9%	8%	7%	6%

	For 1-1/4" Bolt								
	Spacing in Inches								
Plate Thickness	2	4	6	8	10	12	14	16	18
3/16	28%	79%	65%	49%	39%	33%	28%	24%	22%
1/4	28%	79%	65%	49%	39%	33%	28%	24%	22%
5/16	28%	79%	65%	49%	39%	33%	28%	24%	22%
3/8	28%	79%	65%	49%	39%	33%	28%	24%	22%
1/2	28%	79%	65%	49%	39%	33%	28%	24%	22%
3/4	28%	79%	65%	49%	39%	33%	28%	24%	22%
1	28%	76%	51%	38%	30%	25%	22%	19%	17%

= Governed by Critical
#= Governed by 2.4dtFu
#= Governed by net section rupture
#= Governed by bolt failure

range for Boston MKA project

Selected Case

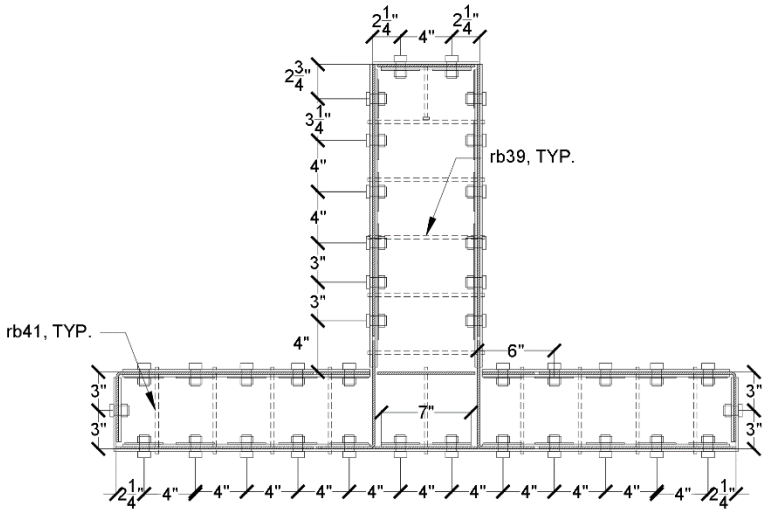


Figure 7-5. Cross Section of T-shaped Wall with Horizontal Splice

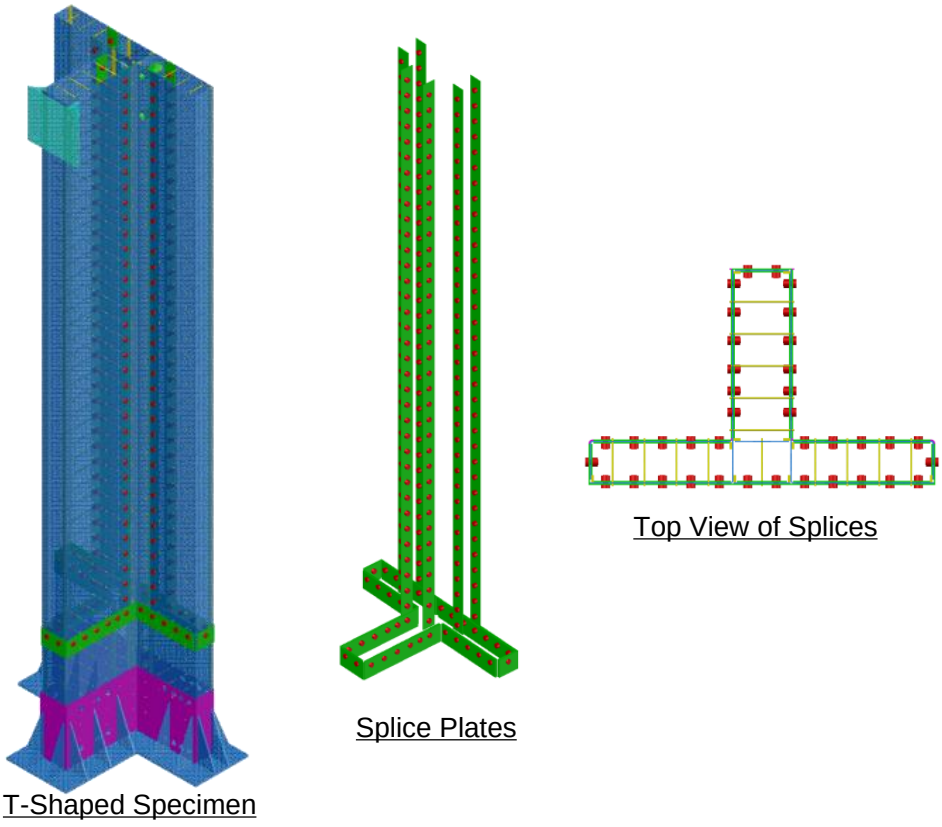


Figure 7-6. 3D Assembly of the Wall Specimen

7.2.2 Flexural Strength of Faceplates

The previous section introduced a simplified method using a tributary area approach to design the bolt spacings for horizontal splice of the wall, aiming for a bolted detail able to develop 60% of the yield strength ($0.6F_y$) of the faceplates in tension. This section provides details on the calculation of the moment capacity of the T-shaped section when the stress in the faceplates on the tension edge of the wall reaches $0.6F_y$.

Figure 7-7 shows the stress profiles of the T-shaped C-PSW/CF when the web is in compression. The figure shows three cases (Cases a to c) corresponding to three different neutral axis locations when the web is under compression. In these stress profiles, α and β represent the percentage of yield stress developed in tension and compression edge of faceplates, respectively. The value of α is set to be 0.6 in all cases, while the value of β is derived using similar triangles, assuming a linear stress profile along the depth of the wall. For a given cross-section geometry, an increase in axial force can push the compressive stress in the web past the yielding point. Consequently, Figure 7-8 provides a stress profile that accounts for the yielding of the web in compression. Similarly, Figure 7-9 shows the stress profiles when the flange is in compression.

Considering an expected yield strength (R_yF_y) of 55 ksi and concrete compressive strengths ranging from 4 ksi to 8 ksi, the P-M interaction curve for the test specimen has been determined using the stress profiles obtained for various axial loads, corresponding to the condition when the maximum axial tension stress reaches 60% of F_y. The resulting P-M interaction curves are plotted in Figure 7-10, with the corresponding locations of the neutral axis presented in Figure 7-11.

The detailed calculation of the resulting flexural strength of the wall is provided in Appendix J2 and J3.

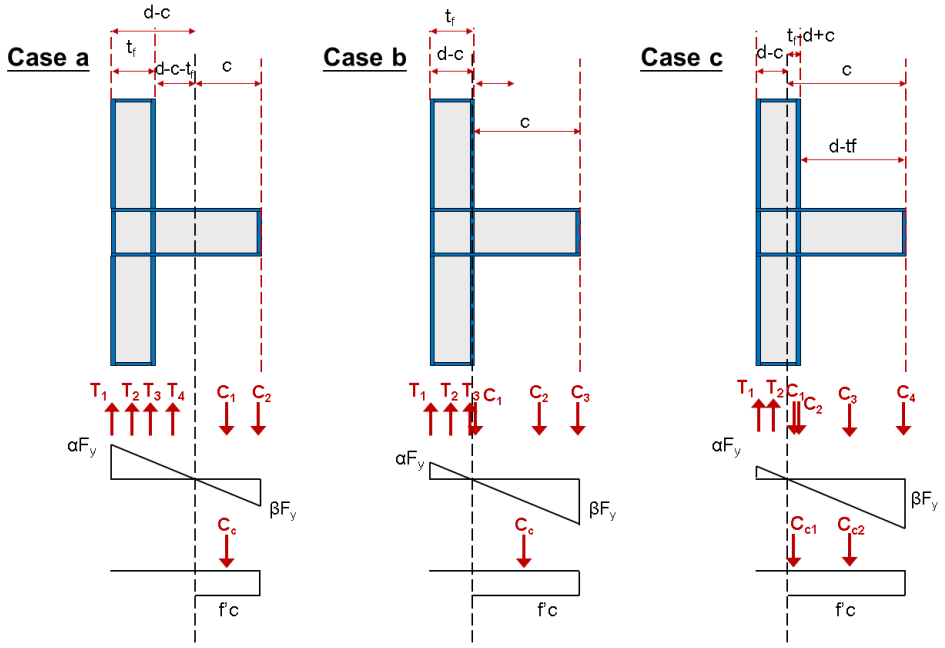


Figure 7-7. Stress Profile of T-Shaped C-PSW/CF (Web in Compression, Elastic)

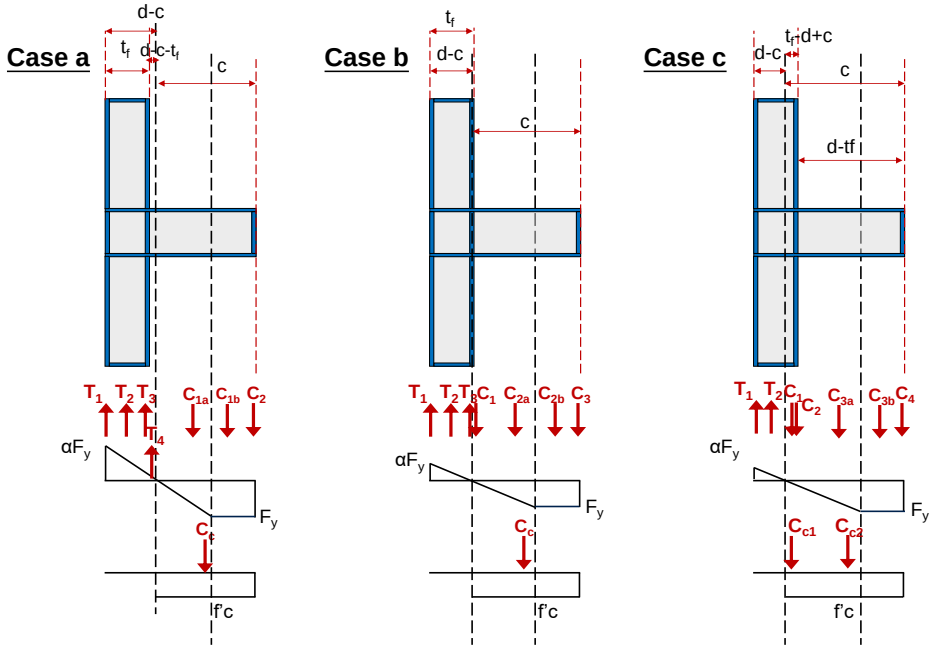


Figure 7-8. Stress Profile of T-Shaped C-PSW/CF (Web in Compression, Yielding Stage)

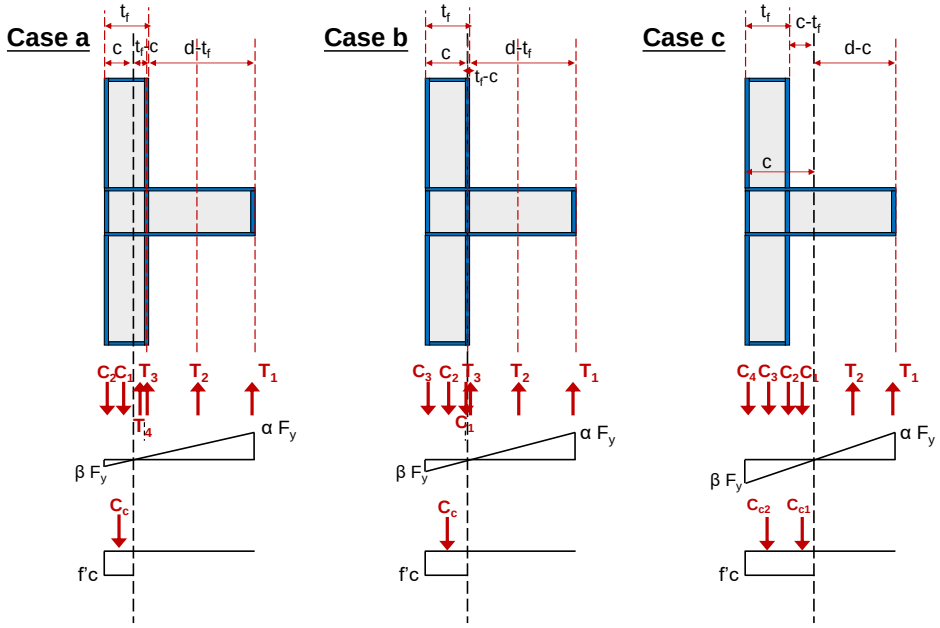


Figure 7-9. Stress Profile of T-Shaped C-PSW/CF (Flange in Compression, Elastic)

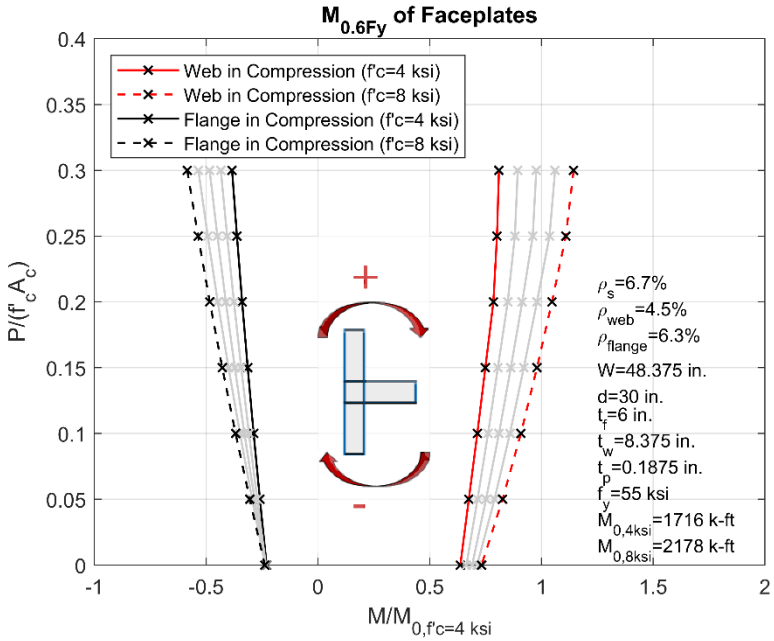


Figure 7-10. P-M Interaction Curve for the T-shaped Section for a maximum tension stress limited to $0.6F_y$

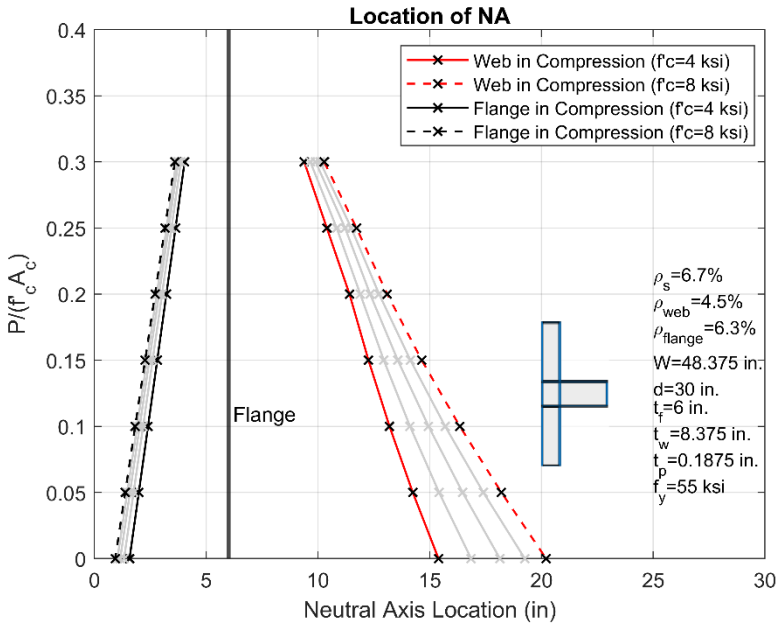


Figure 7-11. Neutral Axis Location of the T-shaped Section for a maximum tension stress limited to $0.6F_y$

7.2.3 Flexural Strength of Horizontal Splices

The C-PSW/CF with bolted connections exhibited ductile behavior in component-level tests when the design was controlled by bearing. Bearing strengths obtained in these tests were achieved with significant deformation. This was therefore selected as the preferred failure mode in designing the wall specimen. Furthermore, while all bolted concepts performed well during the component tests, for practical reasons, blind bolts or Shurikens were deemed to be more convenient for installation by (generally) allowing the bolts to be pre-tensioned before concrete is poured, saving construction time and providing better control over pretension values. For the connection with through rods, pipe-sleeves are needed in the connection. If the compressive strength of the pipe-sleeves is not strong enough to resist the compressive forces impacted by the pretension, the rods can only be torqued after concrete is infilled and partially cured. Therefore, with agreement by the Project Advisory Group, it was decided to use Shurikens for the wall test, and to design the horizontal splice to be governed by the bearing limit state.

This section describes how the flexural strength of the horizontal splice was calculated when the design is governed by bearing strength. Figure 7-12 shows the force distribution of bolts in the horizontal splices for the designed bolt layout (for the ten locations of bolts along the wall depth, accounting for the multiple bolts along the wall width at each location). The bolts at the tension edge are assumed to develop their bearing strength (either $2.4dtF_u$ or $3.0dtF_u$, to calculate and compare the strength of the splice for both conditions), while the other bolt forces are determined by similar triangles assuming a linear force distribution profile, as shown in Figure 7-12 (a). However, for walls having a greater axial load, the neutral axis will shift towards the flange (as shown in Figure 7-12 (b)), and the forces on the bolts on the compression side might exceed the bearing strength designated for the bolts on the tension edge. In such instances, a compression limit is defined to ensure that the compression strengths considered do not exceed the bearing strength at each of the bolt locations, as shown in Figure 7-12 (b). Note that for this compression

bearing strength to develop, the concrete must be compressed by a value equal to the hole elongation needed to develop this bearing strength, something that is not known to be possible at the onset.

Similarly, when the flange is in compression, the distribution of bolt forces is assumed to follow a linear pattern, as shown in Figure 7-13. For this given geometry of the T-shaped section, the neutral axis is consistently located within the flange region. Unlike the scenario when the web is under compression, for this specific specimen geometry, the compressive forces that bolts can develop are relatively small.

Given a tensile strength (F_u) of the faceplates of 71.5 ksi, a bolt diameter of 0.75 in., and concrete compressive strengths ranging from 4 ksi and 8 ksi, the P-M interaction curves of the specimen's horizontal splice can be calculated for various axial loads. For the bearing strength equal to *2.4dtFu*, the P-M interaction curves are shown in Figure 7-14, with the corresponding neutral axis locations in Figure 7-15. For the bearing strength equal to *3.0dtFu*, the P-M interaction curves are shown in Figure 7-16, with the corresponding neutral axis locations illustrated in Figure 7-17.

The detailed calculation of the moment capacity for the specimen's horizontal splice is provided in Appendix J4 and J5.

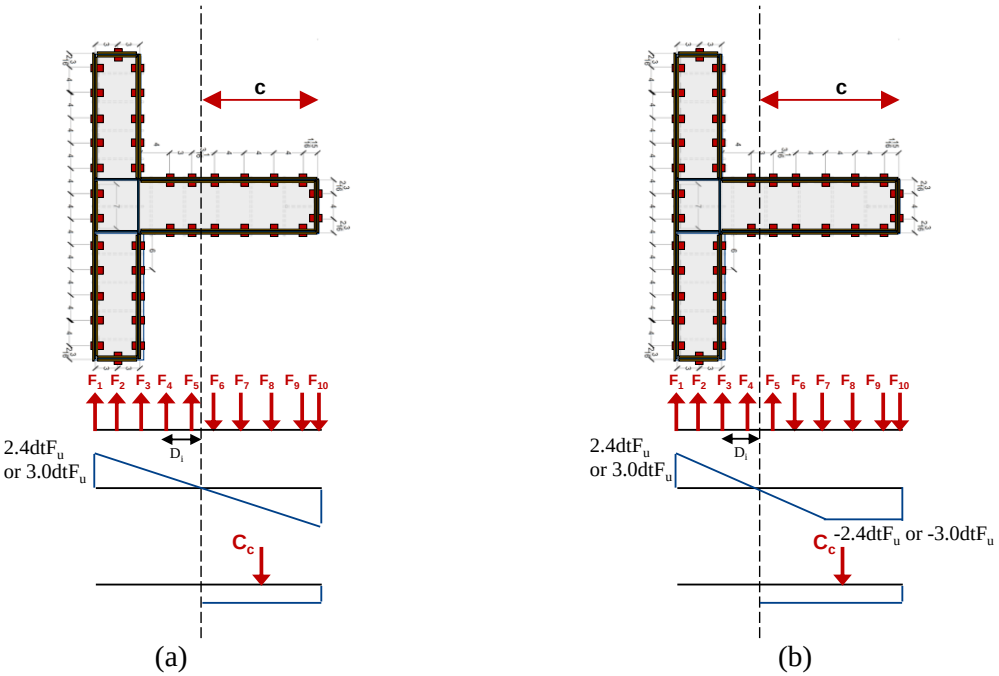


Figure 7-12 Force Distribution of Bolts in Horizontal Splices (Web in Compression)
(a) Elastic Distribution (b) Elastic Distribution with Compression Limit

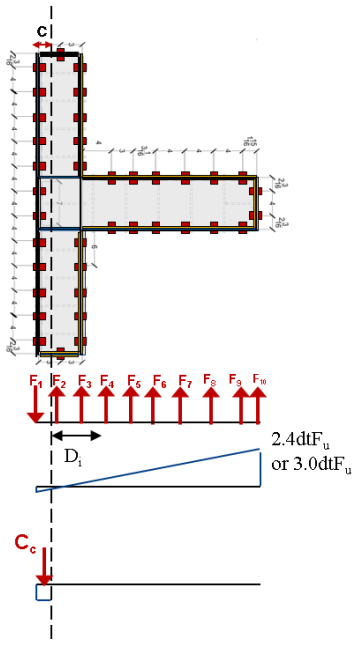


Figure 7-13. Force Distribution of Bolts in Horizontal Splices (Flange in Compression)

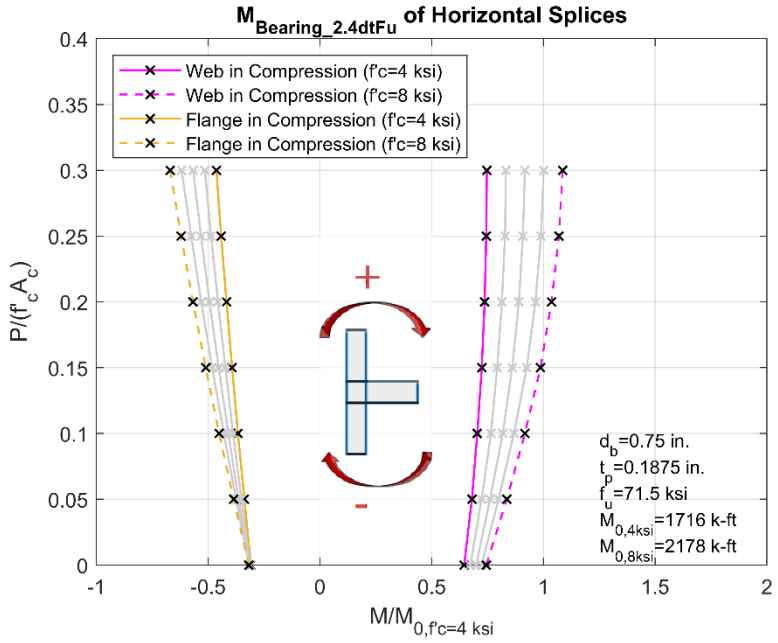


Figure 7-14. P-M Interaction Curve for the Horizontal Splices (Bearing Strength = $2.4dtF_u$)

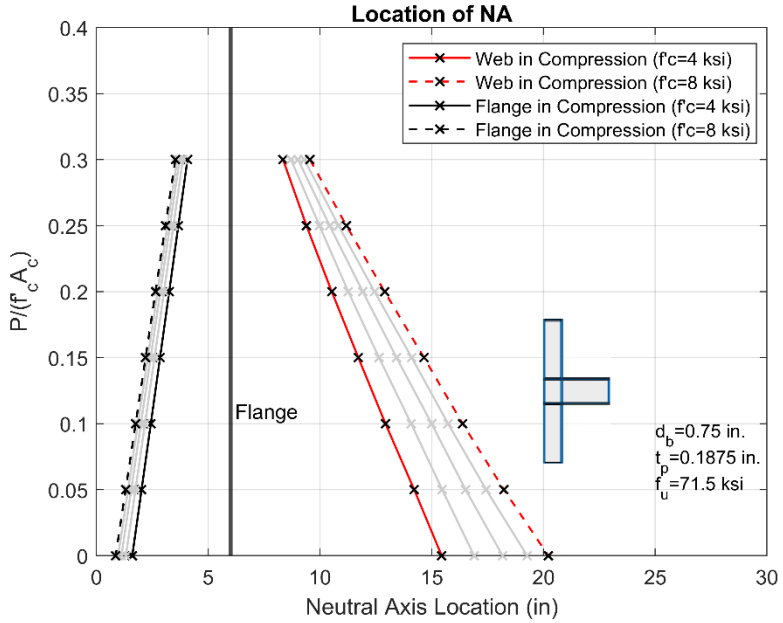


Figure 7-15. Neutral Axis Location of the T-shaped Section (Bearing Strength = $2.4dtF_u$)

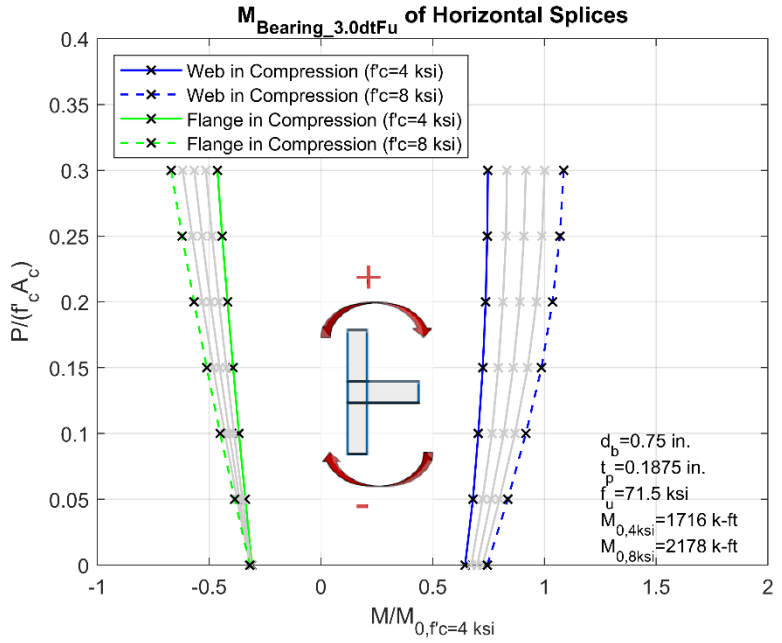


Figure 7-16. P-M Interaction Curve for the T-shaped Section (Bearing Strength = $3.0dtF_u$)

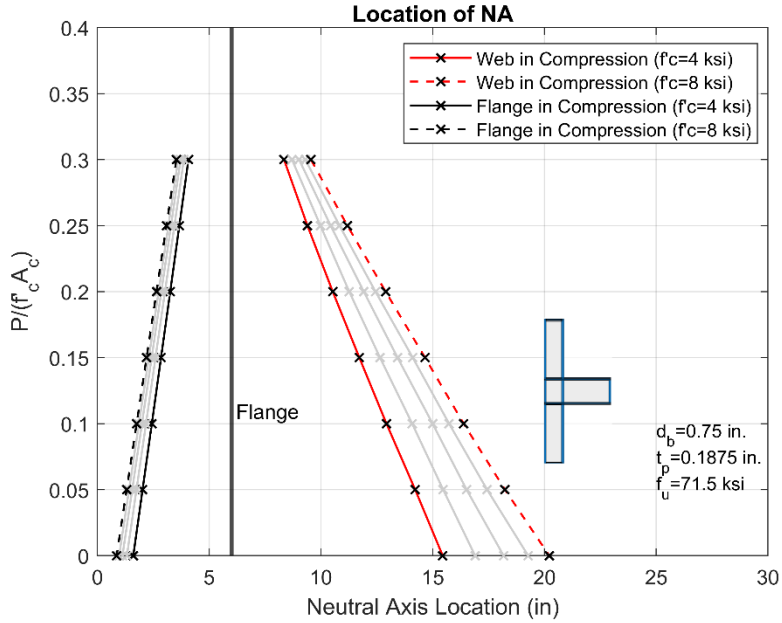


Figure 7-17. Neutral Axis Location of the Horizontal Splices (Bearing Strength = $3.0dtF_u$)

7.2.4 Summary of Moment Capacity for Test Specimen

The previous sections have outlined the process for calculating the P-M interaction curves for both the faceplates and the horizontal splices of the T-shaped C-PSW/CF specimen. The axial load to be applied to the specimen, specified to be proportionally similar to values representative of the aforementioned Boston project, was determined to be 10% of the concrete's compressive strength ($10\%A_c f'_c$). At the specimen design stage, the yield strength (F_y) and tensile strength (F_u) of the faceplates were assumed to be 55 ksi and 71.5 ksi, respectively, and the compressive strength of concrete (f'_c) was taken as 6 ksi. Table 7-2 summarizes the resulting flexural strength of the test specimen obtained at the design stage considering these properties, corresponding to various limit states. Additionally, the actual material strength were obtained from material testing (i.e., from steel coupon and concrete cylinders): the average yield strength (F_y) and tensile strength (F_u) of the faceplates were 63.62 ksi and 71.75 ksi, respectively, and the compressive strength of concrete (f'_c) on the day of testing was 6.75 ksi (as reported in Section 7.5). Consequently, Table 7-3 summarizes the flexural strengths of the test specimen for the actual material strength and same limit states considered previously. Differences are on the order of 5~15%, and mainly due to the differences between the expected and actual material strengths. More specifically: (1) a 0.2% difference in flexural strength is due to the 0.35% difference between expected and actual ultimate tensile strength (F_u) when calculating bearing strength; (2) a 10% difference in flexural strength is attributed to the actual yield strength being 15.6% greater than the expected yield strength (F_y) when calculating $M_{0.6Fy}$,M_y,and M_p, and; (3) a 4.4% to 5.4% differences in positive direction and 2.2% to 4.3% differences in negative direction of flexural strength are due to actual concrete strength being 12.5% greater than expected concrete compressive strength alone for all cases.

Table 7-2. Summary of Moment Capacity for Test Specimen (Design Stage)

	Positive Dir.	**Negative Dir.**	
$M_{0.6Fy}$	1422.59	657.70	k-ft
M_y	1869.76	799.32	k-ft
M_p	2011.84	1311.16	k-ft
$M_{bearing_2.4dtFu}$	1225.14	604.22	k-ft
$M_{bearing_3.0dtFu}$	1404.28	702.94	k-ft

Table 7-3. Summary of Moment Capacity for Test Specimen (Actual Material Strength)

	Positive Dir.	**Negative Dir.**	
$M_{0.6Fy}$	1629.57	754.65	k-ft
M_y	2138.84	917.72	k-ft
M_p	2297.98	1509.38	k-ft
$M_{bearing_2.4dtFu}$	1290.54	631.55	k-ft
$M_{bearing_3.0dtFu}$	1470.78	731.29	k-ft

7.3 Design of Vertical Splices

This section presents two approaches to calculate the shear flows in vertical splices on the T-shaped C-PSW/CF. The first approach considers that the shear is only resisted by the steel components, which results in a more conservative design. The second approach considers the composite section, including the contribution of concrete, which is likely more realistic than the previous approach. The steel component approach is presented in Section 7.3.1, and the composite section approach is presented in Section 7.3.2. Figure 7-18 shows the T-shaped section with vertical splices. Note that, in this case, single interior splice plates are used.

7.3.1 Shear Strength by Steel Component Approach

This section outlines the first approach adopted to design the vertical splices for the T-shaped wall specimen, relying only on the steel to resist the vertical shear forces. Figure 7-19 shows the elevation of the T-shaped C-PSW/CF. To determine the required shear force for the vertical splices, the shear force at the horizontal splice level, denoted as V_{sp} , is used, as defined by the following equation:

$$V_{sp} = \frac{M_{sp}}{H_{sp}} \qquad \text{Equation 7-2}$$

where M_{sp} is the required moment at the horizontal splice level, calculated as the maximum of $M_{0.6F_y}$ and $M_{bearing_3.0dtF_u}$ defined in the previous sections, and H_{sp} is the height from the center of the horizontal actuator applying load at the top of the wall specimen to the center of the horizontal splices.

Figure 7-20 shows the shear flows from the top of flange to the location of the vertical splices. To determine the vertical bolt spacing for the vertical splices, the formula of shear flow is applied, as shown in the equation below:

$$f_{sp} = \frac{V_{sp} Q_{sp}}{I_s}$$ Equation 7-3

where Q_{sp} is the first moment of area from the top of the flange to the center of vertical splices, I_s is the moment of inertia of the steel alone.

The detailed calculation of the shear flow is provided in Appendix J6. The result shows a corresponding shear flow f_{sp} of 2.348 k/in when the horizontal shear splice design strength is reached. To ensure that the wall behaves as a single composite member, the design objective was to prevent slippage along the vertical splices. Note that all vertical splices for the specimen only used internal splice plates, with all bolts in the vertical splices therefore acting in single shear. For a 3/4-in. diameter A490 bolt in single shear condition, the slip-critical resistance R_{slip} is 11.9 kips. Therefore, the required maximum vertical spacing (S_v) of bolts was calculated to be 5.07 in. Since all tie bars in the C-SPW/CF specimen were spaced at 4.5 in., the bolt spacing (S_v) along the vertical splices was therefore arranged to match the spacing of the tie bars, ensuring that the spacings between tie bars and bolts can be equally distributed, as shown in Figure 7-21.

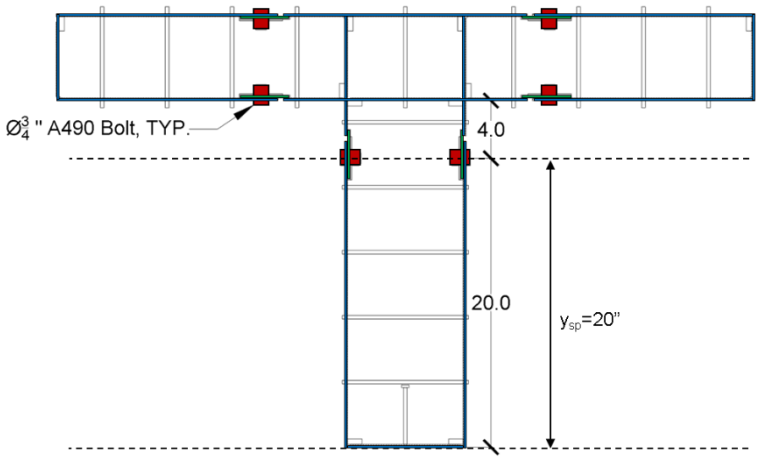


Figure 7-18. Cross Section of Vertical Splices

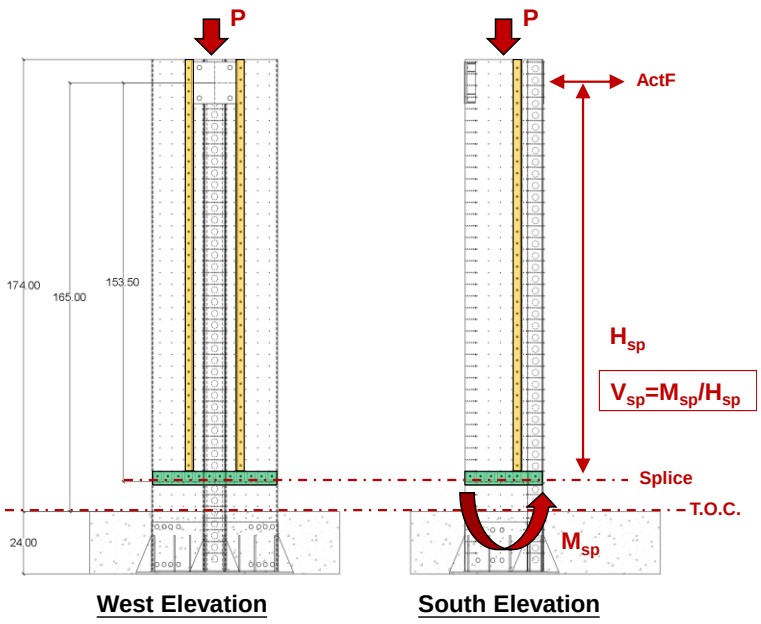


Figure 7-19. Elevations of T-shaped C-PSW/CF

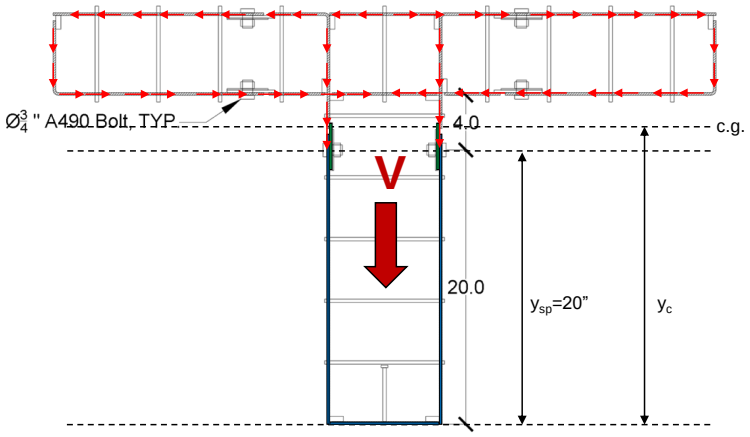


Figure 7-20. Shear Flow on the T-shaped Section

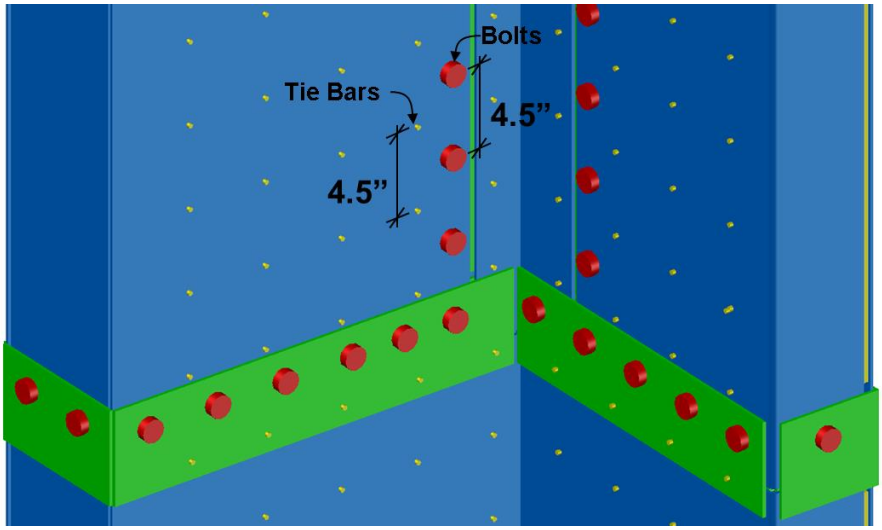


Figure 7-21. Designed Bolt Spacing for Vertical Splices

7.3.2 Shear Strength by Composite Section Approach

This section describes the design of the vertical splices considering the composite section of the T-shaped wall. Figure 7-22 shows the elevation of the T-shaped wall above the horizontal splices with applied axial load P and applied shear force V. Figure 7-23 provides a free-body diagram that separate the T-shaped wall into left and right components along the vertical splices. This diagram shows the distribution of the applied axial loads (αP and βP), and section forces (T_1 to T_4, C_1 to C_2, and C_c). Similarly to Figure 7-7, T_1 and T_2 represent the tensile forces acting on the flange, T_3 and T_4 represent the tensile forces acting on the web, C_1 and C_2 represent the compressive forces acting on the web, and C_c represent the compressive forces on the concrete.

The applied axial load is distributed to the left and right parts of the wall (i.e., on each side of the vertical splice) in proportion to the axial stiffness of each part, calculated as:

$$\alpha = \frac{(EA)_L}{(EA)_L + (EA)_R}$$

$$\beta = \frac{(EA)_R}{(EA)_L + (EA)_R}$$

Equation 7-4

where $(EA)_L$ and $(EA)_R$ represent the axial stiffness on the left and right parts of the wall.

As shown in Figure 7-23, the total shear forces (F_L and F_R) along the vertical splice can be obtained from vertical equilibrium of each part of the wall, namely:

$$F_L = T_1 + T_2 + T_3 + T_4' + \alpha P$$

$$F_R = C_1 + C_2 + C_c - T_4'' - \beta P$$

Equation 7-5

The detailed calculation is provided in Appendix J7. The result shows that the required shear force is 683.15 kips, and the corresponding shear flow is 2.225 k/in. This is 5.2% smaller than the value calculated by the method in Section 8.3.1. For a 3/4-in. diameter A490 bolt in single shear condition, the slip-critical resistance R_{slip} is equal to 11.9 kips. Therefore, the required vertical spacing (S_v) of bolts is calculated to be 5.35 in. As mentioned in the previous section, a spacing of 4.5 in. was adopted for the vertical splices to ensure that the spacing between tie bars and bolts be consistent along the wall height.

The detailed calculation of the shear flow is provided in Appendix J7.

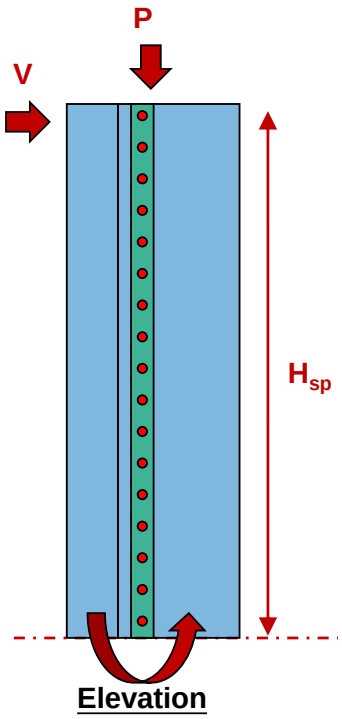


Figure 7-22. Elevations of T-shaped C-PSW/CF above Horizontal Splices

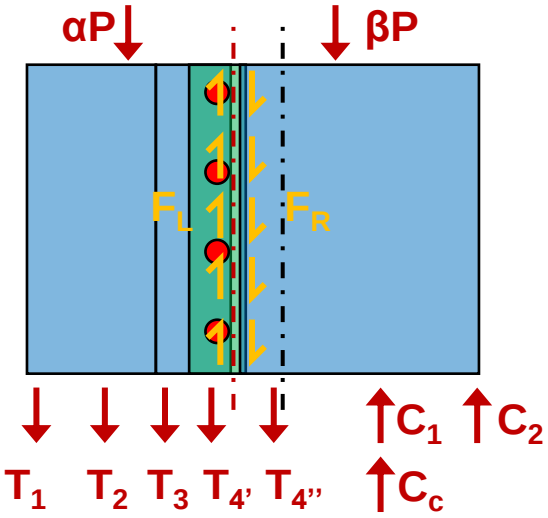


Figure 7-23. Section Forces of T-shaped C-PSW/CF (Web in Compression)

7.4 Test Setup

A test setup previously designed and used for the testing of T-shaped walls by Kizilarslan and Bruneau (2023) was adopted for the T-shaped wall specimen with bolted splices. Per the configuration shown in Figure 7-1, the test setup and the wall specimen were assembled at Structural Engineering and Earthquake Simulation Laboratory (SEESL) at the University at Buffalo.

The height of the wall, measured from the top of the footing to the centerline of the horizontal actuator, is 13.75 ft. The entire test setup measured from the strong floor to the top of the wall is 16.5 ft. The dimension of the reinforced concrete footing is 8 ft. by 8 ft. in plan and 2 ft. in height. 16-DYWIDAG rods are used to tie the concrete footing to the strong floor. Each rod was pretensioned to 130 kips to prevent uplift during the test.

Figure 7-24 shows the elevation of the diagonal actuators, which are anchored to both the strong floor and the top of the wall at angles of 64.2° and 65.5°, respectively. These angles changed by about ±5º during the test as the top of the wall drifted back and forth (considering the maximum displacement reached during the test).

Figure 7-25 shows preparation for casting concrete into the wall specimen. A first batch of concrete was ordered to pour the footing on 12/22/2023 (no concrete in the wall itself), and a second batch to fill the wall specimen on 1/19/2024. Figure 7-26 shows the photo of the complete test setup with wall specimen in place (and under axial load).

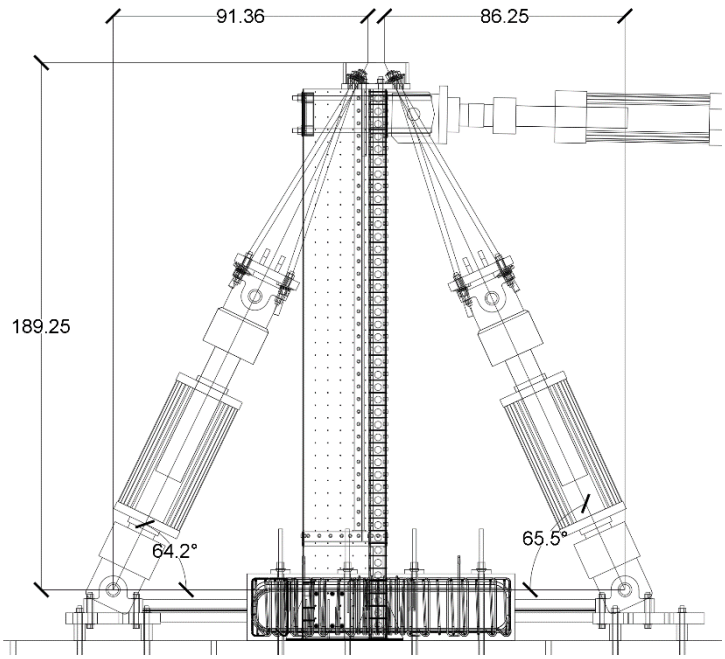


Figure 7-24. Elevation of the Vertical Actuators

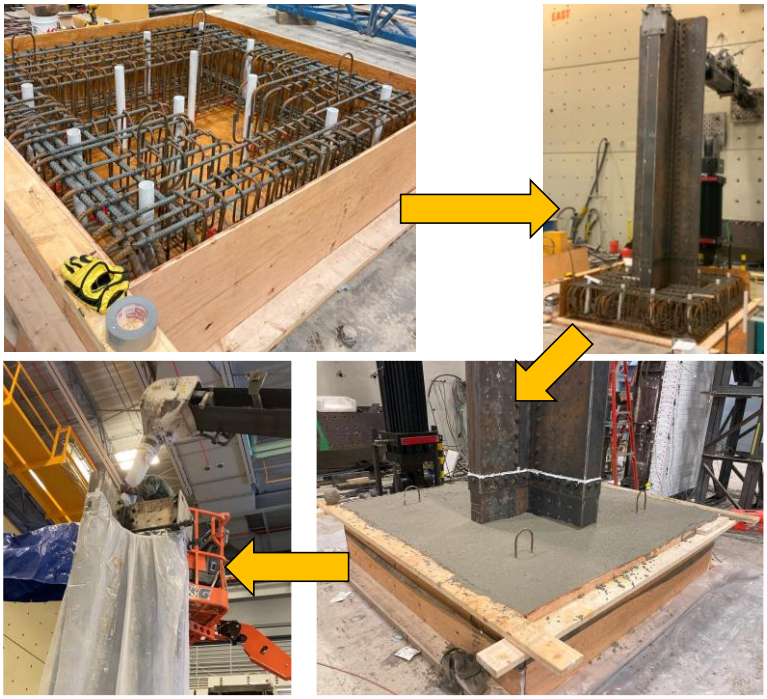


Figure 7-25. Construction Sequence of the Test Specimen

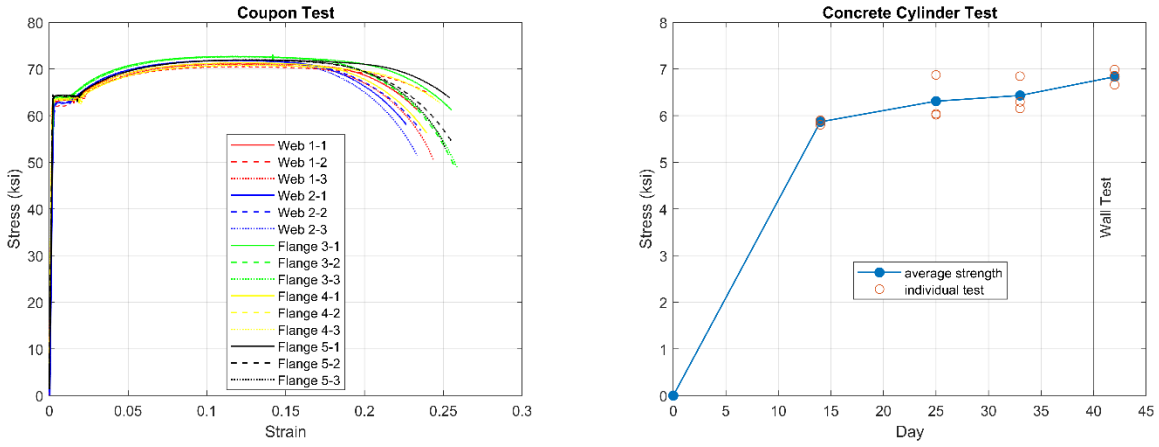


Figure 7-26. Finished Test Setup for the Wall Test

7.5 Material Properties

A572 Gr. 50 steel was used in the construction of all specimens. All of the 3/16 in. thick steel plates used for the wall specimens came from the same heat. Fifteen coupon specimens were cut from an extra length of the 3/16-in. steel plates provided for this purpose, and the coupon specimens were tested under uniaxial tension. Results are presented in Figure 7-27 (a) and Table 7-4. A "Yield plateau" was observed in the stress-strain behavior of the tested coupons. The average yield strength, F_y, for the steel plate is 63.62 ksi, and the average ultimate strength, F_u, for each coupon test is 71.75 ksi.

For concrete, twelve 6in. x12in. cylinders were taken on the day of pouring from the concrete batch used for the infill of the wall specimen. This number of cylinders was taken to periodically test some to keep track of concrete strength over time. Figure 7-27 (b) shows the development of concrete strength over time, and the number of days of curing on the date of the wall test is marked in the figure.



(a) Steel Coupon Test (b) Concrete Cylinder Test

Figure 7-27. Material Test of Wall Specimen

Table 7-4. Coupon Test Results

Coupon Specimen		F_y (ksi)	F_u (ksi)
Web	1-1	63.63	71.30
Web	1-2	62.48	70.53
Web	1-3	63.43	71.06
Web	2-1	62.92	71.84
Web	2-2	62.79	71.91
Web	2-3	62.80	71.88
Flange	3-1	64.17	72.75
Flange	3-2	64.31	72.74
Flange	3-3	63.78	73.23
Flange	4-1	63.75	71.38
Flange	4-2	63.47	70.84
Flange	4-3	63.54	70.85
Flange	5-1	64.37	72.03
Flange	5-2	64.26	71.94
Flange	5-3	64.58	71.94
Average		**63.62**	**71.75**

7.6 Instrumentations

Strain gauges, string pots, and linear pots were used to measure the deformation of the wall specimen during cyclic lateral loadings. The measurements focused on documenting the flexural deformation of the specimens and tracking some local effects of the connection and test setup.

Figure 7-28 shows 46 strain gauges installed on the specimen. The strain gauges were placed at 6.5 in., 15.5 in., and 24.5 in. from the top of the foundation on the faceplates of the wall. These three levels were selected to capture the strain profiles under the horizontal splice, above but near the horizontal splice, and above and some distance away from the horizontal splice. This setup was intended to capture the changes in strain profile along the wall's height, with a focus on areas near the bolted connections where phenomena such as bearing and sliding are likely to occur. Figure 7-29 shows the photograph of the installed strain gauges from a southwest view. The strain gauges were placed along the perimeter of the T-shaped wall to record the strain profile on the cross section, and use those strains to monitor if the faceplate yielded locally under cyclic lateral loads.

Figure 7-30 shows 26 linear potentiometers (LPs) placed on the specimen, positioned at the top and bottom of the horizontal splices. Since the horizontal splices were welded on the bottom, the linear pots on the bottom were not expected to record significant displacement (other than those corresponding to strains over the gage length spanned by the linear pots). The linear pots on the top of the horizontal splices were intended to measure the slip of bolts and to obtain information on splice rotation under cyclic lateral loads. Figure 7-31 shows the installed linear potentiometers from a southwest view.

Figure 7-32 shows the 12 vertical string potentiometers installed around the perimeter of the T-shaped wall specimen. These string pots were used to measure vertical displacements from the top of the concrete to

4.9 in. above the horizontal splices (20 in. above the foundation). These devices were installed to measure vertical deformation around the wall and to calculate the rotation of the wall about its flexural axis (Figure 7-33). The rotation, θ, of the wall can be calculated by the following equation:

$$\theta = \frac{(\Delta VSP_{East} - \Delta VSP_{West})}{Wall\ Depth} \qquad \text{Equation 7-6}$$

where ΔVSP_{East} and ΔVSP_{West} represent the deformations recorded by the vertical string potentiometers on the east and west sides of the wall, respectively.

Finally, Figures 7-34 and 7-35 show the plan and elevation views of the wall specimen with horizontal string potentiometers. Eleven horizontal string pots were installed to measure the lateral displacement at different heights from bottom to top of the wall, to obtain information on the wall's deflected shape.

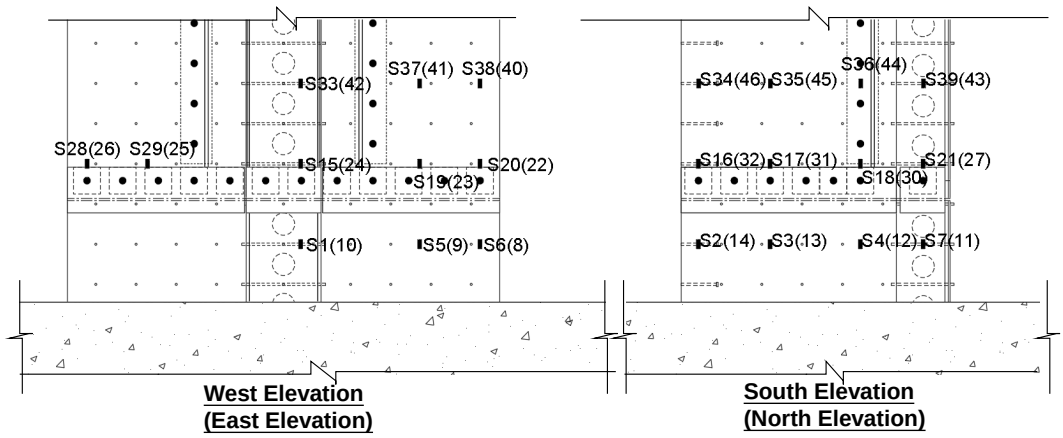


Figure 7-28. Strain Gauges on Wall Specimen

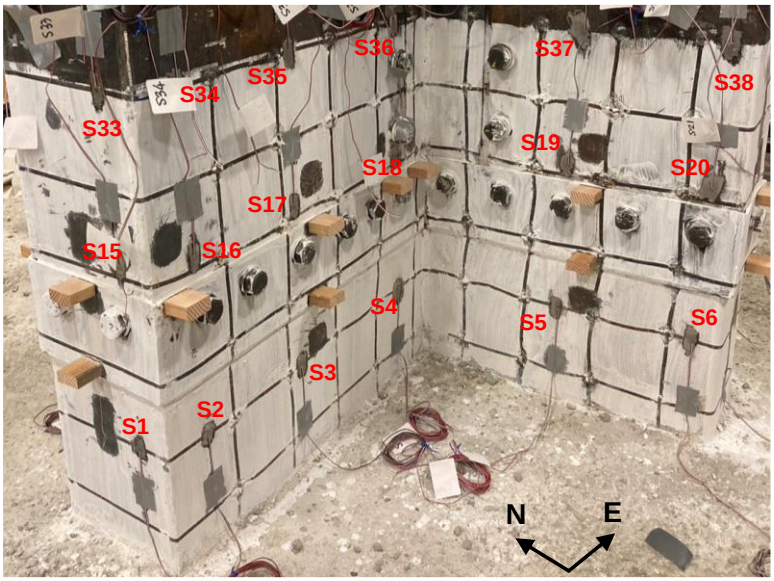


Figure 7-29. Installed Strain Gauges from Southwest View

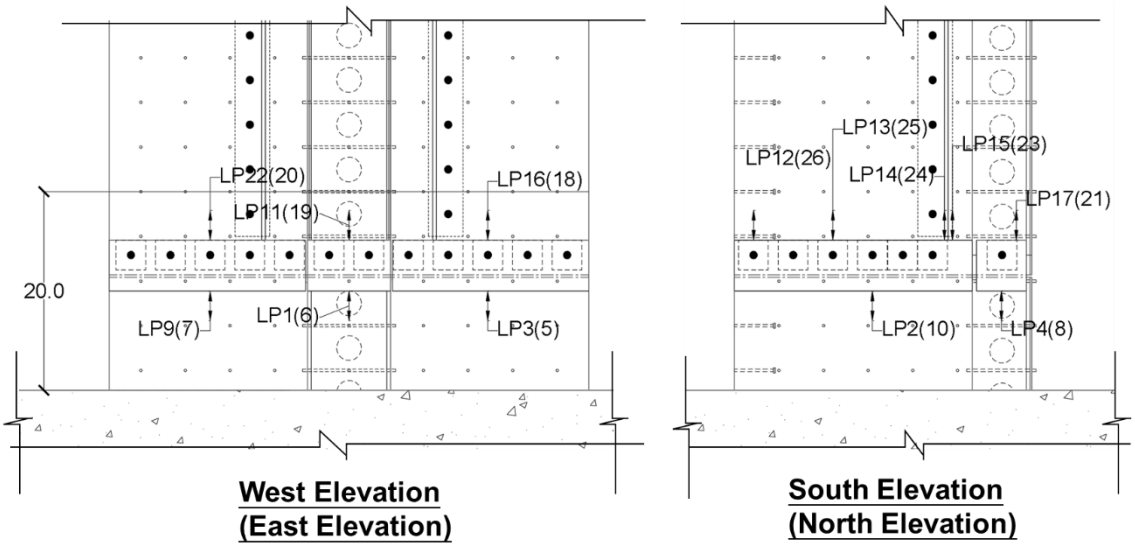


Figure 7-30. Linear Potentiometers on Wall Specimen

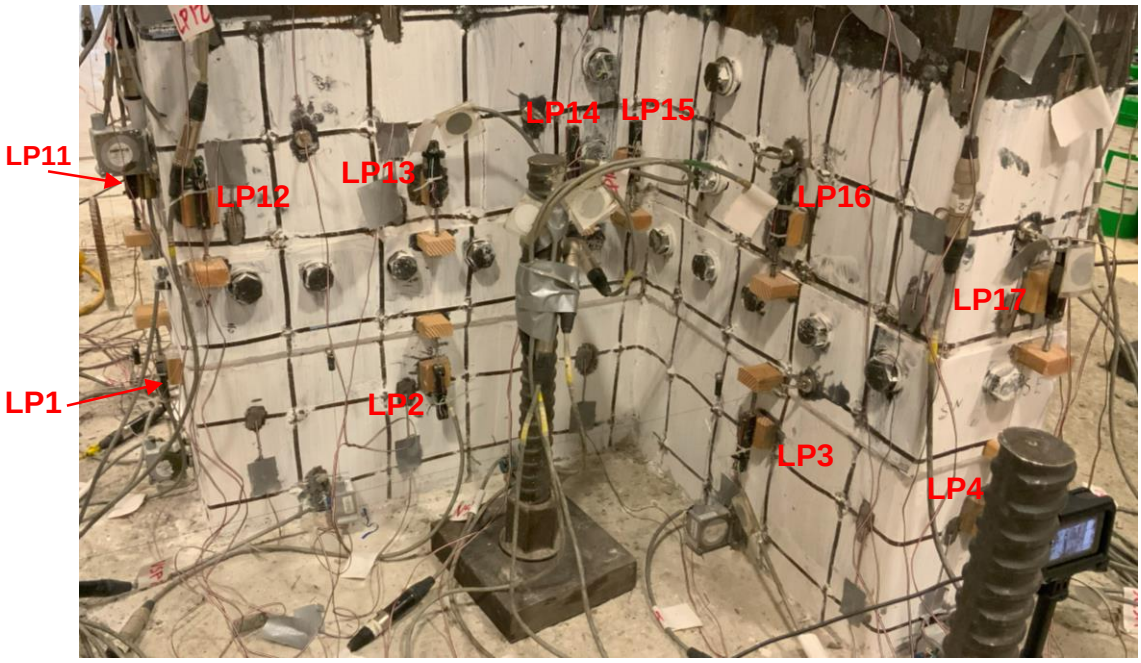


Figure 7-31. Linear Potentiometers from Southwest View

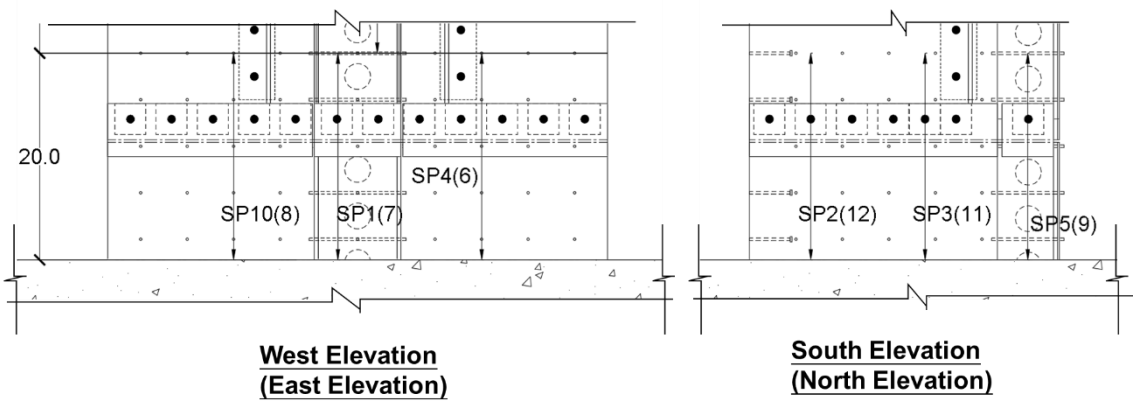


Figure 7-32. Vertical String Potentiometers on Wall Specimen

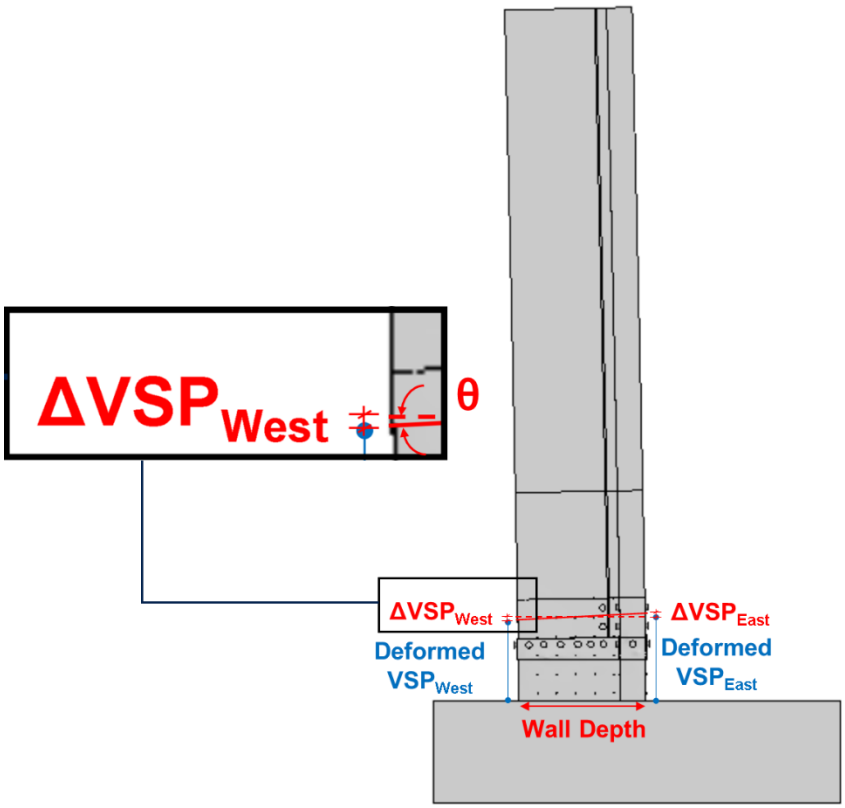


Figure 7-33. Deformed VSP on West and East Sides of the Wall

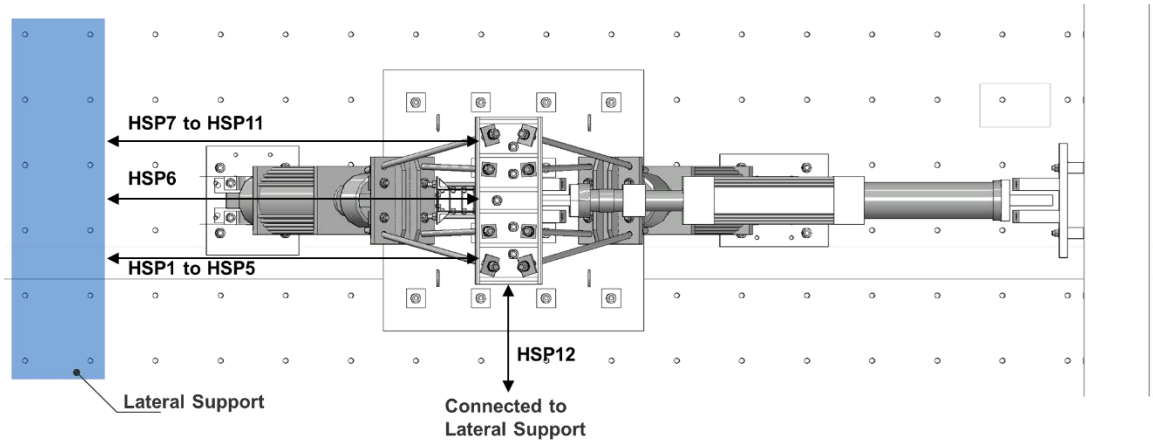


Figure 7-34. Horizontal String Potentiometers on Wall Specimen (Plan View)

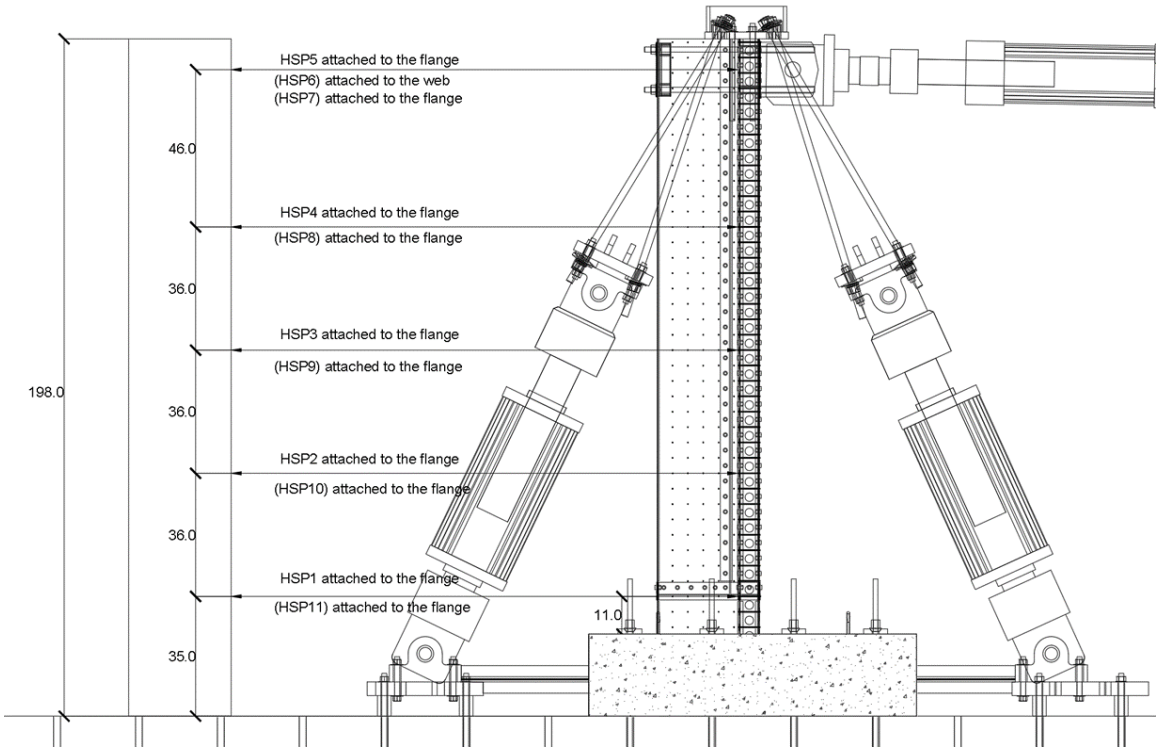


Figure 7-35. Horizontal String Potentiometers on Wall Specimen (Elevation View)

7.7 Loading Protocol

Figure 7-36 shows the force-displacement behavior of the wall as predicted from a preliminary finite element analysis result. The analysis was performed to capture the monotonic pushover behavior of the wall in the positive and negative directions before the test. In this analysis, bolts were arbitrarily pretensioned to, 23 kips, which is 66% of the minimum pretension value specified by AISC Table J3.1 for the A490 3/4" bolts used in the specimen. The figure shows the lateral force V_1 corresponding to the point when the first bolt starts developing bearing stress. The lateral force V_{BT} in the figure defines the load at which a slip plateau is observed in the force-displacement curve when significant slip behavior occurs in the splice.

Table 7-5 presents the originally planned loading protocol for the wall test. The previously mentioned lateral forces from finite element analysis are listed in the table as reference points. The design load, P_w, defined as Step 5 in the table, refers to the design strength required to develop the moment capacity of the horizontal splices for bearing strength limit state of $2.4dtF_u$, as described in Section 7.2.3. Additionally, the test Steps 1 to 3 were determined as corresponding to 25%, 50%, and 75% of the design load, respectively. An additional step (Step 4 in the table) was introduced to capture the possible slip plateau. If the slip was to occur after 100% P_w, then the intent was to skip Step 4. After Step 5 (design load stage), the loading protocol was intended to increase deformations in somewhat regular steps to determine the ductility, maximum strength, and rate of strength degradation of the connection, as it undergoes its failure mechanism.

During testing, in each step, the protocol was to follow a force-controlled mode until the load reaches the design load P_w. However, for safety, this force-controlled mode only means that the load was applied up to the target value in each step – for safety, the horizontal actuator was controlled by increasing displacements

until the target loads were achieved. Beyond the design load, the loading protocol switched to displacement control, with the displacement increments to be determined in real-time during the test based on observed displacement values obtained in prior steps such as to provide relatively regular increments of displacement ductility.

All the steps in the loading protocol were intended to consist of at least 3 cycles, but also to include more cycles if needed to assess the presence of stiffness or strength degradation upon repeated cycling. The displacement values listed in the table were derived from the preliminary finite element analysis, and it was expected that these would be updated as needed during the test. As mentioned earlier, this loading protocol was to be slightly modified based on observations while running the test. The actual loading protocol used during the test is presented in the next section.

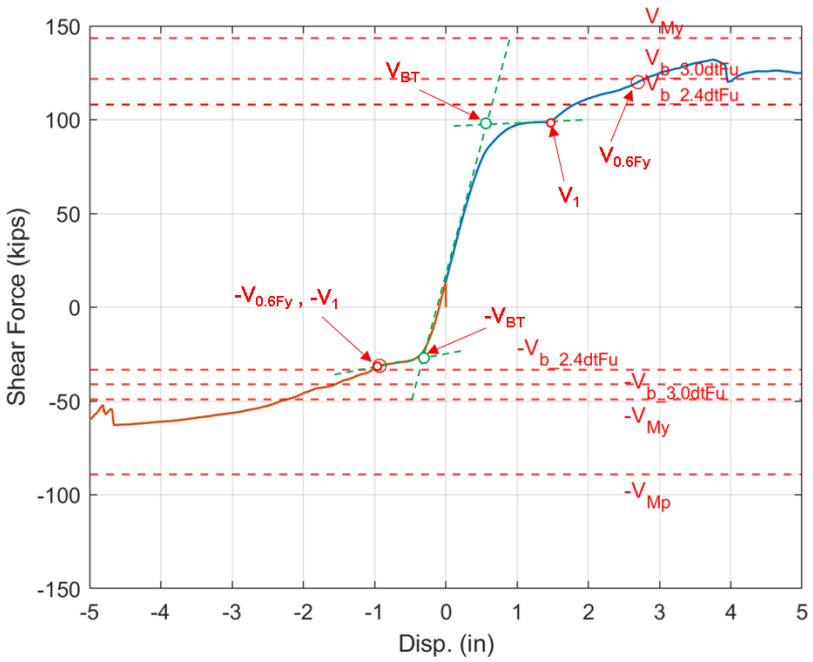


Figure 7-36. Force-displacement behavior predicted from preliminary Finite Element Analysis Result

Table 7-5. Original Loading Protocol for Wall Test

Spliced T-Wall Load Protocol									
Step	Disp. (in) +	Drift (%) +	Force (kips) +	Disp. (in) -	Drift (%) -	Force (kips) -	Cycles	Note 1	Note 2
0	0.00	0.00	0	0.00	0.00	0	-		
1	0.45	0.27	24	-0.13	-0.08	-8	3	0.25Pw	
2	0.90	0.55	49	-0.30	-0.18	-17	3	0.5Pw	
3	1.35	0.82	73	-0.50	-0.30	-25	3	0.75Pw	
4	-	-	-	-	-	-	3	V_{slip}	TBD
REF	0.60	0.36	97	-0.29	-0.18	-28	-	V_{BT}	Bilinear Tangent
REF	1.48	0.90	99	-0.92	-0.56	-31	-	V_1	1st Bearing
REF	2.70	1.64	120	-1.00	-0.61	-31	-	V_0.6Fy	
5	1.80	1.09	97	-1.00	-0.61	-33	3	1.0Pw	Vb_2.4dtFu
6	2.30	1.39	110	-1	-1	-37	3		Transition
7	2.80	1.70	122	-1.55	-0.94	-41	3		Vb_3.0dtFu
8	-	-	144	-2.24	-1.36	-49	3		V_{My}
*Pw=Design Load									

7.8 Proposed Repair Scheme for Resilience of Bolted CPSW/CF

In addition to investigating the flexural strength and ductility of the horizontal splice and the shear strength of the vertical splices, a proposed repair scheme (Figure 7-37) was developed. Because the intended failure mode was bearing failure of the faceplate along the horizontal splice, it was foreseen that it would be possible to re-center the wall, and weld the top of the horizontal outside splice plate. The objective was to use the filet welding strength to substitute for the bearing strength of the failed bolted connection. The following calculations shows that the welding strengths (R_{weld}) along the top edge of the outside splice plate is greater than the bearing strength ($R_{bearing}$) of $3.0dtF_u$, at both locations of maximum stresses on the web and flange of the wall.

Strength at the tip of the web (west face of the specimen), where two bolts are used:

$$R_{weld} = 1.5 \times 0.6F_{Exx} \times 0.707a \times L_{web} = 69.94\ kips$$

$$R_{bearing} = 2 \times 3.0 \times dtF_u = 60.54\ kips \qquad \text{Equation 7-7}$$

$$R_{weld} > R_{bearing}, OK!$$

Strength at the tip of the flange (east face of the specimen), where twelve bolts are used:

$$R_{weld} = 1.5 \times 0.6F_{Exx} \times 0.707a \times L_{flange} = 404\ kips$$

$$R_{bearing} = 12 \times 3.0 \times dtF_u = 363.23\ kips \qquad \text{Equation 7-8}$$

$$R_{weld} > R_{bearing}, OK!$$

where the welding material strength F_{Exx} is equal to 70 ksi, the welding dimension a is equal to 3/16 in., and the length of weld on edges of web and flange (L_{web} and L_{falnge}) are equal to 8.375 in. and 48.375 in.

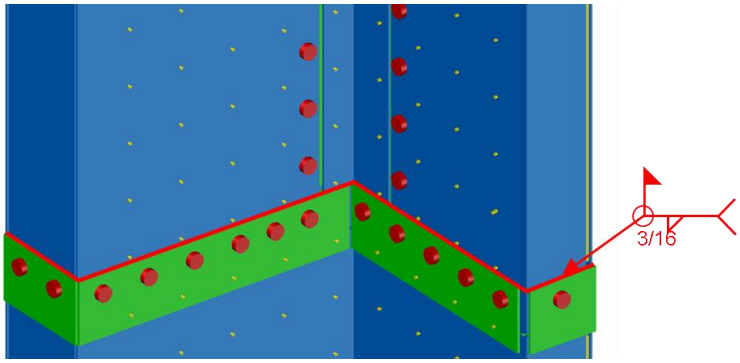


Figure 7-37. Proposed Repair Scheme by Welding at the Top of the Horizontal Splice

SECTION 8
WALL SPECIMEN TEST

8.1 General

This chapter presents the results and findings of the wall specimen test. The objective of the wall test was to verify several aspects of its structural performance under axial and cyclic lateral loads. Specifically, it aimed to confirm the flexural strength of the horizontal splice, governed by bearing strength, and to validate the shear strength of the vertical splices, which are governed by slip-critical resistance. Observations and results from the wall specimen tests are outlined in Section 8.2. Post-test observations are discussed in Section 8.3. Data analysis from the tests is presented in Section 8.4. Finally, a summary of the wall test findings is provided in Section 8.5. Actual material strengths were used for all test data analysis in this chapter. Recall that the actual yield strength (F_y) and tensile strength (F_u) of the faceplates were 63.62 ksi and 71.75 ksi, respectively, and the actual compressive strength of concrete (f'_c) is 6.75 ksi (as reported in Section 7.5).

8.2 Test Observations and Results of Wall Specimens

Testing of wall specimen started on 2/27/2024. The test began with the application of axial loads using the vertically inclined actuators, while the horizontal actuators remained at zero displacement. The forces in each vertical actuator were gradually increased until toward the target loads of 152.7 kips and 151.1 kips calculated to each apply and axial loads of 137.5 kips for the theoretical actuator angles (from AudtoCad drawings) of 64.2° and 65.5°, thereby applying an axial force equivalent to 10% of $A_c f'_c$ (=275 kips) on the cross-section of the T-shaped wall. At that point, the angles of the west and east vertically inclined actuators were measured to be 63.6° and 64.7°, and the respective axial loads were 152.4 kips and 151.8 kips, resulting in an axial load of 237.8 kips. Figure 8-1shows the axial strains observed in the specimen after the vertical loads were applied, with recorded strains ranging from 50με to 150με; fluctuations were attributed

to strain-gage proximity to tie bars (an effect observed from finite element analysis, as will be demonstrated later). These values correspond to 2.3% to 6.8% of the yielding strain, ε_y. The results obtained from the strain gauges confirm that the cross-section experienced relatively uniform stresses under the applied axial load.

Figure 8-2 shows the history of the axial force on the wall. The vertical actuators were driven in a force-controlled mode, and the resulting axial force on the wall was the summation of the vertical forces from the two vertical actuators. The wall was tested over two days, and the vertical loading and unloading of the actuators on 1st and 2nd days are marked in the figure. During the cyclic lateral loadings, some fluctuations occurred during the reversals of "travel direction" along a given displacement cycle, after reaching a peak target displacement amplitude. Also, a sudden sliding of both eastern and western actuators was observed during the test on the 1st day, which created an instantaneous axial loading fluctuation; however, after adjusting the position of wide flange beams that span between the bottom of the vertical actuators and the concrete footing (Figure 8-3), no further sliding was observed during testing.

Cyclic testing proceeded following the loading protocol shown in Table 8-1 (slightly modified from the reference protocol shown in Table 7-5). Figure 8-4 shows the corresponding displacement and load history from the horizontal actuator during the test (note that horizontal loading was typically "held constant" for periods of time to allow taking close pictures of the specimen near peak displacements). The test began with the horizontal loads being applied in force control mode, from Steps 1 to 4, which corresponded to 25% to 100% of the design strength, P_w. The design strength P_w represents the shear force applied to the wall when the flexural strength of the horizontal splice reaches the bearing strength ($2.4dtF_u$), as calculated in Section 7.2. Note that the small horizontal component force resulting from the vertical actuators as top of the wall drifted was neglected when calculating the shear force of the wall in the loading protocol (but

was duly taken into account during data analysis, as shown later). After Step 4, the horizontal loads changed to be displacement control (note that "force control" in the previous steps is a bit of a misnomer, because horizontal actuator were still in displacement control mode for safety, but the displacements were applied up to the point where the target load for each step was reached, which required applying the first cycle of displacement manually to determine the values where the positive and negative cycle target loads were reached, and automating the subsequent cycles to apply those displacements). Cycles at progressively increasing displacement amplitudes were applied in Steps 5 to 9. Starting from Step 10, single-sided displacements were applied due to severe buckling observed on the horizontal web splice plates during Step 9, prompting a decision to continue testing with cycles only in the negative direction. Figure 7-1 provides a definition of the cardinal directions used throughout this report to monitor the condition of the specimens, and to describe movements of parts of the connection throughout the entire test program for the wall.

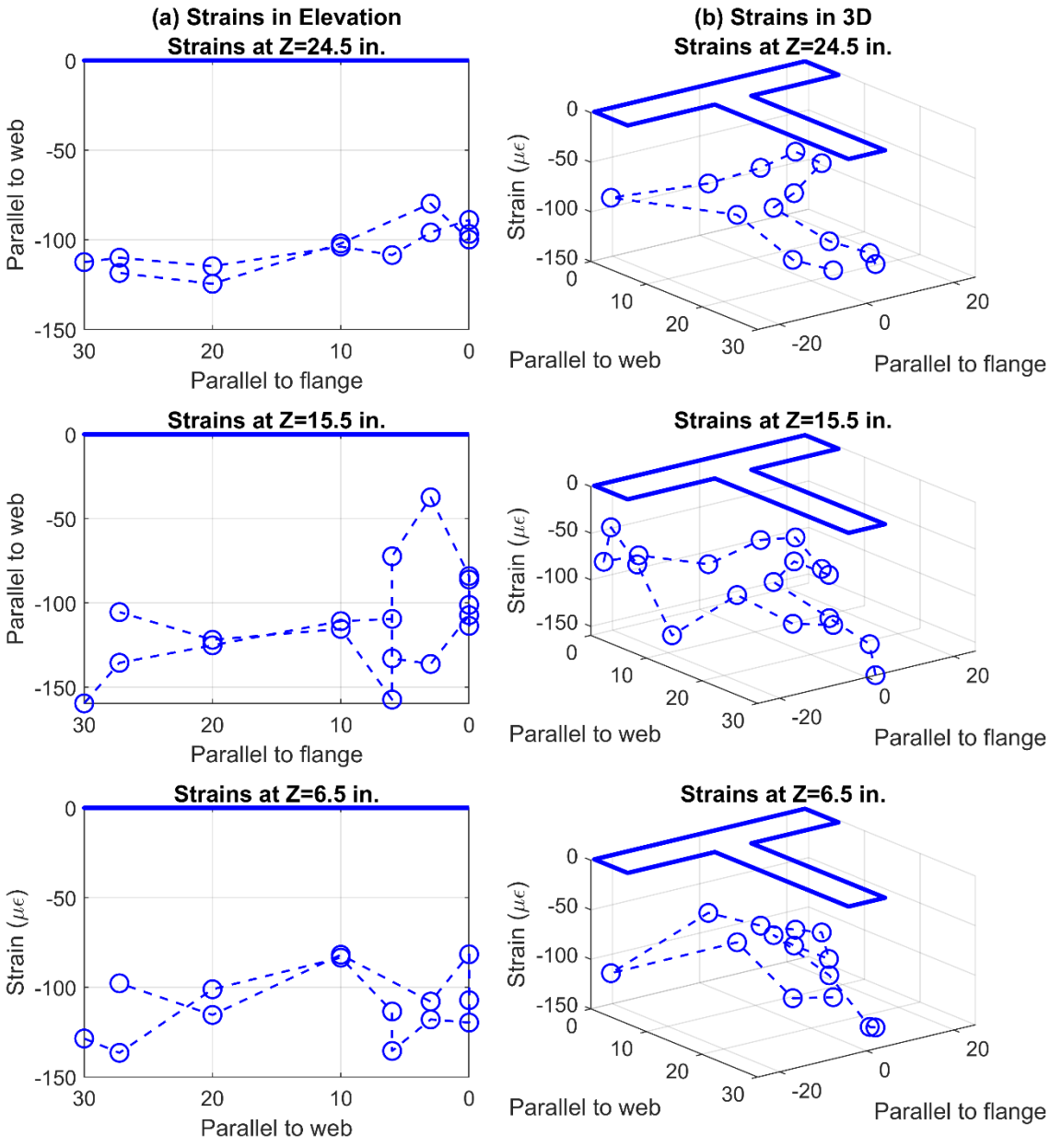


Figure 8-1. Axial Strains at Vertical Loading Stage in (a) Elevation and (b) 3D

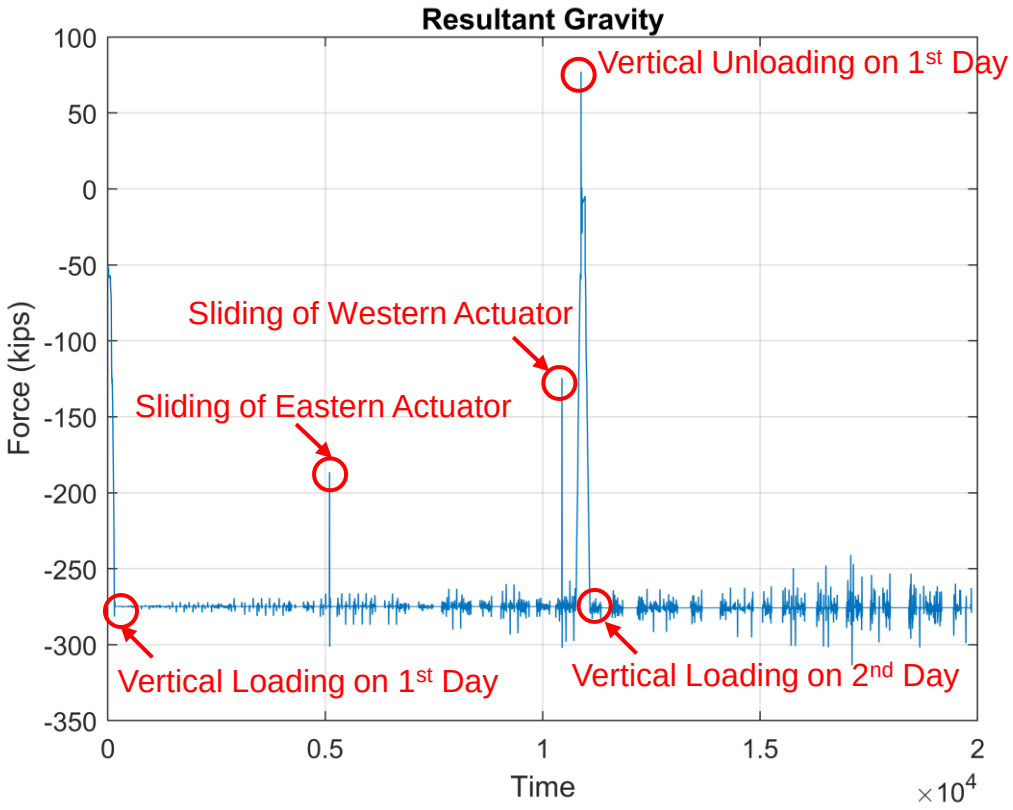


Figure 8-2. Vertical Loading History



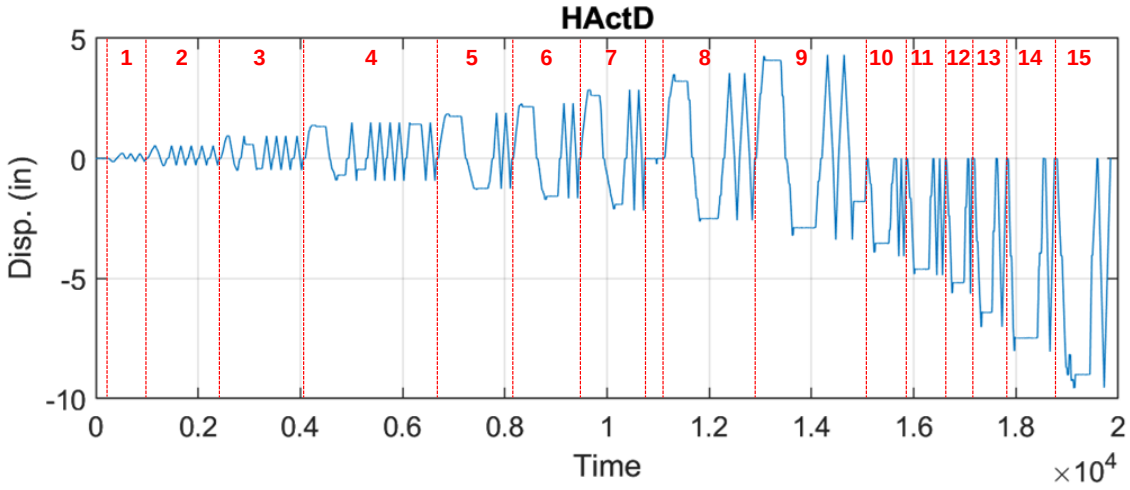
(a) Western Bottom of Vertical Actuator

(b) Eastern Bottom of Vertical Actuator

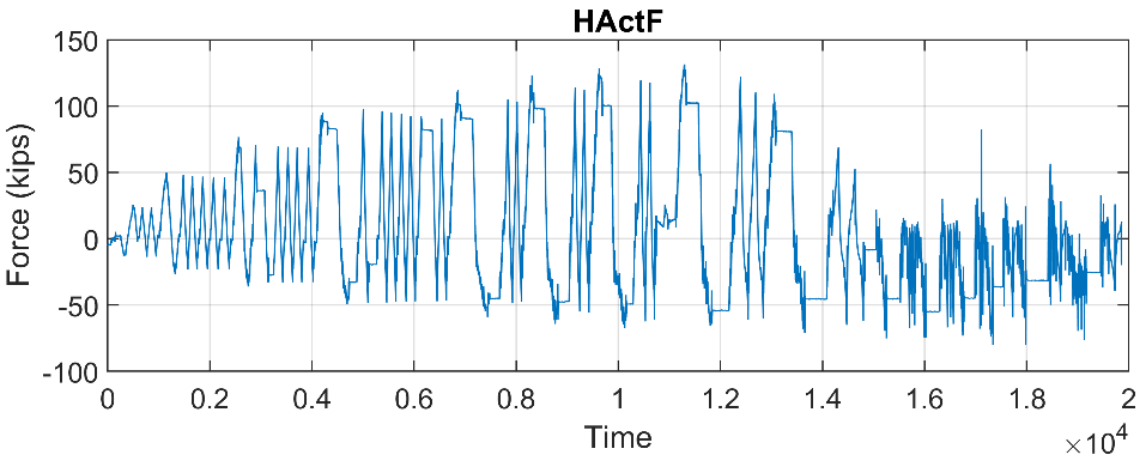
Figure 8-3. Reinforcing Bottom of Vertical Actuators with Wide Flange Beams

Table 8-1. Modified Loading Protocol

Step	Disp. (in) +	Drift (%) +	Force (kips) +	Disp. (in) -	Drift (%) -	Force (kips) -	# of Cycles	Note 1	Note 2
0	0.00	0.00	0	0.00	0.00	0	-		
1	0.21	0.13	26	-0.13	-0.08	-14	3	0.25Pw	
2	0.53	0.32	50	-0.30	-0.18	-27	6	0.5Pw	
3	0.94	0.57	77	-0.50	-0.30	-36	6	0.75Pw	
4	1.38	0.84	98	-0.90	-0.55	-49	8	1.0Pw	Vb_2.4dtFu
5	1.85	1.12	112	-1.30	-0.79	-59	3		Vb_3.0dtFu
6	2.35	1.42	123	-1.70	-1.03	-64	3		
7	2.85	1.73	129	-2.10	-1.27	-67	3		
8	3.50	2.12	132	-2.60	-1.58	-66	3		
9	4.25	2.58	109	-3.20	-1.94	-71	3		
10	-	-	-	-3.90	-2.36	-75	3		
11	-	-	-	-4.60	-2.79	-75	3		
12	-	-	-	-5.60	-3.39	-73	2		
13	-	-	-	-7.00	-4.24	-59	2		
14	-	-	-	-8.00	-4.85	-42	2		
15	-	-	-	-9.50	-5.76	-39	2		



(a) Horizontal Displacement History



(b) Horizontal Load History

Figure 8-4. Actuator Displacement and Load History

To obtain the actual shear force V_u acting on the wall while considering the forces from horizontal and vertical actuators, a free-body diagram was developed accounting for the equilibrium when the wall is subjected to lateral displacement at the top. Figure 8-5 provides the free-body diagrams showing the forces from the vertical horizontal actuators at the top of the wall and the shear force V_{sp} and moment M_{sp} at the center of the horizontal splice level. In the figure, *HActF* represents the force from the horizontal actuator, and *VAct1F* and *VAct2F* represent the axial forces from the west and east actuators, respectively. In addition, $VActF_y$ represents the summation of vertical forces from vertical actuators, and $VActF_x$ represents the resultant horizontal forces from the west and east actuators. From force equilibrium in the horizontal direction, the shear force V_{sp} can be expressed as in the following equation:

$$V_{sp} = HActF + VActF_x \qquad \text{Equation 8-1}$$

The test began under force control at Step 1. This step involved conducting 3 cycles at 25% of the design strength ($0.25P_w$). The corresponding forces from the horizontal actuator in the positive and negative directions were 26 kips and -14 kips, respectively. The lateral displacements in the positive and negative directions were 0.21 in. and -0.13 in., respectively. The test then proceeded to Step 2, which involved 6 cycles at 50% of the design strength ($0.5P_w$). The applied loads in the positive and negative directions reached 50 kips and -27 kips, respectively, while the displacements were 0.53 in. and -0.3 in., respectively. No sound that would suggest sliding in the splice connection was heard during these steps. In this step, the minimum and maximum strains (ε_{min} and ε_{max}) read on the web were -1000 με and 600 με (corresponding to -46% and 27% ε_y). Figure 8-6 shows the recorded LP deformation in Step 2 at positive and negative peaks. No significant difference of deformation was observed between the readings from the LP above (welded) and below (bolted) the horizontal splice plate, which also indicate that slipping had not occurred.

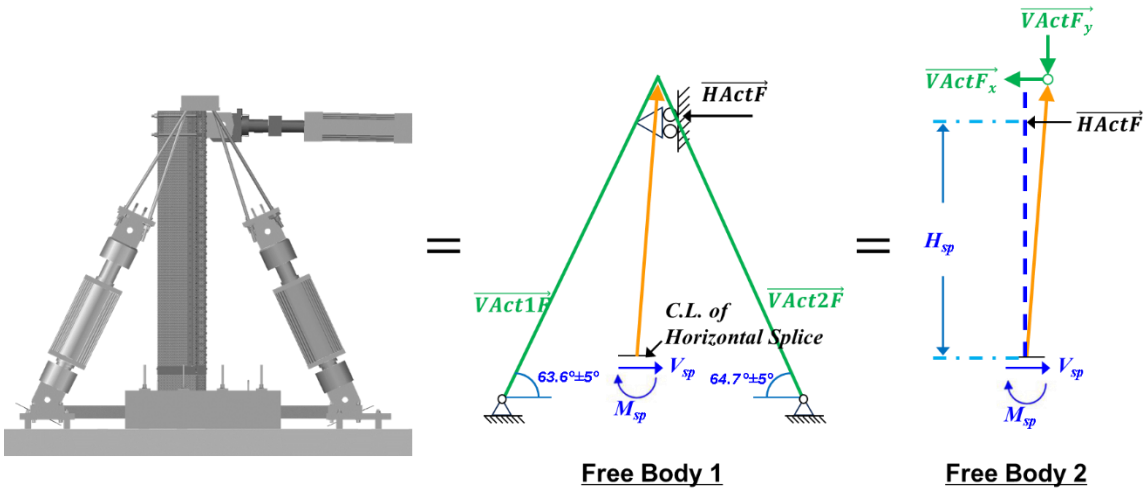


Figure 8-5. Free-Body Diagram for Calculating the Shear Force of the Wall

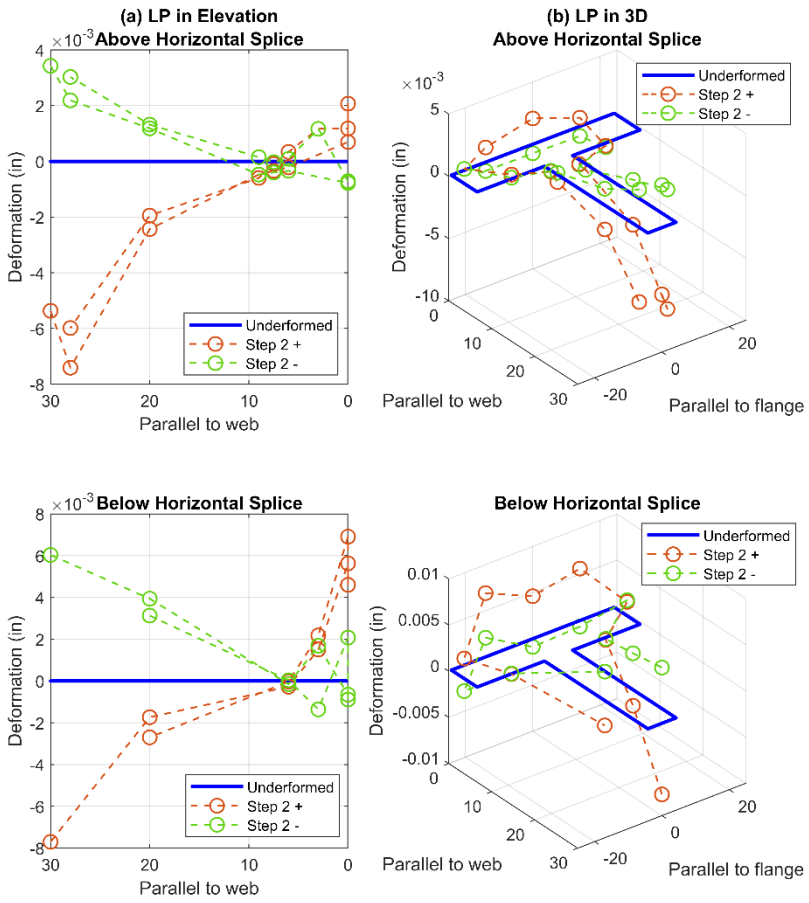


Figure 8-6. LP Deformation at Positive and Negative Peaks in Step 2 in (a) Elevation and (b) 3D

The test then proceeded to Step 3, with 77 kips and -36 kips applied as the positive and negative peak horizontal forces, respectively. The corresponding horizontal displacements in positive and negative peak were 0.94 inches and -0.5 in., respectively. During this step, a single “thump-like” sound was heard. The source of the sound could not be identified; it could have been concrete cracking or some slip occurring between the splice plates and faceplates. However, any evidence of sliding could not be visually observed, as shown in Figures 8-7 and 8-8. In this step, the minimum and maximum strains (ε_{min} and ε_{max}) read on the web were -1500με and 800 με (-68% and 36% ε_y). Figure 8-9 shows the LP deformations recorded in this

step. Similarly, again there was no significant difference between the LP deformations above and below the horizontal splice.

The following step was Step 4, which targeted the design load (P_w). In this step, the actuator forces reached positive and negative peaks of 98 kips and -49 kips, respectively. The corresponding displacements were 1.38 in. in the positive direction and -0.90 in. in the negative direction. Figures 8-10 and 8-11 show the southwest and northeast views of the specimen at the positive and negative peaks, respectively. Figure 8-12 shows the condition of the horizontal splice on the web at the negative peak, and there was no gap initiation visually observed when the web was in tension. In this step, the minimum and maximum strains (ε_{min} and ε_{max}) read on the web were -2000με and 1200 με (-91% and 55% ε_y). At the beginning of the 2nd cycle in Step 4, a loud "bang" was heard, followed by the dislodging of numerous linear potentiometers during this cycle as if impacted by the jerk of a shock wave near the splice plates. Consequently, LP deformation data could not be obtained starting from Step 4 (in spite of numerous attempts to re-glue the LPs, most fell-off when loud sounds were heard in later part of the test, particularly as sliding developed in subsequent steps).

Figure 8-13 shows the hysteresis curve resulting from Steps 1 to 4. In Step 1, the calculated elastic stiffness was 96 k/in. in both the positive and negative loading directions. However, through the loading cycles from Steps 1 to 4, the stiffness gradually decreased to 47 k/in. in the positive direction and 31 k/in. in the negative direction. It was speculated that the stiffness changes might be due to the concrete cracking along greater the height of the wall as the moment increases, lowering the stiffness progressively (something investigated in Section 10). Note that there was no visual sign of sliding observed up to that point.



(a) Southwest View



(b) Northeast View

Figure 8-7. Step 3, Peak Actuator Displacement=0.94”



(c) Southwest View



(d) Northeast View

Figure 8-8. Step 3, Peak Actuator Displacement=-0.5”

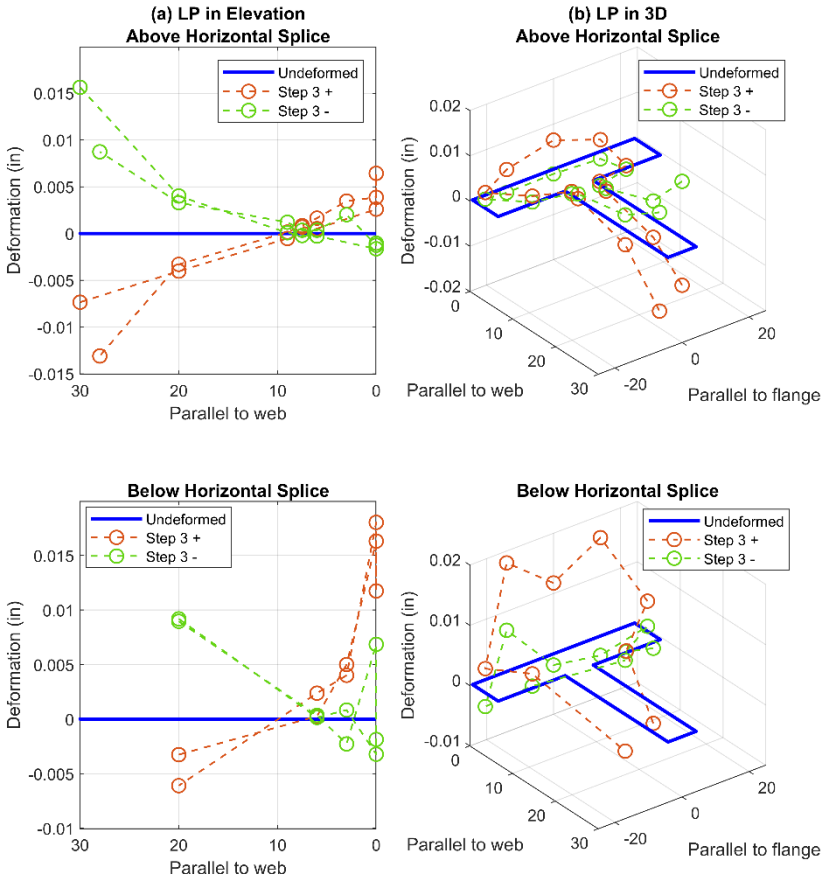


Figure 8-9. Deformation of LP in Step 3 in (a) Elevation and (b) 3D



(a) Southwest View

(b) Northeast View

Figure 8-10. Step 4, Peak Actuator Displacement=1.38”



(a) Southwest View (b) Northeast View

Figure 8-11. Step 4, Peak Actuator Displacement=-0.9”



Figure 8-12. No Gap Initiation on Web in Step 4, Peak Actuator Displacement=-0.9”

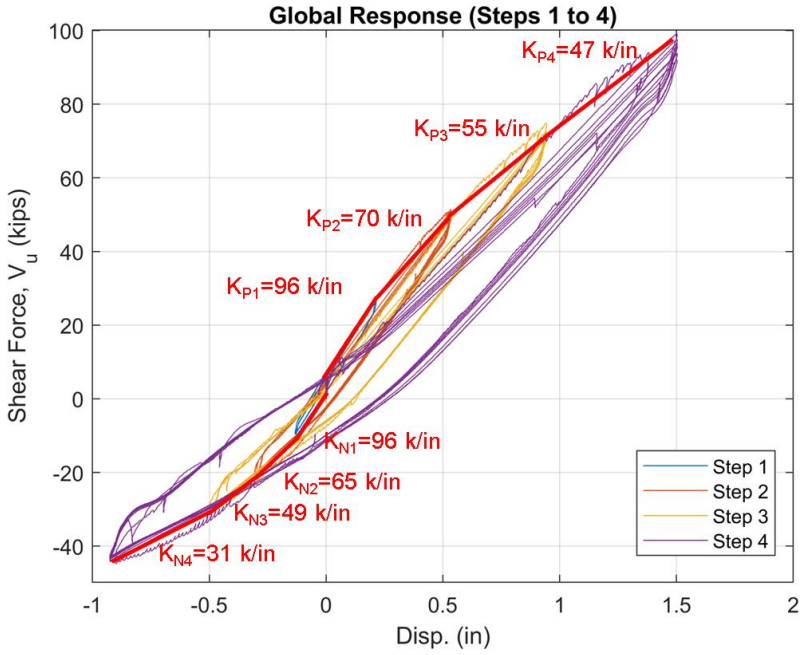


Figure 8-13. Hysteresis Curve in Steps 1 to 4

Starting from Step 5, the horizontal actuator changed from force control to displacement control. In Step 5, the positive and negative peak displacements increased to 1.85 in. and -1.30 in., respectively. The corresponding peak actuator forces were 112 kips in the positive direction and -59 kips in the negative direction. Starting from this step, loud "bang" noises were heard consistently throughout the cycles, which suggested sliding during the loading cycles (by comparison with the similar noises heard during component testing). Figures 8-14 and 8-15 show the southwest and northeast views of the specimen at the positive and negative peaks, respectively. As shown in Figure 8-16, yielding lines were observed around the bolts on the horizontal splice plate on the north side. Figure 8-17 shows an 1/8-in. gap that was visually observed above the horizontal splice when the web was in tension. During Step 6, the applied displacements increased to 2.35 in. and -1.70 in. with 123-kips and -64-kips forces at positive and negative peaks, respectively – these being 10% and 8.5% greater than the values obtained at the previous displacement amplitude, for corresponding displacement amplitude increases of 27% and 31%. In this step, the minimum and maximum strains (ε_{min} and ε_{max}) read on the web were -2000με and 1300 με (-91% and 59% ε_y). Figures 8-18 and 8-19 show the southwest and northeast views of the specimen at the positive and negative peaks, respectively. More severe yielding (Figure 8-20)was observed on the horizontal plate on the northern flange. Figure 8-21 shows the gap increased to about 3/16 to 1/4 in.

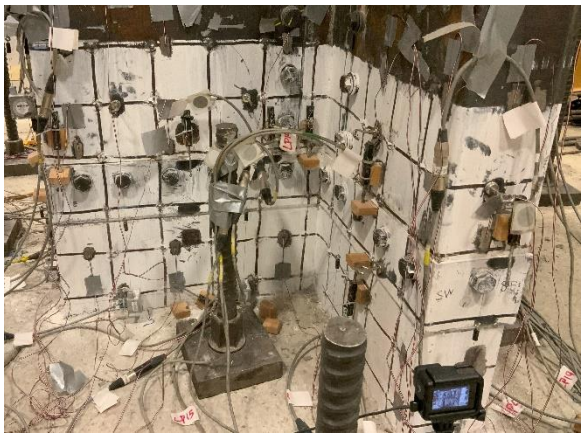


(a) Southwest View



(b) Northeast View

Figure 8-14. Step 5, Peak Actuator Displacement=1.85”



(a) Southwest View



(b) Northeast View

Figure 8-15. Step 5, Peak Actuator Displacement=-1.3”

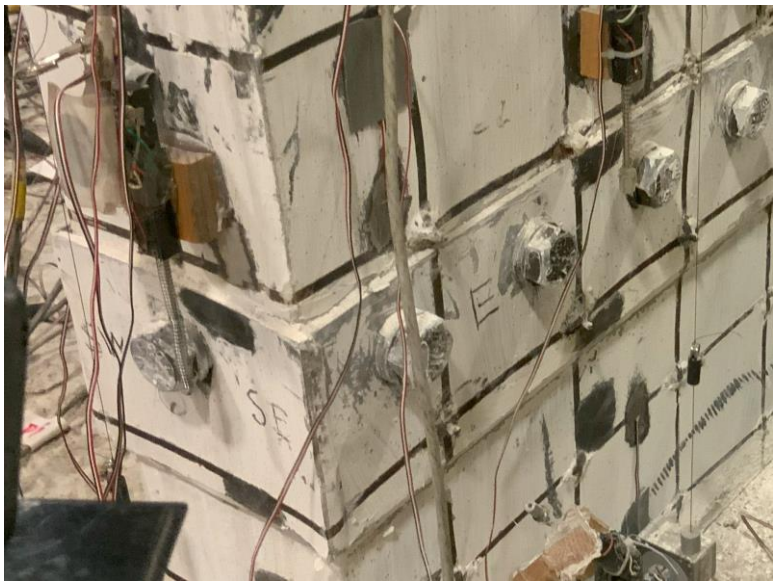


Figure 8-16. Yielding Lines Near Bolts on the North Side of the Wall in Step 5, Peak Actuator Displacement=1.85”



Figure 8-17. Gap Visible on the Web in Step 5, Peak Actuator Displacement=-1.3”



(a) Southwest View



(b) Northeast View

Figure 8-18. Step 6, Peak Actuator Displacement=2.35”



(a) Southwest View



(b) Northeast View

Figure 8-19. Step 6, Peak Actuator Displacement=-1.7”

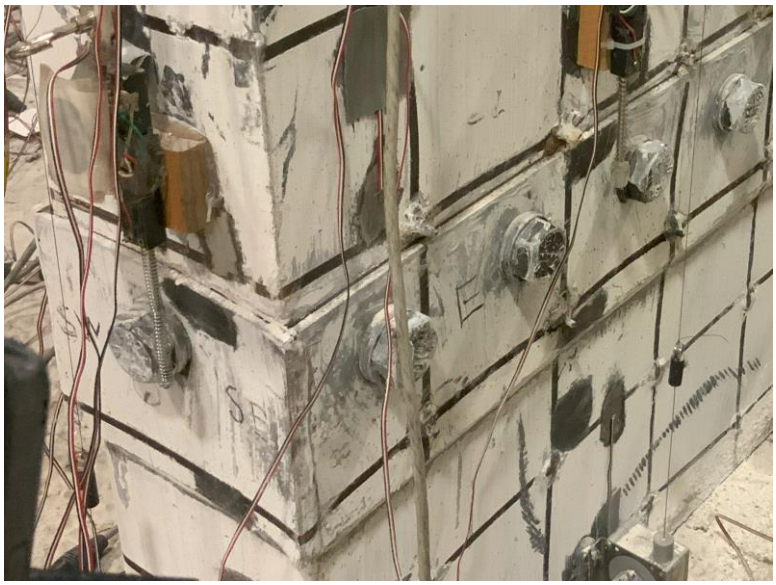


Figure 8-20. Yielding Lines on the North Side of the Wall in Step 6, Peak Actuator Displacement=2.35”



Figure 8-21. Gap on the Web in Step 6, Peak Actuator Displacement=-1.7”

The loading cycles continued to Steps 7 and 8. In Step 7, the displacements further increased to 2.85 in. and -2.10 in. with 129-kips and -67-kips forces at positive and negative peaks, respectively. During Step 8, the displacements were 3.50 in. and -2.60 in. with 132-kips and -66-kips forces at positive and negative peaks, respectively. In essence, forces applied had plateaued, with values in Steps 7 and 8 being nearly similar to those in Step 6. Figures 8-22 to 8-25 show the southwest and northeast view of the specimen at positive and negative peaks during Steps 7 and 8. In Step 8, the minimum and maximum strains (ε_{min} and ε_{max}) read on the web were -3900με and 1300 με (-178% and 59% ε_y). Yielding in compression on the web became severe, and slight buckling on the horizontal splice on the web was observed, as shown in Figures 8-26 and 8-27.

In Step 9, the displacements reached 4.25 in. and -3.20 in. with 109-kips and -71-kips forces at positive and negative peaks, respectively. This corresponds to a strength degradation in the positive direction, and a sustained strength in the negative direction, compared to cycles at the previous displacement amplitude. More specifically, compared to Step 8, the positive peak force dropped by 17.5%, while the negative peak

force increased by 7.6%. Figures 8-28 and 8-29 show the southwest and northeast views of the specimen. The figures show more severe buckling on the web (Figure 8-30) at the positive peak and a larger gap due to sliding at the negative peak. Two tie bars fractured ("popped off") due to this buckling during loading cycles in Step 9, as shown in Figure 8-31. As buckling on the web splice plate further developed, the vertical corner welds on the horizontal splice plate started to fracture (Figure 8-32), and some concrete dust was observed to escape through the gap after Step 9. Figure 8-33 shows the hysteresis curves from Steps 7 to 9, showing that the shear force decreased from its peak of 130 kips to 50 kips in the positive direction after the Step 9 loading cycles. To avoid further damaging the buckled horizontal web splice plate and crush the specimen in a way that would preclude continued testing, it was decided to continue testing by applying cycles only in the negative direction (as shown in Figure 8-4)



(a) Southwest View



(b) Northeast View

Figure 8-22. Step 7, Peak Actuator Displacement=2.85"



(a) Southwest View



(b) Northeast View

Figure 8-23. Step 7, Peak Actuator Displacement=-2.1”



(a) Southwest View



(b) Northeast View

Figure 8-24. Step 8, Peak Actuator Displacement=3.50”



(a) Southwest View



(b) Northeast View

Figure 8-25. Step 8, Peak Actuator Displacement=-2.6”

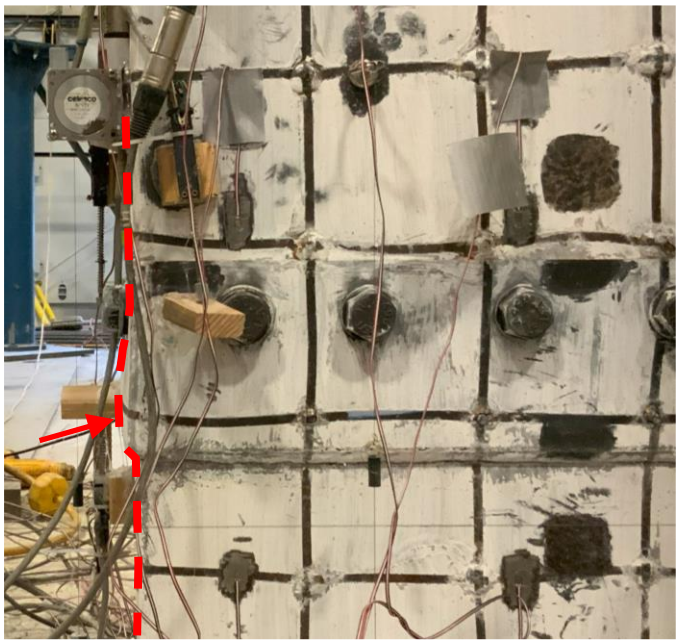


Figure 8-26. Buckling on Horizontal Splice on Web in Step 8, Peak Actuator Displacement=3.5”

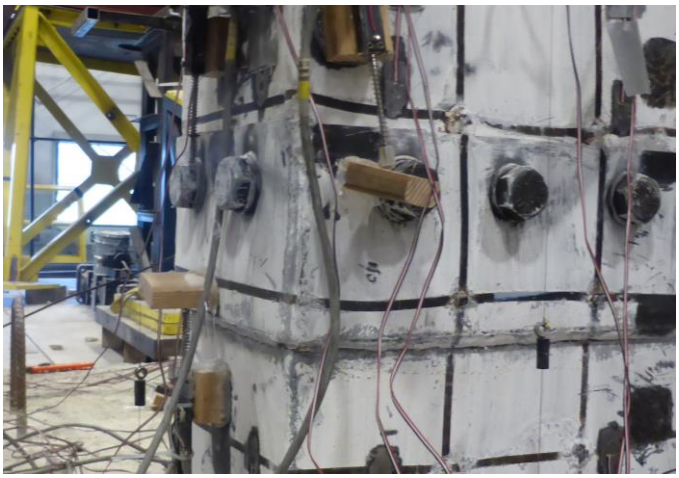


Figure 8-27. Close View of Buckling on Horizontal Splice on Web in Step 8, Peak Actuator Displacement=3.5”



(a) Southwest View



(b) Northeast View

Figure 8-28. Step 9, Peak Actuator Displacement=4.25”



(a) Southwest View



(b) Northeast View

Figure 8-29. Step 9, Peak Actuator Displacement=-3.2”

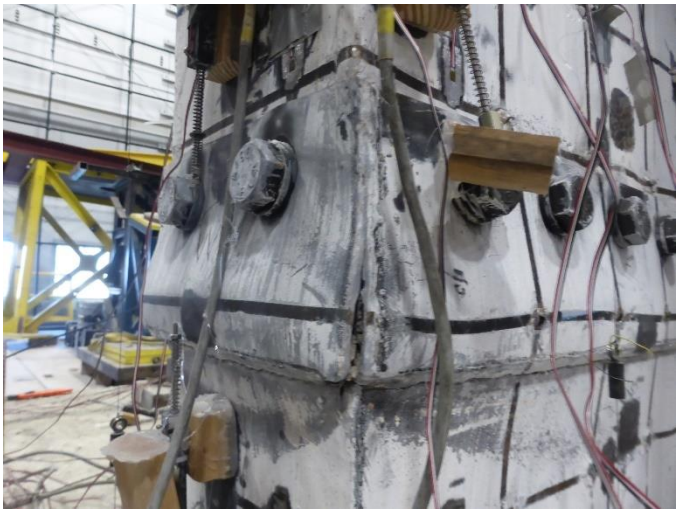


Figure 8-30. Close View of Buckling on Horizontal Splice on Web in Step 9, Peak Actuator Displacement=4.25”



Figure 8-31. Close View of Fractures of Tie-Rods during Step 9



Figure 8-32. Concrete Spalling Observed after Step 9

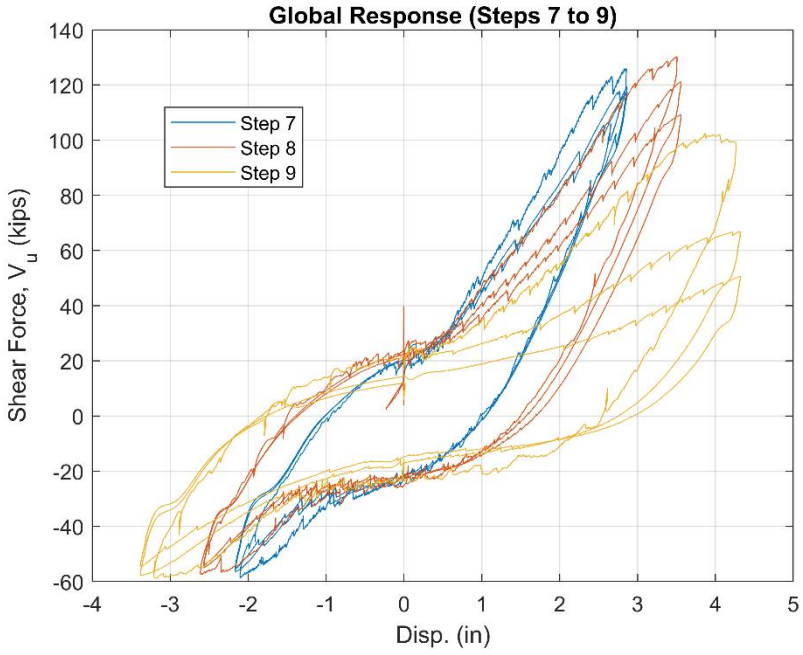


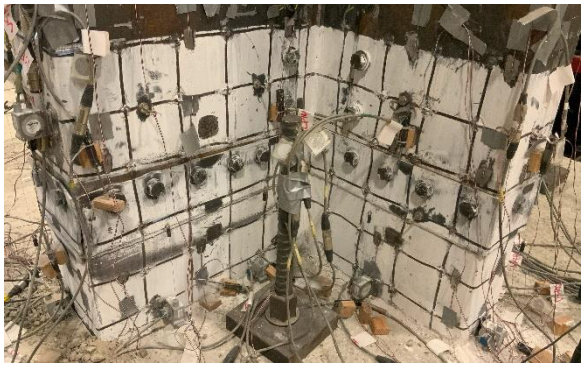
Figure 8-33. Hysteresis Curve in Steps 7 to 9

In Steps 10 and 11, the displacements increased to -3.90 in and -4.6 in., and the corresponding actuator force in both of these two steps was -75 kips, which was the peak force in the negative direction. Figures 8-34 and 8-35 show the southwest and northeast views of the specimen in these steps. With increasing displacement in negative direction, the bearing deformation (Figure 8-36)on the edge of the horizontal splice plate could be observed, especially at the bolts on the web on the south, north, and west surfaces. After the negative peak, the test then proceeded with Steps 12 to 15, with displacement increased from -5.6 in. to -9.5 in., aiming to fail the horizontal splice on the web in tension. Figures 8-37 to 8-40 show the northwest and southeast views of these steps, with progressive bearing failure developing along the horizontal splice plate on the web. As shown in Figure 8-41, bearing failures were first observed starting from Step 14, affecting the first to third rows of bolts on both the southern and northern surfaces of the web. Figure 8-42 shows the hysteresis curve obtained from Steps 10 to 15, showing that the shear force decreased from a negative peak of -60 kips down to -24 kips. Since the residual shear force was only 40% of the peak value obtained in all cycles, the test was terminated.



(a) Southwest View (b) Northeast View

Figure 8-34. Step 10, Peak Actuator Displacement=-3.9”



(a) Southwest View



(b) Northeast View

Figure 8-35. Step 11, Peak Actuator Displacement=-4.6”

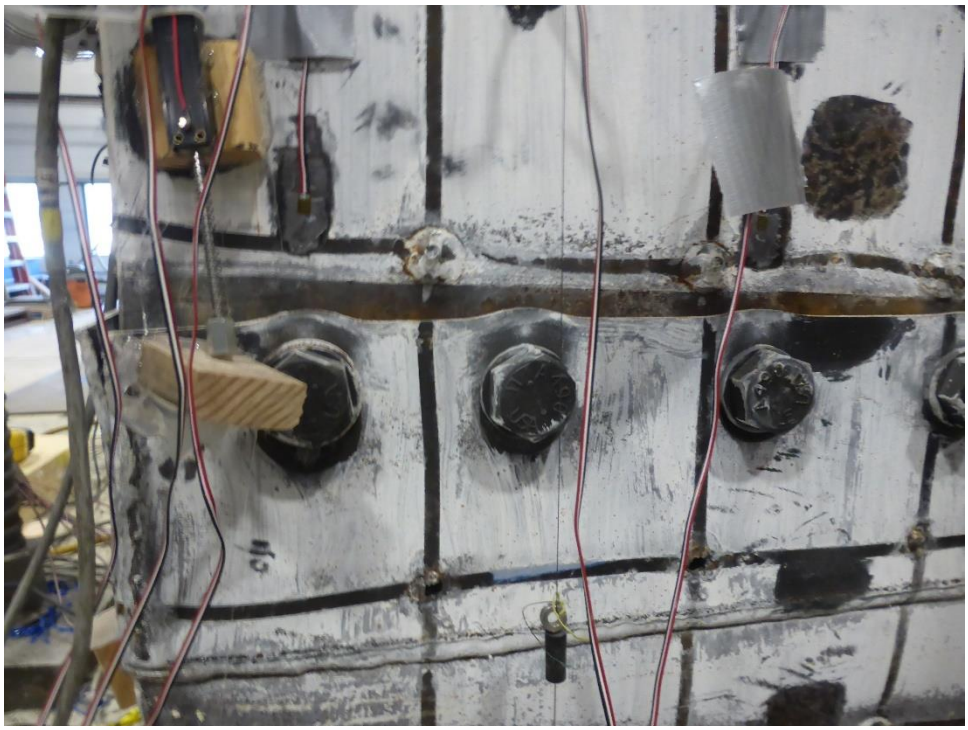


Figure 8-36. Bearing Deformation on Splice Plate Web at Step 11, Peak Actuator Displacement=-4.6”



(a) Southwest View



(b) Northeast View

Figure 8-37. Step 12, Peak Actuator Displacement=-5.6”



(a) Southwest View



(b) Northeast View

Figure 8-38. Step 13, Peak Actuator Displacement=-7.0”



(a) Southwest View

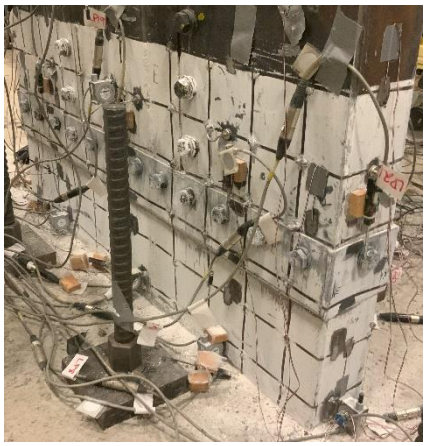


(b) Northeast View

Figure 8-39. Step 14, Peak Actuator Displacement=-8.0”



(a) Southwest View



(b) Northeast View

Figure 8-40. Step 15, Peak Actuator Displacement=-9.5”

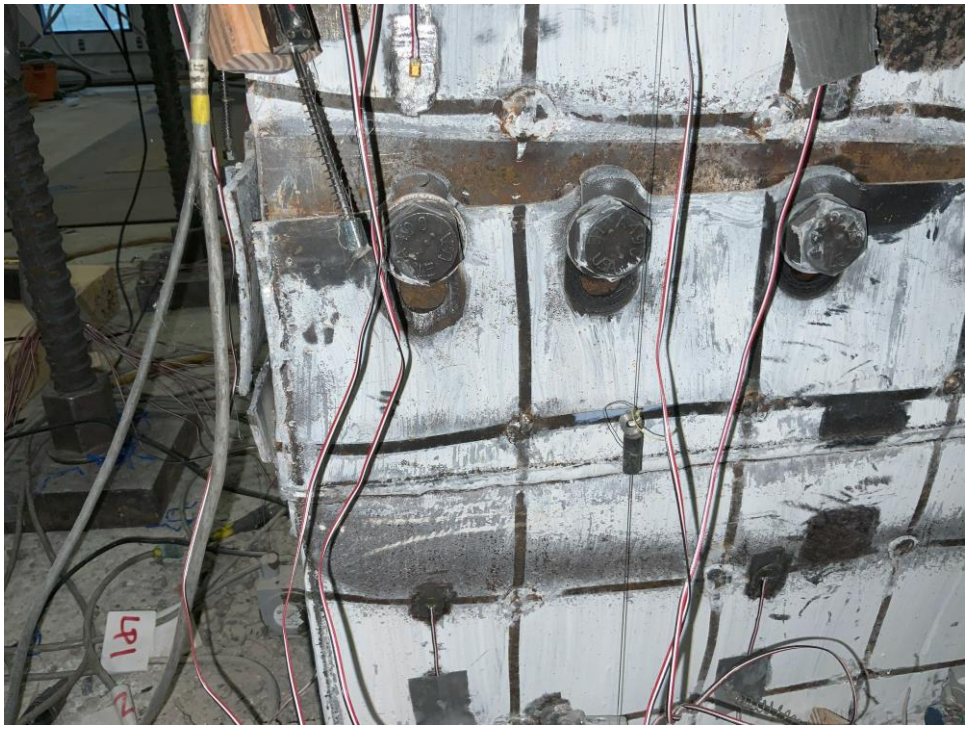


Figure 8-41. Fractures due to Bearing Failure Observed at Step 14, Peak Actuator Displacement=-8.0”

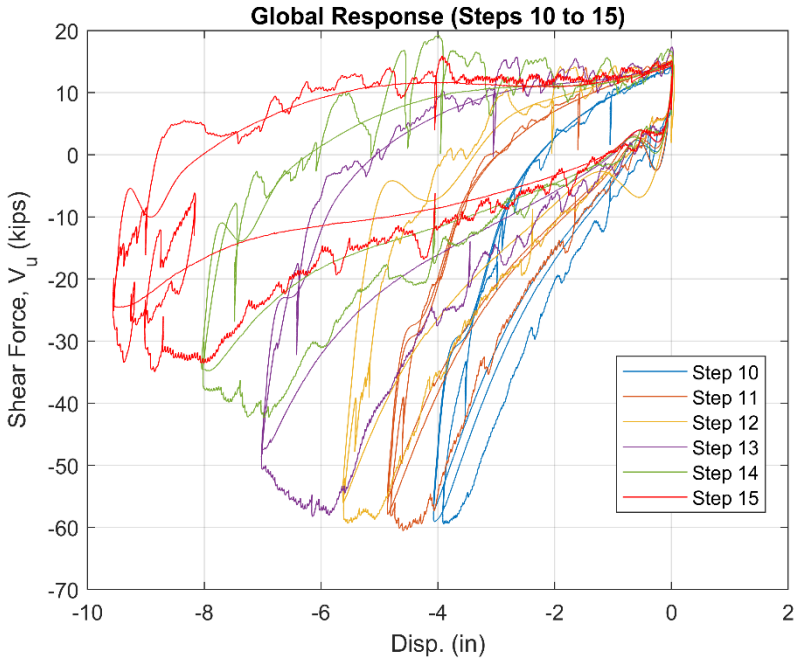


Figure 8-42. Hysteresis Curve in Steps 10 to 15

Figures 8-43 to 8-48 present a collection of photos documenting the splice region from the southwest, southeast, and northwest views of the wall specimen. These photographs illustrate the behavior at different displacement amplitudes, complementing the descriptions provided earlier.



Figure 8-43. Southwest View of the Specimen (Steps 7 to 10)

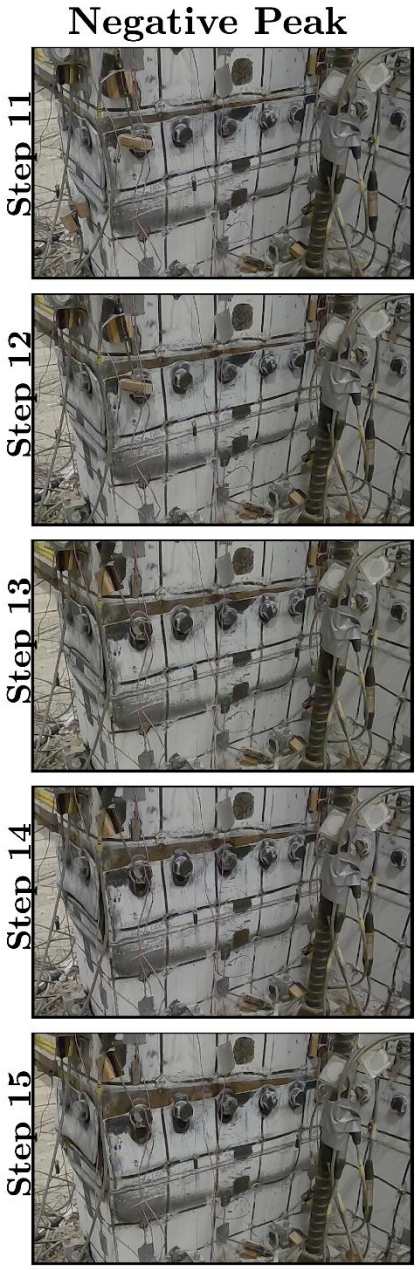


Figure 8-44. Southwest View of the Specimen (Steps 11 to 15)

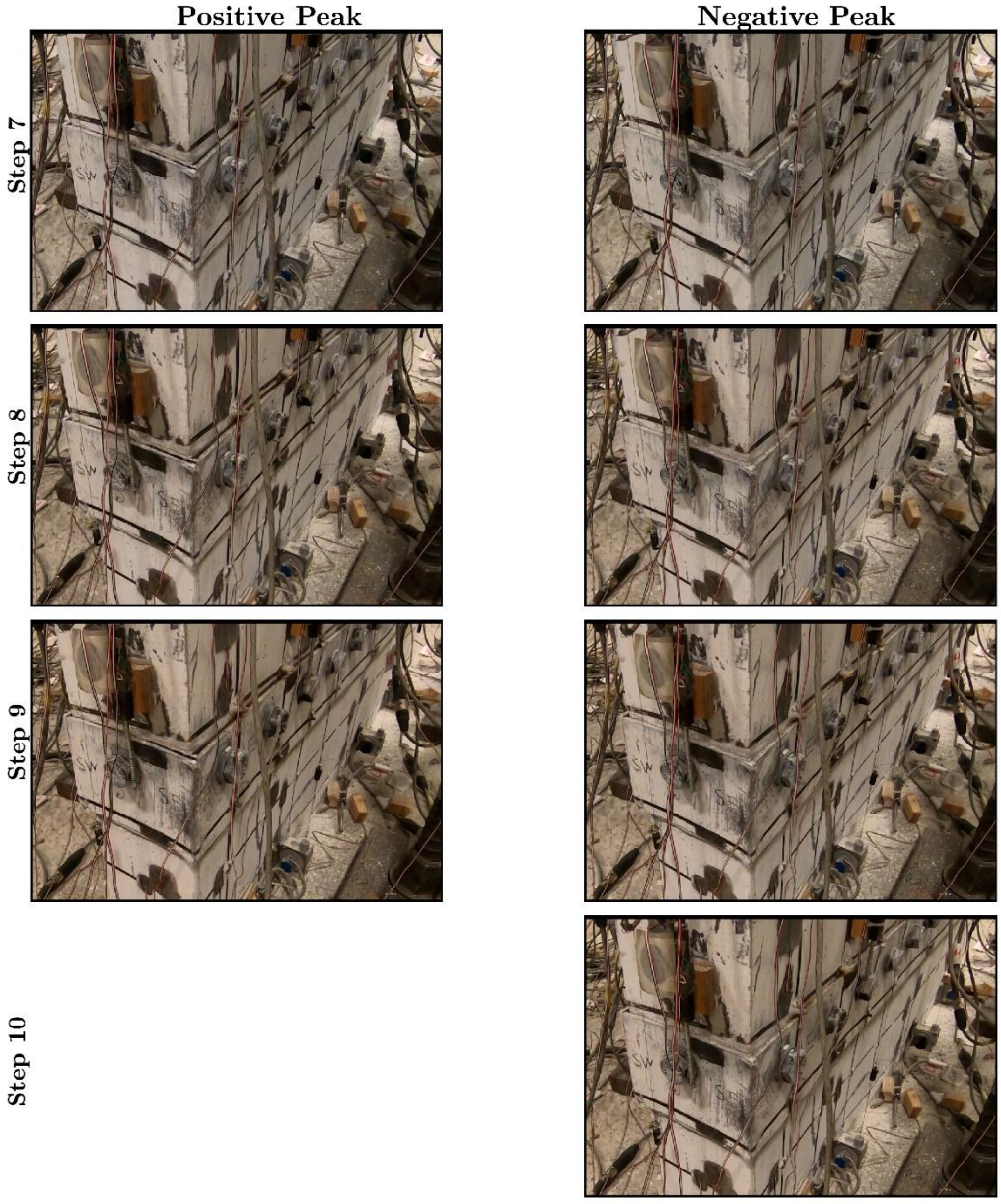


Figure 8-45. Southeast View of the Specimen (Steps 7 to 10)

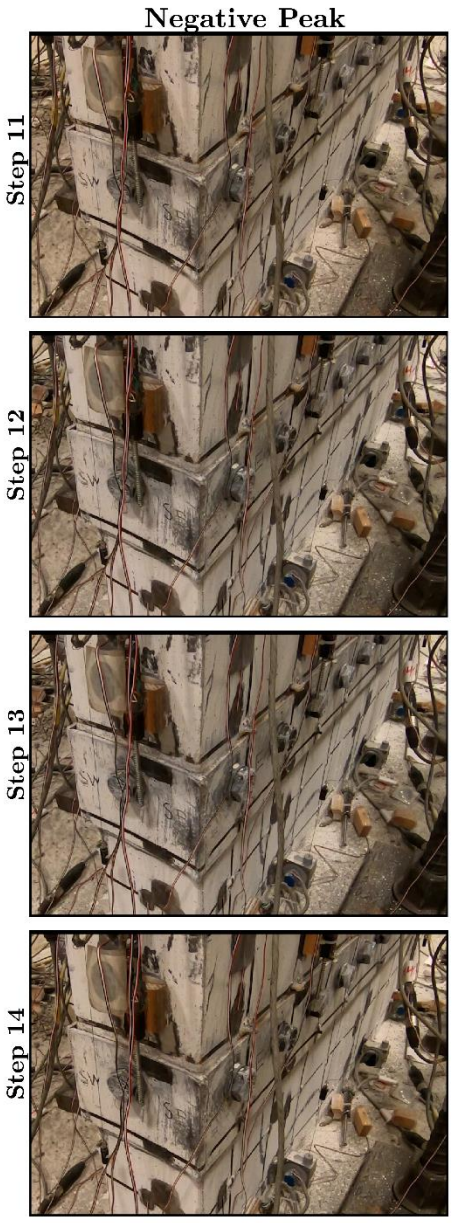


Figure 8-46. Southeast View of the Specimen (Steps 11 to 14)

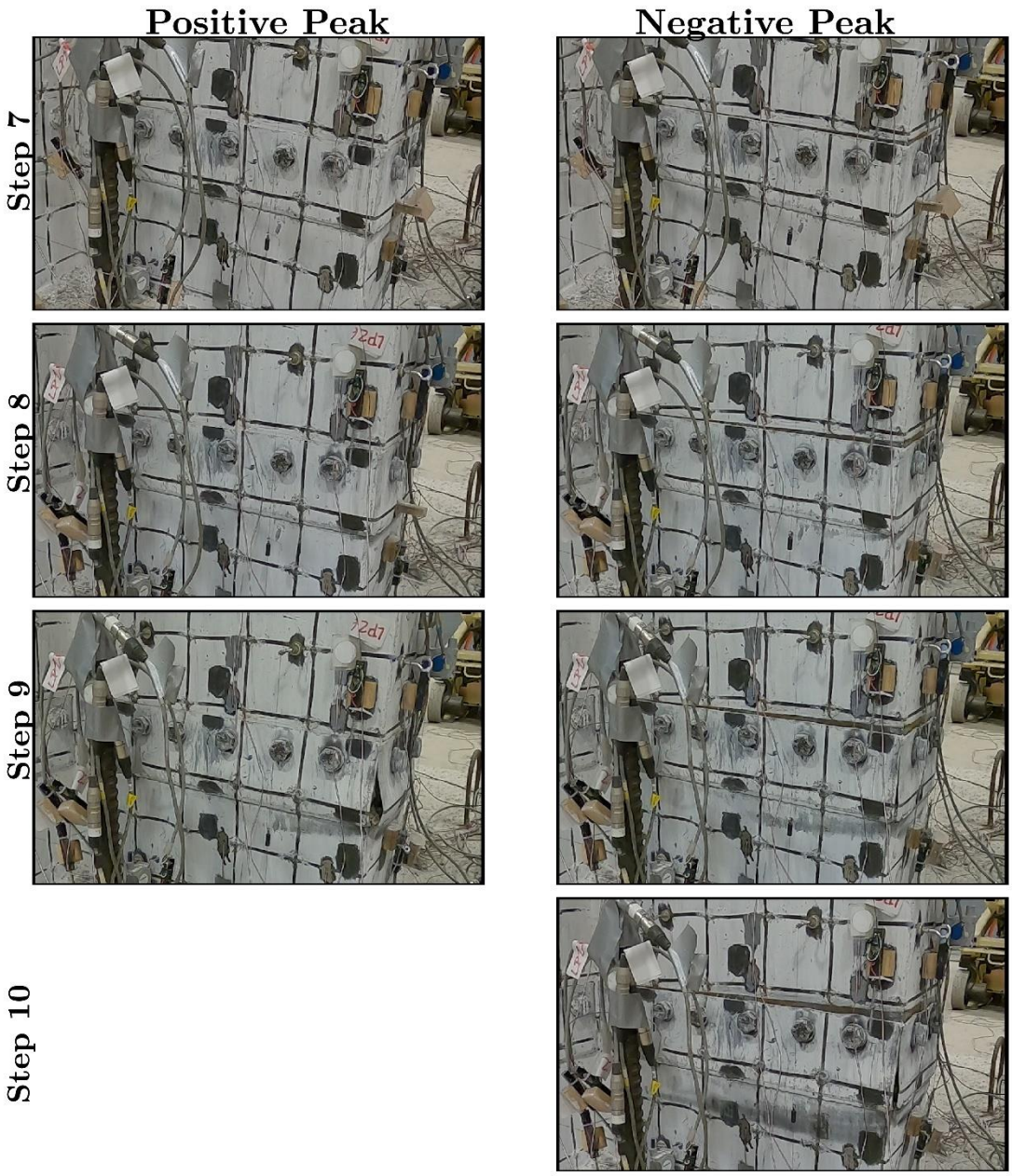


Figure 8-47. Northwest View of the Specimen (Steps 7 to 10)

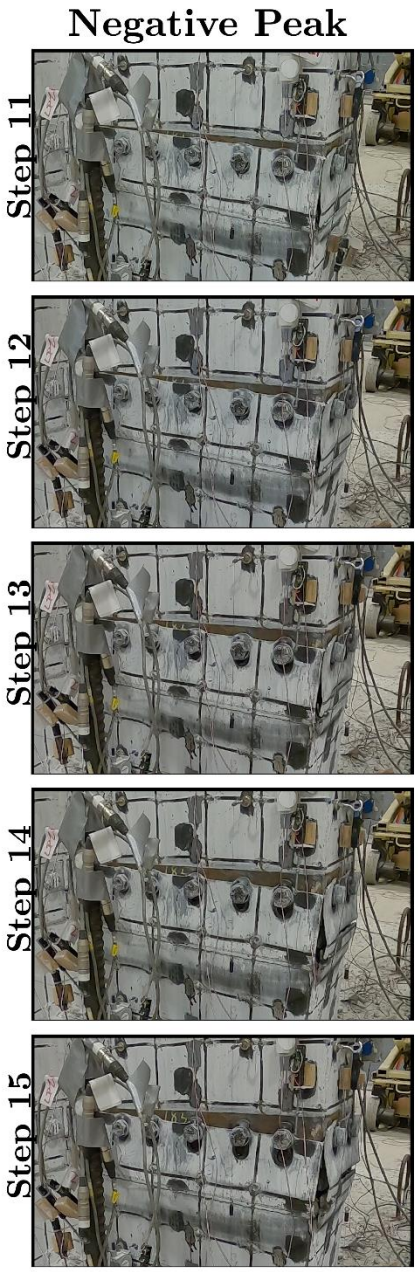


Figure 8-48. Northwest View of the Specimen (Steps 11 to 15)

8.3 Post-Test Observations

After the test, all bolts and the horizontal splice plates were first removed to reveal the faceplates inside, as shown in Figures 8-49 and 8-50. Then the top part of the wall specimen was separated from its lower part, and wall specimen was laid on the ground. This allowed inspection of the cross section surface above and below the splice location, as shown in Figures 8-51 and 8-52, as well as the condition of concrete after test.

At that point, it was discovered that all inside horizontal splice plates had not been welded along their bottom, as shown in Figure 8-53, contrary to what had been requested in the design. Figure 8-54 illustrates the request for welding the bottom surfaces of both inside and outside horizontal splice plates, made when reviewing the shop drawings. The fabricator confirmed that the shop drawing detail (Figure 8-63) indicated that fillet welding was to be applied to both horizontal splice plates (i.e., the inside and outside splice plates). However, on the disassembled specimen, a clean-cut surface is visible at the bottom of the inside splice plate, without any sign of welding. The absence of welding on the inside horizontal splice plates effectively transformed the connection into a single shear connection. This absence of welding helps explain why the outside horizontal splice failed during the loading cycles, instead of the faceplate (the 1.5 in. bolt edge distance on the splice plates being smaller than the 2 in. one on the faceplate). Recall that the intended failure surface was bearing failure of the faceplates, and that the intent was also to repair the connection by welding at the top of outside horizontal splice (as described in Section 7.8). With the outside horizontal splice place buckled and failed instead of the faceplate, the repair scheme was not possible to implement. However, note that failure on the splice plate instead of the faceplate was of no other major consequence as the specimen was still able to reach its design strength, since bearing strength of the splice plate in this case was the same as that of the faceplate (both plates being of the same thickness).

Figure 8-56 shows all the outside horizontal splice plates after test. All the deformed bolt hole dimensions on the outside horizontal splice plates and faceplates were measured; these are reported in Tables 8-2 and 8-3. Based on Tables 8-2, hole deformations of 2/16 in., 5/16 in., and 8/16 in. are obtained for bolt locations #6, #5, and #4 respectively. A nearly rigid body rotation of the wall can be determined from these hole deformations and bolt spacings on web splice. Figure 8-57 shows the measured hole deformations and the wall rotation at the horizontal splice level, alongside a test photo taken at the negative peak in Step 15. The measurements indicate that the maximum rotation of the wall is approximately -3.6 degrees.

As described in Section 7.2.1, the holes on the faceplates of the specimen were designed to be 15/16 in. oversized holes, to replicate how it would be specified in actual projects (to facilitate field erection). However, the measured hole dimensions on the faceplates were 13/16 in., which correspond to standard hole sizes for the ¾ in. bolts used. These discrepancies were not observable before the test since they were concealed by the horizontal splice plates.



(a) Southwest View (b) Northwest View

Figure 8-49. Photos revealing Faceplates after Test



Figure 8-50. Photo revealing Faceplates on Western Web after Test



Figure 8-51. Cross Section View of Lower Part of Wall after Test



Figure 8-52. Cross Section View of Upper Pat of Wall after Test



Figure 8-53. Clean-Cut on the bottom Inside Horizontal Splice Plates

6	4004	Add annotate of fillet welds on the bottom of splice plates. (Inside and Outside Splice Plates) (**Figure 6**)

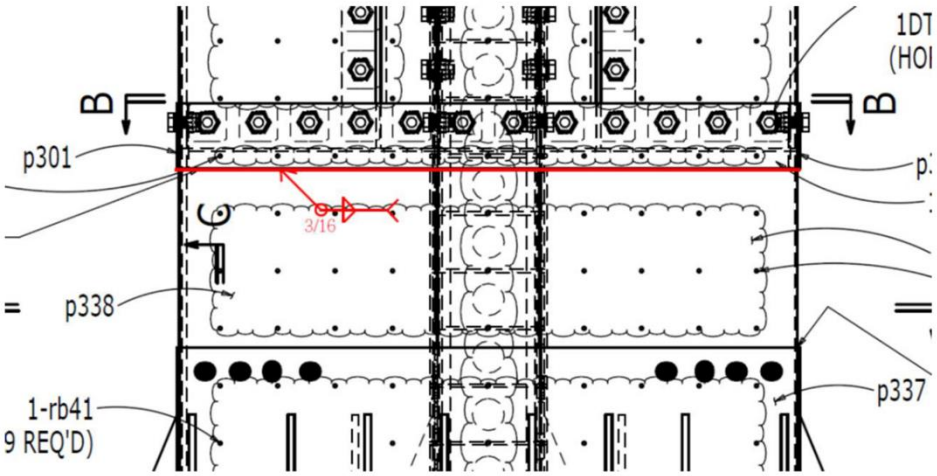


Figure 8-54. Requested Welding on bottom of Inside and Outside Splice Plates

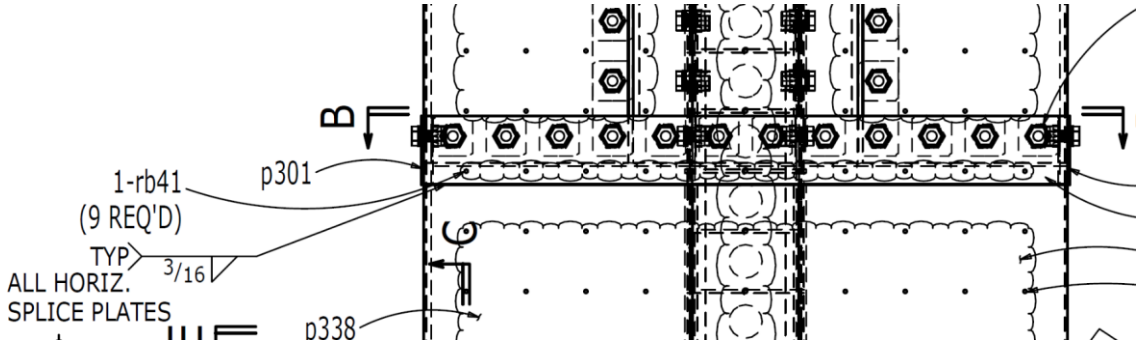


Figure 8-55. Welding on Bottom of Horizontal Splice in Shop Drawing

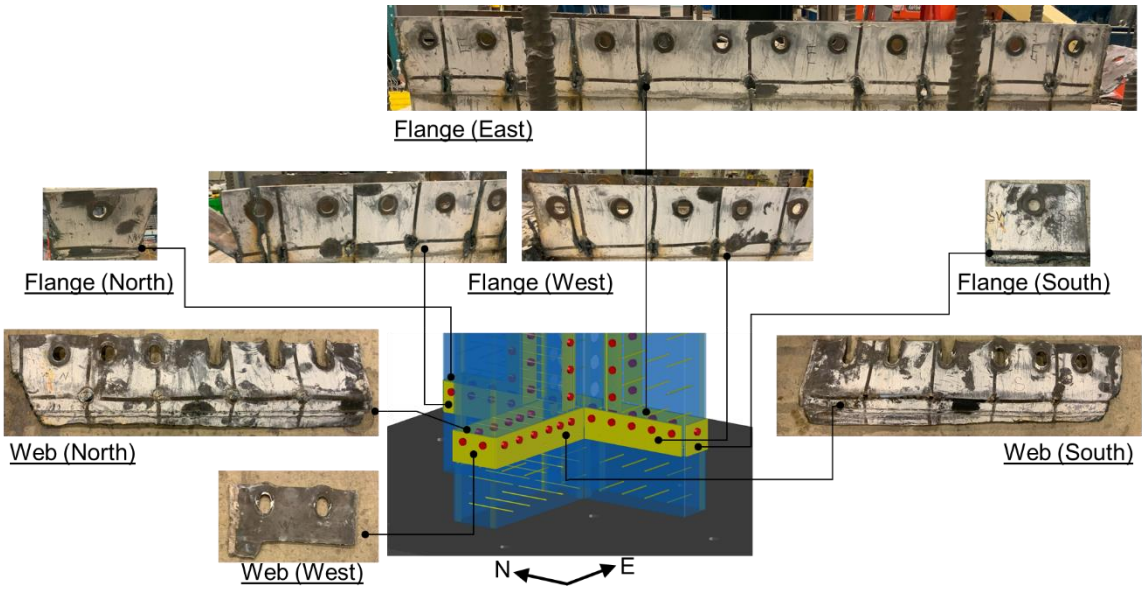


Figure 8-56. Photos showing all Outside Horizontal Splice Plates after Test

Table 8-2. Deformed Hole Dimensions on Outside Splice Plates (Unit: in.)

Part	Location	Bolt #1	Bolt #2	Bolt #3	Bolt #4	Bolt #5	Bolt #6
Web	West	1 5/16	1 6/16				
Web	North	B	B	B	1 5/16	1 2/16	15/16
Web	South	B	B	B	1 5/16	1 2/16	15/16
Flange	North	14/16	for all				
Flange	South	13/16	for all				
Flange	West	13/16	for all				
Flange	East	14/16	for all				

Note:

1. B=Bearing Failure
2. Hole Size=13/16"

Table 8-3. Deformed Hole Dimensions on Faceplates (Unit: in.)

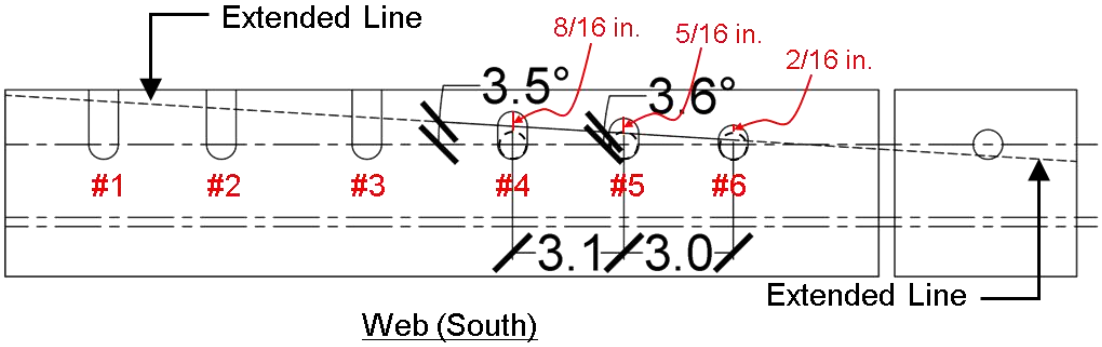
Part	Location	Bolt #1	Bolt #2	Bolt #3	Bolt #4	Bolt #5	Bolt #6
Web	West	15/16	15/16				
Web	North	15/16	15/16	14/16	14/16	14/16	15/16
Web	South	15/16	15/16	14/16	13/16	14/16	14/16
Flange	North	13/16	for all				
Flange	South	13/16	for all				
Flange	West	13/16	for all				
Flange	East	13/16	for all				

Note:

1. Hole Size=13/16"



Web (South) at Step 15, Peak Actuator Disp. = -9.5 in.



Web (South)

Figure 8-57. Measured Rotation at Horizontal Splice After Test

8.4 Test Data Analysis

8.4.1 Shear Force of the Wall

As indicated in Figure 8-5, the shear force V_{sp} of the wall can be determined by Equation 8-1. Figure 8-58 shows the hysteresis curves for the test results, comparing the curve of the horizontal actuator force (*HActF*) as a function of the top lateral displacement curve, with the curve for the shear force versus top lateral displacement curve. Figure 8-59 shows the hysteresis curve of the shear force versus top lateral drift. The top lateral drift was calculated by dividing the displacement from the horizontal actuator by the distance from the top of the foundation to the centerline of the horizontal actuator, which is 165 in. The points when some of the key observations were made during the test (corresponding to the peak loads, the onset of local buckling on the web, and bearing failures of bolts) are marked on the curve. The shear force peaked at 129 kips in the positive direction and -59 kips in the negative direction, corresponding to drifts of 2.09% and -2.92%, respectively. The shear force sustained above 80% of its peak flexural strength up to drifts of 2.4% in the positive direction and -4.3% in the negative direction.

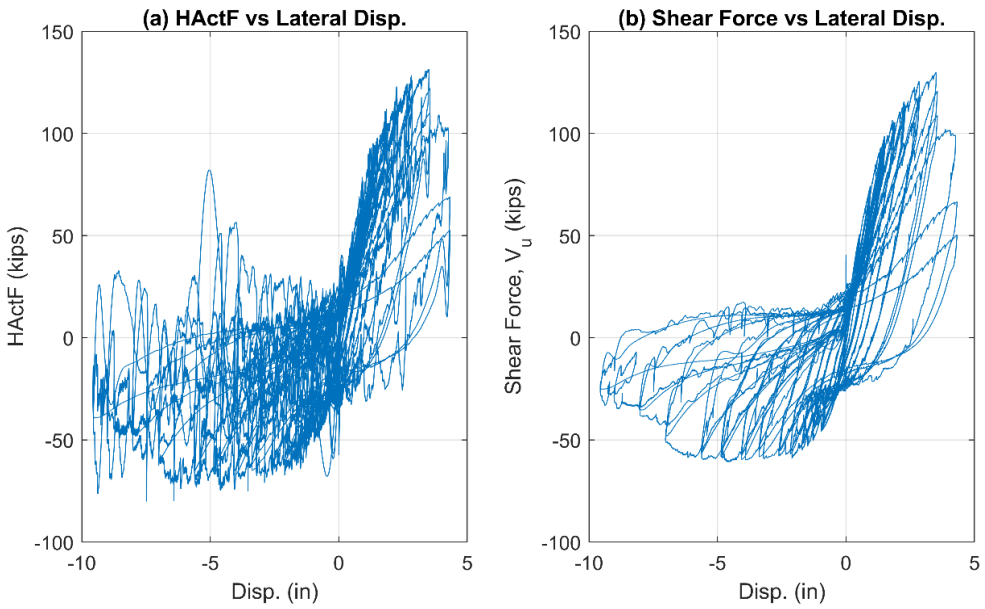


Figure 8-58. Hysteresis Curves of (a) HActF vs Top Lateral Displacement (b) Shear Force vs Top Lateral Displacement

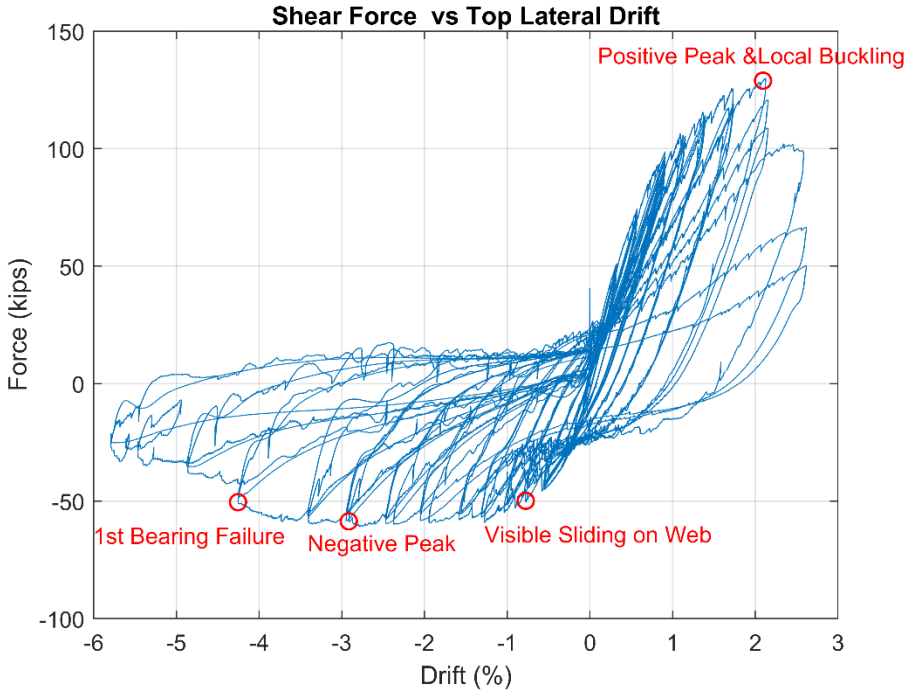


Figure 8-59. Hysteresis Curves of Shear Force vs Top Lateral Drift

8.4.2 Flexural Strength of the Wall

Referring to the T-shaped wall tested by Kizilarslan and Bruneau, 2023, the moment resisted by the wall at its base was calculated by subtracting the resultant of the horizontal components of the force of the two near-vertical actuators that applied axial load from the horizontal force obtained from the horizontal actuator applying loading to the wall. As shown in Figure 7-24, the west and east actuators used for the axial load application were designed with an inclination angle under applied axial loading of 64.2/65.5 degrees respectively, which is slightly different than the values measured during the test, which were 63.6/64.7 degrees. The actual values measured in the test were used for the data analysis. The free-body diagram of the moment at the wall base considering forces from the horizontal and vertical actuators is shown in Figure 8-60. However, the location of interest for this research is the horizontal splice (rather than the wall base). As shown in Figure 8-61, the free-body diagram above was therefore slightly adjusted to show the moment equilibrium at the center line of the horizontal splice. The moment resisted by the wall at the horizontal splice (M_{sp}) can be calculated by the following cross-products:

$$\overrightarrow{M_{sp}} = \overrightarrow{r_{act}} \times \overrightarrow{HActF} + \overrightarrow{r_{top}} \times \left(\overrightarrow{VActF1} + \overrightarrow{VActF2}\right) \qquad \text{Equation 8-2}$$

Figure 8-62 shows the calculated M_{sp} resisted by the wall against the top lateral drift. The flexural strength corresponding to the bearing strengths of $2.4dtF_u$ and $3.0dtF_u$, as well as the yielding moment M_y, are marked in the figure. The peak M_{sp} in the positive drift is 1548 k-ft, which exceeds the flexural strength required to reach a bearing strength of $3.0dtF_u$ (1470.78 k-ft). In the negative drift, the peak M_{sp} is -867 k-ft, which is also larger than the flexural strength required to develop $3.0dtF_u$ (-731.29 k-ft).

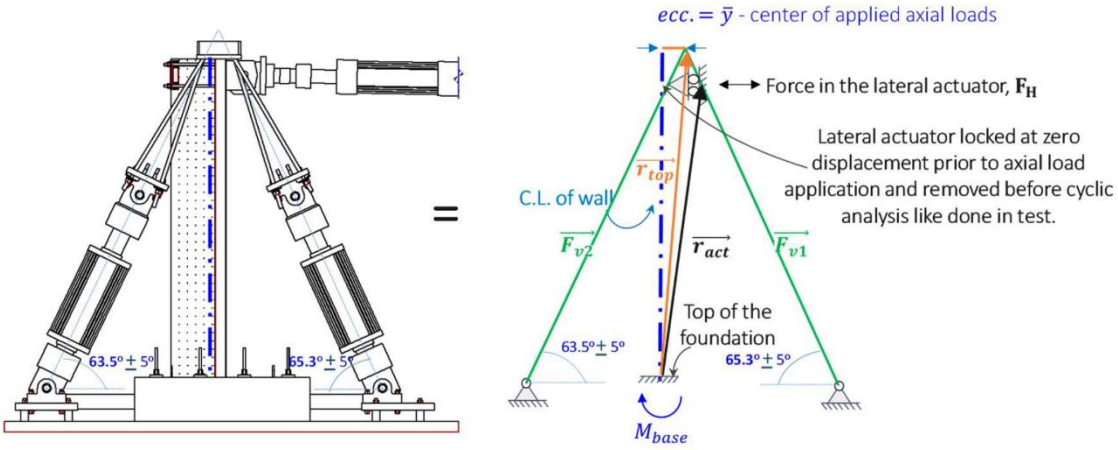


Figure 8-60. Inclination angle of vertical actuators at zero displacement and Free body diagram of the wall specimen at zero displacement (Kizilarslan and Bruneau, 2023)

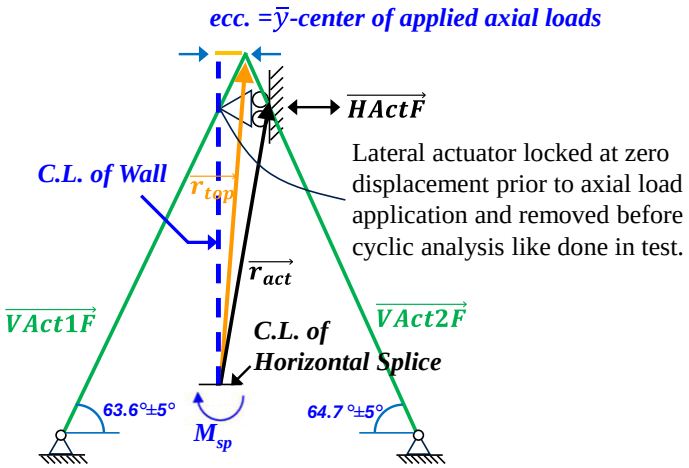


Figure 8-61. Adjusted Free body diagram of the wall specimen at zero displacement

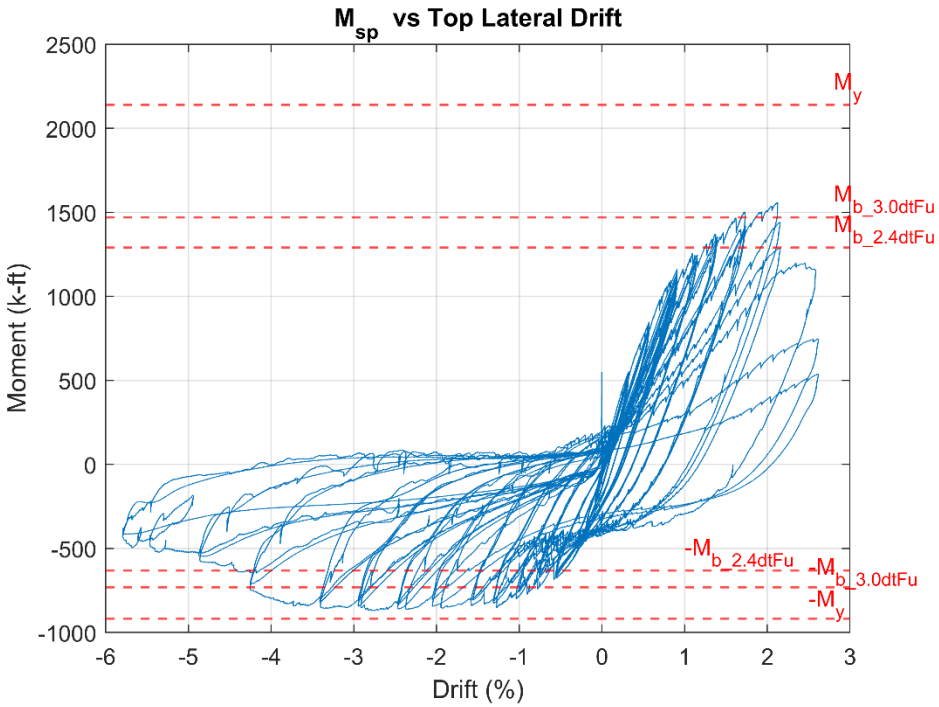


Figure 8-62. Calculated Experimental M_{sp} vs Top Lateral Drift Curve

8.4.3 Records from Strain Gauges and Vertical and Horizontal String Potentiometers

For the wall specimen, the strains on the steel plates were recorded by strain gauges placed at 6.5 in., 15.5 in., and 24.5 in. from the top of the foundation on the faceplates of the wall (Figure 7-28). The strain profiles at these three levels are shown in Figures 8-63 to 8-82 at the peak displacements from Steps 2 to 15 of loading cycles. Until Step 7 of the loading cycle, the faceplates exhibited elastic behavior. However, at the positive peak of Step 7, the maximum strains recorded at z=6.5 in., z=15.5 in., and z=24.5 in. were 2684με, 2308με, and 2137με, respectively. These measurements correspond to 122%, 105%, and 97% of the yield strain (ε_y), indicating some yielding, likely due to stress concentrations given that the moment applied to the wall at these heights during that step were 70%M_y, 66%M_y and 61%M_y and thus did not exceed M_y.

Given that the upper part of the wall is connected to the lower part through bolted horizontal splice plates, the load transfer initiates from the upper part of the faceplates to the bolts, subsequently moving to the lower part of the faceplates. The interaction, including sliding and friction between the horizontal splice plates and faceplates, also contributes to the load transfer process. As a result, the strain profiles observed on the faceplates do not always remain linear, even when the faceplates are not yielded (this is investigated in SECTION 9).

Figures 8-83 and 8-84 show the lateral displacements and drifts at positive and negative peaks in each step. Additionally, Figures 8-85 and 8-86 provide the normalized lateral displacement at positive and negative peaks in each step. To aid in understanding the deformed shapes of the wall observed in the test records, the elastic deformation of the wall was calculated. This calculation is based on the free-body diagrams shown in Figure 8-87, incorporating both first and second-order analyses. The formulae for calculating the elastic deformation are presented as follows:

$$x = \left(\frac{P}{EI_{eff}}\right) \times \left[-\frac{z^3}{6} + \left(\frac{H_{sp}}{2}\right) z^2\right] - \left(\frac{M_g}{EI_{eff}}\right) \times \left[\left(\frac{1}{6H_{sp}}\right) z^3 + \frac{z^2}{2}\right] \quad \text{Equation 8-3}$$

where x represents the lateral elastic deformation of the wall at height z, EI_{eff} is the effective flexural stiffness of the wall, calculated as $E_s I_s + 0.35 E_c I_c$, as defined in AISC 360-22 Equation I1-1, P is the net lateral force applied to the wall, equivalent to the shear force V_{sp} acting on the wall in Equation 8-1, and M_g represents the moment at the top of the wall due to the vertical actuators, calculated as indicated below for first and second-order analyses:

$$First - Order\ Analysis: M_g = VActF_x \times e_z - VActF_y \times e_x$$
$$Second - Order\ Analysis: M_g = VActF_x \times e_z - VActF_y \times (e_x + D) \quad \text{Equation 8-4}$$

where e_x and e_z represent the horizontal and vertical eccentricities from the vertical actuator intersection point to the center line of the wall, while D is the lateral displacement at the top of the wall.

Figures 8-88 and 8-91 compare the wall deformations recorded during the test with the elastic deformations calculated using first and second-order analyses at each step for both positive and negative peaks. These figures illustrate that during initial response, the deflected shape of the wall matched the elastic deformation curves, but started to depart from that elastic response as soon as Steps 4 and 5, exhibiting a progressively more concentrated rotational behavior centered around the horizontal splice location. This is expected, as the predominant inelastic deformations, including slip, plate deformation, and bearing deformation, all occur at the horizontal splice. Therefore, the horizontal splice functions as a plastic hinge for the wall specimen. The calculated hinge rotations, based on the differences between the angles of the elastic curve and the test curve, at positive and negative peaks in Steps 4, 5, 6, 8, and 9 are 0.25°/-0.34°, 0.45°/-0.45°, 0.58°/-0.59°, 1.05°/-0.87°, and 1.42°/-1.08°. The calculated rotation of the wall at negative peaks in Steps 10 to 15 are -1.34°, -1.66°, -1.95°, -2.44°, -2.80°, and -3.35°.

Figures 8-92 and 8-107 provide the deformation of vertical string potentiometers around the perimeter of the wall, as reported in Figure 7-32. The rotation of the wall, as shown in Figure 7-33, including the deformation of horizontal splice plates, faceplates, and sliding, can be determined by Equation 7-6. The calculated rotation of the wall at positive and negative peaks in Steps 4, 5, 6, 8, and 9 are 0.11°/-0.12°, 0.27°/-0.25°, 0.39°/-0.37°, 0.71°/-0.79°, and 1.10°/-1.07°. The calculated rotation of the wall at negative peaks in Steps 10 to 15 are -1.39°, -1.75°, -2.07°, -2.67°, -3.14°, and -3.82°. The calculated rotation of the wall are slightly smaller up to Step 9, and slightly larger in Steps 10 to 15, than the hinge rotations calculated from Figures 8-88 and 8-91, but both sets of values indicate that the hinge rotation contributed by the horizontal splice constitutes a major part of the overall wall rotation.

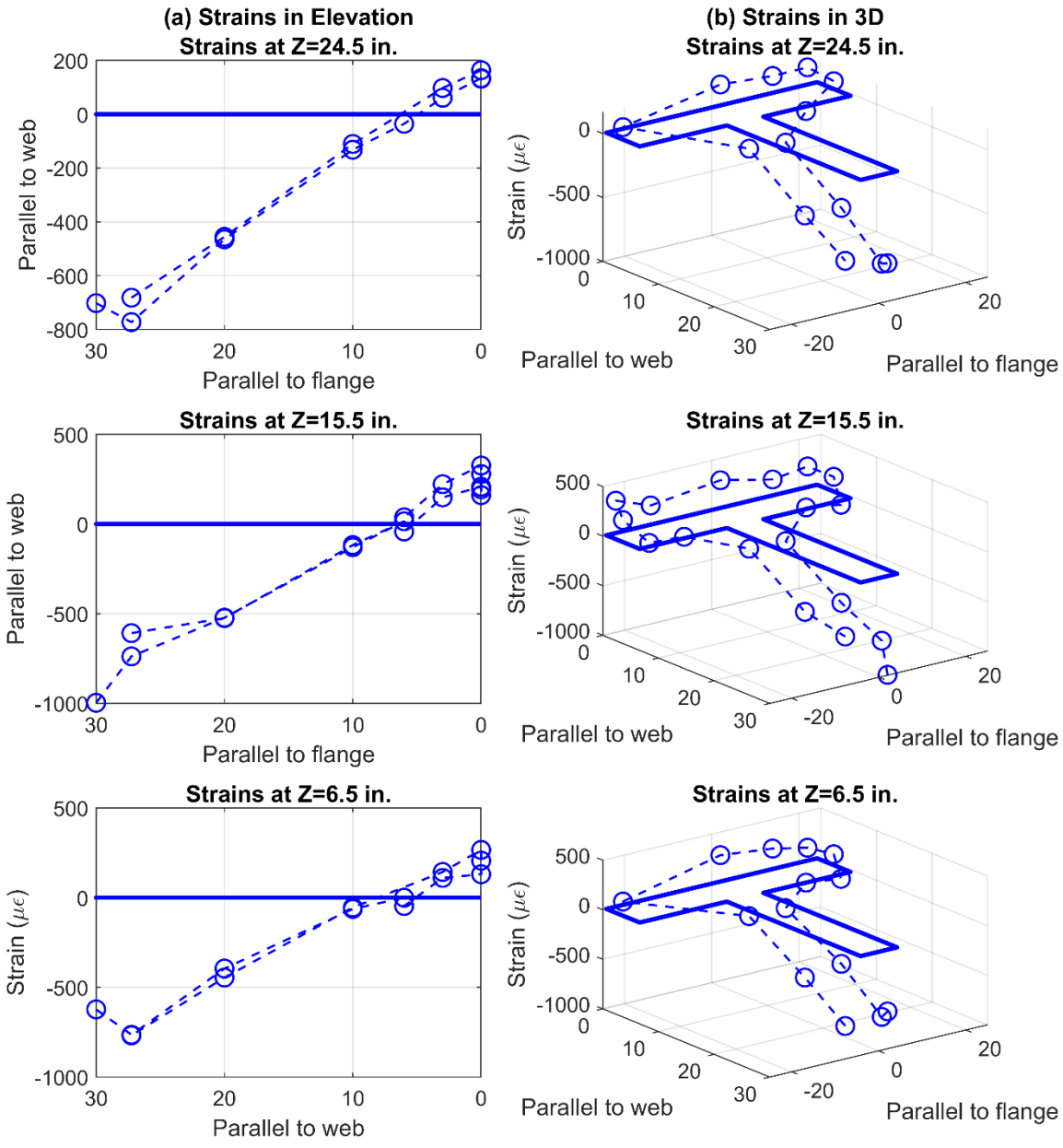


Figure 8-63. Axial Strains at Positive Peak in Step 2 in (a) Elevation and (b) 3D

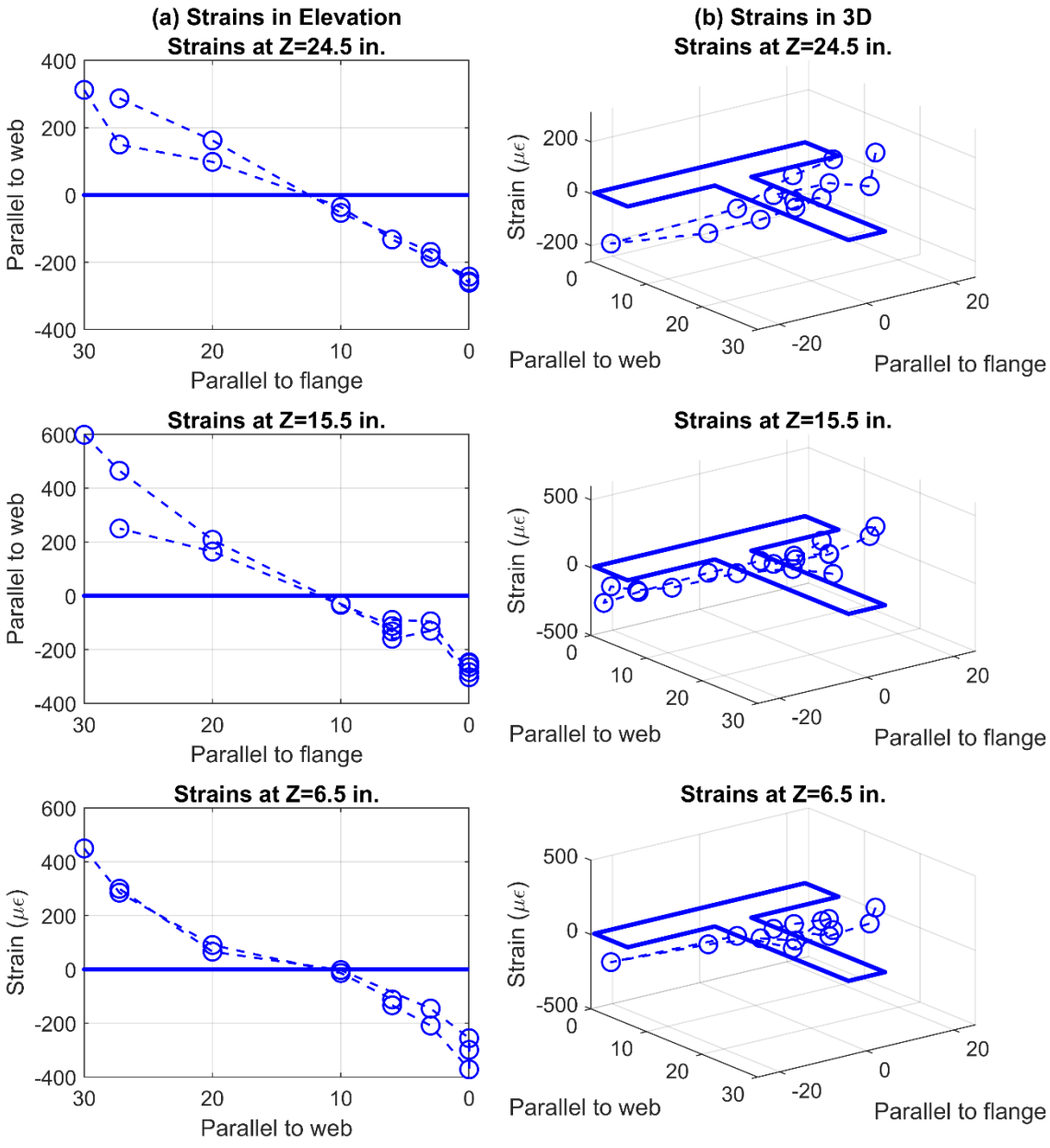


Figure 8-64. Axial Strains at Negative Peak in Step 2 in (a) Elevation and (b) 3D

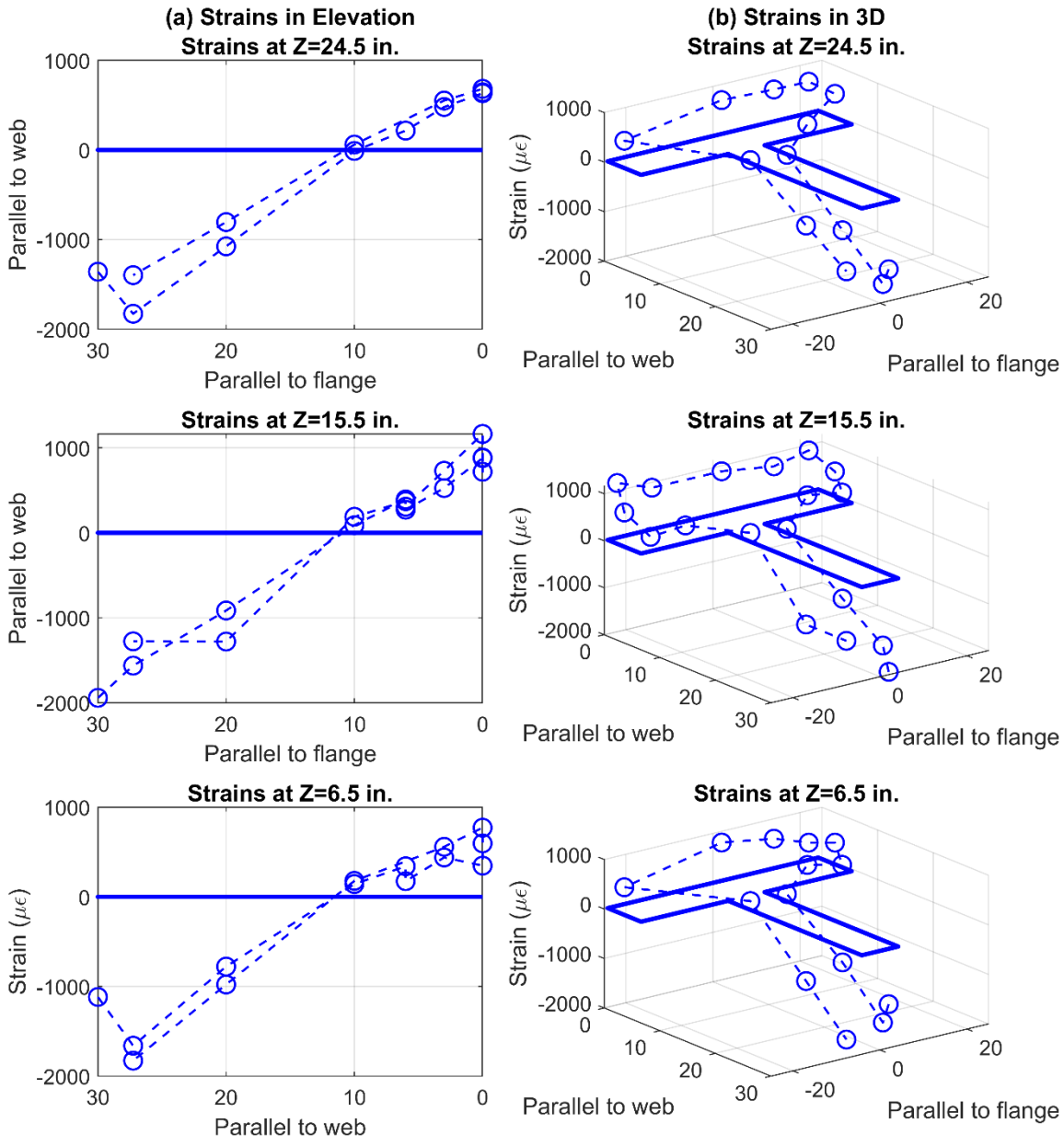


Figure 8-65. Axial Strains at Positive Peak in Step 4 in (a) Elevation and (b) 3D

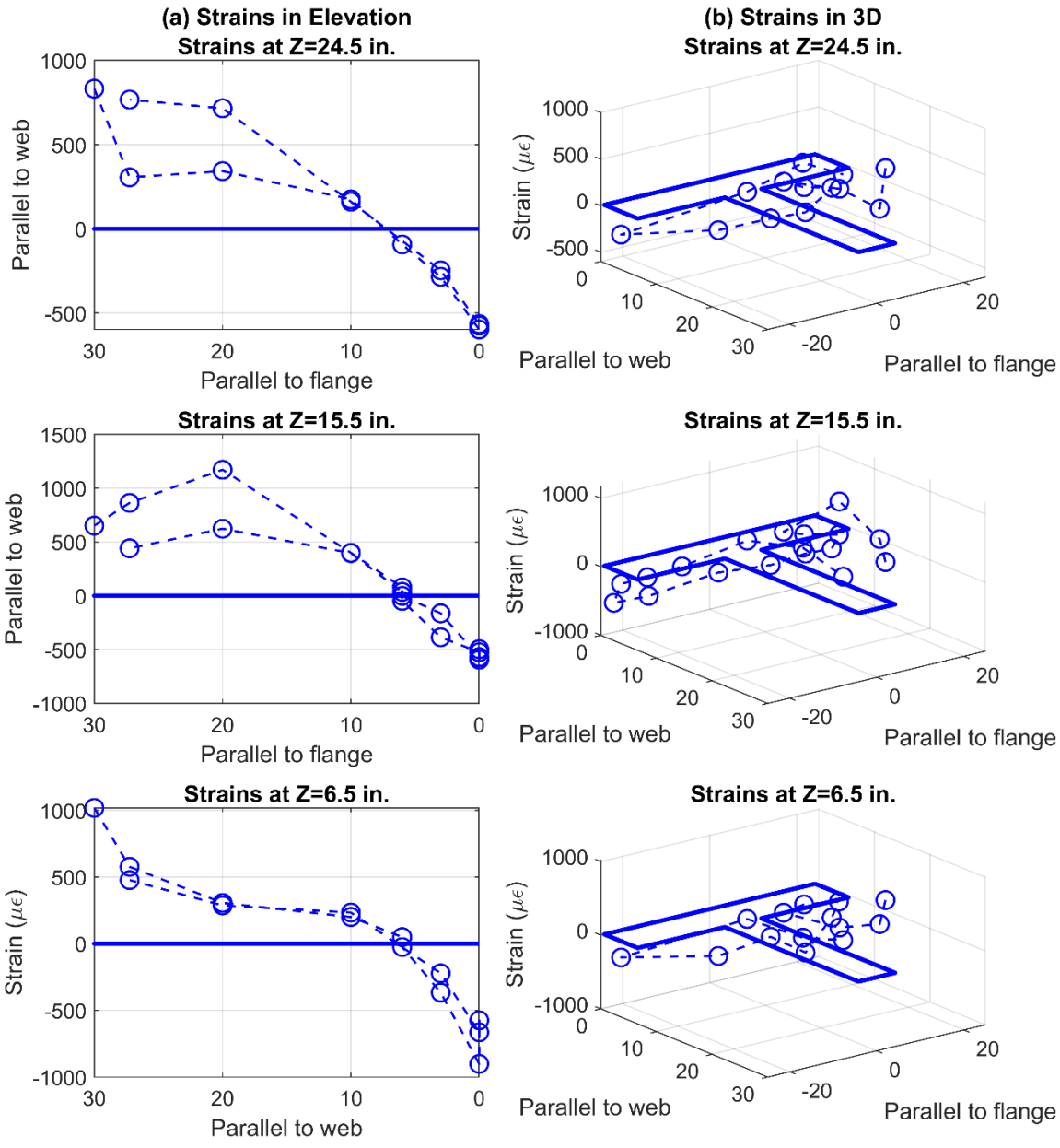


Figure 8-66. Axial Strains at Negative Peak in Step 4 in (a) Elevation and (b) 3D

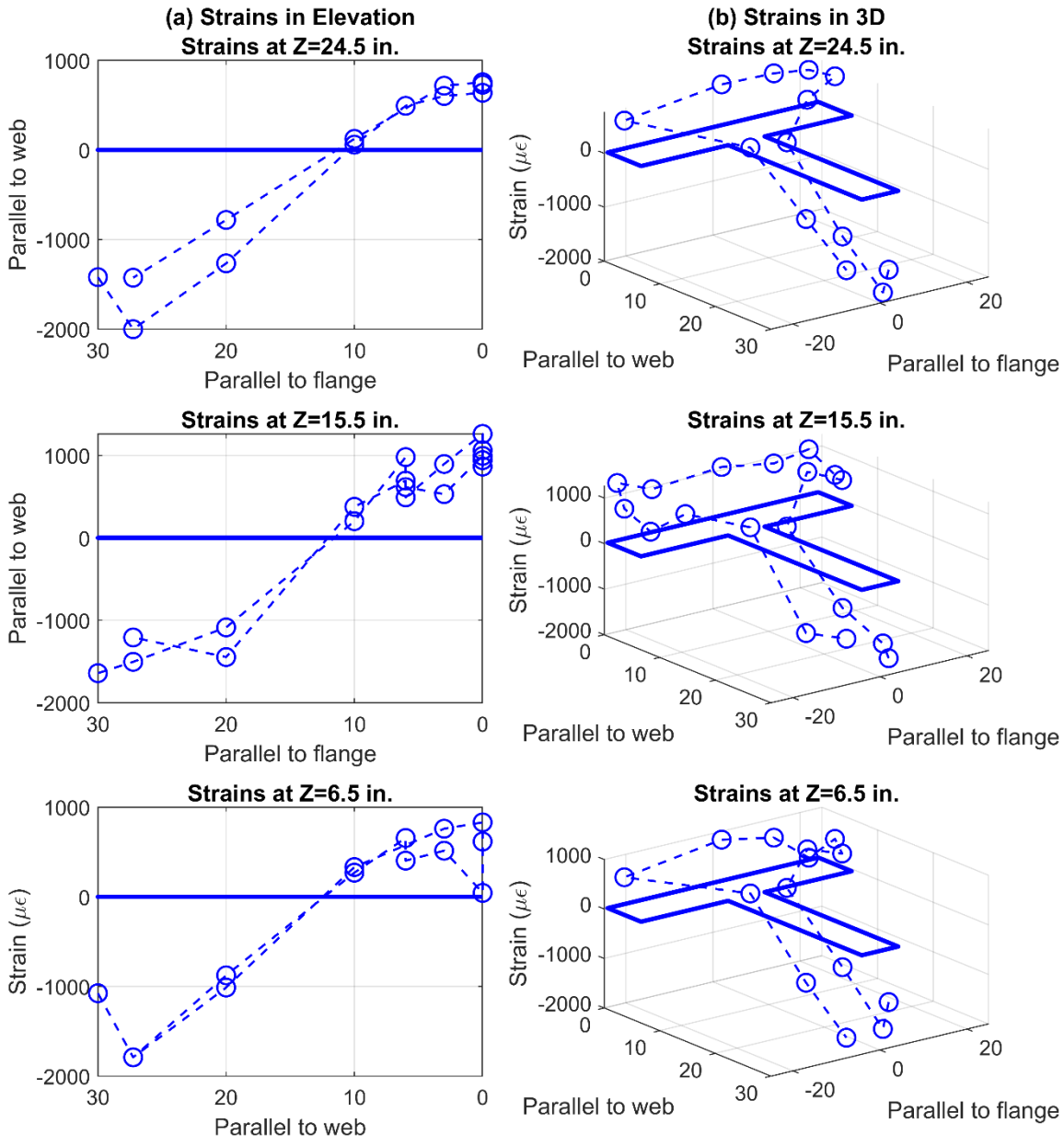


Figure 8-67. Axial Strains at Positive Peak in Step 5 in (a) Elevation and (b) 3D

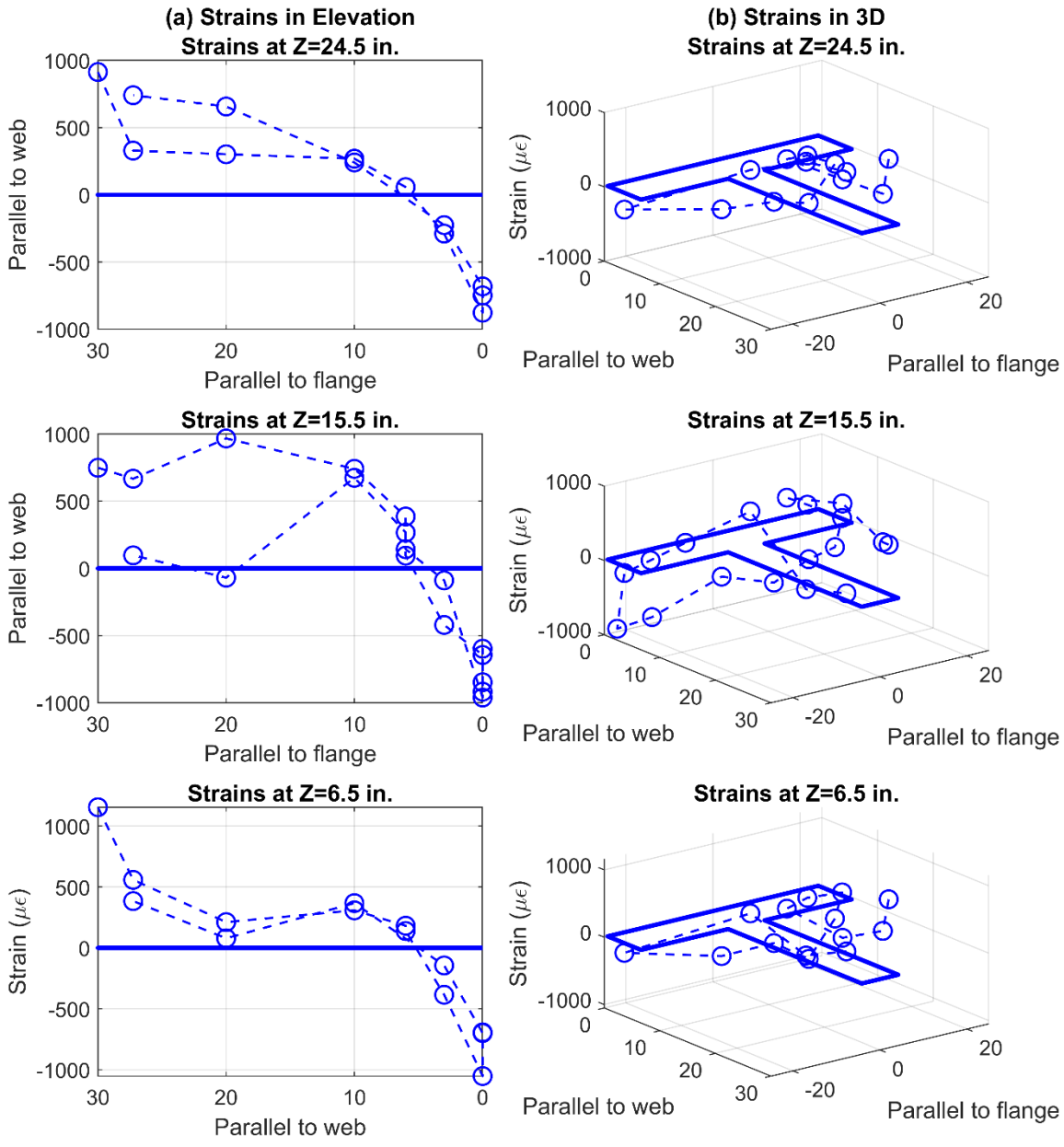


Figure 8-68. Axial Strains at Negative Peak in Step 5 in (a) Elevation and (b) 3D

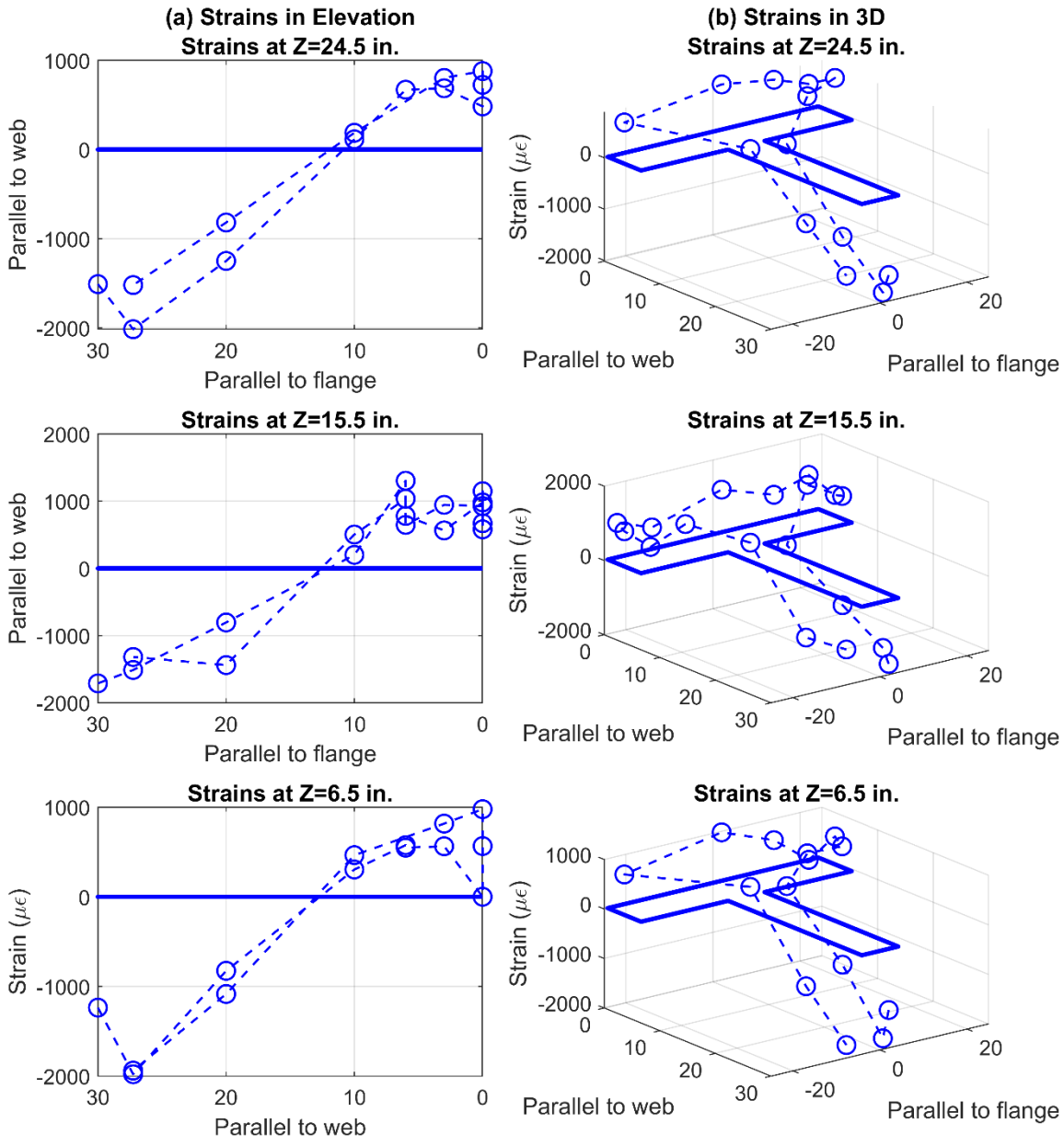


Figure 8-69. Axial Strains at Positive Peak in Step 6 in (a) Elevation and (b) 3D

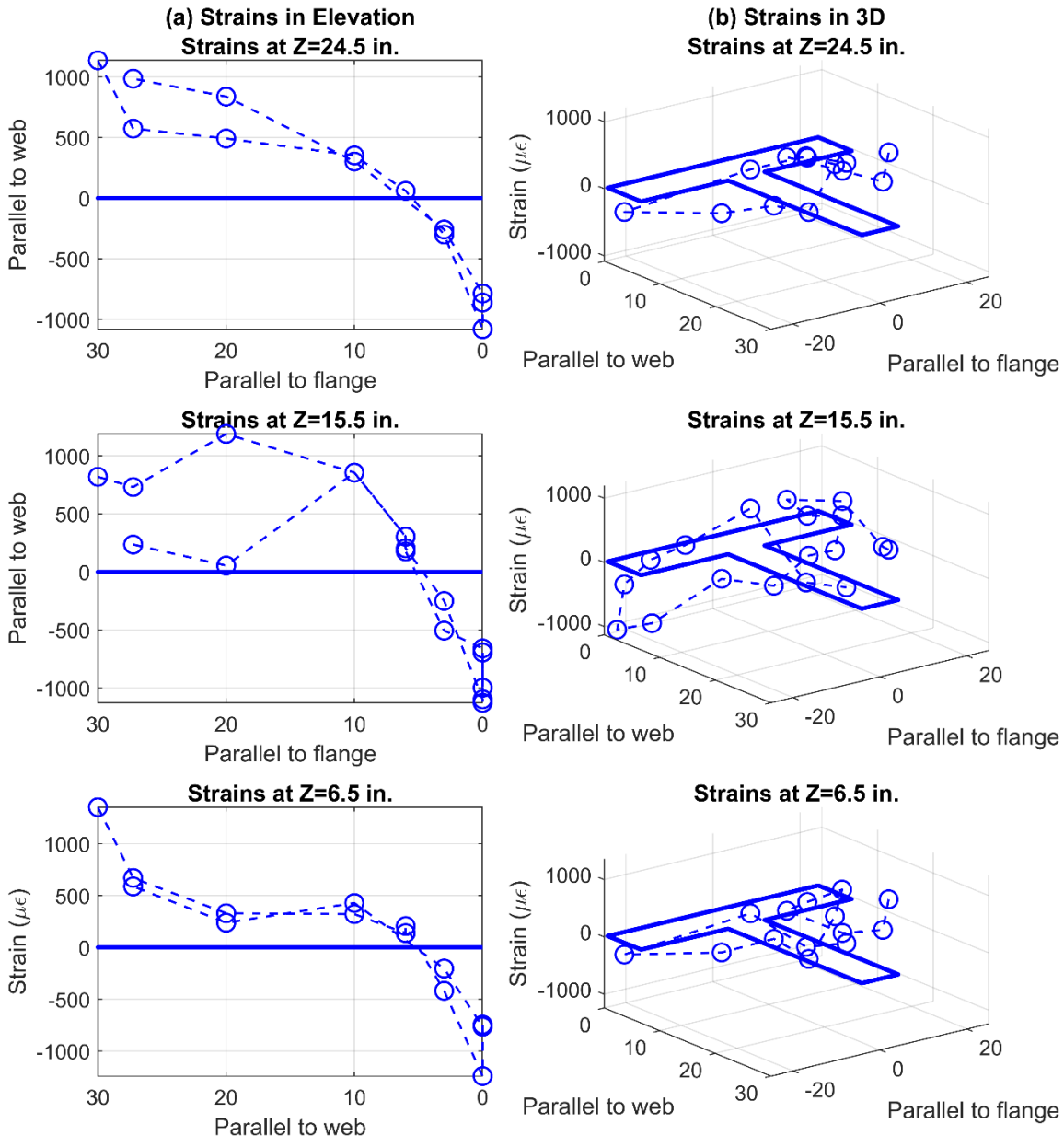


Figure 8-70. Axial Strains at Negative Peak in Step 6 in (a) Elevation and (b) 3D

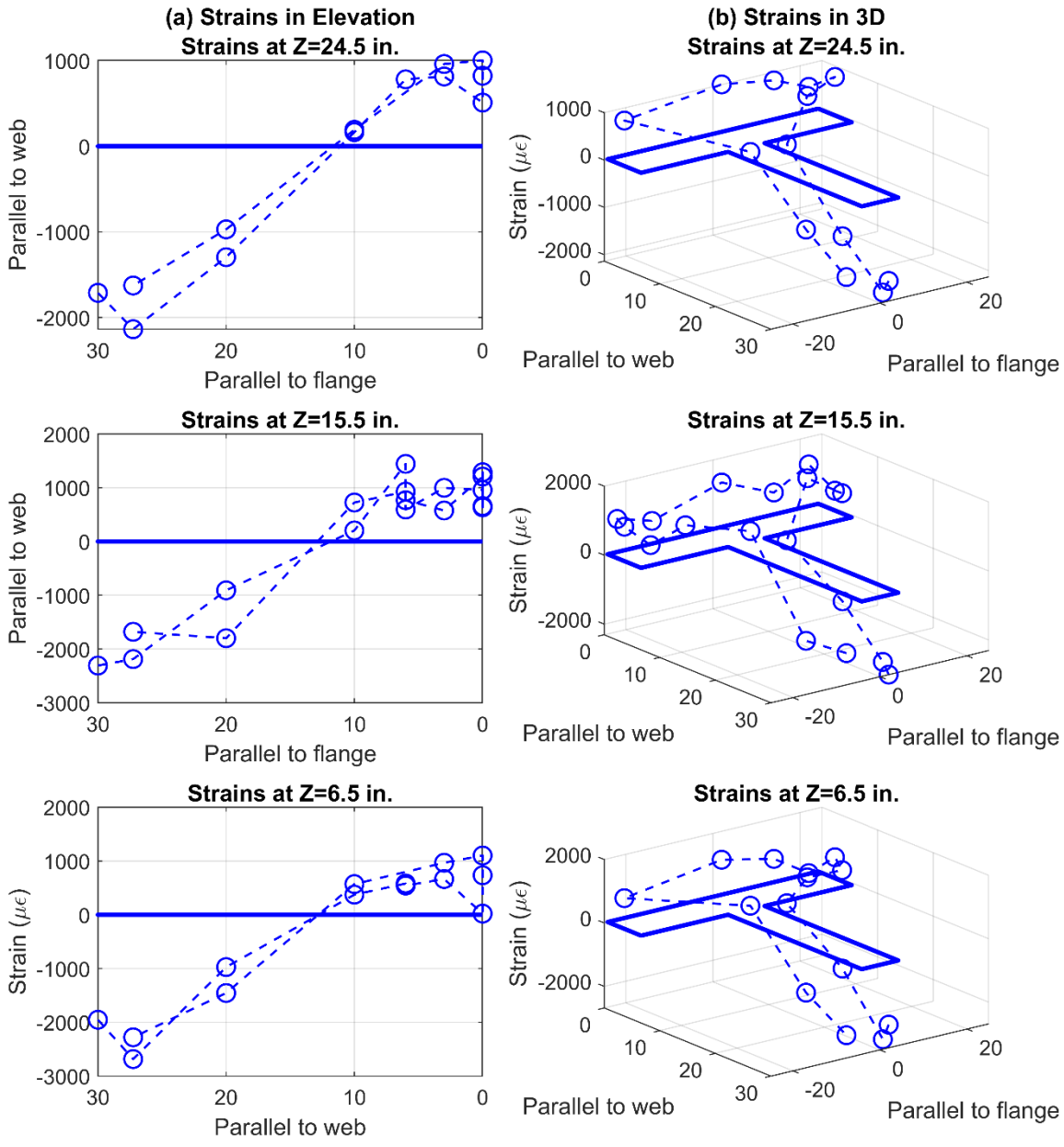


Figure 8-71. Axial Strains at Positive Peak in Step 7 in (a) Elevation and (b) 3D

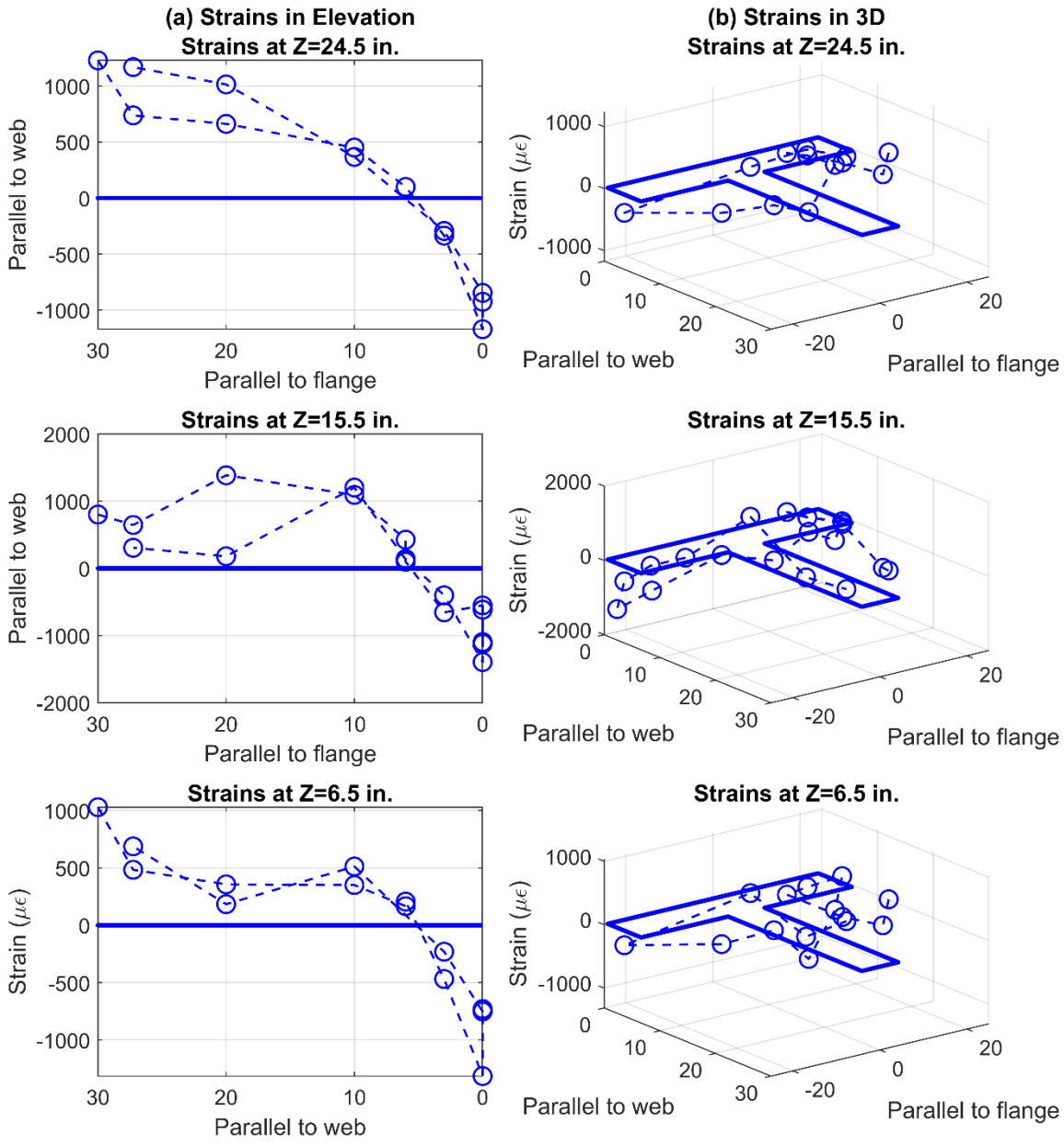


Figure 8-72. Axial Strains at Negative Peak in Step 7 in (a) Elevation and (b) 3D

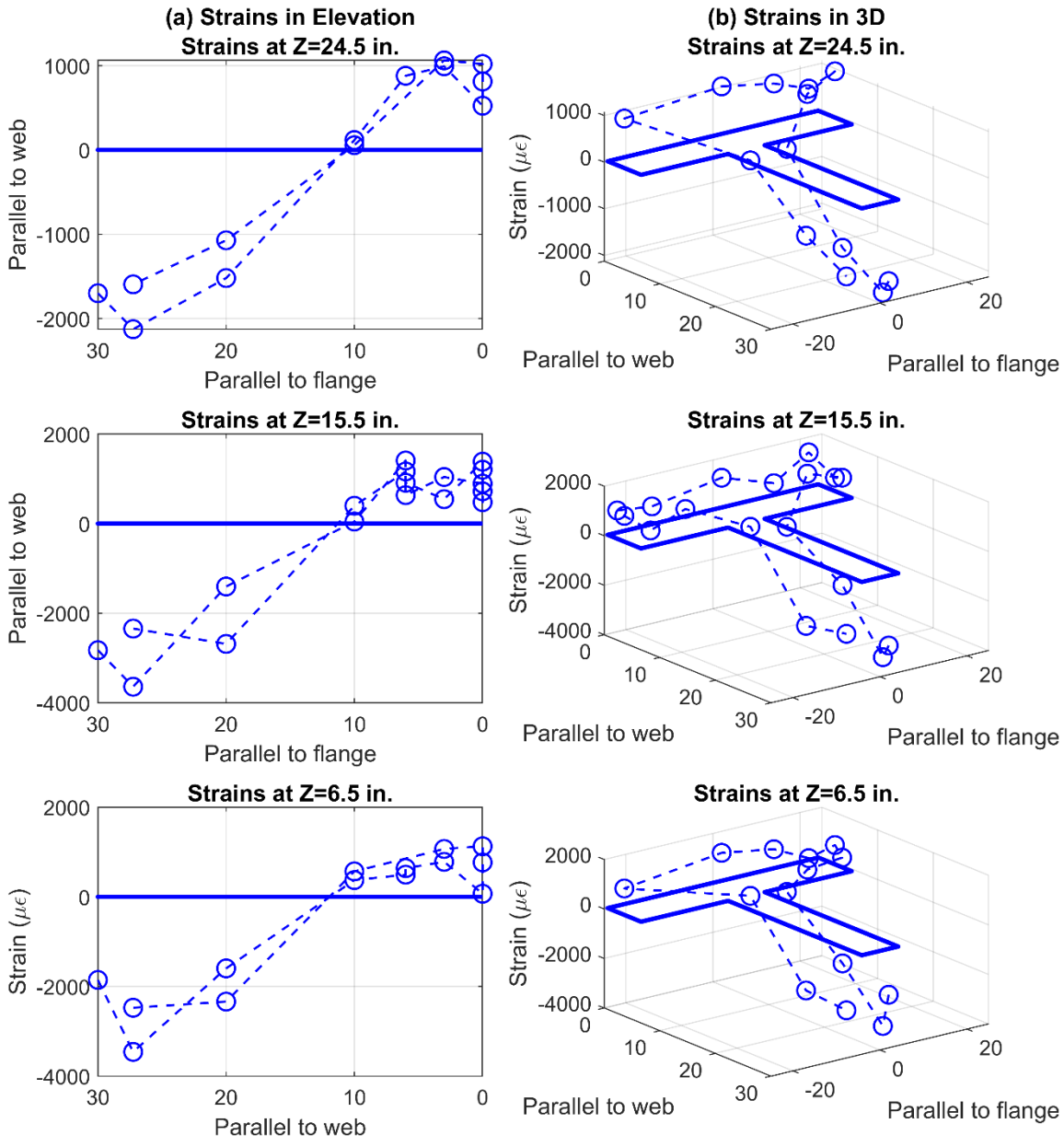


Figure 8-73. Axial Strains at Positive Peak in Step 8 in (a) Elevation and (b) 3D

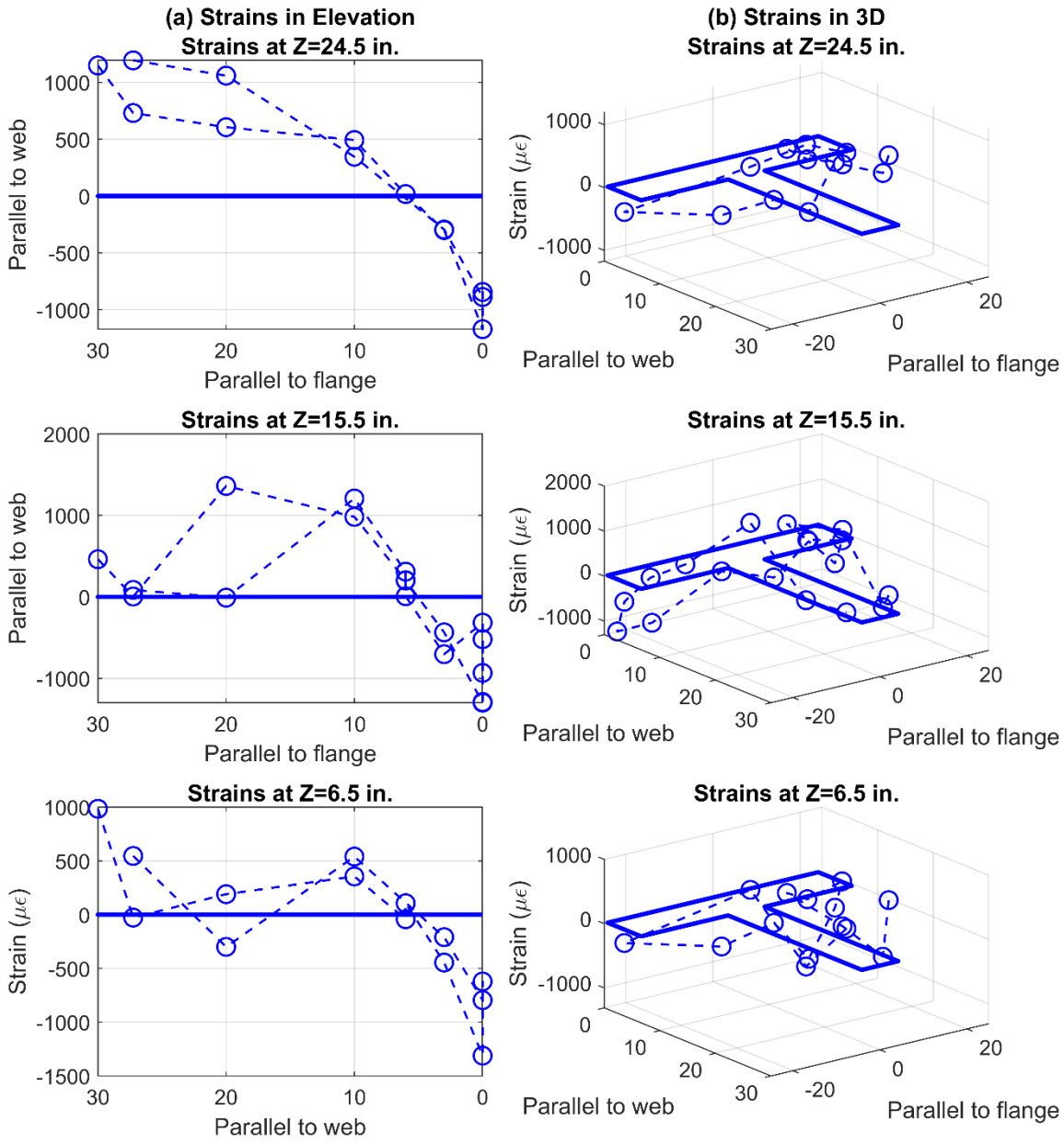


Figure 8-74. Axial Strains at Negative Peak in Step 8 in (a) Elevation and (b) 3D

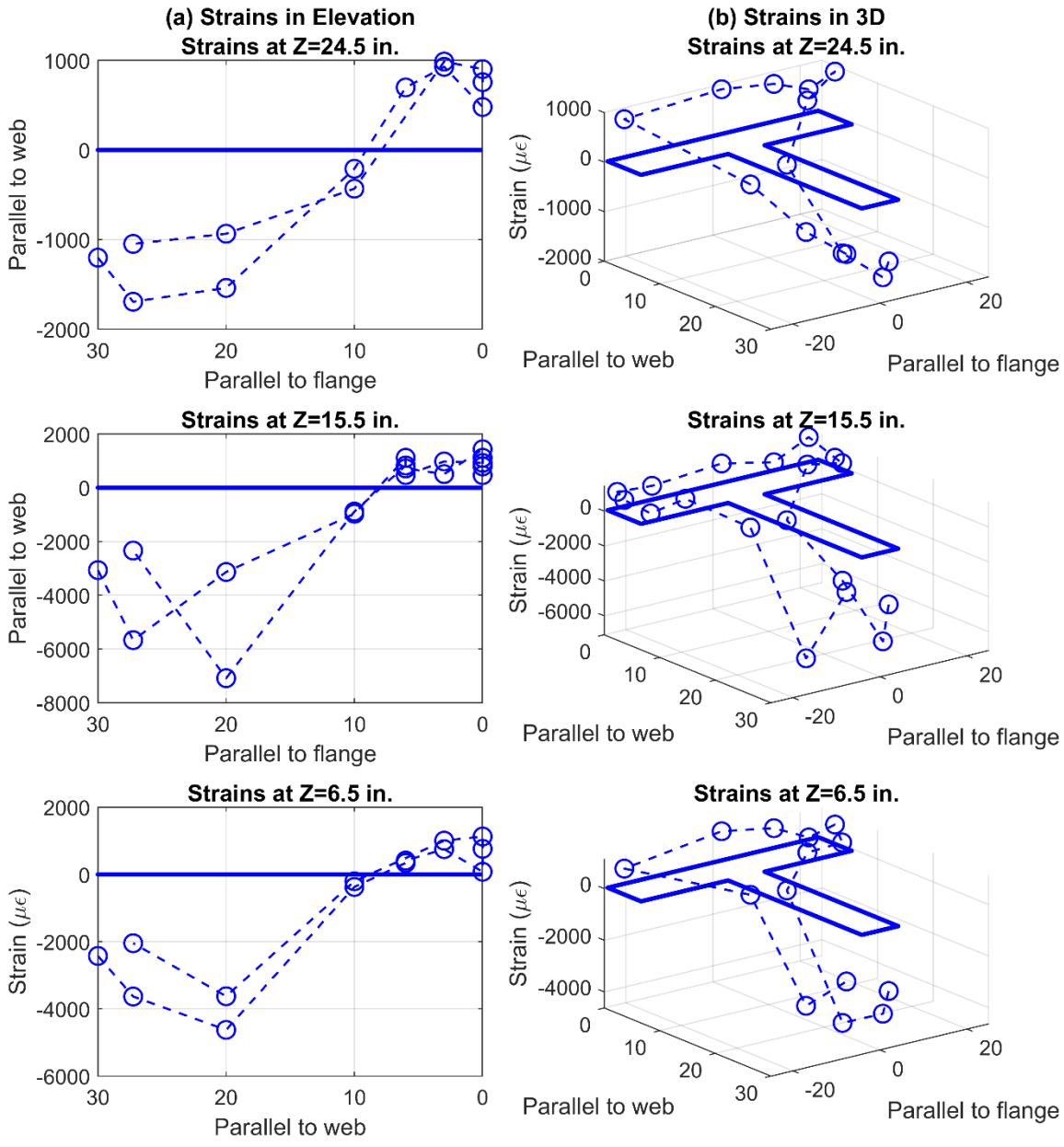


Figure 8-75. Axial Strains at Positive Peak in Step 9 in (a) Elevation and (b) 3D

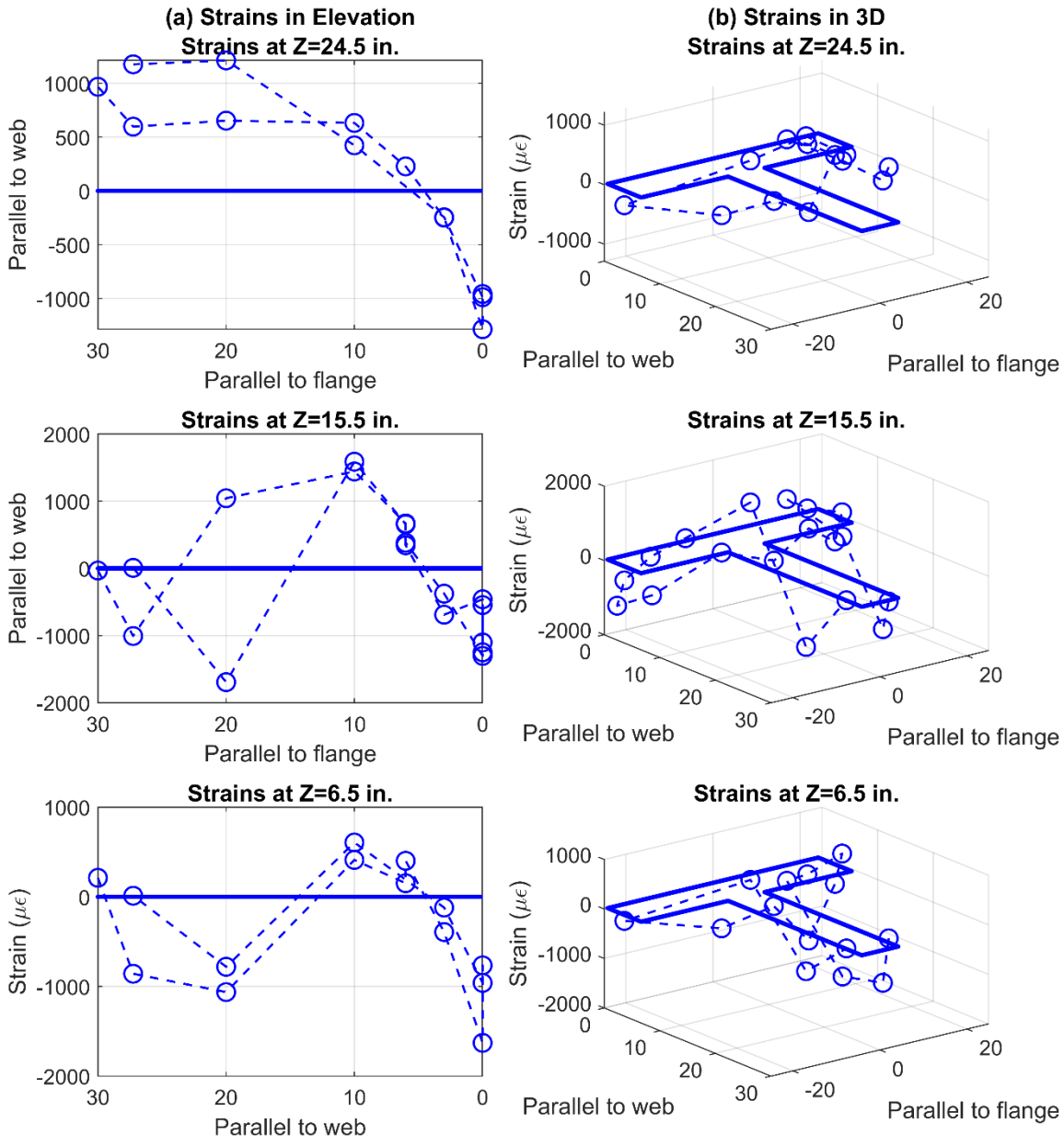


Figure 8-76. Axial Strains at Negative Peak in Step 9 in (a) Elevation and (b) 3D

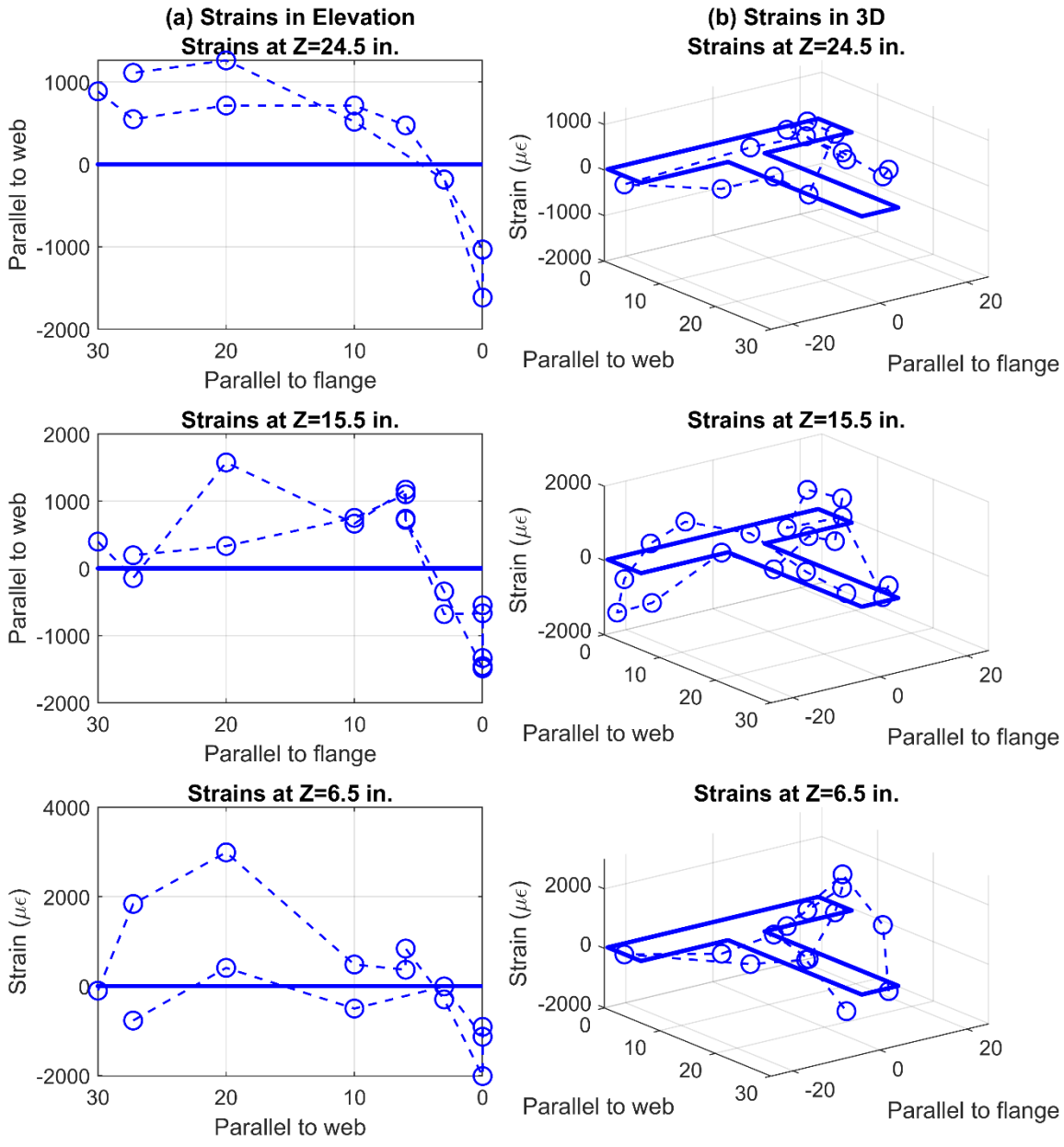


Figure 8-77. Axial Strains at Negative Peak in Step 10 in (a) Elevation and (b) 3D

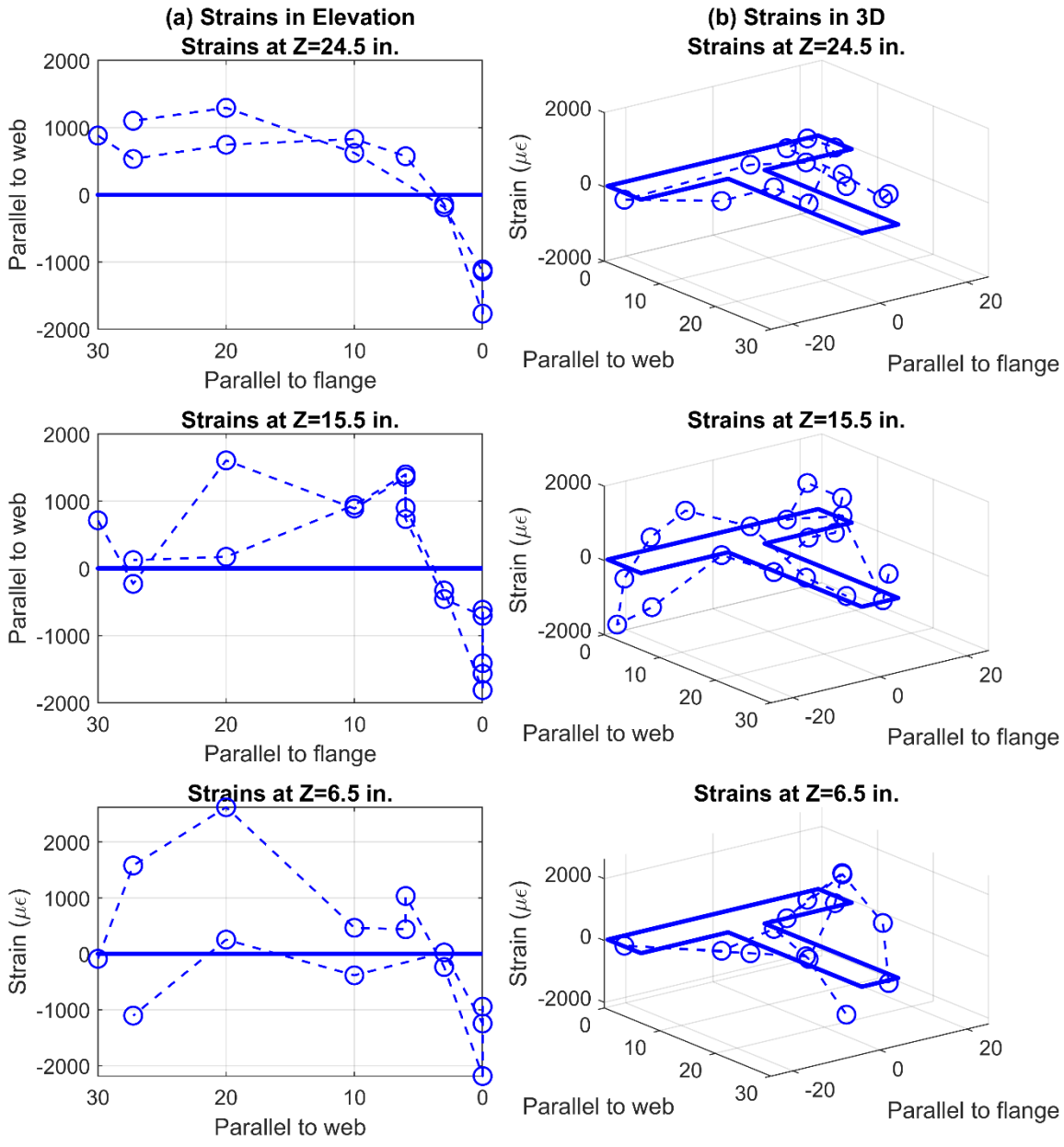


Figure 8-78. Axial Strains at Negative Peak in Step 11 in (a) Elevation and (b) 3D

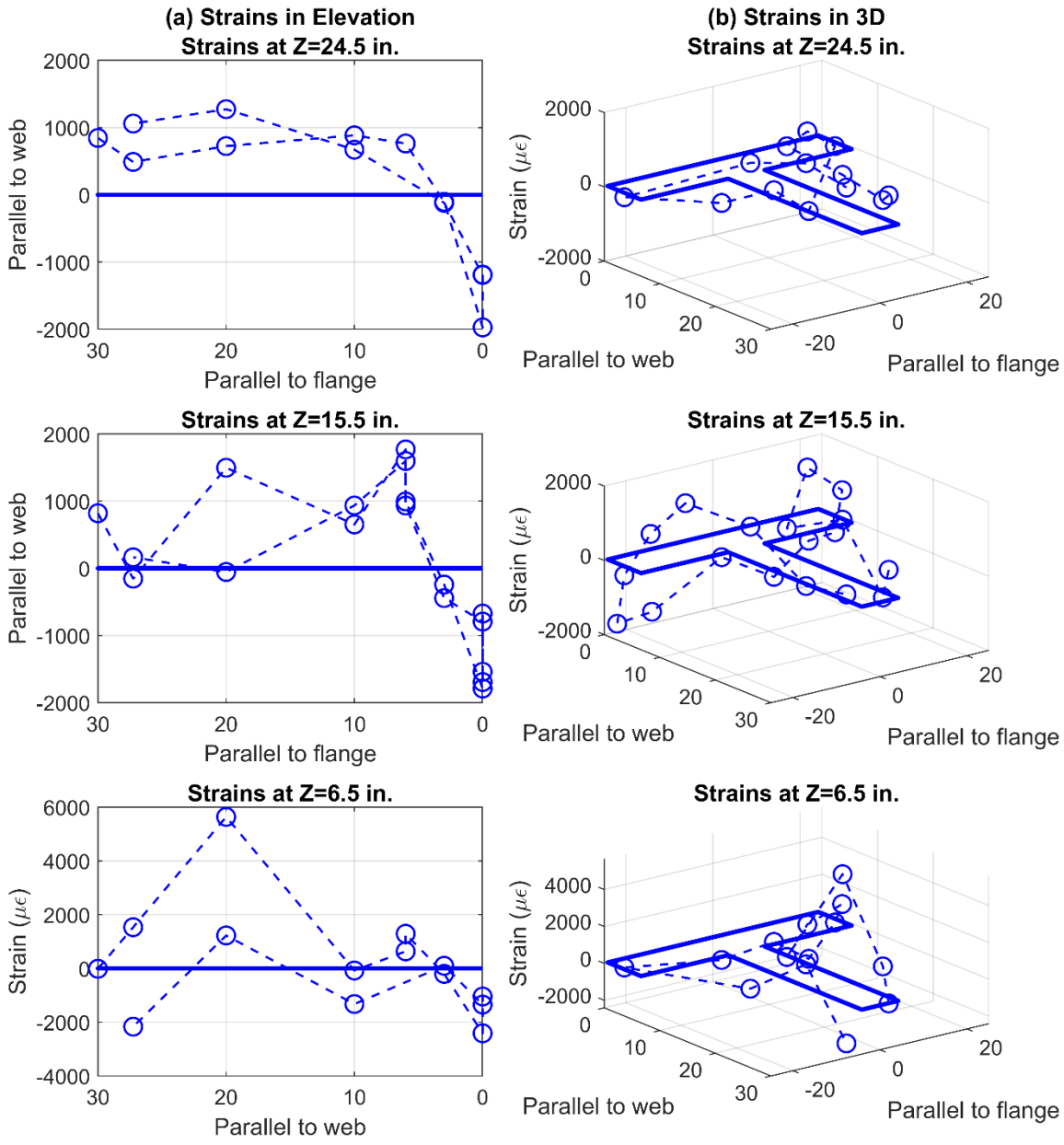


Figure 8-79. Axial Strains at Negative Peak in Step 12 in (a) Elevation and (b) 3D

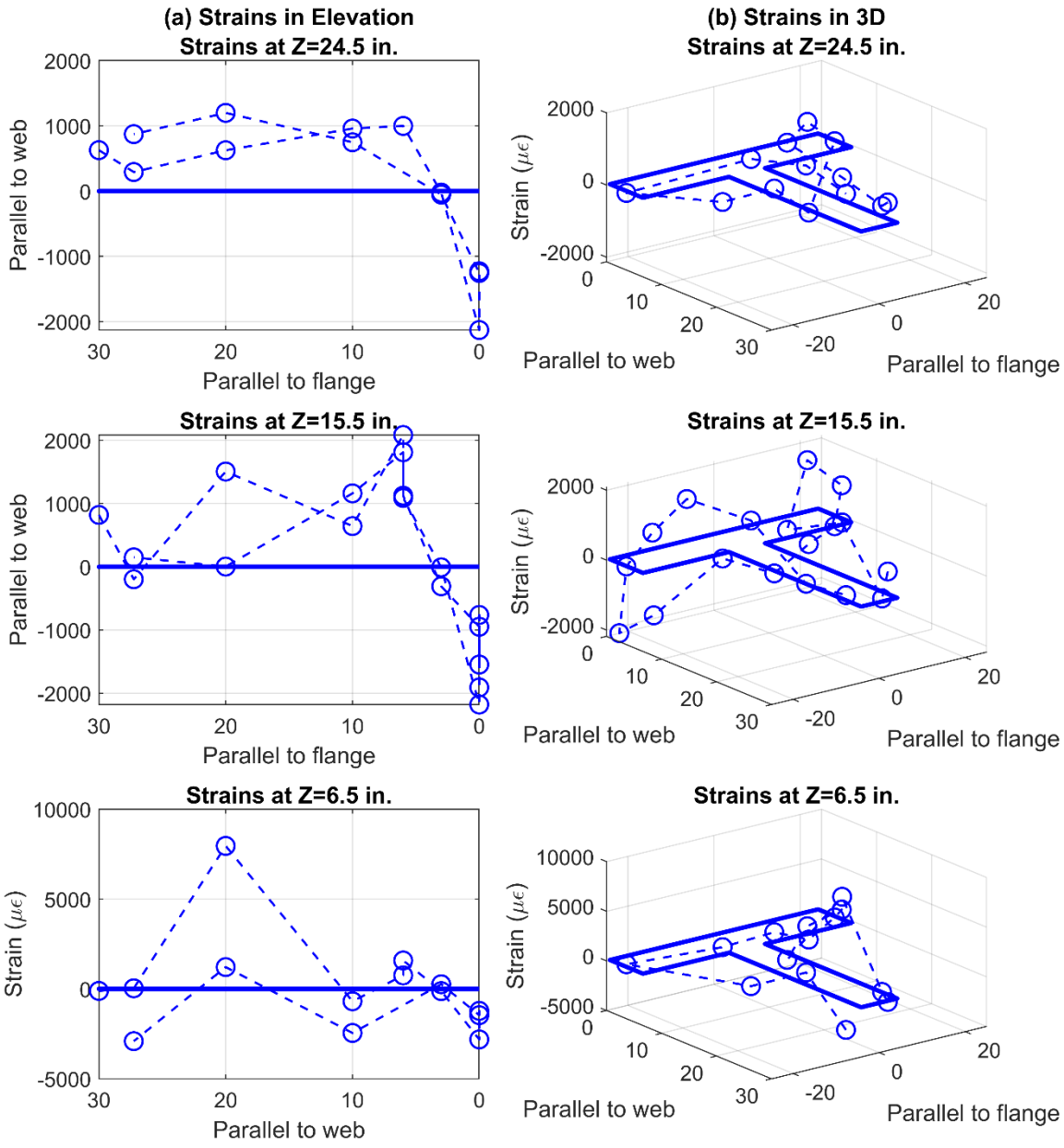


Figure 8-80. Axial Strains at Negative Peak in Step 13 in (a) Elevation and (b) 3D

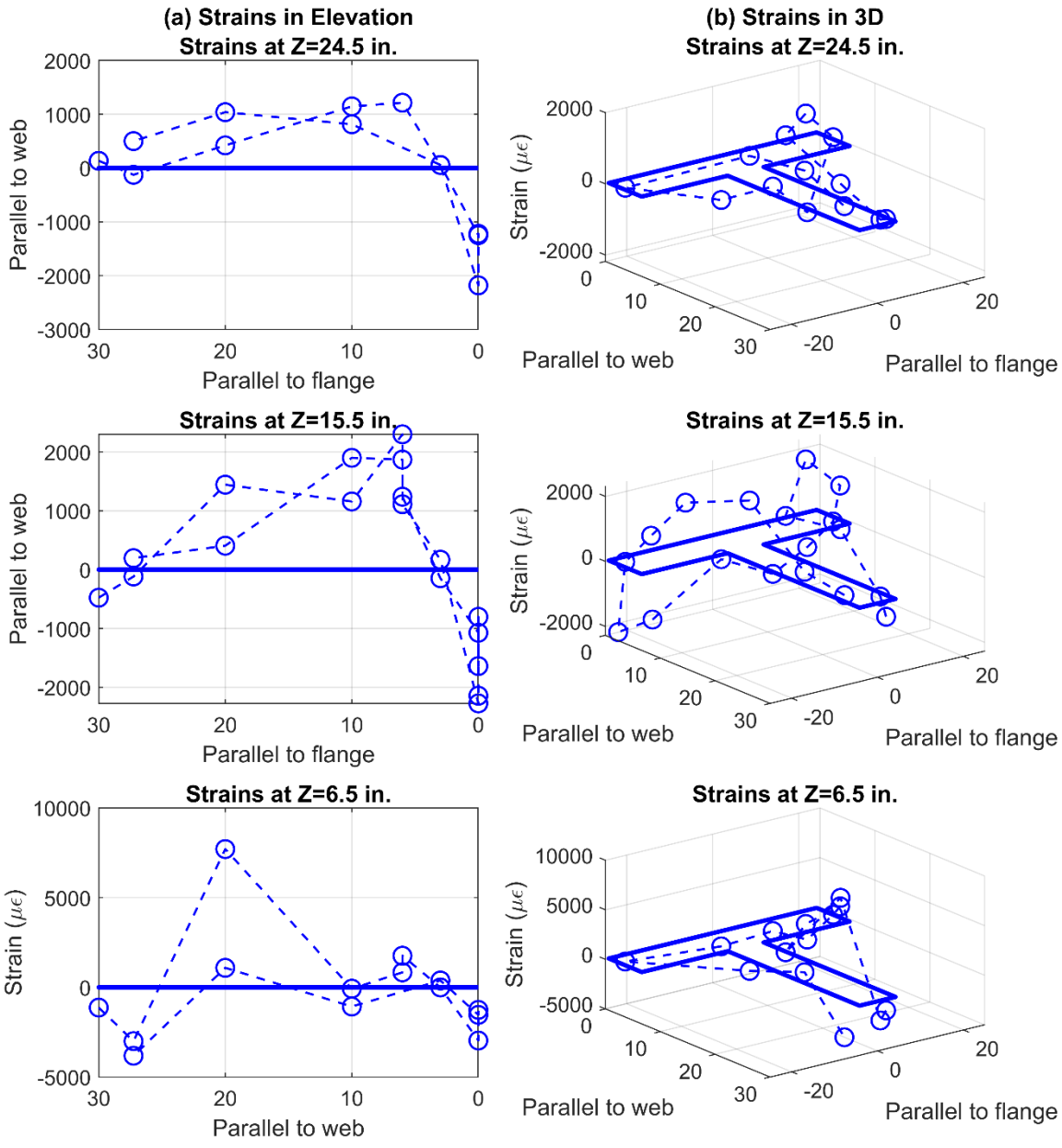


Figure 8-81. Axial Strains at Negative Peak in Step 14 in (a) Elevation and (b) 3D

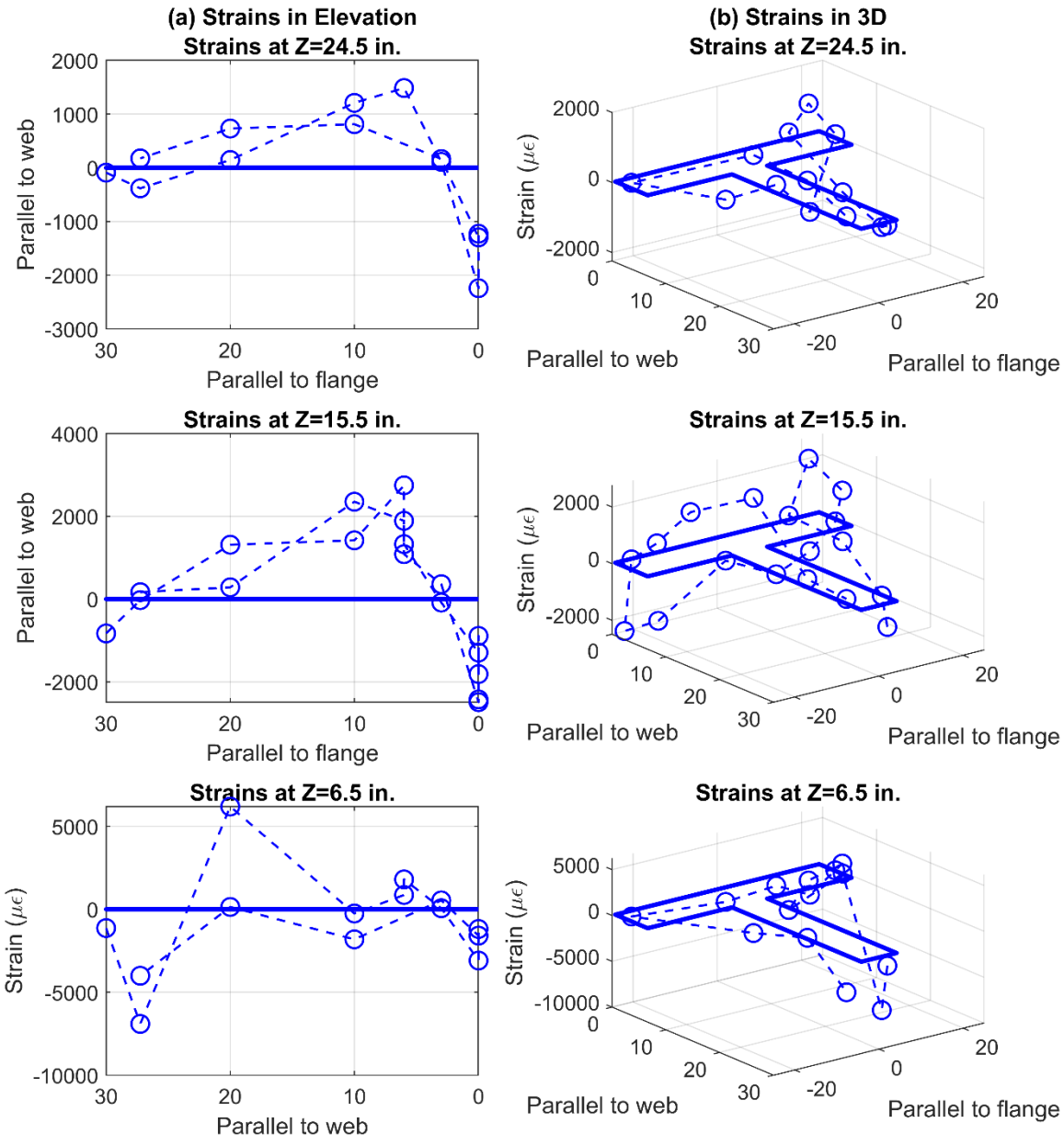


Figure 8-82. Axial Strains at Negative Peak in Step 15 in (a) Elevation and (b) 3D

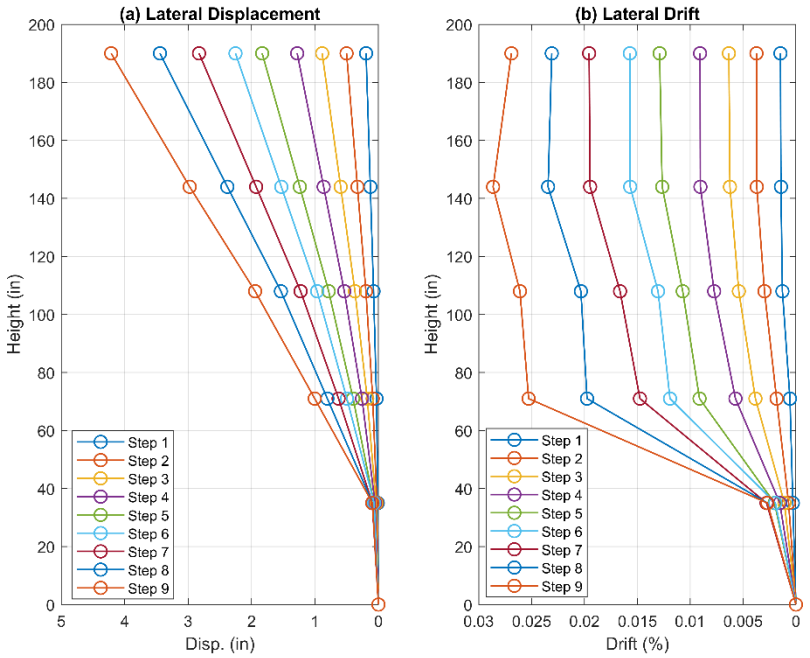


Figure 8-83. Lateral Displacement and Drift at Positive Peaks in each Step

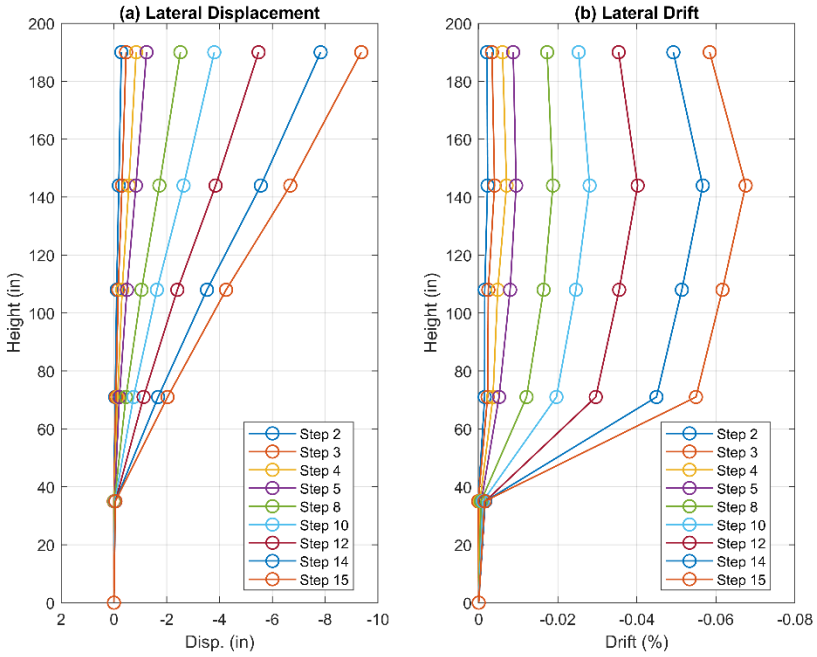


Figure 8-84. Lateral Displacement and Drift at Negative Peaks in each Step

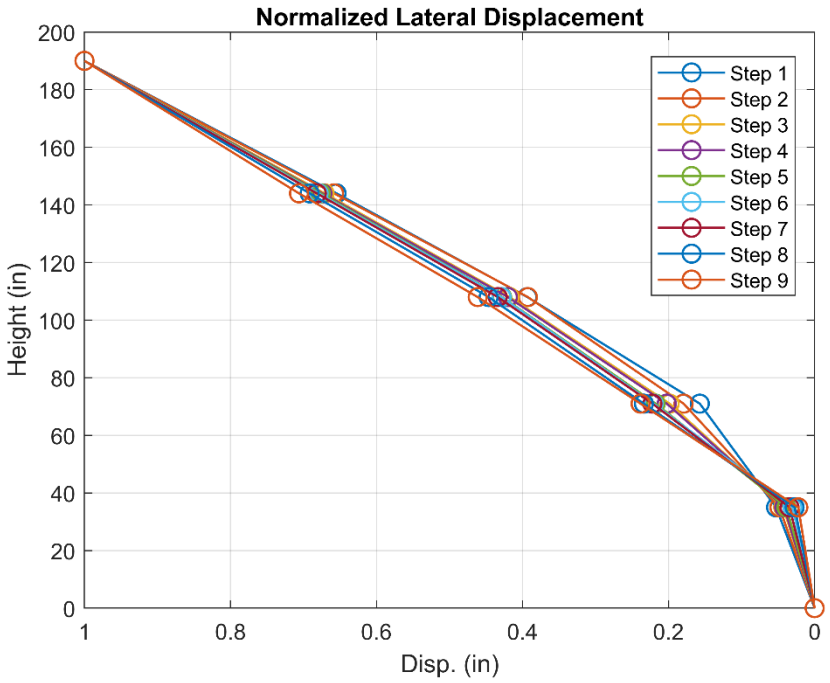


Figure 8-85. Normalized Lateral Displacement at Positive Peaks in each Step

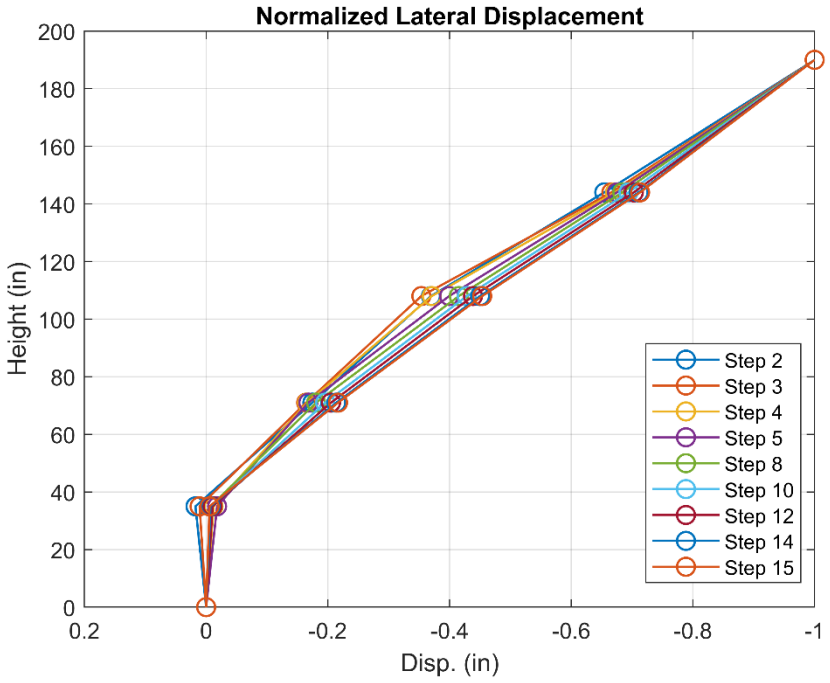


Figure 8-86. Normalized Lateral Displacement at Negative Peaks in each Step

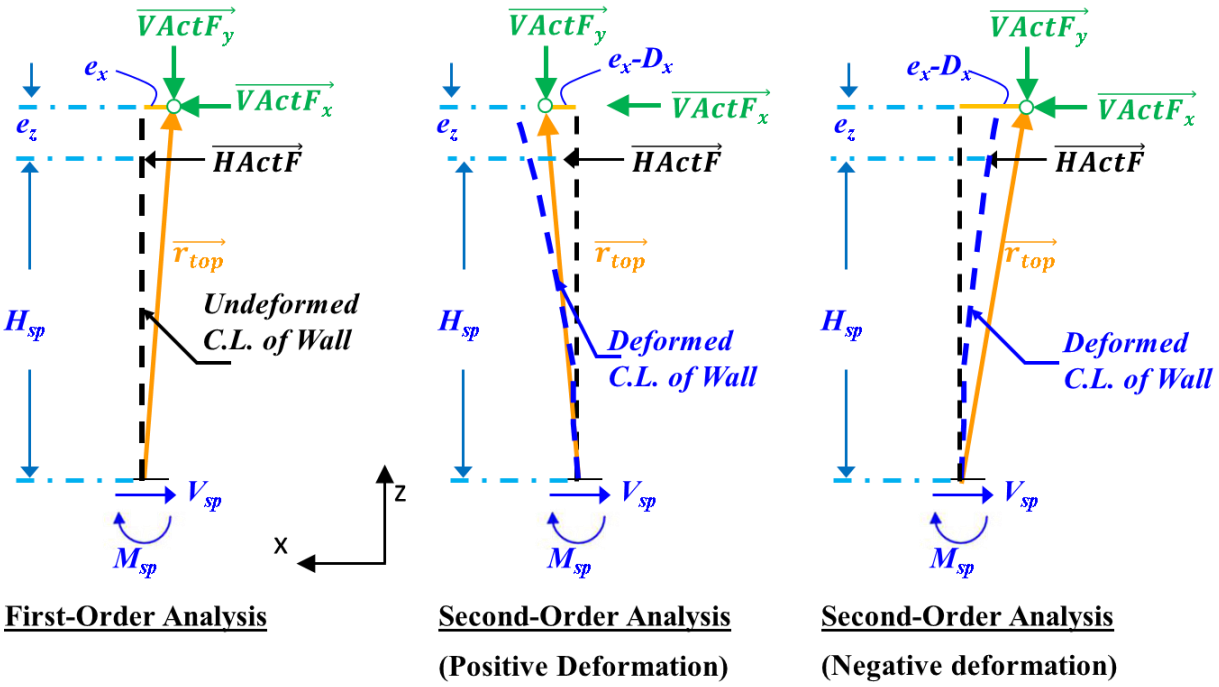


Figure 8-87. Free-Body Diagram of Wall for First and Second-Order Analyses

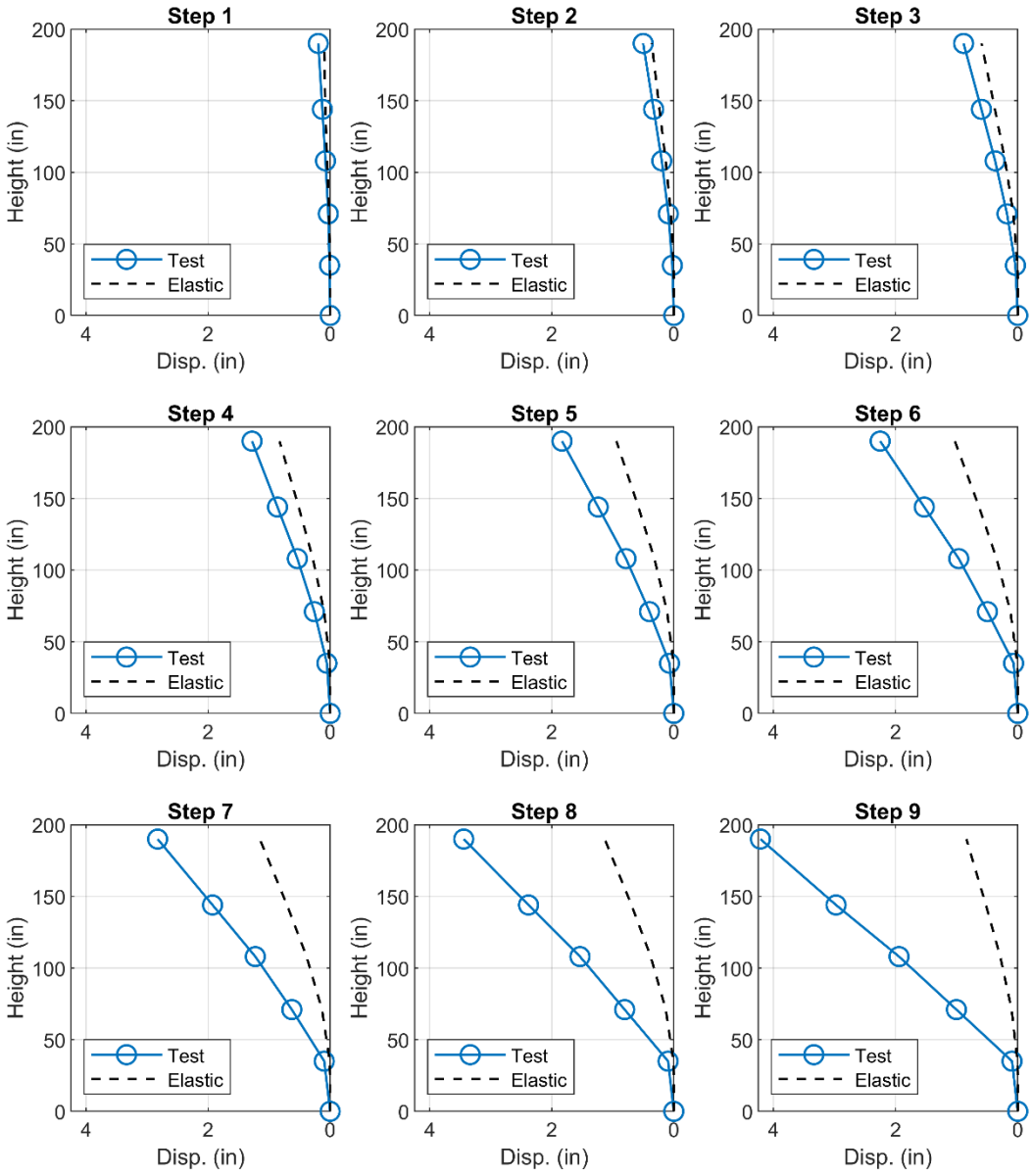


Figure 8-88. Lateral Displacement at Positive Peaks in each Step (First-Order Analysis)

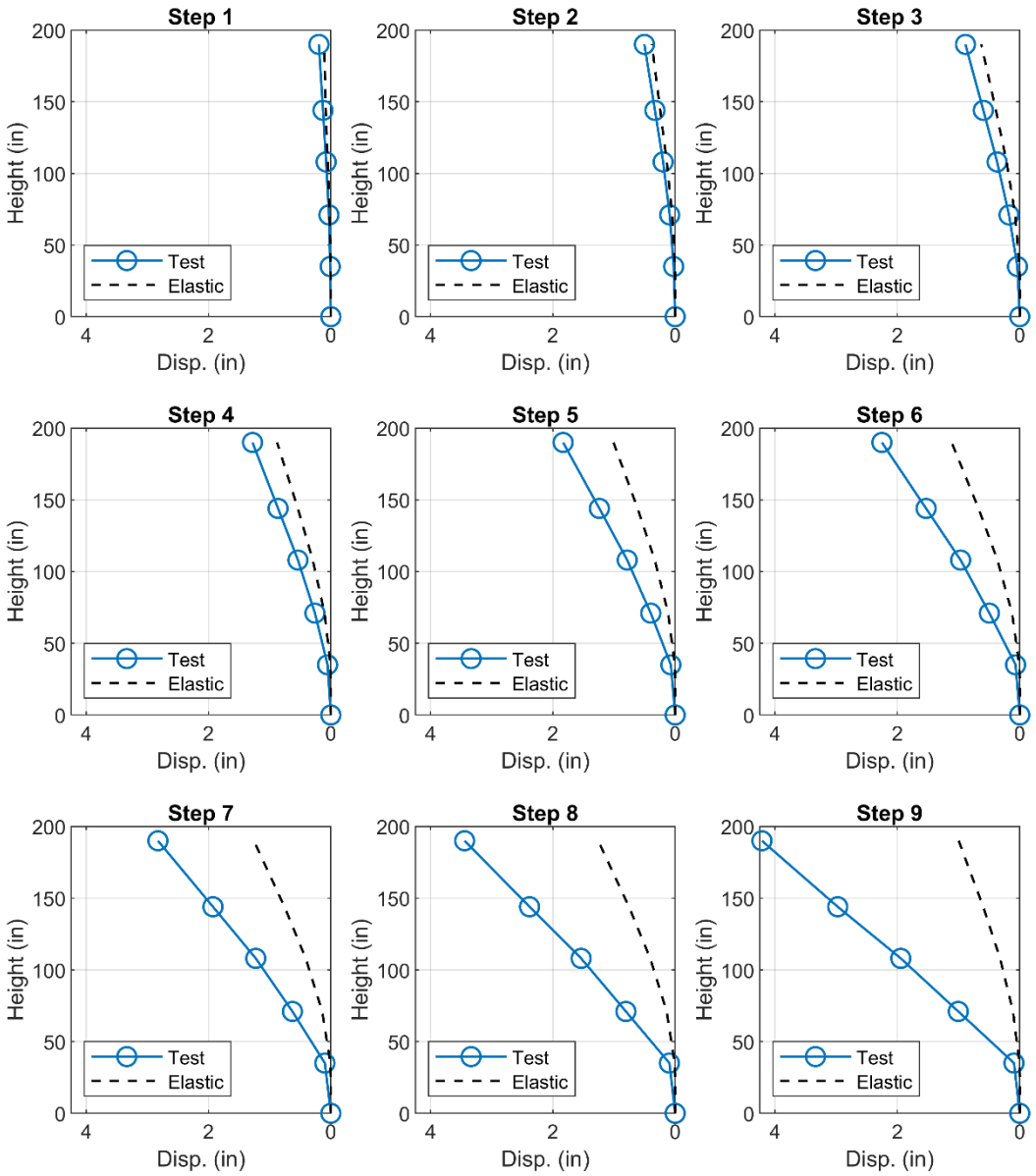


Figure 8-89. Lateral Displacement at Positive Peaks in each Step (Second-Order Analysis)

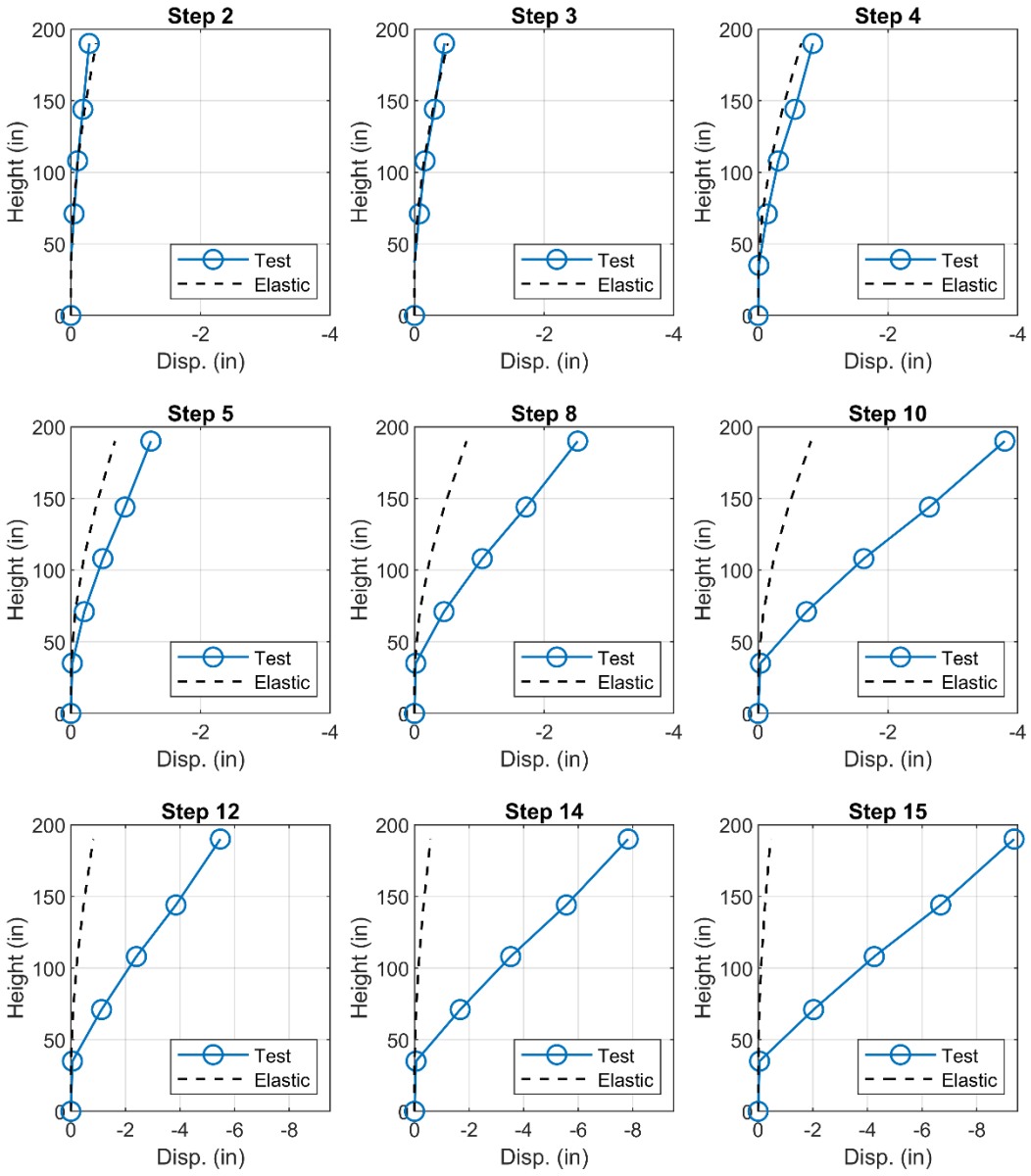


Figure 8-90. Lateral Displacement at Negative Peaks in each Step (First-Order Analysis)

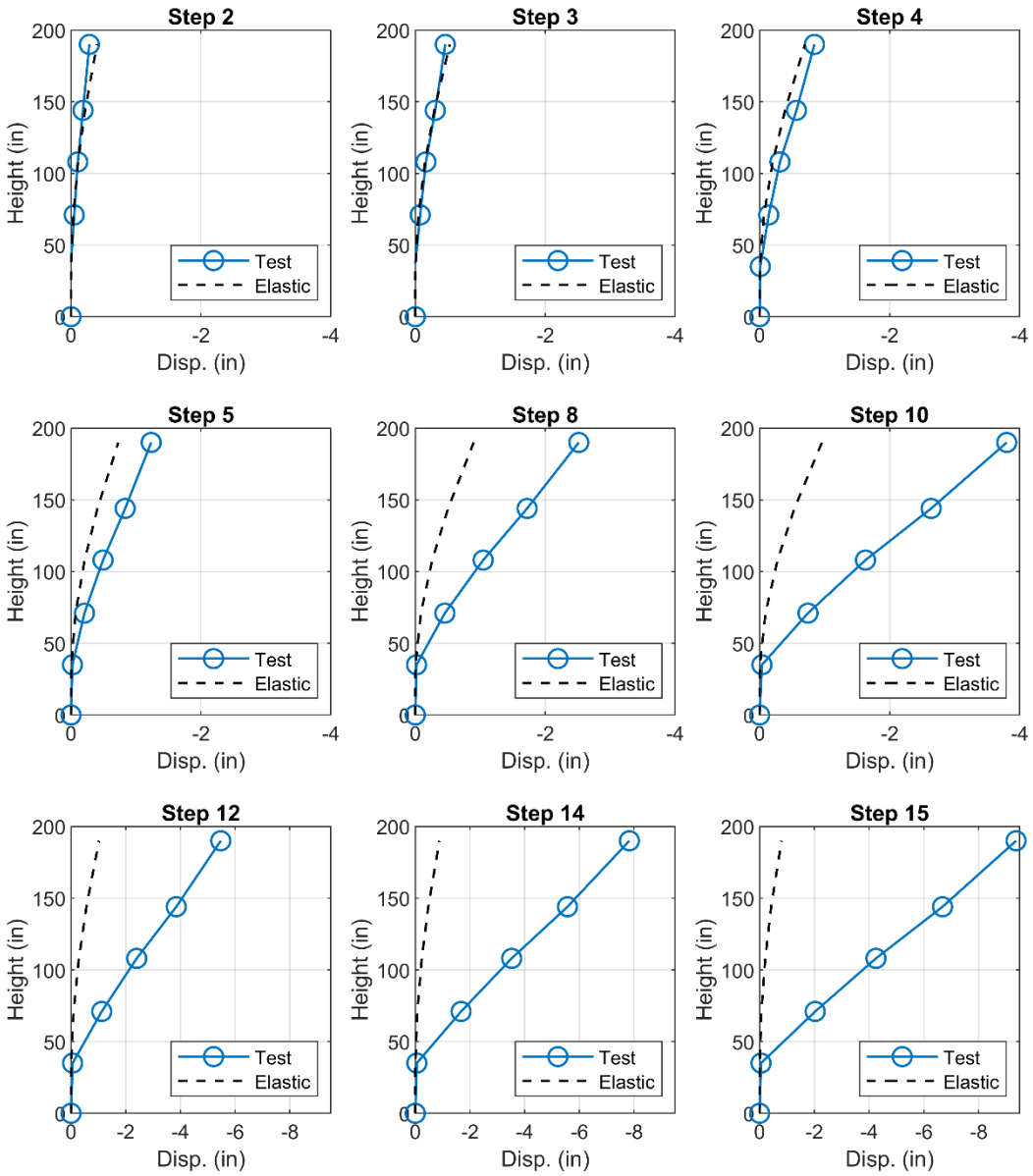


Figure 8-91. Lateral Displacement at Negative Peaks in each Step (Second-Order Analysis)

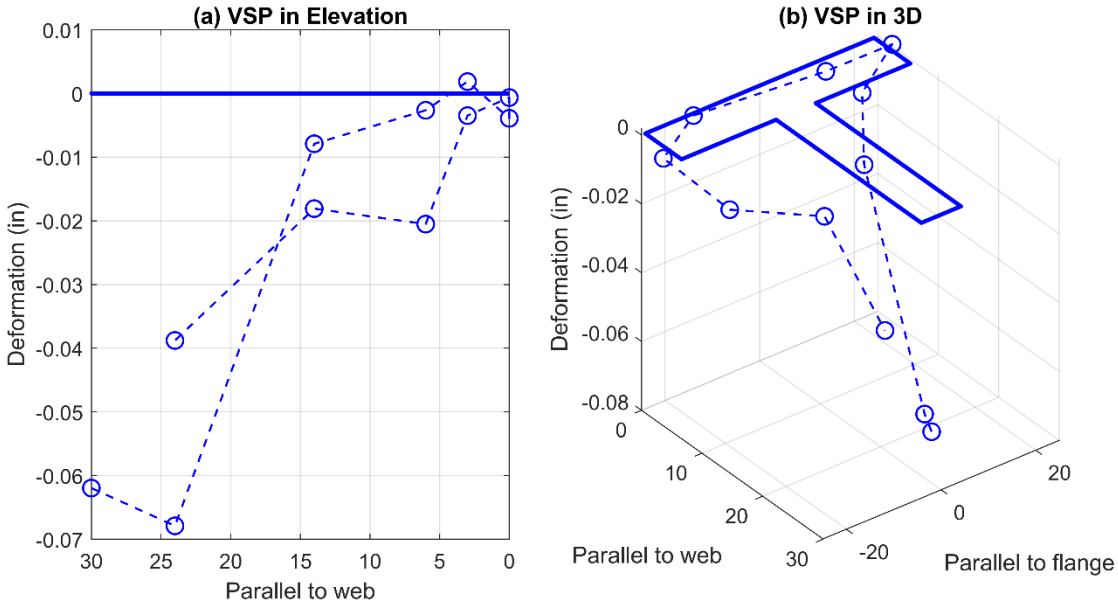


Figure 8-92. Deformation of VSP at Positive Peak in Step 4 in (a) Elevation and (b) 3D

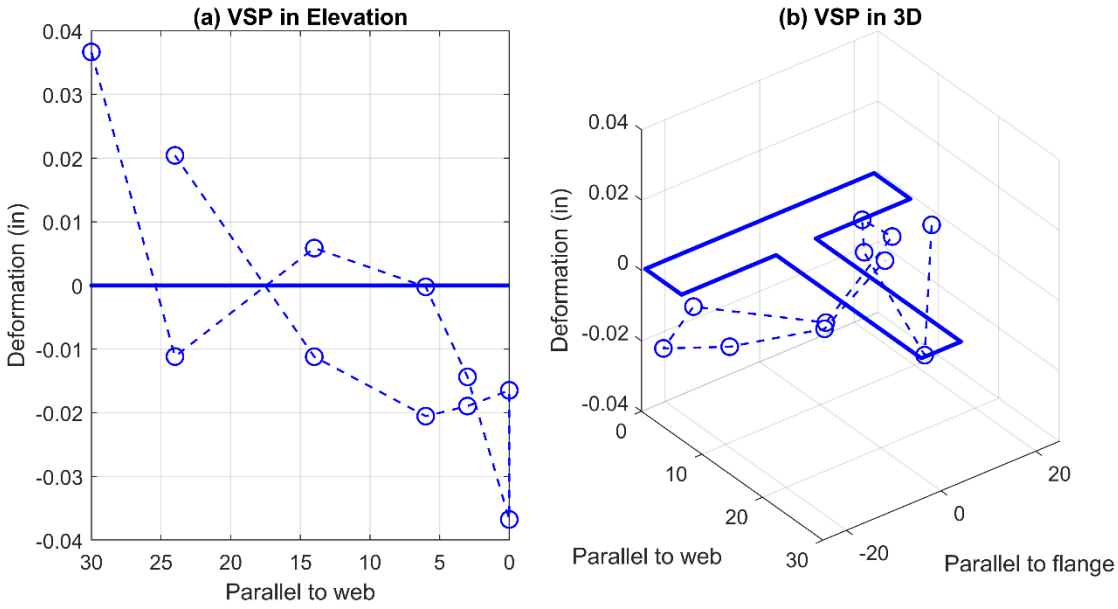


Figure 8-93. Deformation of VSP at Negative Peak in Step 4 in (a) Elevation and (b) 3D

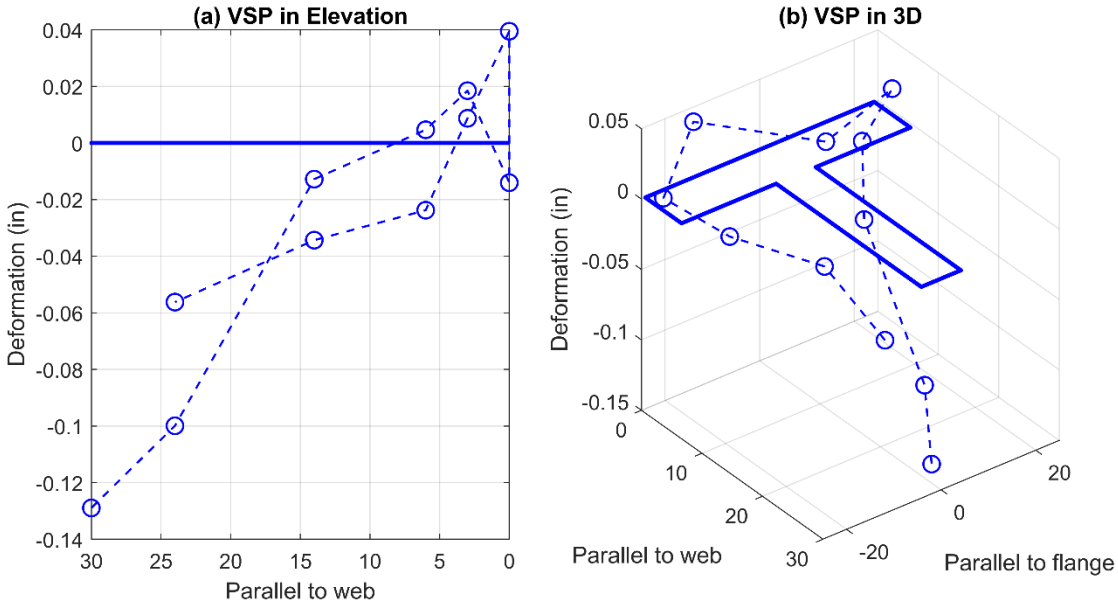


Figure 8-94. Deformation of VSP at Positive Peak in Step 5 in (a) Elevation and (b) 3D

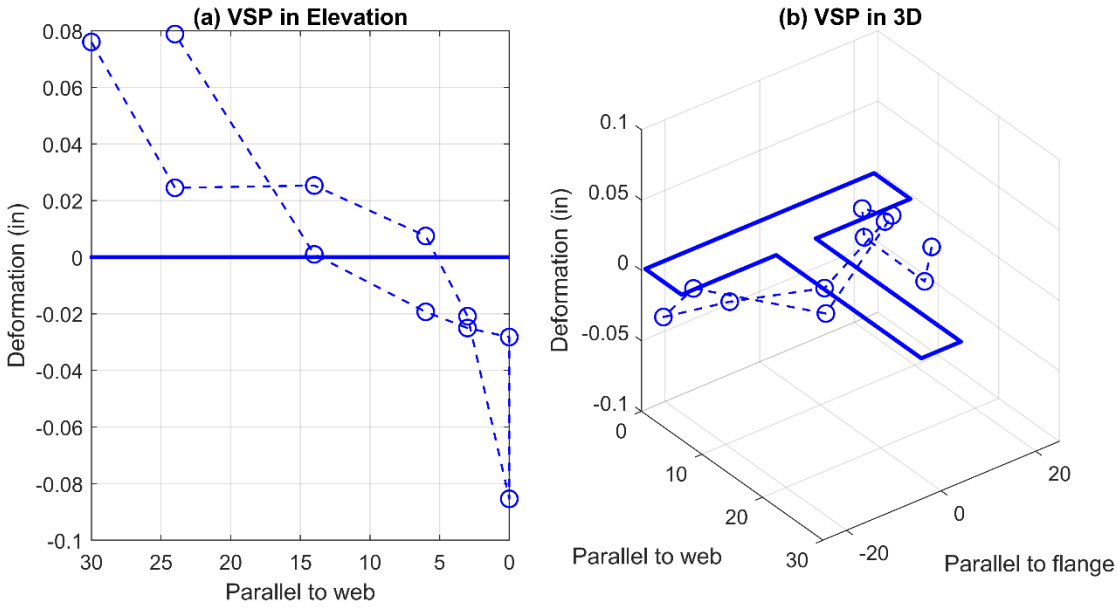


Figure 8-95. Deformation of VSP at Negative Peak in Step 5 in (a) Elevation and (b) 3D

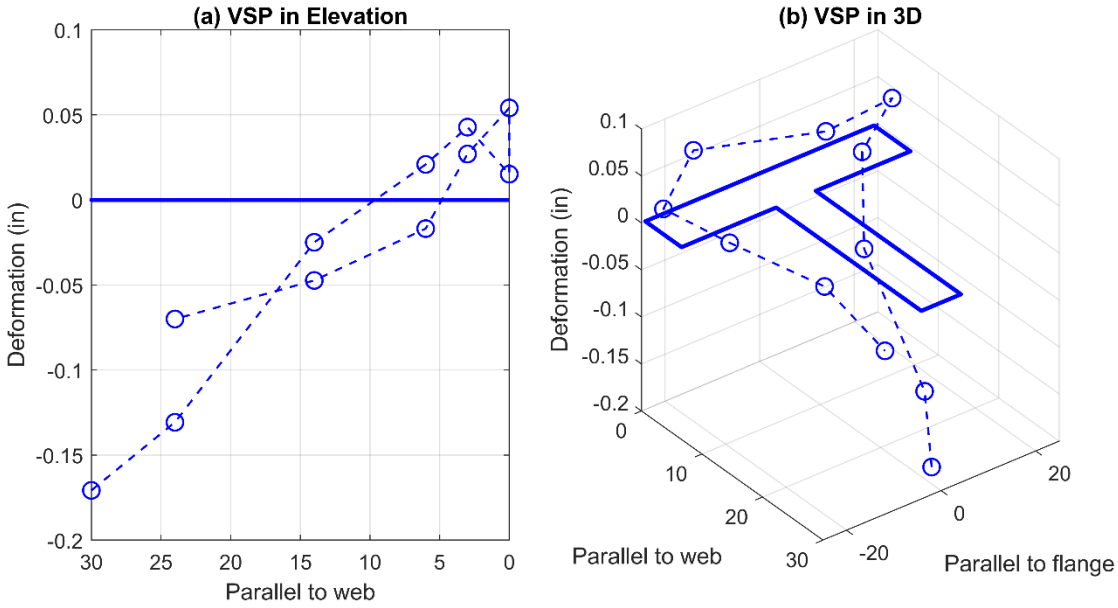


Figure 8-96. Deformation of VSP at Positive Peak in Step 6 in (a) Elevation and (b) 3D

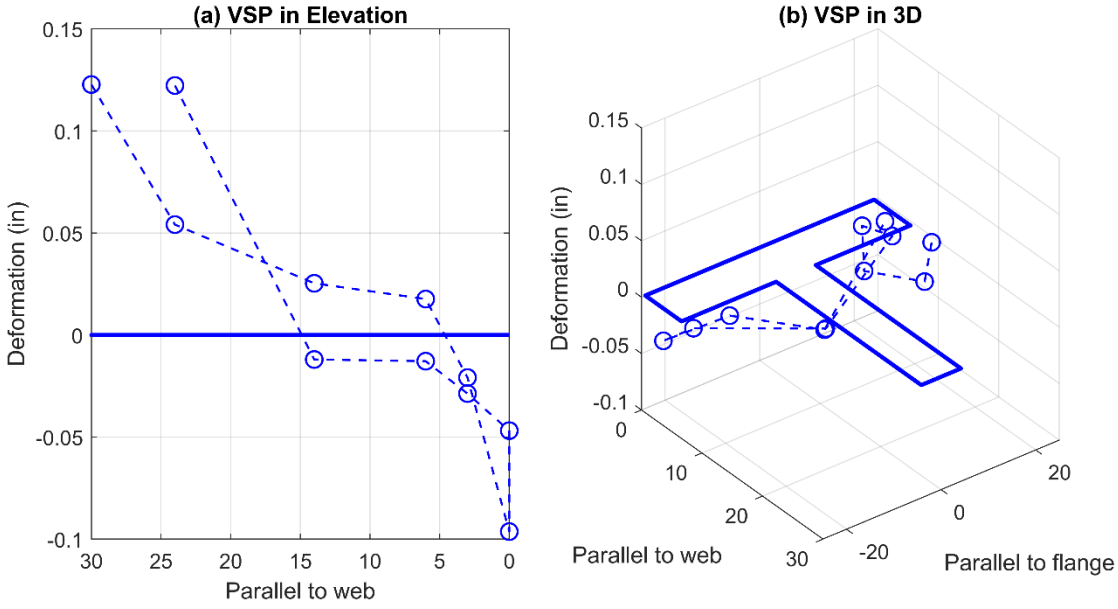


Figure 8-97. Deformation of VSP at Negative Peak in Step 6 in (a) Elevation and (b) 3D

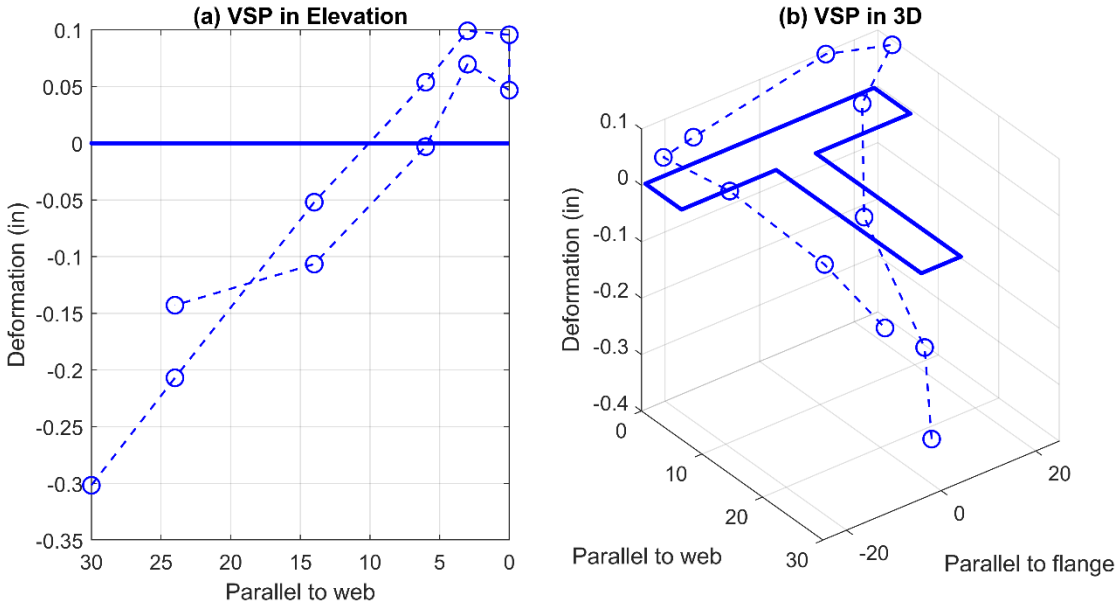


Figure 8-98. Deformation of VSP at Positive Peak in Step 8 in (a) Elevation and (b) 3D

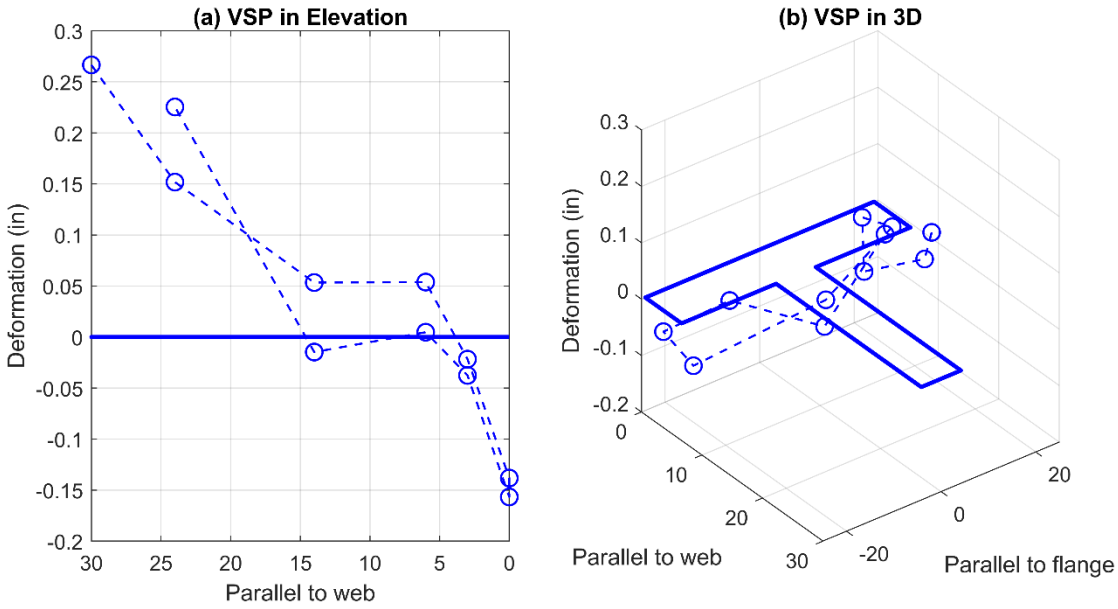


Figure 8-99. Deformation of VSP at Negative Peak in Step8 in (a) Elevation and (b) 3D

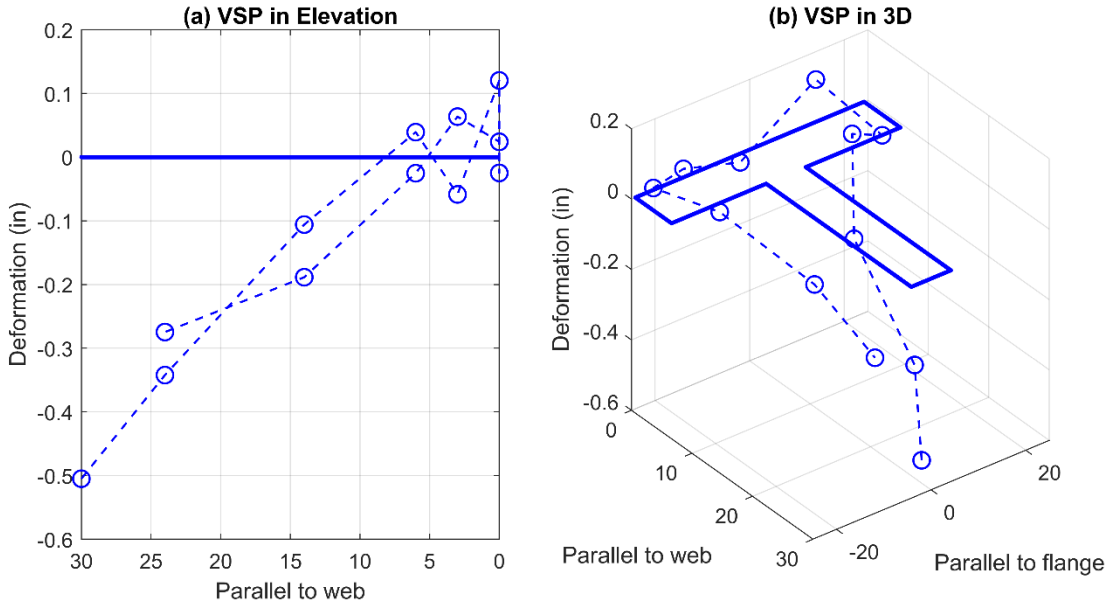


Figure 8-100. Deformation of VSP at Positive Peak in Step 9 in (a) Elevation and (b) 3D

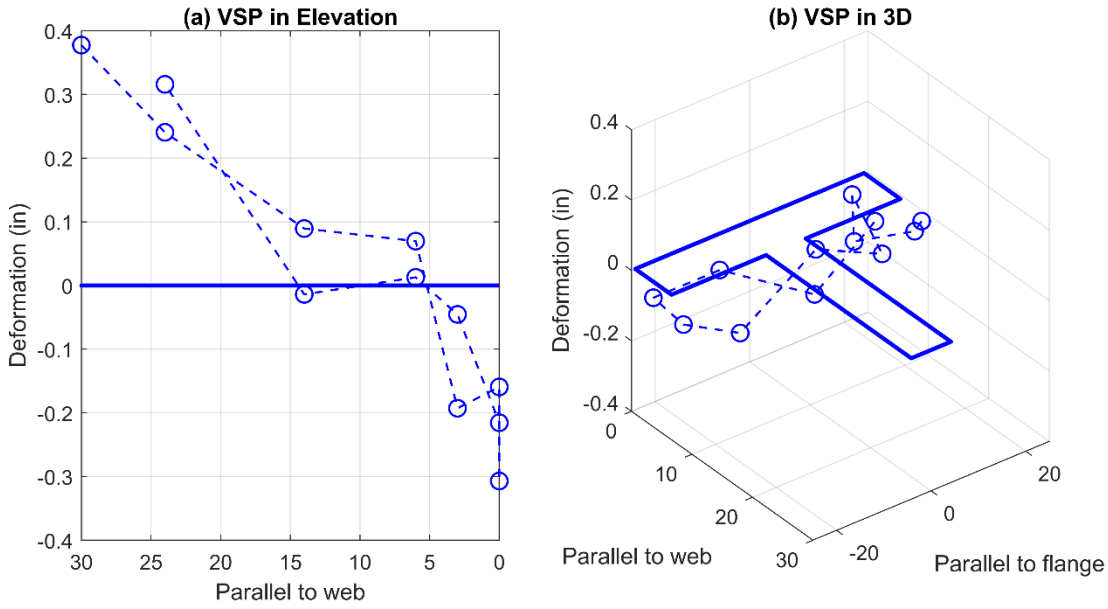


Figure 8-101. Deformation of VSP at Negative Peak in Step 9 in (a) Elevation and (b) 3D

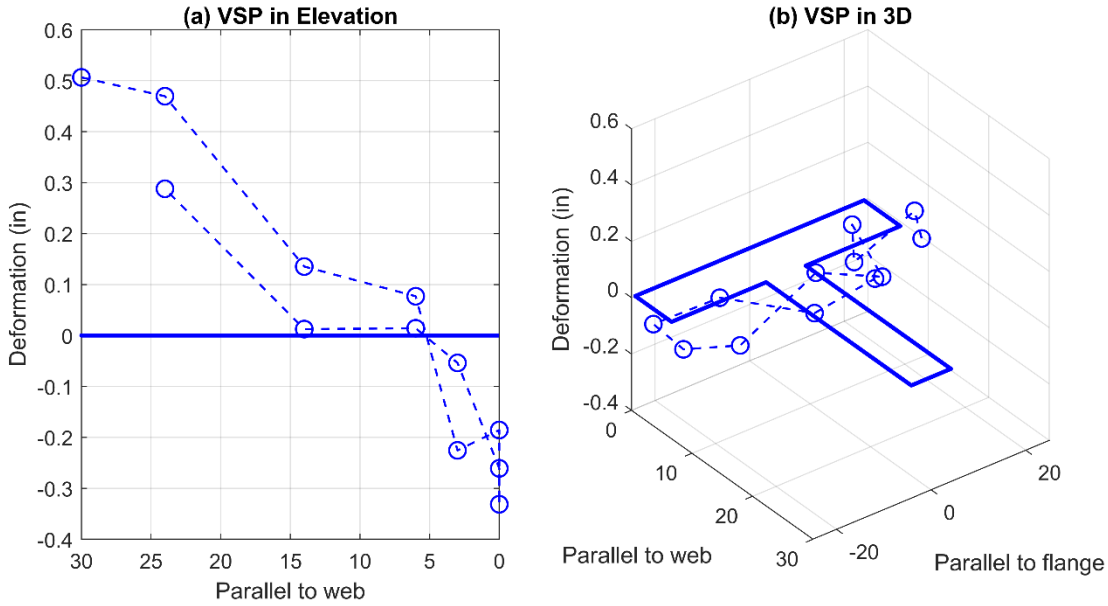


Figure 8-102. Deformation of VSP at Negative Peak in Step 10 in (a) Elevation and (b) 3D

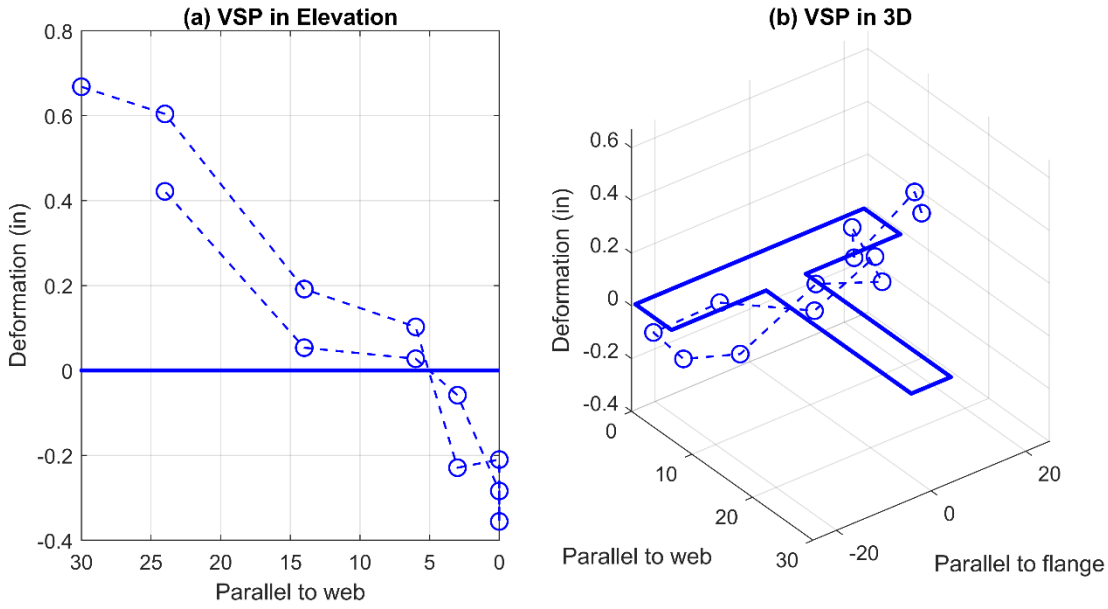


Figure 8-103. Deformation of VSP at Negative Peak in Step 11 in (a) Elevation and (b) 3D

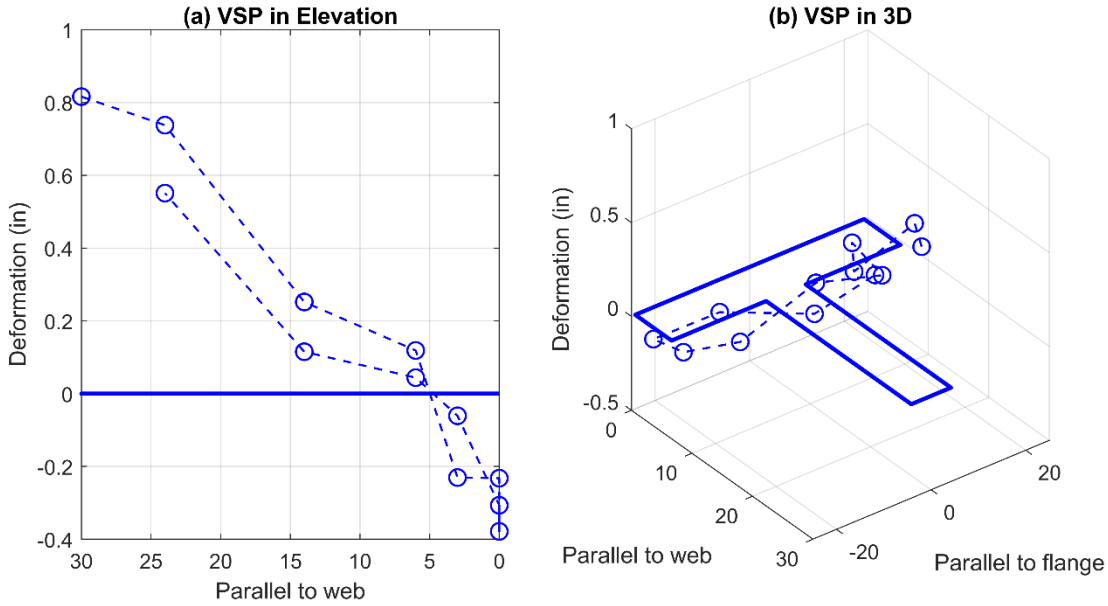


Figure 8-104. Deformation of VSP at Negative Peak in Step 12 in (a) Elevation and (b) 3D

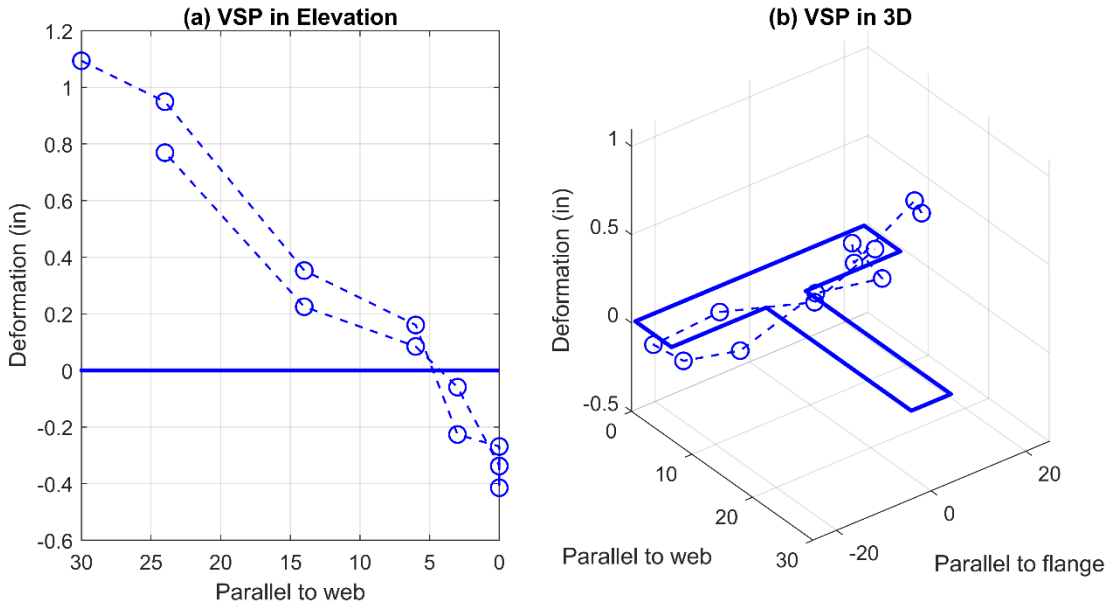


Figure 8-105. Deformation of VSP at Negative Peak in Step 13 in (a) Elevation and (b) 3D

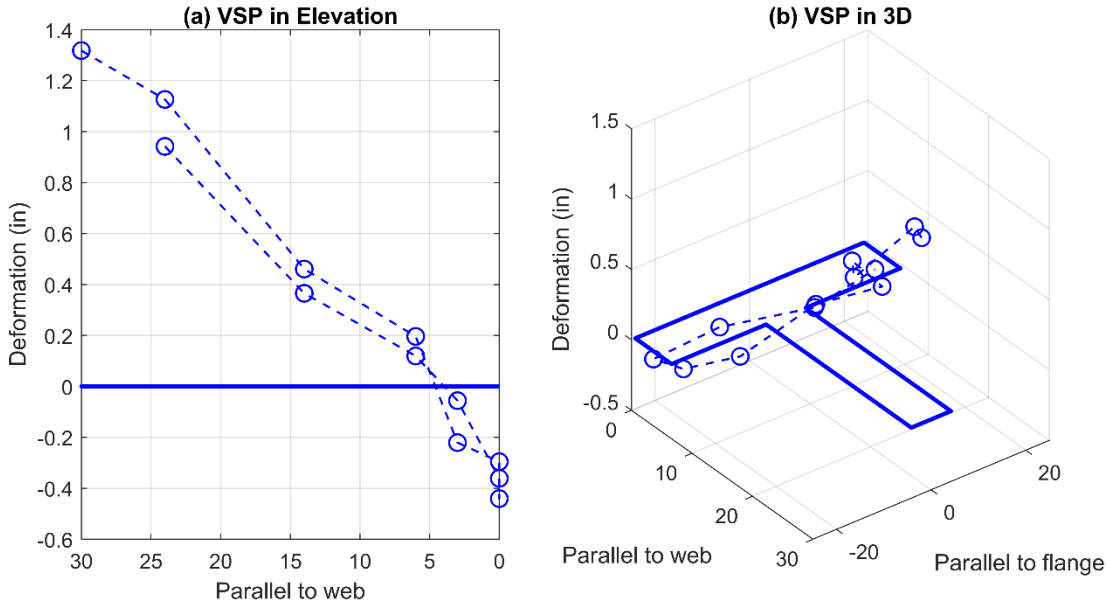


Figure 8-106. Deformation of VSP at Negative Peak in Step 14 in (a) Elevation and (b) 3D

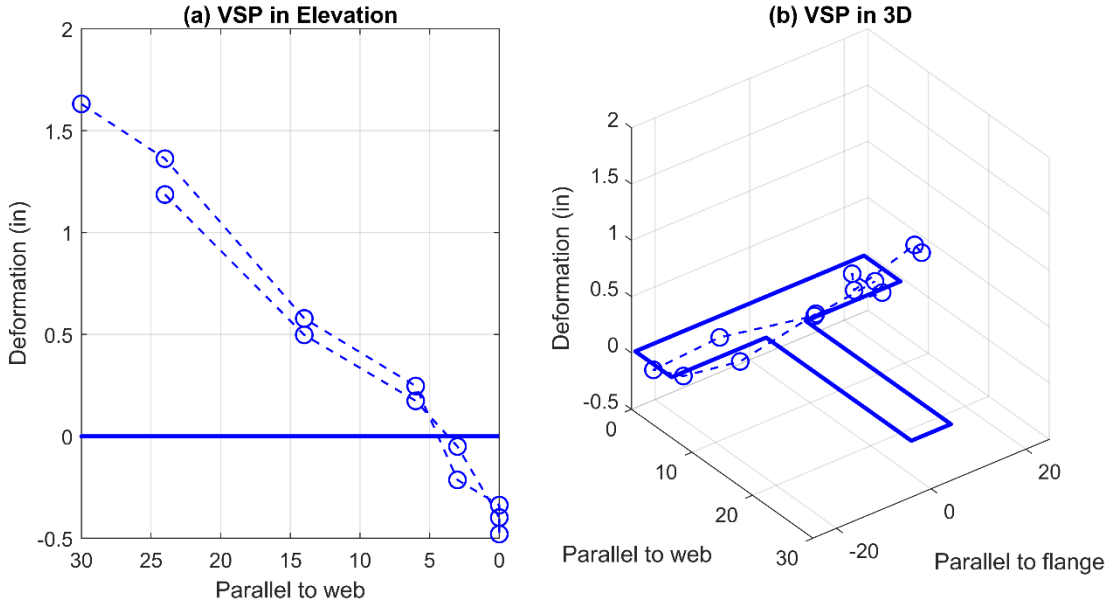


Figure 8-107. Deformation of VSP at Negative Peak in Step 15 in (a) Elevation and (b) 3D

8.5 Summary of Wall Specimen Test

A large-scale T-shaped CPSW/CF subjected to axial and cyclic flexural loading was tested. The wall was subjected to 10% of the crushing load of concrete (i.e. $A_c f'_c$) as an axial load representative of a design case scenario governed by wind load.

The wall specimen, featuring bolted splices, underwent 52 cycles of cyclic loading. The test commenced under force control, with the initial steps representing 25%, 50%, and 75% of the design strength. After reaching 100% of the design strength, the loading protocol switched to displacement control and cyclic displacements at progressively increasing amplitude, up to maximum displacements recorded at 4.25 in. (2.58% drift) in the positive direction (web in compression) and -9.5 in. (5.75% drift) in the negative direction (flange in compression). Shear force peaked at 129 kips in the positive direction and -59 kips in the negative direction, corresponding to drifts of 2.09% and -2.92%, respectively. Flexural strength of no less than 80% of the peak value reached was sustained until reaching drifts of 2.4% in the positive direction and -4.3% in the negative direction. The peak flexural strength at the horizontal splice in positive drift was 1548 k-ft, surpassing the flexural strength required for developing a bearing strength of $3.0dtF_u$ (1470.78 k-ft). In the negative drift, the peak flexural strength at the horizontal splice was -867 k-ft, exceeding the flexural strength required to develop $3.0dtF_u$ (-731.29 k-ft).

Due to a fabrication error, welding was not added at the bottom of the inside horizontal splice plates. This error changed the behavior of the horizontal splice from double-shear connection to single-shear connection. Since the failure mechanism was designed to be governed by bearing strength, and the edge distance of bolt holes on horizontal splice plates (1.5 in.) is shorter than that on faceplates (2.0 in.), failure developed in the outside horizontal splice plates instead of in the faceplates. However, the design horizontal splice strength was still achieved because both the faceplate and the splice plate were 3/16-in. thick plates.

Having the failure develop on the outside splice plate instead of the faceplate prevented implementation of a proposed repair scheme that could have shown how the wall could be rapidly repaired if damaged beyond the design level.

Vertical splices designed to be slip-resistant performed as intended as no slippage was observed in any of the six vertical splices.

SECTION 9
NUMERICAL ANALYSES OF WALL SPECIMEN TESTS

9.1 General

This section presents the results and findings from numerical analyses of the wall specimen tests presented in Chapter 9. The numerical model of the wall specimen is described in Section 9.2, followed by the results from the finite element analyses in Section 9.3. A summary of the finite element analyses is provided in Section 9.4. The overarching objectives of this section are to replicate the hysteretic behavior of the tested specimens and to address issues that could not be investigated or measured solely by physical testing of the wall specimen.

9.2 Finite Element Models

9.2.1 Finite Element Model of the Wall Specimen

Figure 9-1 shows the finite element model of the wall specimen built using the LS-DYNA software, including the reference coordinate system (X, Y, and Z directions). The model comprises the wall specimen and a concrete foundation, with only half of the wall section modeled for simplicity and efficiency. It includes components such as faceplates, vertical and horizontal splice plates, bolts, infill concrete, and tie bars. Additional elements like doubler plates, bottom stiffeners, and a base plate are embedded within the concrete foundation. The model features various "Layers", including the Foundation Layer, Bottom Layer, and Upper Layers 1 and 2. In Upper Layers 1 and 2, no bolts and tie bars were modeled, and all nodes between concrete and steel were merged for simplicity.

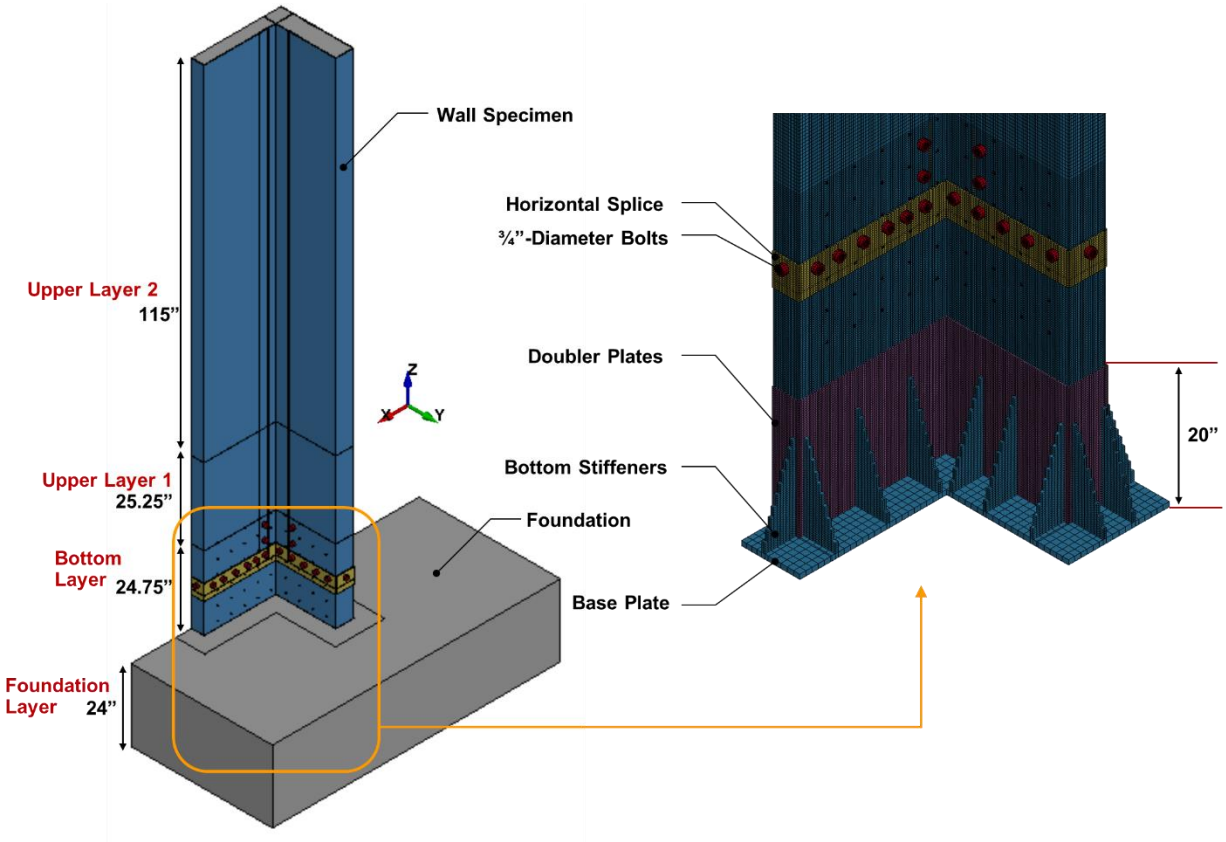


Figure 9-1. Finite Element Model of Wall Specimen and Foundation

9.2.2 Wall Properties

Element types, material properties, and contact and constraint properties for the wall model were the same as for the properties in the finite element models of tension components described in Section 5.3, except for the following differences:

- The element sizes in the wall model vary along the height of the wall. For the steel plates, finer mesh sizes were used in the Bottom and Foundation Layers. As shown in Figure 9-2, the mesh size on the steel surface in the bottom and Foundation Layers was 0.25 × 0.25 in. (width × height), and it increased to 0.25 in. × 0.5 in. and 0.25 in. × 1.0 in. in the Upper Layers 1 and 2, respectively. For the infilled concrete, the element size of the solid elements was 0.5 in. × 0.5 in. × 0.5 in. in the Bottom and Foundation Layers, while the element size increased to 0.5 in. × 1.0 in. × 0.5 in. in the Upper Layers 1 and 2. Finally, for the concrete foundation (Figure 9-3), the element size varied from 0.25 in. × 0.5 in. × 1.0 in. to 2.0 in. × 2.0 in. × 1.0 in., the more refined mesh being used next to the specimen.
- The material properties for the steel and concrete elements were those corresponding to the wall specimen, as summarized in Table 9-1 and Table 9-2. Elastic steel material properties were assigned to the baseplate, bottom stiffeners, and doubler plates, while elastic concrete properties were assigned to the foundation concrete. Note that the elastic modulus of concrete, E_c, calculated by Equation 5-1, was adjusted by a factor of 0.8 to better align with the initial cycle from the test results, as shown in Figure 9-4. This adjustment was informed by a study by Schlumpf (2004), which reported that the elastic modulus of self-compacting concretes tends to be around 20% lower than that of conventional concrete with similar strength.
- The contact properties between faceplates and concrete foundation and between doubler plates and concrete foundation were neglected. The overturning moment applied to the wall embedded

in the footing was assumed to be achieved by bearing reaction of the wall base plate and bottom stiffeners to the concrete footing. Figure 9-5 shows the maximum von Mises stresses for drifts of +3% and -2% from positive and negative pushover finite element analyses, respectively. In the positive direction (+3% drift), local yielding was observed near the top of the bottom stiffeners. Conversely, no yielding occurred in the negative direction (-2% drift). At +3% drift, the moment at the section above the stiffeners reached 2016 k-ft, which represents 94% of the M_y of the wall.

- The different boundary conditions applicable to the wall specimens are shown in Figure 9-6. A fixed end boundary condition was applied at the bottom of the foundation. To simulate symmetry, node restraints were placed in the middle of the wall model. Equal displacements were imposed on all nodes at the top of the wall in the X-direction. Additionally, axial loads were applied to selected nodes at the top of the wall, ensuring that the center of the resultant axial load aligns with the center of the axial loading top fixture, as detailed in Figure 7-1.
- Pretension values of 52.5 ksi, 78.75 ksi, and 105 ksi were assigned on the bolts in the finite element model during monotonic pushover analyses.
- The nodes located at the bottom of the outside horizontal splice plates were merged with those of the faceplates at the same location to simulate welded connections, while those at the bottom of the inside horizontal splice plates remained separate. Consequently, the horizontal splice connection operates as a single shear connection to match the condition of the tested wall. Unless noted otherwise, the finite element analysis in this section assumes this configuration for the horizontal splice.

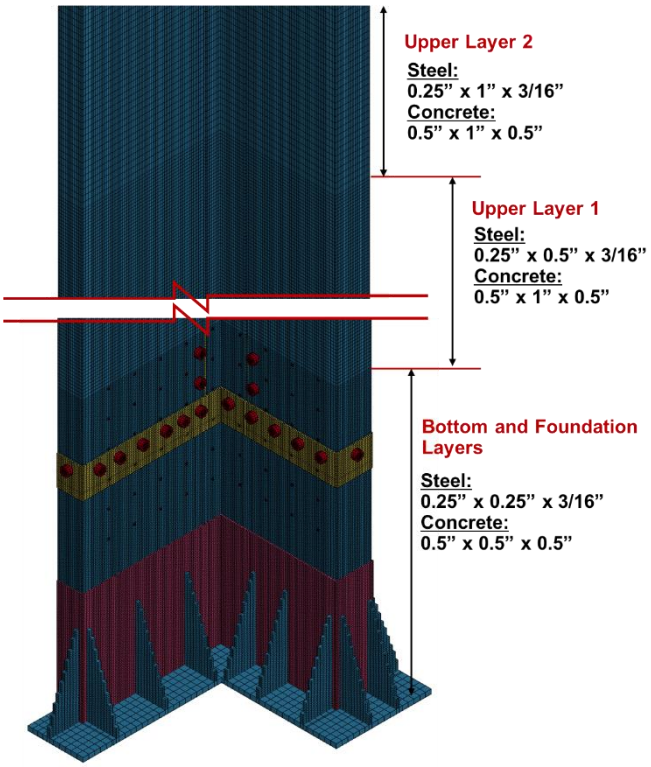


Figure 9-2. Mesht Size Details of the Wall Specimen

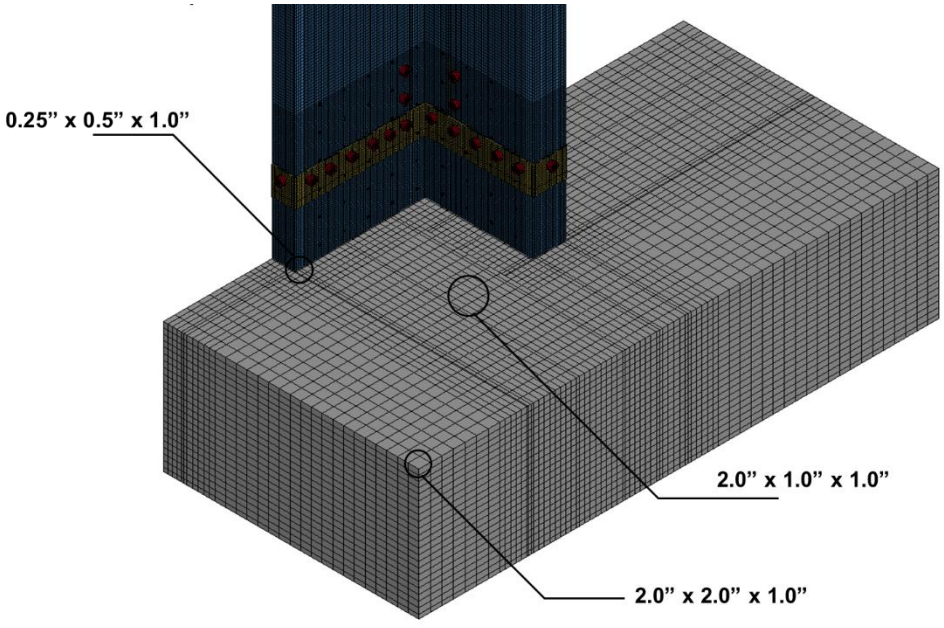


Figure 9-3. Mesh Size Details of the Concrete Foundation

Table 9-1. Material Properties for Steel Parts

Part	E (ksi)	Possion's Ratio	Fy (ksi)	Et (ksi)	β
Face Plates	29000	0.3	63.6	59.1	0.0
Splice Plates	29000	0.3	63.6	59.1	0.0
Bolts	29000	0.3	120.0	221.2	0.0
Tie Bars	29000	0.3	55	108.8	0.0
Steel_Elastic	29000	0.3	-	-	-

Table 9-2. Material Properties for Concrete Parts

Part	E_c (ksi)	Possion's Ratio	f'_c (psi)	f_t (psi)	FE	ASIZE
Infill Concrete	3746	0.2	6750	675	0.0015	0.500
Foundation	3746	0.2	-	-	-	-

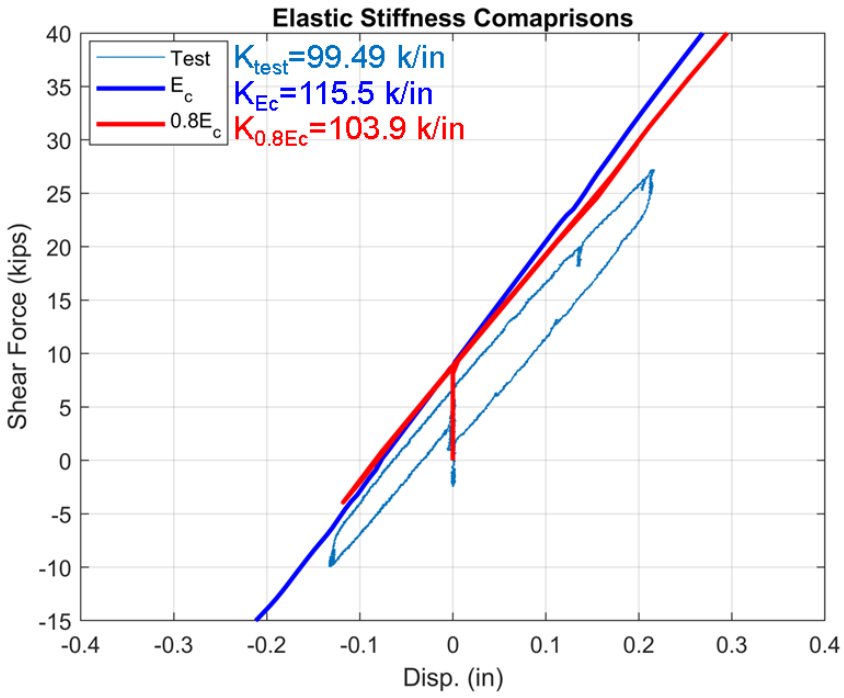


Figure 9-4. Finite Element Elastic Stiffness of Wall Specimen for Various Elastic Modulus of Concrete Compared to First Cycle from Wall Specimen Test

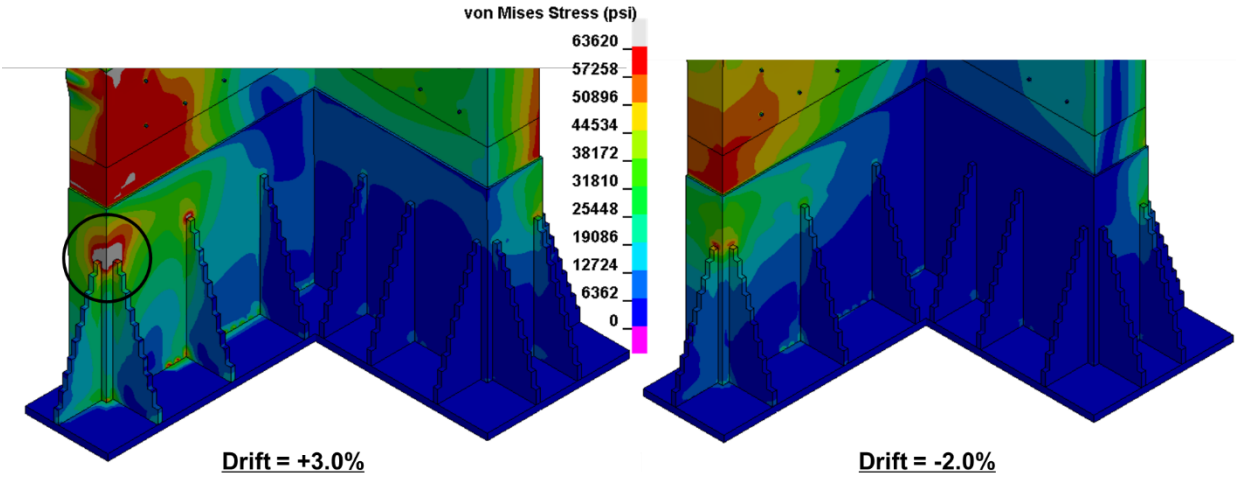


Figure 9-5. Maximum von Mises Stress on Steel in Foundation from Positive and Negative Finite Element Analyses

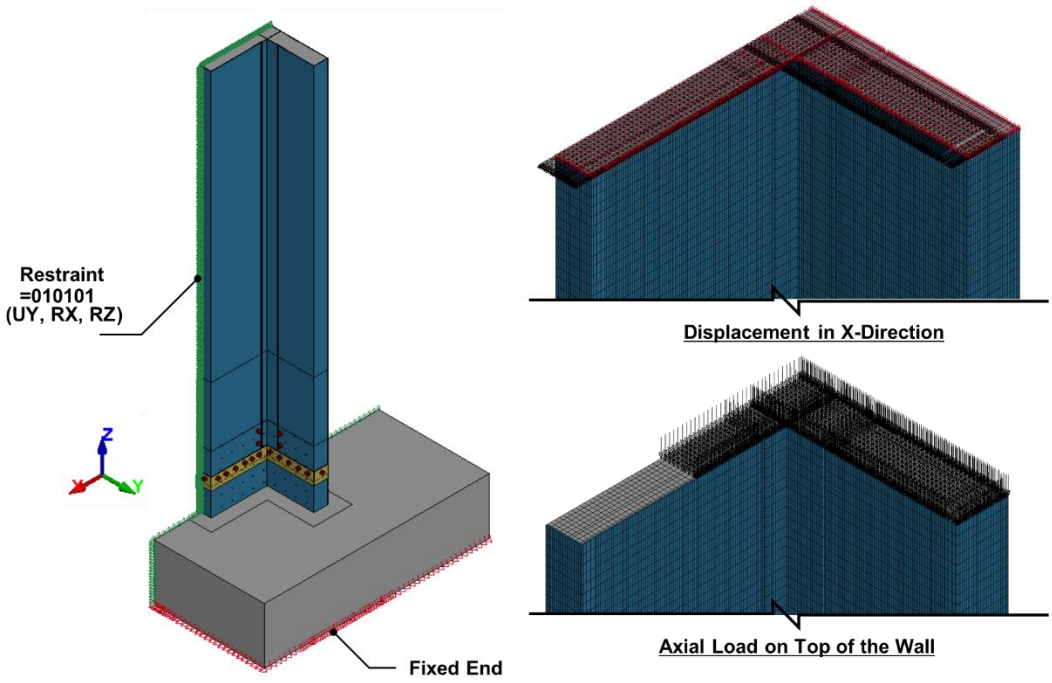


Figure 9-6. Boundary Condition of the Wall Model

9.3 Results of Finite Element Analysis

This section provides analysis results obtained from the finite element model described in Section 9.2. The wall model was subjected to top lateral displacements and a constant axial load to apply flexural deformations similar to what was done to the specimen during testing.

9.3.1 Monotonic Pushover Analyses

9.3.1.1 Impact of Pretension Values

Pretension values of 52.5 ksi, 78.75 ksi, and 105 ksi (corresponding to 66%, 99%, and 132% of the AISC specified pretension force, respectively). were assigned to the bolts in the finite element model during monotonic pushover analyses, as shown in Figure 9-7. While none of the results perfectly enveloped the experimentally observed hysteresis curves, results obtained with a pretension of 52.5 ksi closely matched the sliding plateau observed in the negative loading direction and the peak forces at larger drifts in the positive direction of the hysteresis curve obtained from the test. For this reason, this pretension value was retained for the subsequent pushover analyses.

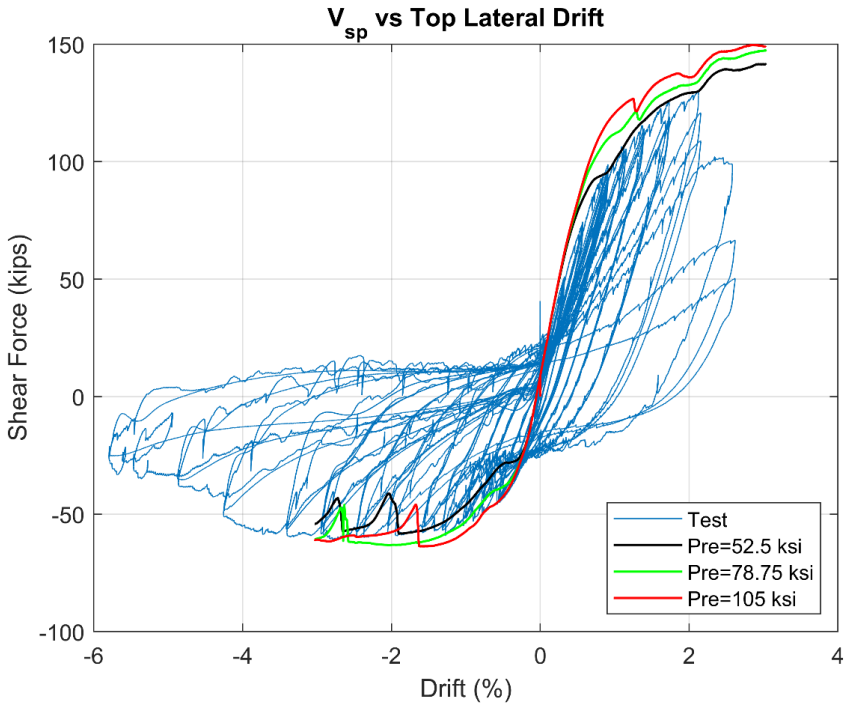


Figure 9-7. Impact of Pretension of Bolts from Pushover Analysis

9.3.1.2 Pushover Analysis with 52.5 ksi Pretension

Figures 9-8 and 9-9 compare the shear force and moment versus top lateral drift from the monotonic loading of the finite element model with the hysteresis curves from the test. The monotonic pushover finite element analyses were first performed, independently in the positive and the negative directions, to investigate the ultimate behavior of the bolted splices in the wall model. The finite element results align well with the strength observed in the test result up to drifts of +2.0 % and -1.9 % in the positive and negative directions, respectively. Recall that during the test at +2.0% drift, the horizontal splice experienced buckling which worsened with further cyclic loading, leading to strength degradation in the positive direction. However, the pushover analysis model did not capture this cyclic behavior, and consequently, results from this analysis did not exhibit a drop in strength after reaching +2.0% drift.

Figures 9-10 and 9-11 show the von Mises stresses in the finite element wall model from the southwest and southeast views during positive pushover finite element analysis. The figures compare stresses on the horizontal splice (left) and faceplates (right) in the horizontal splice region at various values of drift. These figures show that the faceplates and horizontal splice mostly stayed within the elastic range ($\sigma < 63{,}620$ *psi*), except for regions near the bolt holes and in small localized parts of the faceplates at 3.0% drift. As shown in Figure 9-12, buckling was initially observed on the horizontal splice plate at a drift of 1.5%. Subsequently, buckling occurred on the faceplates close to the tip of the web, both above and below the horizontal splice, as shown in Figure 9-13. Figure 9-14 provides a close view of the tip of the web, showing that at a drift of 2.3%, the upper and lower parts of the faceplates began to contact each other as the gap closed. Similarly, Figures 9-15 and 9-16 show the von Mises stresses during negative pushover finite element analysis. Progressive yielding due to bearing of bolts were observed on the web of the wall. The faceplates and horizontal splice plate remained elastic except for small regions near the bolts (Figure 9-17).

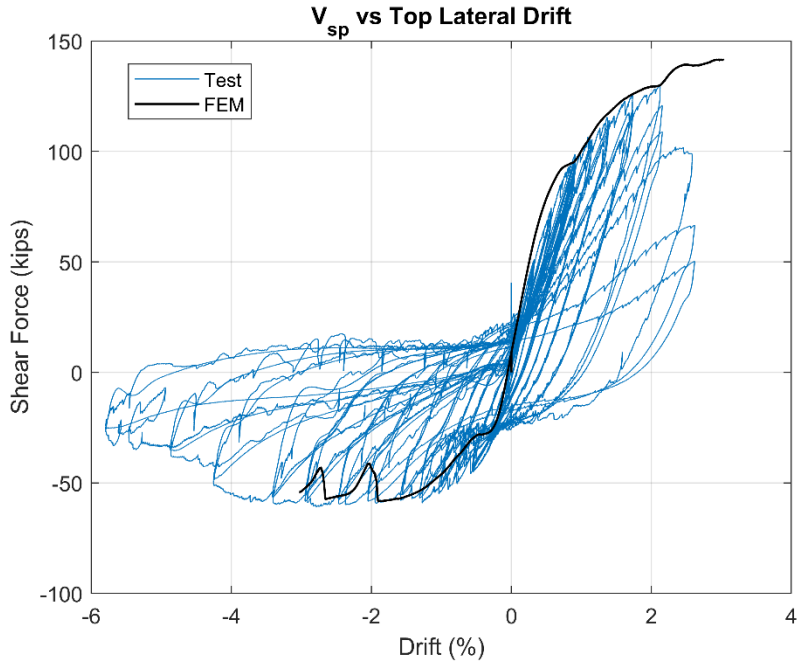


Figure 9-8. Shear Force and Top Lateral Drift Curve from Test and Finite Element Analysis

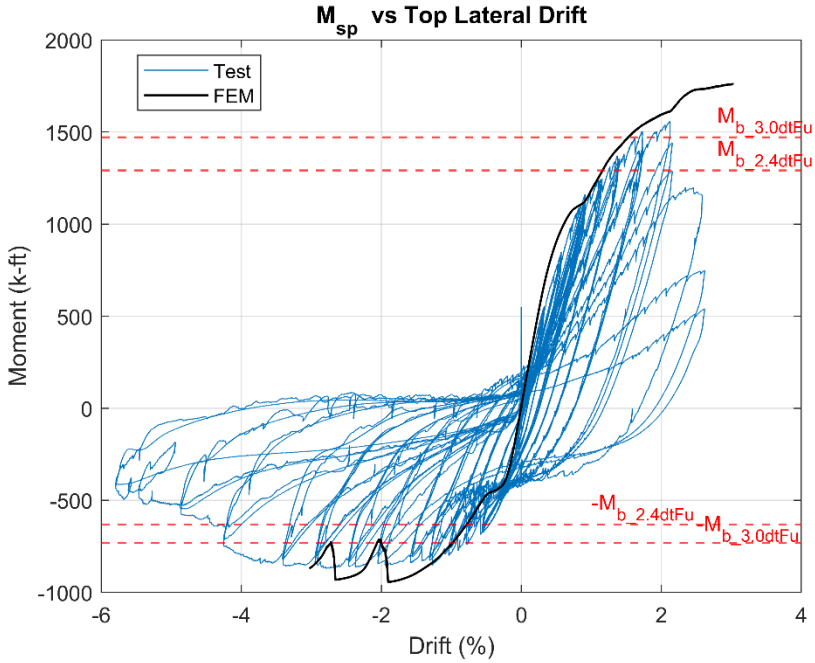


Figure 9-9. Moment and Top Lateral Drift Curve from Test and Finite Element Analysis

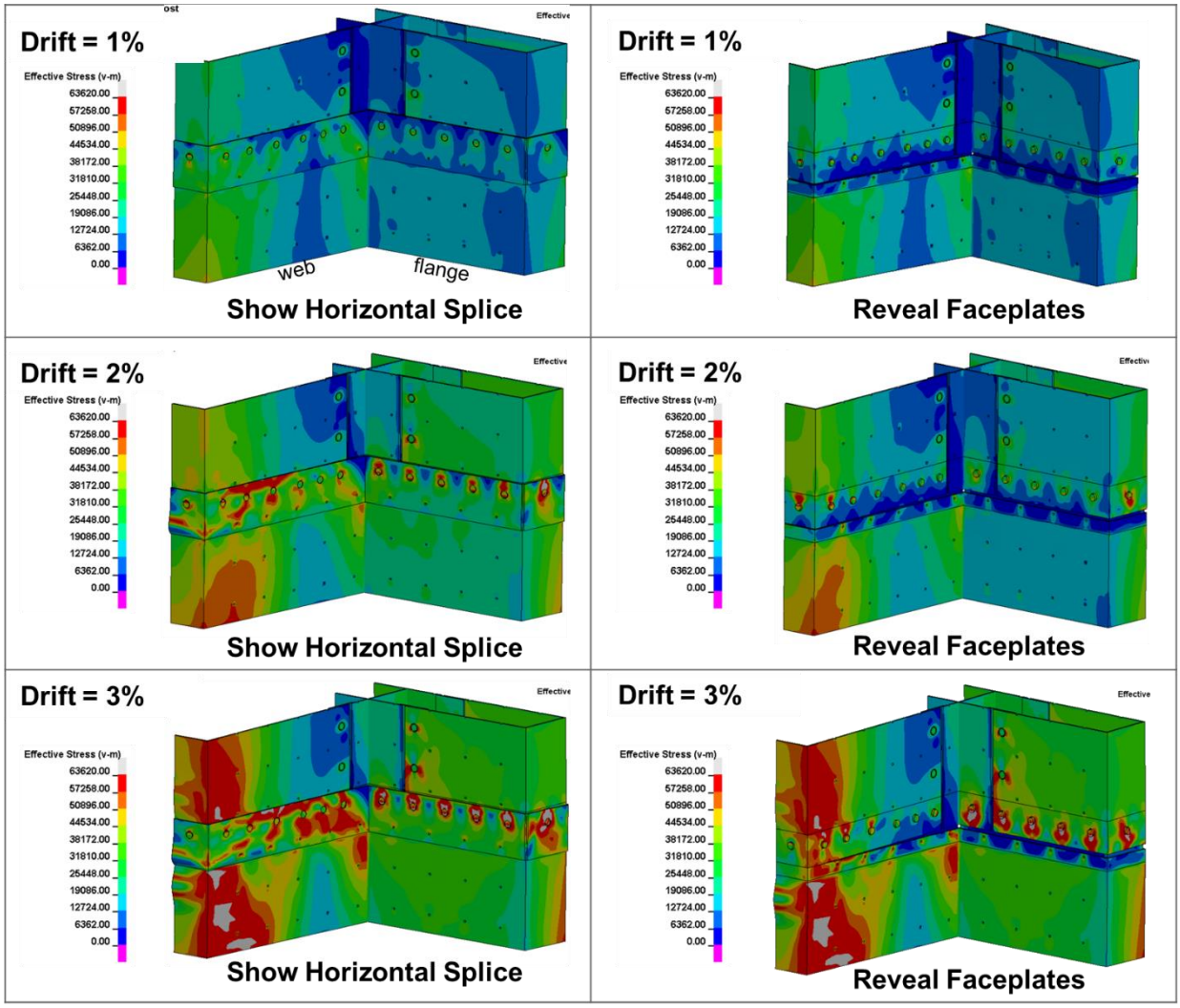


Figure 9-10. von Mises Stresses of the Wall Model in Positive Pushover Analysis (Southwest View)

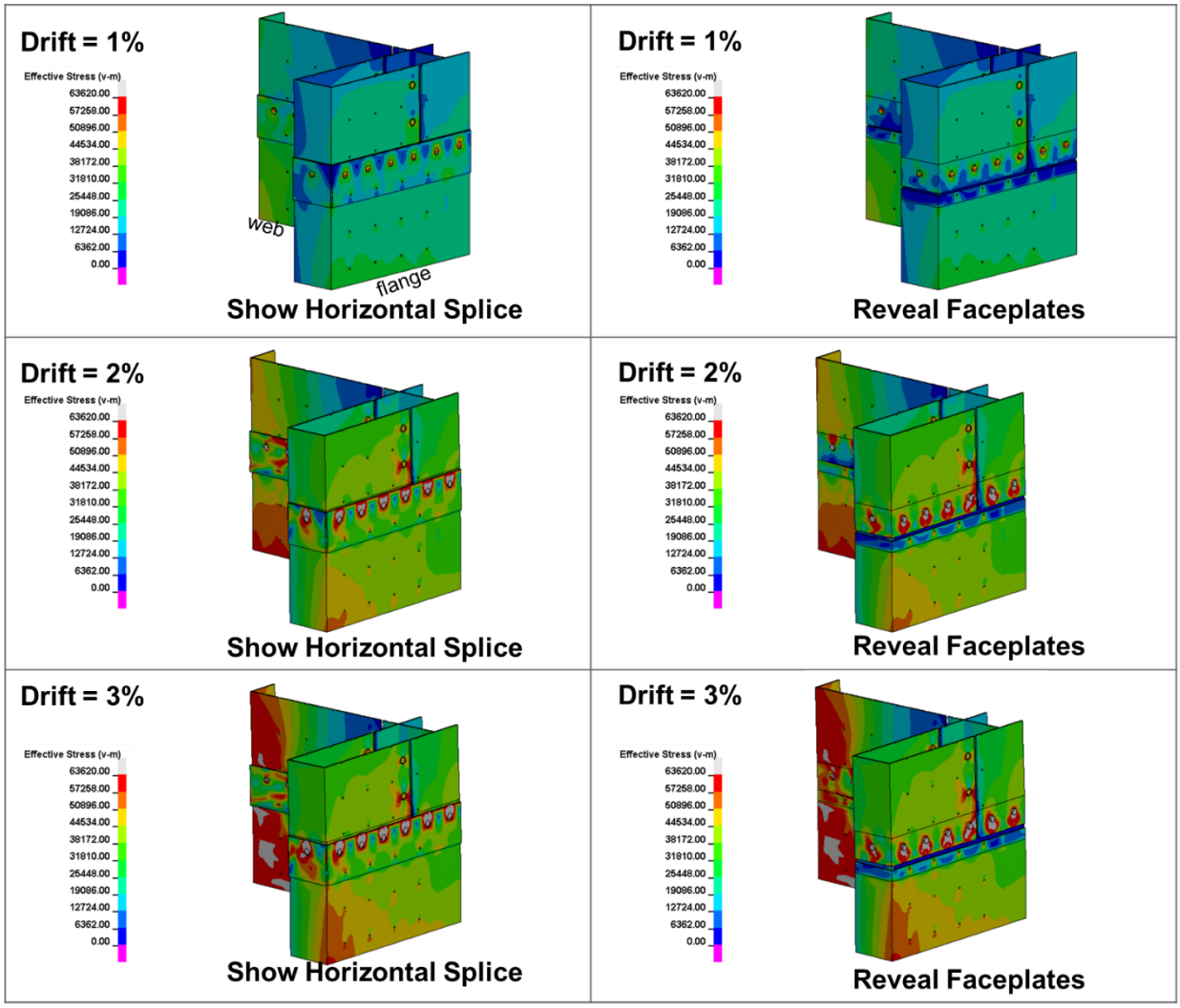


Figure 9-11. von Mises Stresses of the Wall Model in Positive Pushover Analysis (Southeast View)

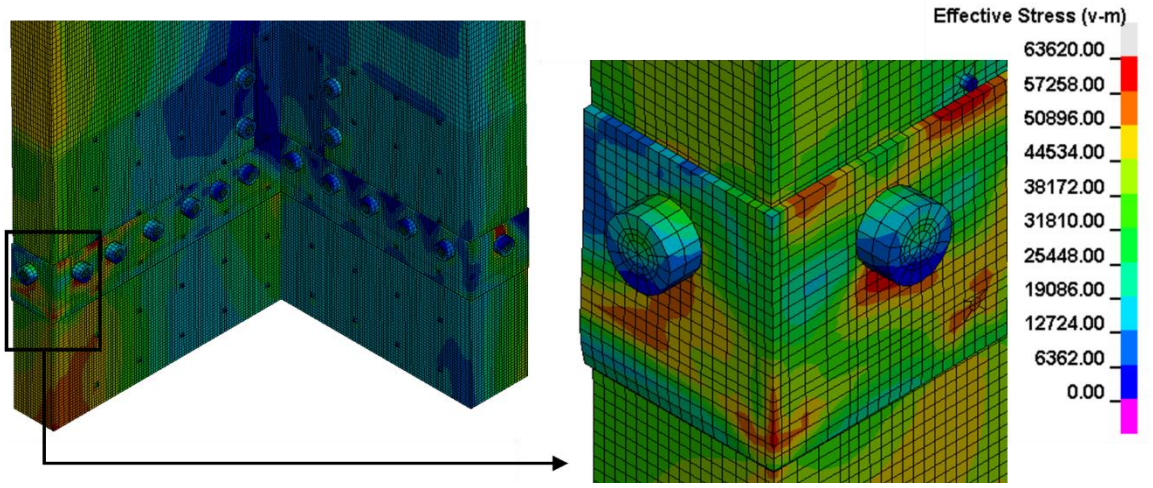


Figure 9-12. Buckling of Horizontal Splice at 1.5% Drift

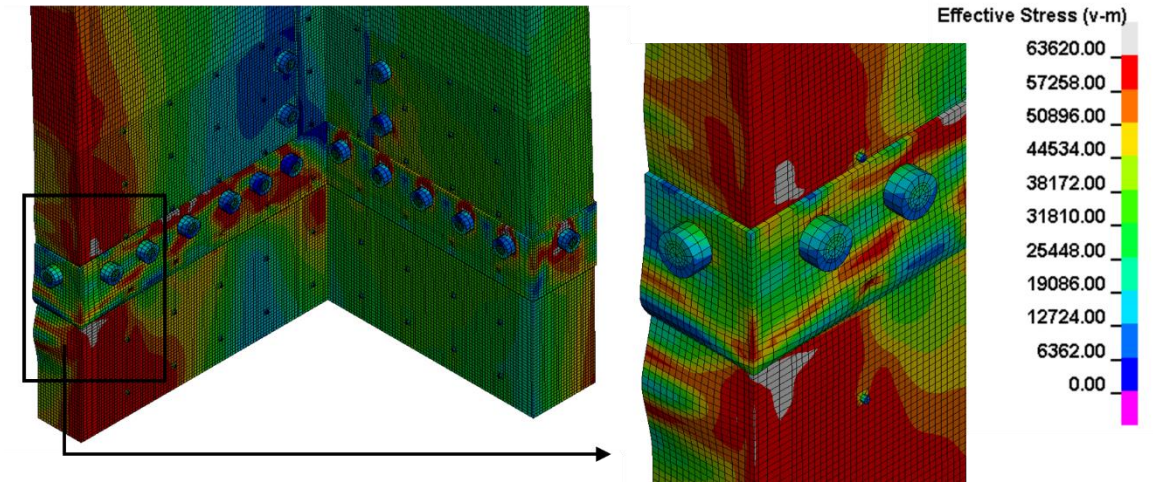


Figure 9-13. Buckling of Faceplate and Horizontal Splice at 3.0% Drift

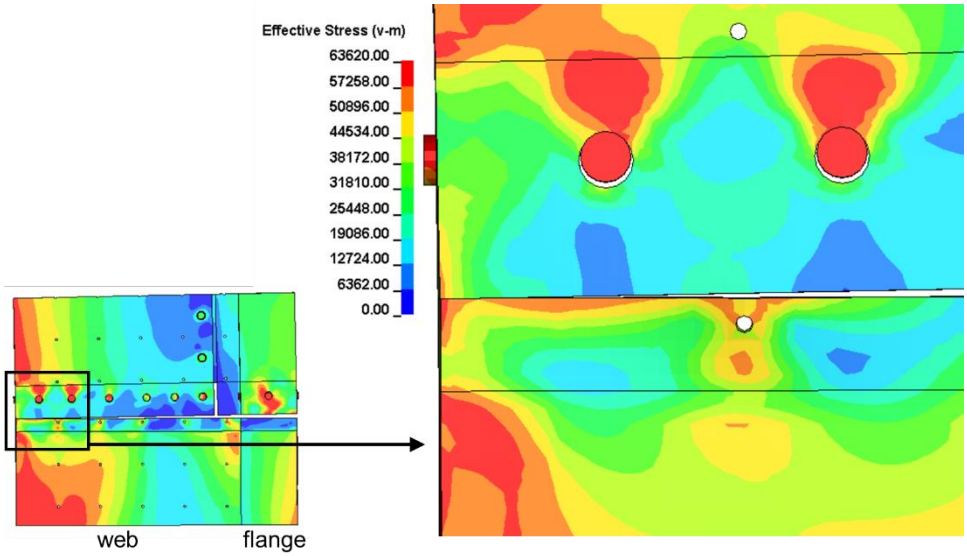


Figure 9-14. Contact between Upper and Lower Parts of Faceplates at Drift of 2.3%

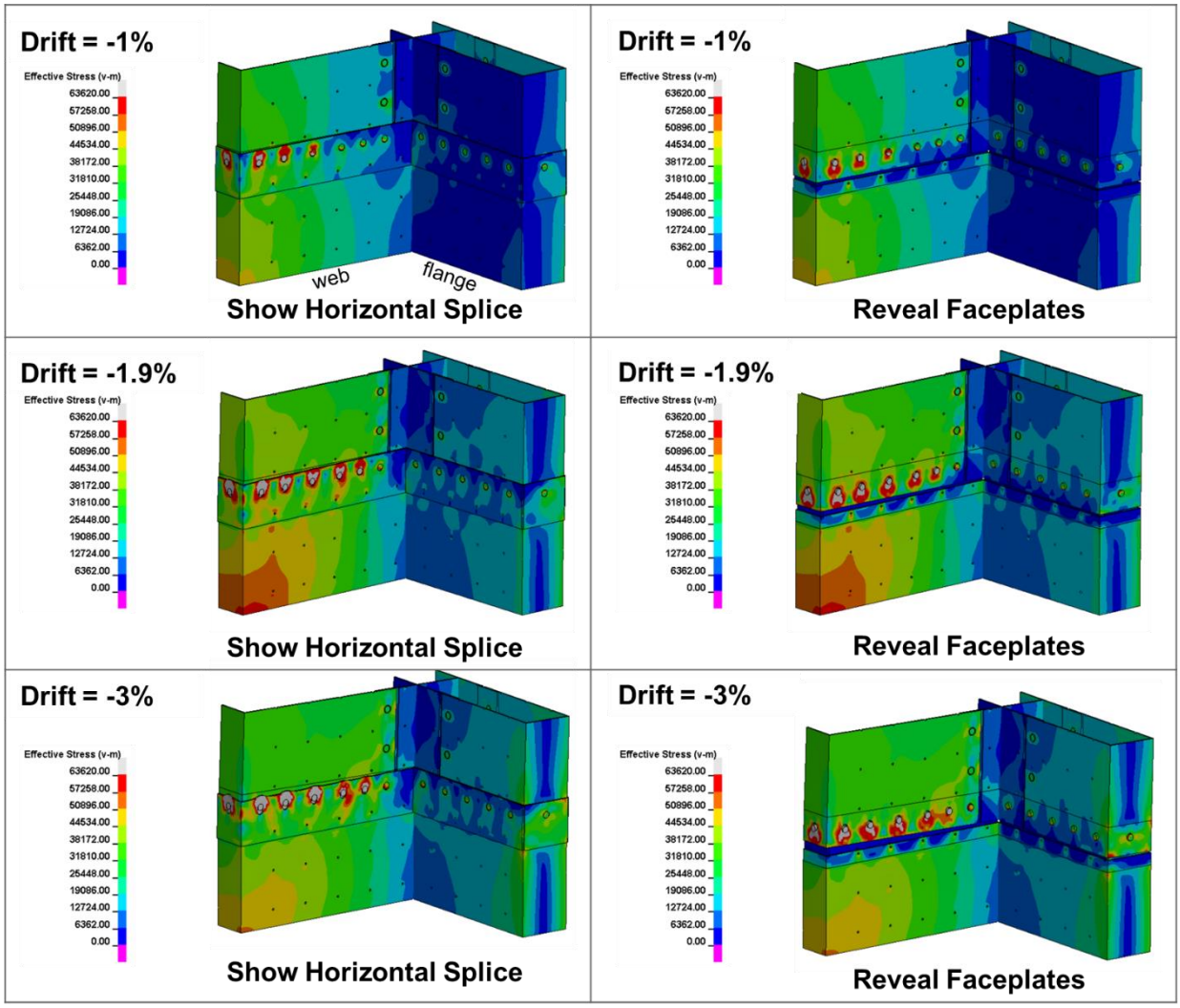


Figure 9-15. von Mises Stresses of the Wall Model in Negative Pushover Analysis (Southwest View)

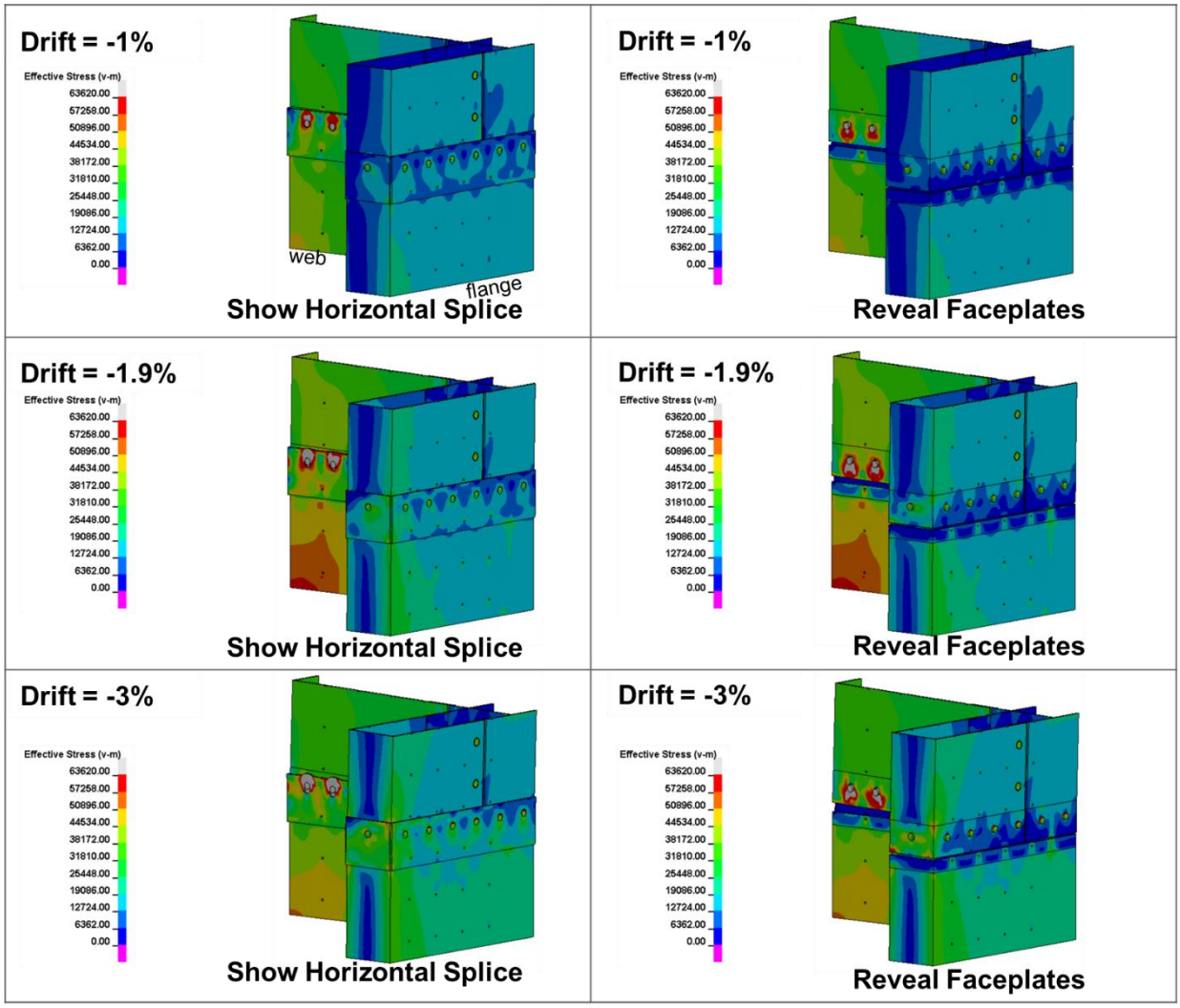


Figure 9-16. von Mises Stresses of the Wall Model in Negative Pushover Analysis (Southeast View)

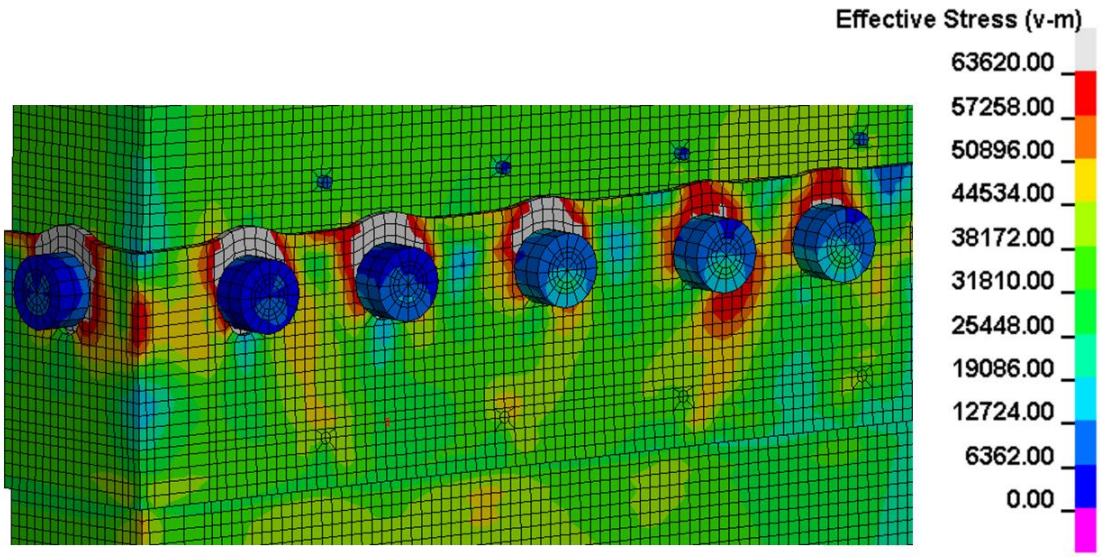


Figure 9-17. Yielding near Bolt Holes on Splice Web at -3% Drift

As previously mentioned, the stiffness of the wall gradually diminishes as the moment increases. It is hypothesized that concrete cracking along the height of the wall contributes to this stiffness reduction. Figure 10-18 illustrates the progression of cracks in the infill concrete during monotonic pushover analysis. Notably, as concrete cracks initiate, the stiffness of the wall begins to decline. With further lateral displacement, the stiffness decreases progressively until reaching a flat plateau. The results shown in that figure indicate a concentration of cracking in the splice region, which is expected since the concrete cross-area is less in the splice region due to the presence of the interior splice plate. Note that LS-DYNA plots only show cracks when the tensile strength reaches a zero value. However, in the concrete model used here, the reduction in tensile stress in concrete occurs linearly from the peak cracking stress (at a strain of 0.0002) down to a user specified-value (the LS-DYNA recommended 0.0015 value was used here), so reduction in stiffness due to tension cracking is already happening even if a crack is not shown graphically. The calculated value of M_{cr} for this wall in the positive direction is 331.68 k-ft, which is 26% of the value of $0.6M_y$, so cracking theoretically occurred over 83% of the height of the wall at 3% drift.

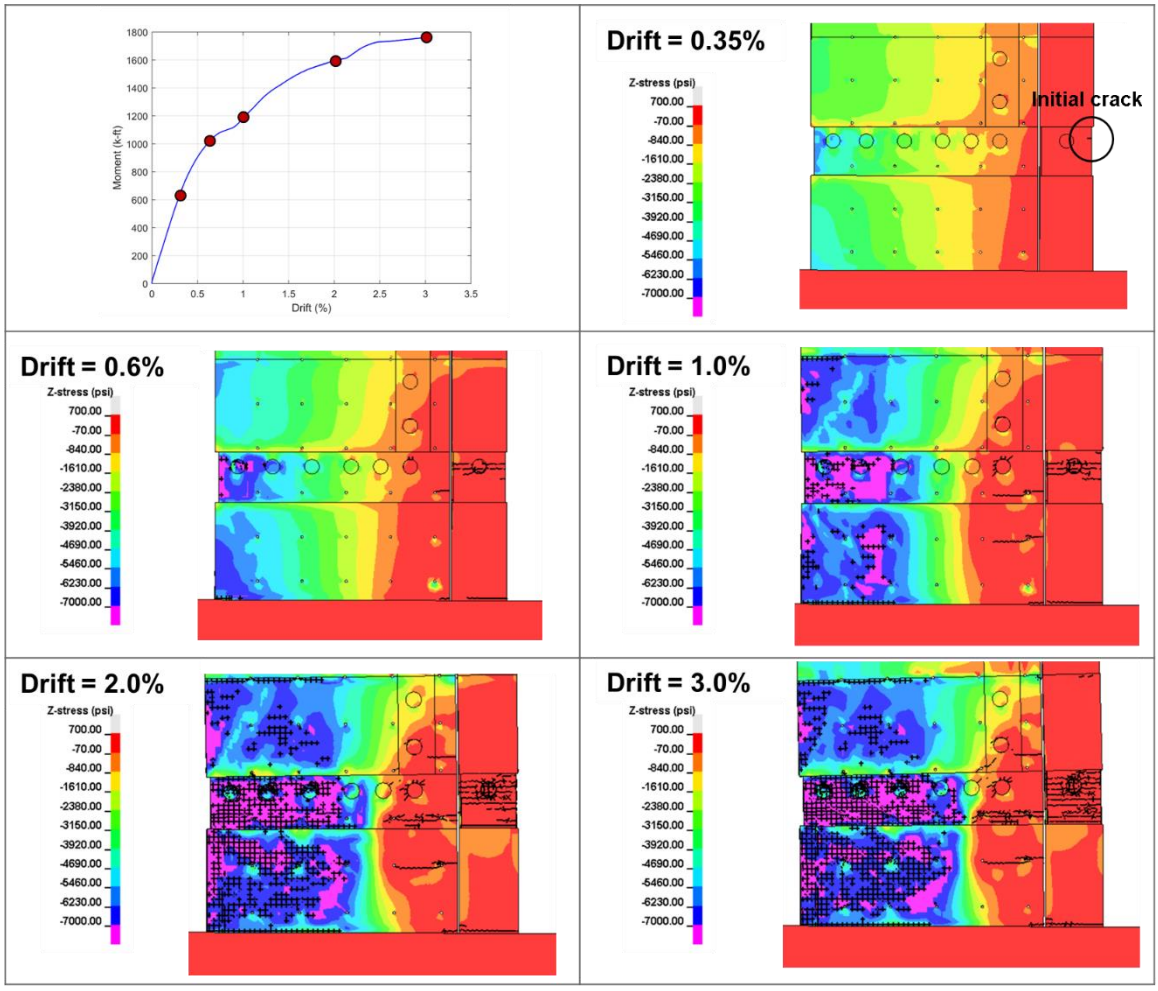


Figure 9-18. Development of Cracks of Concrete in Positive Pushover Analysis (South View)

Figures 9-19 to 9-24 present the friction and bearing forces acting on each row of bolts during positive pushover finite element analysis, with pretension values set at 52.5 ksi and 78.75 ksi (corresponding to 66% and 99% of the AISC specified pretension force, respectively). The friction and bearing forces for each row of bolts, as presented in the figures, were extracted from the finite element model. Friction forces were obtained from the interface between faceplates and the two horizontal splice plates, with the tributary width calculated from the midpoint of bolt spacings. Bearing forces were obtained by summing the forces acting on the bolt holes. Note that the forces displayed for each row correspond to individual bolts. If a row contains multiple bolts, the total force is divided by the number of bolts in that row to represent a single bolt on each row of bolts.

Initially, up to a drift of 1%, only friction forces are observed at the bolt locations. According to the LS-DYNA theory manual (Hallquist 2006), the friction algorithm employs an equivalent elastic-plastic spring. The "yield" force of this friction spring equals the friction limit, calculated as the friction coefficient (μ) multiplied by the normal force (f_n). Hence, the distribution of friction forces along each row of bolts is linear until the friction force reaches its "yielding" point, which is the friction sliding strength (13.9 kips and 18.0 kips for pretension values of 52.5 ksi and 78.75 ksi, respectively). Observations from Figure 9-20 corroborate this behavior, indicating an earlier "yield" of the friction force for the case with bolts pretensioned to a value of 52.5 ksi, while the friction force profile remains linear for the case with bolt pretensioned to the higher value of 78.75 ksi.

The bolt pretension value significantly influences the development of bearing forces on the bolts. As demonstrated in Figure 9-22, at a drift of 1.0%, the bearing forces are notably higher under a pretension value of 52.5 ksi compared to those observed under a pretension value of 78.75 ksi. This phenomenon illustrates how lower pretension values can lead to earlier engagement and greater magnitudes of bearing

forces at the same lateral drift. As the drift increased to 2.0% and 3.0%, bearing forces further increase on the bolts. As anticipated, the bearing forces on the bolts where plates were in tension were greater compared to those on the compression side. This discrepancy is due to the presence of concrete, which provides additional resistance, on the compression side. Figure 9-25 illustrates this, showing a comparison of bolt hole deformation at the compression and tension edges; the hole deformation on the tension edge was 0.054 in., which is three times larger than that on the compression edge (0.017 in.). Recall from Section 2.4 that bearing forces increase with hole elongation.

Figures 9-26 to 9-31 present the friction and bearing forces acting on each row of bolts during negative pushover finite element analysis, for the same pretension values of 52.5 ksi and 78.75 ksi. Before -0.5% drift, only friction forces are evident on each row of bolts. As the drift increases, there is a gradual development of bearing forces, particularly on the tension side (web), as shown in the figures. Again, the lower pretension value (52.5 ksi) lead to earlier development of bearing forces for a given lateral drift.

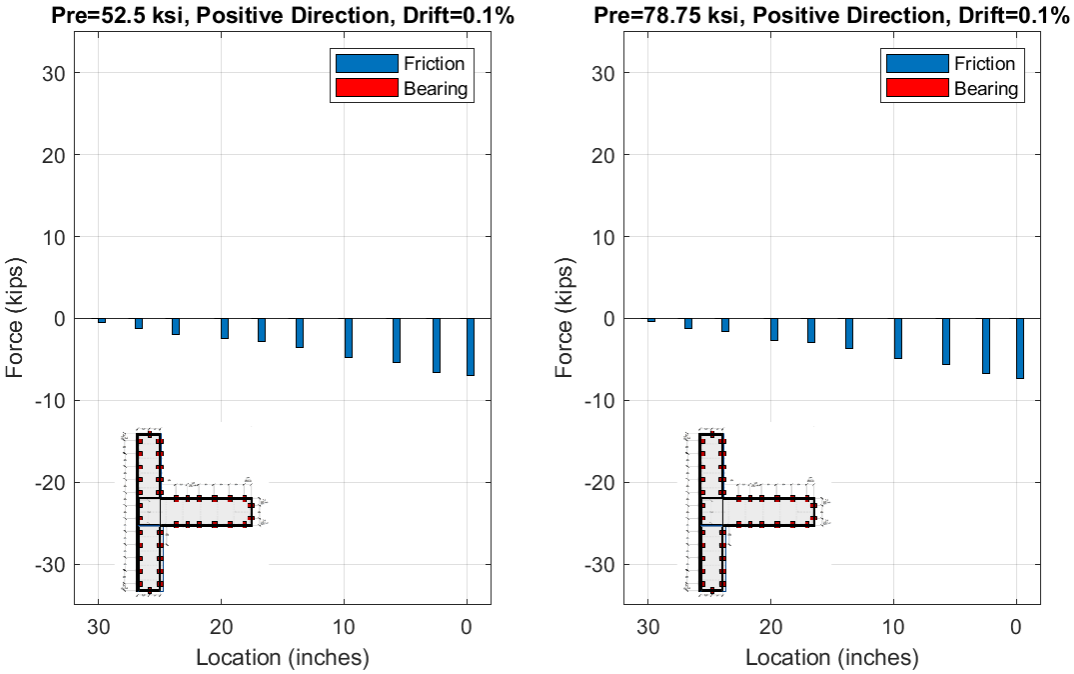


Figure 9-19. Friction and Bearing Forces at Each Row of Bolt (Drift = 0.1%)

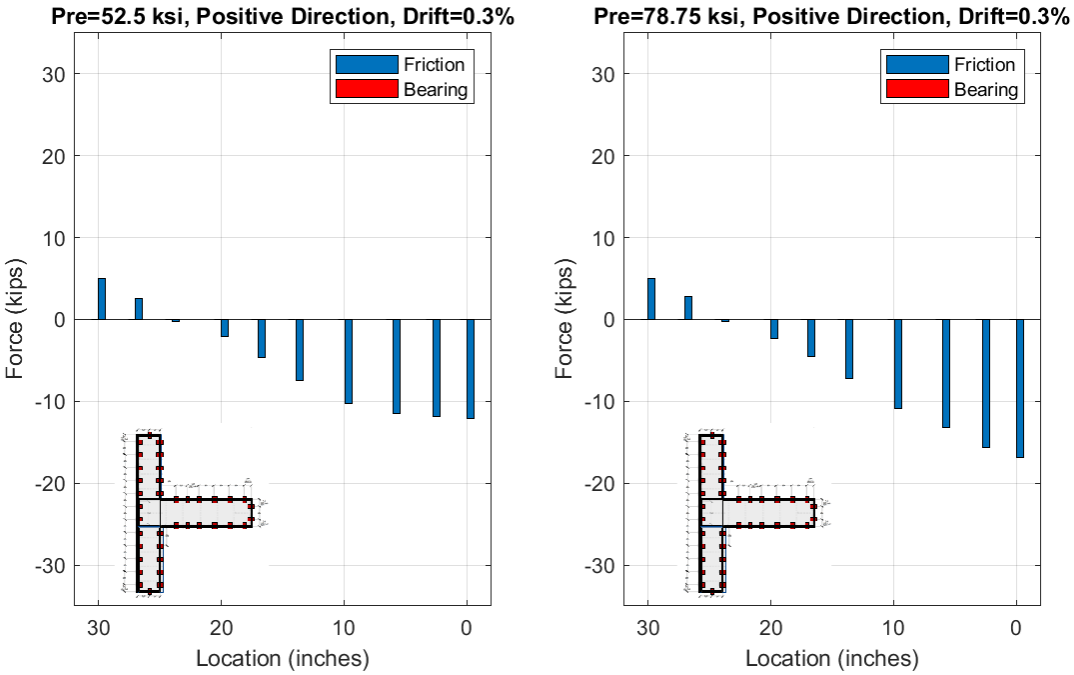


Figure 9-20. Friction and Bearing Forces at Each Row of Bolt (Drift = 0.3%)

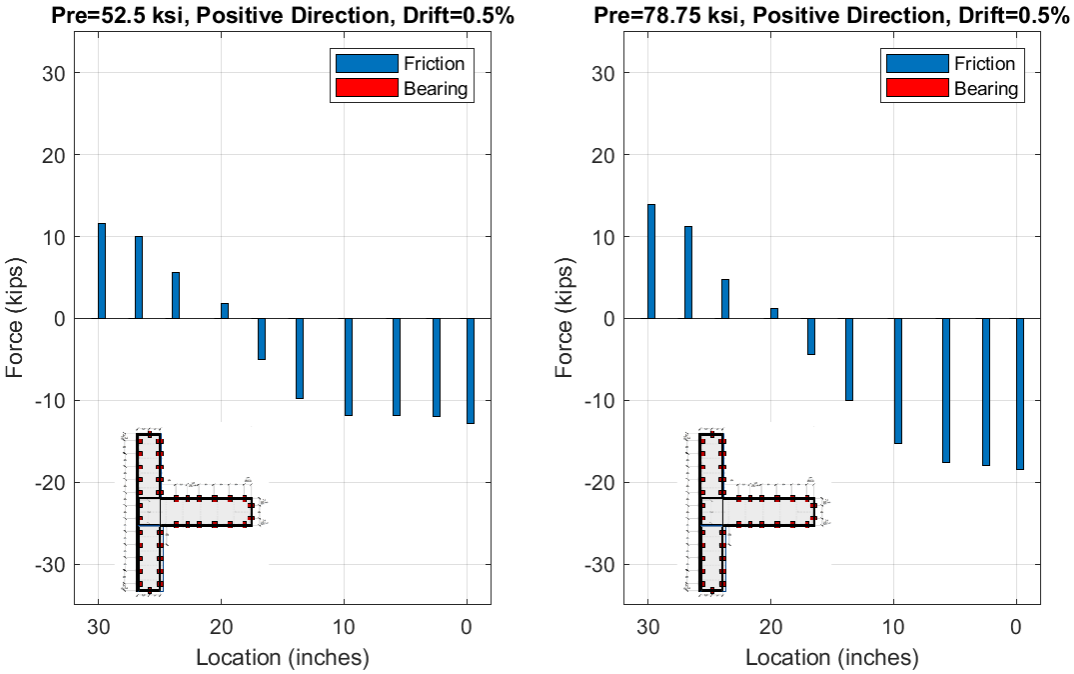


Figure 9-21. Friction and Bearing Forces at Each Row of Bolt (Drift = 0.5%)

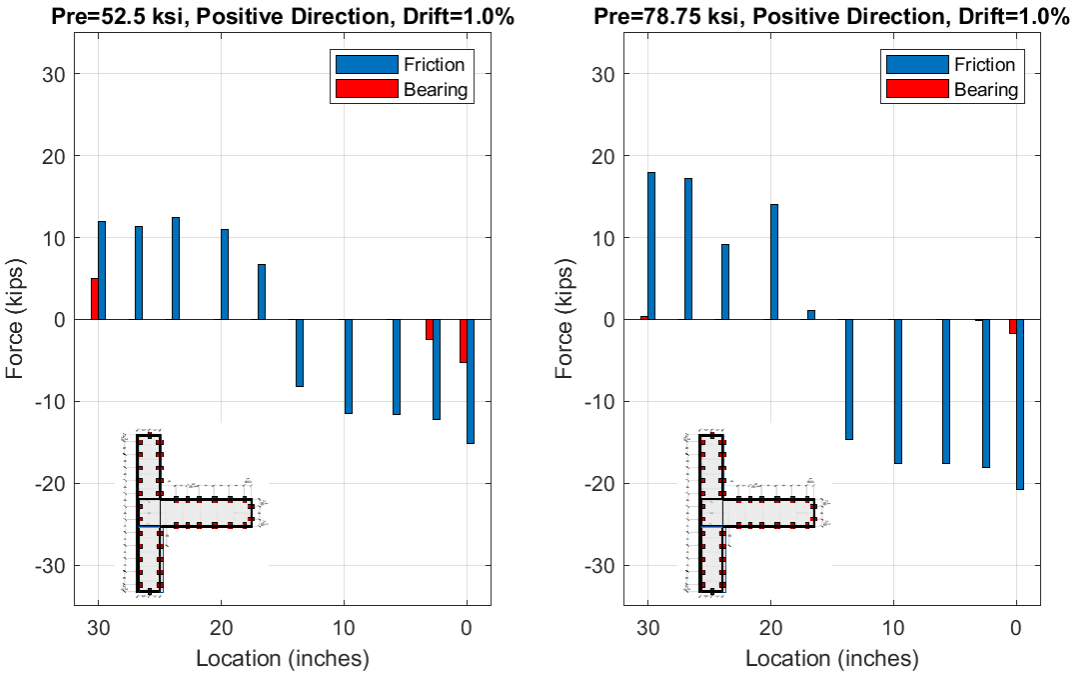


Figure 9-22. Friction and Bearing Forces at Each Row of Bolt (Drift = 1.0%)

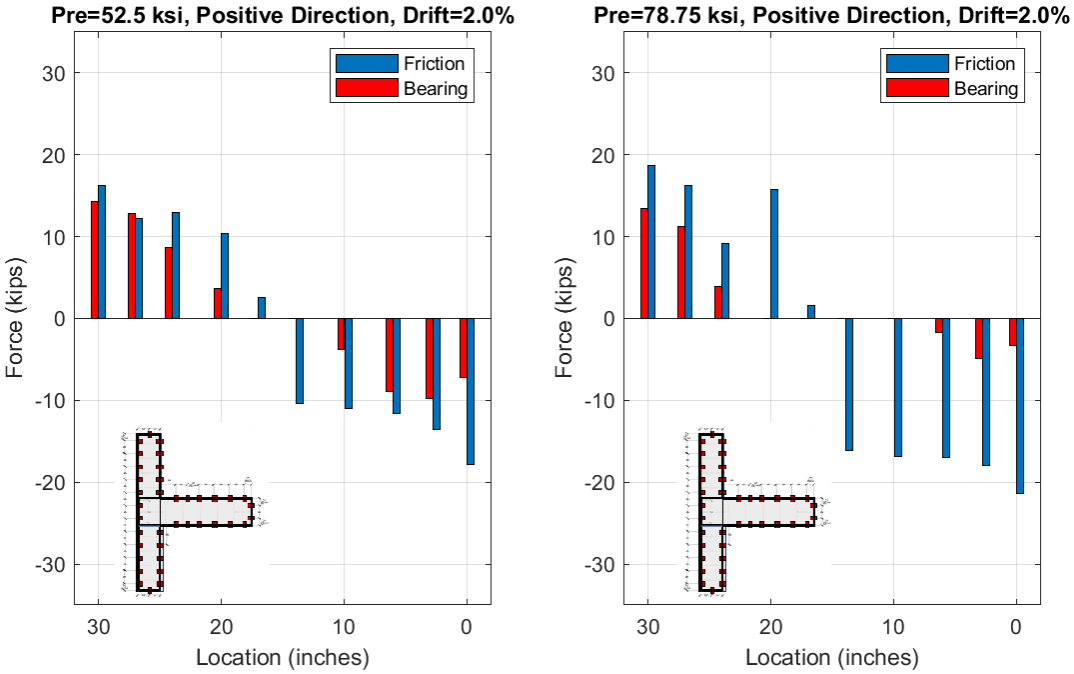


Figure 9-23. Friction and Bearing Forces at Each Row of Bolt (Drift =2.0%)

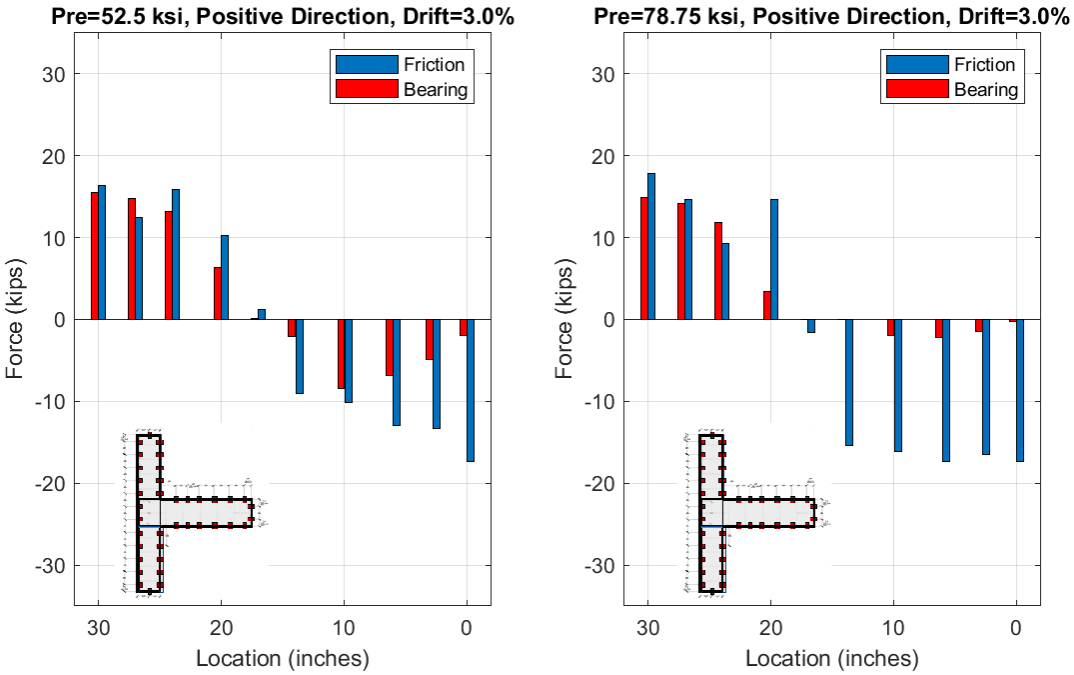


Figure 9-24. Friction and Bearing Forces at Each Row of Bolt (Drift = 3.0%)

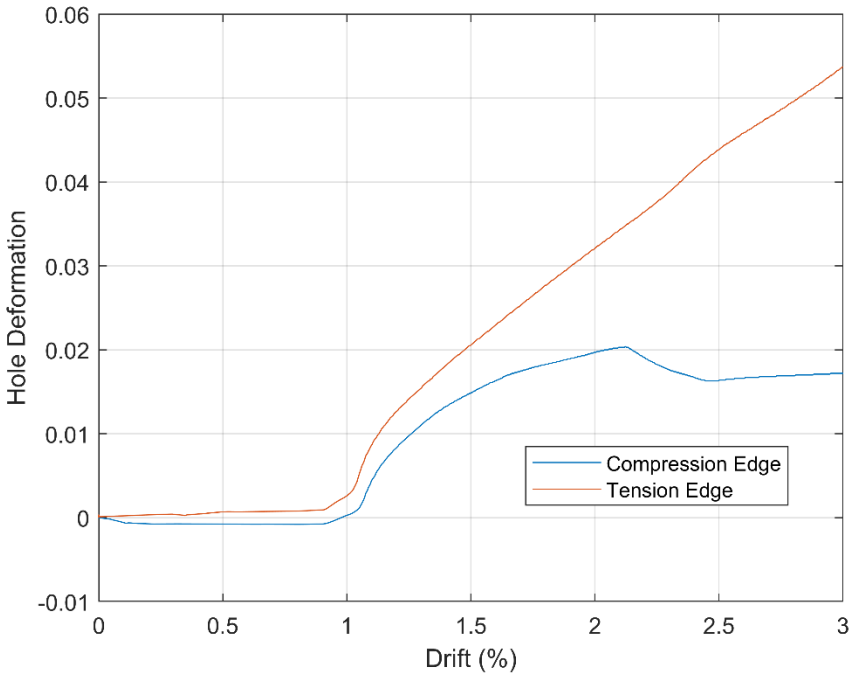


Figure 9-25. Development of Bolt Hole Deformation on Compression and Tension Edges

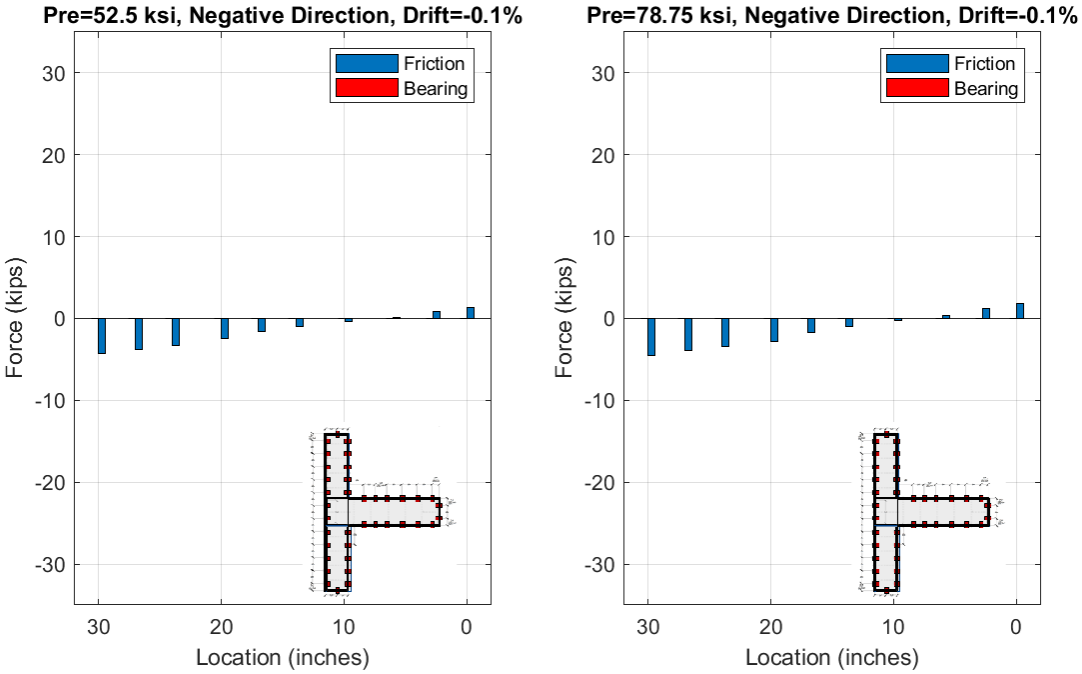


Figure 9-26. Friction and Bearing Forces at Each Row of Bolt (Drift = -0.1%)

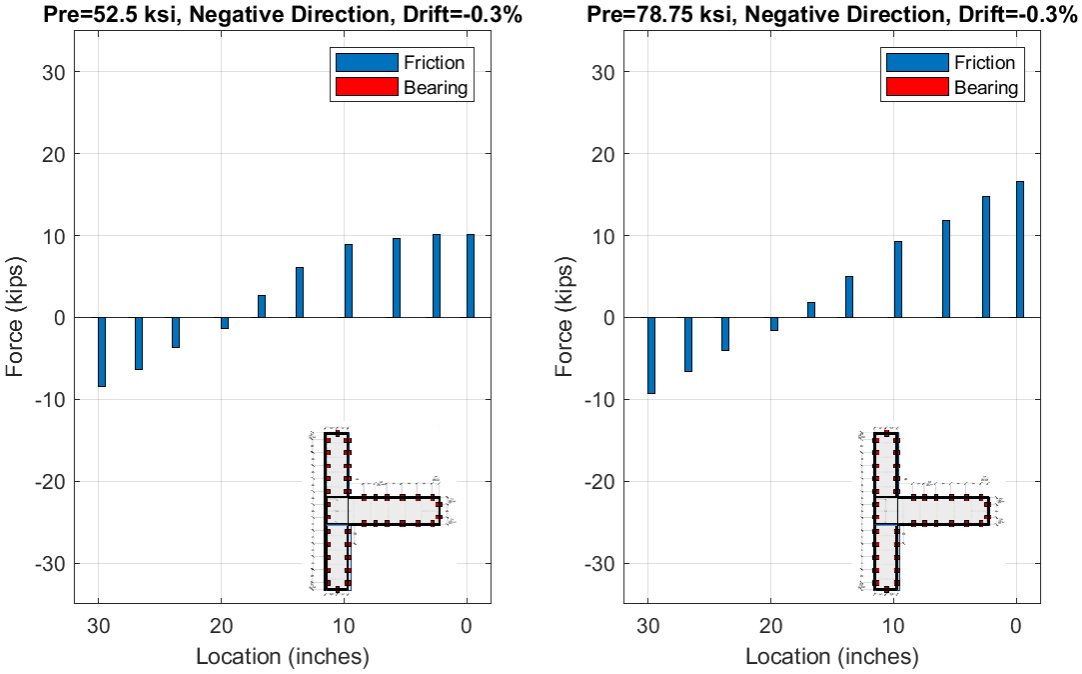


Figure 9-27. Friction and Bearing Forces at Each Row of Bolt (Drift = -0.3%)

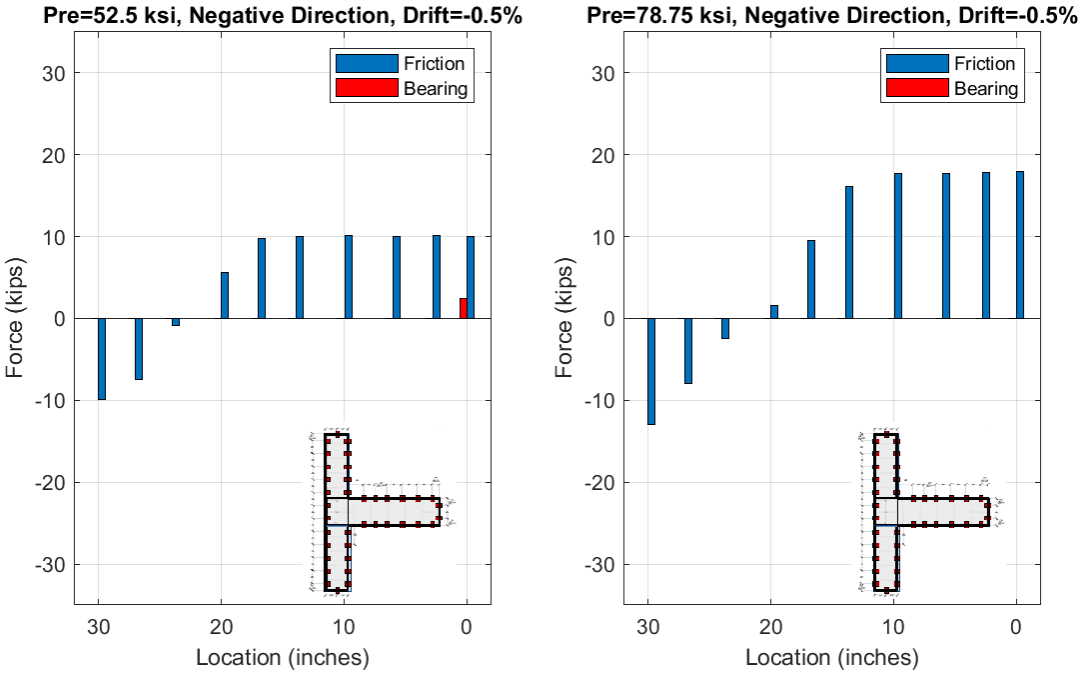


Figure 9-28. Friction and Bearing Forces at Each Row of Bolt (Drift = -0.5%)

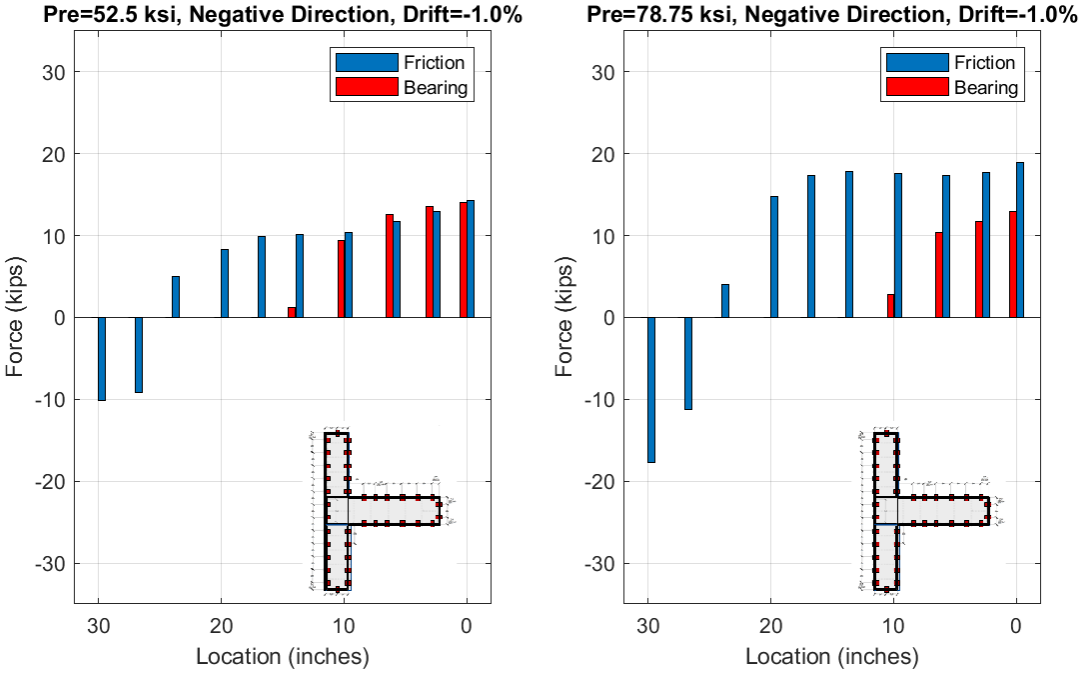


Figure 9-29. Friction and Bearing Forces at Each Row of Bolt (Drift = -1.0%)

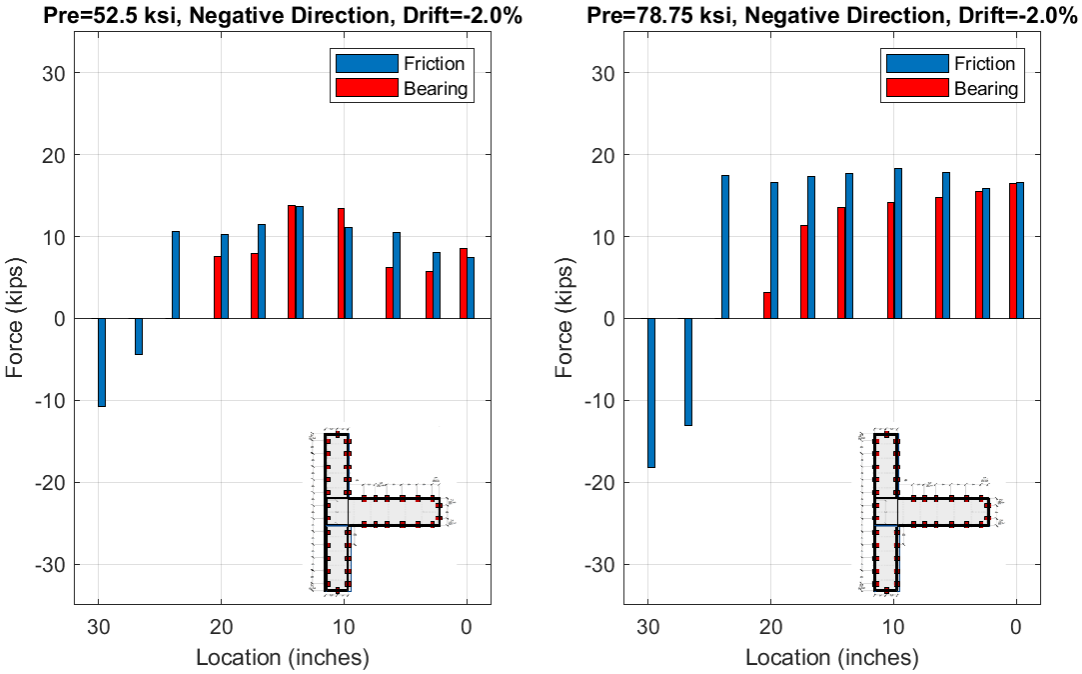


Figure 9-30. Friction and Bearing Forces at Each Row of Bolt (Drift = -2.0%)

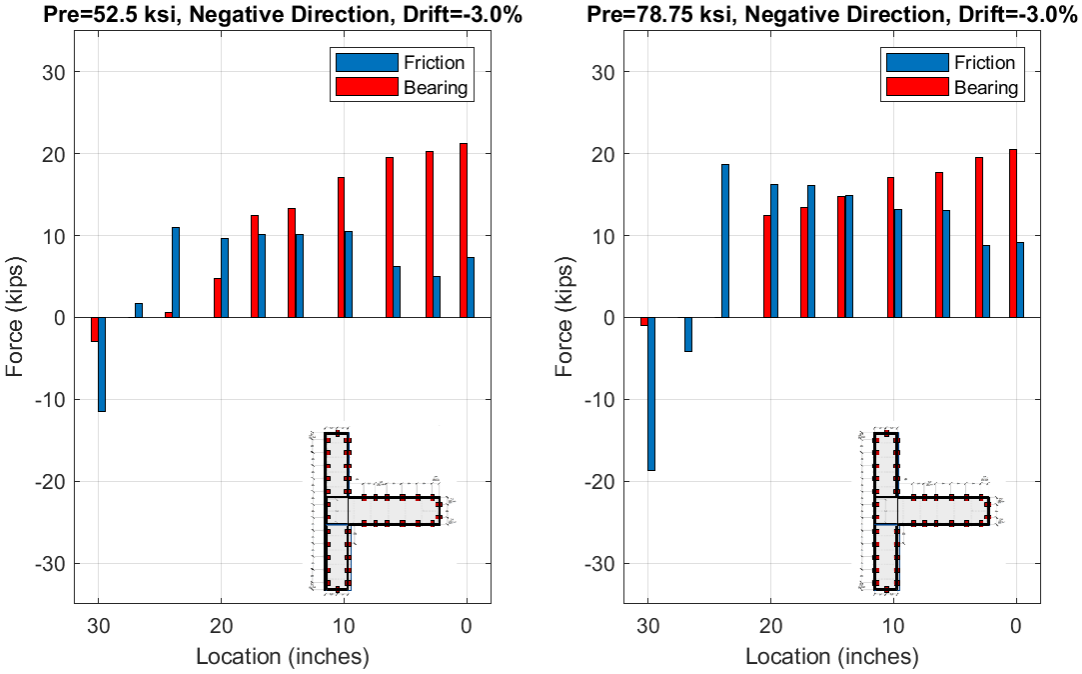


Figure 9-31. Friction and Bearing Forces at Each Row of Bolt (Drift = -3.0%)

These finite element results were also used to investigate the appropriateness of the simplified model presented in Section 7.2.3. Recall that in that simplified model, the bolts at the tension edge are assumed to develop their bearing strength (either $2.4dtF_u$ or $3.0dtF_u$), while the other bolt forces are determined by interpolation using similar triangles assuming a linear force distribution profile. As shown in Figure 9-9, the moment curve reaches the flexural strength to develop bearing strength of $2.4dtF_u$ and $3.0dtF_u$ at 1.17% and 1.54% drifts in positive direction, while it reaches the flexural strength to develop bearing strength of $2.4dtF_u$ and $3.0dtF_u$ at -0.77% and -1.0% in negative direction. Therefore, results from the simplified bolt force distribution are compared with results obtained from the finite element model at those drifts. The friction and bearing forces at each bolt row were summed to obtain the total force on each row of bolts, and divided by the number of bolts on that row to obtain the forced demand on single bolt on each row. Results are shown in Figures 9-32 to 9-35. The simplified model force distributions (corresponding to either the $2.4dtF_u$ or $3.0dtF_u$ limits) are plotted as straight lines in the figures, and bars are used to show the force demand on single bolts in each row obtained from finite element analysis. Table 9-3 compares the flexural strength contributions from bolts, as determined by both simplified methods and finite element analysis, corresponding to $2.4dtF_u$ or $3.0dtF_u$ in both the positive and negative directions. The results indicate that the simplified method achieves over 90% accuracy when compared to pushover finite element analysis.

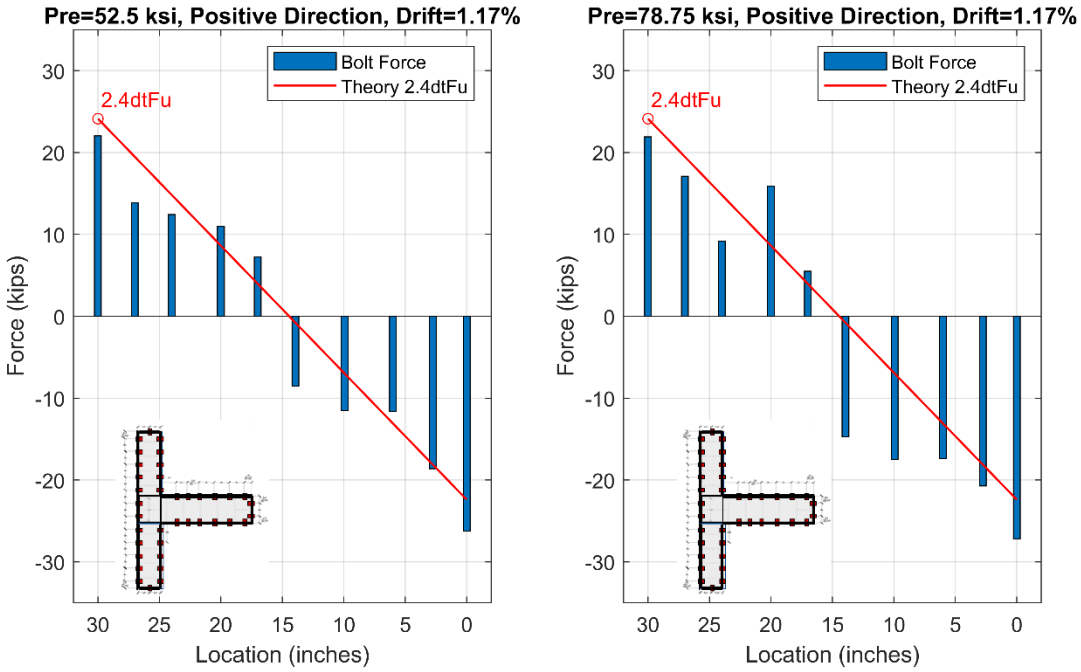


Figure 9-32. Summation of Friction and Bearing Forces at Each Row of Bolt (Drift = 1.17%)

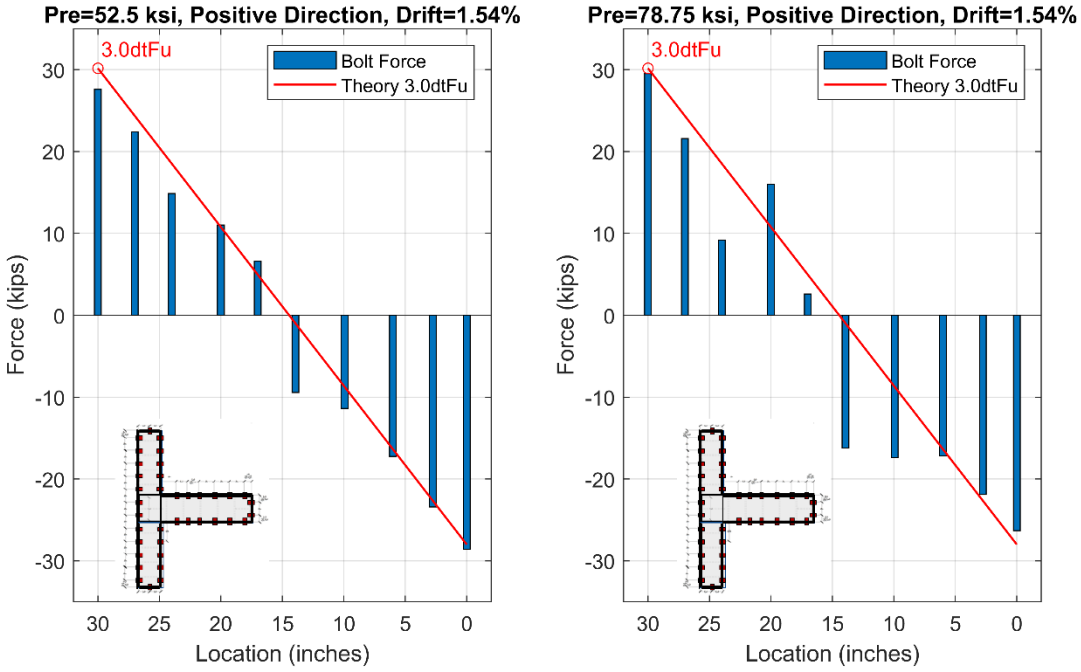


Figure 9-33. Summation of Friction and Bearing Forces at Each Row of Bolt (Drift =1.54%)

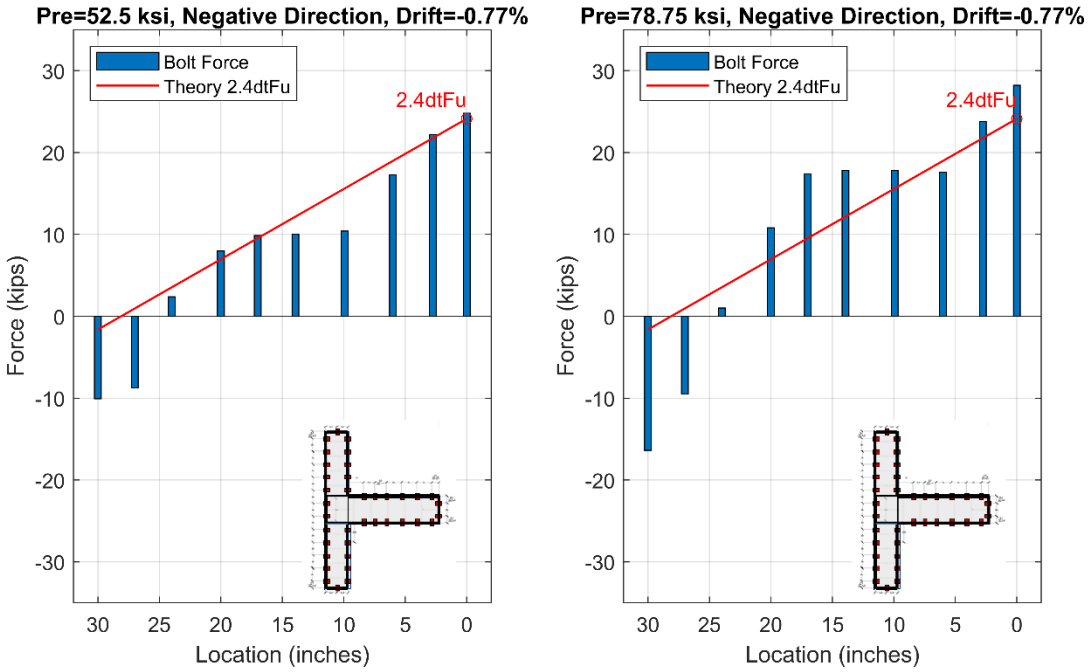


Figure 9-34. Summation of Friction and Bearing Forces at Each Row of Bolt (Drift = -0.77%)

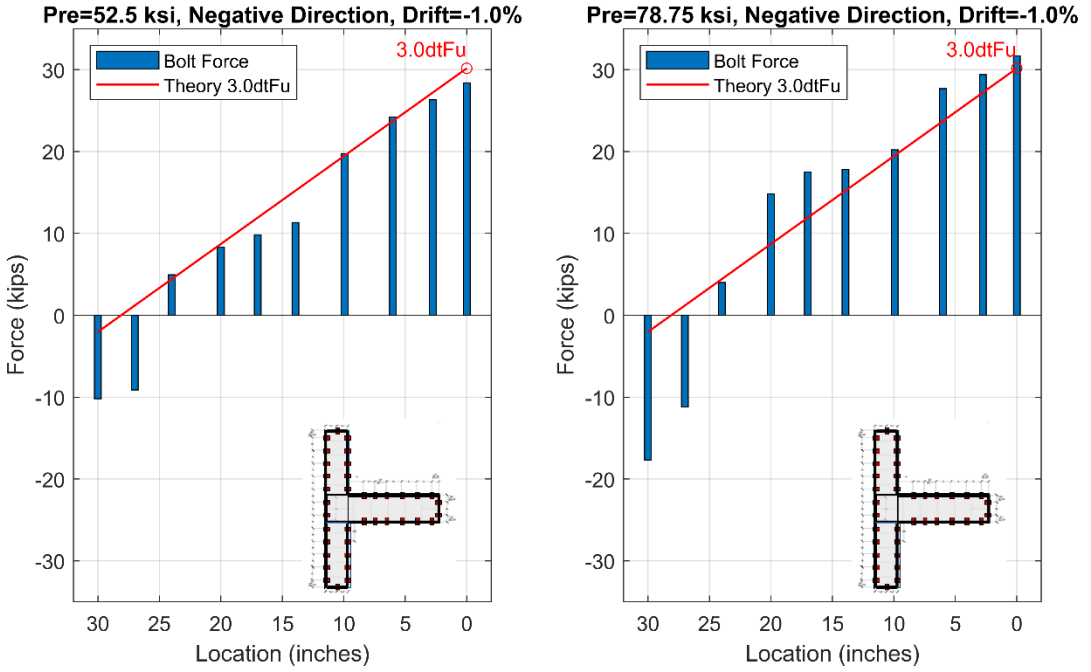


Figure 9-35. Summation of Friction and Bearing Forces at Each Row of Bolt (Drift =-1.0%)

Table 9-3. Flexural Strength of Bolts from Simplified Method and Finite Element Analysis

	Positive Direction		**Negative Direction**	
	$M_{bolt_2.4dtFu}$ (k-ft)	**$M_{bolt_3.0dtFu}$ (k-ft)**	**$M_{bolt_2.4dtFu}$ (k-ft)**	**$M_{bolt_3.0dtFu}$ (k-ft)**
Simplified Method	683.68	821.16	397.90	491.86
FEM	631.48	752.98	384.85	483.99
Accuracy (%)	92.36%	91.70%	96.72%	98.40%

9.3.2 Cyclic Loading Analysis

9.3.2.1 Impact of Pretension Values

To assess the impact of bolt pre-tension values on the hysteretic behavior of bolted splices, pretension values of 52.5 ksi, 78.75 ksi, and 105 ksi were assigned to the bolts in the finite element model for the cyclic loading pushover analyses. Results are shown in Figure 9-36, for the range over which the finite element analysis was run (i.e., -1.3% to 2.1%) and the full experimental range. Figure 9-37 shows the results over a smaller range, focusing on the hysteresis curves for Steps 1 to 3 at drifts ranging from -0.3% to 0.8% (recall that comparison for the initial elastic stiffness was previously performed in Figure 9-4 from monotonic analysis, and is not addressed anew here). The finite element analyses over that smaller range show the presence of an initial overstrength in the positive direction. The reasons for this initial overstrength are unknown, but it is speculated to be caused by either an initial out-of-straightness of the faceplates and horizontal splice plate (not accounted for by the finite element model) or assumptions in the finite element model that produced a wall numerically stiffer than the actual specimen over that range of displacement. Initial out-of-straightness would lead to some initial bending of the plates when the web was in compression during positive drifts, resulting in an earlier softening of the stiffness.

Figure 9-38 focuses on the results from Steps 1 to 8 for which the finite element analysis was conducted, by comparing hysteresis curves with test results. This figure shows the effects of three different pretension values on the bolted connections and juxtaposes these computational results with actual test outcomes. In the results of Steps 4 to 7, the finite element analysis with a pretension of 52.5 ksi closely align with the positive peaks in the test, and it shows a slightly lower sliding plateau and strength in the negative peaks. The finite element analysis conducted with a pretension value of 105 ksi yielded more results up to Step 8 (2.1% drift). It reasonably matched the test data in both the positive peak at 2.1% drift and in the negative peaks. Therefore, this pretension value was retained for the subsequent cyclic loading analyses. Note that

beyond this point, the implicit analysis of the finite element program could not converge due to a negative volume issue, and the analysis terminated.

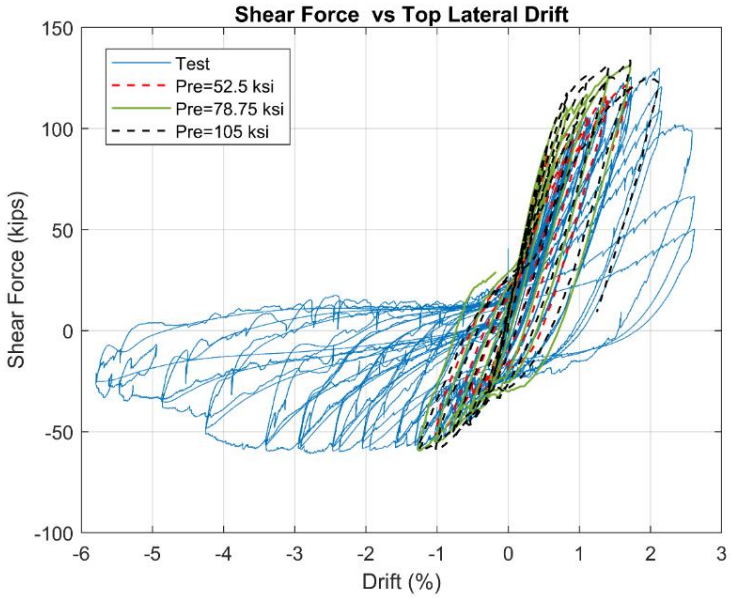


Figure 9-36. Impact of Pretension of Bolts from Cyclic Loading Analysis

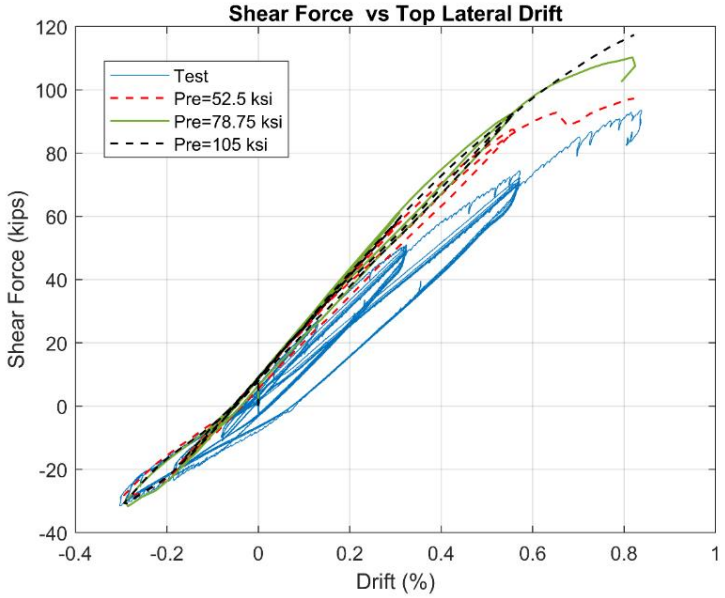


Figure 9-37. Impact of Pretension of Bolts from Cyclic Loading Analysis (-0.3% to 0.8% Drift)

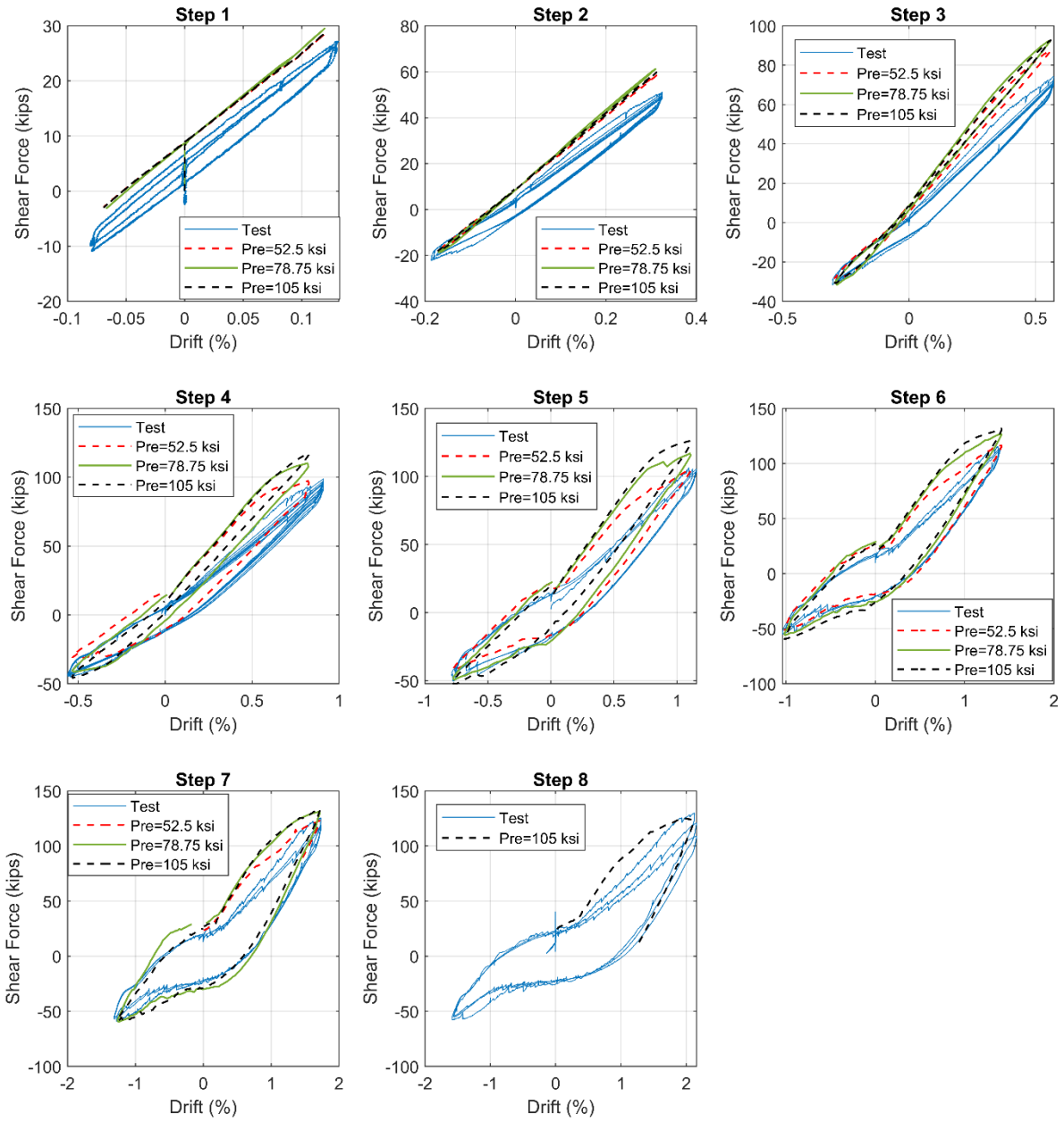


Figure 9-38. Impact of Pretension of Bolts from Cyclic Loading Analysis (Steps 1 to 8)

9.3.2.2 Cyclic Loading Analysis with 105 ksi Pretension

Figure 9-39 shows the load protocol for the cyclic load finite element analysis (matching experimentally obtained displacements), while Figures 9-40 and 9-41 compare the shear force and moment versus top lateral drift from the cyclic loading finite element analysis with the hysteresis curves from the test. Figures 9-42 and 9-43 show the von Mises stresses of the steel plates during cyclic loading from southwest and southeast views. Five arbitrary points were selected to demonstrate the distribution of stress and deformation of the faceplates and horizontal splice plates. Similar to what was observed in the pushover analyses, the horizontal splice buckled at a lateral drift close to 1.42% (Figure 9-44), and progressive yielding due to bearing of bolts can be seen on web and flange splice plates in positive and negative peaks(Figure 9-45).

Finite element results were also used to assess the relative contributions of steel and concrete to the total wall strength and how these contributions evolved throughout the entire cyclic response. Figure 9-46 and 9-47 show the numerically obtained hysteretic curves for the shear and flexural strengths of concrete, steel, and their combined total at the horizontal splice level, plotted as a function of lateral drift. The shear strengths in Figure 9-46 were compared by plotting at three levels—(a) above, (b) at, and (c) below the horizontal splice level—to account for the influence of severe concrete cracks in the connection zone. It was observed that the concrete shear strength degraded dramatically at or below the horizontal splice level. This prompted an investigation into the relationship between crack propagation and the shear strength of concrete in cyclic loading analysis.

Figures 9-48 to 9-50 show the progression of shear and flexural strengths of concrete, steel, and their combined total strengths at and above the horizontal splice level, as the cyclic history unfolded over the loading protocol time. The contribution from concrete at each peak was quantified by comparing the

concrete strength (V_c for shear or M_c for moment) against the total strength (V_{Total} or M_{Total}), with the results expressed as percentages. In 9-48, when the shear strength was read from above the horizontal splice level, the contribution of concrete was progressively dropped from 62% at 0.57% drift to 55% at 2.12% drift in the positive. In the negative direction, the V_c contribution declined from 44% at -0.3% drift to 32% at -0.55% drift, and then the percentage started increasing to 62% at -1.27% drift.

In Figure 9-49, when the shear strength was measured at the horizontal splice level, a more severe decrease was observed, primarily due to the cracking of concrete. At a drift of 0.57%, coinciding with the initiation of concrete cracking as shown in Figure 9-51, the contribution of V_c was 58%. Then, following in Figure 9-51 the progression of concrete cracking at different drifts reached during cyclic loading, it is seen that the contribution of concrete to the total shear strength decreased as drift amplitude increased. By the time positive drift reached 1.42%, the contribution of V_c significantly decreased to 16%. The proportional contribution of concrete to total shear strength slightly increased to 23% beyond 1.42% drift, as web horizontal buckling developed, but by 2.12% drift, this contribution had dropped again to only 8% of V_{Total}, reflecting that the loss of shear strength due to severe concrete cracking was more severe than the loss due to buckling of the web horizontal splice. A similar trend was observed at the negative drift's peaks.

At horizontal splice level, the contribution of M_c (flexural strength of concrete) did not decrease as dramatically as V_c; rather, it progressively dropped from 62% to 58% in the positive direction up to a drift of 1.73%, only dropping to 54% at a drift of 2.12%. In the negative direction, however, the M_c contribution declined from 50% at -0.3% drift to 25% at -1.27% drift. This reduction was more significant in the negative moment, likely due to the more severe propagation of cracks along the web, which led to losses of tensile forces on concrete's web. On the other hand, the reduction was less significant in the positive moment because the cracks on the web were closed when the concrete was compressed during positive drift.

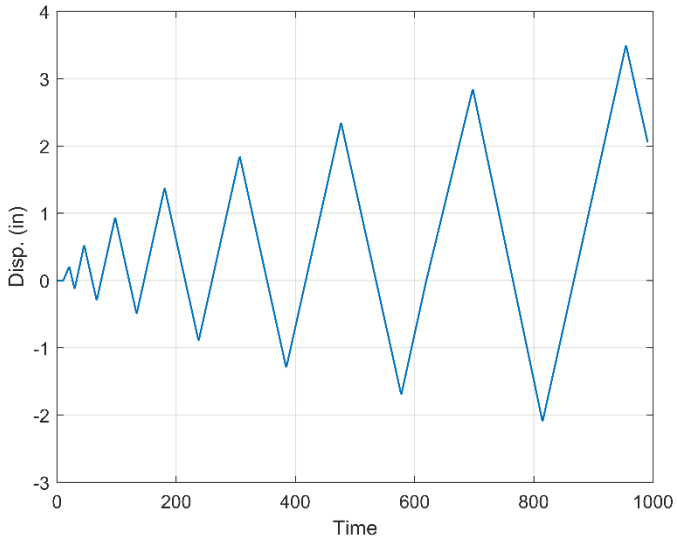


Figure 9-39. Cyclic Loading Protocol of Finite Element Model

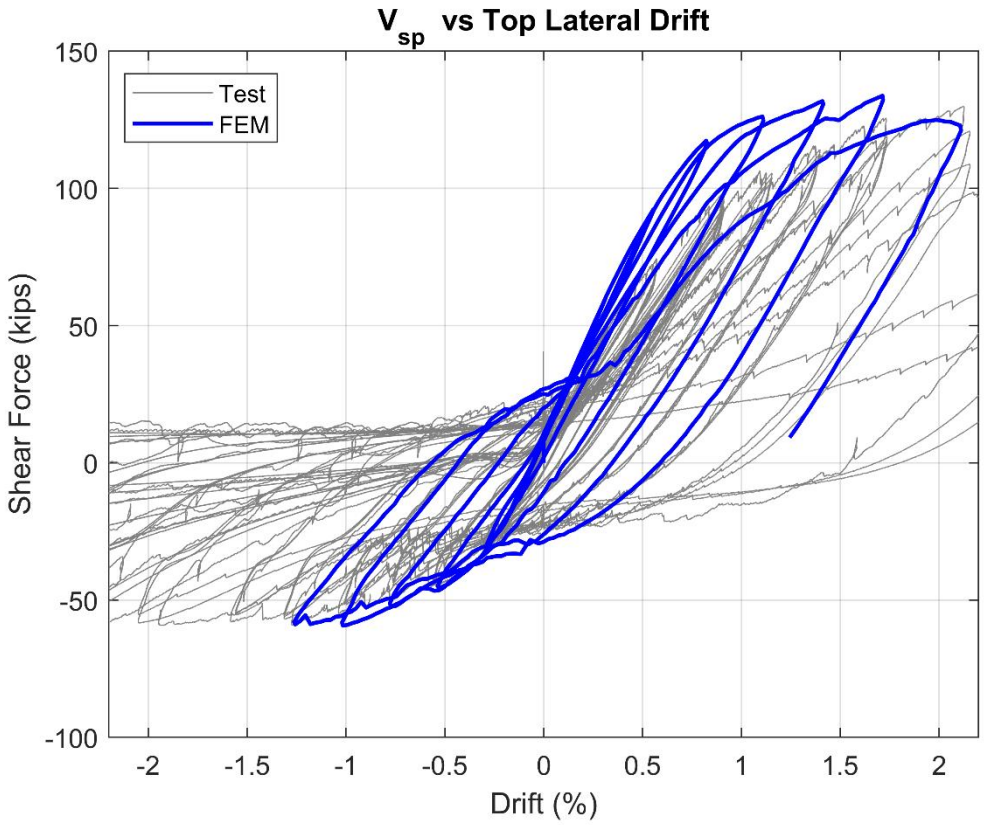


Figure 9-40. Shear Force and Top Lateral Drift Curve from Test and Finite Element Analysis

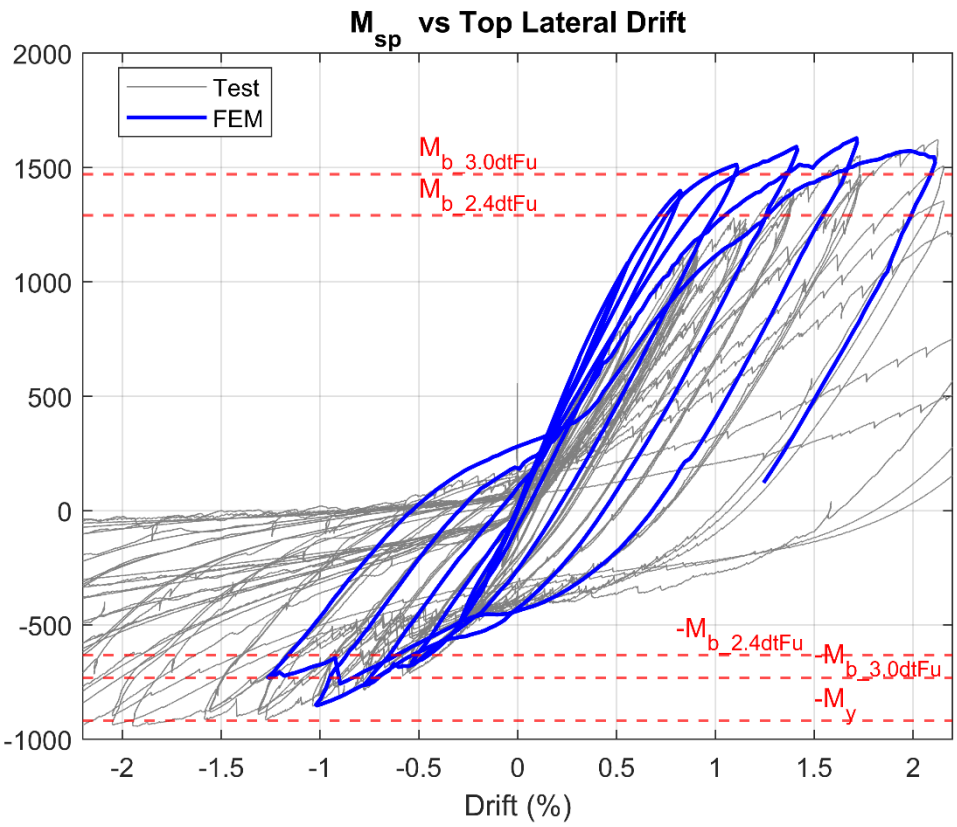


Figure 9-41. Moment and Top Lateral Drift Curve from Test and Finite Element Analysis

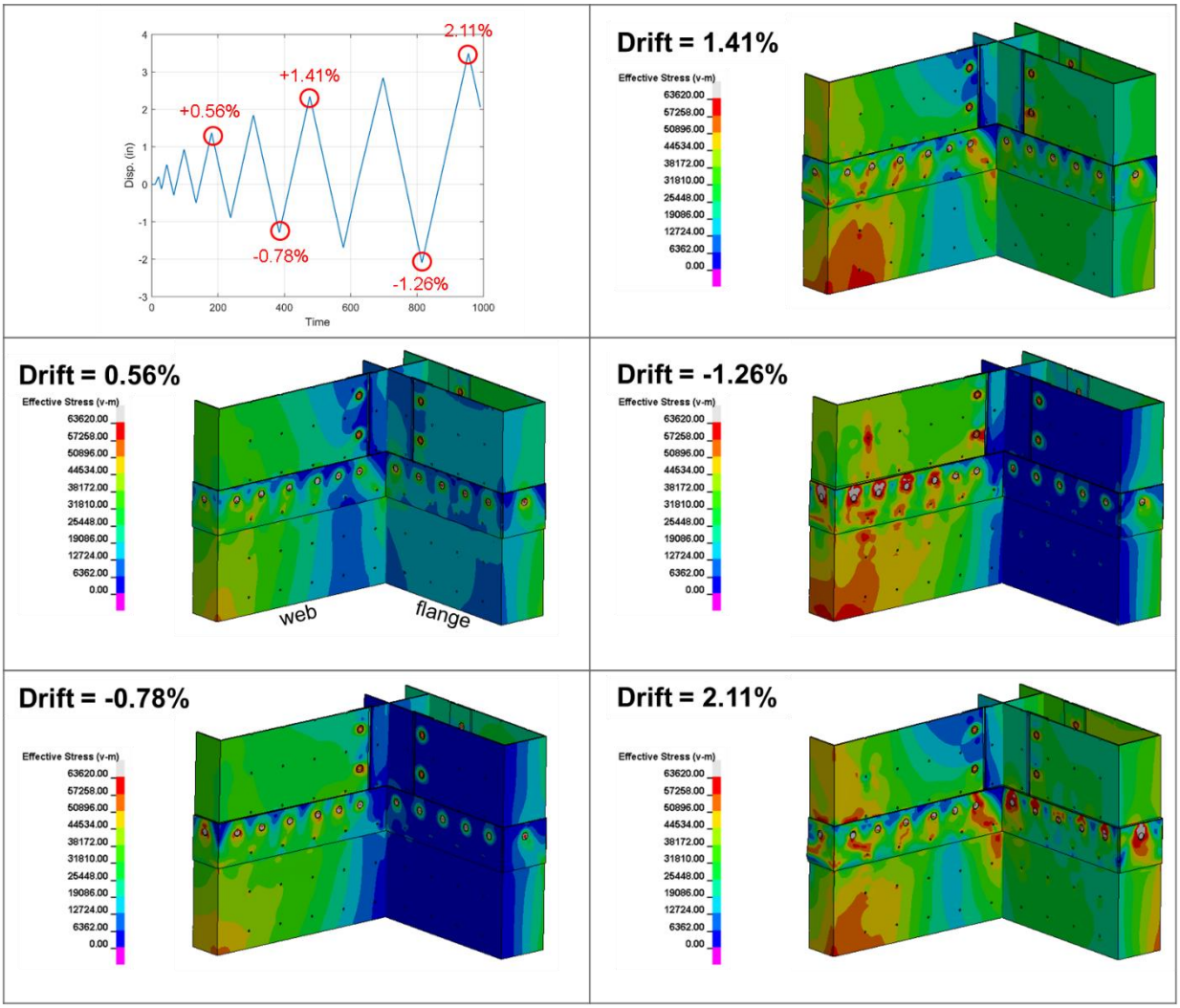


Figure 9-42. von Mises Stresses of the Wall Model in Cyclic Loading Analysis (Southwest View)

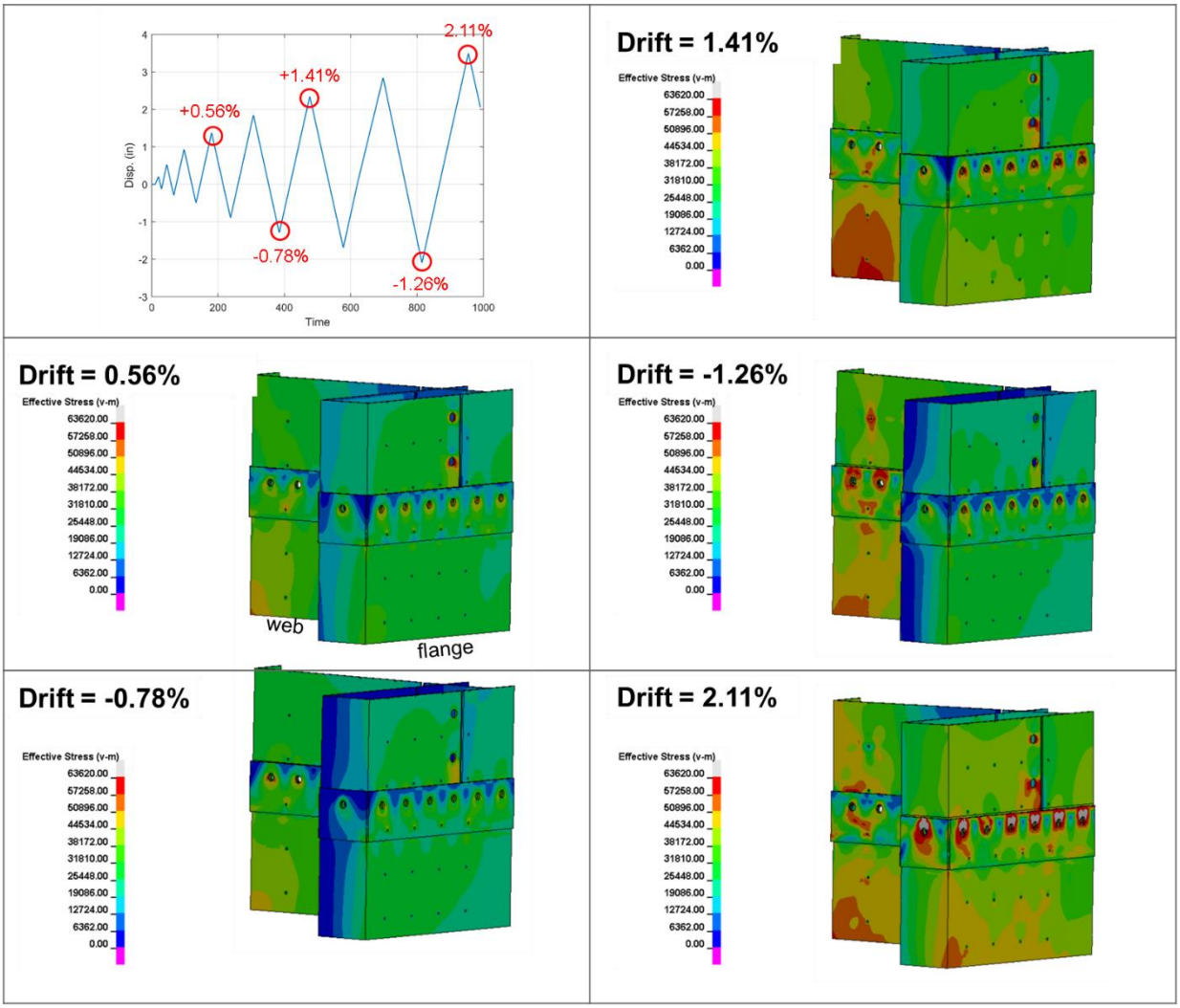


Figure 9-43. von Mises Stresses of the Wall Model in Cyclic Loading Analysis (Southeast View)

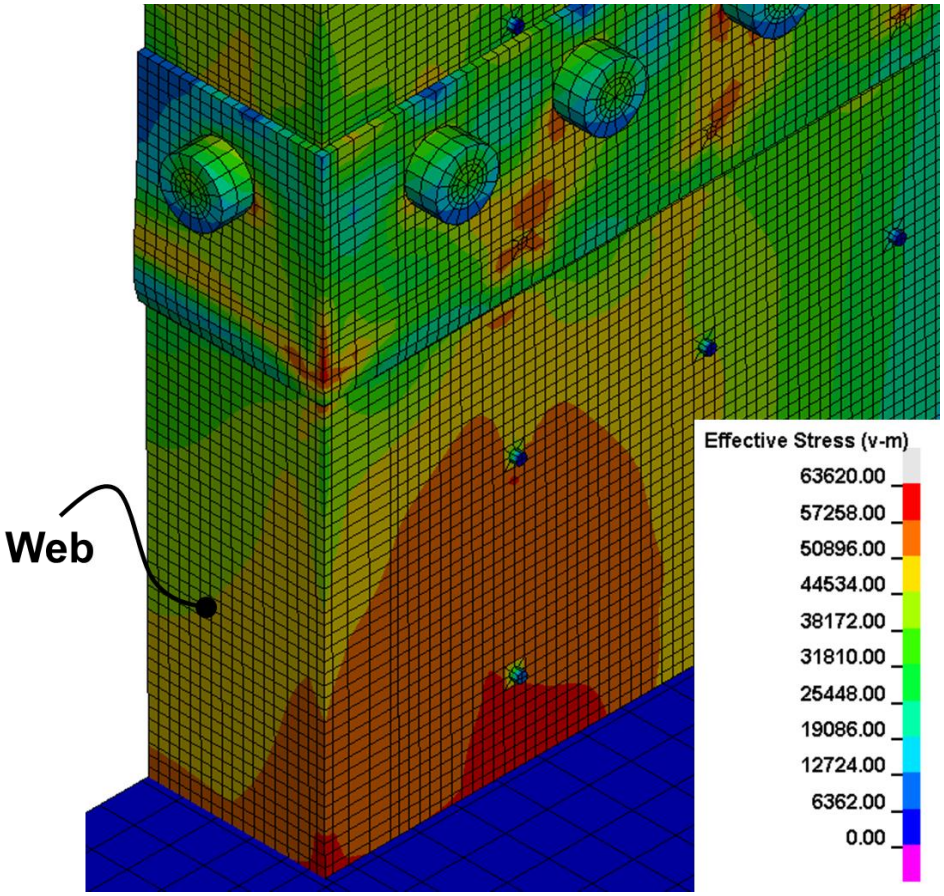


Figure 9-44. Buckling of Web Horizontal Splice at 1.41% Drift

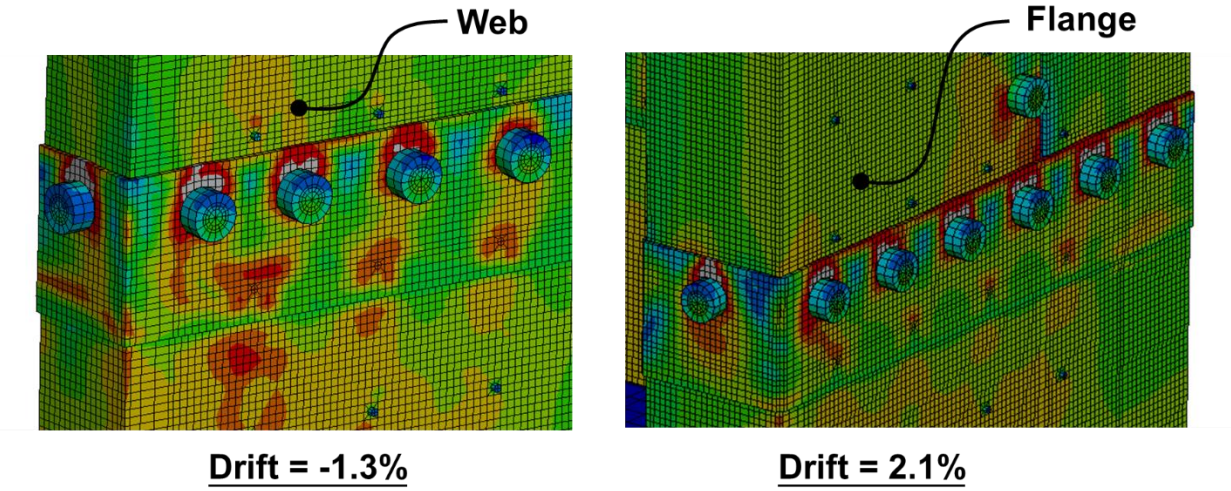


Figure 9-45.Yielding near Bolts at Positive and Negative Peaks

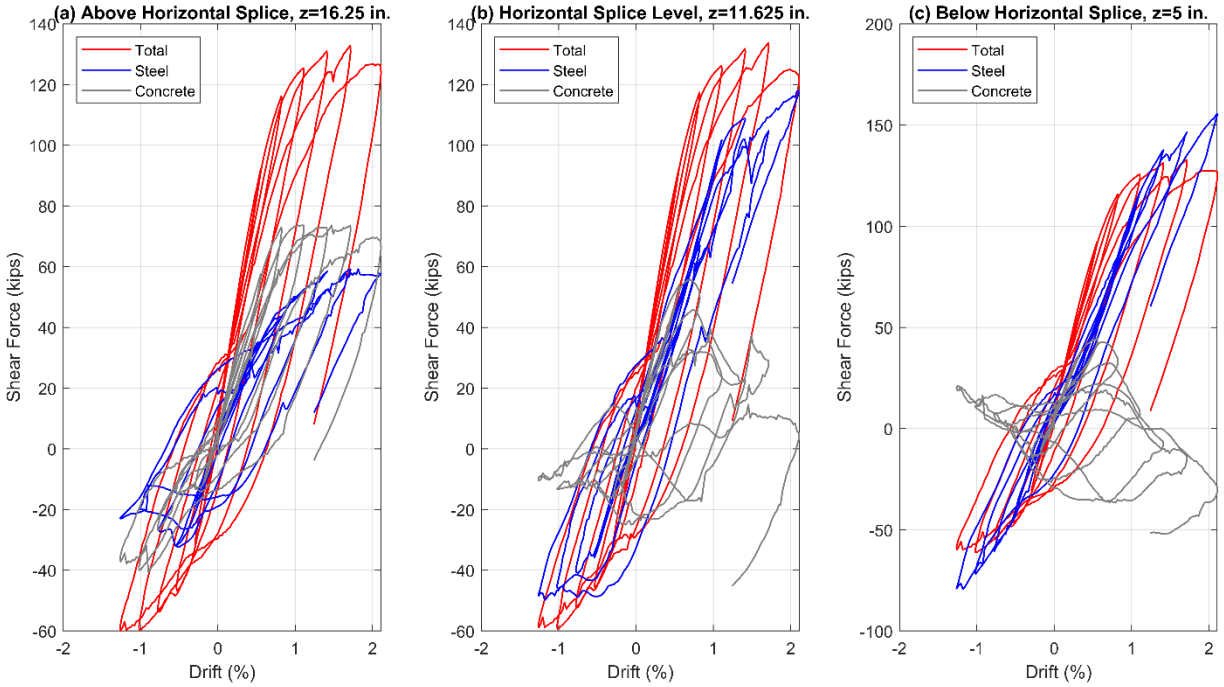


Figure 9-46. Shear Strengths of Concrete and Steel, depicting (a) above, (b) at, (c) below Horizontal Splice Level

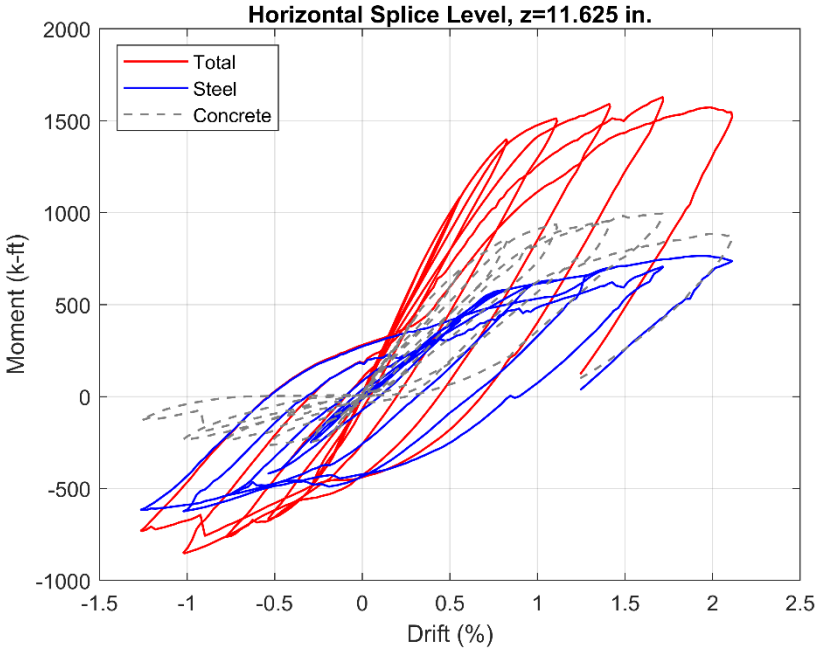


Figure 9-47. Flexural Strengths of Concrete and Steel at Horizontal Splice Level

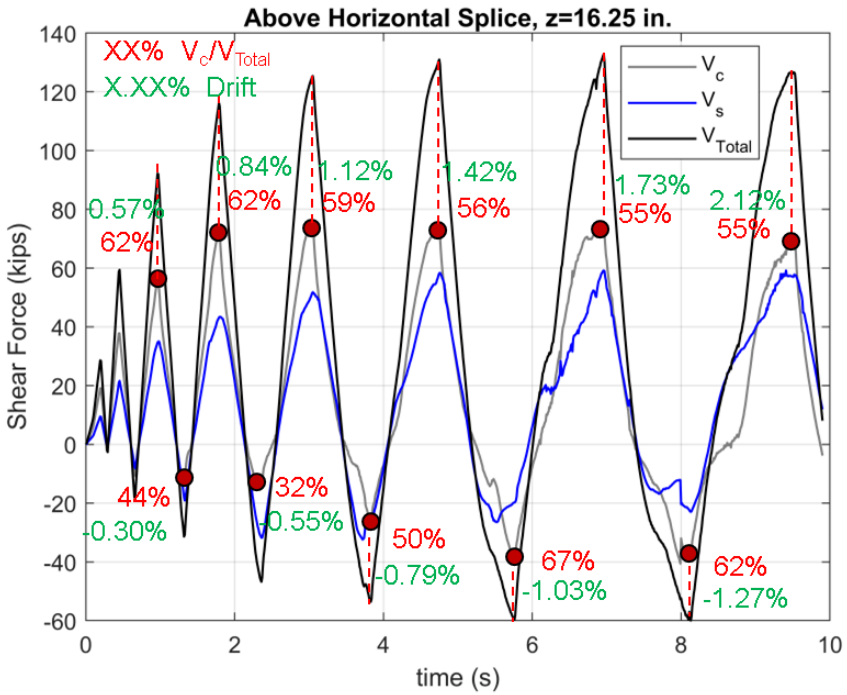


Figure 9-48. Percentage of Concrete Shear Force in Cyclic Loading History (Above Horizontal Splice Level)

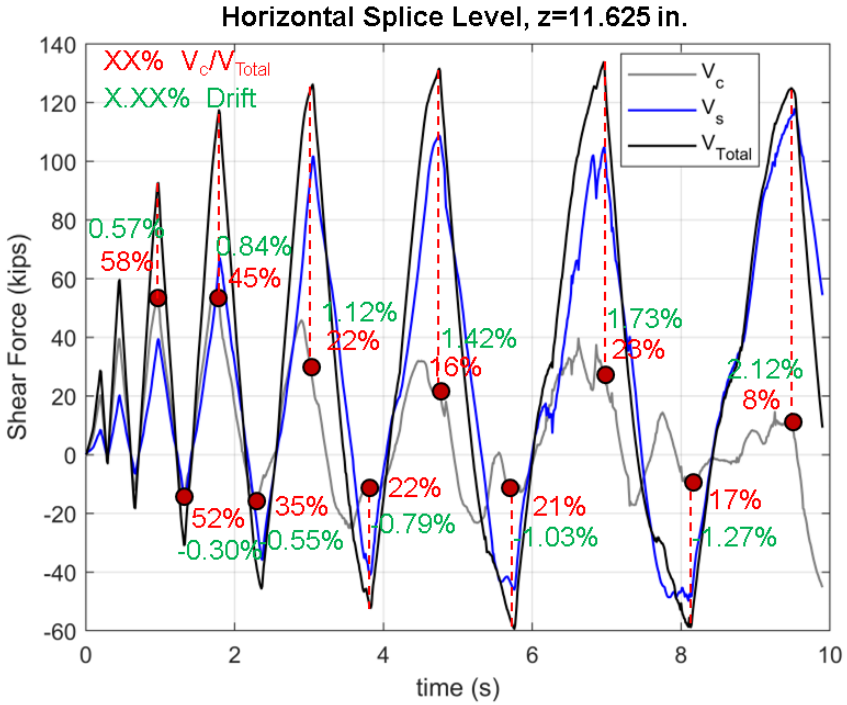


Figure 9-49. Percentage of Concrete Shear Force in Cyclic Loading History (Horizontal Splice Level)

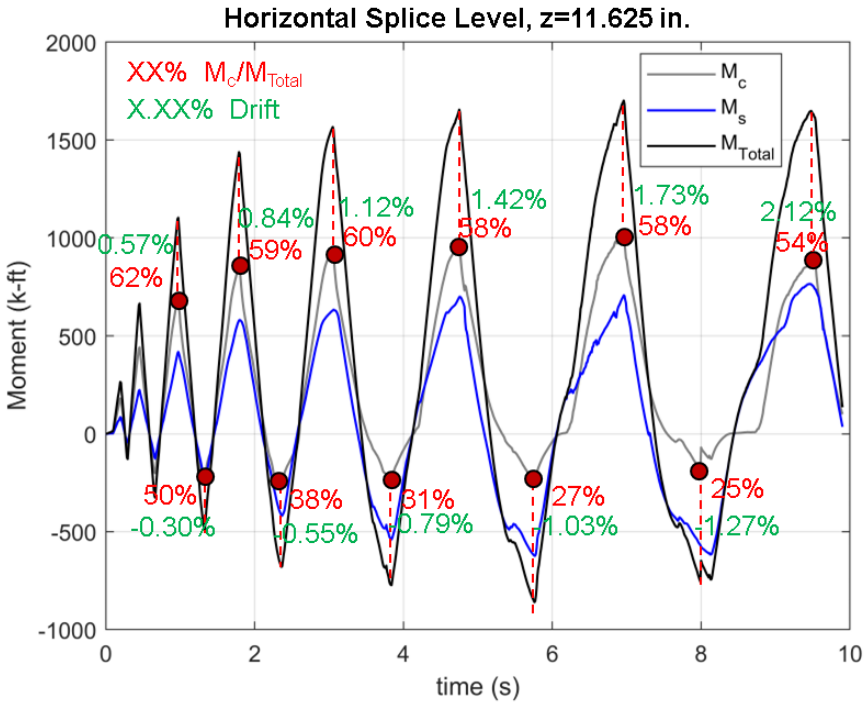


Figure 9-50. Percentage of Concrete Moment in Cyclic Loading History (Horizontal Splice Level)

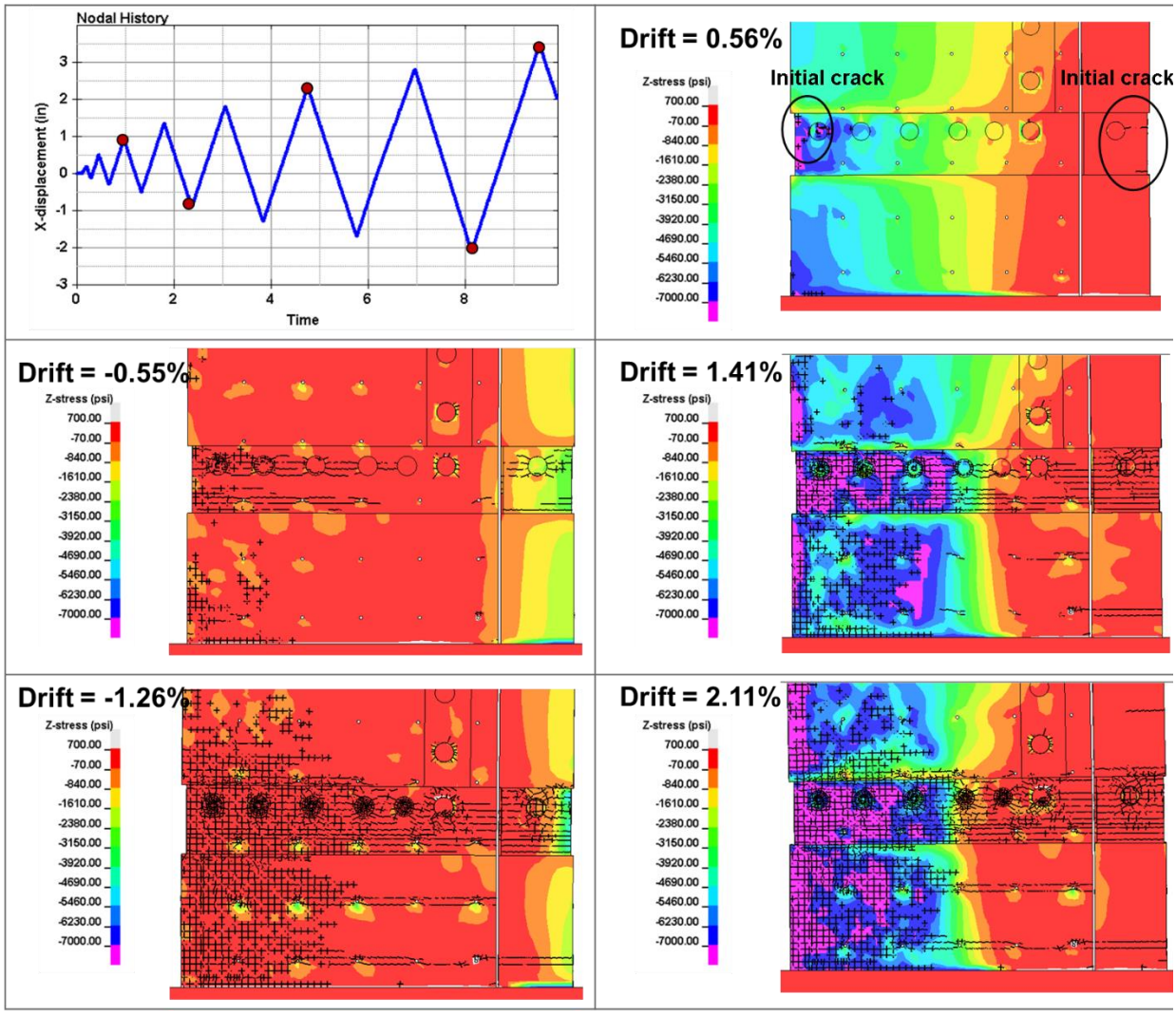


Figure 9-51. Development of Cracks of Concrete in Cyclic Loading Analysis (South View)

Figures 9-52 to 9-63 present the friction and bearing forces acting on each row of bolts corresponding to Steps 2 to 7 from the test loading protocol. It can be observed that bearing forces only started to developed at both positive and negative peaks in Step 5, which is consistent with the fact that during the test, the noise created due to sliding occurred after Step 4. In addition, as shown in Figure 9-41, the moment curve reaches the flexural strength to develop bearing strength of $3.0dtF_u$ at 1.0% and -0.7% drifts in positive and negative peaks. Similar to the pushover analyses, the simplified method was compared with the finite element model under cyclic loading analysis. As mentioned in Section 9.3.1.2, the friction and bearing forces at each bolt row were summed to obtain the total force on each row, and divided by the number of bolts on that row to obtain the force on single bolt on each row. Results are shown in Figures 9-64 and 9-65, the summation of friction and bearing forces at each row were plotted at the drift developing the flexural strength mentioned above. The simplified model force distribution corresponding to $3.0dtF_u$ was plotted in the figure for comparison. Table 9-4 reveals that the flexural strengths corresponding to bearing strengths of $3.0dtF_u$, as obtained from the simplified method, are 821.16 k-ft and -491.86 k-ft in the positive and negative directions, respectively. Conversely, in the finite element model, these flexural strengths are 642.6 k-ft and -451.19 k-ft in the positive and negative directions, respectively, accounting for 78% and 92% of the theoretical values obtained from the simplified model. Note that in the pushover analysis, the moments calculated by the simplified method were compared at 1.54% and -1.0% drift to assess the flexural strength required to develop 3dtFu. In contrast, for the cyclic loading analysis, the compared drifts were smaller, at 1.0% and -0.7%. Additionally, a higher pretension value of 105 ksi was assigned compared to the pushover analysis, which used a pretension value of 52.5 ksi. Therefore, this difference in pretension values and the smaller drifts used in the cyclic loading analysis might explain why the flexural strength contributed by the bolts was lower at that stage in the finite element analysis results compared to the simplified model.

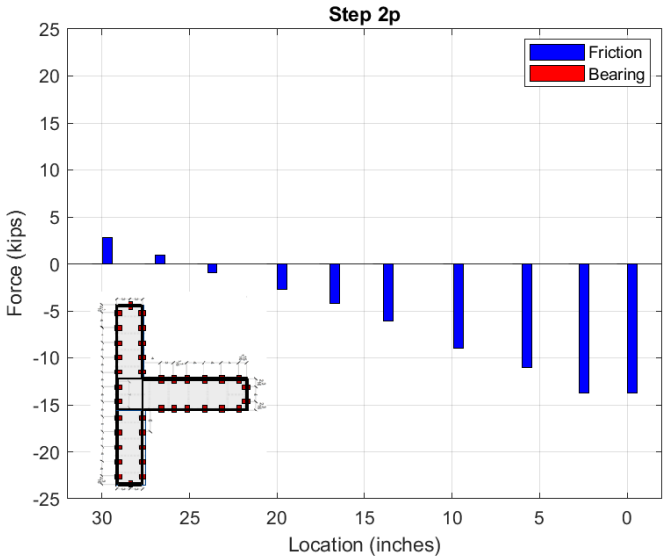


Figure 9-52. Friction and Bearing Forces at Each Row of Bolt (Step 2 Positive, Drift =0.32%)

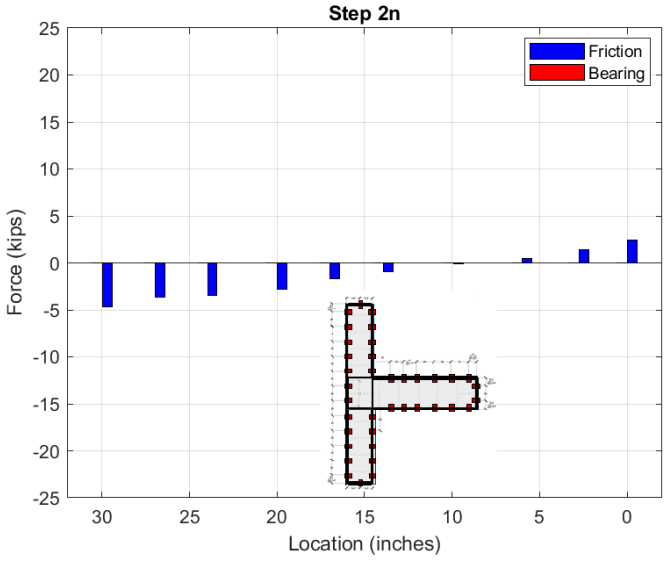


Figure 9-53. Friction and Bearing Forces at Each Row of Bolt (Step 2 Negative, Drift =-0.18%)

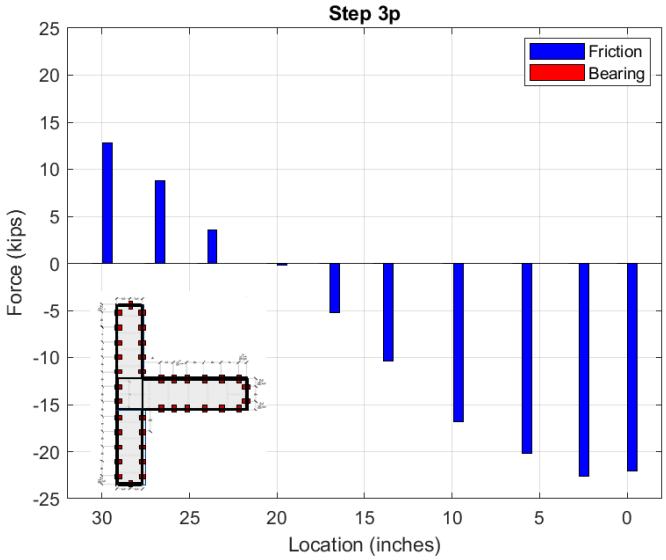


Figure 9-54. Friction and Bearing Forces at Each Row of Bolt (Step 3 Positive, Drift =0.57%)

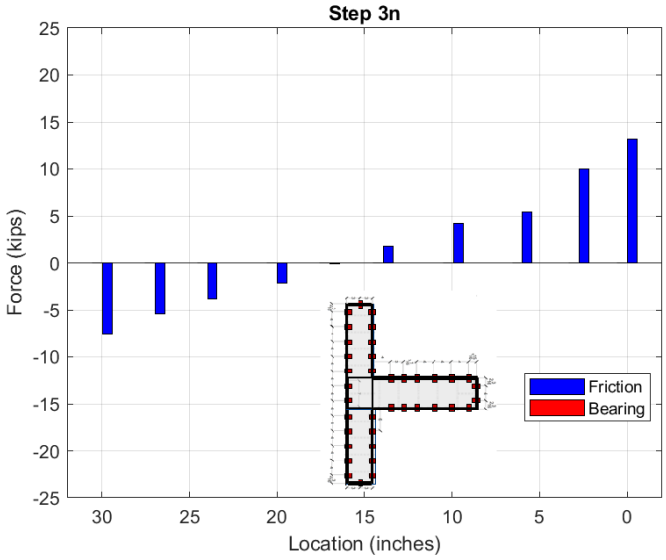


Figure 9-55. Friction and Bearing Forces at Each Row of Bolt (Step 3 Negative, Drift =-0.30%)

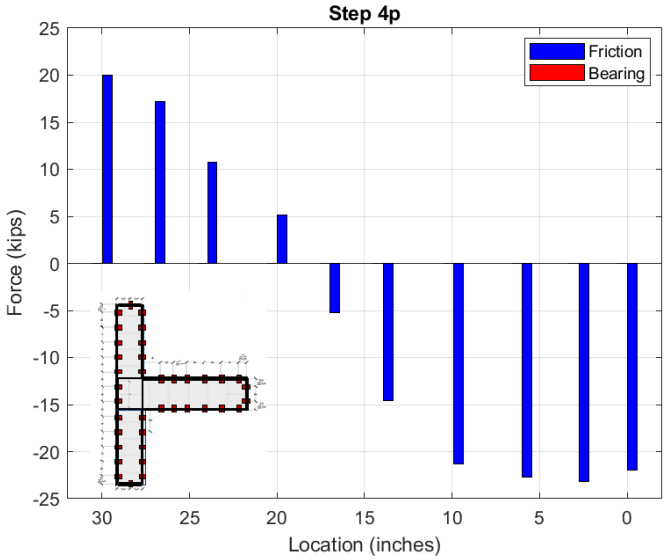


Figure 9-56. Friction and Bearing Forces at Each Row of Bolt (Step 4 Positive, Drift =0.84%)

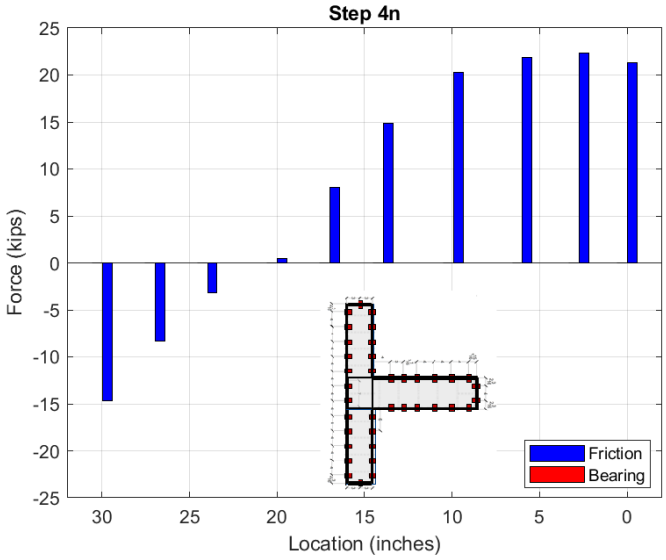


Figure 9-57. Friction and Bearing Forces at Each Row of Bolt (Step 4 Negative, Drift =-0.55%)

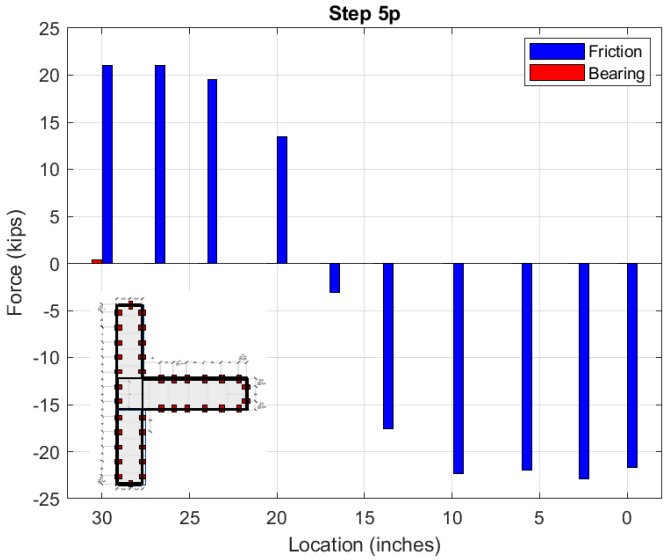


Figure 9-58. Friction and Bearing Forces at Each Row of Bolt (Step 5 Positive, Drift =1.12%)

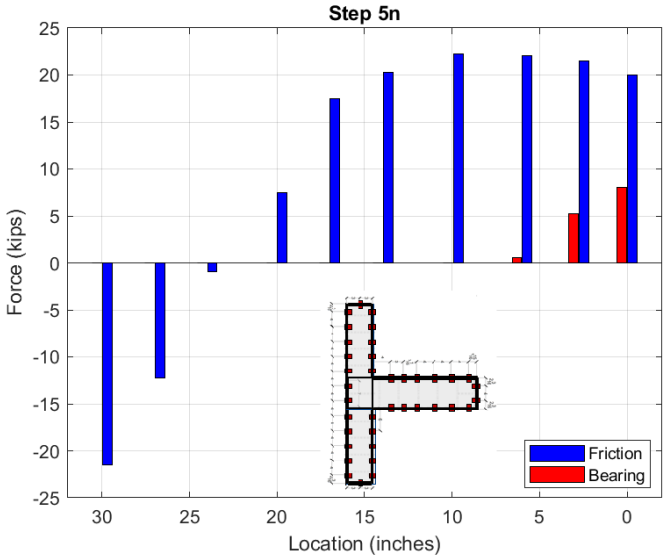


Figure 9-59. Friction and Bearing Forces at Each Row of Bolt (Step 5 Negative, Drift =-0.79%)

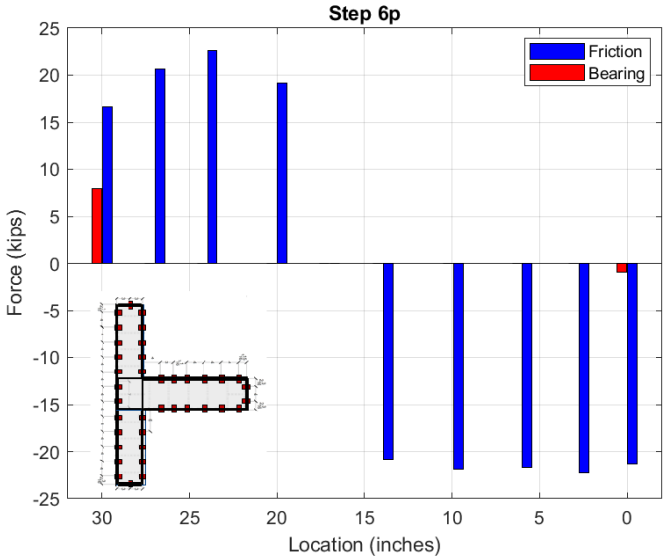


Figure 9-60. Friction and Bearing Forces at Each Row of Bolt (Step 6 Positive, Drift =1.42%)

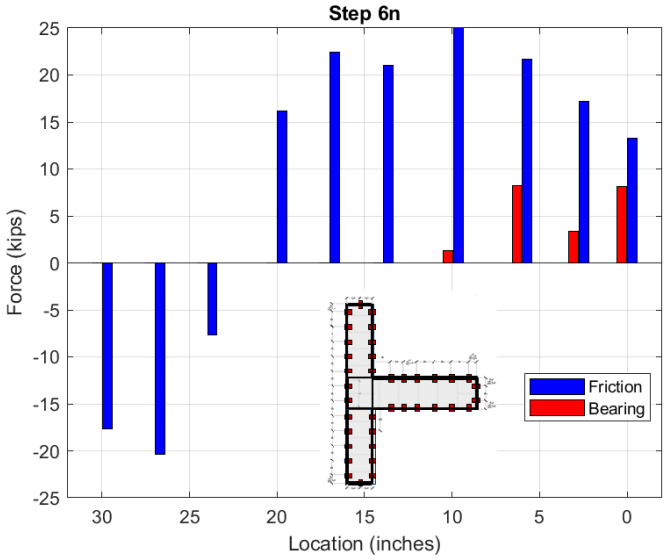


Figure 9-61. Friction and Bearing Forces at Each Row of Bolt (Step 6 Negative, Drift =-1.03%)

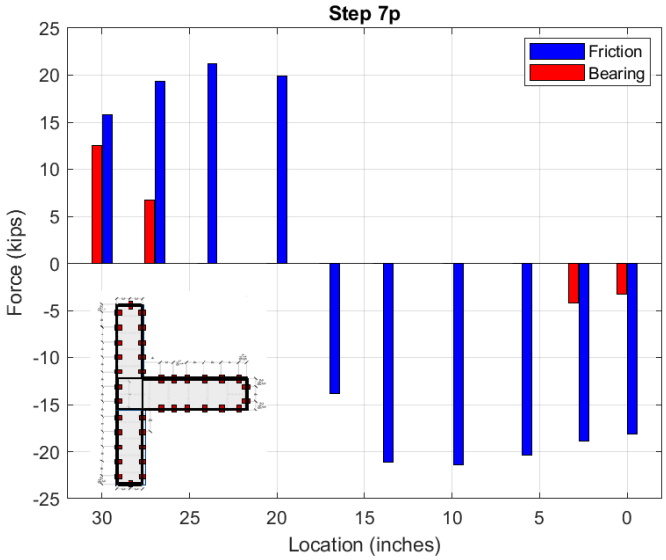


Figure 9-62. Friction and Bearing Forces at Each Row of Bolt (Step 7 Positive, Drift =1.73%)

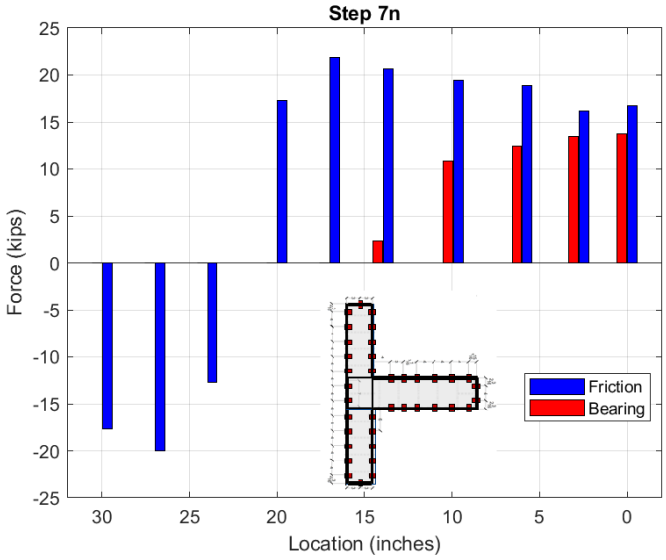


Figure 9-63. Friction and Bearing Forces at Each Row of Bolt (Step 7 Negative, Drift =-1.27%)

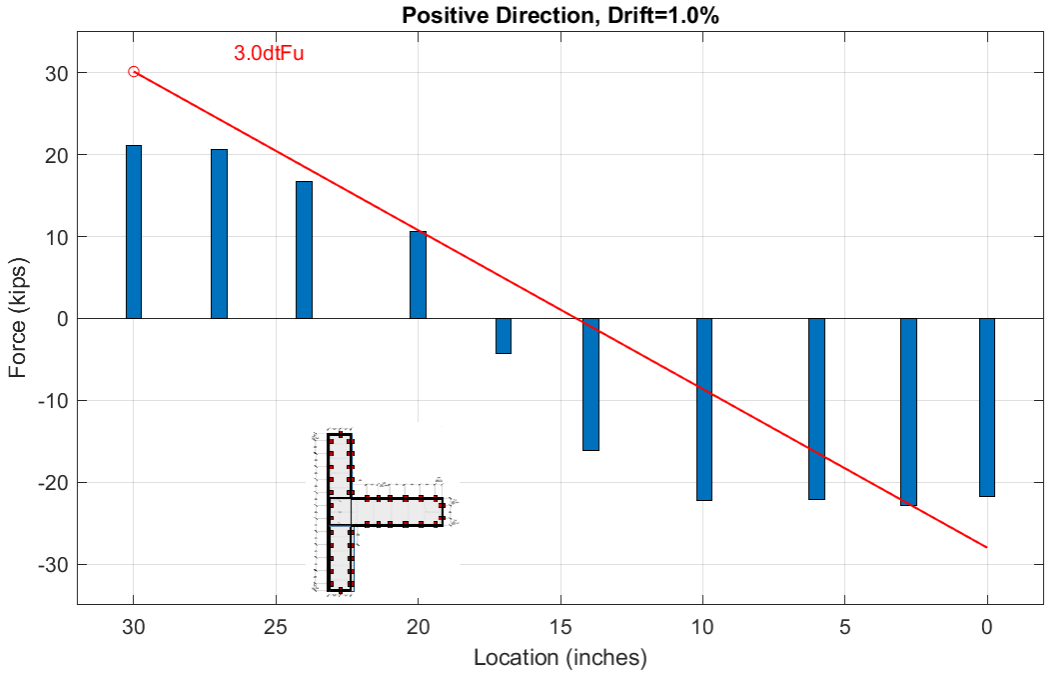


Figure 9-64. Summation of Friction and Bearing Forces at Each Row of Bolt (Drift =1.00%)

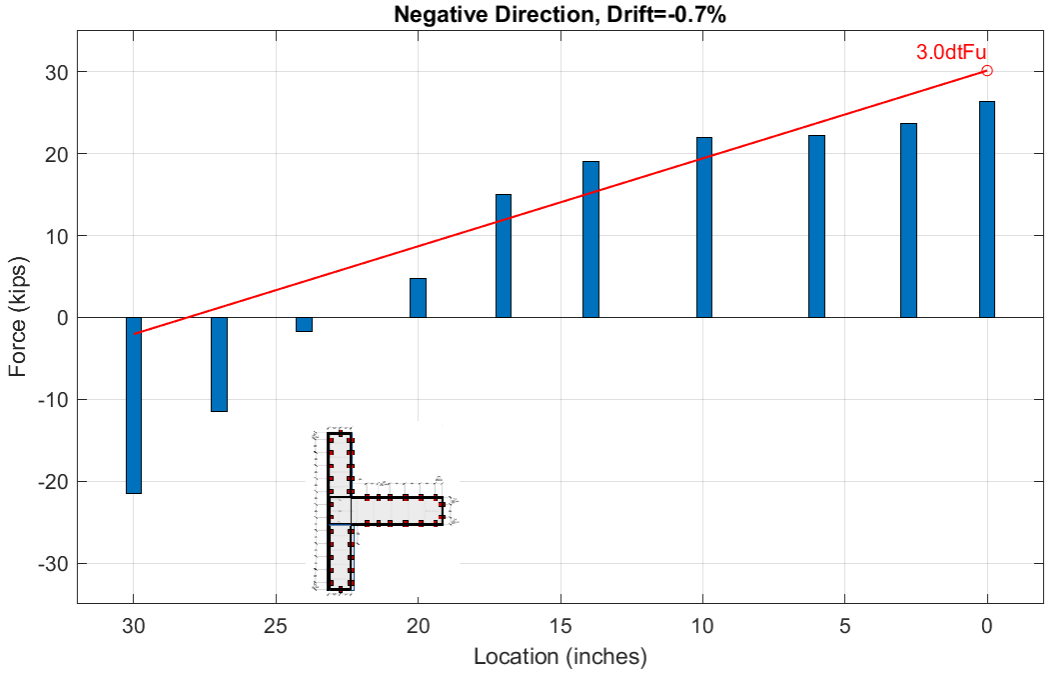


Figure 9-65. Summation of Friction and Bearing Forces at Each Row of Bolt (Drift = -0.70%)

Table 9-4. Flexural Strength of Bolts from Simplified Method and Finite Element Analysis

	Positive Direction	**Negative Direction**
	$M_{bolt_3.0dtFu}$ (k-ft)	**$M_{bolt_3.0dtFu}$ (k-ft)**
Simplified Method	821.16	491.86
FEM_Cyc	642.60	451.19
Accuracy (%)	78.26%	91.73%

9.3.3 Comparison between Test Data and Finite Element Analysis

In this section, the test data from strain gauges and linear potentiometers are analyzed alongside results from corresponding finite element models. Recall that strain measurements were recorded at various points, at the heights of 6.5 in., 15.5 in., and 24.5 in. from the top of the foundation on the faceplates of the wall. These measurements are plotted and compared with the outputs from finite element analyses in Figures 9-66 to 9-75. The correlation between the finite element analysis results and the actual test data was found to be reasonably matched.

Notably, both the test results and the finite element simulations indicated a decrease in strain values at the tip of the web, as illustrated in Figure 9-76, which shows the principal stress vectors S11 on the web of the faceplates in the negative direction at Step 4. The figure also shows the locations of strain gauges, which is helpful to correlate the measured strains directly with the specific stress regions on the web. To facilitate a comprehensive comparison of the principal stress vectors at each step, Figures 9-77 and 9-78 show the principal compression stress vectors (i.e., stress S33) in the positive direction and principal tension stress (i.e., stress S11) in the negative direction, respectively. These figures encompass Steps 4 to 7, offering a detailed insight into the evolution of stress distribution throughout these stages. These vector plots highlight the load transfer paths through the bolted connections. According to Figures 9-77 and 9-78, principal stresses close to the first row of bolts on the web were sometimes higher (Steps 4 and 7) than the ones close to the bolt on the tip of the web. However, the magnitude of the decrease in strain on the west edge of the web compared to the other web faceplate are less significant compared to the test. These decreases in strain in the test were especially apparent in the positive direction, and this cannot be explained from the results. However, similarly to what was done in Section 9.3.2.1, it can be speculated that the finite element did not account for initial imperfections of the web horizontal splice and some bending of the web plates that caused local bending, or buckling, leading to greater a decrease in strain at the tip of the web.

The data presented in Figures 9-79 to 9-86 provide comparisons of the deformations measured by linear potentiometers during Steps 1 to 4 of testing, alongside the results obtained from the finite element model. However, some caution is warranted in the interpretation of these measurements. As schematically illustrated in Figure 9-87 it was identified that the readings from the linear potentiometers were in part influenced by the rotation and bending of the horizontal splice plate. Since the linear potentiometers were affixed to both the horizontal splice plate and the faceplates, any relative rotation between these components could skew the readings. As such rotations have been observed as reported above (such as during buckling of the splice plates), this can partly explain why deformations measured by the LP are higher than the axial deformation of faceplates calculated by the strain gauges.

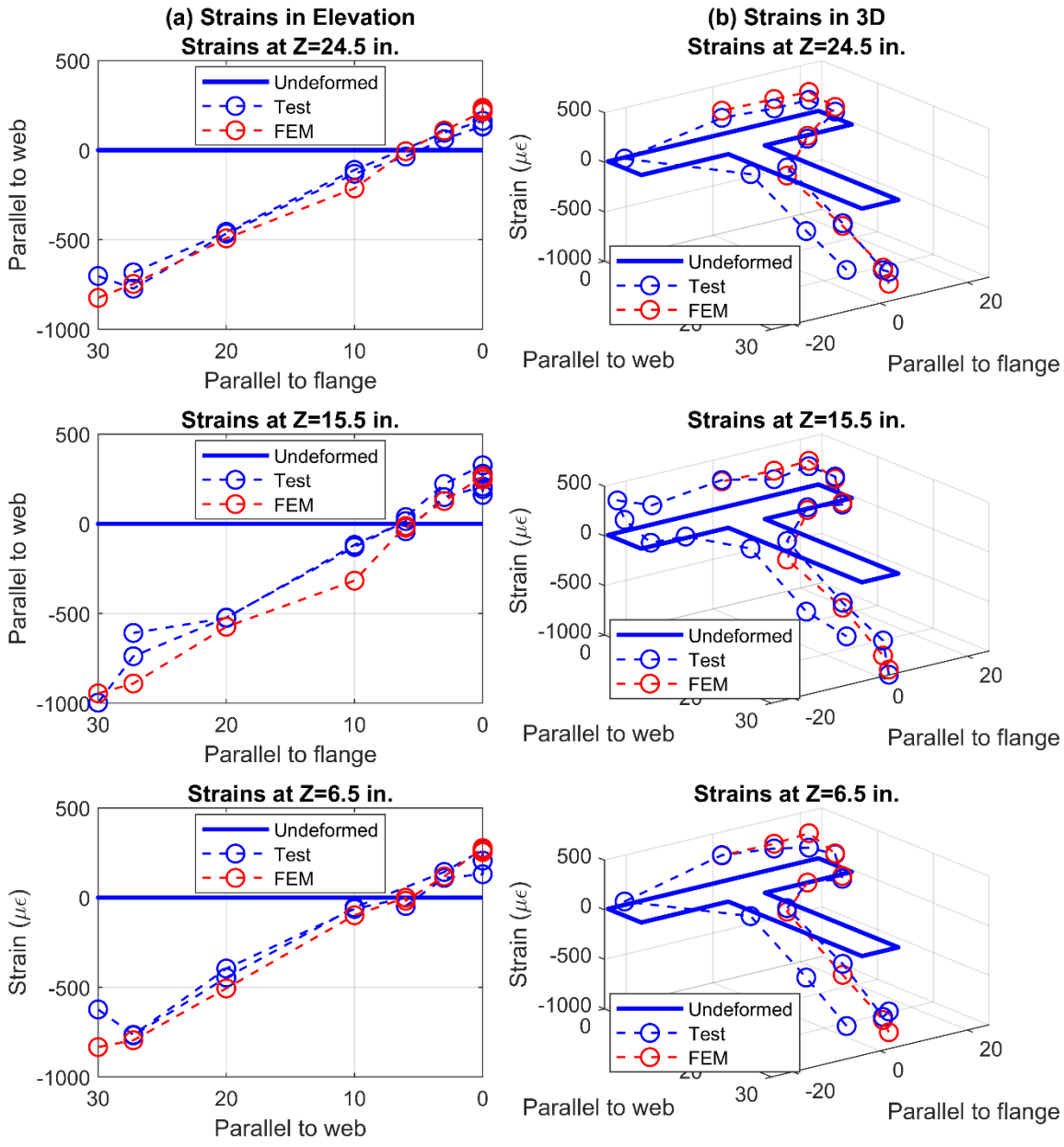


Figure 9-66. Axial Strains at Positive Peak in Step 2 in (a) Elevation and (b) 3D

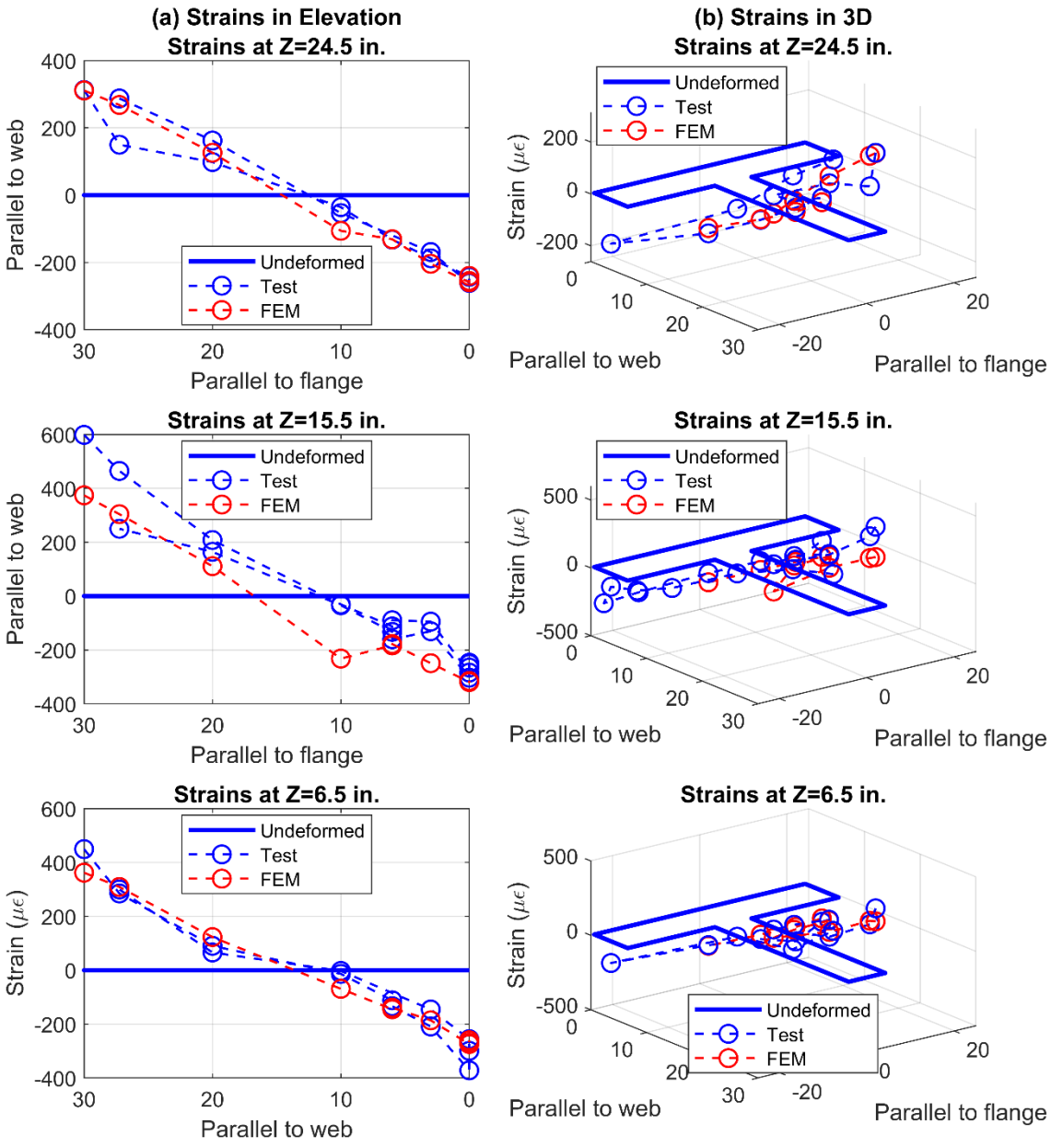


Figure 9-67. Axial Strains at Negative Peak in Step 2 in (a) Elevation and (b) 3D

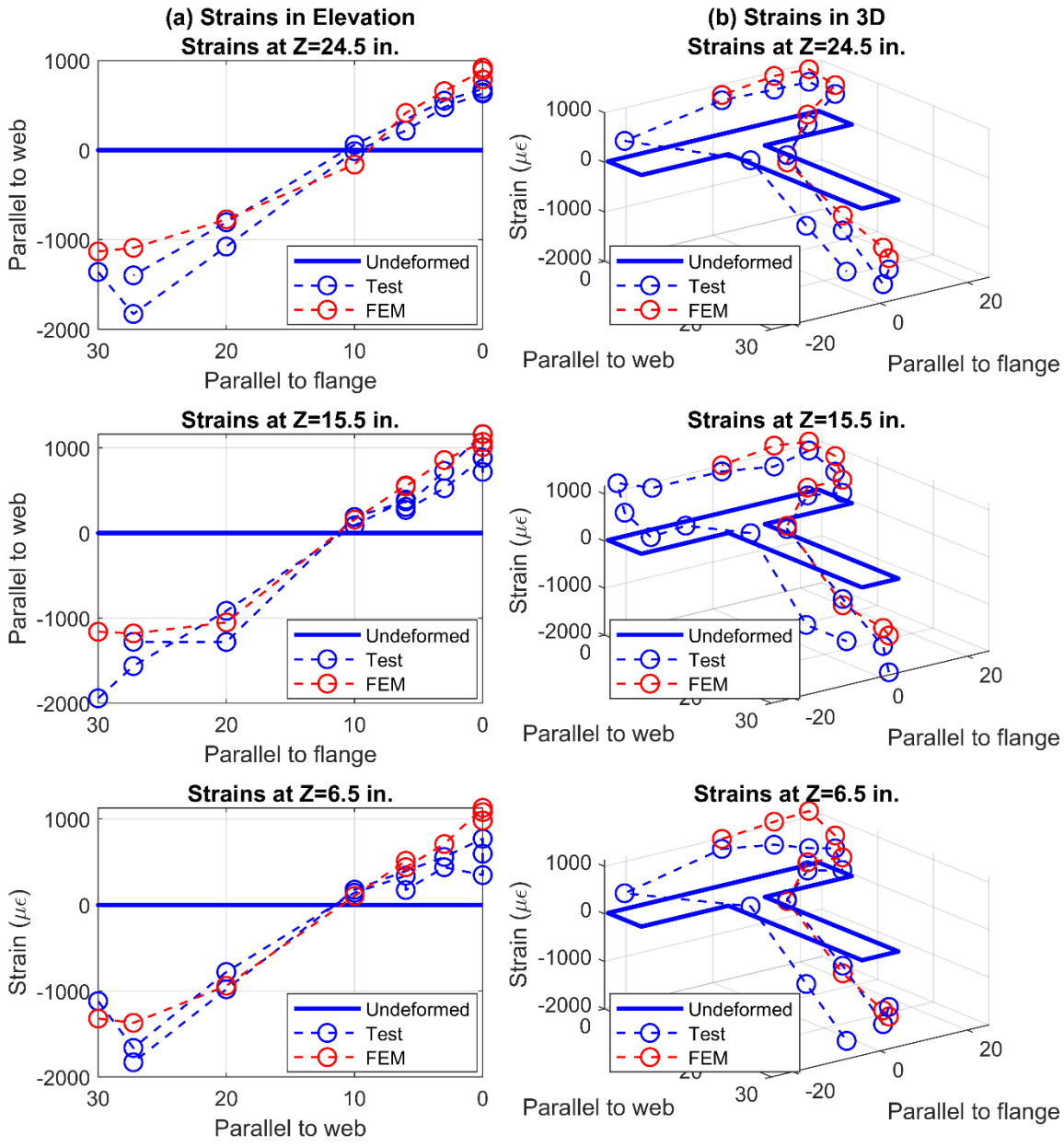


Figure 9-68. Axial Strains at Positive Peak in Step 4 in (a) Elevation and (b) 3D

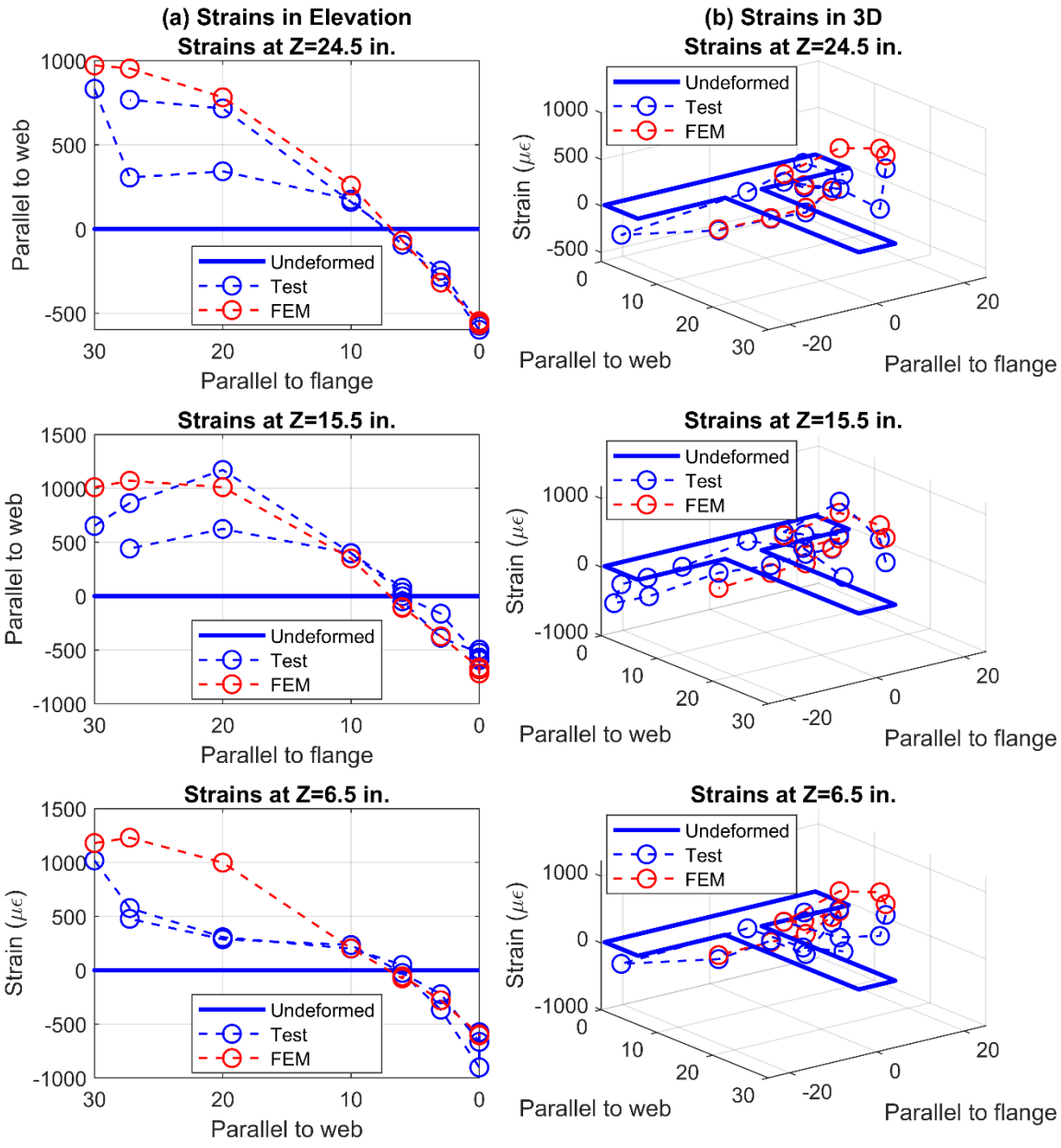


Figure 9-69. Axial Strains at Negative Peak in Step 4 in (a) Elevation and (b) 3D

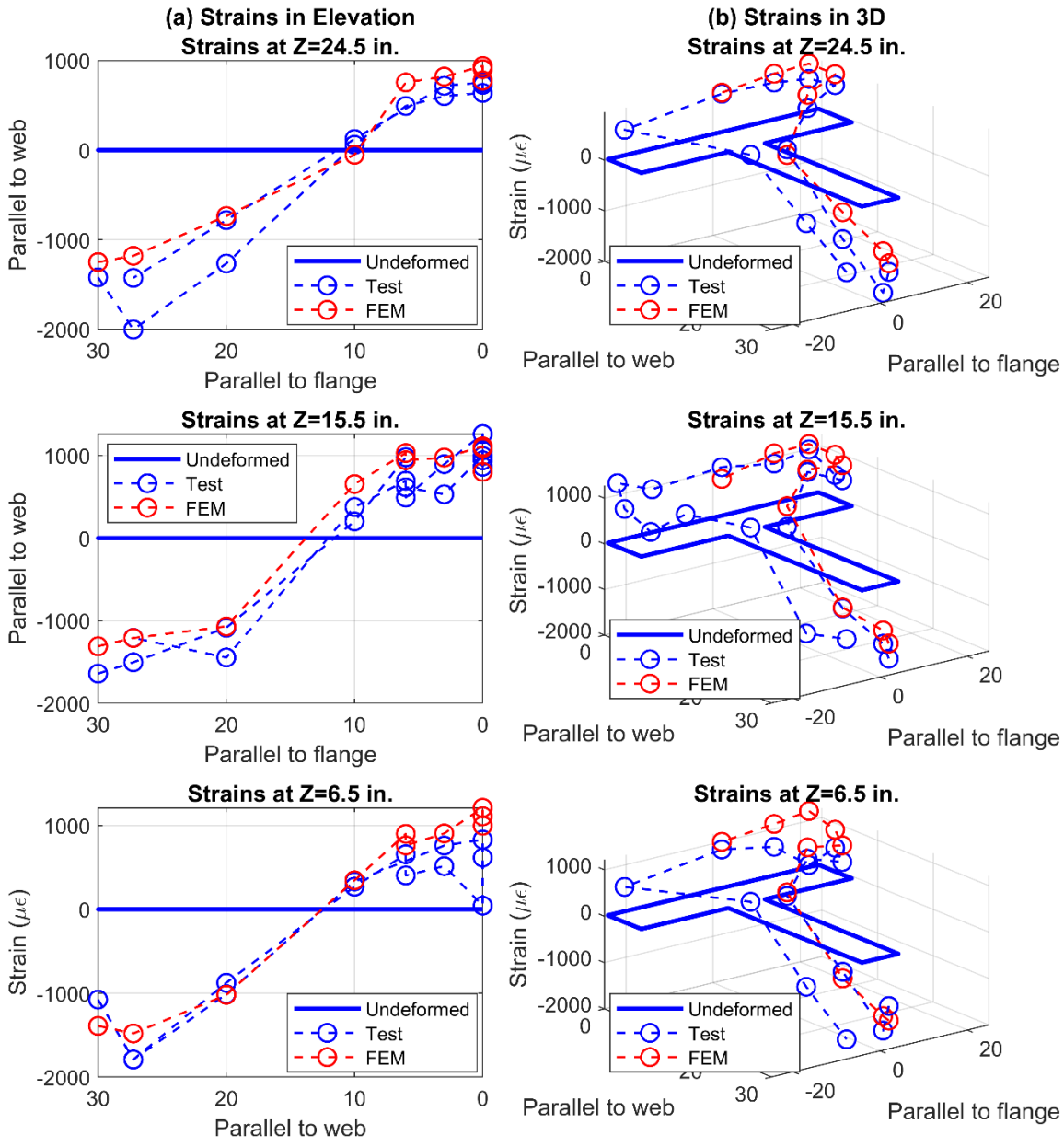


Figure 9-70. Axial Strains at Positive Peak in Step 5 in (a) Elevation and (b) 3D

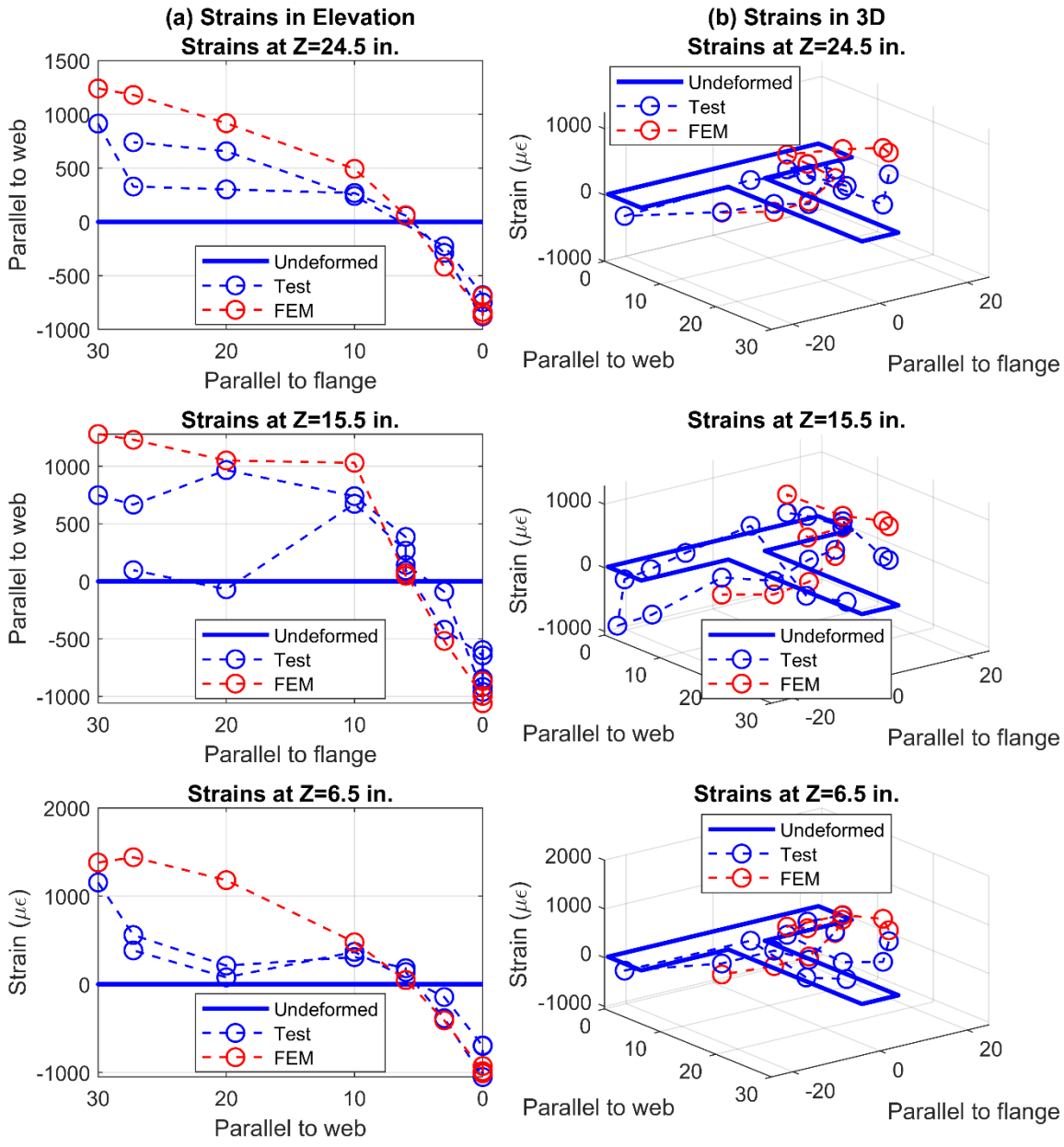


Figure 9-71. Axial Strains at Negative Peak in Step 5 in (a) Elevation and (b) 3D

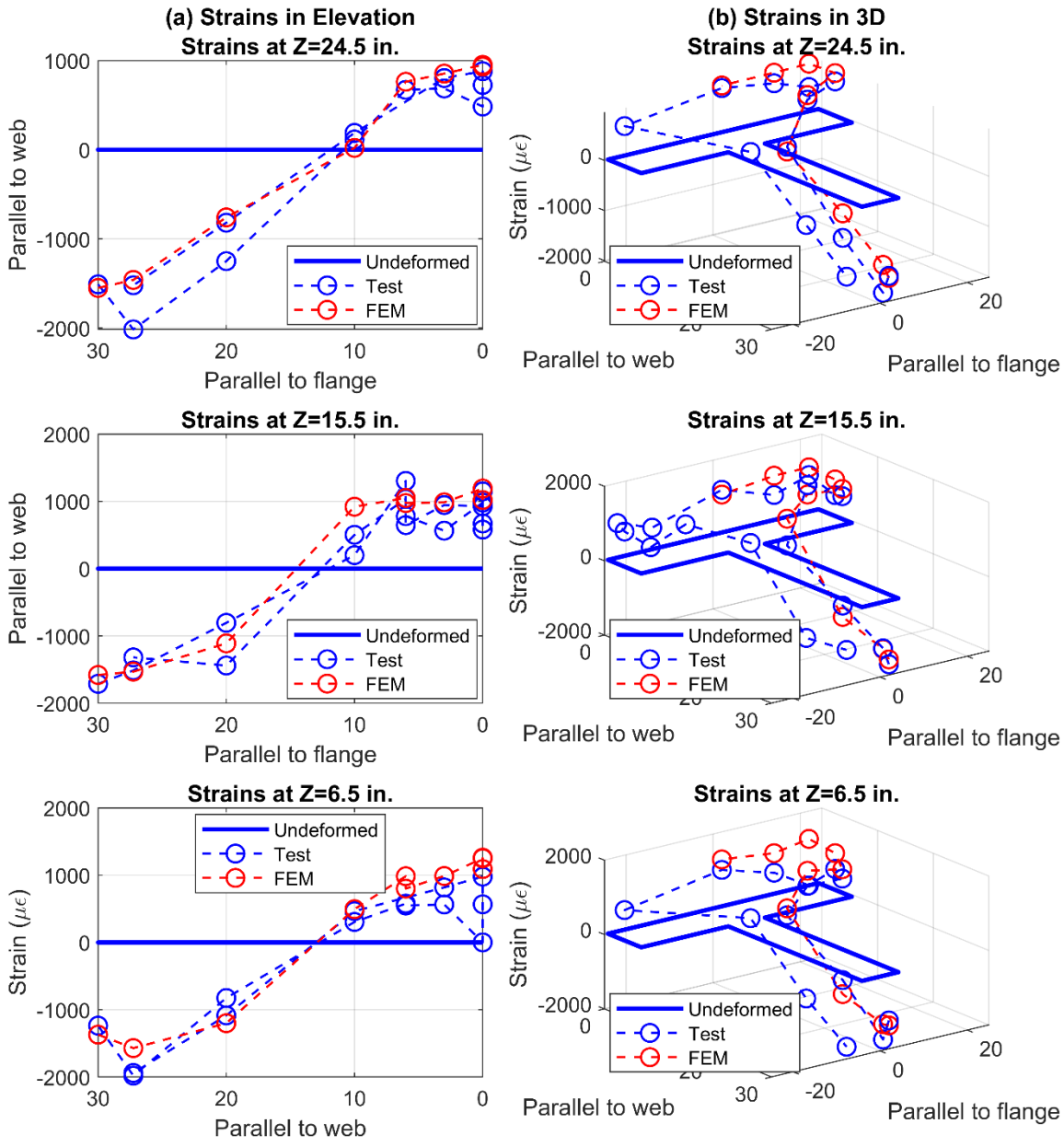


Figure 9-72. Axial Strains at Positive Peak in Step 6 in (a) Elevation and (b) 3D

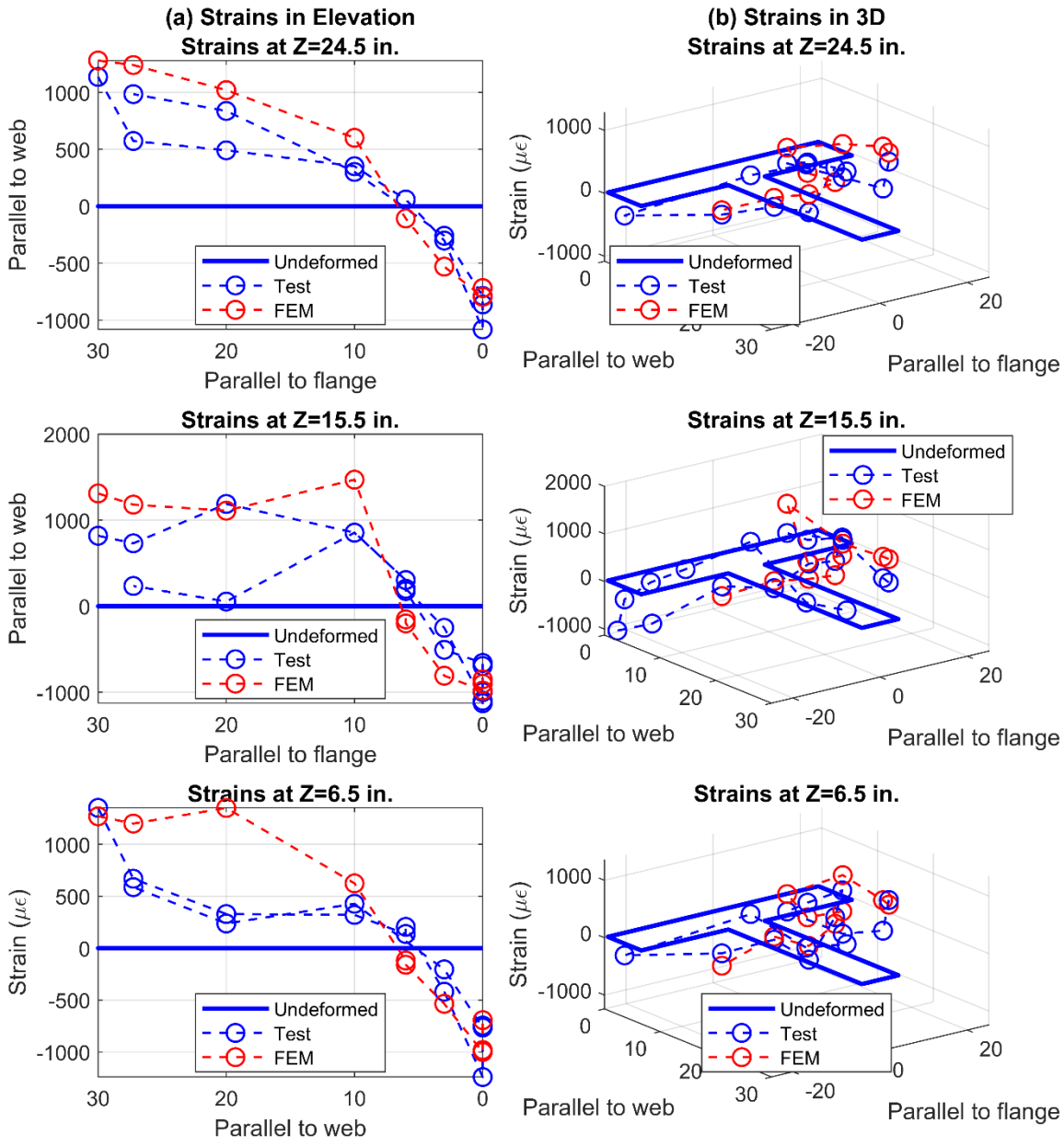


Figure 9-73. Axial Strains at Negative Peak in Step 6 in (a) Elevation and (b) 3D

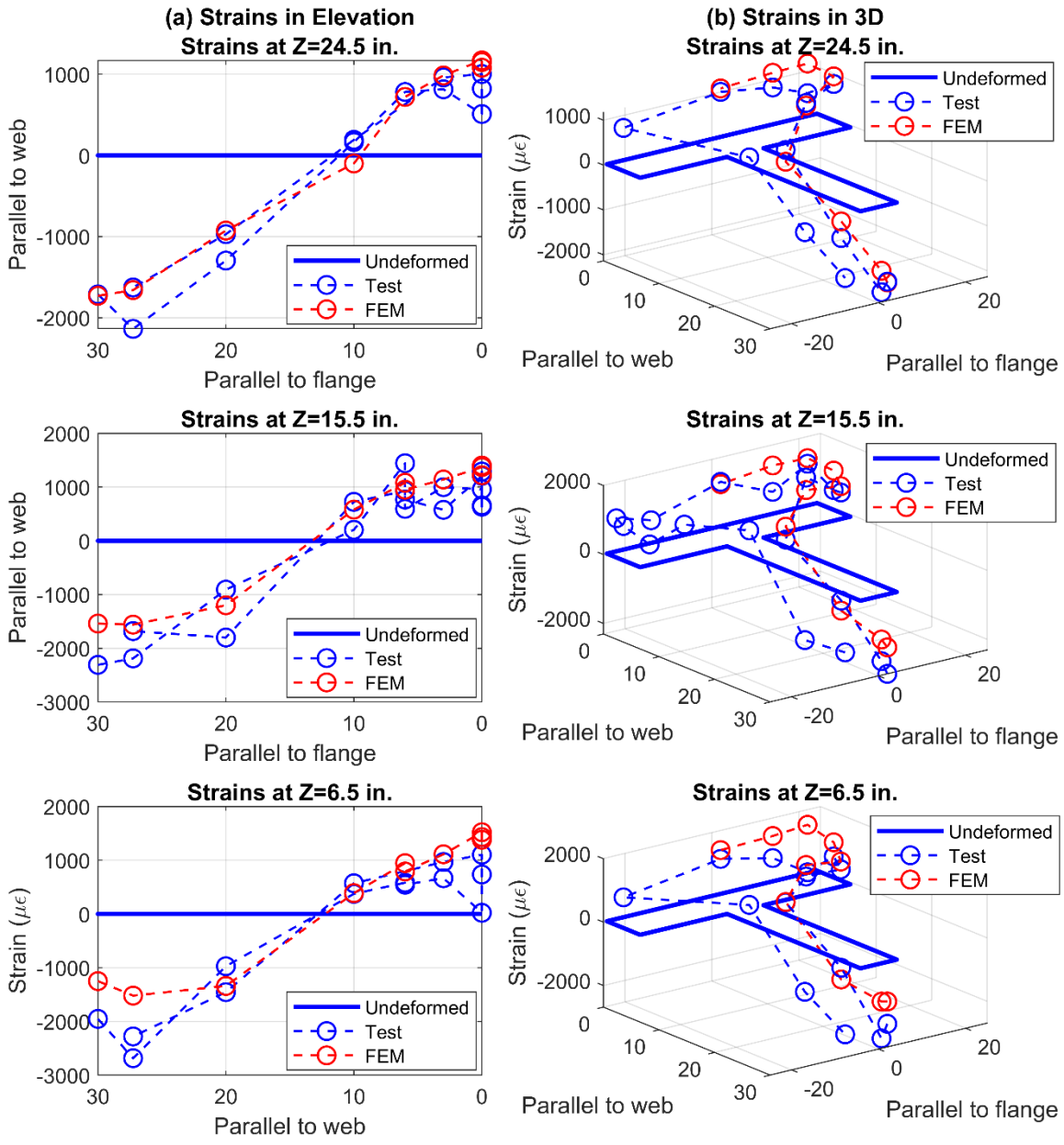


Figure 9-74. Axial Strains at Positive Peak in Step 7 in (a) Elevation and (b) 3D

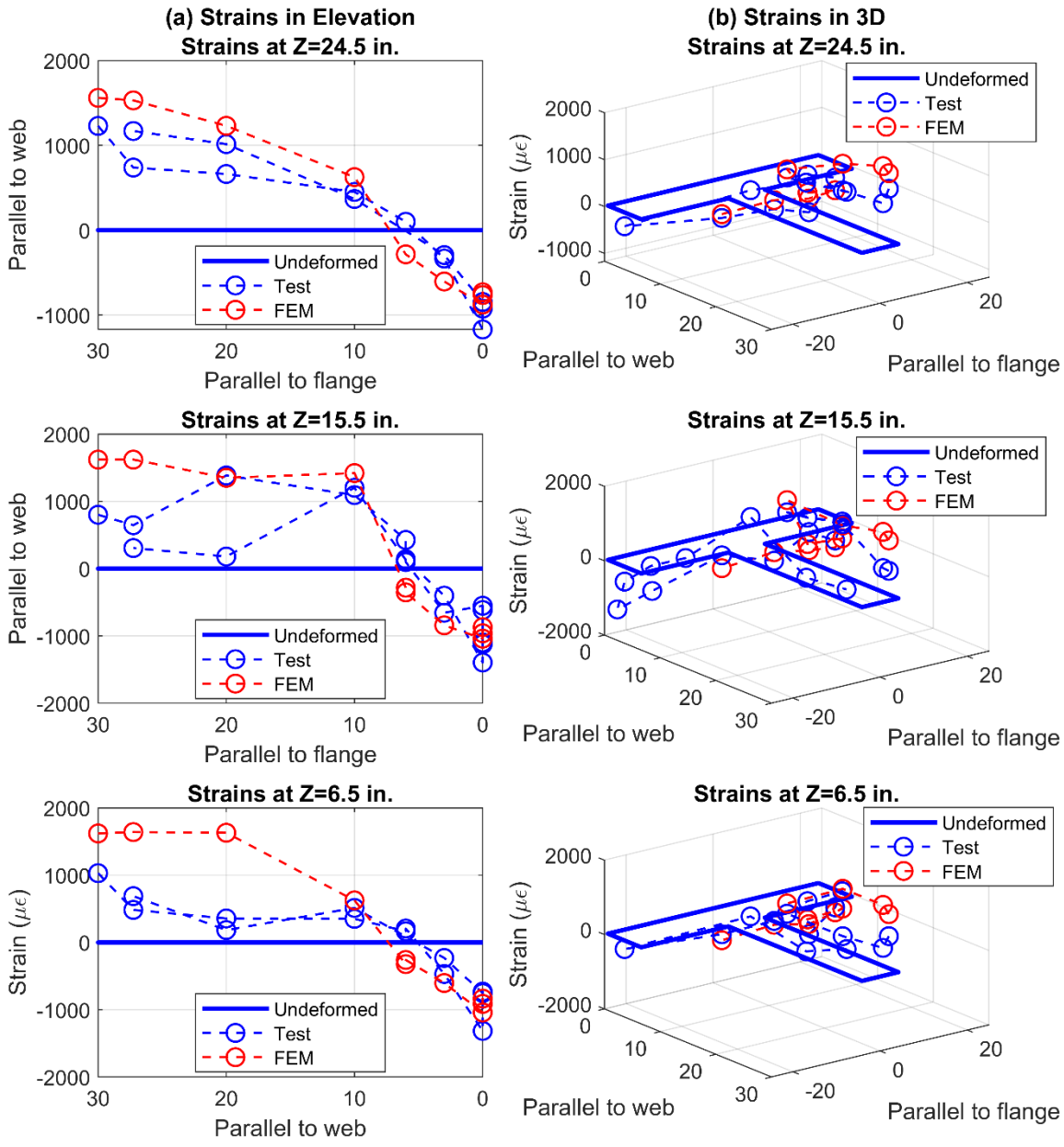


Figure 9-75. Axial Strains at Negative Peak in Step 7 in (a) Elevation and (b) 3D

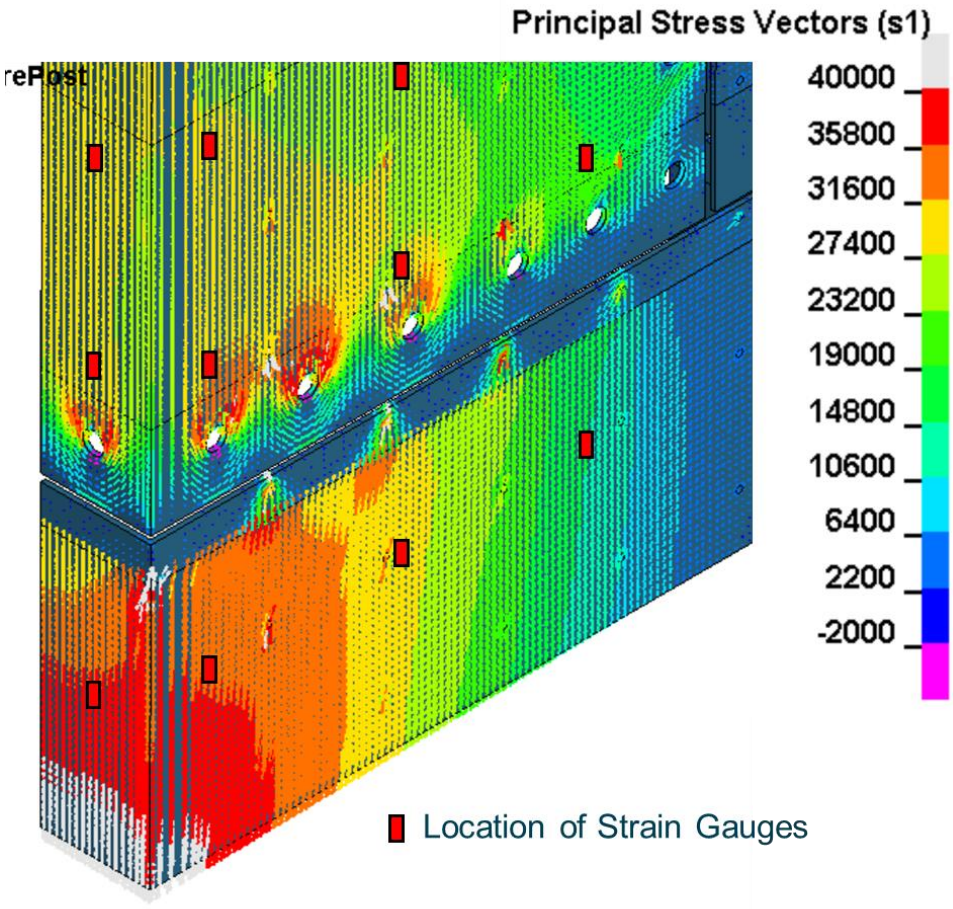


Figure 9-76. Principal Stress Vectors S11 with Location of Strain Gauges (Step 4, Drift =-0.55%)

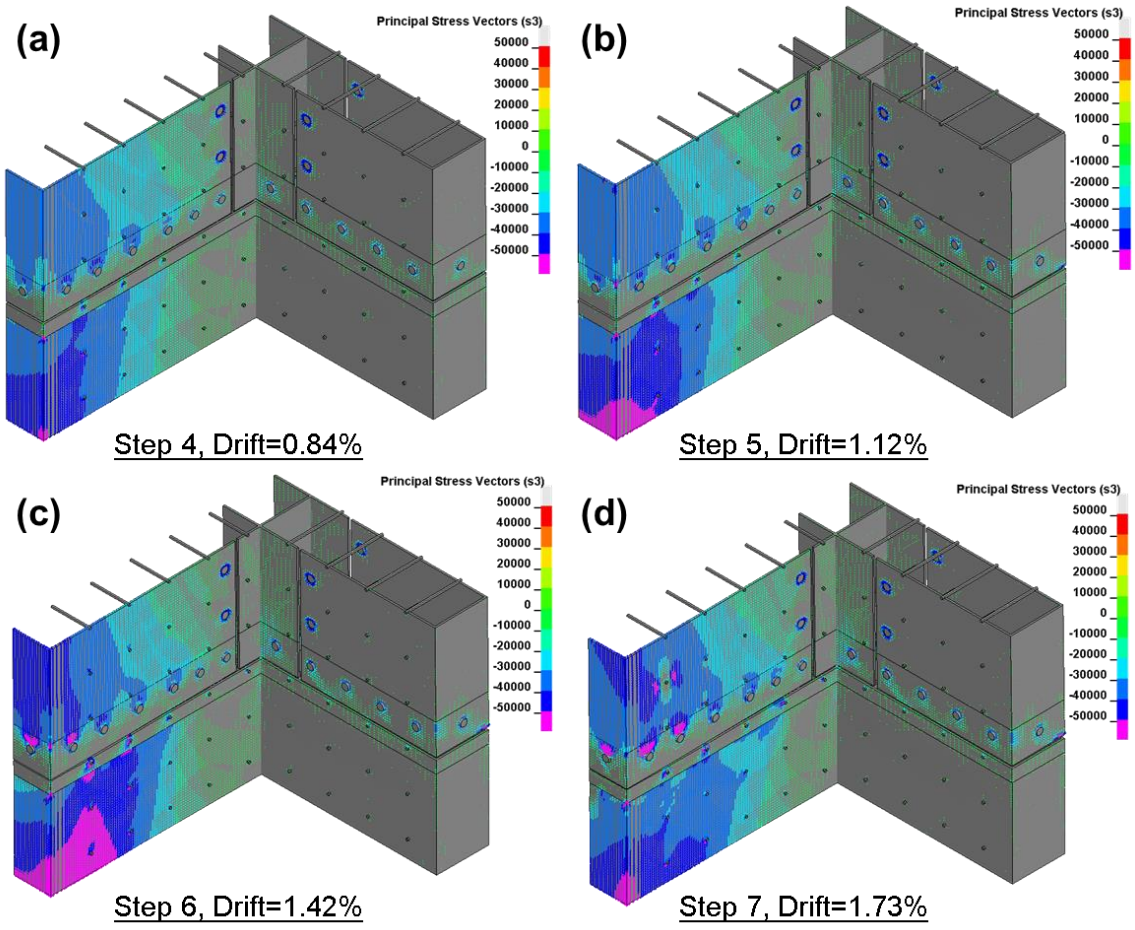


Figure 9-77. Principal Stress Vectors S33 in Positive Direction at (a) Step 4 (b) Step 5 (c) Step 6 (d) Step 7

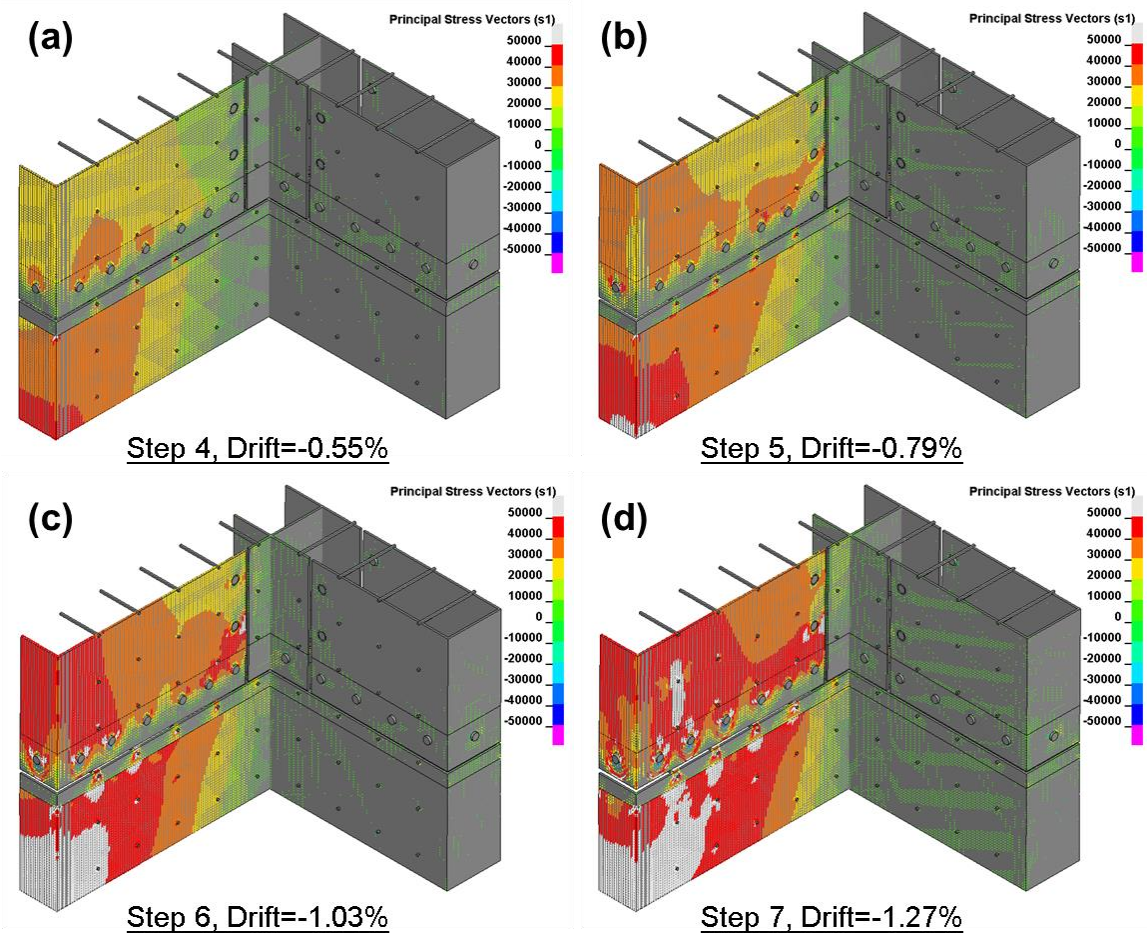


Figure 9-78. Principal Stress Vectors S11 in Negative Direction at (a) Step 4 (b) Step 5 (c) Step 6 (d) Step 7

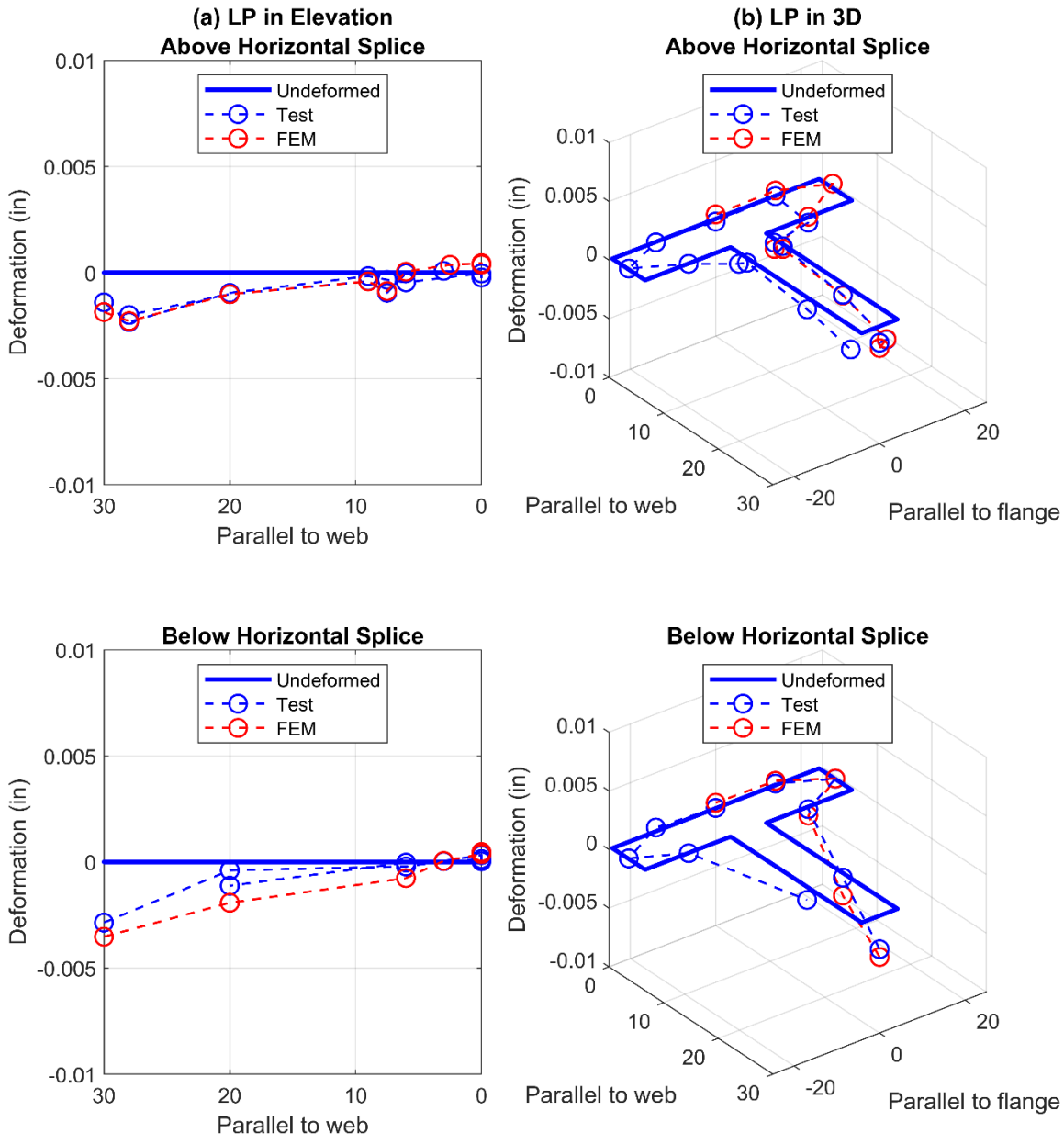


Figure 9-79. Record of Linear Potentiometer at Positive Peak in Step 1 in (a) Elevation and (b) 3D

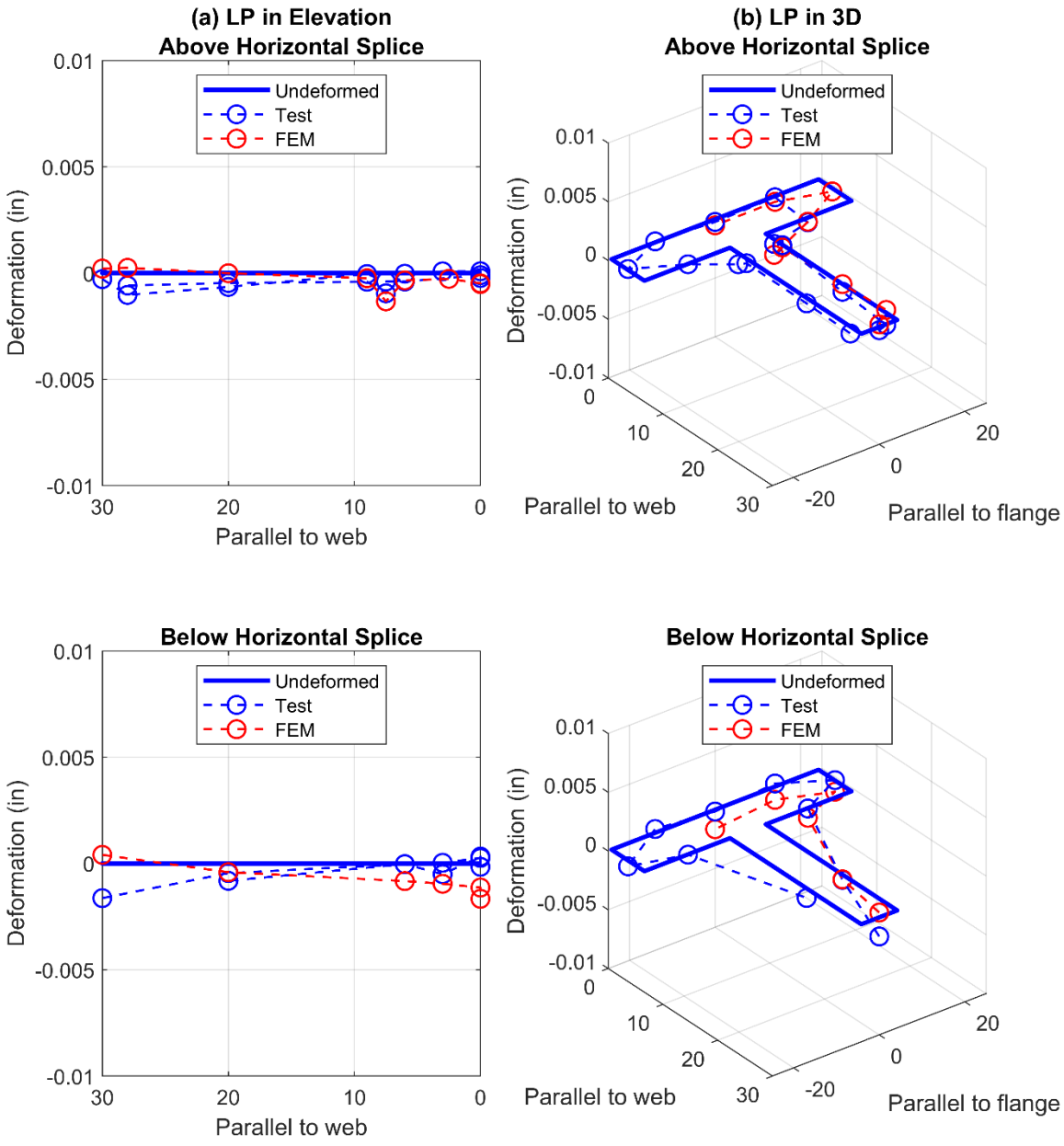


Figure 9-80. Record of Linear Potentiometer at Negative Peak in Step 1 in (a) Elevation and (b) 3D

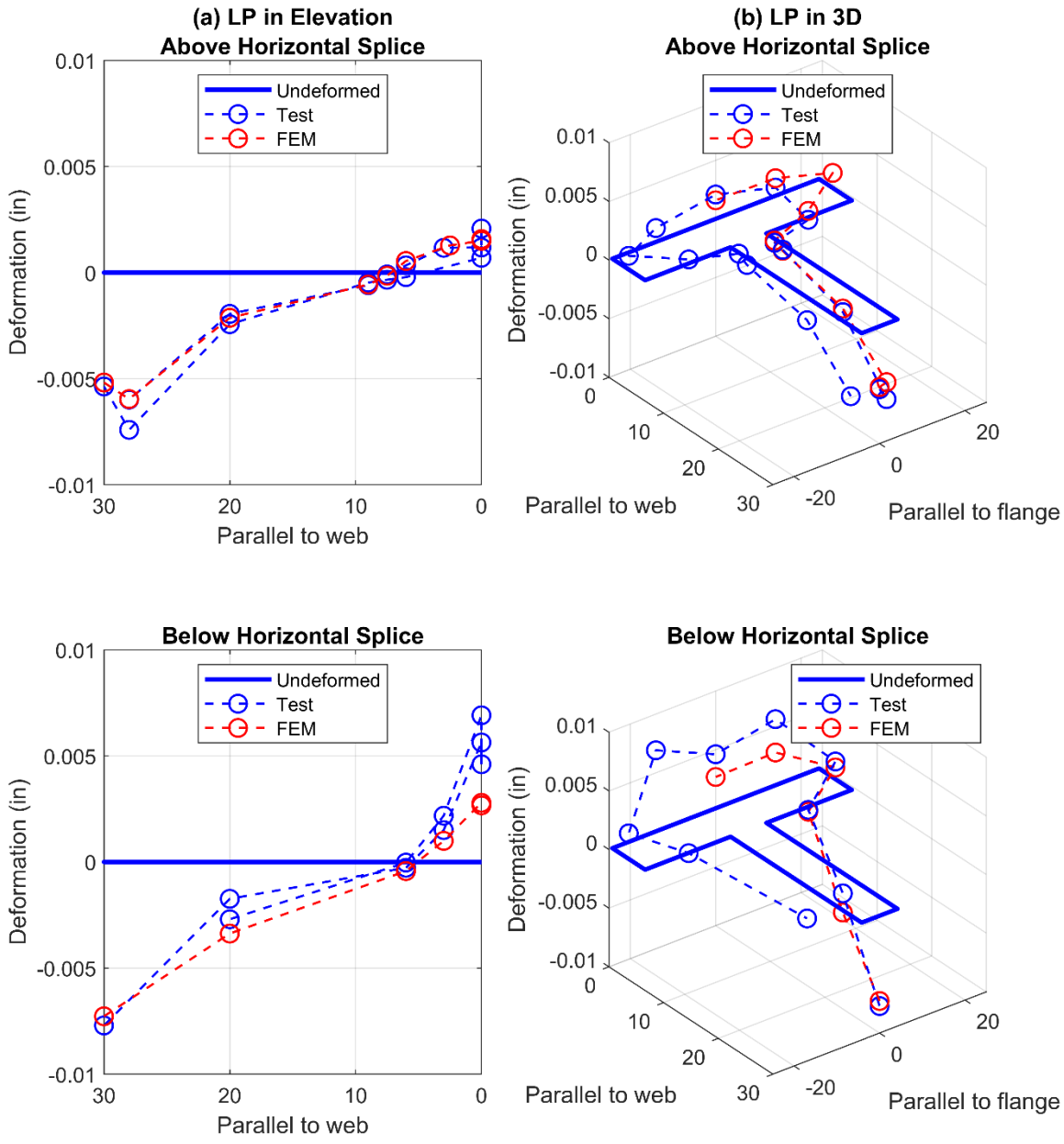


Figure 9-81. Record of Linear Potentiometer at Positive Peak in Step 2 in (a) Elevation and (b) 3D

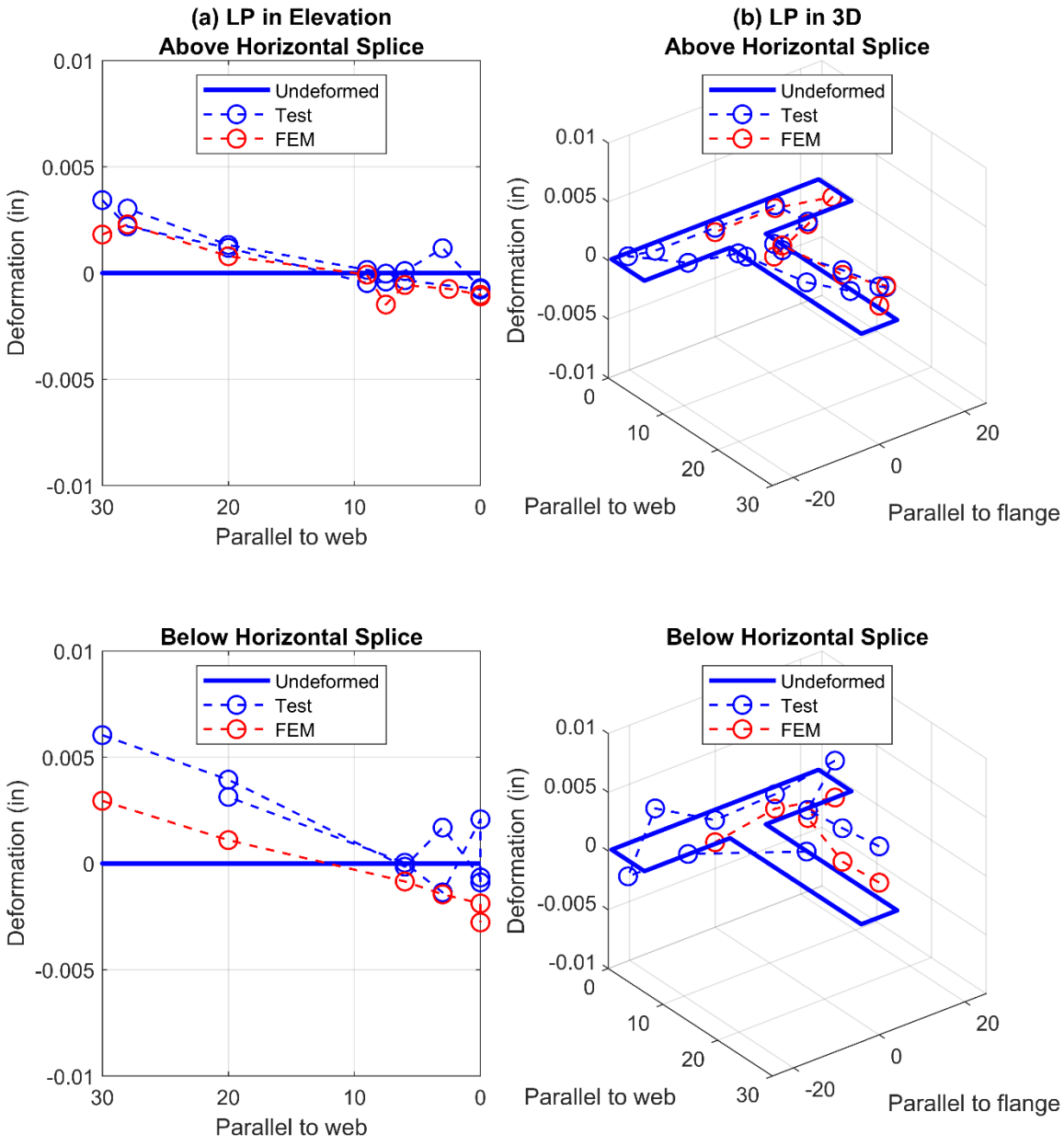


Figure 9-82. Record of Linear Potentiometer at Negative Peak in Step 2 in (a) Elevation and (b) 3D

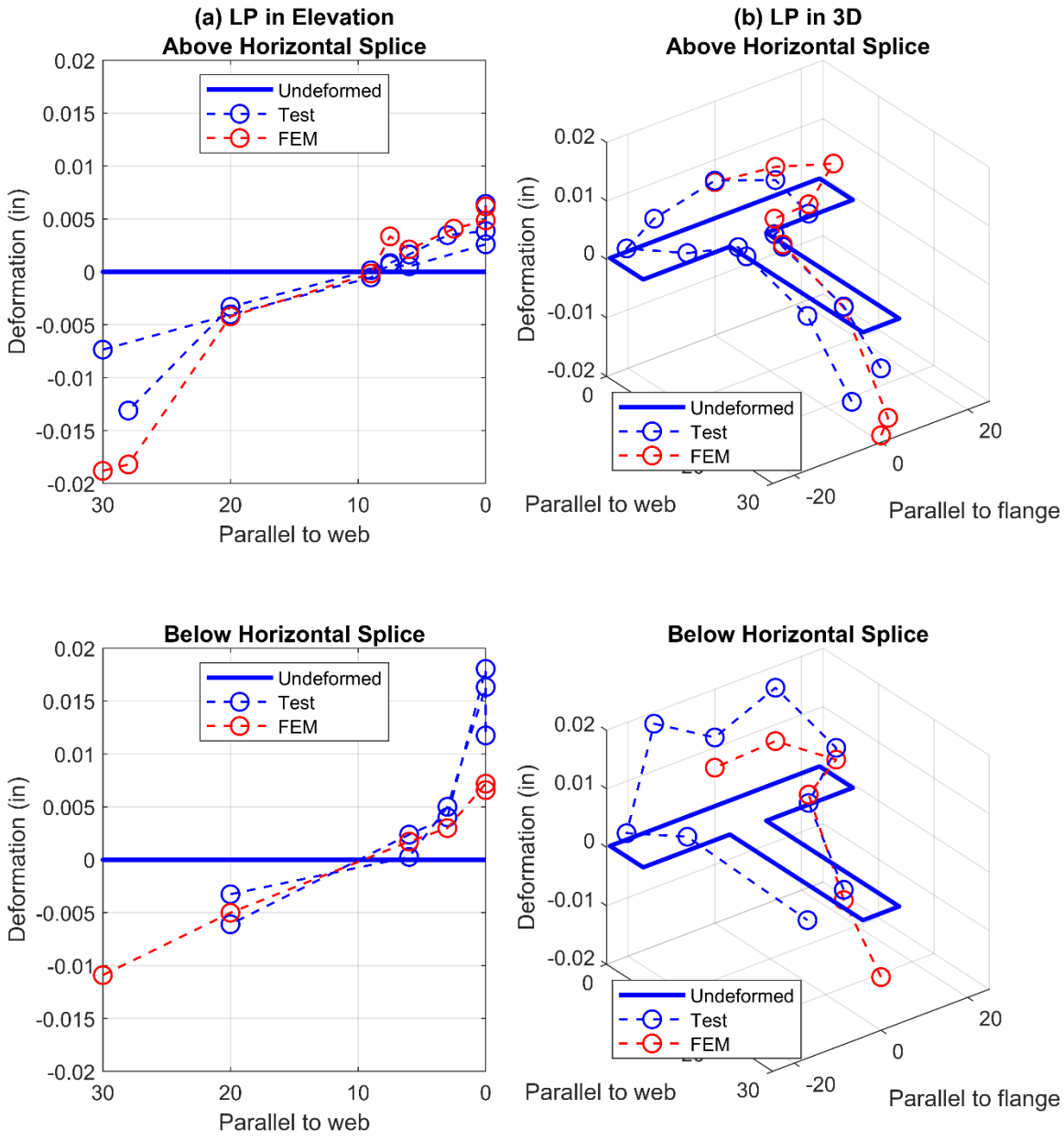


Figure 9-83. Record of Linear Potentiometer at Positive Peak in Step 3 in (a) Elevation and (b) 3D

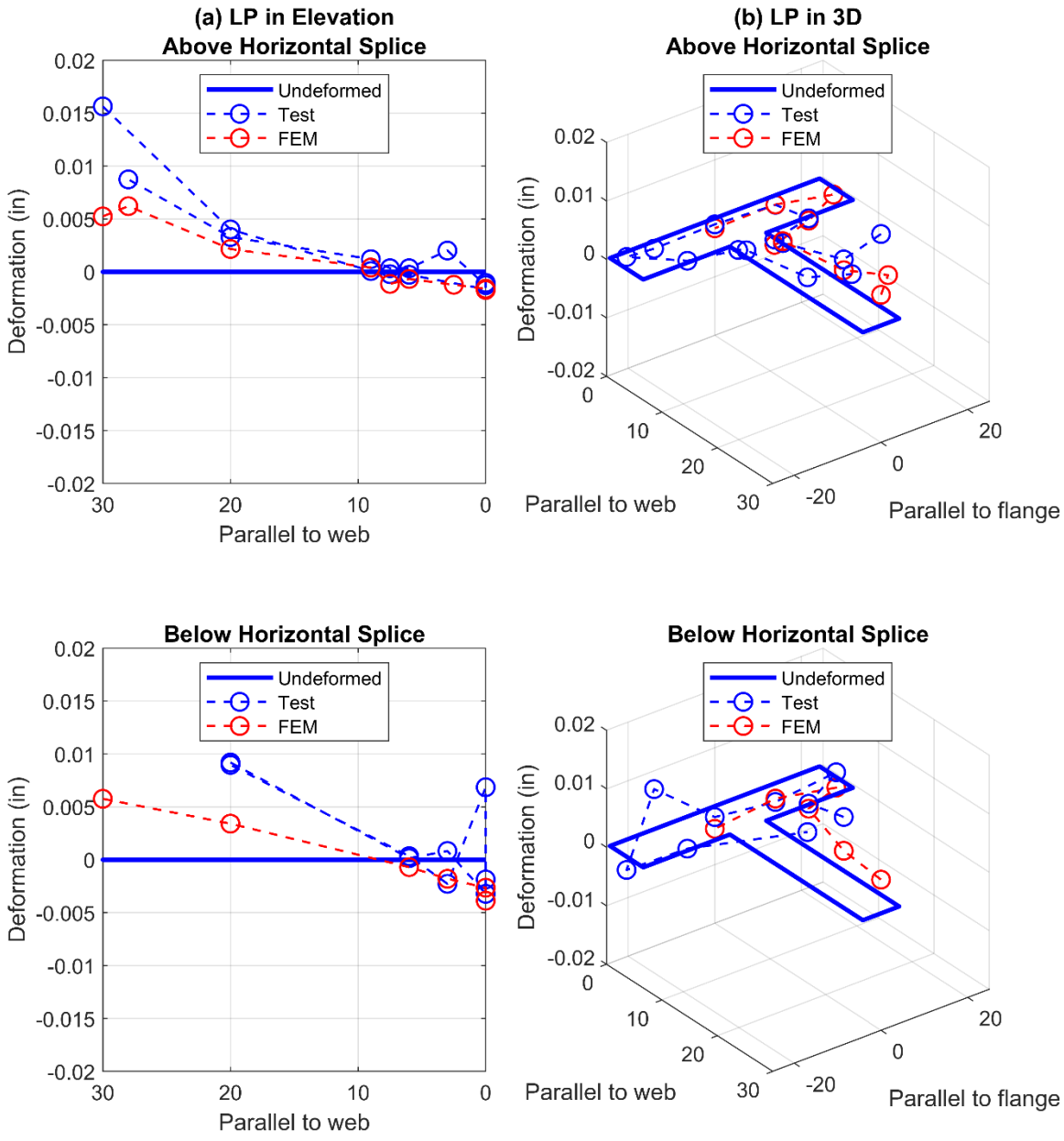


Figure 9-84. Record of Linear Potentiometer at Negative Peak in Step 3 in (a) Elevation and (b) 3D

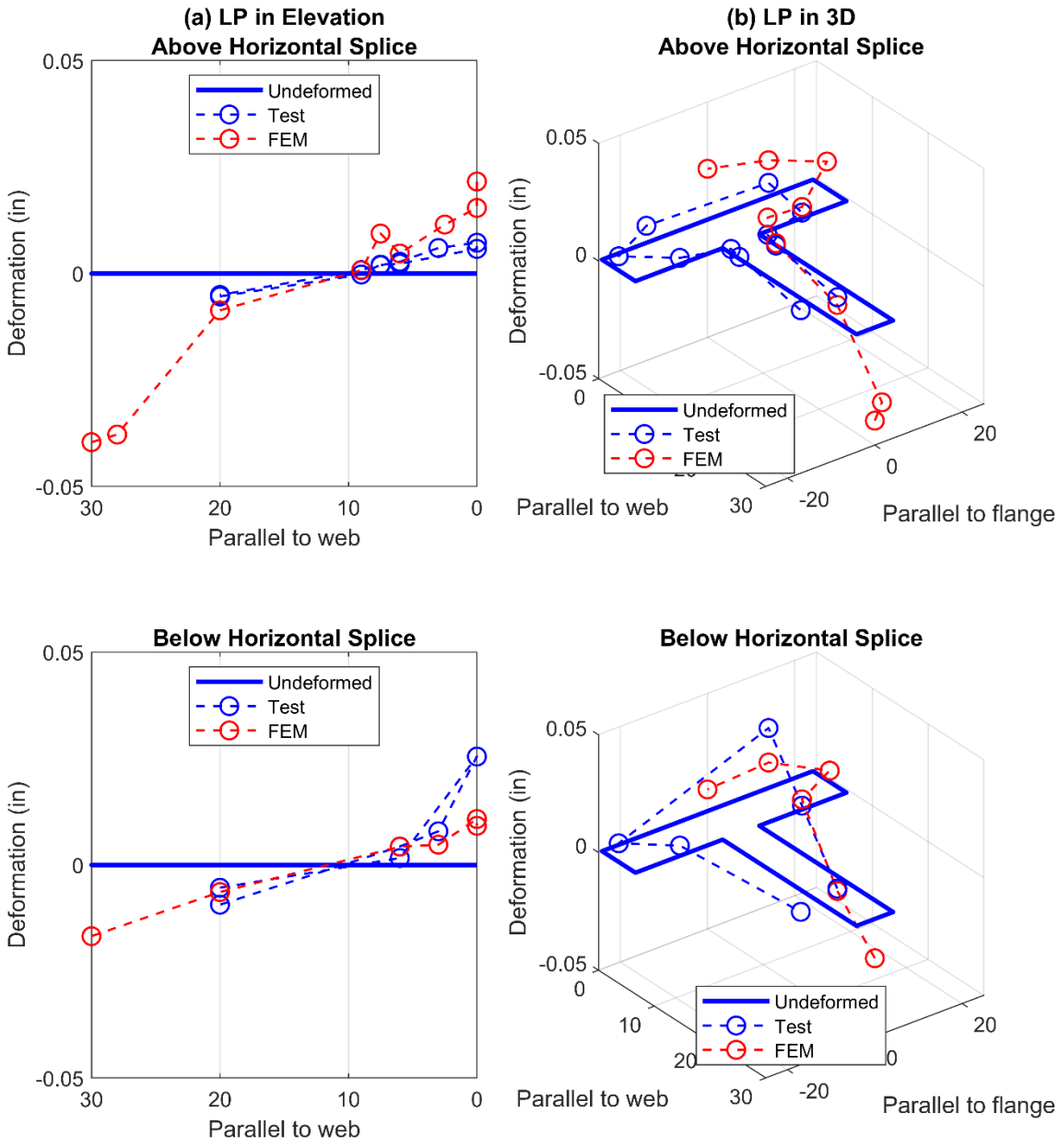


Figure 9-85. Record of Linear Potentiometer at Positive Peak in Step 4 in (a) Elevation and (b) 3D

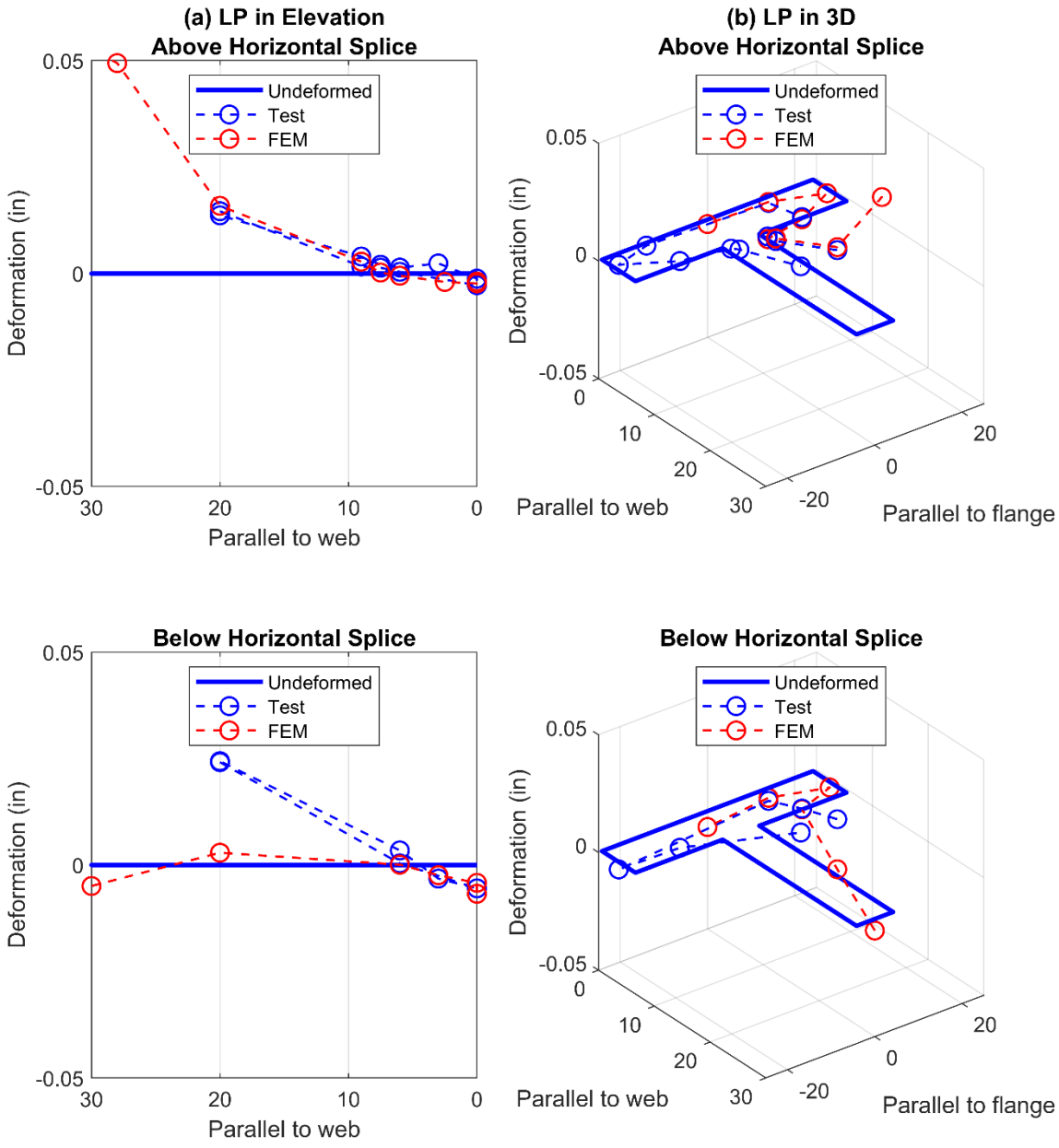


Figure 9-86. Record of Linear Potentiometer at Negative Peak in Step 4 in (a) Elevation and (b) 3D

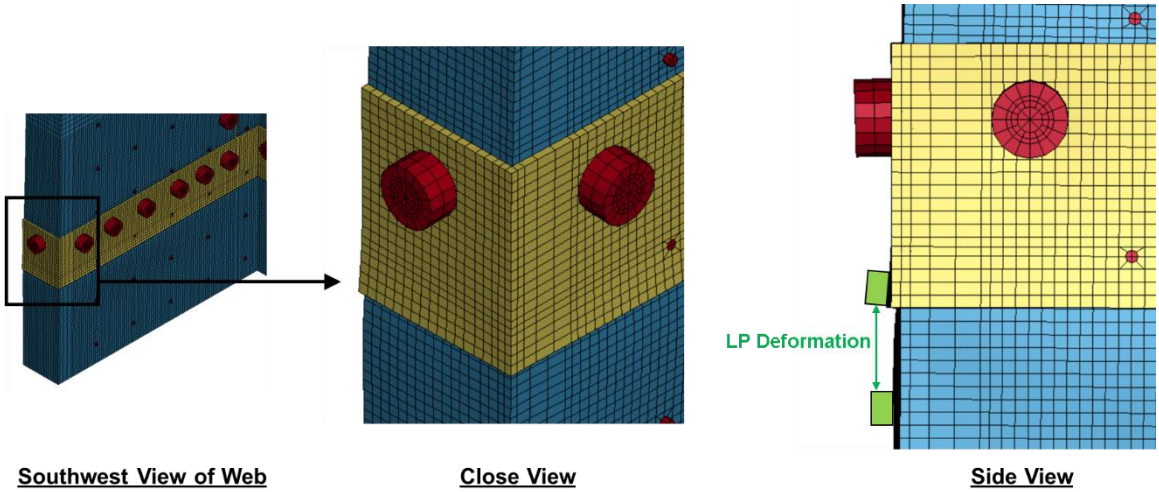


Figure 9-87. LP Deformation Affected by Bending and Rotation of Steel Plates

9.3.4 Double-Shear Connection for Horizontal Splices

This section provides finite element analysis results demonstrating how the behaviors of the T-shaped wall would have differed if the inside horizontal splice plate had been welded, as originally intended. Using the same finite element model introduced in Section 9.2 and shown in Figure 9-88, the only change made was to merge the nodes at the bottom of the inside and outside horizontal splice plates to simulate the horizontal splice functioning as a double-shear connection. Similar to the approach in Section 9.3.1, monotonic pushover analyses were performed to compare the differences between single-shear and double-shear horizontal splices.

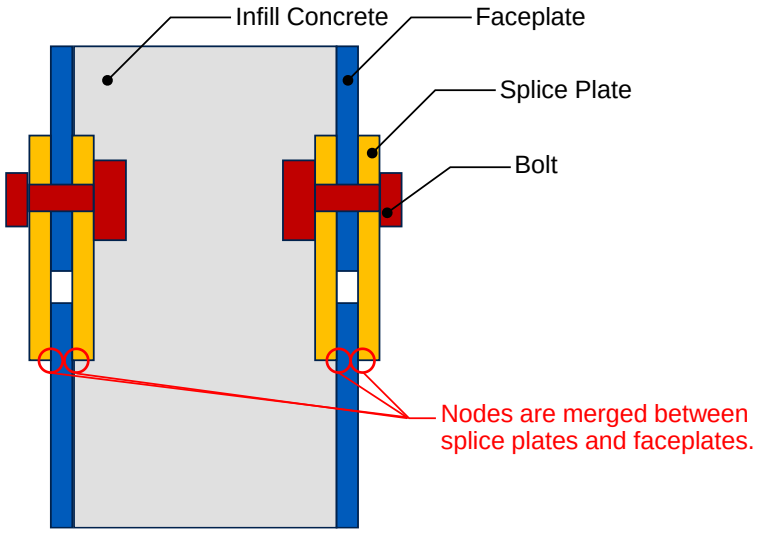


Figure 9-88. Merge of Nodes for Double-Shear Connection

9.3.4.1 Pushover Analysis with 52.5 ksi Pretension (Double-Shear)

Figures 9-89 and 9-90 compare the shear force and moment versus top lateral drift from the monotonic pushover analysis of the single-shear and double-shear finite element models. The analyses were performed independently in both positive and negative directions to investigate the ultimate behavior of the bolted splices in the wall model under both connection types.

The analysis revealed notable differences in both shear and flexural strengths between the two connection types, as shown in Table 9-5. In the positive direction, the values for both shear and flexural strength are remarkably close between single-shear and double-shear connections, because peak strength in both models was limited by local buckling of steel plates in the web of the T-shaped wall for loading in that direction. However, buckling in the single-shear connection occurred both in the splice plate and in the faceplate under the splice, while in the double shear connection it only occurred in the faceplate under the splice. In the negative direction, the double-shear connection demonstrates notably higher strength for both shear force and flexural strength. This increased strength can be attributed to the higher friction resistance provided by the double-shear connection, which offers a more shear friction interface (as demonstrated in Section 6). In other words, sliding in the double-shear model occurred at a higher load than in the single-shear model, resulting in an initial higher strength than in the double-shear model.

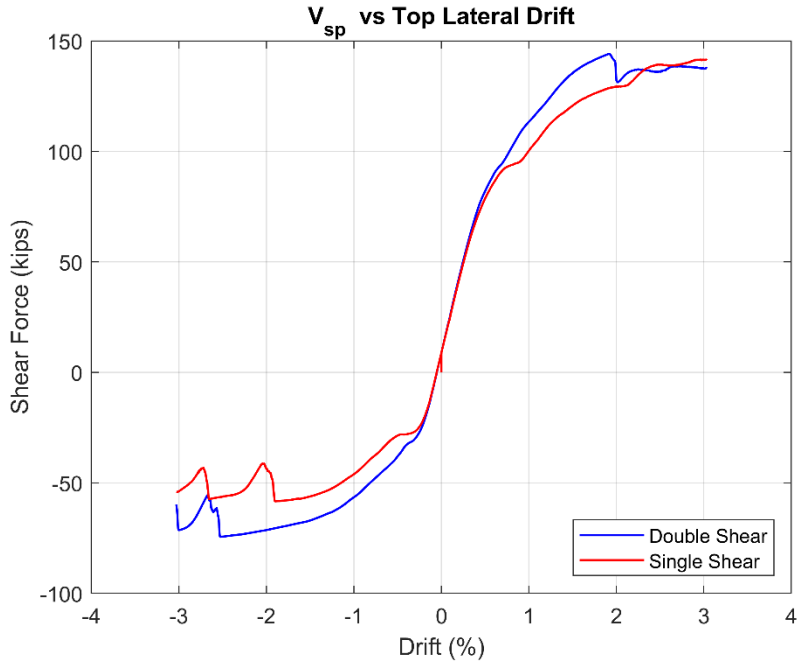


Figure 9-89. Shear Force and Top Lateral Drift Curve from Single-Shear and Double-Shear Finite Element Analysis

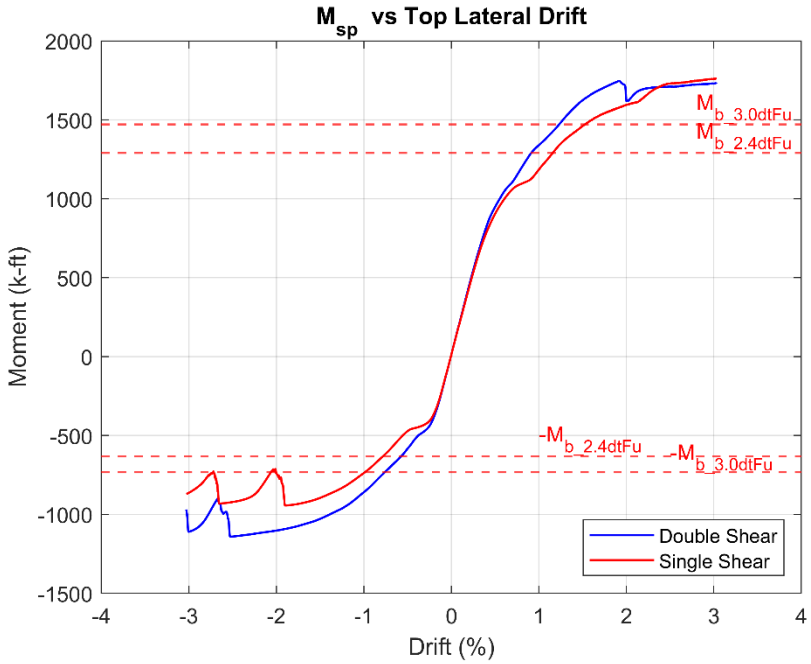


Figure 9-90. Moment and Top Lateral Drift Curve from Single-Shear and Double-Shear Finite Element Analysis

Table 9-5. Shear and Flexural Strength Comparisons between Single-Shear and Double-Shear Models

	Shear Strength (kips)		Flexural Strength (k-ft)	
	Positive Peak	**Negative Peak**	**Positive Peak**	**Negative Peak**
Single-Shear	141.20	-58.40	1759.60	-942.30
Double-Shear	144.10	-74.40	1745.20	-1141.50
Percentage Increase (%)	2.05%	27.40%	-0.82%	21.14%

Figures 9-91 and 9-92 show the von Mises stresses in the double-shear model from the southwest and southeast views during finite element pushover analysis in the positive direction. These figures, similar to those presented in Section 9.3.1.2, compare stresses on the horizontal splice (left) and faceplates (right) in the horizontal splice region at various values of drift.

Referring to similar results presented in Section 9.3.1.2, in the single-shear model (Figures 9-10 and 9-11), the yielding region due to bearing in the tension side of the wall only occurred on the web horizontal splice plates; in contrast, in the double-shear model, the yielding region occurred only on the faceplates, and the horizontal splice plates remained in elastic. As shown in Figure 9-93, buckling was initially observed on the web faceplate at a drift of 1.7% (which is a slightly larger drift than the 1.5% value when buckling was first observed in the single shear case). Subsequently, severe buckling on the web faceplate propagated over a distance at a drift of 3.0%, as shown in Figure 9-94. Unlike the single-shear model, no buckling occurred on horizontal splice plate in the double-shear model (buckling occurred only in the faceplate below the splice).

Similarly, Figures 9-95 and 9-96 show the von Mises stresses in the double-shear model during r finite element pushover analysis in the negative direction. As expected, progressive yielding due to the bearing of bolts was observed only on the faceplates on the tension side of the wall. Figure 9-97 shows the bearing deformation on the web faceplate, and all rows of bolts experienced bearing yielding a drift of -3%.

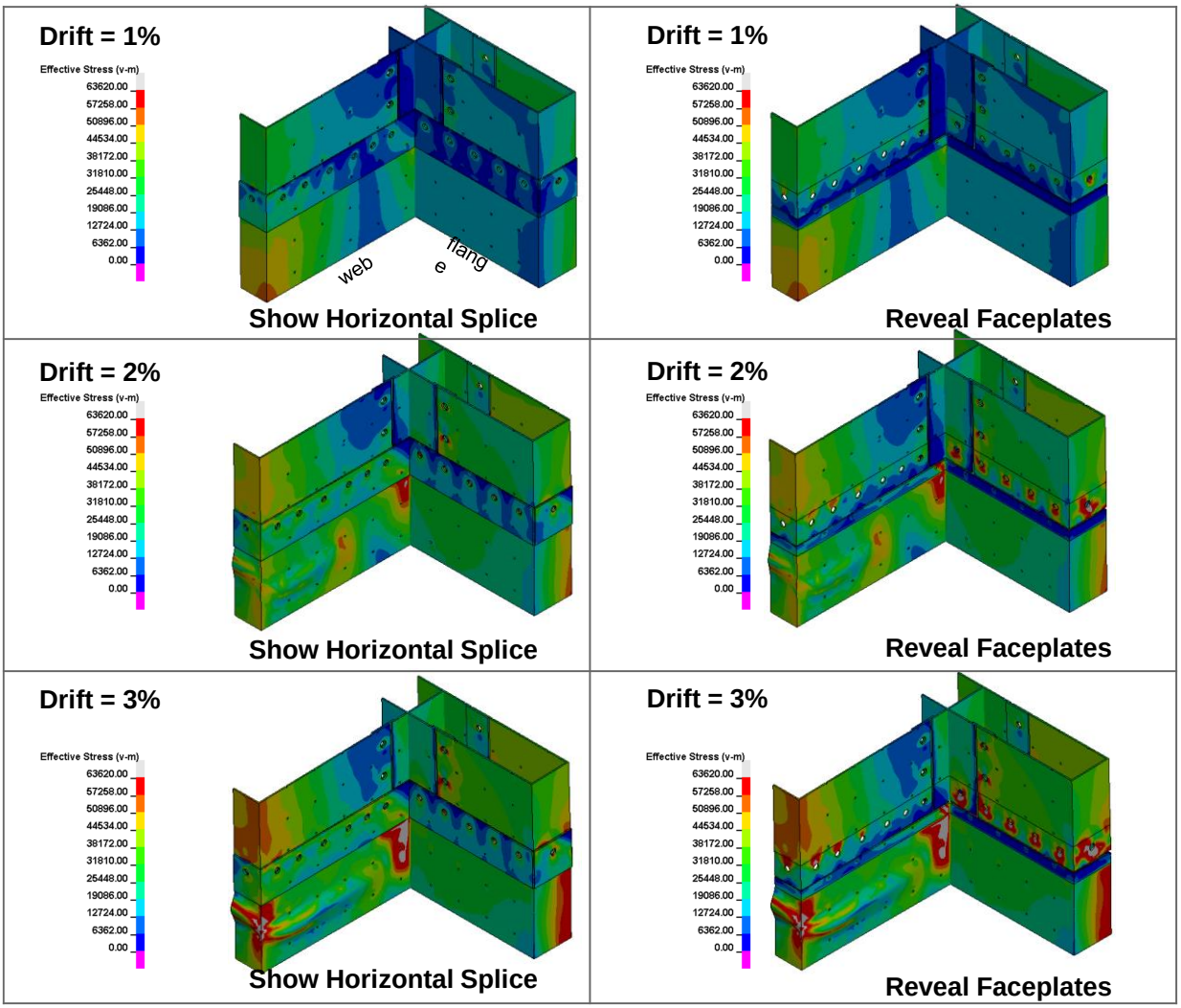


Figure 9-91. von Mises Stresses of the Double-Shear Wall Model in Positive Pushover Analysis (Southwest View)

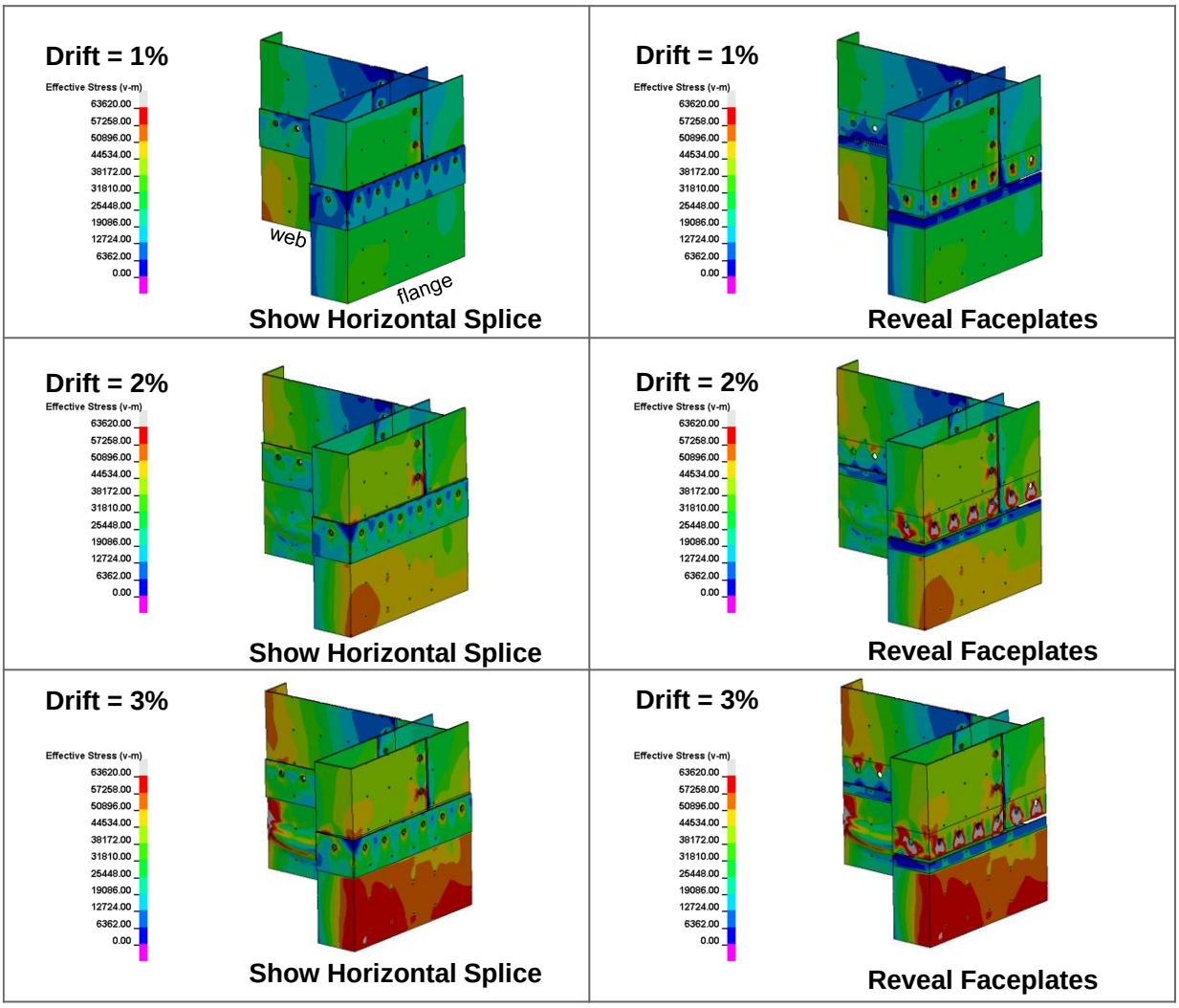


Figure 9-92. von Mises Stresses of the Double-Shear Wall Model in Positive Pushover Analysis (Southeast View)

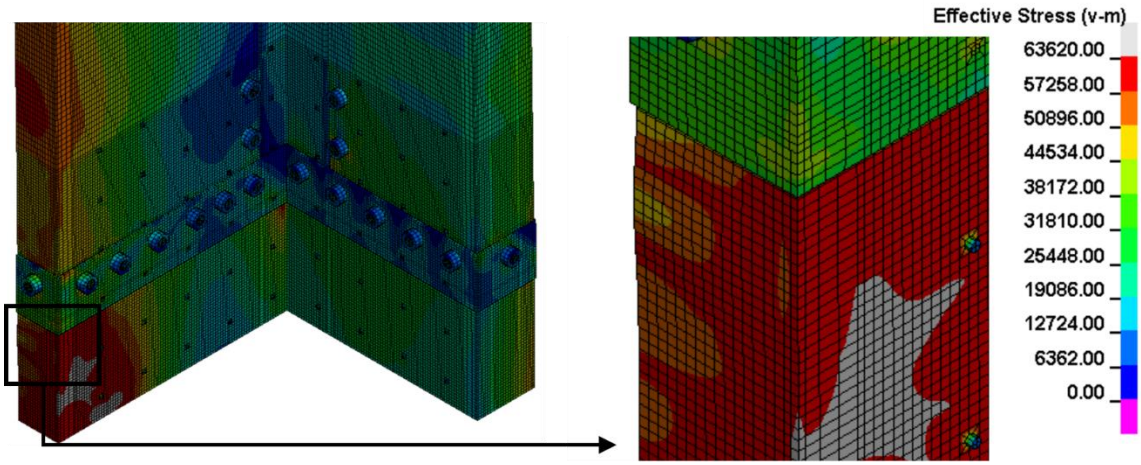


Figure 9-93. Buckling of Horizontal Splice at 1.65% Drift (Double-Shear)

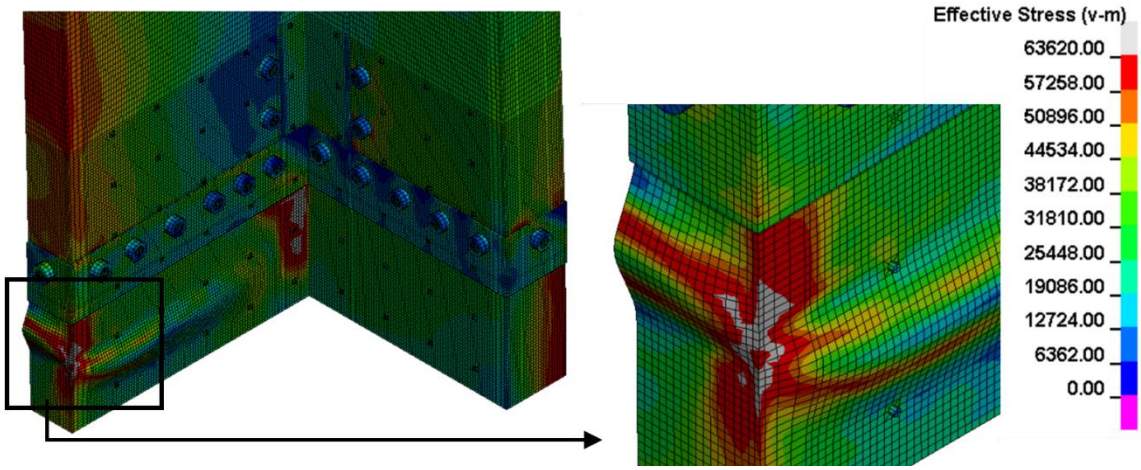


Figure 9-94. Buckling of Faceplate and Horizontal Splice at 3.0% Drift (Double-Shear)

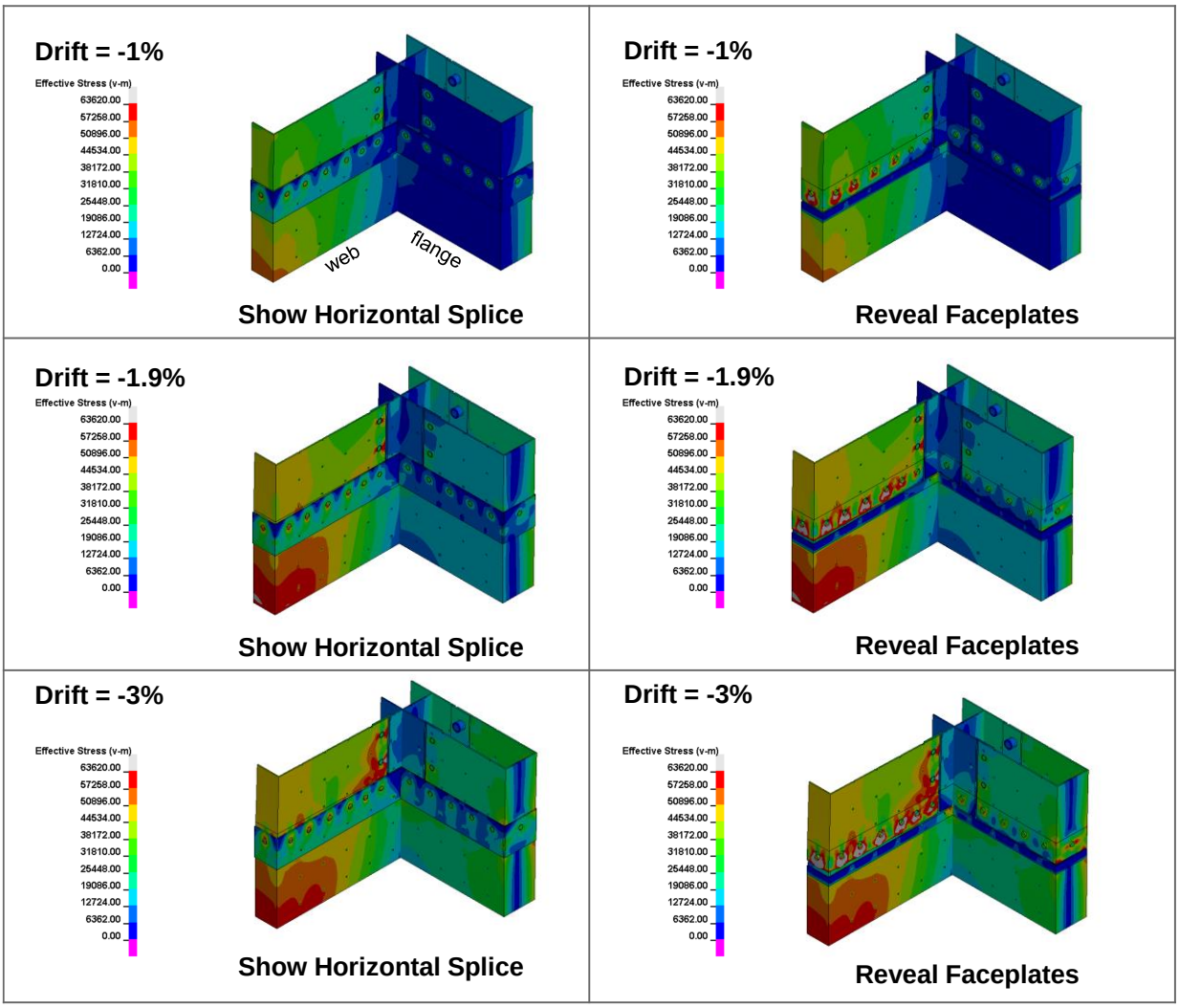


Figure 9-95. von Mises Stresses of the Double-Shear Wall Model in Negative Pushover Analysis (Southwest View)

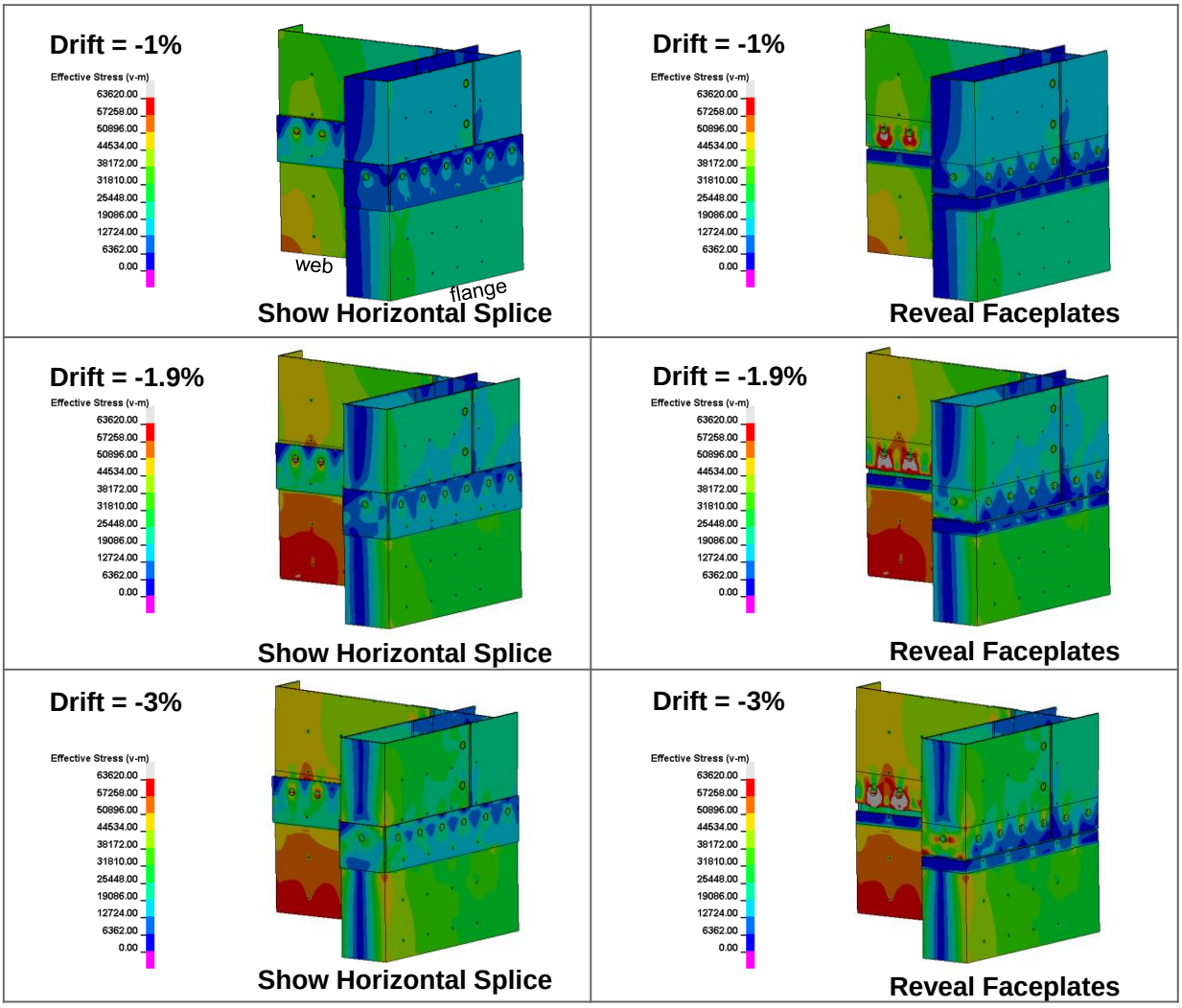


Figure 9-96. von Mises Stresses of the Double-Shear Wall Model in Negative Pushover Analysis (Southeast View)

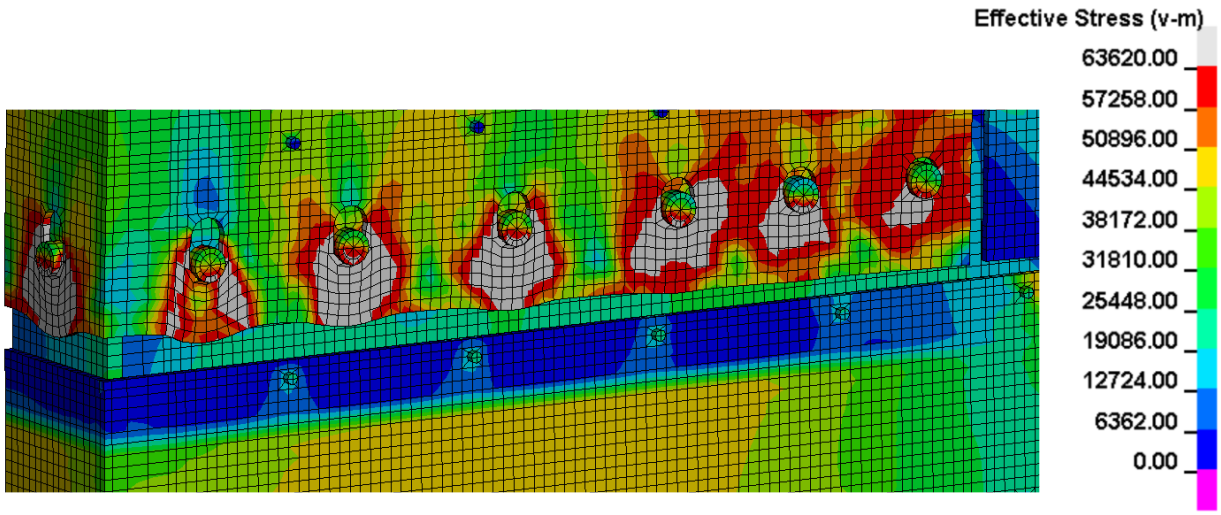


Figure 9-97. Yielding near Bolt Holes on Faceplate Web at -3% Drift

9.4 Summary of Finite Element Analysis

Finite element models of the wall specimen featuring bolted splices were developed to investigate the inelastic behavior of the tested wall specimen. Limited sensitivity analyses were performed to assess the effect of variations in the elastic modulus of concrete and in the pretension values of bolts.

Monotonic pushover analyses were conducted to assess the ultimate behavior of the bolted splices within the wall model. The pushover analysis, conducted with a 52.5 ksi pretension, closely matched the sliding plateau in the negative direction and aligned well with both positive and negative peaks up to drifts of +2.0% and -1.9%, respectively. In addition, cyclic loading analyses were conducted to investigate the inelastic behavior of the bolted C-PSW/CF, comparing these results with test data. The analyses extended up to +2.1% and -1.3% in the positive and negative drifts, respectively. However, the model did not capture the force degradation observed in the test results, which was attributed to convergence issues within the finite element program. A smaller mesh size would have been necessary to capture the ultimate bearing failure when the broken steel separates from the splice plate. However, this was unattainable within a reasonable runtime and sufficient computer memory given the scale of the model and the computational resources available, even with access to the most powerful supercomputers from the Center for Computational Research at the University at Buffalo. Despite this limitation, the cyclic loading analysis with a pretension value of 105 ksi aligned well with the test results, reaching the positive peak at 2.1% drift and matching well with the negative peaks up to -1.3% drift.

In cyclic loading analysis, the contribution of concrete was investigated by comparing the shear and flexural strength when measured from above, at, and below the horizontal splice level. The contribution of concrete shear strength (V_c/V_{Total}) above the horizontal splice level progressively decreased from 62% at 0.57% drift to 55% in the positive direction up to a drift of 2.12%, while in the negative direction, the V_c contribution

declined from 44% at -0.3% drift to 32% at -0.55% drift first, and then increased to 62% at -1.27% drift. However, at the horizontal splice level, the V_c contribution plummeted from 58% at 0.57% drift to only 8% at 2.12% drift, and from 52% at -0.3% drift to 17% at -1.27% drift. This greater reduction in V_c contribution was attributed to more severe crack propagation in the connection zone. In contrast, the contribution of M_c at the horizontal splice level progressively decreased from 62% at 0.57% to 54% at 2.12% in the positive direction, while it declined from 50% at -0.3% drift to 25% at 1.27% drift. The level of loss in M_c contribution at the horizontal splice level is almost comparable to that of the V_c contribution above the horizontal splice level in the positive direction. This indicates that the influence of cracks propagated in the connection zone has a less significant impact on positive flexural strength compared to shear strength.

This section also delved into the development of friction forces, measured at the contact interfaces between the two horizontal splice plates and faceplates, and bearing forces, determined by summing all forces acting on bolt holes. Initially, the distribution of friction forces exhibited linear behavior, with magnitude of forces related to the distance of bolts from the neutral axis, reaching a plateau once the friction limit was attained. Subsequent to the development of sliding, bearing stresses began to develop on the bolt holes in the plates. The finite element model successfully captured this progressive development of bearing stresses under monotonic pushover and cyclic loading conditions. By calculating the cumulative friction and bearing forces on the bolts, the total force of each bolt in every row was plotted and compared with the theoretical force distributions outlined in Section 8. In the finite element pushover analysis, drifts of 1.54% and -1.0% were chosen to compare with the simplified method, aligning with the flexural strength required to develop $3.0dtF_u$ as per the simplified method. Similarly, in the cyclic loading analysis, the same calculated flexural strength was compared with the simplified method at 1.0% and -0.7% drifts. Note that the pretension value differed between the two analyses, being 52.5 ksi in the pushover analyses and 105 ksi in the cyclic loading analyses. The comparison revealed that the simplified method for predicting the flexural strength of bolts

achieved over 90% accuracy in the pushover analyses, while in the cyclic loading finite element analysis, the accuracy of the flexural strength predicted by the simplified method ranged from 78% to 92%.

Local measurements from strain gauges and linear potentiometers were used to compare the finite element model with the actual test results. Strain decreases at the tip of web were found to be more significant in the test than in the finite element analysis. This was especially apparent in the positive direction. It was speculated that initial imperfections of the web horizontal splice and some bending of the web plates caused local bending, or buckling, leading to a greater strain decrease during the test, especially when the web was in compression. Such plate bending and rotations were observed to affect the measurement of the linear potentiometers. This partly explains why deformations measured by the linear potentiometers are higher than the axial deformation of faceplates calculated by the strain gauges.

The T-shaped wall with single-shear and double-shear horizontal splices was analyzed and compared under monotonic pushover analysis, up to +3% and -3% drift. The double-shear model exhibited delayed sliding and provided higher initial strength due to increased friction resistance. In the positive lateral movement, the double-shear model showed similar strength to the single-shear model, as both experienced local buckling on the web. In the negative direction, the double-shear model demonstrated notably higher strength, attributed to the higher friction resistance provided by the double-shear connection. Unlike the single-shear model, where bearing yielding occurred on the horizontal splice plates, the double-shear model showed all bearing yielding occurring on the faceplates.

SECTION 10 SUMMARY AND CONCLUSIONS

10.1 Summary and Detailed Findings

This research focused on investigating the behavior of Composite Plate Shear Wall/Concrete Filled (C-PSW/CF, a.k.a. SpeedCore) having bolted splices, for applications in regions where wind loading governs over seismic considerations and where established construction practice relies on field bolting. As such, this work is intended to answer the critical need to develop and experimentally validate the knowledge and details essential for designing and constructing this innovative type of walls where field bolting is the practice.

The initial phase of this research investigated the behavior of Component Level Tests for bolted C-PSW/CF connections. This included a "Tension Component Test," that consisted of six splice connection specimens subjected to cyclic axial loads (namely, Specimens T1 to T6), and a "Shear Component Test" that featured six shear splices to assess connection behavior under cyclic shear and flexural forces (Specimens S1 to S6). During the design of the specimens, various ductile behavior limit states were considered, including bearing, slip-critical, net section yielding, and gross section yielding, and design aimed to avoid relatively more brittle failure modes such as net section rupture, block shear failure, tear-out failure, and shear failure of bolts. The cross-sectional dimensions of the specimens were constrained to 14 in. in width and 12 in. in thickness due to laboratory constraints and the load capacity of the test setups, which were capped at 840 kips in tension and 420 kips in shear.

Since the emphasis of this study lies on non-seismic regions, where design considerations primarily revolve around wind loads, four of the Tension Components were designed to be governed by wind load.

Accordingly, their corresponding test protocol was devised to evaluate the component behaviors under a range of force demand representative of both typical and performance-based wind loading. In contrast, two of the Tension Components were designed to induce gross section yielding. These specimens were subjected to loading protocols that included fewer cycles, somewhat similar to those typically used in earthquake engineering, to reflect the conditions under median or high seismic regions.

All the tension and shear component specimens, for all the different connection details considered, were able to develop their calculated design strength. Specimens with splices that used "blind bolts" and bolts with Shuriken inside the wall generally developed their theoretical slip-critical strength, unlike those designed with threaded rods through pipe sleeves. All bearing strength obtained in the test were developed with significant deformations. More specifically:

- For Specimens T1 and T2, both designed to be governed by their bearing strength limit state, the test results show that both specimens reached and exceeded the design strength of $2.4dtF_u$. The initial stiffness of Specimen T1 was notably smaller than that of Specimen T2, which can be attributed to the observation that Specimen T1 undesirably developed excessive out-of-plane bending (the only one to do so) and had a lower slip-critical resistance that Specimen T2. The test for Specimen T1 was terminated prior to bearing failure. Conversely, Specimen T2 reached an ultimate strength of $3.84dtF_u$ when the specimen was pulled to a 3-in. deformation.
- Specimen T3 was designed to be governed by slip-critical resistance, but the test results revealed that slip occurred at an axial load of 170 kips that amounted to only 43% of the design value (393 kips). This was a connection type that used through rods running through pipe sleeves; the rods were torqued in the laboratory, albeit with difficulty due to equipment limitations. Consequently, the rods did not attain the specified minimum pretension as stipulated by AISC

standards. Nonetheless, beyond the premature connection slip, Specimen T3 developed net section yielding and progressed to a load plateau as anticipated. The specimen ultimately failed due to net section rupture at a tension force of 622 kips, closely aligning with the calculated net section rupture strength of 614 kips.

- The ductility of the connection in Specimen T2 was calculated to be 5.5 (2.48/0.45=5.5), while the ductility in T3 was determined to be 2.25 (2.25/1.00=2.25). Based on component test results, splices designed to develop their bearing limit states are found to be more ductile than those for which net section failure (when not preceded by gross-section yielding) is the ultimate limit state.
- Specimen T4 was designed with a proposed I-shaped anchor concept to counteract tensile forces by relying on the development of compression struts inside the connection. While the test results indicated that the specimen achieved its design strength, it exhibited a brittle behavior beyond that point, upon severe concrete cracking.
- Departing slightly from the main objective, to investigate possible application in seismic regions, Specimens T5 and T6 were designed to achieve gross section yielding, and the test results confirm that both specimens reached this design objective, exhibiting full hysteresis loops. Specimen T5 demonstrated less stability in compression due to the presence of three rows of Shurikens in the connection, which increased the splice unbraced length. Conversely, in Specimen T6, three rows of through rods served as a lateral bracing system, enhancing the stability of the connection, particularly in compression.
- A “slip plateau” (i.e., constant force while slippage occurs before increasing again once bearing develops) was not observed on the hysteretic curve when using blind bolts or Shurikens, due to the resistance from the embedded nuts in contact with the concrete. Conversely, a slip plateau was

observed with the use of through rods in pipe sleeves, which is attributable to the gaps that allow the rods to slide within the sleeves.

- Specimens S1 and S2 were designed to be governed by the bearing limit state, both with (S2) and without (S1) concrete infill. The test results indicate that both specimens achieved the shear strength necessary to develop the bearing strength of $2.4dtF_u$. As bearing strength increased upon larger hole deformation, Specimen S2 was able to develop net section shear rupture strength ($0.6A_eF_u$) in the positive direction. Both specimens ultimately failed due to the increasing bearing deformation, which eventually caused tear-out at the bolt holes.
- Specimens S3 and S4 were designed governed by slip-critical resistance, both with (S4) and without (S3) concrete infill. In Specimen S3, the test result shows a 144 kips initial slip force, which is close to the calculated slip-critical resistance of 142.38 kips. No sliding plateau was visible in Specimen S4. Both specimens were able to develop net section shear rupture strength ($0.6A_eF_u$) prior to failure, and Specimen S4 also achieved the gross section yielding strength ($0.6A_gF_y$) before failure. Both specimens had a combined failure mechanism involving bearing failure and net section fracture.
- Specimens S5 and S6 were designed to develop their gross section shear yielding strength ($0.6A_gF_y$), both with (S6) and without (S5) concrete infill. For Specimen S5, the test results indicate that the peak strength (258 kips) in the test, was 3.7% lower than the target limit state of gross section shear yielding, which was 268 kips, which could be attributed to the effect of eccentric loading (i.e., shear and torsion) on the connection. Specimen S6 was able to exceed the gross section yielding strength. Both specimens had a combined failure mechanism involving bearing failure and net section fracture.

- The composite sections were initially stiffer and reached peak force with significantly less sliding in the splice compared to non-composite sections. The peak shear strength of the composite section was typically sustained over larger deformations, whereas that of the non-composite sections progressively increased with larger deformations up to failure. However, as deformations increased beyond 1-in deformation, the strength of the composite sections progressively degraded to approach that of the non-composite sections before failure. This indicates that, ultimately, as the concrete severely cracked, its contribution to shear strength decreased.
- In the above Shear Component tests (S1 to S6), bearing strengths were calculated in the direction parallel to the splice. However, strength was also verified using the elastic method for eccentric connections (per procedure in AISC manual), which considers an eccentric bolt group to develop bearing strengths of $2.4dtF_u$ and $3.0dtF_u$, and all specimens were able to develop and exceed these strengths during the tests. Moreover, despite all specimens—both non-composite and composite—exceeding the shear strength necessary to develop a bearing strength of $2.4dtF_u$, diagonal deformation was observed in the bolt holes of the splice plates in all shear specimens, indicating a combined behavior of shear and torsion on the splices due to the fact that some flexure was unavoidably applied to the specimen simultaneously with the shear force.

The behavior of all the component tension specimens was first simulated using proposed simplified spring models. The simplified spring models successfully replicated the hysteresis curves observed from the test results. In addition, the assumed spring properties modeled well the various components of behavior of the tension specimens, including friction sliding, development of bearing strength, net section yielding, gross section yielding, and concrete behaviors. This provided valuable insights into the mechanisms contributing to development of the ultimate strength of the tension specimens. In particular:

- For T1 and T2 (for which design was governed by the bearing strength limit state), it demonstrated that bearing strength and friction resistance are not additive at the point where bearing strength is achieved.
- For T3 (for which design was governed by the net section yielding limit state), it demonstrated that when the connection is designed such that gross section yielding will not be reached, the net section spring exhibited a dominant part of the hysteretic behavior until failure at extreme strains.
- For T5 and T6, it demonstrated that if the specimen had been subjected to cyclic loading to equal tension and compression strength, and if the connection was designed to develop the faceplate gross section yielding, the net section would yield once and then settle into an extended elastic range response.

An advantage of these spring models is that they can be used by engineers doing simple hand calculations to assess the behavior of connections for the types of limit states considered. Also, although it has not been attempted here, a modified version of the model could be implemented in fiber hinge models (such as those in OpenSEES) to model the inelastic behavior of composite members (including C-PSW/CF or other) having bolted splices.

Finite element models were then developed to verify the behavior of the tension and shear component specimens. For analysis of the tension specimens, the finite element models were subjected to monotonic and cyclic loading, and both captured well the overall and localized behaviors. The analyses confirmed the observations made above for the simpler models, but also provided insights into other aspects of behavior, particularly with respect to the relationship between strength and elongation of bolt holes due to bolt bearing, and to other deformation behaviors of the face plates and other members under different governing limit states. More specifically:

- For Specimens T1 and T2, bearing strength reached $2.4dtF_u$ and $3.0dtF_u$ at deformations of 0.21 in. and 0.9/0.8 in., respectively. This is close to the values of 0.25 and 1.0 mentioned in the literature.
- For Specimen T3, the bearing strength of $2.4dtF_u$ was reached at a hole deformation of 0.6 in., but this 0.6-in. deformation was primarily attributed to net section elongation around the rod holes (which was the governing limit state for this connection).
- Threaded rods in Specimen T2 and T3 were observed to bend slightly in single curvature, with bending deformations from middle to top of no more than 1/8 in. when specimen elongation reached 2 in.
- For Specimen T4, up to the theoretical design strength, the angle of the compression struts observed in the analyses was approximately 50˚, which is close to the theoretical value of 45˚ assumed for design. When the theoretical expected strength of 396.6 kips is reached, equilibrium at the mid-length of the splice indicates that the splice plates transfer 44% of the total tension force, while the web of the I-shaped anchor transfers 52% of it. The finite element analysis also showed that concrete cracks that developed in the connection led to a different behavior beyond the theoretical strength, with significant cracking developing in the connection and modifying behavior. Finite element analysis also showed that the threaded rods that were not in a sleeve were bent significantly in double curvature at large specimen tension deformations, which concurs with observations (and failure of the rods) during the tests.
- For Specimens T5 and T6, the net section deformation contributed the largest portion of the overall deformation in this subassembly, but one must keep in mind that gross section yielding would actually extend over a much longer distance than only the localized splice plate region that was the focus of analysis here, and would therefore contribute most substantially to the wall deformation over the entire length of gross section yielding.

In addition, different analyses were conducted for the tension specimens to consider the boundaries conditions replicating both the test specimen and actual walls, to investigate the difference between results in both of these scenarios, and differences were found to be negligible.

For shear component specimens, finite element models were employed and compared with the test results. Monotonic loading analysis was performed for all specimens and cyclic analysis was performed for all the composite specimens. The finite element models generally captured similar ultimate behavior compared to the test results, but at strength with +8% to - 14% accuracy. The contribution of shear strength provided by concrete was found to be 25 to 31% of the total shear strength at peak shear strength of the composite shear specimens. In addition, wider walls with bolted connections were examined to investigate shear connections where eccentricity of the bolt group is not significant. A proposed equation combining the bearing strength of $2.4dtF_u$ and the ACI concrete shear strength (Equation 18.10.4.1) was developed to provide a conservative approach for estimating the shear strength of C-PSW/CF bolted splices. Overall, all analyses conducted validated the design equations used to calculate the strength of bolted wall splices in tension and in shear.

To better understand the mechanisms developing during bearing failure, the impact of bolt pretension on bearing strength in bolted connections was explored. Initially, finite element models of all-steel bolted connections were developed. These models included a single-bolt configuration as well as three double-bolt connection models. The analysis examined the influence of varying numbers of bolts, along with comparisons of different bearing ratios and bolt diameters. More specifically, it was found that:

- The friction forces decrease as the bolt hole elongation increases. In Model 1, which utilized a single-bolt connection, friction forces experienced significant reductions of 66% and 41% when the bolts were modeled with elastic-plastic material (i.e., regular bolts) and elastically, respectively. In Models 2 to 4, which featured double-bolt connection with regular bolts, the reductions in friction forces were 59%, 66%, and 78% respectively, as bolt diameters decreased from 1.0 in. to 0.625 in. These results suggest that the inelastic deformation and bending of bolt shanks significantly impact the development of friction, particularly as the tension force in the bolt decreases due to yielding or bending.
- Even in bolted connections without pretension, friction forces develop due to the relative movement between splice plates and faceplates. These forces are generated from the contact interfaces between the steel plates, and they typically first increase up to a peak value and then decrease as bolt hole elongations increase.
- Using both finite element analysis and simplified analysis using free-body diagram with contact springs helped understand how the initial contact spring loses contact area and contact stiffness due to hole elongation and thinning of the faceplate in tension due to Poisson's effect.
- When a bolted C-PSW/CF connection is subjected to compression, the presence of concrete typically prevents the connection from experiencing significant deformation. Consequently, the elongation of bolt holes due to bearing forces is restricted in this scenario.
- When in compression, the slip-critical resistance was reached initially, after which the axial force was immediately transferred to the concrete. Subsequently, the concrete reached its compressive strength and began to crack. As the cracks propagated, the contribution of concrete decreased, and slip started to develop in the steel connection.

A large-scale T-shaped C-PSW/CF specimen with bolted splices was then designed and tested. The horizontal splice was designed to develop approximately 60% of the yield strength ($0.6F_y$) of the faceplates in tension, using a Tributary Area Approach by which the bearing strength over a width equal to the bolt spacing was set equal to the force developed over that width by a stress equal to 60% of F_y. The specimen had 3/16 in. faceplates and horizontal splice used 3/4-in. diameter bolts typically at 4-in. spacing. In addition, a method was proposed to calculate the flexural strength of the horizontal splice, assuming that the bolts at the tension edge develop a bearing strength of $2.4dtF_u$ or $3.0dtF_u$. This approach assumes a linear distribution of bolt forces, offering another method to evaluate the flexural strength of the horizontal splice.

For the vertical splices, a shear flow analysis was used to design the required bolt spacings for vertical splices to achieve a slip-resistant connection. This shear flow was computed considering either the properties of the steel alone (i.e., the Steel Component Approach) or of the entire composite section (i.e., the Composite Section Approach). The results from both calculations were compared with the slip-critical resistance of the 3/4-in. diameter A490 bolt to determine the appropriate vertical spacing. The resulting designed vertical bolt spacing was 4.5 in. on center.

This T-shaped CPSW/CF specimen was subjected to cyclic flexural loading while under a constant axial load equal to 10% of the crushing load of concrete (i.e. $0.1A_c f'_c$). More specifically:

- The specimen was cycled to increasing amplitudes up to 4.25 in. (2.58% drift) in the positive direction (web in compression) and -9.5 in. (5.75% drift) in the negative direction (flange in compression).

- Flexural strength of no less than 80% of the peak value reached was sustained until reaching drifts of 2.4% in the positive direction and -4.3% in the negative direction.
- The wall specimen was able to develop the flexural strength corresponding to point when bearing strength of $2.4dtF_u$ and $3.0dtF_u$ was reached in the bolts farthest to the neutral axis, as calculated from the above simplified methods.
- Lateral drifts of the wall specimen at each test step were compared with the theoretical elastic deflection curve for a cantilever wall and found to be in good agreement up to the design strength. Beyond the design strength, as slippage and bearing started to develop in the splice, the angle between the theoretical elastic curve and actual test deflections highlighted the development of hinge rotations in the horizontal splice. The rotation was 0.25°/-0.34° at the design strength level (Step 4, 0.84%/-0.55% drift), and reached 1.42°/-1.08° at in Step 9 (2.58%/-1.94% drift). Ultimately, the rotation developed to -3.35° in the negative peak in Step 15 (-5.76% drift). The hinge rotation generated at the horizontal splice due to bolt sliding and concrete cracks introduces flexibility that must be accounted for in wall design if post-design deflections are of interest.
- Due to a fabrication error, the bottom of the inside horizontal splice plates was not welded (contrary to design intent), altering the connection behavior from double-shear to single-shear. Despite this, failure occurred by bearing failure, albeit in the outside splice plates instead of in the faceplates due to shorter edge distances there. The design strength was still achieved as both plates were 3/16-in. thick. Unfortunately, because failure developed on the outside splice plate instead of the faceplate, this prevented implementation of a proposed repair scheme that could have shown how the wall could be rapidly repaired if damaged beyond the design level.

Finite element models of the wall specimen featuring bolted splices were developed and analyzed to investigate the inelastic behavior of the tested wall specimen. Limited sensitivity analyses were performed to assess the effect of variations in the elastic modulus of concrete and in the pretension values of bolts. Monotonic pushover analyses were used to assess the ultimate behavior of the wall specimen, while cyclic loading analyses compared its inelastic behavior with test results. More specifically:

- The pushover analysis with a 52.5 ksi bolt pretension (equal to 66% of the AISC-specified pre-tension load) closely matched the sliding plateau in the negative direction and aligned well with both positive and negative peaks up to drifts of +2.0% and -1.9%, respectively.
- Cyclic loading analysis using a pretension value of 105 ksi (equal to 132% of the AISC-specified pre-tension load) showed good alignment with test results, accurately matching the positive peak at 2.1% drift, and closely fitting the negative peaks up to -1.3% drift.
- The cyclic loading analysis results show an initial overstrength in the positive direction regardless of the pretension value being assigned. The reasons for this initial overstrength are unknown, but it is speculated to be caused by either an initial out-of-straightness of the faceplates and horizontal splice plate (not accounted for by the finite element model) or assumptions in the finite element model that produced a wall numerically stiffer than the actual specimen over that range of displacement.
- The cyclic loading analyses were conducted up to +2.1% and -1.3% in the positive and negative drifts, respectively. However, the model did not capture the additional force degradation observed in the test results beyond those drifts, which was attributed to convergence issues within the finite element program. A smaller mesh size would have been needed to capture the ultimate bearing failure when the broken steel separates from the splice plate. This was unattainable within a

reasonable runtime and sufficient computer memory given the scale of the model and the computational resources available, even with access to the most powerful supercomputers from the Center for Computational Research at the University at Buffalo.

- The contribution of concrete to the total shear strength of the horizontal splice level, as obtained from the cyclic loading analyses, varied from 58% at 0.57% drift to 8% at 2.12% drift in the positive direction, and from 52% at -0.3% drift to 17% at -1.27% drift in the negative direction. Conversely, where cracking in the concrete was less significant, such as above the horizontal splice, the concrete shear strength contributed slightly more than 50% of the total strength irrespective of drift. From the same analyses, the contribution of concrete to the total flexural strength at the horizontal splice level varied between 50% and 62% of the total strength in the positive direction, while it dropped from 50% at -0.3% drift to 25% at -1.27% drift in the negative direction. These findings underscore the significant impact of crack propagation on the shear strength of concrete, as well as its effect on the moment strength of concrete, particularly in the negative direction.

10.2 Overarching Conclusions

More generally, it can be concluded from the experimental and analytical research conducted on C-PSW/CF having bolted splices that:

- All splice details considered were able to develop the design strength calculated on the basis of existing AISC equations for bolted steel connections in tension and shear.
- Connections having blind-bolt or Shuriken performed well, and may be easier to fabricate, with the drawback of possibly having a longer unsupported splice zone when multiple rows of bolts are used.
- Connection details using through rods with pipe-sleeves exhibited a more easily observable slippage before developing their bearing strength. This may be due to challenges in applying the required pre-tension forces in the threaded rods. Note that from a fabrication perspective, another challenge arises from the fact that the pipes need to resist the clamping force during the pretension process, which can result in substantial pipe-sleeve sizes. Alternatively, if pretension is accomplished after concrete is infilled and develops its compressive strength f'_c, this results in construction delays. Both outcomes make this connection detail less attractive.
- Horizontal bolted splices in C-PSW/CF designed to be governed by the bearing strength limit state of $2.4dtF_u$ have been shown to perform well up to that limit provide that the slip resistance of the connection is at least equal to that value. It is unknown how walls with lower slip resistance would perform, as this would likely require the connection to develop hole elongations that may not be acceptable in service following development of the bearing strength.
- Bolted C-PSW/CF connections must experience large bolt hole deformation to develop their bearing strength of $3.0dtF_u$, regardless of the pretension value assigned, because friction forces due to clamping between the steel plates start to progressively decrease starting from hole elongations

of approximately 0.1 in. Residual friction forces typically converge to a low value at large deformations that is the same regardless of the pretension value assigned. This indicates that under large deformations, the bearing strength and slip-resistance strengths cannot be combined together to calculate the strength of a bolted connection.

- Using the simplified method to predict the flexural strength of horizontal splices to develop bearing strength of $2.4dtF_u$ and (ultimately, at large deformations) $3.0dtF_u$ produces a conservative estimate compared to the test results.
- The effective flexural stiffness (EI_{eff}) as defined in AISC 360-22 Equation I1-1 can predict well the initial stiffness of the wall specimen compared to the test result.
- Vertical splices designed to be slip-resistant performed as intended as no slippage was observed in any of the six vertical splices. It indicates that the design approach, either considering steel component or composite section, are adequate for designing vertical splices.
- The finite element analyses show that higher pretension value results in higher initial strength. The result indicates a 20% increment of peak shear force when increasing the pretension value from 52.5 ksi to 105 ksi. (equal to 66% to 132% of the AISC-specified pre-tension load)

10.3 Future Research

The following are potential areas for future research:

- Finding the optimum aspect ratio and material strengths (such as high-strength steel) for bolted C-PSW/CF systems. Walls with larger or smaller reinforcement ratios (and different material strengths) may be more advantageous than the one analyzed in this study. However, there might be a limit where thicker plates become incompatible with bolted connections, necessitating further investigation.
- Exploring the use of doubler plates at the bolted regions to provide a ductile connection suitable for seismic regions, especially for connections with single row of bolts instead of multiple rows, simplifying the design and construction while maintaining adequate seismic performance.
- Modifying the proposed connection detail with an I-shaped anchor or investigate alternative designs to better engage the concrete infill in resisting tensile forces.

SECTION 11
REFERENCES

ACI (2019). Building Code Requirements for Structural Concrete (ACI 318-19) and commentary, American Concrete Institute.

Agrawal, S. (2020). SEISMIC DESIGN COEFFICIENTS FOR COMPOSITE PLATE SHEAR WALLS - CONCRETE FILLED (C-PSW/CF). Civil Engineering. West Lafayette, Indiana, Purdue University.

AISC (2017). Steel Construction Manual 15th Edition, American Institute of Steel Construction.

AISC (2022). AISC 341-22 Seismic Provisions for Structural Steel Buildings. Chicago, Ill., American Institute of Steel Construction.

AISC (2022). AISC 360-22 Specification for Structural Steel Buildings. Chicago, Ill., American Institute of Steel Construction.

Alzeni, Y. (2014). Cyclic inelastic behavior of concrete filled sandwich panel walls subjected to in-plane flexure. Department of Civil, Structural, and Environmental Engineering. Buffalo, NY, State University of New York at Buffalo.

Alzeni, Y. and M. Bruneau (2017). "In-Plane Cyclic Testing of Concrete-Filled Sandwich Steel Panel Walls with and without Boundary Elements." Journal of Structural Engineering 143(9).

Amit H. Varma, P. M. B. S. S., PhD; Ataollah Anvari Taghipour (2023). Design Guide 38: SpeedCore Systems for Steel Structures, American Institute of Steel Construction.

ASCE (2019). Prestandard for Performance-Based Wind Design. United States, American Society of Civil Engineers.

Brown (2007). Evaluation of Influence of Hole Making Upon the Performance of Structural Steel Plates and Connections.

Crawford, S. F. and G. L. Kulak (1971). "Eccentrically Loaded Bolted Connections." Journal of the Structural Division 97: 765-783.

ENR (2023). "Tall Buildings - Steel Group Publishes Design Guide for SpeedCore System." Engineering New-Record.

Fortmeyer, R. (2021). Rainier Square by NBBJ, Architectural Record.
<Retrieved from https://www.architecturalrecord.com/articles/15099-rainier-square-by-nbbj>.

Frank, K. H. and J. A. Yura (1981). An Experimental Study of Bolted Shear Connections.

Gomes, V., et al. (2019). "Monotonic and Fracture Behaviours of Bolted Connections with Distinct Bolt Preloads and Surface Treatments." Frattura ed Integrità Strutturale 13(48): 304-317.

Hallquist, J. O. (2006). LS-DYNA® THEORY MANUAL. Livermore, California, Livermore Software Technology Corporation (LSTC).

J. Schlumpf, Self-compacting concrete structures in Switzerland, Tunn. Undergr. Space Technol. 19 (2004) 480, https://doi.org/10.1016/j.tust.2004.02.080.

Kim, D.-K. and C.-H. Lee (2020). "Generalized Load Deformation Relationship for Bearing-Type Single-Bolted Connections." Journal of Structural Engineering 146(7).

Kim, H. J. and J. A. Yura (1996). The Effect of End Distance on the Bearing Strength of Bolted Connections. The University of Texas at Austin.

KIZILARSLAN, E. (2021). EXPERIMENTAL AND ANALYTICAL INELASTIC BEHAVIOR OF C- AND TSHAPED COMPOSITE PLATE SHEAR WALLS/CONCRETE-FILLED (C-PSW/CF). Department of Civil, Structural and Environmental Engineering. Buffalo, NY, State University of New York at Buffalo.

Kizilarslan, E. and M. Bruneau (2021). "Hysteretic behavior of repaired C-shaped concrete filled-composite plate shear walls (C-PSW/CF)." Engineering Structures 241.

Kizilarslan, E. and M. Bruneau (2023). "Cyclic Behavior of T-Shaped Composite Plate Shear Walls–Concrete Filled." Journal of Structural Engineering 149(8).

Kulak, G. L., et al. (1987). Guide to Design Criteria for Bolted and Riveted Joints. American Institute of Steel Construction.

Lewis, B. E. and F. J. Zwememan (1996). EDGE DISTANCE, SPACING, AND BEARING IN BOLTED CONNECTIONS.

LS-DYNA (2021). LS-DYNA® KEYWORD USER'S MANUAL R13, Volume I. Livermore, California, LIVERMORE SOFTWARE TECHNOLOGY (LST), AN ANSYS COMPANY. I.

LS-DYNA (2021). LS-DYNA® KEYWORD USER'S MANUAL R13, Volume II. Livermore, California, LIVERMORE SOFTWARE TECHNOLOGY (LST), AN ANSYS COMPANY. II.

Može, P. (2018). "Bearing strength at bolt holes in connections with large end distance and bolt pitch." Journal of Constructional Steel Research 147: 132-144.

Schwer, L. (2011). The Winfrith Concrete Model: Beauty or Beast ? Insights into the Winfrith Concrete Model. 8th European LS-DYNA Users Conference. Strasbourg, Schwer Engineering & Consulting Services.

Sener, K. C. and A. H. Varma (2014). "Steel-plate composite walls: Experimental database and design for out-of-plane shear." Journal of Constructional Steel Research 100: 197-210.

Shafaei, S., et al. (2021). "Cyclic Lateral Loading Behavior of Composite Plate Shear Walls/Concrete Filled." Journal of Structural Engineering 147(10).

Varma, A. H., et al. (2011). "STEEL-PLATE COMPOSITE (SC) WALLS FOR SAFETY RELATED NUCLEAR FACILITIES: DESIGN FOR IN-PLANE AND OUT-OF-PLANE DEMANDS."

Appendix A.

PowerPoint slides presented at first Project Advisory Group

(October 7, 2021)

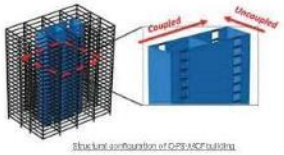
BOLTED SPLICE DETAILS FOR COMPOSITE PLATE SHEAR WALLS—CONCRETE FILLED

Student: Jia-Hau Liu
Advisor: Michel Bruneau
Date: 10/7/2021
Department of Civil, Structural and Environmental Engineering

PROJECT SCOPE

Topic

- This project seeks to develop and experimentally validate bolted splice details for Composite Plate Shear Walls—Concrete Filled (C-PSW/CF), to enable nationwide application of this structural system.



Structural configuration of C-PSW/CF building

Industry Need

- There is a growing interest to use C-PSW/CF in non-seismic regions, such as New York City and Boston, where bolted splices are preferred over welded ones.
- Bolted splices can be used in regions of moderate seismicity, such as Nevada, Idaho, Utah, South Carolina, and many more, where wind demands exceed elastic seismic demands and govern splice design.
- Cyclic response up to the limits permitted by the ASCE Pre standard for Performance-Based Wind Design may also be considered.
- Bolted splices are also desirable in some regions where seismic design governs, such as in the Midwest's New Madrid seismic zone, even though splices in that case would have to resist the full yield strength of the connected plates.

Proposed Research

Research Plan by Tasks

- Task 1: Review/Develop Bolted Splice Alternatives and Selection of Specimens
  - A set of different bolted details will be developed and evaluated, both at the prototype and specimen scale. The experience of steel fabricators and structural engineers will instruct many of the configurations considered. While the connections should be simple enough to be designed using simple hand-calculation methods, preliminary finite element simulations will be performed to predict expected ultimate performance beyond the target service level. Performance under demands from wind load is the primary focus, but details applicable in seismic regions will also be considered for a few component specimens. Final set of splice specimens to be tested will be jointly selected by the Project Advisory Group and research team, on the basis of findings from the above analyses.

Proposed Research

Research Plan by Tasks

- Task 2: Experimental Investigation – Component-level Tests
  - Testing will be accomplished at the component level using a test set-up that makes it possible to swap and test multiple splice details relatively expeditiously. Testing protocol may consist of cyclic testing representative of wind-demands, followed by monotonic loading to failure; or of other protocol agreed upon by the Project Advisory Panel. It is envisioned that axial tests (650 kips) would be accomplished using the set-up schematically laid out in plan-view in Figure 1a. Shear tests (420 kips) would be conducted using the pantograph shown in elevation in Figure 1b (a set-up successfully used previously to produce shear failure in large diameter concrete filled steel tubes).

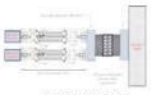


Fig. 1a Axial Tests



Fig. 1b Shear Tests

Proposed Research

Research Plan by Tasks

- Task 3: Post-Processing Experimental Results and Reporting – Component-level Tests
  - Post-processing of the experimental results will be performed, and results will be used to revisit and calibrate the finite element models, in turn used to investigate variations in the details considered and provide broader validation of the splice concepts considered. A report on Tasks 1 to 3 will be produced.

9

Proposed Research

Research Plan by Tasks

- Task 4: Experimental Investigation – Wall-level Test
  - A C-shaped C-SPW/CF wall similar to the one previously tested at UB, but having all (vertical and horizontal) bolted-splices, will be subjected to an axial load and cyclic load protocol. One of the bolted splice concepts investigated in Tasks 1-3 will be used. The objective is to validate the global performance of these walls entirely built of bolted splices.



10

Proposed Research

Research Plan by Tasks

- Task 5: Post-Processing and Formulation of Design Recommendations
  - Further to post-processing of the experimental results, finite element analysis will be used to investigate behavior of the walls having bolted splices. A report on Tasks 4 and 5 will be produced. The two reports (i.e., produced in Tasks 3 and 5) would together provide validation of C-SPW/BF bolted splice concepts, supported by experimental, numerical, and analytical research, to be considered for pre-qualification by relevant committees, for broad adoption by the engineer design community.

11

Industry Support

Industry Champions for this project are:

- Ron Klemencic, Chairman and CEO, Magnusson Klemencic Associates
- Larry Kruth, Vice President, AISC

They would be members of the Project Advisory Group, together with other individuals who have been involved as advisors and peer reviewers for previous research projects on C-SPW/CF, such as (tentatively):

- Devin Huber, Director of Research, AISC
- Glen Bell, Consulting Engineer, Director, CROSS-US
- Jim Malley, Senior Principal, Degenkolb Engineers
- Rafael Sabelli, Principal and Director of Seismic Design, Walter P. Moore & Associates

The PI plans meetings with the Project Advisory Group, per a schedule to be established upon consultation with members of this group.

12

Proposed Timing

Task	*Duration*	*Tentative Schedule*
1 – Review/Develop Bolted Splice Alternative	4 months	9/1/2021 - 12/31/2021
2 – Component-level Tests	4 months	1/1/2022 – 04/30/2022
3 – Post-Processing and Reporting	4 months	5/1/2022 – 8/31/2022
4 – Wall-level Test (Planning and Execution)	8 months	9/1/2022 – 4/30/2023
5 – Post-Processing and Design Recommendations	4 months	5/1/2023 – 8/31/2023

13

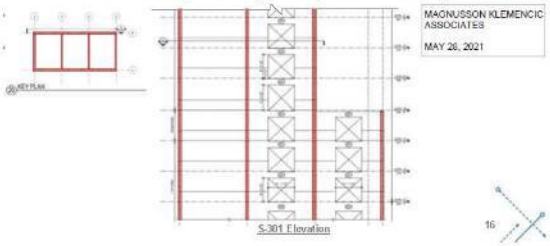
What Need To Be Decided Today

Item	Question	Decision
1	Specific connection details to be in the test? (Type of Splice and Bolt)	
2	Loading Protocol for Tension/Shear Test (TYP. Wind/P. B. Wind/Seismic)	
3	Specific requirements for geometry? (Test Layout, Wall width, thickness, etc.)	

14

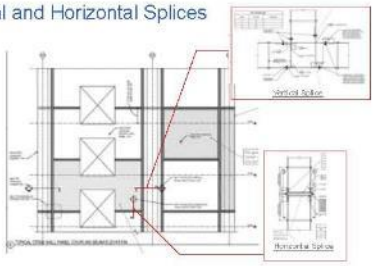
INTRODUCTION

Elevation of the Design Core (Examples from MKA)



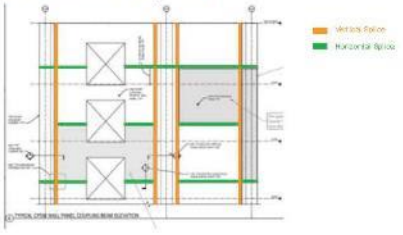
16

Vertical and Horizontal Splices



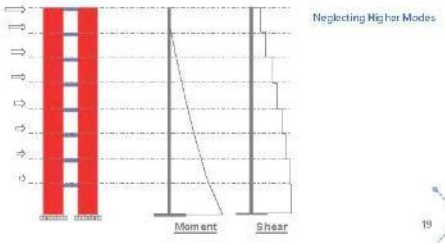
17

Vertical and Horizontal Splices



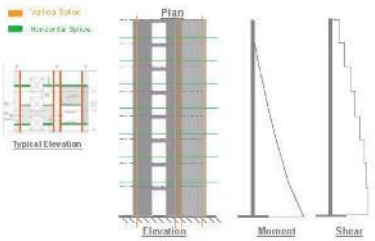
18

Typical Structural Behavior of CPSW



19

Typical Structural Behavior of CPSW



20

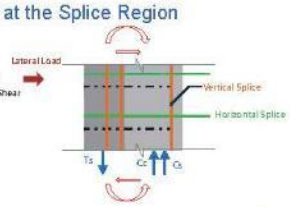
Typical Structural behavior at the Splice Region

For Horizontal Splice

→ Transfer Tension Force in the section
→ Splice need to take Tensile Forces coming from OTM
→ Splice need to take Shear Forces coming from Story Shear

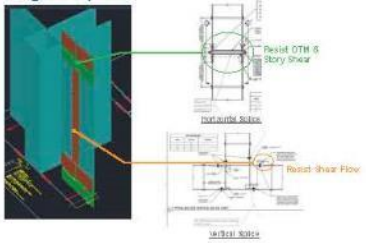
For Vertical Splice

→ No Tension Force in the Section
→ Splice need to take Shear Force from Shear Flow
$v = V(t)/I_x$ (might be very small)



21

3D Drawing for Splice



22

TENSION TEST DESIGN

SHEAR TEST DESIGN

Test Specimen Design (Tension Test)

- Target Loading & Strain T_s & ε_{max}
- Bolt Type (Through Bolt/Blind Bolt)
- Design Slip-Critical Bolts
- Base Material Design (Rupture/Bearing…)
- Splice Dimension
- Test Layout
- Loading Protocol

24

Test Specimen Design (Tension Test)

- Target Loading & Strain T_s & ε_{max}
- Bolt Type (Through Bolt/Blind Bolt)
- Design Slip-Critical Bolts
- Base Material Design (Rupture/Bearing…)
- Splice Dimension
- Test Layout
- Loading Protocol

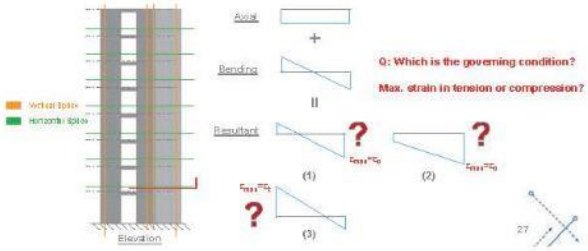
25

Target Load and Strain

- (1) Typical Wind Load (Elastic Design)
  Max. Load →
  Targe Strain → ?
- (2) Performance-Based Wind Design
- (3) Seismic Load

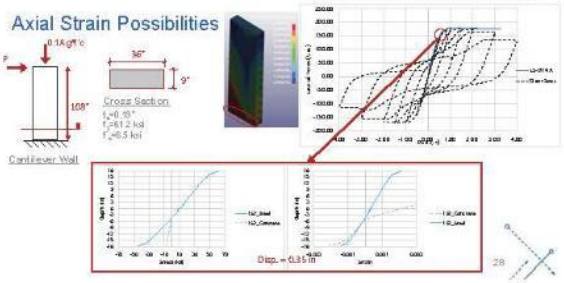
26

Axial Strain Possibilities



27

Axial Strain Possibilities



28

Target Load and Strain

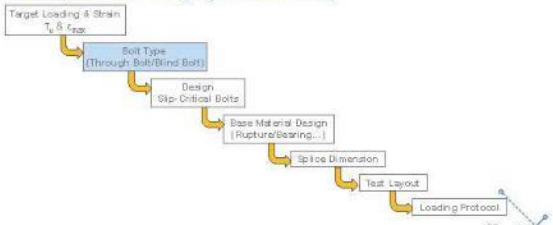
- (1) Typical Wind Load (Elastic Design)
  - Max. Load → T_a= Design Wind Load T_w
  - Targe Strain → Strain at Design Wind Load Level
- (2) Performance-Based Wind Design:
  - Max. Load = $T_a = R_y F_y A_g$
  - Targe Strain → $\varepsilon_{max} = 1.5\ \varepsilon_y = 0.003$
- (3) Seismic Load
  - Max. Load = $T_a = R_y F_y A_g$
  - Targe Strain → ε_{max} up to 4.0 ε_y or higher (until failure)

Commentary: Inelastic strain at 1.5 times section yield should be limited to approximately 10 cycles. Higher inelastic strains or number of inelastic cycles may be shown acceptable through testing. Higher number of lesser magnitude inelastic cycles are acceptable if shown through calculations or testing to result in stable behavior. Recognized methods

ASCE Performance-Based Wind Design

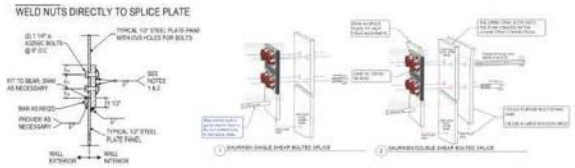
29

Test Specimen Design (Tension Test)



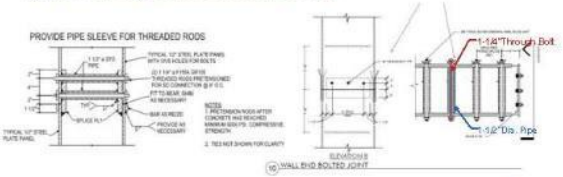
30

Type 1 Blind Blot



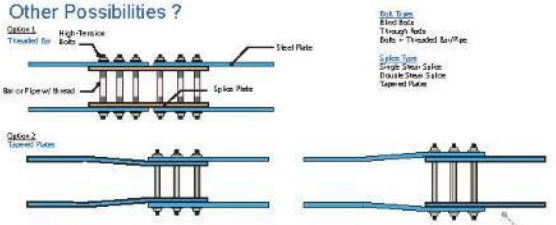
31

Type 2 Through Bolts with Inner Pipe



32

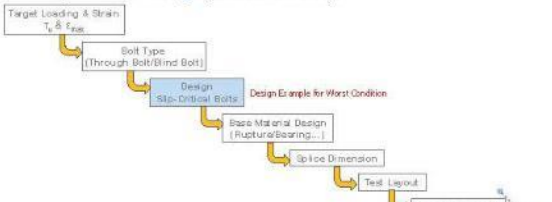
Other Possibilities ?



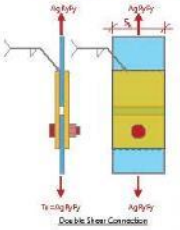
Bolt Types
Blind Bolts
Through Bolts
Bolts + Threaded Bar/Pipe

Splice Type
Single Shear Splice
Double Shear Splice
Tapered Plates

Test Specimen Design (Tension Test)



Double Shear Connection



Assume loading width=bolt lot/unit spacing = s_u (Unit in)

Welding Strength

t=0.5 in

$\phi R_n = 0.75x(1.5x0.6xX70 ksi)x(0.707xL/2xL_w)=31.83L_w$

$T_u=\phi A_g F_y F_y=(0.5 \times s_u)\times 1.1 \times 50 ksi=27.5s_u$

$L_w > 0.91s_u$

Bolt Strength (Slip-Critical Connection, Class A, μ=0.30)

Use bolt diameter = 1 in

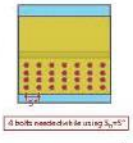
Slip-Critical (Double Shear)		
$Rn=\phi D_h T_b n_s \mu$	34.6	kips
$D_h=$	1.13	
$n_s=$	2	
$T_b=$	53	kips
$F_{nt}=$	2	
$\mu=$	0.3	

Assume bolts spacing=s_u=5 in

$T_u=\phi A_g F_y F_y=(0.5 \times 5)\times 1.1 \times 50 ksi=137.5$ kip

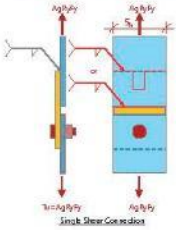
N.Bolts > $T_u \rightarrow$ N=3.9

Need 4 bolts.



4 bolts needed while using s_u=5"

Single Shear Connection



Assume loading width=bolt lot/unit spacing = s_u (Unit in)

Welding Strength

t=0.5 in

$\phi R_n = 0.75x(1.5x0.6xX70 ksi)x(0.707xL/2xL_w)=1.67L_w$

$T_u=\phi A_g F_y F_y=(0.5 \times s_u)\times 1.1 \times 50 ksi=27.5s_u$

$L_w > 1.65s_u$

Bolt Strength (Slip-Critical Connection, Class A, μ=0.30)

Use bolt diameter = 1 in

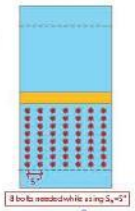
Slip-Critical (Single Shear)		
$Rn=\phi D_h T_b n_s \mu$	17.3	kips
$D_h=$	1.13	
$n_s=$	1	
$T_b=$	51	kips
$F_{nt}=$	1	
$\mu=$	0.3	

Assume bolts spacing=s_u=5 in

$T_u=\phi A_g F_y F_y=(0.5 \times 5)\times 1.1 \times 50 ksi=137.5$ kip

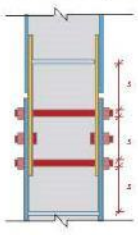
N.Bolts > $T_u \rightarrow$ N=8

Need 8 bolts



8 bolts needed while using s_u=5"

Tied Bar Spacing Issue



Steel Plate Slenderness (AISC 341-22 H7-6)

$$\frac{b}{t_p} \le 1.65\sqrt{\frac{E_s}{R_y F_y}}$$

Max. Tie Spacing Requirement (AISC 341-22 H7-7)

$$\frac{s}{t_p} \le 1.08\sqrt{\frac{E_s}{2\alpha+1}}$$

$$\alpha = 1.7\left[\frac{t_{sc}}{t_p} - 2\right]\frac{t_p}{w_{col}}$$

Max. Tie Spacing Requirement (AISC 341-16 H7-2)

$$w_1 = 1.08\sqrt{\frac{E}{F_y}}$$

Summary of S.C. Bolt Design

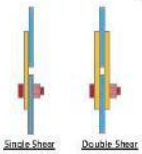
1. General Information

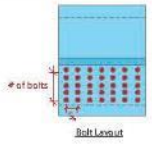
$n_s=$	1.0	bolt
$n_b=$	8.0	bolt
$n_{sh}=$	2.0	
L_w (in)		in
Bolt Dia.	1	in

2. Slip-Critical Bolt

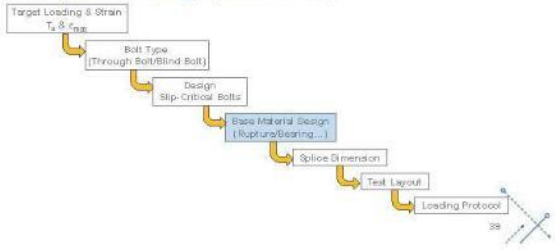
	Single Shear	
T_u (in)	T_u (kip)	# of bolts
2	55.0	3
4	110	5
5	137.5	8
6	165	10
7	192.5	12
8	220	12
9	247.5	15
10	275	18

	Double Shear	
T_u (in)	T_u (kip)	# of bolts
2	55.0	2
4	110	4
5	137.5	4
6	165	5
7	192.5	6
8	220	7
9	247.5	8
10	275	9



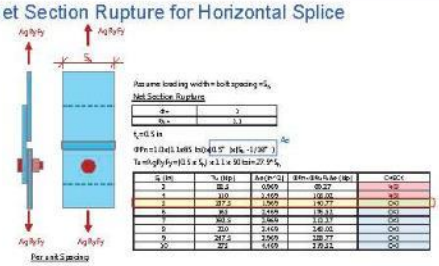


Test Specimen Design (Tension Test)



39

Net Section Rupture for Horizontal Splice



Assume loading width = bolt spacing = S_h

Net Section Rupture

Φ_n	1
R_n	1.1

t_p=0.5 in

$\Phi R_n = 1.0 x 1 x 1.65 x [0.5" (4$ S_h $-1/16")]$ F_u

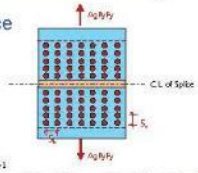
$T_n = 0.9 F_y A_g = 0.9 x F_y x 1 x 1 x 50 min ZF$ S_h

S_h (in)	T_n (kip)	A_{nt} (in^2)	$\Phi R_n = \Phi R_n F_u A_{nt}$ (kip)	CHECK
3	112.5	0.969	85.27	NG
4	150	1.469	108.01	NG
5	187.5	1.969	140.77	OK!
6	225	2.469	178.11	OK!
7	262.5	2.969	210.37	OK!
8	300	3.469	248.01	OK!
9	337.5	3.969	280.77	OK!
10	375	4.469	318.11	OK!

Per unit Spacing

40

Bearing and Tear-Out for Horizontal Splice



Φ=1

S_h (in)	T_n (kip)	S_v (in)	ΦR_n (kip)	# of bolts	R_n (in)	$\Phi R_n = 2.4 \Phi d t F_u + \Phi 1.2 L_c t F_u$ (kip)	$\Phi R_n = 2.4 \Phi d t F_u + \Phi 1.2 L_c t F_u$ (kip)	CHECK
3	112.5	1	1	3	2.34375	317.4	259.22	OK!
4	150	1	1	4	7.59375	343.2	312.37	OK!
5	187.5	1	1	4	7.59375	343.2	312.37	OK!
6	225	1	1	5	9.21875	429	390.46	OK!
7	262.5	1	1	6	10.84375	514.8	468.55	OK!
8	300	1	1	7	12.46875	600.6	546.64	OK!
9	337.5	1	1	8	14.09375	686.4	624.73	OK!
10	375	1	1	9	15.71875	686.4	624.73	OK!

41

DOUBLE-TEE MOMENT CONNECTIONS(Swanson et. al, 2000)

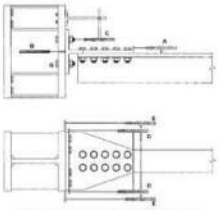


FIG. 5. Instrumentation Scheme for Component Tests

Because of the different stiffnesses of the components in tension and compression, a system of force and displacement limits was used for the cyclic tests.

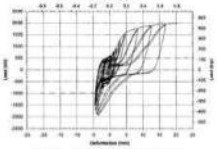


FIG. 6. Cyclic Force-Deformation Curve

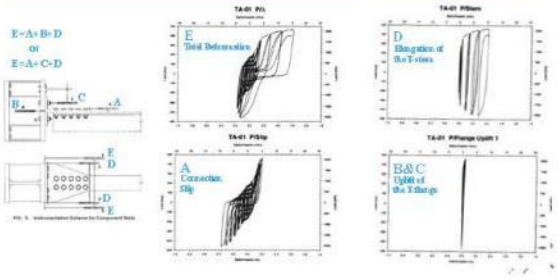
42

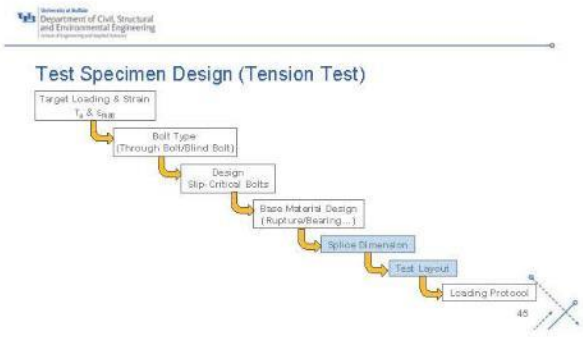
DOUBLE-TEE MOMENT CONNECTIONS(Swanson et. al, 2000)

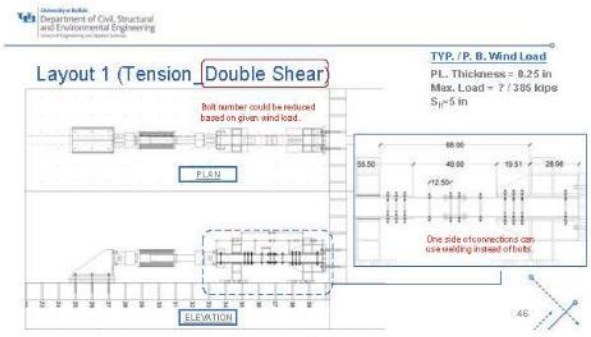
Test ID	Section	Bolt Designation	Tension Bolts #	Tension Bolts s (mm)	Tension Bolts g (mm)	Tension Bolts C_{slip} (kN)	Shear Bolts #	Shear Bolts s (mm)	Shear Bolts g (mm)	Shear Bolts C_{slip} (kN)	Loading	Failure Mode	Peak Load (kN)
TA-01	W16 x 100	7/8" - A490	8	76.20	101.60	353.8	10	88.68	88.90	213.7	Cyclic	Net Sec.	2010.2
TA-02	W16 x 100	7/8" - A490	8	76.20	127.00	340.6	10	88.68	88.90	213.7	Cyclic	Net Sec.	2030.2
TA-03	W16 x 100	7/8" - A490	8	76.20	152.40	340.6	10	88.68	88.90	213.7	Cyclic	T-Bolt	2006.5
TA-04	W16 x 100	7/8" - A490	8	76.20	177.80	340.6	10	88.68	88.90	224.9	Cyclic	T-Bolt	1728.8
TA-05	W16 x 100	7/8" - A490	8	76.20	101.60	340.6	10	88.68	88.90	213.7	Mono	Net Sec.	2105.4
TA-07	W16 x 100	7/8" - A490	8	76.20	152.40	340.6	10	88.68	88.90	213.7	Mono	T-Bolt	1930.4
TA-08	W16 x 100	1" - A490	8	76.20	101.60	441.2	8	76.20	88.90	284.7	Cyclic	Net Sec.	1924.0
TA-10	W16 x 100	1" - A490	8	76.20	127.00	441.2	8	76.20	88.90	284.7	Cyclic	Net Sec.	1897.3
TA-11	W16 x 100	1" - A490	8	76.20	152.40	441.2	8	76.20	88.90	284.7	Cyclic	Net Sec.	1860.1
TA-12	W16 x 100	1" - A490	8	76.20	177.80	441.2	8	76.20	88.90	284.7	Cyclic	Net Sec.	1807.4
TA-13	W16 x 100	1" - A325	8	76.20	101.60	383.2	8	76.20	88.90	239.3	Cyclic	Net Sec.	1903.7
TA-15	W16 x 100	1" - A325	8	76.20	152.40	383.2	8	76.20	88.90	239.3	Cyclic	Net Sec.	1891.8
TA-17	W16 x 100	7/8" - A490	4	203.20	101.60	340.6	10	88.68	88.90	213.7	Cyclic	T-Bolt	1403.1
TA-18	W16 x 100	7/8" - A490	4	203.20	127.00	340.6	10	88.68	88.90	213.7	Cyclic	T-Bolt	1297.5
TA-19	W16 x 100	7/8" - A490	4	203.20	152.40	340.6	10	88.68	88.90	213.7	Cyclic	T-Bolt	1144.9
TA-20	W16 x 100	7/8" - A490	4	203.20	177.80	340.6	10	88.68	88.90	213.7	Cyclic	T-Bolt	1043.8
TA-25	W16 x 100	1" - A490	4	76.20	101.60	441.2	8	88.68	88.90	284.7	Cyclic	Net Sec.	1847.9
TA-26	W16 x 100	1" - A490	4	76.20	101.60	441.2	8	63.50	88.90	284.7	Cyclic	Bik Shr	1771.9

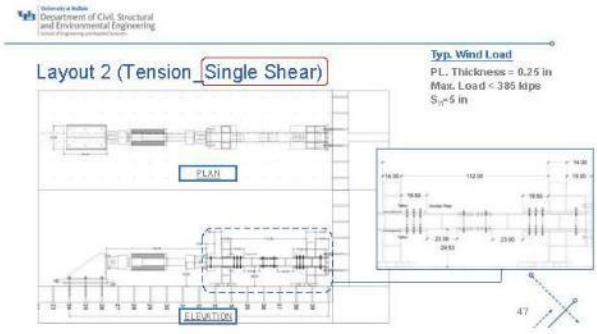
43

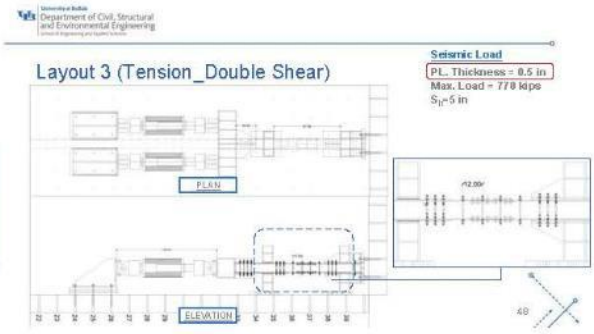
Swanson et. al, 2000

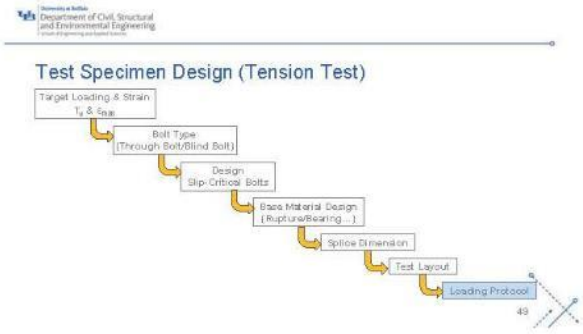


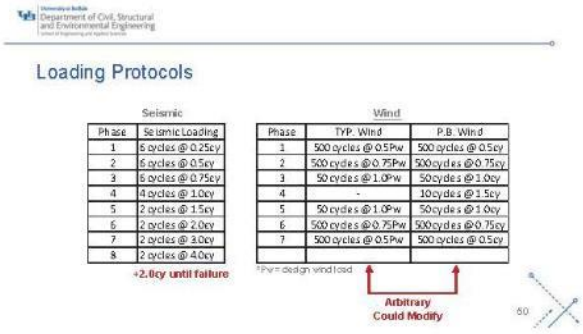

Department of Civil, Structural and Environmental Engineering
Test Specimen Design (Tension Test)
Target Loading & Strain
Bolt Type (Through Bolt/Blind Bolt)
Design Slip Critical Bolts
Base Material Design (Rupture/Bearing...)
Splice Dimension
Test Layout
Loading Protocol
45


Department of Civil, Structural and Environmental Engineering
Layout 1 (Tension_Double Shear)
TYP. /P. B. Wind Load
PL. Thickness = 0.25 in
Max. Load = ? / 385 kips
Bolt number could be reduced based on given wind load.
PLAN
ELEVATION
One side of connections can use welding instead of bolts
46


Department of Civil, Structural and Environmental Engineering
Layout 2 (Tension_Single Shear)
Typ. Wind Load
PL. Thickness = 0.25 in
Max. Load < 385 kips
PLAN
ELEVATION
47


Department of Civil, Structural and Environmental Engineering
Layout 3 (Tension_Double Shear)
Seismic Load
PL. Thickness = 0.5 in
Max. Load = 770 kips
PLAN
ELEVATION
48

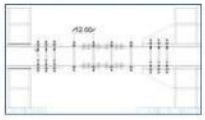

Department of Civil, Structural and Environmental Engineering
Test Specimen Design (Tension Test)
Target Loading & Strain
Bolt Type (Through Bolt/Blind Bolt)
Design Slip Critical Bolts
Base Material Design (Rupture/Bearing...)
Splice Dimension
Test Layout
Loading Protocol
49


Department of Civil, Structural and Environmental Engineering
Loading Protocols
Seismic
Phase | Seismic Loading
1 | 6 cycles @ 0.25cy
2 | 6 cycles @ 0.5cy
3 | 6 cycles @ 0.75cy
4 | 4 cycles @ 1.0cy
5 | 2 cycles @ 1.5cy
6 | 2 cycles @ 2.0cy
7 | 2 cycles @ 3.0cy
8 | 2 cycles @ 4.0cy
+2.0cy until failure
Wind
Phase | TYP. Wind | P.B. Wind
1 | 500 cycles @ 0.5Pw | 500 cycles @ 0.5cy
2 | 500 cycles @ 0.75Pw | 500 cycles @ 0.75cy
3 | 50 cycles @ 1.0Pw | 50 cycles @ 1.0cy
4 | - | 10 cycles @ 1.5cy
5 | 50 cycles @ 1.0Pw | 50 cycles @ 1.0cy
6 | 500 cycles @ 0.75Pw | 500 cycles @ 0.75cy
7 | 500 cycles @ 0.5Pw | 500 cycles @ 0.5cy
*Pw = design wind load
Arbitrary
Could Modify
50

Summary of Specimens for Tension Test

Specimen	Layout	Load Type	Bolt Type	End Block (width)	Plate Th. (in)	Web Width (in)	Max. Load (kip)
1	1	F.S. Wind	Blind Bolt	4	0.25	14	386
2	1	F.S. Wind	Through Bolt	4	0.25	14	386
3	2	TYP. Wind	Blind Bolt	?	0.25	14	?
4	2	TYP. Wind	Through Bolt	?	0.25	14	?
5	3	F.S. Wind	Blind Bolt	4	0.5	14	770
6	3	Seismic	Blind + Through	4	0.5	14	770

Adjustable Combination



TENSION TEST DESIGN
SHEAR TEST DESIGN

Test Specimen Design (Shear Test)

- Target Loading & Strain V_u & γ_{max}
- Bolt Type (Through Bolt/Blind Bolt)
- Design Slip Critical Bolts
- Base Material Design (Rupture…)
- Splice Dimension
- Test Layout
- Loading Protocol

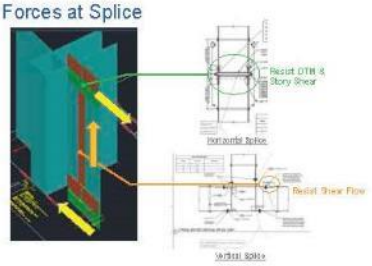
Test Specimen Design (Shear Test)

- Target Loading & Strain V_u & γ_{max}
- Bolt Type (Through Bolt/Blind Bolt)
- Design Slip Critical Bolts
- Base Material Design (Rupture…)
- Splice Dimension
- Test Layout
- Loading Protocol

Target Load and Strain

- (1) Typical Wind Load (Elastic Design)
  Max. Load → ?
- (2) Performance-Based Wind Design
- (3) Seismic Load

Shear Forces at Splice



Target Load and Strain

- (1) Typical Wind Load (Elastic Design)
  Max. Load → V_t= Design Wind Load V_e ?
- (2) Performance-Based Wind Design
  Max. Load = $V_t = 0.6 R_y F_y A_g$
  Targe Strain → γ_{max}=1.5 γ_y=0.003
- (3) Seismic Load
  Max. Load = $V_t = 0.6 R_y F_y A_g$
  Targe Strain → γ_{max} up to 4.0 γ_y or higher

Commentary: Inelastic slopes of 1.5 times section yield should be limited to approximately 10 cycles. Higher inelastic strains or number of inelastic cycles may be shown acceptable through testing. Higher number of lesser magnitude inelastic cycles are acceptable if shown through calculations or testing to result in stable behavior. Recognized methods

ASCE Performance-Based Wind Design

57

Test Specimen Design (Shear Test)

Target Loading & Strain
$V_e \leq V_{max}$

→ Bolt Type (Through Bolt/Blind Bolt)

→ Design Slip-Critical Bolts

→ Base Material Design (Rupture...)

→ Splice Dimension

→ Test Layout

→ Loading Protocol

58

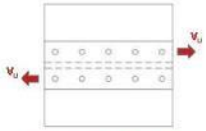
Slip-Critical Bolt Design

Slip-Critical Bolt Design

N_s =	10	bolt
N_b =	02	bolt
N_p =	1.5	
μ (Class A)	0.3	in
Bolt Dia.	1	in

Slip-Critical (Single Shear)		
$\Phi R_n = \phi D h^2 \mu N_s N_p$ =	37.3	kips
C_1 =	1.13	
N_s =	1	
T_b =	51	kips
n_b =	1	
μ =	0.3	

Slip-Critical (Double Shear)		
$\Phi R_n = \phi D h^2 \mu N_s N_p$ =	74.6	kips
C_1 =	1.13	
N_s =	1	
T_b =	51	kips
n_b =	2	
μ =	0.3	



Number of Bolts=$V_u/\Phi R_n$

59

Base Material Design and Expected Shear Strength

A. Typical Arrangement

Gap (in)	s_1 (in)	Bolt Number n_x	Bolt Number n_y	Z_x (in)	Z_y (in)
	3	2	2	3	3
Wall Width (in)	Wall Thickness (in)	S_x (in)	Bolt Dia. (in)	F_y (ksi)	F_u (ksi)
24	1	6.00	1	50	65
ΣY_i^2 (in^2)	Σz_i (ksi)	S_y (ksi)	A_{gv} (in^2)	A_{nt} (in^2)	
2100	25500	3000	13800	7	161

Assume 50% R_y=0.6 F_y/F_{ue} ?

B. Bolt Shear Strength

Bolt Composite		
V_{bn}= R_y0.6 F_{ub} A_b =	221.00	kips
Concrete		
R_y =	29000	
E_c =	2000	
f'_c =	7075.42	
E_s =	29000000	
$V_n = A_{gv}(F_y/\sqrt{3}) + 0.5 f'_c A_{nt} \sqrt{E_c/E_s} \leq 0.6 F_u A_{nv}$ =	345.32	kips

(AISC 360, J4.2)

C. Check Number of Bolts

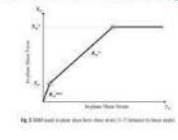
Load Type =	TYP. Wind	
Bolt Type=	Bearing-Shear	
ΦR_n =	34.378	kips
Composite or not?	Non-Composite	
Required Bolt #=	6	

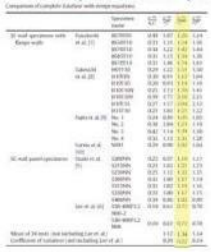
D. Base Material Design (TYP. Wind Design)

A_{gv} =	7.00	in^2				
A_{nt} =	3.41	in^2				
$\Phi R_n = \phi 0.6 A_{gv} F_y$ =	210	kips	>	W	OK	
$\Phi R_n = \phi 0.6 A_{nt} F_u$ =	187.84	kips	>	W	OK	

60

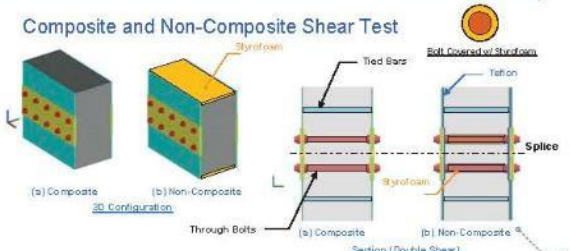
In-Plane Shear Strength of C-PSW (Varma et al. (2014))



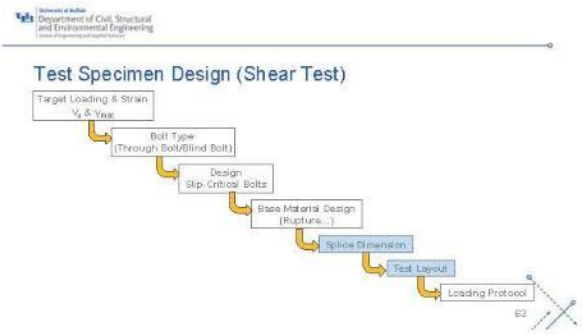


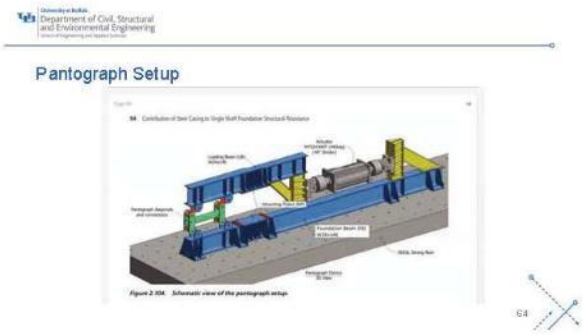
61

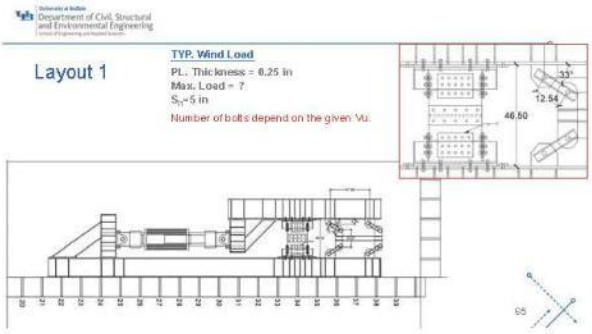
Composite and Non-Composite Shear Test

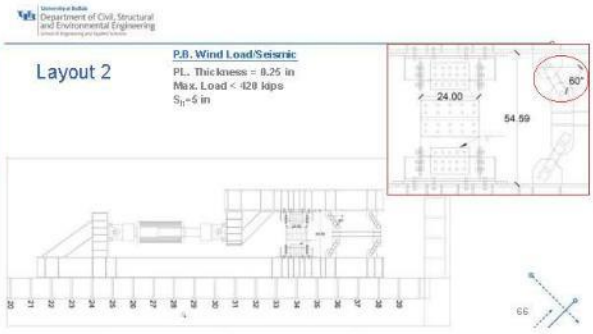


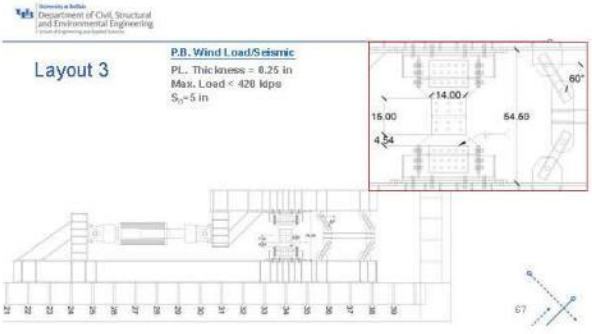
62

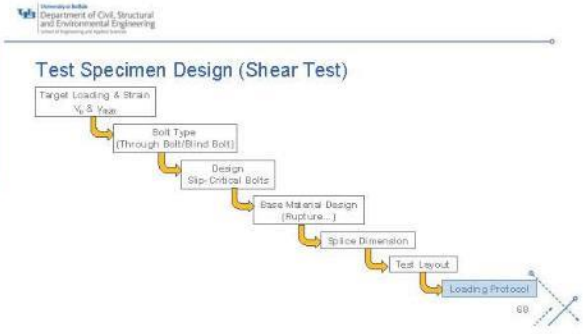

Department of Civil, Structural and Environmental Engineering
Test Specimen Design (Shear Test)
Target Loading & Strain
Bolt Type (Through Bolt/Blind Bolt)
Design Slip Critical Bolts
Base Material Design (Rupture...)
Splice Dimension
Test Layout
Loading Protocol
63


Department of Civil, Structural and Environmental Engineering
Pantograph Setup
64


Department of Civil, Structural and Environmental Engineering
Layout 1
TYP. Wind Load
PL. Thickness = 0.25 in
Max. Load = ?
Sh=5 in
Number of bolts depend on the given Vu.
33°
12.54
46.59
65


Department of Civil, Structural and Environmental Engineering
Layout 2
P.B. Wind Load/Seismic
PL. Thickness = 0.25 in
Max. Load < 420 kips
Sh=5 in
60°
24.00
54.59
66


Department of Civil, Structural and Environmental Engineering
Layout 3
P.B. Wind Load/Seismic
PL. Thickness = 0.25 in
Max. Load < 420 kips
Sh=5 in
60°
14.00
15.00
54.59
4.54
67


Department of Civil, Structural and Environmental Engineering
Test Specimen Design (Shear Test)
Target Loading & Strain
Bolt Type (Through Bolt/Blind Bolt)
Design Slip Critical Bolts
Base Material Design (Rupture...)
Splice Dimension
Test Layout
Loading Protocol
68

Department of Civil, Structural and Environmental Engineering

Loading Protocols

Seismic

Phase	Seismic Loading
1	6 cycles @ 0.25yy
2	6 cycles @ 0.5yy
3	6 cycles @ 0.75yy
4	4 cycles @ 1.0yy
5	2 cycles @ 1.5yy
6	2 cycles @ 2.0yy
7	2 cycles @ 3.0yy
8	2 cycles @ 4.0yy

+2.0yy until failure

Wind

Phase	TYP. Wind	P.B. Wind
1	500 cycles @ 0.5Pw	500 cycles @ 0.5yy
2	500 cycles @ 0.75Pw	500 cycles @ 0.75yy
3	50 cycles @ 1.0Pw	50 cycles @ 1.0yy
4	-	30 cycles @ 1.5yy
5	50 cycles @ 1.0Pw	50 cycles @ 1.0yy
6	500 cycles @ 0.75Pw	500 cycles @ 0.75yy
7	500 cycles @ 0.5Pw	500 cycles @ 0.5yy

*Pw = design wind load

Arbitrary
Could Modify

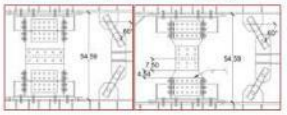
69

Department of Civil, Structural and Environmental Engineering

Summary of Specimens for Shear Test

Specimen	Layout	Load Type	Bolt Type	Shear Interface	Bolt Number (N*W)	Plate Th. (in)	Wall Width (in)	Composite ?	Max. Load (kip)
1	1	TYP. Wind	Bilad Bolt	Sliga /Double ?	?	0.25	?	X	?
2	1	TYP. Wind	Tkoega Bolt	Sliga /Double ?	?	0.25	?	X	?
3	2	P.B. Wind	Bilad Bolt	Double	5x2	0.25	24	X	396
4	2	Seism ic	Bilad Bolt	Double	5x2	0.25	24	X	396
5	3	Seism ic	Bilad Bolt	Double	3x2	0.25	14	X	231
6	3	Seism ic	Bilad Bolt	Double	3x2	0.25	14	V	373

Adjustable Combination



70

Department of Civil, Structural and Environmental Engineering

What Need To Be Decided Today

Item	Question	Decision
1	Specific connection details to be in the test? (Type of Splice and Bolt)	
2	Loading Protocol for Tension/Shear Test (TYP. Wind/P. B. Wind/Seismic)	
3	Specific requirements for geometry? (Test Layout, Wall width, thickness, etc.)	

71

Appendix B.

PowerPoint slides presented at second Project Advisory Group

(December 9, 2021)

BOLTED SPLICE DETAILS FOR COMPOSITE PLATE SHEAR WALLS—CONCRETE FILLED

Jia-Hau Liu
Michel Bruneau

Date: 12/8/2021

University at Buffalo
Department of Civil, Structural and Environmental Engineering



Objectives of this Meeting

- Review proposed connection details for tension and shear tests
  - Budgeted for 4 tests of each but may be able to do 6 tension + 6 shear
- Review proposed loading protocol
- Green light to finalize test set-up design
- Discuss timetable (to reserve lab space accordingly)
  - Drawing submission by UB
  - Fabrication schedule

University at Buffalo
Department of Civil, Structural and Environmental Engineering

Research Project Objectives and Constraints

- Based on input from previous Project Advisory Group Meeting and further discussions with Sponsor:
  - Focus is on developing details to resist wind (not seismic) for cities like Chicago
    1. Priority is strength-based wind resistance (satisfactory performance and no failure of specimens at design strength)
    2. Testing of specimens to continue to investigate Performance-Based Wind Resistance, with the 1.5δ_y target referring to yielding inside the splice zone (requires setting-up a hierarchy of limit states)
  - Number of bolts in splice to be minimized
  - One of the specimens in tension and one of the specimens in shear to have Shurliken connectors (only 3/4" diameter available in U.S.)
  - Minimum plate thickness of specimen = 3/8" (if possible)
  - Slip-critical strength maybe not necessary

University at Buffalo
Department of Civil, Structural and Environmental Engineering

Considered Limit States in Bolted Connections

Limit States Deemed Non-Ductile	Limit States Deemed "Ductile"
Bolt Shear Failure	Sliding
Tear-out (1.2 Lc t Fu)	Bearing (2.4dtFu)
Net Section Failure (AeFu)	Net Section Yielding (AeFy)
Fillet Weld Strength	Gross Section Yielding (AgFy)

* (RyFy) and (RuFu) actually used in all calculations

University at Buffalo
Department of Civil, Structural and Environmental Engineering

Proposed Connection Details (Nomenclature)

MKA original details	Proposed Details for Testing Splices		
	Tension Testing of Splices	Shear Testing of Splices	
		Non-Composite (Forced, for comparison purpose)	Composite (Expected Behavior)
Type 1	Case 1 1A: Bearing Strength 1B: Slip + AeFy 1C: AgFy (option)	Case 5 5A: Bearing Strength 5B: Slip + 0.6 AeFy 5C: 0.6 AgFy (option)	Case 5 5Ac: Bearing Strength 5Bc: Slip + 0.6 AeFy 5Cc: 0.6 AgFy (option)
Type 2	Case 2 2A: Bearing Strength 2B: Slip + AeFy 2C: AgFy (option)	Case 6 6A: Bearing Strength 6B: Slip + 0.6 AeFy 6C: 0.6 AgFy (option)	Case 6 6Ac: Bearing Strength 6Bc: Slip + 0.6 AeFy 6Cc: 0.6 AgFy (option)
-	Case 4 (composite strength)		

* ACase 3 considered earlier has been eliminated

University at Buffalo
Department of Civil, Structural and Environmental Engineering

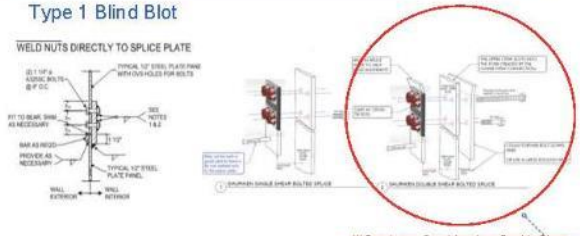
Proposed Connection Details (Nomenclature)

MKA original details	Proposed Details for Testing Splices		
	Tension Testing of Splices	Shear Testing of Splices	
		Non-Composite (Forced, for comparison purpose)	Composite (Expected Behavior)
Type 1	Case 1 1A: Bearing Strength 1B: Slip + AeFy 1C: AgFy (option)	Case 5 5A: Bearing Strength 5B: Slip + 0.6 AeFy 5C: 0.6 AgFy (option)	Case 5 5Ac: Bearing Strength 5Bc: Slip + 0.6 AeFy 5Cc: 0.6 AgFy (option)
Type 2	Case 2 2A: Bearing Strength 2B: Slip + AeFy 2C: AgFy (option)	Case 6 6A: Bearing Strength 6B: Slip + 0.6 AeFy 6C: 0.6 AgFy (option)	Case 6 6Ac: Bearing Strength 6Bc: Slip + 0.6 AeFy 6Cc: 0.6 AgFy (option)
-	Case 4 (composite strength)		

* ACase 3 considered earlier has been eliminated

Department of Civil, Structural and Environmental Engineering

Type 1 Blind Blot

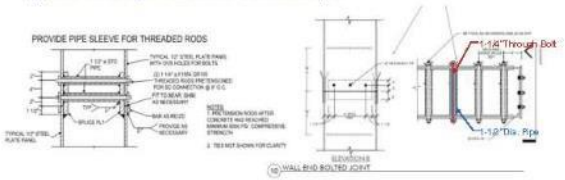


All Specimens Considered are Double Shear

8

Department of Civil, Structural and Environmental Engineering

Type 2 Through Bolts with Inner Pipe

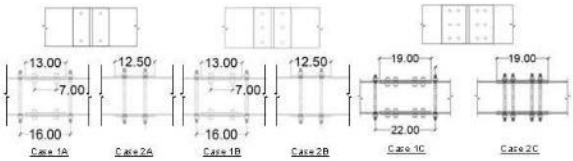


10

Department of Civil, Structural and Environmental Engineering

Case 1 and 2

Case 1: Blind Bolts A: Bearing Control C: Tu=RyFyAg
Case 2: Thru. Bolts B: Slip-Critical Control

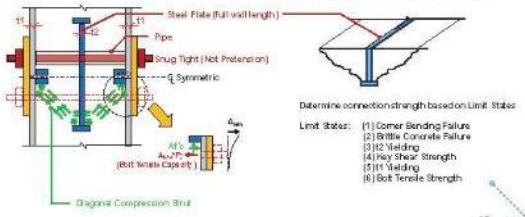


12

Department of Civil, Structural and Environmental Engineering

Strut Model Connection (Case 4)

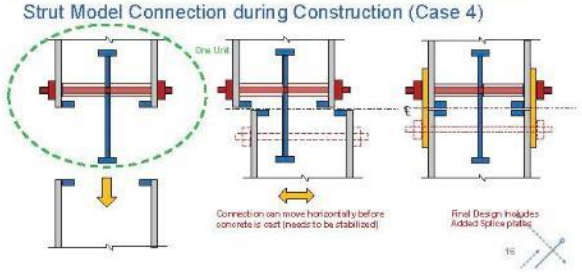
Use a Compression Strut in the Concrete to resist the tensile force from OTM



15

Department of Civil, Structural and Environmental Engineering

Strut Model Connection during Construction (Case 4)



16

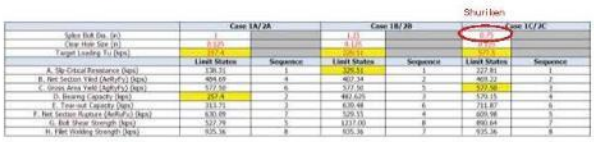
Department of Civil, Structural and Environmental Engineering

Design Approach

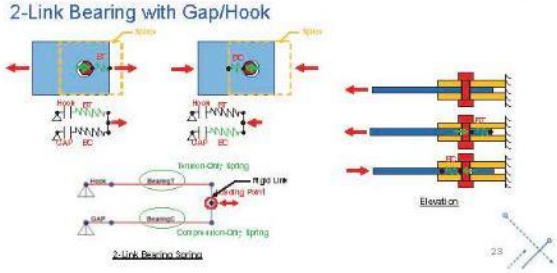
- Cases 1 and 2 are designed as standard steel component
  - Strength-based approach using standard AISC-360 equations for each limit state
  - Hysteretic spring models used for each part of the wall and modeled in SAP2000 to predict possible hierarchy of yielding and development of extended elastic range
- Case 4
  - Simplified design models for hand calculation
  - Simplified finite element model
  - Composited finite element models to validate expected behavior

17

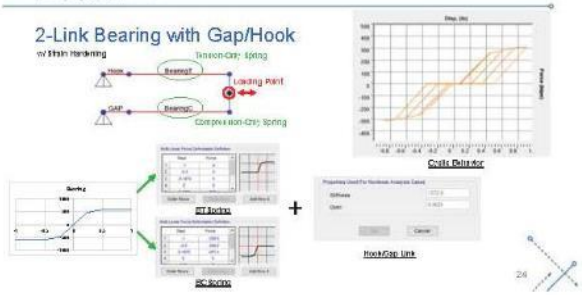
Summary of Case 1/2 A/B/C



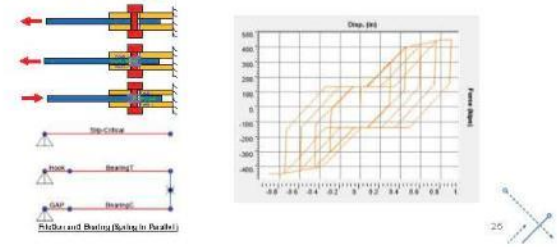
2-Link Bearing with Gap/Hook



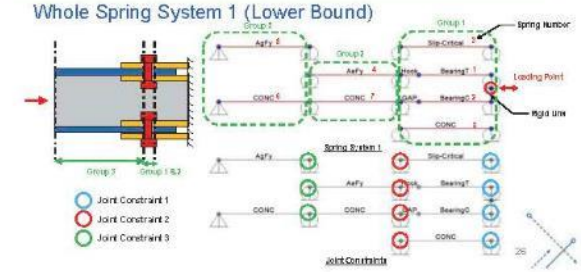
2-Link Bearing with Gap/Hook



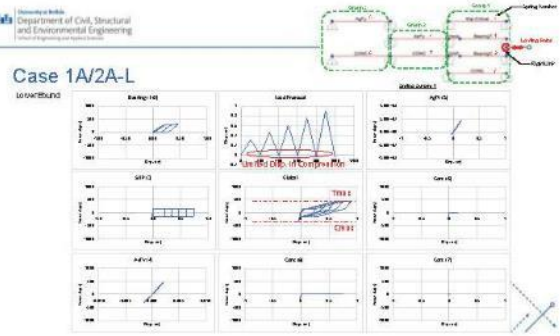
Friction + Bearing

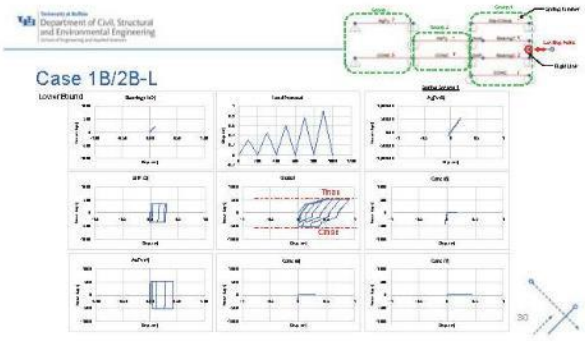


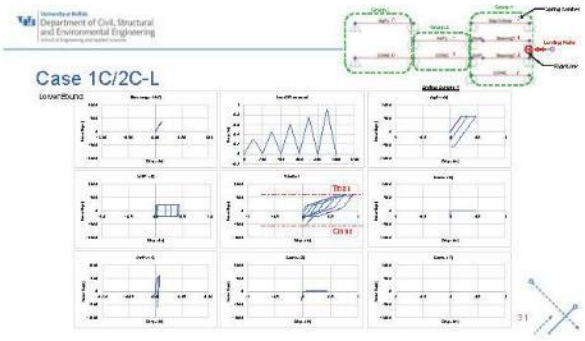
Whole Spring System 1 (Lower Bound)

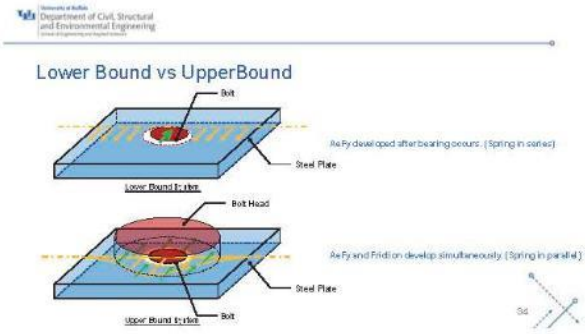


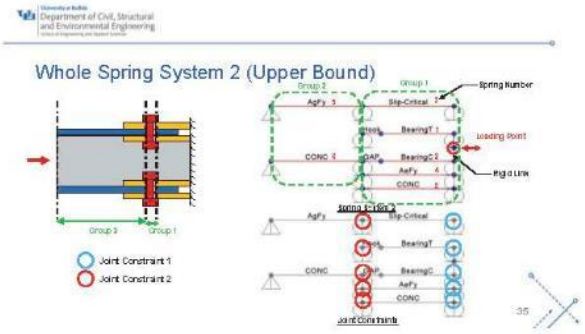
Case 1A/2A-L

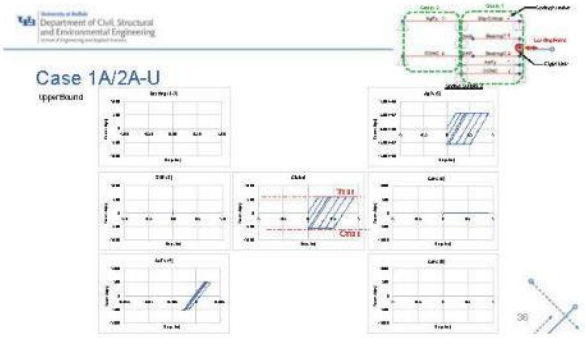


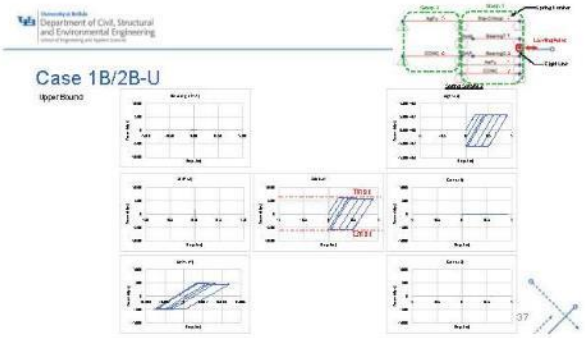

Department of Civil, Structural and Environmental Engineering
Case 1B/2B-L
Lower Bound
Thick
Case
30

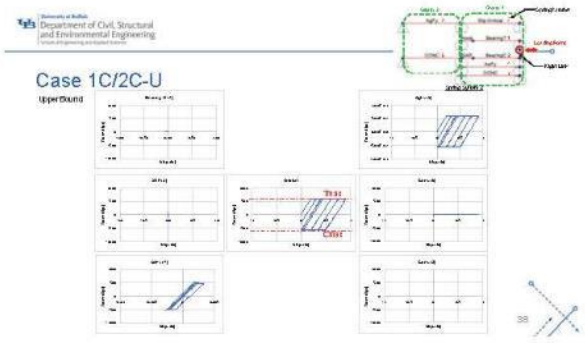

Department of Civil, Structural and Environmental Engineering
Case 1C/2C-L
Lower Bound
Thick
Case
31

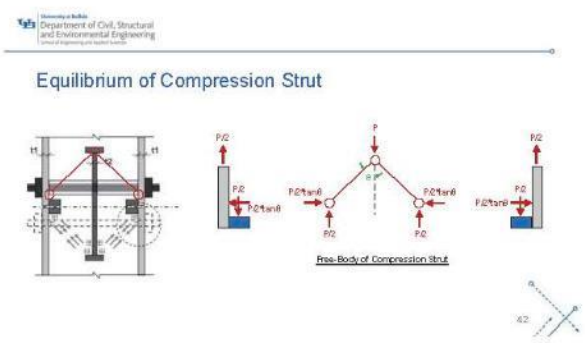

Department of Civil, Structural and Environmental Engineering
Lower Bound vs UpperBound
Bolt
As Fy developed after bearing occurs. (Spring in series)
Steel Plate
Lower Bound Strike
Bolt Head
As Fy and Friction develop simultaneously. (Spring in parallel)
Steel Plate
Upper Bound Strike
Bolt
34

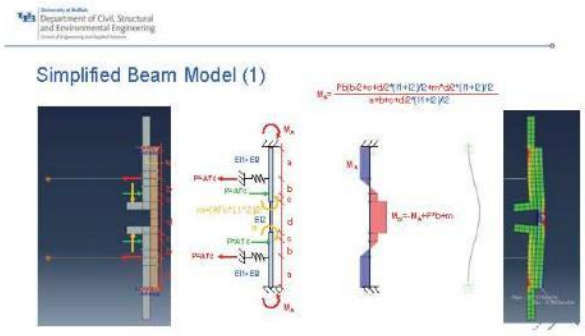

Department of Civil, Structural and Environmental Engineering
Whole Spring System 2 (Upper Bound)
Group 3
Group 1
Joint Constraint 1
Joint Constraint 2
Spring Number
Slip-Critical
BearingT
Loading Point
BearingC
AsFy
CONC
Rigid Link
Spring Set 2
Joint Constraints
35

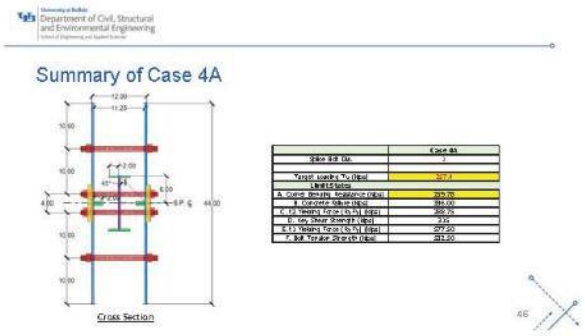

Department of Civil, Structural and Environmental Engineering
Case 1A/2A-U
UpperBound
Thick
Case
36

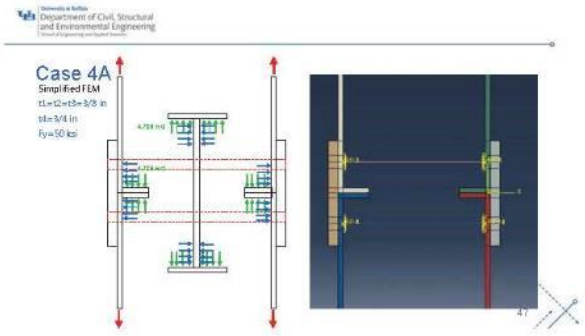

Department of Civil, Structural and Environmental Engineering
Case 1B/2B-U
UpperBound
Thick
Case
37

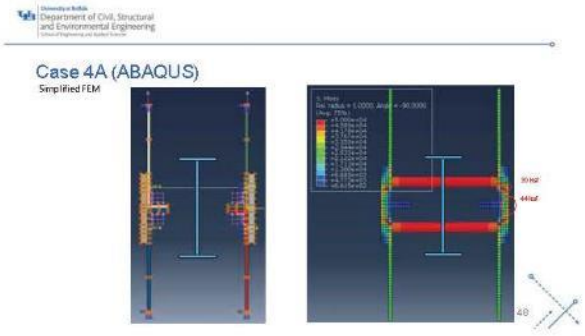

Department of Civil, Structural and Environmental Engineering
Case 1C/2C-U
Upper Bound


Department of Civil, Structural and Environmental Engineering
Equilibrium of Compression Strut
Free-Body of Compression Strut


Department of Civil, Structural and Environmental Engineering
Simplified Beam Model (1)


Department of Civil, Structural and Environmental Engineering
Summary of Case 4A
Cross Section

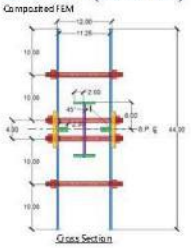

Department of Civil, Structural and Environmental Engineering
Case 4A
Simplified FEM


Department of Civil, Structural and Environmental Engineering
Case 4A (ABAQUS)
Simplified FEM

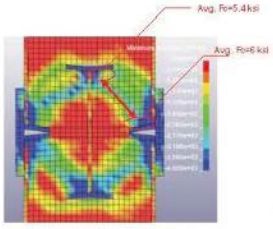
Department of Civil, Structural and Environmental Engineering

Case 4A-1 (LS-DYNA)

Composited FEM



Cross Section

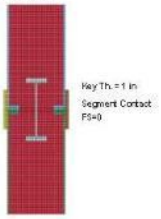


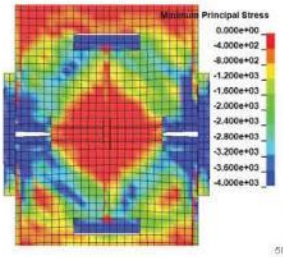
Min. Principal Stress

Department of Civil, Structural and Environmental Engineering

Case 4A-2 (LS-DYNA)

Composited FEM

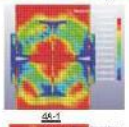




Department of Civil, Structural and Environmental Engineering

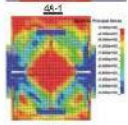
Case 4A-1 vs 4A-2 (LS-DYNA)

Key Th.= 3/8"

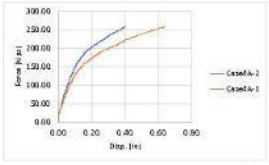


4A-1

Key Th.= 1"



4A-2



Department of Civil, Structural and Environmental Engineering

Proposed Connection Details (Nomenclature)

MKA original details	Proposed Details for Testing Splices		
	Tension Testing of Splices	Shear Testing of Splices	
		Non-Composite (Forced, for comparison purpose)	Composite (Expected Behavior)
Type 1	Case 1 1A: Bearing Strength 1B: Slip + AeFy 1C: AgFy (option)	Case 5 5A: Bearing Strength 5B: Slip + 0.6 AeFy 5C: 0.6 AgFy (option)	Case 5 5Ac: Bearing Strength 5Bc: Slip + 0.6 AeFy 5Cc: 0.6 AgFy (option)
Type 2	Case 2 2A: Bearing Strength 2B: Slip + AeFy 2C: AgFy (option)	Case 6 6A: Bearing Strength 6B: Slip + 0.6 AeFy 6C: 0.6 AgFy (option)	Case 6 6Ac: Bearing Strength 6Bc: Slip + 0.6 AeFy 6Cc: 0.6 AgFy (option)
-	Case 4 (composite strength)		

* ACase 3 considered earlier has been eliminated

Department of Civil, Structural and Environmental Engineering

Design Approach

- Cases 5 and 6 are designed as standard steel component
  - Strength-based approach using standard AISC-360 equations for each limit state
  - Some additional checks performed for diagonal tension field in steel
  - Finite element models to validate expected behavior

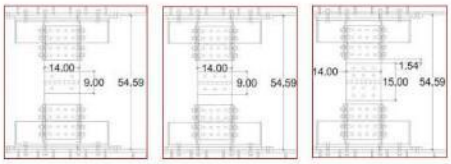
Department of Civil, Structural and Environmental Engineering

Case 5 and 6

Case 5: Blind Bolts
Case 6: Thru. Bolts

A: Bearing Control
B: Slip-Critical Control

C: Vu=0.6RyFyAg
c: Composited

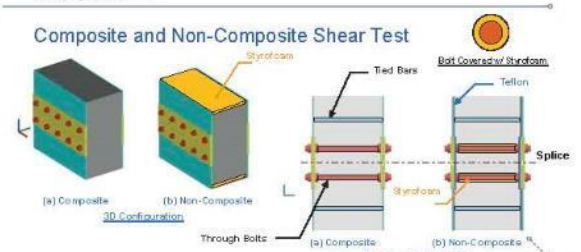


Case 5A/6A
5Ac/6Ac

Case 5B/6B
5Bc/6Bc

Case 5C/6C
5Cc/6Cc

Composite and Non-Composite Shear Test



Summary of Shear Test (1)

Shear Test

Shuri ben

	Case 5A/6A, 5Ac/6Ac		Case 5B/6B, 5Bc/6Bc		Case 5C/6C, 5Cc/6Cc	
ts (in)	0.375		0.375		0.375	
Bolts' Bolt Dia. (in)	0.75		0.75		0.875	
Gage Hole Size (in)	0.938		0.938		0.938	
Target Loading Vu (kips)	333.4		333.4		333.4	
	Limit States	Sequence	Limit States	Sequence	Limit States	Sequence
A. Slip-Critical Resistance (kips)	138.23	1	138.23	1	169.64	1
B. Net Section Yield (0.6AgFy) (kips)	260.63	4	260.63	2	260.63	2
C. Gross Area Yield (0.6AgFy) (kips)	346.50	5	346.50	4	346.50	3
D. Bearing Capacity (kips)	337.4	3	288.576	3	403.45	4
E. Tear-out Capacity (kips)	433.29	9	367.20	8	733.20	8
F. Bolt Tear-out & Bearing (kips)	289.55	3	337.96	5	514.80	7
G. Net Section Rupture (0.6AeFu) (kips)	338.06	6	362.89	6	362.89	4
H. Bolt Shear Strength (kips)	447.79	8	483.31	7	1210.56	9
I. Composite Shear Strength (kips)	480.48	7	480.48	9	341.33	5

Case 5 : Blind Bolts
Case 6 : Thru. Bolts
A : Bearing Control
B: Slip-Critical Control
C: Vu=0.6 Fy*Ag
c : Composite

Summary of Shear Test (2)

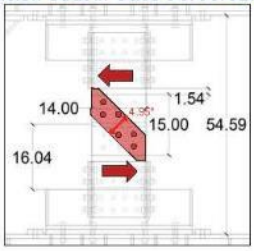
Shear Test

Shuri ben

	Case 5A/6A, 5Ac/6Ac		Case 5B/6B, 5Bc/6Bc		Case 5C/6C, 5Cc/6Cc	
ts (in)	0.375		0.375		0.375	
Bolts' Bolt Dia. (in)	0.75		0.75		0.875	
Gage Hole Size (in)	0.938		0.938		0.938	
Target Loading Vu (kips)	333.4		333.4		333.4	
	Limit States	Sequence	Limit States	Sequence	Limit States	Sequence
A. Slip-Critical Resistance (kips)	138.23	1	138.23	1	169.64	1
B. Net Section Yield (0.6AeFu) (kips)	260.63	4	260.63	2	260.63	2
C. Gross Area Yield (0.6AgFy) (kips)	346.50	5	346.50	4	346.50	3
D. Bearing Capacity (kips)	337.4	3	288.576	3	403.45	4
E. Tear-out Capacity (kips)	433.29	9	367.20	8	733.20	8
F. Bolt Tear-out & Bearing (kips)	289.55	3	337.96	5	514.80	7
G. Net Section Rupture (0.6AeFu) (kips)	338.06	6	362.89	6	362.89	4
H. Bolt Shear Strength (kips)	447.79	8	483.31	7	1210.56	9
I. Composite Shear Strength (kips)	480.48	7	480.48	9	341.33	5

Case 5 : Blind Bolts
Case 6 : Thru. Bolts
A : Bearing Control
B: Slip-Critical Control
C: Vu=0.6 Fy*Ag
c : Composite

Tension Strut in Case 5C/6C/5D/6D



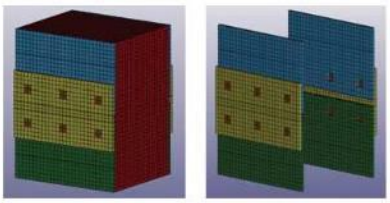
Tension Strut Force
Pu=(0.25*x4.95")x55 ksi=68 kips

Bearing Check
Rn1=2.4dtRuFu=2.4x0.875x0.25x1.1x65x3=112.6 kips > Pu

Edge Tear-Out Check
Lc=2.8"
Rn2= 1.2LctFu=1.2x2.8x0.25x1.1x65x2=120.1 kips > Pu

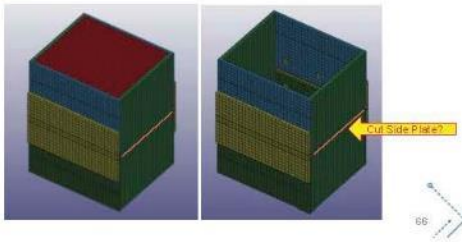
Case 6B-1 (ts=3/8", width=14", no Side Plate)

FE Model



Case 6B-2 (ts=3/8", width=14", Side Plate=0.5")

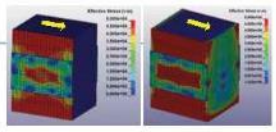
FE Model

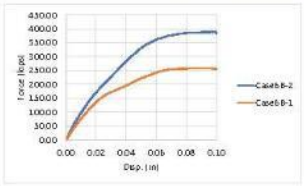


Case 6B-1 vs 6B-2

Expected Shear Strength (Steel Only)

Vn,steel=0.6FyFy
=0.6x(14x0.375x2)x50=315 kips



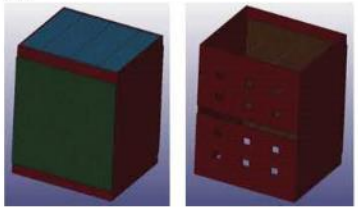


67

Case 6C

(ts=1/4", width=14", Side Plate=1/4")

FE Model

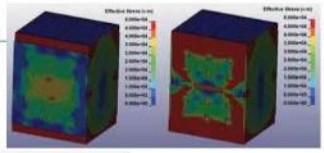


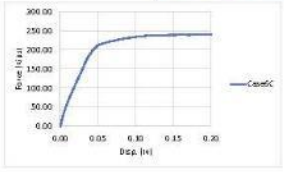
68

Case 6C

Expected Shear Strength (Steel Only)

Vn,steel=0.6FyFy
=0.6x(14x0.25x2)x50=210 kips





69

Loading Protocols

If τ_y is less clear (e.g. bearing)

If τ_y is well defined (as in $A_w F_y$)

P_w = design wind load for Tension/Shear

Tension

Phase	TYP. Wind	P.B. Wind
1	10 cycles @ 0.5 P_w	10 cycles @ 0.5τ_y
2	10 cycles @ 0.75 P_w	10 cycles @ 0.75τ_y
3	10 cycles @ 1.0 P_w	10 cycles @ 1.0τ_y
4	-	10 cycles @ 1.5τ_y
5	-	10 cycles @ 2.0τ_y
6	-	10 cycles @ 3.0τ_y
7	-	10 cycles @ 4.0τ_y
8	-	10 cycles @ 5.0τ_y

Keep increasing until failure

Phase	TYP. Wind	P.B. Wind/Seismic
1	10 cycles @ 0.5 P_w	10 cycles @ 0.5τ_y
2	10 cycles @ 0.75 P_w	10 cycles @ 0.75τ_y
3	10 cycles @ 1.0 P_w	10 cycles @ 1.0τ_y
4	-	10 cycles @ 1.5τ_y
5	-	2 cycles @ 2.0τ_y
6	-	2 cycles @ 3.0τ_y
7	-	2 cycles @ 4.0τ_y
8	-	2 cycles @ 5.0τ_y

Keep increasing until failure

Shear

Phase	TYP. Wind	P.B. Wind
1	10 cycles @ 0.5 P_w	10 cycles @ 0.5τ_y
2	10 cycles @ 0.75 P_w	10 cycles @ 0.75τ_y
3	10 cycles @ 1.0 P_w	10 cycles @ 1.0τ_y
4	-	10 cycles @ 1.5τ_y
5	-	2 cycles @ 2.0τ_y
6	-	2 cycles @ 3.0τ_y
7	-	2 cycles @ 4.0τ_y
8	-	2 cycles @ 5.0τ_y

Keep increasing until failure

Phase	TYP. Wind	P.B. Wind/Seismic
1	10 cycles @ 0.5 P_w	10 cycles @ 0.5τ_y
2	10 cycles @ 0.75 P_w	10 cycles @ 0.75τ_y
3	10 cycles @ 1.0 P_w	10 cycles @ 1.0τ_y
4	-	10 cycles @ 1.5τ_y
5	-	2 cycles @ 2.0τ_y
6	-	2 cycles @ 3.0τ_y
7	-	2 cycles @ 4.0τ_y
8	-	2 cycles @ 5.0τ_y

Keep increasing until failure

Summary Table for Tension Test

Specimen	Load Type	Bolt Type	Bolt Number	Plate Th. (in)	Wall Width (in)	Max. Load (kip)
1A	Wind	Blind Bolt	1x2	3/8	14	257.4
2A	Wind	Through Bolt	1x2	3/8	14	257.4
1B	Wind	Blind Bolt	1x3	3/8	14	339.5
2B	Wind	Through Bolt	1x3	3/8	14	339.5
1C	Wind&Seismic	Blind Bolt	2x3	3/8	14	571.5
2C	Wind&Seismic	Through Bolt	2x3	3/8	14	571.5
4A	Wind	Through Bolt	1x3	3/8	14	257.4

Shuriken



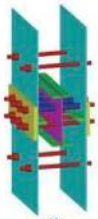
1A/2A



1B/2B



2C



4A

72

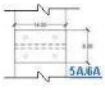
Summary Table for Shear Test

If composited

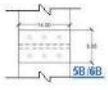
Specimen	Load Type	Bolt Type	Bolt Number	Plate Th. (in)	Wall Width (in)	Target Load (kip)	Expected Composited Load (kip)	Control Limit State
5A/6A	Wind	Blind Bolt	1x2	3/8 or 1/4	14	257.4 or 171.6	480.48 or 341.3	Bearing
6A/6A	Wind	Through Bolt	1x2	3/8 or 1/4	14	257.4 or 171.6	480.48 or 341.3	Bearing
5B/6B	Wind	Blind Bolt	1x3	3/8 or 1/4	14	113.9	480.48 or 341.3	Slip-Critical
6B/6B	Wind	Through Bolt	1x3	3/8 or 1/4	14	113.9	480.48 or 341.3	Slip-Critical
5C/6C	Wind&Seismic	Blind Bolt	2x3	3/8 or 1/4	14	231.0 or	480.48 or 341.3	Shear Yielding
6C/6C	Wind&Seismic	Through Bolt	2x3	3/8 or 1/4	14	346.6 or 231.0	480.48 or 341.3	Shear Yielding

* Actuator Limit = 420 kips

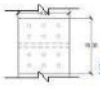
Shuriken



5A/6A



5B/6B



5C/6C

72

Timeline

- Discuss timetable (to reserve lab space accordingly)
  - Drawing submission by UB
  - Fabrication schedule

Task	*Duration*	*Tentative Schedule*
1 – Review/Develop Bolted Splice Alternative	4 months	9/1/2021 - 12/31/2021
2 – Component-level Tests	4 months	1/1/2022 – 04/30/2022
3 – Post-Processing and Reporting	4 months	5/1/2022 – 8/31/2022
4 – Wall-level Test (Planning and Execution)	8 months	9/1/2022 – 4/30/2023
5 – Post-Processing and Design Recommendations	4 months	5/1/2023 – 8/31/2023

74

Appendix – 75% Design of Test Set-up

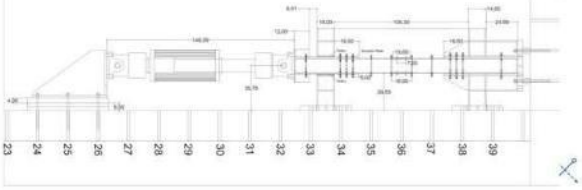
- Test set-up design to be finalized once specimen characteristics decided
- Drawings that follow are provided for general information only
- Shear tests to use existing pantograph (420 kips max loading capacity)

75

CASE 1A/1B TENSION

CASE 1A CASE 1B

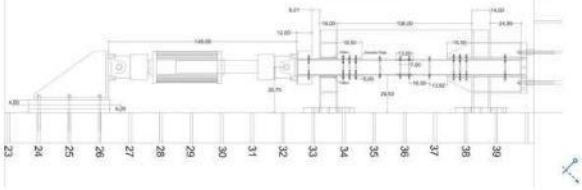
CASE 1A/1B



CASE 2A/2B TENSION

CASE 2A CASE 2B

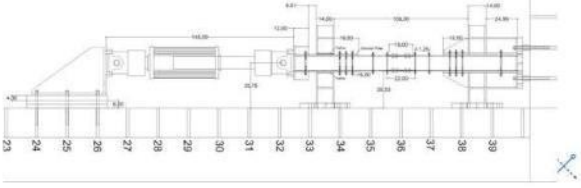
CASE 2A/2B



CASE 1C TENSION

CASE 1C

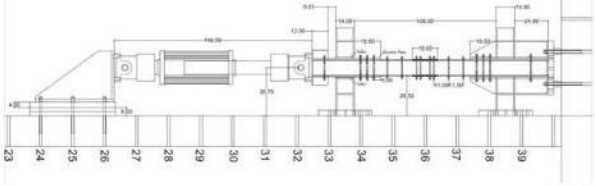
CASE 1C

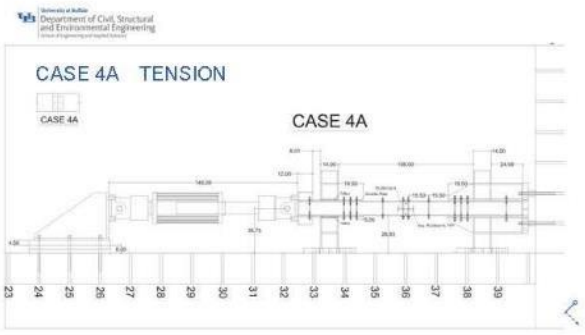


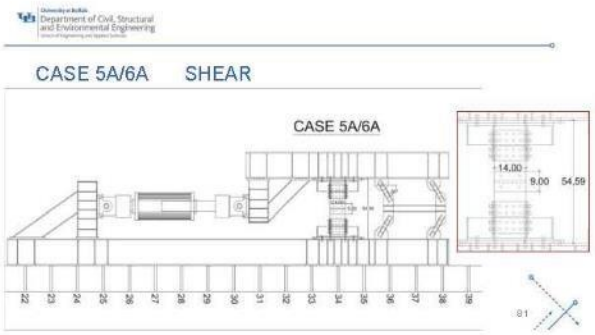
CASE 2C TENSION

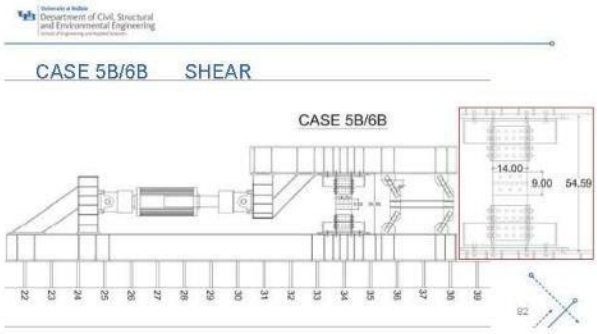
CASE 2C

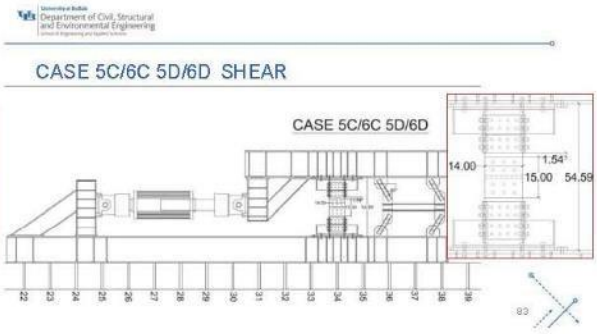
CASE 2C




Department of Civil, Structural and Environmental Engineering
CASE 4A TENSION
CASE 4A
CASE 4A
23 24 25 26 27 28 29 30 31 32 33 34 35 36 37 38 39


Department of Civil, Structural and Environmental Engineering
CASE 5A/6A SHEAR
CASE 5A/6A
14.00
9.00
54.59
22 23 24 25 26 27 28 29 30 31 32 33 34 35 36 37 38 39
81


Department of Civil, Structural and Environmental Engineering
CASE 5B/6B SHEAR
CASE 5B/6B
14.00
9.00
54.59
22 23 24 25 26 27 28 29 30 31 32 33 34 35 36 37 38 39
82


Department of Civil, Structural and Environmental Engineering
CASE 5C/6C 5D/6D SHEAR
CASE 5C/6C 5D/6D
14.00
1.54
15.00
54.59
22 23 24 25 26 27 28 29 30 31 32 33 34 35 36 37 38 39
83

Appendix C.

PowerPoint slides presented at third Project Advisory Group

(December 14, 2022)

BOLTED SPLICE DETAILS FOR COMPOSITE PLATE SHEAR WALLS—CONCRETE FILLED

Jia-Hau Liu
Michel Bruneau

Date: 12/14/2022

University at Buffalo
Department of Civil, Structural and Environmental Engineering
School of Engineering and Applied Sciences

PROJECT SCOPE

Proposed Timing

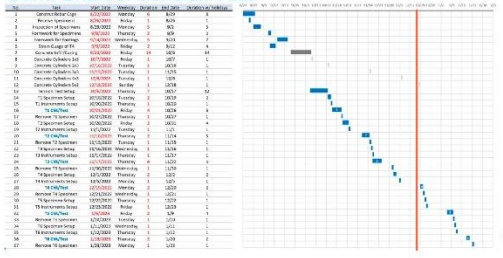
	Project Timing			
	Task	Duration (Month)	Start Date	End Date
Phase 1	1 – Review/Develop Bolted Splice Alternative	5	9/1/2021	1/31/2022
	Fabrication of Components Specimens	7	2/1/2022	8/31/2022
	2 – Component-level Tests	6	9/1/2022	2/28/2023
	3 – Post-Processing and Reporting	2	3/1/2023	4/30/2023
Phase 2	4 – Wall-level Test (Planning and Execution)	4	5/1/2023	8/31/2023
	5 – Post-Processing and Design Recommendations	4	9/1/2023	12/31/2023

Proposed Timing

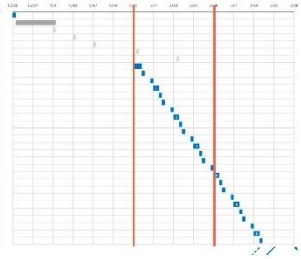
	Project Timing				
	Task	Duration (Month)	Start Date	End Date	End Date (Revised)*
Phase 1	1 – Review/Develop Bolted Splice Alternative	5	9/1/2021	1/31/2022	2/28/2022
	Fabrication of Components Specimens	7	2/1/2022	8/31/2022	8/31/2022
	2 – Component-level Tests	6	9/1/2022	2/28/2023	1/31/2023
	3 – Post-Processing and Reporting	2	3/1/2023	4/30/2023	3/31/2023
Phase 2	4 – Wall-level Test (Planning and Execution)	4	5/1/2023	8/31/2023	7/31/2023
	5 – Post-Processing and Design Recommendations	4	9/1/2023	12/31/2023	11/30/2023

*5/24/2022 Amendment

Gantt Chart of Tension Test



Gantt Chart of Shear Test



University at Buffalo
Department of Civil, Structural and Environmental Engineering
School of Engineering and Applied Sciences

Considered Limit States in Bolted Connections

Limit States Deemed Non-Ductile	Limit States Deemed "Ductile"
Bolt Shear Failure	Sliding
Tear-out (1.2 Lc t Fu)	Bearing (2.4dtFu)
Net Section Failure (AeFu)	Net Section Yielding (AeFy)
Fillet Weld Strength	Gross Section Yielding (AgFy)

* (RyFy) and (RuFu) actually used in all calculations

7

University at Buffalo
Department of Civil, Structural and Environmental Engineering
School of Engineering and Applied Sciences

Proposed Connection Details (Nomenclature)

MKA original details	Proposed Details for Testing Splices		
	Tension Testing of Splices	Shear Testing of Splices	
		Non-Composite (Forced, for comparison purpose)	Composite (Expected Behavior)
Type 1	Case 1 1A: Bearing Strength 1B: Slip + AeFy 1C: AgFy (option)	Case 5 5A: Bearing Strength 5B: Slip + 0.6 AeFy 5C: 0.6 AgFy (option)	Case 5 5Ac: Bearing Strength 5Bc: Slip + 0.6 AeFy 5Cc: 0.6 AgFy (option)
Type 2	Case 2 2A: Bearing Strength 2B: Slip + AeFy 2C: AgFy (option)	Case 6 6A: Bearing Strength 6B: Slip + 0.6 AeFy 6C: 0.6 AgFy (option)	Case 6 6Ac: Bearing Strength 6Bc: Slip + 0.6 AeFy 6Cc: 0.6 AgFy (option)
-	Case 4 4A: composite strength		

* A Case 3 considered earlier has been eliminated

8

University at Buffalo
Department of Civil, Structural and Environmental Engineering
School of Engineering and Applied Sciences

Proposed Connection Details (Nomenclature)

MKA original details	Proposed Details for Testing Splices		
	Tension Testing of Splices	Shear Testing of Splices	
		Non-Composite (Forced, for comparison purpose)	Composite (Expected Behavior)
Type 1	Case 1 1A: Bearing Strength ~~1B: Slip + AeFy~~ 1C: AgFy (option)	Case 5 5A: Bearing Strength 5B: Slip + 0.6 AeFy 5C: 0.6 AgFy (option)	Case 5 5Ac: Bearing Strength 5Bc: Slip + 0.6 AeFy 5Cc: 0.6 AgFy (option)
Type 2	Case 2 2A: Bearing Strength 2B: Slip + AeFy 2C: AgFy (option)	Case 6 6A: Bearing Strength 6B: Slip + 0.6 AeFy 6C: 0.6 AgFy (option)	Case 6 6Ac: Bearing Strength 6Bc: Slip + 0.6 AeFy 6Cc: 0.6 AgFy (option)
-	Case 4 4A (composite strength)		

* A Case 3 considered earlier has been eliminated

9

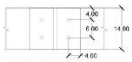
University at Buffalo
Department of Civil, Structural and Environmental Engineering
School of Engineering and Applied Sciences

Tension Splice Details (Case 1A, Case 2A/2B)

T1: Case 1A



Blind Bolt Detail
(N.T.S.)



Bolt Layout (Case 1A/2A)

T2 & T3:Case 2A/2B



Through Rod Detail
(N.T.S.)



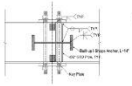
Bolt Layout (Case 2B)

P6

University at Buffalo
Department of Civil, Structural and Environmental Engineering
School of Engineering and Applied Sciences

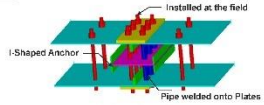
Tension Splice Details (Case 4A)

T6: Case 4A



Note:
1. PROVIDE PIPE SLEEVE ON ONE SIDE FOR THREADED RODS
2. PRETENSION RODS AFTER CONCRETE HAS REACHED MINIMUM 6000 PSI COMPRESSIVE STRENGTH
3. CONCRETE NOT SHOWN FOR CLARITY

I-Shaped Anchor Detail
(N.T.S.)



3D View (Case 4A)

P8

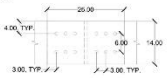
University at Buffalo
Department of Civil, Structural and Environmental Engineering
School of Engineering and Applied Sciences

Tension Splice Details (Case 1C, Case 2C)

T4: Case 1C



Blind Bolt Detail
(N.T.S.)



Bolt Layout (Case 1C/2C)

T5: Case 2C

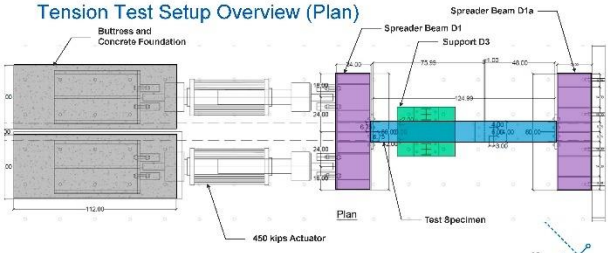


Through Rod Detail
(N.T.S.)

P7

University at Buffalo
Department of Civil, Structural and Environmental Engineering
School of Engineering and Applied Sciences

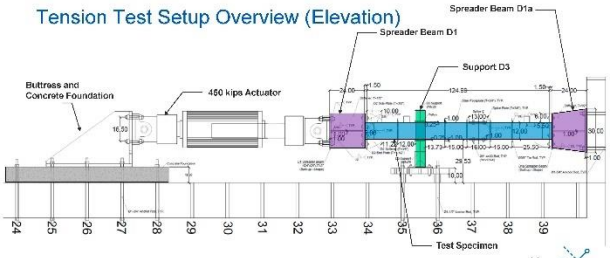
Tension Test Setup Overview (Plan)



13

University at Buffalo
Department of Civil, Structural and Environmental Engineering
School of Engineering and Applied Sciences

Tension Test Setup Overview (Elevation)



14

University at Buffalo
Department of Civil, Structural and Environmental Engineering
School of Engineering and Applied Sciences

Photo of Tension Test 1



15

University at Buffalo
Department of Civil, Structural and Environmental Engineering
School of Engineering and Applied Sciences

Design Summary of Tension Test

Case 1A: Blind Bolt
Case 2A/2B/2C: Through Rod
Case 1C: Shuriken
Case 4A: I-Shaped Anchor

	Case 1A/2A		Case 2B		Case 1C/2C	
T_b (in)	0.375		0.375		0.375	
Spice Bolt Dia. (in)	1		1.25		0.75	
Thread per Inch (n)	13		12		16	
Target Applied Tu (kips)	300.86		323.15		85.00	
Limit States	**Strength (kips)**	**Sequence**	**Strength (kips)**	**Sequence**	**Strength (kips)**	**Sequence**
1. Slip Critical Resistance	187.24	1	303.13	1	265.08	2
2. Net Section Yield ($A_n F_y$)	545.38	3	458.19	3	569.63	3
3. Gross Area Yield ($A_g F_y$)	503.81	2	593.00	2	697.50	1
4. Bearing Capacity	300.86	2	564.50	4	677.40	4
5. Tearout Capacity	300.86	2	737.00	5	1024.15	5
6. Net Section Rupture ($A_n F_u$)	726.73	5	610.98	6	759.08	6
7. Bolt Shear Strength	300.86	5	1240.63	8	885.41	7
8. Block Shear Strength	476.06	4	552.58	7	825.36	6

Case 4A	
Specimen Dia.	1
Concrete Strength f'_c (psi)	9333
Target Applied T_u (kips)	259.78
Limit States	**Strength (kips)**	**Sequence**
1. Screw Bearing Resistance	259.78	1
2. Concrete Failure	333.00	3
3. M_p Yielding - Screw (kips)	574.56	7
4. ϕ Shear Strength	393.6	4
5. M_p Yielding - Inner Plate	661.00	5
6. Plate Tension Strength	533.14	5

16

University at Buffalo
Department of Civil, Structural and Environmental Engineering
School of Engineering and Applied Sciences

Loading Protocols

*Pw = design wind load for Tension/Shear

Tension

Phase	TYP. Wind	P.B. Wind
1	10 cycles @ 0.5Pw	10 cycles @ 0.5cy
2	10 cycles @ 0.75Pw	10 cycles @ 0.75cy
3	10 cycles @ 1.0Pw	10 cycles @ 1.0cy
4	-	10 cycles @ 1.5cy
5	-	10 cycles @ 2.0cy
6	-	10 cycles @ 3.0cy
7	-	10 cycles @ 4.0cy
8	-	10 cycles @ 5.0cy

Keep increasing until failure

Phase	TYP. Wind	P.B. Wind/Seismic
1	10 cycles @ 0.5Pw	10 cycles @ 0.5cy
2	10 cycles @ 0.75Pw	10 cycles @ 0.75cy
3	10 cycles @ 1.0Pw	10 cycles @ 1.0cy
4	-	10 cycles @ 1.5cy
5	-	2 cycles @ 2.0cy
6	-	2 cycles @ 3.0cy
7	-	2 cycles @ 4.0cy
8	-	2 cycles @ 5.0cy

Keep increasing until failure

Shear

Phase	TYP. Wind	P.B. Wind
1	10 cycles @ 0.5Pw	10 cycles @ 0.5cy
2	10 cycles @ 0.75Pw	10 cycles @ 0.75cy
3	10 cycles @ 1.0Pw	10 cycles @ 1.0cy
4	-	10 cycles @ 1.5cy
5	-	10 cycles @ 2.0cy
6	-	10 cycles @ 3.0cy
7	-	10 cycles @ 4.0cy
8	-	10 cycles @ 5.0cy

Keep increasing until failure

Phase	TYP. Wind	P.B. Wind/Seismic
1	10 cycles @ 0.5Pw	10 cycles @ 0.5cy
2	10 cycles @ 0.75Pw	10 cycles @ 0.75cy
3	10 cycles @ 1.0Pw	10 cycles @ 1.0cy
4	-	10 cycles @ 1.5cy
5	-	2 cycles @ 2.0cy
6	-	2 cycles @ 3.0cy
7	-	2 cycles @ 4.0cy
8	-	2 cycles @ 5.0cy

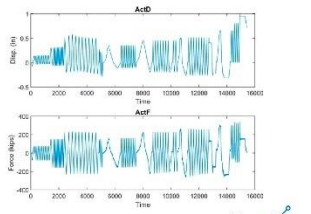
Keep increasing until failure

17

University at Buffalo
Department of Civil, Structural and Environmental Engineering
School of Engineering and Applied Sciences

Test 1 Disp. Protocol

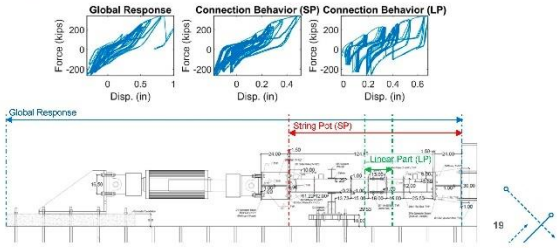
Phase	Disp. (in) + Disp. (in)	Force (kips) + Force (kips)	Cycles	Note 1	Note 2
1	0.14	0.35	75	10	0.5Pw
2	0.2	0.37	110	110	10	0.5Pw	
3	0.3	0.3	215	225	10	0.75Pw	Base Slip
4	0.35	0.31	150	150	10	1.0Pw	
5	0.44	0.4	220	220	10	0.5Pw	
6	0.565	0.735	260	260	10	0.75Pw	
7	0.61	0.75	300	300	1	1.0Pw	
8	0.64	0	300	-	-		
9	0.6	0	250	-	-		
10	0.56	0	210	-	-		Base Slip



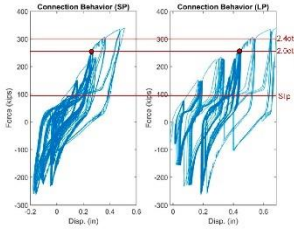
18

University at Buffalo
Department of Civil, Structural and Environmental Engineering
School of Engineering and Applied Sciences

Test 1 Test Result



Test 1 Test Result and Limit States

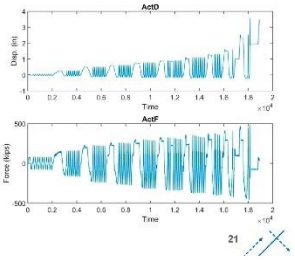


	Case 1A	
Target Loading Tu (kips)	300.96	
Limit States	Strength (kips)	Sequence
1. Slip-Critical Resistance	173.57	①
2. Net Section Yiled (AeRyFy)	546.38	6
3. Gross Area Yield (AgRyFy)	651.00	7
4. Bearing Capacity	300.96	②
5. Tear-out Capacity	366.80	③
6. Net Section Rupture (AeRuFu)	736.73	8
7. Bolt Shear Strength	527.79	5
8. Block Shear Strength	473.06	4

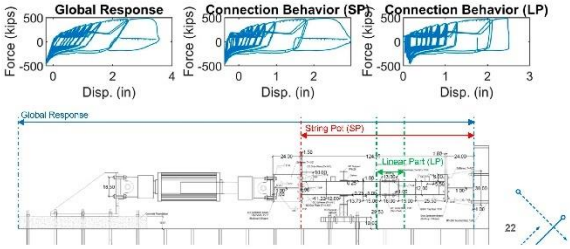
Test 2 Disp. Protocol

T2 Load Protocol

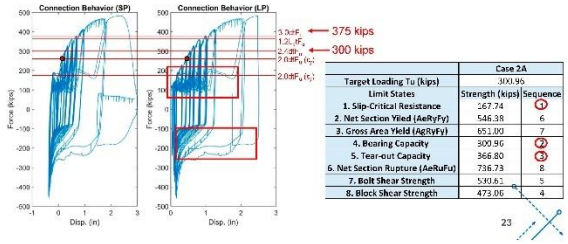
Phase	Disp.Cyc1 (in)	Disp.Cyc2 (in)	Force (kips)	Cycles	Note 1	Note 2
1	0.075	0.05	75	12	0.25Fu	
2	0.225	0.15	150	12	0.50Fu	Conn Slip
3	0.5	0.225	225	12	0.75Fu	
4	0.6	0.3375	300	12	1.00Fu	
5	0.75	0.495	330	330	1.0Fu	
6	0.9	0.555	367	367	1.1	-
7	1.1	0.735	490	490	1.5	-
8	1.5	0.98	490	490	5	-
9	1.5	0.98	490	490	4	Failure
10	2.5	0.98	490	490	1	Failure
11	5	-	490	-	-	-



Test 2 Test Result



Test 2 Test Result and Limit States

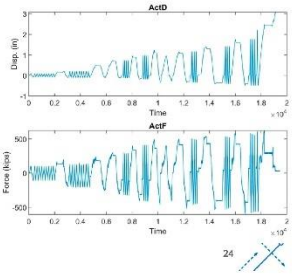


	Case 2A	
Target Loading Tu (kips)	300.96	
Limit States	Strength (kips)	Sequence
1. Slip-Critical Resistance	267.74	①
2. Net Section Yiled (AeRyFy)	546.38	6
3. Gross Area Yield (AgRyFy)	651.00	7
4. Bearing Capacity	300.96	②
5. Tear-out Capacity	366.80	③
6. Net Section Rupture (AeRuFu)	736.73	8
7. Bolt Shear Strength	530.61	5
8. Block Shear Strength	473.06	4

Test 3 Disp. Protocol

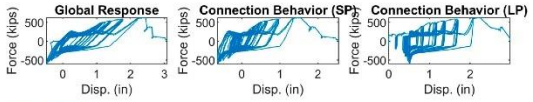
T3 Load Protocol

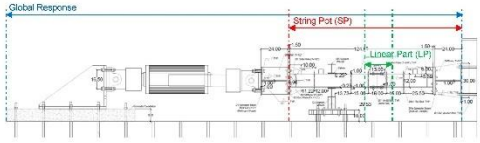
Phase	Disp.Cyc1 (in)	Disp.Cyc2 (in)	Force (kips)	Force (kips)	Cycles	Note 1	Note 2
1	0.05	0.03	50	50	12	0.1Fu	
2	0.225	0.09	150	150	12	0.3Fu	
3	0.5	0.20	240	240	1	0.48Fu	
4	0.725	0.315	300	300	5	0.6Fu	
5	1.00	0.45	420	420	5	0.8Fu	
6	1.25	0.6	505	505	5	AeRy	Str.
7	1.75	0.75	505	505	1		
8	2.25	0.90	505	505	1	Ag_y	
9	2.5	0.4	540	550	5		
10	2.75	0.45	600	590	5		
11	3.0	0.45	640	640	5		
12	3	-	640	-	-	-	



University at Buffalo
Department of Civil, Structural and Environmental Engineering

Test 3 Test Result



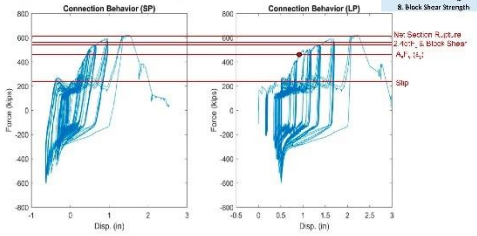


25

University at Buffalo
Department of Civil, Structural and Environmental Engineering

Test 3 Test Result and Limit States

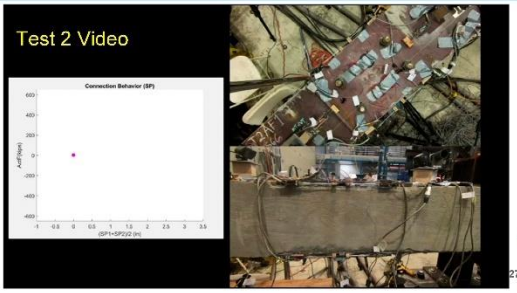
Target Loading Tu (kips)	Case 2B 353.13	
Limit States	Strength (kips)	Sequence
1. Slip Critical Resistance	494.14	
2. Net Section Yield (AgFy/Py)	424.78	2
3. Gross Area Yield (AgFy/Py)	453.00	6
4. Bearing Capacity	644.50	4
5. Tear-out Capacity	362.79	7
6. Net Section Rupture (AeFu/Fu)	612.15	5
7. Bolt Shear Strength	1243.63	8
8. Block Shear Strength	552.58	3



26

University at Buffalo
Department of Civil, Structural and Environmental Engineering

Test 2 Video



27

University at Buffalo
Department of Civil, Structural and Environmental Engineering

T2 Failure Mode



Top Plate



Bottom Plate

28

University at Buffalo
Department of Civil, Structural and Environmental Engineering

T2 Failure Mode



University at Buffalo
Department of Civil, Structural and Environmental Engineering

T2 Failure Mode



University at Buffalo
Department of Civil, Structural and Environmental Engineering
School of Engineering and Applied Sciences

T2 Failure Mode



University at Buffalo
Department of Civil, Structural and Environmental Engineering
School of Engineering and Applied Sciences

Test 3 Video



University at Buffalo
Department of Civil, Structural and Environmental Engineering
School of Engineering and Applied Sciences

T3 Failure Mode



Top Plate



Bottom Plate

University at Buffalo
Department of Civil, Structural and Environmental Engineering
School of Engineering and Applied Sciences

T3 Failure Mode



University at Buffalo
Department of Civil, Structural and Environmental Engineering
School of Engineering and Applied Sciences

T3 Friction

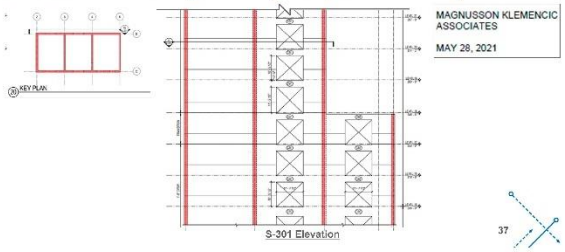


University at Buffalo
Department of Civil, Structural and Environmental Engineering
School of Engineering and Applied Sciences

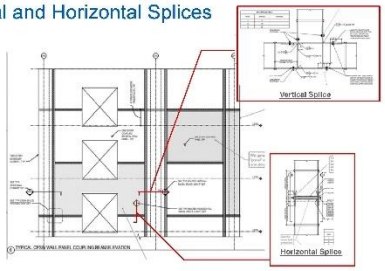
T3



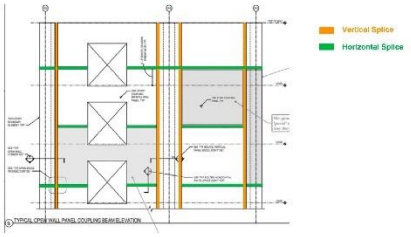
Elevation of the Design Core (Examples from MKA)



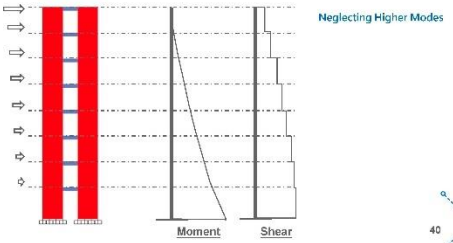
Vertical and Horizontal Splices



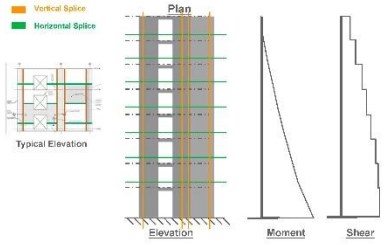
Vertical and Horizontal Splices



Typical Structural Behavior of CPSW



Typical Structural Behavior of CPSW



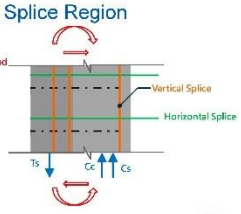
Typical Structural behavior at the Splice Region

For Horizontal Splice

- → Transfer Tension Force in the section
- → Splice need to take Tensile Forces coming from OTM
- → Splice need to take Shear Forces coming from Story Shear

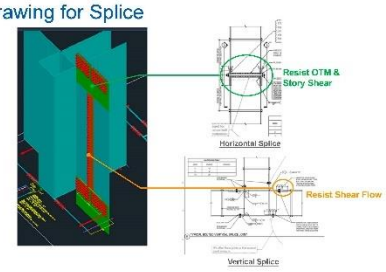
For Vertical Splice

- → No Tension Force in the Section
- → Splice need to take Shear Force from Shear Flow
  $v = VQ/It$ (might be very small)



University at Buffalo
Department of Civil, Structural and Environmental Engineering

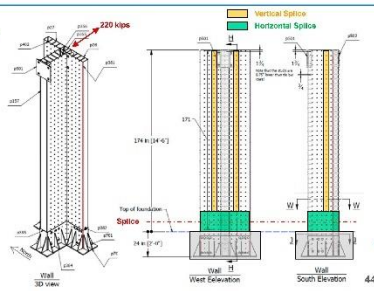
3D Drawing for Splice



43

University at Buffalo
Department of Civil, Structural and Environmental Engineering

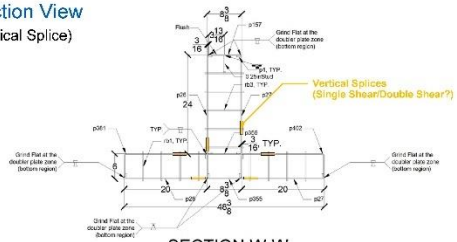
Elevation View



44

University at Buffalo
Department of Civil, Structural and Environmental Engineering

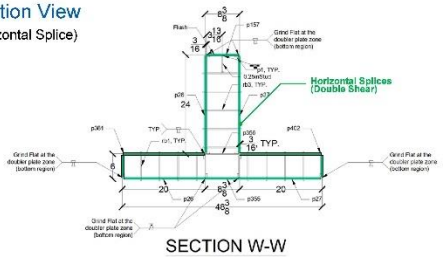
Section View
(Vertical Splice)



45

University at Buffalo
Department of Civil, Structural and Environmental Engineering

Section View
(Horizontal Splice)



46

University at Buffalo
Department of Civil, Structural and Environmental Engineering

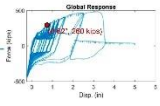
Discussion

- Wall test fabrication schedule (depends on geometry of wall test selected and has an impact on wall testing schedule)
- Suggests same as welded T-walls (to expedite fabricator selection)
- Shop drawings to start now, with splices details (i.e., number and locations of bolts) to be provided later)
- Need to agree on location of splice plates (Vertical/Horizontal)
- Need to agree on selected preferred failure mechanism for connections in wall test (Bearing/Net section fracture/…)

47

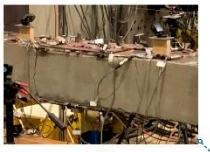
University at Buffalo
Department of Civil, Structural and Environmental Engineering

Test 2 Test Photos





South View

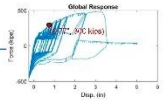


North View

48

Department of Civil, Structural and Environmental Engineering

Test 2 Test Photos





South View

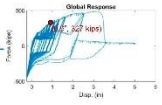


North View

49

Department of Civil, Structural and Environmental Engineering

Test 2 Test Photos





South View

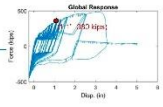


North View

50

Department of Civil, Structural and Environmental Engineering

Test 2 Test Photos





South View

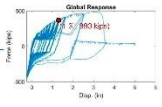


North View

51

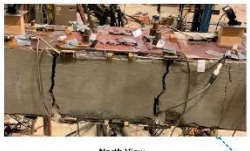
Department of Civil, Structural and Environmental Engineering

Test 2 Test Photos





South View

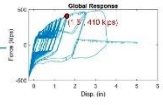


North View

52

Department of Civil, Structural and Environmental Engineering

Test 2 Test Photos





South View

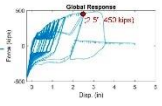


North View

53

Department of Civil, Structural and Environmental Engineering

Test 2 Test Photos





South View



North View

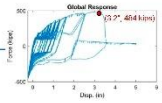
54

University at Buffalo
Department of Civil, Structural and Environmental Engineering
School of Engineering and Applied Sciences

Test 2 Test Photos
(Failure)



Bearing Deformation





South View

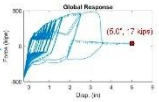


North View



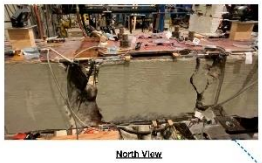
University at Buffalo
Department of Civil, Structural and Environmental Engineering
School of Engineering and Applied Sciences

Test 2 Test Photos
(Max. Disp. =5")





South View



North View



Appendix D.

PowerPoint slides presented at fourth Project Advisory Group

(April 26, 2023)

BOLTED SPLICE DETAILS FOR COMPOSITE PLATE SHEAR WALLS—CONCRETE FILLED

Jia-Hau Liu
Michel Bruneau

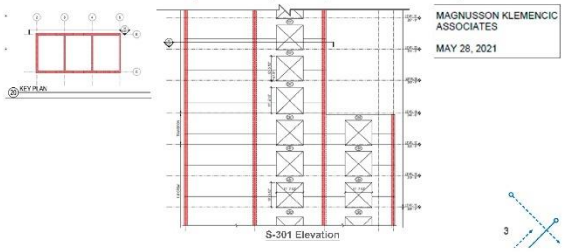
Date: 4/26/2023

University at Buffalo
Department of Civil, Structural and Environmental Engineering
School of Engineering and Applied Sciences

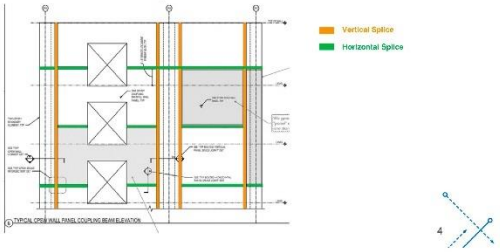
Project Phase 2: Testing of Bolted T-Shaped Wall Specimen

- Constraint: Single Specimen – Geometry selected to be same of previously tested welded wall (time constraint)
- Selected governing limit state for Horizontal Splice:
  - Bearing Failure (2.4 d t Fu) with understanding that bolts will be pre-tensioned per AISC requirements, which will give some slip-resistance prior to bearing failure).
  - (Note: Elastic limit at ~ 2.0 d t Fu ; ¾" bolt hole elongation at 2.4 d t Fu)
  - Double shear
- Vertical Splice:
  - Single Shear / Slip resistant design
- Hierarchy of limit states: Failure to happen in horizontal splice before slippage in vertical splice
- Strength of specimen splices (as % of AgFy for area tributary to bolts) to match values of MKA Boston project
- Consider possible repair/retest post-failure of bolted connection (TBD)
  - Keep outside splice plate and weld it (objective: to restore flexural strength but without removing/replacing concrete)

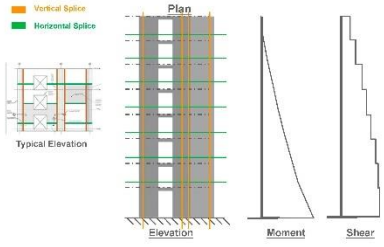
Elevation of the Design Core (Examples from MKA)



Vertical and Horizontal Splices



Typical Structural Behavior of CPSW



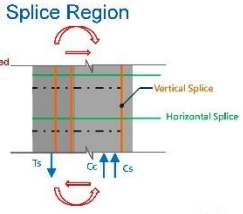
Typical Structural behavior at the Splice Region

For Horizontal Splice

→ Transfer Tension Force in the section
→ Splice need to take Tensile Forces coming from OTM
→ Splice need to take Shear Forces coming from Story Shear

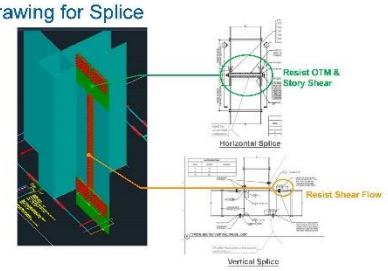
For Vertical Splice

→ No Tension Force in the Section
→ Splice need to take Shear Force from Shear Flow
$\tau = VQ/It$ (might be very small)



University at Buffalo
Department of Civil, Structural and Environmental Engineering

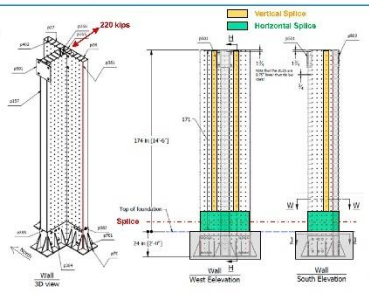
3D Drawing for Splice



7

University at Buffalo
Department of Civil, Structural and Environmental Engineering

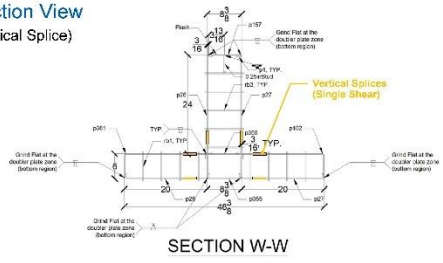
Elevation View



8

University at Buffalo
Department of Civil, Structural and Environmental Engineering

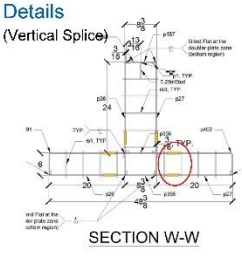
Section View
(Vertical Splice)

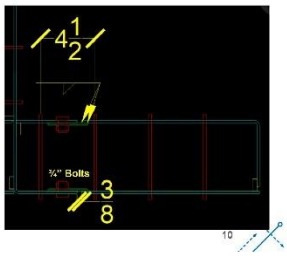


9

University at Buffalo
Department of Civil, Structural and Environmental Engineering

Details
(Vertical Splice)

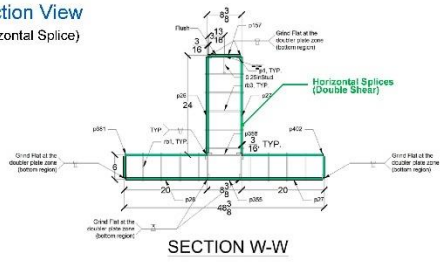




10

University at Buffalo
Department of Civil, Structural and Environmental Engineering

Section View
(Horizontal Splice)



11

University at Buffalo
Department of Civil, Structural and Environmental Engineering

# =	Governed by Critical
#=	Governed by 2.4dtFu
#=	Governed by net section rupture
#=	Governed by bolt failure

Bolt Option for Horizontal Splice (1) Designed by Bearing

For 3/4" bolt
Spacing in inches

Plate Thickness	2	4	6	8	10	12	14	16	18	Type
3/16	117%	59%	39%	29%	23%	20%	17%	15%	13%	3
1/4	117%	59%	39%	29%	23%	20%	17%	15%	13%	3
5/16	117%	59%	39%	29%	23%	20%	17%	15%	13%	3
3/8	117%	59%	39%	29%	23%	20%	17%	15%	13%	3
1/2	109%	55%	36%	27%	22%	18%	16%	14%	12%	F
3/4	73%	36%	24%	18%	15%	12%	10%	9%	8%	F
1	55%	27%	18%	14%	11%	9%	8%	7%	6%	F

for 1-1/4" bolt
Spacing in inches

Plate Thickness	2	4	6	8	10	12	14	16	18	Type
3/16	195%	98%	65%	49%	39%	33%	28%	24%	22%	B
1/4	195%	98%	65%	49%	39%	33%	28%	24%	22%	B
5/16	195%	98%	65%	49%	39%	33%	28%	24%	22%	B
3/8	195%	98%	65%	49%	39%	33%	28%	24%	22%	B
1/2	195%	98%	65%	49%	39%	33%	28%	24%	22%	B
3/4	195%	98%	65%	49%	39%	33%	28%	24%	22%	B
1	152%	76%	51%	38%	30%	25%	22%	19%	17%	-

range for factor MEA project

12

University at Buffalo
Department of Civil, Structural and Environmental Engineering

# =	Governed by Critical
#=	Governed by 2.4dtFu
#=	Governed by net section rupture
#=	Governed by bolt failure

Bolt Option for Horizontal Splice (2) Designed by Slip

For 3/4" Bolt									
Spacing in inches									
Plate Thickness	2	4	5	8	10	12	14	16	18	Type
3/16	115%	57%	38%	29%	23%	19%	16%	14%	13%	S
1/4	80%	40%	26%	20%	16%	13%	11%	10%	9%	S
5/16	60%	34%	23%	17%	14%	11%	10%	9%	8%	S
3/8	57%	29%	19%	14%	11%	10%	8%	7%	6%	S
1/2	43%	22%	14%	11%	9%	7%	6%	5%	5%	S
3/4	29%	14%	10%	7%	6%	5%	4%	4%	3%	S
1	22%	11%	7%	5%	5%	4%	3%	3%	2%	S

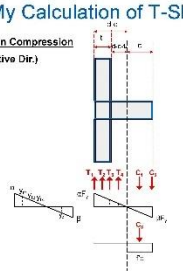
For 1-1/4" Bolt									
Spacing in inches									
Plate Thickness	2	4	6	8	10	12	14	16	18	Type
3/16	195%	98%	65%	49%	39%	33%	28%	24%	22%	B
1/4	195%	98%	65%	49%	39%	33%	28%	24%	22%	B
5/16	195%	98%	65%	49%	39%	33%	28%	24%	22%	B
3/8	168%	84%	56%	42%	34%	28%	24%	21%	19%	S
1/2	126%	63%	42%	31%	25%	21%	18%	16%	14%	S
3/4	84%	42%	28%	21%	17%	14%	12%	10%	9%	S
1	63%	31%	21%	16%	13%	10%	9%	8%	7%	S

Change "In Bolted Mfg Joint" to 1

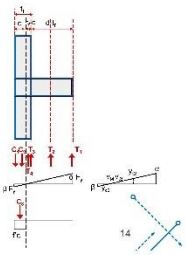
13

My Calculation of T-Shaped Specimen

Web in Compression
(Positive Dir.)



Flange in Compression
(Negative Dir.)



14

Material Property			
f'c (ksi)		Fy (ksi)	Fu (ksi)
6		55	70

My Calculation (Web in Compression)

Positive Direction

--My Calculation (Web in Compression)--						
Ac=(tw-2c)*(d-tf-tp)+(W-4tp)*(F-2)=	456.39	in2				
P=0.1Ag*f'c=	270	kips	(Positive = Tension)			
Try c=	15.80	in	Check sum F=	270		
Stress Profile						
α=	0.65		y1=0.5(13-c)*α=	0.98		
y2=(d-c-tf)/(d-c)*α=	0.51		β=α/(d-c)*α=	0.72		
y3=(c-c-tf)/(d-c)*α=	0.38					
y4=(d-c-tf)/2(d-c)*α=	0.10					
Forces						
T1=W*y1*Fy=	324.26	kip	C1=2*(c-tf)*tf*Fy=	110.44	kip	
T2=4*(tf-2c)*tp*y2*Fy=	110.99	kip	C2=w*tp*Fy=	82.46	kip	
T3=(W-4tp)*y3*Fy=	187.25	kip	C3=c*tw*2=*Fy=	750.48	kip	
T4=2*(d-c-tf)*tw*y4*Fy=	31.74	kip				
Lever Arms						
LT1=d-c=	14.20	in	LC1=c/2=	7.90	in	
LT2=d-c-tf/2	11.20	in	LC2=c	15.80	in	
LT3=(d-c-tf)=	8.20	in	LC3=c/2=	7.90	in	
LT4=(d-c-tf)/2=	4.10	in				
Yield Moment						
My=ΣCi,Ci x LCi=	5600.96	k-in	=	1291.72	k-ft	

15

Material Property			
f'c (ksi)		Fy (ksi)	Fu (ksi)
6		55	70

My Calculation (Flange in Compression)

Negative Direction

--My Calculation (Flange in Compression)--						
Ac=(tw-2c)*(d-tf-tp)+(W-4tp)*(tf-2c)=	456.39	in2				
P=0.1Ag*f'c=	270	kips	(Positive = Tension)			
Try c=	2.68	in	Check sum F=	270		
Stress Profile						
β=(d-c)/c=	0.65		α=	0.65		
y2=(d-tf-c)/c*α=	0.62		y2=(d-tf-3c)/(d-c)*α=	0.37		
y3=(tf-c)/c*α=			y3=(tf-c)/(c-c)*α=	0.09		
y4=(d-tf-c)/2c*α=			y4=(d-tf-c)/2(d-c)*α=	0.08		
Forces						
C1=W*tf*Fy=	24.16	kip	T1=W*tp*y1*Fy=	56.14	kip	
C2=4*(c-tf)*tp*y2*Fy=	1.89	kip	T2=2*(d-tf-tp)*y2*Fy=	183.46	kip	
C3=(W-4tp)*(c-tf)*c*Fy=	843.78	kip	T3=W*tp*y3*Fy=	45.52	kip	
			T4=4*(d-c-tf)*tp*y4*Fy=	7.03	kip	
Lever Arms						
LC1=c/2=	1.34	in	LT1=d-c=	27.32	in	
LC2=(c-tf)/2=	0.95	in	LT2=(d-tf)/2-c=	15.92	in	
LC3=(c-tf)/2=	0.95	in	LT3=d-c=	3.62	in	
			LT4=(d-c-tf)/2=	1.87	in	
Yield Moment						
My=ΣCi,Ci x LCi=	5243.63	k-in	=	436.95	k-ft	

16

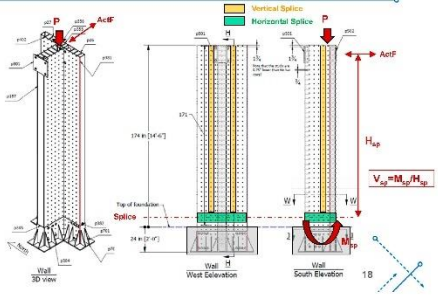
Summary of Moment (P=0.1*Ac*f'c)

Material Property		
f'c (ksi)	Fy (ksi)	Fu (ksi)
6	55	70

	Positive Dir.	Negative Dir.	
0.65My	1291.72	436.95	k-ft
My	1793.55	651.62	k-ft
Mp	2041.57	1186.87	k-ft

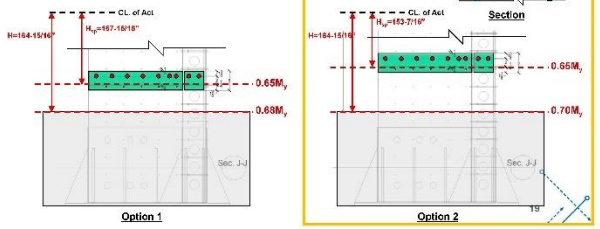
17

Splice Location

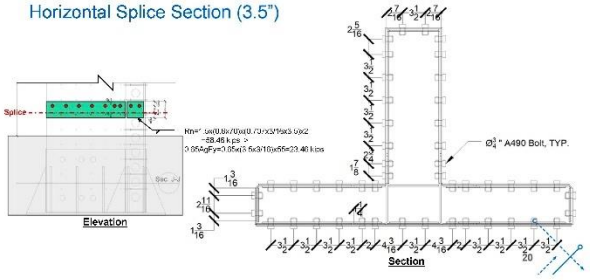


18

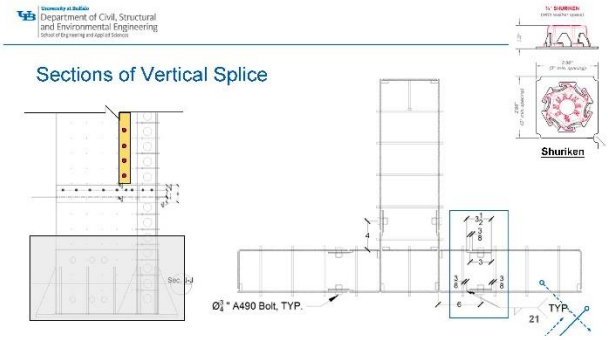
Horizontal Splice Location



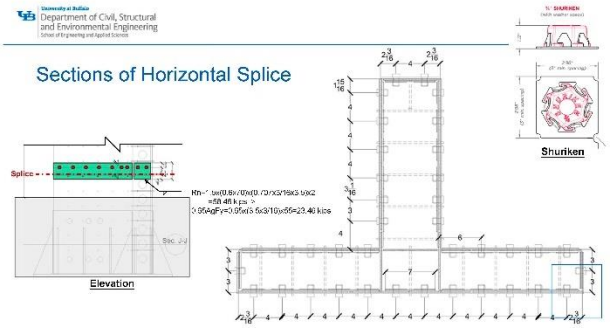
Horizontal Splice Section (3.5")



Sections of Vertical Splice



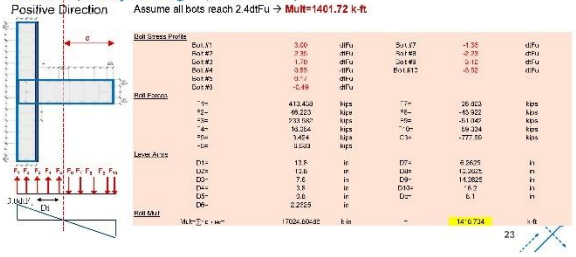
Sections of Horizontal Splice



Bolt Capacity Design (Section 2)

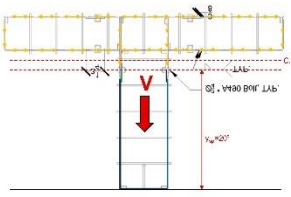
Positive Direction

Assume all bots reach 2.4dtFu → **Mult=1401.72 k-ft**



Vertical Splice (Pure Steel)

(Shear Flow Calculation)



Shear Flow

V=101 kips ← **Based on 0.65My**

V=**111** kips ← **Based on Mult**

Ix=2771.488 in4

Q=120.170 in3

f=VQ/2I=**2.406 k/in**

Vertical Spacing of Vertical Splices

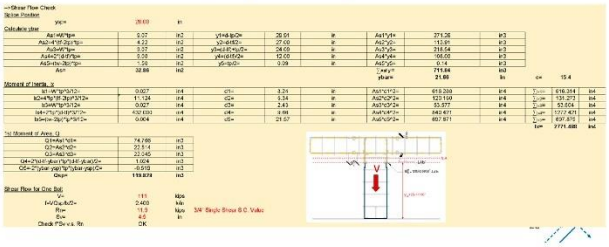
For ¾" Single Shear Slip-Critical Resistance → R_n=11.9 kips

f*S_v < R_n → S_v < 4.9" **(Use S_v=4.5")**

Sv (in)	V (kips)	Moment	Bearing Stress
5.4	101	0.65My	2.4dtFu
4.9	111	0.71My	2.64dtFu
4.5	122	0.79My	2.88dtFu

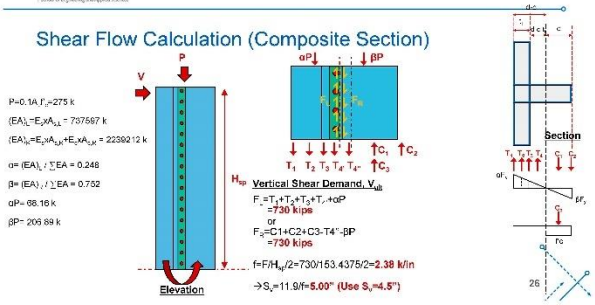
University at Buffalo
Department of Civil, Structural and Environmental Engineering

Shear Flow Calculation (Pure Steel)



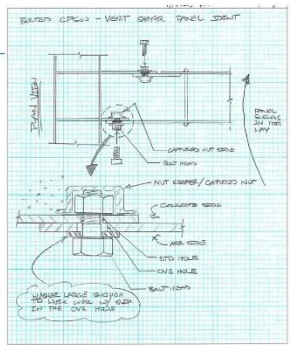
University at Buffalo
Department of Civil, Structural and Environmental Engineering

Shear Flow Calculation (Composite Section)



University at Buffalo
Department of Civil, Structural and Environmental Engineering

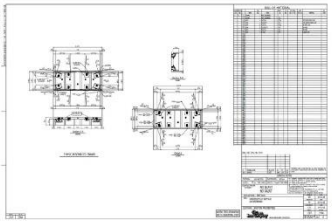
Discussion 1



27

University at Buffalo
Department of Civil, Structural and Environmental Engineering

Discussion 2 (Drawing from T1&2)



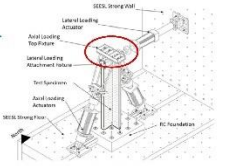


Figure 4-2. 3D view of the test setup



Figure 1-2: Axial Loading setup

28

University at Buffalo
Department of Civil, Structural and Environmental Engineering

Discussion 3

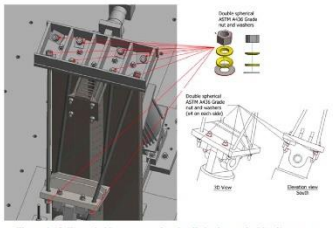


Figure 4-15. Threaded bars connection details in the vertical loading system

29

Appendix E.

PowerPoint slides presented at fifth Project Advisory Group

(February 13, 2024)

BOLTED SPLICE DETAILS FOR COMPOSITE PLATE SHEAR WALLS—CONCRETE FILLED

Jia-Hau Liu
Michel Bruneau

Date: 2/13/2024

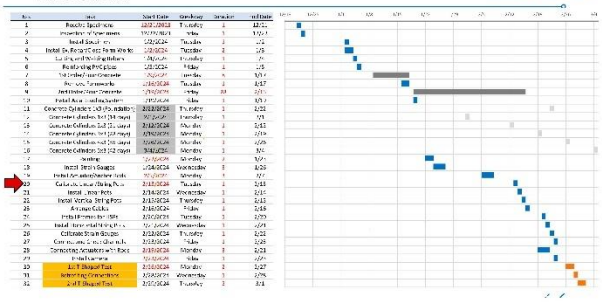
University at Buffalo
Department of Civil, Structural and Environmental Engineering
School of Engineering and Applied Sciences

Outline

- Schedule
- Test Setups
- Wall Test Design
- Finite Element Analysis
- Loading Protocol

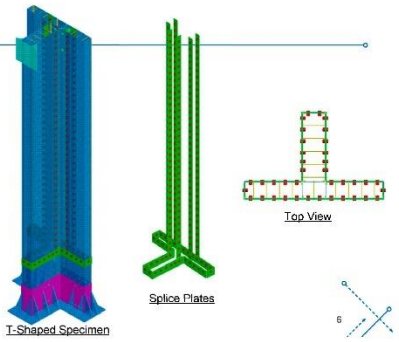
SCHEDULE

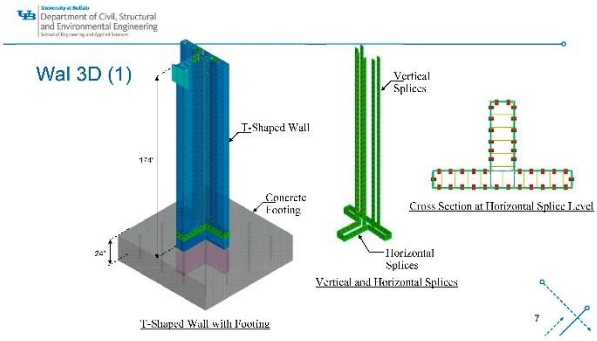
Gantt Chart

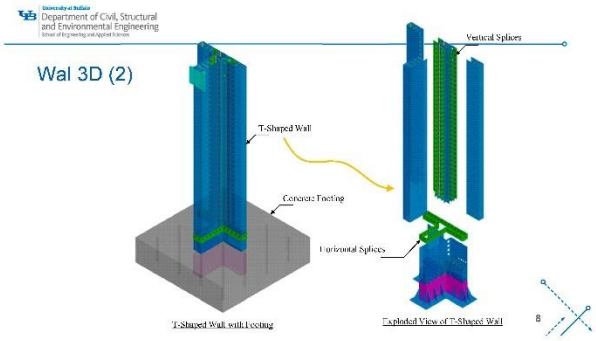


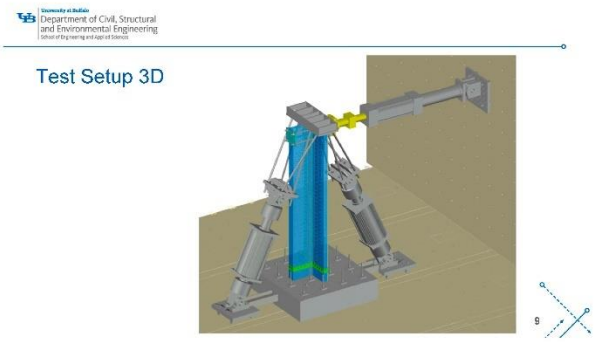
SPECIMEN AND TEST SETUPS

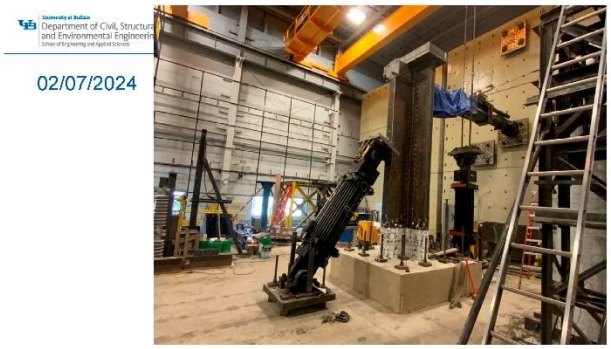
T-Wall Specimen

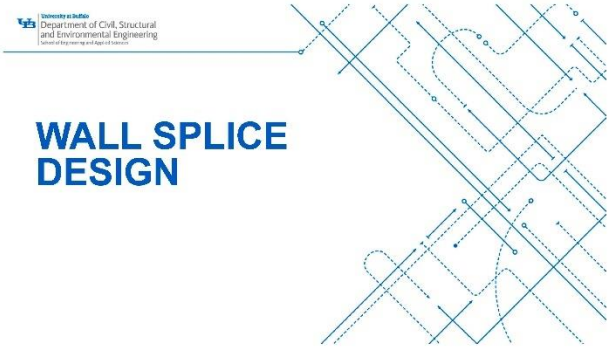


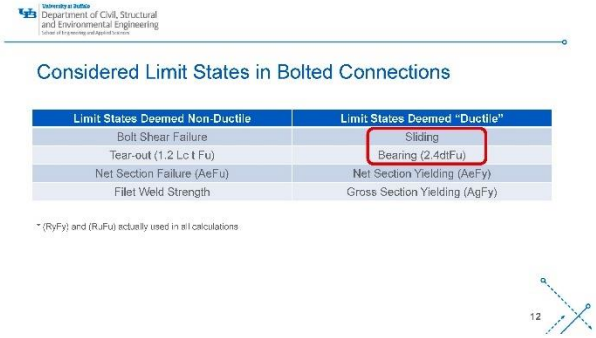

Department of Civil, Structural and Environmental Engineering
Wal 3D (1)
T-Shaped Wall
174"
Concrete Footing
24"
Vertical Splices
Horizontal Splices
Cross Section at Horizontal Splice Level
Vertical and Horizontal Splices
T-Shaped Wall with Footing
7


Department of Civil, Structural and Environmental Engineering
Wal 3D (2)
Vertical Splices
T-Shaped Wall
Concrete Footing
Horizontal Splices
T-Shaped Wall with Footing
Exploded View of T-Shaped Wall
8

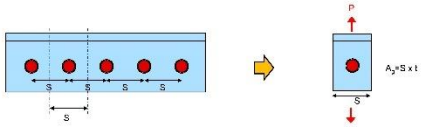

Department of Civil, Structural and Environmental Engineering
Test Setup 3D
9


Department of Civil, Structural and Environmental Engineering
02/07/2024


Department of Civil, Structural and Environmental Engineering
WALL SPLICE DESIGN


Department of Civil, Structural and Environmental Engineering
Considered Limit States in Bolted Connections
Limit States Deemed Non-Ductile
Limit States Deemed "Ductile"
Bolt Shear Failure
Sliding
Tear-out (1.2 Lc t Fu)
Bearing (2.4dtFu)
Net Section Failure (AeFu)
Net Section Yielding (AeFy)
Fillet Weld Strength
Gross Section Yielding (AgFy)
* (RyFy) and (RuFu) actually used in all calculations
12

Tributed Area Approach



$R_{bearing}=2.4dtF_u > P=A_g\ (\%F_y)$

13

Bolt Option for Horizontal Splice (1) Designed by Bearing

# =	Governed by Critical
#=	Governed by 2.4dtFu
#=	Governed by net section rupture
#=	Governed by bolt failure

For 3/4" Bolt

Spacing in inches

Plate thickness	2	3	4	5	6	8	10	12	14	16	18	Type
3/16	117%	59%	59%	59%	59%	59%	59%	59%	59%	59%	59%	S
1/4	117%	59%	59%	59%	59%	59%	59%	59%	59%	59%	59%	S
5/16	117%	59%	59%	59%	59%	59%	59%	59%	59%	59%	59%	S
3/8	117%	59%	59%	59%	59%	59%	59%	59%	59%	59%	59%	S
1/2	109%	55%	55%	55%	55%	55%	55%	55%	55%	55%	55%	F
5/8	73%	36%	36%	36%	36%	36%	36%	36%	36%	36%	36%	F
1	55%	27%	18%	18%	18%	18%	18%	18%	18%	18%	18%	F

For 1-1/4" Bolt

Spacing in inches

Plate Thickness	2	3	4	5	6	8	10	12	14	16	18	Type
3/16	195%	98%	65%	49%	39%	33%	28%	24%	22%	22%	22%	B
1/4	195%	98%	65%	49%	39%	33%	28%	24%	22%	22%	22%	B
5/16	195%	98%	65%	49%	39%	33%	28%	24%	22%	22%	22%	B
3/8	195%	98%	65%	49%	39%	33%	28%	24%	22%	22%	22%	B
1/2	195%	98%	65%	49%	39%	33%	28%	24%	22%	22%	22%	B
5/8	195%	98%	65%	49%	39%	33%	28%	24%	22%	22%	22%	B
3/4	195%	98%	65%	49%	39%	33%	28%	24%	22%	22%	22%	B
1	152%	76%	51%	38%	30%	25%	22%	19%	17%	-	-	-

Target Value = 60%F_y

$R_{Bearing,\ Test}$ = 59%$A_g F_y$

$R_{Bearing}$ = 65%$A_g F_y$

14

Bolt Option for Horizontal Splice (2) Designed by Slip

# =	Governed by Critical
#=	Governed by 2.4dtFu
#=	Governed by net section rupture
#=	Governed by bolt failure

For 3/4" Bolt

Spacing in inches

Plate Thickness	2	3	4	5	6	8	10	12	14	16	18	Type
3/16	112%	57%	38%	29%	23%	17%	14%	11%	10%	9%	8%	S
1/4	86%	43%	29%	22%	17%	14%	12%	11%	10%	9%	8%	S
5/16	69%	34%	23%	17%	14%	11%	10%	9%	8%	7%	6%	S
3/8	57%	29%	19%	14%	11%	10%	9%	8%	7%	6%	6%	S
1/2	43%	22%	14%	11%	9%	7%	6%	5%	5%	4%	4%	S
3/4	29%	14%	10%	7%	6%	5%	4%	4%	3%	3%	3%	S
1	22%	11%	7%	5%	4%	4%	3%	3%	2%	2%	2%	S

For 1-1/4" Bolt

Spacing in inches

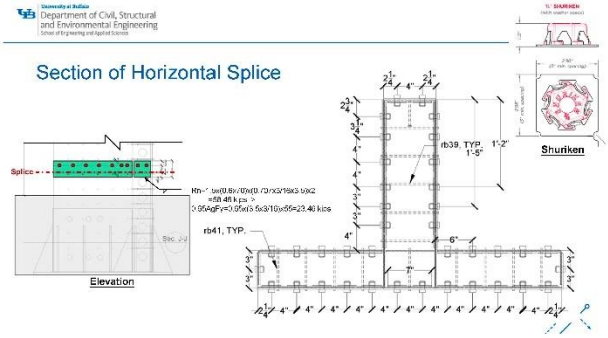
Plate thickness	2	3	4	5	6	8	10	12	14	16	18	Type
3/16	195%	98%	65%	49%	39%	33%	28%	24%	22%	22%	22%	B
1/4	195%	98%	65%	49%	39%	33%	28%	24%	22%	22%	22%	B
5/16	195%	98%	65%	49%	39%	33%	28%	24%	22%	22%	22%	B
3/8	168%	84%	56%	42%	34%	28%	24%	21%	19%	19%	19%	S
1/2	126%	63%	42%	31%	25%	21%	18%	16%	14%	13%	13%	S
3/4	84%	42%	28%	21%	17%	14%	12%	10%	9%	8%	8%	S
1	65%	31%	21%	16%	13%	10%	9%	8%	7%	6%	6%	S

$R_{slip,Test}$ = 57%$A_g F_y$

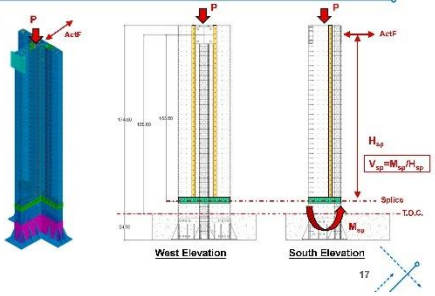
R_{slip} = 56%$A_g F_y$

15

Section of Horizontal Splice

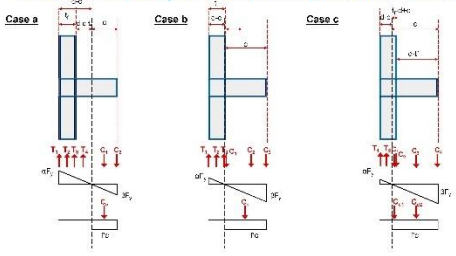


Splice Location



17

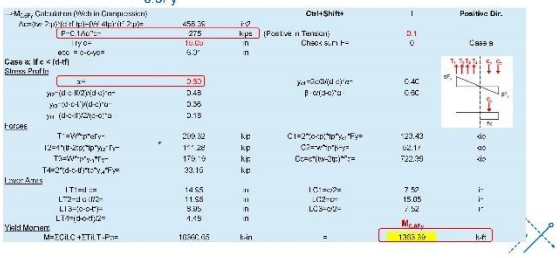
Moment Capacity of Faceplates (Positive, Elastic Stage)



18

University at Buffalo
Department of Civil, Structural and Environmental Engineering
School of Engineering and Applied Sciences

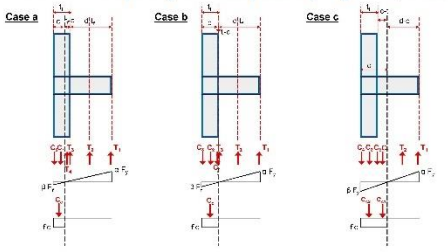
Calculation of $M_{0.6Fy}$



University at Buffalo
Department of Civil, Structural and Environmental Engineering
School of Engineering and Applied Sciences

Moment Capacity of Faceplates (Negative, Elastic Stage)

Case a | Case b | Case c



$\alpha=0.6 \rightarrow -M_{0.6Fy}$

University at Buffalo
Department of Civil, Structural and Environmental Engineering
School of Engineering and Applied Sciences

Summary of Moment (P=0.1*Ac*f'c)

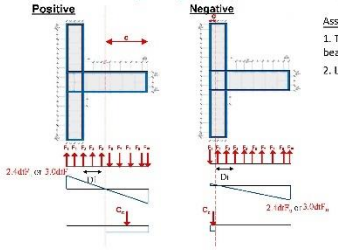
Material Property		
f'c (ksi)	Fy (ksi)	Fu (ksi)
6	55	70

	Positive Dir.	Negative Dir.	
$M_{0.6Fy}$	1363.39	564.18	k-ft
M_y	1666.38	799.01	k-ft
M_u	2011.84	1311.16	k-ft

University at Buffalo
Department of Civil, Structural and Environmental Engineering
School of Engineering and Applied Sciences

Moment Capacity of Splice Plates (Bearing Type)

Positive | **Negative**



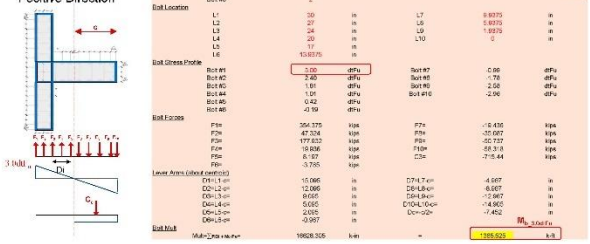
Assumption

1. The outer row of bolts on the tension edge develops bearing strength ($2.4dtF_u$ or $3.0dtF_u$).
2. Linear bolt force distribution.

University at Buffalo
Department of Civil, Structural and Environmental Engineering
School of Engineering and Applied Sciences

$M_{bearing}$ Calculation

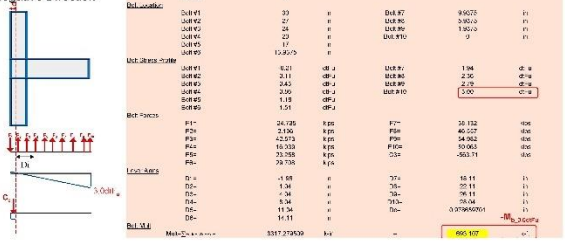
Positive Direction



University at Buffalo
Department of Civil, Structural and Environmental Engineering
School of Engineering and Applied Sciences

$M_{bearing}$ Calculation

Negative Direction



University at Buffalo
Department of Civil, Structural and Environmental Engineering
School of Engineering and Applied Sciences

Summary of Moment (P=0.1*Ac*f'c)

Material Property		
f'c (ksi)	Fy (ksi)	Fu (ksi)
6	55	70

	Positive Dir.	Negative Dir.	
$M_{0.6F_y}$	1363.39	564.18	k-ft
M_y	1666.38	799.01	k-ft
M_c	2011.84	1311.16	k-ft
$M_{bearing,\ 2.4dF_c}$	1210.07	596.25	K-ft
$M_{bearing,\ 3.6dF_c}$	1385.53	693.11	K-ft

25

University at Buffalo
Department of Civil, Structural and Environmental Engineering
School of Engineering and Applied Sciences

FINITE ELEMENT ANALYSIS

University at Buffalo
Department of Civil, Structural and Environmental Engineering
School of Engineering and Applied Sciences

T Wall FEM
General Info.



Plan View

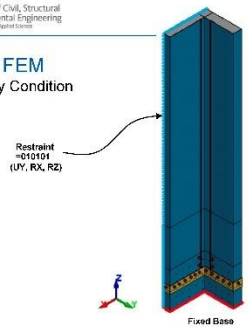

3D Model

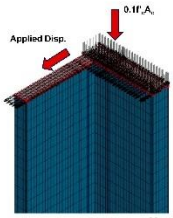

Splice Plates


Bottom Parts

University at Buffalo
Department of Civil, Structural and Environmental Engineering
School of Engineering and Applied Sciences

T Wall FEM
Boundary Condition





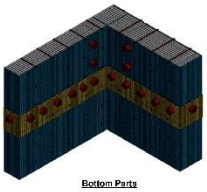
28

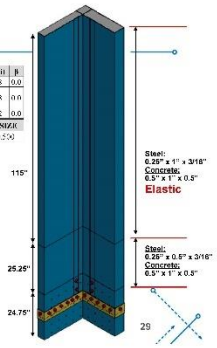
University at Buffalo
Department of Civil, Structural and Environmental Engineering
School of Engineering and Applied Sciences

T Wall FEM
Material and Meshes

Part	E_c (ksi)	Poisson's Ratio	F_y (ksi)	E_s (ksi)	β
Face Plates	29000	0.3	55.0	138.8	0.0
Splice Plates	29000	0.3	55.0	138.8	0.0
Bolts	29000	0.3	120.0	231.2	0.0

Part	E_c (ksi)	Poisson's Ratio	F_c (psi)	f_t (psi)	FL	ASDZC
Concrete	4415	0.2	6000	600	0.00200	0.550

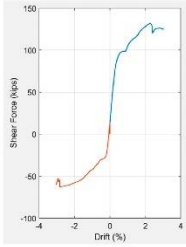

Steel:
0.25" x 0.25" x 3/16"
Concrete:
0.5" x 0.5" x 0.5"
Bottom Parts

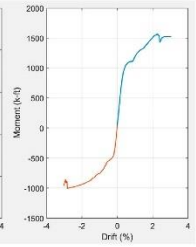


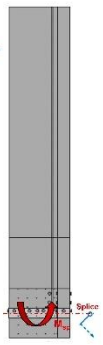
29

University at Buffalo
Department of Civil, Structural and Environmental Engineering
School of Engineering and Applied Sciences

Shear Force and Moment at Splice

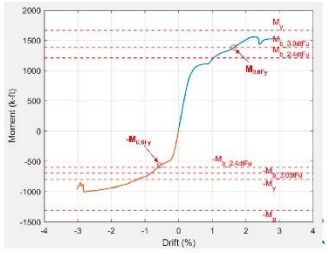




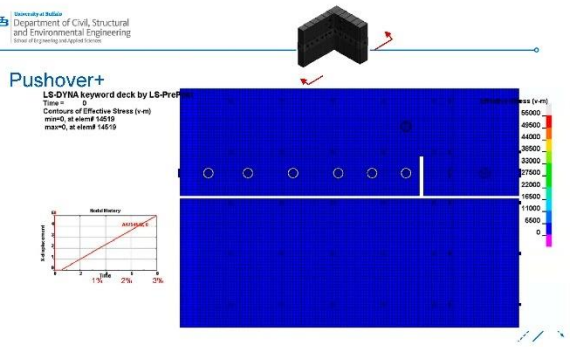


Moment Curve from FEM

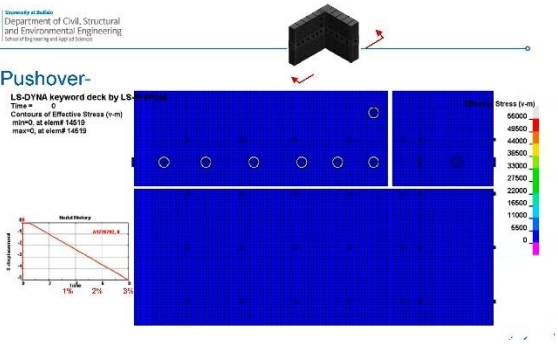
	Positive Dir.	Negative Dir.	
$M_{1.5\%y}$	1363.38	564.18	k-ft
M_y	1668.38	799.01	k-ft
M_u	2011.84	1311.16	k-ft
$M_{beamg_2.4dFu}$	1210.07	596.25	K-ft
$M_{beamg_3.0dFu}$	1385.53	693.11	K-ft



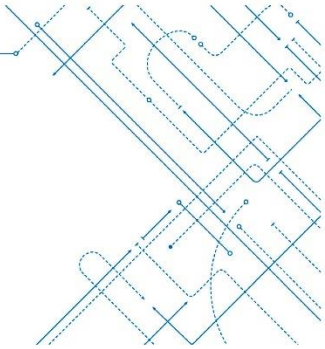
Pushover+



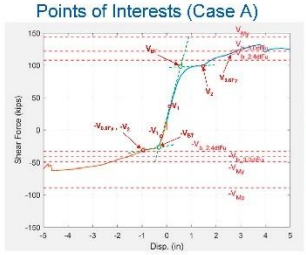
Pushover-



LOAD PROTOCOL



Points of Interests (Case A)



Points before Bearing

Disp. (in)	Force (kips)	Disp. (in)	Force (kips)	Note
0.00	0	0.00	0	
0.16	88	0.26	76	V_1
0.60	97	0.75	98	V_{BT}
1.48	95	1.50	97	V_2

1st Sliding
B: Linear Tangent Point
1st Bearing

Calculated Shear Force

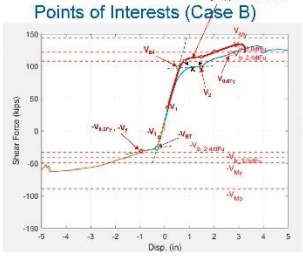
Disp. (in)	Force (kips)	Disp. (in)	Force (kips)	Note
2.40	120	0.93	92	$V_{0.93in}$
2.80	108	1.86	88	$V_{1.86in}$
3.30	115	3.28	97	Translation
3.86	123	3.86	40	$V_{3.86in}$
-	44	2.24	46	V_{sq}

*Displacement values obtained from FEA

Actual displacements are decided in real-time during the test.

Points of Interests (Case B)

Sliding happen after 2.4dFu



Calculated Shear Force

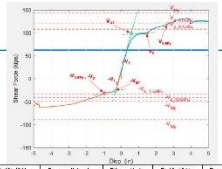
Disp. (in)	Force (kips)	Disp. (in)	Force (kips)	Note
2.40	120	0.93	92	$V_{0.93in}$
2.80	108	1.86	88	$V_{1.86in}$
3.30	115	3.28	97	Translation
3.86	123	3.86	40	$V_{3.86in}$
-	44	2.24	46	V_{sq}

*Displacement values obtained from FEA

Actual displacements are decided in real-time during the test.

University at Buffalo
Department of Civil, Structural and Environmental Engineering
School of Engineering and Applied Sciences

Load Protocol (Case A)

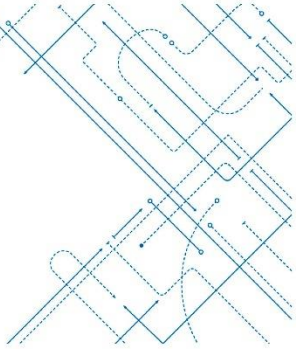


*Displacement values obtained from FEA
*P_w = Target Load / Design Value

Step	Disp. (in)	Drift (%)	Force (kips)	Disp. (in) -	Drift (%) -	Force (kips) -	Cycles	Note 1	Note 2
0	0.00	0.00	0	0.00	0.00	0	-		
REF1	0.16	0.10	38	-0.26	-0.16	-39		V_c	1st Slicing
1	0.45	0.27	-	0.25	0.15	-	3	0.25Pw	
2	0.90	0.55	-	-0.50	-0.30	-	3	0.5Pw	
3	1.35	0.82	-	-0.75	-0.45	-	3	0.75Pw	
4	-	-	-	-	-	-	3	V_{1st}	TBD
REF2	0.60	0.36	97	-0.25	-0.15	-29	-	V_{BL}	Bilinear Tangent
REF3	1.48	0.90	99	-0.92	-0.56	-31	-	V_3	1st Bearing
REF4	2.70	1.64	120	0.93		31		V 0.6Fy	
5	1.80	1.09	108	-1.00	-0.61	-33	3	Vb_2.4dtFu	1.0Pw
6	2.30	1.39	115	-1.28	-0.77	-37	3	Transition	Transition
7	2.80	1.70	122	-1.55	-0.94	-41	3	Vb_3.0dtFu	
8	-	-	144	-2.24	-	-49	2	V_{BA}	

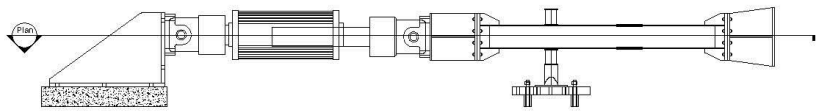
University at Buffalo
Department of Civil, Structural and Environmental Engineering
School of Engineering and Applied Sciences

DISCUSSION

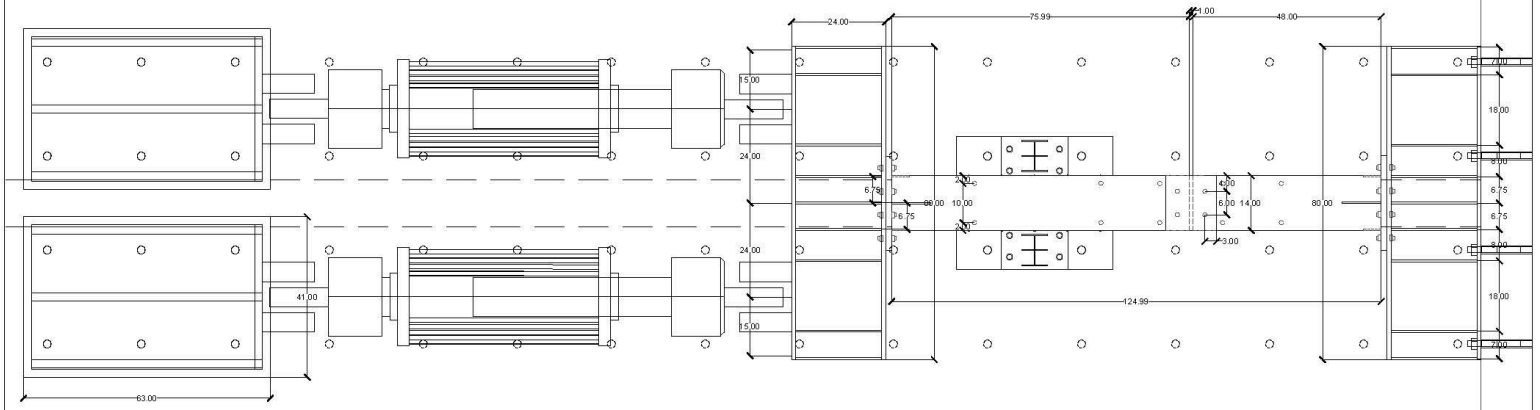


Appendix F.

Drawings of Specimens (Component Level Test)



Key Elevation

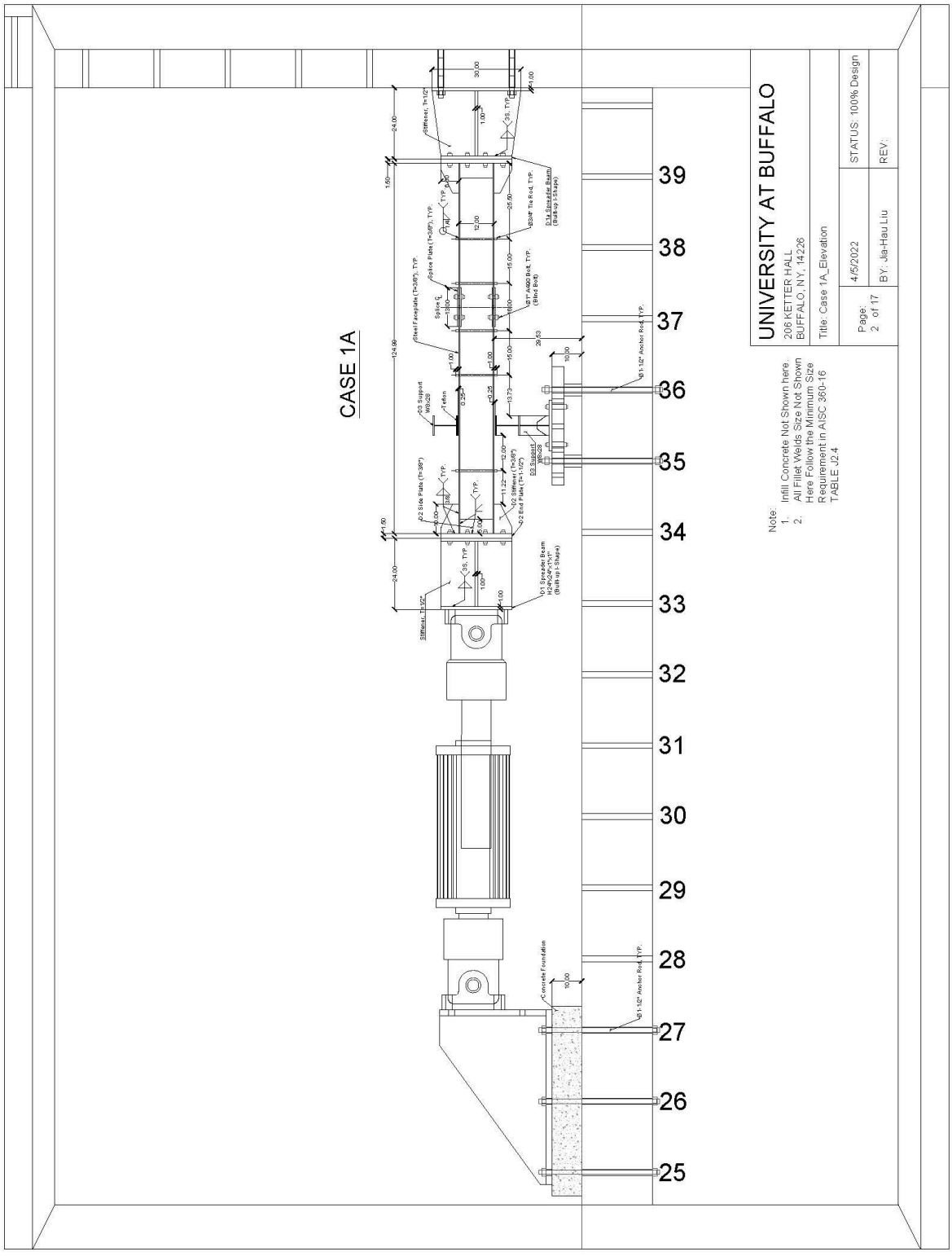


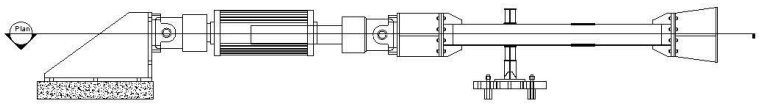
Plan

UNIVERSITY AT BUFFALO
206 KETTER HALL
BUFFALO, NY, 14226

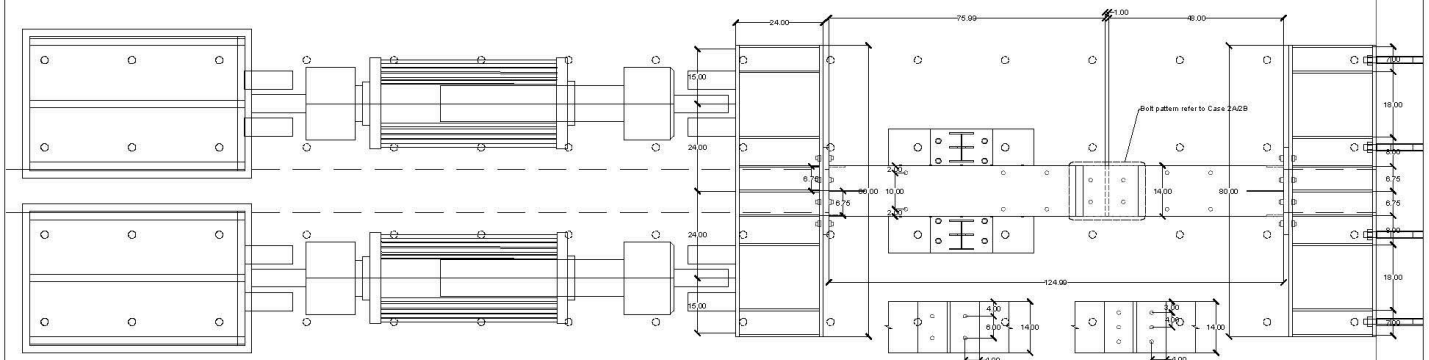
Title: Case 1A_Plan

Page: 1 of 17	4/5/2022	STATUS: 100% Design
	BY: Jia-Hau Liu	REV:


CASE 1A
UNIVERSITY AT BUFFALO
206 KETTER HALL
BUFFALO, NY, 14226
Title: Case 1A_Elevation
Page: 2 of 17
4/5/2022
BY: Jia-Hau Liu
STATUS: 100% Design
REV:
Note:
1. Infill Concrete Not Shown here.
2. All Fillet Welds Size Not Shown Here Follow the Minimum Size Requirement in AISC 360-16 TABLE J2.4
39
38
37
36
35
34
33
32
31
30
29
28
27
26
25

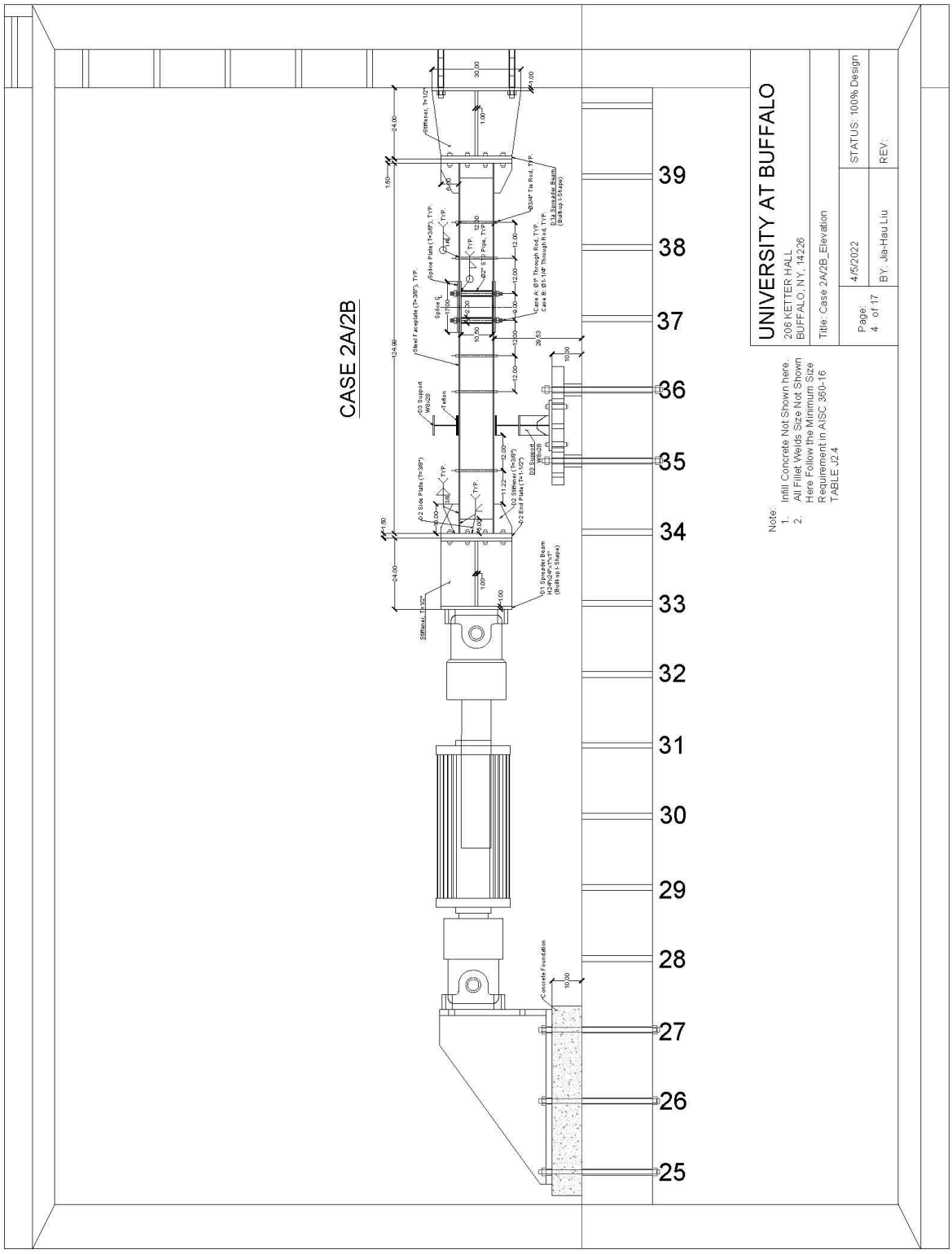


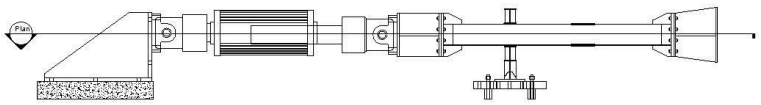
Key Elevation



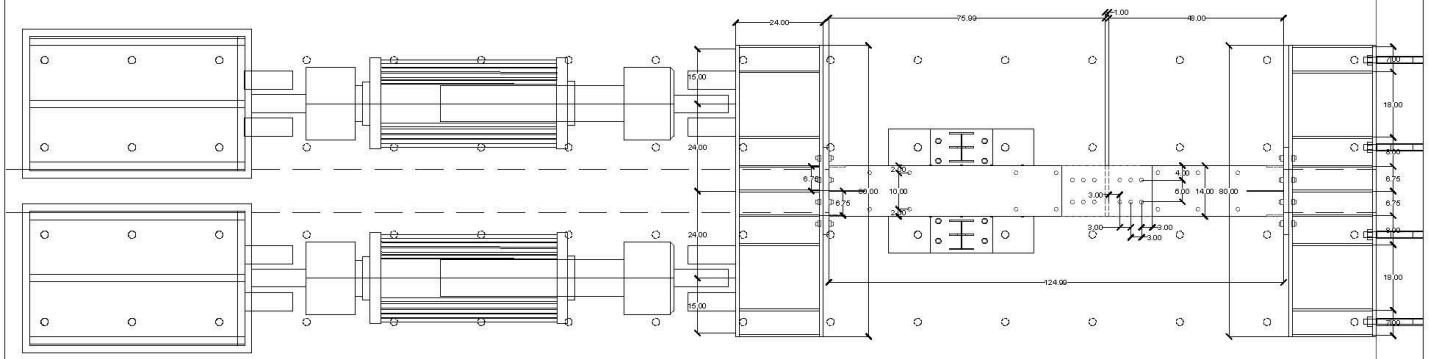
CASE 2A CASE 2B

UNIVERSITY AT BUFFALO 206 KETTER HALL BUFFALO, NY, 14226		
Title: Case 2A/2B_Plan		
Page: 3 of 17	4/5/2022	STATUS: 100% Design
	BY: Jia-Hau Liu	REV:


CASE 2A/2B
39
38
37
36
35
34
33
32
31
30
29
28
27
26
25
UNIVERSITY AT BUFFALO
206 KETTER HALL
BUFFALO, NY, 14226
Title: Case 2A/2B_Elevation
Page: 4 of 17
4/5/2022
BY: Jia-Hau Liu
STATUS: 100% Design
REV:
Note:
1. Infill Concrete Not Shown here.
2. All Fillet Welds Size Not Shown Here Follow the Minimum Size Requirement in AISC 360-16 TABLE J2.4

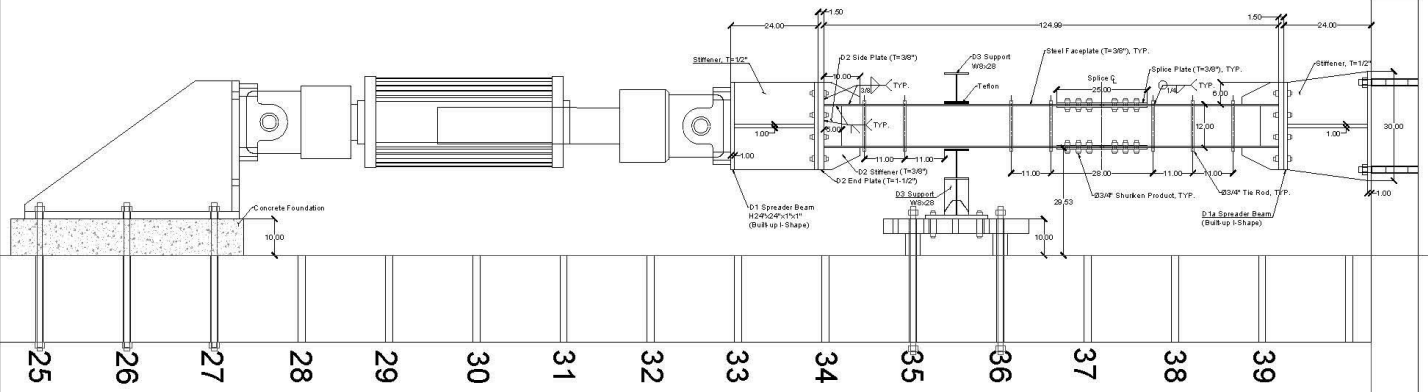


Key Elevation



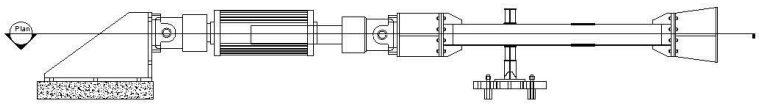
UNIVERSITY AT BUFFALO 206 KETTER HALL BUFFALO, NY, 14226		
Title: Case 1C_Plan		
Page: 5 of 17	4/5/2022	STATUS: 100% Design
	BY: Jia-Hau Liu	REV:

CASE 1C

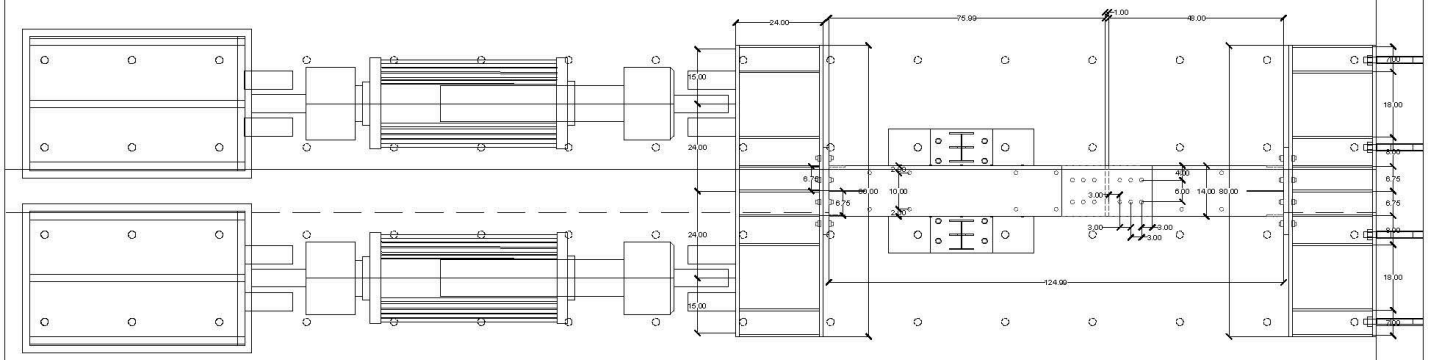


Note:
1. Infill Concrete Not Shown here.
2. All Fillet Welds Size Not Shown Here Follow the Minimum Size Requirement in AISC 360-16 TABLE J2.4

UNIVERSITY AT BUFFALO 206 KETTER HALL BUFFALO, NY, 14226		
Title: Case 1C_Elevation		
Page: 6 of 17	4/5/2022	STATUS: 100% Design
	BY: Jia-Hau Liu	REV:

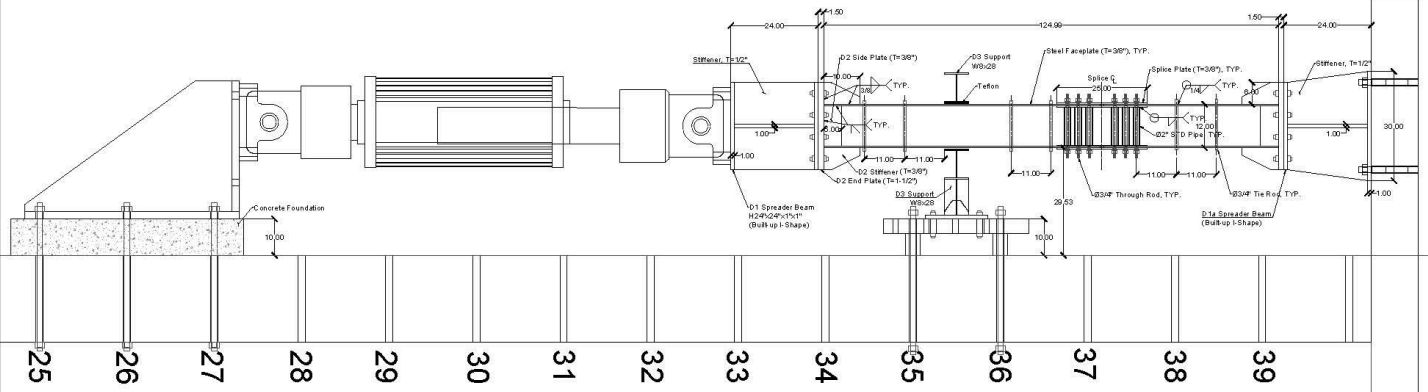


Key Elevation



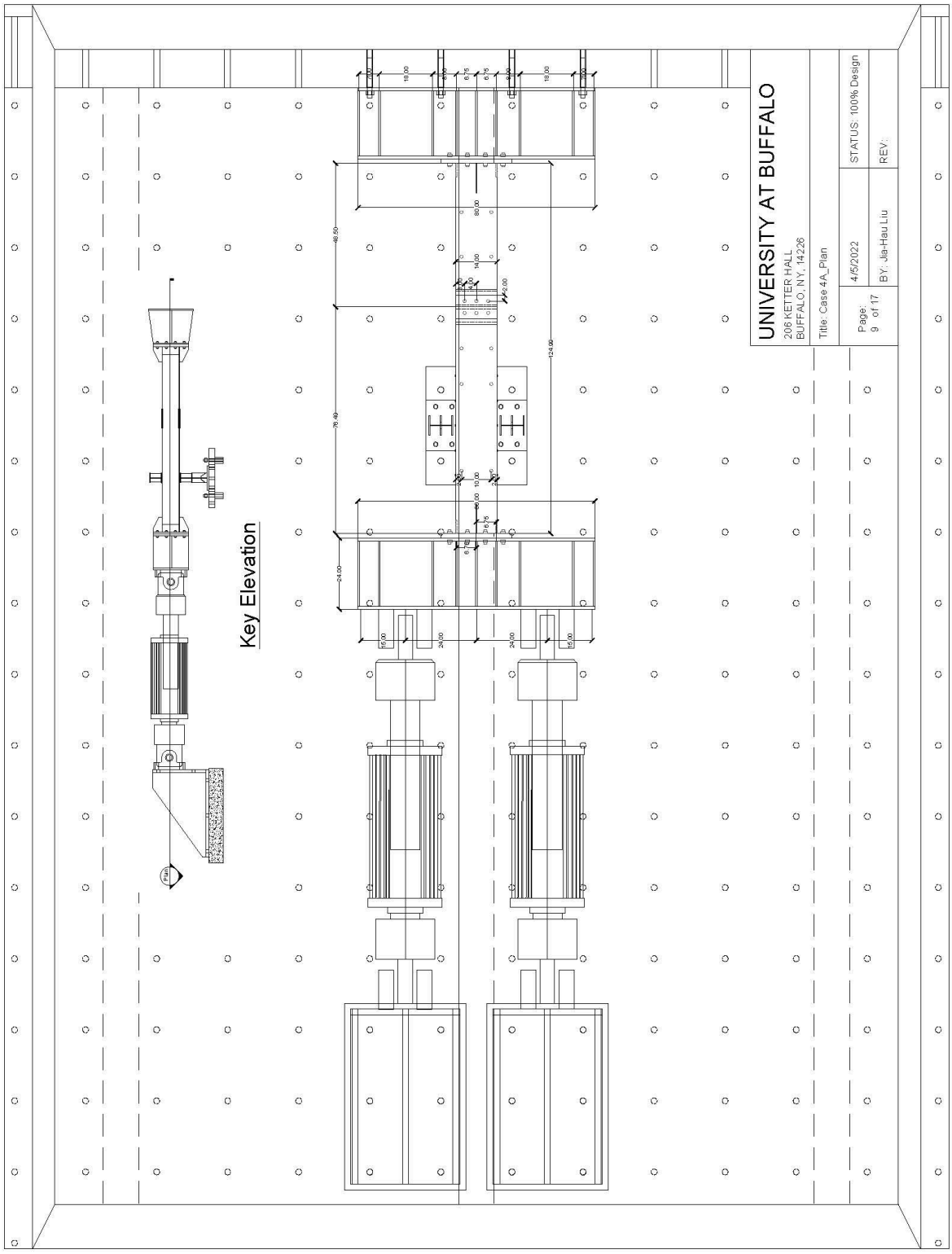
UNIVERSITY AT BUFFALO 206 KETTER HALL BUFFALO, NY, 14226		
Title: Case 2C_Plan		
Page: 7 of 17	4/5/2022	STATUS: 100% Design
	BY: Jia-Hau Liu	REV:

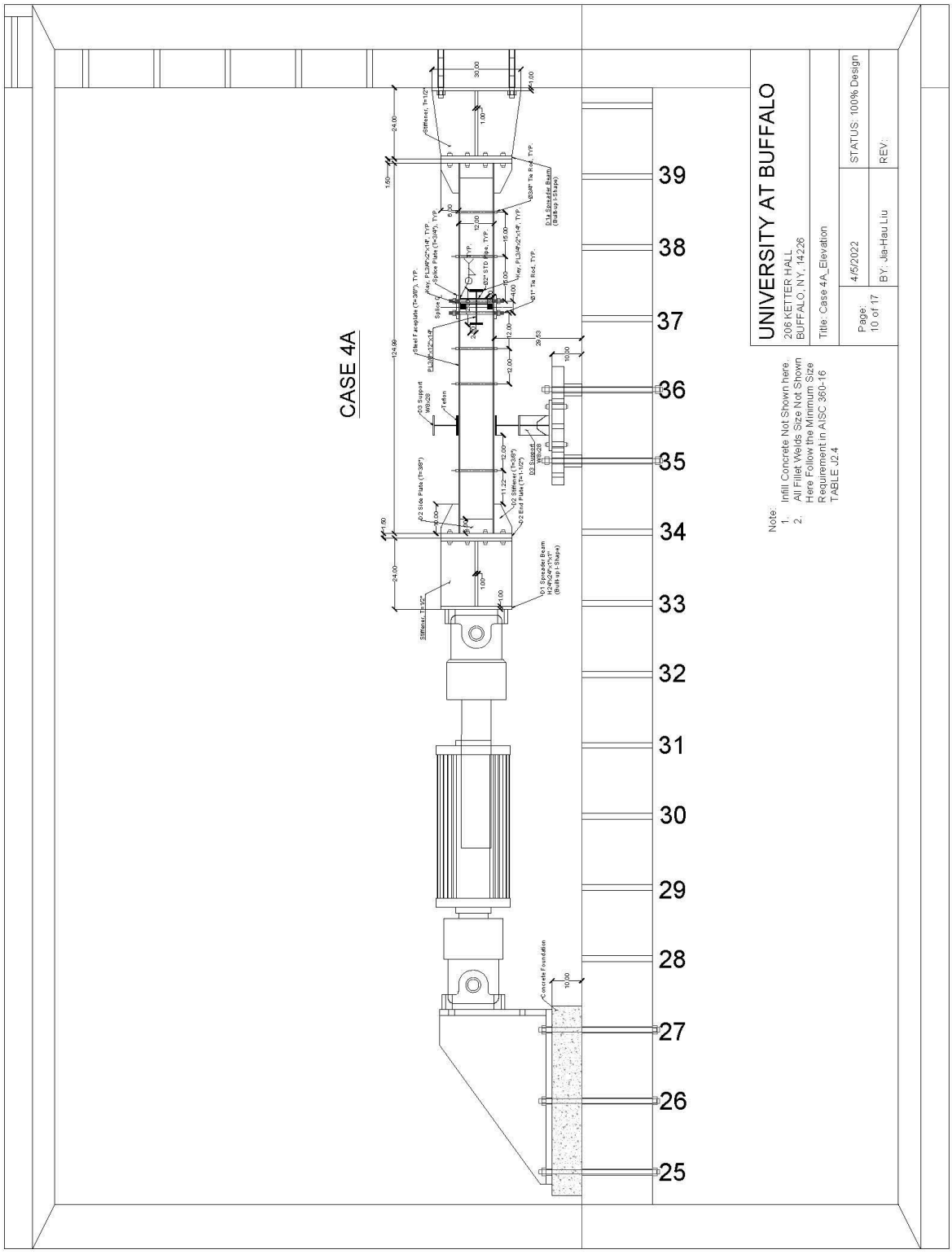
CASE 2C

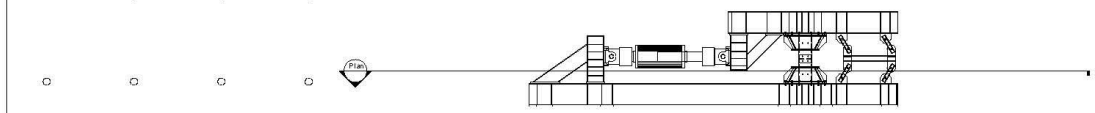


Note:
1. Infill Concrete Not Shown here.
2. All Fillet Welds Size Not Shown Here Follow the Minimum Size Requirement in AISC 360-16 TABLE J2.4

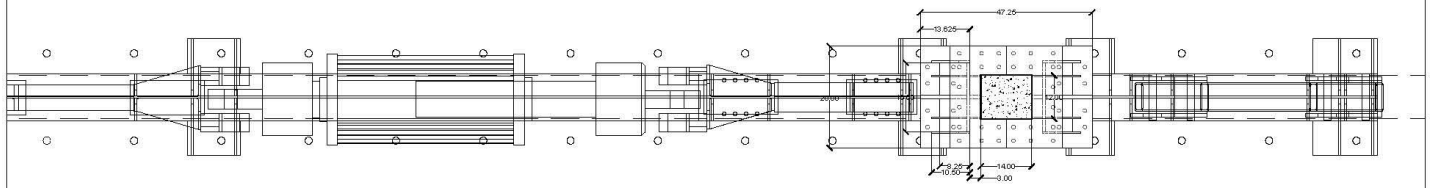
UNIVERSITY AT BUFFALO 206 KETTER HALL BUFFALO, NY, 14226		
Title: Case 2C_Elevation		
Page: 8 of 17	4/5/2022	STATUS: 100% Design
	BY: Jia-Hau Liu	REV:


Key Elevation
UNIVERSITY AT BUFFALO
206 KETTER HALL
BUFFALO, NY, 14226
Title: Case 4A_Plan
4/5/2022
BY: Jia-Hau Liu
STATUS: 100% Design
REV:
Page:
9 of 17


CASE 4A
39
38
37
36
35
34
33
32
31
30
29
28
27
26
25
UNIVERSITY AT BUFFALO
206 KETTER HALL
BUFFALO, NY, 14226
Title: Case 4A_Elevation
Page: 10 of 17
4/5/2022
BY: Jia-Hau Liu
STATUS: 100% Design
REV:
Note:
1. Infill Concrete Not Shown here.
2. All Fillet Welds Size Not Shown Here Follow the Minimum Size Requirement in AISC 360-16 TABLE J2.4

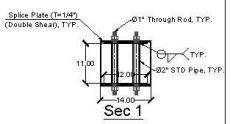


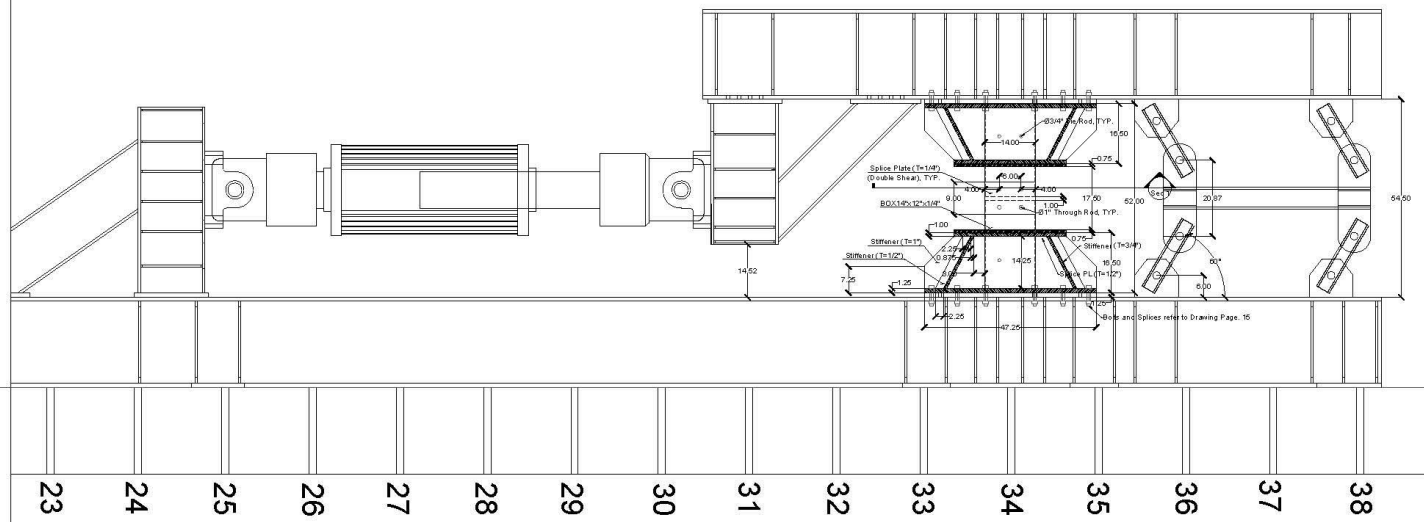
Key Elevation



UNIVERSITY AT BUFFALO		
206 KETTER HALL BUFFALO, NY, 14226		
Title: Shear Test Setup_Plan		
Page: 11 of 17	4/5/2022	STATUS: 100% Design
	BY: Jia-Hau Liu	REV:

CASE 6A/6Ac

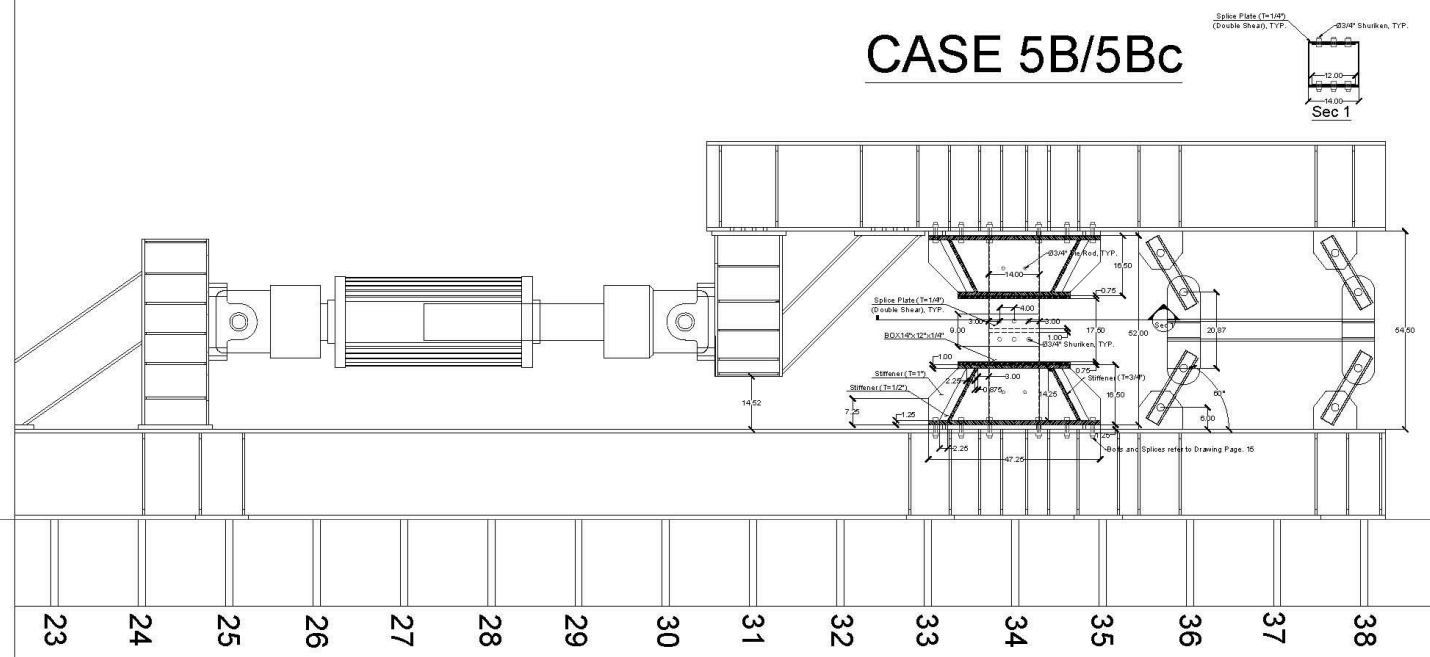




Note:
1. All Fillet Welds Size Not Shown Here Follow the Minimum Size Requirement in AISC 360-16 TABLE J2.4

UNIVERSITY AT BUFFALO 206 KETTER HALL BUFFALO, NY, 14226		
Title: Case 6A/6Ac_Elevation		
Page: 12 of 17	4/5/2022	STATUS: 100% Design
	BY: Jia-Hau Liu	REV:

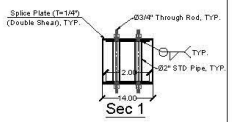
CASE 5B/5Bc

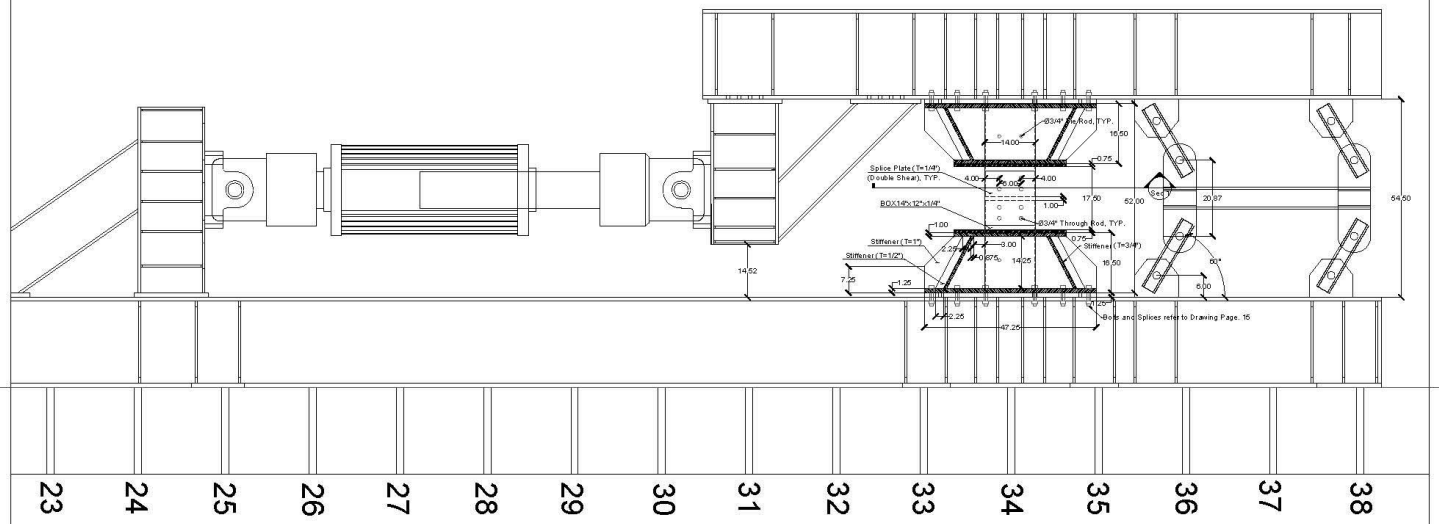


Note:
1. All Fillet Welds Size Not Shown Here Follow the Minimum Size Requirement in AISC 360-16 TABLE J2.4

UNIVERSITY AT BUFFALO 206 KETTER HALL BUFFALO, NY, 14226		
Title: Case 5B/5Bc_Elevation		
Page: 13 of 17	4/5/2022	STATUS: 100% Design
	BY: Jia-Hau Liu	REV:

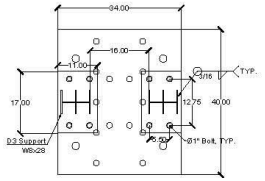
CASE 6C/6Cc



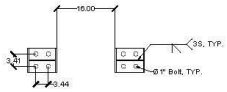


Note:
1. All Fillet Welds Size Not Shown Here Follow the Minimum Size Requirement in AISC 360-16 TABLE J2.4

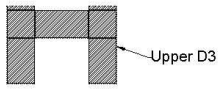
UNIVERSITY AT BUFFALO 206 KETTER HALL BUFFALO, NY, 14226		
Title: Case 5B/5Bc_Elevation		
Page: 14 of 17	4/5/2022	STATUS: 100% Design
	BY: Jia-Hau Liu	REV:



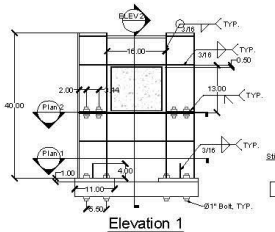
Plan 1



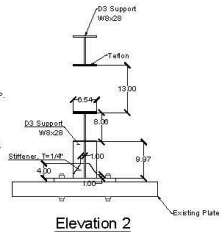
Plan 2



Decomposition of D3



Elevation 1

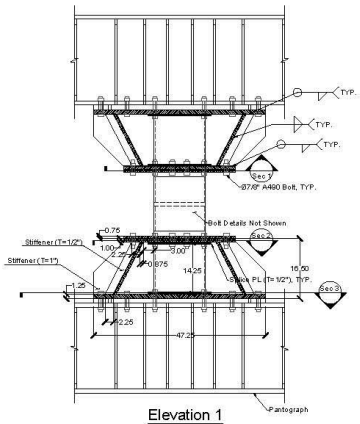


Elevation 2

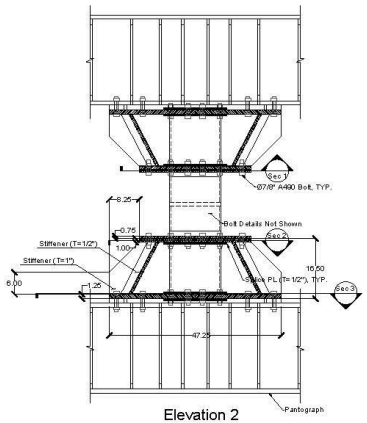
D3 Support for Tension Test

Note:
1. All Fillet Welds Size Not Shown Here Follow the Minimum Size Requirement in AISC 360-16 TABLE J2.4

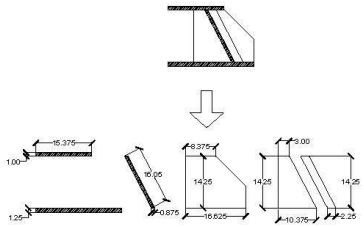
UNIVERSITY AT BUFFALO		
206 KETTER HALL BUFFALO, NY, 14226		
Title: D3 Support Details		
Page: 15 of 17	4/5/2022	STATUS: 100% Design
	BY: Jia-Hau Liu	REV:



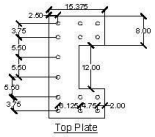
Elevation 1



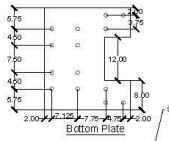
Elevation 2



Details of Reusable Part (Elevation)



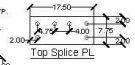
Top Plate



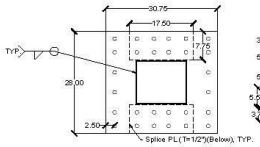
Bottom Plate



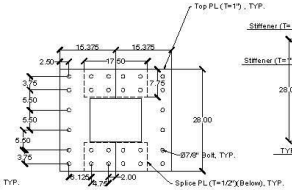
Bottom Splice PL



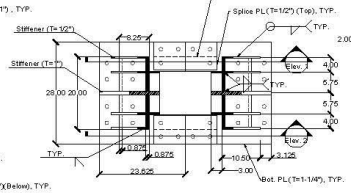
Top Splice PL



Sec 1 (Connection PL)



Sec 2



Sec 3

Reusable Part for Shear Test

Note:
1. All Fillet Welds Size Not Shown Here Follow the Minimum Size Requirement in AISC 360-16 TABLE J2.4

UNIVERSITY AT BUFFALO 206 KETTER HALL BUFFALO, NY, 14226		
Title: Reusable Part for Shear Test		
Page: 16 of 17	4/5/2022	STATUS: 100% Design
	BY: Jia-Hau Liu	REV:

1. Tension Test Specimens

(1) Case 1A

ITEM	QTY	PART NAME	MATERIAL	DESCRIPTION
1	2	PL 3/8x14x76	A572 Gr. 50	Faceplates-L
2	2	PL 3/8x14x48	A572 Gr. 50	Faceplates-R
3	4	PL 3/8x14x13	A572 Gr. 50	Splice Plate
4	8	Φ1" Bolt, L=3-1/8"	Grade A490	For Splice
5	10	Φ3/4" Tie Rod, L=14"	A572 Gr. 55	-
6	2	PL 1-1/2x24x24	A572 Gr. 50	D2 End Plate
7	4	PL 3/8x5x11.25	A572 Gr. 50	D2 Side Plate
8	4	PL 3/8x10x6	A572 Gr. 50	D2 Stiffener
9	32	Φ1" Bolt, L=4.5"	Grade A490	For D2 End Plate
10	2	PL 3/32x14x10	Teflon	In D3 region

(2) Case 2A/2B

ITEM	QTY	PART NAME	MATERIAL	DESCRIPTION
1	4	PL 3/8x14x76	A572 Gr. 50	Faceplates-L
2	4	PL 3/8x14x48	A572 Gr. 50	Faceplates-R
3	8	PL 3/8x14x17	A572 Gr. 50	Splice Plate
4	4	Φ1" Through Rod, L=15"	A354 Gr. BD	For Splice (Case 2A)
5	6	Φ1-1/2" Through Rod, L=15"	A354 Gr. BD	For Splice (Case 2B)
6	10	Φ2" STD Pipe, L=10.5"	A53 Gr. B	Rod Sleeve
7	20	Φ3/4" Tie Rod, L=14"	A572 Gr. 55	-
8	4	PL 1-1/2x24x24	A572 Gr. 50	D2 End Plate
9	8	PL 3/8x5x11.25	A572 Gr. 50	D2 Side Plate
10	8	PL 3/8x10x6	A572 Gr. 50	D2 Stiffener
11	64	Φ1" Bolt, L=4.5"	Grade A490	For D2 End Plate
12	4	PL 3/32x14x10	Teflon	In D3 region

(3) Case 1C

ITEM	QTY	PART NAME	MATERIAL	DESCRIPTION
1	2	PL 3/8x14x76	A572 Gr. 50	Faceplates-L
2	2	PL 3/8x14x48	A572 Gr. 50	Faceplates-R
3	4	PL 3/8x14x25	A572 Gr. 50	Splice Plate
4	24	Φ3/4" Shuriken, L=3-1/8"	Grade A490	For Splice
5	14	Φ3/4" Tie Rod, L=14"	A572 Gr. 55	-
6	2	PL 1-1/2x24x24	A572 Gr. 50	D2 End Plate
7	4	PL 3/8x5x11.25	A572 Gr. 50	D2 Side Plate
8	4	PL 3/8x10x6	A572 Gr. 50	D2 Stiffener
9	32	Φ1" Bolt, L=4.5"	Grade A490	For D2 End Plate
10	2	PL 3/23x14x10	Teflon	In D3 region

(4) Case 2C

ITEM	QTY	PART NAME	MATERIAL	DESCRIPTION
1	2	PL 3/8x14x76	A572 Gr. 50	Faceplates-L
2	2	PL 3/8x14x48	A572 Gr. 50	Faceplates-R
3	4	PL 3/8x14x25	A572 Gr. 50	Splice Plate
4	12	Φ3/4" Through Rod, L=15"	A354 Gr. BD	For Splice
5	12	Φ2" STD Pipe, L=10.5"	A53 Gr. B	Rod Sleeve
6	12	Φ3/4" Tie Rod, L=14"	A572 Gr. 55	-
7	2	PL 1-1/2x24x24	A572 Gr. 50	D2 End Plate
8	4	PL 3/8x5x11.25	A572 Gr. 50	D2 Side Plate
9	4	PL 3/8x10x6	A572 Gr. 50	D2 Stiffener
10	32	Φ1" Bolt, L=4.5"	Grade A490	For D2 End Plate
11	2	PL 3/23x14x10	Teflon	In D3 region

(5) Case 4A

ITEM	QTY	PART NAME	MATERIAL	DESCRIPTION
1	2	PL 3/8x14x76.5	A572 Gr. 50	Faceplates-L
2	2	PL 3/8x14x48.5	A572 Gr. 50	Faceplates-R
3	4	PL 3/8x14x8	A572 Gr. 50	Splice Plate
4	6	Φ1" Through Rod, L=14.75"	A354 Gr. BD	For Splice
5	3	Φ2" STD Pipe, L=10.5"	A53 Gr. B	Rod Sleeve
6	10	Φ3/4" Tie Rod, L=14"	A572 Gr. 55	-
7	2	PL 1-1/2x24x24	A572 Gr. 50	D2 End Plate
8	4	PL 3/8x5x11.25	A572 Gr. 50	D2 Side Plate
9	4	PL 3/8x10x6	A572 Gr. 50	D2 Stiffener
10	32	Φ1" Bolt, L=4.5"	Grade A490	For D2 End Plate
11	2	PL 3/23x14x10	Teflon	In D3 region
12	8	PL 3/4x2x14	A572 Gr. 50	Anchor PL_Key
13	1	PL3/8x12x14	A572 Gr. 50	Anchor PL_Web

2. Shear Test Specimens

(1) Case 6A/6Ac

ITEM	QTY	PART NAME	MATERIAL	DESCRIPTION
1	4	BOX 14x12x1/4, L=24.25"	A572 Gr. 50	Faceplates
2	4	PL 1/4x14x9	A572 Gr. 50	Splice Plate
3	4	PL 1/4x12x9	A572 Gr. 50	Splice Plate
4	8	Φ1" Through Rod, L=14.75"	A354 Gr. BD	For Splice
5	8	Φ2" STD Pipe, L=11"	A53 Gr. B	Rod Sleeve
6	8	Φ3/4" Tie Rod, L=14"	Grade A490	-
7	4	PL 3/4x30.75x28	A572 Gr. 50	Conn. PL
8	64	Φ7/8" Bolt, L=4.25"	Grade A490	Conn. Bolt
9	48	Φ7/8" Bolt, L=4.25"	Grade A490	Conn. Bolt

(2) Case 5B/5Bc

ITEM	QTY	PART NAME	MATERIAL	DESCRIPTION
1	4	BOX 14x12x1/4, L=24.25"	A572 Gr. 50	Faceplates
2	4	PL 1/4x14x9	A572 Gr. 50	Splice Plate
3	4	PL 1/4x12x9	A572 Gr. 50	Splice Plate
4	24	Φ3/4" Shuriken, L=3.125"	Grade A490	For Splice
5	8	Φ3/4" Tie Rod, L=14"	A572 Gr. 55	-
6	4	PL 3/4x30.75x28	A572 Gr. 50	Conn. PL
7	64	Φ7/8" Bolt, L=4.25"	Grade A490	Conn. Bolt
8	48	Φ7/8" Bolt, L=4.25"	Grade A490	Conn. Bolt

(2) Case 6C/6Cc

ITEM	QTY	PART NAME	MATERIAL	DESCRIPTION
1	4	BOX 14x12x1/4, L=24.25"	A572 Gr. 50	Faceplates
2	4	PL 1/4x14x9	A572 Gr. 50	Splice Plate
3	4	PL 1/4x12x9	A572 Gr. 50	Splice Plate
4	16	Φ3/4" Through Rod, L=12.75"	A354 Gr. BD	For Splice
5	16	Φ2" STD Pipe, L=10.5"	A53 Gr. B	Rod Sleeve
6	8	Φ3/4" Tie Rod, L=14"	A572 Gr. 55	-
7	4	PL 3/4x30.75x28	A572 Gr. 50	Conn. PL
8	64	Φ7/8" Bolt, L=4.25"	Grade A490	Conn. Bolt
9	48	Φ7/8" Bolt, L=4.25"	Grade A490	Conn. Bolt

3. Tension Test Setup

ITEM	QTY	PART NAME	MATERIAL	DESCRIPTION
1	1	WF24x24x1x1 ($d*b_f*t_w*t_f$)	A572 Gr. 50	D1 Spreader Beam (Built-up Section)
2	18	PL 1/2x11.5x22	A572 Gr. 50	D1 Stiffener
3	1	H24xWx1x1 (W varies from 24" to 30")	A572 Gr. 50	D1a Spreader Beam (Built-up Section)
4	18	PL 1/2xWx22 (W varies from 11.5" to 14.5")	A572 Gr. 50	D1a Stiffener
5	2	W8x28, L=40"	A572 Gr. 50	D3 Column
6	2	W8x28, L=16"	A572 Gr. 50	D3 Beam
7	20	PL 1/4x3x7.5	A572 Gr. 50	D3 Stiffener
8	2	PL 1x11x17	A572 Gr. 50	D3 Base Plate
9	4	PL 1/4x4x4	A572 Gr. 50	D3 Base Stiffener
10	2	PL 3/23x14x6.54	Teflon	In D3 region
11	8	Φ1" Bolt, L=2.5"	Grade A490	For D3 Column Conn.
12	8	Φ1" Bolt, L=7"	Grade A490	For D3 Base Conn.
13	8	Φ1-1/2" Through Rod, L=45"	A354 Gr. BD	Anchor Rods

4. Shear Test Setup

ITEM	QTY	PART NAME	MATERIAL	DESCRIPTION
1	4	PL 1x15.375x28	A572 Gr. 50	Top Plate
2	4	PL 1-1/4x23.625x28	A572 Gr. 50	Bottom Plate
3	2	PL 1xWx14.25 (W varies from 8.375" to 16.625")	A572 Gr. 50	Stiffener
4	4	PL 7/8x9x16	A572 Gr. 50	Stiffener
5	4	PL 1/2xWx14.25 (W varies from 3" to 10.375")	A572 Gr. 50	Stiffener
6	8	PL 1/2x2.25x14.25	A572 Gr. 50	Stiffener
7	24	Φ7/8" Bolt, L=4.25"	Grade A490	Base Bolt
8	32	Φ7/8" Bolt, L=6.0"	Grade A490	Base Bolt
9	4	PL 1/2x4.0x17.5	A572 Gr. 50	Splice Plate
10	8	PL 1/2x7.75x17.5	A572 Gr. 50	Splice Plate

UNIVERSITY AT BUFFALO
206 KETTER HALL
BUFFALO, NY, 14226

Title: Material List

Page: 17 of 17	4/5/2022	STATUS: 100% Design
	BY: Jia-Hau Liu	REV:

Appendix G.

Analysis of Specimens (Component Level Test)

Design of Test Specimen T1 (Case 1A)

0. Typical Information

Use A572 Gr. 50 Steel

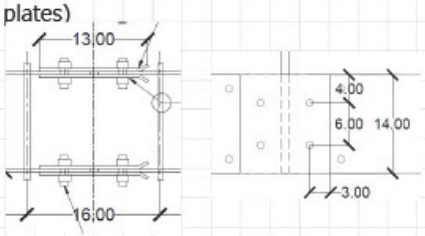
$F_y = 63\ ksi \quad R_y = 1 \quad F_u = 83\ ksi \quad R_u = 1$

$t_s = 0.375\ in \quad B = 14\ in$ (B=Wall Width)

Bolt Layout

$d_b = 1\ in \quad d_H = 0.125\ in$ (d_H=clearance between bolts and steel plates)

$N_{rows} = 1 \quad N_b = 2 \quad L_{e1} = 3\ in \quad S_v = 3\ in \quad L_{e2} = 4\ in$



Plan Elevation

1. Slip-Critical Resistance

Use Grade A490 Bolts (Double-Shear)

$\phi := 1$

$T_b := 64\ kip \quad D_u := 1.13 \quad h_f := 1 \quad \mu := 0.3$

$\phi R_{n1} := (\phi \cdot \mu \cdot D_u \cdot h_f \cdot T_b \cdot 2) \cdot N_{rows} \cdot N_b \cdot 2 = 173.568\ kip$ (AISC 360-16 J3-4)

2. Net Area Yielding

$\phi := 1$

$A_e := (B - N_b \cdot (d_b + d_H)) \cdot t_s \cdot 2 = 8.813\ in^2$

$\phi R_{n2} := A_e \cdot R_y \cdot F_y = 555.188\ kip$

3. Gross Area Yielding

$\phi := 1 \quad A_g := t_s \cdot B \cdot 2 = 10.5\ in^2$

$\phi R_{n3} := A_g \cdot R_y \cdot F_y = 661.5\ kip$ (AISC 360-16 J4-1)

4&5. Bearing and Tear-out Capacity

$\phi := 1$

$L_c := L_{e1} - \frac{(d_b + d_H)}{2} = 2.438\ in$

$\phi R_{n4} := 2.4 \cdot d_b \cdot t_s \cdot R_u \cdot F_u \cdot N_{rows} \cdot N_b \cdot 2 = 298.8\ kip$ (Bearing) (AISC 360-16 J3-6a)

$\phi R_{n5} := 1.2 \cdot L_c \cdot t_s \cdot R_u \cdot F_u \cdot N_b \cdot 2 = 364.163\ kip$ (Tear-out) (AISC 360-16 J3-6c)

6. Net Area Rupture

$\phi := 1$

$\phi R_{n6} := A_e \cdot R_u \cdot F_u = 731.438\ kip$ (AISC 360-16 J4-2)

7. Bolt Shear Strength

Use Grade A490 Bolts (Double-Shear)

$\phi := 1$

$F_v := 84\ ksi$ (AISC 360-16 Table J3.2) $A_b := \pi \cdot \frac{d_b^{\,2}}{4} = 0.785\ in^2$

$\phi R_{n7} := \left(\phi \cdot F_v \cdot A_b \cdot 2\right) \cdot N_{rows} \cdot N_b \cdot 2 = 527.788\ kip$

8. Block Shear Strength

$\phi := 1 \quad U_{bs} := 1$

$A_{nv} := L_c \cdot t_s \cdot 2 \cdot 2 = 3.656\ in^2 \quad A_{gv} := L_{e1} \cdot t_s \cdot 2 \cdot 2 = 4.5\ in^2 \quad A_{nt} := \left(N_b - 1\right) \cdot \left(S_h - d_b - d_H\right) \cdot t_s \cdot 2 = 3.656\ in^2$

$S_1 := 0.6\ R_u \cdot F_u \cdot A_{nv} = 182.081\ kip \quad S_2 := 0.6\ R_y \cdot F_y \cdot A_{gv} = 170.1\ kip$

$T_1 := U_{bs} \cdot R_u \cdot F_u \cdot A_{nt} = 303.469\ kip$

$\phi R_{n8} := \left|\begin{array}{l} \text{if } S_1 > S_2 \\ \quad \left\| T_1 + S_2 \right. \\ \text{else} \\ \quad \left\| T_1 + S_1 \right. \end{array}\right| = 473.569\ kip$ (AISC 360-16 J4-5)

9. Summary of Design Limit States

Limit_States	*Strength* (*kip*)	*Sequence*
"1. Slip–Critical Resistance"	173.57	1
"2. Net Section Yileding"	555.19	6
"3. Gross Area Yielding"	661.50	7
"4. Bearing Capacity"	298.8	2
"5. Tear–out Capacity"	364.16	3
"6. Net Section Rupture"	731.44	8
"7. Bolt Shear Strength"	527.79	5
"8. Block Shear Strength"	473.57	4

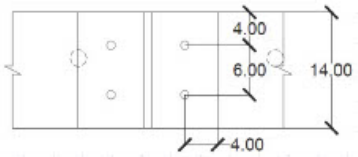
Design of Test Specimen T2 (Case 2A)

0. Typical Information

Use A572 Gr. 50 Steel

$F_y = 63\ ksi$ $R_y = 1$ $F_u = 83\ ksi$ $R_u = 1$

$t_s = 0.375\ in$ $B = 14\ in$ (B=Wall Width)

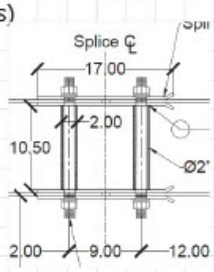


Plan

Bolt Layout

$d_b = 1\ in$ $d_H = 0.125\ in$ (d_H=clearance between bolts and steel plates)

$N_{rows} = 1$ $N_b = 2$ $L_{e1} = 3\ in$ $S_v = 3\ in$ $L_{e2} = 4\ in$



Elevation

1. Slip-Critical Resistance

Use A354 Gr. BD Rods (Double-Shear)

$\phi := 1$ $F_{u_rod} := 150\ ksi$

$A_b := \pi \cdot \frac{d_b^2}{4} = 0.785\ in^2$ $A_{b_thread} := 0.75 \cdot A_b = 0.589\ in^2$

$T_b := 0.7 \cdot F_{u_rod} \cdot A_{b_thread} = 61.85\ kip$ $D_u := 1.13$ $h_f := 1$ $\mu := 0.3$

$\phi R_{n1} := \left(\phi \cdot \mu \cdot D_u \cdot h_f \cdot T_b \cdot 2\right) \cdot N_{rows} \cdot N_b \cdot 2 = 167.737\ kip$ (AISC 360-16 J3-4)

2. Net Area Yielding

$\phi := 1$

$A_e := \left(B - N_b \cdot \left(d_b + d_H\right)\right) \cdot t_s \cdot 2 = 8.813\ in^2$

$\phi R_{n2} := A_e \cdot R_y \cdot F_y = 555.188\ kip$

3. Gross Area Yielding

$\phi := 1$ $A_g := t_s \cdot B \cdot 2 = 10.5\ in^2$

$\phi R_{n3} := A_g \cdot R_y \cdot F_y = 661.5\ kip$ (AISC 360-16 J4-1)

4&5. Bearing and Tear-out Capacity

$\phi := 1$

$L_c := L_{e1} - \frac{\left(d_b + d_H\right)}{2} = 2.438\ in$

$\phi R_{n4} := 2.4 \cdot d_b \cdot t_s \cdot R_u \cdot F_u \cdot N_{rows} \cdot N_b \cdot 2 = 298.8\ kip$ (Bearing) (AISC 360-16 J3-6a)

$\phi R_{n5} := 1.2 \cdot L_c \cdot t_s \cdot R_u \cdot F_u \cdot N_b \cdot 2 = 364.163\ kip$ (Tear-out) (AISC 360-16 J3-6c)

6. Net Area Rupture

$\phi := 1$

$\phi R_{n6} := A_e \cdot R_u \cdot F_u = 731.438\ kip$ (AISC 360-16 J4-2)

7. Bolt Shear Strength

Use A354 Gr. BD Rods (Double-Shear)

$\phi := 1$

$F_v := 0.563 \cdot F_{u_rod} = 84.45\ ksi$ (AISC 360-16 Table J3.2) $A_b := \pi \cdot \frac{d_b^2}{4} = 0.785\ in^2$

$\phi R_{n6} := \left(\phi \cdot F_v \cdot A_b \cdot 2\right) \cdot N_{rows} \cdot N_b \cdot 2 = 530.615\ kip$

8. Block Shear Strength

$\phi := 1 \quad U_{bs} := 1$

$A_{nv} := L_c \cdot t_s \cdot 2 \cdot 2 = 3.656\ in^2 \quad A_{gv} := L_{e1} \cdot t_s \cdot 2 \cdot 2 = 4.5\ in^2 \quad A_{nt} := \left(N_b - 1\right) \cdot \left(S_h - d_b - d_H\right) \cdot t_s \cdot 2 = 3.656\ in^2$

$S_1 := 0.6\ R_u \cdot F_u \cdot A_{nv} = 182.081\ kip \quad S_2 := 0.6\ R_y \cdot F_y \cdot A_{gv} = 170.1\ kip$

$T_1 := U_{bs} \cdot R_u \cdot F_u \cdot A_{nt} = 303.469\ kip$

$\phi R_{n8} := \begin{vmatrix} \text{if } S_1 > S_2 \\ \quad \| T_1 + S_2 \\ \text{else} \\ \quad \| T_1 + S_1 \end{vmatrix} = 473.569\ kip$ (AISC 360-16 J4-5)

9. Summary of Design Limit States

Limit_States	*Strength* (*kip*)	*Sequence*
"1. Slip–Critical Resistance"	167.74	1
"2. Net Section Yileding"	555.19	6
"3. Gross Area Yielding"	661.50	7
"4. Bearing Capacity"	298.8	2
"5. Tear–out Capacity"	364.16	3
"6. Net Section Rupture"	731.44	8
"7. Bolt Shear Strength"	530.61	5
"8. Block Shear Strength"	473.57	4

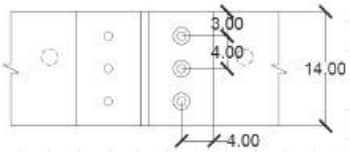
Design of Test Specimen T3 (Case 2B)

0. Typical Information

Use A572 Gr. 50 Steel

$F_y = 63\ ksi \quad R_y = 1 \quad F_u = 83\ ksi \quad R_u = 1$

$t_s = 0.375\ in \quad B = 14\ in$ (B=Wall Width)

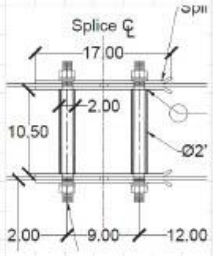


Plan

Bolt Layout

$d_b = 1.25\ in \quad d_H = 0.125\ in$ (d_H=clearance between bolts and steel plates)

$N_{rows} = 1 \quad N_b = 3 \quad L_{e1} = 4\ in \quad S_v = 3\ in \quad L_{e2} = 3\ in$



Elevation

1. Slip-Critical Resistance

Use A354 Gr. BD Rods (Double-Shear)

$\phi := 1 \quad F_{u_rod} := 150\ ksi$

$A_b := \pi \cdot \frac{d_b^2}{4} = 1.227\ in^2 \quad A_{b_thread} := 0.75 \cdot A_b = 0.92\ in^2$

$T_b := 0.7 \cdot F_{u_rod} \cdot A_{b_thread} = 96.641\ kip \quad D_u := 1.13 \quad h_f := 1 \quad \mu := 0.3$

$\phi R_{n1} := \left(\phi \cdot \mu \cdot D_u \cdot h_f \cdot T_b \cdot 2\right) \cdot N_{rows} \cdot N_b \cdot 2 = 393.135\ kip$ (AISC 360-16 J3-4)

2. Net Area Yielding

$\phi := 1$

$A_e := \left(B - N_b \cdot \left(d_b + d_H\right)\right) \cdot t_s \cdot 2 = 7.406\ in^2$

$\phi R_{n2} := A_e \cdot R_y \cdot F_y = 466.594\ kip$

3. Gross Area Yielding

$\phi := 1$

$A_g := t_s \cdot B \cdot 2 = 10.5\ in^2$

$\phi R_{n3} := A_g \cdot R_y \cdot F_y = 661.5\ kip$ (AISC 360-16 J4-1)

4&5. Bearing and Tear-out Capacity

$\phi := 1$

$L_c := L_{e1} - \frac{\left(d_b + d_H\right)}{2} = 3.313\ in$

$\phi R_{n4} := 2.4 \cdot d_b \cdot t_s \cdot R_u \cdot F_u \cdot N_{rows} \cdot N_b \cdot 2 = 560.25\ kip$ (Bearing) (AISC 360-16 J3-6a)

$\phi R_{n5} := 1.2 \cdot L_c \cdot t_s \cdot R_u \cdot F_u \cdot N_b \cdot 2 = 742.331\ kip$ (Tear-out) (AISC 360-16 J3-6c)

6. Net Area Rupture

$\phi := 1$

$\phi R_{n6} := A_e \cdot R_u \cdot F_u = 614.719\ kip$ (AISC 360-16 J4-2)

7. Bolt Shear Strength

Use A354 Gr. BD Rods (Double-Shear)

$\phi := 1$

$F_v := 0.563 \cdot F_{u_rod} = 84.45\ ksi$ (AISC 360-16 Table J3.2) $A_b := \pi \cdot \frac{d_b^2}{4} = 1.227\ in^2$

$\phi R_{n6} := \left(\phi \cdot F_v \cdot A_b \cdot 2\right) \cdot N_{rows} \cdot N_b \cdot 2 = \left(1.244 \cdot 10^3\right)\ kip$

8. Block Shear Strength

$\phi := 1 \quad U_{bs} := 1$

$A_{nv} := L_c \cdot t_s \cdot 2 \cdot 2 = 4.969\ in^2 \quad A_{gv} := L_{e1} \cdot t_s \cdot 2 \cdot 2 = 6\ in^2 \quad A_{nt} := \left(N_b - 1\right) \cdot \left(S_h - d_b - d_H\right) \cdot t_s \cdot 2 = 3.938\ in^2$

$S_1 := 0.6\ R_u \cdot F_u \cdot A_{nv} = 247.444\ kip \quad S_2 := 0.6\ R_y \cdot F_y \cdot A_{gv} = 226.8\ kip$

$T_1 := U_{bs} \cdot R_u \cdot F_u \cdot A_{nt} = 326.813\ kip$

$\phi R_{n7} := \text{if } S_1 > S_2 \ \| \ T_1 + S_2 \ \text{else} \ \| \ T_1 + S_1 = 553.613\ kip$ (AISC 360-16 J4-5)

9. Summary of Design Limit States

Limit_States	*Strength* (*kip*)	*Sequence*
"1. Slip–Critical Resistance"	393.13	1
"2. Net Section Yileding"	466.59	2
"3. Gross Area Yielding"	661.50	6
"4. Bearing Capacity"	560.25	4
"5. Tear–out Capacity"	742.33	7
"6. Net Section Rupture"	614.72	5
"7. Bolt Shear Strength"	1243.63	8
"8. Block Shear Strength"	553.61	3

Design of Test Specimen T4 (Case 4A)

0. Typical Information

Use A572 Gr. 50 Steel and Concrete Strength

$F_y = 63\ ksi \quad R_y = 1 \quad f'_c = 6.6\ ksi$

Geometries of Anchor System

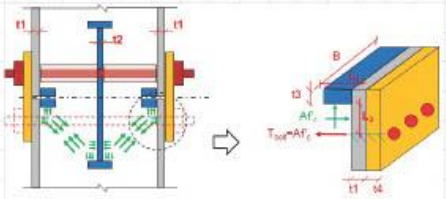
$L_1 = 2\ in \quad L_2 = 1.5\ in \quad B = 14\ in \quad N_{strut} = 1$

$t_1 = 0.375\ in \quad t_2 = 0.375\ in \quad t_3 = 0.375\ in \quad t_4 = 0.75\ in$

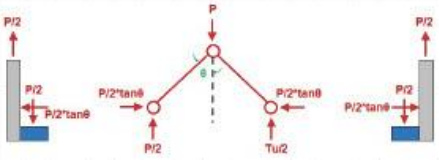
$$I_1 := \frac{B \cdot t_1^{\,3}}{12} = 0.062\ in^4 \qquad I_4 := \frac{B \cdot t_4^{\,3}}{12} = 0.492\ in^4$$

Target Loads

$$T_u := 327.3\ kip \qquad f'_{c_target} := \frac{T_u}{2 \cdot (L_1 \cdot B) \cdot N_{strut}} = 5.845\ ksi$$



Geometry of Case 4A



Free-Body of Compression Strut

1. Corner Bending (Simplified Beam Assumption)

Geometries of Simplified Beam Model

$a = 2\ in \quad b = 1\ in \quad c = 1.188\ in \quad d = 0.375\ in \quad \theta = 45\ °$

Bending Moment in Simplified Beam Model

$$P_v := \frac{T_u}{2 \cdot N_{strut}} = 163.65\ kip \qquad P_h := \left(\frac{T_u}{2 \cdot N_{strut}}\right) \cdot \tan(\theta) = 163.65\ kip$$

$$m := \begin{cases} 0\ kip \cdot in & \text{if } d \le t_3 \\ P_h \cdot \frac{L_1}{2} & \text{else} \end{cases} = 0\ (kip \cdot in)$$

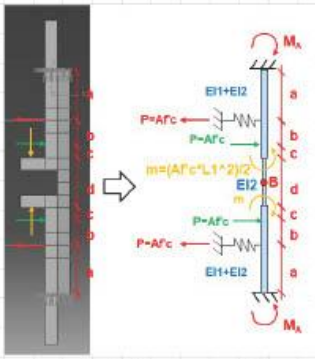
When d <= t3, Key Plates contact with each other, and m=0

$$M_A := \frac{P_h \cdot b \cdot \left(\frac{b}{2} + c + \frac{d}{2} \cdot \left(\frac{I_1 + I_4}{I_4}\right)\right) + m \cdot \frac{d}{2} \cdot \left(\frac{I_1 + I_4}{I_4}\right)}{a + b + c + \frac{d}{2} \cdot \left(\frac{I_1 + I_4}{I_4}\right)} = 70.634\ kip \cdot in$$

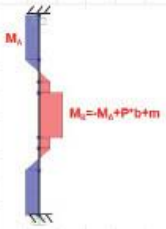
$$M_B := -M_A + P_h \cdot b + m = 93.016\ kip \cdot in$$

$$M_{u_face} := M_A \cdot \frac{I_1}{I_1 + I_4} = 7.848\ kip \cdot in$$

$$M_{u_splice} := \max(M_A, M_B) \cdot \frac{I_4}{I_1 + I_4} = 82.681\ kip \cdot in$$



Simplified Beam Model



Moment Diagram

Design of Face Plates

$\phi := 1$

$\sigma_{T_face} := \frac{T_u}{t_1 \cdot B \cdot 2} = 31.171\ ksi$ $\sigma_{M_face} := \frac{M_{u_face} \cdot t_1}{I_1 \cdot 2} = 23.918\ ksi$

$\sigma_{u_face} := \sigma_{T_face} + \sigma_{M_face} = 55.09\ ksi$

$Chk := \text{if } \sigma_{u_face} \le \phi \cdot F_y \text{ "OK" else "NG"} = \text{"OK"}$

Design of Splice Plates

$\sigma_{T_splice} := 0$ (Assume there is no tensile stress transferred from Face Plates)

$\sigma_{M_splice} := \frac{M_{u_splice} \cdot t_4}{I_4 \cdot 2} = 62.995\ ksi$

$\sigma_{u_splice} := \sigma_{T_splice} + \sigma_{M_splice} = 62.995\ ksi$

$Chk := \text{if } \sigma_{u_splice} \le \phi \cdot F_y \text{ "OK" else "NG"} = \text{"OK"}$

Since the flexural stress of splice plates is nearly equal to its yield strength, we defined the tensile load in this state as the Corner Bending Failure Strength.

$\phi R_{n1} := T_u = 327.3\ kip$

2. Concrete Failure Strength

Refer to the free-body of compression strut, the concrete fails when Tu=2Ac*f'c

$\phi := 1$

$f'_c = 6.6\ ksi$ $A_c := B \cdot L_1$

$\phi R_{n2} := \phi \cdot f'_c \cdot A_c \cdot 2 = 369.6\ kip$

3. t2 Yielding Strength

$\phi := 1$

$A_{g_t2} := B \cdot t_2 = 5.25\ in^2$

$\phi R_{n3} := \phi \cdot R_y \cdot F_y \cdot A_{g_t2} = 330.75\ kip$

4. t3 (Key Plate) Shear Strength

$\phi := 1$

$A_{g_t3} := B \cdot t_3 = 5.25\ in^2$

$\phi R_{n4} := \phi \cdot 0.6 \cdot F_y \cdot A_{g_t3} \cdot 2 = 396.9\ kip$

5. t1 Yielding Strength

$\phi := 1$

$A_{g_t1} := B \cdot t_1 \cdot 2 = 10.5\ in^2$

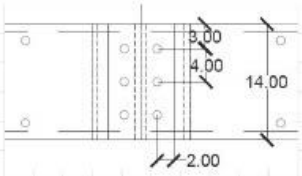
$\phi R_{n5} := \phi \cdot R_y \cdot F_y \cdot A_{g_t1} = 661.5\ kip$

6. Bolt Tension Failure Strength

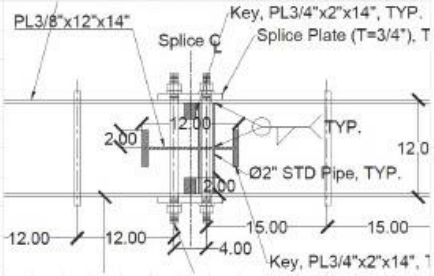
$\phi := 1$

$T_{n_bolt} := 88.36\ kip \qquad N_b = 3$

$\phi R_{n6} := \phi \cdot T_{n_bolt} \cdot N_b \cdot \frac{1}{\tan(\theta)} \cdot 2 = 530.16\ kip$



Plan



Elevation

7. Summary of Design Limit States

Limit_States	*Strength* (kip)	*Sequence*
"1. Corner Bending Resistance"	327.30	1
"2. Concrete Failure"	369.60	3
"3. t2 Yielding Force (RyFy)"	330.75	2
"4. t3 Shear Strength"	396.90	4
"5. t1 Yielding Force (RyFy)"	661.50	6
"6. Bolt Tension Failure"	530.16	5

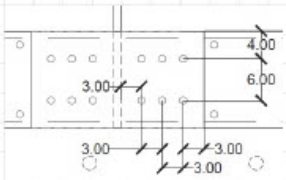
Design of Test Specimen T5 (Case 1C)

0. Typical Information

Use A572 Gr. 50 Steel

$F_y = 63\ ksi \quad R_y = 1 \quad F_u = 83\ ksi \quad R_u = 1$

$t_s = 0.375\ in \quad B = 14\ in$ (B=Wall Width)

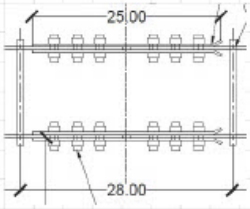


Plan

Bolt Layout

$d_b = 0.75\ in \quad d_H = 0.125\ in$ (d_H =clearance between bolts and steel plates)

$N_{rows} = 3 \quad N_b = 2 \quad L_{e1} = 3\ in \quad S_v = 3\ in \quad L_{e2} = 4\ in$



Elevation

1. Slip-Critical Resistance

Use Grade A490 Bolts (Double-Shear)

$\phi := 1$

$T_b := 35\ kip \quad D_u := 1.13 \quad h_f := 1 \quad \mu := 0.3$

$\phi R_{n1} := (\phi \cdot \mu \cdot D_u \cdot h_f \cdot T_b \cdot 2) \cdot N_{rows} \cdot N_b \cdot 2 = 284.76\ kip$ (AISC 360-16 J3-4)

2. Net Area Yielding

$\phi := 1$

$A_e := (B - N_b \cdot (d_b + d_H)) \cdot t_s \cdot 2 = 9.188\ in^2$

$\phi R_{n2} := A_e \cdot R_y \cdot F_y = 578.813\ kip$

3. Gross Area Yielding

$\phi := 1$

$A_g := t_s \cdot B \cdot 2 = 10.5\ in^2$

$\phi R_{n3} := A_g \cdot R_y \cdot F_y = 661.5\ kip$ (AISC 360-16 J4-1)

4&5. Bearing and Tear-out Capacity

$\phi := 1$

$L_c := L_{e1} + (N_{rows} - 1) \cdot S_v - (0.5 + (N_{rows} - 1)) \cdot (d_b + d_H) = 6.813\ in$

$\phi R_{n4} := 2.4 \cdot d_b \cdot t_s \cdot R_u \cdot F_u \cdot N_{rows} \cdot N_b \cdot 2 = 672.3\ kip$ (Bearing) (AISC 360-16 J3-6a)

$\phi R_{n5} := 1.2 \cdot L_c \cdot t_s \cdot R_u \cdot F_u \cdot N_b \cdot 2 = (1.018 \cdot 10^3)\ kip$ (Tear-out) (AISC 360-16 J3-6c)

6. Net Area Rupture

$\phi := 1$

$\phi R_{n6} := A_e \cdot R_u \cdot F_u = 762.563\ kip$ (AISC 360-16 J4-2)

7. Bolt Shear Strength

Use Grade A490 Bolts (Double-Shear)

$\phi := 1$

$F_v := 84\ ksi$ (AISC 360-16 Table J3.2) $A_b := \pi \cdot \frac{d_b^{\,2}}{4} = 0.442\ in^2$

$\phi R_{n6} := \left(\phi \cdot F_v \cdot A_b \cdot 2\right) \cdot N_{rows} \cdot N_b \cdot 2 = 890.642\ kip$

8. Block Shear Strength

$\phi := 1 \quad U_{bs} := 1$

$A_{nv} := L_c \cdot t_s \cdot 2 \cdot 2 = 10.219\ in^2 \quad A_{gv} := \left(L_{e1} + \left(N_{rows} - 1\right) \cdot S_v\right) \cdot t_s \cdot 2 \cdot 2 = 13.5\ in^2$

$A_{nt} := \left(N_b - 1\right) \cdot \left(S_h - d_b - d_H\right) \cdot t_s \cdot 2 = 3.844\ in^2$

$S_1 := 0.6\ R_u \cdot F_u \cdot A_{nv} = 508.894\ kip \quad S_2 := 0.6\ R_y \cdot F_y \cdot A_{gv} = 510.3\ kip$

$T_1 := U_{bs} \cdot R_u \cdot F_u \cdot A_{nt} = 319.031\ kip$

$\phi R_{n7} := \left|\begin{array}{l} \text{if } S_1 > S_2 \\ \quad \left\| T_1 + S_2 \right. \\ \text{else} \\ \quad \left\| T_1 + S_1 \right. \end{array}\right. = 827.925\ kip$ (AISC 360-16 J4-5)

9. Summary of Design Limit States

Limit_States	*Strength* (kip)	*Sequence*
"1. Slip–Critical Resistance"	284.76	1
"2. Net Section Yileding"	578.81	2
"3. Gross Area Yielding"	661.50	3
"4. Bearing Capacity"	672.3	4
"5. Tear–out Capacity"	1017.79	8
"6. Net Section Rupture"	762.56	5
"7. Bolt Shear Strength"	890.64	7
"8. Block Shear Strength"	827.93	6

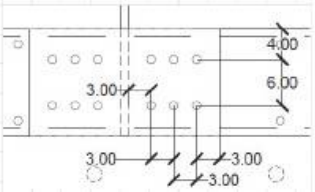
Design of Test Specimen T6 (Case 2C)

0. Typical Information

Use A572 Gr. 50 Steel

$F_y = 63\ ksi \quad R_y = 1 \quad F_u = 83\ ksi \quad R_u = 1$

$t_s = 0.375\ in \quad B = 14\ in$ (B=Wall Width)

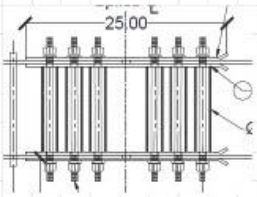


Plan

Bolt Layout

$d_b = 0.75\ in \quad d_H = 0.125\ in$ (d_H =clearance between bolts and steel plates)

$N_{rows} = 3 \quad N_b = 2 \quad L_{e1} = 3\ in \quad S_v = 3\ in \quad L_{e2} = 4\ in$



Elevation

1. Slip-Critical Resistance

Use A354 Gr. BD Rods (Double-Shear)

$\phi := 1 \quad F_{u_rod} := 150\ ksi$

$A_b := \pi \cdot \frac{d_b^2}{4} = 0.442\ in^2 \quad A_{b_thread} := 0.75 \cdot A_b = 0.331\ in^2$

$T_b := 0.7 \cdot F_{u_rod} \cdot A_{b_thread} = 34.791\ kip \quad D_u := 1.13 \quad h_f := 1 \quad \mu := 0.3$

$\phi R_{n1} := \left(\phi \cdot \mu \cdot D_u \cdot h_f \cdot T_b \cdot 2\right) \cdot N_{rows} \cdot N_b \cdot 2 = 283.057\ kip$ (AISC 360-16 J3-4)

2. Net Area Yielding

$\phi := 1$

$A_e := \left(B - N_b \cdot \left(d_b + d_H\right)\right) \cdot t_s \cdot 2 = 9.188\ in^2$

$\phi R_{n2} := A_e \cdot R_y \cdot F_y = 578.813\ kip$

3. Gross Area Yielding

$\phi := 1$

$A_g := t_s \cdot B \cdot 2 = 10.5\ in^2$

$\phi R_{n3} := A_g \cdot R_y \cdot F_y = 661.5\ kip$ (AISC 360-16 J4-1)

4&5. Bearing and Tear-out Capacity

$\phi := 1$

$L_c := L_{e1} + \left(N_{rows} - 1\right) \cdot S_v - \left(0.5 + \left(N_{rows} - 1\right)\right) \cdot \left(d_b + d_H\right) = 6.813\ in$

$\phi R_{n4} := 2.4 \cdot d_b \cdot t_s \cdot R_u \cdot F_u \cdot N_{rows} \cdot N_b \cdot 2 = 672.3\ kip$ (Bearing) (AISC 360-16 J3-6a)

$\phi R_{n5} := 1.2 \cdot L_c \cdot t_s \cdot R_u \cdot F_u \cdot N_b \cdot 2 = \left(1.018 \cdot 10^3\right)\ kip$ (Tear-out) (AISC 360-16 J3-6c)

6. Net Area Rupture

$\phi := 1$

$\phi R_{n6} := A_e \cdot R_u \cdot F_u = 762.563\ kip$ (AISC 360-16 J4-2)

7. Bolt Shear Strength

Use Grade A490 Bolts (Double-Shear)

$\phi := 1$

$F_v := 0.563 \cdot F_{u_rod} = 84.45\ ksi$ (AISC 360-16 Table J3.2) $A_b := \pi \cdot \frac{d_b^2}{4} = 0.442\ in^2$

$\phi R_{n6} := \left(\phi \cdot F_v \cdot A_b \cdot 2\right) \cdot N_{rows} \cdot N_b \cdot 2 = 895.413\ kip$

8. Block Shear Strength

$\phi := 1 \quad U_{bs} := 1$

$A_{nv} := L_c \cdot t_s \cdot 2 \cdot 2 = 10.219\ in^2 \quad A_{gv} := \left(L_{e1} + \left(N_{rows} - 1\right) \cdot S_v\right) \cdot t_s \cdot 2 \cdot 2 = 13.5\ in^2$

$A_{nt} := \left(N_b - 1\right) \cdot \left(S_h - d_b - d_H\right) \cdot t_s \cdot 2 = 3.844\ in^2$

$S_1 := 0.6\ R_u \cdot F_u \cdot A_{nv} = 508.894\ kip \quad S_2 := 0.6\ R_y \cdot F_y \cdot A_{gv} = 510.3\ kip$

$T_1 := U_{bs} \cdot R_u \cdot F_u \cdot A_{nt} = 319.031\ kip$

$\phi R_{n7} := \begin{vmatrix} \text{if } S_1 > S_2 \\ \quad \| T_1 + S_2 \\ \text{else} \\ \quad \| T_1 + S_1 \end{vmatrix} = 827.925\ kip$ (AISC 360-16 J4-5)

9. Summary of Design Limit States

Limit_States	*Strength* (kip)	*Sequence*
"1. Slip–Critical Resistance"	283.06	1
"2. Net Section Yileding"	578.81	2
"3. Gross Area Yielding"	661.50	3
"4. Bearing Capacity"	672.3	4
"5. Tear–out Capacity"	1017.79	8
"6. Net Section Rupture"	762.56	5
"7. Bolt Shear Strength"	895.41	7
"8. Block Shear Strength"	827.93	6

Design of Test Specimen S1/S2 (Case 6A/6Ac)

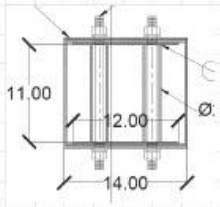
0. Typical Information

Use A572 Gr. 50 Steel

$E_s = (2.9 \cdot 10^4)\ ksi \quad E_c = (3.122 \cdot 10^3)\ ksi \quad G_s = (1.115 \cdot 10^4)\ ksi$

$F_y = 63.86\ ksi \quad R_y = 1.1 \quad F_u = 72.94\ ksi \quad R_u = 1.1$

$t_s = 0.25\ in \quad B = 14\ in$ (B=Wall Width) $\quad T = 12\ in$ (T=Wall Thickness)



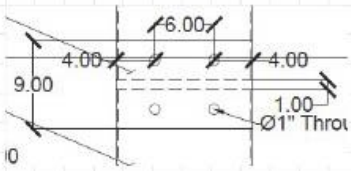
Plan

$A_{sw} := B \cdot t_s \cdot 2 = 7\ in^2 \quad A_c := (T - 2 \cdot t_s) \cdot B = 161\ in^2$

Bolt Layout

$d_b = 1\ in \quad d_H = 0.125\ in \quad L_{ex} = 4\ in \quad L_{ey} = 2\ in$

$g = 1\ in \quad N_{bx} = 2 \quad N_{by} = 1 \quad S_h = 6\ in \quad S_v = 3\ in$



Elevation

1. Slip-Critical Resistance

Use A354 Gr. BD Rods (Double-Shear)

$\phi := 1 \quad F_{u_rod} := 150\ ksi$

$A_b := \pi \cdot \frac{d_b^2}{4} = 0.785\ in^2 \quad A_{b_thread} := 0.75 \cdot A_b = 0.589\ in^2$

$T_b := 0.7 \cdot F_{u_rod} \cdot A_{b_thread} = 61.85\ kip \quad D_u := 1.13 \quad h_f := 1 \quad \mu := 0.3$

$\phi R_{n1} := (\phi \cdot \mu \cdot D_u \cdot h_f \cdot T_b \cdot 2) \cdot N_{bx} \cdot N_{by} \cdot 2 = 167.737\ kip$ (AISC 360-16 J3-4)

Note that for non-composite connection, the pipe sleeves inside the connection does not have sufficient compressive strength to resist the clamping to develop full pretension of threaded rods. Therefore, a smaller bolt pretension and slip-critical resistance are predictred.
In the summary table, a 80-kips slip-critical resistance was assumed based on developing 50% of the full bolt pretension.

2. Net Area Yielding

$\phi := 1$

$A_e := (B - N_{bx} \cdot (d_b + d_H)) \cdot t_s \cdot 2 = 5.875\ in^2$

$\phi R_{n2} := 0.6 \cdot A_e \cdot R_y \cdot F_y = 247.617\ kip$

3. Gross Area Yielding

$\phi := 1 \quad A_g := t_s \cdot B \cdot 2 = 7\ in^2$

$\phi R_{n3} := 0.6 \cdot A_g \cdot R_y \cdot F_y = 295.033\ kip$ (AISC 360-16 J4-3)

4~6. Bearing, Tear-out, and Combined Bearing and Tear-out Capacity

$\phi := 1$

$L_c := L_{ex} - \frac{(d_b + d_H)}{2} + (N_{bx} - 1) \cdot (S_h - d_b - d_H) = 8.313\ in$

$L_{c_end} := L_{ex} - \frac{(d_b + d_H)}{2} = 3.438\ in$

$\phi R_{n4} := 2.4 \cdot d_b \cdot t_s \cdot R_u \cdot F_u \cdot N_{bx} \cdot N_{by} \cdot 2 = 192.562\ kip$ (Bearing, AISC 360-16 J3-6a)

$\phi R_{n5} := 1.2 \cdot L_c \cdot t_s \cdot R_u \cdot F_u \cdot N_{by} \cdot 2 = 400.167\ kip$ (Tear-out, AISC 360-16 J3-6c)

$\phi R_{n6} := 2.4 \cdot d_b \cdot t_s \cdot R_u \cdot F_u \cdot (N_{bx} - 1) \cdot N_{by} \cdot 2 + 1.2 \cdot L_{c_end} \cdot t_s \cdot R_u \cdot F_u \cdot N_{by} \cdot 2 = 261.763\ kip$
(Combined Bearing and Tear-out)

7. Net Section Rupture

$\phi := 1$

$\phi R_{n7} := 0.6 \cdot A_e \cdot R_u \cdot F_u = 282.825\ kip$ (AISC 360-16 J4-3)

8. Bolt Shear Failure Strength

Use A354 Gr. BD Rods (Double-Shear)

$\phi := 1 \quad F_{u_rod} := 150\ ksi$

$F_v := 0.563 \cdot F_{u_rod} = 84.45\ ksi$ (AISC 360-16 TABLE J3.2)

$A_b := \pi \cdot \frac{d_b^2}{4} = 0.785\ in^2$

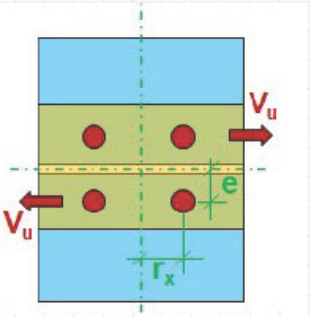
$\phi R_{n7} := (\phi \cdot F_v \cdot A_b \cdot 2) \cdot N_{by} \cdot N_{bx} \cdot 2 = 530.615\ kip$

9. Bearing Strength in Eccentrically Loaded Bolt Group

Geometries

$e := (N_{by} - 1) \cdot \frac{S_v}{2} + L_{ey} + \frac{g}{2} = 2.5\ in$

$r_x := (N_{bx} - 1) \cdot \frac{S_h}{2} = 3\ in \qquad r_y := (N_{by} - 1) \cdot \frac{S_v}{2} = 0\ in$



Eccentrically Loaded Bolt Group

Bolt Group Moment of Inertia

$N_I_x := \text{if } \mathrm{mod}(N_{bx}, 2) = 0 \ \|\ \frac{N_{bx}}{2} \ \text{else} \ \|\ \frac{N_{bx} - 1}{2} = 1 \qquad N_I_y := N_{by} = 1$

$I_x := \text{for } i \in 1..N_I_x \ \|\ \text{if } \mathrm{mod}(N_{bx}, 2) = 1 \ \|\ b \leftarrow b + 2 \cdot N_{by} \cdot S_h^2 \cdot i \ \text{else} \ \|\ b \leftarrow b + 2 \cdot N_{by} \cdot S_h^2 \cdot (i - 0.5)^2 = 18\ in^2$

$I_y := \text{for } i \in 1..N_I_y \ \|\ \text{if } i < N_I_y \ \|\ b \leftarrow b + N_{bx} \cdot \left(L_{ey} + \frac{g}{2}\right)^2 \ \text{else} \ \|\ b \leftarrow b + 0 \cdot in^2 = 0\ in^2$

$I_p := I_x + I_y = 18\ in^2$

Bolt Resultant Force Calculation (Elastic Method)

$M_v := V_u \cdot e$

$P_V_x := \frac{V_u}{N_{bx} \cdot N_{by} \cdot 2}$ $P_M_x := \frac{M_v \cdot r_x}{2 \cdot I_p}$ $P_M_y := \frac{M_v \cdot r_y}{2 \cdot I_p}$

$P_Result := \sqrt{\left(\left(P_V_x + P_M_y \right)^2 + P_M_x{}^2 \right)}$

Use Elastic Method above, the Eccentric Bearing Capacity can be derived as below:

Check with 2.4dtFu Bearing Strength for Single Hole (AISC 360-16 J3-6a)

$$\phi R_{n8} := \frac{2.4 \cdot d_b \cdot t_s \cdot F_u}{\sqrt{\left(\frac{1}{N_{bx} \cdot N_{by} \cdot 2} + \frac{e \cdot r_y}{2 \cdot I_p} \right)^2 + \left(\frac{e \cdot r_x}{2 \cdot I_p} \right)^2}} = 134.482 \ kip$$

Check with 3.0dtFu Bearing Strength for Single Hole (AISC 360-16 J3-6b)

$$\phi R_{n9} := \frac{3.0 \cdot d_b \cdot t_s \cdot F_u}{\sqrt{\left(\frac{1}{N_{bx} \cdot N_{by} \cdot 2} + \frac{e \cdot r_y}{2 \cdot I_p} \right)^2 + \left(\frac{e \cdot r_x}{2 \cdot I_p} \right)^2}} = 168.102 \ kip$$

10. Composite Shear Strength

$E_c A_c := E_c \cdot A_c = \left(5.026 \cdot 10^5 \right) \ kip$

$E_s A_{sw} := E_s \cdot A_{sw} = \left(2.03 \cdot 10^5 \right) \ kip$

$$K_{sc} := \frac{0.7 \cdot \left(E_c A_c \right) \cdot \left(E_s A_{sw} \right)}{4 \ E_s A_{sw} + E_c A_c} = \left(5.433 \cdot 10^4 \right) \ kip$$

$K_s := G_s \cdot A_{sw} = \left(7.805 \cdot 10^4 \right) \ kip$

$$V_n := \frac{A_{sw} \cdot F_y \cdot \left(K_s + K_{sc} \right)}{\sqrt{\left(3 \ K_s{}^2 + K_{sc}{}^2 \right)}} = 406.168 \ kip$$ (AISC 360-22 I4-2)

$\phi R_{n10} := V_n = 406.168 \ kip$

11. Summary of Limit States

Limit_States	*Strength* (*kip*)	*Sequence*
"1. Slip–Critical Resistance"	167.74	2
"2. Net Section Yiled (0.6AeRyFy)"	225.11	5
"3. Gross Area Yield (0.6AgRyFy)"	268.21	8
"4. Bearing Capacity"	175.06	4
"5. Tear–out Capacity"	363.79	9
"6. End Tear–out & Bearing"	237.97	6
"7. Net Section Rupture (0.6AeRuFu)"	257.11	7
"8. Bolt Shear Strength"	530.61	11
"9. Eccentrically Bearing Capacity (2.4dtFu)"	134.48	1
"10. Eccentrically Bearing Capacity (3.0dtFu)"	168.10	3
"11. Composite Shear Strength"	406.17	10

Design of Test Specimen S3/S4 (Case 5B/5Bc)

0. Typical Information

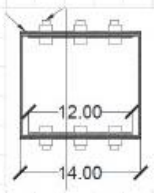
Use A572 Gr. 50 Steel

$E_s = (2.9 \cdot 10^4)\ ksi$ $E_c = (3.122 \cdot 10^3)\ ksi$ $G_s = (1.115 \cdot 10^4)\ ksi$

$F_y = 63.86\ ksi$ $R_y = 1.1$ $F_u = 72.94\ ksi$ $R_u = 1.1$

$t_s = 0.25\ in$ $B = 14\ in$ (B=Wall Width) $T = 12\ in$ (T=Wall Thickness)

$A_{sw} := B \cdot t_s \cdot 2 = 7\ in^2$ $A_c := (T - 2 \cdot t_s) \cdot B = 161\ in^2$

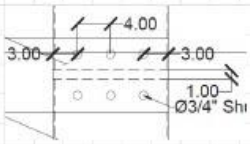


Plan

Bolt Layout

$d_b = 0.75\ in$ $d_H = 0.125\ in$ $L_{ex} = 3\ in$ $L_{ey} = 2\ in$

$g = 1\ in$ $N_{bx} = 3$ $N_{by} = 1$ $S_h = 4\ in$ $S_v = 3\ in$



Elevation

1. Slip-Critical Resistance

Use Grade A490 Bolts (Double-Shear)

$\phi := 1$

$A_b := \pi \cdot \frac{d_b^2}{4} = 0.442\ in^2$

$T_b := 35\ kip$ $D_u := 1.13$ $h_f := 1$ $\mu := 0.3$

$\phi R_{n1} := (\phi \cdot \mu \cdot D_u \cdot h_f \cdot T_b \cdot 2) \cdot N_{bx} \cdot N_{by} \cdot 2 = 142.38\ kip$ (AISC 360-16 J3-4)

2. Net Area Yielding

$\phi := 1$

$A_e := (B - N_{bx} \cdot (d_b + d_H)) \cdot t_s \cdot 2 = 5.688\ in^2$

$\phi R_{n2} := 0.6 \cdot A_e \cdot R_y \cdot F_y = 239.714\ kip$

3. Gross Area Yielding

$\phi := 1$ $A_g := t_s \cdot B \cdot 2 = 7\ in^2$

$\phi R_{n3} := 0.6 \cdot A_g \cdot R_y \cdot F_y = 295.033\ kip$ (AISC 360-16 J4-3)

4~6. Bearing, Tear-out, and Combined Bearing and Tear-out Capacity

$\phi := 1$

$L_c := L_{ex} - \frac{(d_b + d_H)}{2} + (N_{bx} - 1) \cdot (S_h - d_b - d_H) = 8.813\ in$

$L_{c_end} := L_{ex} - \frac{(d_b + d_H)}{2} = 2.563\ in$

$\phi R_{n4} := 2.4 \cdot d_b \cdot t_s \cdot R_u \cdot F_u \cdot N_{bx} \cdot N_{by} \cdot 2 = 216.632\ kip$ (Bearing, AISC 360-16 J3-6a)

$\phi R_{n5} := 1.2 \cdot L_c \cdot t_s \cdot R_u \cdot F_u \cdot N_{by} \cdot 2 = 424.237\ kip$ (Tear-out, AISC 360-16 J3-6c)

$\phi R_{n6} := 2.4 \cdot d_b \cdot t_s \cdot R_u \cdot F_u \cdot (N_{bx} - 1) \cdot N_{by} \cdot 2 + 1.2 \cdot L_{c_end} \cdot t_s \cdot R_u \cdot F_u \cdot N_{by} \cdot 2 = 267.781\ kip$
(Combined Bearing and Tear-out)

7. Net Section Rupture

$\phi := 1$

$\phi R_{n7} := 0.6 \cdot A_e \cdot R_u \cdot F_u = 273.799\ kip$ (AISC 360-16 J4-4)

8. Bolt Shear Failure Strength

Use A354 Gr. BD Rods (Double-Shear)

$\phi := 1$

$F_v := 84\ ksi$ (AISC 360-16 TABLE J3.2) $A_b := \pi \cdot \frac{d_b^2}{4} = 0.442\ in^2$

$\phi R_{n7} := (\phi \cdot F_v \cdot A_b \cdot 2) \cdot N_{by} \cdot N_{bx} \cdot 2 = 445.321\ kip$

9. Bearing Strength in Eccentrically Loaded Bolt Group

Geometries

$e := (N_{by} - 1) \cdot \frac{S_v}{2} + L_{ey} + \frac{g}{2} = 2.5\ in$

$r_x := (N_{bx} - 1) \cdot \frac{S_h}{2} = 4\ in$ $r_y := (N_{by} - 1) \cdot \frac{S_v}{2} = 0\ in$

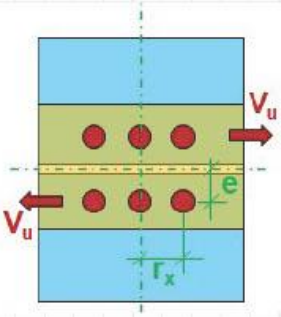
Bolt Group Moment of Inertia

$N_I_x :=$ if $\text{mod}(N_{bx}, 2) = 0$ then $\frac{N_{bx}}{2}$ else $\frac{N_{bx} - 1}{2}$ $= 1$ $N_I_y := N_{by} = 1$

$I_x :=$ for $i \in 1..N_I_x$ (if $\text{mod}(N_{bx}, 2) = 1$ then $b \leftarrow b + 2 \cdot N_{by} \cdot S_h^2 \cdot i$ else $b \leftarrow b + 2 \cdot N_{by} \cdot S_h^2 \cdot (i - 0.5)^2$) $= 32\ in^2$

$I_y :=$ for $i \in 1..N_I_y$ (if $i < N_I_y$ then $b \leftarrow b + N_{bx} \cdot \left(L_{ey} + \frac{g}{2}\right)^2$ else $b \leftarrow b + 0 \cdot in^2$) $= 0\ in^2$

$I_p := I_x + I_y = 32\ in^2$



Eccentrically Loaded Bolt Group

Bolt Resultant Force Calculation (Elastic Method)

$M_v := V_u \cdot e$

$P_V_x := \frac{V_u}{N_{bx} \cdot N_{by} \cdot 2}$ $P_M_x := \frac{M_v \cdot r_x}{2 \cdot I_p}$ $P_M_y := \frac{M_v \cdot r_y}{2 \cdot I_p}$

$P_Result := \sqrt{\left(\left(P_V_x + P_M_y \right)^2 + P_M_x{}^2 \right)}$

Use Elastic Method above, the Eccentric Bearing Capacity can be derived as below:

Check with 2.4dtFu Bearing Strength for Single Hole (AISC 360-16 J3-6a)

$$\phi R_{n8} := \frac{2.4 \cdot d_b \cdot t_s \cdot F_u}{\sqrt{\left(\frac{1}{N_{bx} \cdot N_{by} \cdot 2} + \frac{e \cdot r_y}{2 \cdot I_p} \right)^2 + \left(\frac{e \cdot r_x}{2 \cdot I_p} \right)^2}} = 143.674 \ kip$$

Check with 3.0dtFu Bearing Strength for Single Hole (AISC 360-16 J3-6b)

$$\phi R_{n9} := \frac{3.0 \cdot d_b \cdot t_s \cdot F_u}{\sqrt{\left(\frac{1}{N_{bx} \cdot N_{by} \cdot 2} + \frac{e \cdot r_y}{2 \cdot I_p} \right)^2 + \left(\frac{e \cdot r_x}{2 \cdot I_p} \right)^2}} = 179.592 \ kip$$

10. Composite Shear Strength

$E_c A_c := E_c \cdot A_c = \left(5.026 \cdot 10^5 \right) \ kip$

$E_s A_{sw} := E_s \cdot A_{sw} = \left(2.03 \cdot 10^5 \right) \ kip$

$$K_{sc} := \frac{0.7 \cdot \left(E_c A_c \right) \cdot \left(E_s A_{sw} \right)}{4 \ E_s A_{sw} + E_c A_c} = \left(5.433 \cdot 10^4 \right) \ kip$$

$K_s := G_s \cdot A_{sw} = \left(7.805 \cdot 10^4 \right) \ kip$

$$V_n := \frac{A_{sw} \cdot F_y \cdot \left(K_s + K_{sc} \right)}{\sqrt{\left(3 \ K_s{}^2 + K_{sc}{}^2 \right)}} = 406.168 \ kip$$ (AISC 360-22 I4-2)

$\phi R_{n10} := V_n = 406.168 \ kip$

11. Summary of Limit States

Limit_States	*Strength* (*kip*)	*Sequence*
"1. Slip–Critical Resistance"	142.38	1
"2. Net Section Yiled (0.6AeRyFy)"	217.92	5
"3. Gross Area Yield (0.6AgRyFy)"	268.21	8
"4. Bearing Capacity"	196.94	4
"5. Tear–out Capacity"	385.67	9
"6. End Tear–out & Bearing"	243.44	6
"7. Net Section Rupture (0.6AeRuFu)"	248.91	7
"8. Bolt Shear Strength"	445.32	11
"9. Eccentrically Bearing Capacity 2.4dtFu"	143.67	2
"10. Eccentrically Bearing Capacity 3.0dtFu"	179.59	3
"11. Composite Shear Strength"	325.55	10

Design of Test Specimen S5/S6 (Case 6C/6Cc)

0. Typical Information

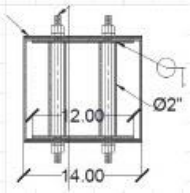
Use A572 Gr. 50 Steel

$E_s = (2.9 \cdot 10^4)\ ksi \quad E_c = (3.122 \cdot 10^3)\ ksi \quad G_s = (1.115 \cdot 10^4)\ ksi$

$F_y = 63.86\ ksi \quad R_y = 1.1 \quad F_u = 72.94\ ksi \quad R_u = 1.1$

$t_s = 0.25\ in \quad B = 14\ in$ (B=Wall Width) $\quad T = 12\ in$ (T=Wall Thickness)

$A_{sw} := B \cdot t_s \cdot 2 = 7\ in^2 \quad A_c := (T - 2 \cdot t_s) \cdot B = 161\ in^2$

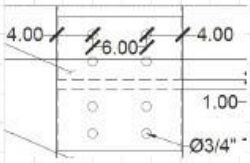


Plan

Bolt Layout

$d_b = 0.75\ in \quad d_H = 0.125\ in \quad L_{ex} = 4\ in \quad L_{ey} = 2\ in$

$g = 1\ in \quad N_{bx} = 2 \quad N_{by} = 2 \quad S_h = 6\ in \quad S_v = 3\ in$



Elevation

1. Slip-Critical Resistance

Use A354 Gr. BD Rods (Double-Shear)

$\phi := 1 \quad F_{u_rod} := 150\ ksi$

$A_b := \pi \cdot \frac{d_b^2}{4} = 0.442\ in^2 \quad A_{b_thread} := 0.75 \cdot A_b = 0.331\ in^2$

$T_b := 0.7 \cdot F_{u_rod} \cdot A_{b_thread} = 34.791\ kip \quad D_u := 1.13 \quad h_f := 1 \quad \mu := 0.3$

$\phi R_{n1} := (\phi \cdot \mu \cdot D_u \cdot h_f \cdot T_b \cdot 2) \cdot N_{bx} \cdot N_{by} \cdot 2 = 188.705\ kip$ (AISC 360-16 J3-4)

2. Net Area Yielding

$\phi := 1$

$A_e := (B - N_{bx} \cdot (d_b + d_H)) \cdot t_s \cdot 2 = 6.125\ in^2$

$\phi R_{n2} := 0.6 \cdot A_e \cdot R_y \cdot F_y = 258.154\ kip$

3. Gross Area Yielding

$\phi := 1 \quad A_g := t_s \cdot B \cdot 2 = 7\ in^2$

$\phi R_{n3} := 0.6 \cdot A_g \cdot R_y \cdot F_y = 295.033\ kip$ (AISC 360-16 J4-3)

4~6. Bearing, Tear-out, and Combined Bearing and Tear-out Capacity

$\phi := 1$

$L_c := L_{ex} - \frac{(d_b + d_H)}{2} + (N_{bx} - 1) \cdot (S_h - d_b - d_H) = 8.688\ in$

$L_{c_end} := L_{ex} - \frac{(d_b + d_H)}{2} = 3.563\ in$

$\phi R_{n4} := 2.4 \cdot d_b \cdot t_s \cdot R_u \cdot F_u \cdot N_{bx} \cdot N_{by} \cdot 2 = 288.842\ kip$ (Bearing, AISC 360-16 J3-6a)

$\phi R_{n5} := 1.2 \cdot L_c \cdot t_s \cdot R_u \cdot F_u \cdot N_{by} \cdot 2 = 836.439\ kip$ (Tear-out, AISC 360-16 J3-6c)

$\phi R_{n6} := 2.4 \cdot d_b \cdot t_s \cdot R_u \cdot F_u \cdot (N_{bx} - 1) \cdot N_{by} \cdot 2 + 1.2 \cdot L_{c_end} \cdot t_s \cdot R_u \cdot F_u \cdot N_{by} \cdot 2 = 487.422\ kip$
(Combined Bearing and End Tear-out)

7. Net Section Rupture

$\phi := 1$

$\phi R_{n7} := 0.6 \cdot A_e \cdot R_u \cdot F_u = 294.86\ kip$ (AISC 360-16 J4-4)

8. Bolt Shear Failure Strength

Use A354 Gr. BD Rods (Double-Shear)

$\phi := 1$

$F_v := 84\ ksi$ (AISC 360-16 TABLE J3.2) $A_b := \pi \cdot \frac{d_b^2}{4} = 0.442\ in^2$

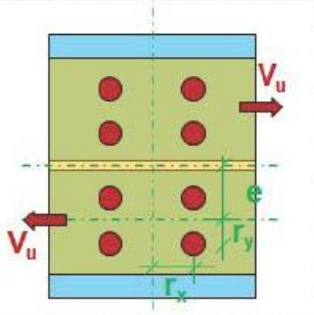
$\phi R_{n7} := (\phi \cdot F_v \cdot A_b \cdot 2) \cdot N_{by} \cdot N_{bx} \cdot 2 = 593.761\ kip$

9. Bearing Strength in Eccentrically Loaded Bolt Group

Geometries

$e := (N_{by} - 1) \cdot \frac{S_v}{2} + L_{ey} + \frac{g}{2} = 4\ in$

$r_x := (N_{bx} - 1) \cdot \frac{S_h}{2} = 3\ in$ $r_y := (N_{by} - 1) \cdot \frac{S_v}{2} = 1.5\ in$



Eccentrically Loaded Bolt Group

Bolt Group Moment of Inertia

$N_I_x := \text{if } \mathrm{mod}(N_{bx}, 2) = 0 \ \| \ \frac{N_{bx}}{2} \ \text{else} \ \| \ \frac{N_{bx} - 1}{2} = 1$ $N_I_y := N_{by} = 2$

$I_x := \text{for } i \in 1..N_I_x \ \| \ \text{if } \mathrm{mod}(N_{bx}, 2) = 1 \ \| \ b \leftarrow b + 2 \cdot N_{by} \cdot S_h^2 \cdot i \ \text{else} \ \| \ b \leftarrow b + 2 \cdot N_{by} \cdot S_h^2 \cdot (i - 0.5)^2 = 36\ in^2$

$I_y := \text{for } i \in 1..N_I_y \ \| \ \text{if } i < N_I_y \ \| \ b \leftarrow b + N_{bx} \cdot \left(L_{ey} + \frac{g}{2}\right)^2 \ \text{else} \ \| \ b \leftarrow b + 0 \cdot in^2 = 12.5\ in^2$

$I_p := I_x + I_y = 48.5\ in^2$

Bolt Resultant Force Calculation

$M_v := V_u \cdot e$

$P_V_x := \frac{V_u}{N_{bx} \cdot N_{by} \cdot 2}$ $P_M_x := \frac{M_v \cdot r_x}{2 \cdot I_p}$ $P_M_y := \frac{M_v \cdot r_y}{2 \cdot I_p}$

$P_Result := \sqrt{\left(\left(P_V_x + P_M_y \right)^2 + P_M_x{}^2 \right)}$

Use Elastic Method above, the Eccentric Bearing Capacity can be derived as below:

Check with 2.4dtFu Bearing Strength for Single Hole (AISC 360-16 J3-6a)

$$\phi R_{n8} := \frac{2.4 \cdot d_b \cdot t_s \cdot F_u}{\sqrt{\left(\frac{1}{N_{bx} \cdot N_{by} \cdot 2} + \frac{e \cdot r_y}{2 \cdot I_p} \right)^2 + \left(\frac{e \cdot r_x}{2 \cdot I_p} \right)^2}} = 146.468 \ kip$$

Check with 3.0dtFu Bearing Strength for Single Hole (AISC 360-16 J3-6b)

$$\phi R_{n9} := \frac{3.0 \cdot d_b \cdot t_s \cdot F_u}{\sqrt{\left(\frac{1}{N_{bx} \cdot N_{by} \cdot 2} + \frac{e \cdot r_y}{2 \cdot I_p} \right)^2 + \left(\frac{e \cdot r_x}{2 \cdot I_p} \right)^2}} = 183.085 \ kip$$

10. Composite Shear Strength

$E_c A_c := E_c \cdot A_c = \left(5.026 \cdot 10^5 \right) \ kip$

$E_s A_{sw} := E_s \cdot A_{sw} = \left(2.03 \cdot 10^5 \right) \ kip$

$$K_{sc} := \frac{0.7 \cdot \left(E_c A_c \right) \cdot \left(E_s A_{sw} \right)}{4 \ E_s A_{sw} + E_c A_c} = \left(5.433 \cdot 10^4 \right) \ kip$$

$K_s := G_s \cdot A_{sw} = \left(7.805 \cdot 10^4 \right) \ kip$

$$V_n := \frac{A_{sw} \cdot F_y \cdot \left(K_s + K_{sc} \right)}{\sqrt{\left(3 \ K_s{}^2 + K_{sc}{}^2 \right)}} = 406.168 \ kip$$ (AISC 360-22 I4-2)

$\phi R_{n10} := V_n = 406.168 \ kip$

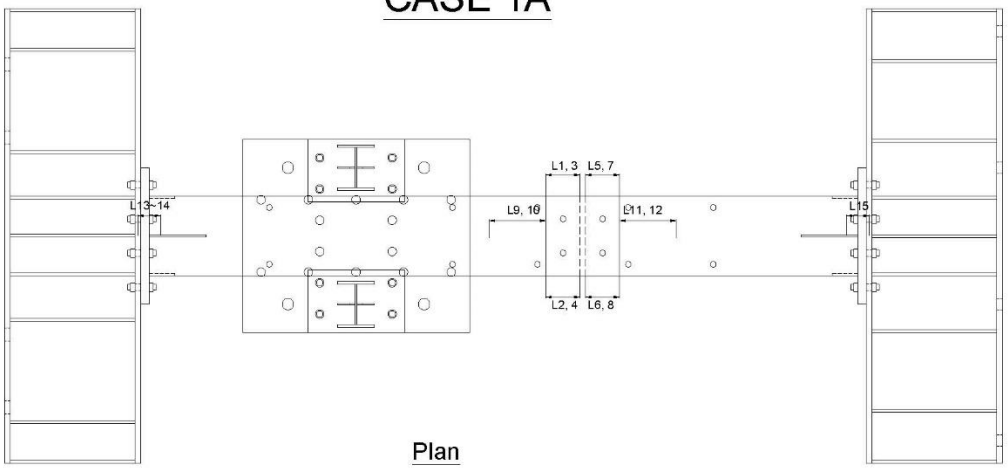
11. Summary of Limit States

Limit_States	*Strength* (*kip*)	*Sequence*
"1. Slip–Critical Resistance"	188.70	3
"2. Net Section Yiled (0.6AeRyFy)"	234.69	4
"3. Gross Area Yield (0.6AgRyFy)"	268.21	7
"4. Bearing Capacity"	262.58	5
"5. Tear–out Capacity"	760.40	11
"6. End Tear–out & Bearing"	443.11	9
"7. Net Section Rupture (0.6AeRuFu)"	268.05	6
"8. Bolt Shear Strength"	593.76	10
"9. Eccentrically Bearing Capacity 2.4dtFu"	146.47	1
"10. Eccentrically Bearing Capacity 3.0dtFu"	183.08	2
"11. Composite Shear Strength"	406.17	8

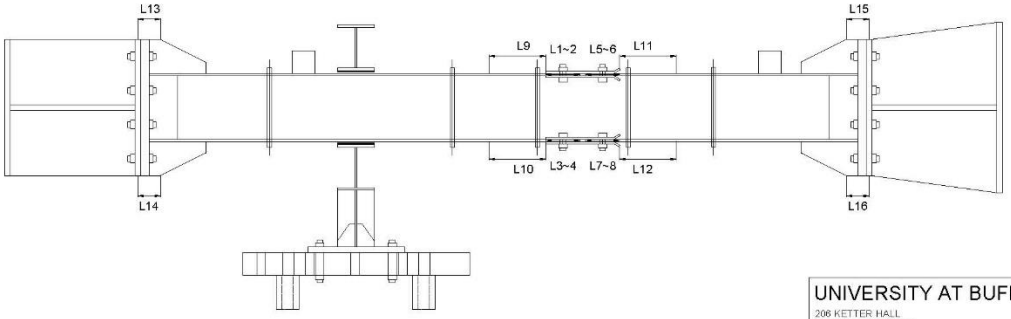
Appendix H.

Instrumentation (Component Level Test)

CASE 1A

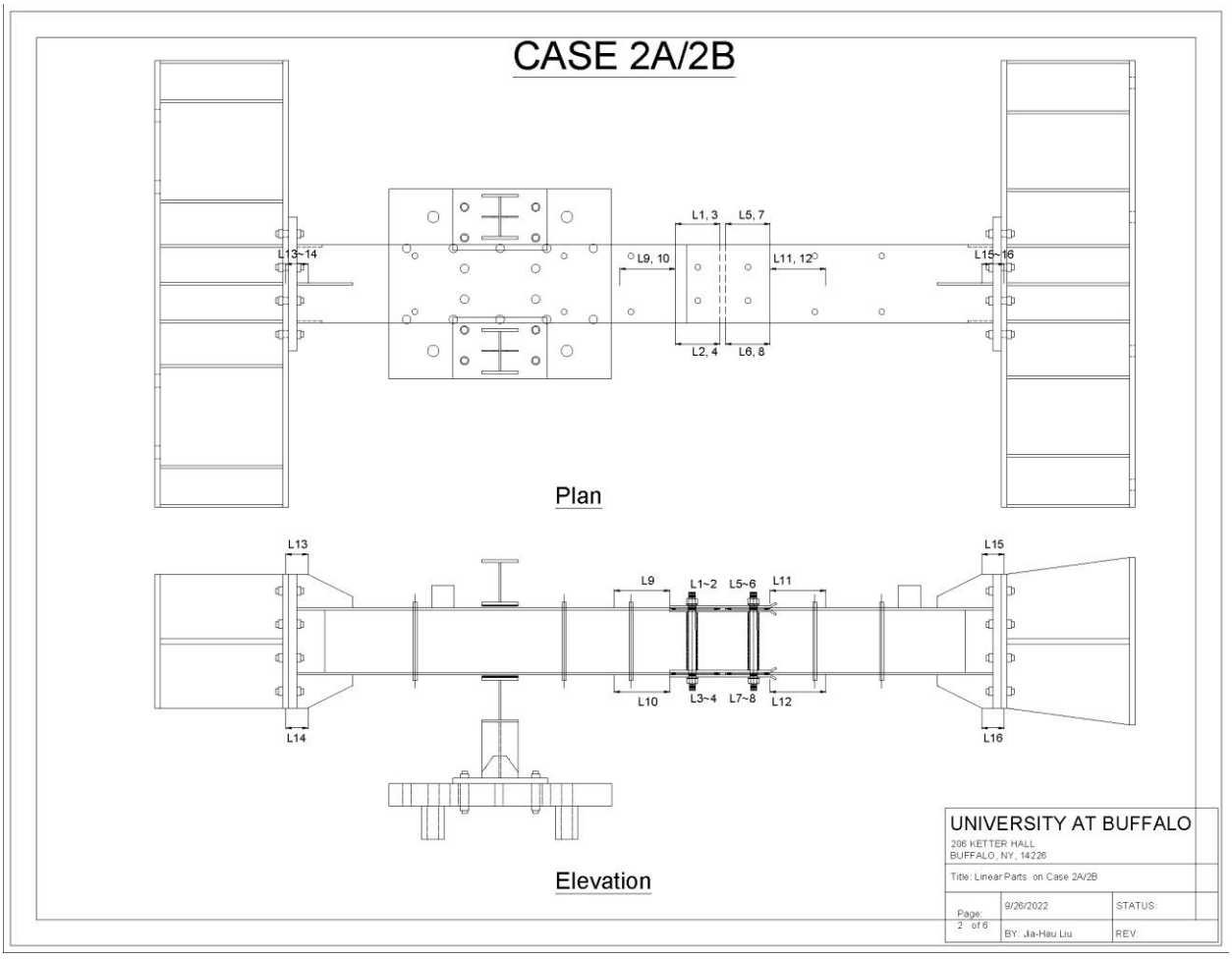


Plan

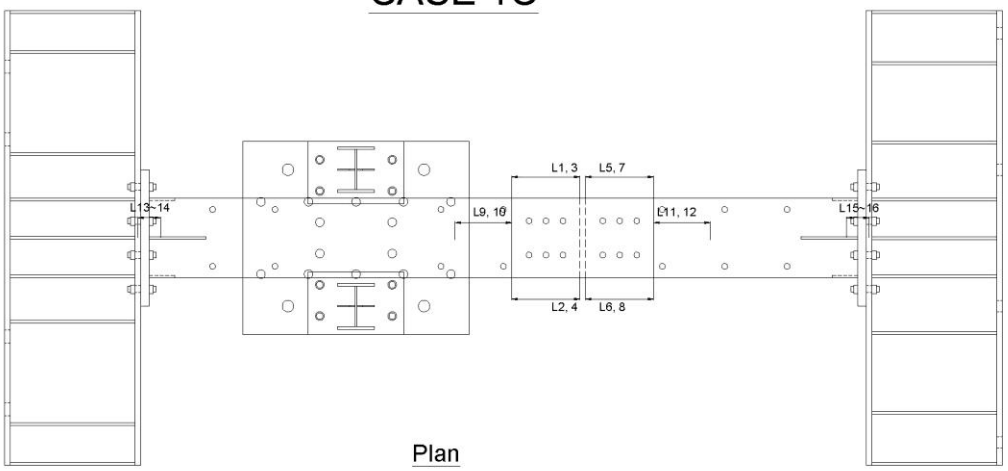


Elevation

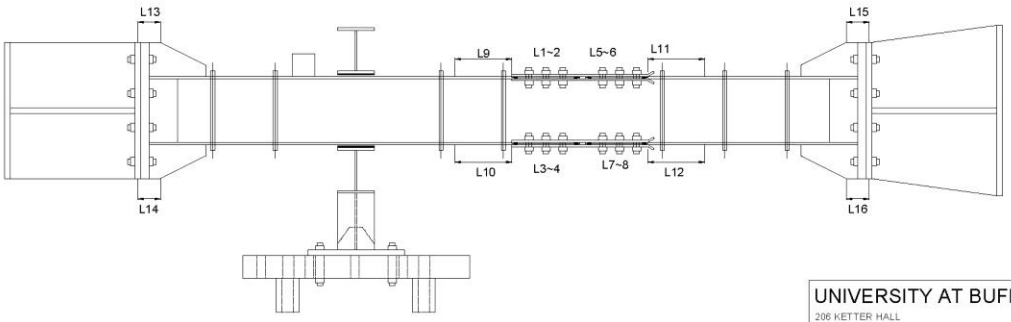
UNIVERSITY AT BUFFALO		
206 KETTER HALL BUFFALO, NY, 14226		
Title: String Pots on Case 1A		
Page: 1 of 6	9/28/2022 BY: Jia-Hau Liu	STATUS: REV:


CASE 2A/2B
L13~14
L9, 10
L1, 3
L5, 7
L11, 12
L2, 4
L6, 8
L15~16
Plan
L13
L9
L1~2
L5~6
L11
L15
L10
L3~4
L7~8
L12
L14
L16
Elevation
UNIVERSITY AT BUFFALO
206 KETTER HALL
BUFFALO, NY, 14226
Title: Linear Parts on Case 2A/2B
Page: 2 of 6
9/26/2022
STATUS:
BY: Jia-Hau Liu
REV:

CASE 1C



Plan

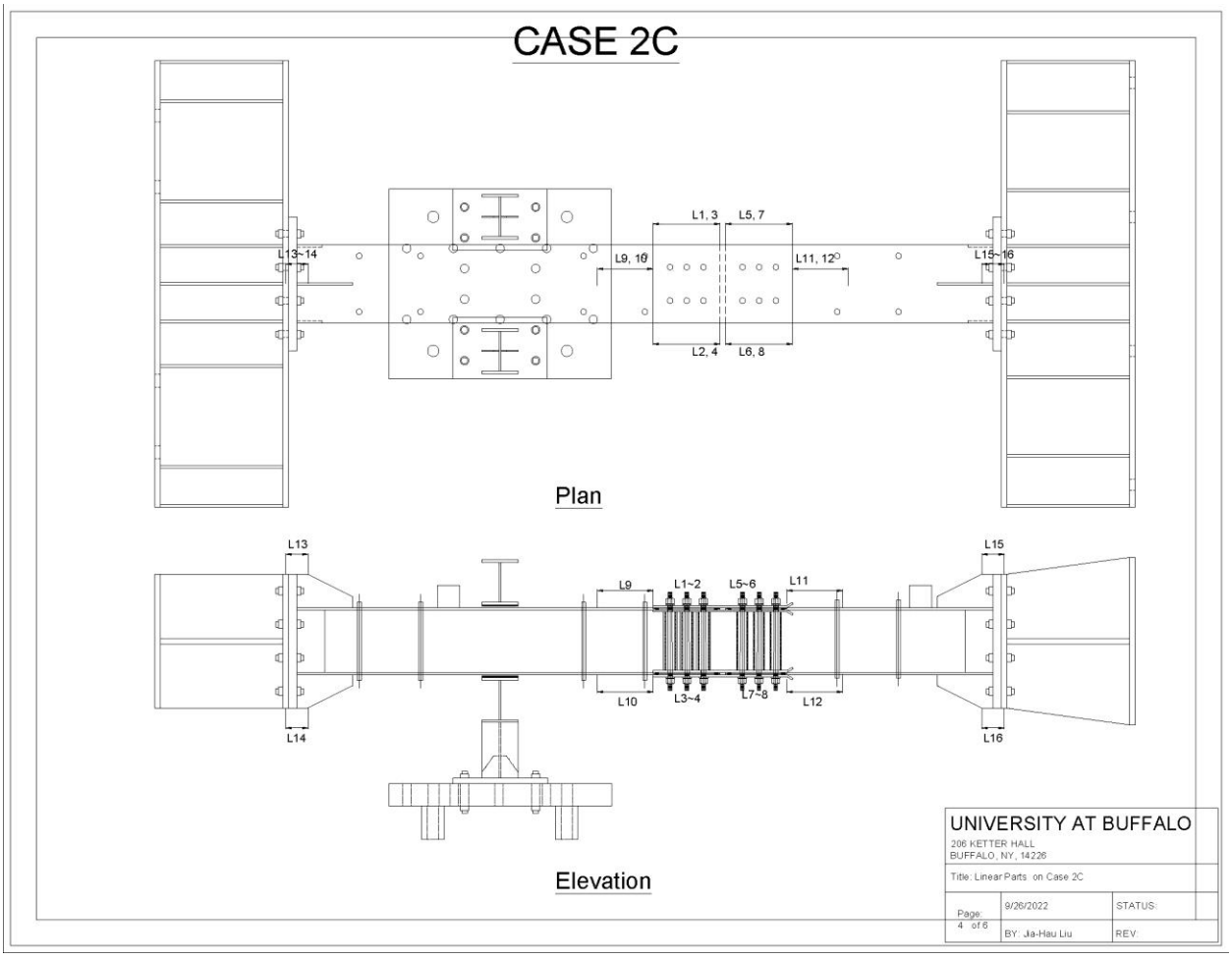


Elevation

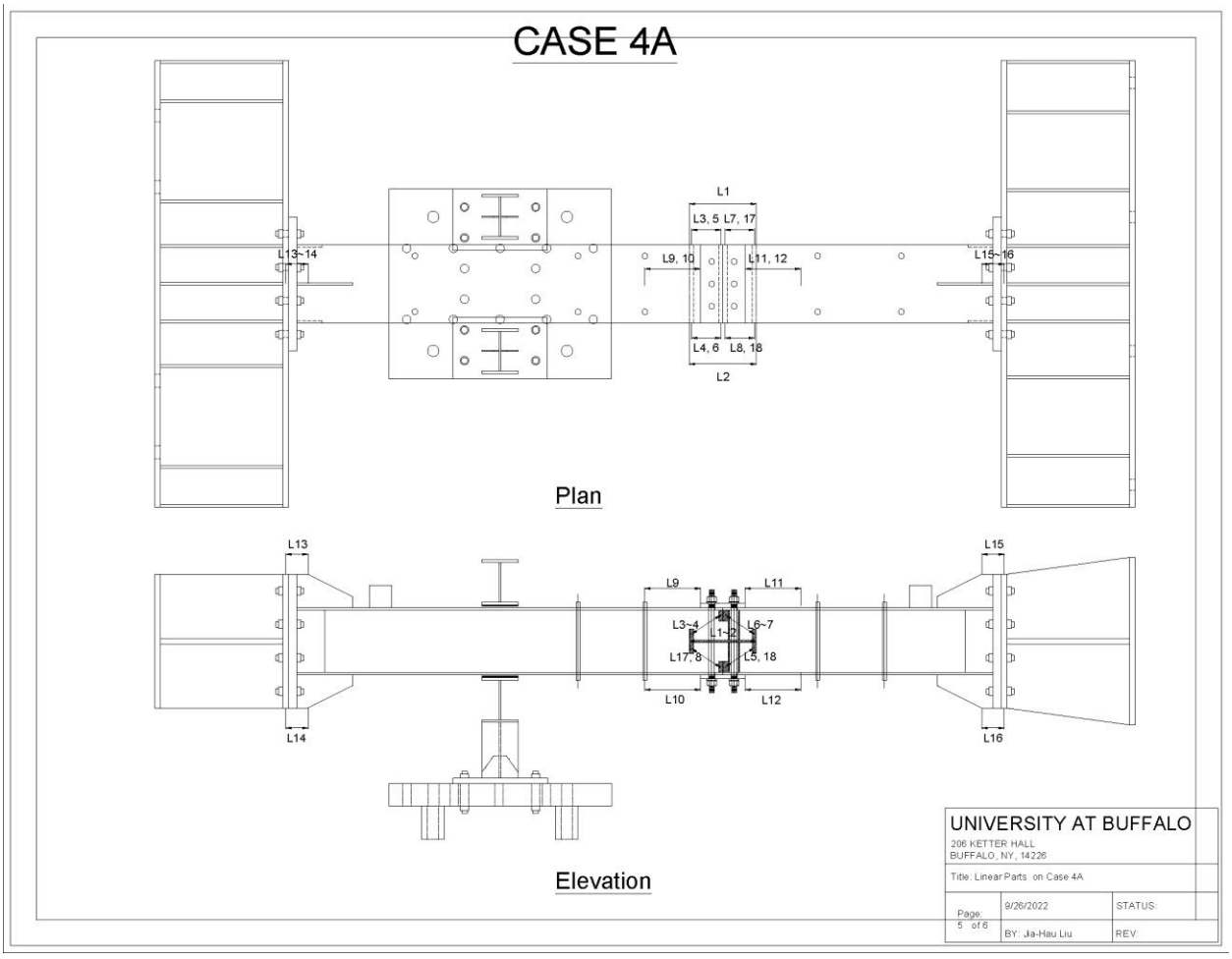
UNIVERSITY AT BUFFALO
206 KETTER HALL
BUFFALO, NY, 14226

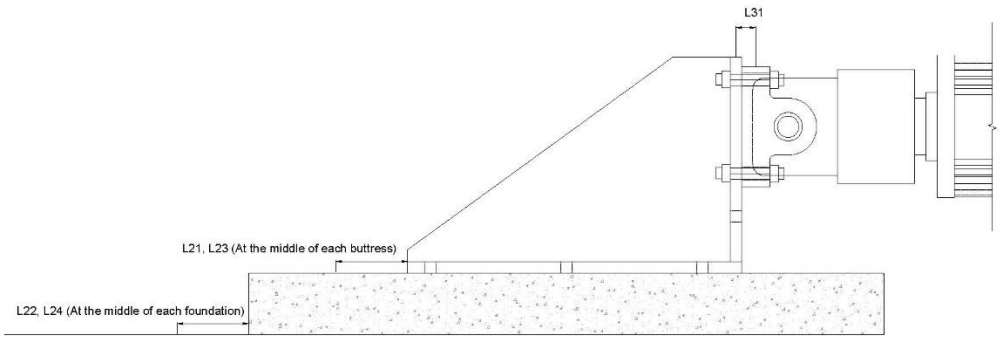
Title: Linear Parts on Case 1C

Page: 3 of 6	9/26/2022	STATUS:
	BY: Jia-Hau Liu	REV:

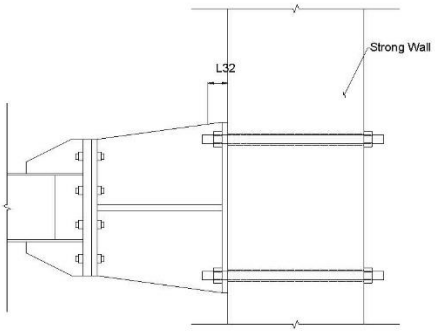

CASE 2C
L13~14
L9, 10
L1, 3
L5, 7
L2, 4
L6, 8
L11, 12
L15~16
Plan
L13
L14
L9
L1~2
L5~6
L11
L10
L3~4
L7~8
L12
L15
L16
Elevation
UNIVERSITY AT BUFFALO
206 KETTER HALL
BUFFALO, NY, 14226
Title: Linear Parts on Case 2C
Page: 4 of 6
9/26/2022
STATUS:
BY: Jia-Hau Liu
REV:

CASE 4A


L1
L3, 5 L7, 17
L13~14
L9, 10
L11, 12
L15~16
L4, 6
L8, 18
L2
Plan
L13
L15
L9
L11
L3~4
L6~7
L1~2
L17, 8
L5, 18
L10
L12
L14
L16
Elevation
UNIVERSITY AT BUFFALO
206 KETTER HALL
BUFFALO, NY, 14226
Title: Linear Parts on Case 4A
Page: 5 of 6
9/26/2022
STATUS:
BY: Jia-Hau Liu
REV:



Buttress and Foundation

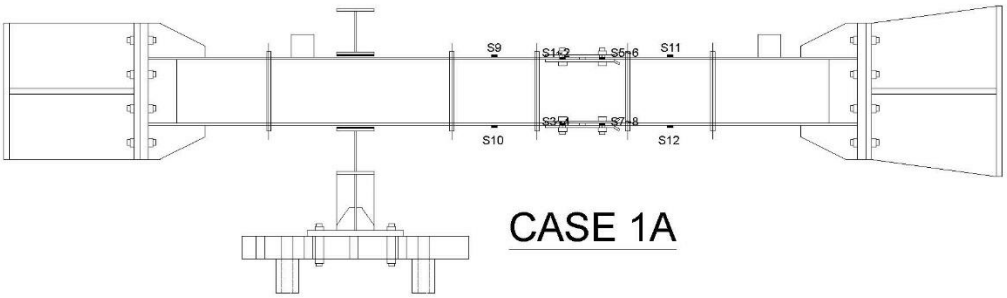


On Strong Wall

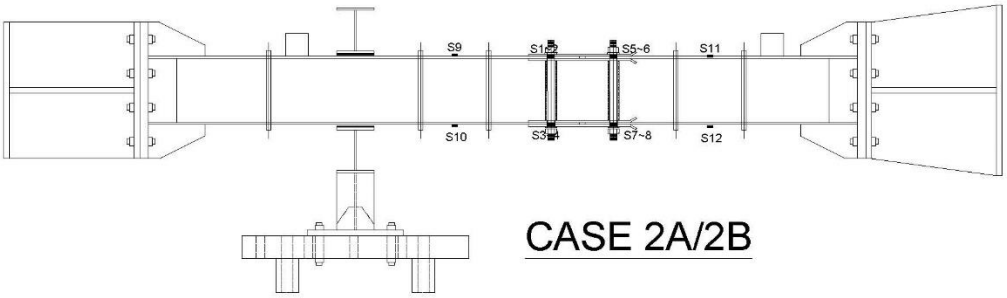
UNIVERSITY AT BUFFALO
206 KETTER HALL
BUFFALO, NY, 14226

Title: Linear Parts on Foundation

Page: 8 of 8	9/28/2022	STATUS:
	BY: Jia-Hau Liu	REV:



CASE 1A

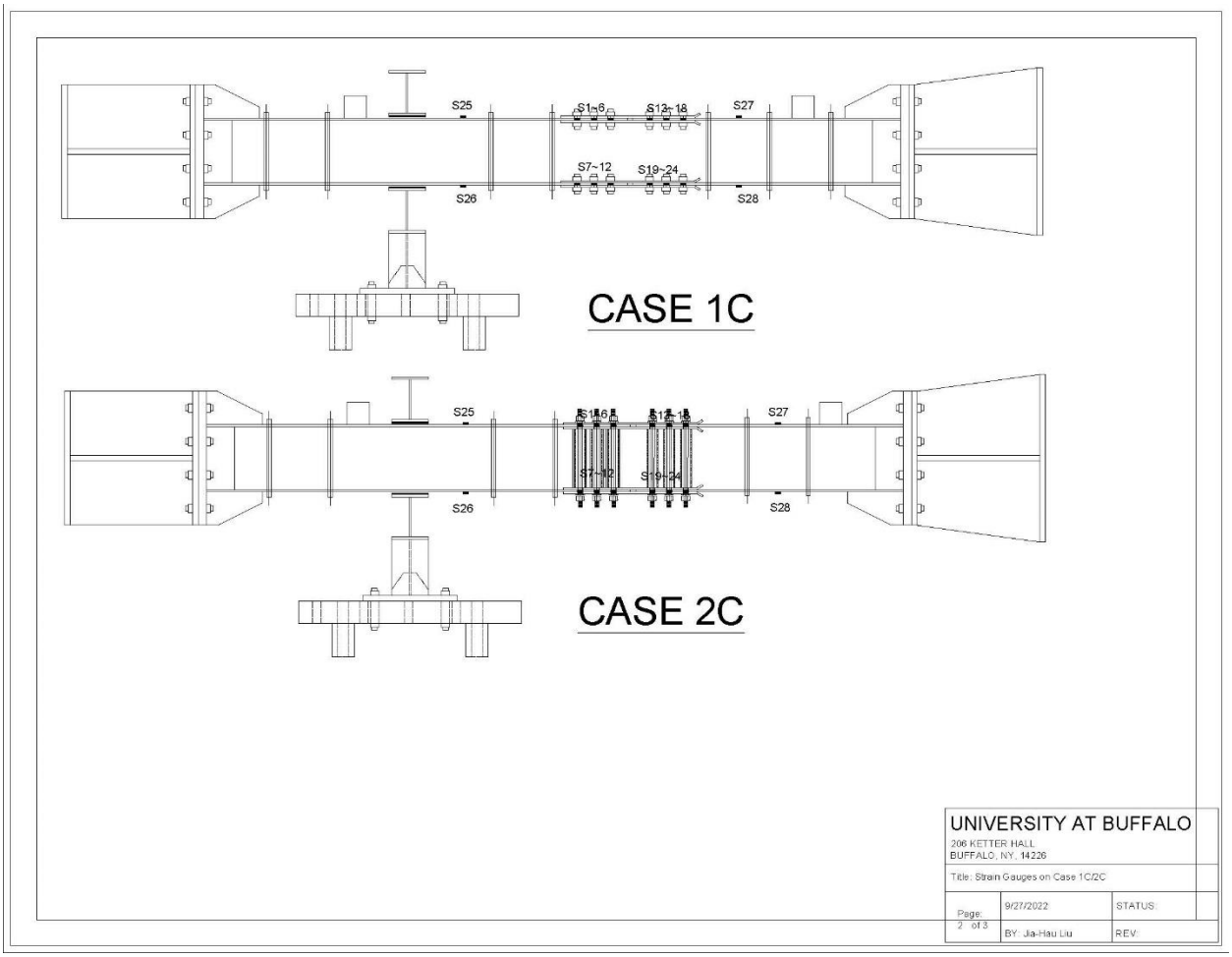


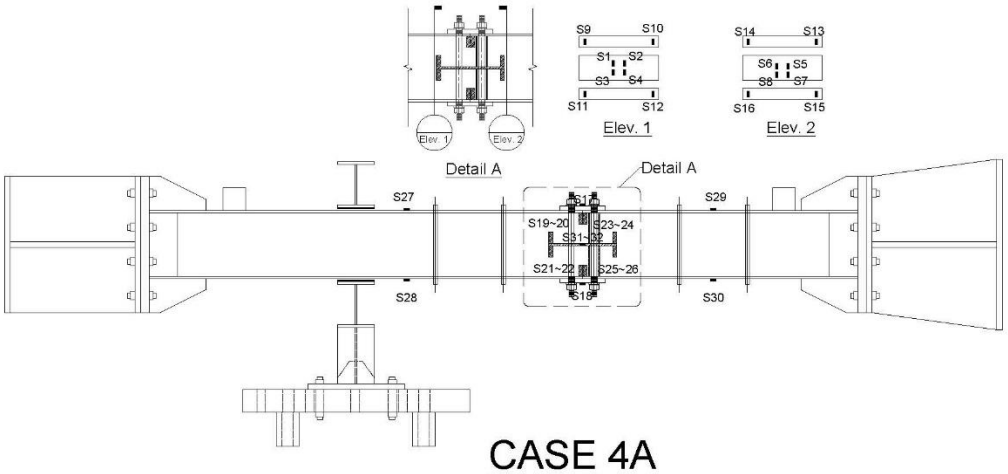
CASE 2A/2B

UNIVERSITY AT BUFFALO
206 KETTER HALL
BUFFALO, NY, 14226

Title: Strain Gauges on Case 1A/2A/2B

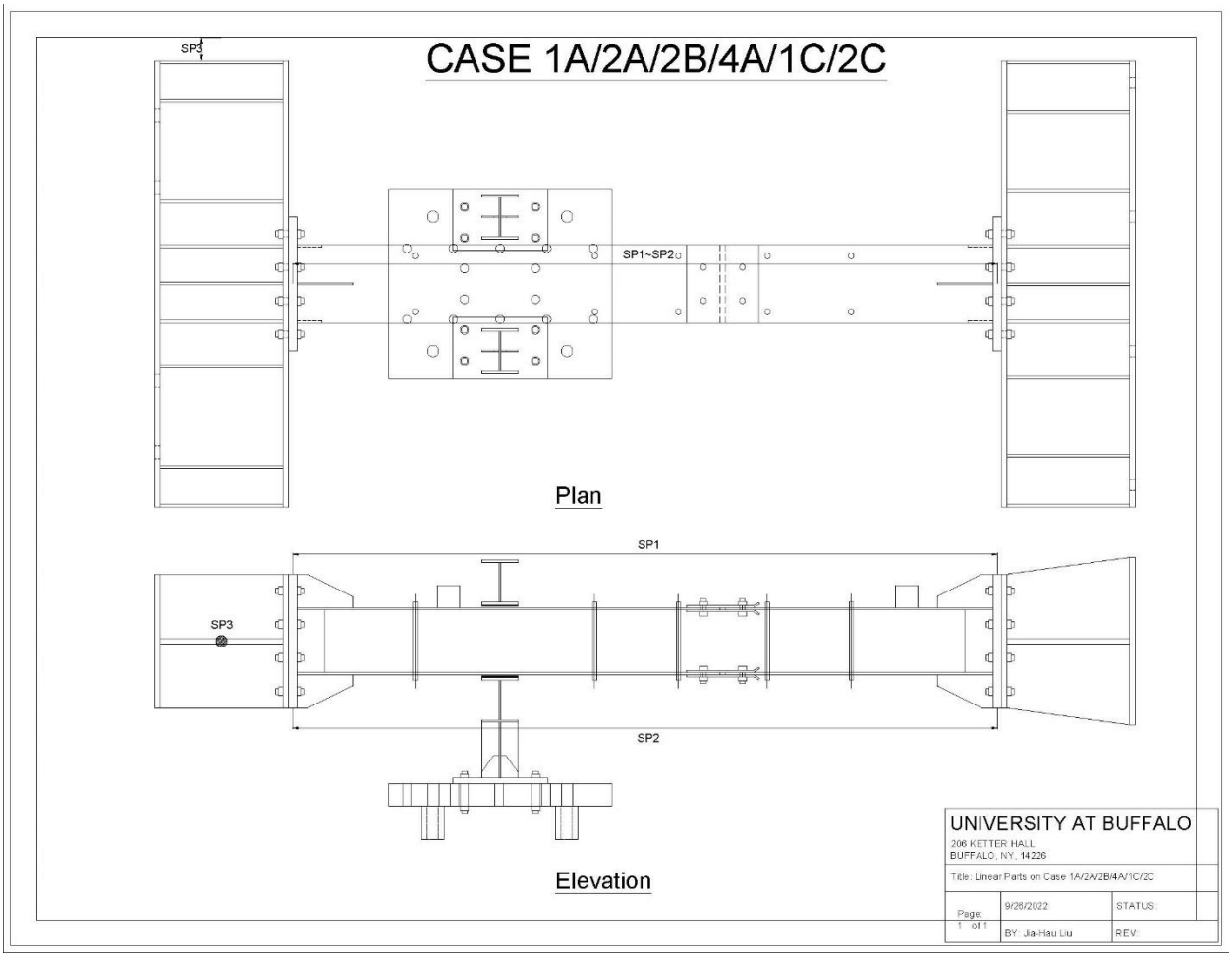
Page:	9/27/2022	STATUS:
1 of 3	BY: Jia-Hau Liu	REV:


S25
S1~6
S13~18
S27
S7~12
S19~24
S26
S28
CASE 1C
S25
S27
S26
S28
CASE 2C
UNIVERSITY AT BUFFALO
206 KETTER HALL
BUFFALO, NY, 14226
Title: Strain Gauges on Case 1C/2C
Page: 2 of 3
9/27/2022
STATUS:
BY: Jia-Hau Liu
REV:



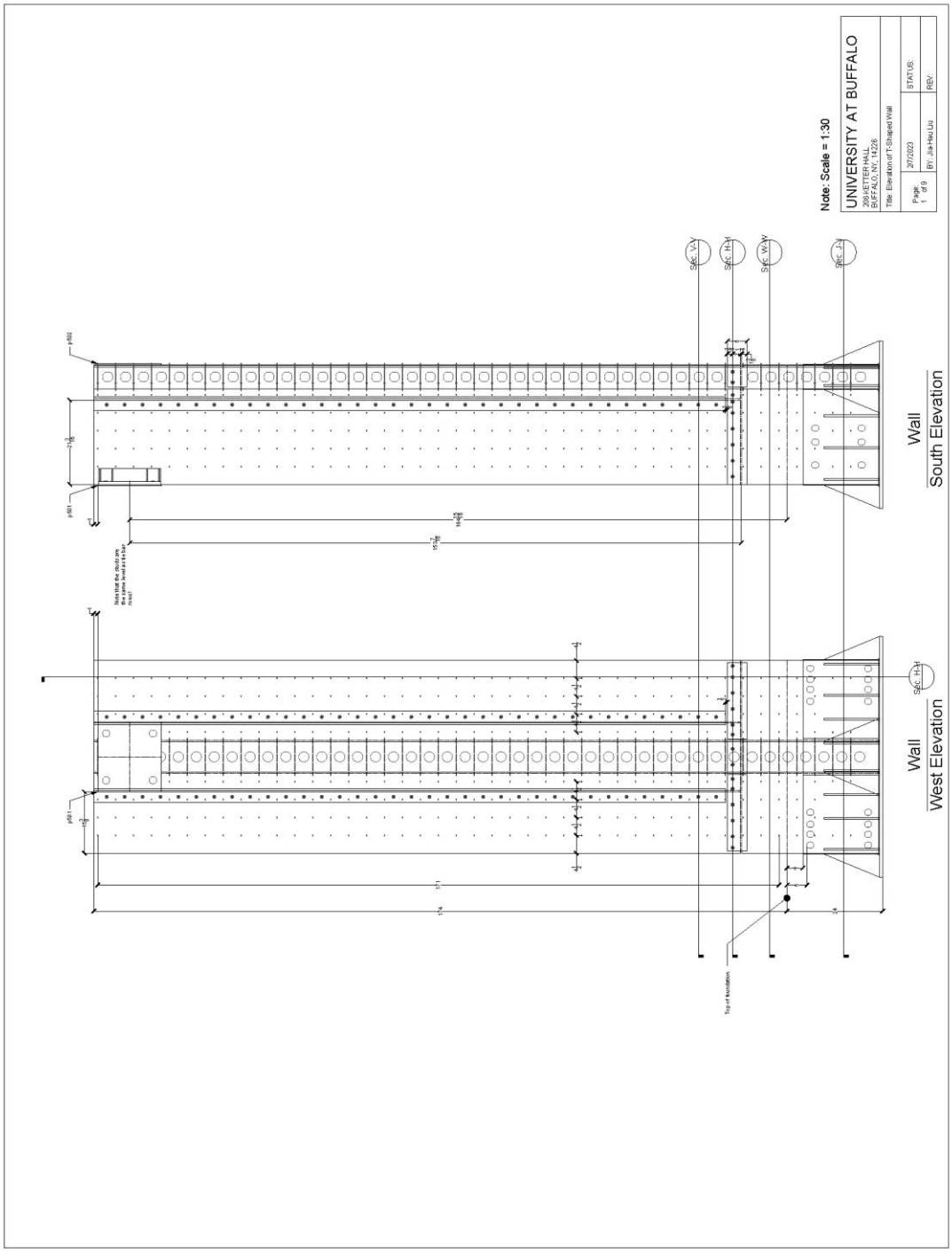
CASE 4A

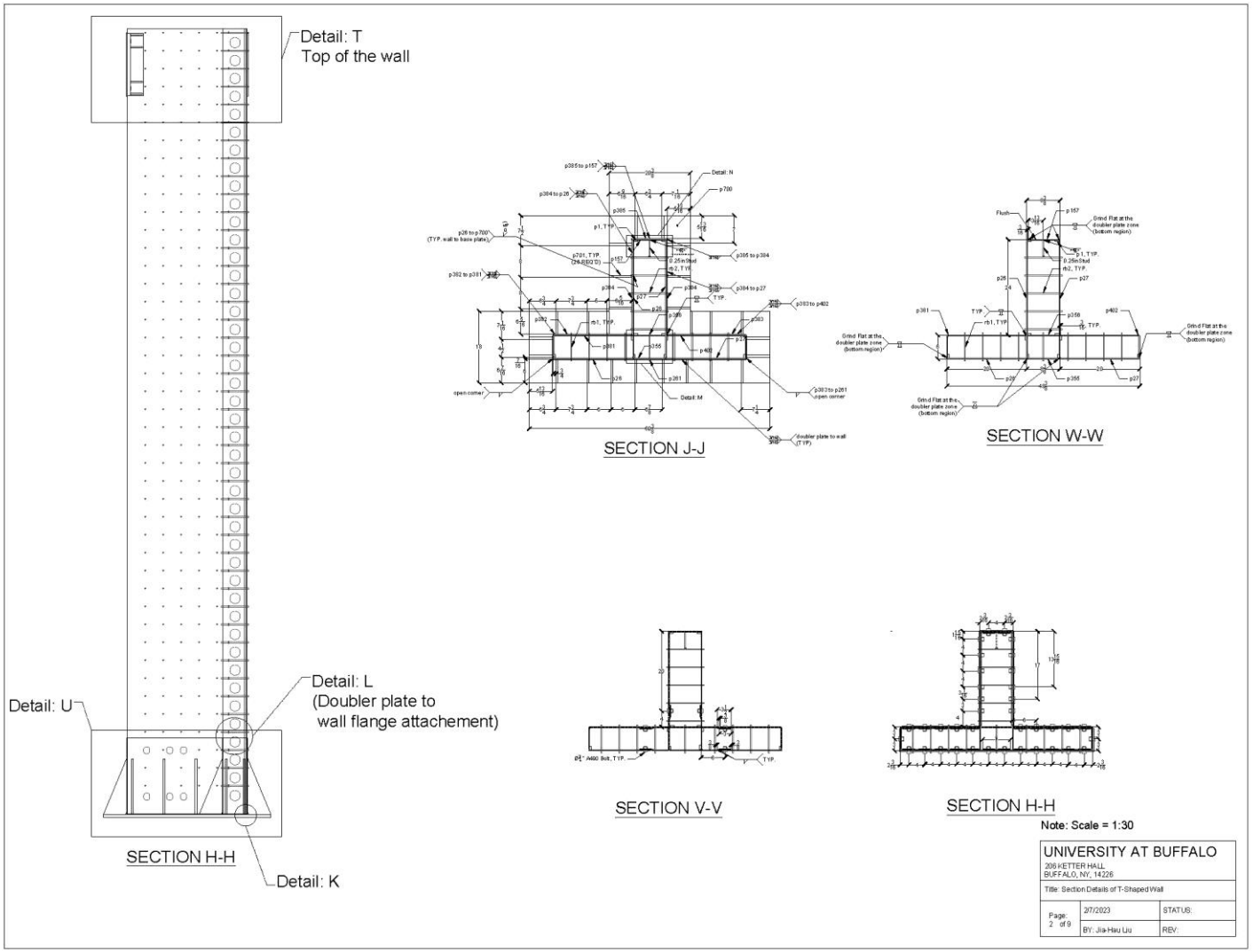
UNIVERSITY AT BUFFALO		
206 KETTER HALL BUFFALO, NY, 14226		
Title: Strain Gauges on Case 4A		
Page: 3 of 3	9/27/2022 BY: Jia-Hau Liu	STATUS: REV:

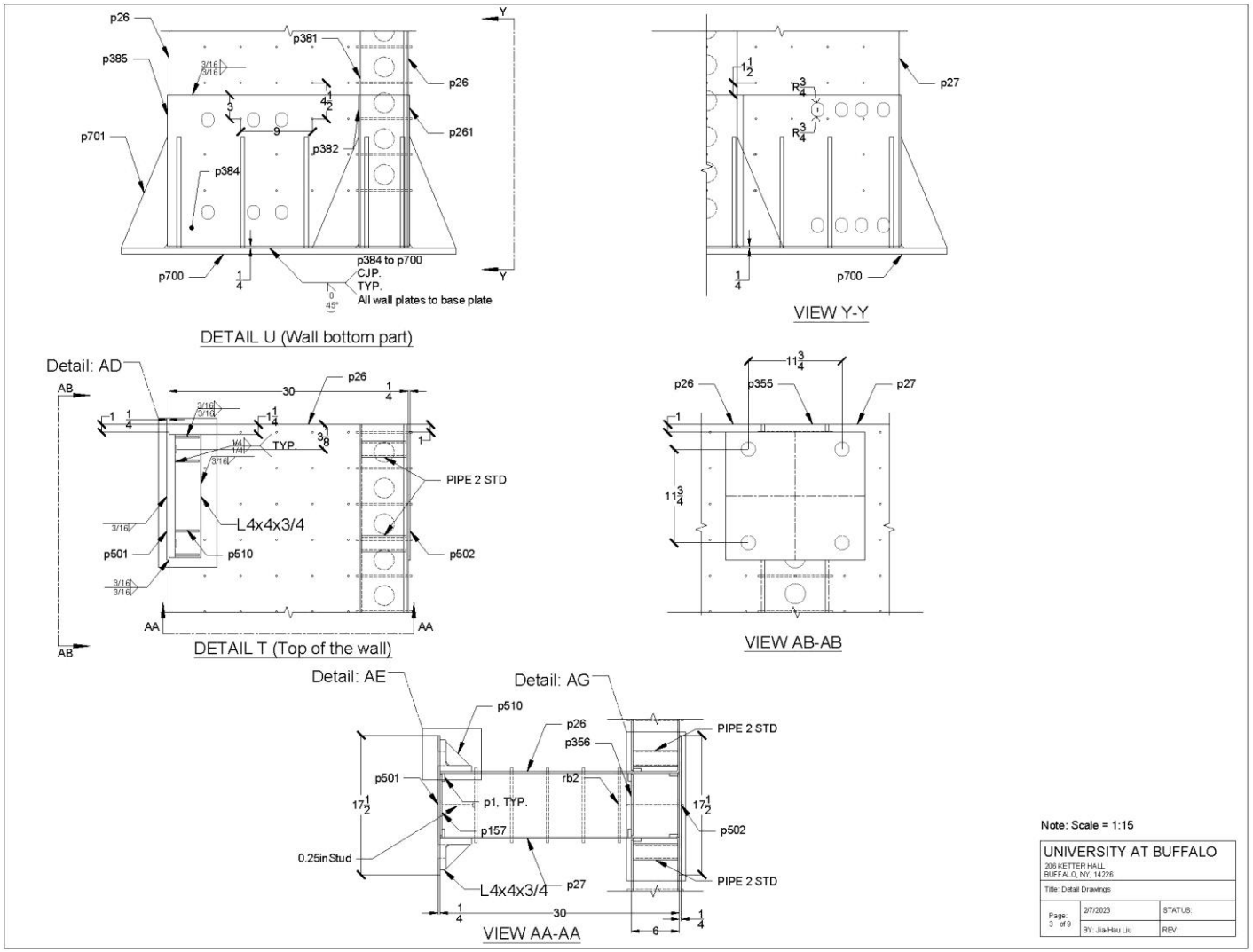

CASE 1A/2A/2B/4A/1C/2C
SP3
SP1~SP2
Plan
SP1
SP3
SP2
Elevation
UNIVERSITY AT BUFFALO
206 KETTER HALL
BUFFALO, NY, 14226
Title: Linear Parts on Case 1A/2A/2B/4A/1C/2C
Page: 1 of 1
9/28/2022
STATUS:
BY: Jia-Hau Liu
REV:

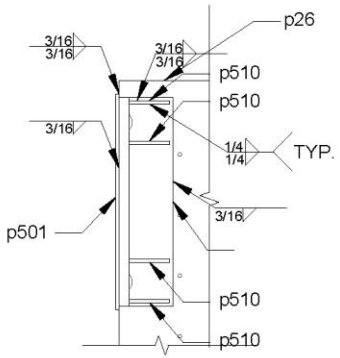
Appendix I.

Drawings of the Specimen (Wall Specimen Test)

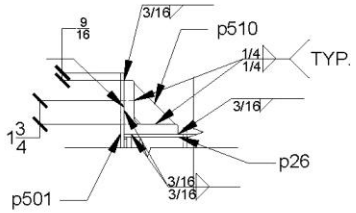

Note: Scale = 1:30
UNIVERSITY AT BUFFALO
JACOBS HALL
BUFFALO, NY, 14226
Title: Elevation of T-Shaped Wall
Page: 1 of 9
2/7/2023
BY: Jia-Hau Liu
STATUS:
REV:
Wall
South Elevation
Wall
West Elevation
Sec. V-V
Sec. H-H
Sec. W-W
Sec. J-J
Top of foundation


Detail: T
Top of the wall
Detail: U
Detail: L
(Doubler plate to
wall flange attachement)
Detail: K
SECTION H-H
SECTION J-J
SECTION W-W
SECTION V-V
SECTION H-H
Note: Scale = 1:30
UNIVERSITY AT BUFFALO
208 KETTER HALL
BUFFALO, NY, 14226
Title: Section Details of T-Shaped Wall
Page: 2 of 9
2/7/2023
STATUS:
BY: Jia-Hau Liu
REV:

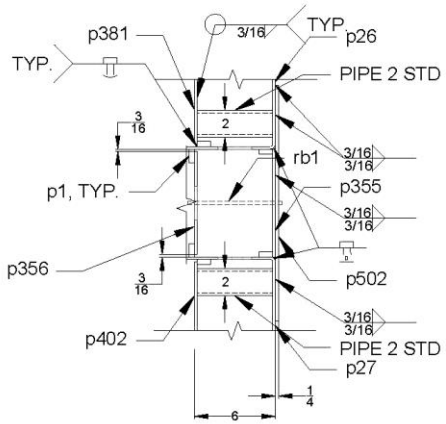

p26
p381
p385
p26
p701
p261
p382
p384
p700
p384 to p700
CJP.
TYP.
All wall plates to base plate
DETAIL U (Wall bottom part)
p27
p700
VIEW Y-Y
Detail: AD
AB
p26
TYP.
PIPE 2 STD
L4x4x3/4
p501
p510
p502
AA
DETAIL T (Top of the wall)
p26
p355
p27
VIEW AB-AB
Detail: AE
Detail: AG
p510
p26
p356
PIPE 2 STD
p501
rb2
p1, TYP.
p157
p502
0.25inStud
L4x4x3/4
p27
PIPE 2 STD
VIEW AA-AA
Note: Scale = 1:15
UNIVERSITY AT BUFFALO
208 KETTER HALL
BUFFALO, NY, 14226
Title: Detail Drawings
Page: 3 of 9
2/7/2023
STATUS:
BY: Jia-Hau Liu
REV:



DETAIL AD



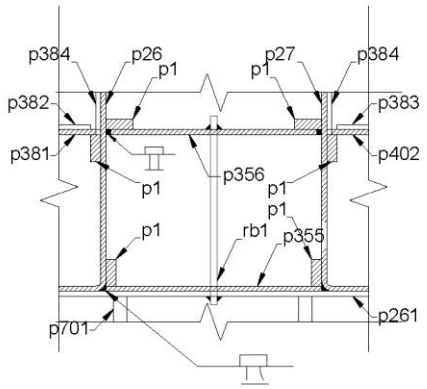
DETAIL AE



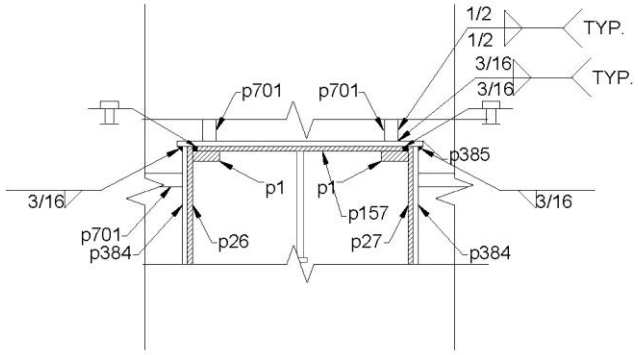
DETAIL AG

Note: Scale = 1:10

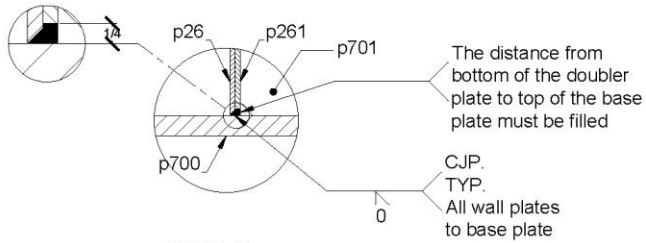
UNIVERSITY AT BUFFALO 208 KETTER HALL BUFFALO, NY, 14226		
Title: Detail Drawings		
Page: 4 of 9	2/7/2023	STATUS:
	BY: Jia-Hau Liu	REV:



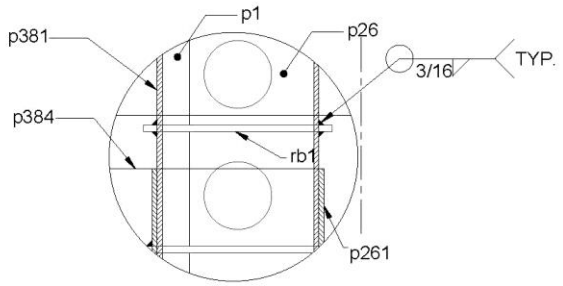
DETAIL M



DETAIL N



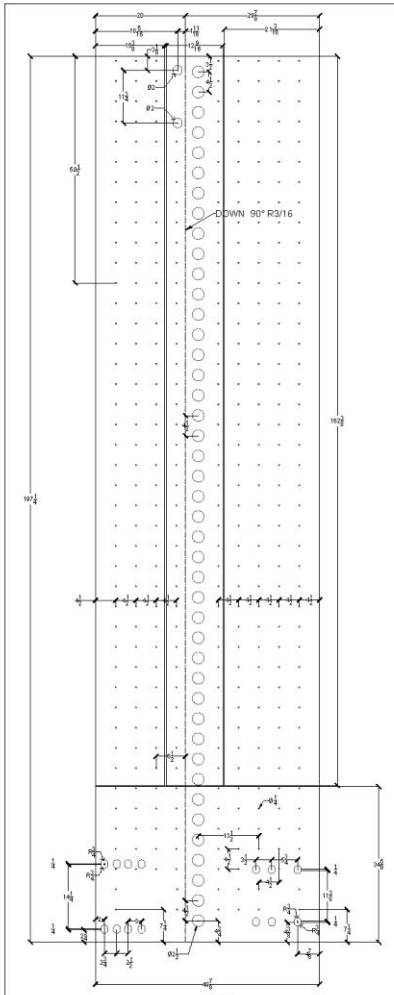
DETAIL K



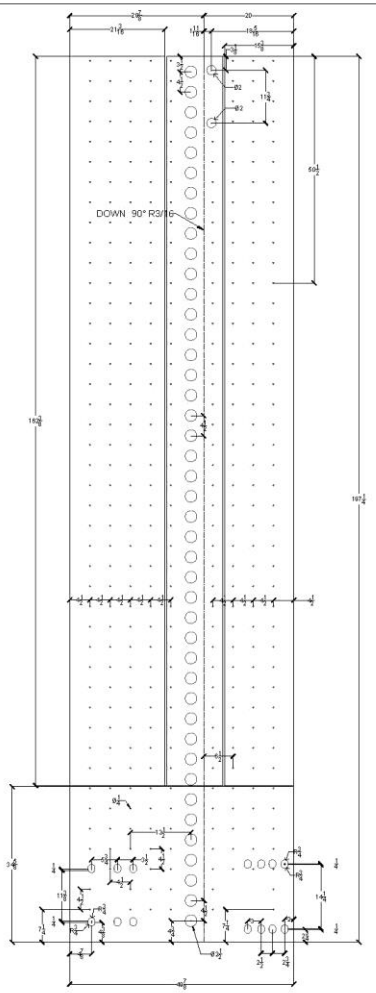
DETAIL L

Note: Scale = 1:5

UNIVERSITY AT BUFFALO 208 KETTER HALL BUFFALO, NY, 14226		
Title: Detail Drawings		
Page: 5 of 9	2/7/2023	STATUS:
	BY: Jia-Hau Liu	REV:



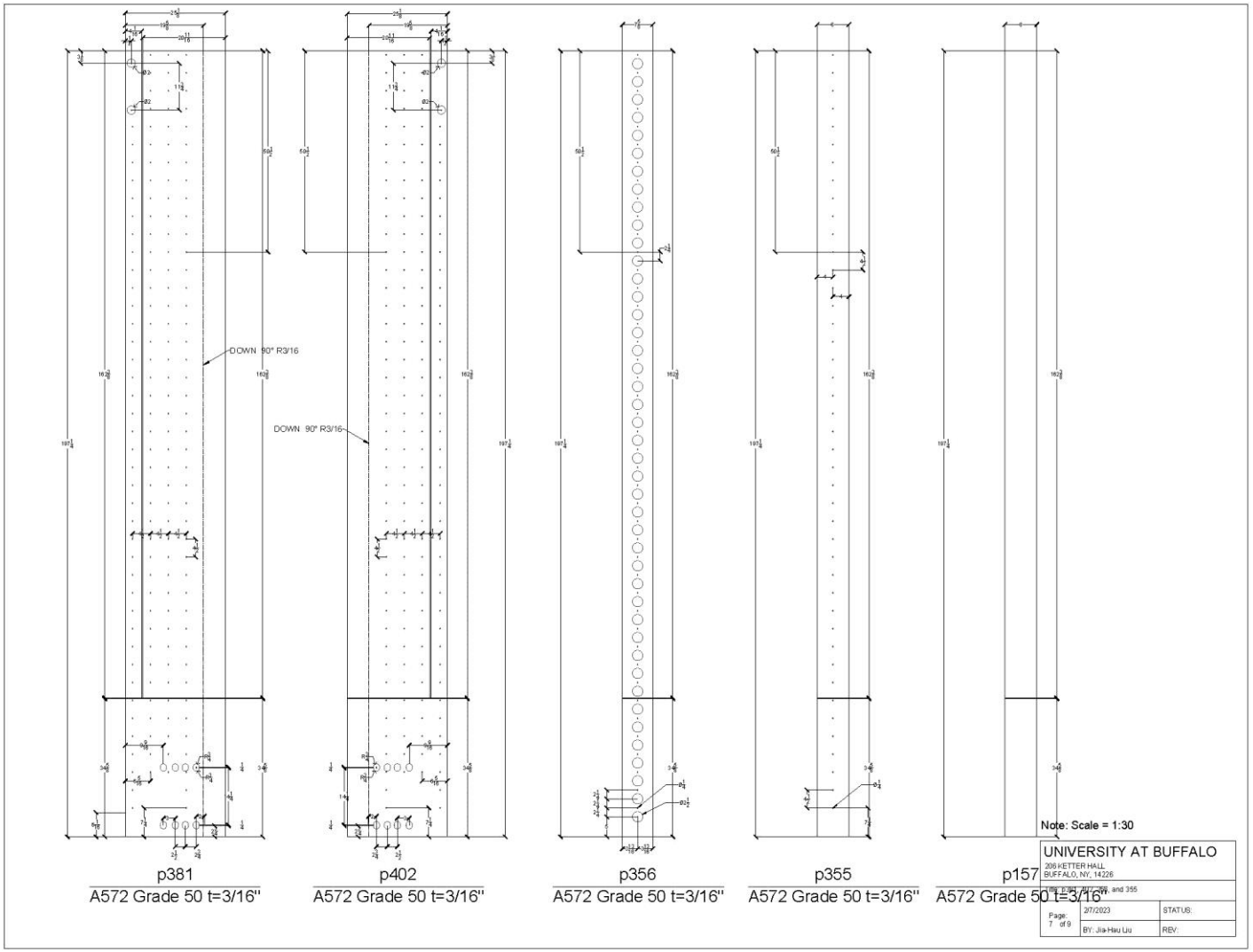
p26
A572 Grade 50 t=3/16"



p27
A572 Grade 50 t=3/16"

Note: Scale = 1:30

UNIVERSITY AT BUFFALO 206 KETTER HALL BUFFALO, NY, 14226		
Title: p26 and p27		
Page: 6 of 9	2/7/2023	STATUS:
	BY: Jia-Hau Liu	REV:



p381
A572 Grade 50 t=3/16"

p402
A572 Grade 50 t=3/16"

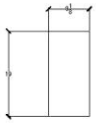
p356
A572 Grade 50 t=3/16"

p355
A572 Grade 50 t=3/16"

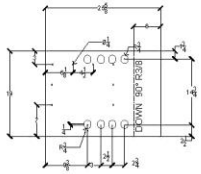
p157
A572 Grade 50 t=3/16"



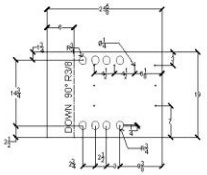
p1
Baking bar t=3/8"



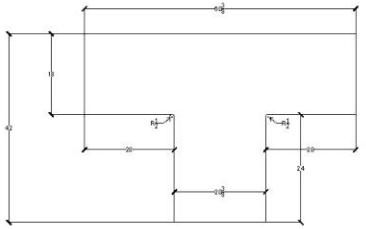
p385
Doubler Plate
A572 Grade 50 t=3/16"



p382
Doubler Plate
A572 Grade 50 t=3/16"



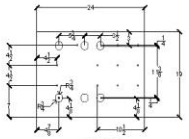
p383
Doubler Plate
A572 Grade 50 t=3/16"



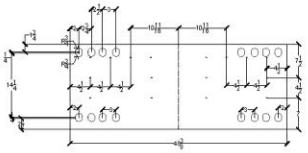
p700
Base Plate
A572 Grade 50 t=3/4"



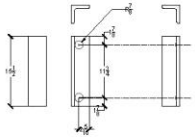
rb1
Grade: F1554GR55
(Round bar)



p384
Doubler Plate
A572 Grade 50 t=3/16"



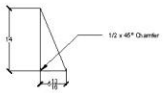
p261
Doubler Plate
A572 Grade 50 t=3/16"



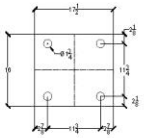
L4x4x3/4



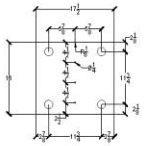
rb2
Grade: F1554GR55
(Round bar)



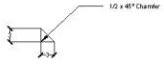
p701
A572 Grade 50 t=1/2"



p501
A36 Grade 36 t=1/4"



p502
A36 Grade 36 t=1/4"



p510
A36 Grade 36 t=1/2"



0.25 in. Stud
Grade: F1554GR55
(Stud)

Note: Scale = 1:30

NOTE:
1. Holes on the doubler plate should be aligned with the holes on the wall flange.
2. The hole drilling can be performed before or after welding to the wall flange.

UNIVERSITY AT BUFFALO		
208 KETTER HALL BUFFALO, NY, 14226		
Title: Detail Drawings		
Page: 8 of 9	2/7/2023	STATUS:
	BY: Jia-Hau Liu	REV:

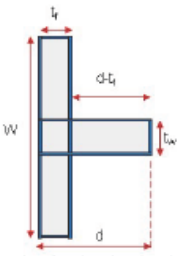
Appendix J.

Analysis of Specimens (Wall Specimen Test)

Analysis of Wall Specimen

0. Typical Information

Material and Section Properties



$F_y = 55\ ksi$ $F_u = 71.5\ ksi$ $E_s = (2.9 \cdot 10^4)\ ksi$

$f_c = 6\ ksi$ $E_c = (4.415 \cdot 10^3)\ ksi$ $n := \frac{E_s}{E_c} = 6.568$

$t_p = 0.1875\ in$ $W = 48.375\ in$ $d = 30\ in$ $t_f = 6\ in$ $t_w = 8.375\ in$

1. Calculate Center of Gravity

$A_1 := W \cdot t_p = 9.07\ in^2$ $y_1 := \frac{t_p}{2} = 0.094\ in$

$A_2 := 4 \cdot (t_f - 2 \cdot t_p) \cdot t_p = 4.219\ in^2$ $y_2 := \frac{t_f}{2} = 3\ in$

$A_3 := W \cdot t_p = 9.07\ in^2$ $y_3 := t_f + \frac{t_p}{2} = 6.094\ in$

$A_4 := 2 \cdot (d - t_f - t_p) \cdot t_p = 8.93\ in^2$ $y_4 := t_f + \frac{(d - t_f - t_p)}{2} = 17.906\ in$

$A_5 := t_w \cdot t_p = 1.57\ in^2$ $y_5 := d - \frac{t_p}{2} = 29.906\ in$

$A_6 := (W - 4 \cdot t_p) \cdot \frac{(t_f - 2 \cdot t_p)}{n} = 40.786\ in^2$ $y_6 := \frac{t_f}{2} = 3\ in$

$A_7 := (d - t_f - t_p) \cdot \frac{(t_w - 2 \cdot t_p)}{n} = 29.003\ in^2$ $y_7 := t_f + \frac{(d - t_f - t_p)}{2} = 17.906\ in$

$\Sigma A_i := A_1 + A_2 + A_3 + A_4 + A_5 + A_6 + A_7 = 102.649\ in^2$

$\Sigma A_i y_i := A_1 \cdot y_1 + A_2 \cdot y_2 + A_3 \cdot y_3 + A_4 \cdot y_4 + A_5 \cdot y_5 + A_6 \cdot y_6 + A_7 \cdot y_7$ $y_c := \frac{\Sigma A_i y_i}{\Sigma A_i} = 8.937\ in$

2. Calculate $M_{0.6Fy}$ on Faceplates (Web in Compression)

2.1 Gravity Load, Eccentricity, and NA

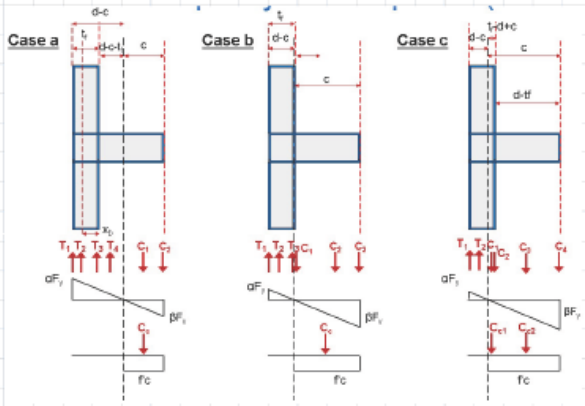
$A_c := (t_w - 2 \cdot t_p) \cdot (d - t_f - t_p) + (W - 4 \cdot t_p) \cdot (t_f - 2 \cdot t_p) = 458.391\ in^2$

$P := -0.1 \cdot A_c \cdot f_c = -275.034\ kip$ **(10% $A_c f_c$)**

Try $c := 15.288\ in$ $e := d - c - y_c = 5.775\ in$

2.2 Stress Profile

if $c < (d - t_f)$ = "Case a"
  "Case a"
else if $c > (d - t_f + t_p)$
  "Case c"
else
  "Case b"



$\alpha := 0.6$

$x := \frac{d-c}{\alpha} = 24.52\ in$

$y_{t3} := \frac{d-c-t_f}{d-c} \cdot \alpha = 0.355$

$y_{c1a} := \text{if } c \le x \left\| \frac{2\,c}{3\cdot(d-c)} \cdot \alpha \right. \text{ else } \left\| \frac{2}{3} \right. = 0.416$

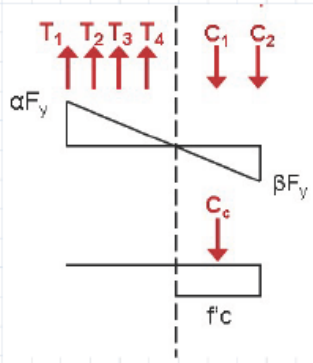
$x_b := t_f \cdot \frac{4\,\alpha - y_{t3}}{3\cdot(\alpha + y_{t3})} = 4.281\ in$

$y_{t2} := \frac{d-c-t_f+x_b}{d-c} \cdot \alpha = 0.53$

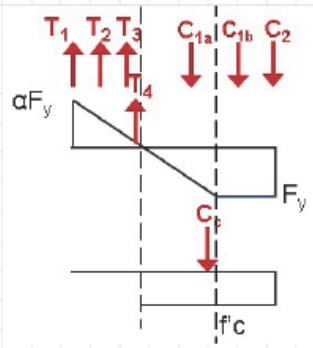
$y_{c1b} := \text{if } c \le x \left\| 0 \right. \text{ else } \left\| 1 \right. = 0$

$y_{t4} := \frac{(d-c-t_f)\cdot\frac{2}{3}}{(d-c)} \cdot \alpha = 0.237$

$\beta := \text{if } c \le x \left\| \frac{c}{d-c} \cdot \alpha \right. \text{ else } \left\| 1 \right. = 0.623$



Case a (Elastic)



Case a (Yielding Stage)

2.3 Forces

$T_1 := W \cdot t_p \cdot \alpha \cdot F_y = 299.32\ kip$

$C_{1a} := 2 \cdot t_p \cdot y_{c1a} \cdot F_y \cdot \text{if } c \le x \left\| c - t_p \right. \text{ else } \left\| x \right. = 129.457\ kip$

$T_2 := 4 \cdot (t_f - 2 \cdot t_p) \cdot t_p \cdot y_{t2} \cdot F_y = 122.949\ kip$

$C_{1b} := 2 \cdot t_p \cdot y_{c1b} \cdot F_y \cdot \text{if } c \le x \left\| 0\ in \right. \text{ else } \left\| c - x - t_p \right. = 0\ kip$

$T_3 := W \cdot t_p \cdot y_{t3} \cdot F_y = 177.248\ kip$

$C_2 := t_w \cdot t_p \cdot \beta \cdot F_y = 53.849\ kip$

$T_4 := 2 \cdot (d - c - t_f) \cdot t_p \cdot y_{t4} \cdot F_y = 42.562\ kip$

$C_c := c \cdot (t_w - 2 \cdot t_p) \cdot f_c = 733.824\ kip$

Check $\Sigma F_i := T_1 + T_2 + T_3 + T_4 - C_{1a} - C_{1b} - C_2 - C_c - P = -0.016\ kip$ **~=0, OK!**

2.4 Lever Arms

$L_{T1} := d - c = 14.712\ in$

$L_{C1a} := \text{if } c \le x \ \| \ 2\frac{c}{3} \ \text{else} \ \| \ 2\frac{x}{3} = 10.192\ in$

$L_{T2} := d - c - t_f + x_b = 12.993\ in$

$L_{C1b} := \text{if } c \le x \ \| \ 0\ in \ \text{else} \ \| \ x + \frac{(c-x)}{2} = 0\ in$

$L_{T3} := d - c - t_f = 8.712\ in$

$L_{C2} := c = 15.288\ in$

$L_{T4} := \frac{d - c - t_f}{2} = 4.356\ in$

$L_{Cc} := \frac{c}{2} = 7.644\ in$

2.5 Moments (Positive Dir./Web in Compression)

$\Sigma C_i L_{Ci} := C_{1a} \cdot L_{C1a} + C_{1b} \cdot L_{C1b} + C_2 \cdot L_{C2} + C_c \cdot L_{Cc} = (7.752 \cdot 10^3)\ (kip \cdot in)$

$\Sigma T_i L_{Ti} := T_1 \cdot L_{T1} + T_2 \cdot L_{T2} + T_3 \cdot L_{T3} + T_4 \cdot L_{T4} = (7.731 \cdot 10^3)\ (kip \cdot in)$

$pos.M_{0.6Fy} := \Sigma C_i L_{Ci} + \Sigma T_i L_{Ti} - P \cdot e = (1.423 \cdot 10^3)\ kip \cdot ft$

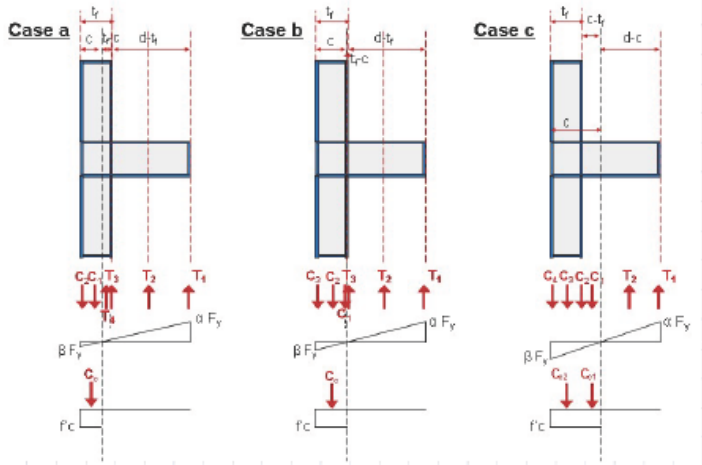
3. Calculate $-M_{0.6Fy}$ on Faceplates (Flange in Compression)

3.1 Eccentricity and NA

Try $c := 2.12175\ in$ $\quad e := c - y_c = -6.815\ in$

3.2 Stress Profile

$\text{if } c < (t_f - t_p) \ \| \ \text{“Case a”} \ \text{else if } c > t_f \ \| \ \text{“Case c”} \ \text{else} \ \| \ \text{“Case b”} = \text{“Case a”}$



$\beta := \frac{c}{(d-c)} \cdot \alpha = 0.046$

$\alpha := 0.6$

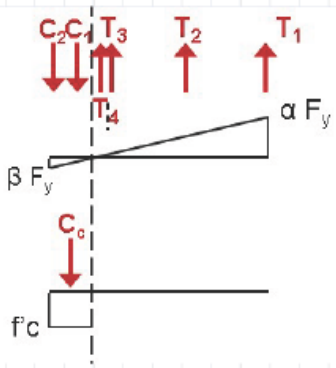
$y_{c2} := \frac{2\,\beta}{3} = 0.03$

$y_{t3} := \frac{(t_f - c)}{d-c} \cdot \alpha = 0.083$

$x_b := (d-t_f) \cdot \frac{(y_{t3} + 2\,\alpha)}{3\,(y_{t3}+\alpha)} = 15.023\ in$

$y_{t2} := \frac{x_b + t_f - c}{d-c} \cdot \alpha = 0.407$

$y_{t4} := \frac{\frac{2}{3}\,(t_f - c - t_p)}{c} \cdot \beta = 0.053$



Case a (Elastic)

3.3 Forces

$C_1 := W \cdot t_p \cdot \beta \cdot F_y = 22.781\ kip$

$T_1 := t_w \cdot t_p \cdot \alpha \cdot F_y = 51.82\ kip$

$C_2 := 4\,(c - t_p) \cdot t_p \cdot y_{c2} \cdot F_y = 2.429\ kip$

$T_2 := 2 \cdot (d - t_f) \cdot t_p \cdot y_{t2} \cdot F_y = 201.364\ kip$

$C_c := (W - 4 \cdot t_p) \cdot (c - t_p) \cdot f_c = 552.712\ kip$

$T_3 := W \cdot t_p \cdot y_{t3} \cdot F_y = 41.64\ kip$

$T_4 := 4 \cdot (t_f - c - t_p) \cdot t_p \cdot y_{t4} \cdot F_y = 8.062\ kip$

Check $\Sigma F_i := T_1 + T_2 + T_3 + T_4 - C_1 - C_2 - C_c - P = -0.001\ kip$ **~=0, OK!**

3.4 Lever Arms

$L_{C1} := c = 2.122\ in$

$L_{T1} := d - c = 27.878\ in$

$L_{C2} := \frac{2\,(c - t_p)}{3} = 1.29\ in$

$L_{T2} := t_f - c + x_b = 18.901\ in$

$L_{Cc} := \frac{(c - t_p)}{2} = 0.967\ in$

$L_{T3} := t_f - c = 3.878\ in$

$L_{T4} := \frac{(t_f - c - t_p) \cdot 2}{3} = 2.461\ in$

3.5 Moments (Negative Dir./Flange in Compression)

$\Sigma C_i L_{Ci} := C_1 \cdot L_{C1} + C_2 \cdot L_{C2} + C_c \cdot L_{Cc} = 48.834\ kip \cdot ft$

$\Sigma T_i L_{Ti} := T_1 \cdot L_{T1} + T_2 \cdot L_{T2} + T_3 \cdot L_{T3} + T_4 \cdot L_{T4} = 452.668\ kip \cdot ft$

$neg.M_{0.6Fy} := \Sigma C_i L_{Ci} + \Sigma T_i L_{Ti} + P \cdot e = 657.697\ kip \cdot ft$

4. Calculate $M_{Bearing}$ of Horizontal Splices (Web in Compression)

4.1 NA, Eccentricity, Bolt Diameters

Try $c := 15.005\ in$ $e := d - c - y_c = 6.058\ in$ $d_b := 0.75\ in$

4.2 Bolt Number, Nb

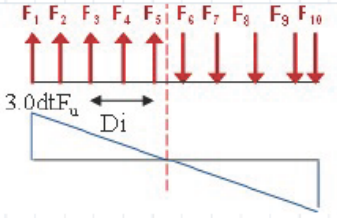
$N_{b\#1} := 12$ $N_{b\#6} := 2$

$N_{b\#2} := 2$ $N_{b\#7} := 2$

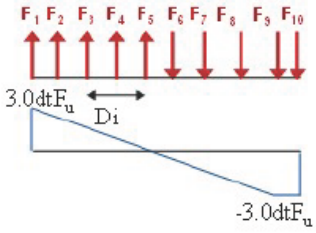
$N_{b\#3} := 10$ $N_{b\#8} := 2$

$N_{b\#4} := 2$ $N_{b\#9} := 2$

$N_{b\#5} := 2$ $N_{b\#10} := 2$



Case a (Elastic)



Case a (With Compression Limit)

4.3 Bolt Locations

$L\#1 := 30\ in$ $L\#6 := 13.9375\ in$

$L\#2 := 27\ in$ $L\#7 := 9.9375\ in$

$L\#3 := 24\ in$ $L\#8 := 5.9375\ in$

$L\#4 := 20\ in$ $L\#9 := 1.9375\ in$

$L\#5 := 17\ in$ $L\#10 := 0\ in$

4.3 Bolt Stress Profile (NA in Web, Case a)

$TLim := 3.0$ dtFu (Tension Limit) $CLim := -3.0$ dtFu (Compression Limit)

$B\#1 := TLim = 3$ dtFu

$B\#2 := \max\left(\frac{(L\#2 - c)}{d - c} \cdot B\#1, CLim\right) = 2.4$ dtFu

$B\#3 := \max\left(\frac{(L\#3 - c)}{d - c} \cdot B\#1, CLim\right) = 1.8$ dtFu

$B\#4 := \max\left(\frac{(L\#4 - c)}{d - c} \cdot B\#1, CLim\right) = 0.999$ dtFu

$B\#5 := \max\left(\frac{(L\#5 - c)}{d - c} \cdot B\#1, CLim\right) = 0.399$ dtFu

$B\#6 := \max\left(\frac{(L\#6 - c)}{d - c} \cdot B\#1, CLim\right) = -0.214$ dtFu

$B\#7 := \max\left(\frac{(L\#7 - c)}{d - c} \cdot B\#1, CLim\right) = -1.014$ dtFu

$B\#8 := \max\left(\frac{(L\#8 - c)}{d - c} \cdot B\#1, CLim\right) = -1.814$ dtFu

$B\#9 := \max\left(\frac{(L\#9 - c)}{d - c} \cdot B\#1, CLim\right) = -2.614$ dtFu

$B\#10 := \max\left(\frac{(L\#10 - c)}{d - c} \cdot B\#1, CLim\right) = -3$ dtFu

4.4 Bolt Forces

$F_1 := B\#1 \cdot d_b \cdot t_p \cdot F_u \cdot N_{b\#1} = 361.969\ kip$

$F_2 := B\#2 \cdot d_b \cdot t_p \cdot F_u \cdot N_{b\#2} = 48.258\ kip$

$F_3 := B\#3 \cdot d_b \cdot t_p \cdot F_u \cdot N_{b\#3} = 180.944\ kip$

$F_4 := B\#4 \cdot d_b \cdot t_p \cdot F_u \cdot N_{b\#4} = 20.096\ kip$

$F_5 := B\#5 \cdot d_b \cdot t_p \cdot F_u \cdot N_{b\#5} = 8.026\ kip$

$F_6 := B\#6 \cdot d_b \cdot t_p \cdot F_u \cdot N_{b\#6} = -4.295\ kip$

$F_7 := B\#7 \cdot d_b \cdot t_p \cdot F_u \cdot N_{b\#7} = -20.388\ kip$

$F_8 := B\#8 \cdot d_b \cdot t_p \cdot F_u \cdot N_{b\#8} = -36.481\ kip$

$F_9 := B\#9 \cdot d_b \cdot t_p \cdot F_u \cdot N_{b\#9} = -52.573\ kip$

$F_{10} := B\#10 \cdot d_b \cdot t_p \cdot F_u \cdot N_{b\#10} = -60.328\ kip$

$C_c := -c \cdot f_c \cdot (t_w - 2\ t_p) = -720.24\ kip$

Check $\Sigma F_i := F_1 + F_2 + F_3 + F_4 + F_5 + F_6 + F_7 + F_8 + F_9 + F_{10} + C_c - P = 0.024\ kip$ **~=0, OK!**

4.5 Lever Arms

$D_1 := L\#1 - c = 14.995\ in$

$D_2 := L\#2 - c = 11.995\ in$

$D_3 := L\#3 - c = 8.995\ in$

$D_4 := L\#4 - c = 4.995\ in$

$D_5 := L\#5 - c = 1.995\ in$

$D_6 := L\#6 - c = -1.068\ in$

$D_7 := L\#7 - c = -5.068\ in$

$D_8 := L\#8 - c = -9.068\ in$

$D_9 := L\#9 - c = -13.068\ in$

$D_{10} := L\#10 - c = -15.005\ in$

$D_c := \frac{-c}{2} = -7.503\ in$

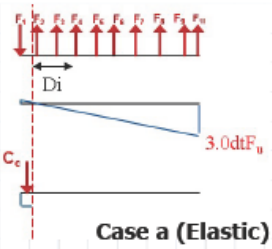
4.6 Bearing Moment Capacity (Positive Dir./Web in Compression)

$\Sigma F_i D_i := F_1 \cdot D_1 + F_2 \cdot D_2 + F_3 \cdot D_3 + F_4 \cdot D_4 + F_5 \cdot D_5 + F_6 \cdot D_6 + F_7 \cdot D_7 + F_8 \cdot D_8 + F_9 \cdot D_9 + F_{10} \cdot D_{10} = 815.123\ kip \cdot ft$

$pos.M_{bearing} := \Sigma F_i D_i + C_c \cdot D_c - P \cdot e = (1.404 \cdot 10^3)\ kip \cdot ft$

5. Calculate $-M_{Bearing}$ of Horizontal Splices (Flange in Compression)

5.1 NA, Eccentricity



Try $c := 1.9908\ in$ $\quad e := c - y_c = -6.946\ in$

5.2 Bolt Stress Profile (NA in Flange, Case a)

$TLim := 3.0$ dtFu (Tension Limit) Case a (Elastic)

$B\#1 := \frac{(d-c-L\#1)}{d-c} \cdot TLim = -0.213$ dtFu $\quad B\#6 := \frac{(d-c-L\#6)}{d-c} \cdot TLim = 1.507$ dtFu

$B\#2 := \frac{(d-c-L\#2)}{d-c} \cdot TLim = 0.108$ dtFu $\quad B\#7 := \frac{(d-c-L\#7)}{d-c} \cdot TLim = 1.936$ dtFu

$B\#3 := \frac{(d-c-L\#3)}{d-c} \cdot TLim = 0.429$ dtFu $\quad B\#8 := \frac{(d-c-L\#8)}{d-c} \cdot TLim = 2.364$ dtFu

$B\#4 := \frac{(d-c-L\#4)}{d-c} \cdot TLim = 0.858$ dtFu $\quad B\#9 := \frac{(d-c-L\#9)}{d-c} \cdot TLim = 2.792$ dtFu

$B\#5 := \frac{(d-c-L\#5)}{d-c} \cdot TLim = 1.179$ dtFu $\quad B\#10 := TLim = 3$ dtFu

5.3 Bolt Forces

$F_1 := B\#1 \cdot d_b \cdot t_p \cdot F_u \cdot N_{b\#1} = -25.728\ kip$ $\quad F_6 := B\#6 \cdot d_b \cdot t_p \cdot F_u \cdot N_{b\#6} = 30.309\ kip$

$F_2 := B\#2 \cdot d_b \cdot t_p \cdot F_u \cdot N_{b\#2} = 2.174\ kip$ $\quad F_7 := B\#7 \cdot d_b \cdot t_p \cdot F_u \cdot N_{b\#7} = 38.924\ kip$

$F_3 := B\#3 \cdot d_b \cdot t_p \cdot F_u \cdot N_{b\#3} = 43.176\ kip$ $\quad F_8 := B\#8 \cdot d_b \cdot t_p \cdot F_u \cdot N_{b\#8} = 47.54\ kip$

$F_4 := B\#4 \cdot d_b \cdot t_p \cdot F_u \cdot N_{b\#4} = 17.251\ kip$ $\quad F_9 := B\#9 \cdot d_b \cdot t_p \cdot F_u \cdot N_{b\#9} = 56.155\ kip$

$F_5 := B\#5 \cdot d_b \cdot t_p \cdot F_u \cdot N_{b\#5} = 23.712\ kip$ $\quad F_{10} := B\#10 \cdot d_b \cdot t_p \cdot F_u \cdot N_{b\#10} = 60.328\ kip$

$C_c := -c \cdot f_c \cdot (W - 4\ t_p) = -568.871\ kip$

Check $\Sigma F_i := F_1 + F_2 + F_3 + F_4 + F_5 + F_6 + F_7 + F_8 + F_9 + F_{10} + C_c - P = 0.004\ kip$ ~=0, OK!

5.4 Lever Arms

$D_1 := d - c - L\#1 = -1.991\ in$ $\quad D_6 := d - c - L\#6 = 14.072\ in$

$D_2 := d - c - L\#2 = 1.009\ in$ $\quad D_7 := d - c - L\#7 = 18.072\ in$

$D_3 := d - c - L\#3 = 4.009\ in$ $\quad D_8 := d - c - L\#8 = 22.072\ in$

$D_4 := d - c - L\#4 = 8.009\ in$ $\quad D_9 := d - c - L\#9 = 26.072\ in$

$D_5 := d - c - L\#5 = 11.009\ in$ $\quad D_{10} := d - c - L\#10 = 28.009\ in$

$D_c := \frac{c}{2} = 0.995\ in$

5.5 Bearing Moment Capacity (Positive Dir./Web in Compression)

$\Sigma F_i D_i := F_1 \cdot D_1 + F_2 \cdot D_2 + F_3 \cdot D_3 + F_4 \cdot D_4 + F_5 \cdot D_5 + F_6 \cdot D_6 + F_7 \cdot D_7 + F_8 \cdot D_8 + F_9 \cdot D_9 + F_{10} \cdot D_{10} = 496.561\ kip \cdot ft$

$neg.M_{bearing} := \Sigma F_i D_i - C_c \cdot D_c + P \cdot e = 702.945\ kip \cdot ft$

6. Check Shear Flow of Vertical Splices (Steel Section)

6.1 Calculate ȳ, yc

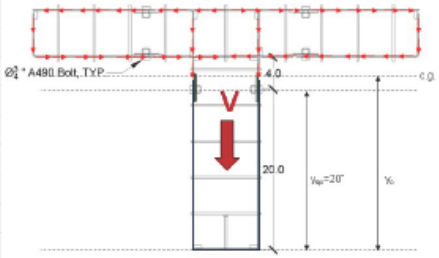
$A_{s1} := W \cdot t_p = 9.07\ in^2$ $\quad y_1 := d - \frac{t_p}{2} = 29.906\ in$ $\quad y_{sp} := 20\ in$

$A_{s2} := 4 \cdot (t_f - 2 \cdot t_p) \cdot t_p = 4.219\ in^2$ $\quad y_2 := d - \frac{t_f}{2} = 27\ in$

$A_{s3} := W \cdot t_p = 9.07\ in^2$ $\quad y_3 := (d - t_f) + \frac{t_p}{2} = 24.094\ in$

$A_{s4} := 2 \cdot (d - t_f) \cdot t_p = 9\ in^2$ $\quad y_4 := \frac{(d - t_f)}{2} = 12\ in$

$A_{s5} := (t_w - 2\ t_p) \cdot t_p = 1.5\ in^2$ $\quad y_5 := \frac{t_p}{2} = 0.094\ in$



$\Sigma A_{si} := A_{s1} + A_{s2} + A_{s3} + A_{s4} + A_{s5} = 32.859\ in^2$

$\Sigma A_{si} y_i := A_{s1} \cdot y_1 + A_{s2} \cdot y_2 + A_{s3} \cdot y_3 + A_{s4} \cdot y_4 + A_{s5} \cdot y_5 = 711.844\ in^3$

$y_c := \frac{\Sigma A_{si} y_i}{\Sigma A_{si}} = 21.663\ in$

6.2 Calculate Moment of Inertia, Ix

$I_{x1} := W \cdot \frac{t_p^3}{12} = 0.027\ in^4$ $\quad d_1 := \mathrm{abs}(y_1 - y_c) = 8.243\ in$ $\quad A_{s1} \cdot d_1^2 = 616.288\ in^4$

$I_{x2} := 4 \cdot t_p \cdot \frac{(t_f - 2 \cdot t_p)^3}{12} = 11.124\ in^4$ $\quad d_2 := \mathrm{abs}(y_2 - y_c) = 5.337\ in$ $\quad A_{s2} \cdot d_2^2 = 120.15\ in^4$

$I_{x3} := W \cdot \frac{t_p^3}{12} = 0.027\ in^4$ $\quad d_3 := \mathrm{abs}(y_3 - y_c) = 2.43\ in$ $\quad A_{s3} \cdot d_3^2 = 53.577\ in^4$

$I_{x4} := 2 \cdot t_p \cdot \frac{(d - t_f)^3}{12} = 432\ in^4$ $\quad d_4 := \mathrm{abs}(y_4 - y_c) = 9.663\ in$ $\quad A_{s4} \cdot d_4^2 = 840.421\ in^4$

$I_{x5} := (t_w - 2 \cdot t_p) \cdot \frac{t_p^3}{12} = 0.004\ in^4$ $\quad d_5 := \mathrm{abs}(y_5 - y_c) = 21.57\ in$ $\quad A_{s5} \cdot d_5^2 = 697.871\ in^4$

$\Sigma I_{xi} := I_{x1} + I_{x2} + I_{x3} + I_{x4} + I_{x5} = 443.181\ in^4$

$\Sigma A_i d_i d_i := A_1 \cdot d_1^2 + A_2 \cdot d_2^2 + A_3 \cdot d_3^2 + A_4 \cdot d_4^2 + A_5 \cdot d_5^2 = (2.354 \cdot 10^3)\ in^4$

$I_{total} := \Sigma I_{xi} + \Sigma A_i d_i d_i = (2.798 \cdot 10^3)\ in^4$

6.3 1st Moment of Area, Q

$Q_1 := A_1 \cdot d_1 = 74.766\ in^3$ $\quad Q_3 := A_3 \cdot d_3 = 22.045\ in^3$

$Q_2 := A_2 \cdot d_2 = 22.514\ in^3$ $\quad Q_4 := 2 \cdot (d - t_f - y_c) \cdot t_p \cdot \frac{(d - t_f - y_c)}{2} = 1.024\ in^3$

$Q_5 := -2 \cdot (y_c - y_{sp}) \cdot t_p \cdot \frac{(y_c - y_{sp})}{2} = -0.519\ in^3$

$Q_{total} := Q_1 + Q_2 + Q_3 + Q_4 + Q_5 = 119.829\ in^3$

6.4 Check Shear Flow for One Bolt and Determine Bolt Spacing

$$V := \frac{\max\left(pos.M_{0.6Fy}, pos.M_{bearing}\right)}{153.5\ in} = 111.212\ kip$$

$$f := \frac{V \cdot Q_{total}}{2 \cdot I_{total}} = 2.382\ \frac{kip}{in}$$

Slip-Critical Resistance of a 3/4-in. diameter A490 Bolt -> $R_{slip} := 11.9\ kip$

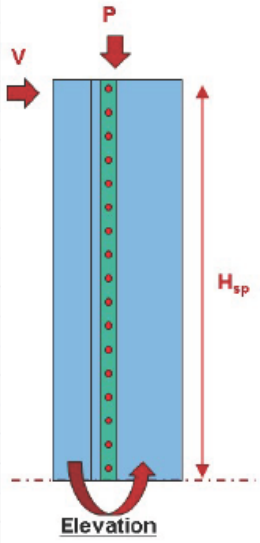
Use $S_v := 4.5\ in$

Check

if $f \cdot S_v \le R_{slip}$ = "OK"
    "OK"
else
    "NG"

7. Check Shear Flow of Vertical Splices (Composite Section)

7.1 Calculate Axial Load Distribution



$A_c = 458.391\ in^2$

$P = -275.034\ kip$

$c := 15.05\ in$ **(From Section 2.1)**

$A_{s4'} := 2 \cdot \left(d - t_f - c - 4\ in\right) \cdot t_p = 1.856\ in^2$

$A_{s4''} := 2 \cdot \left(y_{sp} - c\right) \cdot t_p = 1.856\ in^2$

$A_{sL} := A_{s1} + A_{s2} + A_{s3} + A_{s4'} = 24.216\ in^2$

$A_{sR} := \Sigma A_{si} - A_{sL} = 8.644\ in^2$

$EA_L := E_s \cdot A_{sL} = \left(7.023 \cdot 10^5\right)\ kip$

$EA_R := E_s \cdot A_{sR} + E_c \cdot A_c = \left(2.275 \cdot 10^6\right)\ kip$

$\alpha_p := \frac{EA_L}{EA_L + EA_R} = 0.236$ --> $\alpha P := \text{abs}\left(\alpha_p \cdot P\right) = 64.883\ kip$ **(Axial Load on the Left)**

$\beta_p := \frac{EA_R}{EA_L + EA_R} = 0.764$ --> $\beta P := \text{abs}\left(\beta_p \cdot P\right) = 210.152\ kip$ **(Axial Load on the Right)**

7.2 Check Shear Flow

Recall Section 2.3

$T_1 := 299.32\ kip$ $C_1 := 123.43\ kip$

$T_2 := 111.28\ kip$ $C_2 := 52.17\ kip$

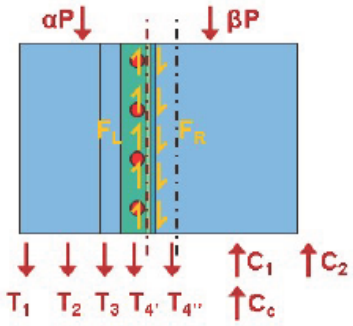
$T_3 := 179.19\ kip$ $C_c := 722.39\ kip$

$T_4 := 33.15\ kip$

$F_{s4'} := \frac{(d - t_f - c - 2\ in)}{(d - c)} \cdot 0.6 \cdot F_y = 15.341\ ksi$

$T_{4'} := A_{s4'} \cdot F_{s4'} = 28.477\ kip$

$T_{4''} := T_4 - T_{4'} = 4.673\ kip$



Total Shear Force at Vertical Splices

$F_L := T_1 + T_2 + T_3 + T_{4'} + \alpha P = 683.15\ kip$

$F_R := C_1 + C_2 + C_c - T_{4''} - \beta P = 683.165\ kip$

Shear Flow

$H_{sp} := 153.5\ in$

$f := \frac{F_L}{2\ H_{sp}} = 2.225\ \frac{kip}{in}$

Slip-Critical Resistance of a 3/4-in. diameter A490 Bolt -> $R_{slip} := 11.9\ kip$

Use $S_v := 4.5\ in$

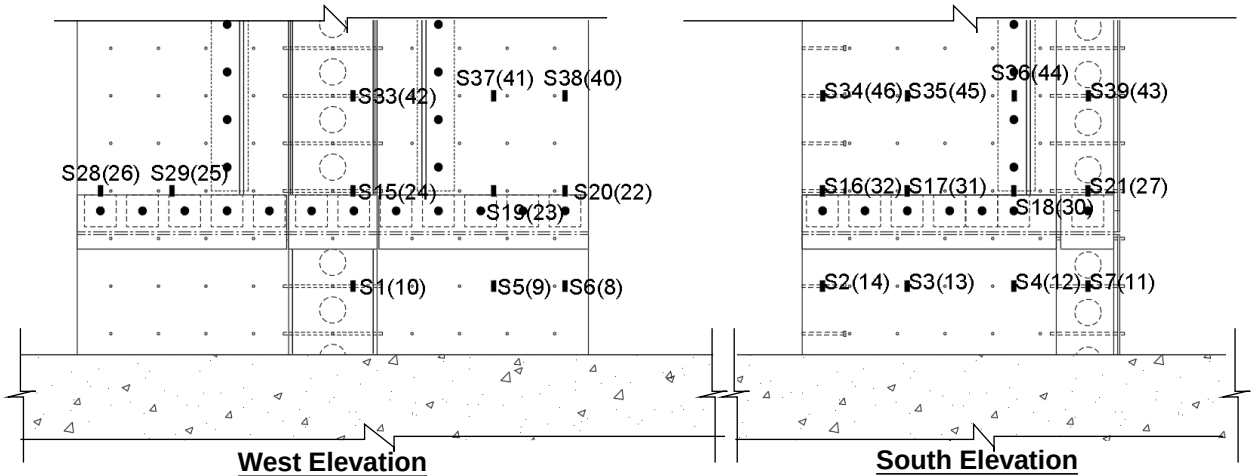
Check

```
if f · S_v ≤ R_slip
    "OK"
else
    "NG"
= "OK"
```

Appendix K.

Instrumentation (Wall Specimen Test)

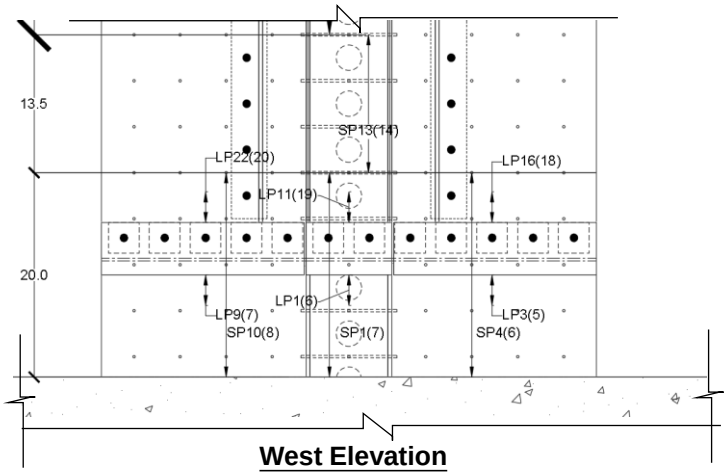
K1. Strain Gauges



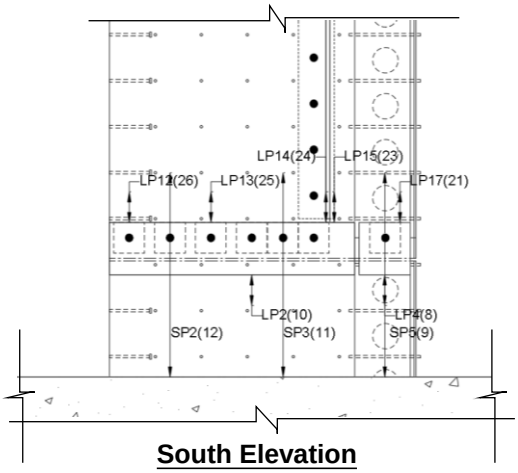
West Elevation
(East Elevation)

South Elevation
(North Elevation)

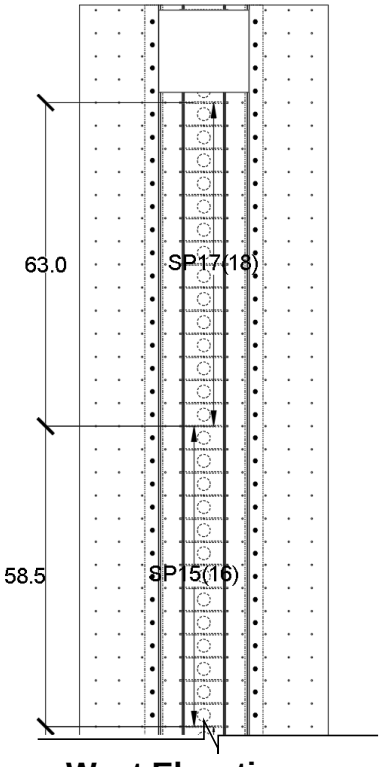
K2. Vertical String Potentiometers and Linear Potentiometers



West Elevation
(East Elevation)

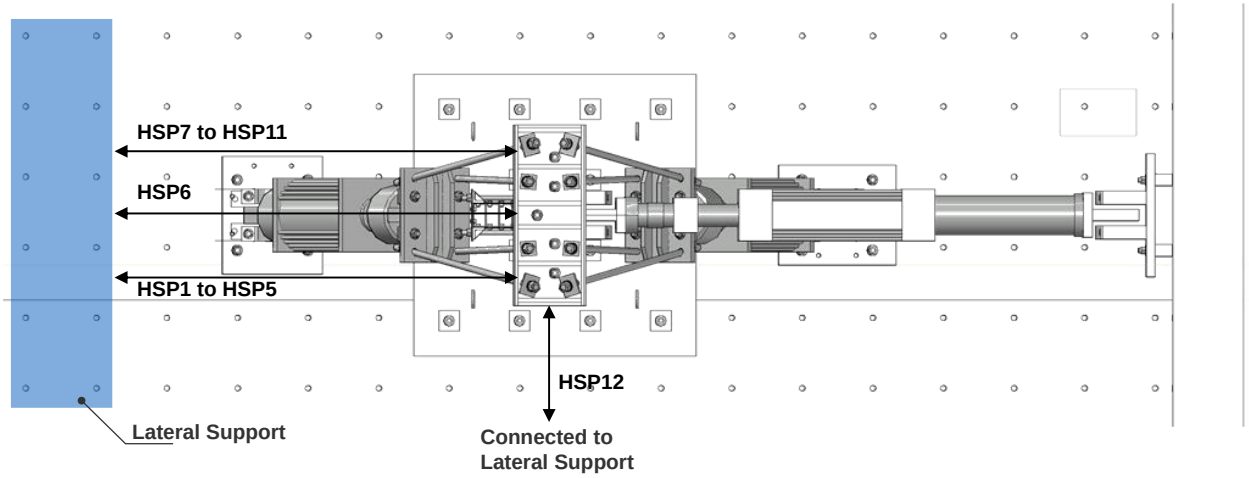


South Elevation
(North Elevation)

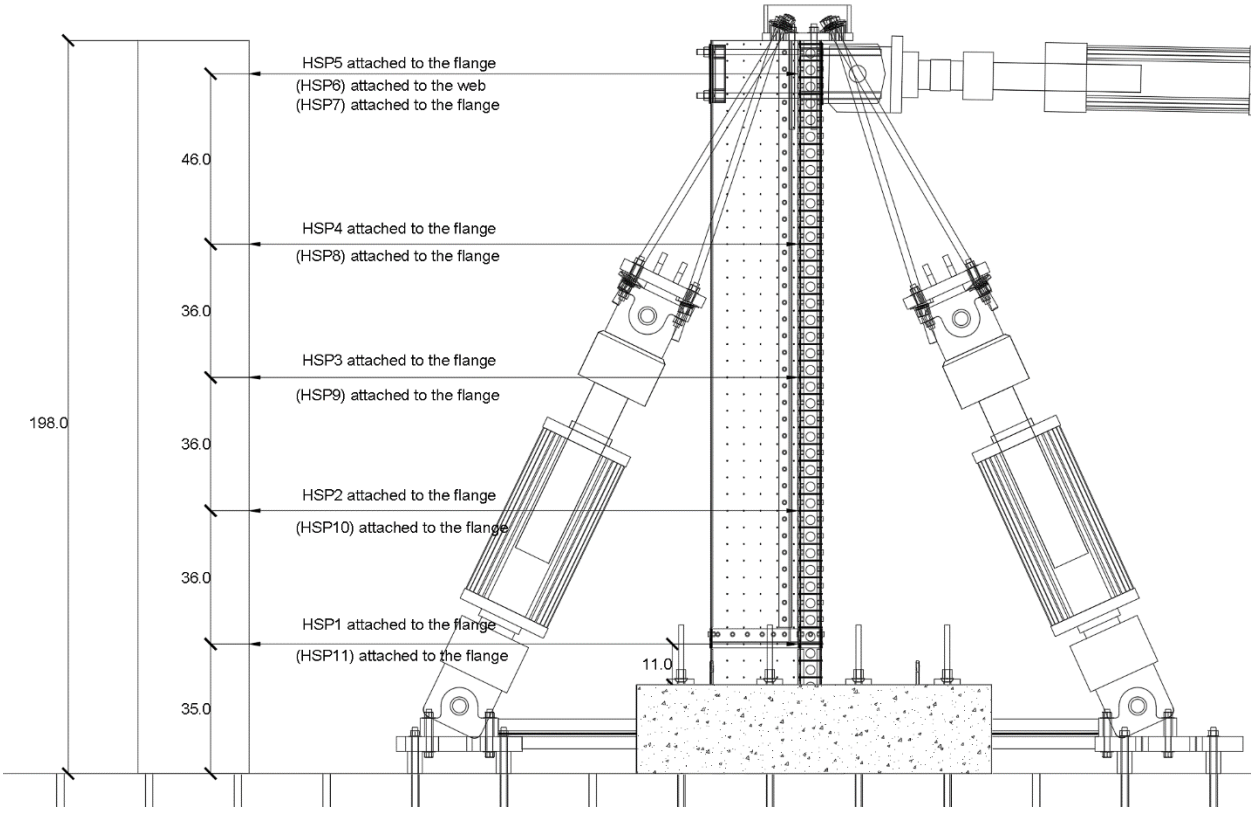


West Elevation
(East Elevation)

K3. Horizontal String Potentiometers



Plan View



Elevation View

Appendix L.

Bill of Material (Component Level Test)

F1. Specimens

Table F-1 and Table F-2 provide a detailed bill of material for all the tension and shear test specimens. This bill of material is provided to help suppliers willing to provide material and fabrication of the specimen assess the scope of work and extent of material needed.

Table F-1. Material List of Tension Test Specimens

ITEM	QTY	PART NAME	MATERIAL	DESCRIPTION
1	2	PL 3/8x14x76	A572 Gr. 50	Faceplates-L
2	2	PL 3/8x14x48	A572 Gr. 50	Faceplates-R
3	4	PL 3/8x14x13	A572 Gr. 50	Splice Plate
4	8	Φ1" Bolt, L=3-1/8"	Grade A490	For Splice
5	10	Φ1" Tie Rod, L=14"	A572 Gr. 55	-
6	2	PL 1-1/2x24x24	A572 Gr. 50	D2 End Plate
7	4	PL 3/8x5x11.25	A572 Gr. 50	D2 Side Plate
8	4	PL 3/8x10x6	A572 Gr. 50	D2 Stiffener
9	32	Φ1" Bolt, L=4.5"	Grade A490	For D2 End Plate
10	2	PL 3/23x14x10	Teflon	In D3 region

(a) Case 1A

ITEM	QTY	PART NAME	MATERIAL	DESCRIPTION
1	4	PL 3/8x14x76	A572 Gr. 50	Faceplates-L
2	4	PL 3/8x14x48	A572 Gr. 50	Faceplates-R
3	8	PL 3/8x14x17	A572 Gr. 50	Splice Plate
4	4	Φ1" Through Rod, L=14.75"	A354 Gr. BD	For Splice
5	6	Φ1-1/2" Through Rod, L=14.75"	A354 Gr. BD	For Splice
6	10	Φ2" STD Pipe, L=10.5"	A53 Gr. B	Rod Sleeve
7	20	Φ1" Tie Rod, L=14"	A572 Gr. 55	-
8	4	PL 1-1/2x24x24	A572 Gr. 50	D2 End Plate
9	8	PL 3/8x5x11.25	A572 Gr. 50	D2 Side Plate
10	8	PL 3/8x10x6	A572 Gr. 50	D2 Stiffener
11	64	Φ1" Bolt, L=4.5"	Grade A490	For D2 End Plate
12	4	PL 3/23x14x10	Teflon	In D3 region

(b) Case 2A/2B

ITEM	QTY	PART NAME	MATERIAL	DESCRIPTION
1	2	PL 3/8x14x76	A572 Gr. 50	Faceplates-L
2	2	PL 3/8x14x48	A572 Gr. 50	Faceplates-R
3	4	PL 3/8x14x25	A572 Gr. 50	Splice Plate
4	24	Φ3/4" Shuriken, L=3-1/8"	Grade A490	For Splice
5	14	Φ1" Tie Rod, L=14"	A572 Gr. 55	-
6	2	PL 1-1/2x24x24	A572 Gr. 50	D2 End Plate
7	4	PL 3/8x5x11.25	A572 Gr. 50	D2 Side Plate
8	4	PL 3/8x10x6	A572 Gr. 50	D2 Stiffener
9	32	Φ1" Bolt, L=4.5"	Grade A490	For D2 End Plate
10	2	PL 3/23x14x10	Teflon	In D3 region

(c) Case 1C

ITEM	QTY	PART NAME	MATERIAL	DESCRIPTION
1	2	PL 3/8x14x76	A572 Gr. 50	Faceplates-L
2	2	PL 3/8x14x48	A572 Gr. 50	Faceplates-R
3	4	PL 3/8x14x25	A572 Gr. 50	Splice Plate
4	12	Φ3/4" Through Rod, L=14.75"	A354 Gr. BD	For Splice
5	12	Φ2" STD Pipe, L=10.5"	A53 Gr. B	Rod Sleeve
6	12	Φ1" Tie Rod, L=14"	A572 Gr. 55	-
7	2	PL 1-1/2x24x24	A572 Gr. 50	D2 End Plate
8	4	PL 3/8x5x11.25	A572 Gr. 50	D2 Side Plate
9	4	PL 3/8x10x6	A572 Gr. 50	D2 Stiffener
10	32	Φ1" Bolt, L=4.5"	Grade A490	For D2 End Plate
11	2	PL 3/23x14x10	Teflon	In D3 region

(d) Case 2C

ITEM	QTY	PART NAME	MATERIAL	DESCRIPTION
1	2	PL 3/8x14x76.5	A572 Gr. 50	Faceplates-L
2	2	PL 3/8x14x48.5	A572 Gr. 50	Faceplates-R
3	4	PL 3/8x14x8	A572 Gr. 50	Splice Plate
4	6	Φ1" Through Rod, L=14.75"	A354 Gr. BD	For Splice
5	3	Φ2" STD Pipe, L=10.5"	A53 Gr. B	Rod Sleeve
6	10	Φ1" Tie Rod, L=14"	A572 Gr. 55	-
7	2	PL 1-1/2x24x24	A572 Gr. 50	D2 End Plate
8	4	PL 3/8x5x11.25	A572 Gr. 50	D2 Side Plate
9	4	PL 3/8x10x6	A572 Gr. 50	D2 Stiffener
10	32	Φ1" Bolt, L=4.5"	Grade A490	For D2 End Plate
11	2	PL 3/23x14x10	Teflon	In D3 region
12	8	PL 3/4x2x14	A572 Gr. 50	Anchor PL_Key
13	1	PL3/8x12x14	A572 Gr. 50	Anchor PL_Web

(e) Case 4A

Table F-2. Material List of Shear Test Specimens

ITEM	QTY	PART NAME	MATERIAL	DESCRIPTION
1	4	BOX 14x12x1/4, L=24.25"	A572 Gr. 50	Faceplates
2	8	PL 1/4x14x9	A572 Gr. 50	Splice Plate
3	8	Φ1" Through Rod, L=14.75"	A354 Gr. BD	For Splice
4	8	Φ2" STD Pipe, L=10.5"	A53 Gr. B	Rod Sleeve
5	8	Φ1" Tie Rod, L=14"	Grade A490	-
6	4	PL 1x30.75x28	A572 Gr. 50	Conn. PL
7	64	Φ7/8" Bolt, L=4.25"	Grade A490	Conn. Bolt
8	48	Φ7/8" Bolt, L=4.25"	Grade A490	Conn. Bolt

(a) Case 6A/6Ac

ITEM	QTY	PART NAME	MATERIAL	DESCRIPTION
1	4	BOX 14x12x1/4, L=24.25"	A572 Gr. 50	Faceplates
2	8	PL 1/4x14x9	A572 Gr. 50	Splice Plate
3	24	Φ3/4" Shuriken, L=3.125"	Grade A490	For Splice
4	8	Φ1" Tie Rod, L=14"	A572 Gr. 55	-
5	4	PL 1x30.75x28	A572 Gr. 50	Conn. PL
6	64	Φ7/8" Bolt, L=4.25"	Grade A490	Conn. Bolt
7	48	Φ7/8" Bolt, L=4.25"	Grade A490	Conn. Bolt

(b) Case 5B/5Bc

ITEM	QTY	PART NAME	MATERIAL	DESCRIPTION
1	4	BOX 14x12x1/4, L=24.25"	A572 Gr. 50	Faceplates
2	8	PL 1/4x14x9	A572 Gr. 50	Splice Plate
3	16	Φ3/4" Through Rod, L=12.75"	A354 Gr. BD	For Splice
4	16	Φ2" STD Pipe, L=10.5"	A53 Gr. B	Rod Sleeve
5	8	Φ1" Tie Rod, L=14"	A572 Gr. 55	-
6	4	PL 1x30.75x28	A572 Gr. 50	Conn. PL
7	64	Φ7/8" Bolt, L=4.25"	Grade A490	Conn. Bolt
8	48	Φ7/8" Bolt, L=4.25"	Grade A490	Conn. Bolt

(c) Case 6C/6Cc

F2. Test Set-up

Table F-3 and Table F-4 provide a detailed bill of material for the tension and shear test setups.

Table F-3 Material List of Tension Test Setup

ITEM	QTY	PART NAME	MATERIAL	DESCRIPTION
1	1	WF24x24x1x1 ($d*b_f*t_w*t_f$)	A572 Gr. 50	D1 Spreader Beam (Built-up Section)
2	18	PL 1/2x11.5x22	A572 Gr. 50	D1 Stiffener
3	1	H24xWx1x1 (W varies from 24" to 30")	A572 Gr. 50	D1a Spreader Beam (Built-up Section)
4	18	PL 1/2xWx22 (W varies from 11.5" to 14.5")	A572 Gr. 50	D1a Stiffener
5	2	W8x28, L=39"	A572 Gr. 50	D3 Column
6	2	W8x28, L=14.5"	A572 Gr. 50	D3 Beam
7	20	PL 1/4x3x7.5	A572 Gr. 50	D3 Stiffener
8	2	PL 1x10x17	A572 Gr. 50	D3 Base Plate
9	4	PL 1x4x4	A572 Gr. 50	D3 Base Stiffener
10	2	PL 3/23x14x6.54	Teflon	In D3 region
11	8	Φ1" Bolt, L=2.5"	Grade A490	For D3 Column Conn.
12	8	Φ1" Bolt, L=7"	Grade A490	For D3 Base Conn.

Table F-4. Material List of Shear Test Setup

ITEM	QTY	PART NAME	MATERIAL	DESCRIPTION
1	2	PL 1x30.75x28	A572 Gr. 50	Top Plate
2	2	PL 1.5x47.25x28	A572 Gr. 50	Bot. Plate
3	2	PL 1x16.62x14.25	A572 Gr. 50	Stiffener
4	8	PL 1/2x2.25x14.25	A572 Gr. 50	Stiffener
5	4	PL 1-1/4x3x14.25	A572 Gr. 50	Stiffener
6	56	Φ7/8" Bolt, L=6.10"	Grade A490	Base Bolt